

9th Annual Review of Progress in

APPLIED
COMPUTATIONAL
ELECTROMAGNETICS

at

Naval Postgraduate School
Monterey, CA

March 22-26, 1993

CONFERENCE PROCEEDINGS

DISTRIBUTION STATEMENT A

Approved for public release;
Distribution Unlimited

CONFERENCE PROCEEDINGS

9th Annual Review of Progress in

APPLIED

COMPUTATIONAL

ELECTROMAGNETICS

at the

Naval Postgraduate School

Monterey, CA

March 22-26, 1993

SYMPOSIUM PROGRAM COMMITTEE CHAIRMAN

Perry Wheless

Sponsored by

The Applied Computational Electromagnetics Society

and CEFC, DOD/USA CECOM, USAIESA, NCCOSC NRaD, NPS, AND DOE/LLNL

THE NAVAL POSTGRADUATE SCHOOL

19970910 154

FORM 10-1-81 (REV. 1-81) 4/

Contents

Table of Contents	i
1994 Call for Papers	x
1993 Symposium Program Committee	xii
Conference Chairman's Summary	xiii
ACES President's Statement	xiv
ACES93 Short Courses	xv

Session 1: Canonical Problems for Software Validation Chair: Dr. Andrew Peterson, Co-Chair: Capt. Dennis Andersh

RCS of High Permittivity Cubes by FDTD and by Measurement <i>C.W. Trueman, S.J. Kubina, R.J. Luebbers, S.R. Mishra, and C. Larose</i>	2
Asymptotic Prediction Validation Using Measured Data <i>B.B. Halama, D.J. Andersh, and A.J. Terzouli, Jr.</i>	11
TLM Computation of an Iris-Coupled Waveguide Cavity — A Canonical Problem <i>Qi Zhang and W.J.R. Hoefer</i>	19
A Technique for Determining Non-Integer Eigenvalues for Canonical Analysis of Boundary Value Problems <i>D. Reuster and M. Kaye</i>	27
Evaluation of Method of Moments Codes: University of Houston JUNCTION and Numerical Electromagnetic Code, Version 4 <i>C.A. Deneris, J.C. Logan, and J.W. Rockway</i>	37
NEC2, NEC3, and NEC4 on a Convex Mini-Supercomputer <i>Lance Koyama</i>	45

Session 2: Canonical Problems Workshop (no published papers) Moderators: Dr. Andrew Peterson and Capt. Dennis Andersh

Session 3: Moment Method Theory and Applications Chair: Dr. Paul M. Goggans

Development of a Bandlimited Basis Set for Thin Wire Method of Moments Scattering Problems <i>G.E. Mortensen and C.C. Cha</i>	56
A Moment Method Formulation for Electromagnetic Radiation and Scattering from Composite Bodies of Revolution <i>Pierre Steyn and David B. Davidson</i>	64
Scattering and Radiation from Partially Coated 3-D Triangular Patched Bodies <i>J.M. Putnam</i>	Presentation Only

Session 3, continued

Calculation of Transient Scattering from Two-Dimensional Objects using a Frequency Domain Method of Moments Approach <i>Paul M. Goggans</i>	72
RCS of Structures with Apertures and Slots <i>S. Kashyap, A. Louie, S. Mishra, and C. Larose</i>	81

Session 4: GTD/UTD/PO Analysis

Chair: Dr. A.K. (Tony) Brown, Co-Chair: Dr. Shian U. Hwu

Overview of Analytic Techniques used in OSU Reflector Antenna Code <i>Teh-Hong Lee and Roger C. Rudduck</i>	90
Space Station Freedom (SSF) Antenna Pattern Predictions Using Geometrical Theory of Diffraction <i>Shian U. Hwu, Jon S. Fournet, Robert J. Panneton, and G. Dickey Arndt</i>	97
An 'Object-Oriented' Approach to GTD/UTD Modeling <i>Edgar L. Coffey</i> (Late Submission)	901
The Multi-Point GTD and Extended Aperture Integration Techniques for Analysis of Reflector Antenna <i>Roger C. Rudduck, Yueh-Chi Chang, and Teh-Hong Lee</i>	105

Session 5: Computational Electromagnetics — The Next Generation

Chair: Kenneth R. Siarkiewicz

The Electromagnetic Modeling and Simulation Environment for Systems (EMSES) <i>Kenneth R. Siarkiewicz</i>	114
A Proposed Approach for Developing Next-Generation Computational Electromagnetics Software <i>E.K. Miller, R.P. Kruger, and Steve Moraites</i>	122
Hybrid Approach for Large 3-D Platforms <i>L.N. Medgyesi-Mitschang, J.M. Putnam, and Dau-Sing Wang</i>	Presentation Only

Session 6: Transients

Chair: Dr. Paul M. Goggans

Transient Internal and Scattered Fields of a Sphere Illuminated with a Pulsed Gaussian Beam <i>Elsayed Esam M. Khaled, Dipakbin Q. Chowdhury, Steven C. Hill, and Peter W. Barber</i>	140
---	-----

Session 7: High-Frequency Techniques and Asymptotic Solutions

Chair: Dr. A.K. (Tony) Brown, Co-Chair: Dr. Shian U. Hwu

ISAR Image Formation Using Bistatic Data from 'XPATCH'	
<i>Rajan Bhalla and Hao Ling</i>	150
Time Domain Smyth-Kirchhoff Approximation to Aperture Coupling	
<i>K.S. Kunz and S.A. Blocher</i>	158
A Hybrid Approach to Trailing Edges and Trailing Ends	
<i>David Ingham</i>	166
High Frequency Approximations to the Physical Optics Scattering Integral for Curved Edged Surfaces	
<i>William B. Gordon</i>	173

Session 8: Visualization and I/O Issues

Chair: Dr. Ed Miller Co-Chair: Dr. Stan Kubina

Numerical Imaging of Finite Element Frequency Domain Solutions	
<i>R. Craig Baucke and John D'Angelo</i>	182
Visualization of Electromagnetic Fields Using the Finite Difference Time Domain Method	
<i>John H. Beggs, Deirdre A. Ryan, and Raymond J. Luebbers</i>	189
Creation, Visualization and Analysis -- The Dynamics of Complex Models	
<i>S.J. Kubina, C.W. Trueman, D. Gaudine and A. Ramos</i>	195
Scientific Visualization of 3D Radar Cross Section Data	
<i>Thomas G. Wojszynski, Andrew J. Terzouli, Jr., and Martin R. Stytz</i>	213
Rapid Visual Computation of Physical Optics Backscattering (Invited Paper)	
<i>R.A. Shepherd, T.D. Olson, and C.S. Liang</i>	Presentation Only
EM Visualization on a SGI 4D Workstation	
<i>L.C. Russell and J.W. Rockway</i>	221
WinGAUGE Graphical Aids for the Users of GEMACS for the Windows Environment	
<i>Jeffrey A. Evans</i>	228
NECDRAW for 3-D Images of NEC Wire Grid Models	
<i>Ron Bardarson and Robert Just</i>	235
The Electromagnetic Modeler's Workbench for GEMACS	
<i>Edgar L. Coffey and Robert Fisher</i>	(Late Submission) 888
Graphical Shell for Numerical Electromagnetics Code	
<i>M.J. Packer, R.A. Powers, and A.P. Tsitsopoulos</i>	243

Session 9: Microwave Circuits

Chair: Dr. Peter Russer Co-Chair: Professor Linda P.B. Katehi

Field Matching Analysis of Complex Waveguides with Anisotropic Materials	
<i>M. Okoniewski</i>	252
Advance in Analyzing Passive Planar Radiating Structures with Method of Moments Matrices	
<i>Sebastian Sattler and Peter Russer</i>	260
S-Parameter Modeling of Planar Transmission Line Discontinuities and MMIC Module Interconnections	
<i>Hang Jin, Rüdiger Vahldieck and Peter Russer</i>	266

Session 9, continued

Theoretical Analysis of Microshield Transmission Lines With Dual-Plane Discontinuities (Invited Paper)	
<i>T.M. Weller and P.B. Katehi</i>	273
Symmetry Analysis of Large Two-Dimensional Clusters of Coupled Cavity Resonators	
<i>Ross A. Speciale</i>	281
Analysis of a Millimeter-wave Filter using Transmission Line Matrix and Mode Matching Methods and Comparison with the Measurements (Invited Paper)	
<i>W. Menzel, F. Alessandri, M. Mongiardo, R. Sorrentino, C. Eswarappa, P.P.M. So, and W.J.R. Hoefer</i>	289
Coupling-of-Modes Analysis of SAW-Multistrip Coupler	
<i>R. Weigel, G. Scholl, and P. Russer</i>	297
Description of Conductor-Loss Effects in Planar Transmission Lines	
<i>Wolfgang Heinrich</i>	305
Dynamic Electrical Modeling of Gap Discontinuities on Lossy Monolithic Microstrip Line	
<i>Anne Vilcot and Smaïl Tedjini</i>	313

Session 10: Time-Domain Techniques I (featuring FDTD)

Chair: Dr. Ray Luebbers, Co-Chair: Dr. Jiayuan Fang

Absorbing Boundary Treatments in the Simulation of Wave Propagation in Microwave Integrated-Circuits	
<i>Jiayuan Fang</i>	322
A Hybrid Ray/FDTD Method for Computing Electromagnetic Scattering from an Engine Cavity with a Complex Termination	
<i>R. Lee and T.T. Chia</i>	330
FDTD Modeling of the Resonance Characteristics of Realistic Enclosures	
<i>Kent Chamberlin, Lauchlan Gordon, and Bruce Archambeault</i>	338
A Method for Reducing Run-Times of Out-of-Core FDTD Problems	
<i>J. Raley Marek and Jeff MacGillivray</i>	344
Investigation of the Use of Chimera for Solving Maxwell's Equations for Electromagnetic Propagation in the Time Domain	
<i>M.D. White and J.J. Chattot</i>	352
Radar-Cross-Section and Aerodynamic-Force Calculations using Finite-Difference Methods	
<i>H. Vinh, C.P. van Dam, and H.A. Dwyer</i>	360

Session 11: Remote Sensing and Monte Carlo Techniques

Chair: Professor Leung Tsang, Co-Chair: Dr. Chi Chan

Monte Carlo PO Simulation of Scattering from Rough Surfaces Near Grazing Incidence	
<i>H. Bender, R. Suchar, and P. Russer</i>	370
Polarimetric Thermal Emission from Rough Ocean Surfaces: A Numerical Study (Invited Paper)	
<i>J.T. Johnson, J.A. Kong, R.T. Shin, S.H. Yueh, S.V. Nghiem, and R. Kwok</i>	376
A Banded Matrix Iterative Approach to Monte Carlo Simulations of Large-Scale Random Rough Surface Scattering: TE Case (Invited Paper)	
<i>Leung Tsang, Chi H. Chan and Haresh Sangani</i>	384

Session 11, continued

- A Banded Matrix Iterative Approach to Monte Carlo Simulations of
Large-Scale Random Rough Surface Scattering: Penetrable Case (Invited Paper)
C.H. Chan, L. Li and L. Tsang 391

Session 12: Bioelectromagnetic Computations

Chair: Dr. Imre Gyuk

- Bio-electromagnetic Computation in the Low Frequency Range:
An Introduction (Invited Paper)
Imre Gyuk 400
- Calculation of Electric and Magnetic Fields near Ground Level in 187KV
AC Substation (Invited Paper)
K. Isaka, N. Hayashi, and Y. Yokoi 403
- Numerical Methods for Dosimetric Calculations: ELF to Microwave
Frequencies (Invited Paper)
Om P. Gandhi (Abstract Only) 411
- Current Distribution Tomography for Determination of Internal Current
Density Distributions (Invited Paper)
Paul C. Gailey (Late Submission) 923
- A Matrix Formulation of Dielectric Imaging, Dosimetry and Computation
of Vector Electromagnetic Fields (Invited Paper)
Wendy W. Guo and Theodore C. Guo 413
- Explanation of Biological Effects of Low-intensity Electric, Magnetic and
Electromagnetic Fields by Nonlinear Dynamics (Invited Paper)
F. Kaiser 424
- Calculation of Absorbed Power Density in the Human Arm Due to Induced
Currents at 1-30 MHz
P.R. Wainwright 432

Session 13: Time-Domain Techniques II (featuring TLM)

Chair: Dr. Wolfgang J.R. Hoefer, Co-Chair: Dr. Fred German

- A Comparison of Currents Induced on Scattering Bodies Using the
Transmission Line Modeling (TLM) Method and the Method of Moments (MOM)
Griffin K. Gothard and Sadasiva M. Rao 442
- Transmission Line Matrix (TLM) Modeling of a Stepped-Septum Square-
Waveguide Polarizer
*Lloyd S. Riggs, G.K. Gothard, Fred J. German,
and Chuck Chandler* 450
- Discrete Time-Domain Greens Functions for Three-Dimensional TLM Modelling
of the Radiating Boundary Conditions (Invited Paper)
M. Krumpholz and P. Russer 458
- Transmission Line Matrix Method on Massively Parallel Processor Computers
*Poman P.M. So, Channabasappa Eswarappa,
and Wolfgang J.R. Hoefer* 467
- Fast Frequency-Domain TLM Analysis of 3D Circuit
Discontinuities (Invited Paper)
Jifu Huang, Ruediger Vahldieck and Hang Jin 475
- Infinitesimally Adjustable Boundaries in Symmetrical Condensed Node
TLM Simulations (Invited Paper)
Fred J. German 482

Session 14: General Purpose Code Applications

Chair: Dr. Jim Breakall, Co-Chair: George Hagn

Rhombic Illuminator Performance at High Frequency <i>J. Patrick Donohoe and Clayborne D. Taylor</i>	492
Recent Enhancements to GEMACS 5.2 <i>Edgar L. Coffey</i> (Late Submission)	894
High Resolution Spectral Analysis of HF Coupling Modes on the EC-130 Aircraft <i>Q.C. Luu, S.J. Kubina, C.W. Trueman, and D. De Carlo</i>	500
Helicopter Antenna Pattern Analysis Using NEC-BSC <i>R.M. Herkert, J.A. Woody, D.W. Acree, and D.P. Millard</i>	513
Airborne TX/RX Antenna Pair Location Investigation — Experimental and NEC-BSC Results <i>Scott Townley</i>	521
The Analysis of Asymmetric Log-Periodic Dipole Antennas Using NEC <i>Jacqueline A. Schaefer</i>	529

Session 15: CAEME

Chair: Dr. Magdy Iskander

Interactive Video Lessons for Electromagnetic Education <i>Magdy F. Iskander and Thomas Reed</i>	538
A Generic Finite Element Model for Plane Problems <i>Kyran D. Mish and LaDawn Haws</i>	549
Analysis of Electromagnetic Fields in Electrical Machines from Experimental Data for Educational Purposes <i>Osama A. Mohammed, Howard Gordon, and Abd A. Arkadan</i>	556
Learning About EM Theory and EM Modeling by Analyzing Printed Circuit Boards in an Enclosure <i>T.H. Hubing and M.W. Ali</i>	564
EMAG — Electromagnetic Software Development at Rose-Hulman Institute of Technology (Invited Paper) <i>J. Lebaric and Roger P. Manke, Jr.</i> (Late Submission)	915
Relativistic Foundation of Electric Current — A Model for Transmission Lines (Invited Paper) <i>Zvonko Fazarinc</i>	569
Making Computer Tutorials in Electrodynamics With The CAEME Software <i>Rodney Cole, Curtis Brune, and Scott Tooker</i> (Late Submission)	908
Reflector Antenna Analysis Software: An Educational Approach <i>B. Houshmand and Y. Rahmat-Samii</i>	577
Computer-Graphics-Aided Teaching and Learning Tool for Antennas <i>Hamid Moradi, Swapan Chakrabarti, and Prasad Gogineni</i>	586
Introducing Spherical Harmonics to Undergraduates <i>Glen Erickson</i>	Presentation Only
Interactive Analysis of Antenna Arrays with a Personal Computer <i>Atef Z. Elsherbeni and Patrick H. Ginn</i>	594

Session 16: RCS

Chair: Dr. Shian U. Hwu, Co-Chair: Dr. A.K. (Tony) Brown

Xpatch: a High Frequency RCS Code	
<i>S.W. Lee and Dennis J. Andersh</i>	Presentation Only
Computing the Time Domain EM Scattering from Large Open-Ended Cavities Using the SBR and GRE Ray Shooting Methods	
<i>Robert J. Burkholder and Prabhakar H. Pathak</i>	602
Target Facetization Level and the Effect on Xpatch Predictions	
<i>E.M. Miller, D.J. Andersh, and A.J. Terzouli, Jr.</i>	610

Session 17: Multipole Techniques

Chair: Dr. Richard K. Gordon

Comparison of Multipole and Multifilament Techniques	
<i>D. Reuster and M. Kaye</i>	620
New Thin Wire Expansions for Long Wires in the MMP-Code	
<i>Pascal Leuchtman and Marcel Gnos</i>	630

Session 18: Numerical Modelling in Complex Media

Chair: Dr. Weng Chew

Toward an FDTD Analysis of the Standard Approximations for Propagation in Randomly Structured Ionization	
<i>L.J. Nickisch and P.M. Franke</i>	640
A Ray-Based Approach to Scattering from Inhomogeneous Dielectric Objects	
<i>Hao Ling and Hyeongdong Kim</i>	649
Applications of Discrete Methods to Optical Pulse Propagation in Linear and Nonlinear Materials	
<i>R.W. Ziolkowski and J.B. Judkins</i>	Presentation Only
Heirarchical Basis Functions for 3D Finite Element Methods	
<i>John R. Lovell</i>	657
NEPAL - The Use of Huygens' Equivalence Principle for Solving the Volume Integral Equation of Scattering	
<i>Weng Cho Chew and Cai-Cheng Lu</i>	664
A CG-FFHT Method for the Solution of EM Field in Axisymmetric Inhomogeneous Media	
<i>Qing-Huo Liu and Weng Cho Chew</i>	672
Scattering Computations for Multi-Region Cylindrical Objects	
<i>Michael A. Morgan</i>	678

Session 19: Low-Frequency Techniques and Applicaitons

Chair: Dr. Osama Mohammed, Co-Chair: Dr. Abd A. Arkadan

Computation of Electric Machines Parameters in the ABC Frame of Reference Using Finite Element Analysis	
<i>A.A. Arkadan and R.H. VanderHeiden</i>	688
An Efficient 3-D Finite Element Mesh Generator for Electromagnetic Analysis in Complex Volumes	
<i>Fuat G. Uler and Osama A. Mohammed</i>	696

Session 19, continued

Modern Numerical Techniques for High Precision MRI Magnet Design (Invited Paper) <i>Sergio Pissanetzky</i>	704
An Artificial Neural Network Environment for the Optimal Design of Geometric Boundaries in Electromagnetic Devices <i>Osama A. Mohammed, Dong C. Park, Riaz Merchant, and Fuat Üler</i>	712
Sensitivity Analysis of the Integrodifferential Finite Element — Green's Function Method <i>Qiushi Chen, A. Konrad and P.P. Biringer</i>	720

Session 20: EMC/EMI

Chair: Dr. Todd Hubing, Co-Chair: Dr. Reinaldo Perez

EMI Analysis of Transient Events via Method of Moments on the Titan IV/Centaur Rocket Main Batteries <i>Reinaldo Perez</i>	728
Detailed Analysis of a Realistic Canonical Structure in Electromagnetic Radiation Problems <i>Shahrokh Daijavad and Barry J. Rubin</i>	738
EMI Prediction Using Wire Mesh Boxes in NEC <i>Bruce Archambeault and Rich Mellitz</i>	747
The Application of Different Meshing Techniques to EMC Problems <i>J.L. Herring and C. Christopoulos</i>	755
Optimization of FDTD for EMI Modeling Applications <i>Bruce Archambeault and Louise Lemaire</i>	763
Applications of MiniNEC to EMI Modeling <i>Colin E. Brench</i>	771
Nonlinear Effects Errors Encountered in Performing Interference Analysis Using an RF Circuit Analysis Code <i>Frank E. Walker and Sperry H. Goodman</i>	777

Session 21: Antennas

Chair: Dr. Roger Radcliff, Co-Chair: Dr. Al Christman

Computer Model for Axially Symmetric Dielectric Radomes in the Near Field of a Circular Aperture <i>D.C. Jenn, R.M. Francis, and K.A. Klopp</i>	784
An Exact Expression for the Vector Potential of a Uniform Current Cylindrical Antenna <i>D.H. Werner and P.L. Werner</i>	792
A Simplified Approach for Modeling a Log Periodic Antenna <i>Steven C. Merrill and Malcolm J. Packer</i>	800
Phased Array Radiating Element Design Software <i>H.K. Schuman</i>	813
Spectral-Domain Analysis of Patch Radiators on Lossy Ferrite Substrates <i>Zhenglian Cai and Jens Bornemann</i>	821

Session 22: Finite Element Method and Applications at High Frequencies

Chair: Dr. Richard K. Gordon, **Co-Chair:** Dr. Jin-Fa Lee

ABC Finite Elements for Open Boundary Electromagnetic Problems of Frequencies from DC to GHz <i>John R. Brauer, Brian S. Brown and Mark M. Jenich</i>	830
Application of Explicit Finite Elements to Maxwell's Equations <i>M. Hafez and P. English</i>	838
Microstrip Discontinuity Analysis by Time Domain Finite Elements <i>J.O.Y. Lo, A. Konrad, J.L. Coulomb, and J.C. Sabonnadiere</i>	846
On the Optimization of a Finite Element Code for 3D Scattering Computation <i>A. Chatterjee, J.L. Volakis, and D. Windheiser</i>	855
Performance Evaluation of MEI-Based Mesh Truncation Conditions for Finite Element Modeling of Electromagnetic Scattering by Penetrable Bodies <i>Diana B. Wright and Andreas C. Cangellaris</i>	863
Finite Element Method for Determining the Scattering from Lossy Cylinders Illuminated by Obliquely Incident Plane Waves <i>Richard K. Gordon and Ahmed A. Kishk</i>	871
Numerical Analysis of Microwave Cavities with Anisotropic Materials <i>Shirley Min, Jin-Fa Lee and Richard Gordon</i>	879
Author Index	932

THE APPLIED COMPUTATIONAL ELECTROMAGNETICS SOCIETY

1994

CALL FOR PAPERS

1994

The Tenth Annual Review of Progress in Applied Computational Electromagnetics March 21-25, 1994

at the

**Doubletree Hotel at Fisherman's Wharf and Convention Center
(Tentative)
Monterey, California**

Share your knowledge and expertise with your colleagues

The Naval Postgraduate School has hosted the conference for the last eight years. Plan on joining our 10th Anniversary Celebration tentatively scheduled for the Doubletree Hotel and Convention Center.

The 1994 Annual Review of Progress in Applied Computational Electromagnetics will be the tenth yearly Symposium to bring analysts together to share information and experience about the practical application of EM analysis using computational methods. All aspects of computational electromagnetic analysis will be represented but particular emphasis at the 1994 Symposium will be placed on general purpose code applications, code performance analysis, and validation. Attendance and professional program paper participation from non-ACES and from outside North America are encouraged and welcome. The Symposium features four areas of interest to the EM analysis enthusiast: short courses, demonstrations, vendors' booths and technical paper sessions which are solicited from all areas of electromagnetic computation. The Symposium will also include invited speakers and interactive forums.

1994 ACES

Symposium Chairman

Andy Terzuoli
Air Force Institute of Technology
2950 P Street
Wright-Patterson AFB, OH 455433
Tel (513) 255-3576
Fax (513) 476-4055

Symposium Advisor

Richard W. Adler
Naval Postgraduate School
Code EC/AB
Monterey, CA 93943
Tel (408) 656-2352
Fax (408) 649-0300
E-Mail: 5541304@mcimail.com

Symposium Facilitator

Jodi Nix
Veda Incorporated
5200 Springfield Pike
Suite 200
Dayton, OH 45431
Tel (513) 476-3550
Fax (513) 476-3577

Co-Chairmen:

Dennis Andersh & Jeff Fath
Wright Laboratories/AARA-2
Wright-Patterson AFB OH 45433
Tel (513) 255-1115
Fax (513) 476-4414
E-Mail: dandersh@mbvlab.wpafb.af.mil
E-Mail: Jeff_fath@qm.mbvlab.wpafb.af.mil

1995 ACES Symposium Chairman

Ray Luebbers
Penn State University
Dept. of Electrical Engineering
University Park, PA 16802
Tel (814) 865-2362
Fax (814) 865-7065
E-Mail: LU4@psuvm.psu.edu

Sponsored by: ACES, DOD/USA CECOM, DOE, LLNL, NCCOSC/NRAD, NPS and USAJESA
In cooperation with: The IEEE Antennas and Propagation Society, the IEEE Electromagnetic Compatibility Society, USNC/URSI and the CEFC

THE APPLIED COMPUTATIONAL ELECTROMAGNETICS SOCIETY

1994

CALL FOR PAPERS

1994

The Tenth Annual Review of Progress in Applied Computational Electromagnetics

Papers may address general issues in applied computational electromagnetics, or may focus on specific applications, techniques, codes, or computational issues of potential interest to the Applied Computational Electromagnetics Society membership. Areas and topics include:

- Code validation
- Code performance analysis
- Computational studies of basic physics
- "Tricks of the Trade" in selecting and applying codes and techniques
- New Codes, algorithms, code enhancements, and code fixes
- Code input/output issues
- Computer hardware issues
- Partial List of applications:

antennas
static fields
shielding
EMP,EMI/EMC
charge transport
microwave components
fiberoptics
communications systems
particle accelerators
wave propagation
dielectric & magnetic
materials

eddy currents
radar cross section
bioelectromagnetics
power transmission
inverse scattering
MMIC technology
remote sensing & geophysics
plasmas
generators & motors
non-destructive evaluation
networks

- Partial list of techniques:

frequency-domain & time-domain techniques
integral equation & differential equation techniques
finite differences & finite element techniques
diffraction theories
modal expansions
hybrid methods
physical optics
perturbation methods
moment methods

TIMETABLE

October 1, 1993	Summary Submission Submit four (4) copies of a 300-500 word summary to the Symposium Chairman (Address on other side of this sheet).
November 17, 1993	Authors notified of acceptance
January 12, 1994	Submission deadline for camera-ready copy, not more than eight (8) pages including all figures. For both summary and final paper, please supply the following data for the principal author - name, address, e-mail address, FAX, and telephone numbers for both work and home.

Registration fee per person for the Symposium will be approximately \$200. The exact fee amount will be announced later.

SHORT COURSES

Short courses will be offered in conjunction with the Symposium, covering numerical techniques, computational methods, surveys of EM analysis and code usage instruction. It is anticipated that short courses will be conducted principally on Monday, March 21, and Friday, March 25. Fee for a short course is expected to be approximately \$80.00 per person for a half-day course and \$130.00 for a full-day course, if booked before March 4, 1994. Full details of 1994 Symposium will be available by November of 1993.

EXHIBITS

Vendor booths and demonstrations will feature commercial products, computer hardware and software demonstrations, and small company capabilities.

**1993 Symposium Program Committee
for the
9th Annual Review of Progress in
APPLIED COMPUTATIONAL ELECTROMAGNETICS
at the
Naval Postgraduate School
Monterey, CA**

Symposium Chairman: Perry Wheless
University of Alabama
Dept. of Elec. Engr.
Box 870286
Tuscaloosa, AL 35487
Phone: (205)348-1757

Symposium Administrator: Dr. Richard W. Adler
Naval Postgraduate School
Code EC/AB
Monterey, CA. 93943
(408) 656-2352

Symposium Short Course Chairman: Dr. John Rockway
NCCOSC/Code 805
San Diego, CA. 92152-5000
(619) 553-3791

CAEME Director: Dr. Magdy Iskander
Electrical Engineering Dept.
University of Utah
Salt Lake City, UT. 84112
(801) 581-6944

1994 Symposium Chairman: Andy Terzuoli
Air Force Institute of Technology
P.O. Box 3402
Dayton, OH 45401-3402
(513)255-3576

Conference Secretary: Mrs. Pat Adler

Advisory Committee: Dr. Ed Miller, Los Alamos Labs.
Dr. Robert Bevensee, Consultant
Dr. Harold Sabbagh, Sabbagh Assoc., Inc.
Jim Logan, NCCOSC
Dr. Ray Luebbers, Penn State Univ.
Dr. Andrew Peterson, Georgia Inst. of Tech.

CONFERENCE CHAIRMAN'S SUMMARY

I extend to you my warmest welcome to the beauty of Monterey and the *9th Annual Review of Progress in Applied Computational Electromagnetics* Symposium. The ACES Symposium has become a highly influential outlet for promoting awareness of recent technical contributions to the advancement of computational electromagnetics (CEM). The Symposium's technical papers and slate of short courses address the needs of newcomers to the field of computational electromagnetics as well as the needs of experienced practitioners, so the CEM community now eagerly anticipates Monterey in March of each year.

My special thanks go to Dick and Pat Adler for their invaluable assistance and advice throughout. Dr. John Rockway has coordinated an outstanding lineup of timely and applicable short courses for ACES93, and we are all grateful for his efforts on this extremely important component of the Symposium. Both Frank Walker and Pat Foster generously shared their experiences as Symposium Chair in 1991 and 1992, respectively, and their positive influence is evident in ACES93; Frank Walker, furthermore, maintained oversight responsibility for exhibits and industry liaison again this year. David Lizius and Robert Paknys provided publicity for ACES93 in Europe and North America, respectively, and their contribution to the success of ACES93 is greatly appreciated.

While some ACES members will view the parallel sessions at ACES93 with mixed emotions, I believe that, overall, the necessity for parallel sessions to accommodate the record number of papers is a good sign for ACES. It appears that many organizations and institutions will fall by the wayside in the 1990's, so I am encouraged by the growth and increased activity we have been fortunate enough to achieve with ACES93.

Several new session topics are conspicuous in ACES93. While the emphasis is retained on ACES traditional strengths such as software performance analysis and validation, canonical problems, and general purpose code applications, the new topics provide valuable enrichment for the ACES membership. External financial support was solicited, and obtained, for the Bioelectromagnetic Computations session; appreciation is expressed to Dr. Harold Sabbagh, ACES President, and Dr. Imre Gyuk, Session Chair, for their initiatives in connection with this special session.

The ACES93 Technical Program is fortunate to have a group of exceptional session chairs and co-chairs. They have contributed extensively to the number and quality of papers, the involvement of new participants, and interest in the Symposium. We are all thankful for their time and achievements.

The support of the Department of Electrical Engineering and the College of Engineering at The University of Alabama is gratefully acknowledged. Completion of my duties as Symposium Chairman would not have been possible without their active support and encouragement.

Finally, ACES commits to make your visit to Monterey and participation in ACES93 informative and enjoyable. As you take these *Proceedings* home with you, we hope you also take a satisfaction that you contributed to and benefited from this effort to advance the field of computational electromagnetics and to serve the needs of individual CEM professionals.

Perry Wheless
1993 Symposium Chairman

ACES PRESIDENT'S STATEMENT

Welcome to California! This has been a stormy winter in California, but by now the sun should be shining in Monterey. If not in fact, then surely in spirit, for that is the nature of ACES Conferences, and this, the 9th Annual Conference will be no exception.

Perry Wheless has done an exceptional job in organizing the conference, and we note one novel feature of this conference. The session on Bioelectromagnetic Computations, which consists mostly of invited papers, has the partial support of the Department of Energy. This means more to me than simply having DOE pick up part of the tab. It means that ACES is acknowledged as a preeminent technical society, in which significant scientific and engineering work is reported. Dr. Imre Gyuk, who gave a very interesting talk at last year's conference, was responsible for DOE's support of this session. Our thanks to Dr. Gyuk for this strong endorsement of ACES.

But conferences are more than just papers and short courses and banquets. They are intimate get-togethers with colleagues and friends, people that we see only once a year, perhaps. They are opportunities to meet new colleagues, from this country and abroad. They are chances to recharge ourselves with the help of our colleagues. Let's take advantage of these opportunities and make ACES the best that it can be.

Best wishes for a successful conference experience.

Harold A. Sabbagh
ACES President

SHORT COURSES

MONDAY MARCH 22 **FULL-DAY COURSE:** (Approximately 6 hour Course)

0830 "Solving Practical Problems with GEMACS"
by Buddy Coffey, Advanced Electromagnetics

MONDAY MARCH 22 **FULL-DAY COURSE** (Approximately 6 hour Course)

0830 "EM Modeling Using TSAR FDTD Code Suite"
by Dr. K.S. Kunz, Pennsylvania State University and S.T. Pennock, Lawrence Livermore National Laboratory

MONDAY MARCH 22 **MORNING HALF-DAY COURSE**

0830 "The Generalized Multipole Technique (GMT) and the Multipole Program (MMP: Theory and Practical Use in Computational Electromagnetics"
by Dr. Pascal Leuchtman, Swiss Federal Institute of Technology

MONDAY MARCH 22 **AFTERNOON HALF-DAY COURSE**

1300 "CEM Modeling Options and Tradeoffs"
by E.K. Miller, Los Alamos National Laboratory

TUESDAY MARCH 23 **AFTERNOON HALF-DAY COURSE**

1300 "Starting Your Own Small Business"
by Buddy Coffey, Advanced Electromagnetics

FRIDAY MARCH 26 **FULL-DAY COURSE** (Approximately 6 hour Course)

0830 "Wire Antenna Modeling: 20 Years of Successes, Failures and Lessons Learned, Modeling Guide lines and Some Useful Utility Programs"
by R.W. Adler, Naval Postgraduate School, J. Breakall, Pennsylvania State University, and G.J. Burke, Lawrence Livermore National Laboratory

FRIDAY MARCH 26 **FULL-DAY COURSE** (Approximately 6 hour Course)

0830 "TLM Techniques for Electromagnetic Wave Modeling"
by Wolfgang J.R. Hoefer, Professor, University of Victoria

FRIDAY MARCH 26 **FULL-DAY COURSE** (Approximately 6 hour Course)

0830 "Reflector Antenna Code Modeling"
by Dr. Roger C. Rudduck and Teh Hong Lee, The Ohio State University Electroscience Laboratory

SESSION 1 - "CANONICAL PROBLEMS

FOR

SOFTWARE VALIDATION"

Chair: Dr. Andrew Peterson, Co-Chair: Capt. Dennis Andersh

RCS of High Permittivity Cubes by FDTD and by Measurement

C.W. Trueman
S.J. Kubina
Concordia University,
Montreal, Quebec,
Canada

R.J. Luebbers
The Pennsylvania
State University,
University Park,
Pennsylvania

S.R. Mishra
C. Larose
David Florida Laboratory,
Canadian Space Agency,
Ottawa, Ontario,
Canada.

Abstract—This paper compares the measured radar cross-section(RCS) of dielectric cubes of relative permittivity 37.84 and 79.46 with calculations using the finite-difference time-domain method(FDTD). Such cubes ring for a very long time, and the effect of computing the RCS from a truncated time response is explored. The dependence of the RCS on the number of free-space cells separating the cube from the Mur absorbing boundary is investigated, and it is demonstrated that there is considerable interaction with the boundary. This paper shows that Yee's FDTD algorithm computes the RCS of a cube which is larger than the number of dielectric cells times the cell size. By adjusting the cell size to allow an extra half-cell of dielectric material on all faces of the cube, the computed RCS is brought into reasonable alignment with the measured data.

Introduction

The "finite difference time domain"(FDTD) method solves Maxwell's Equations by approximating the space derivatives and time derivatives with central difference formulas[1]. Thus space is subdivided into cells of size Δx by Δy by Δz and material properties are assigned to each cell. A finite volume of space consisting of N_x by N_y by N_z cells must contain both the scattering object and a sufficiently thick layer of free-space or "whitespace" separating the boundaries of the object on all sides from the outer boundary of the cell space. The outer boundary is designed to absorb any energy incident upon it, by imposing the Mur second-order boundary condition on the electric field[2].

Previous papers[3,4] used FDTD to model perfectly-conducting(PEC) targets, and obtained remarkably good agreement with measured RCS data over a frequency range as wide as 20 to 1[4]. "Guidelines" for choosing the cell size, the thickness of the whitespace and the number of time steps were proposed for PEC targets. Ref. [5] used FDTD to model dielectric cubes and rods made of plexiglas, of $\epsilon_r \approx 2.35$, and showed that both more whitespace and more time steps were needed for such low-permittivity targets compared to PEC targets. This paper extends the study to high permittivity dielectric cubes having $\epsilon_r = 37.84$ and 79.46 using measured data from 3.5 to 8 GHz. Modelling such cubes reveals that Yee's FDTD algorithm makes a systematic error in the size of the dielectric target, and hence in its resonant frequencies.

This paper uses the Penn State FDTD Code[6,7] which splits the total field into the incident field, which analytically satisfies Maxwell's Equations, plus the scattered field, which is found using the Yee FDTD update equations[1]. The outer boundary of the cell space uses the Mur second-order boundary condition[2]. The incident field is a Gaussian pulse, of width chosen to limit its energy content to frequencies where the cell size in the dielectric is less than a tenth of a wavelength. The field components in the FDTD cell space are used to find the far-zone scattered field with the near- to far-zone transformation described in Ref. [8].

High Permittivity Dielectric Material

The dielectric materials used for the measurements in this paper are high permittivity, low loss ceramics manufactured by Trans-Tech, Inc., for dielectric resonator applications. It comes in the form of discs roughly 1 cm thick and 2 cm in diameter. The manufacturer provides a measured permittivity for each individual sample showing that the permittivity is nearly constant over the frequency range from 0.5 GHz to 5 GHz for which data is given. A type D-8811 disc of diameter 1.99 cm and thickness 0.90 cm having $\epsilon_r = 37.84$ and loss tangent less than 1/6000 was

used to make a cube 8.97 mm on each side. A type D-8623 disc of diameter 1.71 cm and thickness 0.77 cm of $\epsilon_r = 79.46$ and loss tangent less than 1/3000 had sufficient material for a 7.72 mm cube.

Measuring the RCS

The RCS of each dielectric cube was measured with the electric field vector parallel to an edge of the cube and normally incident on one face. The cube was mounted in a 6 by 6 by 6 m anechoic chamber on a slim, tapered styrofoam column 1.2 m from a pair of horns, for a bistatic angle of about 8 degrees. The amplitude and phase was measured at each frequency for three configurations: the cube on the column, a reference sphere on the column, and the column alone. Then the room is calibrated as follows. The measured target response is the difference at each frequency between the response of the target on the column and the response of the column alone; and the sphere response is the difference between the response of the sphere on the column and the response of the column alone. Hence the scattered field of the target is the target response divided by the sphere response, times the exact scattered field of the sphere evaluated using the Mie series[9] with the appropriate bistatic angle. The scattered field of the target was obtained in this way from 3.5 to 8 GHz. For perfectly-conducting(PEC) targets[3,10], the Fourier transform was used to obtain the time response of the target in the chamber, and then time-gating was used to remove the direct coupling between the horns and also the reflections from the room after the target response subsides. However, it was found that the high-permittivity cubes "ring" for such a long time that a satisfactory setting for the length of the time gate could not be found, and so no time gating was used. The 3.5 to 8 GHz measurement obtains the RCS of the dielectric cube to a cube size of about $0.24\lambda_0$ for the $\epsilon_r = 37.84$ cube, where λ_0 is the free-space wavelength.

FDTD Model of a Dielectric Cube

FDTD models are usually based on the guideline that the cell size should be smaller than a tenth of a wavelength. If N by N by N cells are used to model a cube of side length a , this rule-of-thumb limits the frequency such that the cell size $\Delta x = a/N$ is smaller than $\lambda_d/10$, where λ_d is the wavelength in the dielectric. For the $\epsilon_r = 37.84$ cube, the measured data extends to a maximum cube size of $1.476\lambda_d$, hence $14.76 \approx 15$ cells must be used to represent the cube.

The user must choose the number of cells of free-space or "whitespace" separating the cube surfaces from the Mur absorbing boundary. In modelling PEC targets[3,4], it was found that separating the target surfaces from the Mur boundary by 20 cells is adequate to reduce interactions of the target and the boundary to acceptable levels. For low-permittivity dielectric cubes[5], it was found that 30 cells of whitespace were required. In the following, 20 cells of whitespace will be used to determine the time period over which the solution must be run, then the effect of larger whitespace will be explored.

Time Interval Requirement

To complete the model, the user must specify the total number of time steps for which the solution will be run. For highly-conducting targets, it was found[3] that sufficient time must be allowed for propagation at the free-space speed of light along a distance of 10 times the longest diagonal dimension of the target, D . Thus for PEC targets the time interval was chosen to be $T = 10D/c$. Using the Courant Limit time step of $\Delta t = \Delta x/(\sqrt{3}c)$, the number of time steps for a PEC cube with diagonal $D = N\sqrt{3}\Delta x$ is $N_t = 30N$, or 450 steps for a 15 cell cube. For a dielectric cube, the same time step is used as for a PEC cube[5]. In the dielectric case, the user might expect that sufficient time for 10 trips of distance D at the speed of propagation in the dielectric would be enough, thus $N_t = 30\sqrt{\epsilon_r}N$. Indeed, this is more than enough steps for a dielectric cube of low permittivity such as $\epsilon_r = 2.35$ [5]. But with $\epsilon_r = 37.84$ and $N = 15$, $N_t = 2770$ steps proves to be totally inadequate.

Fig. 1 shows the time response of the 15x15x15 cell model of cube having $\epsilon_r = 37.84$, using 20 cells of whitespace. The cell size is $8.97/15 = 0.598$ mm. Very early in the time response there are large positive and negative excursions, likely due to reflection of the incident field from the front face of the cube. The transient sustains its amplitude fully to about 16000 time steps, then gradually attenuates. The calculation was terminated after 65,536 steps. The solution could be continued further: it would be of interest to determine whether the oscillation eventually subsides.

RCS With Increasing Numbers of Time Steps

The data of Fig. 1 was used to compute the RCS shown in Fig. 2(a) to (c) with "time windows" of 16,384, 32,768, and 65,536 time steps, respectively. The figure plots the cube RCS in dB relative to the free-space square wavelength as a function of the cube size expressed in wavelengths in the dielectric, a/λ_d . Thus the horizontal axis is proportional to the frequency,

$a/\lambda_d = (a/u)f$, where u is the speed of propagation in the dielectric. As discussed in Ref. [11], when the time response is truncated to the period from zero to T , then the true spectrum is convolved with the function $\sin(\pi T f)/(2\pi f)$. This broadens the peaks in the RCS curve and introduces the series of closely spaced maxima and minima which are seen, for instance, at the left side of Fig. 2(a). The spacing of these spurious minima is $\Delta f = 1/T$, becoming closer and closer as the time window is broadened. If $T = N_s \Delta t$, then the minima are spaced by $\Delta(a/\lambda_d) = \sqrt{3\epsilon_r} N_s / N_t$. The 65,536 step window is sufficiently wide that the windowing effect is seen only as a spreading of the width of the curve between cube sizes of 1.18 and 1.22 wavelengths.

Figs. 2(a) to (c) show that the frequencies of the resonance peaks do not change as the number of time steps in the time window increases. Only the sharpness of these features changes. Thus computation of the response with 16,384 steps is sufficient to allow a quick comparison of the alignment of the computed resonant behavior with the measured RCS curve. Ref. [11] points out that Prony's method could be used to extract the resonant frequencies and Q factors using a very narrow time window.

Whitespace Thickness

Figs. 2(a), 3(a) and 3(b) show the RCS of the cube as the whitespace thickness is increased from 20 to 30 to 40 cells, substantially increasing the computation time. These curves were obtained using 16,384 time steps. Comparing Fig. 2(a) and 3(a) shows that the peak at cube size $0.77\lambda_d$ changes from 7.4 dB to -2.6 dB as the whitespace is increased from 20 to 30 cells, but the frequency or cube size at which the peak falls is unchanged. When the whitespace is increased to 40 cells, Fig. 3(b), the resonance peak changes to -3.33 dB, still at cube size $0.77\lambda_d$. The resonance peak at cube size $1.05\lambda_d$ changes from -0.1 dB to -0.2 dB to -2.4 dB as the whitespace increases from 20 to 30 to 40 cells, respectively. The "windowing" peaks are substantially reduced in Fig. 3(a) compared to Fig. 2(a), but change little as the whitespace is increased to 40 cells in Fig. 3(b). Thus in Fig. 2(a) the "close" Mur boundary only 20 cells away interacts strongly with the cube surface. Comparing Fig. 3(a) and (b) suggests that 30 cells is sufficient whitespace for the cube having $\epsilon_r = 37.84$.

Comparison With The Measured RCS

Comparing the computed and measured RCS curves in Fig. 3(a) shows remarkable similarity. The two curves correspond very well on a feature-by-feature basis, with every peak and every minimum in the measured curve clearly seen in the computation. But there is a systematic shift in frequency of the computed data towards lower frequencies. Thus the lowest resonance peak falls at $0.77\lambda_d$ cube side length in the computation compared to $0.83\lambda_d$ side length in the measurement. It appears that the Yee FDTD algorithm computes the RCS of a larger cube than that specified by setting the cell size to be the cube side length of 8.97 mm divided by 15 cells.

Half-Cell Margin Model

In Ref. [4] it was noted that, for perfectly-conducting rod targets, the RCS computed with Yee's FDTD algorithm is that of a larger rod than would be expected by multiplying the size of the cell by the number of PEC cells. Ref. [4] shows that the effective size of a PEC rod is larger than its size in cells by about one-quarter cell on all boundaries. For a high-permittivity dielectric cube, the size increase is more like one-half a cell. Thus a dielectric cube should be modelled by choosing the cell size allowing a half-cell margin all around the cube, so that the effective size of an N cell cube is $(N + 1/2 + 1/2)\Delta x = a$. For the $\epsilon_r = 37.84$ cube of side length

$a = 8.97$ mm, with $N = 15$ cells the cell size is $\Delta x = 8.97/(15 + 1) = 0.5606$ mm. Fig. 4 compares the RCS of the cube having this cell size with the measured RCS, using 16,384 time steps and 30 cells of whitespace. Comparing Figs. 3(a) and 4 shows that computing the cube's RCS allowing a half-cell margin on all sides dramatically improves the agreement between the measurement and the computation. Thus the resonance peak at $0.77\lambda_d$ in Fig. 3(a) falls at $0.82\lambda_d$ in Fig. 4, in much better agreement with the measured position at $0.83\lambda_d$. The second resonance peak falls at $1.05\lambda_d$ in Fig. 3(a), and at $1.12\lambda_d$ in Fig. 4, compared to $1.12\lambda_d$ in the measurement. Note that the half-cell margin adjustment is not perfect, and indeed better alignment of the sharp minima might be had using a size adjustment of 0.6 cell.

Cube With $\epsilon_r = 79.46$

To compute the RCS in Fig. 5(a), the 7.72 mm cube having $\epsilon_r = 79.46$ was modelled with $15 \times 15 \times 15$ cells and 40 cells of whitespace. The cell size was initially chosen with no margin adjustment, $\Delta x = 7.72/15 = 0.5147$ mm, and the computation carried out with 16,384 time steps. Note that the windowing effect in Fig. 5(a) is much more noticeable than in Fig. 3(b), even though the thickness of the whitespace is the same. Evidently, more time steps are required to control the windowing effect, and more whitespace might be needed for the higher permittivity cube.

Comparing the measured and computed curves for the RCS in Fig. 5(a) shows that there is again good correspondence of the peaks and minima in the measurement and the calculation, although the comparison tends to be obscured by the windowing problem. The first resonance peak of -3.5 dB falls at $0.78\lambda_d$ cube size, compared to a peak of -2.1 dB at $0.836\lambda_d$ in the measurement, and the second resonance of -4.8 dB at $1.07\lambda_d$, compared to -2.2 dB at $1.157\lambda_d$ in the measurement. Thus once again the Yee FDTD algorithm computes the RCS of a larger cube than expected.

To test the half-cell margin hypothesis, the cell size was reset to $\Delta x = 7.72/(15 + 1) = 0.4825$ mm, and the calculation was repeated to obtain Fig. 5(b). However, only 30 cells of whitespace could be used, and so more interaction with the Mur boundary is expected than in Fig. 5(a). Fig. 5(b) compares the measured and computed RCS. The fundamental resonance falls at $0.828\lambda_d$ cube size and agrees much better with the measured peak at $0.836\lambda_d$ than it did in Fig. 5(a). The peak height of 0.4 dB is larger than in Fig. 5(a), likely due to boundary interaction, as was the case between Fig. 2(a) and 3(a). The second resonance peak of -5.3 dB at $1.146\lambda_d$ aligns better with the measured peak at -2.2 dB at $1.157\lambda_d$ in Fig. 5(b) than it did in Fig. 5(a). The "doublet" in the measurement, with a sharp peak at -4.2 dB at $1.259\lambda_d$ cube size and a sharp minimum of -35.0 dB at $1.263\lambda_d$ size, is smeared by windowing in the computation. The computed minimum falls at $1.251\lambda_d$ cube size.

Conclusion

This paper has compared the measured RCS of high-permittivity cubes having $\epsilon_r = 37.84$ and 79.46 with the RCS computed using FDTD. This paper has clearly demonstrated that when the RCS of a high-permittivity dielectric cube is computed using Yee's FDTD algorithm, the peaks and minima occur at lower frequencies than those in the measurement. Evidently, FDTD computes the RCS of a larger cube than is expected by choosing the cell size to be the cube size divided by the number of dielectric cells. If the cell size is adjusted by considering the effective size of the cube to be one-half cell larger on all faces than its size in cells, then the computed RCS is in much better alignment with the measurement, although the correction is imperfect.

In doing extensive computations for this paper, problems were occasionally encountered with growing oscillations. Thus if the RCS of the $\epsilon_r = 79.46$ cube is computed with a 20 cell model surrounded by 40 cells of whitespace, then the oscillation in the transient response grows steadily beyond 32,768 time steps. It is not clear whether the problem is entirely due to the Mur absorbing boundary.

It is of interest to note that there are no peaks or minima in the RCS as a function of frequency in that do not appear in the measurement. Thus the frequencies present in the long sustained oscillation in the transient response of Fig. 1 are likely to have a physical basis and not simply be an artefact of the computation. It has been suggested that the Gaussian pulse excitation is unsuitable for this type of FDTD computation because of its energy content at zero frequency. The computations were repeated using a double Gaussian pulse excitation, having zero D.C. energy and being bandlimited to frequencies where the cell size in the dielectric is less than one-tenth wavelength. This excitation did not at all change the computed resonant frequencies of the cube. However, problems were encountered with additional sharp narrow resonance peaks introduced into the response by this excitation, not corresponding to any peaks seen in the measurement.

Further work on high-permittivity dielectric cube RCS will include tests with the Liao absorbing boundary condition[12], and results for cubes of permittivity approximately 10 and 20, as well as for the two permittivity values discussed here.

References

1. K.S. Yee, "Numerical Solution of Initial Value Problems Involving Maxwell's Equations in Isotropic Media", IEEE Trans. on Antennas and Propagation, Vol. AP-14, No. 3, pp. 302-307, May, 1966.
2. G. Mur, "Absorbing Boundary Condition for the Finite-Difference Approximation of the Time-Domain Electromagnetic Field Equations", IEEE Trans. on Electromagnetic Compatibility, Vol. EMC-23, No. 4, Nov. 1981.
3. C.W. Trueman, S.J. Kubina, R.J. Luebbers, K.S. Kunz, S.R. Mishra and C. Larose, "RCS of Cubes, Strips, Rods and Cylinders by FDTD", 8th Applied Computational Electromagnetics Society Symposium, Monterey, California, March, 1992.
4. C.W. Trueman, S.J. Kubina, R.J. Luebbers, S.R. Mishra and C. Larose, "Quarter-Cell Surface Adjustment for PEC FDTD Targets", submitted for review to the IEEE Trans. on Antennas and Propagation.
5. C.W. Trueman, S.J. Kubina, R.J. Luebbers, S.R. Mishra and C. Larose, "RCS of Dielectric Cubes and Rods by FDTD and by Measurement", Proceedings of the Symposium on Antenna Technology and Applied Electromagnetics, pp. 481-492, Winnipeg, Canada, August 5-7, 1992.
6. J.H. Beggs, R.J. Luebbers, K.S. Kunz and H.S. Langdon, "User's Manual for Three Dimensional FDTD Version A Code for Scattering from Frequency-Independent Dielectric Materials", Electrical and Computer Engineering Department, The Pennsylvania State University, University Park, Pennsylvania, March 25, 1992.
7. R. Holland, L. Simpson, and K.S. Kunz, "Finite Difference Analysis of EMP Coupling to Lossy Dielectric Structures", IEEE Trans. on Electromagnetic Compatibility, Vol. EMC-22, No. 3, pp. 203-209, August, 1980.

8. R.J. Luebbers, K.S. Kunz, M. Schneider and F. Hunsberger, "A Finite-Difference Time-Domain Near Zone to Far Zone Transformation", IEEE Trans. on Antennas and Propagation, Vol. AP-39, No. 4, April, 1991.
9. C.A. Balanis, "Advanced Engineering Electromagnetics", Wiley, New York, 1989.
10. S.R. Mishra, C. Larose, and C.W. Trueman, "Radar Cross-Section Measurements for Computer Code Validation", Antenna Measurement Techniques Association, 1991 Symposium Digest, Boulder, Colorado, Oct. 7-11, 1991.
11. J.A. Pereda, L.A. Vielva, A. Vegas and A. Prieto, "Computation of Resonant Frequencies and Quality Factors of Open Dielectric Resonators by a Combination of the Finite-Difference Time-Domain (FDTD) and Prony's Method", IEEE Microwave and Guided Wave Letters, Vol. 2., No. 11, November, 1992.
12. Z. Liao, H.L. Wong, B. Yang and Y. Yuan, "A Transmitting Boundary for Transient Wave Analyses," Scientia Sinica(Series A), Vol. XXVII, No. 10, pp. 1062-1076, Oct. 1984.

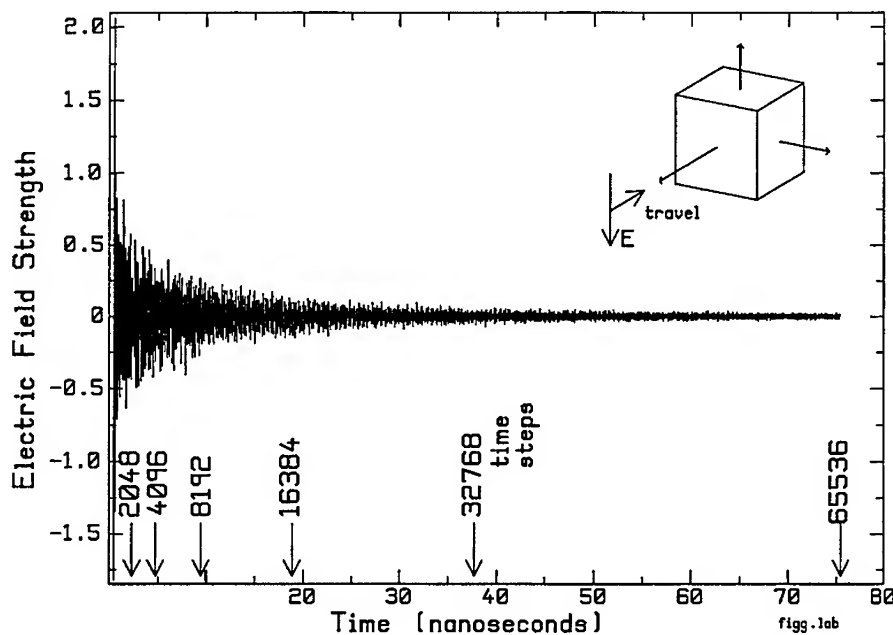


Fig. 1 The transient response of the cube with $\epsilon_r = 37.84$, computed with 20 cells of "whitespace" and 65,536 time steps.

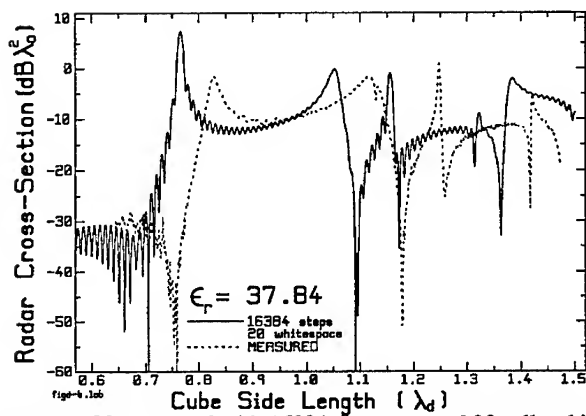


Fig. 2(a) RCS computed with 16384 time steps and 20 cells whitespace.

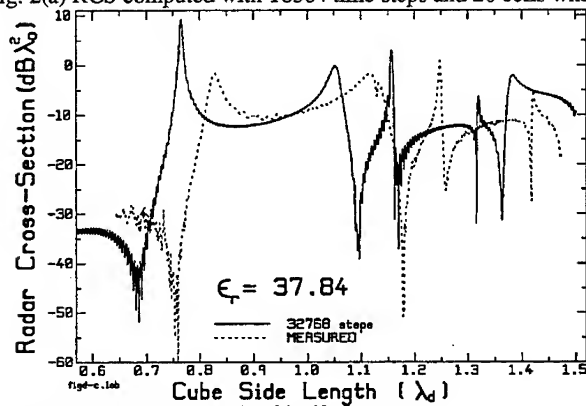


Fig. 2(b) RCS computed with 32768 time steps.

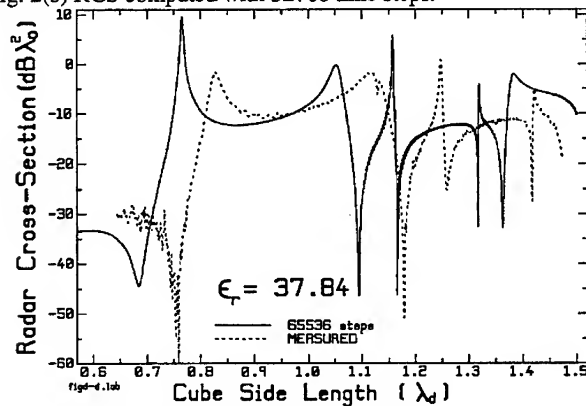


Fig. 2(c) RCS computed with 65536 time steps.

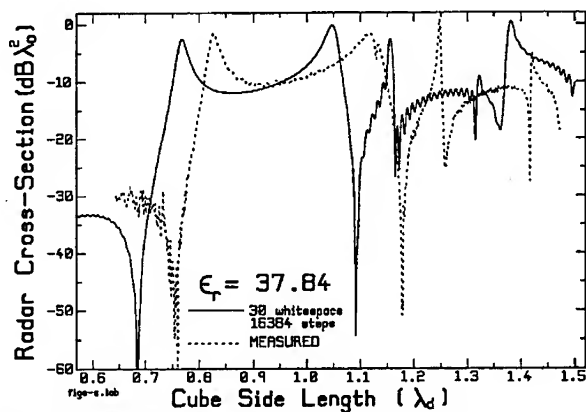


Fig. 3(a) RCS computed with 30 cells of whitespace.

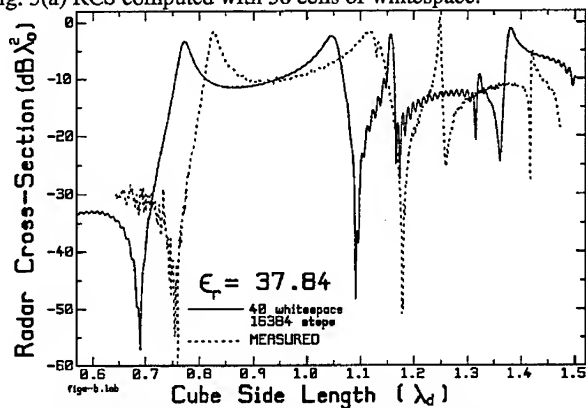


Fig. 3(b) RCS computed with 40 cells of whitespace.

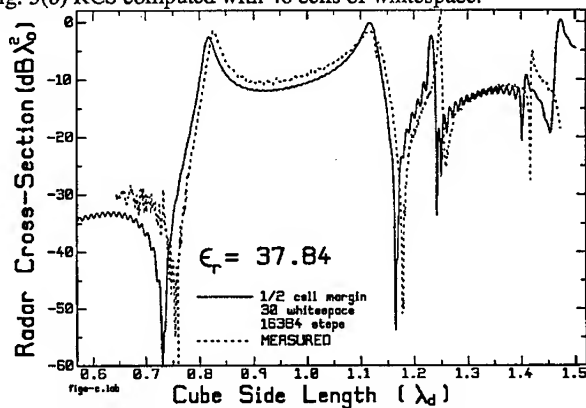


Fig. 4 RCS computed with a 1/2 cell size adjustment.

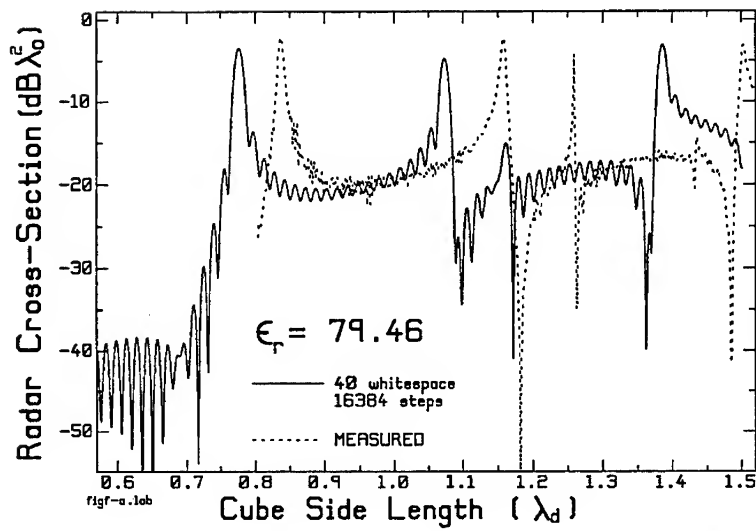


Fig. 5(a) RCS with $\epsilon_r = 79.46$ computed with 40 cells of whitespace.

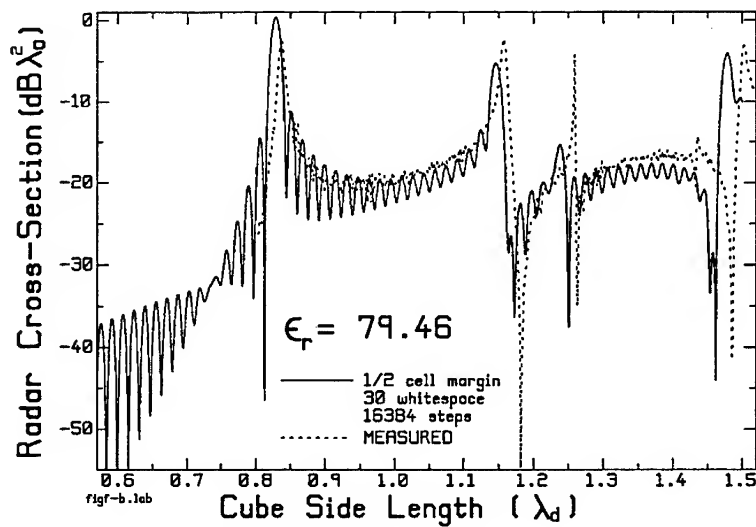


Fig. 5(b) RCS computed with a 1/2 cell size adjustment.

Asymptotic Prediction Validation Using Measured Data

B.B. Halama, D.J. Andersh, A.J. Terzuoli Jr.
School of Engineering · Air Force Institute of Technology
Wright-Patterson AFB, Ohio 45433

1 Abstract

Software implementation of asymptotic prediction methods requires validation against target geometries exhibiting both specular and non-specular scattering mechanisms. Additional, use of precise Computer Aided Design (CAD) target models are essential for adequate prediction model accuracy. Validation of radar signature predictions using measured signature data requires that accurate test target dimensions and proper test range calibration data is available.

This paper¹ compares CADDSCAT[1] synthetic predictions to monostatic RADAR signature measurements for a 'standard' set of primitive and complex targets. Prediction accuracy is compared for temporal, spatial and spectral signature accuracy. The limitations of the asymptotic predictions are validated based on the measured data. The full thesis report on the CADDSCAT validation can be found in, "Validation of CADDSCAT Radar Signature Predictions Using Measured Data"[2].

2 Introduction

Validation of asymptotic prediction methods is required to determine the frequency and geometry range over which accurate predictions are obtainable. This paper presents validation results of a radar signature prediction code called CADDSCAT. The CADDSCAT code was developed by McDonnell Douglas Corporation². CADDSCAT implements the Physical Optics (PO) and Incremental Length Diffraction Coefficient (ILDC) asymptotic methods for prediction of surface specular fields and edge diffracted fields. Multi-bounce field contributions are incorporated via the Shooting and Bouncing Rays (SBR) Method. All three theories require electrically large smooth targets. CADDSCAT radar signature predictions are implemented through the use of Computer Aided Design (CAD) based target models.

The collection of measured signature data and the creation of Advanced Computer Aided Design (ACAD)³ models was the primary effort in this study. The validation used measured radar signature data and is thus limited by the accuracy of the measurements. The validation method will be discussed in terms of target choices, CAD modeling and measurement used for the CADDSCAT validation.

3 Test Targets and Validation Methodology

The first step in the validation process was to choose appropriate test targets. Initially 25 appropriate test objects were considered for this validation. Targets were chosen so as to have five wavelengths along their surfaces when possible as suggested by Knott.[4, 113] The next criteria was to ensure that the target set as a whole exhibited scattering due to specular reflection, edge diffraction and multi-bounce scattering. Specifically, simple targets exhibiting well defined scattering features (edge diffraction, specular reflection, cavities,

¹This research was sponsored by the US Air Force Wright Laboratory, Avionics Directorate, Target Recognition Branch

²Jim Roedder, from McDonnell Douglas, was the key consultant concerning the CADDSCAT prediction code.

³ACAD ver. 7.3k solid modeling software was used for all IGES format target models in this study

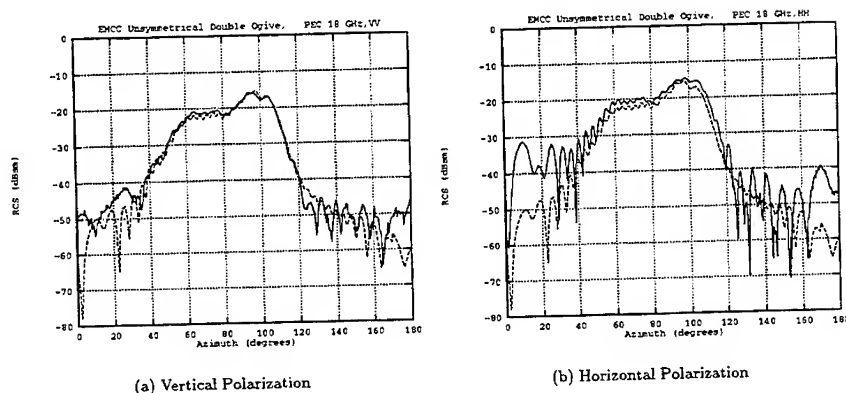


Figure 1: Unsymmetric Ogive Predictions, Elevation = 0° , Length = 7.5 inches, Radius = 1 inch, SOLID curves are measured data, DASHED curves are synthetic data

etc.) were essential to isolate major code problems. In addition objects with doubly curved surfaces were also required to test the CAD geometry modeling accuracy. Complex target's tested the codes performance in predicting combined effects. A missile model was chosen as the complex test target exhibiting scattering centers from curved surfaces, edges, cavities, and surface shadowing features. Accurate accounting of shadowing between surfaces of a complex geometry is needed to obtain a correct radar signature prediction. Both Perfect Electrical Conductor (PEC) and dielectric test targets were used for the CADDSCAT validation.

This study used measured data from the Naval Weapons Center at China Lake⁴. [5] The China Lake data provided low radar signature target measurements of conespheres, ogives, and an almond target. Measurements were completed for the missile target at The Ohio State University anechoic chamber. The validation process was completed using the measurement data. The methodology of building accurate ACAD models from known target dimensions and then comparing to CADDSCAT predictions allowed for several aspects of the code to be validated.

4 Validation Results

CADDSCAT's use of bi-cubic spline models allows for accurate radar signature predictions. The results presented illustrate the prediction accuracy obtained when using ACAD target models. The following results also show the deficiencies of high frequency methods in predicting traveling wave effects.

4.1 Unsymmetric Ogive

Figures 1(a) and 1(b) show the PO predictions for an unsymmetric ogive target that is illustrated in Figure 3(a). No calibration data was available for the ogive measurements. The data was shifted down by 10 dBsm to account for the 14 inch calibration sphere data that was not available. Lack of proper target configuration

⁴Data measurements for the Electromagnetic Code Consortium(EMCC) were completed by personnel from the Ames Research Center and The China Lake Naval Weapons Center.

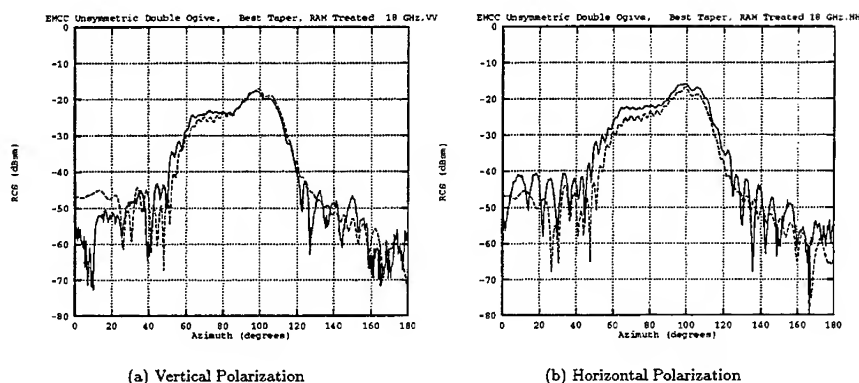


Figure 2: RAM Coated Unsymmetric Ogive Predictions, Elevation = 0° , Length = 7.5 inches, Radius = 1 inch, SOLID curves are measured data, DASHED curves are synthetic data

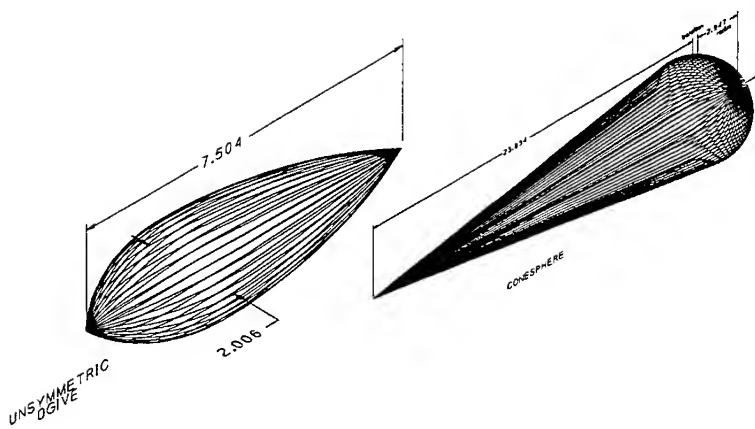
data adds some uncertainty to the measured data. Additional Predictions shown in Figures 2(a) and 2(b) are for an identical size dielectric coated ogive at 18 gigahertz (GHz) using constitutive parameters measured at 10 GHz. Nonavailability of constitutive parameters over the frequency band contributes to further uncertainty when validating the ogive prediction accuracy. The ogive predictions show that a PO only prediction does well at predicting this simple target, except for the traveling wave effects near 0° and 180° . The higher order effects are the primary limitation for high frequency asymptotic predictions.

4.2 Conesphere

The next low signature target analyzed was a 7° half-angle conesphere at 9 GHz. The conesphere geometry file contained 711 bi-cubic patch surfaces and is shown in Figure 3(b). Since no edges exist on the conesphere, a PO prediction was analyzed. The PEC conesphere predictions are similar to the ogive results. The results have been shifted so that the radar signature value of both the predicted and measured data match at the 0° point. The PO prediction matches both measurement polarizations of Figures 3(c) and 3(d) very well.

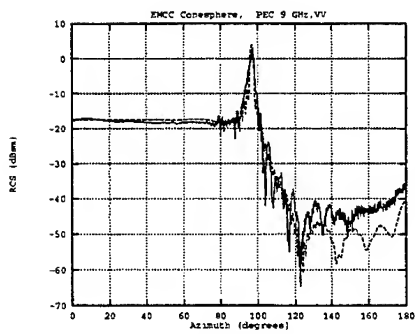
4.3 Trihedral

The measurements of a 6 inch triangular corner reflector, and a 12 inch by 3 inch cylindrical cavity with a flat plate termination were used to validate the multi-bounce predictions from CADDSCAT. These targets test significantly different aspects of the CADDSCAT multi-bounce calculation method. For the trihedral target, no divergence is required due to its flat surfaces. The trihedral prediction tests that CADDSCAT's bounce point calculation provides an accurate result over the aperture of the trihedral and that the shadowing effects are properly predicted over the rear of the trihedral. Figure 4(a) shows that a reasonably accurate results is obtained. The effect of shadowing in this prediction is seen by comparing Figures 4(a) and 4(b). These figures clearly show the effects of the various shadowing options available in CADDSCAT. Without any shadowing the trihedral prediction tends to over predict the radar signature where a null in the pattern should be. A Slightly less over prediction is obtained when using the centroid shadowing option. Note in Figure 4(b) the

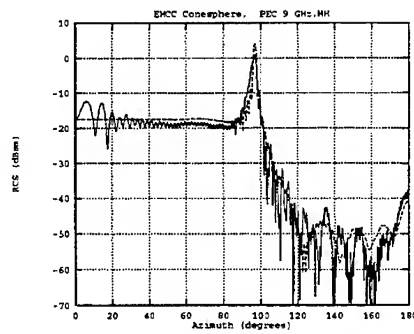


(a) Unsymmetric Ogive ACAD Model

(b) Conesphere ACAD Model



(c) Vertical Polarization



(d) Vertical Polarization

Figure 3: Conesphere Predictions, Elevation= 0 degrees, 9 GHz, **SOLID** curves are measured data, **DASHED** curves are the synthetic data

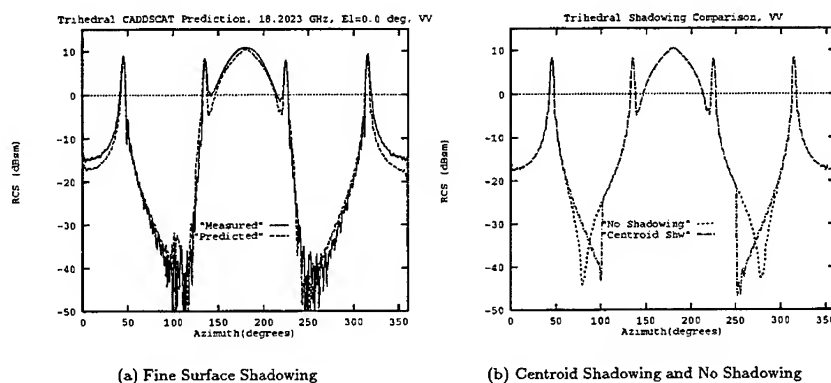


Figure 4: Trihedral Measurement Compared to CADDSCAT Predictions, Elevation= 0 degrees (Trihedral measured and predicted with one side horizontal during azimuth scan.), **SOLID** curves are measured data, **DASHED** curves are the synthetic data

drastic discontinuity caused by the centroid shadowing analysis. The trihedral model contained only one facet per side and so the fine shadowing option was required in order to obtain a good prediction. Typically, a CADDSCAT user must decide on whether to use centroid shadowing to save time or to use fine shadowing to get a more accurate prediction. This can be decided based on the facet (or bi-cubic patch) sizes used in the target model.

4.4 Cylindrical Cavity

A cylinder geometry provides a more rigorous test of the CADDSCAT multi-bounce capability. CADDSCAT [1] provides three important runtime parameters of LIMBC, NSAMPR, and IDIV for control of the multi-bounce accuracy. LIMBC controls the number of multi-bounce calculations completed for each Geometric Optic (GO) ray tube. NSAMPR controls the density of GO ray tubes that are initially shot at the target. Finally, IDIV determines whether the multi-bounce contribution is calculated with or without the GO ray tube divergence being calculated. Changing these parameters will drastically change the radar signature predicted for a cavity structure. For the prediction of Figure 5 the divergence factor was turned off. Runtime parameters of LIMBC=15, NSAMPR =20, and IDIV=0 (no divergence) were used. The prediction accuracy is not very good over the open end of the cavity. In general, the SBR method is not expected to provide very good results for this electrically small cavity as is discussed by Ling.[6] This illustrates how the SBR method is limited to large cavities on the order of 10 or 20 λ in diameter.

4.5 Missile Target

For a more complex target a validation can look at both time domain (or impulse response) signatures as well as frequency domain (azimuth scan) data in order to access a prediction codes accuracy. Impulse response predictions were obtained by an inverse Fourier transform of the frequency domain data. Impulse response analysis is used to validate a prediction's accuracy through comparison of scattering center location and

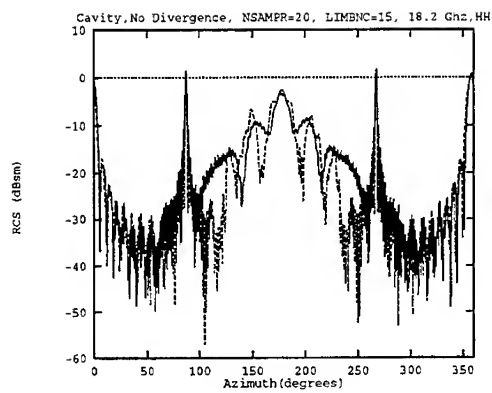


Figure 5: Circular Cavity Multi-bounce Prediction, No Divergence, HH, Dimensions(inches): $l=12.26$, $r(\text{inner})=1.37$, $r(\text{outer})=1.5$, **SOLID** curve is measured data, **DASHED** curve is synthetic data

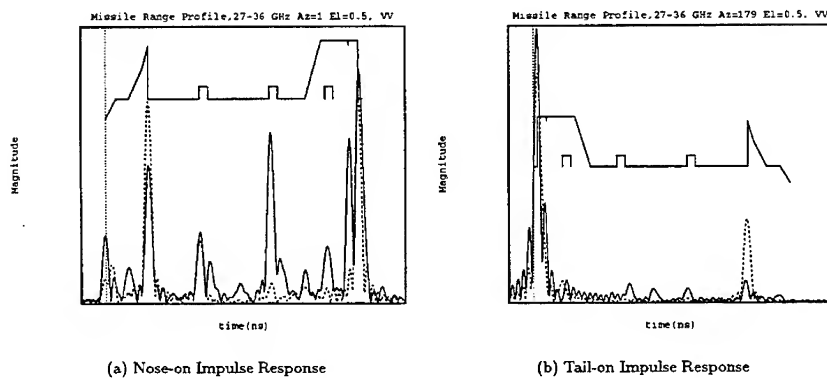
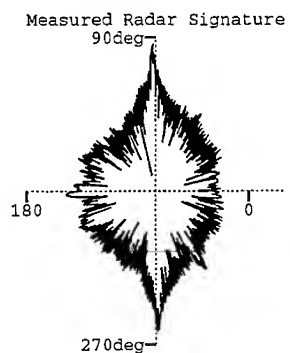
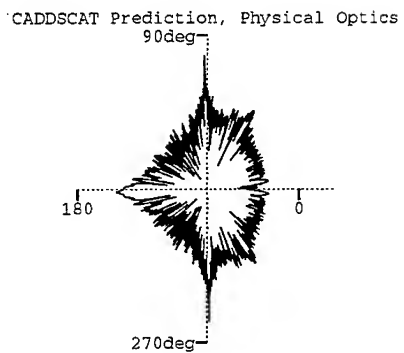


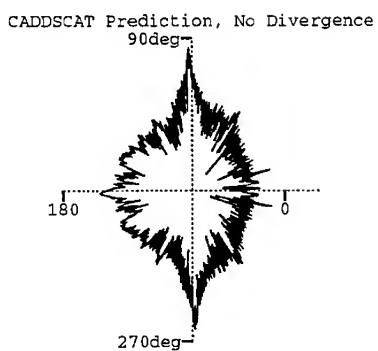
Figure 6: Time Domain Missile Data versus Predictions, **SOLID** curves are measured data, **DASHED** curves are synthetic data



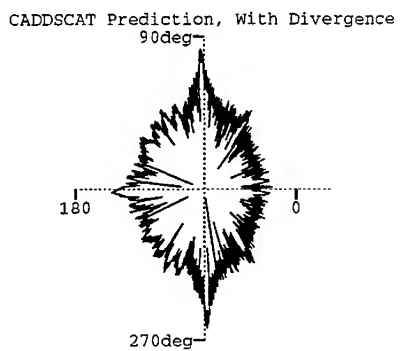
(a) Measured Data



(b) PO Prediction



(c) Multi-bounce Prediction, No Divergence



(d) Multi-bounce Prediction, With Divergence

Figure 7: Measured Missile Data Compared to Predictions, 36 GHz, 0.15° Granularity, Elevation= 0 degrees, Vertical Polarization (VV), (Identical Scale used for all plots)

amplitudes. This was difficult to do because of measurement alignment uncertainties. Small changes in the missile alignment caused variations in the missile's impulse response amplitudes. For illumination of the missile's nose CADDSCAT accurately predicts two major scattering center locations at the trailing edges of the fins (see Figure 6(a)). Alignment uncertainties of $\pm 0.5^\circ$ in elevation and $\pm 1^\circ$ in azimuth and elevation constitute a significant error source when comparing time domain predictions. Similar results are noted in Figure 6(b) for a tail-on prediction. In general, these impulse responses indicate that both the asymptotic predictions and possible small alignment errors prevent anything other than major scattering centers from being predicted.

The physical model's radar signature is not as symmetric as the ACAD model's predicted radar signature. The model's asymmetries are easily seen, in Figure 7(a), above and below the 0° line marker as well as at 180° . Not all of these asymmetries are due to the physical model. Pedestal alignment errors of $\pm 0.5^\circ$ in elevations and $\pm 2^\circ$ in azimuth also played a factor in the skewing of the measured radar signature. Comparing Figure 7(a) to the prediction of Figure 7(d) shows that CADDSCAT adequately predicts the radar signature. The most noticeable discrepancy is the additional lobes predicted near $\pm 45^\circ$ off of the tail sector due to the divergence calculations of CADDSCAT. The missile prediction was repeated with the multi-bounce divergence factor turned off. The no divergence result plotted in figure 7(c), shows better agreement to the measured data overall. Finally, Figure 7(b) illustrates a CADDSCAT physical optics result for comparison. The PO prediction provides an extremely gross error near the tail-on sector and at broadside due to no calculation of the multi-bounce contribution. These predictions show how the PO prediction doesn't provide sufficient accuracy to for a complex target. Also, the addition of multi-bounce predictions and GO ray tube divergence calculations can provide erroneous predictions for electrically small targets.

5 Conclusions

CADDSCAT's implementation of the PO, ILDC and the SBR prediction methods provides excellent first-order radar signature predictions for complex, electrically large targets. The target measurements used have highlighted the limitation of PO only predictions. The extension of the PO predictions for specular predictions of dielectric coated targets was validated. The validation targets used are a candidate set for use in future code validation efforts.

References

- [1] J. Roedder, *CADDSCAT User's Manual for CADDSCAT version 3 Jan 1992*. McDonnell Douglas, McDonnell Douglas, Saint Louis, MO 63166-0516, Jan. 1992.
- [2] B. B. Halama, "Validation of caddscat radar signature predictions using measured data," afit/ge/eng/92d-18, Air Force Institute of Technology, AFIT, Wright-Patterson AFB OH 45433-6583, Dec. 1992.
- [3] General Dynamics, General Dynamics Corporation, Fort Worth, TX, *Advanced Computer Aided Design Version 7.2 User's Manual*, 1991.
- [4] E. F. Knott, J. F. Shaeffer, and M. T. Tuley, *Radar Cross Section*. Artech House, 1985.
- [5] H. T. G. Wang, M. L. Sanders, and A. Woo, "Radar cross section measurement data on low-cross-section targets: Part 1 and 2," Informal Report TM-7002, Radio Frequency Guidance Division Intercept Weapons Department, Naval Weapons Center, China Lake, CA 93555-6001, Oct. 1991.
- [6] H. Ling, S.-W. Lee, and R.-C. Chou, "High frequency rcs of open cavities with rectangular and circular cross sections," *IEEE Transactions on Antennas and Propagation*, vol. 37, pp. 648-654, May 1989.

TLM Computation of an Iris-Coupled Waveguide Cavity - A Canonical Problem

Qi Zhang and W.J.R. Hoefer

NSERC/MPR Teltech Research Chair in RF Engineering
Department of Electrical and Computer Engineering
University of Victoria
Victoria, British Columbia, Canada V8W 3P6

Abstract

In this paper, a canonical problem is solved with the TLM method. The TE_{101} resonant frequency and Q-factor of an iris-coupled rectangular waveguide cavity are determined. The sources of errors affecting the numerical results are discussed, and methods for minimizing or eliminating them are pointed out.

1 Introduction

The purpose of this study is to provide reference data obtained with the TLM method for the canonical problem in Fig. 1. Shown is a square waveguide cavity coupled to a rectangular waveguide of equal width and height by a symmetrical inductive iris. Computed are the TE_{101} resonant frequency and the loaded Q-factor. These were determined for three iris openings ($d/a = 1/3, 1/2$ and $2/3$) and the following cases:

1. Lossless case: Walls are perfectly conducting ($\sigma = \infty$), $t = 0$ and $t = a/12$
2. Lossy case: Walls are made of coin silver ($\sigma = 4.7 \times 10^7$ s/m), $t = a/12$, size WR(28)

It was assumed that in the lossy case the thickness of the iris was much larger than the skin depth, and the waveguide size was WR(28).

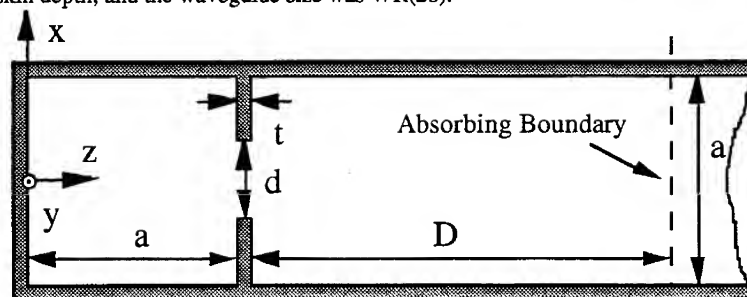


Fig.1 A square cavity coupled to a rectangular waveguide through a centered inductive iris. The inner height of the structure is b . The waveguide is air-filled, and the iris has thicknesses $t = 0$ and $t = a/12$. The distance D between the absorbing boundary and the iris wall is $2a$. The normalized widths of the iris are: $d/a = 1/3, 1/2$ and $2/3$. The waveguide size is WR(28) with $a = 7.112$ mm and $b = 3.556$ mm.

2 TLM Analysis of the Structure

All configurations were discretized by a uniform square (2D) or cubic (3D) TLM mesh and solved in the time domain. Procedures are described in a number of previous publications [1] - [4]. Details of the modeling procedures are given for each case below.

2.1 Lossless Case: 2D-TLM Analysis

When all walls are assumed lossless, the problem becomes two-dimensional since all quantities are independent of the height b . The structure can thus be represented by a two-dimensional shunt-connected network of transmission lines which are short-circuited at the wall positions. In order to model an infinitely long (or matched) waveguide, an absorbing boundary condition of high return loss must be introduced. In order to achieve such a condition with reasonable numerical expenditure, the absorbing boundary was placed at a distance $D = 2a$ from the iris to ensure that all higher order modes are decayed sufficiently to be negligible. Fig. 2 shows the discretization of the structure using a coarse mesh with $\Delta/a = 1/12$, when $d/a = 1/2$, and $t/a = 1/12$. Fig. 3 shows how the cavity is excited: at the beginning of the simulation, a single impulse is injected at each

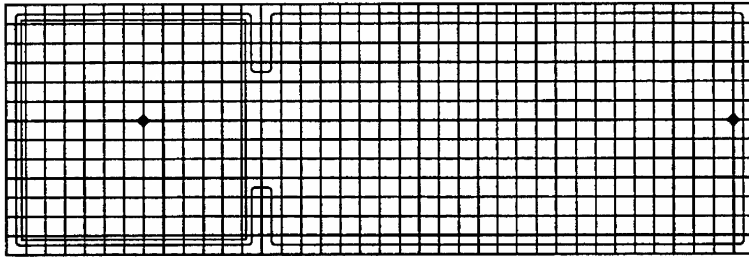


Fig. 2 Discretization of the structure using a coarse mesh with $\Delta/a = 1/12$, when $d/a = 1/2$, and $t/a = 1/12$. The time domain response is extracted at the output points in the center of the cavity and in front of the absorbing boundary

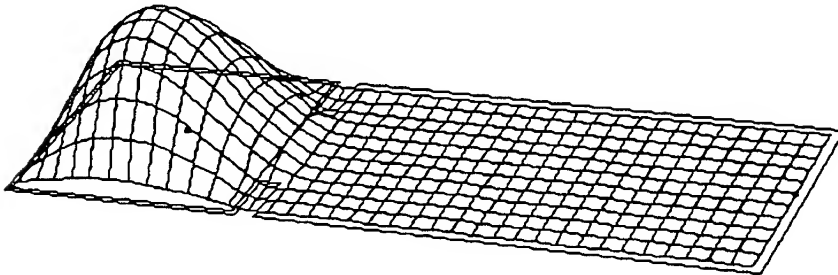


Fig. 3 Electric field distribution after the first computation step. This initial field distribution excites essentially the TE_{101} mode which then decays exponentially as shown in Fig. 4.

node inside the cavity, with an amplitude distribution corresponding to the TE₁₀₁ mode. The system is then left to itself, and the cavity oscillation decays exponentially.

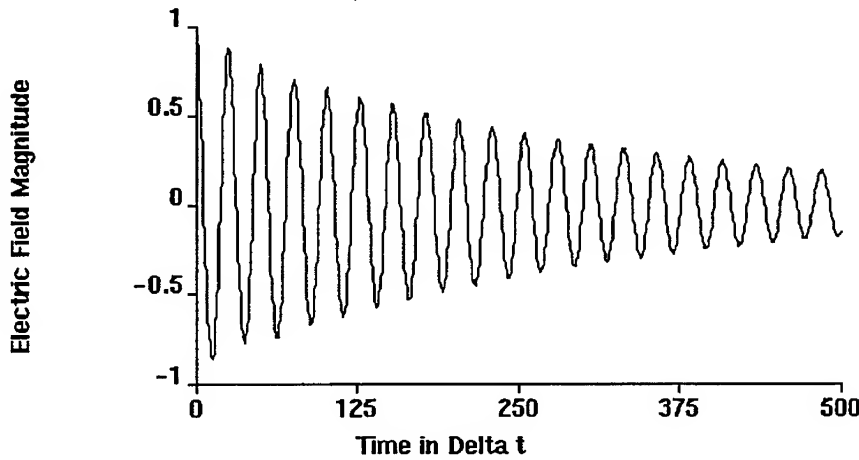


Fig. 4 Exponential decay of the TE₁₀₁ mode field in the center of the cavity

The time domain response picked up at the output point in the center of the cavity is shown in Fig. 4. The resonant frequency is obtained by computing the discrete Fourier Transform (DFT) of the time response and determining the location of the maximum of the resulting resonance curve. The loaded Q can be extracted either from the decay time by the following equation [5]:

$$E_y = E_0 e^{-\frac{\omega t}{2Q}} \quad (1)$$

or from the frequency domain response by the following formula:

$$Q = \frac{f_c}{f_1 - f_2} \quad (2)$$

where f_c is the resonant frequency, f_1 and f_2 are frequencies corresponding to the 3dB points. In the lossless case, the Q-factor is equal to the external Q. Since we can directly compute the decay in the time domain, we use Eq. (1) to determine the Q-factor.

The frequency dispersive absorbing boundary is modeled by a single mode Johns Matrix [4], which is the impulse response of an infinitely long waveguide, computed for 1000 time steps and convolved with the impulses incident upon it.

2.2 Lossless Case: 3D-TLM Analysis

In order to compare the 2D-TLM results with 3D-TLM computations we have also modeled the lossless case with a uniform cubic 3D mesh being only 1 Δl high in the third dimension. The structure was excited in the same manner as the 2D mesh.

However, the absorbing boundary was represented by a single impulse reflection coefficient rather than a Johns Matrix. This reflection coefficient was computed for the resonant frequencies obtained with 2D computations. Data extraction was the same as in 2D.

2.3 Lossy Case: 3D-TLM Analysis

When wall losses due to finite conductivity are taken into account, the absolute dimensions of the structure must be given, and the entire structure must be discretized fully in all three dimensions. We have chosen the standard WR(28) dimensions and assumed a finite thickness $t = a/12$ of the iris. Since the situation is a narrow-band problem, the wall losses have been included by evaluating the surface impedance of coin silver at the resonant frequency of the cavity, yielding a wall reflection coefficient of about -0.9997. Surface roughness and screening effects are not included in that value, so that the computed losses represent a lower bound. All other aspects of the lossy simulation are the same as in the lossless 3D case discussed in section 2.2. The results do not differ significantly because coin silver is a good conductor.

3 Results

Numerical results obtained from the above simulations are summarized in the following tables. These contain all data necessary to reproduce and verify these results.

Tables 1 and 2 show the resonant frequencies and Q-factors obtained with a 2D-TLM Electromagnetic Simulator [2],[4] for zero and finite thickness of the iris, assuming perfectly conducting walls everywhere. The TE_{101} normalized resonant frequency $\Delta l / \lambda$ is computed for three iris openings and using three mesh densities. The number of computation steps (often called "Number of Iterations" in the literature) must be increased proportionally with the mesh density. In all cases the number of computations was sufficient to reach a stable value of the resonant frequency. The results are then extrapolated for $\Delta l = 0$ and denormalized for WR(90) and WR(28) waveguide sizes. The Q-factor is determined from the decay time of the resonance using Eq. (1). It can be seen that the resonant frequency is only slightly affected by the thickness of the iris, while the Q-factor depends very strongly upon it.

Tables 3 and 4 show results for identical geometries obtained with a 3D-Electromagnetic Simulator, assuming that the structure is one mesh parameter high.

Table 5 presents resonant frequencies and Q-factors for the lossy case, assuming that the walls are made from coin silver, and using standard WR(28) dimensions where $a=7.112$ mm, $b=3.556$ mm. The thickness of the iris is 0.593 mm. Only two mesh densities ($\Delta l/a = 1/12$ and $1/24$) were chosen, and frequency values were extrapolated linearly for $\Delta l/a = 0$.

4 Errors and their Correction

The most important error in the TLM simulation is the coarseness error which is due to imperfect resolution of the fields in the vicinity of sharp edges. This error has been reduced by at least one order of magnitude by computing each structure with two or three different discretization steps and linearly extrapolating the results for $\Delta l=0$. The systematic error after extrapolation is estimated to be less than ± 0.1 percent of the resonant frequency. Velocity error due to the finite discretization is eliminated by the extrapolation process and thus negligible.

Table 1
2D-TLM simulation of TE₁₀₁ mode. Lossless walls. Iris thickness $t = 0$

d/a	$\Delta l/a$	Number of Computation Steps	Δl (mm)	Norm. Reso- nant Freq. $\Delta l / \lambda$	Extrapolated Resonant Freq. (GHz)	Loaded Q-factor
1/3	1/48	4000	0.25	0.01431	WR(90): 9.0367	85.4
	1/24	2000	0.50	0.02854	WR(28): 29.0466	
	1/12	1000	1.00	0.05675		
1/2	1/48	4000	0.25	0.01378	WR(90): 8.7086	16.7
	1/24	2000	0.50	0.02744	WR(28): 27.9921	
	1/12	1000	1.00	0.05445		
2/3	1/48	4000	0.25	0.01305	WR(90): 8.2246	5.6
	1/24	2000	0.50	0.02599	WR(28): 26.4364	
	1/12	1000	1.00	0.05190		

Table 2
2D-TLM simulation of TE₁₀₁ mode. Lossless walls. Iris thickness $t = a/12$

d/a	$\Delta l/a$	Number of Computation Steps	Δl (mm)	Norm. Reso- nant Freq. $\Delta l / \lambda$	Extrapolated Resonant Freq. (GHz)	Loaded Q-factor
1/3	1/48	4000	0.25	0.01441	WR(90): 9.0944	472.8
	1/24	2000	0.50	0.02879	WR(28): 29.2322	
	1/12	1000	1.00	0.05734		
1/2	1/48	4000	0.25	0.01395	WR(90): 8.8136	46.9
	1/24	2000	0.50	0.02785	WR(28): 28.3295	
	1/12	1000	1.00	0.05538		
2/3	1/48	4000	0.25	0.01337	WR(90): 8.4583	10.8
	1/24	2000	0.50	0.02664	WR(28): 27.1873	
	1/12	1000	1.00	0.05283		

Table 3

3D-TLM simulation of TE₁₀₁ mode. Lossless walls. Iris thickness $t = 0$
 (Percentage values indicate deviation from 2D-TLM results in Table 1)

d/a	$\Delta l/a$	Number of Computat. Steps	Δl (mm)	Reflect. Coeff. of Abs. Wall	Norm.Res. Frequency $\Delta l / \lambda$	Extrapol. Res. Frequ. (GHz)	Loaded Q-factor
1/3	1/48	4000	0.25	0.1859492	0.01432	WR(90) 9.0383	91.0 (+ 6.5 %)
	1/24	2000	0.50	0.1871245	0.02859	WR(28) 29.0517	
	1/12	1000	1.00	0.1897106	0.05690	(+ 0.02 %)	
1/2	1/48	4000	0.25	0.2069948	0.01380	WR(90) 8.7160	18.7 (+ 11 %)
	1/24	2000	0.50	0.2093416	0.02751	WR(28) 28.0157	
	1/12	1000	1.00	0.2135141	0.05468	(+ 0.08 %)	
2/3	1/48	4000	0.25	0.2337197	0.012997	WR(90) 8.2325	5.0 (- 11 %)
	1/24	2000	0.50	0.2322035	0.025829	WR(28) 26.4618	
						(+ 0.1 %)	

Table 4

3D-TLM simulation of TE₁₀₁ mode. Lossless walls. Iris thickness $t = a/12$
 (Percentage values indicate deviation from 2D-TLM results in Table 2)

d/a	$\Delta l/a$	Number of Computat. Steps	Δl (mm)	Reflect. Coeff. of Abs. Wall	Norm.Res. Frequency $\Delta l / \lambda$	Extrapol. Res. Frequ. (GHz)	Loaded Q-factor
1/3	1/48	4000	0.25	0.182135	0.01442	WR(90) 9.0918	450.5 (- 4.7 %)
	1/24	2000	0.50	0.182837	0.02881	WR(28) 29.2238	
	1/12	1000	1.00	0.184542	0.05744	(- 0.03 %)	
1/2	1/48	4000	0.25	0.199111	0.01397	WR(90) 8.8162	50.1 (+ 6.8 %)
	1/24	2000	0.50	0.201042	0.02790	WR(28) 28.3380	
	1/12	1000	1.00	0.203544	0.05553	(+ 0.03 %)	
2/3	1/48	4000	0.25	0.227341	0.01341	WR(90) 8.4650	13.6 (+ 26 %)
	1/24	2000	0.50	0.232152	0.02663	WR(28) 27.2092	
	1/12	1000	1.00	0.235718	0.05299	(+ 0.08 %)	

Table 5
3D-TLM simulation of TE₁₀₁ mode. Lossy walls made of coin silver. WR(28)
waveguide size. Iris thickness $t = a/12$
(Percentage values indicate deviation from lossless 3D-TLM results in Table 4)

d/a	$\Delta l/a$	No. of Compu- tation Steps	Δl (mm)	$t/\Delta l$	Impulse Reflect. Coef. of Absorb. Boundar	Impulse Reflect. Coef. of coin silver	TE ₁₀₁ Reson. Freq. in GHz	Extrapo- lated Reson. Freq. in GHz	Loaded Q-factor
1/3	1/24	2000	0.29633	2	0.18280	-0.9997	29.1533	29.246	410.5
	1/12	1000	0.58267	1	0.18449	-0.9997	29.0605	(+0.08%)	(-9 %)
1/2	1/24	2000	0.29633	2	0.20111	-0.9997	28.2246	28.339	46.3
	1/12	1000	0.58267	1	0.22291	-0.9997	28.1105	(+0.004 %)	(-8 %)
2/3	1/24	2000	0.29633	2	0.23262	-0.9997	26.9397	27.054	11.6
	1/12	1000	0.58267	1	0.23604	-0.9997	26.8102	(-0.5 %)	(-15 %)

The number of computation steps was chosen in each case such that no change in resonant frequency could be detected when increasing it any further. The only other error of consequence is due to the finite return loss of the absorbing boundaries used in the simulation. This error has been determined to be less than ± 0.15 percent of the resonant frequency by placing the absorbing boundary at different distances from the iris and measuring the corresponding variations in the resonant frequency. This is the equivalent of the sliding load measurements used in S-parameter measurements. **The overall estimated error in the computation of the resonant frequencies is thus less than ± 0.25 percent.**

The deviations in percent among resonant frequencies for the lossless cases as obtained with 2D-TLM and 3D-TLM are included in tables 3 and 4. All results agree well indeed within the estimated maximum error of ± 0.25 percent. The wider the opening, the more sensitive the resonant frequency value is to the return loss of the absorbing boundary. The accuracy of the Q-factor is much worse, (typically ± 10 percent), and deteriorates when the iris becomes very wide and the loaded Q drops to extremely low values.

Resonant frequencies for the 3D lossy case are compared with the 3D lossless case in Table 5. As expected, the losses are so small that they do not sensibly affect the resonant frequency at narrow iris openings. For $d/a = 2/3$ the resonant frequency of the lossy system is 0.5 percent lower than that for the lossless case, and thus exceeds the error margin mentioned above. This is attributed to the strong coupling between the cavity and the absorbing boundary which is no longer perfectly matched to the lossy waveguide section. The Q-factor in the lossy case is typically 10 percent lower than in the lossless case. Since the same procedure has been used to compute these two sets of values, the reduction of Q with increasing d/a is quite consistent.

5 Conclusion

A canonical problem has been solved with the TLM method. The TE_{101} resonant frequency and loaded Q-factor of a square cavity coupled to a commensurate waveguide through a symmetrical inductive iris are computed. Numerical errors are reduced to less than 0.25 percent using extrapolation with successive mesh refinement. Numerical results for the resonant frequency computed both with 2D-TLM and 3D-TLM Electromagnetic Simulators agree well within that error margin. The Q-factor is more difficult to compute with high accuracy, particularly in the cases of strong coupling between the cavity and the waveguide. An accuracy of about 10 percent is the best that can be achieved with the time decay method. The method based on the 3 dB bandwidth is even less accurate, particularly when the Q-factor is very low. The consistency of the results obtained with different TLM models indicates that the values obtained are reliable and accurate within about 0.1 percent for the resonant frequencies, and about 10 percent for the loaded Q.

Acknowledgement

The authors thank P. So and C. Eswarappa for their helpful suggestions and discussions.

References

- [1] P. B. Johns and R. L. Beurle, "Numerical solution of 2-dimensional scattering problems using a transmission-line matrix", *Proc. Inst. Elec. Eng.*, Vol. 118, No. 9, pp 1203-1208, Sept. 1971.
- [2] P.P.M. So, C. Eswarappa, and W.J.R. Hoefer, "A Two-dimensional TLM Microwave Field Simulator using New Concepts and Procedures," *IEEE Trans. Microwave Theory Techniques*, Vol. MTT-37, No. 12, pp. 1877-1884, Dec. 1989.
- [3] W.J.R. Hoefer, "The Transmission Line Matrix (TLM) Method", Chapter 8 of "Numerical Techniques for Passive Microwave and Millimeter-Wave Structures," edited by T. Itoh, John Wiley & Sons, New York 1989, pp. 496-591.
- [4] W.J.R. Hoefer, P.P.M. So, "The Electromagnetic Wave Simulator, A Visual Electromagnetics Laboratory based on the 2D TLM Method", John Wiley & Sons, Chichester, U.K., 1991.
- [5] R. E. Collin, "Foundations for Microwave Engineering", McGraw-Hill, New York 1966, Chapter 7, pp 313-362.

A TECHNIQUE FOR DETERMINING NON-INTEGGER EIGENVALUES FOR CANONICAL ANALYSIS OF BOUNDARY VALUE PROBLEMS

D. Reuster and M. Kaye

University of Dayton
Department of Electrical Engineering
Dayton, OH 45469-0226

ABSTRACT

A study of the determination of non-integer eigenvalues for ordinary differential equations with transcendental solutions is presented. An algorithm based on expansion in terms of Chebyshev polynomials and collocation is presented. The method is applied to the problem of computing the modal fields external to a biconical radiating structure and to the computation of the modal fields in a curved section of rectangular waveguide. Eigenfunction solutions for both problems are presented.

I. INTRODUCTION

Canonical analysis of boundary value problems commonly produce series solutions of transcendental functions, [1-3] where the index of summation is a set of eigenvalues (ν) determined by the boundary conditions of the problem. When considering perfectly conducting boundaries, the eigenvalues are those values such that the transcendental function of order ν , or its derivative, is equal to zero at the boundaries. Unfortunately, the determination of the eigenvalues that provide such results is usually limited to special cases, often when ν is an integer. Difficulty in determining the correct values for ν , when ν is not an integer, has limited the use of canonical analysis for these problems.

This paper presents a generalized numerical approach for determining the eigenvalues of transcendental functions subject to the Dirichlet and Neumann boundary conditions. The method proposed is based upon expanding the unknown function in a series of Chebyshev polynomials [4] and using the method of collocation [3] to obtain a well conditioned system of linear homogeneous equations. The eigenvalues (ν) are then found by using a bracketing and bisection technique [5].

II. MATHEMATICAL FORMULATION

Assume that the physical problem under consideration is described by the function $y_v(x)$, which is defined on the closed region $[a,b]$, and satisfies a second order ordinary differential equation (ODE) of the following form:

$$A(x) \frac{d^2 y_v(x)}{dx^2} + B(x) \frac{dy_v(x)}{dx} + C(x, v) y_v(x) = 0 \quad (2.1)$$

The functions $A(x)$, $B(x)$, and $C(x, v)$ are taken to be continuous on the open region (a, b) . The sought solutions are subject to boundary conditions which can be separated into different types according to the physical problem under consideration. Typical boundary conditions are:

$$y_v(a) = y_v(b) = 0 \quad (2.2)$$

$$y_v'(a) = y_v'(b) = 0 \quad (2.3)$$

$$y_v(a) = y_v'(b) = 0 \quad (2.4)$$

$$y_v'(a) = y_v(b) = 0 \quad (2.5)$$

Let $y_v(x)$ be expressed by the following Chebyshev polynomial expansion:

$$y_v(x) = \sum_{n=0}^{\infty} \alpha_n^v T_n[\ell(x)] \quad a \leq x \leq b \quad (2.6)$$

where $T_n(z)$ is the n^{th} Chebyshev polynomial of the first kind, and $\ell(x)$ is a linear mapping which maps the interval $[a, b]$ to $[-1, 1]$

$$T_n(z) = \cos(n \cos^{-1}(z)) \quad -1 \leq z \leq 1 \quad (2.7)$$

$$\ell(x) = \left[\frac{2}{(b-a)} \right] x - \frac{2a}{(b-a)} - 1 \quad a \leq x \leq b \quad (2.8)$$

Since the set of Chebyshev polynomials are continuous on $[-1, 1]$, the first and second derivatives of $y_v(x)$ may be expressed as follows:

$$\frac{dy_v(x)}{dx} = \sum_{n=0}^{\infty} \alpha_n^v T_n'[\ell(x)] \frac{d\ell(x)}{dx} \quad (2.9)$$

$$\frac{d^2 y_v(x)}{dx^2} = \sum_{n=0}^{\infty} \alpha_n^v T_n''[\ell(x)] \left[\frac{d\ell(x)}{dx} \right]^2 \quad (2.10)$$

$T'_n[\ell(x)]$ and $T''_n[\ell(x)]$ are the first and second derivatives of $T_n[\ell(x)]$ with respect to $\ell(x)$, and are given by:

$$T'_n(z) = \frac{1}{(1-z^2)} [-nz T_n(z) + n T_{n-1}(z)] \quad (2.11)$$

$$T''_n(z) = \frac{1}{(1-z^2)^2} [T_n(z) ((nz)^2 - nz^2 - n) + T_{n-1}(z) (-2n^2z + 3nz) + T_{n-2}(z) (n^2 - n)] \quad (2.12)$$

Substituting Eqs. (2.9) and (2.10) in Eq. (2.1) and approximating the series expansion for $y_\nu(x)$ by the first N terms, yields the following linear homogeneous equation for the expansion coefficients (α_n^ν):

$$\sum_{n=0}^{N-1} M_n^\nu(x) \alpha_n^\nu = 0 \quad (2.13)$$

where,

$$M_n^\nu(x) = A(x) T_n''[\ell(x)] \left[\frac{d\ell(x)}{dx} \right]^2 + B(x) T_n'[\ell(x)] \frac{d\ell(x)}{dx} + C(x, \nu) T_n[\ell(x)] \quad (2.14)$$

Enforcing Eq. (2.14) at N points, $\{x_i, i=1, N\}$, on the interval $[a, b]$ leads to a system of N linear homogeneous equations, which may be written as the following matrix equation:

$$\begin{bmatrix} M_0^\nu(x_1) & M_1^\nu(x_1) & \dots & M_{N-1}^\nu(x_1) \\ M_0^\nu(x_2) & M_1^\nu(x_2) & \dots & M_{N-1}^\nu(x_2) \\ \vdots & \vdots & \ddots & \vdots \\ M_0^\nu(x_N) & M_1^\nu(x_N) & \dots & M_{N-1}^\nu(x_N) \end{bmatrix} \begin{bmatrix} \alpha_0^\nu \\ \alpha_1^\nu \\ \vdots \\ \alpha_{N-1}^\nu \end{bmatrix} = \begin{bmatrix} 0 \\ 0 \\ \vdots \\ 0 \end{bmatrix} \quad (2.15)$$

Note that the matrix M is solely a function of ν , the desired eigenvalues of the given ODE. Since Eq. (2.13) is a homogeneous equation, it will have non-trivial solutions if and only if the determinant of the matrix M is zero. However, taking the determinant of the matrix M in its present form yields zero for any value of ν . This is because solutions exist for any given

value of ν due to the fact that the boundary conditions have not yet been imposed. Hence, it is necessary to first impose the boundary conditions in order to obtain the desired values for ν .

Boundary conditions are imposed by replacing the first and last rows of the matrix M with the series representation for the boundary conditions. Thus if, $y(a) = y(b) = 0$ the first row of the matrix M is replaced by

$$\sum_{n=0}^{N-1} \alpha_n^\nu T_n[\ell(a)] = 0 \quad (2.16)$$

and the last row is replaced by

$$\sum_{n=0}^{N-1} \alpha_n^\nu T_n[\ell(b)] = 0 \quad (2.17)$$

The new matrix obtained will be denoted by \tilde{M} . Because the boundary conditions require the function, or the derivative of the function, to be zero at the boundaries, the matrix equation remains homogeneous; thus, non-trivial solutions still exist if and only if the determinant of the matrix \tilde{M} is zero. Hence, the permissible values of ν , subject to the given boundary conditions, are obtained by requiring $\det(\tilde{M}) = 0$.

III. COMPUTER IMPLEMENTATION

Numerical estimation of the eigenvalues ν_p ($p=1,\dots,P$), is based on the fact that the $\det(\tilde{M})$ is an oscillatory function of ν , with the $\det(\tilde{M}^{\nu_p}) = 0$ ($p = 1,\dots,P$). Hence, over any interval containing a single eigenvalue, $\det(\tilde{M})$ will change sign. This behavior allows the eigenvalues (ν_p) to be determined using a bracketing and bisection technique [5]. Scanning $\det(\tilde{M})$ for changes in sign over a given interval on the ν axis, provides the bracketing intervals for the eigenvalues. Care must be taken in selecting a maximum scan distance which is less than the minimum distance between any two adjacent roots. Scan distances which are too large may cause roots to be missed. Once the roots are bracketed the bisection technique may be implemented to compute the particular eigenvalue to the desired degree of accuracy. Since the bisection method requires only the computation of the sign of the determinant, the common problem of numerical overflow, associated with determinant calculations, is avoided.

IV. BICONICAL RADIATING STRUCTURE

Under radiation conditions, the electric field external to the biconical radiating structure has series solution of the following form:

$$E_r = \sum_{\nu} c_{\nu} H_{\nu+1/2}^{(2)}(kr) L_{\nu}(\cos\theta) \quad (4.1)$$

where $H_{\nu+1/2}^{(2)}(kr)$ is a modified Hankel function of the second kind, and $L_{\nu}(\cos\theta)$ is an odd Legendre polynomial [6]. Boundary conditions require that $L_{\nu}(\cos\theta_1) = L_{\nu}(\cos\theta_2) = 0$. Thus, it is necessary to determine the eigenvalues whose eigenfunctions satisfy the given boundary conditions. For Legendre's differential equation, $A(x) = 1-x^2$, $B(x) = -2x$ and $C(x,\nu) = \nu(\nu+1)$.

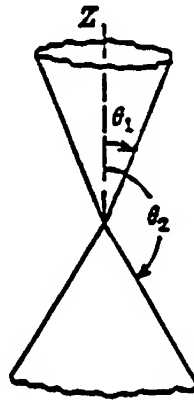


Figure 4.1 Geometry of the biconical radiating structure

Two different biconical radiating structures were chosen for analysis: Structure 1, $\theta_1 = 30^\circ$ and $\theta_2 = 150^\circ$; Structure 2, $\theta_1 = 10^\circ$ and $\theta_2 = 170^\circ$. Tables I and II provide the first four eigenvalues for each structure and compares the calculated eigenvalues with the eigenvalues estimated by Grimes using an asymptotic expansion technique [7]. Graphs of the corresponding eigenfunctions are shown in figures 4.2 and 4.3. For both radiating structures under study, convergence of the calculated eigenvalues occurred for matrix sizes on the order of $N = 50$ to 60.

TABLE I

Structure 1 $\theta_1 = 30^\circ$, $\theta_2 = 150^\circ$

Eigenvalue	Calculated Value	Grimes' Result
nu-1	2.439212	2.439211
nu-2	5.466996	5.466996
nu-3	8.477510	8.477309
nu-4	11.482985	-

TABLE II

Structure 2 $\theta_1 = 10^\circ$, $\theta_2 = 170^\circ$

Eigenvalue	Calculated Value	Grimes' Result
nu-1	1.621407	1.620624
nu-2	3.916836	3.915488
nu-3	6.188799	6.187171
nu-4	8.451585	8.450112

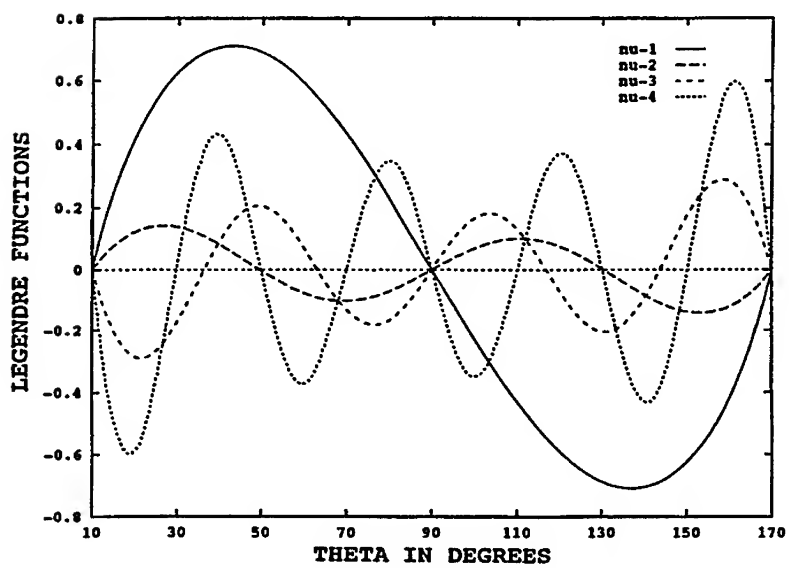


Figure 4.2 First four Legendre functions (eigenfunctions) for 10° biconical structure

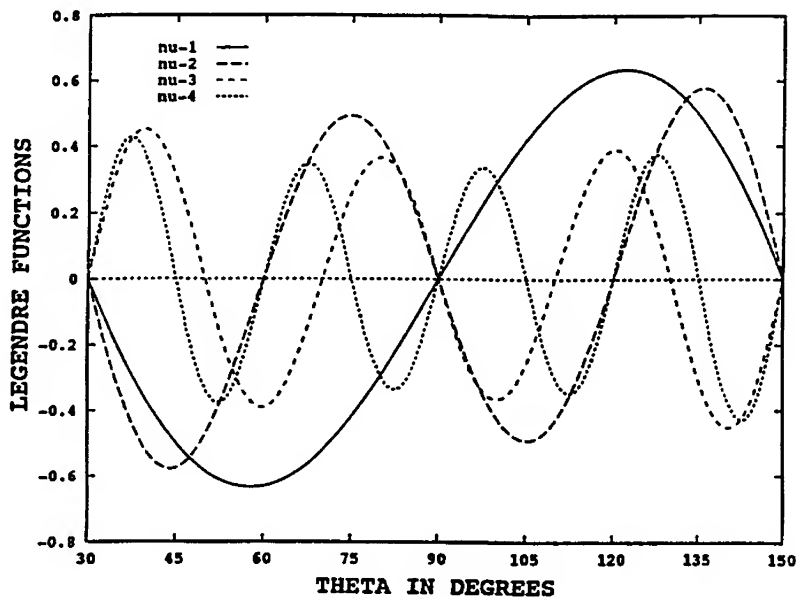


Figure 4.3 First four Legendre functions (eigenfunctions) for 30° biconical structure

V. CURVED RECTANGULAR WAVEGUIDE

The radial variation of the LM modal fields in a curved section of rectangular waveguide may be expressed as a superposition of Bessel functions:

$$y_v(r) = C_1 J_v(k_r r) + C_2 J_{-v}(k_r r) \quad (5.1)$$

where C_1 , C_2 , and v are determined by

$$J_{-v}(k_r r_1) J_v(k_r r_2) - J_{-v}(k_r r_2) J_v(k_r r_1) = 0 \quad (5.2)$$

$$y_v(k_r r_1) = y_v(k_r r_2) = 0 \quad (5.3)$$

Thus, it is necessary to determine the eigenvalues whose eigenfunctions satisfy Eqs. (5.2) and (5.3). For Bessel's differential equation: $A(x) = x^2$, $B(x) = x$ and $C(x, v) = x^2 - v^2$, in Eq. (2.1).

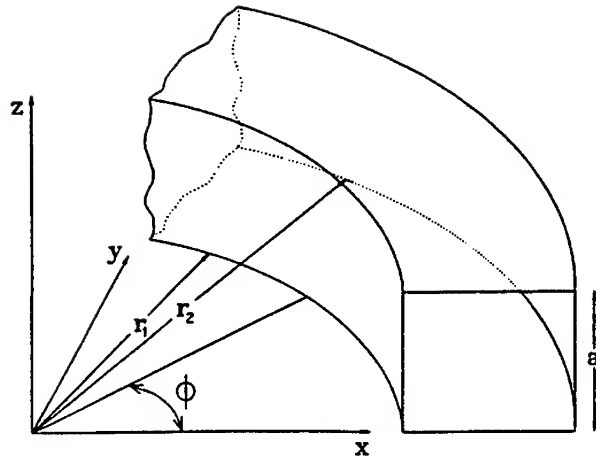


Figure 5.1 Geometry of curved rectangular waveguide

A curved section of rectangular waveguide with $k_r r_1 = 3$ and $k_r r_2 = 9$ was chosen for analysis. Table III shows the first five eigenvalues and figure 5.2 shows the corresponding eigenvalues. it should be noted that for this particular waveguide there is only one propagating mode (nu-1) and all the remaining modes a evanescent.

TABLE III
Eigenvalues (ν)

nu-1	5.1793
nu-2	1.5893i *
nu-3	6.5009i *
nu-4	9.9471i *
nu-5	13.1245i *

* non-propagating modes

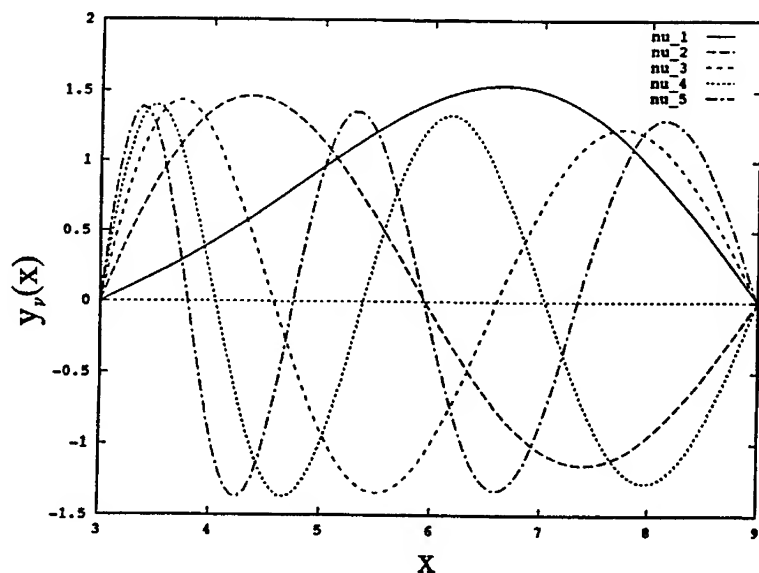


Figure 5.2 First five eigenfunctions for given waveguide

VI. CONCLUSIONS

This paper presents a generalized technique for determining non-integer eigenvalues for ordinary differential equations with transcendental solutions. The method was applied to a biconical radiating structure and to a section of a curved waveguide of rectangular cross section. To verify the technique the computed eigenvalues for the biconical structure were compared with results obtained by Grimes [7] using an asymptotic method. Excellent agreement was established between the two methods. The method proposed here is completely general and has the advantages that only the sign of the determinant needs to be computed and that the matrix size needed for convergence is small.

ACKNOWLEDGEMENT

The authors would like to thank Dr. Warren Perger for the use of his hypergeometric evaluator program [8] which was used for generating the numerical values of the eigenfunctions.

REFERENCES

1. S.A. Schelkunoff and H.T. Friis, Antennas Theory and Practice, (John Wiley and Sons, New York, 1952).
2. R.F. Harrington, Time-Harmonic Electromagnetic Fields, (McGraw-Hill Book Co., New York, 1961).
3. D.S. Jones, The Theory of Electromagnetism, (Pergamon Press, New York, 1964).
4. T.J. Rivlin, The Chebyshev Polynomials (John Wiley and Sons, New York, 1974).
5. W.H. Press, B.P. Flannery, S.A. Teukolsky and W.T. Vetterling, Numerical Recipes, (Cambridge University Press, New York, 1990), p. 243.
6. J.R. Wait, Electromagnetic Radiation for Conical Structures, in Antenna Theory, Part I, edited by R.E. Collin and F.J. Zucker (McGraw-Hill, New York, 1969), Chapter 12.
7. D.M. Grimes, Biconical receiving antenna, J. Math. Phys. **23**, 897, 1982.
8. M. Nardin, W.F. Perger and A. Bhalla, Numerical evaluation of the confluent hypergeometric function for complex arguments of large magnitudes, J. Comput. Appl. Math. **39**, 193, 1992.

**Evaluation of Method of Moments Codes:
University of Houston JUNCTION
and
Numerical Electromagnetic Code, Version 4**

**C. A. Deneris, J. C. Logan, J. W. Rockway
Naval Command Control and Ocean Surveillance Center
RDT&E Division
San Diego, CA 92152-5000**

ABSTRACT

The progress in the development of two advanced computer programs for antenna modeling is evaluated. Both codes use the method of moments to solve the appropriate surface and wire integral equations. The performance of the JUNCTION code, under development at the University of Houston, is compared to the performance of the Numerical Electromagnetic Code - Version 4 (NEC4), developed by the Lawrence Livermore National Laboratory. JUNCTION uses the electric field integral equation (EFIE) for both wires and surfaces, while NEC4 models bodies either as a wire mesh, or as a surface of magnetic field integral equation (MFIE) patches. Results are presented comparing the convergence and stability of NEC4 and JUNCTION for both wire antennas and wire antennas mounted on simple structures. These results contribute to a user's perception of the "value" of both codes.

1. INTRODUCTION

Electromagnetic (EM) modeling codes are an important tool in the Navy's analysis of shipboard antennas. As modeling costs increase and new composite materials come into service on board ships, the ability to quickly and accurately model the performance of shipboard EM systems becomes increasingly important. EM modeling codes provide a means to do this efficiently and cost effectively. A comparison is presented for two of these codes, the Numerical Electromagnetic Code - Version 4 (NEC4), developed at the Lawrence Livermore National Laboratory (LLNL) [1,2]; and JUNCTION, developed at the University of Houston [3,4,5]. Both codes use the method of moments (MOM) [6] to solve the appropriate surface and wire integral equations. A brief introduction is presented for both programs. Results are computed for a series of canonical problems to illustrate code performance. Where available, the computed results are compared with measurements.

1.1 Numerical Electromagnetic Code - Version 4 (NEC4)

Representing over twenty years of Department of Defense investment, the method of moments NEC4 is a fairly mature program. It is probably the best documented and most powerful wire antenna code available. NEC4 is user-oriented code, offering a comprehensive capability to analyze interactions of electromagnetic waves with conducting structures. To model complex structures, NEC4 uses an electric-field integral equation (EFIE) for wires and a magnetic-field integral equation (MFIE) for surfaces. The EFIE is well suited for thin wires, while the MFIE is attractive for modeling smooth surfaces which bound closed volumes. The EFIE wire grid is preferred for surfaces that are not smooth and not closed.

Principal advantages of the wire grid approach are that the geometry is easily specified for computer input and only one-dimensional integrals need to be evaluated. The wire grid modeling approach, however, often proves unsatisfactory where near field quantities such as surface currents or input impedance are desired. One obvious difficulty is in interpreting computed wire currents as equivalent surface currents. Also, the storage of energy in the neighborhood of a wire mesh is not completely equivalent to that of a continuous surface. As a result, computed resonant frequencies and reactive components of computed impedances are often shifted from their correct values. Modeling using the MFIE patch is limited to surfaces that are closed and smooth and, therefore, lacks application to many "real world" problems.

1.2 JUNCTION

JUNCTION, recently developed at the University of Houston, also attempts to improve modeling complex geometries. The JUNCTION computer code invokes the method of moments to solve a coupled electric field integral equation (EFIE) for the currents induced on an arbitrary configuration of perfectly conducting bodies and wires. There are three principal advantages to the JUNCTION formulation. First, the EFIE formulation for the surfaces of bodies, in contrast to the magnetic field integral equation (MFIE), applies to open bodies as well as closed bodies. Second, JUNCTION allows voltage and load conditions to be easily specified at terminals defined on the structure. Third, the triangular patches of JUNCTION are the simplest planar surfaces which can be used to model arbitrary surfaces and boundaries, and triangular patches permit patch densities to be varied locally so as to model a rapidly varying current distribution.

2. EVALUATION

An evaluation is performed to contribute to a user's perception of the validity for an electromagnetic modeling code. A perception of validity implies that the user has confidence that "within his or her modeling experience" he or she can produce "credible" analysis with a given electromagnetic code. The validity of an electromagnetic computer code is measured, in part, by its ability to replicate the results or solutions of known canonical problems with some degree of accuracy. There is, however a difference between the "actual" validity of a code and a user's perception of the validity.

2.1 Wire antennas

An evaluation of wire antennas usually begins with studies of dipole antennas of different lengths. These studies include both measured and theoretical data. Convergence tests for various lengths of dipoles demonstrate the accuracy that can be expected. A convergence test also provides the rationale for selection of segmentation density (i.e., the number of unknowns per wavelength of wire). The accuracy of the method of moments depends on meeting the thin wire criteria. Next, a study is made of the variation of conductance and susceptance as a function of dipole radius and changes in radius (i.e. stepped radius junction). Finally, convergence tests are made for antenna structures of multiple wires.

Both JUNCTION and NEC4 were tested for these various wire antenna problems. Both JUNCTION and NEC4 showed definite convergence and stability for short dipoles, and dipoles near resonance and anti-resonance. NEC4 converged somewhat faster. NEC4 reaches a stable answer with fewer unknowns than JUNCTION, as the number of unknowns is increased. For either code, however, the accuracy with respect to measurements is acceptable, if a sufficient number of unknowns is used. NEC4 performs satisfactorily for dipoles with both thin and thick wires, but JUNCTION produces an unacceptable anomaly in the transition from thin to thicker wires. This anomaly in JUNCTION has since been resolved. Both codes perform well for antennas with stepped wire radii. For short segments, NEC4 gives the appropriate dipole behavior for segments at least as short as 10^{-8} wavelengths. JUNCTION will provide proper dipole behavior for segments down to only about 10^{-4} segments. This limitation in JUNCTION can be resolved, but has not been coded at this time. The performance for multiple wire junctions was tested against measurements for TEE antennas. Both JUNCTION and NEC4 show similar behavior as the number of unknowns is increased. JUNCTION showed somewhat faster convergence and somewhat better accuracy than NEC4 for the problems chosen. Finally, both codes were tested for small loop behavior using a 22-sided wire polygon with one unknown per side as a model of a circular loop. NEC4 showed appropriate admittance behavior for loops as small as .005 wavelength in circumference, while JUNCTION was correct down to a circumference of .05 wavelength.

2.2 Wire antennas on structures

Three canonical problems were used to compare the structure modeling capabilities of the two codes. The first two problems consider the impedance over a range of frequency for a monopole mounted on a square plate. The plate measures 0.914 square meters, while the monopole is 0.421 meters long with a radius of 0.008 meters. Fifteen unknowns were used to model the monopole in both JUNCTION and NEC4. For the JUNCTION calculation, the surface is modeled by the EFIE triangular patch, while in NEC4, the plate is modeled as a wire grid equivalent. In the first problem, the input impedance is calculated for the monopole centered on the plate. Figure 1 compares the results of both programs with measurements [7]. The graphs present the data parametrically for the number of patches or segments used along a side of the plate. Table 1 gives the total number of unknowns for each calculation.

Figures 1 (a) and (b) show good agreement between JUNCTION and the measurements for both conductance and susceptance. Note that all the models are converged and stable over the given frequency band. Figures 1 (c) and (d) also show reasonable agreement between NEC4 and the measurements when the plate has at least six segments per side (99 unknowns). However, for all NEC4 models, the conductance diverges from the measurement after the first resonance. JUNCTION appears to converge more quickly (55 unknowns) and is more stable.

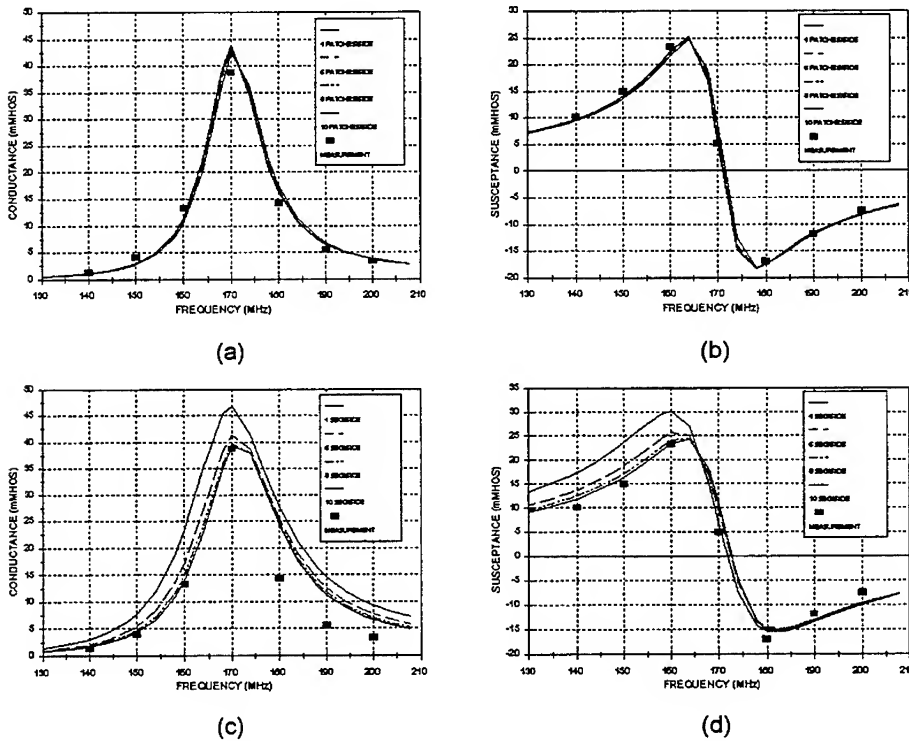


Figure 1. Input admittance of a 0.42 m. monopole centered on a square plate, (a),(b) JUNCTION; (c),(d) NEC4.

For the second problem the monopole is mounted vertically at the plate corner. The number of unknowns used for each case are the same as in the first problem. Figure 2 presents the calculated results for this model. Measurements were not available for comparison. Although no comparative measurements were available, some qualitative statements can be made. As in the first problem, figures 2 (a) and (b)

JUNCTION		NEC4	
Patches Per Side	Total Unknowns	Segments Per Side	Total Unknowns
4	55	4	55
6	111	6	99
8	191	8	159
10	295	10	235

Table 1. Number of unknowns used for monopole on a square plate calculation.

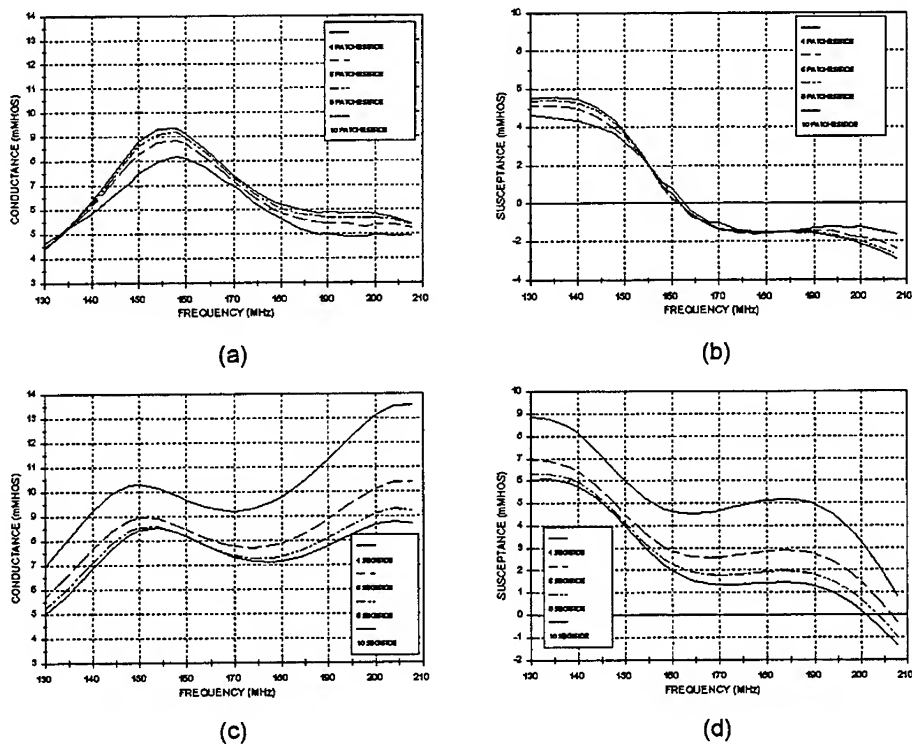


Figure 2. Input admittance of a 0.42 m. monopole at the corner of a square plate, (a),(b) JUNCTION; (c),(d) NEC4

show that JUNCTION converges quickly and is stable. Results for the models with six (111 unknowns) to ten patches per side are close to each other. In the case of NEC4 however, figures 2 (c) and (d) show that the results do not converge until the eight segment per side model (159 unknowns). Also, similar to the first problem, the conductance calculation diverges after the first resonance.

For the last problem, the impedance is calculated over a range of frequency for a monopole centered on a 0.1 square meter box. It is 0.06 meters high, with a radius of 0.008 meters, and it is modeled with fifteen unknowns. As with the plate, the NEC4 model of the box is a wire grid, while the JUNCTION model uses EFIE surface patches. Table 2 presents the total number of unknowns for each calculation.

Figure 3 presents the JUNCTION and NEC4 calculations compared with measurements found in [8]. The results are presented parametrically for the number of

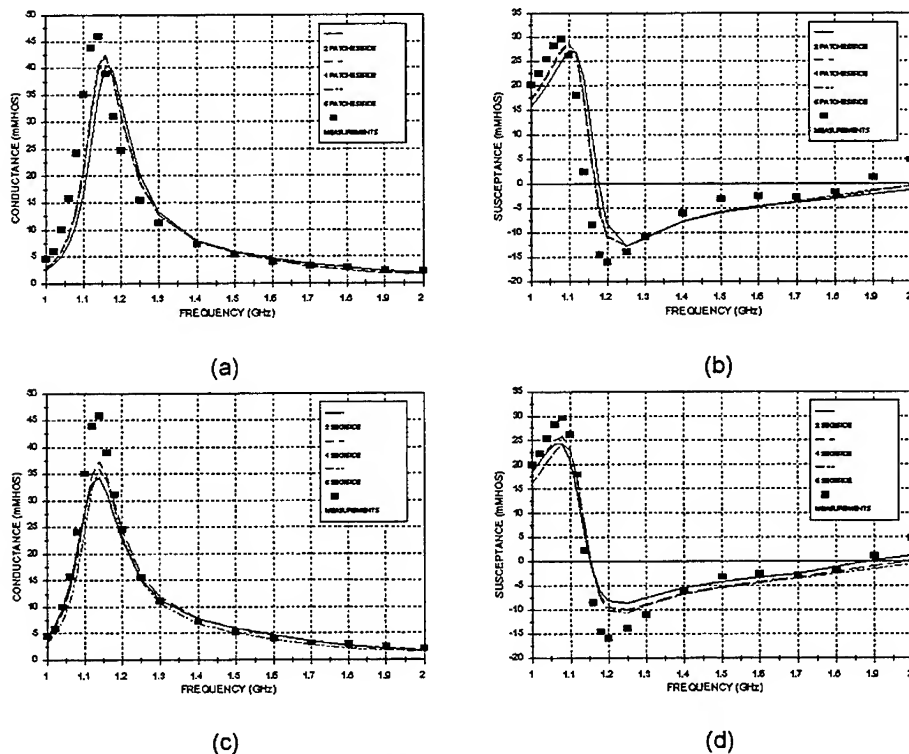


Figure 3. Input admittance of a 0.06 m. monopole centered on a square box, (a),(b) JUNCTION; (c),(d) NEC4.

JUNCTION		NEC4	
Patches Per Side	Total Unknowns	Segments Per Side	Total Unknowns
2	79	2	51
4	263	4	167
6	567	6	364

Table 2. Number of unknowns used for monopole on a square box calculation.

patches or segments on a side of the box. The graphs show that both codes converge quickly -- JUNCTION with 79 unknowns and NEC4 with 51 unknowns. Note that at resonance, both the conductance and susceptance calculations of JUNCTION approach the measurements better than the NEC4 calculations. This is especially true for the conductance (figures 3 (a) and (c)). It appears that JUNCTION would provide a slightly more accurate answer, but at the cost of more unknowns.

3. SUMMARY

The performance of JUNCTION and NEC4 has been explored. As expected, NEC4 is a mature wire antenna modeling code, that out performs JUNCTION in most respects for wire configurations. On the other hand, JUNCTION shows improved performance over NEC4 for wires mounted on simple structures (e.g., flat plates and boxes). At this stage in the development of JUNCTION, there is much improvement to be done to be competitive with NEC4. Improvements are necessary to make JUNCTION a viable competitor to NEC4 for general wire type problems. Many of these improvements have been identified. In addition the computational efficiency for wires and patches must be addressed. JUNCTION's performance for structures is encouraging. The JUNCTION approach also shows promise for modeling dielectric and magnetic surfaces. In summary, JUNCTION shows much promise for a future improved capability to model shipboard antenna configurations.

REFERENCES

- [1] G. J. Burke and A. J. Poggio, "Numerical Electromagnetic Code (NEC)—Method of Moments," NOSC Technical Document 116, Naval Ocean Systems Center, San Diego, CA, Jan. 1981.
- [2] G. J. Burke, "Recent Advances in NEC: Applications and Validation," UCRL-100651, Lawrence Livermore National Laboratory, Livermore, CA, Mar. 1989.
- [3] D. R. Wilton and S. U. Hwu, "Junction Code User's Manual: Electromagnetic Scattering and Radiation by Arbitrary Configurations of Conducting Bodies and

Wires," NOSC Technical Document 1324, Naval Ocean Systems Center, San Diego, CA, Dec. 1988.

- [4] S. U. Hwu and D. R. Wilton, "Electromagnetic Scattering and Radiation by Arbitrary Configurations of Conducting Bodies and Wires," NOSC Technical Document 1325, Naval Ocean Systems Center, San Diego, CA, Aug. 1988.
- [5] D. R. Wilton and S. U. Hwu, "JUNCTION: A Computer Code for the Computation of Radiation and Scattering by Arbitrary Conducting Wire/Surface Configurations," *6th Annual Review of Progress in Applied Computational Electromagnetics*, Mar. 1989.
- [6] R. F. Harrington, *Field Computations by Moment Methods*. New York: Macmillan, 1968.
- [7] E. T. Newman and D. M. Pozar, "Electromagnetic Modeling of composite Wire and Surface Geometries," *IEEE Trans. Antennas Propagat.*, vol. AP-26, no. 6, Nov. 1978.
- [8] S. Bhattacharya, S. A. Long, and D. R. Wilton, "The Input Impedance of Monopole Antenna Mounted on a Cubical Conducting Box," *IEEE Trans. Antennas Propagat.*, vol. AP-35, no. 7, Jul. 1987.

NEC2, NEC3, AND NEC4 ON A CONVEX MINI-SUPERCOMPUTER

Lance Koyama
NCCOSC RDTE DIV
Code 824
SAN DIEGO, CA 92152-7304

Abstract

A methodology was desired for optimizing the Numerical Electromagnetics Code (NEC) on a given platform. The platform chosen was the Convex mini-supercomputer. The matrix fill and factor times were the gauges of optimizing for speed. The software tool for choosing where to optimize was the profiler that comes with the FORTRAN compiler.

NEC2, NEC3, and NEC4 were evaluated. The test cases were models of 44, 300, 722, and 2286 segments. Three levels of built-in compiler optimizations were used. Additional optimizations were sought. The greatest speedup in runtime came with the use of LINPACK library routines specifically optimized for the Convex.

INTRODUCTION

This study gives a methodology for optimizing the NEC codes (or any method of moments code) for a given platform, in this case, a Convex mini-supercomputer.

The Convex Computer Corporation mini-supercomputers have become very popular because of their high power for the dollar. The model used for this study was the Convex C240 which is commonly classified as a mini-supercomputer. Its vector architecture makes it a supercomputer and it is smaller than a Cray, making it a mini. Its cogent features are as follows:

- 4 processors - 50 MegaFLOPS each
- Each processor includes scalar and vector processing units
- Peak performance - 200 MegaFLOPS
- LINPACK1000 benchmark: 162 MegaFLOPS
(Cray Y-MP): 305 MegaFLOPS
- Whetstone benchmark: 38 MIPS
(Cray Y-MP): 26 MIPS
- MULTIfunits benchmark: 4900
(Cray Y-MP): 6000

Each processor has

- 8 vector registers of 128 elements each
- Each element (word) consists of 64 bits
- There are 3 independent functional unit controllers:
 - Load and Store
 - Multiply and Divide
 - Add and Logical

SCOPE

NEC runs were made on various combinations of the following parameters:

Codes

<u>Name</u>	<u>Number of Lines</u>	<u>Number of Routines</u>
NEC2	8,734	81
NEC3	9,780	99
NEC4	16,039	207

NEC2 was chosen for its complete documentation; NEC4, for being the latest and greatest and NEC3 to round out the family.

Compiler Optimizations - None, Scalar, Vector, Parallel -

There are three types of automatic optimizations that come with the FORTRAN compiler. The scalar optimization performs a great many types of both machine dependent and machine independent optimizations on the scalar level. The vector optimization seeks loops that are actually dealing with arrays. As much as possible, the entire loop is converted to vector operations. The parallel optimization operates only within individual routines. It tries to spread the processing among the four processors if it would be more efficient.

In the following discussion, the optimizations are labeled as follows.

<u>Optimization</u>	<u>Types</u>
0	None
1	Scalar
2	Scalar + Vector
3	Scalar + Vector + Parallel

Models - 44 segment, 300 segment, 722 segment, 2286 segment -

The 44 segment model is a one wavelength loop. The 300 segment model is a monopole on a ground plane. The 722 segment model is the US Navy's Spruance (DD-963) class destroyer segmented for up to 6 MHz problems. The 2286 segment model is the same ship segmented for 30 MHz problems.

Information Gathered

For each run, the following information was gathered:

- Matrix fill, matrix factor, and total run-time
- A profile of the run listing each routine and operation used and for each:
 - Percentage of total run-time used in calls to the routine or operation
 - The number of calls to the routine or operation
 - The time used in a call to the routine or operation

For some of the runs, some additional information was gathered: the percent used of all the processors, the amount of memory used, the physical reads and writes, the number of page faults, and the number of page faults paged out to disk.

Manual Optimization

Looking at the profiles of the runs, routines were chosen to be optimized beyond the automatic optimizations of the quite intelligent compiler.

RESULTS

Verification

The impedance of an antenna on each of the models was used to verify that a run was valid.

Profiles

To gauge the performance of each run, the profiler that comes with the FORTRAN compiler was used. There is some overhead in its use as it performs its counts and timings as seen in the examples below for a 722 segment model.

	<u>Fill</u>	<u>Factor</u>	<u>Total</u>
NEC3, optim.2, w/o profiler	106.943	37.999	148.343
with profiler	120.596	32.316	157.349
NEC4, optim.3, w/o profiler	128.441	49.368	187.582
with profiler	155.841	45.500	213.442

All times in the following data and discussion presume the use of the profiler. You will see in the following profiles an item called "mcount". This is one of the profiler overhead items.

The following series of profiles shows the differences between NEC2, NEC3, and NEC4 for a 722 segment model using compiler optimization 2 in all cases. The routines or functions that take up more than 5% of the total runtime are shown.

NEC2		<u>Fill</u>	<u>Factor</u>	<u>Total</u>
		177.541	32.436	213.422
%time	cumsecs	#call	ms/call	name
15.7	34.84	521284	0.07	_efld_
15.4	69.07	1021498	0.03	_eksc_
15.2	102.82	1	33750.00	_factr_
14.7	135.38	4901342	0.01	_gf_
9.8	157.13		21750ms	mcount
9.1	177.24	1021498	0.02	_intx_
7.5	194.00	2042996	0.01	_gx_
6.5	208.49	722	20.07	_cmww_

NEC3		<u>Fill</u>	<u>Factor</u>	<u>Total</u>
		120.596	32.316	157.349
%time	cumsecs	#call	ms/call	name
20.5	33.62	1	33620.00	_factr_
17.1	61.58	887915	0.03	_eksc_
15.7	87.28	521284	0.05	_efld_
11.5	106.19		18910ms	mcount
10.6	123.57	722	24.07	_cmww_
5.5	132.50	1351794	0.01	_mth\$e_exp

NEC4		Fill	Factor	Total
		146.313	32.366	190.199
%time	cumsecs	#call	ms/call	name
17.1	33.82	286	118.25	_factr_
14.9	63.24	887913	0.03	_eksclr_
13.5	89.95		26710ms	mcount
10.8	111.23	1042568	0.02	_efldsg_
8.6	128.22	722	23.53	_cmww_

The following show the differences in profiles as the size of the model changes. (NEC4 is used with optimization 3).

300 segments		Fill	Factor	Total
		23.873	4.436	30.287
%time	cumsecs	#call	ms/call	name
21.0	6.00	177310	0.03	_eksclr_
20.9	11.96		5965ms	mcount
10.4	14.95	180000	0.02	_efldsg_
9.0	17.52	300	8.60	_cmww_
6.3	19.32	1	1800.00	_factr_
5.8	20.98	544795	0.00	_mth\$C_div

722 segments		Fill	Factor	Total
		155.841	45.500	213.442
%time	cumsecs	#call	ms/call	name
19.8	38.00		38000ms	mcount
15.5	67.62	887913	0.03	_eksclr_
9.7	86.29	1042568	0.02	_efldsg_
9.2	103.96	286	61.78	_factr_
9.2	121.52	722	24.32	_cmww_
5.0	131.03	3178604	0.00	_mth\$C_div

2286 segments		Fill	Factor	Total
		1437.447	5678.125	7220.752
%time	cumsecs	#call	ms/call	name
52.3	1747.24	756	2311.16	_factr_
10.0	2082.34		335105ms	mcount
9.8	2410.93	9918973	0.03	_eksclr_
5.6	2596.86	10451592	0.02	_efldsg_
5.4	2776.95	2286	78.78	_cmww_

2286 segments	LINPACK routines			
		Fill	Factor	Total
		1451.863	700.771	2304.245
%time	cumsecs	#call	ms/call	name
18.4	334.04		334040ms	mcount
18.3	665.41	9918973	0.03	_eksclr_
10.6	858.13	10451592	0.02	_efldsg_
10.4	1046.93		188800ms	_cgefa_
9.7	1223.06	2286	77.05	_cmww_
5.3	1319.97	10451592	0.01	_ekscsz_
5.0	1410.89	31597174	0.00	_mth\$C_div

The last profile was of a run using LINPACK routines, discussed next.

Manual Optimization

A widely available set of routines for solving linear equations, called LINPACK, was available specifically optimized for the Convex hardware. Two routines were chosen to replace the matrix factor and solve portions of the NEC codes.

Function	NEC routine	LINPACK routine
Factor matrix	factr	cgefa
Solve matrix	solve	cgesl

In both cases, because of the way NEC stores matrices, the interaction matrix had to be transposed before and after the LINPACK routines were used.

Next, routines high in the profile list were sought that could benefit from manipulation so that the compiler could vectorize them. In NEC2: *efld*, *eksc*, *gf*, *intx*, and *test* all had no loops. In NEC4: *eksclr*, *efldsg*, and *ekscsz* all had no loops. In both: *cmww* was already automatically 70% vectorized by the compiler. All other routines consumed less than 5% of the total runtime. It was not considered worthwhile to continue the optimization effort.

Runtimes

The following lists the impedances and runtimes of the significant runs.

Segments	NEC	Optim	LinPack	Impedance		Times (seconds)		TOTAL
				R	X	FILL	FACTOR	
44	2	2		100.6	-139.1	0.36	0.02	0.47
44	4	3		100.3	-140.6	0.47	0.05	0.69
44	4	3	yes	100.3	-140.6	0.47	0.01	0.66
300	2	0		232.3	-36.4	9.54	19.28	29.86
300	2	1		232.3	-36.4	9.20	12.97	22.98
300	2	2		232.3	-36.4	10.23	2.36	13.30
300	2	3		232.3	-36.4	10.63	4.39	15.80
300	4	3		240.3	-37.1	23.87	4.44	30.29
300	4	3	yes	240.3	-37.1	24.12	1.71	27.86
722	2	0		20.3	-0.5	168.27	268.14	441.56
722	2	1		20.3	-0.5	176.80	180.83	361.73
722	2	2		20.3	-0.4	177.54	32.44	213.42
722	2	2	yes	20.3	-0.4	176.06	22.08	202.21
722	2	3		20.3	-0.4	179.58	45.46	228.81
722	3	2		19.7	-2	120.60	32.32	157.35
722	4	2		23	0.5	146.31	32.37	190.20
722	4	3		23	0.5	155.84	45.50	213.44
722	4	3	yes	23	0.5	157.37	22.18	193.51
2286	4	3		34	20.8	1437.45	5678.13	7220.75
2286	4	3	yes	34	20.8	1451.86	700.77	2304.25

In matrix format

FILL RUNTIMES (sec)

Segments	NEC	Optimization				LinP	3	LinP
		0	1	2				
44	2			0.36				
44	4					0.47	0.47	
300	2	10	9	10		11		
300	4					24	24	
722	2	168	177	178	176	180		
722	3			121				
722	4			146		156	157	
2286	4					1437	1452	

FACTOR RUNTIMES (sec)							
Segments	NEC	Optimization			LinP	3	LinP
		0	1	2			
44	2			0.02			
	4					0.05	0.01
300	2	19	13	2		4	
	4					4	2
722	2	268	181	32	22	45	
	3			32			
	4			32		46	22
2286	4					5678	701

TOTAL RUNTIMES (sec)							
Segments	NEC	Optimization			LinP	3	LinP
		0	1	2			
44	2			0.47			
	4					0.69	0.66
300	2	30	23	13		16	
	4					30	28
722	2	442	362	213	202	229	
	3			157			
	4			190		213	194
2286	4					7221	2304

Figures 1, 2, 3, 4, and 5 graphically show the trends in the data.

CONCLUSIONS

Just as important as the speed of the machine is the way the software utilizes its resources. For the case of the Convex computer used in this study, the automatic optimizations supplied with its FORTRAN compiler cut the time for a NEC run in half for a 722 segment model.

Library routines optimized for a machine's hardware should be used whenever possible to replace existing code. Two routines especially appropriate for a method of moments code are the matrix factor and matrix solve routines from the LINPACK library. These had been optimized for the Convex hardware. For a 2,286 segment model, they cut the factor time by a factor of 8 resulting in an overall runtime improvement of a factor of 3.

REFERENCES

1. G. J. Burke and A. J. Poggio, *Numerical Electromagnetics Code (NEC) - Method of Moments*, Lawrence Livermore National Laboratory, Report UCID-18834, January 1981
2. A. Ralston, *A First Course in Numerical Analysis*, McGraw-Hill Book Company, 1965
3. "VECLIB Programmer's Reference", CONVEX Computer Corporation, August 1991

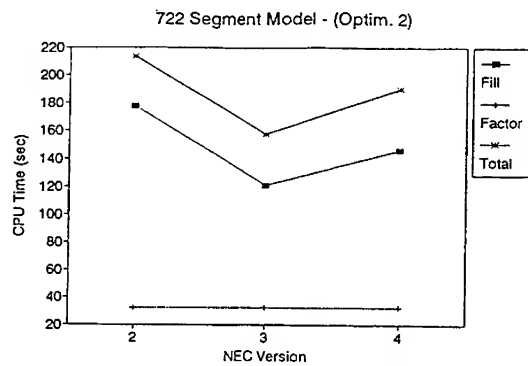


Figure 1. Runtime Variation with NEC Version Number

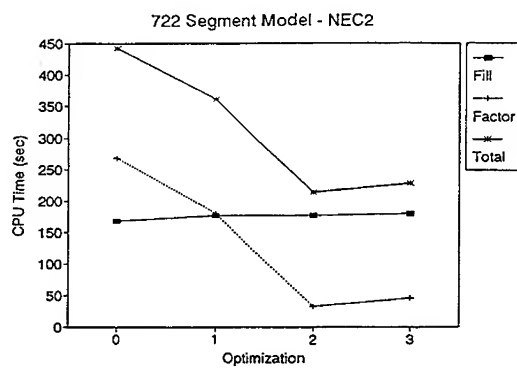


Figure 2. Runtime Variation with Optimization Level

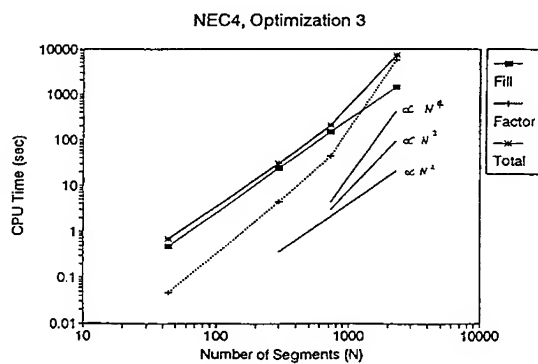


Figure 3. Runtime Variation with Number of Segments

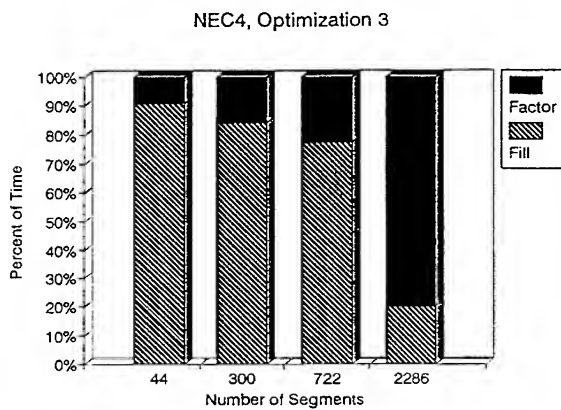


Figure 4. Percentage of Time in Fill and Factor for Different Model Sizes

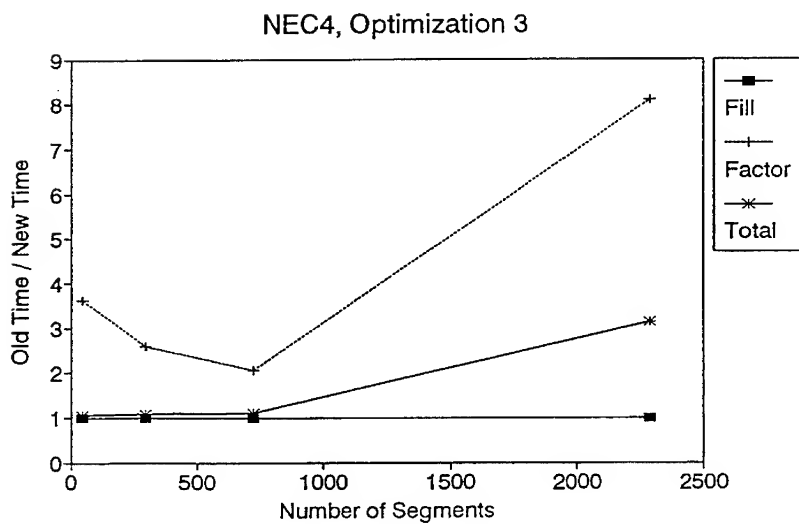


Figure 5. Improvement by Using LINPACK Routines

SESSION 2 - "CANONICAL PROBLEMS WORKSHOP"

(NO PUBLISHED PAPERS)

Moderators: Dr. Andrew Peterson and Capt. Dennis Andersh

SESSION 3 - "MOMENT METHOD THEORY AND APPLICATIONS"

Chair: Dr. Paul M. Goggans

DEVELOPMENT OF A BANDLIMITED BASIS SET FOR THIN WIRE METHOD OF MOMENTS SCATTERING PROBLEMS

G.E. Mortensen, C.C. Cha
Syracuse Research Corporation
Merrill Lane
Syracuse, NY 13210

ABSTRACT: A method of moments formulation based on the cardinal series expansion for bandlimited signals is described. It is demonstrated that the induced current on wire scatterers tends to be spatially bandlimited. A thin wire code is described and results are presented which demonstrate that the code requires significantly fewer unknowns than an equivalent code with triangle basis functions to achieve similar accuracy. Extension of the approach to surface scattering is discussed.

1.0 INTRODUCTION

In applying the Method of Moments (MOM) solution to scattering problems, the primary limitation is the often excessive computation required for the solution of the resulting matrix equations. In order to reduce the matrix size in the MOM solution, one must find an efficient representation for the unknown function (usually the induced current) so that fewer unknowns are required to achieve sufficient accuracy.

Recent work by Bucci and Franceschetti [1] has suggested that the scattered fields in the near zone are nearly spatially bandlimited ("quasibandlimited") and, therefore, may be efficiently represented according to the concepts of sampling theory. We claim that the induced currents on many targets share similar quasibandlimited properties. In this paper, we numerically demonstrate that the induced currents on finite wire scatterers are, in fact, quasibandlimited. We, furthermore, describe the use of a bandlimited current expansion basis set that provides an accurate current representation and tends to minimize the effect of residual representation error on the MOM solution.

A similar approach has been applied recently by Herrmann [2] on 2-dimensional cylinder scattering problems. We will present the results of a 3-dimensional thin wire code. This code is shown to provide a 50% or better savings in matrix dimension for a given accuracy when compared to other traditional (e.g., pulse, triangle) implementations over a variety of wire geometries.

The cost of this reduction in unknowns is an increase in matrix fill time per unknown due to the increased complexity of the basis set. However, the ultimate motivation for this approach is to reduce the computational cost of large 3-dimensional *surface* problems. On a surface, a factor of 2 savings in unknowns per wavelength translates to a factor of 4 savings in unknowns, a factor

of 16 in matrix elements to be filled, and a factor of 64 in matrix factor time (LU decomposition). Therefore, the potential computational savings are quite large, easily offsetting the increased fill time per unknown.

2.0 SPATIAL BANDWIDTH OF INDUCED CURRENTS

The spectrum of the current on an arbitrarily shaped wire scatterer cannot be determined analytically. We have empirically examined the spectrum (the Fourier transform of $I(l)$, where l represents distance along the wire) of the computed current for a variety of wire geometries. These results were computed using an "exact" (converged) MOM solution using the thin-wire formulation (current expanded on a filament, tested on a wire surface) [3] with linear (triangle) basis functions.

The current spatial frequency spectrum versus incident angle of a finite straight wire is shown in Figure 1. As expected, at each angle of the spectrum consists primarily of three peaks centered at spatial radian frequencies k , $-k$, and $-k \cos \theta$, where k is the wavenumber of the incident plane wave and θ is the incident angle. The width of the peaks is inversely proportional to the length of the wire. Almost all of the spectral energy is confined to a lowpass band slightly larger than k ; the current is said to be "quasibandlimited".

The quasibandlimited spectral characteristic is not limited to straight wires. For curved and bent wires of moderate to large electrical size, we have observed that the spectrum is essentially limited to a band slightly larger than k as in the straight wire case. Examples of currents and resulting spectra for a bent wire and a circular wire loop are shown in Figures 2 and 3, respectively.

One may observe that the spectral distribution for the straight wire lends itself to a "physical" expansion of the form

$$I(z) = c_1 e^{jk \cos \theta z} + c_2 e^{-jkz} + c_3 e^{jkz} \quad |z| < L/2.$$

This form may be utilized directly in MOM by using the three exponential terms as full-domain expansion functions and solving for the unknowns c_1, c_2, c_3 [4]. However, such an approach is not readily generalized to arbitrary curved wires or surfaces. A robust approach relying only on the bandwidth properties and not the specific form is described in the next section.

3.0 SAMPLING THEORY AND EXPANSION FUNCTIONS

In Section 2, we demonstrated that the current on a wire scatterer is essentially spatially bandlimited to a lowpass band, B , where B is only slightly larger than the frequency of the incident plane wave. Sampling theory states that a function whose spectrum is limited to the frequency band $[-B, B]$ may be exactly represented by the cardinal series expansion

$$f(x) = \sum_i f(iX) \frac{\sin(\frac{\pi}{X}(x-iX))}{\frac{\pi}{X}(x-iX)} \quad \text{for } X < \frac{1}{2B}$$

Assuming that the current is a quasibandlimited function, a good choice for the current expansion on a thin wire is seen to be

$$J(l) = \sum_{k=1}^N J(k\Delta l) b(l - k\Delta l) \quad \text{with basis function} \quad b(l) = \text{sinc}\left(\frac{l}{\Delta l}\right) = \frac{\sin(\pi \frac{l}{\Delta l})}{\pi \frac{l}{\Delta l}}$$

where Δl is the sample increment along the wire length. Because the current is limited to a frequency only slightly higher than that of the illuminating field, we should be able to achieve a very good current representation and, consequently, an accurate MOM solution with marginally more than 2 basis functions per wavelength. This is contrary to the widely held belief that 6 to 10 basis functions per wavelength are required for an accurate MOM solution.

The sinc basis functions have a number of advantageous properties in addition to representation accuracy. They are "quasilocalized" in that a basis function has a large impact mainly on the fields in its vicinity. This property, which is shared by subdomain basis functions such as pulses and triangles, tends to lead to well-conditioned impedance matrices. The nulls of the basis function occur at the neighboring sample points (nodes). Therefore, the current is easily forced to zero at the wire ends by omitting the basis functions that would be associated with the end nodes. To reduce matrix fill time, the sinc functions may be truncated to a finite domain with small loss in accuracy, as described in Section 4.

4.0 MOM IMPLEMENTATION AND RESULTS

The bandlimited (sinc) basis function was incorporated into a thin wire code. Galerkin's approach is used for testing. The potential and testing integrals are performed numerically using 5 rectangular rule integration points per subsection for the potentials and 3 points for testing. This integration procedure was found empirically to provide low error levels. The basis function is a truncated sinc function that spans $2M$ subsections including the sinc mainlobe and $M-1$ sidelobes on each side. Typically $M=2$ is adequate, although the error due to truncation is somewhat reduced for larger M . Other sampling-theoretic basis functions with reduced truncation error could be used at the cost of a slight increase in sampling rate. Truncation error in the context of interpolating antenna fields is discussed in [5]. The results from the bandlimited basis function are compared to those from a triangle basis function code with all other relevant parameters constant.

A comparison of 5λ wire current solutions for linear (triangle) and truncated sinc basis functions is shown in Figure 4. The resulting bistatic RCS comparison is shown in Figure 5. An RCS comparison for a 10λ wire is shown in Figure 6. In this case, it is seen that the bandlimited basis functions with 2.5 samples per wavelength ($M=4$) perform approximately as well as the triangles with 7 samples per wavelength. Similar results have been obtained over a variety of incident angles and wire lengths.

The current spectrum of a 5λ circumference wire loop was shown previously in Figure 3 and seen to be quasibandlimited. The corresponding RCS results are displayed in Figure 7. Similar results were obtained at various aspects and for other bent and curved wires as well.

5.0 CONCLUSIONS AND FUTURE INVESTIGATION

The truncated sinc basis functions have been shown to have the desirable properties of subdomain basis functions and to be more efficient than the triangle (linear) functions on wire scatterers in terms of unknowns required for a desired accuracy. We are currently developing a 3-dimensional surface scattering code using bandlimited basis functions. Our preliminary results indicate that surface currents on smooth objects are quasibandlimited and that, even on objects with surface discontinuities, the bandlimited functions are more efficient than the widely used Rao-Wilton-Glisson (RWG) basis functions. Implementation issues being addressed include current expansion in parameteric space, the bandwidth characteristics of typical target geometries, the use of non-uniform sampling, and fast algorithms for matrix filling.

REFERENCES

- [1] O. Bucci and G. Franceschetti, "On the Spatial Bandwidth of Scattered Fields", *IEEE Trans. AP*, Vol. AP-35, No. 12, Dec. 1987
- [2] G. Herrmann, "Note on Interpolational Basis Functions in the Method of Moments", *IEEE Trans. AP*, Vol. 38 No. 1, Jan. 1990
- [3] R. Harrington, Field Computation by Moment Methods, Robert E. Krieger Co., Malabar, Florida, 1968, 1982
- [4] A. Chatterjee, J. Volakis, and W. Kent, "Scattering by a Perfectly Conducting and a Coated Thin Wire Using a Physical Basis Model", *IEEE Trans. AP*, Vol. 40, No. 7, July 1992
- [5] O. Bucci and G. Di Massa, "The Truncation Error in the Application of Sampling Series to Electromagnetic Problems", *IEEE Trans. AP*, Vol. 36, No. 7, July 1988

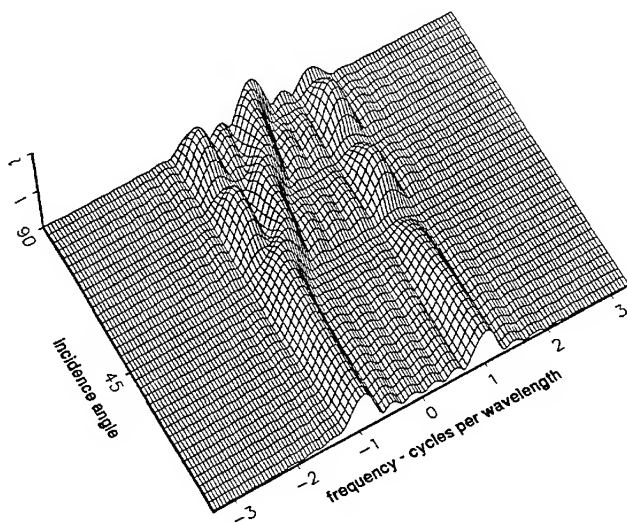


Figure 1. Current Spectrum versus Incident Angle for 3λ Wire

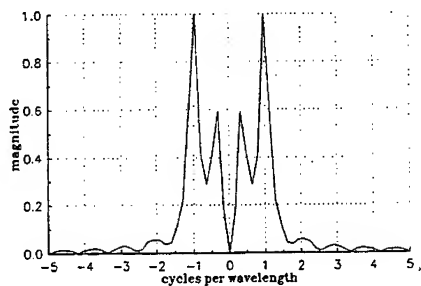
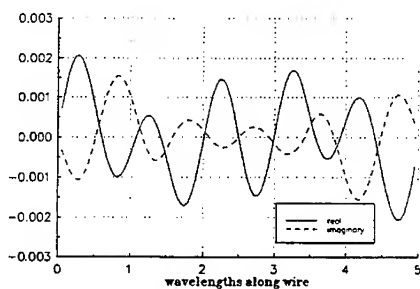
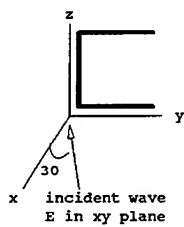


Figure 2. Current on 5λ Bent Wire

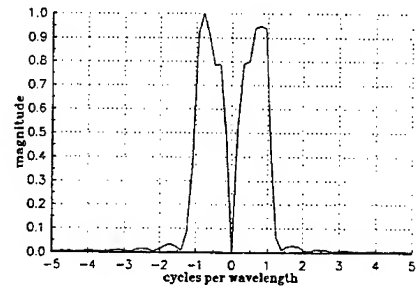
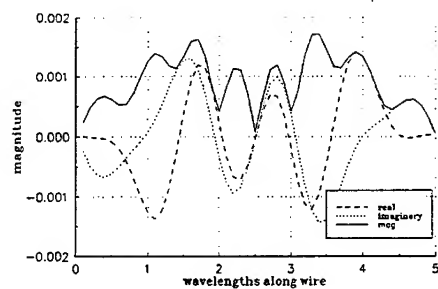
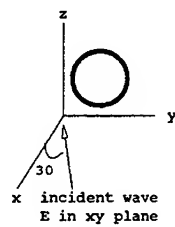


Figure 3. Current on 5λ Circumference Wire Loop

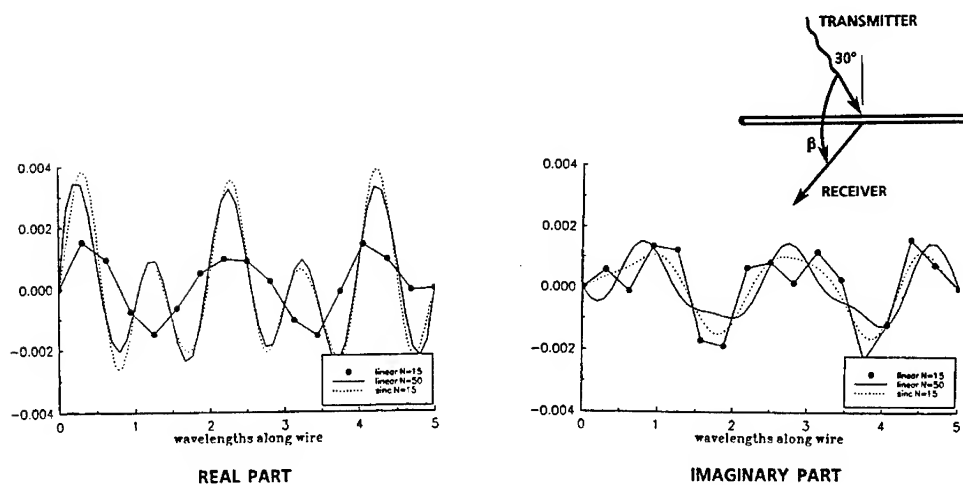


Figure 4. Current Solution for 5λ Wire

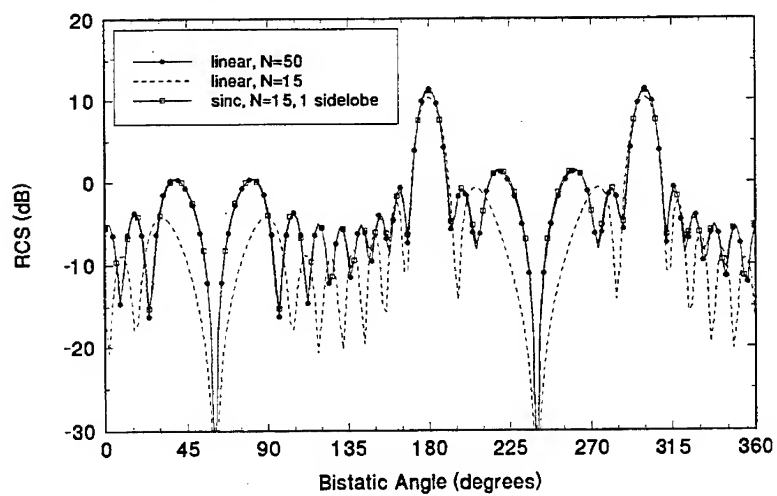


Figure 5. RCS Solution for 5λ Wire

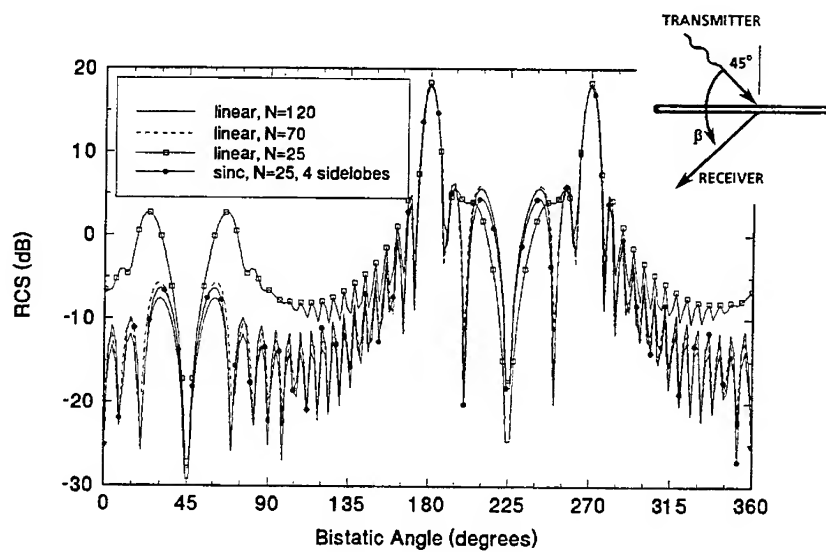


Figure 6. RCS Solutions for 10λ Wire

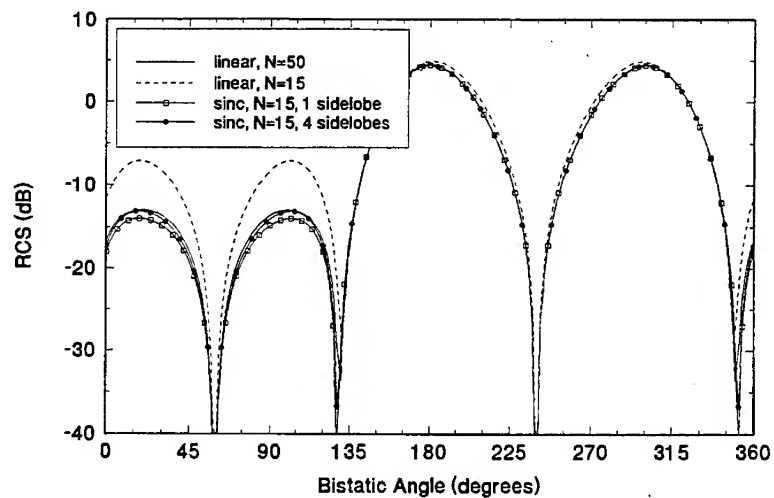


Figure 7. RCS Solutions for 5λ Circumference Loop

A Moment Method Formulation for Electromagnetic Radiation and Scattering from Composite Bodies of Revolution

Pierre Steyn and David B. Davidson
Department of Electrical Engineering
University, Stellenbosch, 7600

Abstract

A Moment Method (MM) code has been developed for the prediction of radiation and scattering from composite bodies of revolution. A composite body of revolution (BOR) is one composed of different homogeneous dielectric regions as well as, but not necessarily including, a conducting region. The various regions can be arranged in such a way that the BOR is inhomogeneous in both the radial and axial dimensions. The dielectric regions may be lossy, but the conducting regions are perfect electrical conductors. Radiation is from apertures mounted in a conducting region of the BOR. The integral equation formulation and the particular MM used is described briefly. Numerical results for scattering from a composite cylinder, compared to measurements, are presented. A practical antenna configuration consisting of a monopole mounted on a disc is described. The antenna is modeled with and without a radome. Numerical results of the antenna's input reflection and radiation pattern are compared to measurements.

1 Introduction

A Moment Method (MM) code has been developed for the prediction of radiation and scattering from composite bodies of revolution. A body of revolution (BOR) is a body obtained by rotating a two dimensional curve, referred to here as the generatrix, around an axis. In this paper a composite BOR is one composed of different homogeneous dielectric regions as well as, but not necessarily including, a conducting region. The dielectric regions may be lossy. The various regions can be arranged in such a way that the BOR is inhomogeneous in both the radial and axial dimensions. A generic example of such a BOR is shown in figure 1.

The code is based on the formulation presented in [1], which is for plane wave scattering. The formulation has been extended to predict radiation from rotationally asymmetrical apertures (as well as rotationally symmetric apertures which is a special case) mounted in a conducting portion of the BOR. The code was partly described in a previous paper [2]. It could then only handle problems consisting of layered geometries but has since been extended to cope with problems involving intersections of three regions, as occur in figure 1.

The code has been developed to investigate the suitability of the formulation to predicting radiation from antennas mounted on bodies that are penetrable by electromagnetic fields. Analytical solutions of such problems are in many cases impossible, thus a numerical approach is necessary. Examples of such problems are antennas covered by dielectric radomes, dielectrically clad low profile antennas, antennas mounted on composite vehicles and medical applications of electromagnetics. As the code was intended merely to demonstrate the suitability of the formulation it was specialized to problems involving BOR's to limit complexity and computational costs. The formulation does not carry this restriction, however, and a code based on it could be developed for more general bodies.

In [2] numerical results were presented for problems involving spherical layered geometries which compared favorably with solutions obtained using spherical wave function expansions (SWFE). Results are presented here for problems involving region intersections.

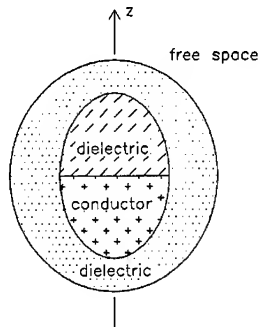


Figure 1: Cross section through the axis of rotation of a generic composite body of revolution.

2 Formulation and Moment Method solution

The formulation of the problem and the MM solution is summarized here, details are given in [1] and [2]. The latter reference also discusses the equivalence principle on which the formulation is based.

In the formulation of the problem the boundary enclosing each dielectric region, including free space, is replaced by equivalent electric and magnetic surface currents. The electric and magnetic fields within each region are then expressed as a sum of excitation fields, that may exist within that region, and integro-differential operators of the equivalent surface currents. The equations for all of the regions are then coupled via the boundary conditions on each of the interfaces between the regions. On a dielectric-dielectric interface the tangential components of the fields are continuous, while on a dielectric-conductor interface the tangential electric field is zero (thus the magnetic surface currents are also zero). The resultant equations constitute a set of coupled Fredholm equations which can be solved for the equivalent surface currents.

The MM solution is specialized for BOR's. The equivalent surface currents are expanded in terms of coefficients and expansion functions. Overlapping triangular expansion functions are used along the generatrix (in the plane of the generatrix) while modal expansion functions are used around the BOR.

The generatrix of the BOR is approximated by a finite set of points. Each triangle function spans five of these points. The number of points used to describe the generatrix depends on the frequency of the excitation – the spacing of the points should be such that the distances between apexes of the triangle functions are less than or equal to a tenth of the wavelength.

The modes of the modal expansion, which is a Fourier series expansion are orthogonal and thus uncoupled. Each mode can thus be solved independently from all the other modes. The number of modes, i. e. the number of terms in the Fourier series, required for a converged solution depends on the electrical size of the problem. However, a rotationally symmetric excitation, such as a rotationally symmetric aperture, only couples with the zero mode, thus only this mode need be solved in such a case; and an axially incident plane wave only couples with modes ± 1 , thus only these modes need be solved in this case.

The Galerkin form of the MM solution is used, thus the testing functions are the complex conjugate of the expansion functions (the symmetric inner product is used). The current expansions are substituted into the integral equations and the inner products are formed with the testing functions. This results in a set of matrix equations, one for each mode, which are then solved to yield the expansion coefficients. Computationally tractable formulas for the elements of the interaction matrix (often referred to as the impedance matrix) are given in [1]. The interaction matrix is symmetric thus only

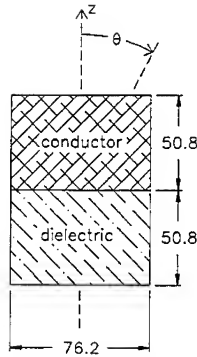


Figure 2: Cross section through a aluminium-plexiglas cylinder. Dimensions are in mm.

the lower triangle matrix need be computed and stored.

For scattering problems plane wave excitations are used, while for radiation problems the excitation is an aperture in a conducting surface of the BOR. The algorithms used for incorporating apertures in the geometry and for computing the excitation array were taken from [3] and the theory is described in [4].

3 Scattering by a composite cylinder

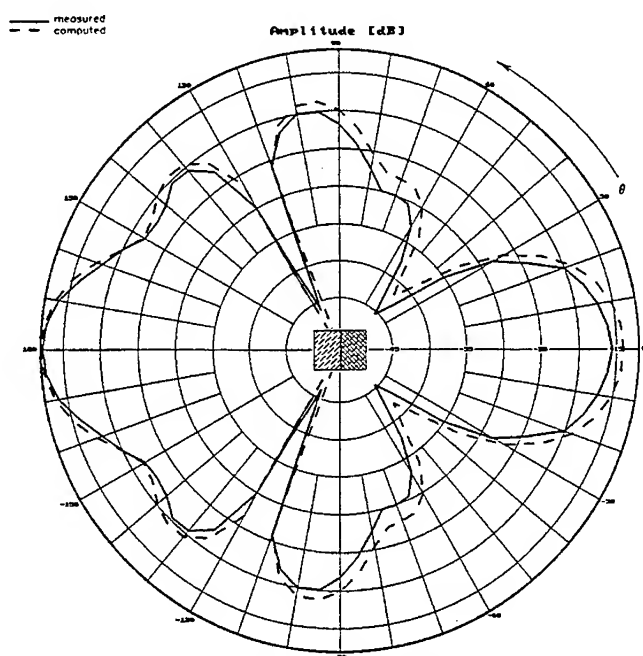
Several results for scattering by composite BOR's are given in [1] which have been successfully repeated by our code. One of these results, which we present here, is scattering by a conductor-dielectric cylinder. The geometry of the problem is shown in which figure 2. The dielectric is plexiglas and the conductor is aluminium.

The backscatter cross section of the cylinder was computed at 3 GHz at which plexiglas has a relative permittivity of $\epsilon_r = 2.6 - j0.015$ [5, Appendix B]. The computations required 4 circumferential modes with 68 unknown coefficients per mode. Results computed by our code are compared to measurements in figure 3. The measurements were taken from figure 8 of [1] where the measurement set up is also described. There is also good agreement between our result and the computed result in [1] although the latter computation ignored the loss. It appears that if the imaginary part of ϵ_r is less than a hundredth of the real part, it can be safely ignored in this case.

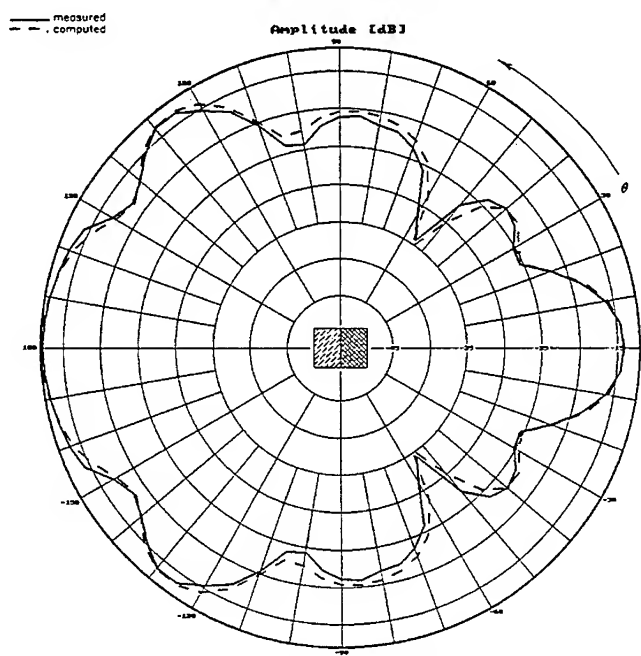
The number of triangle functions used on the dielectric surface was such that the segment length is less than or equal to one tenth of the free space wavelength. It was found that if the segment length was reduced to one tenth or less of the wavelength in the dielectric, the computed result is unchanged. Thus, at least for a relative permittivity of this magnitude and this geometry, the free space wavelength can be used in determining the number of triangle functions required.

4 Radiation from a monopole on a disc

In order to verify the capabilities of the code in predicting radiation, a practical antenna configuration was designed. The configuration is shown in figure 4. It consists of a monopole mounted on a disc which is mounted on a larger disc. The monopole is merely the centre conductor of an SMA connector. To include a dielectric region the configuration was designed so that a radome can be press-fitted over the smaller disc. The radome used here is a 40 mm polyvinyl chloride (PVC) end cap. The discs are made of aluminium.



(a) $\phi\phi$ -polarization.



(b) $\theta\theta$ -polarization.

Figure 3: Computed and measured backscatter cross sections at 3 GHz for the conducting-dielectric cylinder.

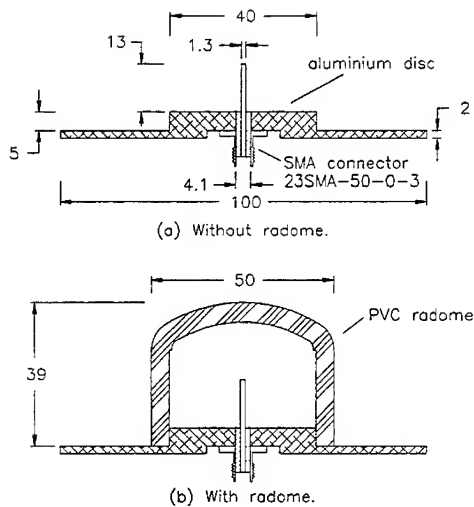


Figure 4: Cross section through the disc mounted monopole. Dimensions are in mm.

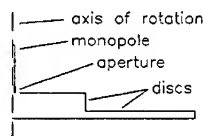


Figure 5: Generatrix of the disc mounted monopole without the radome.

The input reflection coefficient (S_{11}) of the monopole was measured from 2 to 18 GHz with and without the radome. The radiation pattern was measured at 5.52 GHz, the first resonance of the monopole, for the two cases.

Computations were first done without the radome. The generatrix for this case is shown in figure 5. The excitation is modeled as an aperture with a TEM field distribution corresponding to the coaxial feed. The input impedance at the aperture is computed by dividing the voltage across the aperture by the equivalent electric current on the aperture (the surface current is integrated around the BOR). The input reflection is computed using the input impedance in a 50 Ω system. As the aperture is rotationally symmetric, only mode zero needs to be solved.

For the S_{11} computation the configuration was modeled with a discretization sufficiently fine for 18 GHz. The result is compared with the measurement in figure 6. The curve labelled "MM/BOR(1)" computed with 1 triangle function on the aperture which resulted in 156 unknowns. The curve labelled "MM/BOR(3)" was done with 3 triangle functions on the aperture, in order to model the $1/\rho$ dependence of the aperture field more accurately, which resulted in 160 unknowns.

The computed results predict the behavior of S_{11} quite well up to about 15 GHz. Using 3 triangle functions on the aperture gives only a slightly better result. The anomalies in the computed results at about 5.5, 7.7, 13.7 and 17 GHz are due to internal resonances supported by the closed conducting surface. For a conducting surface (on which there are no magnetic currents) the formulation is purely

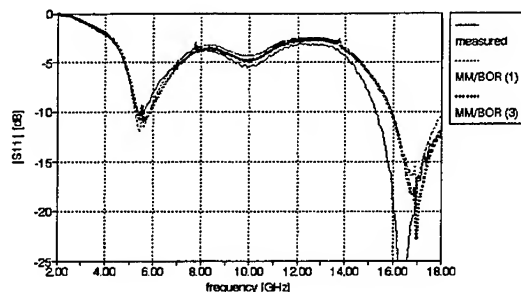


Figure 6: Input reflection coefficient of the disc mounted monopole. The computations were done with 1 and 3 triangle functions on the aperture. The minima in the measured result at 16.4 GHz is -43.42 dB.

the EFIE. At frequencies at which internal resonances can occur the total current flowing on the surface of the structure is not uniquely determined by the EFIE and the excitation. The surface current due to the internal resonance influences the solution for the external problem. This is due to the discretization error – the error introduced when reducing the integral equations to a finite matrix equation. As an example one can consider the smaller disc on which the monopole is mounted. This disc has a radius of 20 mm and a length of 5 mm. The frequency of the dominant mode of a circular cavity with these dimensions can be calculated using equations in [5, pages 213-214] and is found to be 5.74 GHz. This disc forms a slightly longer cavity with the larger disc which will reduce the resonance frequency of the dominant mode, thus explaining the anomaly at 5.5 GHz. The susceptibility of the MM solution of the EFIE is well documented in the literature [6, 7, 8].

The radiation pattern of the monopole without the radome at 5.52 GHz is compared to the measurement in figure 7. The computation was first done using the generatrix as in figure 5 using 88 unknowns (sufficient discretization for up to 10 GHz). This result, the curve labelled “MM/BOR” in figure 7, agrees reasonably with the measurement in the range $-80^\circ \leq \theta \leq 80^\circ$ but deviates somewhat outside of this. However, the position of the peak at $\pm 170^\circ$ was successfully predicted. Some of the deviation was believed to be due to interaction with the feed cable which was then modeled by adding a 4.1 mm diameter (the outside diameter of SMA cable) cylinder to the base of the model. The curve labelled “MM/BOR(c30)” in figure 7 is the computation for when this cylinder is 30 mm long. This computation required 56 triangle functions, resulting in 112 unknowns. It agrees very well with the measurement in the range $-80^\circ \leq \theta \leq 80^\circ$ indicating that the cable influences the currents above the discs quite strongly. There is also an improvement in the computed result in the ranges $\pm 80^\circ$ to $\pm 110^\circ$. The remaining deviations are probably due to interference with obstacles in the anechoic chamber, such as the antenna support. The addition of the cable to the numerical model does not influence the input reflection results.

The input reflection coefficient of the monopole with the PVC radome was computed using two values for the relative permittivity of PVC. The first value was obtained from a table in [9, Appendix E] which is $\epsilon_r = 2.84 - j0.016$ at 3 GHz (and 20° centigrade). However, it is uncertain whether this is the correct value to use for the particular PVC used here. PVC comes in a variety of colours and the authors are not sure how this affects the dielectric properties. It was decided thus to measure a sample of the PVC using a waveguide measurement technique. The setup used is reliable in the frequency range of 8 to 12 GHz. At 10 GHz the value was measured as $\epsilon_r = 2.7$. The measured magnitude of the imaginary part was of the order of the measurement error that can be expected using this technique – the technique is more suited to dielectrics with higher loss – it was thus ignored.

The S_{11} computations using the two relative permittivity values are compared with the mea-

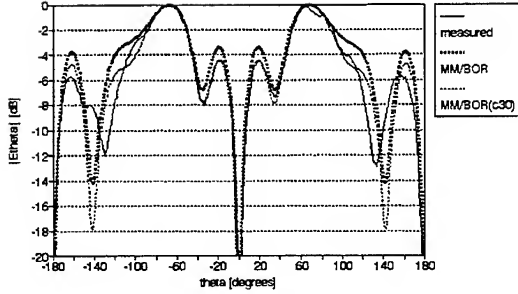


Figure 7: Normalized far field of the disc mounted monopole at 5.52 GHz.

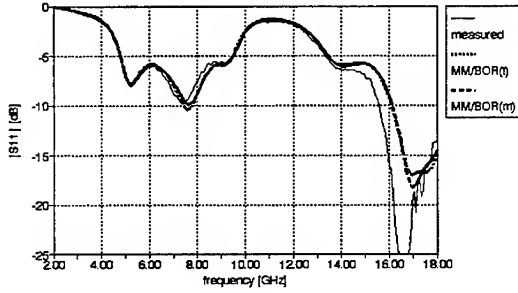


Figure 8: Input reflection coefficient of the disc mounted monopole with radome. The minima in the measured result at 16.64 GHz is -37.60 dB.

surement in figure 8. The configuration was modeled using a sufficiently fine discretization for 18 GHz which resulted in 430 unknowns. The curve labelled “MM/BOR(t)” is the result using $\epsilon_r = 2.84 - j0.016$ and that marked “MM/BOR(m)” used $\epsilon_r = 2.7$. The difference between the two ϵ_r values has little effect on the result except at the higher frequencies. A loss of this small magnitude can also be neglected. Both computed curves predict the behavior of S_{11} well below 14 GHz except for the minima at 7.5 GHz which is shifted slightly. The ϵ_r values used here are valid at the lower frequencies thus the deviation from the measured result at the higher frequencies can partly be explained by this. The anomalies due to internal resonances in the conductor are suppressed which is probably due to the antenna interacting with three different dielectric regions.

The radiation pattern was computed using $\epsilon_r = 2.7$ with and without the cable at 5.52 GHz. The results are compared to the measurement in figure 9. The improvement with the cable added is not as dramatic as the result for the monopole without the radome.

5 Conclusions

A MM code has been described which predicts radiation and scattering from composite BOR's. It has been demonstrated that the code can successfully predict scattering from composite BOR's. Further, the capability of the code to predicting radiation from practical antenna configurations has been demonstrated.

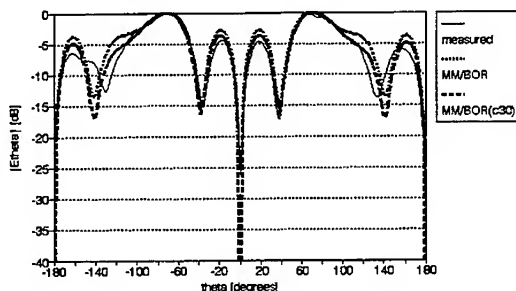


Figure 9: Normalized far field of the disc mounted monopole with radome at 5.52 GHz.

To date, the code has only been applied to relatively lossless dielectrics with low relative permittivity. Problems involving materials with higher loss and higher relative permittivities are to be investigated.

The formulation suffers from numerical problems at frequencies near to internal resonances supported by a conducting region. Methods of avoiding this problem are being investigated.

6 Acknowledgement

The authors wish to thank Jeandre Botha for helping with the antenna measurements and Marius du Plessis for the waveguide dielectric measurement.

References

- [1] L. N. Medgyesi-Mitschang and J. M. Putnam, "Electromagnetic scattering from axially inhomogeneous bodies of revolution," *IEEE Trans. Antennas Propagat.*, vol. AP-32, pp. 797-806, August 1984.
- [2] P. Steyn and D. B. Davidson, "Electromagnetic radiation and scattering from axially inhomogeneous bodies of revolution," in *AP/MTTS-91 Proceedings, Symposium on Antennas & Propagation and Microwave Theory & Techniques*, pp. 81-89, SAIEE & IEEE, August 1991.
- [3] D. B. Davidson and D. A. McNamara, "A boundary element program package for electromagnetic excitation of conducting bodies of revolution by an asymmetrical slot," *Computer Physics Communications*, vol. 56, pp. 249-257, 1989.
- [4] D. B. Davidson, "Predicting electromagnetic radiation from and coupling between antennas mounted on a body of revolution using the method of moments technique," Master's thesis, University of Pretoria, 1986.
- [5] R. F. Harrington, *Time-harmonic electromagnetic fields*. New York: McGraw-Hill, first ed., 1961.
- [6] J. R. Mautz and R. F. Harrington, "H-field, E-field, and combined-field solutions for conducting bodies of revolution," *AEU*, vol. 32, pp. 157-164, 1978.
- [7] P. L. Huddleston, L. N. Medgyesi-Mitschang, and J. M. Putnam, "Combined field integral equation formulation for scattering by dielectrically coated conducting bodies," *IEEE Trans. Antennas Propagat.*, vol. AP-34, pp. 510-520, April 1986.
- [8] F. X. Canning, "Singular value decomposition of integral equations of EM and applications to the cavity resonance problem," *IEEE Trans. Antennas Propagat.*, vol. AP-37, pp. 1156-1163, September 1989.
- [9] J. Musil and F. Žáček, *Microwave Measurements of Complex Permittivity by Free Space Methods and Their Applications*. New York: Elsevier Science Publishing Company, Inc., first ed., 1986.

Calculation of Transient Scattering from Two-Dimensional Objects using a Frequency Domain Method of Moments Approach¹

Paul M. Goggans
Department of Electrical Engineering
University of Mississippi
University, MS 38677

Abstract- This paper describes the calculation of the time domain field scattered from a two-dimensional body due to an incident transient plane wave. The incident wave is band-limited with bandwidth Δf and has a center frequency f_0 . The scattering body has dimensions on the order of a few wavelengths at the frequency f_0 . Return from bodies of this size is interesting because it can exhibit both strong local scattering (specular and edge diffraction) as well as strong resonant behavior. Scattering bodies considered here include a circular cylinder, a flat strip, and a rectangular cavity. The inverse fast Fourier transform is used to calculate the transient scattered field at discrete times from the steady state scattered field at discrete frequencies. The steady state scattered field is determined using the moment method.

Introduction

Engineers are often interested in calculating the transient received signal in radar systems. This interest may be due to a need to analyze the response of the radar system to a particular target (scattering object) or the interest may be in studying the transient scattering characteristics of a particular class of targets. This work was motivated by a desire to study the ability of a scattering center representation to model the transient return from structures with local as well as resonant scattering behavior. For this study, two-dimensional (2-D) conducting bodies in the upper resonance region were chosen because they are the simplest targets that demonstrate all of the desired scattering behavior. In this paper, calculation of the time domain field scattered from a two-dimensional body is described. A frequency domain moment method (MM) and inverse Fourier transform technique was chosen for these calculations because of its ability to treat arbitrary shaped targets and because of its accuracy. The disadvantages of this method are the long execution time required and the possibility of aliasing in the time domain.

This paper begins with a section that outlines the calculation of the received signal for the general three-dimensional (3-D) target case. In this section the target impulse response, equivalent transmitted signal, and radar profile are defined. Although similar expressions are given in other places (references [1] and [2] for example) they are repeated here for clarity. The next section specializes the general expressions for the two-dimensional target case. This section also briefly describes the MM solution of the time-

¹ This work was supported by the MICOM Research, Development, and Engineering Center (Dr. C. Ray Smith) under the auspices of the U.S. Army Research Office Scientific Services Program administered by Battelle (Delivery Order 0182, Contract No. DAAL03-91-C-0034).

harmonic scattered fields and the use of the inverse Fourier transform to determine the envelope of the returned signal. The final section gives calculated results for a circular cylinder, a flat strip, and a rectangular cavity.

The Radar Profile

For a particular target the received signal is here referred to as the target signature. The target signature, $g(t)$, represents some field, voltage, or current quantity in the radar receiver. If the target is stationary and has no moving parts the target signature is described by the following equation in which convolution is denoted by an asterisk (*):

$$g(t) = a_R(t) * a_p(t) * h(t) * a_p(t) * a_T(t) * f(t). \quad (1)$$

In the expression above, $h(t)$ is the target impulse response function, $a_T(t)$ is the impulse response of the transmitter and transmit antenna, $a_R(t)$ is the impulse response of the receiver and receive antenna, and $f(t)$ is the transmitted signal. The signal $f(t)$ represents some field, voltage, or current quantity in the radar transmitter. In (1), $a_p(t)$ accounts for propagation of the signal between the radar and the target and is taken to be

$$a_p(t) = \frac{\delta(t - R/c)}{R} \quad (2)$$

where R is the range from the radar to the target, c is the speed of light and δ is the Dirac delta function. Equation (2) can be rewritten using the commutative property of convolution to obtain the following:

$$g(t) = \left\{ \frac{a_T(t) * a_R(t) * f(t - 2R/c)}{R^2} \right\} * h(t) \quad (3)$$

where the total time delay is accounted for in $f(t)$. The quantities in the curly brackets in (3) are assumed known and so it is convenient to combine them and define them as a single quantity. This quantity is here referred to as the equivalent transmitted signal, $\tilde{f}(t)$.

$$\tilde{f}(t) = \frac{a_T(t) * a_R(t) * f(t - 2R/c)}{R^2}. \quad (4)$$

Using the equivalent transmitted signal the target signature can be expressed as

$$g(t) = \tilde{f}(t) * h(t). \quad (5)$$

The form of (3) above is useful because $\tilde{f}(t)$ includes the effect of the receive antenna and receiver, the transmit antenna and transmitter, and the range to the target; while the target impulse response $h(t)$ isolates the scattering characteristics of the target (note however that $h(t)$ is also a function of the transmit and receive polarization).

The target impulse is easiest to define in terms of its Fourier transform, $H(f)$, the target transfer function.

$$H(f) = \int_{-\infty}^{\infty} h(t) e^{-j2\pi ft} dt. \quad (6)$$

The value of $H(f)$ at a particular frequency f can be determined by considering a time-harmonic plane-wave incident on the target and traveling in the direction of the unit vector $\hat{\mathbf{k}}$. The incident electric and magnetic fields written in phasor form (with $e^{j2\pi ft}$ time variation assumed and suppressed) are

$$\mathbf{E}_i(\mathbf{r}) = E_o \hat{\mathbf{p}} e^{-j2\pi f \mathbf{r} \cdot \hat{\mathbf{k}} / c} \quad (7)$$

and

$$\mathbf{H}_i(\mathbf{r}) = (E_o / \eta_o) (\hat{\mathbf{k}} \times \hat{\mathbf{p}}) e^{-j2\pi f \mathbf{r} \cdot \hat{\mathbf{k}} / c} \quad (8)$$

where E_o is the constant amplitude of the incident electric field, $\hat{\mathbf{p}}$ in the unit polarization vector (here linear polarization is assumed for simplicity) and η_o is the characteristic impedance of free space. The origin of the coordinate system used to define \mathbf{r} is picked at a convenient point close to, inside, or on the target. For a monostatic radar system, the Fourier transform of the target impulse response is given by the expression

$$H(f) = \frac{\mathbf{E}_s(-R\hat{\mathbf{k}}) \cdot \hat{\mathbf{p}}}{E_o} [R e^{(j2\pi f R/c)}] \quad (9)$$

where it is assumed that the polarization of the received antenna is matched to the polarization of the incident wave. The distance R from the origin to the receiving antenna is assumed to be electrically large so that the scattered electric field due to the target, \mathbf{E}_s , can be calculated using the standard far-field approximations.

Because the Fourier transform of the equivalent transmitted signal is band-limited, it is only necessary to determine $H(f)$ for frequencies in the pass band of $\tilde{F}(f)$ in order to calculate $g(t)$. To investigate the target signature any suitable band-limited function can be chosen for the equivalent transmitted signal. Here the Blackman window function [3] is used so that:

$$\begin{aligned} \tilde{F}(f) = \text{rect}[(f - f_o) / \Delta f] & \left\{ 1 + \frac{.50}{.42} \cos[2\pi(f - f_o) / \Delta f] + \frac{.08}{.42} \cos[4\pi(f - f_o) / \Delta f] \right\} \\ & + \text{rect}[(f + f_o) / \Delta f] \left\{ 1 + \frac{.50}{.42} \cos[2\pi(f + f_o) / \Delta f] + \frac{.08}{.42} \cos[4\pi(f + f_o) / \Delta f] \right\} \end{aligned} \quad (10)$$

where

$$\text{rect}(x) = \begin{cases} 1 & \text{for } |x| \leq \frac{1}{2} \\ 0 & \text{otherwise} \end{cases} \quad (11)$$

In (10), f_o is the center frequency and Δf is the bandwidth. Because it is a band-limited function $g(t)$ can be expressed in the form

$$g(t) = i(t) \cos(2\pi f_o t) + q(t) \sin(2\pi f_o t) \quad (12)$$

where $i(t)$ and $q(t)$ are the in-phase and quadrature portions of $g(t)$. Papoulis [4] gives expressions for calculating $i(t)$ and $q(t)$. If the positive frequency portion of $\tilde{F}(f)$ is symmetric about f_o , these expressions can be manipulated into the following form:

$$i(t) + jq(t) = \int_{-\Delta f/2}^{\Delta f/2} \tilde{F}(f + f_o) H^*(f_o - f) e^{j2\pi f t} df \quad (13)$$

where H^* is the complex conjugate of H .

Equation (12) can also be written in envelope and phase form.

$$g(t) = p(t) \cos\{2\pi f_o t + \tan^{-1}[q(t)/i(t)]\}. \quad (14)$$

Because it is a lowpass function, the envelope of $g(t)$ is used to display the return signal rather than $g(t)$ itself. The envelope of the target signature is here referred to as the radar profile and is denoted $p(t)$. The radar profile is the magnitude of (13) and can be determined from the in-phase and quadrature portions of $g(t)$ using the expression

$$p(t) = \sqrt{i^2(t) + q^2(t)}. \quad (15)$$

In summary, the radar profile is calculated using equations (9), (10), (13), and (15).

Two-Dimensional Targets

A two-dimensional target is infinite in the axial direction (here considered to be the z direction) and has the same physical cross section in any plane cut which is orthogonal to the axis (any plane cut parallel to the x - y plane). The incoming wave in the 2-D case always travels on a ray that is orthogonal to the axis of the body, hence the direction of propagation is given by the expression $\hat{k} = \hat{\rho}$ where $\hat{\rho}$ is the ρ directed unit vector (ρ is the distance from the z -axis in the cylindrical coordinate system). In the 2-D case, an incoming wave of arbitrary polarization can always be written as the sum of waves that are transverse electric (TE) and transverse magnetic (TM) to the axis of the target. For TM polarization the polarization vector is given by the expression $\hat{p} = \hat{z}$ and for TE polarization by the expression $\hat{p} = \hat{z} \times \hat{\rho}$ where \hat{z} is the z directed unit vector.

The equations outlining the calculation of the radar profile in the previous section are for the three-dimensional target case. Only the equation of the target transfer function must be modified for the 2-D case. For the 2-D case

$$H(f) = \frac{\mathbf{E}_s(-\rho\hat{\mathbf{k}}) \cdot \hat{\mathbf{p}}}{E_o} \left[\sqrt{\rho} e^{(j2\pi\rho/c)} \right]. \quad (16)$$

The 2-D radar profile is calculated using Equations (10), (13), (15), and (16). Here the time harmonic far scattered electric field is calculated at discrete frequencies using a 2-D moment method code [5]. The MM program solves the combined field integral equation for closed bodies and the electric field integral equation for open bodies using pulse basis functions and point matching. The inverse Fourier transform in (13) is calculated using the fast inverse Fourier transform [6].

Results

Figure 1 illustrates the envelope of the equivalent transmitted signal $\tilde{f}(t)$. For this illustration and the calculations in this section the center frequency, f_o , is 10 GHz and the bandwidth, Δf , is 4 GHz. The center frequency was chosen arbitrarily; however, the bandwidth was chosen so that a time resolution of approximately 1 ns is achieved.

The idea of a reference plane is useful in interpreting the radar profile. The reference plane passes through the origin and is orthogonal to $\hat{\mathbf{k}}$, the unit normal pointing in the direction of the incident wave. A local scatterer on the target will result in a peak in the radar profile at a time corresponding to twice the distance from the reference plane to the scatterer along a $\hat{\mathbf{k}}$ directed path.

Figure 2a illustrates a 1 m wide perfect electric conductor (PEC) strip with a TE polarized incident wave. The strip is at a 45 degree angle to the direction of the incident wave and the origin is 1 m from the center of the strip. The Figure 2b illustrates the radar profile of the PEC strip. The first two return pulses in Figure 2b are due to edge diffraction from the lower and upper edges of the strip. The latter pulses are due to waves traveling up and down the strip that are then diffracted at the upper or lower edge.

Figure 3a illustrates a 24 cm diameter PEC cylinder with a TE polarized incident wave. The center of the cylinder lies on the $x = 0$ plane and the origin is 1 m from the center of the cylinder. Figure 3b illustrates the radar profile of the PEC cylinder. The first return pulses in Figure 3b is due to the specular point on the front of the cylinder. The second return pulse is due to the creeping wave.

Figure 4a illustrates a 45 cm by 10 cm rectangular cavity with a TM polarized incident wave. The center of the open face of the cavity is 1 m from the origin. Figure 4b illustrates the radar profile of the rectangular cavity. The calculations for Figure 4b were set up to achieve a 64 ns period to limit aliasing; however, only the first 32 ns are plotted. The first return pulse in Figure 4b is due to edge diffraction from the front edge of the cavity. The second return pulse is due to the wave which travels down the parallel-plate waveguide in the lowest order TM mode and is reflected from the back inside face of the cavity. The third return pulse appears to be due to a wave which travels down the waveguide in a higher order mode and is reflected from the back face of the cavity. The return after the third pulse cannot be classified as separate return pulses. This portion of the radar profile is the resonant response of the cavity.

References

- [1] E. M. Kennaugh and D.L. Moffatt, "Transient and Impulse Response Approximations, *Proc. IEEE*, vol. 53, no.8, August 1965.
- [2] A.K. Dominek, L. Peters, and W.D. Burnside, "A Time Domain Technique for Mechanism Extraction," *IEEE Trans. Antennas Propagat.*, vol. AP-35, March 1987.
- [3] F. J. Harris, "On the Use of Windows for Harmonic Analysis with the Discrete Fourier Transform," *Proc. IEEE*, vol. 66, no. 1, January 1978.
- [4] A. Papoulis, *The Fourier Integral and Its Applications*, New York, Mc-Graw Hill, 1962, Chap. 7.
- [5] P. M. Goggans and T. H. Shumpert, "CFIE MOM Solution for TE and TM Incidence on a 2-D Conducting Body with a Dielectric Filled Cavity," *IEEE Trans. Antennas Propagat.*, vol. AP-38, October 1990.
- [6] W. H. Press et al., *Numerical Recipes*, Cambridge, Cambridge University Press, 1986, Chap. 12.

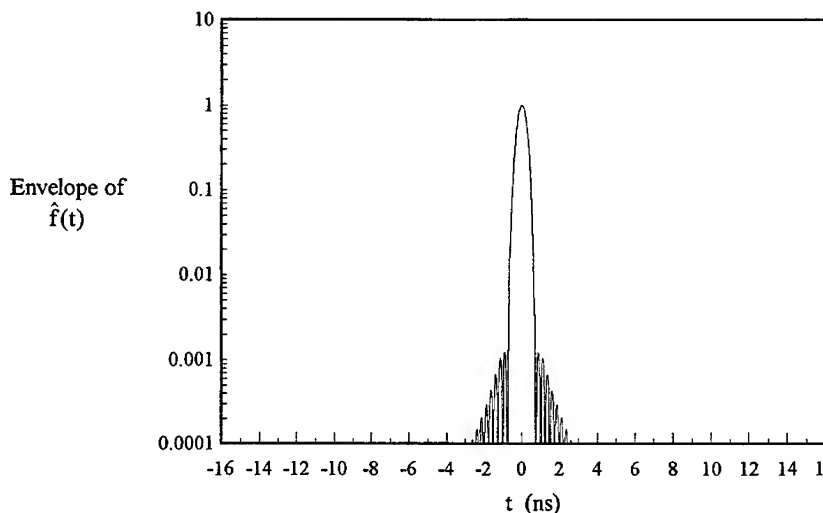


Figure 1. Envelope of the equivalent transmitted signal versus time.

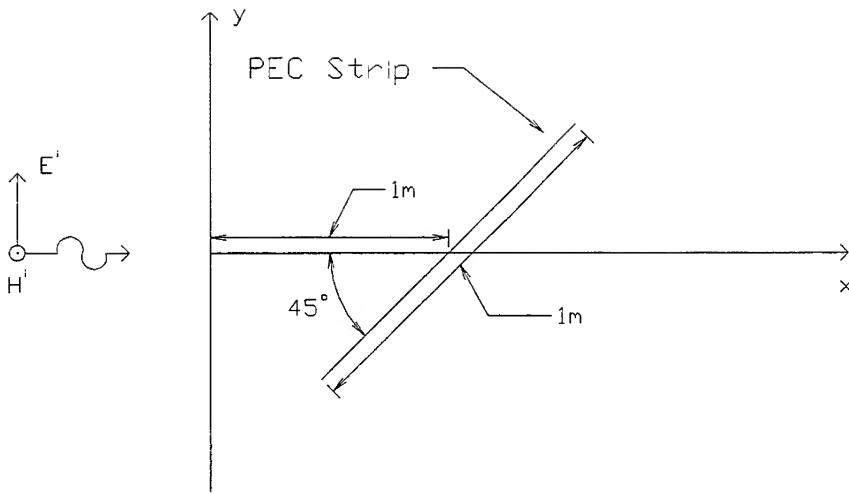


Figure 2a. Illustration of a PEC strip with a TE polarized incident wave.

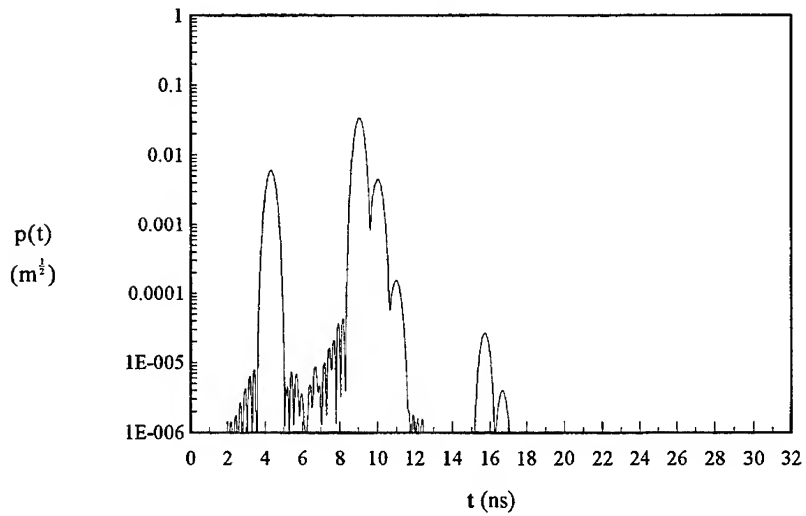


Figure 2b. Radar profile of the PEC strip.

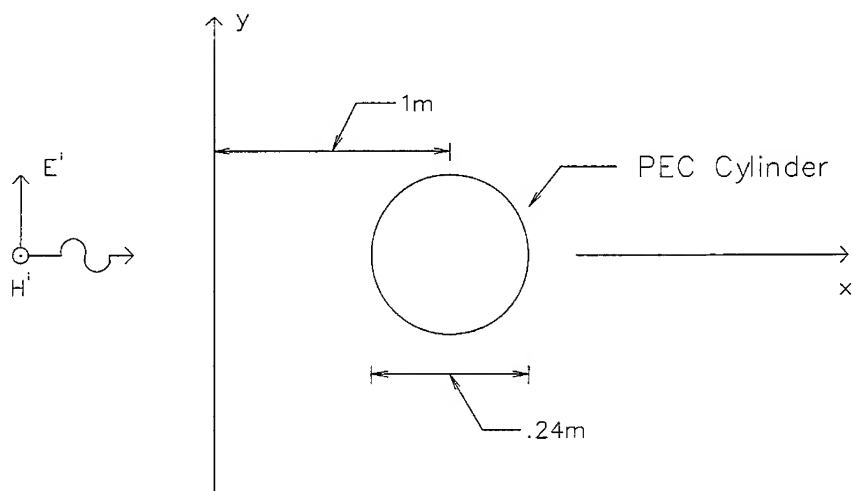


Figure 3a. Illustration of a PEC cylinder with a TE polarized incident wave.

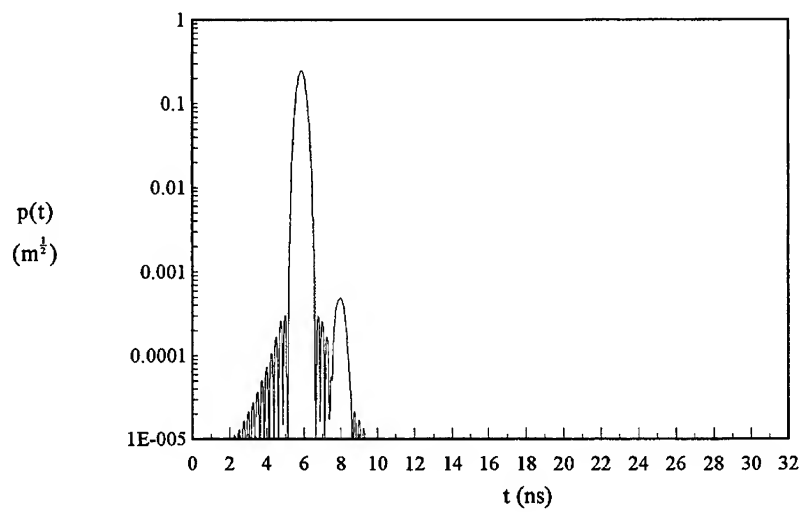


Figure 3b. Radar profile of the PEC cylinder.

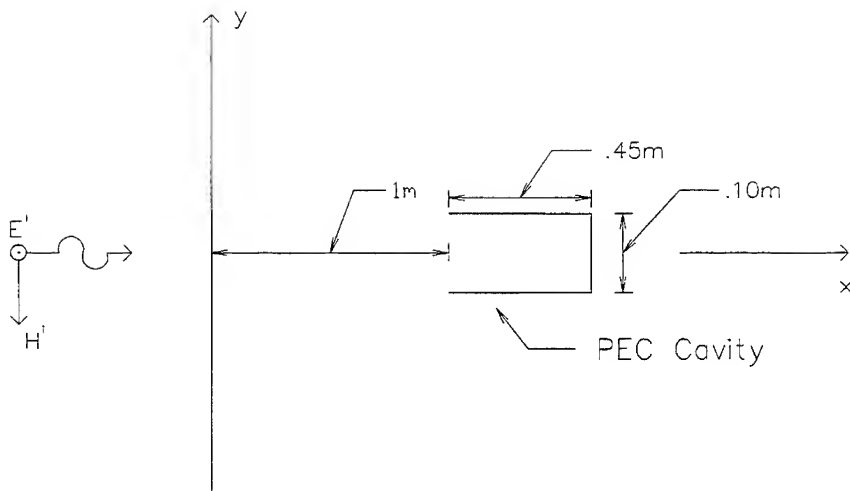


Figure 4a. Illustration of a rectangular PEC cavity with a TM incident wave.

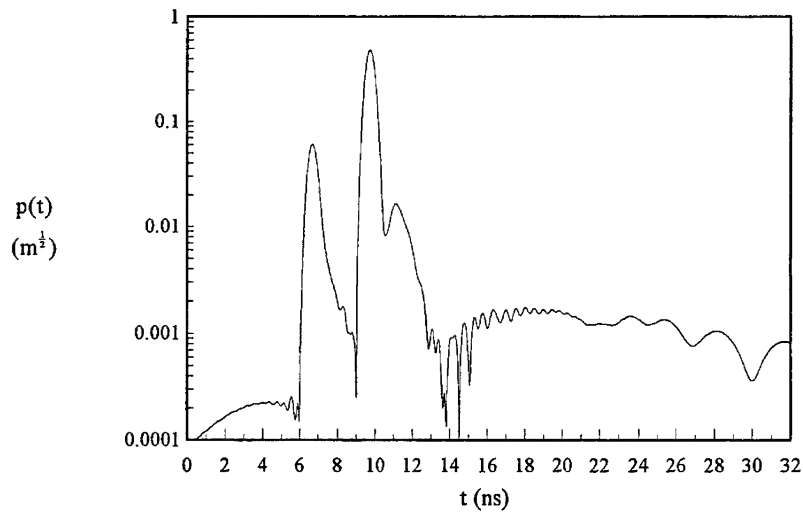


Figure 4b. Radar profile of the rectangular cavity.

RCS of Structures with Apertures and Slots

S. Kashyap
A. Louie
Electronics Division
Defence Research Establishment
Ottawa, Canada

S. Mishra
C. Larose
David Florida Laboratory
Canadian Space Agency
Ottawa, Canada

ABSTRACT

This paper concerns the calculation and measurement of the radar cross-section (RCS) of conducting cylindrical structures with slots and circular apertures. The calculations are made using a moment method (MM) solution of the electric-field integral equation (EFIE). The measurements are made on 1/6 (approx.) scale models. Good agreement is shown between the measurements and the calculations.

INTRODUCTION

Many structures, such as airplanes, helicopters, and missiles, have some apertures and slots through which electromagnetic fields may leak in. The radar cross-section (RCS) of such structures is affected by these openings, and its study is of practical importance.

Pathak and Burkholder [1] have analyzed the electromagnetic scattering of open-ended waveguide cavities using a hybrid combination of asymptotic and modal techniques. Ling, Lee, and Chou [2] have also done RCS analysis of open-ended waveguides using the waveguide modal approach and the shooting and bouncing ray (SBR) approach. In this paper, the RCS of conducting cylinders with various apertures and slots is computed by using a moment method (MM) solution of the electric-field integral equation (EFIE). The calculations are compared with results of measurements made on 1/6 (approx.) scale models in the range 2-18 GHz. At the highest frequency the cylinders are about 5 wavelengths long and thus are not electrically small targets.

Various modelling and measurement issues such as discretization, resonances, and gating are discussed.

PROCEDURE

Figure 1 shows schematically a generic cylinder used in this study. It is a perfectly conducting cylinder with a zero-thickness wall, and has one circular aperture on one end and three slots on the cylindrical wall. Note the overall dimensions of 0.25m in diameter and 0.50m in length. The frequency range of interest is 300 MHz to 3 GHz.

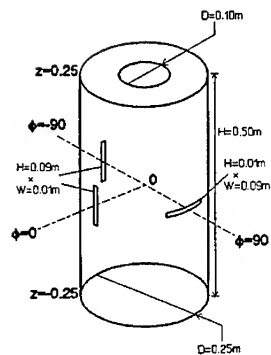


Figure 1. The generic cylinder.

Five cylinders with various combinations of aperture and slots (Figure 2) are studied. A plane wave (at different frequencies, orientations, and polarizations) is incident on the cylinder and the RCS is computed.

Reference [3] describes a simple and efficient procedure for scattering by arbitrarily shaped bodies, using the moment method to solve the electric field integral equation. The object surface is modelled by using planar triangular patches. In JUNCTION [4], the EFIE approach is extended to analyze an arbitrary configuration of conducting wires and bodies. A modified version of JUNCTION is used here for the calculations. The mathematical model of the cylinders in our study is a triangulation of the wall into roughly

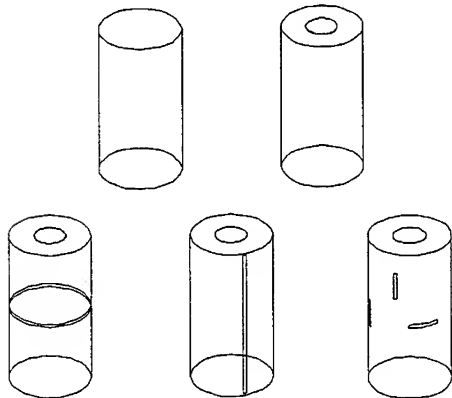


Figure 2. The five cylinders under study.

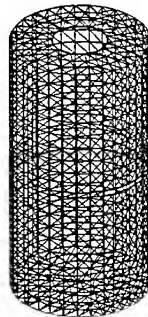


Figure 3. The triangulated patch model of the generic cylinder.

1500 patches with about 2500 edges. The triangulated-patch model of the generic cylinder of Figure 1 is shown in Figure 3. The core of the moment method solution is the creation and factorization of a 2500×2500 complex matrix. On a VAX 6420 equipped with a vector processor, the JUNCTION run takes about 2.5 hours per frequency.

Because of the limitations of the measuring apparatus, the actual physical model on which the measurements are done is a scaled-down version, with the approximate dimensions of 43mm in diameter and 86mm in length, and a wall thickness of 0.89mm. A few of the JUNCTION runs were done on the full-size cylinder, while the rest were done on the scaled-down versions. For a proper comparison of RCS values of similar bodies differing by a scaling factor s , one must note that the corresponding frequencies are scaled by $1/s$, and the RCS values are scaled by s^2 , which in dBsm terms translates to $RCS(dBsm)_2 = RCS(dBsm)_1 + 20 \log s$.

WALL THICKNESS

While in the idealized mathematical model of the cylinder it is possible to have zero-thickness walls, in the physical model one must deal with the effect of the wall thickness. Although the metal sheet from which the model cylinders are made is only 0.89mm thick, the effect is still significant when compared to a slot width of 1.7mm in the scaled-down cylinders. The physical models actually have the following dimensions:

external diameter	= 44.45mm
internal diameter	= 42.67mm
external length	= 87.12mm
internal length	= 85.34mm.

For the case of the closed cylinder, the dimensions to take are clearly the external ones. But for the case of the cylinders with apertures, the only reasonable choice is to take the average of the external and internal diameters as the diameter, and the average of the external and internal lengths as the length. In most of our simulations we actually use cylinders with the average diameter = $\frac{1}{2} \times (44.45 + 42.67) = 43.56\text{mm}$, and the average length = $\frac{1}{2} \times (87.12 + 85.34) = 86.23\text{mm}$. Note that the "aspect ratio" of diameter::length is no longer exactly 1::2 as in the full-size 0.25m::0.50m cylinder, and a further averaging to adjust this minor discrepancy is necessary. Thus the scaling factor s is an overall average, taking wall thickness and aspect ratio into account. Henceforth we present the results in terms of the scaled-down cylinders.

MEASUREMENTS

The measurements presented in this paper are done in a 6m×6m×6m cubic anechoic chamber. Each of the target cylinders is mounted, in turn, on a slim, tapered styrofoam column on a Scientific Atlanta turntable at the centre of the chamber. The procedure of aligning the cylinders is a combination of the use of laser beam reflections

from the cylinders and visual sighting techniques, depending on the target orientation. The measurement set-up has a range of about 1.25m: see Figure 4a. A set of two Daimo Victor dual-polarized quadridged horns, model A6100, is used: one to illuminate the targets and the other to receive the scattered field. This introduces a bistatic angle of about 8° , hence an error in the RCS. The error incurred, however, was assessed using the Numerical Electromagnetic Code (NEC) [5] by comparing the monostatic and the bistatic RCS on a wide variety of metallic and dielectric targets, and was found to be negligible for small metallic targets.

Figure 4b illustrates the fully-automated RCS measurement set-up. An HP Series 9000 Model 320 Instrument Controller is used for process control, data acquisition, and

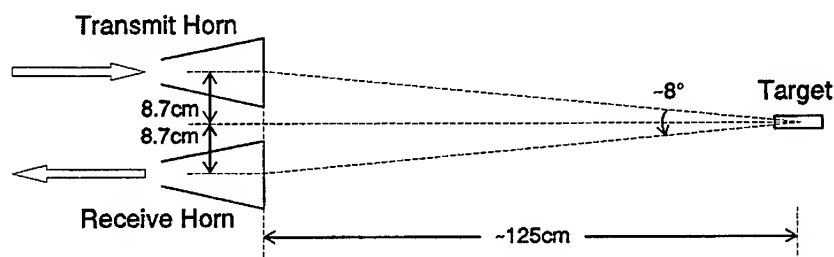


Figure 4a. The geometry of the measurement set-up as seen from above.

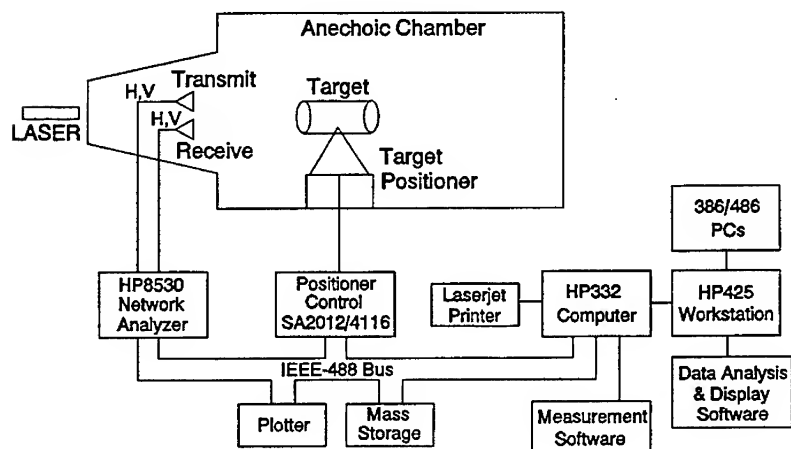


Figure 4b. Block diagram of the RCS measurement system.

processing. An HP 8510 or 8530 Network Analyzer System, with an HP 8511A Frequency Converter as the receiver front end, is used to determine the scattered field amplitude and phase in the 2-18 GHz frequency range. Time-gating, with a gate span of several nanoseconds, isolates the target response. The response of a reference sphere is measured as the difference at each frequency between the response of the sphere with the column and chamber together, and the response of the column and chamber alone. The response of the target (i.e. our cylinders) is measured in a similar way. The exact Mie series for the back-scattered field of the sphere [6], evaluated with the appropriate bistatic angle, is used to find a calibration factor for the system at each frequency.

The scattered field values (amplitude and phase) are collected at 801 frequencies generated by an HP 83631A Synthesizer, and averaged over at least 32 measurements at each frequency. A Fourier transform gives the time response of the scattered field. A time-gate is then used to eliminate direct coupling between the horns at early times and unwanted room reflections at late times. The gate starts about 1.5 ns before the main time response. A proper choice of the "gate stop" ensures that the full target response is obtained, while excluding unwanted reflections.

The range, bistatic angle, and gate stop relative to the target location were 1.28m, 7.8°, and 4.5 ns, respectively, for the measurements of Figures 5, 6, and 9, and 1.20m, 8.3°, and 6.5 ns for those of Figures 7 and 8.

RESULTS

Figure 5 shows the RCS versus frequency for a closed cylinder, the simplest of the five, when a plane wave is incident on it axially and transversally. The average length

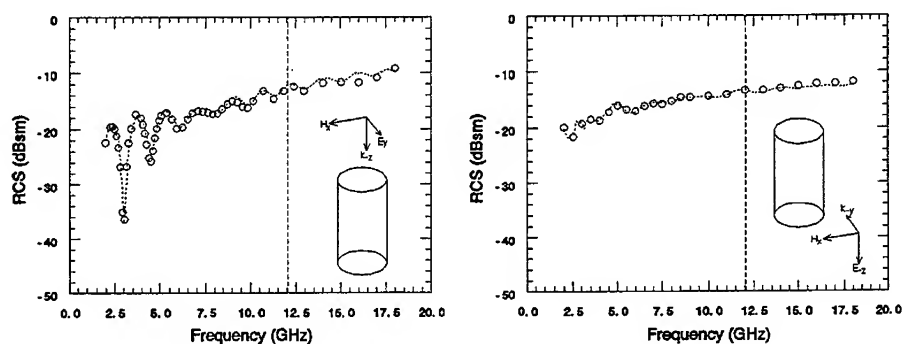


Figure 5. RCS of a solid cylinder.
Dashed curve = Measurement. Circles = JUNCTION.
Vertical dashed line = $\lambda/5$ simulation limit.

of the edges of the triangles in the mathematical model is about 5mm, whence by the one-fifth wavelength rule in EFIE/MM simulations, the results are reliable up to about 12 GHz. This is what the vertical dashed lines in the graphs signify. The comparison between measurement (the dashed curves) and simulation (the circles) is very good. The one-fifth wavelength rule is a guideline for obtaining reliable currents at specific surface

locations. For "integrated quantities" over the whole structure, such as RCS and near-field, the guideline is sometimes more stringent than necessary, and that is why the comparison is also not bad above 12 GHz.

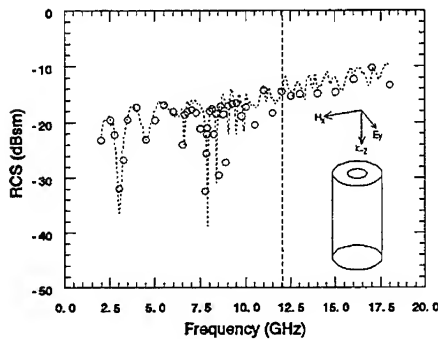


Figure 6. RCS return of a cylinder with a circular aperture at one end.
Dashed curve = Measurement.
Circles = JUNCTION.
Vertical dashed line = $\lambda/5$ simulation limit.

Figure 6 shows the RCS versus frequency for a cylinder with a circular aperture of diameter 17.02mm at one end, on which a y-polarized plane wave is incident. Again the match between simulation and measurement is very good, except on a small interval around 7 GHz.

Figure 7 shows the comparison for a cylinder with the same end-cap circular aperture and an equatorial slot of width 1.57mm. The only discrepancies in the otherwise good

match occur in the case of the axial pulse between 5.0 and 6.0 GHz and between 6.5 and 7.5 GHz. We will discuss some possible causes of the mismatch in the next section.

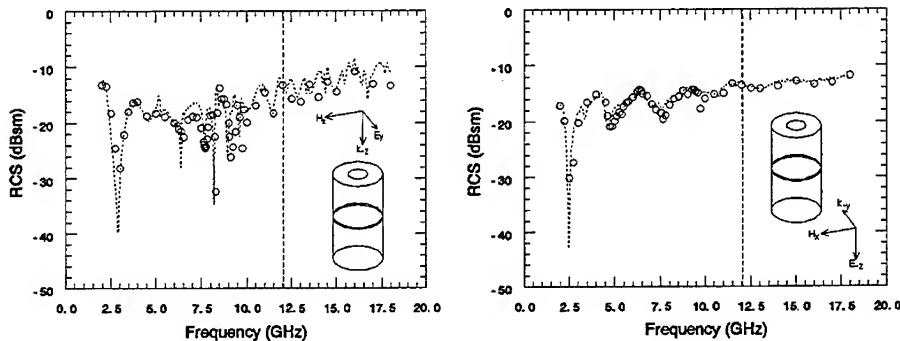


Figure 7. RCS of a cylinder with aperture and equatorial slot.
Dashed curve = Measurement. Circles = JUNCTION.
Vertical dashed line = $\lambda/5$ simulation limit.

Figure 8 shows the comparison for a cylinder with a circular aperture and a longitudinal slot of width 1.78mm. Note the different polarization of the incident pulses for this cylinder. Again the only discrepancies (although to a lesser extent than in Figure 7) occur between 5.0 and 6.0 GHz and between 6.5 and 7.5 GHz.

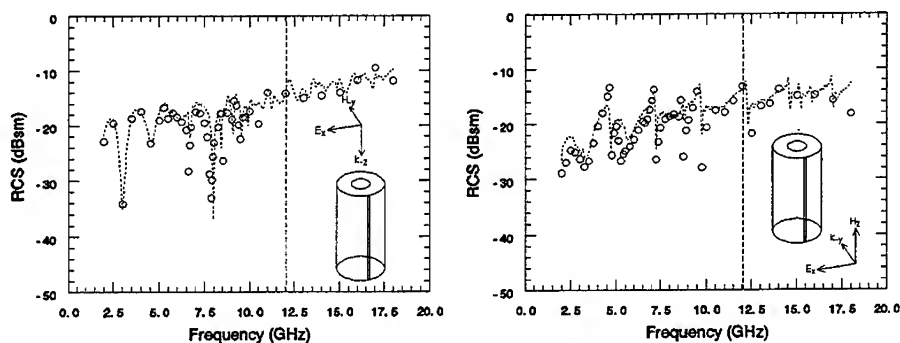


Figure 8. RCS of a cylinder with aperture and longitudinal slot.
Dashed curve = Measurement. Circles = JUNCTION.
Vertical dashed line = $\lambda/5$ simulation limit.
[Note the different polarization of the incident pulses for this cylinder.]

Figure 9 shows the comparison of the calculated and measured RCS for the (scaled-down) generic cylinder of Figure 1. Mismatches occur for the axial pulse between 6.5 and 7.5 GHz, and for the transverse pulse between 6.5 and 8.5 GHz.

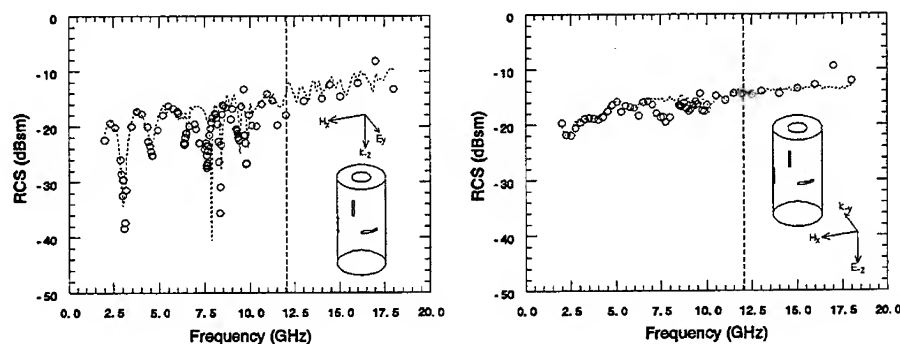


Figure 9. RCS of the generic cylinder: with aperture and three slots.
Dashed curve = Measurement. Circles = JUNCTION.
Vertical dashed line = $\lambda/5$ simulation limit.

DISCUSSION AND CONCLUSIONS

We have made a comparison of the computed and measured RCS of conducting cylinders with aperture and slots and have shown the degree of agreement that we have been able to obtain. It is very good except for minor discrepancies at some frequencies.

There are several possible causes of these discrepancies. The mismatch may be due to an inadequate "gating window" in the measurement process. It could be from problems with the EFIE-method near the internal resonant frequencies of the cylinders. A third reason could be the averaging of the cylindrical dimensions we use in approximating the 0.89mm-thick walls by ones with zero thickness. Another contribution to the mismatch may be that computations assume the mathematical models of the bodies to have infinite conductivity, while the metallic physical models have a large but nonetheless finite conductivity. The agreement may improve when some or all of these factors are taken into account.

REFERENCES

- [1] P. H. Pathak and R. J. Burkholder, "Modal, Ray, and Beam Techniques for Analyzing the EM Scattering by Open-Ended Waveguide Cavities", *IEEE Trans. Antennas Propagat.*, AP-37, 635-647, May 1989.
- [2] H. Ling, S.-W. Lee, and R.-C. Chou, "High-Frequency RCS of Open Cavities with Rectangular and Circular Cross Sections", *IEEE Trans. Antennas Propagat.*, AP-37, 648-654, May 1989.
- [3] S. M. Rao, D. R. Wilton, and A. W. Glisson, "Electromagnetic Scattering by Surfaces of Arbitrary Shape", *IEEE Trans. Antennas Propagat.*, AP-30, 409-418, 1982.
- [4] S.-U. Hwu and D. R. Wilton, "Electromagnetic Scattering and Radiation by Arbitrary Configurations of Conducting Bodies and Wires", *University of Houston, Technical Report 87-17*, 1988.
- [5] G.J. Burke and A.J. Poggio, "Numerical Electromagnetic Code", *Technical Document 116, Naval Electronic Systems Command*, 18 July 1977.
- [6] R. F. Harrington, *Time-Harmonic Electromagnetic Fields*, Chapter 6, McGraw-Hill, New York, 1961.

SESSION 4 - "GTD/UTD/PO ANALYSIS"

Chair: Dr. A.K. (Tony) Brown, Co-Chair: Dr. Shian U. Hwu

Overview of Analytic Techniques Used in OSU Reflector Antenna Code

Teh-Hong Lee and Roger C. Rudduck
The Ohio State University ElectroScience Laboratory
1320 Kinnear Road, Columbus, Ohio 43212-1191
Phone: (614)292-7981 Fax: (614)292-7297
E-mail: thl@tiger.eng.ohio-state.edu
E-mail: rudduck@tiger.eng.ohio-state.edu

Abstract

This paper presents theoretical techniques and capabilities of the current OSU Reflector Antenna Computer Code. The previous OSU NEC-Reflector Antenna Code has been widely used in analysis of reflector antennas. It has the capability for both near-field and far-field computation for reflector antennas with paraboloidal surfaces. A key feature of the code is its capability for a general reflector rim shape. The theoretical approach for computing the fields of the reflector is based on a combination of Geometrical Theory of Diffraction (GTD) and Aperture Integration (AI) techniques. The advantages of using AI and GTD are discussed in this paper. Other capabilities of the code include modeling commonly used feed horn antennas, feed blockage and strut scattering analysis. Recently, a different version of the code which contains many new options, such as Cassegrain and Gregorian dual reflectors and surface distortion analysis, have been developed internally at OSU. The overview of major techniques used in this computer code are presented in this paper.

Introduction

The NEC Reflector Antenna Code (NEC-REF) [1] which was developed under the support of the Navy has been widely used by government agencies, universities and industries for reflector antenna pattern analysis. It has the capability for both near-field and far-field computation for reflector antennas with paraboloidal surfaces. Subsequently, subreflectors with hyperbolic and elliptic surfaces were implemented in a different version of the computer code [2]. A key feature of the code is its capability for treating reflectors with general rim shapes. The theoretical approach used in the NEC Reflector Antenna Code for computing the fields of the reflector antenna is based on a combination of Geometrical Theory of Diffraction (GTD) and Aperture Integration (AI). Typically, AI is used to compute the main beam and near sidelobes for parabolic reflector and GTD is used to compute the wide-angle sidelobes. For subreflectors, GTD is used to compute the complete patterns. For near field calculations, GTD is sometimes used for the whole region.

The computer code also provides options for calculating patterns of several commonly used feed horn antennas. With calculated feed patterns, or user input feed

patterns, the code can be used to compute complete 360° patterns for the subreflector for a dual-reflector and then the main reflector. In addition, scattering due to blockage by the feed and its supporting struts can also be included in the analysis. In the following sections, the basic theoretical techniques for pattern analysis will be discussed.

Aperture Integration

The Aperture Integration method has been used for many years to compute the radiation patterns of reflector antennas. By this method the radiated field of a large aperture antenna can be determined from the aperture field distribution. Two efficient techniques have been employed in the NEC-REF Code to carry out the aperture integration which is performed over the portion of the aperture plane inside the reflector rim. One is the large subaperture method and the other is the rotating grid method [3]. The subaperture can be electrically large, thus minimizing the computer storage and also the amount of numerical integration required. The major feature of the rotating grid method is that it reduces the two-dimensional aperture integration into two one-dimensional integrations [3]. Computational advantages on the order of 10 to 100 in computer time ratios are frequently encountered because of the rotating grid feature.

Geometrical Theory of Diffraction

The GTD approach is used to analyze the wide-angle sidelobes and near field patterns for reflector antennas. A "segmented-rim GTD" method is implemented in the original NEC-REF Code. This method is similar to that of the diffraction by a flat plate in that the reflector rim is subdivided into segments and each segment is treated as an edge of a flat plate which is tangent to the reflector surface. Edge diffracted field and corner diffracted field for each rim segment are then calculated. Consequently, general reflector rim shapes with corners and edges can be analyzed. Smooth rim shapes can also be modeled by segmentation. Accurate results can be obtained if the rim segments are sufficient small. However, for a large reflector, the segmented-rim GTD may require significant computation time since contributions from all the rim segments and corners have to be calculated.

A different method, called multi-point GTD [4], has been implemented in the latest code. This approach applies numerical techniques to find the diffraction points and caustic distances. The edge diffracted field from each "true" diffraction point is then calculated numerically with the edge as part of the curved surface, instead of flat plate. Corner diffraction is added only if there is a "true corner" in the reflector rim. This method is much more efficient than the segmented-rim GTD approach. The disadvantage of multi-point GTD is that it cannot be used when the field point is near or at the caustic of the reflector, because a very large number of diffraction points will be found. In this case, the multi-point GTD method must be supplemented by the segmented-rim GTD method.

Feed Pattern Calculation

It is necessary to have feed pattern data in order to compute the reflector patterns. There are several ways to input feed pattern data in the code. One can input piece-wise feed pattern data (from either measured or calculated), or specify the feed pattern analytically, or specify the input feed horn geometry. Many types of feed antennas can be treated, such as circular waveguides, rectangular waveguides, rectangular pyramidal horns, and circular symmetric horns. For waveguide feeds, aperture integration is used to determine the feed patterns. For pyramidal horns, the GTD approach is used to calculate full 360° patterns. For circularly symmetric horns, the Aperture Integration (only for forward region) or Moment Method (for full 360°) is used.

Feed/Subreflector Blockage Calculation

The blockage effects caused by the feed or subreflector will reduce the gain and raise the sidelobe level of the reflector antenna. Blockage effects are analyzed by finding the incident fields on the blockage aperture and then calculating the forward scattered fields from this aperture by aperture integration of physical optics. The scattered fields are then subtracted from the main reflector pattern to determine the total fields. For a blockage aperture located within the projected geometrical optics (GO) region of the main reflector, only the geometrical optics field is necessary to be used as the incident field. On the other hand, if the blockage aperture is close to the edge of the projected GO region, or even outside the GO region, such as in offset reflector case, then the GO field is not sufficient and the edge diffracted field from the main reflector has to be included as the incident field [5].

Strut Scattering Calculation

Similar to feed/subreflector blockage, feed supporting struts can also reduce the antenna gain and raise the sidelobe level. Perfectly conducting struts with circular or general cross sections can be calculated in the computer code. By the input locations of the struts, the scattered fields from the struts are calculated by multiplying the incident field on the strut with a strut diffraction coefficient. The diffraction coefficients are determined from eigenfunction solutions of the scattering from a circular cylinder for struts with circular cross sections [6] and moment method solutions for struts with general cross sections [7].

Numerical Example

In this section, calculated and measured results for a 8 ft diameter prime focus fed reflector antenna at 11.0 GHz are presented. The antenna geometry is shown in Figure 1. The measured and calculated (AI and Moment method) patterns of the conical horn feed for the reflector are shown in Figure 2. Very good agreement

between the measured and moment method calculated patterns have been obtained. The AI result is not as accurate because the aperture of the horn antenna is only about 1.2λ in diameter where AI does not work as well. From these feed patterns, the main reflector patterns can be determined. The measured and calculated reflector E-plane patterns are shown in Figure 3. Note that both the feed and strut scattered fields have been included in the calculation. As can be seen good agreement has been obtained. Note that the two distinct lobes at $\theta \simeq \pm 75^\circ$ are caused by the four struts which appear in both the measured and calculated patterns.

Summary

The basic techniques used in the OSU Reflector Antenna Code have been presented in this paper. An example of an 8 ft diameter prime focus fed reflector antenna has been shown to validate the computer code. The agreement between the measured and calculated patterns indicates the accuracy of the code. The code also has the capabilities for analyzing reflector with array feeds [4], reflectors with imperfect surface profiles [8], and also reflectors with flat plates present in their vicinity. However, higher order terms such as multiple bounces between the reflector and the feed/subreflector and its supporting structure are not included. These higher order terms may not be important in some cases but they can affect the performance of the reflector in other situations. Consequently, it may be necessary to consider these higher order interaction terms in the analysis in order to obtain more accurate results.

References

- [1] R.C. Rudduck and Y.C. Chang, "Numerical Electromagnetic Code - Reflector Antenna Code, NEC-REF (Version 2), Part I: User's Manual," Report 712242-16, December 1982, The Ohio State University ElectroScience Laboratory, Department of Electrical Engineering, prepared under Contract No. N00123-79-C-1469 for Naval Regional Procurement Office.
- [2] T.H. Lee "Geometrical Optics and GTD Analysis of Subreflectors in Cassegrain and Gregorian Reflector Antennas," M.Sc. Thesis, The Ohio state University, Department of Electrical Engineering, June, 1984.
- [3] S.H. Lee and R.C. Rudduck "Aperture Integration and GTD Techniques Used in the NEC Reflector Antenna Code," IEEE Trans. Antennas Propagation, Vol. AP-33, pp. 189-194, February 1985.
- [4] Y.C. Chang, "Analysis of Reflector Antennas with Array Feeds Using Multi-Point GTD and Extended Aperture Integration," Technical Report 715559-3, The Ohio State University ElectroScience Laboratory, Department of Electrical

Engineering; prepared under Contract No. NAS1-17450 for NASA Langley Research Center, March 1984. (This report is also a Ph.D. dissertation, The Ohio State University, 1984).

- [5] R.C. Rudduck, Y.C. Chang and T.H. Lee, "The Multi-Point GTD and Extended Aperture Integration Techniques for Analysis of Reflector Antennas," in this proceeding.
- [6] S.H. Lee, R.C. Rudduck, C.A. Klein and R.G. Kouyoumjian, "A GTD Analysis of the Circular Reflector Including Feed and Strut Scatter," Report 4381-1, The Ohio State University ElectroScience Laboratory, Department of Electrical Engineering, May 1977.
- [7] J.H. Richmond, "An Integral-Equation Solution for TE Radiation and Scattering from Conducting Cylinders," Report 2902-7, The Ohio State University ElectroScience Laboratory, Department of Electrical Engineering, prepared under Contract No. NGL 36-008-138 for NASA Langley Research Center, October 1972.
- [8] T.H. Lee, R.C. Rudduck and M.C. Bailey "A Surface Distortion Analysis Applied to the Hoop/Column Deployable Mesh Reflector Antenna," IEEE Trans. Antennas Propagation, Vol. AP-37, pp. 452-458, April 1989.

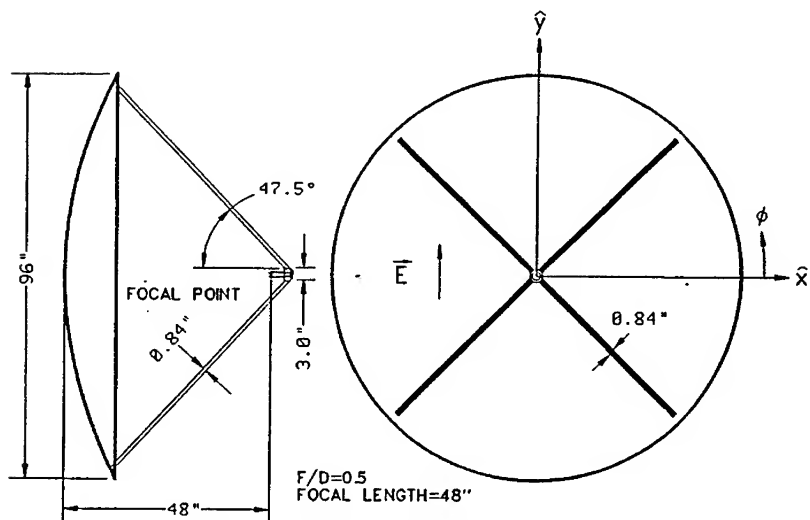


Figure 1. A prime focus fed reflector antenna.

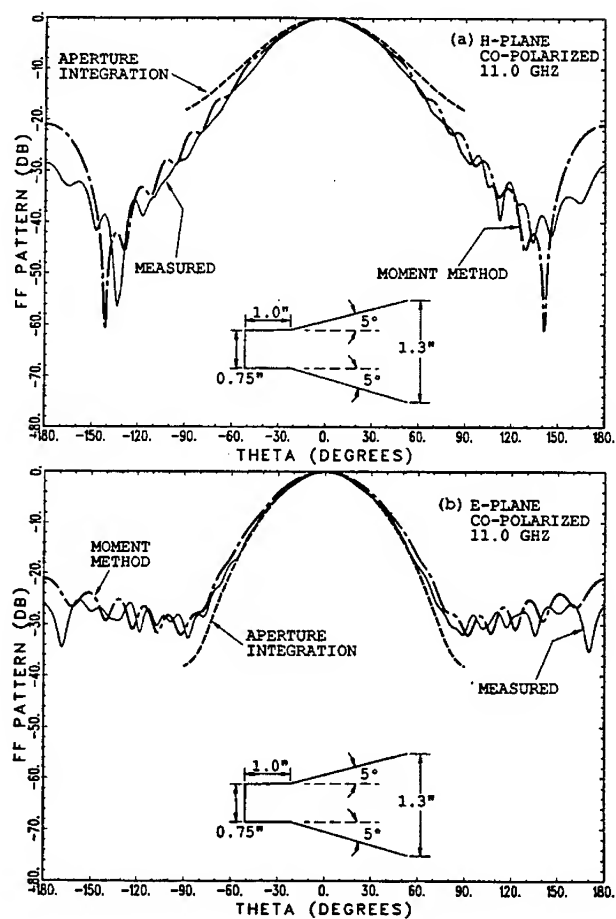


Figure 2. Measured and calculated feed patterns.

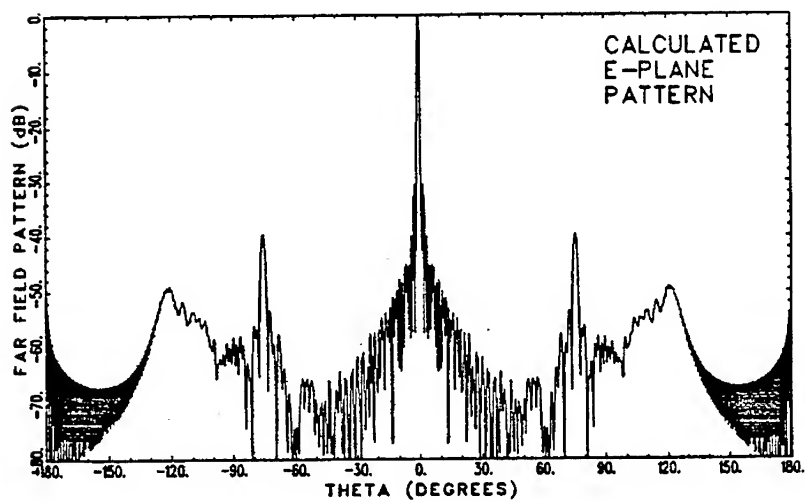
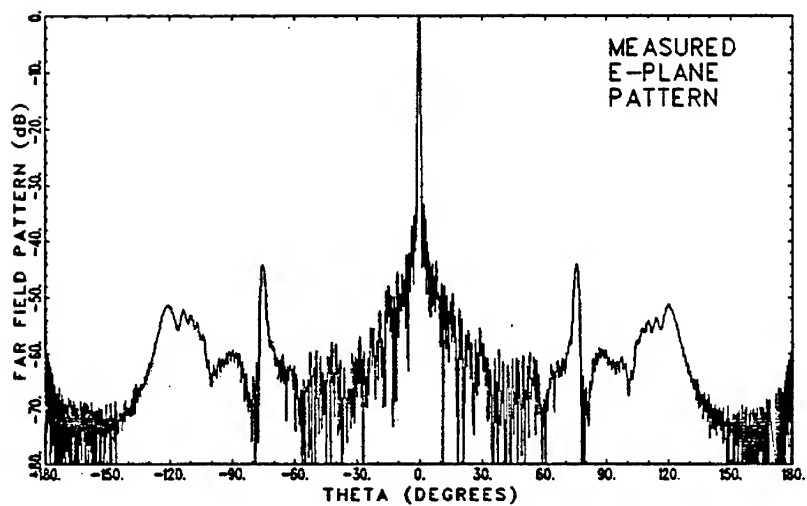


Figure 3. Measured and calculated reflector patterns.

SPACE STATION FREEDOM (SSF) ANTENNA PATTERN PREDICTIONS USING GEOMETRICAL THEORY OF DIFFRACTION

Shian U. Hwu and Jon S. Fournet
Lockheed Engineering & Sciences Company ¹
Houston, Texas 77058

Robert J. Panneton and G. Dickey Arndt
NASA/Lyndon B. Johnson Space Center
Houston, Texas 77058

Abstract

The ability of SSF Ultrahigh Frequency (UHF) antennas to communicate with an Extravehicular Activity (EVA) astronaut one meter behind SSF major structures is analyzed. The two UHF antenna booms should be mounted separately so that one boom is on the port side and the other boom is on the starboard side - one above the truss and one below the truss.

The scattering effects of the SSF structural elements on the Assembly/Contingency Subsystem (ACS) high gain steerable antenna patterns are analyzed. If a ± 15 degree cone is used to protect the ACS antenna boresight pattern, up to 1 dB of link budget will be required to compensate for the gain degradation in the ± 4 degree boresight region.

The scattering effects of a solar panel on the SSF Space-to-Ground Subsystem (SGS) steerable reflector antenna when the antenna is operated in the tracking (difference) mode are analyzed. It was shown that the solar panel scattering interference causes a shift in null position, a decrease in the depth of the null, as well as a decrease in the gain on the antenna difference mode patterns.

The electric field strength around the S-band and Ku-band high gain antennas was computed. The regions in which the electric fields exceed the specified maximum permitted Radio Frequency (RF) exposure to the Extravehicular Mobility Unit (EMU) electronic equipment are identified.

I. Introduction

It is important to be able to predict antenna performance in the SSF environment since the antenna patterns will be distorted due to electromagnetic reflection and diffraction by SSF obstructions. To ensure the antennas can meet design requirements, the system design must take into account such antenna pattern distortions. The system should be able to compensate for the distortion of the antenna patterns, but the antennas must provide reasonable gain throughout their assigned areas of coverage for the systems to function effectively.

Formerly, conventional antenna pattern prediction was based on full-scale mockup measurements. The large dimensions of a full-scale SSF mockup requires a large quiet zone for the illuminating field, which leads to high towers and, in conjunction with the far-field condition requirements, to a very large test range.

Another approach in solving the measurement problem is using an electromagnetic modeling technique capable of computing both near-field and far-field patterns. A reliable analytical tool provides for the early detection of problems and helps to find the best solutions. Modern high-speed computers with large storage capacity have made possible the theoretical calculation of the radiation pattern of antennas mounted on complex structures such as space vehicles. The main advantage of this mathematical method is that, once the shape of the vehicle has been represented in the computer, the influence of different positions of the individual antennas can be easily evaluated. If the position of an antenna has been selected on the basis of a computer evaluation, the number of measurements can be cut down to a minimum.

¹This work was supported by NASA/Johnson Space Center under contract NAS9-17900.

Since the SSF is large in terms of wavelength, the Geometrical Theory of Diffraction (GTD) is the best candidate for the task. The scattering effects of the SSF structural elements on the SSF antenna patterns are analyzed using the GTD.

II. Ultrahigh Frequency (UHF) Antenna

The SSF UHF antennas are designed to provide a UHF communications link between the SSF, Extravehicular Activity (EVA) astronauts, and the Space Shuttle Orbiter (SSO). The ability of two UHF antennas to communicate with an EVA immediately behind SSF major structures is a concern.

The purpose of this study is to determine the signal strength behind SSF major structures (solar panels, thermal radiators, trusses and modules). These regions are expected to have the most significant shadowing effects due to the large electrical size of the structures. The EVA directly behind these structures may be blocked from both antennas. The only signal present in these regions is due to the diffracted fields from edges and corners, which are usually very small compared to the direct and reflected fields. Since diffracted fields are the dominant terms in these regions, accurate computations are required.

The computed signal strength in terms of the electric field behind SSF major structures is presented and compared to the signal strength corresponding to the 0 dB link margin. Based on the results obtained, in order to increase the signal strength and to minimize the major structure near field shadowing effects when the EVA is working behind SSF major structures, the two UHF antenna booms should be mounted separately so that one boom is on the port side and the other boom is on the starboard side - one above the truss and one below the truss.

Analysis

The Permanently Manned Configuration (PMC) phase at the Local Vertical Local Horizontal (LVLH) flight mode is considered for the SSF. In all cases, the solar panels are oriented at $\alpha = 0^\circ$ and $\beta = 90^\circ$ and the thermal radiators are at 0° (vertical in the X-Z plane). The antennas are pointed in the $\pm X$ axis direction. The Space Station structural elements are modeled as perfect electrical conductors.

The SSF UHF antenna is a 1/2-turn quadrifilar helical antenna with a beamwidth of $\pm 90^\circ$ from boresight at -4 dBic. A frequency of 415 MHz was used in this analysis. The locations of the UHF antennas examined are referenced to the origin of the SSF coordinate system. Antenna boom locations, at (1.44, ± 15.15 , ± 3.26) meters, are shown in Fig. 1. Three combinations for two antennas operating simultaneously were analyzed as follows :

1. Case 1: Ant. 3+ pointed at +X and Ant. 3- pointed at -X
2. Case 2: Ant. 3+ pointed at +X and Ant. 4- pointed at -X
3. Case 3: Ant. 3+ pointed at +X and Ant. 2- pointed at -X

In the near field, there are three orthogonal components of the electric field with arbitrary relative amplitudes and phases. The tip of the electric vector traces out an ellipse lying in an arbitrary plane. The average value of the square of the instantaneous electric field vector is

$$|E(\text{volts/meter})|^2 = \frac{1}{2} (E_x^2 + E_y^2 + E_z^2).$$

The results presented in the following section are in dBV/M which is defined as

$$E(\text{dBV/M}) = 10 \log[|E(\text{volts/meter})|^2].$$

Based on the SSF UHF system to EVA link margin data, there is a 17.4 dB link margin for the UHF antenna with a -18 dBW EIRP at 100 M range. This corresponds to an electric field of -40.22 dBV/M. The 0 dB link margin corresponds to an electric field of -57.62 dBV/M.

Results

Fig. 1 shows the front view of the SSF and the antenna locations. Fig. 2 shows a top view of the SSF. Signal strength along the dashed lines was computed and presented in the Figs. 3-6.

The critical regions where signal strengths fall below the 0 dB margin were identified as behind the solar panel, behind the thermal radiator and under the truss.

The most critical regions, where the UHF communications link to the EVA may not be maintained for all three antenna combinations examined, are the regions immediately behind the solar panels. These significant shadow regions are due to the large electrical size of the solar panels and the long path of travel between the UHF antennas and the solar panels.

In order to increase the signal strength and to minimize the major structure near field shadowing effects when the EVA astronaut is working behind SSF major structures, the two UHF antenna booms should be mounted separately so that one boom is on the port side and the other boom is on the starboard side - one above the truss and one below the truss (Ant. 3+ & 2-).

Placement of the two antennas on opposite sides of the SSF reduces shadow regions and gives a more uniform distribution of radiated energy for both port and starboard sides of the SSF.

In the near field, the polarization ellipse is not necessarily within the $\theta - \phi$ plane of the outward traveling direction as in the far field case. In order to obtain the major component and to avoid the minor component of the polarization ellipse, EVA astronaut maneuvering may be required.

III. ACS High Gain Steerable Antenna

The S-band subsystem, also known as the ACS subsystem, is a bi-directional Radio Frequency (RF) link utilizing the Tracking and Data Relay Satellite System (TDRSS) S-band Single Access (SSA) service to receive audio, software uploads, and commands from the ground station, and to transmit audio and core element telemetry to the ground station. In addition, the S-band subsystem is utilized to support ground based tracking services for station orbit determination.

The scattering effects of the SSF structural elements on the ACS high gain antenna patterns are analyzed. The predicted antenna patterns were computed using the GTD technique. Based on the results accomplished, if a ± 15 degree cone is used to protect the ACS high gain antenna boresight pattern, up to 1 dB of link budget will be required to compensate for the gain degradation in the ± 4 degree boresight region due to multipath interference from SSF structure.

Analysis

The ACS inboard antenna is located at $x, y, z = -0.2, 20.72, -3.99$ meters and the outboard antenna is located at $x, y, z = 0.38, 22.68, -3.99$ meters referenced to the origin of the SSF coordinate system, as shown in Fig. 7. A frequency of 2.175 GHz was used.

The major structure elements causing interference to the ACS high gain antenna patterns were identified as the RCS module, the starboard side thermal radiator and the starboard side solar panel.

There are four different flight orientation modes that have been considered for SSF operation. These are the Local Vertical Local Horizontal (LVLH), Arrow, Gravity Gradient (GG), and Inverted Gravity Gradient (IGG) flight modes.

Since the ACS high gain antenna has a directive pattern, it is not necessary to include all structural elements of the SSF in the model. Instead, only major components such as solar panels, RCS modules, and thermal radiators are modeled in this analysis. The SSF structure elements are modeled as perfect electrical conductors.

The ACS antenna patterns with various antenna orientations for each major interfering structure are computed using the GTD technique.

Results

Fig. 8 shows a summary of the maximum antenna gain degradation in the $\pm 4^\circ$ antenna boresight region due to each major interfering structure. Also, shown in Table 1, is the maximum antenna gain degradation in the antenna $\pm 4^\circ$ boresight region with various size cone protection.

The results indicate that, if significant interference (more than 1 dB antenna gain loss) with ACS antenna patterns is to be avoided, the ACS steerable antenna 3 dB beamwidth must be kept clear of SSF structural blockage. This means that the ACS high gain antennas should not be pointed within 15 degrees of obstructions.

IV. SGS Steerable Reflector Antenna

The Ku-band SGS subsystem is a single direction RF link utilizing the TDRSS Ku-band Single Access (KSA) service to transmit payload data and video to the ground station.

The SSF is very large in terms of physical and electrical size and is a complex structure. The solar panels and the thermal radiators are rotated to maintain a preferential orientation with respect to the sun. The SGS antenna must track signals in the upper hemisphere and will encounter scattering interference from the SSF structure, especially the solar panels.

The scattering effects of a solar panel on the SGS steerable reflector antenna when the antenna is operated in the tracking (difference) mode are analyzed. To verify the analytical model, measurements were performed on the far-field antenna test facility. Good agreement between computed and measured results was obtained. It was shown from computation and experiment that the solar panel scattering interference causes a shift in null position, a decrease in the depth of the null, as well as a decrease in the gain on the antenna difference mode patterns.

Analysis

A 4-foot reflector antenna operated at 13.5 GHz was used to simulate the SGS antenna.

The solar panel is a very complex structure which consists of many small solar cells and connected copper wires. Such detailed modeling will require large amounts of computer resources in storage memory and computing time.

To characterize the electromagnetic property of the solar array, two electromagnetic measurements of the solar array sample have been performed at Ku-band frequencies.

The measured results from the backscattering measurements indicate that the solar array sample exhibited about 1 to 2 dB less signal return than a flat metal plate of the same area. The results from the insertion loss measurements show the transmission loss of the solar array sample to be approximately 20 dB. Both measurements indicate that the solar array is highly reflective at Ku-band. A conducting plate is assumed to be a reasonable electromagnetic model for the solar panel.

To verify the analytical model, measurements were performed on the far-field antenna test facility.

Results

As shown in Figs. 9-12, the computed and measured antenna difference mode patterns show that the tracking lobes of the 4-foot reflector antenna operated at 13.5 GHz were significantly affected due to the blockage by the solar panel. It was illustrated by both computed and measured antenna difference mode patterns that the scattering effects from the solar panel significantly affect not only the near-in sidelobes but also the main lobes.

When the antenna was blocked by the solar panel, the strong reflection from the solar panel increases the backlobes to a very high level. These backlobes raise Electromagnetic Compatibility/Electromagnetic Interference (EMC/EMI) concerns to nearby equipment EVA.

The conclusion observed and supported by both computed and measured results was that a gain loss in the main lobes and a shift in null position, as well as a decrease in the depth of the null, were observed for the antenna difference mode patterns with the solar panel penetrating into the projected antenna aperture cylinder.

In order to avoid significant scattering interference, the SGS antenna projected aperture cylinder must be kept clear from any SSF structural blockage. This means that the SGS antenna projected aperture cylinder should not be pointed onto any SSF structure, otherwise significant antenna pattern degradation will occur.

V. Radiation Hazard Analysis

Predicting the near field intensities (strengths) around an antenna and structures is important in assessing personnel and electronic equipment RF exposure hazards.

There are serious concerns about the possible high levels of electric field strength produced by the SSF ACS S-band conical horn antenna and the SGS Ku-band reflector antenna.

The regions in which the electric fields exceed the specified maximum permitted RF exposure to the Extravehicular Mobility Unit (EMU) electronic equipment and Extravehicular Activity (EVA) astronaut are identified for the SSF ACS antenna and the SGS antenna.

ACS High Gain Steerable Antenna

The near-field intensity levels around the SSF produced by the ACS high gain antenna are a concern because of the high radiated power. The electric field strength levels that an astronaut or sensitive electronic equipment might experience due to S-band antenna system operation are required to comply with specified RF radiation protection criterion.

A maximum of 40 watts (16 dBW) radiated power at the antenna aperture was estimated for the S-band high gain steerable horn antenna. These estimates are based on the maximum estimated Effective Isotropic Radiated Power EIRP (29 dBW) and the specified minimum antenna gain (13 dBic):

$$\text{RADIATED POWER}_{\text{max}}(16 \text{ dBW}) + \text{GAIN}_{\text{antenna}}(13 \text{ dBic}) = \text{EIRP}_{\text{max}}(29 \text{ dBW})$$

The transmit frequency for the ACS antenna is 2.265 GHz. The maximum permitted RF exposure to the EMU has recently been recertified to 106 V/m peak at the S-band frequencies from a previous 20 V/m peak. The regions in which the electric fields are greater than the maximum permitted RF exposure are identified in Fig. 13. Based on the results obtained, a cylindrical region of 1 meter diameter and 2.3 meters in length, extending outward from the antenna and centered about the boresight axis, should be avoided to reduce the risk associated with excessive S-band antenna RF exposure to the EMU electronic equipment.

SGS Steerable Reflector Antenna

A maximum of 10 watts (10 dBW) radiated power at the antenna aperture was estimated for the Ku-band SGS reflector antenna. These estimates are based on the maximum allowable EIRP (56 dBW) and the specified minimum antenna gain (46 dBic):

$$\text{RADIATED POWER}_{\text{max}}(10 \text{ dBW}) + \text{GAIN}_{\text{antenna}}(46 \text{ dBic}) = \text{EIRP}_{\text{max}}(56 \text{ dBW})$$

The transmit frequency for the Ku-band antenna is 15 GHz. The maximum permitted RF exposure to the EMU is 20 V/m peak (or 14.14 V/m rms) at the Ku-band frequencies. The regions in which the electric fields are greater than the maximum permitted RF exposure are identified in Fig. 14. Based on the results obtained, a cylindrical region of 2.5 meters diameter and 230 meters in length, extending outward from the antenna and centered about the boresight axis, should be avoided to protect the EMU electronic equipment and reduce the risk associated with the Ku-band antenna RF exposure.

References

- [1] R. J. Marhefka, and J. W. Silvestro, "Near Zone - Basic Scattering Code User's Manual with Space Station Applications", NASA Contractor Report 181944, ElectroScience Laboratory, Ohio State University, December 1989.
- [2] R. C. Rudduck and Y. C. Chang, " Numerical Electromagnetic Code - Reflector Antenna Code (NEC-REF), " ElectroScience Laboratory, The Ohio State University, December 1982.

Table 1: Maximum gain degradation in the antenna $\pm 4^\circ$ boresight region with various size cone protection.

Cone	RCS Module	Thermal Radiator	Solar Panel
$\pm 0^\circ$	13.9 dB	10.1 dB	15.3 dB
$\pm 5^\circ$	4.11 dB	4.3 dB	3.31 dB
$\pm 10^\circ$	1.13 dB	1.13 dB	0.58 dB
$\pm 15^\circ$	0.73 dB	0.81 dB	0.36 dB
$\pm 20^\circ$	0.33 dB	0.35 dB	0.26 dB
$\pm 25^\circ$	0.11 dB	0.21 dB	0.06 dB
$\pm 30^\circ$	0.07 dB	0.09 dB	0.06 dB

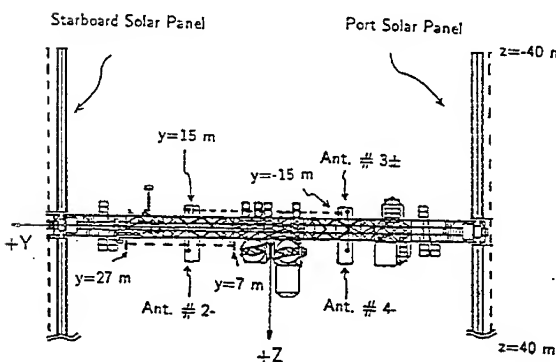


Figure 1: Front view of the Space Station. Signal strength along the dashed lines was computed.

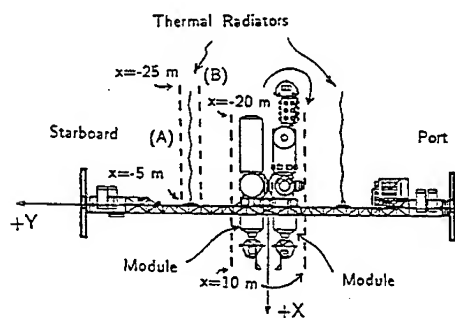


Figure 2: Top view of the Space Station. Signal strength along the dashed lines was computed.

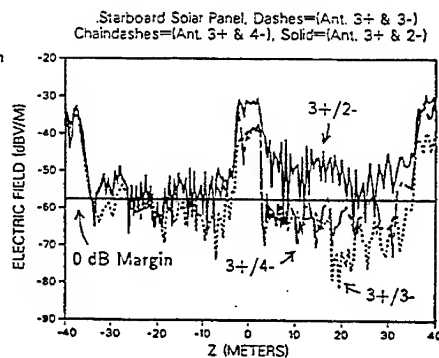


Figure 3: Signal strength along a line ($x=0$ m, $y=41$ m, -40 m $\leq z \leq 40$ m) at 1 meter behind the starboard side solar panel, outboard of panel.

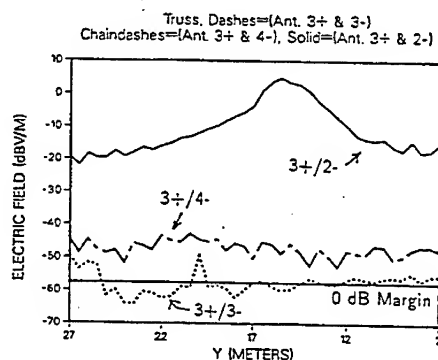


Figure 4: Signal strength along a line ($x=0$ m, 7 m $\leq y \leq 27$ m, $z=3$ m) at 1 meter below the starboard side truss.

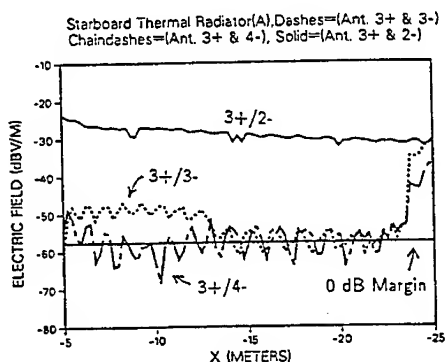


Figure 5: Signal strength along a line $(-25 \text{ m} \leq x \leq -5 \text{ m}, y=15.6 \text{ m}, z=0 \text{ m})$ at 1 meter from the starboard side thermal radiator along line (A), outboard of the radiator.

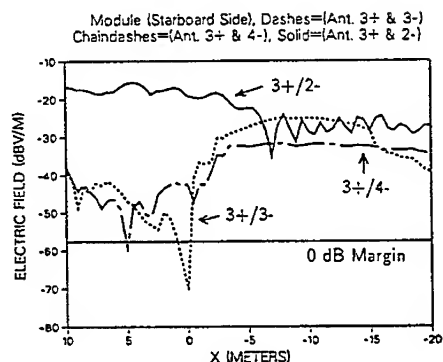


Figure 6: Signal strength along a line $(-20 \text{ m} \leq x \leq 10 \text{ m}, y=6.5 \text{ m}, z=4.5 \text{ m})$ at 1 meter from the starboard side module, outboard of the module.

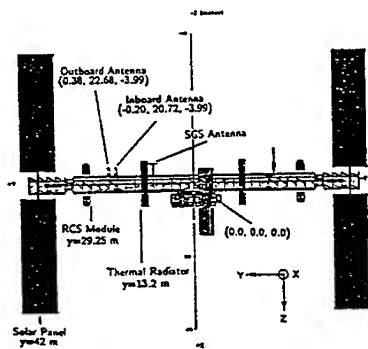


Figure 7: The proposed ACS antenna locations.

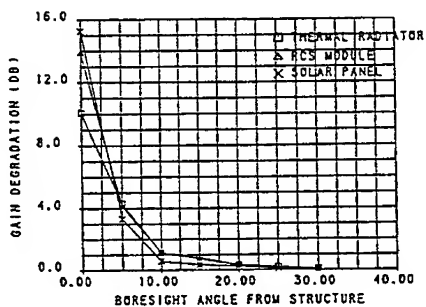


Figure 8: Maximum antenna gain degradation in the $\pm 4^\circ$ antenna boresight region due to each major interfering structure.

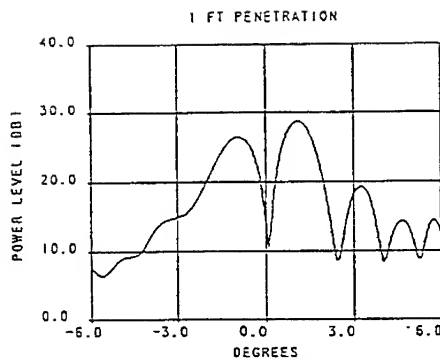


Figure 9: Computed difference pattern for the 4-foot reflector with the solar panel penetrating 1 foot into the projected aperture cylinder.

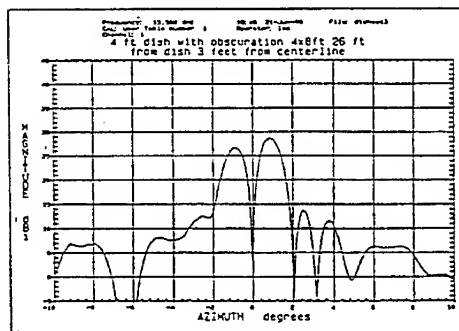


Figure 10: Measured difference pattern for the 4-foot reflector with the solar panel penetrating 1 foot into the projected aperture cylinder.

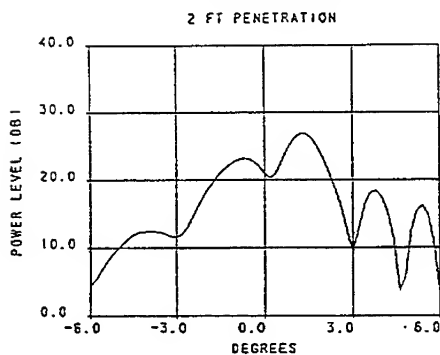


Figure 11: Computed difference pattern for the 4-foot reflector with the solar panel penetrating 2 feet into the projected aperture cylinder.

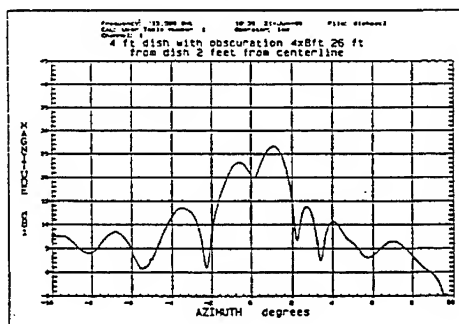


Figure 12: Measured difference pattern for the 4-foot reflector with the solar panel penetrating 2 feet into the projected aperture cylinder.

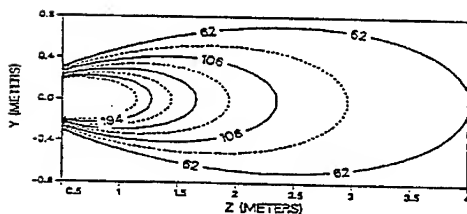


Figure 13: The electric field intensities produced by the ACS high gain antenna with a maximum of 40 watts radiated power.

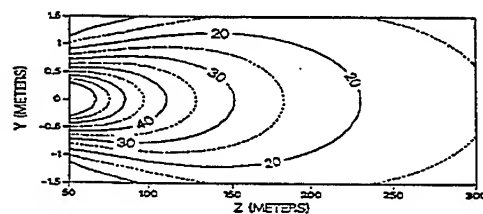


Figure 14: The electric field intensity produced by the SGS reflector antenna with a maximum of 10 watts radiated power.

The Multi-Point GTD and Extended Aperture Integration Techniques for Analysis of Reflector Antennas

Roger C. Rudduck and Teh-Hong Lee
The Ohio State University ElectroScience Laboratory
1320 Kinnear Road, Columbus, Ohio 43212-1191
Phone: (614)292-7981 Fax: (614)292-7297
E-mail: rudduck@tiger.eng.ohio-state.edu
E-mail: thl@tiger.eng.ohio-state.edu

Yueh-Chi Chang
Raytheon Company
430 Boston Post Road, Mail Stop LL1, Wayland, MA01778
Phone: (508) 440-1940 Fax: (508) 440-6468

Abstract

The NEC Reflector Antenna Code incorporate a rather flexible approach called segmented rim GTD for calculating the wide-angle sidelobes and near zone patterns of reflector with general rim shapes. One purpose of this paper is to describe an approach called multi-point GTD which has almost as much flexibility as the segmented rim GTD approach but is typically 10-20 times more efficient. Another purpose is to describe an approach called the extended aperture integration (AIE). The AIE method adds the diffracted fields from the reflector rim to the Geometrical Optics fields in the aperture plane. The AIE is more accurate than conventional aperture integration, especially for offset reflectors. More importantly, the AIE is useful for modeling scattering by structures within or near the projected aperture of the reflector.

Introduction

The NEC Reflector Antenna Code incorporates a rather flexible approach which uses GTD or what has become known as UTD (Uniform Geometrical Theory of Diffraction) [1] for calculating the wide-angle sidelobes and near zone patterns of reflectors with general rim shapes. By this approach, which we call segmented rim GTD, the reflector rim is subdivided into many straight segments and corner diffraction is used to calculate the contributions from each of the rim segments. One purpose of this paper is to describe a new approach called multi-point GTD which has almost as much flexibility as the segmented rim GTD approach but is typically 10-20 times more efficient.

Another purpose is to describe an approach called the Extended Aperture Integration (AIE). The AIE is more accurate than conventional aperture integration, especially for offset reflectors. More importantly, the AIE is useful for modeling scattering by structures within or near the projected aperture of the reflector.

The validity of the AIE methods are demonstrated by comparing results with those from the segmented rim GTD method. The capability of the AIE method for modeling scatterers is illustrated by an example of an offset reflector in which the feed support structures is located outside of the projected aperture of the reflector.

Segmented Rim GTD

The advantage of the segmented rim GTD which is used in the NEC-REF Code [2, 3] is that it can treat rather general rim shapes. An example of a reflector with a projected rim shape which is rectangular is shown in Figure 1. Note that the resulting rim is curved in three-dimensions. Since the corner diffraction solution [4] for a straight edge is used, the curved rim needs to be subdivided into many segments to achieve a good piece-wise fit to the 3-D rim. Similarly, many segments are needed to model a circular rim shape, at least 36, even for small reflector diameters. Thus, the segmented rim GTD is rather time-consuming because of the large number of corner diffraction contributions.

Multi-Point GTD

This approach, which we have designated multi-point GTD, combines the flexibility of the segmented rim GTD with the high efficiency of the basic analytic GTD approach. With the latter approach, the diffracted field contributions are determined for reflector rim shapes that can be specified analytically. In the frequent case of circular rim shapes, the locations of the two diffraction points are easily determined.

With the multi-point GTD approach [5], the reflector rim geometry is specified in the same way as with the segmented rim GTD approach. However, instead of summing the corner diffraction contribution from each segment, the edge diffraction points and true corner points, if any, are determined by a numerical search. Numerical approaches are also used to calculate the caustic distance used in the GTD calculation by determining the "spreading" or angle between two closely spaced diffracted rays. Then the contributions from the edge diffraction rays and the corner diffraction rays are summed as indicated by Figure 2a. In some cases, these will be more than two edge diffracted rays as in the near zone case of a circular reflector shown in Figure 2b.

The multi-point GTD was tested for both far zone and near zone calculations and for circular, elliptical and rectangular rim shapes. The multi-point GTD and the segmented rim GTD gave essentially the same results. The multi-point GTD was found to be typically 10-20 times faster. This improvement in computational efficiency permits practical computations with the AIE method described in the following section.

Extended Aperture Integration

The Extended Aperture Integration (AIE) method is based on adding the diffracted fields from the reflector rim to the aperture fields as shown in Figure 3a. The multi-

point GTD is used to improve the efficiency of the near field calculations. Since the diffracted fields contribute significantly outside the projected aperture, the integrating aperture must be extended as shown in Figure 3b. In theory, the aperture integration should extend to infinity. However, it was found that the aperture fields beyond the stationary phase point do not contribute much to the integral. The addition of the diffracted fields yields more accurate aperture fields although they are still not the true fields because multiple diffraction terms are not included. Note that the extended aperture plane should be located a few wavelengths in front of the original reflector aperture plane in order to reduce the double diffraction effect. This distance (DZ) should not be too long; otherwise, the new aperture needs to be extended a lot to cover the stationary phase point.

The offset reflector example used by Chu and Turrin [6] was chosen to demonstrate the AIE technique. The position and size of the extended aperture used for the AIE are shown in Figure 4. The far zone pattern in the $\phi = 0^\circ$ (horizontal) and 90° (vertical) planes as calculated by the AIE, GTD and AIC are shown in Figure 5. The AIC and GTD sidelobes overlap well for the $\phi = 0^\circ$ pattern but do not overlap for $\phi = 90^\circ$ pattern. It can be seen that the AIC is not adequate for the $\phi = 90^\circ$ plane in this case. On the other hand, the AIE results agree well with AIC in the main beam region and with GTD in the wider angle sidelobes.

The AIE approach provides good insight into the limitation of conventional aperture integration. However, the well-known approach of integrating the currents on the reflector surface or surface current method overcomes this limitation. Consequently, the AIE method is more useful for modeling obstacles in or near the reflector aperture as discussed in the next section.

Modeling of Aperture Blockage

One of the most common types of aperture blockage is caused by the feed in a center-fed reflector. In this case the feed blockage area is usually small and its illumination can be treated as uniform. Consequently, the forward scattering by a typical feed can be approximated as that of a flat plate with either a circular or rectangular shape. The scattered field can then be determined by simple analytic formula. The scattered field is then subtracted from the reflector fields, as is done in the NEC Reflector Code [2].

This simple feed blockage model cannot be used for offset reflectors because the feed and its supporting structure is usually outside or near the edge of the projected geometrical optics (GO) aperture of the reflector. Thus, the feed structure is illuminated by a non-uniform aperture field which includes a strong diffracted field component. The aperture field illumination of the feed structure consists entirely of diffracted fields for structures located entirely outside the projected aperture. In this case the simple feed blockage model predicts zero scattering, when, in fact, there will be some.

The AIE method provides an approach for modeling the feed scattering effects in offset reflectors, as well as other obstacles near reflector apertures. One example is the pie-shaped reflector shown in Figure 6a. The feed and its support mast are located outside of the projected GO aperture. With the AIE approach, we model the feed and mast by a flat plate located on the aperture plane. The rim of the flat plate is determined by the outline of the feed and mast projected onto the aperture plane as shown in Figure 6b. The fields incident on this equivalent plate area are calculated by using the multi-point GTD. These incident fields are integrated by the AIE approach to determine the forward scattered fields as shown in Figure 7a. The scattered fields are then subtracted from the reflector fields, given in Figure 7b, to determine the total reflector pattern as shown in Figure 7c. The measured pattern is shown in Figure 7d. Comparing Figures 7b, 7c and 7d, it is found that the agreement between calculated and measured patterns for $-10^\circ \leq \theta \leq 0^\circ$ is improved after the feed scattering effect is included. The differences for $0^\circ \leq \theta \leq 10^\circ$ are probably due to the fact that reflections from the feed mast are not modeled in the calculation.

References

- [1] R.G. Kouyoumjian and P. Pathak, "A Uniform Geometrical Theory of Diffraction for an Edge of a Perfectly Conducting Surface," *Proc. IEEE*, Vol. 62, No. 11, pp. 1448-1461, November 1974.
- [2] R.C. Rudduck and Y.C. Chang, "Numerical Electromagnetic Code - Reflector Antenna Code, NEC-REF (Version 2), Part I: User's Manual," Report 712242-16, December 1982, The Ohio State University ElectroScience Laboratory, Department of Electrical Engineering; prepared under Contract No. N00123-79-C-1469 for Naval Regional Procurement Office.
- [3] S.H. Lee and R.C. Rudduck, "Aperture Integration and GTD Techniques Used in the NEC Reflector Antenna Code," *IEEE Trans. Antennas Propagation*, Vol. AP-33, pp. 189-194, February 1985.
- [4] F.A. Sikta, W.D. Burnside, T.T. Chu and L. Peters, Jr., "First-Order Equivalent Current and Corner Diffraction Scattering From Flat Plate Structures," *IEEE Trans. Antennas Propagation*, Vol. AP-31, pp. 584-589, July 1983.
- [5] Y.C. Chang, "Analysis of Reflector Antennas with Array Feeds Using Multi-Point GTD and Extended Aperture Integration," Technical Report 715559-3, The Ohio State University ElectroScience Laboratory, Department of Electrical Engineering; prepared under Contract No. NAS1-17450 for NASA Langley Research Center, March 1984. (This report is also a Ph.D. dissertation, The Ohio State University, 1984).

- [6] T.S. Chu and R.H. Turrin, "Depolarization Properties of Offset Reflector Antennas," IEEE Trans. Antennas Propagation, Vol. AP-21, pp. 339-345, May 1973.

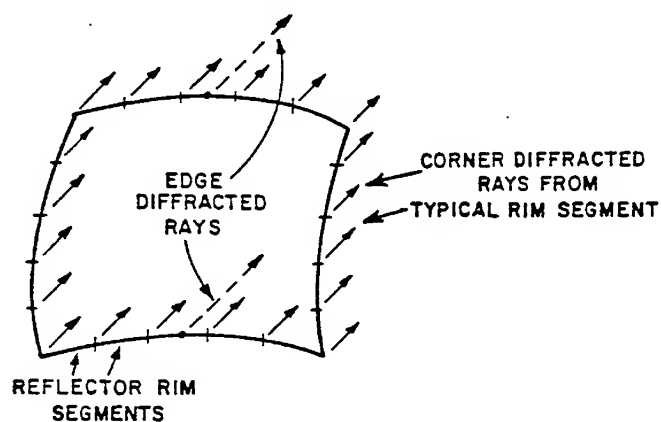


Figure 1. Diffracted rays in the segmented rim GTD.

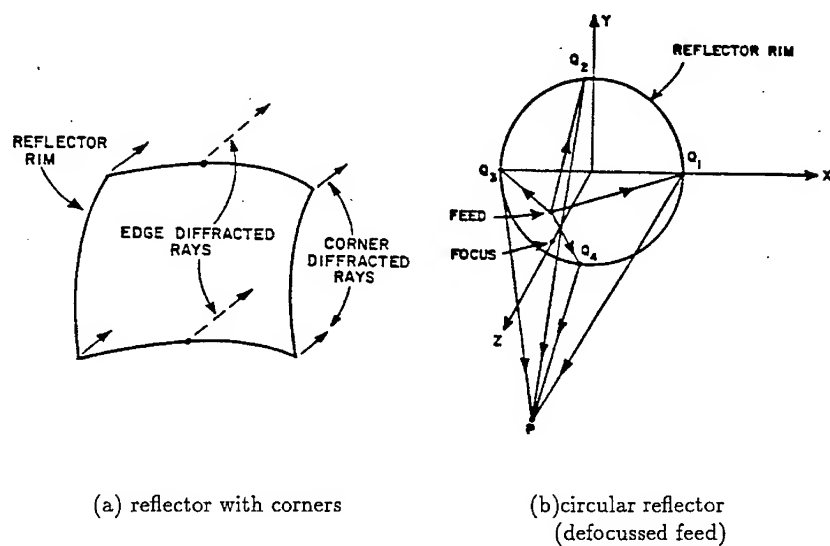
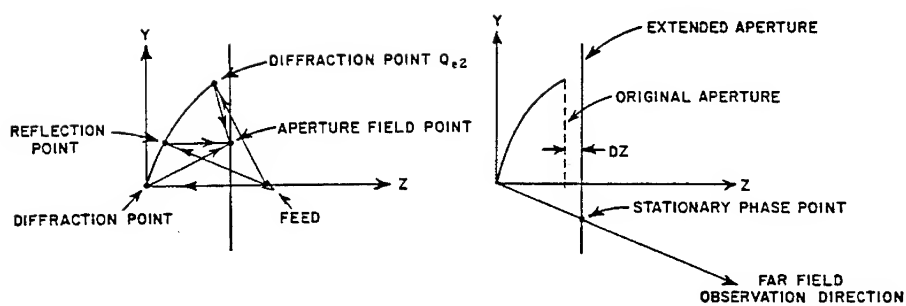


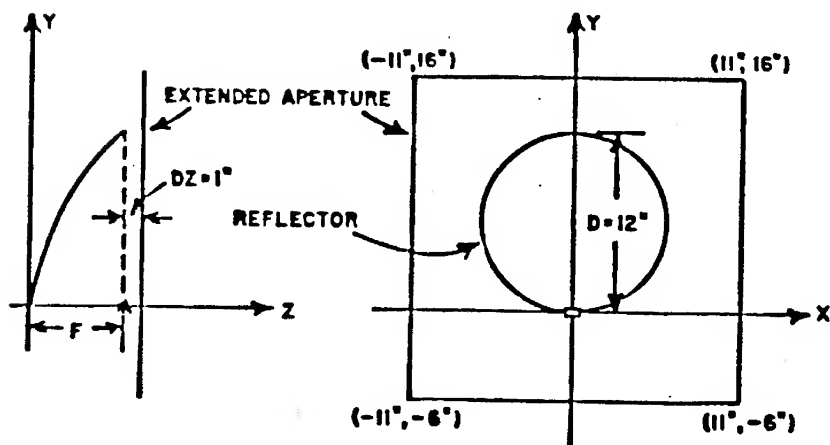
Figure 2. Diffracted rays in the segmented rim GTD.



(a) diffracted and GO fields

(b) extended aperture

Figure 3. The features in the AIE.



$D=12''$, $F=6''$, $\psi_T = \theta_c = 45^\circ$, $f=18.5$ GHz

Figure 4. The extended aperture for an offset reflector [6].

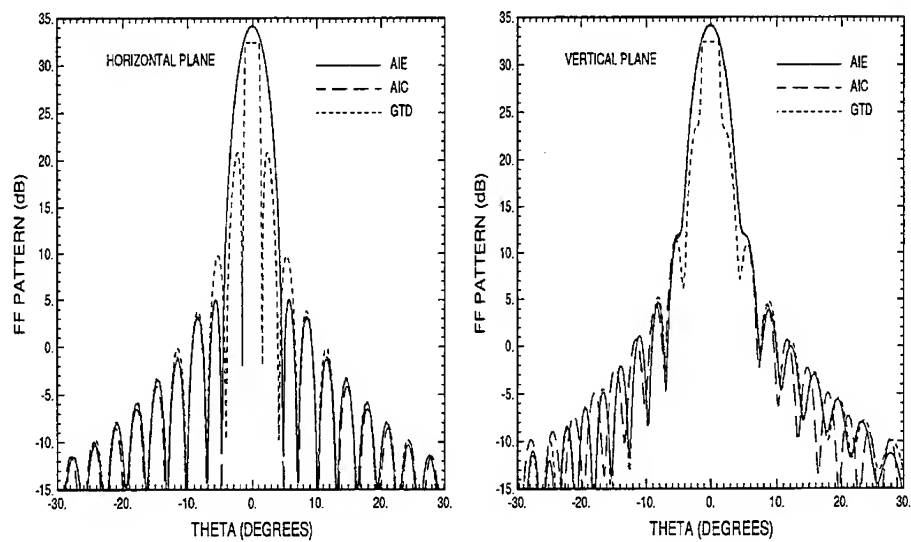


Figure 5. Calculated far-field pattern of the offset reflector.

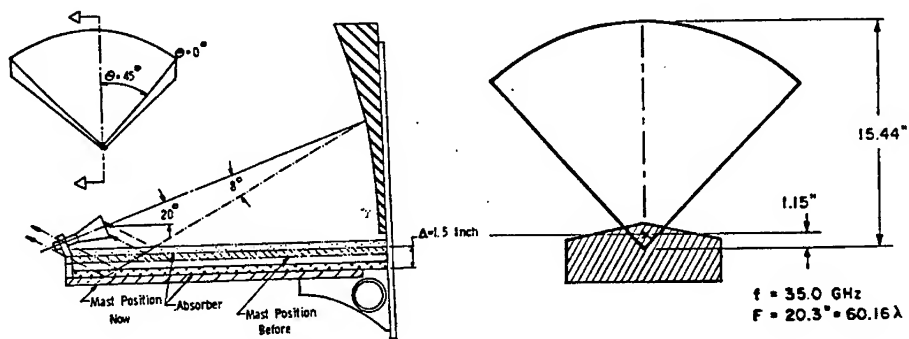
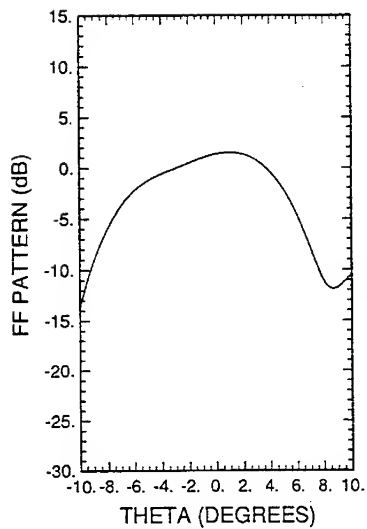
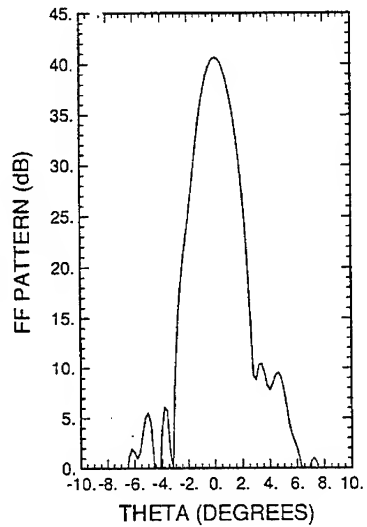


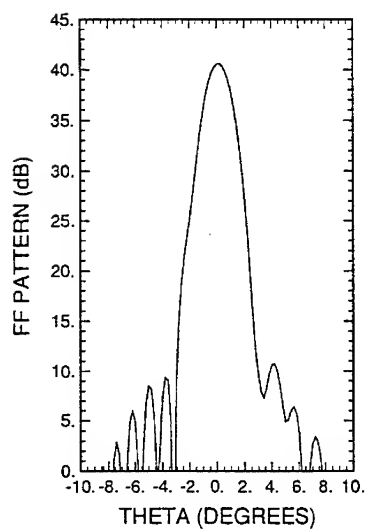
Figure 6. A pie-shaped reflector.



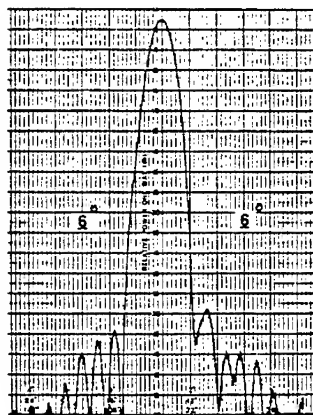
(a) feed blockage



(b) reflector field



(c) total field



(d) measured pattern

Figure 7. Far field patterns of the pie-shaped reflector.

SESSION 5 - "COMPUTATIONAL ELECTROMAGNETICS

THE NEXT GENERATION"

Chair: Mr. Kenneth R. Siarkiewicz

THE ELECTROMAGNETIC MODELING AND SIMULATION ENVIRONMENT FOR SYSTEMS (EMSES)

Kenneth R. Siarkiewicz
Rome Laboratory/ERPT
525 Brooks Road
Griffiss AFB NY 13441-4505

Introduction

For more than twenty years Government and commercial agencies have been using a small number of generally available, general purpose computer programs to characterize the electromagnetic (EM) phenomena associated with radiating and scattering systems. These include the Numerical Electromagnetic Code (NEC), the Basic Scattering Code (BSC), and the General Electromagnetic Model for the Analysis of Complex Systems (GEMACS). Each of these codes has undergone evolution and revolution during its life in order to incorporate theoretical developments in electromagnetics sciences and to provide some measure of capability to treat new technology being incorporated into the DoD's inventory (e.g., composite materials, high performance phased arrays).

Nonetheless, in spite of the continued enhancements of these tools each of them is hampered by one common characteristic which precludes the possibility of endless evolution—an initial development that occurred at a time when hardware, software, and computational electromagnetics (CEM) technologies were just beginning to develop into the powerful forms that exist today. This is not an indictment of the utility of the codes or a criticism of their developers. It is simply a conclusion based on reflection of the genesis, history, and foreseeable future of CEM.

This paper briefly examines the limitations of the more commonly available tools and just as briefly discusses the driving forces which determine the requirements of future CEM tools. The majority of the paper is devoted to a description of a CEM environment which will provide EM analysts and system designers with an integrated set of tools and procedures to design and develop the complex systems and C³I platforms of the 21st century.

Necessary Characteristics

An example C³I system of the future is a surveillance system whose function is to detect, track, and identify a target with an extremely small radar cross section flying in a high clutter environment. The antenna is a high performance, adaptive phased array whose far-field pattern has a narrow main beam, ultralow sidelobe levels, and is well behaved as a function of scan angle. While the technology exists to design such an antenna, the difficult task is its fabrication to the tolerances required to maintain precise phase relationships. The nearly impossible task is to maintain the desired far-field beam pattern when the phased array is mounted on the airframe, which is a complex structure in terms of shape and material make-up. Other factors of surveillance system design will also impact the design of the antenna. In addition, the mission and theater of operations will also be driving forces which influence the required performance and characteristics of the antenna.

This example and many others like it provide the foundation for the principal factors which underlie the design and development of the next generation EM modeling and simulation

environment for systems (EMSES). Insight and direction for EMSES will also be derived from the body of experience gained in the development, use, maintenance, and enhancement of the current widely used system-level CEM codes. These include as a minimum the following:

- Ability to specify geometrical detail to a high degree of resolution
- Efficient interface with commonly used geometry databases
- Ability to analyze thousands of radiating elements with complex excitation schemes
- Hybridization of numerous CEM formulations
- Extensive graphical visualization options for data input and data output
- Numerous opportunities and flexibility for user intervention, as well as the computer generation of a system-level analysis scheme which can be selectively modified by the analyst
- "Low noise" computational processes (i.e., 70 dB dynamic calculation range)
- Well documented computer programs which are highly transportable across classes of computer platforms (e.g., massively parallel processors, workstations and networks of workstations)
- Extreme modularity to facilitate the maintenance of the code and the incorporation of new EM and computational technology advances
- Flexible database structures and query schemes to generate, maintain, and access the numerous geometric and EM profiles of the system

The CEM tools of today possess few of these characteristics. They each began their initial development during the 1970-1975 time period. It is to their credit that they have been able to undergo numerous major revisions and enhancements during the past twenty years without serious impact to the long-time users of the codes. However, close examination will show that despite the best efforts to reduce and avoid them there still exist numerous twistings and turnings in the program flow, extraneous lines of code and unused variables, and other signs of code revisions which increase the effort required for maintenance, debug, and enhancement, increase the opportunity for error in calculations, and inhibit transportability.

Hybridization schemes are limited, as are the resolution of the modeling elements and the ability to characterize the electrical properties of the platform and antenna geometry and materials. Some graphics-based geometry generation and data input tools exist, and there is a move to interface these processors with one or more airframe database languages (e.g., IGES). However, these are generally neither extensive enough nor widespread in a consistent, standardized format.

Similar comments, both positive and negative, can be made regarding each of the characteristics specified in the preceding list. It is significant that each of these is recognized as an element which must be addressed when one considers CEM technology development. What must be also recognized and addressed is the lack of coherence and consistency with which the work in CEM tool development is being pursued.

The tools that are now being extensively used are powerful and have been adequate to characterize systems to the level required in the past. However, recent experience with the codes has shown them to be inadequate and inefficient to accomplish the types of analysis required by the high performance systems now in the concept stage or in the early design stages of their life cycles. These tools are also powerful from one other perspective. They and the experience associated with their life cycles provide vital data which can inform the community in the design and development of the next generation of tools and the broader, over-arching concepts of the EM modeling and simulation environment.

It is the opinion of this author and the underlying thesis of this paper that it is now time and necessary to design and develop a new generation of CEM tools which together form an integrated and consistent environment in which the EM analyst and system designer can operate with efficiency, effectiveness, accuracy, and flexibility.

The Electromagnetic Modeling and Simulations Environment for Systems (EMSES)

A first fundamental division of the environment based on functions or types of operations results in three major, interrelated categories:

- Input processing; such as model development and specification of ranges of parameters (e.g., frequencies, scan angles)
- The computational engine
- Output processing; such as data reduction and interpretation, and database generation and modification

Input Processing

The input processing phase is critical to the accomplishment of the analysis. It must be carefully designed to provide a great deal of flexibility and visualization for the analyst, interface with numerous geometrical and EM databases, encompass all the modeling elements associated with the various CEM formulations available within the computational engine, and incorporate knowledge-based rules to support the analyst's effort to efficiently develop an accurate model.

The primary function of the input processor is EM model development. Its input is the physical and electrical parameters associated with the system being analyzed. It must account for the shape of the structure; the various materials out of which the structure is fabricated; and the location, shape, and constitutive parameters of the apertures which exist on the surface of the structure.

The most efficient and accurate method of obtaining the required data is for the input processor to access the CAD/CAM database that is used in the manufacture of the system. Since each manufacturer has its own way of storing the data, the input processor will need to have available several distinct translators, each of which can interface with a particular database. The translator will then transform the data into the proper format, units, and sequence which the input processor expects to see. The user will control which part or parts of the structure are to be accessed and treated by the input processor.

One preliminary task that must be pursued is to query each manufacturer to determine the characteristics of the databases in use. What types of data are collected? In what format is the data stored? What are the units of the various physical and electrical quantities associated with the system? These and many other questions need to be answered.

Another early task is the initial design of the input processor. How will the system data be stored in order to expedite the processing that will be performed by later stages of the input processor? How will geometry characteristics affect this storage? What CEM formulations will be incorporated into the computational engine, and what are the modeling requirements for each formulation?

Upon completion of these two tasks, one a data collection and collation and the other a program design process, the individual translators can be designed, developed, and tested. They each need to be flexible so that they can be easily transported across platforms and easily modified to accommodate changes in the manufacturer database and/or the input processor program. Since

it is not anticipated that the translation processes will be time-intensive, the design of the translators can be tuned for flexibility at the sacrifice of computational speed.

A logical platform for execution of the input processing function is the UNIX-based high performance workstation, using X-Windows. This choice is based on the growing proliferation of such machines, their ever-increasing power, and the transportability of code across manufacturers and models. In addition, these machines can execute the expert/knowledge-based systems, such as Prolog, CLEPS, and the Gensym G2. The initial stages of the input processor will obtain data from the appropriate translator. They will execute any final data preparation which is necessary before being operated on by the knowledge-based program.

The heart of the input processor, the knowledge-based engine, will accept the data from the initial stages of the input processor, display it in a format chosen by the analyst, and develop an initial EM model for the system. The design of the processor must provide several tools in order to facilitate analyst visualization. Obvious options include extensive use of color to emphasize or separate elements of the geometry depending on some chosen parameter (e.g., conductivity, aperture); the use of layers (e.g., to separate and manipulate antenna position on an aircraft); and the use of zoom boxes to provide an expanded view of selected areas of the model.

Another option that must be incorporated into the visualization capability is the ability to make notations on the screen. These will aid identification at a later date, or be useful to analysts other than the person originally working with the model. The analyst would have the opportunity to display or hide these notations. Furthermore, they would be stored with the model, although they would not become part of the input data stream for the computational engine.

A versatile print capability must also be available to the analyst. Various levels of resolution would be selectable (e.g., draft mode, screen print, 300 dots per inch). The user will have the ability to select blocks, layers, or colors of the model to print. The screen notations would be printed or suppressed as requested by the analyst.

An extensive capability for dialogue with the analyst is an essential element of the design of the input processor. It will make use of menus and allow for both textual and graphical responses from the user. Information required by the knowledge-based processor includes the specification of the system to be analyzed (the processor will determine the database format), frequency or frequencies of interest, excitations (both incident and antenna), scan angles with respect to the array boresight, and observables of interest and parameters regarding their collection (e.g., far-field patterns over some ranges of theta and phi spatial angles, or field distribution over some volume within the structure).

Using the database and user-provided data the processor will then develop an initial EM model of the system. The model will generally be made up of numerous types of modeling elements, each of which is associated with one of the many CEM formulations available in the computational engine. Typical element types include:

- MOM wires, patches, loads, excitations
- UTD cylinders, endcaps, plates, cone frustums, apertures, materials, excitations
- FD cells, loads, wires, apertures, excitations
- PO and PTD flat and curved triangular facets

The EM model derived by the knowledge-based input processor will be graphically displayed for review and modification by the analyst. Through the use of the various tools available (e.g., zoom boxes, colors) the user may focus on individual sections of the model and modify the model to include a finer grid structure in an area of interest or the use of a more

coarse modeling construct in areas where there is either a lack of detail or which are far removed from sources of excitation or EM scattering phenomena.

After the analyst has completed the "fine-tuning" process, the input processor will then generate one or more input records for the system database, which can then be retrieved and modified as necessary for future analysis runs. The processor will also generate an input data stream for use by the computational engine. This stream will specify which CEM formulations will be used in the analysis (by virtue of the modeling elements used in various parts of the EM model), what the excitations are, what the observables are and where they are to be computed, and the many global parameters needed by the formulations (e.g., frequency of analysis).

Since this part of the input processing function will not be a time-intensive computer process, execution speed will be sacrificed in favor of user flexibility and platform transportability. In addition, the expert system core of the input processor must also be designed and developed such that its growth potential is maximized. Growth (or modification) may be required in expanding the database definition or modifying the characteristics of particular records and fields within records. New physics formulations may be incorporated into the computation engine to handle a very limited, but very common, geometry structure (e.g., engine nacelles). These formulations will bring with them new modeling elements and rules for modeling, both of which will need to be incorporated into the knowledge-based input processor. Finally, graphics-based techniques for visualization are continually evolving. Therefore, sections of the input processor code that implement these functions will be continually updated to reflect the state-of-the-art in these areas.

The Computational Engine

The workhorse of EMSES is the computational engine. It is in this section of the fundamental division that the various and numerous CEM formulations reside in a hybridized schema. Several considerations must be adequately addressed in the design and development of this element of EMSES.

One fundamental decision that must be made is the determination of the class of platform on which the engine will perform. At the present time there are two viable alternatives, each of which has its own advantages and disadvantages. The first is a distributed system of high-performance sequential mainframes or workstations, and the second is the massively parallel processor. It is beyond the scope of this paper to argue for one or the other class. It may very well turn out that implementations of the engine for both platform classes may be possible with minimum development costs.

Regardless of the platform type the code itself must have at least the following characteristics:

- Be modular to facilitate maintenance, enhancement, upgrade
- Be transportable across manufacturers and models within a manufacturer
- Be well documented to facilitate maintenance, transportability, and enhancement
- Possess a robust hybridization scheme to enable the incorporation of new CEM formulations as they become available or as modeling and simulation requirements demand their incorporation
- Minimized and quantified sources of computational error in order to maximize the dynamic range of the computations (critical for the analysis of structures incorporating ultralow sidelobe antennas and/or low observable materials)

- Computational processes which minimize execution time, consistent with the requirements imposed by the characteristics of transportability, modularity, and minimization of computational error

Table 1 contains a list of techniques and capabilities which should be implemented as a minimum set within the computational engine.

Output Processing

The output processor must be as flexible and user-friendly as the input processor described previously. Its user-intensive functions are data reduction and data presentation (or at least data preparation via translators for input to standard commercial-off-the-shelf graphics packages).

The types of data that are to be made available from the execution of the computational engine include as a minimum:

- Electric and magnetic fields at specified points or ranges of points
- Monostatic and bistatic radar cross section
- Current density on the surfaces of the platform and the elements of antennas
- Antenna on-platform far-field patterns
- Antenna-to-antenna coupling
- Field-to-aperture coupling
- Interior field distributions
- Field-to-wire coupling
- Antenna terminal parameters
- System critical frequencies
- Types and locations of EM interaction (e.g., edge diffraction, wing surface reflection)

The types of presentation include as a minimum the following:

- Polar plots (electric and/or magnetic field as a function of angle)
- Rectangular plots (electric and/or magnetic field as a function of position or angle)
- Current density maps drawn on the surface of the structure
- Antenna-to-antenna coupling as a function of frequency
- Antenna-to-antenna coupling as a function of separation distance
- Aperture field distribution as a function of position in the aperture
- Parameterized interaction characterization as specified by the user (may require user-generated data reduction and plotting routines)

Other functions of the output processor include as a minimum:

- Data handling, storage, retrieval, and maintenance: This involves the generation and support of any number of input and output files associated with the EM characterization of the system under assessment. The EM database must maintain its currency with respect to the life cycle and configuration of the system.
- Preparation of the output of the analysis for use as input to related system analyses: One of the output options that will be invoked from the EM analysis is the coupling of external fields to wires and cable bundles located within the system. The coupled energy can then be translated into an open-circuit voltage and short-circuit current at the input to sensitive circuitry within the system. These data can be used by circuit

- I. Hybridized CEM formulations
 - A. Interior
 - 1. Finite differences
 - 2. Finite elements
 - 3. Characteristic modes
 - 4. Wires and cable bundles
 - 5. Conductivity, complex permittivity, complex permeability of the interior structures
 - B. Exterior
 - 1. Ray tracing
 - a. Physical optics
 - b. Uniform theory of diffraction
 - c. Physical theory of diffraction
 - 2. Materials characterization
 - a. Conductivity, complex permittivity, complex permeability
 - b. Options for layered materials
 - (1) Calculation by layer
 - (2) Equivalent surface wave impedance
 - 3. Method of moments
 - a. High resolution models
 - (1) Wire segments and grids
 - (2) Patch areas
 - b. Excitation
 - (1) Antenna elements
 - (2) Arrays
 - (3) Incident field
 - c. Loading
 - (1) Terminations
 - (2) Materials characterization using complex constitutive parameters
 - 4. Radomes
 - C. Apertures
 - 1. Empty
 - 2. Filled, specifying complex constitutive parameters
 - D. Domains
 - 1. Time
 - 2. Frequency
- II. Solution techniques
 - A. Full matrix solution
 - 1. Lower/Upper decomposition
 - 2. Use of rotational or planar symmetry
 - B. Iterative matrix solution techniques
 - 1. Conjugate gradient
 - 2. Banded Matrix Iteration (BMI)
 - C. Model order reduction

Table 1. Computational Engine Considerations

analysis programs to calculate the response of the circuit, heat build-up and propagation within the circuitry, and probability of circuit failure due to environmental circumstances.f

The output processor, like the input processor, is to be installed and executed on a high performance workstation, which may interface to the platform on which the computational engine is executed. It is to run under the UNIX operating system and X-Windows to maximize performance and transportability. As is the case with the input processor, flexibility and user interface capabilities are the major considerations over execution times, memory requirements, and data storage requirements.

Summary

This paper has presented the need for the development of unified and integrated EM modeling and simulation environment for system-level analyses of the RF performance of a radiating and/or scattering platform. Although the author's perspective is focused on Air Force C³I aircraft, it is obvious that the principles and concepts presented here are also applicable to ground-, sea-, and space-based platforms. In addition, the system need not consist of transmitters, receivers, antennas, and equipment bays. The geometry can just as easily be the interior of an automobile engine compartment or the case in which is located a high-performance workstation. The scale and the shape of the geometrical elements and the nature of the sources of radiation and reception may be different, but the concepts and needs are very similar regarding the environment which facilitates the EM analysis and characterization.

The next step is the development of an initial, albeit recognizably incomplete, specification for that environment, which can be used to maintain a perspective for EM researchers and CEM tool developers. There will never be a "final" specification, but there must be a continually and rationally evolving document which can be used as a metric for the development of a national CEM asset supporting the design and analysis of government and civilian radiating and scattering systems.

A PROPOSED APPROACH FOR DEVELOPING NEXT-GENERATION COMPUTATIONAL ELECTROMAGNETICS SOFTWARE

E. K. Miller, Group MEE-3; R. P. Kruger, Group A-10
Los Alamos National Laboratory, Los Alamos, NM 87545
Steve Moraites, Simulated Life Systems, Inc., Chambersburg, PA

ABSTRACT

Computations have become a tool coequal with mathematics and measurements as a means of performing electromagnetic analysis and design. This is demonstrated by the volume of articles and meeting presentations in which computational electromagnetics (CEM) is routinely employed to address an increasing variety of problems. Yet, in spite of the substantial resources invested in CEM software over the past three decades, little real progress seems to have been made towards providing the EM engineer software tools having a functionality equivalent to that expected of hardware instrumentation. Furthermore, the bulk of CEM software now available is generally of limited applicability to large, complex problems because most modeling codes employ a single field propagator, or analytical form, of Maxwell's Equations. The acknowledged advantages of hybrid models, i.e., those which employ different propagators in differing regions of a problem, are relatively unexploited.

The thrust of this discussion is to propose a new approach designed to address both problems outlined above, integrating advances being made in both software and hardware development. After briefly reviewing the evolution of modeling CEM software to date and pointing out the deficiencies thereof, we describe an approach for making CEM tools more truly "user friendly" called EMSES (Electromagnetic Modeling and Simulation Environment for Systems, named selected in collaboration with Kenneth Siarkiewicz of RADC). This will be achieved through two main avenues. One is developing a common problem-description language implemented in a visual programming environment working together with a translator that produces the specific model description needed by various numerical treatments, in order to optimize user efficiency. The other is to employ a new modeling paradigm based on the idea of field propagators to expedite the development of the hybrid models that are needed to optimize computation efficiency. By nature of its design, EMSES will be highly modular, hence more portable, and will exploit progress being made in "scalable" libraries to maximize performance in advanced parallel computational environments.

COMPUTATIONAL ELECTROMAGNETICS

The analysis and design of new materials, subsystems, and systems with specific electromagnetic requirements has led to research into the use of electromagnetic modeling codes on parallel processors. This research has been conducted for several years with the apparent conclusion that electromagnetic codes generally map well onto a wide range on machine architectures [Calalo (1987), Perlik and Moraites (1992), Russel and Rockway (1991), Davidson (1991)]. Both integral-equation (IE) and differential-equation (DE) methods map with high parallel efficiency onto such machines as the CM2 connection machine, the JPL hypercube, and the Cray YMP8. While no limitation of parallel architectures or parallel EM algorithms has been observed, several impediments to full exploitation of new machines have arisen.

A major limiting factor or impediment in achieving more useful and productive CEM CAD (Computer-Aided Design) tools remains the computation resource required, as parallel architectures

at best offer quantitative speedups only in proportion to their increased throughput as opposed to qualitative speedups that alternate formulations might be hoped to provide. Or, as observed by Wandzura (1992) in a recent talk, the former is "evolutionary" while the latter would be "revolutionary." To illustrate both qualitatively and quantitatively the computation-resource problem, Fig. 1 shows how the computational requirements increase with modeling accuracy and the frequency of interest.

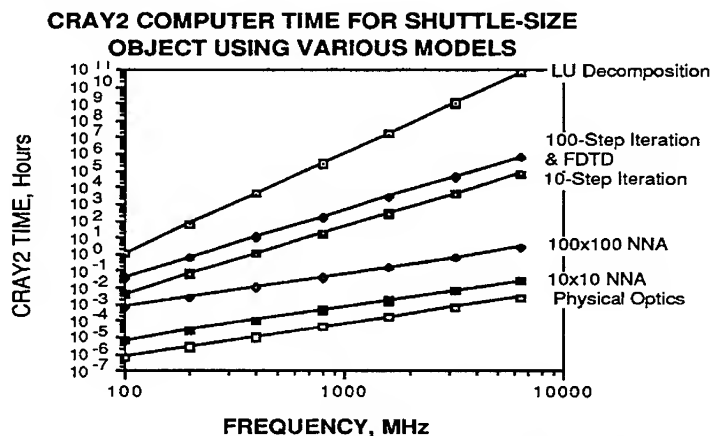


Figure 1: Illustrated here is the effect of frequency on the computational requirements [Miller (1991)]. In electromagnetics, an object size is measured in wavelengths, which is inversely proportional to frequency. Increasing frequency is equivalent to increasing the size of an object. A linear increase in either can cause a much larger rate of increase in the number of operations required to achieve a solution. The operation count for present and anticipated future models increases from the 2nd to as much as the 9th power of the frequency for three-dimensional problems, depending on the specific analysis method used. Note that the operation count for LU decomposition of an IE matrix increases as the 6th power of frequency for a surface-sampled object.

Another impediment to furthering large-scale CEM is that of preparing the input for a problem worthy of a teraflop computer and subsequently making use of the resultant massive amounts of data. Still a third impediment arises as a result of the improved performance of CEM tools where high-accuracy EM solutions for more complex problems such as low-observable targets might be nullified by effects of structural and thermal stress. The CEM software which is genuinely useful today must interface to at least thermal and structural analysis software for many applications. Finally, one of the most critical impediments to progress in CEM is multifaceted but is based primarily on the very rudimentary, one-of-a-kind, user interface that pervades present day CEM software. Rectifying this problem requires development of a standardized interface that provides a modeler access to all of the most widely used CEM tools. Overall, mitigating the impact of these impediments is best met by developing the integrated modeling infrastructure EMSES as illustrated generically in Fig. 2. A system such as EMSES is needed to not only open access to advanced CEM software to geographically remote users but also to permit continual and future additions, modifications, and program control while also providing other capabilities in such areas as verification and validation as is discussed further below.

EMSES would be best developed as the scalable software of the future in CEM for grand-challenge

computing utilizing two complementary and parallel approaches. One approach will be to improve

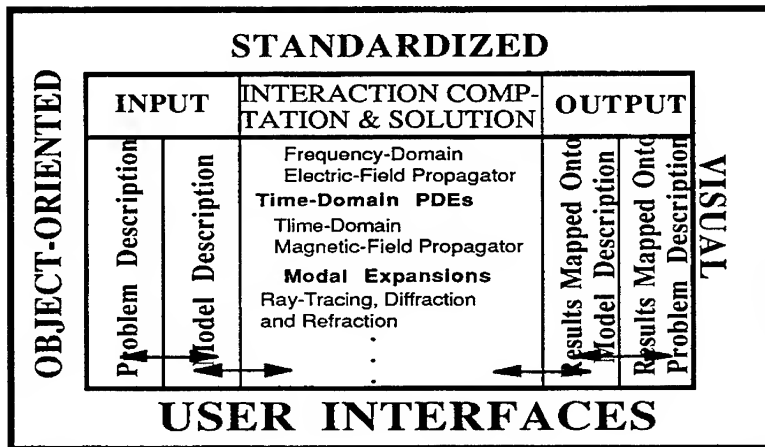


Figure 2: Conceptual block diagram for EMSES to illustrate its modularity with respect to using a field-propagator paradigm and its key components.

CEM software with respect to modeling performance and capabilities, and the other will be to better exploit continuing advances in computer hardware, especially in parallel, scalable and distributed computing. Each area is discussed in turn below.

ADVANCES IN CEM MODELING SOFTWARE

Progress (i.e., solving bigger, more complex problems) in CEM is predicated on advances in solution speed and accuracy commensurate with advances in computing hardware on the one hand and user effort on the other. Driving user effort is the fact that the typical electromagnetics engineer, most often someone who has not written any of the software being used, must become familiar enough with several different software packages that each can be used with some minimum facility. Unfortunately, existing software usually has a limited interface and is generally incapable of incorporating improvements made to other functionally similar software. This situation might be unfavorably compared with the status of hardware instrumentation development. In the latter case, even the most complex instrumentation can be reliably used by someone familiar only with its functionality and application, i.e., the user is not required to know how to design an instrument in order to use it. We suggest that an equivalent approach is needed in designing the next generation of CEM modeling software, and that this might proceed by beginning with developing a model of the modeling process itself, for which the structure shown in Fig. 2 might provide a starting point.

Reducing Computational Complexity and Exploiting Special Hardware

Work to date on reducing model complexity (the number of operations required to achieve acceptable accuracy) spans the spectrum from being either primarily analytical to primarily numerical, or some intermediate combination thereof [Miller (1988) (1991)]. Among the more analytical approaches are the Fast Multipole Method [Engheta et al. (1992)] and the various high-frequency, asymptotic techniques [Stone (1990)]. In the former, the number of mutual interactions, M , needed to be included in an IE like model is reduced from of order N^2 to of order $N \log N$ by representing the "faraway" interactions using multipole expansions together with a fast-

Four transform (FFT). Asymptotic techniques such as the Geometrical Theory of Diffraction and a number of other variations reduce problem complexity by avoiding the need to solve for the current on an object. They instead deal only with the fields caused by specular reflection, refraction at edges, energy shedding on curved surfaces, or diffraction at dielectric interfaces.

Additional numerical approaches include those based on impedance-matrix localization [Canning (1990)]; spatial decomposition [Umashankar et. al. (1990)]; space segmentation [Wang and Ling (1991)]; diakoptics [Butler (1990)]; fast-propagation solutions [Miller and Gilbert (1991)]; various FFT-based procedures [Sarkar et. al. (1986)]; and multigrid methods [Kalbasi (1991)]. Almost all of these also use iterative matrix-solution techniques to reduce solution of a general matrix from being proportional to N^3 to of order IM , where I is the number of iterations required for an acceptably converged solution. All such techniques share the goal of reducing a model's complexity by altering the problem's description through using special basis and testing functions. This divides the problem into parts that are more easily solved by taking advantage of special features the problem might possess to thereby develop a more efficient matrix solution. Other numerically oriented approaches for reducing complexity include the various time-domain DE models [Taflov (1988)] whose primary advantage is that, in their explicit formulation, they are solvable without matrix inversion.

As designing and building special computers for solving certain kinds of problems are becoming more practical, we are beginning to see a blurring between software and hardware design. This development might be typified by computers such as the WaveTracer computer [Miller (1990)] which was designed with particular kinds of DE models in mind. Upon noting the close analogy between signal processing and filtering and such DE models, new hardware paradigms are being developed, one example of which is represented by the "Wave Digital Filter," [Kuo and Levy (1990), Fettweis and Nitsche (1991)].

A Field-Propagator Paradigm for Electromagnetic Modeling

We note that at some point in the process, all electromagnetic modeling involves evaluating the fields caused by specified sources. When the sources are known, the problem is more straightforward, an example being to find the radiation pattern of an antenna. Most often the sources are unknown and are found as the solution of a boundary-value problem with boundary conditions imposed on the fields due to these sources. The source-field relationship, or field propagator, that is employed in this process may be based on:

- 1) the Maxwell curl equations written in differential or integral form to yield what are called finite-difference and finite-element models;
- 2) a Green's function and source integral to produce an IE or boundary-element formulation;
- 3) a mode-based description which leads to techniques such as the T-Matrix and Generalized Multipole Techniques or;
- 4) rays and diffraction coefficients which lead to an optics model.

The vast majority of present CEM modeling software is based wholly on using only one of these approaches for a particular problem. However, it is well known that the applicability of each is limited, and that models for more general problems should employ that field propagator which it is best suited to each subset of the overall problem. Effective implementation of such a hybrid model requires that a new modeling paradigm be employed that recognizes this need, since hybridization offers the only means by which larger and more complex problems can be successfully solved.

We suggest that CEM modeling-software development be reoriented so that field propagators are explicitly incorporated as its most basic ingredient. This means that, whatever the kind of modeling code is under consideration, the building blocks needed for its development and application are formulated and employed as field propagators. These propagators will be written as

modular, scalable, software-library elements that can be easily linked together in a systematic, dataflow oriented, and visual manner. This will greatly simplify developing the source-field relationship of a problem that is geometrically or electrically complex. The input to each propagator will be an appropriate source while its output will be a transformed field produced by a combination of source and propagator. The spatially (and possibly temporally) discrete set of field and source samples that result will generate sets of equations by imposing needed field continuity at common boundaries or in common regions of the separate propagators. Modeling a complex problem thus becomes a process of identifying the propagator types to be assigned to each region of the problem and the boundaries across, or volumes within, of propagator interaction. The computation then proceeds by assembling a set of equations for each spatial region. The collection of all such regions produces the final matrix, generally a combination of dense and sparse matrices because of using different propagators in different regions, that will model the entire problem.

We also suggest that this new approach should permit variations in the numerical treatment by expressing the propagators in a uniform and predefined way. Among the variations to be included would be basis and testing functions employed, model adaptation, and matrix-solution procedures. Allowable variations for a particular problem would depend on the resources available to the modeler on the distributed computational network. Thus, as we expand the computational network resources, the modeling algorithm can also grow and provide, for example, user choices to be made concerning numerical accuracy, spatial resolution, or the density of frequency and angle sampling.

The propagator paradigm approach proposed for EMSES is an inherently modular one. Propagator modules would provide the electric and/or magnetic fields or potentials needed for various single-propagator or multiple-propagator (hybrid) models. For example, one set of libraries would model the frequency-domain electric fields for filamentary, surficial and volumetric electric currents. Other library modules would employ differential, modal, and high-frequency propagators. These propagator modules can also be designed to provide the fields for various kinds of basis and testing functions as selected by the modeler using interactive decision aids.

As a specific example, the integration required to obtain a field involves summing weighted values of the IE kernel function. The subsequent integration required for the field testing involves another weighted summation of similar nature. Thus, the propagator evaluation for integral equations ultimately requires only weighted sums of kernel-function samples. Furthermore, the field samples required for the impedance matrix involve sampling a relatively well-defined parameter space. This provides the opportunity for pre-computing and storing fields in some suitable way so that much of the one-time computing cost of certain problem classes can be subsequently avoided. This approach is known as "function approximation" and "model-based parameter estimation" and is instrumental in reducing the cost of evaluating the Sommerfeld integrals needed for modeling an object near a planar interface by a factor of up to a thousand [Burke and Miller (1984)].

The process of computing fields in an IE context provides the coefficients for an interaction (impedance) matrix. We call this the "system" matrix for, depending on the formulation used, the coefficients will not all have the units of impedance, as they do for the electric-field IE. The system matrix is "assembled" by evaluating the fields of the various propagators that might be employed. Each row of the matrix arises from imposing some boundary condition or continuity condition at various points in the problem space. We note that this kind of modeling-code decomposition is well-suited for interfacing with a user decision aid.

Developing Hybrid Models Using Field Propagators

After the modeler has developed a physical problem description for the application of interest, a decision aid will be used to analyze that description and provide a suggested list of propagators for each different portion of the problem. It will also help in selecting from among the

set of available options, the modeling details that are best suited for each particular spatial region. For example, a large, smooth, conducting segment would best use an IE model that employs entire-domain bases, whereas a region of spatially varying dielectric would best employ a finite-element DE model. An illustration of this type of problem decomposition is shown in Fig. 3. A simplified example of the value of using such a method for a simple problem is shown in Fig. 4 where all curves show the speedup of the proposed type of algorithm under various conditions compared to an IE modeled using LU decomposition.

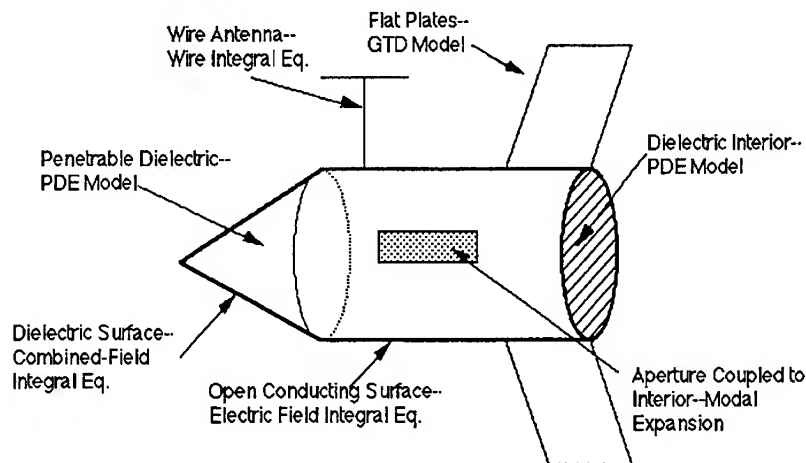


Figure 3. Example of generic problem for a propagator-based, hybrid approach could provide a more efficient model than would one based on a single field propagator.

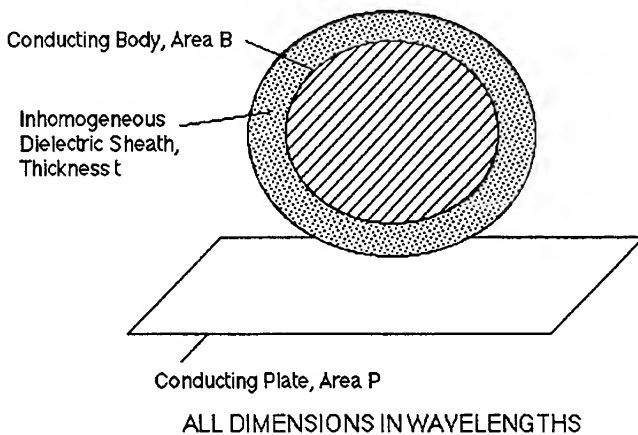


Figure 4a.

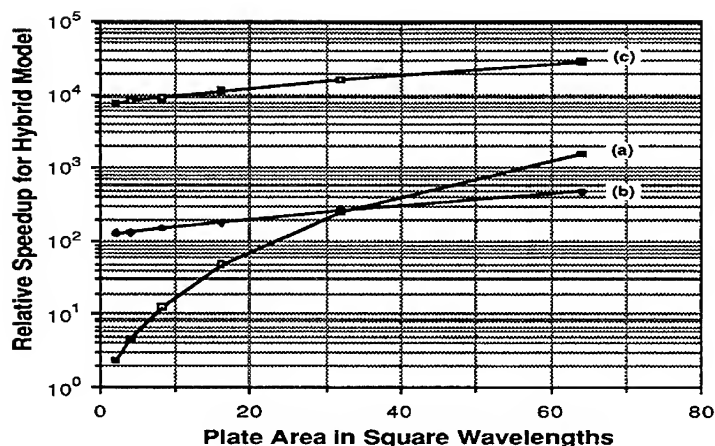


Figure 4b: Some results for a simple problem to illustrate the potential operation-count advantage of hybrid models. For the problem geometry depicted in Fig. 4a, the result for curve (a) applies where $t = 0$ (i.e., then is no sheath), and for (b) and (c) where an inhomogeneous sheath is present. Curve (a) demonstrates the relative speedup [given by $(1+P/B^2)$] achieved using a hybrid model [IE (IE) for the object with geometrical-theory of diffraction (GTD) for the plate-object interaction] over an IE model for both, when solving the Impedance matrix using LU decomposition. Curve (b) shows the speedup [given by $(10t+1+P/B^2)$] achieved by a hybrid IE-GTD-PDE (partial-differential equation) model over an all-IE model using an iterative solution for both, when an inhomogeneous sheath covers the object. Finally, in curve (c) we demonstrate the speedup [given by $\{10B(10t+1+P/B^2)/\eta\}$] achieved by a hybrid Modal-GTD-PDE model over an all-IE, again solved using iteration. In the latter case, we sample only those surface fields whose mode numbers extend from 0.9 to 1.1 ka , where a is the effective sheath radius. We assume that the sampling density is 10 per wavelength in 1D dimension (i.e., 100 per square wavelength and 1000 per cubic wavelength), that the object area is 64×64 square wavelengths, and for (b) and (c) that the integrated sheath thickness is one wavelength.

The properties of the system matrix for a problem will depend on whether the modeling is done in the time domain or frequency domain, and the kinds of propagators chosen. Therefore, the subsequent numerical solution of this matrix must reflect these differences. It is envisioned that EMSES will include LU decomposition, iterative, and various sparse-matrix solution procedures which will provide solution options appropriate for given applications. For example, when an antenna problem is modeled, only one excitation or "right-hand side" is needed, so that an iterative solution would almost always be more efficient than LU decomposition. When a radar-cross section (RCS) is needed for many angles of incidence on the other hand, LU decomposition could be more efficient since an iterative solution may need approximately the same number of iterations for each new incidence angle. There may be some potential in this latter application, however to use the most recent solution as the starting point for a new angle of incidence and thus potentially reduce the number of iterations needed for convergence, which could make iteration more appropriate then. These kinds of options will be provided in EMSES to give the user a convenient, easily exercised menu of choices.

Model Adaption for Error Control

Another potentially important means of improving computation efficiency is provided by adaptive methods. Almost all modeling in CEM currently employs predefined models where the number of unknowns is selected based on experience and modeling guidelines. Not until the computation is finished does the user normally obtain any quantitative indicator of how accurate or numerically converged are the results. If we determine that more spatial unknowns are needed to achieve the accuracy desired, the entire problem normally needs to be redone using a more refined model description.

Model adaptation in EMSES might be achieved by including a capability for checking model performance as the computations are being performed. A field propagator that is especially well-suited to making this feasible is one based on modal expansions of a field due to multipole sources. Present implementations of modal propagators do not require the usual surface-source discretization. They require only that the fields be sampled on boundary surfaces. Consequently, it is numerically efficient to solve a problem using a modal propagator for a given number of unknowns and then check boundary-field errors. If they are too large, new unknowns can be added and more field samples used in regions where the boundary errors are largest. This can be accomplished in a recursive fashion without discarding the first solution which serves as a starting point for the updated solution. Since there is no source-discretized approximation of the problem to be refined, the problem of using more sources and fields is greatly simplified. An IE model that employs entire domain (e.g., a Fourier series) over all or part of a problem boundary can be made adaptive in a similar fashion. The benefit of reducing the boundary error, which is normally the controlling factor in determining the overall solution accuracy, only enough to achieve the needed observable accuracy, will be substantial. This idea is illustrated conceptually in Fig. 5.

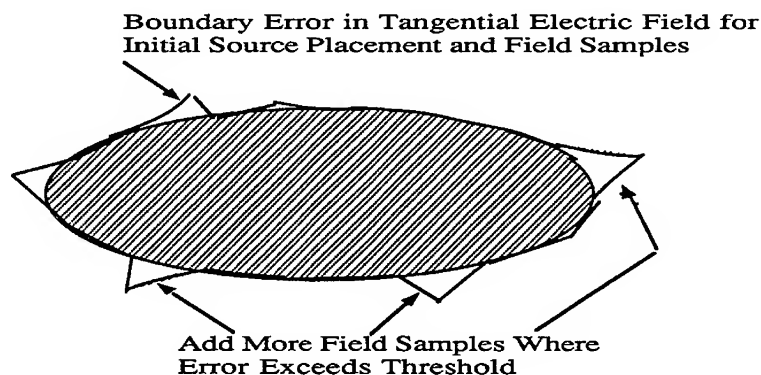


Figure 5: Conceptual example of using field sampling for model adaptation. Key ingredients for efficient adaptation are having available an appropriate error-evaluation procedure and a way of adding more unknown and field samples to the model.

Verification and Validation

Aside from the work required by a user to prepare the input needed to exercise a computer model and access the output it produces, perhaps the greatest integrated effort associated with CEM is that of verifying code operation and validating the results produced. Verification is associated with determining that a modeling code produces results consistent with its design. Validation is concerned with establishing how well its results conform to physical reality. Both are ingredients essential to performing reliable modeling computations. The former is a necessary, but not

sufficient, condition for acceptable code performance, while the latter determines how reliably a given code can be applied to physically meaningful problems.

Thus, computational checks would be advantageous at various points to establish quantitative measures of code performance with respect to both verification and validation. These checks will address the issues of:

- 1) moving codes between computers;
 - 2) confirming continued valid operation of the code over time on a given computer,
- and;
- 3) giving guidance to the user concerning the validity of the computed results.

Computational models would ideally also include features that support "dialable" accuracy to permit an explicit trade-off between the cost of the computation and the accuracy of the results.

The first step in assessing computational accuracy stems from the two sources of error in any modeling exercise. These are the physical modeling error (E_p) which arises from approximating the physical problem of interest with some idealized mathematical representation, and the numerical modeling error (E_n) which occurs because only an approximate numerical solution is obtained to that idealized mode. Determining E_p will require access to measured data since few problems are modeled without employing some physical approximation such as representing a smoothly curved object by plane, triangular facets. Given adequate computational resources, E_n can always be made smaller than E_p . The essence of the verification and validation approach outlined here is to develop a protocol for systematically and consistently estimating E_n in response to the three points above.

There are a number of options that could be considered for this purpose but that are rarely utilized in the modeling codes now available. In connection with (1) and (2) above, for example, it would be advantageous to include a set of precomputed test cases, including the model input, results at various stages of the computation, and the final observables such as radar cross sections and/or thermal emissions. EMSES would then allow the user to automatically compare the results of running these test cases with their precomputed results using appropriate error norms to determine where any significant differences exist. Concerning (3), EMSES could also include a user option to exercise various validation checks that might range from checking far-field reciprocity, to evaluating boundary errors, or even comparing results from two different numerical models. Finally, EMSES could offer the modeler a quantitative "figure of merit" (FoM) which indicates how reliable the computed results might be.

It can be seen that verification and validation options range from being quite easily implemented to posing a research challenge. However, these issues will become increasingly essential as problem complexity and the associated total FLOP count continue to increase with faster computers.

Developing Problem Input

A useful metric in CEM is how large a problem measured in wavelengths or how many unknowns can be solved on a given computer architecture in a given amount of time. A measure like this is informative because it indicates for which size of problem the user might need to consider changing to a different computer platform. It also clearly demonstrates the state-of-the-art of present mainframe or supercomputers in terms of defining what a "large" but possibly solvable a problem actually is. For the present discussion, we will consider the number of unknowns solvable in one hour as the relevant measure.

This number is closely related to the effort needed to prepare the input data required for a computer

solution. When the one-hour problem size involved only a few hundred unknowns, the effort needed to prepare the input manually was feasible. On current supercomputers, the one-hour IE problem size has passed 10,000 unknowns. The input effort has grown commensurately larger, reaching the point where manual data preparation becomes unfeasible. The need for computer-assisted data preparation is even greater for DE equation models, where the number of spatial unknowns is proportionately larger because the model samples represent a volume of space rather than an enclosing surface.

Problem description for CEM actually occurs at two levels on the input side. The more elementary one is where the problem being modeled is described electrically and geometrically in the way required by the specific modeling code being used. For example, for a wire code the model description might include the two endpoints of each wire segment, its diameter, impedance loading, and connection information about wire segments attached to either end. A more advanced level, but one employed by few if any EM models today, is where the problem is described in engineering-oriented terms such as might be associated with engineering drawings. Translation of the latter, physical problem description (PPD) to a numerical model description (NMD) like the former, is then done by the user interface software. Implementing an approach like this for EMSES would have three distinct advantages:

- 1) The PPD would need to be developed only once;
- 2) The NMD can be developed interactively using an appropriate "translator" that follows guidelines needed by a particular modeling approach/library permitting human inspection and intervention where needed; and
- 3) The single PPD can be used to drive any modeling library component to make intermodel comparisons and solution presentation more consistent and accurate.

Visualizing the Model and the Results

Electromagnetics is one of the more mathematical and abstract sciences. There is little opportunity to view field and wave phenomena that are relevant to CEM. While it is true that we live in a visible-light world, we can directly observe none of the phenomena that are important at the size-to-wavelength ratios that are of concern in CEM modeling. Yet visualization of the solutions that are obtained using CEM techniques is becoming more and more important.

One reason visual electromagnetics is needed is the growing complexity and size (number of unknowns, size-to-wavelength ratio) of problems being modeled. As already noted, it is relatively simple to confirm the correctness of the data needed to describe a problem consisting of an array of dipoles such as a logperiodic antenna. However, the physical behavior of even this simple problem, when the observables of interest are the antenna currents as a function of frequency or time or the angle-dependent near and far fields, can be challenging to interpret without a graphical presentation. We believe that graphical presentation of results will become much more important for more complex problems where there is an even greater variety of parameters and variables to be observed. This need has led to an increased emphasis on scientific visualization in electromagnetics, [Miller et. al. (1981) (1988), Cole et. al. (1990)], to provide access to, and understanding of, the results of CEM modeling.

Visualization is also needed to ensure the correctness of problem-description and model-description data. Finding errors manually in numerical data that describes the complex interconnection of triangular facets used to represent a moderately complex conducting body is intimidating and error prone. Visual presentation of the model is the only effective way to inspect the input data. Visualizing the intervening steps in the computation process can also provide insight into the correctness of the numerical results and interpreting the physics being described. For example, in one application involving modeling an antenna near the earth-air interface, we found that a graphical plot of the impedance matrix showed a numerical "noise" on the smaller values of matrix coefficients. This demonstrated that 32-bit accuracy on our VAX computer was inadequate. Only

when 64-bit computations were performed did this noise vanish. Plots of the inverse or admittance matrix for wires have similarly exhibited the problem's physics in ways not otherwise observable [Miller et. al. (1981)]. The EMSES environment would provide easy and convenient visualization of all aspects of modeling and results presentation as part of its computing infrastructure.

Combining CEM in a Multidisciplinary Library Interface

The kinds of structures whose electromagnetic properties are the result of tight specifications and advanced requirements cannot be analyzed without regard to other physical factors that affect shape, size, and material properties. Certain RCS reduction methods degrade severely when structures bend and deform. High gain antenna performance behaves similarly. Thus, as CEM capability progresses to the point where numerical design is feasible for the most advanced structures, a connection must be made to other disciplines such as thermal analysis and structural analysis in order to assess the design in the real world, which includes structural and thermal effects.

EXPLOITING ADVANCES IN HARDWARE ARCHITECTURES AND ASSOCIATED SOFTWARE IN CEM MODEL DESIGN

Rationale for Emulating Hardware Design in Software Development

The present state of CEM may be compared with the situation that prevailed during the initial phases of the industrial revolution. Until machinery made it possible to produce more output per worker, there was little incentive to make interchangeable parts. Each craftsman produced a complete version of a given product. Its various parts though fulfilling the same function as the same part made by another worker, were not required to be interchangeable. However, when the economies of larger-scale production were fast becoming a possibility, it was soon recognized that continuing this kind of arrangement would largely offset the advantages that could otherwise be achieved. It was necessary, in the interest of production efficiency, that the creative control of individual workers be made subordinate to the benefits of standardization and interchangeability. This is a lesson that needs to be applied to software development.

The motivation for software scalability is similar. While the production of analysis software in CEM continues unabated, designers are confronted by a bewildering array of modeling choices. Perhaps the most telling characteristic of the large majority of this software is the fact that each package requires the user to learn a new interface in spite of the fact that all these modeling tools involve a small number of the same basic steps. A major thrust of EMSES will be developing and implementing an integrated user interface to permit a designer to access and use it effectively.

Designing Software for Distributed and Parallel Architectures

Traditional multicomputing has relied on the close coupling of large numbers of homogeneous processors in hypercube distributed memory and shared-memory, bus-based interconnections. Recently, shared, distributed-memory architectures like the Kendal Square with interlocking rings of processors has extended the paradigm of closely coupled multicomputing that is a hybrid of the two earlier architectural types. Within this paradigm, machines have been developed that are either single instruction multiple data (SIMD) or Multiple instruction multiple data (MIMD). The recently announced CM-5 from Thinking Machines Inc., has confirmed the generality of the MIMD distributed memory approach as the dominant approach for the future of scalable closely coupled multiprocessors.

Closely coupled multicomputers have been made possible because of the high speed buses, rings, or hypercube communications mechanisms internal to these machines. These internal communications mechanisms have facilitated low-latency, high-bandwidth communications between processors which has made these machines efficient parallel processing computers. The recent development of very-high bandwidth (800Mb/s) low latency crossbar switches which serve

as local-area-network interconnects, and the promise of wide-area-network extensions of this technology, will enable the multicomputing paradigm to be extended to a much higher level of processor granularity and heterogeneity. Thus, in the near future, heterogeneous networks of architecturally diverse machines will be closely coupled over great physical distances.

Previous research at LANL, and elsewhere, has consistently shown that algorithm performance can be optimized when it is mapped to the hardware and software environment for which it is best suited. Thus, different algorithms map best to distinct architectures. Until the advent of HIPPI-based, high-speed crossbars, it was still often expedient to develop, test, and deliver a multiple-algorithm software system on a single parallel architecture fronted by a workstation network used as the user interfaces, even though the mapping of diverse algorithms to a single architecture was markedly suboptimal. The present and future potential of high-bandwidth, low-latency, crossbar networks, and their wide-area extensions will alleviate this restriction and make overall application-level optimization practical. As a result, high-performance, network-based multicomputing will be extended to include workstations, massively parallel machines, workstations with embedded accelerators, and conventional supercomputers as nodal processors on the network. The network will exploit both message passing and shared-memory capabilities and represents a hardware realization of a "virtual metacomputer".

It is recognized that the EMSES concept encompasses a wide spectrum of applications that will push the computational ability of existing computers. Because of this, it is clear that EMSES system will be designed from a very broad perspective. It will include mechanisms for distributed and parallel computing and interactive visualization. Furthermore, it must provide a working environment that encourages joint development by a geographically dispersed design and development groups. It must also support the rapid prototyping of new applications and enable the easy re-use of previously developed library software.

The key to the successful use of this virtual metacomputer will be the software-based programming environment and its underlying application level communications and control infrastructure which will permit the user to conveniently and seamlessly utilize this resource. EMSES would include this application-level software infrastructure to address the requirements of both the electromagnetic library software developer and the designer/user of this software. This would be accomplished both by integrating existing public-domain, visual-language, network, CAD, mesh-definition software, etc., and by enhancing these existing components to meet both the requirements of the electromagnetic library developer and the eventual designer/user. EMSES would also include scaleable and portable electromagnetics software which can be used by electromagnetics designers from a high level visual programming environment that shields these designers from the details needed to execute complex analyses over this networked virtual metacomputer.

It is no longer reasonable to expect each design and development team to write sophisticated network infrastructure software. EMSES would provide developers with a more abstract and powerful environment that links together existing sealable libraries of application software and "hides" the infrastructure details of this linkage from the user and would also provide the application level user with powerful CASE (Computer Aided Software Engineering) tools that facilitate the creation, compilation, and debugging of new library software. EMSES implementation would include a distributed and parallel software network infrastructure that can be programmed, monitored, and debugged as if it were contained within a single multicomputer.

Using the KHOROS System as a Basis for EMSES

One approach to realizing the distributed and parallel software development infrastructure for EMSES could be based on a public-domain system such as KHOROS whose design is illustrated in Fig. 6 [see Miller (1992)], which would satisfy the following seven design criteria:

1. Produce optimal and balanced computational performance on a heterogeneous computer network while transparently providing a software development CASE-tool environment that enables investigators to develop and test new library components while continuing to utilize a wide variety of existing software written in several high level languages.
2. Provide transparent access to and use of data and electromagnetic libraries over a network of different machine architectures.
3. Support an extended data-flow model of computation that is important for electromagnetic modeling.
4. Provide for network level control, communication, load balancing, fault-tolerant execution, and debugging.
5. Provide 3-dimensional object modeling and mesh generation capability using government owned BRLCAD system and its extensions or commercial solutions when applicable.
6. Provide a convenient means to interact with users who are not electromagnetic experts or programmers through a modern visual programming environment.
7. Be built using public-domain, government-owned, and/or easily affordable commercial software components based on open system principles.

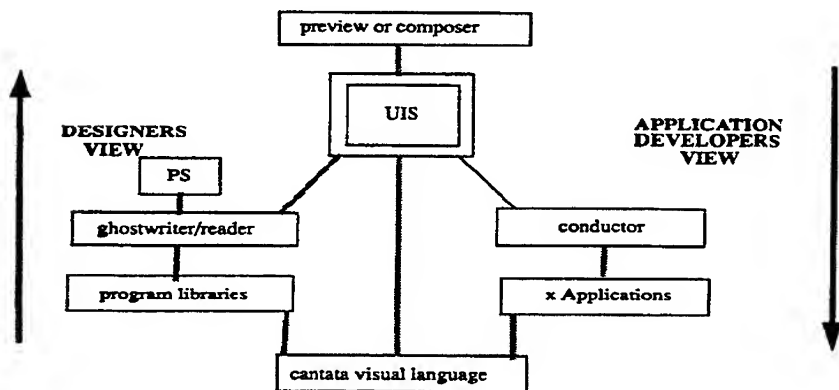


Figure 6: Block diagram of the KHOROS system and CASE tools.

KHOROS is built with the philosophy of being an open and extensible parallel and distributed system. It is the only open scientific computing environment that provides CASE tools for the creation, maintenance, and distribution of user contributed programs. These integrated tools are utilized by a developer to create KHOROS-compatible libraries. KHOROS provides three levels of compatibility:

- 1) Process interface: This minimal level of compatibility allows the developer to integrate in an existing set of executable programs. The developer only needs to edit/configure the user interface of the visual language and to interactively create a graphical user interface for each program. No software development or compiling is required for this level of integration.

2) Procedure interface: This level of compatibility allows the developer to integrate or develop a library of procedures of functions. The developer interactively creates a specification file for each procedure that is used as input to a code generator. The code generator acts as a programmers apprentice to automate the creation of all user interface code. This level of integration allows the developer to utilize the source configuration and maintenance tools provided in KHOROS.

3) Procedure interface and data structure: This highest level of compatibility also allows the developer to utilize the reusable libraries of the KHOROS system.

Application developers work from top to bottom in Fig. 6. They use the various tools provided by the KHOROS environment to extend the capabilities of the system, add new routines to be accessed by the visual language, or create interactive graphical applications. End users/designers (shown at the bottom of the Figure) use the visual language to create custom solutions to their CEM problems.

Preview, composer, ghostwriter and conductor represent specific User Interface Development tools that are provided within the KHOROS software structure. The library of data processing algorithms and the X applications are supported by utility and development libraries. The User Interfaces Specification (UIS) and Program Specification (PS), along with the libraries, act as input to the KHOROS tools which then generate programs. These programs include many of the KHOROS tools themselves, in addition to programs created by application developers using the KHOROS system. All applications developed using KHOROS may be referenced from within Cantata, the visual language programming environment.

"Distributed processing" in KHOROS is currently supported by the ability to manually specify remote machines upon which to execute individual KHOROS programs. The capability to do distributed processing is implemented via employment of remote data transport mechanisms and automatic process scheduling. With distributed processing, one needs a method to execute jobs remotely, as well as a mechanism to transport data back and forth from the remote machine.

KHOROS uses various data-transport mechanisms for local and remote communication. Local-transport mechanisms include shared memory, files, pipes, and streams; remote-transport mechanisms include Sockets and TLI (System V Transport Layer Interface). Custom data transport mechanisms such as HIPPI protocols to support high-speed CM-2-to-Cray communication have been implemented. With the use of remote data transport, the ability to get input from and output to remote machines is implemented. The data transport and distributed processing capability can be taken advantage of either from the cantata visual language, or from individual command line executions of KHOROS programs.

In operation, KHROS provides various kinds of visualization, including windows that display input and output data sets and the computational modules themselves which are shown as "glyphs." Each glyph represents either a process or a data source. The glyphs are connected by lines representing data transport between the different processes, and can be arranged by the user into different data-flow configurations to accomplish various kinds of computations. The modeler thus works in a mode similar to that of a hardware designer who, beginning at the gate, circuit, and chip level, constructs larger circuits and boards from elementary modules to achieve specified design goals. By storing commonly used combinations of modules, some computational "circuits" can be used over and over again to avoid duplicating past effort. Furthermore, by adhering to well-defined design rules, the modeler need not be bother with most of the minutia that characterizes most modeling now. Instead, the modeler can concentrate on conducting electromagnetic experiments on the computer by connecting together the required software components in much the same way that an experimentalist performs various experiments by using available hardware components.

COMPARISON WITH OTHER ONGOING CEM RESEARCH

The preponderance of CEM software developed to date consists of research programs intended to accomplish specific goals. A much smaller set of modeling codes has been developed in industry and at government laboratories for sponsors. A few of the codes originating in this fashion have become widely distributed because they have been well documented and supported and are available at a small cost and with few restrictions. A short, but representative, list of examples include:

- NEC [Breakall, Burke, and Miller (1985)]
- EM-TRANAIR [Bussolletti, et. al. (1988)]
- ESP [Newman and Pozar (1978)]
- EMPAC [Wilton, et. al. (1989)]
- FERM [Lee, Shnidman, and Lichauco (1987)]
- GEMACS [Siarkiewicz (1988)]
- JUNCTION [Wilton and Hwu (1989)]
- MININEC [Rockway, et. al. (1988)]
- PATCH [Johnson, Wilton, and Sharp (1988)]
- RCS BSC V2 [Marhefka and Brinkley (1988)]
- SPEX [Ludwig (1986)]
- TSAR [Ray (1991)]

A still smaller set of codes have been developed in the commercial arena. These are usually available without restriction, but can be quite expensive. Most work to date has concentrated on traditional code design where a single computational model is developed for application to a limited set of suitable problems.

One exception to this rule is GEMACS (Generalized Electromagnetic Model for the Analysis of Complex Systems). This software represents an early effort to develop an integrated modeling environment that was expected to evolve eventually into a package that offers a variety of modeling options. GEIMACS was originally developed at BDM Corporation with continuing support provided from Rome Air Development Center. It contains several different kinds of models, including frequency-domain integral equations and time-domain differential equations, but seems not to have gained as wide acceptance in the CEM community as, for example, the NEC package. One reason for this may be that GEMACS is a large (approaching 150,000 lines of code) package with limited modularity and portability. It was also developed prior to the advent of distributed and parallel computing, so that porting it to these new computing environments would require major changes. While GEMACS offers some capability for hybrid modeling, it now seems relatively limited in scope compared with evolving requirements. However, GEMACS provides a number of valuable lessons learned which will be valuable in designing a package like EMSES.

Another, more recent, modeling package is EMPACK. It is being developed by a Wilton and his students at the University of Houston. Their goal is to develop modular CEM tools suitable for a wide variety of applications. Although some of the concepts behind EMPACK are attractive, its eventual realization as a solid, user-friendly package is not assured. In addition, EMPACK addresses only the CEM part of the problem and does not address the scaling of this software to a distributed highly parallel computing environment.

Much of the current work in CEM is devoted to adapting existing models to parallel machines. A typical example is Davidson (1991), in which NEC (Numerical Electromagnetics Code) was ported to a 32-transputer PC-based system. Other work is targeted at reducing the operation count of modeling by developing new techniques [for example, Gurel and Chew (1990), Kalbasi (1991)] or refining or approximating existing models [Butler (1990), Canning (1990)]. There are no efforts

we are aware of that develop the field-propagator approach proposed for EMSES. While a fair amount of work has been done on developing more convenient and automatic procedures for preparing the computer-model descriptions, there also are no comprehensive efforts that target the problem-model-description approach we propose. Verification and validation has also recently received increasing attention recently [Miller (1989)].

Concluding Comments

Taken as a whole, we believe that it is absolutely essential to develop as a next-generation CEM software package an integrated system such as EMSES. This is necessary both to better exploit evolving computer hardware and systems, and to provide the more productive environment for analysts and designers which will permit them to concentrate on electromagnetics issues rather than computer and numerical issues as is now so often the case. We envision that, following an approach such as proposed here in the form of EMSES, next-generation CEM tools should provide a computational capability to electromagnetics designers and analysts that is functionally equivalent to the measurement capability now expected by electromagnetics experimentalists.

REFERENCES

- Bussolette, J.E., E.T. Johnson, K.W. Sidwell, B.L. Everson, D.P. Young, R.H. Burkhart, and S.S. Samant (1988), EM-TRANAIR: A Computer Program for the Solution of Maxwell's Equation in Three Dimensions, Boeing Military Airplane Company, AFWAL-TR-87-3082.
- Breakall, J.K., G.J. Burke, and E.K. Miller (1985), "The Numerical Electromagnetic Code (NEC)," in Proceedings of 6th Symposium and Technical Exhibition on Electromagnetic Compatibility, Zurich, March 5-7, pp. 301-308.
- Burke, G.J. and E.K. Miller (1984), "Modeling Antennas Near to and Penetrating a Lossy Interface", IEEE Transactions on Antennas and Propagation, AP-32, pp. 1040-1049.
- Butler, C.M. (1990), "Diakopic Theory and the Moment Method," in digest of IEEE Antennas and Propagation Society Symposium, pp. 72-75.
- Calalo, R. et. al. (1987) "Hypercube Matrix Computation Task," JPL Publication 87-18, Jet Propulsion Laboratory, Pasadena, CA
- Canning, E.X. (1990), "The Impedance Matrix Localization (IML) Method for Moment-Method Calculations," IEEE Antennas and Propagation Magazine, 32, pp. 18-28.
- Cole, R.J., E.K. Miller, S. Chakrabarti, and G. Prasad (1990), "Learning About Fields and Waves using Visual Electromagnetics," IEEE Transactions on Education, 33, February, pp. 81-94.
- Davidson, D.B. (1991), "Parallel Algorithms for Electromagnetic Moment Method Formulations," Ph.D. Dissertation, U. of Stellenbosch, Stellenbosch, South Africa.
- Engheta, N., W.D. Murphy, V. Rokhlin, and M.S. Vassiliou (1992), "The Fast Multipole Method (FMM) for Electromagnetic Scattering Problems," to be published in IEEE Transactions Antennas and Propagation.
- Fettweis, A. and G. Nitsche (1991), "Numerical Integration of Partial Differential Equations Using Principles of Multidimensional Wave Digital Filters," J. of VLSI Signal Processing.
- Johnson, W. A., D. R. Wilton, and R.M. Sharpe (1988), Patch Code Users Manual, Sandia National Laboratory, SAND87-2991.
- Kalbasi, Khalil (1991), "DSP-based Multilevel Iterative Technique for the Moment Method Solution of Large Electromagnetic Problems," Ph.D. Dissertation, U. of Kansas, Lawrence.
- Kuo, C.C. Jay, and B.C. Levy (1990), "Discretization and Solution of Elliptic PDEs--A Digital Signal Processing Approach," IEEE Proceedings, 12, pp. 1808-1842.
- Lee, S., D.A. Shnidman, and E.A. Kichauco (1987), "Numerical Modeling of RCA and Antenna Problems," Lincoln Laboratory, Massachusetts Institute of Technology, ESD-TR-87-036.
- Ludwig, A.C. (1986), "A Comparison of Spherical Wave Boundary Value Matching Versus Integral Equation Scattering Solutions for a Perfectly Conducting Body," IEEE Antennas and Propagation Society Transactions, AP-34, pp. 857-65.
- Marhefka, R.J., and T.J. Brinkley (1988), "Comparison of Methods for Far Zone Scattering from

- a Flat Plate and Cube," *Applied Computational Electromagnetics Society Journal*, Vol. 3, No. 2.
- Miller, E.K. (1986), Editor of "Time-Domain Measurements in Electromagnetics", Van Nostrand Reinhold, New York, NY.
- Miller, E.K. (1988), "A Selective Survey of Computational Electromagnetics," Invited Tutorial-Review Paper, *IEEE Transactions Antennas and Propagation*, pp. 1281-1305.
- Miller, E. K. (1990), "PCs for AP," Column in *IEEE AP-S Magazine*, Vol. 32, No. 3, June.
- Miller, E. K. (1991), "Solving Bigger Problems--By Reducing the Operation Count and Increasing the Computation Bandwidth," invited article, *IEEE Proceedings*, October.
- Miller, E. K. (1992), Description of Khoros system in "PCs for AP," Column in *IEEE AP-S Magazine*, Vol. 32, No. 2, February.
- Miller, E.K., F.J. Deadrick, G.J. Burke and J.A. Landt (1981), "Computer-Graphics Applications in Electromagnetic Computer Modeling, *Electromagnetics*," 1, pp. 135-153.
- Miller, E. K., R. Merrill, and R.J. Cole (1988), "Computer Movies for Education," *IEEE Transactions on Education*, May, 58-68, Education Transactions Best Paper Award for 1988.
- Miller, E.K. and M.A. Gilbert (1991), "Solving the Helmholtz Equation Using Multiply-Propagated Fields," *International J. of Numerical Modeling in Engineering*, 4, pp. 123-138.
- Newman, E.H. and D.M. Pozar (1978), "Electromagnetic Modeling of Composite Wire and Surface Geometries," *IEEE Transactions Antennas and Propagation*, AP-26, pp. 784-788.
- Perlik, A.T., and Moraites, S.C. (1992, to be published), "Electromagnetic Wave Analysis using FDTD and its Implementation on the Connection Machine," Chapter 8, *Progress in Electromagnetics Research*, PIER 7/8, Elsevier Press
- Ray, S. (1991), in "PCs for AP" column by E.K. Miller, in *IEEE Antennas and Propagation Society Magazine*, Vol. 33, No. 6, December.
- Rockway, J.W., J.C. Logan, D.W.S. Tam, and S.T. Li (1988), "The MININEC System: Microcomputer Analysis of Wire Antennas," Artech House, Boston.
- Russell, L.C. and J.W. Rockway (1991), "Parallel Processing Applied to Computational Electromagnetics," Technical Report 1450, Naval Ocean Systems Center, San Diego, CA.
- Sarkar, T.K., E. Arvas, and S.M. Rao (1986), "Application of FFT and the Conjugate Gradient Method for the Solution of Electromagnetic Radiation from Electrically Large and Small Conduction Bodies," *IEEE Transactions Antennas and Propagation*, AP-34, pp. 635-640.
- Siarkiewicz, K.R. (1988), "GEIMACS - The Present and the Future," *Proceedings of 4th Annual Review of Progress in Applied Computational Electromagnetics*.
- Stone, W.R. (1990), "Radar Cross Sections of Complex Objects," *IEEE Press*.
- Taflov, A. (1988), "Review of the Formulation and Applications of the Finite-Difference Time-Domain Method for Numerical Modeling of Electromagnetic Wave Interactions with Arbitrary Structures," *Wave Motion*, 10, pp. 547-582.
- Umashankar, K, S. Nimmagadda, and A. Taflov (1990), "Application of Integral Equation and Method of Moments for Electrically Very Large Scatterers Using Spatial Decomposition Technique," in digest of *IEEE Antennas and Propagation Society Symposium*, pp. 76-79.
- Wandzura (1992), Oral presentation on the Fast-Multipole Method at Workshop on Computational Electromagnetics, Rome Laboratory, Hanscom AFB, MA, December.
- Wang, T. M. and H. Ling (1991), "Electromagnetic Scattering from Three-Dimensional Cavities via a Connection Scheme," *IEEE Antennas and Propagation*, AP-39, pp. 1505-1513.
- Wilton, D. R, and S.U. Hwu (1989), "JUNCTION: A Computer Code for the Computation of Radiation and Scattering by Arbitrary Conducting Wire/Surface Configurations," *Proceedings of 5th Annual Review of Progress in Applied Computational Electromagnetics*, pp. 43-51.
- Wilton, D. R, S.V. Yesantharao, C.M. Cheng, and R.M. Shapre (1989), "EMPACK: Building Block Subroutines for the Method of Moments," *Proceedings of 5th Annual Review of Progress in Applied Computational Electromagnetics*, pp. 34-42.

SESSION 6 - "TRANSIENTS"

Chair: Dr. Paul M. Goggans

Transient Internal and Scattered Fields of a Sphere Illuminated with a Pulsed Gaussian Beam

Elsayed Esam M. Khaled, Dipakbin Q. Chowdhury*,
Steven C. Hill** and Peter W. Barber

Department of Electrical and Computer Engineering,
Clarkson University, Potsdam, NY 13699-5720.

* Department of Applied Physics and Center for Laser Diagnostics,
Yale University, New Haven, CT 06520.

** Atmospheric Sciences Laboratory,
White Sands Missile Range, NM 88002,
and Department of Electrical and Computer Engineering,
New Mexico State University, Las Cruces, NM 88003.

Abstract

Internal and scattered time-dependent intensities are calculated for a dielectric sphere illuminated with a pulsed Gaussian beam. The center frequency of the pulse spectrum is chosen to be on or near a resonant frequency of the sphere. The center of the beam is positioned inside, on the edge, or outside the sphere. The electric field at a point, at each frequency of the incident pulse spectrum, is calculated using the plane-wave spectrum technique and the T-matrix method. The frequency spectrum of the field at a point is calculated using the incident field spectrum and the transfer function at that point. The time-dependence of the electric field at a point inside or outside the sphere is obtained by inverse Fourier transforming the frequency spectrum. Two different decay rates in the internal and scattered time-dependent intensity are observed: a decay rate that depends on the incident pulse spectrum and a rate which depends on the lineshape of the resonant mode of the sphere.

1. Introduction

Transient scattered fields are of interest in areas such as characterizing targets using radar. Internal transient fields are also of interest in areas such as bioelectromagnetics, and electromagnetic hyperthermia.[1] In the visible frequency range, small dielectric objects, e.g., liquid spherical droplets, are often of interest. Both the transient internal intensity and the transient scattered field are important for dielectric spheres. The term "intensity" refers to $\mathbf{E} \cdot \mathbf{E}^*$, which is proportional to the electric energy density, where \mathbf{E} is the complex amplitude of the electric field. When the frequency of the incident wave is on a resonant frequency of the sphere the internal energy density can be very large [2]. Spheres are often illuminated with beams or pulses which have a Gaussian spatial dependence.

Many techniques have been used to compute the transient far-fields scattered by conducting or dielectric objects for plane-wave illumination. The forward and backward scattering by perfectly conducting spheres was computed using Laplace transformation [3]. The singularity expansion method was used to selectively excite the transient response corresponding to a single pole of the transfer function for a perfectly conducting sphere [4]. The backscatter by a sphere illuminated with a short pulse was calculated using a Fourier series expansion [5]. The transient scattering by a conducting sphere was calculated using the integral equation method [6]. The transient responses of dielectric cylinders and spheres for a source located at the center were computed [7]. All of these computations were for far-field transients and for spherical size parameters (circumference/incident wavelength) less than 10. Internal transient fields inside spherical models of dispersive biological materials were computed using Fourier transform techniques. [1]

The time-dependence of the internal intensity of a large sphere illuminated with a plane-wave pulse was calculated [8] where Fourier transformation was used to calculate the internal time-dependent intensity. The transient behavior at different positions inside the sphere was calculated for different detunings. The detuning is the difference in frequency between the center of the incident pulse spectrum and the center of a particular resonant frequency of the sphere.

In this paper the transient build-up and decay of the internal and scattered intensities of a dielectric sphere on and near resonance are calculated and illustrated. The sphere is illuminated with a pulse that has both a Gaussian time dependence, and a Gaussian spatial dependence. The spatial dependence is modeled using the angular spectrum of plane waves. To obtain the transfer function at each frequency of the incident pulse spectrum, the internal and scattered fields are computed using the T-matrix method. Then at each point of interest the internal or the scattered frequency spectrum is computed as the product of the incident field spectrum and the transfer function at that point. The time-dependent fields are computed by inverse-Fourier transforming the field spectrum.

The primary factors determining the time dependence of the intensity inside or outside a sphere are the spatial position and width of the incident Gaussian pulse, the pulse width (in time) of the incident pulse intensity, the lifetime of the nearest high- Q mode, and the detuning of the center frequency of the pulse from the resonant frequency of the mode.

The method of calculation is given in Section 2. The calculated results and a discussion of the internal and scattered transient intensities for a sphere illuminated with different pulses are presented in Section 3. The conclusions are summarized in Section 4.

2. Theoretical Analysis

Figure 1 shows the geometry of the problem. A sphere of radius a is located at the center of a right-handed Cartesian coordinate system (x, y, z) . A spherical coordinate system (r, θ, ϕ) is also shown. The sphere is illuminated with a pulse that is a Gaussian function in time. The incident pulse propagates in the z -direction. The cross-section of the incident pulse, in space, is either a plane wave or a Gaussian function. The pulsed Gaussian beam is polarized in the x - z plane and the minimum spot size of the beam is ω_0 . The focal point is located at an arbitrary point relative to the sphere's center. The amplitude of the field at the beam's focal point is chosen in such a way that the total power carried by the beam is constant for various cases.

For a plane wave, the incident pulse amplitude, polarized in the x -direction, has an electric field given by

$$\mathbf{E}^i(z, t) = \hat{E}^i(t - z/c) \exp[-i\Omega_0(t - z/c)] \mathbf{i}_x \quad (1)$$

where $\hat{E}^i(t - z/c)$ is the envelope of the field, which is real, and c is the velocity of light in free space. The angular frequency is $\Omega_0 = 2\pi f_0$, where f_0 is the frequency and $i = \sqrt{-1}$. The real electric field is the real part of (1) and is given by

$$\mathbf{E}^i(z, t) = \hat{E}^i(\tau) \cos(\Omega_0 \tau) \mathbf{i}_x \quad (2)$$

where τ is the shifted time $t - z/c$.

To compute the time-dependent electric field at an arbitrary point inside or outside the sphere, we compute the Fourier transform of the incident field amplitude and multiply by the Fourier transform of the impulse response function (the transfer function for the linear system) at that particular point. We then take the inverse Fourier transform of the individual field components to obtain the total time-dependent field, i.e.,

$$\mathbf{E}(\tau, \mathbf{r}) = \mathcal{F}^{-1} \left\{ E^i(\Omega) \mathbf{E}^s(\Omega, \mathbf{r}) \right\}, \quad (3)$$

where $\mathbf{E}(\tau, \mathbf{r})$ is either the internal field $\mathbf{E}^{int}(\tau, \mathbf{r})$ or the scattered field $\mathbf{E}^s(\tau, \mathbf{r})$, $E^i(\Omega)$ is the Fourier transform of the incident field, and $\mathbf{E}^\delta(\Omega, \mathbf{r})$ is the Fourier transform of the impulse response function at $P(\tau, \theta, \phi)$. Note that point P in Fig. 1 can be chosen inside or outside the sphere for the internal or the scattered field calculation, respectively. The Fourier transform, $E^i(\Omega)$, of the incident pulse is

$$E^i(\Omega) = \mathcal{F}\{E^i(\tau)\} = \mathcal{F}\{\hat{E}^i(\tau) \exp[-i\Omega_0\tau]\}, \quad (4)$$

where $\hat{E}^i(\tau)$ is the envelope of the incident field. Rewriting (4) using the translation theorem for the Fourier transform [9] we obtain

$$E^i(\Omega) = \hat{E}^i(\Omega + \Omega_0). \quad (5)$$

Combining (3) and (5), the time-dependent field is

$$\mathbf{E}(\tau, \mathbf{r}) = \mathcal{F}^{-1}\{\hat{E}^i(\Omega + \Omega_0)\mathbf{E}^\delta(\Omega, \mathbf{r})\}. \quad (6)$$

The Fourier transform of the impulse response function, $\mathbf{E}^\delta(\Omega, \mathbf{r})$, at the position P is obtained by evaluating the electric field amplitude at P over the frequencies of the incident pulse spectrum. Since there are many optical oscillations within the time period of a pulse, we are interested only in the time development of the pulse envelope. Rewriting the internal or scattered field as $\mathbf{E}(\tau, \mathbf{r}) = \hat{\mathbf{E}}(\tau, \mathbf{r}) \exp(-i\Omega_0\tau)$, where $\hat{\mathbf{E}}(\tau, \mathbf{r})$ is the envelope of the internal or scattered field, and using the translation theorem again, we obtain the expression for the envelope of the field in (6) as

$$\hat{\mathbf{E}}(\tau, \mathbf{r}) = \mathcal{F}^{-1}\{\hat{E}^i(\Omega)\mathbf{E}^\delta(\Omega - \Omega_0, \mathbf{r})\}. \quad (7)$$

For Gaussian beam illumination, the above analysis is used with the exception that $\mathbf{E}^\delta(\Omega, \mathbf{r})$ is the internal or scattered field resulting from Gaussian beam illumination. For an incident pulsed Gaussian beam the expression for an arbitrary incident field is given (at any incident frequency) in terms of vector spherical harmonics [10] by

$$\begin{aligned} \mathbf{E}^i(k\mathbf{r}) = & H \sum_m \sum_n D_{mn} \left[a_{emn}^t \mathbf{M}_{emn}^1(k\mathbf{r}) + a_{omn}^t \mathbf{M}_{omn}^1(k\mathbf{r}) \right. \\ & \left. + b_{emn}^t \mathbf{N}_{emn}^1(k\mathbf{r}) + b_{omn}^t \mathbf{N}_{omn}^1(k\mathbf{r}) \right], \end{aligned} \quad (8)$$

For a unit amplitude incident plane wave, H is unity and the azimuthal mode index $m = 1$. The expression for the internal fields excited in a sphere by an arbitrary incident beam is given [10] by

$$\begin{aligned} \mathbf{E}^{int}(\Omega, \mathbf{r}) = & H \sum_m \sum_n \left[c_{emn}^t \mathbf{M}_{emn}^1(mk\mathbf{r}) + c_{omn}^t \mathbf{M}_{omn}^1(mk\mathbf{r}) \right. \\ & \left. + d_{emn}^t \mathbf{N}_{emn}^1(mk\mathbf{r}) + d_{omn}^t \mathbf{N}_{omn}^1(mk\mathbf{r}) \right], \end{aligned} \quad (9)$$

where H is a constant that depends on the incident beam. Note that m in Roman type indicates the refractive index and m in italics is the azimuthal mode index. The expression for the scattered electric field [10] is

$$\begin{aligned} \mathbf{E}^s(\Omega, \mathbf{r}) = & H \sum_m \sum_n D_{mn} \left[f_{emn}^t \mathbf{M}_{emn}^3(k\mathbf{r}) + f_{omn}^t \mathbf{M}_{omn}^3(k\mathbf{r}) \right. \\ & \left. + g_{emn}^t \mathbf{N}_{emn}^3(k\mathbf{r}) + g_{omn}^t \mathbf{N}_{omn}^3(k\mathbf{r}) \right]. \end{aligned} \quad (10)$$

All the parameters are given previously [10].

3. Results and Discussion

Transient intensities inside and outside a micrometer-sized dielectric sphere illuminated by a pulsed beam that is Gaussian in space and time are calculated for different incident pulse durations and detunings. The detuning is the shift in frequency of the center of the incident pulse spectrum from the resonant frequency. The results for illumination with Gaussian beams are normalized relative to the total power carried by the incident beam

$$P_t = \frac{c}{16} E_0^2 \omega_0^2 \quad (11)$$

where c is the speed of light in free space, E_0 is the electric field amplitude at the beam's focal point and ω_0 is the beam's minimum spot size. For plane wave pulses P_t would be infinite. The results for plane wave illumination are normalized by assuming that it carries the same power as a Gaussian beam of width $\omega_0 = 10a$, where a is the sphere radius. When the minimum beam width is much larger than the droplet diameter the computed results show very close agreement with the computed results for plane wave illumination.

The resonant mode investigated here in detail is the $TE_{58,1}$ resonance, which has a resonant size-parameter $x_r (= 2\pi a/\lambda) = 47.3094299$, a dimensionless resonance linewidth $\Delta x = 0.66 \times 10^{-4}$, and $Q = x/\Delta x = 0.72 \times 10^6$ in a sphere having a refractive index of $m = 1.36$. The resonant lifetime, τ_r , is 0.2052 ns. The spot size of the incident Gaussian pulse at its focal point is $\omega_0 = 1 \mu\text{m}$. Although the beam focal point can be shifted along the x and/or y and/or z axes, the results here are shown for $x_0 = 0$ and $z_0 = 0$, i.e., the beam's focal point is shifted along the y -axis only. At the resonant size parameter of the $TE_{58,1}$ resonance the radius of the sphere is $a \approx 4 \mu\text{m}$ at $\lambda = 0.532 \mu\text{m}$. The demonstrations of the calculated results are given in two groups. In the first group the time-dependent internal intensity is shown at a point $P_1 (0.9a, 0^\circ, 0^\circ)$ for different incident beam positions and detuning. The results in this category are illustrated in Figs. 2 - 5. In the second group the time-dependent scattered intensity is shown at a point $P_2 (500a, 180^\circ, 0^\circ)$. The results are shown in Figs. 6 and 7.

3.1. Time-dependence of the internal intensity

Figure 2 shows the time-dependence of the internal intensity at point P_1 . The incident pulse is also shown. The time $t = 0$ is chosen to be at the peak of the incident pulse intensity. The width of the input pulse $\tau_0 = 0.5239$ ns (full width at half maximum of intensity) is larger than the resonance lifetime, $\tau_r = 0.2052$ ns, of $TE_{58,1}$. When the pulse is focused at $y_0 = 1.232a$, the internal intensity is greater than that when the pulse is focused at $y_0 = a$ or $y_0 = 1.5a$. For steady state Gaussian beam illumination, the maximum electric energy is coupled to the $TE_{58,1}$ mode at the illumination position $y_0 = 1.232a$. The time delay between the peak of the incident pulse and the peak of the internal intensity is somewhat longer for $y_0 = 1.232a$ than for the other two pulsed beam positions. For all three cases the internal intensity eventually decays exponentially with a decay rate determined by the resonant lifetime.

Figure 3 shows the time dependent internal intensity as in Fig. 2, but in this case the width of the incident pulse is $\tau_0 = 0.1746$ ns which is shorter than the resonant lifetime ($\tau_r = 0.2052$ ns), i.e., the incident frequency spectrum is broader than linewidth of the resonant mode. There are two differences between the results in Figs. 2 and 3. First, the peaks are higher in Fig. 2 ($\tau_0 > \tau_r$) than in the corresponding cases in Fig. 3 ($\tau_0 < \tau_r$). When $\tau_0 > \tau_r$ the spectrum of the incident pulse overlaps well with the spectrum of the resonant mode. As the time duration of the incident pulse becomes wider the internal intensity has time to build to a higher value. Second, the time delay between the internal intensity peaks and the peak of the incident pulse is larger in Fig. 2, than in Fig. 3. In the cases shown in Fig. 2 and 3, when the Gaussian pulse is focused at the optimal

position to couple maximum energy to the $TE_{58,1}$ mode ($y_0/a = 1.232$), the internal intensity is higher than with the other illumination positions ($y_0/a = 1.0$ and $y_0/a = 1.5$).

The effects of detuning from resonance on the transient internal intensity for different incident pulse illuminations are shown in Fig. 4. The center frequency of the input pulse is

$$\Omega_0 = \Omega_r + N\Delta\Omega_r \quad (12)$$

where $\Delta\Omega_r$ is the resonance linewidth in frequency and N is the number of linewidths. Figure 4 shows the transient internal intensity at the point P_1 when $N = 5$ and the incident pulse width is 0.5239 ns. For all beam positions, the transient internal intensity decreases much faster than when $N = 0$ (compare with Fig. 2(b)). When $N = 5$, the overlap of the incident field spectrum with the resonant linewidth spectra is relatively small. To show the behavior of the transient intensity for a detuned narrow incident pulse, $\tau_0 < \tau_r$, the same calculations as in the case of Fig. 4 are repeated with an incident pulse width of $\tau_0 = 0.1746$ ns. The incident pulse is detuned by $N = 5$ linewidth and all other parameters are the same as in the case of Fig. 3. The calculated results are presented in Fig. 5. The exponential tail is observed in the plots because the incident pulse spectrum is broad enough that the detuned (shifted) part of the incident spectrum overlaps the resonant spectrum. Since only a part of the incident spectrum overlaps significantly with the resonant lineshape, the internal intensity does not build to a value similar to that of a resonant incidence. Also, in the temporal profile of the internal intensity a kink is shown when the incident pulse is detuned. There are two different spectral peaks in the internal field spectrum associated with two different decay rates (a fast decay depends on the incident pulse and an exponential decay depends on the life-time of the resonant mode). One of the peaks is caused by the resonance and the other by the peak of the incident spectrum. In the case of a detuned incident pulse these two peaks are separated causing the kink in the calculated results as shown in Fig. 5. In the internal field spectrum the energy near the peak due to the incident spectrum is responsible for the rapid decay rate while the energy near the peak due to the resonance is responsible for the slower decay rate.

3.2. Time-dependence of the scattered intensity

Figures 6 and 7 show the time-dependent scattered intensity of a sphere illuminated with a Gaussian pulse focused at different positions. Results for plane wave illumination are also included. Figure 7 shows the results of the scattered intensity when the width of the incident pulse $\tau_0 = 0.1746$ ns, is less than the resonant lifetime ($\tau_r = 0.2052$ ns). The scattered intensity for all Gaussian pulse illumination positions follows the input pulse during the time the intensity is rising. The scattered intensity then decays exponentially and smoothly when the input pulsed Gaussian beam is focused at $y_0/a = 1.232$ or 1.5. When the beam is focused at $y_0 = 1.0$ the decay-time consists of two parts: (1) a relatively faster decaying part; and (2) a part that decays with a rate determined by the resonant lifetime. The reason for the two decay rates in Fig. 6(a) for $y_0/a = 1$ is that the resonant mode does not completely dominate the internal (and hence the scattered) energy. Other modes share the energy distribution with the resonant mode and contribute to the time dependence of the decay. As the pulse is focused away from the surface of the sphere the resonant (high-Q) mode becomes more dominant and the exponential decay associated with that mode becomes more pronounced. To clarify this, the time-dependence of the backscattered intensity at two more illumination positions $y_0/a = 0.5$ and $y_0/a = 0.75$ are calculated and shown in Fig. 6(b). As the incident pulse is focused near to the center of the sphere the resonant mode ($TE_{58,1}$) is less dominant and the exponential decay starts later.

Figure 7 shows the results of the transient scattered intensity for the same input Gaussian pulse as in the case of Fig. 6, i.e., $\tau_0 = 0.1746$ ns. However the incident pulse is detuned by 5 linewidths from the resonance location of the $TE_{58,1}$ MDR, i.e., $N = 5$. All the other parameters are the

same as in the case of Fig. 6. The kinks in the scattered intensity and the two different decay rates are similar to the case of Fig. 5. There is a difference in temporal behavior between the transient internal, Fig. 5, and scattered, Fig. 7, intensity for different detuned incident beam positions. In Fig. 7, before the exponentially decaying tail starts, the scattered intensity is progressively lower as the beam is focused farther from the sphere. In the transient internal field distribution for the same detuning (Fig. 5), the case for the beam focused at $y_o/a = 1.232$ gave the highest internal intensity for all times. For the scattered intensity in Fig. 7 the beam position $y_o/a = 1$ gave the largest scattered intensity over the duration time before the exponential decay starts. This maximum occurs because of the relatively large contribution of the other modes. After the incident pulse intensity decreases to negligible values, the largest transient scattered intensity is for the beam position $y_o/a = 1.232$, the position for best coupling into the resonant mode.

4. Conclusions

The internal and scattered transient intensities of a dielectric sphere illuminated with a pulse that is Gaussian in space and time are computed. In a sphere, both the internal spectrum and the associated time-dependence vary with spatial location, particularly when the incident frequency is near a resonant mode. The time dependence of the intensity at an internal location at resonance has an exponential tail with a time constant of $1/\Delta\Omega_r$, where $\Delta\Omega_r$ is the resonant linewidth of the resonant mode. This exponential tail is more prominent when the incident spectrum overlaps significantly with the mode, i.e., when $\Delta\Omega \leq \Delta\Omega_o$ and $\Delta\Omega_o \geq \Delta\Omega_r$, where $\Delta\Omega_o$ is the width of the incident pulse spectrum, and $\Delta\Omega$ is the detuning. The pulse duration and its illumination position relative to the center of the sphere, the lifetime of the nearest high-Q resonant mode, the detuning, and the position of the point inside or outside the sphere at which the field is calculated are the primary factors determining the time dependence of the internal or the scattered intensity.

The calculations presented here show that there are different peak intensities and delay times for different focal positions of the incident pulsed Gaussian beam. The results also show that with a slightly detuned incident pulse, the optimal beam position for coupling energy into the resonant mode gives the largest scattered intensity.

References

- [1] K. Moten, C. H. Durney, and T. G. Stockham, "Electromagnetic pulsed-wave radiation in spherical models of dispersive biological substances," *Bioelectromagnetics*, **12**, 319-333 (1991).
- [2] S. C. Hill and R. E. Benner, "Morphology-dependent resonances," in *Optical Effects Associated with Small Particles*, P. W. Barber and R. K. Chang, eds. (World Scientific, Singapore, 1988), 3-61.
- [3] T. Hosono, K. Ikeda, and A. Itoh, "Analysis of transient response of electromagnetic waves scattered by a perfectly conducting sphere. The case of back- and forward-scattering," *Electron. Commun. Japan*, part 1, **71**, 74-86 (1988).
- [4] W. E. Howell and H. Überall, "Selective observation of resonances via their ringing in transient radar scattering, as illustrated for conducting and coated spheres," *IEEE Trans. Antennas Propagat.*, **AP-38**, 293-298 (1990).
- [5] J. Rheinsteint, "Backscatter from spheres: a short pulse view," *IEEE Trans. Antennas Propagat.*, **AP-16**, 89-97 (1968).

- [6] R. Mittra, "Integral equation methods for transient scattering" in *Transient Electromagnetic Fields*, L. B. Felson, Ed. (Springer-Verlag, New York, 1976).
- [7] H. Shirai, "Time Transient Analysis of Waves Scattering by Simple Shapes," Analytic and Numerical Methods in Wave Theory Seminar, Adana, Turkey (1991); H. Shirai and A. Hamakoshi, "Transient Response by a Dielectric Cylinder due to a Line Source at the Center," *Trans. Inst. Electron. Inf. Commun. Eng. (Japan)*, E 74, 157-166 (1991).
- [8] D. Q. Chowdhury, S. C. Hill and P. W. Barber, "Time dependence of internal intensity of a dielectric sphere on and near resonance," *J. Opt. Soc. Am. A*, 9, 1364-1373 (1992).
- [9] Joseph W. Goodman, *Introduction to Fourier Optics*, (McGraw-Hill, New York, 1968).
- [10] E. E. M. Khaled, S. C. Hill and P. W. Barber, "Scattered and internal intensity of a sphere illuminated with a Gaussian beam," accepted for publication in the *IEEE Trans. Antennas Propagat.*

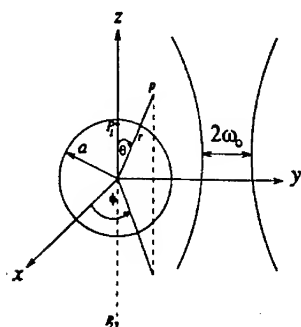


Figure 1. A spherical particle of radius a centered at the origin of a right-handed Cartesian co-ordinate system (x, y, z) along with a spherical coordinate system (r, θ, ϕ) . The incident pulse is a Gaussian function in time propagating along the z direction. The pulsed Gaussian beam has a spot size of $\omega_0 = 1.0 \mu\text{m}$ and the focal point is arbitrarily located at (x_0, y_0, z_0) in the Cartesian coordinate system.

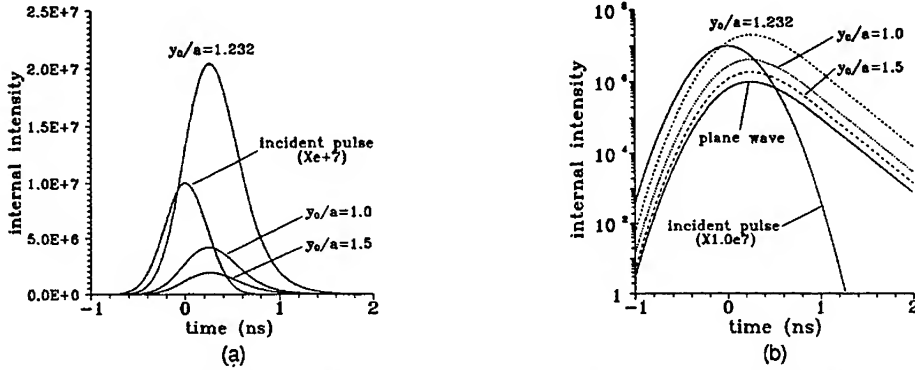


Figure 2. Time-dependence of the internal intensity at $P_1(0.9a, 0^\circ, 0^\circ)$ of a sphere. The incident pulse is either a plane wave or a Gaussian pulse focused at different locations. The incident frequency is on resonance with the $TE_{ss,1}$ mode. The width of the incident pulse is $\tau_0 = 0.5239$ ns and the resonant lifetime is $\tau_r = 0.2052$ ns, $m = 1.36$ and $a \approx 4$ μ m for an incident wavelength of 0.532 μ m. Beam position along the y axis is shown relative to the sphere radius a . (a) Linear scale. (b) Log scale

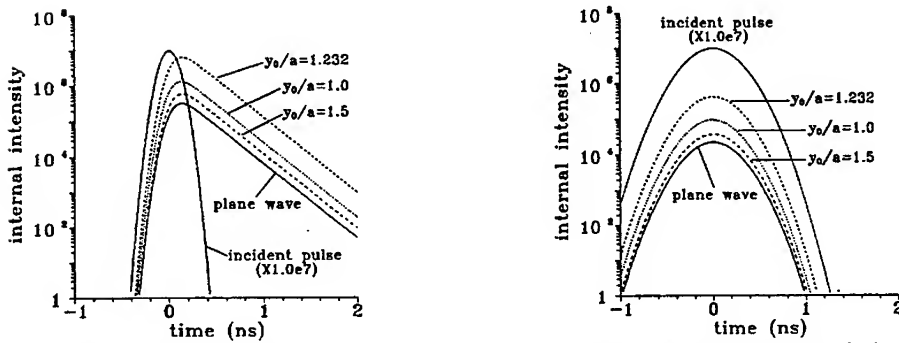


Figure 3. Time-dependence of the internal intensity at $P_1(0.9a, 0^\circ, 0^\circ)$ of a sphere as in Fig. 2 except that the incident pulse width is $\tau_0 = 0.1746$ ns, i.e., $\tau_0 < \tau_r$.

Figure 4. Time-dependence of the internal intensity of a sphere where the incident pulse is either a plane wave or a Gaussian pulse focused at different locations. The incident field frequency is detuned by 5 linewidths from the resonant mode $TE_{ss,1}$. All the other parameters are the same as in Fig. 2.

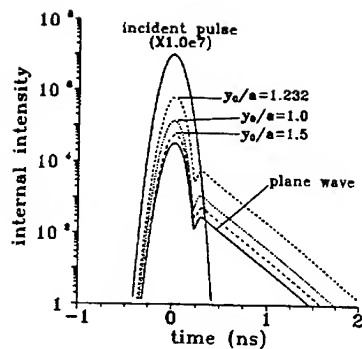


Figure 5. Time-dependence of the internal intensity at $P_1(0.9a, 0^\circ, 0^\circ)$ of a sphere as in Fig. 4 except that the incident pulse width is $\tau_0 = 0.1746$ ns.

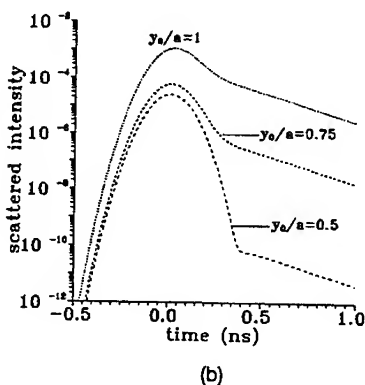
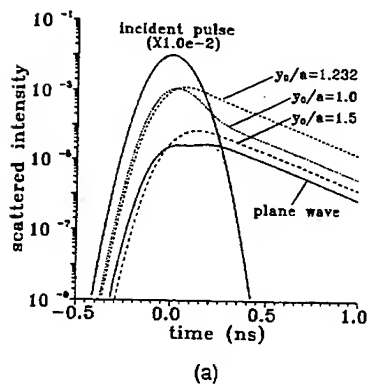


Figure 6. Time-dependence of the backscattered intensity at $P_2(500a, 180^\circ, 0^\circ)$ of a sphere where the incident pulse is either a plane wave or a Gaussian pulse focused at different locations. All the parameters for the sphere and the incident pulse are the same as in Fig. 3.

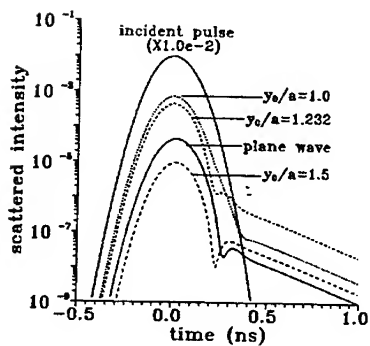


Figure 7. Time-dependence of the backscattered intensity at $P_2(500a, 180^\circ, 0^\circ)$ of a sphere as in Fig. 6 except that the incident frequency is detuned by 5 linewidth away from the $TE_{58,1}$ resonance location.

SESSION 7 - "HIGH - FREQUENCY TECHNIQUES

AND

ASYMPTOTIC SOLUTIONS"

Chair: Dr. A.K. (Tony) Brown, Co-Chair: Dr. Shian U. Hwu

ISAR Image Formation Using Bistatic Data from 'XPATCH'

Rajan Bhalla and Hao Ling

Department of Electrical and Computer Engineering
The University of Texas at Austin
Austin, TX 78712-1084

1. INTRODUCTION

In radar cross section (RCS) applications, it is often desirable to generate the inverse synthetic aperture radar (ISAR) image of a target. The ISAR image can be used: (i) as a visualization tool by displaying the microwave image of the target, (ii) as a diagnostic tool to pinpoint the key scattering centers on the target, and (iii) as an identification tool to distinguish and classify the target from a collection of possible targets. ISAR image formation is typically achieved by utilizing the monostatic scattered field data, obtained through either measurement or numerical simulation, over a finite range of look angles and frequencies. In this work, we investigate the feasibility of utilizing bistatic scattered field data to obtain the ISAR image of a target (Fig. 1).

Our work is motivated by the recent development of a general-purpose high-frequency electromagnetic scattering code, XPATCH [1], which can predict the scattering from complex, realistic targets. XPATCH is based on the shooting and bouncing ray (SBR) technique [2],[3]. The major computation time for the XPATCH code can be attributed to two parts: geometrical ray tracing and electromagnetic computation. The latter includes the computation of the geometrical optics field associated with each ray and the ray tube integration algorithm. As the complexity and size of the target increases the ray tracing time can become a dominant portion of the total computation time. In the usual practice where monostatic data are utilized to generate ISAR images, the ray tracing portion of the code is executed for every look angle. Bistatic scattered field data, on the other hand, is cheaper to acquire, since ray tracing is performed once for the incident direction and only the electromagnetics calculation is needed for every look angle. Hence microwave image formation using XPATCH in the bistatic arrangement can result in time savings.

2. FORMULATION

The equivalence between the monostatic and bistatic RCS data under the physical optics approximation is not new and has been discussed earlier by Kell [4]. However, this equivalence has not been fully evaluated for image formation applications. Farhat *et al.* [5] utilized measured far field data collected under a fixed bistatic angle for image formation. In this section we will derive the relationship between the bistatic scattered far field data and the microwave image of the scatterer. Our derivation will parallel closely with the formulation found in [6]. Consider a perfectly conducting object illuminated by a plane wave with $\exp(j\omega t)$ time dependence and an incident wave vector \mathbf{k}^i . The incident electric field is $\mathbf{E}^i(\mathbf{r}) = \hat{\ell} E_0 \exp(-jk^i \cdot \mathbf{r})$ where E_0 and $\hat{\ell}$ are respectively the magnitude and direction of the incident electric field and $|\mathbf{k}^i| = k_0$. The scattered far field at the observation point \mathbf{r} due to the physical optics current $\mathbf{J}_s = 2 \hat{\mathbf{n}} \times \mathbf{H}^i$ on the target is then given by

$$\mathbf{E}^s(\mathbf{r}) = -j\omega\mu_0 \iint_{S^{ill}} \mathbf{J}_s(\mathbf{r}') G^{ff}(|\mathbf{r}-\mathbf{r}'|) d^2\mathbf{r}' \quad (1)$$

where $G^{ff}(|\mathbf{r}-\mathbf{r}'|) = [\exp(-jk_0 r)/4\pi r] \exp(+jk^{ob} \cdot \mathbf{r}')$ is the free space scalar far-field Green's function with $\mathbf{k}^{ob} = k_0 \hat{\mathbf{r}}$ and the integration is over the illuminated object surface S^{ill} . We will now assume that the component of the scattered field in the $\hat{\mathbf{p}}$ direction will be observed and define a scalar object shape function $O(\mathbf{r}')$ as

$$O(\mathbf{r}') = \hat{\mathbf{p}} \cdot [2\hat{\mathbf{n}}(\mathbf{r}') \times (\hat{\mathbf{k}}^i \times \hat{\mathbf{t}})] \delta(S(\mathbf{r}')) \quad (2)$$

where $\delta(S(\mathbf{r}'))$ is the Dirac delta function with its argument $S(\mathbf{r}')$ defined as zero when $\mathbf{r}' \in S^{ill}$. The observed component of the scattered field in the $\hat{\mathbf{p}}$ direction, by making use of (2) can thus be written as

$$\hat{\mathbf{p}} \cdot \mathbf{E}^s(\mathbf{r}) = -jk_0 E_0 \frac{e^{-jk_0 r}}{4\pi r} \iiint_{-\infty}^{+\infty} O(\mathbf{r}') e^{+j(\mathbf{k}^{ob} - \mathbf{k}^i) \cdot \mathbf{r}'} d^3\mathbf{r}' \quad (3)$$

Note that equation (3) relates the scattered far field to the three-dimensional Fourier transform of the object function, or more explicitly,

$$\hat{\mathbf{p}} \cdot \mathbf{E}^s(\mathbf{r}) = C \tilde{O}(\mathbf{k}^{ob} - \mathbf{k}^i) \quad (4)$$

where $C = -jk_0 E_0 e^{-jk_0 r}/4\pi r$ and the tilde denotes Fourier transform.

In ISAR image formation, we are primarily interested in a two-dimensional projected image of the three-dimensional target. This two-dimensional microwave image is the projection of the object shape function onto a plane. It can be easily shown that the projected object function $O_{proj}(x, z)$ and a central slice of the three-dimensional Fourier space data $\tilde{O}(k_x, 0, k_z)$ form a two-dimensional Fourier transform pair:

$$\tilde{O}(k_x, 0, k_z) = \iint_{-\infty}^{+\infty} O_{proj}(x, z) e^{jk_x x + jk_z z} dx dz \quad (5)$$

This is the well-known projection-slice theorem. Therefore, the scattered field data collected under the $k_y=0$ condition can be used to form the two-dimensional ISAR image O_{proj} of the target. To acquire sufficient data in the Fourier domain for image formation, we can make use of angular and frequency diversity. For a given incident and observation direction in the xz -plane, the scattered field data corresponds to a point $\mathbf{k} = k_x \hat{\mathbf{x}} + k_z \hat{\mathbf{z}} = \mathbf{k}^{ob} - \mathbf{k}^i$ in the Fourier transform domain of the projected object function, as derived in (4). By varying the observation angle while keeping the incident direction fixed, the locus of points

$$(k_x + k_x^i)^2 + (k_z + k_z^i)^2 = k_0^2 \quad (6)$$

is traced out in k -space. Equation (6) defines a circle in the k_x - k_z plane with radius k_0 and its center is at $-k^i$ (see Fig. 2). By collecting the scattered field data over various frequencies, a set of circles with different radii k_0 can be traced out. Fig. 3(a) shows the region of k_x - k_z plane which can be accessed for a finite range of observation angles and frequencies for the case when $k^i = k_0 \hat{z}$. Proper inversion of this sector of data then leads to the two-dimensional microwave image of the target.

3. NUMERICAL RESULTS AND DISCUSSIONS

By using computed data from XPATCH, the performance of the bistatic imaging algorithm will now be illustrated. Shown in Fig. 4 is the results for the NASA almond. The geometry of the target is shown in Figs. 4(a) and 4(b). The monostatic and bistatic images are shown in Figs. 4(c) and 4(d), respectively. These images bear very good resemblance to each other. In both the images we can see the outline of the lit side of the almond. Shown in Fig. 5 is the results for a rhombic cube. The geometry of the target is shown in Figs. 5(a) and 5(b). The monostatic and bistatic images are shown in Figs. 5(c) and 5(d), respectively. The principal scattering centers corresponding to the three corners are distinctly captured by both the images. In the monostatic image, the fourth backside corner is also weakly visible. It is absent in the bistatic image since the corner is in the deep shadow of the incident illumination. Shown in Fig. 6 is the results for a dihedral corner reflector. The geometry of the target is shown in Figs. 6(a) and 6(b). The monostatic and bistatic images are shown in Figs. 6(c) and 6(d), respectively. While the three scattering centers corresponding to the three edges are clearly visible in both images, there are additional ghost artifacts in the two images. In the monostatic image the ghost artifact appears just above the right edge of the bottom plate whereas in the bistatic image it appears in the middle of the bottom plate. Since both the monostatic and bistatic imaging algorithms have been derived based on the physical optics approximation, multiple scattering effect results in ghost artifacts in the images. Furthermore, these ghost artifacts appear at different positions in the monostatic and bistatic images because the path lengths of the multiple scattering effects are strongly dependent on the incident angle and are different for the two arrangements.

The time savings to simulate the bistatic scattered field data over the monostatic data generation using the SBR technique is the main motivation for our investigation into bistatic image formation. If we define T as the time it takes to perform ray tracing for one look angle and E as the electromagnetic computation time, then the total time to simulate monostatic scattered field data for N look angles is $t_M = NT + E$. The time to simulate the bistatic far-field data for N bistatic angles, on the other hand, is $t_B = T + E$. The time savings is $\Delta t = t_M - t_B = (N-1)T$. It increases linearly with the number of look angles N , and the ray trace time T .

To conclude, there exists a tradeoff between image fidelity and time savings for the bistatic imaging scheme. The time savings depends on the ray trace time. The ray trace time for a target is large whenever multiple scattering effect is dominant or the electrical size of the target is large. On the other hand, whenever multiple scattering exists the ghost artifacts in the bistatic image do not agree with those in the monostatic image. This tradeoff is clearly brought out by the dihedral where the time savings for the ISAR generation using the bistatic scheme is a factor of 5 over the monostatic scheme but the image fidelity to that of the monostatic scheme is not as good. Hence bistatic imaging scheme is a preferred way for ISAR image generation if the image degradation due to movement of ghost artifacts is not an important consideration.

ACKNOWLEDGEMENT

This work was supported by NASA Grant NCC3-273 and in part by the Joint Services Electronics Program.

REFERENCES

- [1] S. W. Lee, "Test cases for XPATCH," Electromagnetics Lab. Tech. Rept. ARTI-92-4, Univ. of Illinois, Feb. 1992.
- [2] H. Ling, R. Chou and S. W. Lee, "Shooting and bouncing rays: calculating the RCS of an arbitrary shaped cavity," *IEEE Trans. Antennas Propagat.*, vol. AP-37, pp. 194-205, Feb. 1989.
- [3] J. Baldauf, S. W. Lee, L. Lin, S. K. Jeng, S. M. Scarborough and C. L. Yu, "High frequency scattering from trihedral corner reflectors and other benchmark targets: SBR versus Experiment," *IEEE Trans. Antennas Propagat.*, vol. AP-39, pp. 1345-1351, Sept. 1991.
- [4] R. E. Kell, "On the derivation of bistatic RCS from monostatic measurements," *Proc. IEEE.*, vol. 53, pp. 983-988, Aug. 1965.
- [5] H. J. Li and N. H. Farhat, "Image understanding and interpretation in microwave diversity imaging," *IEEE Trans. Antennas Propagat.*, vol. AP-37, pp. 1048-1057, Aug. 1989.
- [6] T. H. Chu and D. B. Lin, "Microwave diversity imaging of perfectly conducting objects in the near-field region," *IEEE Trans. Microwave Theory Tech.*, vol. MTT-39, pp. 480-487, Mar. 1991.

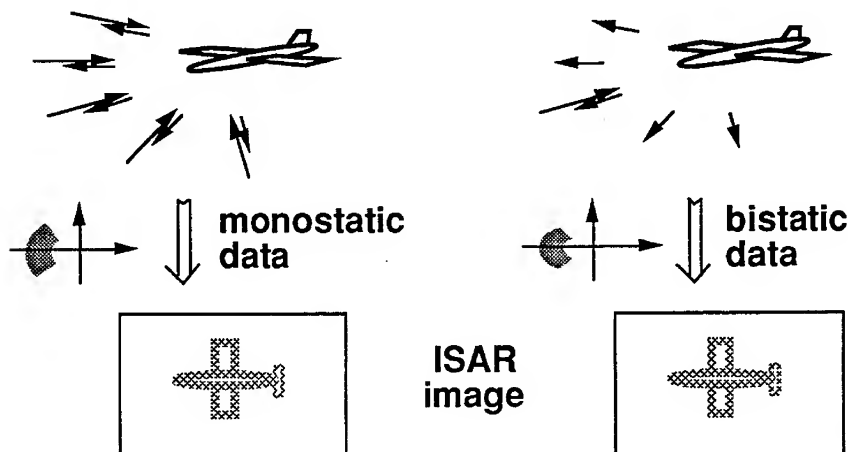


Fig. 1. ISAR image formation using bistatic instead of monostatic scattered field data.

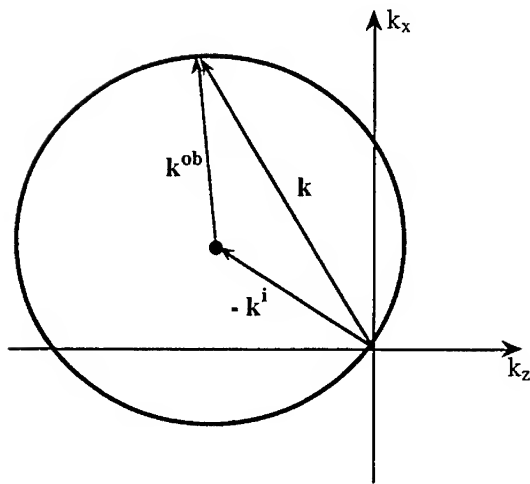


Fig. 2. The locus of points traced out in the plane by varying the observation angles for a fixed incident direction.

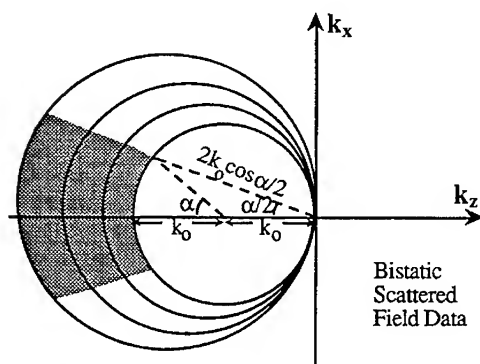
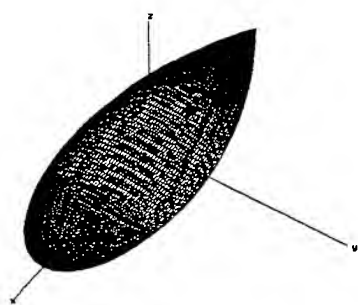
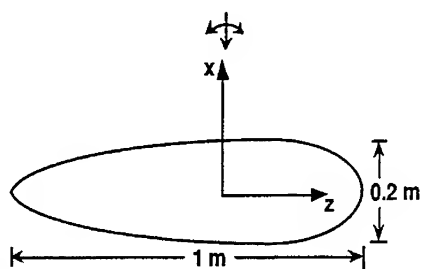


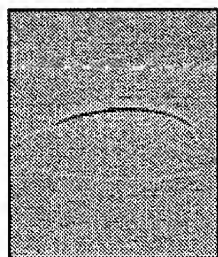
Fig. 3. Fourier space data collected under the bistatic arrangement.



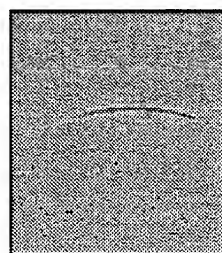
(a) NASA almond



(b) Projection of the NASA almond on the x-z plane

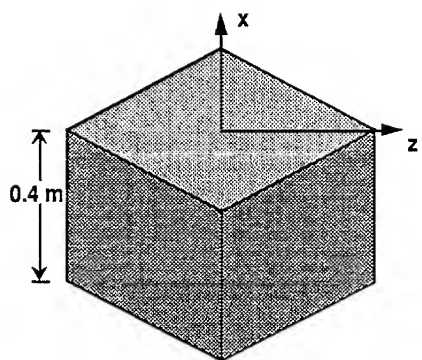


(c) Monostatic image
Freq. scan : 3 - 9 GHz
Angle scan : $(-45^\circ, 45^\circ)$

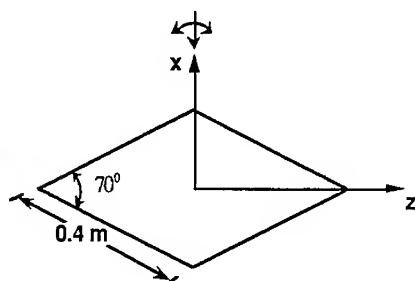


(d) Bistatic image
Freq. scan : 3 - 9 GHz
Incident angle : 0°
Ob. angle scan : $(-90^\circ, 90^\circ)$

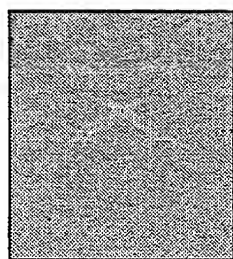
Fig. 4. Monostatic and bistatic ISAR images for the NASA almond.



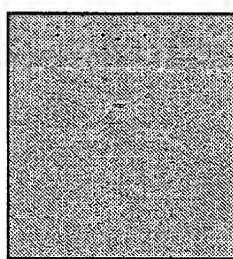
(a) Rhombic cube



(b) Projection of the rhombic cube on the x-z plane

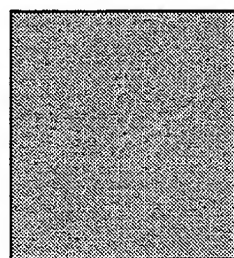
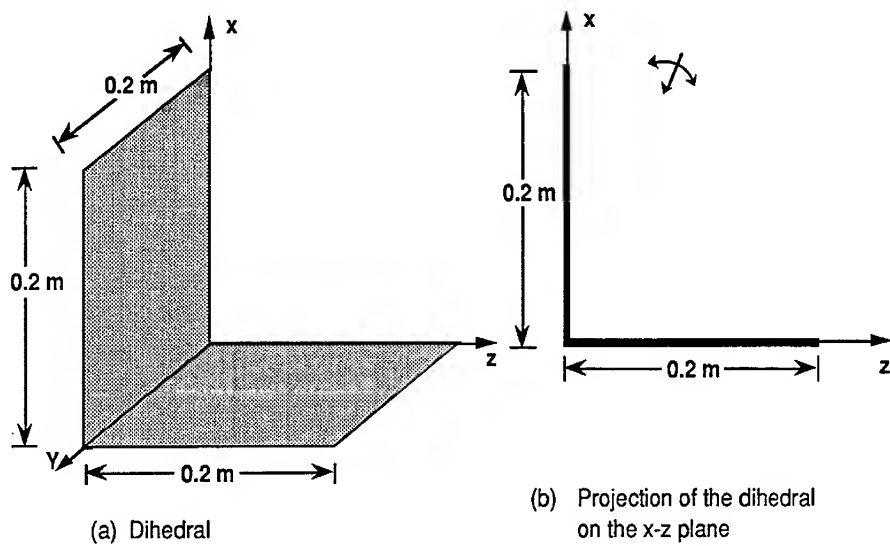


(c) Monostatic image
Freq. scan : 6 - 10 GHz
Angle scan : $(-45^\circ, 45^\circ)$

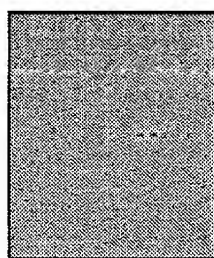


(d) Bistatic image
Freq. scan : 6 - 10 GHz
Incident angle : 0°
Ob. angle scan : $(-90^\circ, 90^\circ)$

Fig. 5. Monostatic and bistatic ISAR images for the rhombic cube.



(c) Monostatic image
 Freq. scan : 4 - 10 GHz
 Angle scan : (17.5°, 62.5°)



(d) Bistatic image
 Freq. scan : 4 -10 GHz
 Incident angle : 35°
 Ob. angle scan : (0° , 90°)

Fig. 6. Monostatic and bistatic ISAR images for the dihedral.

Time Domain Smyth-Kirchhoff Approximation to Aperture Coupling

K.S. Kunz and S.A. Blocher

Penn State and Phillips Laboratory

Introduction

Modeling the interior coupling to complex aerospace systems poises a formidable challenge to the computational electromagnetics community. Resources on the order of Teraflop computers will be needed for complete solutions using techniques such as the Finite Difference Time Domain method. A desirable alternative is to develop computationally efficient approximations, particularly at high frequencies, to complement the more exact but more expensive solutions.

Coupling across an aperture into a cavity can be treated in this fashion using a combination of a time domain Smyth-Kirchhoff approximation to aperture coupling and the method of images to account for the many internal reflections of the transmitted aperture field. The formulation of the time domain Smyth-Kirchhoff approximation to aperture coupling is critical to the technique and will be addressed here.

Formulation

The frequency domain Smyth-Kirchhoff expression for aperture coupling (1) is

$$E(\vec{r}, \omega) = -\frac{j e^{-jkx}}{r} a^2 (E_o \cos \alpha) (\hat{x} \times \vec{k}) \frac{J_1(ka\xi)}{ka\xi} \quad (1)$$

Figure 1 describes the geometry and the attendant parameters.

The $\frac{J_1(\omega x)}{\omega x}$ (where $x = a/c\xi$ and $\omega = kc$) can be expanded (2) as

$$\frac{J_1(\omega x)}{\omega x} = \frac{1}{2} \left[1 - \frac{x^2 \omega^2}{8} + \frac{x^4 \omega^4}{192} - \frac{x^6 \omega^6}{9,216} + \frac{x^8 \omega^8}{1,474,560} - \dots \right] \quad (2)$$

Then a time domain Gaussian pulse, $Ae^{-(\sigma t)^2}$, is assumed incident on the aperture. The corresponding frequency domain content of this pulse is $Be^{-(\Omega\omega)^2}$ where B and Ω can be related to A and σ . Each frequency component is assumed to obey the frequency domain Smyth-Kirchhoff approximation, an assumption only good above aperture cutoff but applied at all frequencies here. Making the substitution yields

$$E(\vec{r}, \omega) = \frac{-j e^{j \frac{\omega}{c} r}}{r} a^2 \cos \alpha (\hat{z} \cdot \hat{u}_k) \frac{\omega}{c} \frac{1}{2} \left[1 - \frac{x^2 \omega^2}{8} + \dots \right] B e^{-(\Omega\omega)^2} \quad (3)$$

where $\hat{u}_k = \frac{\vec{k}}{k}$.

To obtain the time domain Smyth-Kirchhoff approximation we take the inverse Fourier transform of the above expression. A critical step is to observe that terms of the form $\omega^n B e^{-(\Omega\omega)^2}$ transform into $\left(\frac{\partial}{\partial t} \right)^n A e^{-(\sigma t)^2}$. The derivatives in the time domain terms can be readily evaluated so as to obtain the time domain

Smyth-Kirchhoff approximation. Ignoring phase shifts of $-je^{j\frac{\omega}{c}r}$

it is

$$\begin{aligned}
 E(\vec{r}, t) = & \frac{a}{r} (\cos \alpha) (\hat{x} \hat{u}_k) \left(\frac{a}{c} \right) \frac{1}{2} (-2\sigma^2) \left[t + \frac{x^2}{8} (-6\sigma^2 t + 4\sigma^4 t^3) \right. \\
 & + \frac{x^4}{192} (60\sigma^4 t - 80\sigma^6 t^3 + 16\sigma^8 t^5) \\
 & \left. + \frac{x^6}{9216} (-840\sigma^6 t + 1680\sigma^8 t^3 - 692\sigma^{10} t^5 + 64\sigma^{12} t^7) \right] A e^{-(\sigma t)^2} \quad (4)
 \end{aligned}$$

Evaluation

The time domain Smyth-Kirchhoff approximation behaves as expected. The case of $\xi = 1$, boresight field across the aperture is presented here. The aperture acts as a high pass filter and the resulting signal (Figure 2) for $\hat{x} \hat{u}_k = \hat{y}$ or boresight scattering and $r = 1$, oscillates at about the aperture "cutoff frequency" given by $f = c/\lambda = c/(2\pi a)$. The figure shows the effect of including more and more of the terms in equation 4 up to the last term in the approximation. As more terms are included the oscillations approach an asymptotic limit in their period.

The $\frac{J_1(\omega x)}{\omega x}$ term of equation 1 yields a nearly identical

behavior in the frequency domain (Figure 3) as the frequency domain expression on the right-hand side of equation 2 used to

obtain the time domain Smyth-Kirchhoff approximation with the largest number of terms. It is important to note that taking an inverse Fourier transform of the frequency domain expression with $\frac{J_1(\omega x)}{\omega x}$ does not yield an analytically expressible result that

may be readily used in the time domain.

An example is using the method of images to formulate an internal cavity field distribution arising from aperture coupling into the cavity. Here the time domain Smyth-Kirchhoff approximation in the form of a single series expansion is time shifted, scaled by distance and for FDTD applications lumped into time domain bins to form a time history of the fields at desired locations. If greater accuracy is needed an approach such as this will accommodate additional terms in the approximation at not too high a computational cost.

Conclusions

With the increasing popularity of time domain computational electromagnetics codes such as FDTD [3], it is useful to have time domain expressions for fields incident on the interior of a cavity. The development of the time domain Smyth-Kirchhoff approximation is one of the important steps in achieving this goal.

References

- [1] J.D. Jackson, Classical Electrodynamics, 2nd Edition, Wiley and Sons, 1975.

- [2] C. Balanis, Advanced Engineering Electromagnetics, John Wiley and Sons, 1989.

- [3] K.S. Kunz and R.J. Luebbers, The Finite Difference Time Domain Method for Electromagnetics, CRC Press, 1993.

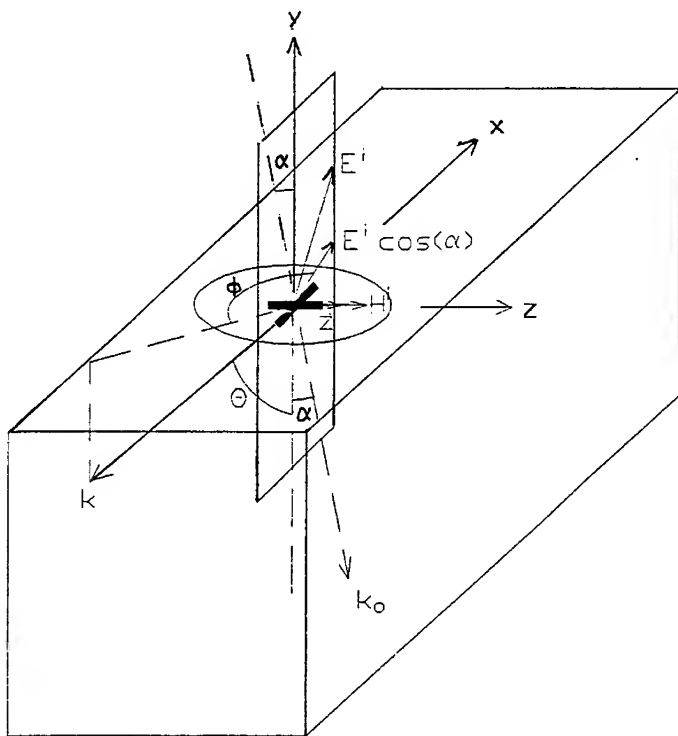


Figure 1. Cavity with aperture model

Time Domain Electric Field Using Smyth-Kirchhoff Approximation

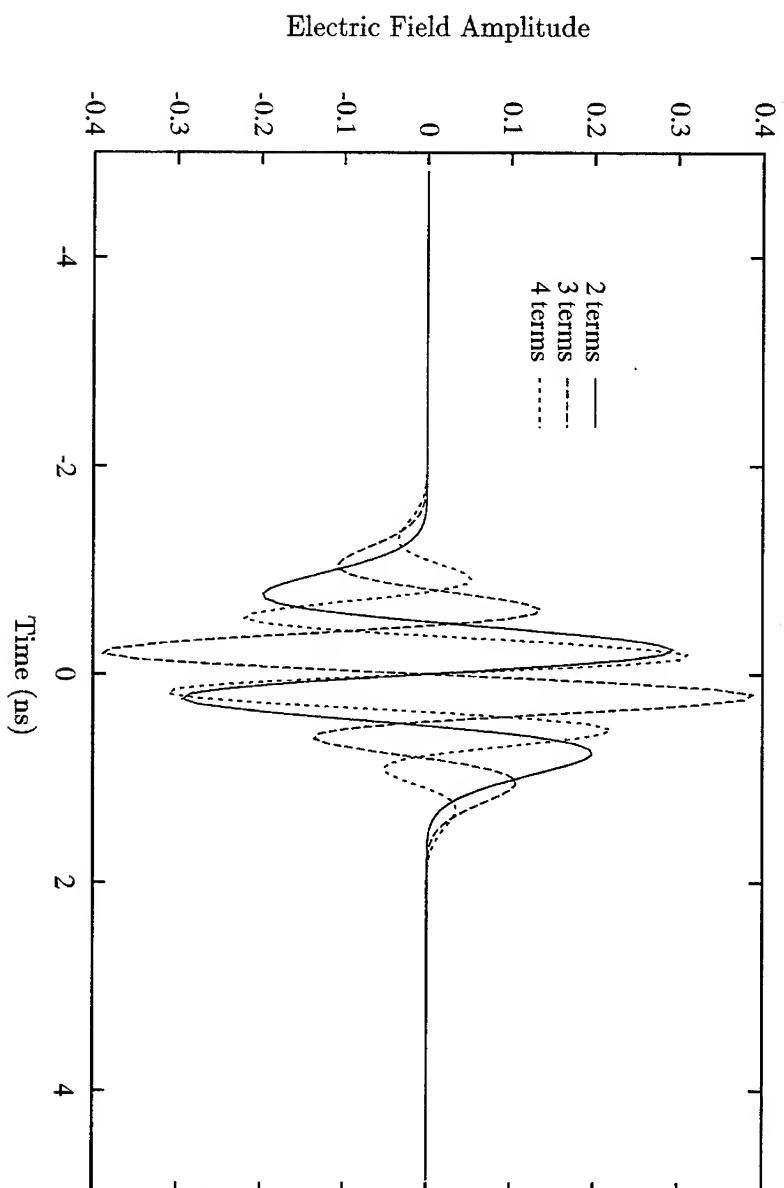


Figure 2: Time domain electric field convergence as successive terms of the Smyth-Kirchhoff approximation are added.

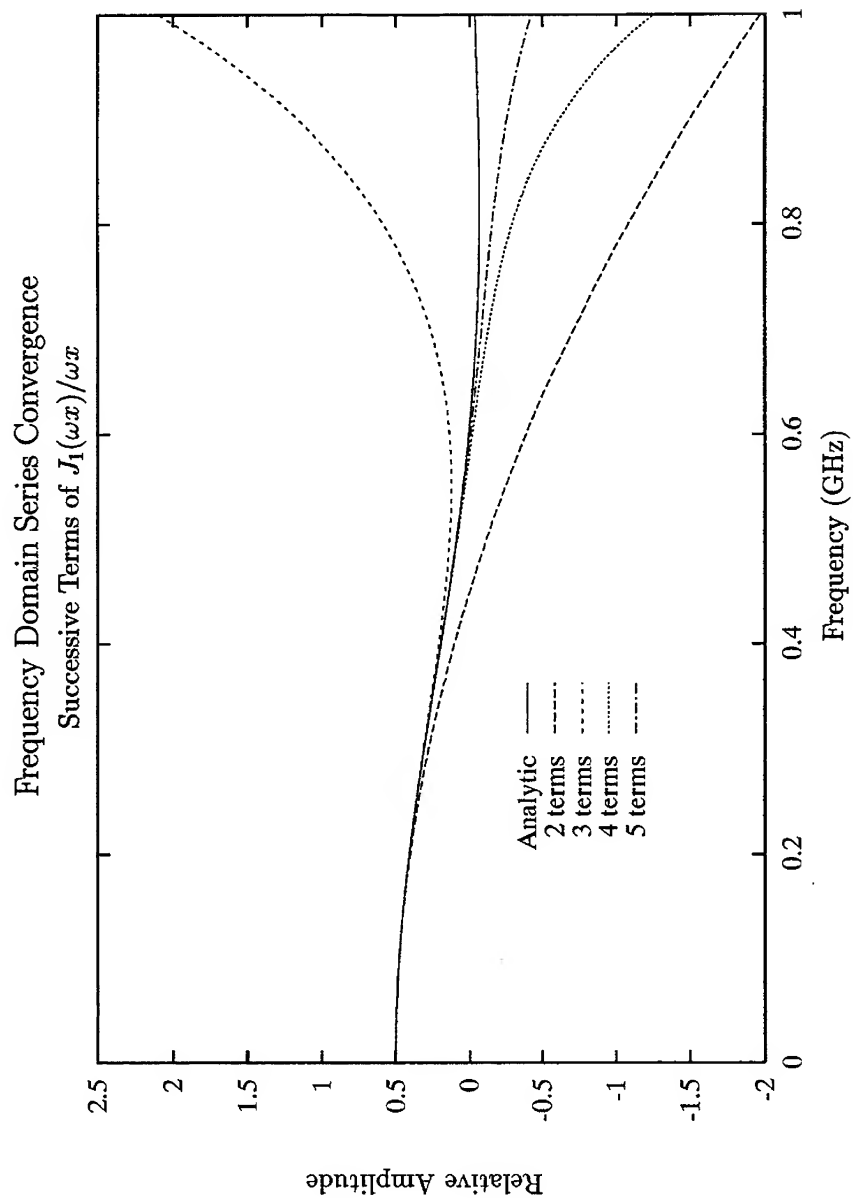


Figure 3: Frequency domain convergence of $J_1(\omega x)/\omega x$ by adding successive terms to series approximation.

A Hybrid Approach to Trailing Edges and Trailing Ends

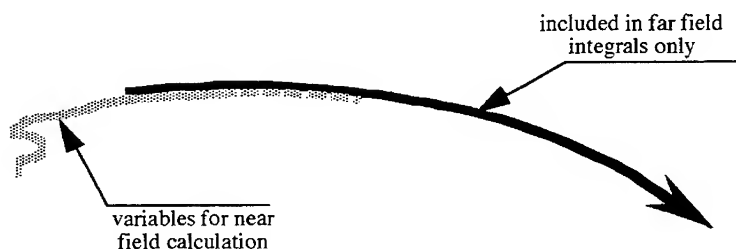
David R. Ingham

A procedure has been developed for combining asymptotic and numerical methods. It handles near field effects numerically and far field effects in high frequency approximation. It was reported in [Ingham 1990] and was justified in terms of scattering theory in [Ingham 1992]. The emphasis here is on implementation. This method eliminates the difficulty encountered by other semi-numerical methods near trailing edge grazing angle. It is a way of connecting a numerical calculation of the edge region to an analytic calculation of the scattering by a large smooth surface. The error can be given a physical interpretation and controlled.

Half plane based calculations have been done and can have broad application in high frequency electromagnetics. Other Applications require further work. The variety, accuracy and generality of numerical programs has increased as computers have become common. There is also a large literature of analytical and asymptotic methods. These are less well known to us, because many of them were developed at times or in places where powerful computers were not available. Since the distorted wave approach provides a relatively simple interface between the two parts, the greatest difficulty in extending it will be matching applications with analytic methods.

INTRODUCTION

THE direct scattering by a leading edge is sometimes calculated by modeling the edge numerically and neglecting smooth parts of the body that significantly contribute to the scattering only in the specular direction. A multiple scattering term that involves scattering by an edge and a smooth surface can be treated by a combination of diffraction and geometric optics if the two are well separated. When the edge terminates the surface, the solution turns out to be a numerical integration, which for a half plane is called the Physical Optics near field.



Some of the work discussed here was done while D. Ingham was with the Lockheed Missiles & Space Company, 3251 Hanover Street, Palo Alto, CA 94304-1191.

Diffraction coefficients for edges of arbitrary shape and composition can be obtained by numerical calculation of a narrow strip at the edge [Herrmann]. One must use special care when a ray coming to or from a part of a body that he treats numerically grazes a part that he treats in a high frequency approximation. The specular reflection point spreads out at grazing angle.

The method discussed deals with this difficulty. One substitutes the Physical Optics near fields (or generalizations of them for curved surfaces) called distorted waves for the incoming and outgoing plane wave fields of a purely numerical calculation. These plane wave fields usually can be identified explicitly in general purpose numerical computer programs. The main difficulty is calculating the distorted waves.

A high frequency approximation that gives an accurate current function far from the edge can account for a large smooth region of a scatterer in the field incident on a small edge region, where the current is calculated numerically [Sahalos], [Mitschang]. Applying reciprocity to exchange the incident and scattered fields accounts for the effect of the smooth region on the wave as it goes away from the edge toward the receiver. In the distorted wave method one takes the latter case and then uses the high frequency approximation again to account for the effect of the large smooth part on the incident wave.

RELATION TO THE METHOD OF IMAGES

The far field effect of a large smooth surface near a form that can be calculated numerically is handled by using geometric optics to generate distorted waves. A well known example is the far field treatment of the ground in antenna programs. In problems involving a half plane or a plane with different properties on its two halves, the Physical Optics near field is needed for the distorted waves. This same method can be used for truncations of other smooth or simple shapes. An accurate treatment requires a solution for an extended geometry, which can be truncated to match the physical geometry outside the numerical region. For example a solution for an infinite cylinder can be used in the calculation of scattering by a semi-infinite cylinder.

For a perfectly conducting full plane, the method of images is geometric optics. The general green's function is:

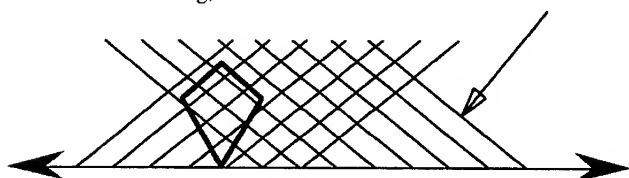
$$\overline{\overline{G}}_{pg}(\vec{r}, \vec{r}') = \overline{\overline{G}}(\vec{r}, \vec{r}') + \overline{\overline{G}}_I(\vec{r}, \vec{r}'),$$

$$\text{where} \quad \overline{\overline{G}}_I(\vec{r}, \vec{r}') = -\overline{\overline{I}}_r \cdot \overline{\overline{G}}(\vec{r}, \overline{\overline{I}}_r \cdot \vec{r}')$$

$$\text{and} \quad \overline{\overline{I}}_r = \widehat{x}\widehat{x} + \widehat{y}\widehat{y} - \widehat{z}\widehat{z} \quad [\text{Burke}]$$

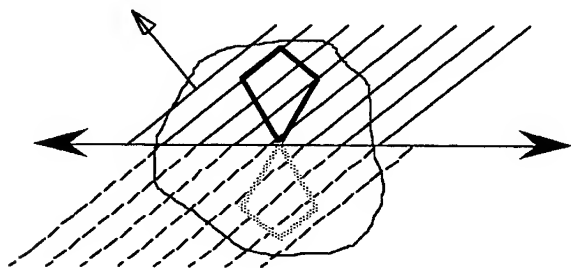
[For a full plane that is not a perfect conductor, the above expression needs only to be multiplied by a reflection coefficient for the far field, but the near field requires, at least, a separate integral to be evaluated for each $\vec{r}-\vec{r}'$.]

If parts of the total system are far away, and relatively small, they can be handled by plane waves. For scattering, the excitation looks like this:

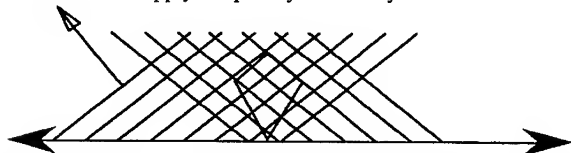


The scatterer is illuminated by the reflection of the source as well as by the physical source.

There are two equivalent ways to think about the reflection by the ground on its way from the scatterer to the receiver. One is to include the reflected currents in the integral over the scatterer according to the green's function expressions above:



The other is to apply reciprocity to the way we think about the excitation:



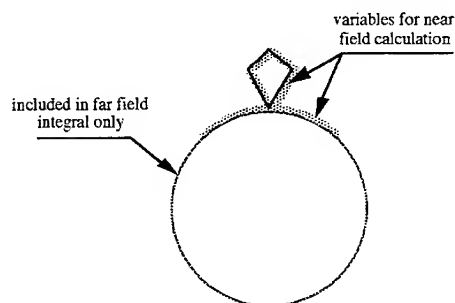
The integral extends only over the physical scatterer, but the excitation of the reflection of the receiver is included.

In complicated scattering problems, the second point of view has the great advantage that one need think only once. For example, with an imperfect ground the reflected scatterer is not so obvious because it does not apply for the near field, but the reflected receiver approach must be valid when its reciprocal case is valid.

The term "incoming distorted wave" describes the wave coming from the transmitter and its reflection. The "outgoing distorted wave" is the wave shown above, including the reflection. It is pointed toward the receiver, as shown by the arrow, if an overlap integral convention is used. It points away from the receiver in the reaction integral convention. Formulas given in [Ingham 1990] and [Ingham 1992] are in the reaction integral form.

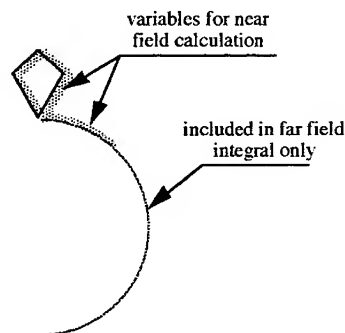
EXAMPLES

Consider the far field radiation of a transmitting antenna on a large lossy sphere:



One approach to this problem is to solve the shaded part of the problem numerically, and then include the effect of the lower part of the sphere by using a Mie series or asymptotic treatment to calculate the outgoing distorted wave.[Yee]

The same method will work if the bottom of the sphere is missing, provided the interaction between the hole and the antenna can be ignored. If the left half of the sphere is missing, specular reflection must be included in a way that accounts for the asymmetry.

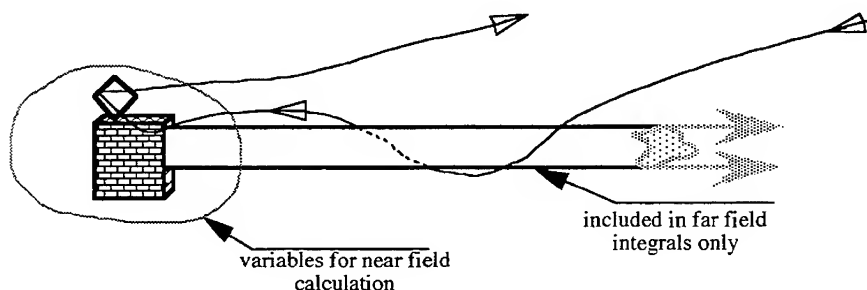


Suppose there is an electrically large thin half sphere with an electrically small antenna at its edge. The field radiated to the left is difficult to calculate because of the concave surface, but if the surface is sufficiently large and lossy, the largest contributions are the direct term and its specular reflection. The direct term can be calculated by numerically including the part of the half sphere near to the antenna, as above. Its reflection can be included by geometric optics.

This approach breaks down for the field radiated to the right when rays coming from the antenna graze a region of the half sphere's surface that is too large to calculate numerically. Optics does not apply at the edge. The exact distorted wave field for the full sphere will not work for the same reason. The calculation can be done, with a distorted wave obtained by integrating the full

sphere solution over the half sphere surface. This is not trivial, but it is much more tractable than solving for currents on the same large surface.

Another type of problem that requires this approach near grazing angle is the radiation or scattering by the ends of long cylinders:



If the transmitter or receiver is close to the cylinder axis, one must find a solution to the two dimensional infinite cylinder problem.

THE METHOD

The method given in [Ingham 1992] is:

- 1) Select a simplified system S_1 that approximates the physical system on the side that is closest to the incident ray.
- 2) Find an analytic expression or approximation for the field on S_1 that is valid at large distances, in the direction nearest to the incident ray. When S_1 is flat, this is geometric optics.
- 3) Repeat steps 1) and 2) for the part of the system near to the outgoing ray, if necessary. These fields now include all that one needs to describe the contribution to the scattering from outside a finite region S_2 .
- 4) Truncate these fields (currents) on S_1 somewhere inside S_2 . (Sometimes, better accuracy will be obtained if this truncation is not done at a sharp edge, but by a smooth window function that forces the current to fade away gradually.)
- 5) Add, to the incident plane wave, the field on S_2 given by the Stratton Chu integral over the above approximate field on S_1 . This new incident field is the incoming distorted wave. For a half plane, this is the Physical Optics near field. Repeat this step to obtain the outgoing distorted wave. If only one ray is near to grazing angle, a plane wave will do for the other one. For monostatic scattering, the two distorted waves are identical. (They have opposite propagation directions in the overlap integral convention.)
- 6) By some standard numerical method, calculate the field (current) induced on S_2 by this incident distorted wave.

- 7) Calculate the scattered field, not directly by the Stratton Chu integral, but as the reaction of the outgoing distorted wave with the field on S_2 . The explicit formula is:

$$\lim_{\substack{|\vec{r}| \rightarrow \infty \\ \text{in direction } \Omega}} |\vec{r}| \vec{E}_2(\vec{r}) \cdot \hat{\epsilon} = \int_{S_2} [\vec{\chi}_{\Omega}^{+e}(\vec{r}') \times \vec{H}_2(\vec{r}') - \vec{E}_2(\vec{r}') \times \vec{\chi}_{\Omega}^{+m}(\vec{r}')] \cdot d\vec{S}'$$

where Ω is shorthand for the angular coordinates of \vec{r} , (θ, ϕ) and specifies the polarization $\hat{\epsilon}$.

- 8) Add the field scattered by S_1 to obtain the total far scattered field.

IMPLEMENTATION

In practice, one has two computer programs (or procedures). One is something like NEC or Trimom^[Wilton] that can handle the small part numerically. The other may come out of an old book on separating Maxwell's equations or on high frequency approximations.

For a half plane, even if composed of many layers, the hardest part has been performing the integral in step 5). Various tricks are used, but this integration still dominates the accuracy and the computer time. Physical Optics has been around a long time. It is likely that a much better method has been reported, but it may or may not work for more complicated shapes. Most of the tricks reported in [Ingham 1992] will work for more complicated shapes, so this problem should not deter one unless very high accuracy is required.

One attaches the high frequency and numerical integration procedures to make a distorted wave subroutine. Electric and/or magnetic fields are required according the forms in which the incident and outgoing plane waves appear in the numerical program.

It is not necessary to understand a numerical program to use it in this way. One finds two expressions that look like $e^{(-jk\hat{\epsilon} \cdot \vec{r})}$, one in the excitation and the other in the far field integration. In some Galerkin's method programs (such as CICERO^[Putnam]) these are the same subroutine, because the symmetry of the problem is reflected in the computer code. More commonly the outgoing plane wave is viewed as a Stratton Chu integral by the author. In this case, the same program could have been written from a reaction integral point of view, and one can still identify the outgoing plane wave and replace it by a distorted wave. The normalization of each distorted wave is the same as that of the plane wave it replaces.

If the program is worn and incompletely documented, it is essential to run several simple test cases. This was the case with the MM2D^[Taylor] based calculations.

ADDITIONAL REMARKS

Since ACES invites negative results, I mention that this method has not been successful for smoothly curved trailing edges. Though arbitrary accuracy is possible, the method used so far to calculate the Physical Optics near field has too much numerical error to handle the very small back scatter from a smoothly rolled trailing edge. Calculations for sharp edges composed of combinations of materials have shown the advantages expected.

Generating the distorted waves has been the limiting step even for half planes and has not

been attempted, in this context, for other surfaces. These problems are reduced, however, from an integral equation on a large surface to an integral over that surface.

In principle, it is very important to be able to handle the coupling between two features on the same large smooth surface, because this is needed for higher order GTD terms. For a large perfect conductor, the far field expression is good at the surface, but it gives zero on lossy surfaces. This difficulty, also, is manageable. It requires a quasi-far field expression.^[Hurst]

REFERENCES

- David R. Ingham, "Hybrid Method Computation of Diffraction by Trailing Edges Using Reciprocity," proceedings of *Int. Symposium of the Antennas and Propagation Society*, p.1574-7, Dallas, 1990
- David Ingham, "A Hybrid Method Based on Reciprocity for the Computation of Diffraction by Trailing Edges," submitted 1992 September to *IEEE Trans. Antennas Propag.*, About 10 pp.
- G. F. Herrmann, "Numerical Computation of Diffraction Coefficients", *IEEE Trans. Antennas Propag.* vol. 35, no. 1, Jan. 1987
- John N. Sahalos and Gary A. Thiele, "On the Application of the GTD-MM Technique and its Limitations", *IEEE Trans. Antennas Propag.*, vol. 29, no. 5, Sept. 1981
- L. N. Medgyesi-Mitschang, and Dau-Sing Wang "Hybrid Solutions for Scattering from Perfectly Conducting Bodies of Revolution", *IEEE Trans. Antennas Propag.* vol. 31, p. 570-583, July 1983
- Burke, et al., NEC II documentation, equations 174-5
- Kane Yee, private communication
- Donald R. Wilton, S. S. Rao and Allen W. Glisson, *Electromagnetic Scattering by Surfaces of arbitrary Shape*, University of Mississippi, March 1980
- John M. Putnam, "CICERO," the MM/D-BOR(EFIE) general metal/dielectric scattering code, McDonnell Douglas Research Labs., 1984.
- Jim Taylor, Bill Lorber, et al., MM2D (*Method of Moments in 2 Dimensions*) Lockheed Burbank, Burbank, CA
- M. P. Hurst, "Improved Numerical Diffraction Coefficients with Application to Frequency-Selective Surfaces", *IEEE Trans. Antennas Propag.* vol. 36, pp. 606-612, June 1992

High Frequency Approximations to the Physical Optics Scattering Integral for Curved Edged Surfaces

William B. Gordon
Radar Division
Naval Research Laboratory
Code 5311
Washington, D.C. 20375

ABSTRACT

Two high frequency (HF) approximations are obtained for the Physical Optics (PO) scattering integral for a general curved edged reflecting surface. In the first, the PO scattering integral is approximated as the sum of a specular effect and an edge effect, where the latter is represented as a line integral evaluated over the boundary edge of the reflector. A closed form result is then obtained by applying the Principle of Stationary Phase to the line integral. These approximations are compared with known closed form results in special cases, with numerically calculated mathematically "exact" results, and with a result from the Geometrical Theory of Diffraction. The approximations are found to work well for surfaces which satisfy certain smoothness and convexity conditions, but they break down for curved surfaces which have flat parts with zero curvature. There are also numerical glitches that can occur at caustics or when the specular point falls on or near the boundary edge.

1. BACKGROUND — THE POLYGON FORMULA

In this paper we consider HF approximations to the PO scattering integral for the radar backscatter from a general curved edged surface viewed at arbitrary aspect. The PO scattering integral for backscatter from a reflecting surface S is the double integral given by

$$(1) \quad J_{po} \equiv (1/\lambda) \int_{S_0} e^{i2ks \cdot X} (s \cdot \eta) dA$$

where λ is the radar wavelength, S_0 is the illuminated portion of S , $k = 2\pi/\lambda$, s is the unit scatter vector (pointing from S to the radar), X is the position vector of a general point on S , η is the unit normal vector to S , and dA is the infinitesimal element of area on S . The scattering integral is normalized so that the radar cross section σ is given by

$$(2) \quad \sigma = 4\pi |J_{po}|^2$$

It is known that (1) can be reduced to a closed form result when S is a flat polygonal plate [Gordon]. Specifically, if S is a polygon with vertices $\{a_1, a_2, \dots, a_N\}$, then (1) reduces to

$$(3) \quad J_{po} = \frac{i \cos \theta}{4\pi \sin^2 \theta} \sum_{n=1}^N \left\{ [(s \times \eta) \cdot \Delta a_n] \frac{\sin(k s \cdot \Delta a_n)}{(k s \cdot \Delta a_n)} e^{i2ks \cdot \frac{a_n + a_{n+1}}{2}} \right\}$$

where θ is the off-normal angle defined by $\cos \theta \equiv (s \cdot \eta)$, $\Delta a_n \equiv a_{n+1} - a_n$, and we set $a_{N+1} \equiv a_1$. When $\theta=0$, (3) becomes indeterminate, but (1) reduces to

$$J_{po} = \frac{A}{\lambda} e^{i2ks \cdot X_0} \quad (\text{flat plate, normal incidence})$$

where A is the area of S and X_0 is the position vector of any point on S . The area A and unit normal η of a flat polygonal plate can be calculated according to

$$2 A \eta = a_1 \times a_2 + a_2 \times a_3 + \dots + a_N \times a_1$$

In the next section, the polygon formula (3) will be used to obtain a HF approximation for curved surfaces.

2. HF APPROXIMATIONS FOR CURVED SURFACES

Suppose now that S is a smooth curved convex surface, or portion thereof, with boundary edge ∂S . From the Fermat Principle, one would expect a HF approximation of the form

$$(4) \quad J_{p_0} \approx J_{\text{spec}} + J_{\text{edge}},$$

where the first and second terms on the right hand side correspond respectively to specular and edge effects. The standard Geometrical Optics formula for J_{spec} is given by [Born & Wolf]

$$(5) \quad J_{\text{spec}} = \frac{e^{i 2 k s \cdot X_0}}{2 \sqrt{|K(p_0)|}} e^{(i\pi/4)[2 - 2 \text{ind}(p_0)]}$$

where X_0 is the position vector of the specular point p_0 , $K(p_0)$ is the Gaussian curvature of S at p_0 , and the "index" of the specular point is defined by

$$\text{ind}(p_0) = \begin{cases} 2 & \text{if } s \cdot X \text{ is a local maximum at } X = X_0, \\ 0 & \text{if } s \cdot X \text{ is a local minimum at } X = X_0, \\ 1 & \text{if } s \cdot X \text{ is a saddle at } X = X_0. \end{cases}$$

To obtain the corresponding result for J_{edge} , we approximate S with a collection of a large number M of small non-overlapping rectangular tiles, as indicated in Figure 1. We then apply (3) to each of the tiles, and sum the results. According to (3), each of the rectangular tiles gives rise to 4 edge terms, so that the scattering integral (1) will be approximated as the sum of $4M$ edge terms. It is anticipated that, in the HF limit, the edge effect J_{edge} will be accurately approximated as the sum of the all contributions from the edges Δa_n lying on ∂S .

Referring to (3), we see that the $\sin x/x$ factors are equal to unity in the limit as the vector differentials Δa_n become infinitely small. Hence, from (3) we get the result

$$(6) \quad J_{\text{edge}} = \frac{i}{4\pi} \int_{\partial S} \frac{s \cdot \eta}{1 - (s \cdot \eta)^2} e^{i2ks \cdot x} (s \times \eta) \cdot dx.$$

In this derivation it was assumed that the entire boundary ∂S is illuminated; if such is not the case, the integral (6) is only taken over the portion of ∂S which is illuminated.

Substituting (5) and (6) into (4), one obtains a HF approximation to J_{p0} which is much easier to calculate (numerically) than the double integral (1). Moreover, a closed form result can be obtained by applying the Principle of Stationary Phase to (6). When this is done, one obtains the result

$$(7) \quad J_{\text{edge}} \approx \sum_p J_0(p)$$

where p varies over the set of *bright points* of ∂S (the points on ∂S at which $s \cdot X$ is a local maximum or minimum), and at each such point

$$(8) \quad J_0(p) = \frac{i\sqrt{\lambda}}{4\pi} e^{i2ks \cdot X_p} \frac{e^{\pm i\pi/4}}{\sqrt{\pm 2s \cdot X_p''}} \times \frac{s \cdot \eta}{1 - (s \cdot \eta)^2} (s \times \eta) \cdot X_p',$$

where the \pm sign is chosen to make the quantity inside the square root positive, and X_p , X_p' , and X_p'' are the position, velocity, and acceleration vectors at p . There are certain obvious breakdowns when either of the denominators is zero, one of them (the case $s \cdot \eta = 1$) occurring when the specular point

falls on ∂S . Also, in the sum (7), one only includes those bright points occurring on the illuminated portion of ∂S .

3. TEST CASES

Let (x, y, z) denote standard rectangular coordinates, and set $r = \sqrt{x^2 + y^2}$. Our first test case is a surface of revolution $z = z(r)$ viewed at axial incidence for which the vertex is at the origin, and the boundary edge is at a height h above the vertex. Then (6) reduces to

$$J_{\text{edge}} = \frac{i r_0}{2 z'(r_0)} e^{-i 2 k h},$$

where r_0 is the radius of circular edge. This result agrees with previously published results on surfaces of revolution viewed at axial incidence [Gordon & Bilow]. Specializing to the case of a paraboloid $z = r^2/2R$, and combining this result with the specular effect, one obtains

$$J_{\text{spec}} = -\frac{i R}{2},$$

$$J_{\text{edge}} = \frac{i R}{2} e^{-i 2 k h}.$$

Hence, from (4),

$$J_{\text{po}} \approx \frac{i R}{2} (-1 + e^{-i 2 k h}),$$

and from (2),

$$\sigma \approx 4 \pi R^2 \sin^2(kh),$$

which happens to be the exact PO result. (The paraboloid is a

special case for which the HF limit is equal to the actual value of J_{po} .)

To test the result (8), we compared the corresponding value of radar cross section with the GTD result obtained by Raybin for the case of a surface of revolution with a circular boundary edge viewed at arbitrary incidence [Raybin]. Letting σ_{PO} and σ_{GTD} denote the values of the edge effects as calculated from (8) and Raybin's formulas, respectively, it turns out that

$$\frac{\sigma_{PO}}{\sigma_{GTD}} = \left(\frac{1 - \cos \psi}{1 + \cos \psi} \right)^{\pm 1},$$

where ψ is the grazing angle between the radar line-of-sight and the surface at the bright point, and the sign in the exponent depends on polarization. This result is a confirmation of (8) since it is generally accepted that the agreement between the PO and GTD calculated edge effects is good when the grazing angle is large, and bad when the grazing angle is small.

In another test, the HF approximations were compared to exact results for paraboloids of revolution viewed at arbitrary (non-axial) incidence. Closed form formulas do not exist in this case, and therefore a 2 dimensional quadrature had to be used to calculate J_{po} . A typical example is shown in Figure 2. The dashed line was obtained by using (6) for calculating the edge effect, whereas the solid line was obtained from the stationary phase approximation (7). The angle θ is the co-latitude, which is zero for nose-on incidence, and the blow-up in the stationary phase result at $\theta=0$ is due to the vanishing of the quantity $s \cdot X_p''$ that occurs in the denominator of (8). The glitch occurring at $\theta \approx 20^\circ$ corresponds to the case when the specular point falls on the edge.

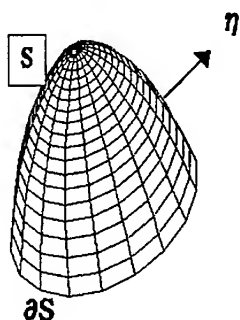


FIGURE 1
A General Edged Surface

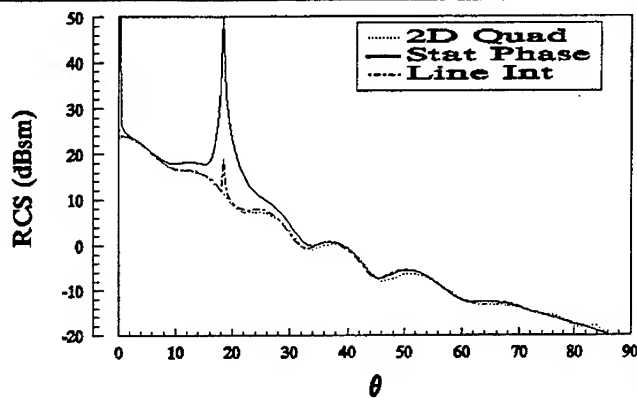


FIGURE 2
Calculated RCS for a Paraboloid

Other calculations have been performed, some of which were designed to push the HF approximations to the limit. As expected, the HF results failed for surfaces with flat parts. The results of these tests will be reported elsewhere in more detail.

REFERENCES

- [M. Born and E. Wolf] *Principles of Optics*, 6th ed., Pergamon Press, Oxford, 1980.
- [W.B. Gordon] *Far field approximations to the Kirchhoff-Helmholtz representations of scattered fields*, *IEEE Trans AP-23*, (July 1975), p.590-592.
- [W.B. Gordon and H.J. Bilow] *High-frequency approximations for edge scatter from surfaces of revolution*, *J. Opt. Soc. Am.* vol 8 (January 1991), p.11-13.
- [D.M. Raybin] *Radar cross section of spherical shell segments*, *IEEE Trans AP-13* (1965), p.754-759.

SESSION 8 - "VISUALIZATION AND I/O ISSUES"

Chair: Dr. Ed Miller, Co-Chair: Dr. Stan Kubina

Numerical Imaging of Finite Element Frequency Domain Solutions

R. Craig Baucke, GE Aircraft Engines
John D'Angelo, GE Corporate Research & Development

Abstract: *A numerical bistatic imaging technique is applied to two dimensional finite element frequency domain solutions. The numerical imaging process efficiently provides information about the location and magnitude of scattering centers at a single frequency. Example images are provided for some EMCC benchmarks and a resistive/conductive strip.*

I. INTRODUCTION

The finite element frequency domain (FEFD) method efficiently computes the near fields of antennas or scatterers [1,2]. In many applications, the near field solutions are transformed to the far field to provide radar cross section (RCS) or antenna gain results. However, far field information does not indicate the location or strength of scattering centers on the scatterer, as images generated from compact range measurements do [3]. In order to provide scattering center information, an efficient numerical bistatic imaging algorithm has been developed and implemented by Shaeffer in a three dimensional method of moments code [4]. In this work, this imaging technique is applied to FEFD analysis.

A brief description of the numerical bistatic imaging (NBI) technique and its incorporation into the FEFD analysis is provided. Example images illustrate the capability of this technique to identify and evaluate the magnitude of scattering centers.

II. DESCRIPTION OF BISTATIC IMAGING ALGORITHM

In a compact range, ISAR images can be created by measuring the target at a large number of discrete frequencies to gather down range data, and by sweeping angle for cross range information [3]. Since a large number of frequencies are required to generate an image with good resolution, this technique is very time consuming when applied to frequency domain analysis. The numerical bistatic imaging technique developed by Shaeffer alleviates this problem. The NBI technique produces images from frequency domain analysis performed at a single frequency by gathering far field bistatic data. Little additional computational effort is required due to the simplicity of gathering bistatic scattering data.

The NBI technique is developed from the following Fourier transform,

$$(1) \quad E^{\alpha,\beta}(\mathbf{r}_r, \mathbf{r}_\theta, \mathbf{r}_\phi) = \iiint W(\mathbf{k}^s) E^{\alpha,\beta}(\mathbf{k}^i, \mathbf{k}^s) e^{j\mathbf{k}^s \cdot \mathbf{R}} d\mathbf{k}_r^s d\mathbf{k}_\theta^s d\mathbf{k}_\phi^s$$

where α, β indicates polarization, k^i is the incident field propagation vector, k^s is the scattered field propagation vector, $E^{\alpha, \beta}(k^i, k^s)$ is the computed scattered field, $E^{\alpha, \beta}(r_r, r_\theta, r_\phi)$ is the transformed scattered field in (r_r, r_θ, r_ϕ) space, and $W(k^s)$ is an FFT window function such as Hanning. The transform variable k^s is given by

$$(2) \quad \vec{k}^s = k_r^s \hat{r} + k_\theta^s \hat{\theta} + k_\phi^s \hat{\phi}.$$

In two dimensions, (2) becomes

$$(3) \quad \vec{k}^s = k_r^s \hat{r} + k_\theta^s \hat{\theta} = k_x^s \hat{x} + k_y^s \hat{y} = k_{\text{down}}^s \hat{e}_{\text{down}} + k_{\text{cross}}^s \hat{e}_{\text{cross}}$$

where the down range and cross range vectors, \hat{e}_{down} and \hat{e}_{cross} , are defined parallel and perpendicular to k^i . When implemented, the far field transform computes the scattered fields for each \vec{k}^s value. The FFT transforms these field values using (1) to produce an array which is the image.

The resolution of the image is given by

$$(4) \quad r = \frac{2\pi}{\Delta k^s}$$

and theoretically has no lower limit. However, the discrete nature of frequency domain analysis limits the resolution. If the resolution is too small, the imaging technique identifies the individual basis functions as scattering centers. In practice, a minimum resolution of $\lambda/2$ preserves the true scattering centers in the image.

III. IMPLEMENTATION OF NUMERICAL BISTATIC IMAGING WITH FEFD

The finite element problem is discretized and solved at a single frequency, as described in detail in [1]. The range resolution and window size of the image are defined and the order of the FFT is computed. A two-dimensional array of k^s values are calculated, centered around the k^s of the backscattered field ($-k^i$). The far fields are computed for each k^s using a near field/far field transform.

Common methods of computing the far fields from FEFD analysis are the harmonic expansion (HE) and Green's theorem integral (GTI) [1,2,6]. The harmonic expansion is not an integral method and is difficult to use with this imaging technique. However, the Green's theorem integral and the newly-developed volume source integral (VSI) can be easily modified in order to compute images using NBI. A description and comparison of these near field/far field transforms is found in [5].

After the array of far field results is computed using GTI or VSI, the they are transformed by the FFT in (1). The resulting array of data is the image of the scatterer, from which the scattering centers can be observed.

IV. EXAMPLE IMAGES

Several example images are computed using NBI with the VSI transform. Figures 1-3 are images of Electromagnetic Code Consortium 2D benchmarks, and the details of each scatterer are described in [7]. Computation of these images required less than 5 minutes in all cases on a VAX 6510.

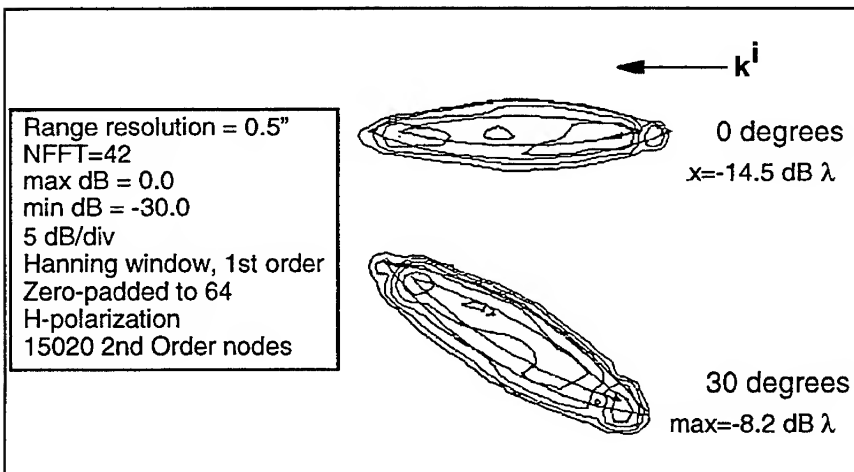


Figure 1. EMCC 2D Benchmark Example 1, Coated Ogive, Images at 0 and 30 degrees Incidence Angles

In figure 1, the image of a coated ogival shape is shown. The incident field impinges on the scatterer from the right side in all of the images. The image is slightly offset from the geometry overlay due to a software problem.

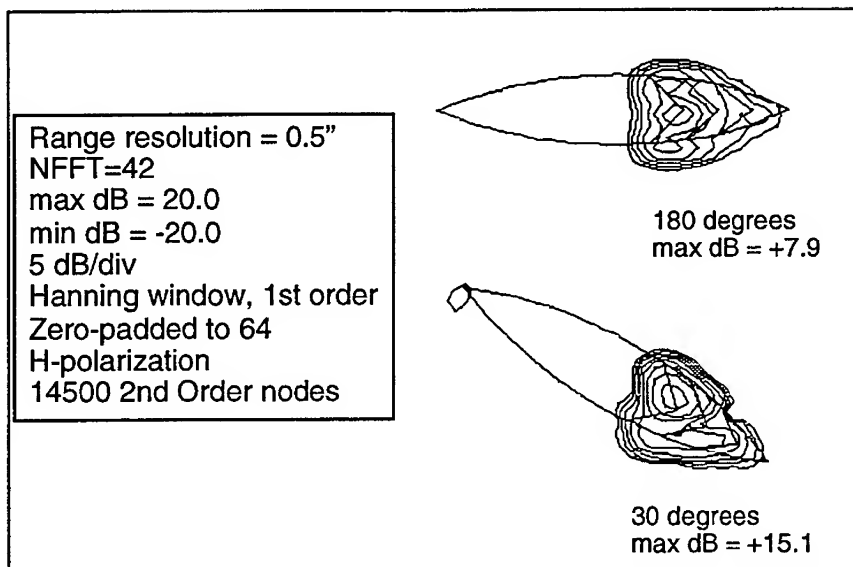


Figure 2. EMCC 2D Benchmark Example 4, Multi-Layer Ogive, Images at 180 and 210 degrees Incidence Angles

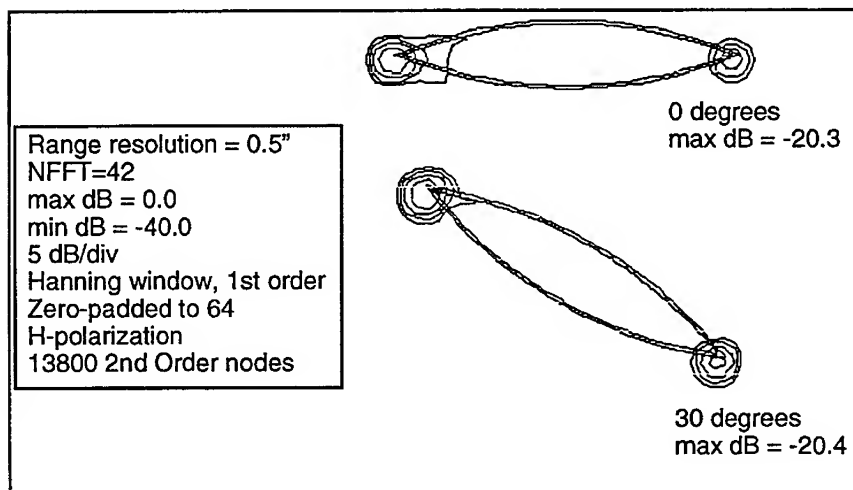


Figure 3. EMCC 2D benchmark Example 5, Thin-Shell Ogive, Images at 0 and 30 degrees Incidence Angle.

Figure 4 illustrates a resistive strip/perfect conductor geometry that is imaged in figure 5. Tapered resistive strips B and C are two wavelengths wide and the perfect conductor A is one wavelength wide. The levels at E-polarization converge slowly when perfect conductor is present and the VSI is used for the far field transform, since the current on the PEC is not directly solved and must be computed from the normal derivative of the electric field near the surface. Increasing the mesh density near a discontinuity in the surface of the PEC improves the image significantly. In figure 4, a much higher mesh density is used around each edge of the PEC strip.

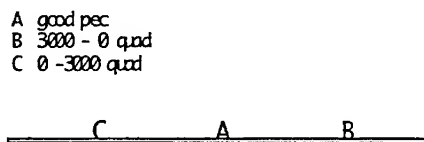


Figure 4. Resistive Strip/PEC configuration for Imaging

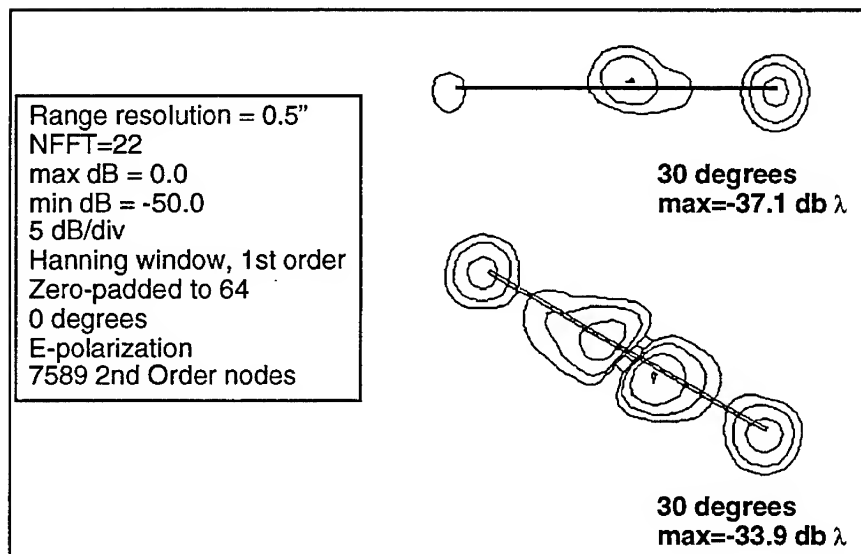


Figure 5. Resistive Strip/PEC Image

V. VALIDATION OF IMAGE RESULTS

Exact validation of this type of image is difficult to define. In practice, images produced by the NBI approach have been compared to ISAR images for geometries which are somewhat "two-dimensional". Agreement on the magnitude and location of most types of scattering centers is fairly good, although no data is available for inclusion in this paper. However, because of the fundamental differences between ISAR and NBI images, some difference should be expected. For instance, dispersive materials will affect scattering centers differently in a single-frequency image (NBI), as compared to an ISAR image that requires a certain bandwidth of data which may average the effects of the dispersion.

A quick check of the accuracy of the image magnitudes can be made by comparing the maximum scattering center magnitude of the NBI image to the magnitude of the echo width pattern at the angle of incidence corresponding to the image. This is shown below for the example cases in this paper.

<u>Figure</u>	<u>Angle</u>	<u>NBI max level</u>	<u>Pattern level</u>
1	0	-14.5	-19.3
	30	-8.2	-9.5
2	180	+7.9	+4.7
	210	+15.1	+6.0
3	0	-20.3	-20.0
	30	-20.4	-32.1
5	0	-37.1	-39.9
	30	-33.9	-28.5

Table 1. Comparison of maximum NBI image magnitudes to scattering pattern magnitudes.

Table 1 illustrates that while this check is by no means conclusive, it does indicate that the scattering center magnitudes on the image are following the same trends as the scattering patterns, and the levels are in general the same order of magnitude.

VI. CONCLUSIONS

The application of the numerical bistatic imaging technique to finite element frequency domain solutions provides an efficient method of identifying scattering centers on computer-generated models. This process is very efficient when used in conjunction with FEFD far field transforms, and

the images provide information which is very useful to the electromagnetic design community.

VII. REFERENCES

- [1] J. D'Angelo and I.D. Mayergoyz, "Finite element methods for the calculation of RF radiation and scattered fields," *Electromagnetics*, vol. 10, no. 1-2, Jan.-Jun., 1990, pp. 177-200.
- [2] M.J. Povinelli and J. D'Angelo, "Finite element analysis of large wavelength antenna radome problems for leading edge and radar phased arrays," *IEEE Trans. Magn.*, vol. 27, no. 5, Sept. 1991, pp. 4299-4302.
- [3] D.L. Mensa, High Resolution Radar Imaging, Artech House, Norwood, MA, 1981.
- [4] J.F. Shaeffer, "MOM3D Method of Moments Code Theory Manual," NASA Contract Report 189594, March, 1992.
- [5] R.C. Baucke, J. D'Angelo and G.D. Crabtree, "Far field transforms for finite element frequency domain solutions," *IEEE Trans. Antennas Propagat.*, accepted paper to be published.
- [6] A.F. Peterson and S.P. Castillo, "A frequency-domain differential equation formulation for electromagnetic scattering from inhomogeneous cylinders," *IEEE Trans. Antennas Propagat.*, vol. 37, no. 5, May 1989, pp. 601-607.
- [7] Electromagnetic Code Consortium, "Two-dimensional benchmark problems for RCS prediction, Tabulation of Results," EMCC Report, January, 1990.

Visualization of Electromagnetic Fields Using the Finite Difference Time Domain Method

by

John H. Beggs*, Deirdre A. Ryan and Raymond J. Luebbers
Department of Electrical and Computer Engineering
The Pennsylvania State University
University Park, PA 16802

1 Introduction

The computing and graphics performance of engineering workstations today are at the point where visualization tools are becoming an important aid in research and education in the scientific and engineering disciplines. With scientific visualization tools, researchers in electromagnetics can enhance their understanding of scattering, radiation and penetration problems. Creating visualization tools will also have a tremendous impact in undergraduate and graduate education by giving students a deeper understanding of both fundamental and more advanced electromagnetic concepts.

As a result of our research using the Finite Difference Time Domain (FDTD) method, we have found a need to have visualization tools which cover three major areas: object generation/definition, object viewing and geometry analysis, and electromagnetic field visualization. Under the object generation/definition category, several programs currently exist that permit a user to generate an object by manipulating canonical objects in three dimensions and then write a geometry file to be translated into an FDTD format. Therefore, we concentrated on the remaining two areas and have developed a software program that permits a user to view objects as defined for the Penn State FDTD code and another program to display electric or magnetic fields, current or Poynting vector, or electric or magnetic field lines in real time.

Previous work in this area include videotape demonstrations of real-time field computation using FDTD during conference presentations [1] and a software package for the Cray family of supercomputers. A paper by Kunz [2] describes a software package designed for educational purposes (i.e. courseware). This paper presents a description of two software programs that were developed at Penn State as research aids in FDTD analyses of electromagnetic problems. This work was done independently and without knowledge of the capabilities of other existing software packages.

2 VIEWOB Program

The VIEWOB program was developed because of the need for a method to verify objects as they are constructed for the Penn State FDTD code. Previous verification methods included line printouts of material types at cell locations and point plots for different material types. These methods were time consuming and some geometry errors often went undetected. With the use of this three-dimensional visualization program, the time required to

construct a correct geometry is substantially lower than what was previously required and geometry errors are readily apparent. The VIEWOB program has saved countless hours of geometry construction, verification and debug time since it has been used on a regular basis at Penn State.

The VIEWOB program is designed to view an object as constructed for the Penn State FDTD code in three-dimensions. VIEWOB reads a geometry file containing the size of the solution space and the material types present at each cell location. This geometry file is written as a binary file and is stored on disk in compressed form. When VIEWOB retrieves a geometry file, it uncompresses the file, reads the data and then recompresses the file on the disk. The different material types are indicated by a colored line that is drawn one cell length long corresponding to a cell edge that has a specific permittivity or conductivity. The outline of the problem space is also drawn and the coordinate axes are labeled. An option box on the right side of the screen displays the size of the problem space and the location of the slice plane (if the slice mode is enabled). Figure 1 shows the main menu of the VIEWOB program and the arrow (\rightarrow) denotes that menu selection has a submenu. A brief description of each of the menu selections will now be presented.

Retrieve	Wire Grid
Shell	Solid
Rotate \rightarrow	Slice \rightarrow
Translate \rightarrow	Reset View
Scale \rightarrow	Grid ON/OFF
Zoom \rightarrow	Help \rightarrow
Exit	Cancel

Figure 1: Main menu for VIEWOB FDTD object visualization program.

The **Retrieve** option is used to retrieve (or load) the geometry files. When Retrieve is selected, the user can list the files and select one with the mouse, or the user can type in the file name manually. The **Shell** option produces a UNIX shell without leaving the VIEWOB program so that the user can execute standard UNIX commands if necessary. The **Rotate** option permits the user to rotate the object in the clockwise or counterclockwise direction around the x , y or z axis. A + and - box are provided in the Rotate submenu for controlling the rotation. The **Translate** option permits the user to translate the object along the x , y or z axis and a + and - box are provided in the submenu for controlling the translation. The **Scale** option permits the user to scale the object along the x , y or z axis and a + and - box are provided in the submenu for controlling the scaling. The **Zoom** option provides the capability to zoom in and out on the object to examine details more closely. The **Wire Grid** option displays the object in wire grid mode: lines are drawn along cell edges that have nonzero conductivity and/or permittivity that differs from free space or for perfectly conducting cell edges. The **Solid** option displays the object in solid form: squares are drawn

if four cell edges in a plane have nonzero conductivity and/or non-free space permittivity. The **Slice** option allows the user to examine details more closely by displaying the object in two-dimensional slice planes. The Slice submenu lets the user choose xy , xz or yz planes and *up* or *down* to move the slice plane through the third dimension. The location of the slice plane along with the problem space size is displayed in the option box on the right side of the screen. The Slice option provides the opportunity to view object details that may otherwise be obscured in a three-dimensional perspective view. The **Reset View** option resets the view from the slice mode back to the original three-dimensional view when the object was first loaded into VIEWOB. The **Grid On/Off** option turns off the outline of the problem space in three-dimensions and turns off the grid in the slice mode. The **Help** option provides a submenu with choices for help information on all main menu selections along with some general information about VIEWOB. The **Exit** option exits the user from the VIEWOB program and is in the same location for all submenus also. The **Cancel** option cancels a menu selection and takes the user back to the main menu if a submenu is active. The Cancel option is also used to dismiss help screens.

Even though the VIEWOB program is an extremely useful visual aid, it does have some limitations. One limitation is that it is currently set up to display only material types corresponding to perfect conductors, lossy dielectrics or dispersive dielectric materials. The capability to display lossy magnetic and dispersive magnetic materials will certainly be a part of a future version of VIEWOB. Another limitation is that the default size of the largest problem space that is displayable by VIEWOB is 140 by 140 by 140 cells. This limit is set so that the VIEWOB program can use the maximum amount of RAM available and still remain in core. If the user has a geometry where one of the problem space dimensions is larger than the default maximum (provided the other two dimensions are smaller than the default maximum), the VIEWOB source code can easily be modified and recompiled to display that particular geometry. The main advantage with the VIEWOB program is that it is generalized because it reads geometry files containing different problem space sizes without the need to modify the VIEWOB source code and recompile. Another advantage is that VIEWOB does not depend on the cell size or any other parameter to display the geometry. With the capabilities and advantages described above, VIEWOB is an important research tool because it displays FDTD geometries for verification and allows the user to examine every cell edge within the problem space.

3 FIELDS3D Program

The FIELDS3D program was developed to visualize electromagnetic field interaction with objects in real time. Such a capability would permit users to easily identify scattering centers and analyze field behavior and structure inside and outside of the object. This type of program could even be used to help design electromagnetic shielding enclosures, devices and circuits.

FIELDS3D is designed to visualize electromagnetic field interaction with objects in real time by displaying color-coded field amplitudes in two-dimensional slice planes. The object is displayed in the same manner as in the slice mode of the VIEWOB program. The Penn State FDTD code performs real-time computations and a separate graphics routine displays the fields, object, option box and menu system. FIELDS3D is completely generalized because it reads a configuration file for each problem that contains all of the relevant analysis

parameters. Many options are available to the user to change the analysis parameters and these options will now be described.

Figure 2 shows the FIELDS3D main menu box with all of the available menu selections.

Retrieve	Magnetic →
Shell	Current
Start FDTD	Poynting
Reset	Options1 →
Slice →	Options2 →
Electric →	Options3 →
Exit	Cancel

Figure 2: Main menu for FIELDS3D FDTD real-time field visualization program.

Note again that the arrow (→) denotes that menu selection has a submenu. FIELDS3D displays an option box on the upper right portion of the screen which contains all of the analysis parameters. These parameters are: problem space size, slice plane (e.g. xy , xz or yz), slice plane location, grid on/off, cell sizes, time step, source type (plane wave or point source), θ and ϕ incidence angles, incident plane wave polarization (θ or ϕ), field display type, scattered or total field, color scale factor, geometry on/off, and square root on/off. The **Retrieve** option functions the same as for VIEWOB and instructs FIELDS3D to read the selected configuration file. The configuration file contains the name of the geometry file (used by VIEWOB) and several parameters to instruct FIELDS3D how to set up the initial excitation and field display. The **Shell** option functions the same as for VIEWOB. The **Start FDTD** option starts (and pauses) the FDTD computations. Thus, the user can pause the computations, change the slice plane view and then restart the computations. The **Reset** option resets the field computations to zero and reinitializes the problem but the geometry being analyzed still remains current. The **Slice** option functions the same as for VIEWOB, and the user can move the slice plane dynamically (while computations are taking place) or while the computations are halted. The **Electric** option provides a choice of electric field components for display including electric field lines. The electric field lines are displayed as a vector with the length and direction of the vector dependent on the magnitude and sign of the appropriate electric field components for the active slice plane view. Thus for an xy slice plane view, the electric field lines depend on the magnitude of the x and y components of electric field. The **Magnetic** option provides a choice of magnetic field components for display including magnetic field lines. The magnetic field lines are displayed in the same manner as the electric field lines. The **Current** option displays the conduction current for dielectric materials and displays the line integral of magnetic field for perfectly conducting objects. The **Poynting** option displays the instantaneous Poynting vector in the same manner as the electric and magnetic field lines.

The **Options1** menu selection allows the user to change some of the analysis parame-

ters of the problem. The parameters available in the Options1 submenu are: turn the grid on/off, display scattered or total field, use plane wave excitation, use point source excitation, select one of four time dependencies for initial excitation (Gaussian, Gaussian derivative, ramped sine wave, and hyperbolic secant), change the frequency for the ramped sine wave, and change the rise time of the ramped sine wave. A + and - button are provided in the submenu for changing the sine wave frequency and rise time.

The Options2 menu selection allows the user to change more of the analysis parameters of the problem. The parameters available in the Options2 submenu are: change the pulse width for Gaussian, Gaussian derivative and hyperbolic secant pulses, change the ϕ and θ incidence angles, change the i , j or k location of the point source, change the point source type to feed E_x , E_y or E_z component. A + and - button are provided in the submenu for changing these parameters.

The Options3 menu selection allows the user to change some of the display characteristics for displaying the geometry and color-coding the field intensities. The parameters available in the Options3 submenu are: scale the color intensity up or down, turn the geometry on/off, display the square root of the field intensity instead of the actual field intensity (sqrt on/off), help and information about FIELDS3D (info). The Sqrt On/Off option levels out the field intensities and makes some of the lower level fields more visible. The Help submenu option provides help information on all the main menu selections and provides a list of the submenu selections for each main menu selection. The Info submenu selection provides general information about FIELDS3D and also provides a section describing how to construct the configuration file and what each parameter in the configuration file means.

When changing analysis parameters, an error message will be displayed if that parameter cannot be changed under the current settings. The analysis parameters cannot be changed while the field computations are taking place, otherwise instabilities may occur. Although FIELDS3D is a generalized program for real time FDTD analysis of electromagnetic problems, it also has some limitations. The maximum problem space size that can be accommodated is 140 by 140 by 140 cells and the cell sizes and time step cannot be changed by the user unless a separate configuration file is loaded. The default problem space maximum is again set so that the FIELDS3D program can use the maximum amount of RAM available while still remaining in core. For large problem space sizes, the the field display screen updates may take several seconds or minutes. Only free space, dielectric, magnetic and perfectly conducting objects can be analyzed with the present version and dispersive material capability will undoubtedly be part of a future version of FIELDS3D. Also, FIELDS3D does not perform any far-field computations at the present time; therefore far-field or Radar Cross Section (RCS) data are unavailable. Additional capabilities are being examined for future versions of FIELDS3D in the form of suggestions and comments provided by users.

4 Conclusion

This paper has described two electromagnetic visualization programs based upon the FDTD method: VIEWOB and FIELDS3D. The VIEWOB program displays objects as defined for the Penn State FDTD code and the FIELDS3D program displays real-time field interaction with objects calculated using the Penn State FDTD code. The programs were

designed for the Silicon Graphics family of workstations and should work on other workstations that have the Silicon Graphics graphics library. The primary advantages of these two programs is that they run on workstations and do not require the use of a supercomputer and they are general enough to not require modifications for each new problem. Even though these programs have some basic limitations, they provide a solid foundation for visualizing objects and electromagnetic fields using the FDTD method and have proven useful in research work at Penn State.

References

- [1] V. P. Cable, S. W. Fisher, M. N. Kosma, L. A. Takacs, R. J. Luebbers, F. P. Hunsberger and K. S. Kunz, "Continuing Progress in Parallel Computational Electromagnetics," *Proc. 1990 URSI Radio Science Meeting*, Dallas, TX, p. 67, May 1990.
- [2] K. S. Kunz, "Progress in Computational Electromagnetic Modeling for EM Courseware: a Personal Perspective at Penn State" *Proc. 1992 IEEE AP-S Int. Symp.*, Chicago, vol. 3, p. 1291, July 1992.

Creation, Visualization and Analysis - The Dynamics of Complex Models

S.J. Kubina, C.W. Trueman, D. Gaudine and A. Ramos
Electromagnetic Compatibility Laboratory
Concordia University
7141 Sherbrooke Street West
Montreal, Quebec, Canada

Abstract-This paper presents an overview of the software system used at Concordia's EMC Lab to construct wire grid models, to display and analyse the resulting current distributions and fields, and to prepare presentation graphics. The "life-cycle" of a wire-grid modelling problem is traced starting with the initial preparation of the input data set, the calculation of the wire radius, and the verification of the model for gross errors and integrity. NEC is often executed at many, many frequencies. Model validation is done by comparing computed and measured radiation patterns on the basis of equal radiation power, at many frequencies. The display and analysis of the current flow on the grid and of the radiated fields at each frequency helps in comprehending their intimate relationship near resonances of the antenna and wire-grid structure. Each software module can produce a drawing file for the preparation of diagrams for publication or Vugraphs or color slides for oral presentations.

Introduction

The EMC Laboratory at Concordia University has been engaged for some time in Computational Electromagnetics directed at the radiation and scattering analysis of complex structures, using wire-grid modelling and the Numerical Electromagnetics Code(NEC)[1,2]. The need to improve upon the error-prone and tedious process of preparing grids representing aircraft and ships had led to the development of the computer-aided modelling software system of Fig. 1, which aids in visualizing the wires of the model, in finding and understanding both gross and subtle errors in grid construction, and in calculating a wire radius for each wire. After solving for the current flow and radiated fields with the NEC program, software modules support the display of wire-grid currents and fields in a variety of formats. This paper describes the EMC software system and its use in developing a model for the analysis of the performance of the HF wire antennas on the aircraft of Fig. 2, as a typical application. The key factors in each step of the problem are discussed: model creation and integrity checking; comprehending and correcting integrity errors with aid of computer graphics; validation relative to measured radiation patterns; the association of currents and patterns as a function of frequency to heighten the understanding of results.

Model Creation and Visualization

The design of a wire-grid model such as the aircraft of Fig. 2 begins by choosing a "nominal" segment length such that the model covers the desired frequency range. Thus to keep the segments in the 32 m aircraft of Fig. 2 shorter than 0.14λ up to 30 MHz, the "nominal" segment length is set to 1.4 m, requiring 22 segments axially. The fuselage diameter of 3.6 m requires 8 segments circumferentially. Hence the wire grid model will have 8 axial wires and 21 cross-sections. The surface of the aircraft must then be covered with wires following the principles for wire placement called "wire-grid modelling guidelines"[3,4]. The basic rule is that the aircraft surface be covered with square "mesh cells" of side length equal to the nominal segment length. Where the cross-section tapers, triangular cells are to be used to change the number of squares around the fuselage periphery. In critical regions such as near antenna feed points, smaller mesh cells and shorter segments are used. Often, the initial design of the wire-grid is sketched with a pencil onto a plastic model, as an aide to three-dimensional visualization.

To construct the wire-grid model of Fig. 2 the (x, y, z) coordinates of each "vertex" or wire end-point are "digitized" from three-view drawings with a tablet using program DIDECD(igitize, Display, Edit and Convert)[5,6] in the chart of Fig. 1. DIDECD displays each vertex point as it is acquired. Complex models are built up in sections, such as forward fuselage, center fuselage, aft fuselage, wings, and tail planes, and each section is drawn with DIDECD and examined for errors as it is constructed. Only one side of symmetrical sections need be digitized. The complete model is assembled by concatenating the individual sections. Sometimes it is convenient to digitize many, many points on an aircraft surface and then derive the wire endpoints by interpolation. DIDECD has been supplemented by Computer-Aided Drafting(CAD) programs which provide an efficient means of approximating cross-sections of the aircraft with smooth interpolation curves to derive the actual wire endpoints.

The wire-grid model is completed by specifying the radius of each wire in the grid. A generalization of the "equal-area rule"[7,8] is used. Thus the wire in Fig. 3 is a member of a four-wire mesh of area A_1 and periphery L_1 , and of a three-wire mesh of area A_2 and periphery L_2 . The wire radius a is calculated according to[9]

$$a = \frac{A_1}{\pi L_1} + \frac{A_2}{\pi L_2} \quad \dots(1)$$

To implement this rule for complex grids, program MESHES[9] is used to search the grid for its mesh content: for each wire of the grid, the wires forming meshes with that wire are determined. Then program FNDRAD(FiND RADius)[9] uses the areas and peripheries of the meshes in Eqn. (1) to find an individual radius for each wire of the grid. (Program names originated when six characters was the maximum in a file name!) DIDECD provides an overview of the wire lengths and wire radii contained in a given wire-grid, by color-coding the wires either by length or radius.

Integrity Checking, Visualization and Gross Errors

The "integrity" of the wire-grid refers to its freedom from gross errors such as missing wires, duplicated wires, wires which cross one another but do not form a junction in the NEC code, and of utmost importance, conformity to NEC's geometry restrictions[1,2], called "NEC modelling guidelines", which are discussed in detail in Ref. [4]. "Integrity checking" is the systematic verification of the grid, both for gross errors and for conformance to the NEC modelling guidelines.

The most basic integrity check is a visual inspection of the grid drawn by program DIDECD or program MODEL, in the format of Fig. 2. Each wire is represented by its centerline. For a complex, three-dimensional grid such as the aircraft, such a drawing is very confusing. Program HIDDENMOD(HIDDEN MODEL) draws the wires as if they were located on the surface of an opaque solid, as shown in Fig. 4. The display is much simpler, and the grid can be inspected to see whether it is an accurate implementation of the original design. Experience has shown that a variety of gross errors are easily missed by visual inspection, but are efficiently found with the mesh search, as described in the following.

Program MESHES[9] is run to identify meshes in the wire-grid representing the aircraft surface. MESHES checks each wire against every other wire to identify duplicated wires. MESHES then carries the mesh search, and produces lists of wires that are members of various kinds of meshes: wires that are part of 3 wire meshes, that are part of 4 wire meshes, of 5 wire meshes, ..., of 8 wire meshes; wires that are members of no meshes at all, that are members of only one mesh, and of more than two meshes. When these lists are displayed with MODEL gross errors are often clearly seen. For example, Fig. 5 shows the forward part of the aircraft grid, with wires that are members of six wire meshes highlighted. The figure illustrates two errors and how they are identified by the mesh search. In one case a wire has been omitted from the grid, creating a six-wire mesh cell, which outlines the location of a missing grid wire. The other error is more subtle. One wire of the grid is not actually connected to the grid at one end: the (x, y, z) coordinates of the wire's endpoint are too different from the (x, y, z) coordinates of the nearby junction. MESHES treats the wire as open-circuited, and thus it is encircled by a six-

wire mesh. The wire would also appear in the list of wires which are not members of any mesh, and again could be seen clearly on the graphics display. The first step in "integrity checking" is the correction of gross errors such as these.

Radius Calculation and Integrity Verification with CHECK

When the grid is first assembled, the radius of every wire in the grid is set to a very thin value. Many of the NEC modelling guidelines involve the wire radius[2,4]. For example, restrictions are placed on the ratio of the segment length to the wire radius; on the ratio of the fattest to the thinnest radius at a wire junction; and on the spacing of wires in terms of wire radius. Full integrity checking cannot go ahead until the "equal-area" radius has been evaluated for each wire, using program FNDRAD to evaluate Eqn. (1) for each wire, given the mesh list compiled by MESHERS.

Program MODEL aids in visualizing relationships among wires involving the wire radius by drawing each wire as a cylinder of appropriate radius, in the format seen in Fig. 6 for the full aircraft grid. Most wires are members of two "square" mesh cells of side length equal to the "nominal" segment length. Eqn. (1) implies that, for square mesh cells of side length Δ , the wire radius is $\Delta/(2\pi)$, hence for most wires, the ratio of the wire length to its diameter is about 3. For wing edge wires, systematic application of Eqn. (1) results in wire radii of about half this value, because edge wires are members of only one mesh. Critical regions of the model which have been subdivided into small mesh cells have thinner wire radii. This is clearly seen at the top of the dorsal fin in Fig. 6.

Program CHECK[4] systematically verifies the grid against the NEC modelling guidelines for individual wires, for wires making up junctions, and for every pair of wires in the model, to ensure adequate spacing. CHECK produces lists of wires which violate each of the modelling guidelines, for display with MODEL. For example, Fig. 7(a) illustrates a geometry in which a "match point error" exists: the center of a segment lies within the volume of another segment. Thus, eight radial wires have been included at the feed point for the starboard wire antenna in the aircraft grid, and short segments have been used adjacent to the feed point. But the "equal-area" wire radius is so fat that the center point of the highlighted feed radial lies within the volume of an adjacent wire: a match point error. Drawing the wires as cylinders in MODEL aids in visualizing the problem and in comprehending how it arises. The solution is illustrated in Fig. 7(b). The radius of each segment connected to the feed point has been reduced by a factor of two.

Model development is an interactive, iterative process. A wire grid is designed, and is constructed with DIDEK. MESHERS identifies gross errors, which are corrected. FNDRAD calculates radii, then CHECK identifies a variety of transgressions of the NEC modelling guidelines, which are displayed with MODEL. Minor problems are often fixed simply by editing the model: moving vertices slightly, or adding a few wires to break large meshes into smaller ones to reduce the radii of the associated wires. Severe problems are often the result of a poorly-conceived wire-grid, and can only be fixed with extensive rethinking of the grid design in critical regions. Few wire-grids are ever completed without several iterations of model editing, radius recalculation, then integrity verification with CHECK. Rapidly accessible computer graphics highlighting the errors found by CHECK, showing the wire radius explicitly, aids enormously in understanding and correcting such problems efficiently.

Executing NEC at Many Frequencies

Once a satisfactory wire-grid model has been developed, the NEC code can be run to obtain the desired results. Typically in an antenna performance study, the volumetric distribution of the radiated electric field strength must be studied over a range of frequencies, such as 2 to 30 MHz for the HF wire antennas on the aircraft of Fig. 2. With the aircraft oriented to "fly" along the x-axis toward positive x, at each frequency the "conical cut" radiation patterns[10] $E_\theta(\theta, \phi)$ and $E_\phi(\theta, \phi)$ are computed to cover the radiation sphere: $\theta = 0, 25, 37, 45, 53, 60, 66, 72, 78, 84, 90, 96, 102, 108, 114, 120, 127, 135, 143, 150$ and 180 , each for $0 \leq \phi \leq 360$. Also, to provide standard "principal plane" patterns, two "elevation cuts" are added: $\phi = 0$ and 90 degrees, each for $-180 \leq \theta \leq 180$. With the power of modern workstation computers, all these patterns

can be computed with a "fine" frequency step, such as 0.1 MHz, from 2 to 30 MHz to trace out sharp resonance peaks and sharp deep troughs associated with antenna and airframe resonance in the HF band.

NEC's rather extensive output file is greatly reduced in size by program STRIP in Fig. 1, which generates a "SOLution" file. The SOLN file consists of a copy of the input file for that run of NEC, which provides full documentation of the "run", and is handy for recycling if further frequencies need to be computed for that model. Then the SOLN file contains, at each frequency, the port impedances, followed by the segment currents, the radiation patterns, and any near fields that were computed, all written using as few ASCII characters as possible. Binary files are not used because they cannot be examined easily with an editor and they are usually incompatible between different computer systems.

For a typical problem, several wire-grid models are usually studied, and each will be "run" at many, many frequencies. Currently we manually keep track of what "runs" have been done for each wire-grid topology, at what frequencies, what the file names are, and where the file for each "run" is stored, using hard-covered "log books". Keeping track of runs is a problem in database management. We recognize the need for a computer-based archiving and retrieval system for this "data base", so that, over a period of years, wire-grid models and "runs" are accumulated and stored in an organized system, logs of runs are accumulated and can be inspected, and specific "runs" efficiently retrieved.

Calculating the Radiated Power

Comparisons of the fields of two different HF antennas, or of fields computed with two different wire-grid models, or of fields obtained by wire-grid calculation and by measurement is usually done on a basis of equal radiated power. The radiated power is obtained by program ISOLEV (ISotropic LEVEL) by integrating the fields over the radiation sphere according to

$$P_{rad} = \int_0^{2\pi} \int_0^{\pi} \frac{E_{\theta}^2 + E_{\phi}^2}{2\eta} \sin \theta d\theta d\phi \quad \dots(2)$$

This is more reliable than calculating the power based on the input impedance. The "isotropic level" is the field strength which, if radiated uniformly over the radiation sphere, obtains the same total radiated power, and is given by

$$E_{iso} = \sqrt{\frac{\eta P_{rad}}{2\pi}} \quad \dots(3)$$

This isotropic level field strength is routinely plotted as a reference level for comparing measured and computed radiation patterns, or two sets of calculations. In HF antenna performance assessment, both the relative field strength in each polarization and pattern shape factor are important.

Visualization of the Radiated Fields

The most basic visualization and comparison tool is the polar plot of radiation patterns, on a basis of equal radiated power. Program PATCMP (PATtern CoMparison) displays individual conical or elevation cuts in the format of Fig. 8. PATCMP is often used in "validating" a wire-grid model by comparing a scale-model measurement of the radiation patterns with wire-grid calculations, pattern-by-pattern and frequency-by-frequency. Thus Fig. 8 shows that although the E_{θ} polarization agrees well at 10 MHz, except in the aft direction, there is a significant difference in the shape, level and orientation of the E_{ϕ} polarization for the port antenna at this frequency. Such differences are usually investigated by comparing the radiated field over the full radiation sphere between the computation and the measurement, and by correlating the fields to the current distribution over the wires of the grid. Once the model is "validated", it can be used

to study the performance of different HF antenna configurations, to evaluate antenna-to-antenna coupling, both in-band and out-of-band provided the wire-grid spans a sufficient frequency range.

The comparison of individual radiation patterns quickly becomes tedious, and a summary format of the performance of the antenna at each frequency is desirable. Figs. 9(a) and (b) show the field components E_θ and E_ϕ drawn with CPLOT(Contour PLOTter) as contour maps on the (θ, ϕ) plane, providing a complete description of the distribution of the radiated field in three-dimensional space at a single frequency. Program CPLOT is a general-purpose contouring program, which produces both line drawing contour maps such as Fig. 9 for publication and false-color contour plots. The "hot scale" uses blue for the weakest fields, through green, yellow and orange to red for the most intense fields. CPLOT can draw cuts of constant θ or ϕ through the surface, and can export individual cuts to RPLOT(Rectangular PLOTter) or PPLOT(Polar PLOTter) for comparison with measured data or other wire-grid calculations. A variety of specialized tools has been developed for displaying the three-dimensional distribution of field strength. Program FLDMAP(FieLD MAP) produces a color-contour map of both E_θ and E_ϕ on a single page that can be printed on a color printer for inclusion in a report. Figs. 10(a) and (b) show E_θ and E_ϕ represented as surfaces above the (θ, ϕ) plane by program SURPAT(SURface PATtern). On a color workstation, SURPAT codes the contours in the same colors as CPLOT or FLDMAP, and the hidden-surface drawing and the contour map can be shown side-by-side in two windows. Figs. 11(a) and (b) show E_θ and E_ϕ as functions of direction in three-dimensional space drawn with program TDPAT(Three-Dimensional PATtern). The aircraft wire-grid is shown in the same orientation as the field strength drawing. The aircraft can be rotated to examine the field strength from various viewing angles. This is a considerable aid to evaluating the directions in which the energy in each field component is radiated. Once again, TDPAT can use the same color scale as other programs to enhance the interpretation of the field strengths. Together, PATCMP, SURPAT, TDPAT, FLDMAP and CPLOT provide an array of tools for visualizing the three-dimensional distribution of field strength surrounding a radiating antenna, and comparing the radiated fields of different antennas or comparing computed and measured results calibrated to the same power level.

Visualizing the Segment Currents

The intimate relationship between the current flow on the antenna and aircraft wire-grid and the radiated fields is of particular interest near frequencies of resonance of the antenna or airframe. Programs SPECTRM(SPECTRuM) and IDIS(I DISplay) were developed to allow the user to display currents on the wire grid. Both SPECTRM and IDIS show current magnitude on the blue-green-yellow-red "hot scale" and phase on a "color-circle" scale, representing phase of -180 degrees with red, through violet and blue to cyan for 0 degrees, then through green and yellow back to red for a phase of 180 degrees. SPECTRM is oriented toward multi-window display of the current flow on the structure seen from different view angles, whereas IDIS provides a variety of display formats and is oriented toward examining the current flow on subsets of wires, as well as the whole structure. IDIS maintains lists of tag numbers and displays the current on the wires named in a given list. The default list is the whole set of wires. Fig. 11 shows the current on the port antenna when it is excited with 1 volt at its base, and the induced current on the starboard antenna, drawn in the "perpendicular line" format with IDIS. The same current can be shown with IDIS as a rectangular plot of magnitude and phase as a function of distance along the wire. But the perpendicular line format is very confusing when used to show the currents over the aircraft wire-grid, and so grid currents are usually shown on the color "hot-scale". Because grid currents usually vary enormously in magnitude, a decibel scale for current flow is often attractive. IDIS can drive a color printer to reproduce current distribution displays for inclusion in reports or as Vugraphs. The contact with and appreciation of the current distribution on the grid is a vital element in building confidence in a wire-grid model and understanding its behavior as a function of frequency.

High Resolution Spectral Analysis

The performance of an HF antenna on an aircraft changes enormously with frequency, and the antenna design is usually a compromise. A summary parameter that is used to assess the antenna's performance across the HF band is the percentage of the power radiated into the E_θ component of the field, because ground stations are usually designed to transmit and receive that field component. The "percent E_θ " parameter is defined as

$$\%E_\theta = \frac{1}{P_{rad}} \left(\int_0^{2\pi} \int_0^\pi \frac{E_\theta^2}{2\eta} \sin\theta d\theta d\phi \right) \times 100 \quad \dots(4)$$

A parameter such as percent E_θ must be calculated at each frequency from the set of conical-cut radiation patterns. Its value at many frequencies is then collected into a data file for graphing with RPLLOT. Fig. 13 shows percent E_θ as a function of frequency with the port antenna excited with one volt and the starboard antenna shorted to the aircraft skin. The figure shows a comparison of two wire-grid calculations, using a wire-grid model with 6 axial wires, "model 4GP", and one with 8-axial wires, "model 7", both compared with a set of 10 measured data points. At 2 MHz, most of the power is radiated into E_θ . As the frequency rises toward the quarter-wave resonant frequency of the port antenna, 3.7 MHz, the fraction of the power in E_θ drops rapidly, to a minimum approximately coinciding with the resonant frequency. Percent E_θ has a sharp minimum closely followed by a sharp, tall peak at the resonant frequency of the starboard antenna, 5.8 MHz, which is shorted to the aircraft skin. The figure illustrates that the resonance associated with the passive antenna is completely missed in the measured data, which is derived from sets of conical cut radiation patterns taken at 2, 6, 10, 15, 20, 22, 24, 26, 28 and 30 MHz. Initial calculations at 2, 3, 4, ..., 30 MHz showed significant differences from the measurement, and were only understood when sufficiently dense frequency sampling was used to trace out the sharp resonance trough and peak seen at 5.7 MHz. The alignment of the resonance peak between the two wire-grid models, and with the measurement, is extremely sensitive to the length of the wire antennas. Thus the wires are slightly different in length in the two models, and the precise length of the wire in the measurement model is not known.

Presentation Graphics

A large part of any engineering activity is the production of the report and its associated drawings and graphs, and so the EMC Lab software system has been engineered to provide solid support for the preparation of presentation graphics. Most programs can "write" a "LABLNG" file, which is an ASCII file containing a line-by-line description of the drawing. Program LABLNG(LABeLiNG) began as a means of adding a few arrows and character strings to dress up a drawing shown in a TEK 613 storage graphics screen, and gradually evolved into a mini-CAD program for manipulating EMC Lab graphics displays. LABLNG is used to specialize the format of standard display "templates" such as the displays produced by PATCMP, RPLLOT or CPLOT. Unwanted text can be removed, new text added, Greek letters added, the size and position of text can be changed. Thus once a drawing has been created with any of the graphics programs as a LABLNG file, it is not cast in stone, but instead any part of it can be changed or specialized to a particular purpose. At present sharp, clean paper copies are obtained by translating the LABLNG file into Postscript format with MAKEPS(MAKE PostScript), and copying it to a laser printer. The Postscript file can be imported directly into a word processor, which scales the drawing and places it in the desired location on the printed page. The LABLNG format file is extremely simple, and would be easily adapted to the HP graphics language, for example, to drive a pen plotter or an HP compatible laser printer.

Color displays such as color contour maps or current distributions on a color scale are a challenge for hard-copy reproduction. Currently the EMC Lab uses HP Paintjet printers to produce color hard-copies. If a graphics program is to drive the color printer directly, then it must maintain a pixel-map in memory into which is stored the color of each pixel on the drawing. This makes most programs too large for the 640 k memory available on the MS-DOS computers, but is not a problem on UNIX workstations. Program LABLNG is small enough to allow the pixel-map on MSDOS machines, and so graphics programs can write a color version of the LABLNG file, then LABLNG can drive the color printer. This has the advantage of allowing color drawings to be manipulated in the same way as any other drawing. Color laser printers are becoming affordable and the next step is the adaptation of our software system to support such printers.

Conclusions

This paper has described the software system used at Concordia's EMC Lab to prepare and visualize wire-grid models, check them for errors and "integrity", and to examine and visualize the radiated fields and current distributions at each frequency. The software system is an evolving tool, that was initially developed on 64 kilobyte PDP-11 computers using storage CRT graphics and later 16 color graphics, that was subsequently adapted to 8088 machines running MSDOS with monochrome graphics, to 80386 machines with 256 color VGA graphics, and most recently to fast UNIX machines running X-Windows. We have chosen to maintain MSDOS compatibility to keep most graphics software available to lab members on inexpensive but fast MSDOS platforms. Many of our graduate students own suitable MSDOS machines. The 640 kilobyte memory limitation has been largely avoided in most programs by using binary disk files for temporary storage, thus reserving most of the machine's memory for code rather than data.

The program set was recently ported to UNIX and X-Windows. An "X interface" in the C language was written in such a way that the FORTRAN source files for a given graphics program for MSDOS are simply re-compiled under UNIX and linked with the X interface to create the UNIX version of the program, which is virtually identical to the MSDOS version. This minimizes the inconvenience to users in switching platforms in the course of the day. The X-windows environment offers significant advantages in speed of execution, and in the display of multiple windows. For example, MODEL can be run in one window to show the wire-grid, IDIS in a second to show the current distribution and SURPAT in a third to show the radiated fields. Additional windows can be opened to show currents and fields at nearby frequencies, allowing the user to form strong associations between changes in current flow and the associated changes in radiated field strength.

Our software system has developed as in Fig. 1, with a separate, medium-scale program implementing each individual function. This has kept the maintenance problem manageable, made it possible to add new features and functions to one module without changing others, and allowed all programs to be implemented in the limited space available on MSDOS machines. From the user point of view, most of the programs of Fig. 1 "look and feel" similar, and learning one program in the set smooths the way to learn others. For instance, in all programs the principal parameters such as look angles are entered into boxes in the main menu, "F3" draws the graphics display, "F4" draws the display with automatic scaling, "F2" zooms using the mouse, and "F10" then "F1" exits. This integration into a single system involves no small amount of effort on the programmer's part: it is terribly difficult to be perfectly consistent across a large set of programs. Further, it is even more difficult to maintain consistency at the sub-menu level in all programs. From the user's point of view, as much commonality of function as possible is an enormous advantage.

The user interface is an especially vexing issue. Our user interface puts most user choices on the function keys, which has in recent years become unfashionable. New users preconditioned to expect a "Graphical User Interface"(GUI) using the mouse find our function key interface a stumbling block! The essential features of the user interface are these. The novice user should be able to obtain a reasonably well-formatted graphics display by doing little more than naming the data file and pressing "draw". Menus should be largely self-explanatory, reducing the need for a "help file" or a printed manual, allowing the user to build up knowledge of the

program by trying its various functions over a period of time. Hidden within such an apparently-simple program must be the full functionality demanded by the expert user, with each function reasonably well explained by a simple menu.

There may be a significant advantage in integrating the software system into two or three major blocks. The "model creation" block would include: DIDEK for entering and modifying wire endpoints, the MESHES and FNDRAD functions for radius calculation, the MODEL program with its radius-drawing capability, the HIDNMOD program, and the CHECK program for integrity verification. This becomes a large-scale program, comparable in size and complexity to commercial CAD or word-processing programs. The data-base manager would systematically archive files to tape cartridges, maintaining a log of what and where, making for easy retrieval. The display-and-visualization block would include MODEL, HIDNMOD, IDIS, PATCMP, SURPAT, FLDMAP, and TDPAT, providing the capability of opening "windows" for each of these functions. Further, such a program should be able to have several "SOLN" files open at once, and show data at several frequencies, in multiple windows. The RPLOT, PPLOT and CPLOT set should become a single, general-purpose graphing tool. In the past, our graphics programs have been developed as needed in our projects but without explicit funding. It is unlikely that this scale of programming effort can be undertaken without support.

The developer of such graphics visualization programs can never be satisfied, because a little imagination rapidly provides exciting new ideas for functionality, hence no program is ever finished. New projects bring new demands for graphics software, most recently for near-field visualization. Intensive use of any program by its developer and others soon reveals weaknesses or points to a better way to implement some function. Consequently, programs are continually evolving toward more convenience and simplicity, better defaults and fewer choices for the inexperienced user, but fuller functionality for the expert.

References

1. G.J. Burke and A.J. Poggio, "Numerical Electromagnetics Code - Method of Moments, Part I: Program Description-Theory", Technical Document 116, Naval Electronic Systems Command(ELEX 3041), July, 1977.
2. G.J. Burke and A.J. Poggio, "Numerical Electromagnetics Code - Method of Moments, Part III: User's Guide," Technical Document 116, Naval Electronic Systems Command(ELEX 3041), July, 1977.
3. C.W. Trueman and S.J. Kubina, "Fields of Complex Surfaces Using Wire Grid Modelling," Fourth Biennial IEEE Conference on Electromagnetic Field Computation, Toronto, October 22-24, 1990.
4. C.W. Trueman and S.J. Kubina, "Verifying Wire-Grid Model Integrity with Program CHECK," Applied Computational Electromagnetics Society Journal, Vol. 5, No. 2, Winter, 1990, pp. 17-42.
5. S.J. Kubina and E. Cerny, "EMC Modelling Computer Graphics Capability", Technical Note No. TN-EMC-82-01, EMC Laboratory, Concordia University, March 31, 1982.
6. P. Bhartia, S.J. Kubina, E. Cerny and D. Gaudine, "Generation of Computer Models for the EMC Analysis and Design of Large Systems", Proceedings of the 1984 International Symposium on Electromagnetic Compatibility, Tokyo, Japan, October, 1984.
7. K.S.H. Lee, L. Marin and J.P. Castillo, "Limitations of Wire-Grid Modelling of a Closed Surface", IEEE Trans. on Electromagnetic Compatibility, Vol. EMC-18, No. 3, pp. 123-129, August, 1976.
8. Ludwig, "Wire-Grid Modelling of Surfaces", IEEE Trans. on Antennas and Propagation, Vol. AP-35, No. 9, pp. 1045-1057, September, 1987.
9. C.W. Trueman, "Automated Radius Calculation for Wire-Grid Models," 7th Annual Review of Progress in Applied Computational Electromagnetics of the Applied Electromagnetics Computational Society, Monterey, California, March 18-22, 1991.
10. MIL-A-9080(USAF)-Military Specifications for Antenna and Liaison Communication Equipment, February 2, 1954.

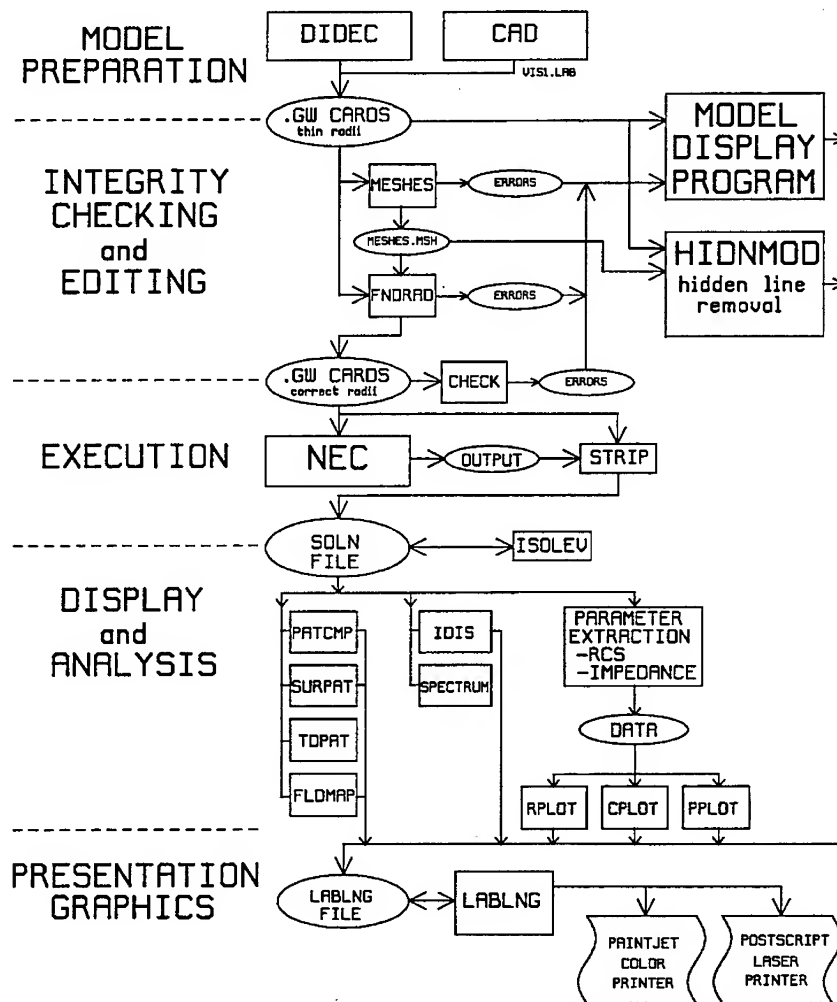


Fig. 1 The EMC Lab software model creation and visualization software system.

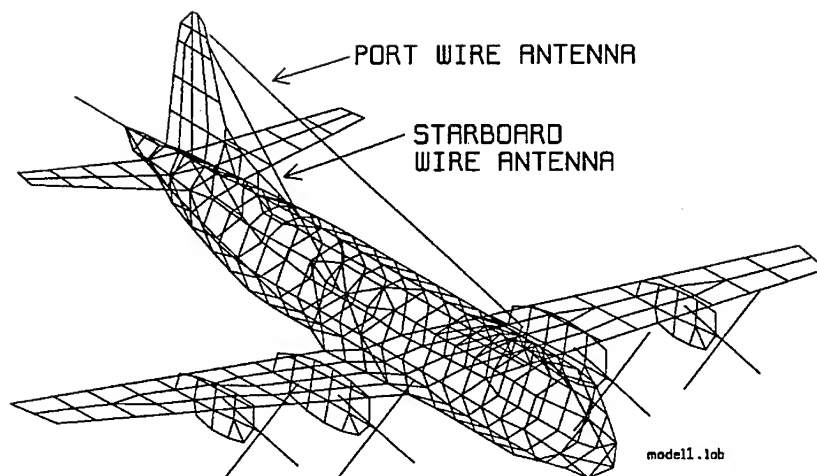


Fig. 2 An aircraft wire-grid model displayed with program MODEL, representing wires with their centerlines.

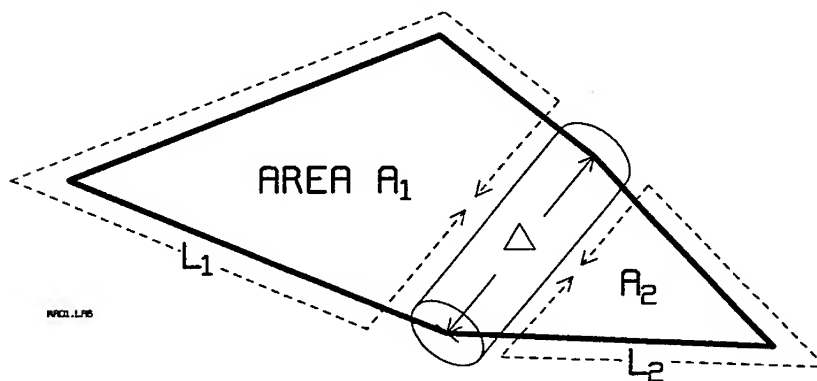


Fig. 3 A wire which is a member of two meshes, of areas A_1 and A_2 , and peripheral lengths L_1 and L_2 .

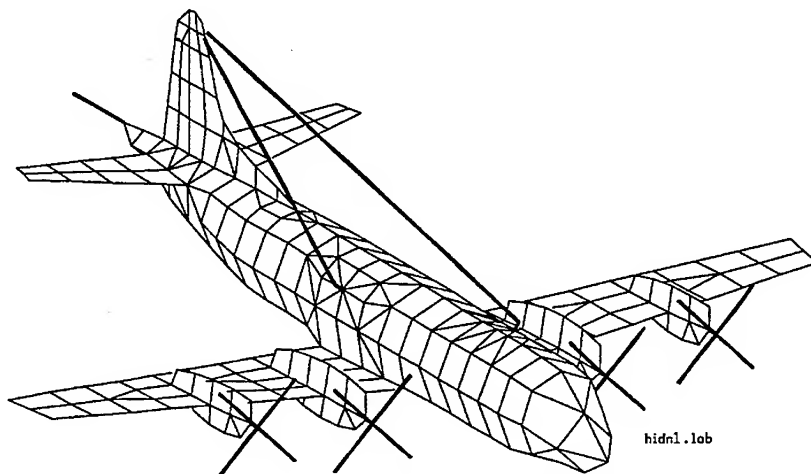


Fig. 4 The aircraft grid drawn by program HINDMOD, as if the wires cover the surface of an opaque solid.

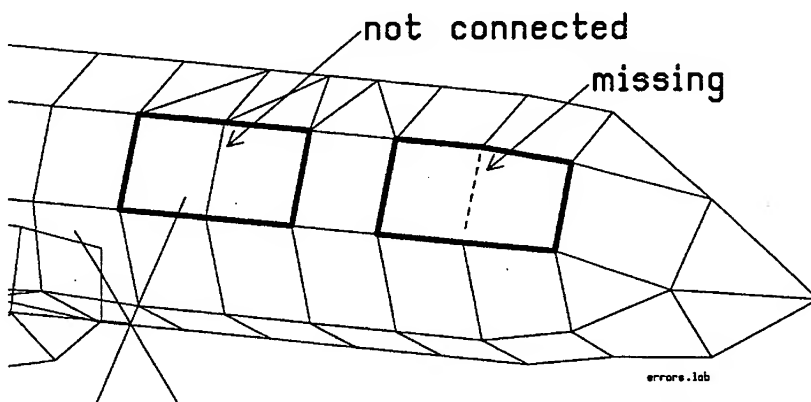


Fig. 5 The aircraft grid with 6-wire meshes highlighted, showing two "gross" errors in the grid.

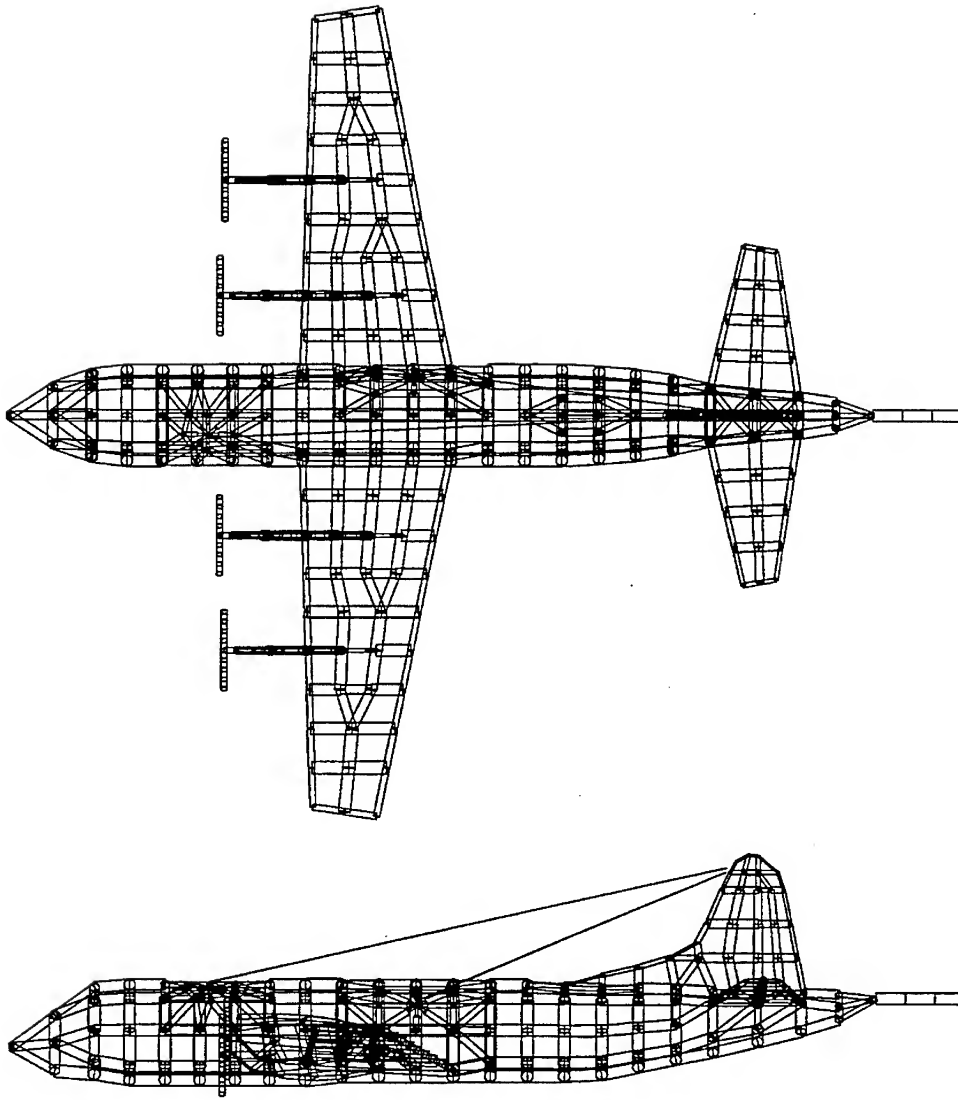


Fig. 6 The full aircraft grid showing the "equal-area" radius for all the wires.

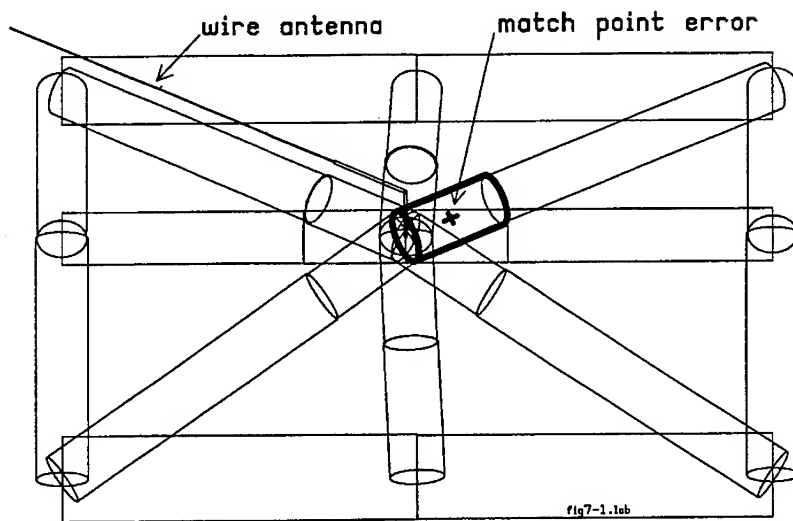


Fig. 7(a) The feed point of the starboard wire antenna, drawn showing the wire radius. The highlighted wire has a "match point error" with its neighbor.

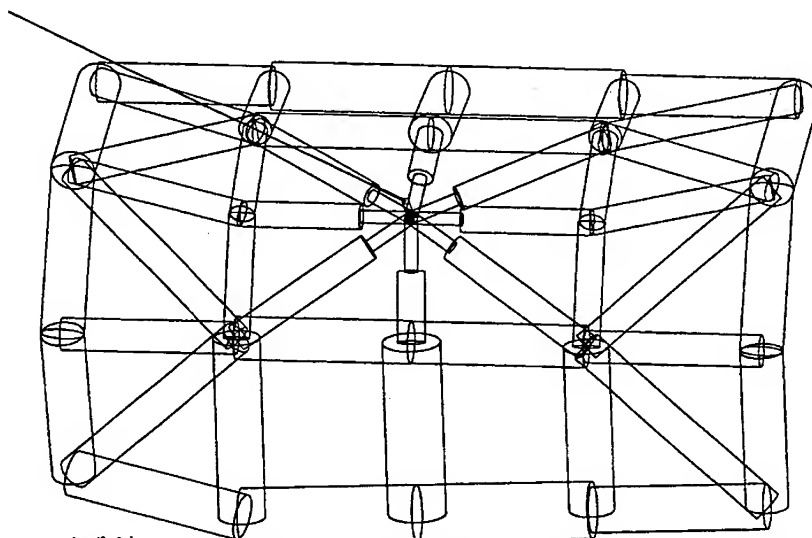
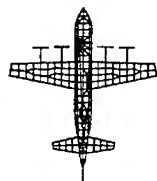


Fig. 7(b) The feed region of the starboard wire, with the match point error corrected.

Aurora Aircraft
Port wire antenna excited
10 MHz



Computed (AUR7)
----- E-THETA
--o-- E-PHI
MEASURED
—— E-THETA
—o— E-PHI
..... ISOTROPIC
LEVEL

EM

CONCORDIA EMC LABORATORY

Fig. 8

The radiation patterns for E_θ and E_ϕ in the $\theta = 90$ degree plane, with the port wire excited at 10 MHz.

RADIATED FIELD
FREQUENCY = 10.00 MHz
LINEAR SCALE
0 TO 0.3520
CONICAL CUT
 $\theta = 90$

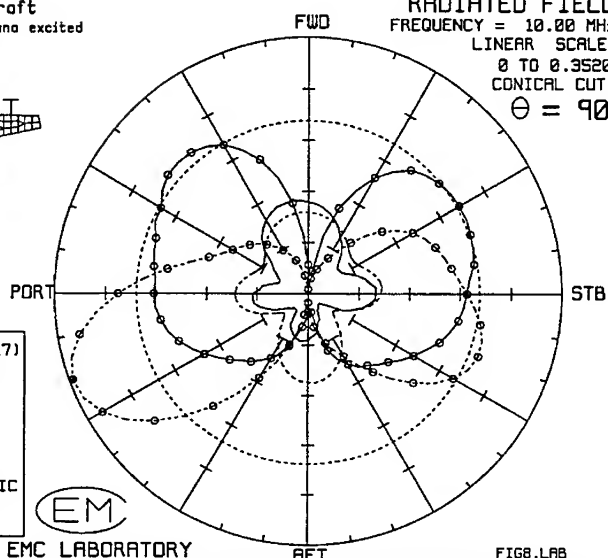


FIG8.LAB

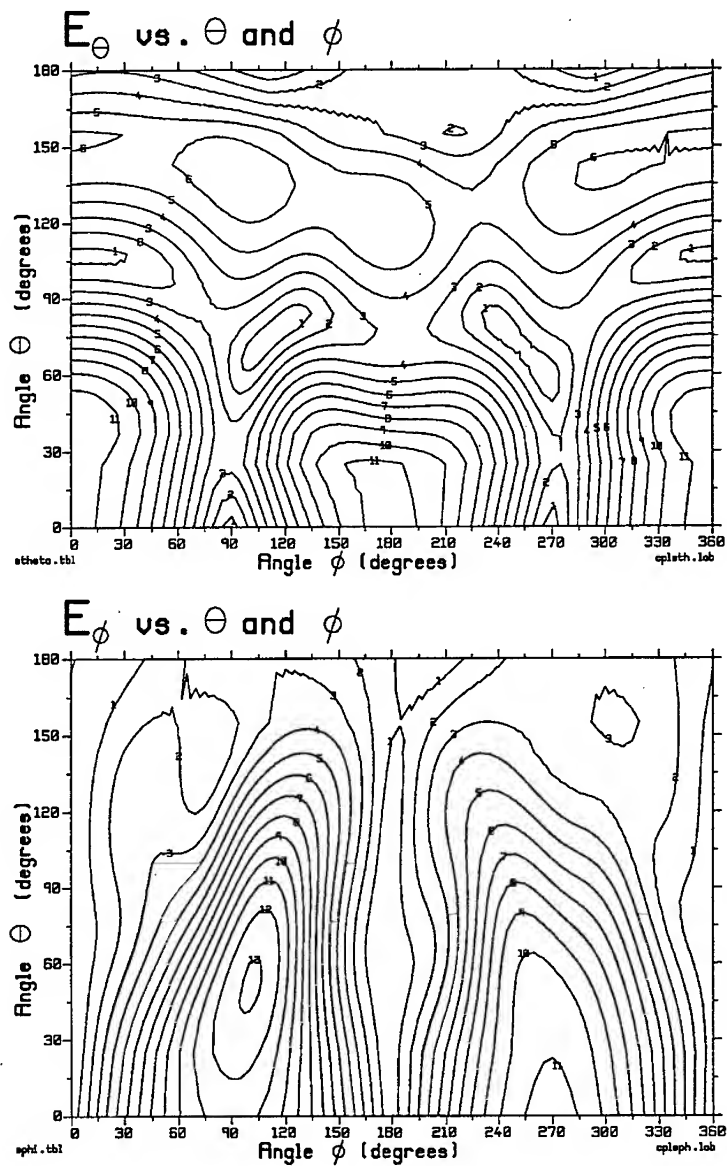
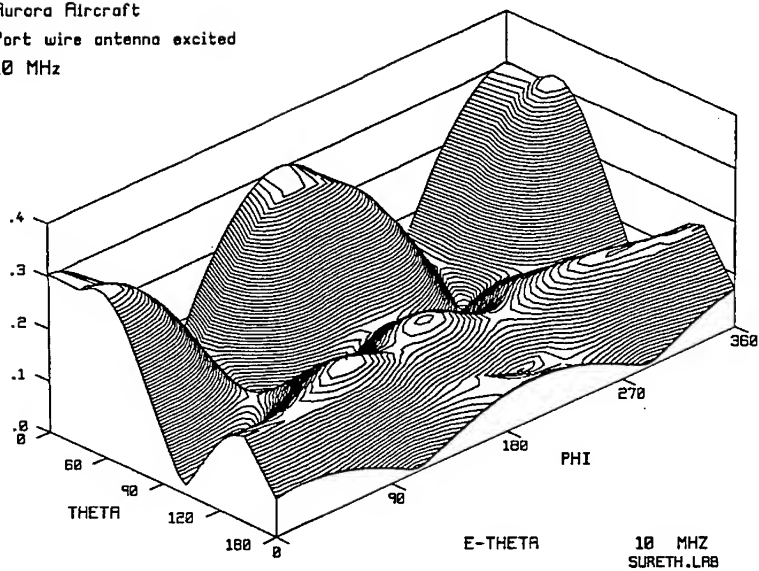


Fig. 9 Contour maps of E_θ and E_ϕ at 10 MHz, with the port wire excited, normalized to a radiated power of 1 watt.

Aurora Aircraft
Port wire antenna excited
10 MHz



Aurora Aircraft
Port wire antenna excited
10 MHz

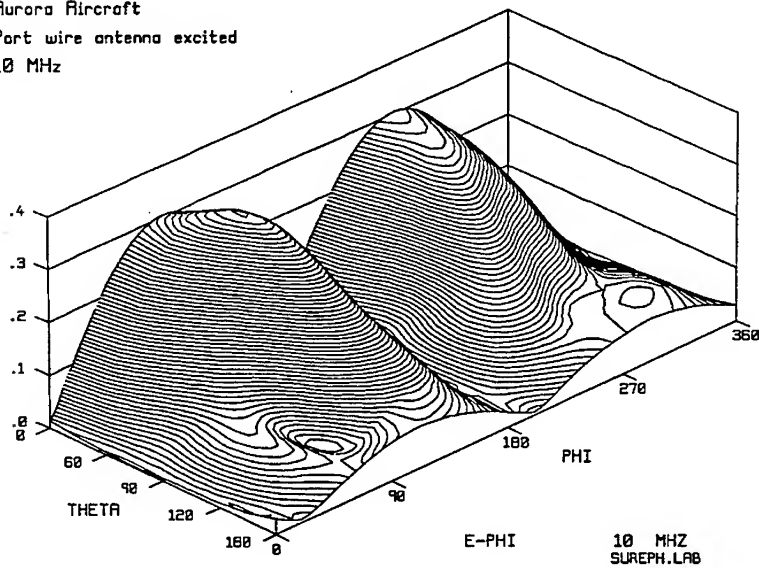
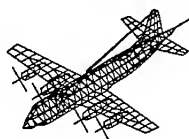


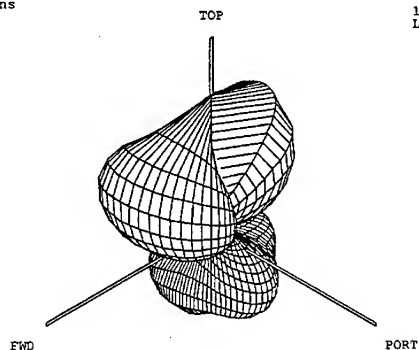
Fig. 10 Surface plots of E_{θ} and E_{ϕ} at 10 MHz, with the port wire excited with 1 volt.

Aurora Aircraft

Port wire antenna excited at 10 MHz
E-theta radiation patterns



TOP VIEW
QUADRANT NO. 1
MINIMUM THETA 0
MAXIMUM THETA 180
MAX FIELD STRENGTH
AT THIS FREQUENCY
0.352E+00 V/M
MAX VALUE PLOTTED
0.319E+00 V/M
ISOTROPIC LEVEL
0.207E+00 V/M
SOLUTION FILE:
AUR7.10



E-THETA

10 MHZ
LINEAR
SCALE

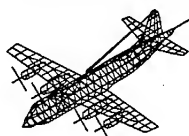
CONCORDIA EMC LABORATORY



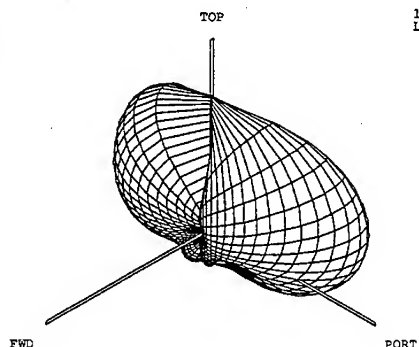
12/14/92

Aurora Aircraft

Port wire antenna excited at 10 MHz
E-phi radiation patterns



TOP VIEW
QUADRANT NO. 1
MINIMUM THETA 0
MAXIMUM THETA 180
MAX FIELD STRENGTH
AT THIS FREQUENCY
0.352E+00 V/M
MAX VALUE PLOTTED
0.352E+00 V/M
ISOTROPIC LEVEL
0.207E+00 V/M
SOLUTION FILE:
AUR7.10



E-PHI

10 MHZ
LINEAR
SCALE

CONCORDIA EMC LABORATORY



12/14/92

Fig. 11 Three-dimensional representations of E_θ and E_ϕ at 10 MHz, with the port wire excited with 1 volt.

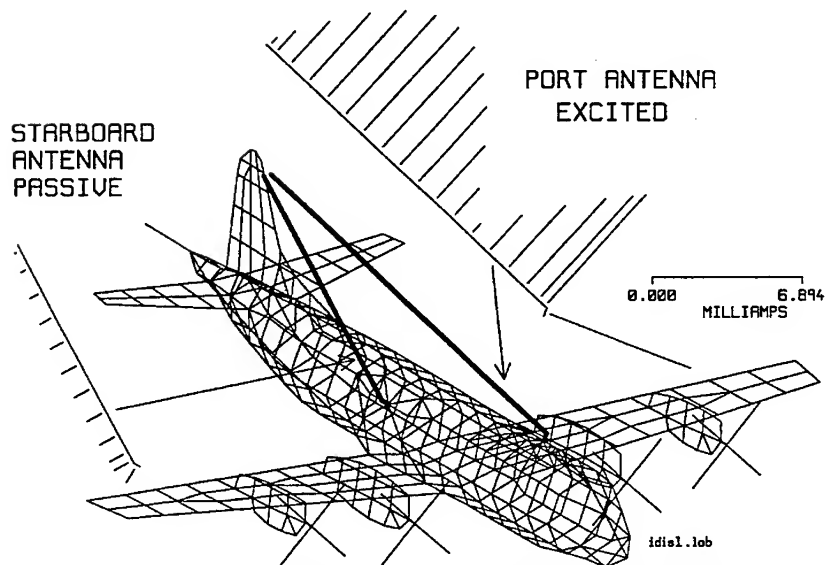


Fig. 12 The current flow on the port and starboard wires at 10 MHz, with the port antenna excited with 1 volt.

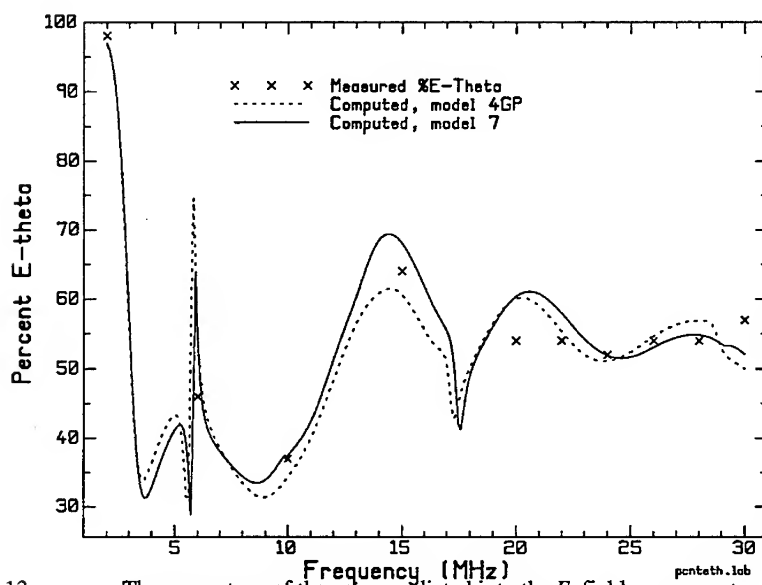


Fig. 13 The percentage of the power radiated into the E_θ field component as a function of frequency, for the port antenna.

Scientific Visualization of 3D Radar Cross Section Data

Thomas G. Wojszynski, Andrew J. Terzuoli, Jr., Martin R. Stytz
School of Engineering, Air Force Institute of Technology
Wright-Patterson AFB, Ohio 45433

Abstract – Aircraft designers, threat analysts, mission planners, and pilots require a Radar Cross Section (RCS) central tendency with its associated distribution about a specified aspect and its relation to a known threat. Historically, RCS data sets have been statically analyzed to evaluate a design or mission profile. However, Scientific Visualization, the application of computer graphics techniques to produce pictures of complex physical phenomena [1], appears to be a more promising tool to interpret this data. We describe a visualization tool to depict RCS distributions in 3D. The tool may be useful for synthesis, design, and analysis of complex targets.

1 INTRODUCTION

Numerous techniques are used to generate RCS data, both predicted (model-based) and measured. Once collected, the data must be analyzed to meet a specific design objective. For example, new military air vehicles require a reduced radar cross section to improve mission effectiveness by decreasing the probability of detection. For operational aircraft, mission planners, threat analysts, and pilots require detailed knowledge of the air vehicle's RCS and its relation to known threats to successfully plan a survivable mission route. Historically, RCS data is collected for a constant elevation angle, typically 0° , with an angular resolution of $0.1^\circ - 1.0^\circ$. The data is then displayed on a 2D polar plot as shown in Figure 1. With the current emphasis on design of low observable air vehicles and increased capability

of computers, however, designers are now collecting data at finer degrees of elevation. Designers must then mentally piece together the additional polar plots of the data set to obtain a 3D representation of the complete RCS. Our approach uses a high-power graphics workstation to render the data set. In this paper we present our methodology and the results of implementing a RCS visualization system. We first describe the input and output data set, then explain the algorithm used to create the complex polyhedron that models the 3D RCS. Finally, we present our results.

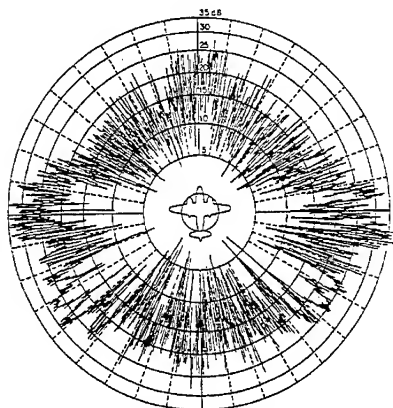


Figure 1: RCS of B-26 at 10 GHz

2 METHODOLOGY

2.1 Data Generation

To visualize a 3D RCS data set of a complex target, sufficient data must be collected. We selected Radar Cross Section-Basic Scattering Code (RCS-BSC), developed at the Ohio State University, ElectroScience Laboratory, to create the data set. RCS-BSC is a fast, simple code based on the Geometrical Theory of

Diffraction (GTD) and provides an accurate first-look of the vehicle's RCS. For a complete description of RCS-BSC, see Marhefka [2].

The input data contained a finite plate, perfectly conducting geometrical description of a modern conventional fighter. We assumed perfect symmetry about the vertical plane and selected a resolution of 0.5° in elevation and varied the azimuthal resolution proportional to the cos of the elevation angle. The data was calculated at a single frequency of 1.0 GHz. This format provided us with sufficient data to create a representative 3D model of the RCS.

The results of RCS-BSC is a series of RCS conical slices. Each slice describes the RCS for a fixed elevation angle and a varying azimuthal angle. Each description, at a particular aspect angle, contains magnitude (dB_{sm}) and phase information for H-pole, V-pole, and cross-pole returns.

2.2 RCS Construction

Since RCS prediction or measurement is a potentially time-consuming process, our tool is designed as a post-processor to create a model of the RCS. The overall approach in constructing the model is to form triangular patches between adjacent slices of data. Many triangulation algorithms fail, however, because they are based on connecting a data point on one contour to the closest point(s) on a contour of an adjacent slice [3]. If the data is completely convex and well-behaved, this approach works well; however, concave contours, such as slices of RCS data, present a problem because the closest-point strategy often fails.

Ekoule [4] proposed using the convex hull of the contour to solve this problem. Thalman [5] states that a set of points is convex if a line segment joining any two pairs of its points is entirely contained within the set. Foley [6] provides a more intuitive definition by describing the convex hull as the polygon created by stretching a rubberband around the data points. All data points are projected onto the convex hull and the hull is used for all closest point calculations as described by Christiansen and Sederberg [7]. The original list of points is used to provide the vertices of the triangles. This triangulation process is then performed over the entire data set. In traditional polar plot methods of RCS data, concentric circles are used to show relative magnitude with the radial distance indicating strength of the RCS for a particular aspect angle. We needed a similar technique to display relative magnitude in 3D. It is well known that color provides an additional visual cue for data comprehension [8] [9]. We chose a monotonically varying color scale [9] and implemented color interpolation between vertices.

3 RESULTS

The computer program was written using AT&T C++, Version 2.1, and implemented on a Silicon Graphics Iris-4D 440/VGXT. The RCS data is converted into a 3D triangle mesh and displayed on the workstation using scan-line conversion techniques [6]. Hidden surface removal is accomplished by the native z-buffer algorithm [10]. Several features were added to improve data comprehension. First, we added a target icon to orient the user with the data set. Second, we added a color scale to help the user identify potential areas of concern. Finally, we added the capability to translate, scale, or rotate the object to easily locate areas of interest.

Figures 2, 3, 4, 5, and 6 show the five views of the raw RCS data set. The radial distance shows the relative magnitude of the RCS for a particular aspect angle and provides a high degree of perceptual data comprehension. Interpolated color is added to reinforce visualization of the data. The designer could display this image and immediately recognize aspect angles of large RCS returns. Notice the small, noisy RCS values at the nose and tail of the air vehicle and the large RCS values as the viewer approaches broad-side. Notice the small lobe at approximately (0, 60) most likely caused by the shaping of the canopy.

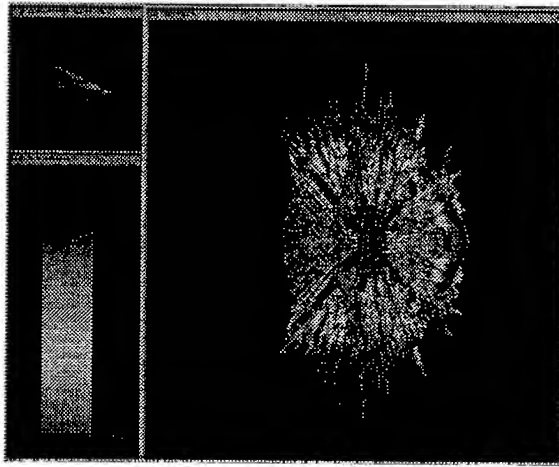


Figure 2: God's-eye view of raw data.

4 CONCLUSIONS

In this article we presented a tool that exploits the high bandwidth of the human visual system by casting 3D RCS data into a visual format. A designer can combine our tool with a CAD-based electromagnetic scattering code during the early stages of air vehicle design to easily detect potential areas of concern. The user can then make changes to the CAD model, recalculate the RCS, and redisplay the RCS in near real-time.

5 ACKNOWLEDGMENTS

Thanks to Ron Marhefka of The Ohio State University for providing the data set for this project and Dave Pond of the Air Force Institute of Technology for designing and providing the initial set of rendering tools.

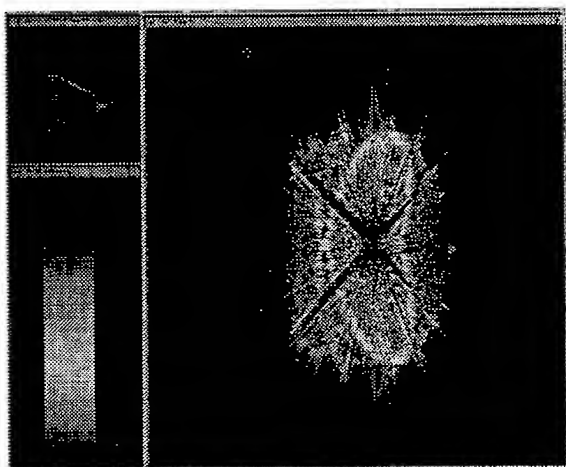


Figure 3: Devil's-eye view of raw data.

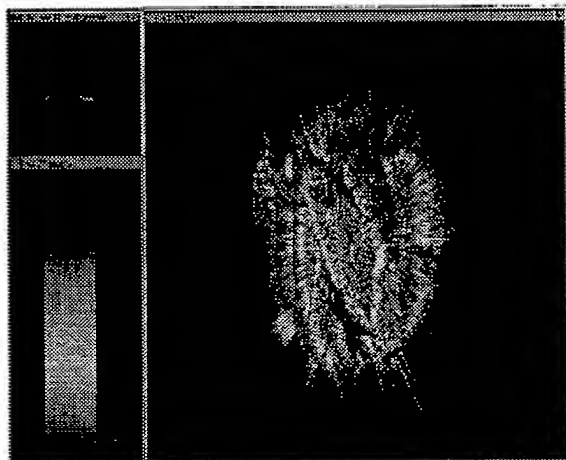


Figure 4: Broad-side view of raw data

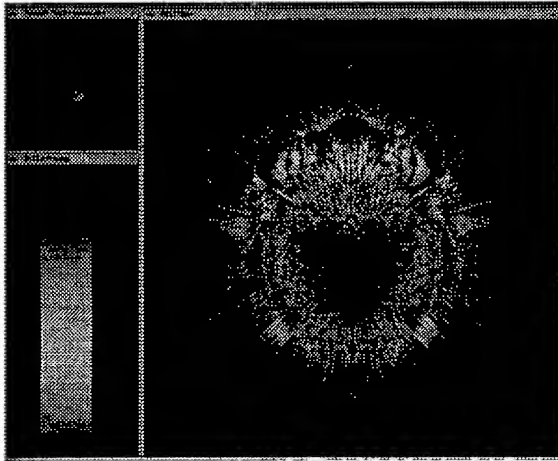


Figure 5: Nose-on view of raw data set.

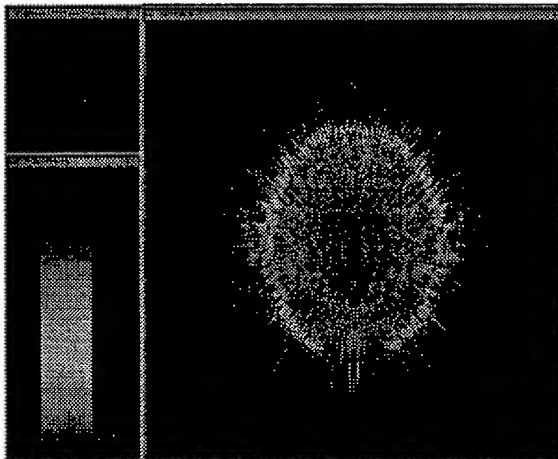


Figure 6: Tail-on view of raw data set.

References

- [1] M. Fruhauf, "Volume visualization on workstations: Image quality and efficiency of different techniques," *Computers and Graphics*, vol. 15, no. 1, pp. 101-107, 1991.
- [2] R. J. Marhefka, *Radar Cross Section - Basic Scattering Code, RCS-BSC (Version 2.0) User's Manual*. The Ohio State University, Department of Electrical Engineering, Columbus, OH 43212, 1990.
- [3] D. Meyers, S. Skinner, and K. Sloan, "Surfaces from contours: The correspondence and branching problem," *Proceeding of Graphics Interface '91*, pp. 246-254, June 1991.
- [4] A. Ekoule, F. Peyrin, and C. Odet, "A triangulation algorithm from arbitrary shaped multiple planar contours," *ACM Transactions on Graphics*, pp. 182-199, April 1991.
- [5] D. Thalman, *Scientific Visualization and Graphics Simulation*. Chichester: John Wiley and Sons, 1990.
- [6] J. D. Foley, A. van Dam, S. K. Feiner, and J. F. Hughes, *Computer Graphics Principles and Practice*. Reading, Massachusetts: Addison-Wesley, 1990.
- [7] H. Christiansen and T. Sederberg, "Conversion of complex contour line definition into polygonal element mosaic," *Computer Graphics*, vol. 12, pp. 187-192, July 1978.
- [8] P. K. Robertson, "Visualizing color gamuts: A user interface for the effective use of perceptual color spaces in data displays," *IEEE Computer Graphics and Applications*, pp. 50-64, September 1988.
- [9] C. Ware, "Color sequences for univariate maps: Theory, experiments, and principles," *IEEE Computer Graphics and Applications*, pp. 41-49, September 1988.
- [10] E. Catmull, "A hidden surface algorithm with anti-aliasing," *Proceedings of SIGGRAPH 78*, pp. 6-11, 1978.

EM Visualization on a SGI 4D Workstation

L.C. Russell, J. W. Rockway

Naval Command Control and Ocean Surveillance Center

RDT&E Division

San Diego, CA 92152-5000

Abstract

The value of high performance visualization techniques for Method of Moments modeling of electromagnetic (EM) field radiation and scattering for antennas in a complex environment is demonstrated. EM visualization was performed on a Silicon Graphics IRIS 4D/320GTX workstation. This application of high performance visualization is demonstrated for the problem definition, computation and solution description phases of the method of moments technique.

1.0 NEED FOR VISUALIZATION

Computational electromagnetics can be thought of as a three step process: problem definition, computation, and solution description. The drawback to using a computational electromagnetics code such as NEC-MoM (Burke and Poggio, 1981) is in the effort required at each of the three steps. Preparing the input model for NEC-MoM and evaluating the output can be an overwhelming task. Performing calculations can be exceedingly time consuming for all but the most simple structures.

To conserve computing resources, input models must be extensively validated before calculations are performed. Enormous quantities of output data are generated including currents and charges on all the wire segments, near field contours, and far fields. The goal of this effort was to demonstrate how advanced visualization techniques could be used to assist in input validation and rapid interpretation of output data.

2.0 VISUALIZATION TECHNIQUES

Decisions have to be made regarding how to effectively visualize the data of interest. In many cases, there were found to be several options. Often it was difficult to decide which display method would have the most utility for the final user. The products of this effort are now being used in support of ship EM design projects. This application of these tools will quantify utility.

One of the main problems encountered was in deciding how to assign color codes. Color coding is an art unto itself. It was often difficult to decide whether color coding should be done using a continuous range of colors or using a discrete set of colors.

There are three components to color. The RGB color model interprets these components as the three colors (red, green, blue) used by the CRT. By varying the amount of each color component the full range of screen colors can be achieved. The Silicon Graphics workstation has 24-bit color, with 8 bits for each component. Each component is an integer value between 0

and 255. In this manner the console is capable of displaying over 16 million different colors. Of course, it is doubtful that the human eye can distinguish all these.

Humans do not perceive colors in the same manner that the console displays them. To humans it is more intuitive to use the HSV color model (hue, saturation, and value). The HSV model is based on the intuitive appeal of the artist's tint, shade, and tone. Hue has a value between 0 and 360. Saturation and value range between 0 and 1. Algorithms exist for translating between the different color models (Foley, 1990).

At one point during this effort it was proposed that various data components could be encoded into the different components of the HSV color model. For example, for complex data the magnitude could be encoded in the hue and the phase could be encoded in the value. This idea was found to not be feasible for two reasons. First, the user becomes overwhelmed by the amount of information contained in slight variations in displayed color. Second, the color printer was totally incapable of reproducing anything but major variations in color, so one could not obtain a hard copy output of the visualization display.

For most data sets a discrete color key coding system was found to provide the most useful visualization of the data. Seven bins were chosen and the data is linearly or logarithmically assigned to the bins. The color key assignments were changed several times. A final decision was made to use colors that gave the best contrast when printed out on the color printer. Phase is displayed as a continuous range of hue, with saturation and value set to unity.

In most cases, it was found that trying to display both components (real and imaginary or magnitude and phase) of a complex data set in one image confused the user unnecessarily. A decision was made to allow the user to display complex data in side by side windows if both components needed to be viewed simultaneously.

Current data, charge data and field data are vectors. A straightforward method for displaying a vector's orientation was never developed. The current and charge vectors are defined relative to the wire's direction. User interaction indicates that the current's direction does not have as much value as the magnitude and phase of the current.

3.0 APPROACH

To perform advanced visualization decisions had to be made regarding hardware and software. The authors were fortunate to have access to a Silicon Graphics Incorporated (SGI) 4D/320GTXB. The SGI 4D/320GTXB is one of the SGI POWER SeriesTM line of computers. It can be configured with up to eight CPUs; the one used for this project has two 33MHz CPUs. It has the following performance ratings (SGI, 1991): 59 MIPS (VAX Dhrystone MIPS), 20 MFLOPS (DP Linpack 1000x1000), 41 SPECmarks. The GTXB has 48 bits color and 24 bits Z buffer. Its graphics performance is rated as 400K Vectors/sec, 150K Triangles/sec, and 100K Polygons/sec. The system used for this effort is configured with 64MB memory and a 19 inch console monitor.

Several graphics software packages were available on this SGI workstation, including PV-Wave, apE, Explorer and the SGI GL (Graphics Library). The available high level languages included C and Fortran. The Graphics Library (GL) provided the greatest flexibility in the development of the required visualization techniques. GL is a set of graphics and utility routines that provide high- and low-level support for graphics. The routines can be called from either C code or Fortran code. GL is quite primitive and yet allows one to access all the

powerful visualization capabilities of the SGIs including 3D drawing, Gouraud shading, device polling, double buffering, coordinate transformations, hidden surface removal (z-buffering), lighting, pick correlation, and texturing, depending on the hardware's capabilities. SGI provides an enormous number of demo programs that can be easily modified. GL provides a straightforward approach to developing the proposed visualization tools.

The NEC-MoM input data set is created by a program called NEEDS (Li, et al., 1988). The data set is an ASCII file in which each line represents a "card". The first two characters on each line refer to an alphabetic code that determines what the data on that line represents. For example, "CM" is a comment line and "GW" is a wire description line. The output from NEC-MoM is an enormous ASCII text file in a format that is very difficult to read from within another computer program. For that reason a parser program is needed to extract the data of interest and put it in a software readable format. A preprocessing filtering program, *filter*, was written in Fortran to put the input and output data in a form that would allow easy display of the data of interest.

4.0 VISUALIZATION PROGRAM STRUCTURE

The visualization programs were written in the ANSI C language using the SGI Graphics Library (GL) to access the visualization tools. The program to visualize the problem definition and solution description is named *view_nec*. The program evolved as feedback was received from users. However, the basic structure using multiple windows, pull-down menus, and transformations was determined from the beginning.

4.1 Windows

The beauty of working in an X-windows type environment, such as that on the SGI machines, is the flexibility it affords the user. That flexibility was retained in the development of *view_nec*. Each data component is displayed using 3D imagery in its own window. At any given moment during the running of the program the user has complete control over how many data windows are displayed as well as their sizes and locations. In addition, multiple copies of *view_nec* can be launched to do side by side comparisons of different NEC-MoM runs.

4.2 Menus

Pressing the right mouse button while the mouse cursor is within any *view_nec* window brings up a "pull-down" menu. This pull-down menu allows the user to select which data windows to open/close, which transformation is active, and whether a coordinate axis is displayed. Once a selection has been made, the affected windows are updated.

4.3 Transformations

The available transformations include rotation, translation, and zooming. Each 3D transformation is represented internally in the workstation by a 4 x 4 matrix. The IRIS Geometry Engines transform all geometric data (vertices of points, lines, and polygons) by multiplying each vertex by the accumulated matrices. In *view_nec* the transformations are actuated with the left mouse button held down and the cursor dragged across the screen.

There are three basic classes of transformations that can be carried out by the Graphics Library: projection transformations, viewing transformations, and modeling transformations. A good analogy is to a camera with a versatile lens. Projection transformations describe the type of lens on the camera. Viewing transformations determine where the camera is positioned and in

which direction it is pointed. Finally, modeling transformations affect the location, orientation, and size of the 3D geometric models in the scene.

There is often more than one way to carry out a transformation of a scene. For instance, instead of moving the camera toward the object, the object could be moved closer to the camera. However, there may be subtle differences. The transformation methods used in *view_nec* were chosen by selecting demo programs that gave the desired effect.

The zoom feature allows the user to expand a selected portion of the model for more detailed display. Zooming is achieved internally by using a projection transformation. The field of view in the y dimension is modified. This has the effect of making the scene appear closer or farther away. The aspect ratio between the field of view in x and the field of view in y, and the distances to the near and far clipping planes are kept constant.

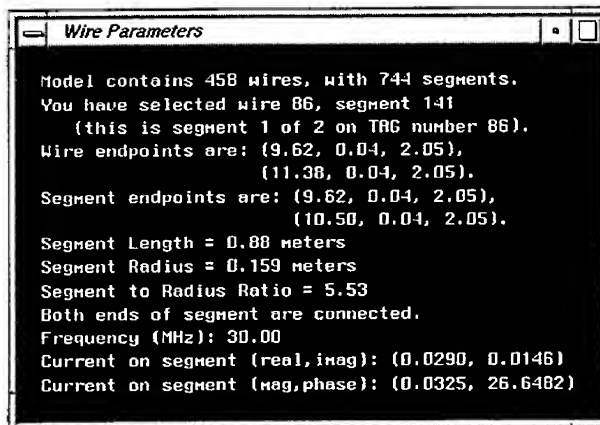
The rotate feature allows the user to rapidly change the orientation of the model. This permits a better feeling for the three dimensional nature of the model and often allows various features of the data to become more apparent. Rotation of the scene is carried out internally using a viewing transformation to move the viewpoint. The distance from the origin is kept constant while the azimuthal angle in the x-y plane and the incidence angle in the y-z plane are modified. This is akin to moving the camera over a spherical surface surrounding the scene.

Translate allows the user to move the model up/down or left/right in the plane of the screen. This shifts the origin and is useful before zooming in on a selected portion of the model. Translation of the scene is carried out internally using a modeling transformation. The program is set up to only allow translation of the object in the plane of the screen. The size of the object is preserved.

4.4 Pick Correlation

It quickly became apparent that a method was needed to selectively choose a single element, such as a wire segment, from the 3D wire object display. This was needed for troubleshooting as well as linking the display back to the NEC-MoM input data set. The middle mouse button was chosen for this purpose. The technique used is known as *pick correlation*. The Graphics Library provides this capability.

Pick correlation identifies objects on the screen that appear near the mouse cursor. Information about these objects is stored in a buffer. *view_nec* uses this information to allow the user to select a single wire segment from the object displayed and list all information about it. A sample wire parameters window is shown below.



Wire Parameters Window

5.0 VISUALIZATION OF METHOD OF MOMENTS

5.1 Problem Definition

The NEC-MoM input file describes the modeled object (such as a ship) as a collection of wires. At this time *view_nec* does not recognize patches. The description of each wire includes: a tag number (for identification purposes), the number of segments on the wire, the (x,y,z) coordinates for both the beginning and end points, and the radius of the wire. Some wires are tapered and so extra information is given for these wires to describe the tapering.

There are four windows that can be opened up to display the model's input geometry. The windows each display one of the following: Wire Segmentation (segment length in meters), Wire Radius (in meters), Segment to Radius Ratio, or Wire Connectivity (none, one, or both ends connected). All of these windows display the model as a 3D wire object. The data is encoded in the color of each wire segment using a linear or logarithmic color assignment scheme. A color key is displayed in the lower left corner of the window.

5.2 Computation Visualization

There has been some speculation that visualizing the method of moments matrix that has been extracted from NEC-MoM might give some insight into the validity of the wire model being used. A Graphics Library program, *view_mom*, was developed to allow display of almost any size method of moments matrix. Its structure is similar to that of *view_nec*, but it is quite a bit simpler.

view_mom allows the user to bring up two different windows. The first window has the data displayed as a 3D surface with the vertical offset and color proportional to the logarithm of the magnitude of the data. The second window is similar except it has the color proportional to the phase of the data. Each window allows the surface to be rotated, translated, and zoomed just as in *view_nec*. The right mouse button brings up the menu. The left mouse button performs the transformations. The middle mouse button performs a pick correlation that allows the user to select a point on the matrix. After a matrix point has been picked an information window

appears in the lower left corner of the console screen. This information window describes the matrix and gives information about the selected point. Included in this information are the row and column number of the point.

5.3 Solution Description Visualization

Many different solution description products are available for display. The visualization products include currents and charges on the wires (real component, imaginary component, magnitude, or phase), total near field, z-component of near field, theta component of far field, and phi component of far field.

5.3.1 Currents and Charges

Currents and charges on the wires are displayed using the same technique as was used for the geometry description products: current and charge are color coded on a 3D wire display of the model. Again, both linear and logarithmic color codes are available. Since currents and charges are complex, each has four different data windows that can be displayed: real component, imaginary component, magnitude, and phase. Most users have found the magnitude window to be most useful.

5.3.2 Near Fields

NEC-MoM allows the user to calculate the near field at selected locations around the model. These locations are usually defined by a 3D grid surrounding the model. The near field is a complex vector. Of most interest is the z-component since this will be the component that is most closely associated with hazards.

Several techniques were evaluated for displaying the near field data points. The most popular was the "fog" technique. *view_nec* displays near fields using a "fog" technique in which the density of activated pixels in the image is linearly proportional to the field intensity at the nearest calculation point. Since the calculation points usually form a 3D grid the image contains square blocks of fog varying in density with the field intensity. The fog is also color coded in a manner similar to that used for the geometry description products. The 3D wire model is drawn using a dark gray color so as not to detract from the near field display.

The near field windows have a thresholding capability. By clicking in the window with the middle mouse button the user is able to selectively change the threshold at which the fields are displayed. This allows the user to quickly determine what areas surrounding the model have fields above a particular cutoff level. The user can select any of the color key bin levels, HERP (Hazardous Electromagnetic Radiation for Personnel), or HERO (Hazardous Electromagnetic Radiation for Ordnance) for the threshold. HERP and HERO are functions of the radiation frequency. The near field windows display the value of this frequency.

5.3.3 Far Fields

There are two windows available for the display of far fields. These windows allow the user to display either the theta component or the phi component of the far electric field. The far field is complex data. This makes display of it somewhat complicated. A method of displaying both the magnitude and phase simultaneously was sought. The selected method involves displaying the fields as a three-dimensional surface. The distance from a point on the surface to the origin is proportional to the field magnitude at that point. The color at the point is determined by the phase of the field at that point. Gouraud shading is used between points to transition the color.

6.0 OBSERVATIONS

During this project the authors learned a great deal about visualization techniques and limitations. One observation is that as more and more features are added to a piece of software, the user interface becomes the limiting factor in the utility of the program. Present efforts are directed toward providing a graphical user interface into *view_nec* and *view_mom*. Another observation is of the limits of hard copy devices such as the color printer that was attached to the SGI. Although it was a very high quality printer, it was extremely limited in its ability to faithfully reproduce the hue, saturation, and brightness displayed on the console. Subtle differences in hue could not be discerned, and saturation variations were washed out. Finally, without viewing the actual SGI display it is difficult to provide an understanding of the power of the EM visualization on a SGI 4D workstation. However, video making capability is available with the SGI. This is the only way to properly demonstrate the utility of the visualization products that were developed.

REFERENCES

- Burke, G. J. and A. J. Poggio. 1981. "Numerical Electromagnetic Code (NEC) - Method of Moments," NOSC Technical Document 116, Naval Ocean Systems Center (January), San Diego, CA.
- Foley, J. D., A. van Dam, S. K. Feiner, J. F. Hughes. 1990. *Computer Graphics: Principles and Practice*, Second Edition, Addison-Wesley Publishing Company, NY.
- Li, S. T., J. C. Logan, and J. W. Rockway. 1988. "Ship EM Design Technology," *Naval Engineers Journal*, May.

WinGAUGE

Graphical Aids for the Users of GEMACS for the Windows Environment

Jeffrey A. Evans
Decision Science Applications, Inc.
1300 Floyd Ave.
Rome, NY 13440

Phone: (315) 339-6184 FAX (315) 339-6923

Introduction

This paper describes the new Microsoft Windows based graphical interface program for GEMACS, WinGAUGE. WinGAUGE provides an intuitive menu and toolbar design for an analyst to use in building electromagnetic models.

WinGAUGE (Graphical Aids for the Users of GEMACS for Windows) is a Microsoft Windows application that provides the electromagnetic (EM) analyst a tool for building, modifying and displaying complex electromagnetic models (Method of Moments (MOM), and Geometric Theory of Diffraction (GTD)) for use by the General Electromagnetic Model for the Analysis of Complex Systems (GEMACS). WinGAUGE also provides a method for displaying currents induced on the wire segments of the geometry. WinGAUGE produces GEMACS ready geometry files and is compatible with GEMACS Versions 4.0 and up.

The standard features of WinGAUGE include:

- | | |
|--|--|
| <input checked="" type="checkbox"/> Standard Windows Menus | <input checked="" type="checkbox"/> True 3-Dimensional Geometry Displays |
| <input checked="" type="checkbox"/> Mouse and Keyboard Interfaces | <input checked="" type="checkbox"/> Hybrid Model Generation |
| <input checked="" type="checkbox"/> Multiple Views of the Geometry | <input checked="" type="checkbox"/> On-Line Help for all Commands |
| <input checked="" type="checkbox"/> Hidden Surface display | <input checked="" type="checkbox"/> Easy Installation |
| <input checked="" type="checkbox"/> GEMACS File Formats | <input checked="" type="checkbox"/> Full Documentation and Tutorial |

User Interface

The WinGAUGE user interface follows the IBM Common User Access (CUA) Advance Interface Design Guide specifications for Window applications. WinGAUGE follows the specification as closely as possible, particularly in the design and function of the menu system, dialog boxes, and keyboard control. Figure 1 shows WinGAUGE as it appears on the Windows screen.

Title Bar

The WinGAUGE title bar shows the name of the application, WinGAUGE.

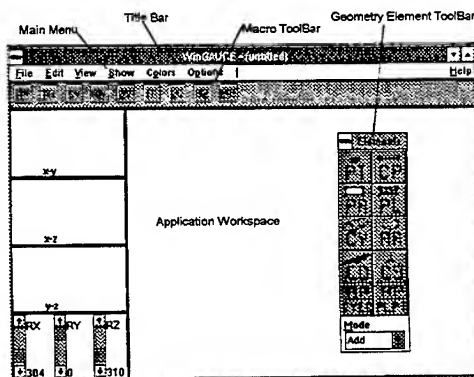


Figure 1 WinGAUGE Interface

It will also display the name, if any, of the current geometry file being used/edited.

Main Menu Bar

The WinGAUGE menu has been designed to allow a logical progression through the steps necessary to generate and display GEMACS geometries. Each menu and menu item has an appropriate keyboard shortcut defined.

Macro ToolBar

The WinGAUGE macro toolbar is just below the main menu and is used to perform global operations on the geometry. Each macro command has an appropriate keyboard shortcut defined.

Geometry Element ToolBar

The WinGAUGE geometry element toolbar is a floating dialog box. This toolbar allows the user to add, edit or delete GEMACS geometry elements. The user can also use the scroll bars at the bottom of the toolbar to rotate the model on the screen. Each geometry command has an appropriate keyboard shortcut defined.

Application Workspace

The Application Workspace is a background where the graphics display is generated with titles and legends. The workspace is normally divided into 4 drawing windows and a rotation bar window in the lower left hand corner. The main window dominates the workspace and is the view that is used in all editing operations. The three smaller drawing windows on the left side of the workspace are the planar projections of the geometry. They include X-Y plane on the top, X-Z in the middle and Y-Z on the bottom. They are always labeled for reference.

The scroll bars in the rotation bar window are used to dynamically change the viewing angle for the main drawing window. Each of the three scroll bars controls one of the three viewing axes.

Main Menu

This section describes the functions performed by each menu item in the WinGAUGE menu bar. Menu items leading to a dialog box are followed by an ellipsis (...). Basic functional operation of the dialog boxes follows CUA. A detailed description of Dialog box operation can be found in the Windows Manuals. Every menu item can be invoked by a keyboard shortcut consisting of two keystrokes: one to select the menu and the second to select the menu item. The first keystroke is modified with the Alt key; the second is not. The keystrokes required to execute the keyboard shortcut are specified in this document and in the software with an underscore. For instance, File Open is invoked with the key sequence Alt-FO. In addition to keyboard shortcuts, some menu items may be invoked with a single keystroke called an accelerator. Keyboard accelerators are specified in parentheses after each menu item that has one.

File

The File menu of WinGAUGE, Figure 2, provides items to start a new editing session, read in an existing model, merge a model from disk with the one in memory, save the geometry in memory to disk, printing the main drawing window and printer setup. The exit menu item also appears in this menu.

File	
New...	
Open...	Ctrl+F12
Merge...	
Save	Shift+F12
Save As...	F12
Print	Ctrl+Shift+F12
Printer Setup...	
Exit	Alt+F4

Figure 2 File Menu

WinGAUGE uses the common dialog boxes for file open and file saveas provided by the Microsoft Windows Software Development Toolkit. This reduces the need to remember drastically different commands from one Windows application to another.

Edit

The Edit menu, Figure 3, gives the user options for copying portions of the geometry display to the Windows clipboard. Selecting the copy menu item places a bitmap copy of the main drawing window into the Windows clipboard. This bitmap can then be copied into any other application that supports bitmap graphics. Selecting the copy-4 menu item will place a bitmap copy of all 4 drawing windows, and the rotation bar widow if active, into the Windows clipboard for further use. As an example all of the geometry graphics in this paper were created in this manner.

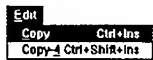


Figure 3 Edit Menu

View

The View menu shown in Figure 4 gives the user options for changing the display of the geometry. It allows the user to set controls to specify exactly how a model is viewed on screen. The 4-view menuitem is a toggle to turn the 3 planar views off or on. A check mark signifies they are being displayed. The Zoom-In and Zoom-Out menu items give the user a chance to select a portion of the geometry in the main drawing window to view more closely or go back to a full display of the geometry. The next 4 menu items set how the geometry will be displayed in the main drawing window. The Rotation Bars menu item is a toggle to remove the rotation bar window from the display to give more room for geometry display. For those who are comfortable with pitch and yaw rotations the last menu item provides a vertical scroll bar (pitch) and a horizontal scroll bar (yaw) in the main drawing window to change the viewing angles of the display.

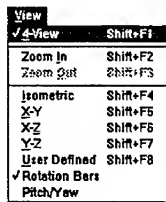


Figure 4 View Menu

Show

"Show/no-show" can be used to partition the model in various ways. Each geometric entity can be in either 'show' or 'no-show' status. Only that portion of the model which is in show status is displayed on the screen. Some other options -- skeleton, translate/rotate, reflect, save -- act only on the geometry in show status.

The different ways of selecting a portion of the model under control of the "show/no-show" option are indicated in the show menu, Figure 5. Each menu item is explained individually under separate subsections. When some of these options are chosen, a further dialog box is presented to determine the status of the selected geometry.

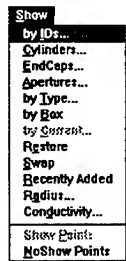


Figure 5 Show Menu

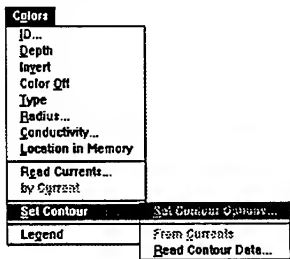


Figure 6 Colors Menu

Colors

WinGAUGE is capable of color coding the elements in several ways as shown in the menu below, and display the color plot on the screen. The Colors menu, Figure 6, gives the user options for setting different color schemes in which to plot the geometry.

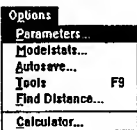


Figure 7 Options Menu

Options

The Options menu, shown in Figure 7, gives the user various global options for working with WinGAUGE. The parameters option is identical to the DOS GAUGE and provides plate and polygon labeling, hidden surface display, shrink plots, etc. The Modelstats option shows the contents of the model database. Autosave is used to set a frequency for automatically saving the model in memory. The time is user selectable. The tools option turns on and off the Geometry toolbar which is described later in the paper. The find distance option gives the user a dialog box to find the distance between any two points in the geometry. Lastly the calculator option pops up the Windows Calculator for manual calculations when building a model.

Help

WinGAUGE help is provided via the help menu, Figure 8, using the standard Windows help system. When help is displayed, a help window is created with help navigation commands available at the top, with navigation icons immediately below. The main body of the window contains the help text itself.

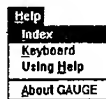


Figure 8 Help Menu

Geometry Toolbar

The WinGAUGE geometry toolbar is a set of custom push buttons in a floating dialog box that can be turned on or off via the options menu. These buttons are used for adding, editing or deleting GEMACS geometry elements during an editing session. Figure 10 shows the geometry toolbar.

From the top left corner of the tool bar going left to right and then down the buttons correspond top the GEMACS point card (PT), connect point (CP), patch (PA), plate (PL), cylinder and endcaps (CY), radius card (RA), conductivity card (CO), coordinate system cards (CS), and finally the bottom two buttons provide the four different types of aperture cards: aperture on a cylinder; aperture on an endcap; aperture on a plate and; aperture defined by points.



Figure 9 Geometry Toolbar

The mode drop down list box at the bottom of the toolbar show the editing mode the program is in. In the add mode dialog boxes will be displayed for a user to enter data for a given geometry element to add it to the model being built. In the delete mode a list of elements of the type selected from the buttons will be displayed in a dialog box along with an empty deletion list. The user then selects elements from the data list to build a deletion list once complete the user accepts the list and those elements are deleted. The edit mode allows the user to change point coordinates, plate normals and conductivities and wire radius values.

Figure 10 shows an example of the add point dialog box that is presented to the user from the geometry tool bar. The user enters the id number and the coordinates and selects OK to enter the point and exit the dialog or Apply to enter the point and

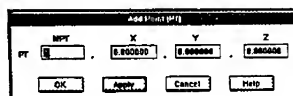


Figure 10 Add Point Dialog Box

remain in the dialog to enter another or selects Cancel to exit the dialog without entering the point.

Macro ToolBar

This section briefly describes the functions performed by items in the WinGAUGE macro toolbar. Figure 11 shows the buttons that are available on the toolbar. The operations are considered macro items because they operate on sections of the geometry rather than generating single geometry items as the geometry toolbar does. The operations/buttons include: Reflect (RF); Translate/Rotate (TR); Convert (CV); Renumber (RN); Delete by Volume (DV); Integrity Checking (IT); Lines and Curves (LC); Bezier Curves (BZ); and the Model Editing (ME).



Figure 11 Macro ToolBar

The following set of figures show an example of the reflect macro dialog box and the result of a reflection operation on one half of a truck geometry.

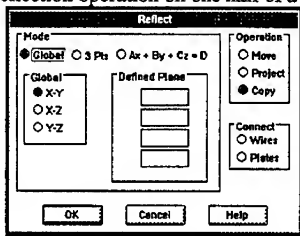


Figure 12 Reflect Macro Dialog Box

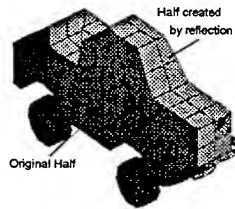


Figure 13 Reflected Truck

The next five figures show examples of other macro operations that are available in WinGAUGE. Each of the macros has many different options available to give it as much power as possible to reduce the workload of the analyst that is building or modifying the geometry.

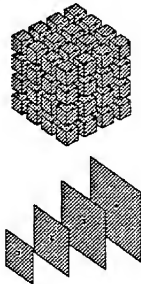


Figure 14 Translated Cubes and Translated and Scaled Plates

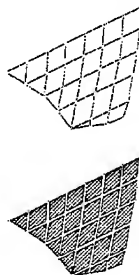


Figure 15 Converting Geometry elements, Wires to Plates

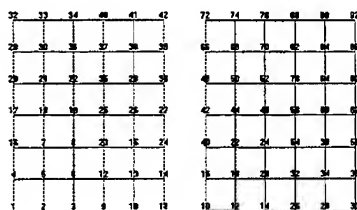


Figure 16 Renumbering Wires



Figure 17 Lines and Curves



Figure 18 Bezier Curve

In addition to the original DOS GAUGE macro functions two macro operations were incorporated into WinGAUGE from the program MODELED. These are the integrity checking capability and the mesh refinement/generation capability. The dialog boxes for these two macro options are given below.

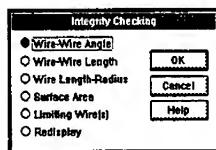


Figure 19 Integrity Checking Dialog Box

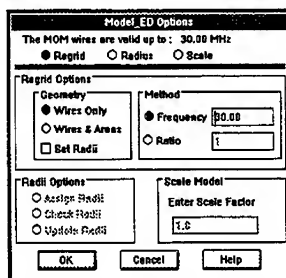


Figure 20 Model Editing Dialog Box

The integrity checking dialog box gives the user a chance to ensure that various aspects of his model fall within electromagnetic modeling guidelines. The ModelEd dialog box allows the user to take an existing MOM model and regrid it via a ratio or frequency based method. Other options include ensure wire radius values are valid and scaling the geometry by a user entered value.

GEMACS Commands Interpreted by WinGAUGE

WinGAUGE can read a subset of the GEMACS geometry command set. These commands are summarized in the following list. Additions and changes to the list over the DOS based GAUGE include adding the multiple point (MP), and wire (WR) cards of GEMACS and allowing multiple segments on any of the wire cards.


```

PT ID x y z
COND  $\sigma_1$   $\sigma_2$  ...  $\sigma_n$ 
RA r1 r2 r3 ... rn
CP p1 p2 NSEG ID NRAD
MP # of points(n) p1 p2 ... pn NSEG ID NRAD
WR x1 y1 z1 x2 y2 z2 NSEG ID NRAD
PL ID # of corners(n) p1 p2 ... pn c_ID
PA # of corners(n) p1 p2 ... pn ID
CS NCS xc yc zc rx ry rz
CY ID xr yr len NCS
EC ID  $\pm$ cyl_ID  $\theta$   $\phi$ 
AP ID CY cyl_ID dl g b z1 z2  $\phi_1$   $\phi_2$ 
AP ID EC endcap_ID dl g b r1 r2  $\phi_1$   $\phi_2$ 
AP ID PL plate_ID dl g b # of corners(n) p1 p2 ... pn

AP ID PT area g b  $\begin{cases} CY \\ EC \\ PL \end{cases}$  element_ID # of points(n) p1 p2 ... pn

```

Figure 21 GEMACS Card Formats Read by WinGAUGE

Differences between WinGAUGE and DOS GAUGE-GP

The following table summarizes some of the key differences between the Windows version of GAUGE and the original DOS based version.

WinGAUGE	DOS GAUGE-GP
variable up to 3000 Points and Polygons	fixed at 1500 Points and Polygons
Automatically updated 4-View drawings	Single updated view
Hardcopy via any Windows Printing Device	Dot Matrix and Laserjet Screendump
Copy image to Windows Clipboard to paste to other applications	N/A
Run Simultaneously with other programs	N/A
Dynamic Allocation of memory	N/A
GEMACS MP and WR cards interpreted	Not implemented
Automatic mesh generation and integrity checking built in to the program	Separate module for mesh generation and integrity checking (MODELED)
Able to directly export models to other CAD data formats	Export of data not supported.

Another key difference between WinGAUGE and the DOS GAUGE is the speed of WinGAUGE reading, saving, hidden surface calculations, etc. is extremely faster. This is due to the use of optimized C functions for sorting, graphics and file handling. The user then is not wasting time waiting for a screen refresh or file operation from WinGAUGE.

Availability

WinGAUGE was developed by Decision-Science Applications, Inc and is being distributed commercially. Anyone interested in ordering a copy of the code can contact the author. Government approval is still required for receiving the code.

***NECDRAW* for 3-D Images of NEC Wire Grid Models**

Ron Bardarson and Robert Just

ESL/TRW
Sunnyvale, California
ronb@antlab.esl.com

Summary

IBM PC program *NECDRAW* provides a three dimensional image of a NEC wire grid model which is rotatable and scalable under user control. Individual segments and wire junctions are identifiable. The NEC validity tests of program *CHECK* have been included, with test failures shown as colorized segments for easy identification. *NECDRAW* is available under the shareware concept for IBM DOS programs.

Introduction

The usefulness of graphical aids while constructing NEC [1] wire grid models has been shown in recent ACES Symposiums and publications. With few exceptions, most of these aids have existed on computer platforms other than the ubiquitous IBM PC. We created a version for our UNIX system some years ago. Due to a recent completion of a 3 dimensional graphics library for the IBM similar to our UNIX package, an opportunity existed to port the *NECDRAW* concepts to the IBM and simultaneously expand it. An IBM PC has two major advantages over mainframes for this application, very fast graphical displays and a larger palette of colors.

Using the NEC Output File

Previous programs similar to *NECDRAW* have used a NEC input file to generate their displayed geometry. *NECDRAW* uses the NEC output file for one reason. Unless NEC code has been bodily moved into a graphics program, the validity of the graphics program geometry engine is open to question, especially when the duplication and rotation/translation cards are considered. With geometry code in two programs, code maintenance or updating is more complex and costly. By simply inserting a segment

loading card that references a non-existent segment, NEC will abort further computations and provide the user with the full geometry of the wire grid model in the output file. *NECDRAW* users utilize this trick in initial model checks. Since segment current plotting is planned for *NECDRAW*, the NEC output file must be read at some point after the geometry has been settled.

CHECK tests

Program *CHECK* [2] tests a NEC wire grid for computational validity. Since that is part of the model generation process, the *CHECK* wire and junction tests have been incorporated into *NECDRAW*. Failures of these tests are displayed to the user and in an optional error logging file. The tests only occur when the user issues a command for the desired test.

NECDRAW Commands

A command listing from the help file follows the parameter definitions. The reference axes for translation or rotation are fixed with respect to the view, not the displayed wire grid model. The user can display the models axis reference with the *gr* command. Toggles implies the alternation between an on and off state.

Axis	is x, y, z, or a for all axes (used in scaling).
Angle	is a numeric quantity in degrees.
Scale_factor	is a numeric quantity.
Trans_factor	is a numeric quantity in meters.
Frequency	is a numeric quantity in Megahertz.

TRANSLATION, ROTATION AND SCALING COMMANDS

tr Axis Trans_factor	Moves model along axis by Trans_factor.
ro Axis Angle	Rotates model around Axis by Angle.
sc Axis Scale_factor	Scales model along Axis by Scale_factor.
<CR>	Repeat last tr, sc or ro command.
re	Returns model to initial view.
un	Undo last tr, sc or ro command.

MISCELLANEOUS COMMANDS

3d	Toggle 3 dimensional segments.
cl	Clears command history listing.
cu Frequency	Toggle frequency's segment current colors.
ep Segment_Number	Displays the segment endpoint coordinates.
gr	Toggles model reference grid.
he	Command reference help.
ma	Toggle markers at segment ends.
nu	Toggle segment numbers.
qu	Quit.
rf	Refresh screen.
ta	Toggle tag numbers.

WIRE MODEL VALIDITY TOGGLES

sl	Segment length check.
sr	Segment radius check.
rr	Segment length to radius ratio check.
sa	All of the above segment checks.
jc	Unconnected segment junction check.
jl	Segment junction length ratio check.
jr	Segment junction radius ratio check.
js	Segment junction length to radius ratio.
ja	All of the above junction checks.

Examples

Figures 1 through 4 are simple examples of *NECDRAW* with a helical antenna. The NEC output file was edited to cause the radius changes shown in figures 2 and 3 in order to verify the segment and junction tests. Figures 1 through 3 are snapshots of a single command stream, while figure 4 is a second command stream. These plots are printed from screen captures on an ink jet printer, the video display has higher resolution.

Availability

NECDRAW will be released as shareware. This is a 'try-before-you-buy' concept used by single programmers to distribute their efforts at low cost. If you decide that the program has value for you, then you are expected to

contribute a nominal sum. The IBM version of *NECDRAW* has been produced solely from unsupported efforts at home. Updates are expected based on user feedback, but as with all shareware, cannot occur in a rapid fashion. At this writing in January, *NECDRAW* is still in beta test but a version is expected to be available at the 93 ACES Symposium Interactive Forum Session. Afterwards, *NECDRAW* will be available through one of the large FTP file servers (SIMTEL20 or it's mirrors) and the IBM BBS network.

Bibliography

- [1] G.J. Burke and A.J. Poggio, "Numerical Electromagnetics Code (NEC) -- Method of Moments," UCID-18834 Lawrence Livermore Laboratory Report January 1981.
- [2] C.W. Trueman and S.J. Kubina, "Verifying Wire-Grid Model Integrity with Program 'CHECK'," Vol. 5, No. 2, Applied Computational Electromagnetics Society Journal Winter 1990.

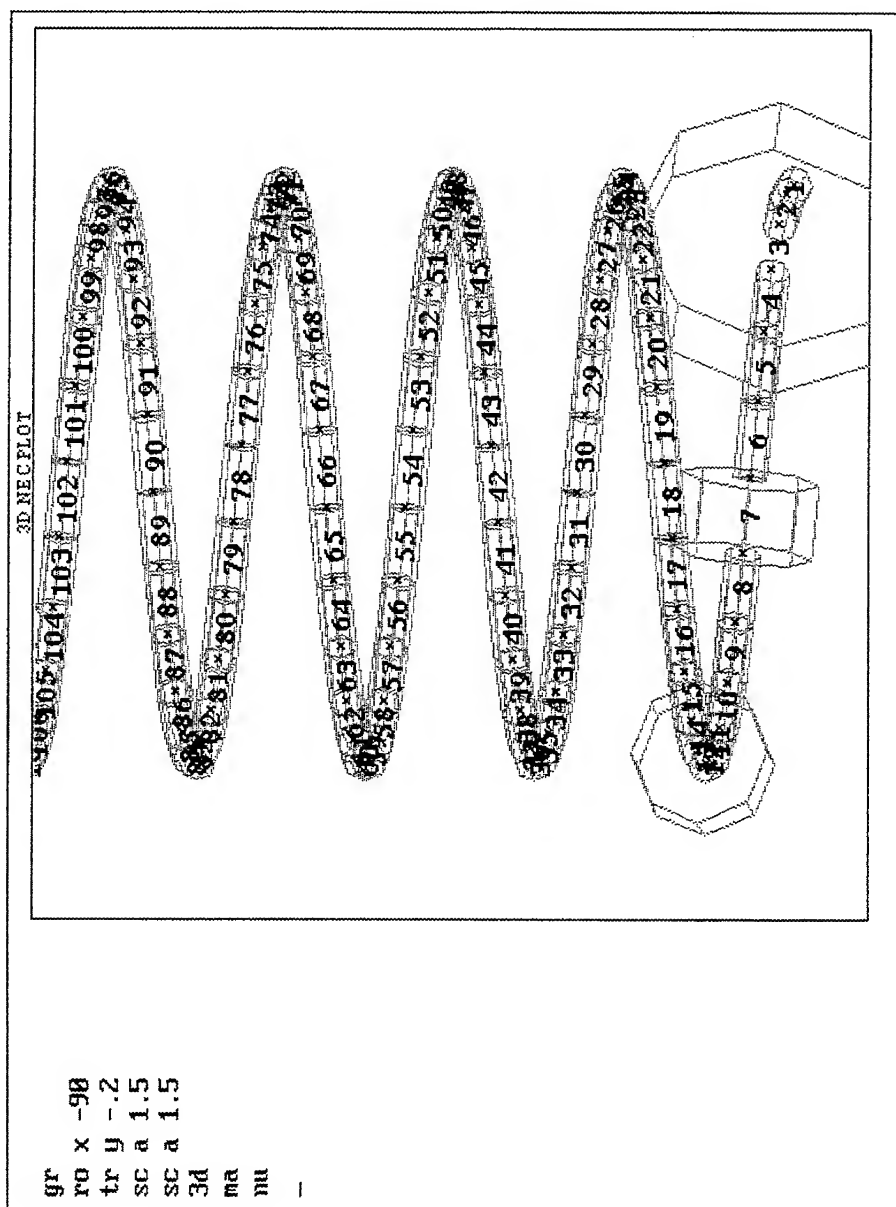


Figure 4

3D NECPLOT

```
ro x 98
ro x 98
ro x 98
ro x 45
ro y 45
gr
gr
tr x -.3
tr x .1
tr x .1
tr y -.1
sc a 2
sc a .75
gr
-
```

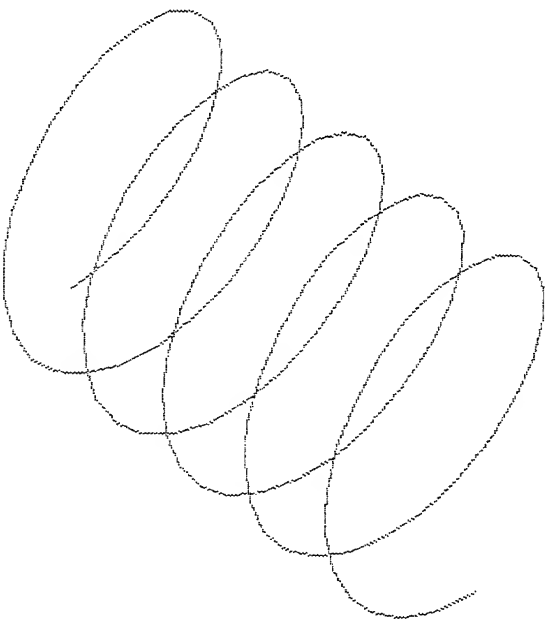


Figure 1

3D NECPLOT

```
ro x 90
ro x 90
ro x 90
ro x 45
ro y 45
gr
gr
tr x -.3
tr x .1
tr x .1
tr y -.1
sc a 2
sc a .75
gr
3d
-
```

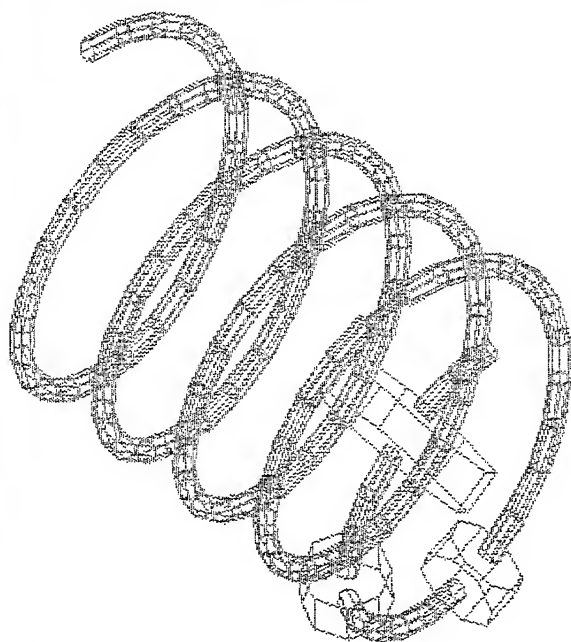


Figure 2


```

r0 x 45
r0 x 45
r0 x 45
r0 x 45
r0 x 45
r0 y
ma
ma
ma
ma
nu
ma
ma
3d
sc a 2
sc a 2
-

```

3D NECPLOT

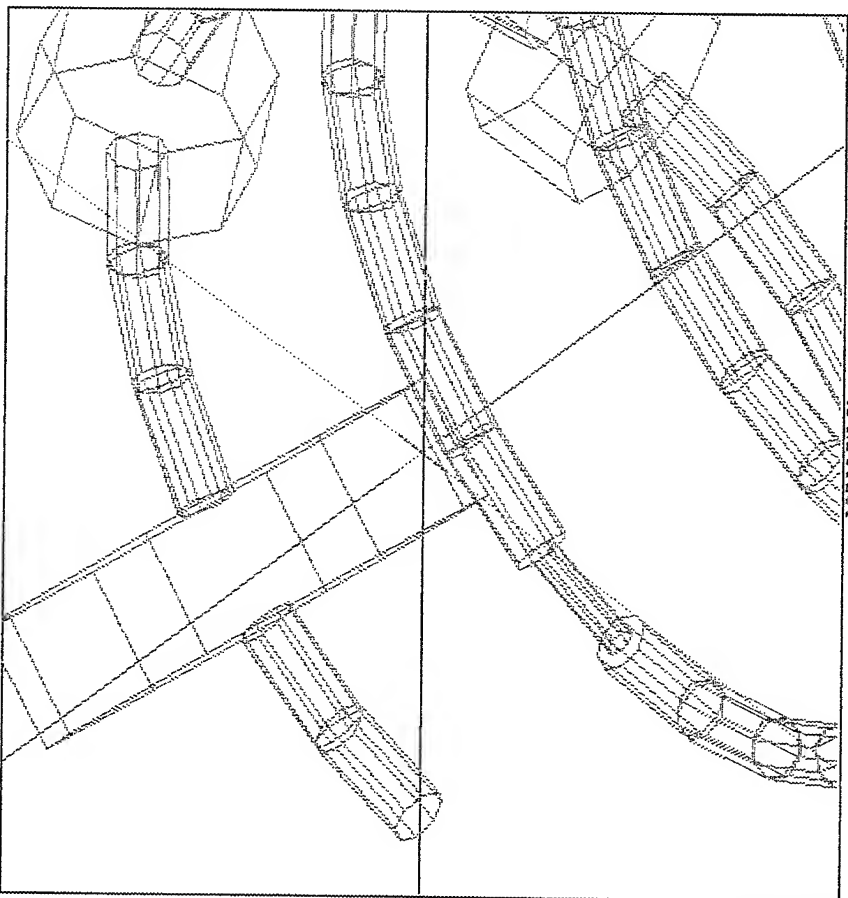


Figure 3

GRAPHICAL SHELL FOR NUMERICAL ELECTROMAGNETICS CODE

by M.J. Packer, R.A. Powers, A.P. Tsitsopoulos

Science Applications International Corporation
Communication Engineering Laboratory
300 Nickerson Road, Marlborough, MA 01752
(508) 460-9500

Abstract

SAIC is currently developing a Windows™-based graphical shell for Numerical Electromagnetics Code, (NEC). The shell, designed for the USAF's Foreign Aerospace Science and Technology Center under a contract with Rome Laboratory, provides a graphical NEC Pre-processor, an unmodified version of NEC, and a data post-processor. The pre-processor is a custom-tailored wire definition/drawing package with the look and feel of a typical Windows™ vector-based drawing package. It enables the user to create, view, and edit a 3-D representation of the antenna structure, as well as control antenna excitation. Extensive error checking is performed before NEC execution, identifying most model definition errors. Data post-processing capabilities presently include color coded current intensities superimposed on the model's geometry, and user specified radiation patterns in polar format. This package is fully compatible with existing NEC-compatible antenna models and NEC-generated output files for NEC versions 2, 3, and 3i.

The package runs on the 80386/486 PC architecture with Windows™ 3.0 or higher running in enhanced mode. This platform configuration allows multi-tasking, so NEC can be executed in a background mode while other Windows™ applications are also running. In addition, all of the typical Windows™ features are available. This includes the ability to view several 3-D antenna structures and/or output plots concurrently within one instance of the shell. The ability to print is also provided.

Introduction

Advances in applied electromagnetic algorithms over the last few decades have made it possible to predict the performance of virtually any type of antenna structure. These rigorous, time-intensive, algorithms have, however, traditionally required the speed and processing power of main-frame computers. As a result, personal computers (PCs) have been restricted to simpler, less-accurate, closed-form solutions. Now, due primarily to recent technological advances in computer architectures, rigorous algorithms can realistically be solved on a PC as well.

One example of a resource intensive electromagnetic (EM) algorithm that has recently been ported over to the PC is The Numerical Electromagnetics Code (NEC) [1,2]. NEC is recognized as a gold-standard in moment method (MM) [3] codes and is used for predicting the performance of antennas less than a few wavelengths in size. Its core computation is the current distribution on a segmented wire/patch model. Computational time is directly related to the

electrical size and segmentation of the antenna model. NEC, like most text-based engineering tools, is user unfriendly and requires extensive knowledge and experience to be used correctly and effectively.

In the past, several government and commercial agencies have produced user-friendly interfaces for NEC. SAIC developed its first DOS-based NEC pre- and post-processors in 1982, each having extensive use and continuous improvement. In 1991, SAIC started development of a Windows™-based graphical shell for NEC under a contract with Rome Laboratory for the USAF's Foreign Aerospace Science and Technology Center. The shell consists of a customized antenna definition/drawing processor and a data post-processor. It is intended to be used for antenna analysis targeted at both novice and experienced EM engineers. Because of the anticipated broad range of user experience, the shell was designed to support all of NEC's sophisticated antenna analysis features while also being intuitive enough to mitigate the most common deficiency of NEC, i.e., user error.

Errors in antenna modeling can result from computer limitations, algorithms and implementation of algorithms, and defining the antenna model. While PCs may not have the processing power of main frame computers, advances in the PC architecture and programming techniques support large matrix inversions required for MM solution. The MM algorithm and its implementation in NEC have been independently validated by many organizations and found to provide accurate antenna predictions. The one remaining error source is due to the user and his/her ability to create error free antenna models which are compatible with NEC. Therefore, SAIC's NEC graphical shell includes a 3D antenna drawing package to help the user visualize the model, error checking, and user-friendly dialog boxes to accurately specify NEC control parameters. These features allow an inexperienced user to climb the NEC learning curve at an accelerated rate.

Graphical Shell

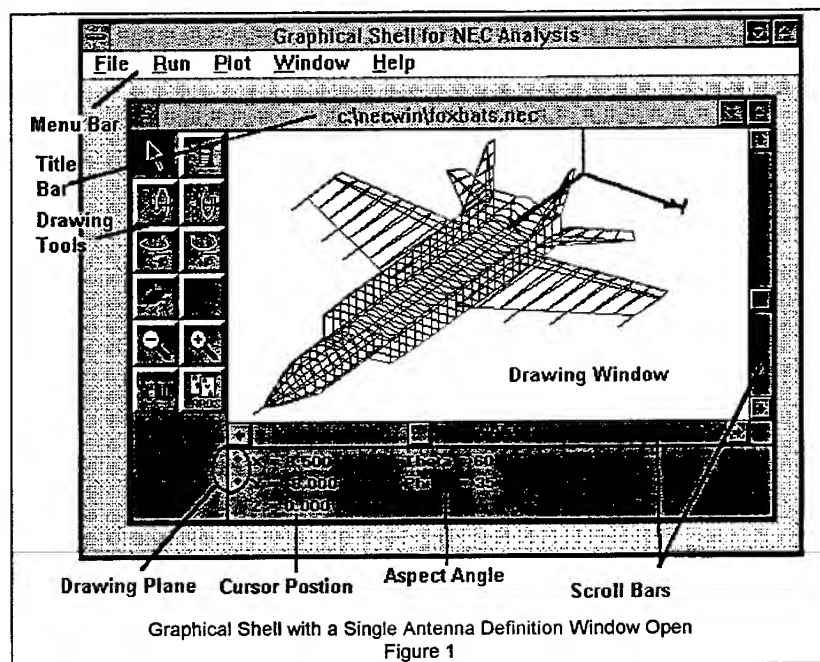
The graphical shell runs on an 80386/486 PC with Windows™ 3.0 or higher in the enhanced mode. The shell is a Windows™ Graphical User Interface (GUI) consisting of a main menu, an antenna definition pre-processor, a NEC execution interface, and a data post-processor.

The graphical shell provides the capability for complete antenna analysis. Using the menu bar as shown in Figure 1, the user can perform file management operations, execute NEC, view output plots, manipulate windows, and access help. The File menu item allows a user to open one or more antenna definition/drawing windows. These windows read numerical data stored in NEC input files and display the data as 3D images. Creating, viewing, editing, and printing antenna models are easily performed. The Run menu item is used to execute NEC in a manner that is transparent to the user. During NEC execution, a rotating dial is displayed to signify that an analysis is being performed. The user is unaware that a separate DOS-based code is being run. Output plotting capability is provided via the Plot menu item. Both polar radiation plots and current intensity diagrams are available. The Window menu item provides conventional window manipulation functions such as Cascade, Tile, Arrange Icons, and Close All Windows. The Help menu item provides assistance for using SAIC's graphical shell.

Antenna Model Definition

A key feature of SAIC's NEC graphical shell is the antenna definition window. The window was designed to have the look and feel of a typical Windows™ vector-based drawing package with additional features for drawing in 3D. This 3D drawing package automates the tedious work of defining and typing wire coordinates in a DOS text file. As shown in Figure 1, the antenna drawing window contains a window title, drawing area, wire and view manipulation tools, scroll bars, and drawing information. Figure 2 illustrates the graphical shell's ability to display multiple orientations and outputs concurrently. Some of the antenna definition window's key features include:

User-defined defaults	Wire stretch/shrink ability	Wire statistics
Wire tag definition	Find wire ends	Find wire segment ends
Three dimensions	3-D Cursor position data	Variable orientation (θ , ϕ)
Zoom up/down	Snap-to-grid	Multiple images (varying θ , ϕ)



Mouse movement

The norm for today's drawing utilities is to perform most drawing functions with a mouse. However, when drawing in 3D, it is mathematically impossible (without fixing other variables) to convert a 2D mouse cursor location to a single 3D coordinate. SAIC's antenna definition window overcomes this reality by limiting mouse movement to orthogonal planes. The plane of mouse movement can be

shifted between x-y, y-z, and z-x by clicking the right-hand mouse button. The

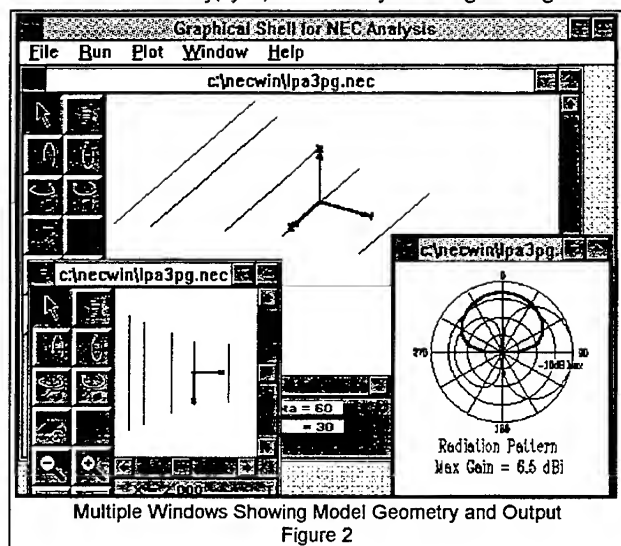


Figure 2

model viewing angle remains unaffected.

Movement along a single axes is accomplished by holding the shift button down while moving the mouse. Keyboard support is also provided. The cursor position is incremented or decremented in any 3D direction by depressing the x, y, or z and ctrl x, ctrl y, or ctrl z keys, respectively.

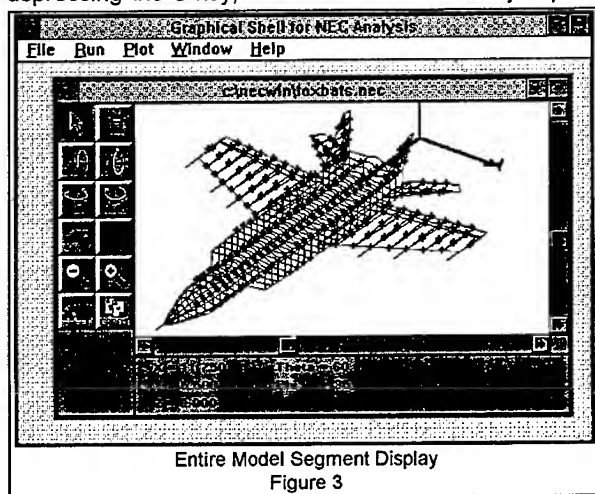
These features allow for quick, easy development of 3D models.

Wire Drawing/Definition

A major advantage of using SAIC's graphical shell is wire definition. Defining a wire using SAIC's antenna definition window is similar to drawing a line in a typical drawing packages. Upon selecting the wire tool, a wire can be drawn in three easy steps. First, the user moves the mouse to the desired wire start coordinate and clicks the left-mouse button. He/She then "rubber bands" the wire, moving to the wire end coordinate. Third, the user releases the mouse button. The wire is displayed on the screen and its end-point coordinates are stored in memory for subsequent creation of a NEC input file. During the "rubber banding" process, a display of the wire's length is continuously updated as the mouse is moved. An existing wire can be edited by using the arrow tool to stretch or shrink the wire from either of its ends in a similar fashion. After a wire is created or edited, it becomes the "selected" wire. When selected, its two endpoints are marked with dissimilar sized black squares to distinguish the start node from the end node.

Connecting two wires requires that the connecting ends have identical 3D floating point coordinate values. This is not easily accomplished when converting mouse cursor locations to 3D coordinates since the distance between screen pixels is much larger than the resolution of a floating point number. SAIC's antenna drawing window provides three features to ensure precise wire connections: Snap-to-Grid, Wire-Segment Find, and Wire-End Find. Snap-to-grid restricts the cursor movement to a user-defined 3D grid resolution. Wire-Segment Find, activated with the "F" key, sets the 3D cursor coordinates to that of the closest wire segment. Wire-End Find, activated with the "Shift F" keys, sets the 3D cursor coordinates to that of the closest wire end.

When constructing an antenna model with many wires, it is often desirable to display wire segments. This can be accomplished on a selected wire by depressing the S key, or for the entire model by depressing the *shift* S keys as shown in Figure 3.



Proper segmentation is extremely important for obtaining accurate NEC predictions with reasonable run-times. For example, a UHF antenna placed on a large platform requires stringent segmentation near the antenna. However, segmentation requirements can be reduced on other parts of the platform.

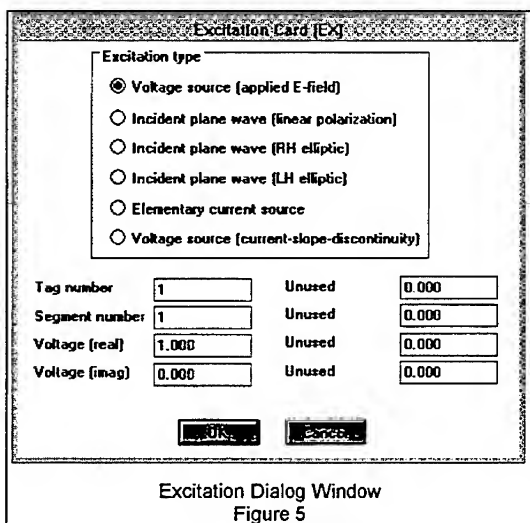
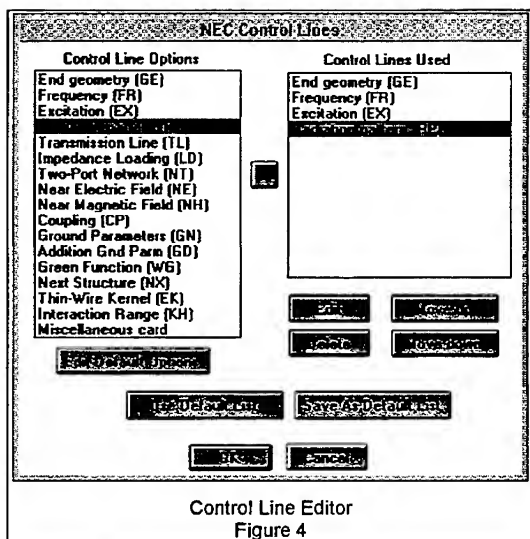
Model Viewing

It is necessary to view antenna models in 3D space using a 2D screen. In actual 3D space, items are viewed from an isometrics view point, so all parallel edges appear to converge or diverge. This is important for the correct simulation of infinite space but is impractical for this application. For finite antenna modeling, the model must be able to be viewed from any spherical coordinate (ρ, θ, ϕ). This is accomplished using scroll bars, zoom buttons, and orientation buttons. Scroll bars are used to change the location of the 3D origin on the screen. Zoom buttons allow a user enlarge a portion of a model to show more detail, or shrink the display to show more area. Orientation buttons allow a user to view a model from any aspect angle (θ, ϕ). Each time a button is pressed, θ or ϕ is incremented or decremented by a user-defined amount.

Control Line Specification

After completion of the model's geometry, the model's control lines, excitation, frequency, and desired output need to be specified. SAIC's graphical shell includes a control line editor that simplifies specification of NEC's control and system parameters. As shown in Figure 4, each available control line is listed in the left section of the editor. Nearly all NEC control lines are listed. The miscellaneous line allows the use of control lines not recognized by the line editor, such as, upper medium, dielectric sheath, and print control. The miscellaneous line can be used by the experienced user for the creation of any line.

The control line editor's right-hand section shows the control lines that have



been selected by the user to be used with the model. When creating a NEC input file the traditional way with an ASCII editor, each control line requires specification of four integer variables and six floating point variables. The definition of each variable is dependent on the particular control line being used. Using the control line editor, the method for specifying each variable is greatly simplified. For example, editing the geometry end (GE) line will open a dialog box with three options: no ground plane, ground plane with an image, or ground plane without an image. The user simply clicks the mouse on the desired option. A more complex example is the excitation line's dialog box (shown in Figure 5). The dialog box is divided into two sections: excitation type and definition fields. The titles of the eight definition fields vary to correspond to the particular excitation type that is selected. In the figure a voltage excitation is selected, therefore four definition fields are necessary. These features provide a simple and intuitive method for control line specification, minimizing the user's dependence on the NEC manual.

NEC Execution

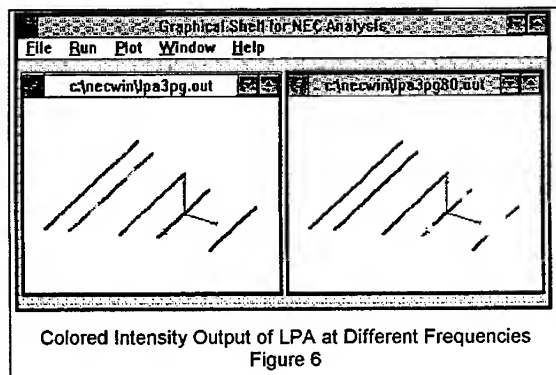
Execution of NEC is accomplished by selecting the Run menu item. NEC will automatically create and save an input file for the active drawing window, and then execute NEC. Once an analysis has begun, the cursor changes to a

rotating wheel, signifying execution is in process. At this time, the user can take advantage of Windows™ multi-tasking abilities and switch to another Windows™ application. SAIC's NEC graphical shell will run both an unmodified NEC-2 FORTRAN from the NEEDS package and NEC-3i compiled for a personal computer running DOS. SAIC will distribute NEC-2 with the graphical shell, however, NEC-3 or NEC-3i must be obtained from its owners. SAIC also has compiled a version of NEC to run under Windows™. If desired, SAIC will distribute NEC-2WIN with the graphical shell.

NEC Data Storage and Graphical Display

NEC generates extremely large output files. These files include input information, segment positions, and other redundant data traditionally used to check the input structures. When using SAIC's shell, most of this information is not required since the model is checked for errors before NEC execution. SAIC contemplated NEC output file reduction by removing redundant data or by using binary storage, but it was decided that interoperability with previous NEC runs is more important. Therefore, the graphical shell does not perform any reformatting of NEC output files. It reads the NEC-generated files for desired information and plots the data in the form of polar radiation plots and color-coded current intensity diagrams. The graphical shell can graphically display data obtained from existing NEC output files as well as output files generated on a main-frame computer. Huge NEC models can be created with the graphical shell, transferred to a main frame computer for fast execution, and then the output file can be transferred back to the PC for graphical display.

Figure 2 displays the graphical shell's polar radiation plots. Both elevation and azimuth patterns can be displayed alone or simultaneously on a single polar plot. The two patterns are distinguished by both line color and thickness. The elevation pattern is red and has two pixels' widths while the azimuth pattern is blue and is one pixel wide. Selection of a specific ϕ (θ) angle for the elevation (azimuth) pattern is performed from the Plot-Options menu item.



Color-coded current intensity diagrams graphically display NEC's output current intensities superimposed with color on the model's geometry (shown in Figure 6). Red (hot) is used for segments with the highest current, while blue (cold) indicates low current. The value associated with each color can be determined automatically or can be defined by the user.

Summary

SAIC is developing a graphical shell for NEC that can be used both by novice and experienced EM engineers and analysts. A user with only a basic understanding of PCs and Windows™ will be able to use the shell to predict the performance of any antenna structure that can be modeled with NEC. The shell automates the otherwise tedious and confusing methods required to specify inputs and to view results. It includes three dimensional drawing capabilities, easy-to-understand output plots, error checking, and help. Presently, the graphical shell is in development; however, a working prototype is available (Version 1.1).

SAIC has three other Windows™-based graphical tools use for electromagnetics and propagation analyses. One uses closed form and simple MM solutions to perform quick parametric studies of twenty standing wave, traveling wave, and aperture antenna types. Since computationally simple solutions are used, predictions for each of the twenty antenna types can be obtained in under ten seconds. Another Windows™-based software package provides a graphical shell for Basic Scattering Code (BSC) [4]. BSC uses UTD algorithms to model large antenna structures that are more than a few wavelengths in size. The graphical shell is similar to that for NEC except that it uses solid geometric shapes for model construction. SAIC's last graphical shell simplifies the use of IONCAP [5], a High Frequency (HF) skywave propagation code. The shell provides input windows, map windows, and plot windows. Input windows provide user-friendly dialog boxes with error checking for defining IONCAP input parameters. Map windows use the Defense Mapping Agency's Digital Chart of the World to display node locations and signal-strength contours on high-resolution maps. Plot windows are used to display IONCAP's numerical output data in the form of nine types of Cartesian and polar plot types. Interoperability is built into all of SAIC's Windows™-based antenna, propagation, and map software. As a result, complete end-to-end communication system performance can be determined quickly, easily, and accurately.

References

Windows™ is a registered trade-mark of Microsoft Corporation..

- [1] Burke G.J., Poggio A.J., *Numerical Electromagnetics Code*, Lawrence Livermore Laboratory, January 1981.
- [2] Burke G.J., *A Model for Insulated Wires in the Method of Moment Code NEC*, Lawrence Livermore National Laboratory, January 1988.
- [3] Harrington R.F., *Field Computation by Moment Methods*, Krieger Publishing Company, 1968.
- [4] Marhefka R.J., Silvestro J.W., *Numerical Electromagnetic Code-Basic Scattering Code-Version 3*, ElectroScience Laboratory, March 1989.
- [5] Teters R.T., Lloyd J.L., Haydon G.W., Lucas D.L., *Ionospheric Communications Analysis and Prediction Program User's Manual*, Institute for Telecommunication Sciences.

SESSION 9 - "MICROWAVE CIRCUITS"

Chair: Dr. Peter Russer, Co-Chair: Professor Linda P. B. Katehi

Field Matching Analysis of Complex Waveguides with Anisotropic Materials

M. OKONIEWSKI

Dept. Of Electrical and Computer Engng, University of Victoria
P.O.Box 3055, Victoria, BC, Canada V8W 3P6

1 Introduction

Many structures, such as ferrite phase shifters, magnetron resonators, fin waveguides have geometries that are difficult to analyze. The mode matching technique [1] has been modified to allow for an accurate analysis of complex shape waveguides loaded with anisotropic materials. The method has been implemented on a PC-386 computer equipped with a Microway i860 board. The method was used for the computations of the properties of a waveguide used to construct a novel polarization rotator for a domestic satellite TV receiver operating in a 10.95-12.75GHz frequency range. The parameters of a model of the device are presented.

2 Analysis

Consider a waveguide of a cross-sectional geometry sketched in fig.1. To facilitate the analysis, the cross-section of the structure is sectioned so that a cylindrical inner guide (CIG), and attached guides (AG) are distinguished (fig.1). The geometry of both CIG and AGs makes it simple to find the general solutions of Maxwell equations in their respective regions.

To solve the boundary problem, the fields — general solutions in the distinguished regions — have to be matched across the common interfaces. To achieve this, continuity conditions for fields components tangential to the interfaces are employed.

2.1 Fields in IG region

The CIG can be inhomogeneous (radially heterogeneous but axially symmetrical). It can be build of an arbitrary number of concentric cylinders made of dielectric or longitudinally magnetized ferrite materials. Fields in the outermost layer of the CIG have to be known to carry out the matching procedure [1]. Transfer matrix concept

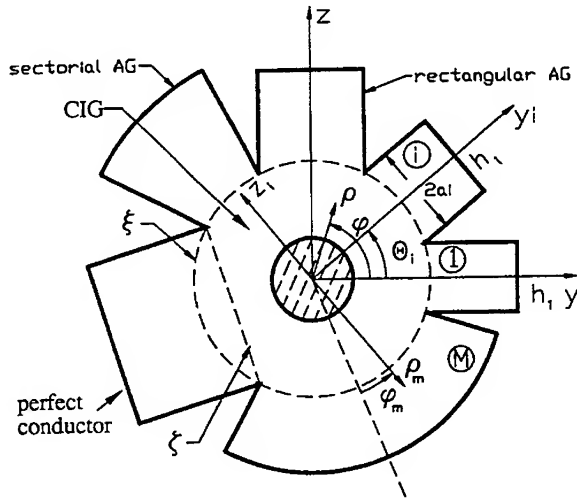


Figure 1: Structure under analysis

[4, 1] adopted for cylindrical ferrite media is used to solve Maxwell equation in the CIG.

In a given, say l -th, ferrite cylinder of IG, the electromagnetic fields are governed by a pair of coupled equations [3]:

$$\begin{aligned} (\nabla_t^2 - \beta^2 + k_0^2 \epsilon_l \mu_{eff_l}) D_x + j\beta k_0 \epsilon_l \frac{\mu_{a_l}}{\mu_l} \widetilde{H}_x &= 0 \\ (\nabla_t^2 - \frac{1}{\mu_l} \beta^2 + k_0^2 \epsilon_l) \widetilde{H}_x - j\beta k_0 \frac{\mu_{a_l}}{\mu_l} D_x &= 0 \end{aligned} \quad (1)$$

where: D is an electric flux and \widetilde{H} is proportional to magnetic field — $\widetilde{H} = \sqrt{\epsilon_0 \mu_0} H$, while μ_{a_l} , μ_l denote the relative off-diagonal and diagonal elements of the permeability tensor, respectively, μ_{eff_l} stands for the relative effective permeability, and ϵ_l is the relative permittivity and $k_0 = \omega \sqrt{\epsilon_0 \mu_0}$.

We seek the solution to (1) in terms of series of eigenfunctions:

$$D_x^{ol} = \sum_{k=-\infty}^{+\infty} D_{xl}^k e^{-j\beta x} \quad \widetilde{H}_x^{ol} = \sum_{k=-\infty}^{+\infty} \widetilde{H}_{xl}^k e^{-j\beta x} \quad (2)$$

Each eigenfunction consists of coupled partial waves \mathcal{D}_x and \mathcal{H}_x :

$$D_{xl}^k = \mathcal{D}_{xl}^k + R_l \mathcal{H}_{xl}^k \quad \widetilde{H}_{xl}^k = S_l \mathcal{D}_{xl}^k + \mathcal{H}_{xl}^k \quad (3)$$

defined as:

$$\mathcal{D}_{xl}^k = [A_{1l}^k J_k(\chi_{l1} \rho) + A_{2l}^k Y_k(\chi_{l1} \rho)] e^{jk\varphi}$$

$$\mathcal{H}_{xl}^k = [B_{1l}^k J_k(\chi_{l2}\rho) + B_{2l}^k Y_k(\chi_{l2}\rho)] e^{jk\varphi} \quad (4)$$

where: k is an integer number, the eigenvalues $\chi_{l1,2}$ can be found from the following expression:

$$\chi_{l1,2} = \sqrt{\frac{1}{2} \left[(a+c) \mp \sqrt{(a+c)^2 - 4(ac-bd)} \right]} \quad (5)$$

where:

$$\begin{aligned} a &= k_0^2 \epsilon_l \mu_{\text{eff}l} - \beta^2 & b &= j\beta k_0 \epsilon_l \frac{\mu_{a1}}{\mu_l} \\ c &= k_0^2 \epsilon_l - \frac{1}{\mu_l} \beta^2 & d &= j\beta k_0 \frac{\mu_{a1}}{\mu_l} \end{aligned}$$

and $J_k(\cdot)$, $Y_k(\cdot)$ are Bessel and Neumann or modified Bessel and McDonald functions, depending on the sign of $k_d^2 - \beta^2$.

Note that the coupling coefficients R_l and S_l :

$$S_l = \frac{\chi_{l1}^2 - a}{b} \quad R_l = \frac{\chi_{l2}^2 - c}{d}$$

vanish when infinite bias magnetization H_i is applied. Once the longitudinal fields are known, transverse field components can also be determined [5]. A sequential application of continuity conditions between subsequent layers leads to a relation between amplitudes of the fields of the innermost and outermost layers of CIG [5]:

$$\underline{A}_L^k = \underline{\mathbf{X}}_{\text{Tr}}^k \underline{A}_1 \quad (6)$$

where $\underline{\mathbf{X}}_{\text{Tr}}^k$ is a *global transfer matrix* which is dependent on the electromagnetic and geometric parameters of CIG only, and is defined in [5]. In the innermost cylinder of the CIG amplitudes A_{21}^k and B_{21}^k vanish, therefore k -th mode in the CIG has only two amplitudes A^k and B^k .

2.2 Fields in AGs

The AGs can have a variety of cross-sectional shapes, ranging from open at one side rectangular waveguides to sectorial guides and parallel plate guides with magnetic or electric walls. It is required however, that the Helmholtz equation formulated in AG region is separable.

The solution of Maxwell equation is postulated as a series of type E and H modes, complete in an AG region:

$$D_x^{\perp i} = \sum_n e_n^i D_{xn}^{\perp i} \quad \widetilde{H}_x^{\perp i} = \sum_n h_n^i H_{xn}^{\perp i} \quad (7)$$

where: i denotes i -th AG, n - n -th eigenfunction, and e_n^i , h_n^i stand for unknown amplitudes. Superscript \perp indicates quantities defined in AGs.

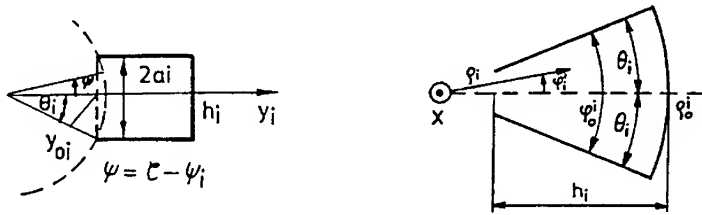


Figure 2: Types of AG implemented: rectangular - a, sectorial - b.

The eigenfunctions $D_x^{\perp i}$ and $H_x^{\perp i}$ are assumed in the following form:

$$D_{xn}^{\perp i} = e^{-j\beta x} \Phi_n^i(q_1) \Upsilon_n^i(q_2) \quad (8)$$

$$\widetilde{H}_{xn}^{\perp i} = e^{-j\beta x} \Psi_n^i(q_1) \Omega_n^i(q_2) \quad (9)$$

where: q_1, q_2 are transverse coordinates of a system in which AG is defined, (y and z in case of fig.1).

Currently two types of AG are implemented: rectangular AG and sectorial AG (Fig.2. For rectangular AG functions $\Upsilon_n^i(q_2)$ and $\Omega_n^i(q_2)$ are defined as:

$$\Upsilon_n^i(z_i) = \sin[k_{zn}^i(z_i - a_i)]$$

$$\Omega_n^i(z_i) = \cos[k_{zn}^i(z_i - a_i)]$$

$$\Phi_n^i(y_i) = \sinh(k_{yn}^i b_i - y_i)$$

$$\Psi_n^i(y_i) = \cosh(k_{yn}^i b_i - y_i)$$

where: $k_{zn}^i = \frac{n\pi}{2a}$

whereas for sectorial AG we have:

$$\Upsilon_n^i(\varphi_i) = \sin[k_{\varphi n}^i(\theta_i - \varphi_i)]$$

$$\Omega_n^i(\varphi_i) = \cos[k_{\varphi n}^i(\theta_i - \varphi_i)]$$

$$\Phi_n^i(\rho_i) = J_{k_{\varphi n}^i}(k_{\rho n}^i \rho_i) + c_{en}^i Y_{k_{\varphi n}^i}(k_{\rho n}^i \rho_i)$$

$$\Psi_n^i(\rho_i) = J_{k_{\varphi n}^i}(k_{\rho n}^i \rho_i) + c_{hn}^i Y_{k_{\varphi n}^i}(k_{\rho n}^i \rho_i)$$

where: $c_{en}^i = -J_{k_{\varphi n}^i}(k_{\rho n}^i \rho_0^i) / Y_{k_{\varphi n}^i}(k_{\rho n}^i \rho_0^i)$, $c_{hn}^i = -J_{k_{\varphi n}^i}'(k_{\rho n}^i \rho_0^i) / Y_{k_{\varphi n}^i}'(k_{\rho n}^i \rho_0^i)$, and $k_{\varphi n}^i = \frac{n\pi}{2\theta_i}$

2.3 Field matching

To obtain the solution of the boundary problem the fields are enforced to fulfill the continuity conditions at the interfaces between distinguished regions. These interfaces are denoted with ζ and ξ lines — ξ circumferences the CIG region, while ζ marks the limits of the AGs.

In general, AGs and CIG can overlap, as it is the case for rectangular AGs. The continuity conditions for E and H field can be then formulated at different interfaces, e.g. H fields can be matched on ξ and E on ζ [5]. With sectorial AG however, the both lines become identical, which facilitates the analysis allowing for analytical calculations of inner products that follow (using symbolic math packages, MATHEMATICA in this case).

Let us consider the continuity conditions for \vec{E} fields on ζ and for the \vec{H} fields on ξ

$$\begin{aligned} \vec{H}_x^\circ &= \sum_{i=1}^M \vec{H}_x^\perp \mathcal{B}_i(\varphi) \\ \vec{H}_\varphi^\circ &= \sum_{i=1}^M \vec{H}^\perp \vec{a}_\varphi \mathcal{B}_i(\varphi) \end{aligned} \bigg|_\xi \quad (10)$$

$$\begin{aligned} E_x^\circ &= \sum_{i=1}^M E_x^\perp \mathcal{B}_i(\varphi) \\ \sum_{i=1}^M \vec{E}^\circ \vec{a}_{z_i} \mathcal{B}_i(\varphi) &= \sum_{i=1}^M E_{z_i}^\perp \mathcal{B}_i(\varphi) \end{aligned} \bigg|_\zeta \quad (11)$$

where: \mathcal{B} is a function selecting i -th AG region.

To transform equation (10) into an algebraic system the inner products are taken of its both sides with every function from the set of IG eigenfunctions, $\{e^{jk\varphi}\}$, with the definition of the inner product ensuring orthogonality

$$\langle f | g \rangle_\xi \stackrel{\text{def}}{=} \oint_\xi f g^* d\xi = \int_0^{2\pi} f g^* R_d d\varphi \quad (12)$$

As a result a matrix formula is obtained:

$$\underline{T} \begin{bmatrix} \underline{A} \\ \underline{B} \end{bmatrix} = \underline{\Delta} \begin{bmatrix} \underline{e} \\ \underline{h} \end{bmatrix} \quad (13)$$

where: \underline{T} is build of diagonal submatrices, $\underline{\Delta}$ is dense and $[\underline{A} \ \underline{B}]^T$ and $[\underline{e} \ \underline{h}]^T$ are vectors storing amplitudes of eigenfunctions of IG and AGs, respectively.

A similar procedure is applied to (11). This time however, an inner product is taken of its both sides with every eigenfunction of AGs. The appropriate inner product for this operation is defined as follows:

$$\langle f | g^{\perp i} \rangle_\zeta \stackrel{\text{def}}{=} \oint_\zeta f (g^{\perp i})^* \mathcal{B}_i(\varphi) d\zeta = \int_{-a_i}^{a_i} f (g^{\perp i})^* dz_i \quad (14)$$

This operation yields the following matrix relation:

$$\underline{V} \begin{bmatrix} \underline{A} \\ \underline{B} \end{bmatrix} = \underline{\Delta} \begin{bmatrix} \underline{e} \\ \underline{h} \end{bmatrix} \quad (15)$$

where: $\underline{\Delta}$ is build of diagonal matrices and \underline{V} is dense [5].

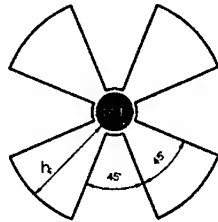


Figure 3: Cross-section of a waveguide used in a polarization rotator. CIG radius=4.mmm, $h_i=14.5\text{mm}$, $M_s=3000\text{Gs}$, $\epsilon=12$.

In both eq. (13) and eq. (15) the same two vectors of unknown amplitudes are present. By the elimination of one of them a homogeneous system of algebraic equations, is obtained, which, after setting its determinant to zero, provides the dispersion equation:

$$\left[\underline{\underline{A}} - \underline{\underline{V}}(\underline{\underline{T}})^{-1} \underline{\underline{A}} \right] \begin{bmatrix} \underline{\underline{e}} \\ \underline{\underline{h}} \end{bmatrix} = 0 \quad (16)$$

3 Verification and results

The program has been written in Fortran, and implemented on a PC-386 computer equipped with a Microway i860 NumberSmusher board. To compute β - f characteristics the root finding subroutine proposed in [6] was used and found very efficient.

A proper behavior of the method applied to compute structures where only rectangular AG were present was verified both numerically and experimentally [1]. Since the core of the algorithm remains unchanged when sectorial AG are also allowed, only few tests were performed – in particular the program was used to compute characteristics of ferrite and dielectric loaded circularly-cylindrical waveguide. The theoretical and computed results compared well. Tests involving more complex structures were not possible however, since no adequate data in the literature were found. Therefore the version of the method involving sectorial AGs was validated experimentally in the design of a waveguiding structure for a novel polarization rotator for a domestic satellite TV receiver operating in 10.95–12.75 GHz frequency band.

The cross-section of the waveguide is shown in Fig.3, and Fig.4 illustrates values of computed phase shift. The measurements of the prototype of the device are shown in Fig.5. Although the two figures do not correspond directly, it may be notice that the measurement results for an actual device were in good agreement with the estimated behavior.

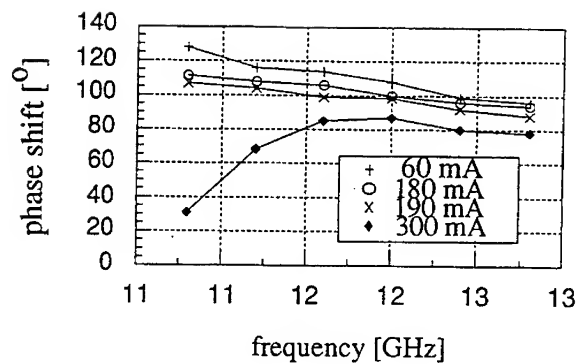


Figure 4: Polarization rotation of a section of a waveguide in Fig.3 Section length - 25mm.

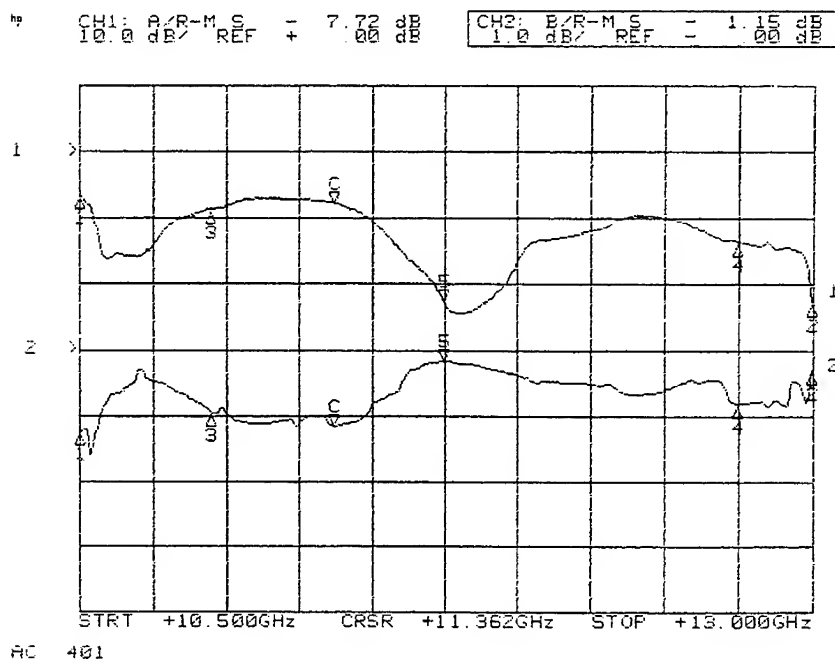


Figure 5: Reflectio - curve 1, and transmission losses -curve 2 of a ferrite polarization rotator, I=186mA.

4 Conclusions

The mode matching method of analysis of waveguides of complex cross-sectional geometry has been modified to allow for analysis of structures containing sectorial AGs. Results of numerical computations of a polarization rotation introduced by a section of complex waveguide were presented. A model of polarization rotator comprising this waveguide was built, and its measured parameters are included.

References

- [1] M.Okoniewski, J.Mazur, "An Accurate, Field Matching Analysis of Waveguides of Complex Cross-Sectional Geometry Loaded with Magnetized Ferrite Rods", *IEEE MTT-S Intern. Symp. Digest*, pp181-184, Boston, 1991.
- [2] M.Okoniewski, J.Mazur, "Waveguides with Complex Cross-Sectional Geometry Containing Longitudinal Dielectric Rods", *Proc. URSI Internat. Symp.*, pp.114-116, Stockholm, 1989.
- [3] A.G.Gurewicz: *Ferrites at microwave frequencies*, in Polish, PWN, Warszawa 1964.
- [4] F.E.Gardiol: "Propagation in rectangular waveguide loaded with slabs of anisotropic materials", PhD thesis, Louvain, 1969.
- [5] M.Okoniewski: "*Branched wave-guiding structures, their theory and analytical applications*", PhD thesis, in Polish, Technical University of Gdańsk, 1990.
- [6] M.Mrozowski, "An efficient algorithm for finding zeros of a real function of two variables", *IEEE trans. Microwave Theory Tech.*, vol.MTT-38, pp.601-604, Mar., 1988.

ADVANCE IN ANALYZING PASSIVE PLANAR RADIATING STRUCTURES WITH METHOD OF MOMENTS MATRICES

Sebastian Sattler¹ and Peter Russer^{1,2}

¹ Technische Universität München, Lehrstuhl für Hochfrequenztechnik

Arcisstraße 21, W-8000 München 2, FRG

Phone: +49 (89) 2105 3380, Fax: +49 (89) 2105 3365

² Ferdinand-Braun-Institut für Höchstfrequenztechnik

Rudower Chaussee 5, O-1199 Berlin, FRG

Phone: +49 (30) 6704 5717, Fax: +49 (30) 6704 4542

Abstract

Integral Equation Techniques (IET) like Spectral Domain Analysis (SDA) or Mixed Potential Integral Equation (MPIE) are preferred methods for the analysis of passive planar radiating structures. Arbitrarily shaped geometries are investigated by the subsectional basis function approach to the Method of Moments and the resulting system matrices are computed with Conjugate Gradient Methods (CGM). The complexity of planar structures that can be modeled is limited by storage space and computation time. These limitations can be overcome by the application of a mapping procedure. This way one can not only save the maximum of computational storage but also minimize the required computation time. Cray computers yield the fastest performance for these highly vectorized algorithms.

Summary

Among the mathematical models for the analysis of passive planar radiating structures, integral equation techniques stand out as one of the most common and popular approaches [1,2]. They can be generally separated into the two numerical methods, the Spectral Domain Analysis (SDA) and the Mixed Potential Integral Equation (MPIE). They provide a different rigorous treatment of printed microwave circuits but yield to the same impedance matrices. Among their principal features, these models are able to handle patches of arbitrary shapes where no suitable first guess of the surface-current distribution is possible. Also there are no limitations in frequency and substrate thickness. The models automatically take into account mutual coupling between elements and can predict the performance of a patch embedded in an array environment. Electromagnetic radiation is fully considered and surface waves are included as well as dielectric and ohmic losses.

The integral equations, the Electrical Field Integral Equation (EFIE) and the Mixed Potential Integral Equation (MPIE) will be treated numerically with the Method of Moments (MoM) [3]. By this way the integral equation is transformed into a matrix algebraic equation

$$\begin{pmatrix} \overline{\overline{C}}^{xx} & \overline{\overline{C}}^{xy} \\ \overline{\overline{C}}^{yx} & \overline{\overline{C}}^{yy} \end{pmatrix} \begin{pmatrix} \mathbf{I}_x \\ \mathbf{I}_y \end{pmatrix} = \frac{1}{jZ_0} \begin{pmatrix} \mathbf{V}_x^{(e)} \\ \mathbf{V}_y^{(e)} \end{pmatrix} \quad (1)$$

which can be solved on a computer. The subsectional basis function approach is successfully applied to arbitrarily shaped geometries [4,5,6]. Concerning the physical size of the structure to be analysed the method is valid from DC to infinity. However, most numerical implementations work at their best with structures whose size is comparable to the wavelength.

Discretization usually requires the solution of large systems of linear equations that maybe exceed the storage of a computer. Because of numerical instabilities Gaussian elimination becomes intractable for higher frequency problems. To overcome these drawbacks we use conjugate gradient methods for the numerical solution of the matrices and apply a mapping procedure to the matrix elements that allows a reduction in computational storage by about one dimension. Hence, these highly vectorized algorithms are very suited to run on vector computers and extend the range of discretization drastically. There are no more barriers to examine passive planar radiating structures with ten thousand and more subsections.

The conjugate gradient algorithm for solving the matrix equation $Ax = b$ in its general form is shown in Table 1:

Initialization:	$p_0 = r_0 = b - Ax$
For $k = 0, 1, 2, 3...$	until convergence do $x_{k+1} = x_k + \alpha_k p_k$ $r_{k+1} = r_k - \alpha_k A p_k$ $p_{k+1} = r_{k+1} + \beta_k p_k$
End do	
where:	$\alpha_k = r_k^T r_k / p_k^T A p_k$ $\beta_k = r_{k+1}^T r_{k+1} / r_k^T r_k$

Table 1:

It provides a viable algorithm for application to indefinite problems [7,8]. The matrix A of order N is complex symmetric and implicitly formed by two storage vectors of order $2N$. One matrix-vector multiplication operation per iteration is necessary. The algorithm theoretically terminates in exact arithmetic in at most N iterations with $\mathbf{r}_{k+1} = 0$ and $\beta_k = 0$. However it has been observed that for every solved system of equations, satisfactory convergence occurs in much fewer than N iterations. The number N of iterations strongly depends on the proper choice of basis- and testfunctions in the subsectional basis function approach to the Method of Moments. For arbitrarily shaped structures we chose rooftop-type and unidimensional pulse functions defined above equivalent rectangles.

The application of the subsectional basis function approach to the Electrical Field Integral Equation in Eq.(2) as well as to the Mixed Potential Integral Equation in Eq.(3) yields a very simple algorithm which reduces the computational storage of the MoM-matrix to a minimum.

$$\mathbf{e}_z \times \mathbf{E}^e = -\mathbf{e}_z \times \int_{S_0} \bar{\bar{G}}_E \mathbf{J}_s dS' + Z_s \mathbf{J}_s \quad (2)$$

$$\mathbf{e}_z \times \mathbf{E}^e = \mathbf{e}_z \times (j\omega \int_{S_0} \bar{\bar{G}}_A \mathbf{J}_s dS' + \nabla \int_{S_0} G_V q_s dS') + Z_s \mathbf{J}_s \quad (3)$$

The algorithm represents a simple law of mapping and allows a reduction in the required computational storage by several orders of magnitude. Taking advantage of the rotational and translational symmetry of the Green's functions in the transverse directions, one can map the whole MoM-matrix onto two rows of the matrix. Only as few matrix elements as absolutely necessary, i.e., only the non-redundant, have to be addressed and thus the information of the $N \times N$ matrix can be stored in the computational memory of a $2 \times N$ matrix. Following [9] we get the required law of mapping:

$$c(A_{i,j}^p(s) \longleftrightarrow A_{m,n}^q(t)) \longmapsto CoS * a((|m-i| + \delta_y) * n_x^q + |n-j| + 1 + \delta_x) \quad (4)$$

Eq.(4) maps all the correspondences c that depend on the mean value of the distance between two weighted subsections $A_{i,j}^p(s)$ and $A_{m,n}^q(t)$ onto an one-dimensional array \bar{a}^T . The superscripts p and q denote the orientation of the specific subsection in p -direction and q -direction, respectively. The symmetric or antisymmetric functions which weight the subsections, are characterized by the indices s and t . Even functions are represented by (e) , odd functions by (o) . In connection with the application of the MoM to the MPIE the function $A_{m,n}^x$, for example, represents the cartesian component of the surface charge generated by a x -directed surface current \bar{I}_x . The subsections $A_{i,j}^q$ refer to the so-called razor test functions.

We have implemented the mapping law to the MPIE [10] and studied the performance of the CG-algorithm. Independent of the CG-convergence rate we plotted for various computers the average time per iteration cycle versus the order N of the system matrix. Fig.1 compares the 33MHz PCs 386 and 486 with the workstation HP720 and the Cray computer Y-MP4/464 of the Leibniz Rechenzentrum München. The available storage space for a matrix (explicitly formed) is limited by the 60 Megawords RAM of the Cray. For the

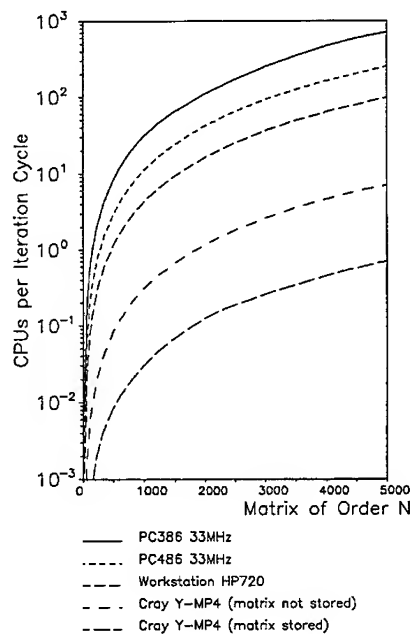


Figure 1: Reference Plot for Various Computers

explicit set up of a complex matrix of order $N = 5000$, for example, we require about 50 Megawords RAM. Supposed that we form the impedance matrix implicitly by our mapping procedure we can reduce computational storage to 60 Kilowords RAM, however. The increase in the computation time amounts to about a factor ten and the Cray computer spends 4.64 CPU seconds for one iteration cycle. The average computation time multiplier for the respective machines listed in Fig.1 is shown in the table below:

	Matrix explicitly formed (60Mwords Cray-RAM)
PC386 33MHz	Factor 1011
PC486 33MHz	Factor 360
HP720	Factor 140
Cray Y-MP4	Factor 10 (with mapping)
Cray Y-MP4	Factor 1 (without mapping)

To become independent of the large memory requirements of more complex printed structures the presented CG-algorithm is in connection with the mapping procedure the favourite candidate for the simulation of passive planar millimeter wave circuits. In Fig.2 we show the appropriate reference. The average computation time for one iteration cycle

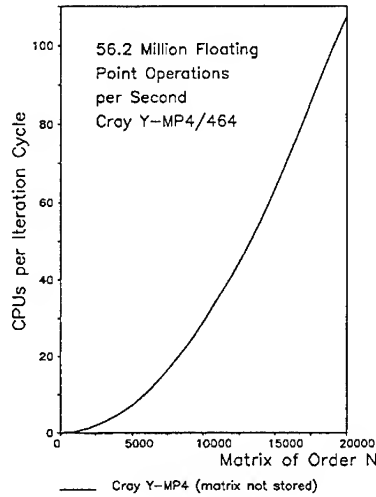


Figure 2: Reference Plot for Cray Y-MP4 with the Matrix Implicitly Formed

is again plotted versus the size of the calculated matrices. But for matrices larger than order fifteen thousand the exponential behaviour in the plots of Fig.1 ends in the strictly linear dependency shown in Fig.2. Therefore the required computation time per iteration cycle of matrices of order N can be easily estimated by linear extrapolation.

Conclusion

The use of the subsectional basis function approach to the Method of Moments and the Conjugate Gradient Method, the iterative procedure for the solution of system matrices, result in a stable numerical algorithm. This way not only the maximum of computational storage is saved but also the demand for computation time is kept within applicable limits. The implementation of the proposed numerical procedure to integral equation techniques, the EFIE and the MPIE, respectively, expands the capabilities of simulation of passive planar radiating structures forwards. Application of the described techniques to these structures provides a means for modeling more complex shaped geometries discretized by ten thousand and more equivalent subsections. Considering the complexity of the passive

planar radiating structures to be analysed an optimal compromise between computational storage on the one hand and computation time on the other hand was found.

Acknowledgement

We thank the Leibniz Rechenzentrum München for the allocation of the Cray computer resources. This work has been financially supported by the Deutsche Forschungsgemeinschaft (DFG).

References

- [1] F. E. Gardiol, "Microstrip Computer-Aided Design in Europe," *IEEE Trans. Microwave Theory Tech.*, MTT-34, pp. 1271-1275, 1986.
- [2] R. H. Jansen, I. G. Eddison, R. G. Arnold, "Recent developments in the CAD of high packing density MMICs," *Microwaves and Optronics 1989 (MIOP)*, (Sindelfingen, Germany), Eröffnungsvortrag 1.3, Feb. 1989.
- [3] R. F. Harrington, *Field Computation by Moment Methods*, Macmillan, New York, 1968.
- [4] G. Splitt, *Effiziente Rechenverfahren zur Analyse von komplexen Einzel- und Gruppenantennen in Streifenleitungstechnik*, Forschungsbericht, DLR, Oberpfaffenhofen, 1990.
- [5] J. R. Mosig, R. C. Hall and F. G. Gardiol, "Numerical Analysis of Microstrip Patch Antennas," in: *Handbook of Microstrip Antennas*, Ed. James & Hall, Peregrinus, London, 1989.
- [6] K. A. Michalski and D. Zheng "Analysis of Microstrip Resonators of Arbitrary Shape," *IEEE Trans. Microwave Theory Tech.*, MTT-40, pp. 112-119, 1992.
- [7] D. A. H. Jacobs, *Generalizations of the conjugate gradient method for solving non-symmetric and complex systems of algebraic equations*, Central Electricity Research Laboratories, Leatherhead, Aug. 1980.
- [8] J. K. Cullum and R. A. Willoughby, *Lanczos Algorithms for Large Symmetric Computations Vol. 1 Theory*, Birkhäuser, Boston, 1985.
- [9] S. Sattler and P. Russer, "A Note on the Computational Storage in the Subsectional Basis Function Approach to the Method of Moments," *International Journal of Numerical Modelling: Electronic Networks, Devices and Fields*, Vol. 5, pp. 245-250, 1992.
- [10] S. Sattler and P. Russer, "Method of Moments Computational Storage Minimization," *Proceedings Int. Symp. on Antennas and Propag. 22-25 Sept. 1992*, (Sapporo, Japan), Vol. 1, pp. 249-252.

S-Parameter Modeling of Planar Transmission Line Discontinuities and MMIC Module Interconnections

Hang Jin¹, Rüdiger Vahldieck^{1,2} and Peter Russer²

¹Laboratory for Lightwave Electronics, Microwaves and Communications (LLiMiC)
Department of Electrical and Computer Engineering
University of Victoria, Victoria, B.C., V8W 3P6, Canada

²Ferdinand-Braun-Institut für Hochfrequenztechnik, Berlin, Germany

Abstract

This paper has introduced a rigorous analysis of a variety of transmission line transition discontinuities and module interconnect assemblies in MMIC and MHMIC circuits using the frequency-domain TLM method. Numerical results of frequency-dependent s-parameters have been presented which include the effect of finite thickness and conductivity of metallization as well as mode interaction between cascaded discontinuities. The effect of inserting an intermediate section of transmission line between two different transmission media has been analysed and it was found that CPW transitions can be made more broadband. The effects of the bonding wire for module assemblies is investigated. It is found that the properties of the interconnect are largely depended on the total length of the wire and are quite insensitive to the shape of the wire. This is in a good agreement with the experimental observations.

1.Introduction

Typical MMIC and MHMIC circuits are composed of a variety of different types of planar transmission lines including microstrip, coplanar waveguide and coplanar stripline as well as slotlines on a single or multiple chips. Low loss transmission of energy between these different transmission media as well as the interconnect between different modules is a frequently encountered problem in the design of MMIC and MHMIC circuits. This problem is not easily solved since the structures present a truly 3-D discontinuity with small circuit dimensions. Furthermore, discontinuities are closely spaced which leads to interactions between circuit parts and makes the use of quasi-static analysis methods unreliable. More sophisticated full-wave techniques which are capable of simulating all aspects of 3-D field interaction at and between discontinuities are usually very CPU-time consuming or memory space intensive which is the reason why they are not in widespread use. On the other hand, design data for discontinuities as shown in Fig.1, as an example, are quite useful for practical applications but are not available from the literature. In this paper we will investigate these transmission line transitions and module interconnections in more detail with a very powerful and flexible new numerical technique, the frequency-domain TLM method, which was published only recently by Jin and Vahldieck [1]. The objectives of this investigation is to simulate such structures and to extract useful information for optimum transition design.

2. Method

The numerical analysis is carried out utilizing the frequency-domain TLM (FDTLM) method. A detailed description of this method has been presented in [2]. Therefore, only some highlights are given here. In the FDTLM method, the space to be analysed is discretized by a transmission line network, as in the conventional time domain TLM (TDTLM) method. A hybrid symmetric condensed node is used which is represented by a 15-port symbolic scattering matrix [4]. However, instead of exciting the network with a single impulse, an impulse train of sinusoidally modulated magnitude is assumed. This impulse train is only used to build a bridge between the time- and the frequency-domain. By choosing the modulation frequency subsequent pulses are related by a factor of $e^{j\omega\Delta t}$ and therefore the entire algorithm is transformed into the frequency-domain and is significantly simplified. Hence the practical implementation of the algorithm does not require an actual impulse excitation of the network. Frequency-domain techniques, such as the diakoptics, can be readily implemented in this new method in order to enhance its computational efficiency. Hence, the FDTLM method has both the flexibility of the conventional TDTLM and the computational efficiency of frequency-domain techniques, and is particularly suitable for structures with complicated geometries such as the transmission line transitions and interconnect assemblies shown in Fig.1.

The general calculation procedure of the frequency-dependent s-parameters with the FDTLM method consist of the following steps. For a given structure we first perform a two dimensional propagation analysis for the attached waveguides, which, in the present cases, are microstrip, CPW or slotline. From this analysis we find the fundamental modal field distribution. Then the discontinuity region is excited from one of the waveguides by an incident wave, which is its fundamental propagation mode obtained from the previous two dimensional analysis. The reflected and transmitted waves are calculated and the s-parameters are obtained. Since the field components for different modes can be separated in the FDTLM method, the reference plane for the s-parameter calculation may be located right in the discontinuity plane. This property allows to minimize the volume of discontinuity area between the reference planes that need to be discretized by the transmission line network.

3. Numerical Results

Fig.1a shows a CPW to slotline transition. While the slotline mode will be totally reflected at the CPW section of the discontinuity if only the odd CPW mode is considered, we have investigated the even CPW mode only (Fig.2). Such a transition is of interest in multiplier, mixer and oscillator applications [5]. Varying the gap g between the CPW and the slotline, it was found that the curves for two different gaps ($g=0.1\text{mm}$ and $g=3.0\text{mm}$) are almost identical, indicating that the properties of this kind of CPW-slotline transition are not sensitive with respect to the distance between the CPW and the slotline. This can be explained by the fact that the centre strip of the CPW has a very narrow width, w_1 , in comparison with the distance between the groundplanes ($2s_1+w_1$). A slotline mode is supported by the two uniplanar groundplanes and its field configuration is not significantly disturbed by introducing a narrow metal strip within the central plane, because this strip acts essentially as an electric wall. Therefore, the reflection from the transition

is mainly due to the slot line step junction. This effect increases with frequency as shown in Fig.2. Fig.3 illustrates the s-parameters as a function of the gap g for two different frequencies $f=10$ GHz and $f=40$ GHz. The flat behaviour of the curves only confirms that the effect of the gap width g is quite marginal.

To reduce the reflection coefficient of the slotline step junction, a quarter wave transformer section with gap $w_m=1$ mm and length $d_1=1.5$ mm is inserted (Fig.1b). The s-parameters for this cascaded transition are plotted in Fig.4. The peak in the S_{11} curve occurs at about 26 GHz where the propagation constant of the intermediate slotline is $\beta=1.1$ (mm^{-1}) and the quarter wavelength is about $\lambda_g=2\pi/4\beta=1.43$, which is very close to the physical length of the added section ($d_1=1.5$ mm).

Fig.5 shows a CPW-microstrip transition (Fig.1c) with an odd mode excitation. Although this transition can be viewed as a CPW to CPW transition, the slot width (s_2) becomes so wide that the field changes from a CPW field to a microstrip field, because the distance to the metallization on the backside is much smaller than to the uniplanar groundplanes (s_2). Due to the additional substrate layer (air $\epsilon_r=1.0$) between the back metallization and the GaAs substrate ($\epsilon_r=9.6$), there are no higher order modes up to 40 GHz. As expected, the reflection coefficient increases with frequency because the transition behaves like a transmission line junction with a parasitic shunt capacitor. Also here the reflection coefficient can be reduced by introducing a quarter wavelength transformer between the CPW and microstrip (Fig.1d). The numerical results for this arrangement are shown in Fig.6. The quarter wavelength transformer is a section of CPW with a relatively wide gap $s_m=0.4$ mm. Comparing Fig.5 and Fig.6, it is found that the reflection coefficient is reduced by 50% at the low end ($f=5$ GHz) and 70% at the high end ($f=40$ GHz) of the frequency spectrum. The peak in the S_{11} curve occurs at about 29 GHz which corresponds to $\beta=1.5$ (mm^{-1}) or a quarter wavelength $\lambda_g \sim 1.05$ mm, which is again approximately the physical length of the intermediate section ($d=1$ mm).

Fig.7 shows the frequency-dependent s-parameters of the interconnection between a microstrip on Al_2O_3 with $\epsilon_r=9.6$ and that of the CPW on GaAs substrate ($\epsilon_r=12.9$). It is found that the reflection of the interconnect increases significantly with the frequency, suggesting that the interconnect assembly of Fig.1e may be considered as a shunt capacitor (open-ended microstrip and CPW), series inductor (wire bond), in a low pass filter p-network. The shunt capacitances are due to the fringing fields at the open ends of the microstrip and the CPW and the series inductance comes from the bonding wire connecting the microstrip and CPW. The inductance is approximately proportional to the length of the bonding wire. Fig.8 shows the s-parameters as a function of the gap g for two different frequencies $f=5$ GHz and $f=25$ GHz. It is obvious that the reflection increases with increasing gap g . This is quite plausible because a wider gap means longer bonding wire and hence larger inductance value with large reflection coefficient. Fig.9 illustrates s-parameters as a function of the bonding wire height $a_m(=a_c)$. Also here, the reflection increases with increasing height because this results in longer bonding wire lengths.

It has been observed that the properties of the interconnect assembly of Fig.1(e) are largely determined by the length of the bonding wire and are quite insensitive to the shape of the bonding wire. This can be confirmed in the following investigation. For a given wire length, we change both the wire height a_m , a_c and the gap g simultaneously in such a way that the length of the wire $L=a_m+a_c+g$ is kept unchanged. The results of the s-parameters with different a_m , a_c and g are shown in Fig.10. The curves are quite flat over a large range of dimensions. In other words, when the bond wire changes from one extreme shape ($g=0.3$, $a_m=a_c=0.1$, Fig. 10) to another ($g=0$, $a_m=a_c=0.25$, Fig.10) the s-parameters change only by a few percent. This simulation results are in a good agreement with experimental observations [3].

4. Conclusions

This paper has introduced a rigorous analysis of a variety of transmission line transition discontinuities and module interconnect assemblies in MMIC and MHMIC circuits using the frequency-domain TLM method. Numerical results of frequency-dependent s-parameters have been presented which include the effect of finite thickness and conductivity of metallization as well as mode interaction between cascaded discontinuities. The effect of inserting an intermediate section of transmission line between two different transmission media has been analysed and it was found that CPW transitions can be made more broadband. The effects of the bonding wire for module assemblies is investigated. It is found that the properties of the interconnect are largely depended on the total length of the wire and are quite insensitive to the shape of the wire. This is in a good agreement with the experimental observations.

References:

- [1] Hang Jin and Ruediger Vahldieck, " A frequency domain TLM method," 1992 IEEE Int. Microwave symp. Dig. pp.775-778
- [2] Hang Jin and Ruediger Vahldieck, " The frequency-domain transmission line matrix method - A new concept," (to be appeared in IEEE Trans. Microwave Theory Tech. December issue, 1992)
- [3] Steve Nelson, Marilyn Youngblood, Jeanne Pavio, Brad Larson, and Rick Kottman, " Optimum microstrip interconnects," 1991 IEEE MTT-S Digest, pp.1071-1074, 1991,Boston.
- [4] R.Scaramuzza and A.J.Lowery, " Hybrid symmetrical condensed node for the TLM method," Electron. Letters, no.23, vol.26, pp1947-1949, 1990
- [5] J.A.Navarro, Y.H.Shu, and K.Chang, " A novel varactor tunable waveguide-slotline Gunn VCO," 1991 IEEE MTT-S Digest, pp.1187-1190, 1991,Boston.

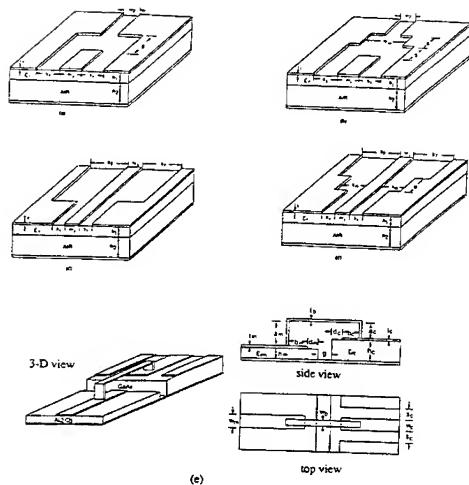


Fig. 1 Examples of discontinuities in MMIC and MMHC circuits:
(a) CPW-slot line without a matching section
(b) CPW-slot line with a matching section
(c) CPW-microstrip without a matching section
(d) CPW-microstrip with a matching section
(e) Interconnect assembly between microstrip and CPW on different substrates

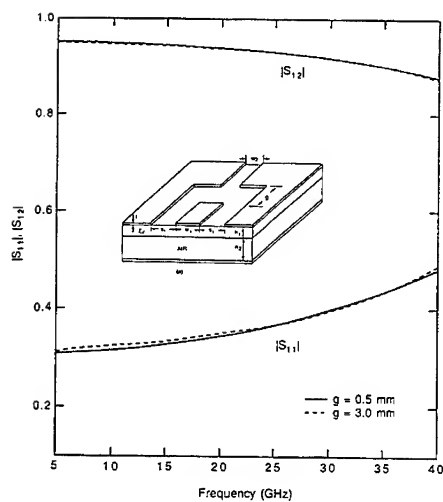


Fig. 2 Frequency-dependent S-parameters of a CPW-slot line transition (Fig. 1(a)) for two different values of gap g ($w_1=0.2$ mm, $s_1=0.6$ mm, $w_2=0.4$ mm, $h_1=0.254$ mm, $h_2=0.4$ mm, $t_w=0.003$ mm, $\epsilon_r=9.6$ and the metallization $\sigma=10000$ s/mm)

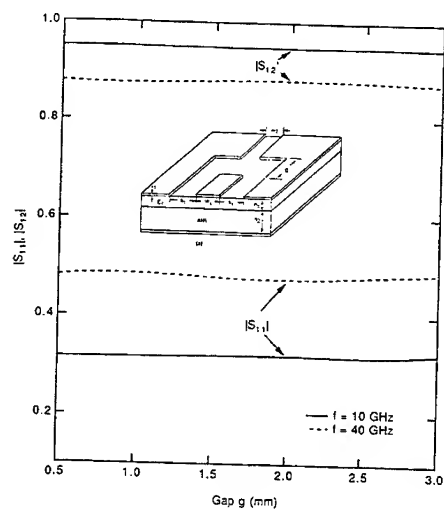


Fig. 3 Variation of the S-parameter versus the gap g of a CPW-slot line transition (Fig. 1(a)) for two different frequencies. Other structure parameters are as same as those in Fig. 2

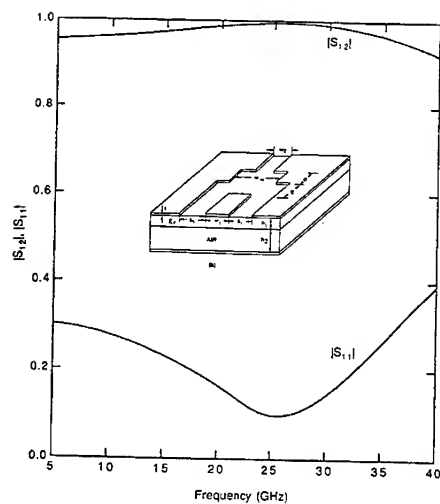


Fig. 4 Frequency-dependent S-parameters of a cascaded CPW-slot line transition as shown in Fig. 1(b). The length and the gap of the intermediate section are, respectively, $d=1.5$ mm and $w_m=1.0$ mm. Other structure parameters are the same as those in Fig. 3

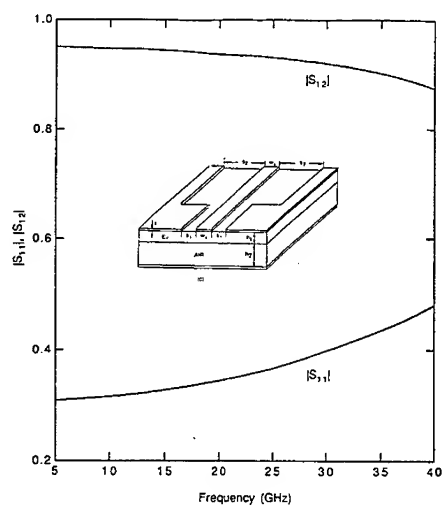


Fig.5 Frequency-dependent S-parameters of a uniplanar CPW-microstrip transition as shown in Fig.1(c) ($w_1=0.2$ mm, $s_1=0.2$ mm, $s_2=5.0$ mm, $h_1=0.254$ mm, $h_2=0.2$ mm, $t=0.003$ mm, $\epsilon_r=9.6$ and the metallization $\sigma=10000$ s/m)

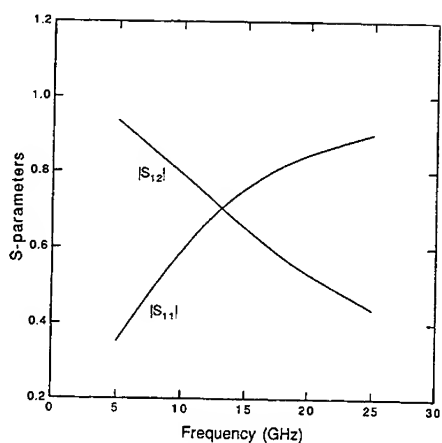


Fig.7 Frequency-dependent s-parameters of the interconnect assembly of Fig.1 ($b_m=b_c=d_m=d_c=0.1$ mm, $h_m=h_c=0.2$ mm, $g=0.3$ mm, $s_m=s_c=0.25$ mm, $w_m=w_c=0.2$ mm, $w_b=0.1$ mm, $s_b=0.2$ mm, $t_c=t_m=t_b=0$, $\epsilon_r=12.9$, $\epsilon_{rm}=9.8$)

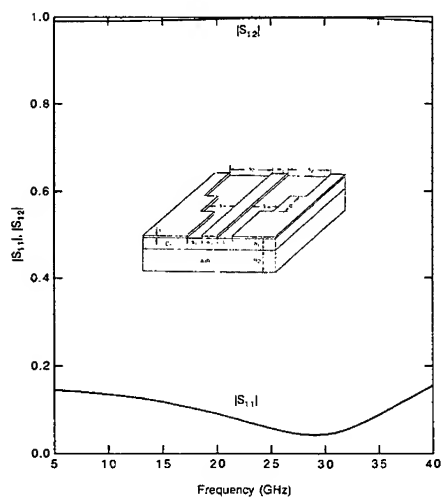


Fig.6 Frequency-dependent S-parameters of a cascaded uniplanar CPW-microstrip transition as shown in Fig.1d. The length and the gap of the intermediate section are, respectively, $d=1.0$ mm and $s_m=0.4$ mm. Other structure parameters are the same as those in Fig.5

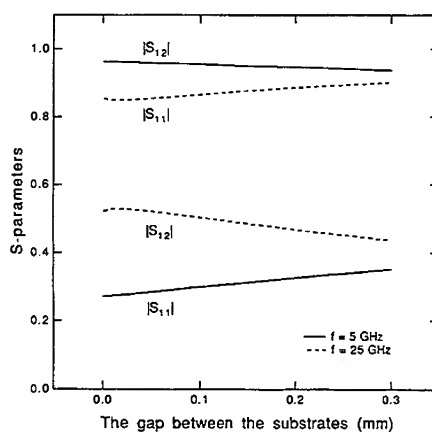


Fig.8 S-parameters as functions of the gap g between the substrates for two different frequencies $f=5$ GHz and $f=25$ GHz ($b_m=b_c=d_m=d_c=0.1$ mm, $h_m=h_c=0.2$ mm, $s_m=s_c=0.25$ mm, $w_m=w_c=0.2$ mm, $w_b=0.1$ mm, $s_b=0.2$ mm, $t_c=t_m=t_b=0$, $\epsilon_r=12.9$, $\epsilon_{rm}=9.8$)

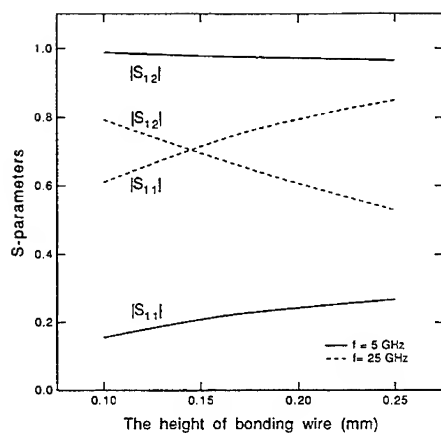


Fig.9 S-parameters as the functions of the height of bonding wire $a_m (=a_n)$ for two different frequencies $f=5$ GHz and $f=25$ GHz ($b_m=b_n=d_m=d_n=0.1$ mm, $h_m=h_n=0.2$ mm, $g=0.001$ mm, $w_m=w_n=0.2$ mm, $w_b=0.1$ mm, $s_c=0.2$ mm, $t_c=t_m=t_n=0$, $\epsilon_{rc}=12.9$, $\epsilon_{rm}=9.8$)

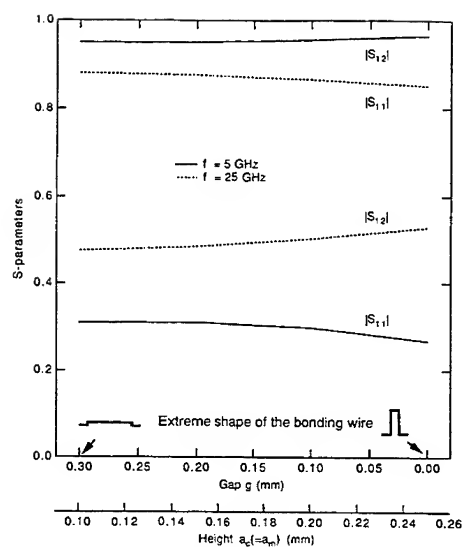


Fig.10.S-parameters as the functions of the height of bonding wire. The gap between the substrates is reduced simultaneously with increasing height so as to keep the total length of the bonding wire constant. ($b_m=b_n=d_m=d_n=0.1$ mm, $h_m=h_n=0.2$ mm, $w_m=w_n=0.2$ mm, $w_b=0.1$ mm, $s_c=0.2$ mm, $t_c=t_m=t_n=0$, $\epsilon_{rc}=12.9$, $\epsilon_{rm}=9.8$)

THEORETICAL ANALYSIS OF MICROSHIELD TRANSMISSION LINES WITH DUAL-PLANE DISCONTINUITIES

T. M. Weller and P. B. Katehi

*NASA Center for Space Terahertz Technology
University of Michigan
Ann Arbor, MI 48109-2122*

Abstract

A method is presented to theoretically characterize "planar" microshield transmission line circuits which may have dual-plane discontinuities. The technique involves a space domain integral equation (SDIE), derived from the application of equivalent magnetic currents in more than one plane, which is solved with the method of moments (Galerkin's method). Microshield is a relatively new type of monolithic transmission line, formed by replacing the substrate of a coplanar waveguide (CPW) with an air-filled metallized cavity connecting the upper ground planes. This line does not require via-holes or air bridges for ground equalization, radiates less than CPW, and can provide a wide range of impedance levels. An accurate and efficient method for computing the free-space admittance matrix will be discussed along with numerical results for some typical discontinuities.

1 INTRODUCTION

This paper presents a method to theoretically characterize "planar" microshield transmission line circuits which may have dual-plane discontinuities. The technique involves a space domain integral equation (SDIE), derived from the application of equivalent magnetic currents in more than one plane, which is solved with the method of moments (Galerkin's method).

Microshield is a relatively new type of monolithic transmission line, formed by replacing the substrate of a coplanar waveguide (CPW) with an air-filled metallized cavity connecting the upper ground planes. As discussed in previous publications [1, 2] microshield does not require via-holes or air bridges for ground equalization, radiates less than CPW, and can provide a wide range of impedance levels. It has been shown [3] that CPW discontinuities can be very accurately modeled using the SDIE technique with equivalent magnetic currents. In this approach the slots (apertures) in the metal are replaced with equivalent currents, and field continuity is enforced in order to generate the integral relations. Because of the similarity between microshield and CPW on the upper metallization plane, the same approach may be used in the analysis of microshield.

A representative microshield circuit is shown in Figure 1. Typical discontinuities in the upper metallization layer consist of step changes in the width of the center conductor, tuning stub geometries, and coupled short-end or open-end lines. In addition to discontinuities in the upper signal lines and ground, however, the microshield line may also possess geometrical or material changes in the lower shielding cavity. These would be in the form of step changes in the cavity height or width, an additional port in the sidewall of a cavity for stubs or a T-junction, or possibly changes in the

dielectric filling material along the length of a circuit. In order to model these effects additional planes of equivalent currents are required.

This paper will present a theoretical analysis for open microshield circuits with dual-plane discontinuities using the SDIE technique and piecewise sinusoidal (rooftop) expansion functions. An accurate and efficient method for computing the free-space admittance matrix will be discussed along with numerical results for some typical discontinuities.

2 FORMULATION

The formulation is a rigorous full-wave analysis which involves a space-domain integral equation (SDIE) that is generated through the application of equivalent magnetic currents. This approach has previously been applied in a variety of electromagnetic problems, such as the analysis of waveguide junctions [4], scattering from microstrip patches [5], and characterization of planar transmission lines such as coplanar waveguide [3]. The distinction, in this case, is the utilization of equivalent current planes both parallel and perpendicular to the direction of signal propagation, which is essentially a combination of the solutions to waveguide and planar line problems. The method is particularly well-suited to the study of microshield transmission lines, however, as it provides a powerful and relatively simple means of studying the broad array of different circuit geometries mentioned above. Furthermore, as will be shown later, a number of steps may be taken to enhance the efficiency of the numerical computation.

The first step in the analysis is the simplification of the circuit geometry, which is obtained through the application of the equivalence principle. This step is illustrated in Figure 1. Here fictitious metal surfaces are introduced which transform each region of the circuit into either a closed metallic cavity or free space, and upon each side of these surfaces magnetic currents have been imposed which act as equivalent sources in each region. To determine the strength of these unknown currents the condition of continuous tangential electric and magnetic fields is then enforced over each of the fictitious planes. Since $\vec{M} = \vec{E} \times \hat{n}$, where \hat{n} is the outward unit normal in each region, continuity of \vec{E}_{tan} is strictly satisfied by setting $\vec{M}_{lower} = -\vec{M}_{upper} = \vec{M}$. The continuity of \vec{H}_{tan} is expressed in terms of the following integral equation:

$$\hat{n} \times \int_{S'} [\vec{G}_{ext}(\vec{r}, \vec{r}') + \vec{G}_{int}(\vec{r}, \vec{r}')] \cdot \vec{M}_s(\vec{r}') ds' = \vec{J}_s \quad (1)$$

where $\vec{G}_{ext,int}$ are the magnetic field dyadic Green's functions external and internal to the metallic cavities, respectively, and \vec{J}_s is the ideal current source assumed with the gap generator model. The solution is obtained by first dividing each surface into subsections and expanding the unknown magnetic currents using localized rooftop basis functions. These functions have a piecewise sinusoidal variation in the longitudinal direction, and are constant in the transverse direction. Equation 1 is then enforced in an average sense over each of the subsections, and is solved by using the method of moments (Galerkin's method) to generate a system of linear equations based on the mutual coupling, or admittance, between each of the currents. The solution of this system yields the complex coefficients of these basis functions, which is equivalent to finding the electric field in the slots. Standard transmission line theory may then be used to analyze the fields in the feedlines since they are in the form of pure standing waves. The details of this analysis may be found in [3].

The implementation of this formulation has been structured to take advantage of the inherent symmetry in typical microshield circuit geometries. An example of this is the manner in which the

magnetic current surfaces are discretized. By selectively creating separate mesh *regions* on these surfaces, and using additional connecting current nodes, the symmetry of the coupling between different regions can easily be exploited to reduce the necessary computations, typically by a factor of 2.5 to 3. In terms of numerical considerations, regions with a uniform discretization are advantageous since the internal Green's function expansions may be written in terms of the sum and difference of the source and observation points, as opposed to the absolute position of each, using the following trigonometric identity:

$$\sin(a)\sin(b) = \frac{1}{2}[\cos(a-b) - \cos(a+b)] \quad (2)$$

This will reduce the required computations for a region by a factor of $\frac{N}{2}$, where N is the number of basis functions in a given direction [6]. A further consideration is the necessary current sampling rate, i.e. subsection size, required to accurately analyze a circuit. Since the current will vary most rapidly in localized areas near a discontinuity, mesh regions with high sampling rates (e.g. 60 samples per λ_0) are used here and regions with low sampling rates (e.g. 30 samples per λ_0) are used in slowly varying areas such as the feeding lines. This technique does not preclude the use of the two previous optimizations and can significantly reduce the required number of unknowns. Finally, the use of vertically oriented equivalent current surfaces may be used to internally couple the elements on the feedlines to elements in other parts of a circuit. Since the cavity heights for microshield circuits are typically on the order of a few hundred μm , a small number of nodes are required on the vertical walls, and thus the coupling is accomplished through fewer element interactions.

2.1 Internal Admittance Evaluation

Evaluation of the internal admittance elements requires the use of dyadic Green's functions for magnetic current sources inside a homogeneously-filled metallic box. The derivation of these expressions is straightforward, and will not be given here. It is worth mentioning, however, that a discreet choice in the way these functions are written can greatly simplify the evaluation of the resulting analytic integrals. As shown in Figure 1, the lower shielding structure is a truncated cavity, rather than a semi-infinite line that extends beyond the source. Due to its location beyond the gap generator, which acts as a fixed boundary condition, this termination will not influence the characteristics of the circuit under analysis. In treating this type of cavity, one has the option of writing Green's functions which are separated in either \hat{x} , \hat{y} , or \hat{z} , i.e. $\bar{G}^{x<, >x'}$, $\bar{G}^{y<, >y'}$, or $\bar{G}^{z<, >z'}$. Since each form is equivalent, they may be interchanged as needed to simplify the analysis, the optimum orientation being with the separation direction always normal to the plane of the source currents, i.e. $\bar{G}^{x<, >x'}$ is used for currents in the y - z plane and $\bar{G}^{z<, >z'}$ for currents in the x - y plane. In this way, the observation coordinates can be kept either above or below the source coordinates, thereby avoiding the complicated integrals that result when two subsections overlap. With a semi-infinite waveguide in the \hat{z} direction, however, the continuous nature of the corresponding eigenfunction forces the use of $\bar{G}^{x<, >x'}$ for all current elements. This in turn leads to relatively tedious expressions for the mutual coupling between currents which overlap in the \hat{z} direction, and will severely complicate an attempt to implement variable discretization on the mesh regions.

2.2 External Admittance Evaluation

An efficient technique has been utilized for the evaluation of the external admittance values which

represent the mutual coupling between current elements on the free-space (upper) side of the microshield geometry. This approach follows the basic structure of the method outlined in [5]. The admittance is expressed as

$$Y^{ext} = -jk_o Y_o \int_S ds \int_{S'} ds' [2\tilde{f}(\vec{r}') \cdot \bar{\Gamma}_o(\vec{r}, \vec{r}')] \cdot \vec{w}(\vec{r}) \quad (3)$$

where S and S' denote the observation and source subsections, \tilde{f} is the current expansion function, \vec{w} is the rooftop weighting function, and $\bar{\Gamma}_o$ is the free space dyadic Green's function

$$\begin{aligned} \bar{\Gamma}_o(\vec{r}, \vec{r}') &= \left\{ \bar{I} + \frac{1}{k_o^2} \nabla \nabla \right\} G_o(\vec{r}, \vec{r}') \\ G_o(\vec{r}, \vec{r}') &= \frac{e^{-jk_o|\vec{r}-\vec{r}'|}}{4\pi|\vec{r}-\vec{r}'|} \\ |\vec{r}-\vec{r}'| &= \sqrt{(y-y')^2 + (z-z')^2} = R \end{aligned} \quad (4)$$

where \vec{r} and \vec{r}' represent the observation and source points, respectively. The factor of two was introduced to account for the presence of the assumed infinite ground plane. Equation 3 may be simplified by using successive integration-by-parts to transfer the derivatives from the Green's function onto the expansion and testing functions. Letting the expansion function for current in the $\hat{\zeta}$ direction be written as $\tilde{f}_{\zeta}(\zeta', \theta') = \hat{\zeta} T(\zeta') P(\theta')$, where T is a piecewise sinusoid and P is a pulse, the expressions for the like- and cross-polarization admittance are then given by

$$Y_{\zeta\zeta}^{ext} = \frac{-2jY_o}{k_o} [k_o^2 A(\zeta\theta, \zeta'\theta') - B(\zeta\theta, \zeta'\theta')] \quad (5)$$

$$Y_{\theta\zeta}^{ext} = \frac{2jY_o}{k_o} B(\theta\zeta, \zeta'\theta') \quad (6)$$

$$\begin{aligned} A(\zeta\theta, \zeta'\theta') &= \int_S ds P(\theta) T(\zeta) \int_{S'} ds' P(\theta') T(\zeta') G_o(\vec{r}, \vec{r}') \\ B(\zeta\theta, \zeta'\theta') &= \int_S ds P(\theta) T'(\zeta) \int_{S'} ds' P(\theta') T'(\zeta') G_o(\vec{r}, \vec{r}') \end{aligned}$$

For the sake of brevity, only the evaluation of the like-polarization element, $Y_{\zeta\zeta}^{ext}$, will be covered here, as the cross-polarization term may be handled in a like manner. Furthermore, in order to easily accommodate variable subsection sizes, each admittance element is broken down into four similar interactions which result from the coupling between the two halves of the rooftop functions. By choosing the scaling parameter of the expansion functions (refer to [3]) to be the free space wavenumber, k_o , and separating the exponent of G_o into real and imaginary parts, the coupling between the first two halves of a source and observation subsection can be expressed as

$$\begin{aligned} Y_{\zeta\zeta}^{ext,11} &= \frac{2jY_o k_o}{\sin(k_o \zeta_1) \sin(k_o \zeta'_1)} \int_{\zeta_1}^{\zeta_2} d\zeta \int_{\zeta'_1}^{\zeta'_2} d\zeta' \int_{\theta_1}^{\theta_2} d\theta \int_{\theta'_1}^{\theta'_2} d\theta' \cos[k_o(\zeta + \zeta') - k_o(\zeta_1 + \zeta'_1)] \\ &\quad \left(\underbrace{\frac{\cos(k_o R)}{R}} - \underbrace{\frac{j \sin(k_o R)}{R}} + \underbrace{\frac{1}{R}} \right) \end{aligned} \quad (7)$$

where $\sin(k_o l_\zeta) \sin(k_o l_{\zeta'})$ is the normalization factor of the expansion functions. Notice that the $\frac{1}{R}$ term has been added and subtracted from the equation, allowing the singularity at the source to be extracted and treated analytically. In the following, the first and second terms in the underbrackets in 7 will be denoted as FT and ST , respectively. For FT ,

$$\lim_{R \rightarrow 0} FT = -jk_o \quad (8)$$

The second term in the underbrackets may be evaluated using an analytic expression for the integration over θ and θ' , since the cosine is a function of only ζ and ζ'

$$\begin{aligned} I_{\frac{1}{R}} &= \int d\theta \int d\theta' \frac{1}{\sqrt{(\zeta - \zeta')^2 + (\theta - \theta')^2}} \\ I_{\frac{1}{R}}|_{\zeta=\zeta'} &= |\theta - \theta'| \{1 - \ln|\theta - \theta'|\} \\ I_{\frac{1}{R}}|_{\zeta \neq \zeta'} &= R - (\theta - \theta') \ln(\theta - \theta' + R) \\ I_{\frac{1}{R}}|_{\zeta=\zeta', \theta_1=\theta'_1, \theta_2=\theta'_2} &= 0 \end{aligned} \quad (9)$$

Equations 8 and 9 are then implemented in a Gauss-Legendre numerical integration routine. For nonoverlapping cells, the ratio, r_d , of the distance between cell centroids and the maximum cell dimension is computed to determine the order of the integration. If $r_d > 10$, a 1-point, 2 sample scheme is sufficient, where the number of samples refers to the number of testing points per cell in each direction. If $r_d < 10$, a 2-point scheme is required with the number of samples ranging from two to four. For the case of overlapping cells, the imaginary part of FT may be computed in the same fashion as for nonoverlapping cells, while the real part requires an 8- or 12-sample 2-point integration for cell sizes which are $> \frac{\lambda_o}{160}$ or $< \frac{\lambda_o}{160}$, respectively. The integration of ST over ζ, ζ' is the most critical contribution, and this is handled using a subroutine based on a 10-point Gauss-Legendre, 21-point Kronrod formula.

The guidelines stated above were determined using a criterion of $\approx 0.5\%$ relative error, and have been tested for cell sizes from $\frac{\lambda_o}{15}$ to $\frac{\lambda_o}{500}$. Utilizing the Toeplitz nature of the external admittance matrix, the time required to compute 500x500 elements on a $1\lambda_o \times .15\lambda_o$ mesh is 20 cpu seconds on an IBM RS/6000 workstation.

3 NUMERICAL RESULTS

In order to demonstrate the formulation, a comparison is made for two variations of the circuit shown in Figure 1. The parameters held constant in both designs are: $P_1 = 250\mu m$, $P_2 = 500\mu m$, $C_1 = 1500\mu m$, and $C_2 = 1900\mu m$. In Figure 2, the center cavity section is air-filled and the length of the coupling section is $C_3 = 5000\mu m$. The response is relatively narrowband and the maximum coupling is limited to -2.35 dB, due to the power lost to radiation. In Figure 3, the center cavity section is filled with silicon ($\epsilon_r = 11.7$) and the coupling length is correspondingly reduced to $C_3 = 1400\mu m$. In this case the response is more broadband, and the coupling increases to -0.33 dB. The reduction in the radiated power is due to higher field concentration in the dielectric, and could be further improved by reducing the width of the coupling section cavity. It is noted that no optimization of either circuit has been performed.

Each of the data points shown in these figures required ≈ 280 basis functions and approximately 20 cpu minutes to compute using an IBM RS/6000 workstation.

4 ACKNOWLEDGEMENTS

This work is supported by the NASA Center for Space Terahertz Technology. The authors would also like to thank Dr. Nihad Dib for his valuable suggestions and his support in supplying theoretical data for comparison purposes.

References

- [1] N. I. Dib, W. P. Harokopus Jr., P. B. Katehi, C. C. Ling and G. M. Rebeiz, "Study of a Novel Planar Transmission Line", *1991 IEEE MTT-S Digest*, pp. 623-626.
- [2] N. I. Dib, P. B. Katehi, "Impedance Calculation for the Microshield Line," *Microwave and Guided Letters*, Vol. 2, No. 10, Oct. 1992, pp. 406-408.
- [3] N. I. Dib and P. B. Katehi, "Modeling of Shielded CPW Discontinuities Using the Space Domain Integral Equation Method (SDIE)," *Journal of Electromagnetic Waves and Applications*, April 1991.
- [4] Z. Shen and R. Hua, "Moment method analysis of rectangular waveguide T-junctions having arbitrary cross-sections", *Int. J. Electronics*, 1991, Vol. 71, No. 3, 463-469.
- [5] K. Barkeshli and J. Volakis, "Electromagnetic Scattering from an Aperture Formed by a Rectangular Cavity Recessed in a Ground Plane," *Journal of Electromagnetic Waves and Applications*, Vol. 5, No. 7, pp. 715-734, 1991.
- [6] L. P. Dunleavy, *Discontinuity Characterization in Shielded Microstrip: A Theoretical and Experimental Study*, Ph.D. Thesis, University of Michigan, 1988.

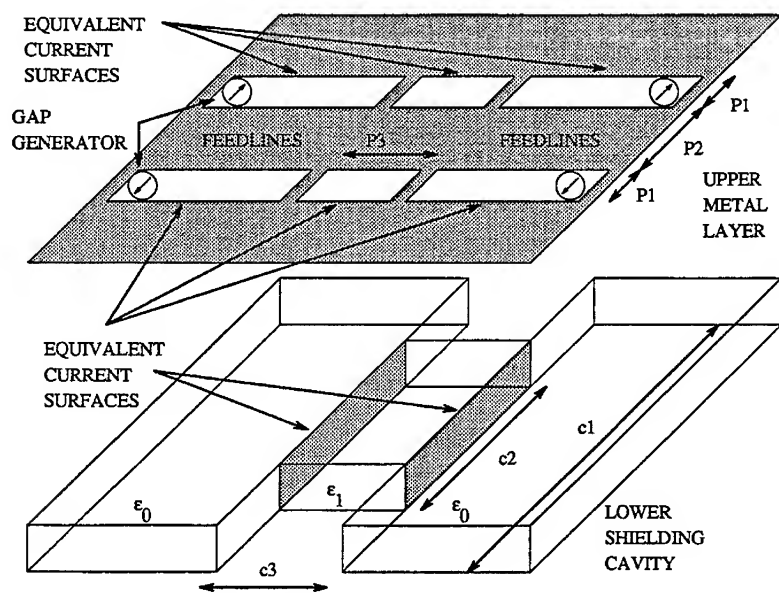


Figure 1: Example of a microshield gap-coupled circuit with dual-plane discontinuities, consisting of the upper metal layer and the lower shielding cavity. The feedlines and gap generators are shown on either side of the slot coupling section. The lower shielding cavity narrows in the center of the circuit and may also have a dielectric material change. All planes where equivalent magnetic currents are used to model the structure are indicated.

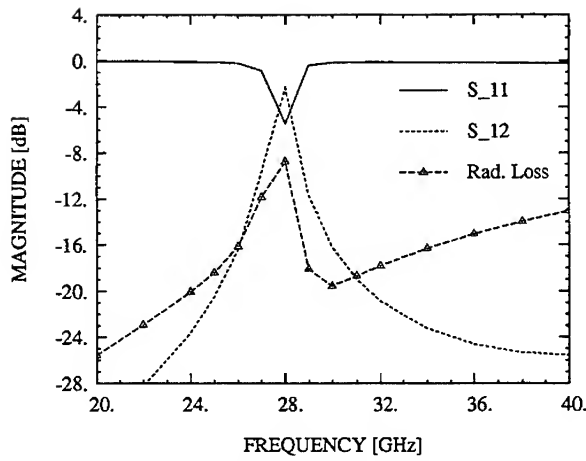


Figure 2: Scattering parameters and radiation loss, $(1 - |S_{11}|^2 - |S_{21}|^2)$, for the gap-coupled circuit using $\epsilon_r=1$, $C_3=5000 \mu\text{m}$, and $P_3=4900 \mu\text{m}$.

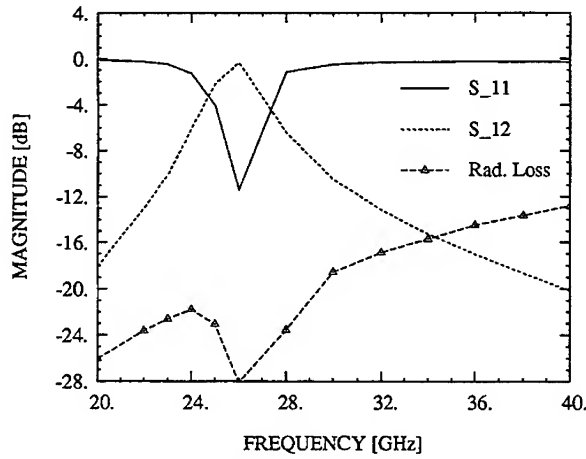


Figure 3: Scattering parameters and radiation loss, $(1 - |S_{11}|^2 - |S_{21}|^2)$, for the gap-coupled circuit using $\epsilon_r=11.7$, $C_3=1400 \mu\text{m}$, and $P_3=1300 \mu\text{m}$.

SYMMETRY ANALYSIS OF LARGE TWO-DIMENSIONAL CLUSTERS OF COUPLED CAVITY RESONATORS

Ross A. Speciale
Hughes Missile System Company
Pomona, California 91769-2507

ABSTRACT

Electrically large, two-dimensional clusters of directly-coupled cavity resonators, ordered in a square or in a hexagonal lattice, perform and can be used as doubly-periodic wave-guiding structures. The considered two-dimensional clusters may extend hundreds of free-space wavelengths in length and width, and can be designed to exhibit wide relative transmission bandwidths. The transmission losses within such large passbands are very low if high-Q cavity resonators are used as 'unit-cells' of such clusters.

Large relative transmission bandwidths are obtained by using resonant-iris coupling between resonators. Further, because of the intrinsic 'multiport impedance match' between mutually-identical multiport resonators, guided traveling electromagnetic waves propagate without reflection through such structures in every arbitrary direction.

Such two-dimensional clusters of coupled cavity resonators can be excited by any arbitrary topological distribution of multiple, mutually-coherent signal sources. Practical cluster-structures of finite physical extent can be excited by sets of signal sources properly aligned around the structure perimeter. Numerous, and very complex two-dimensional patterns of guided, traveling-wave fields can be obtained, by properly controlling the relative amplitudes and phases of the coherent driving sources.

A comprehensive symmetry analysis of such two-dimensional clusters, with either a square or a hexagonal lattice, is being performed, to determine the dependence of the wave-impedance and of the propagation constant upon the frequency and the azimuthal direction of wave-propagation. Further, the boundary conditions for reflection-free, multiport impedance matching around the perimeter of finite clusters are being formally defined.

Generalized matrix-algorithms have been derived that formally express the open-circuit impedance matrix of a cluster of finite extent, as seen from the 'external' ports, aligned around the structure perimeter. The derived generalized matrix-algorithms use a multi-level diakoptic approach, by tearing the cluster into progressively smaller subdivisions, while maintaining geometrical similarity, and conserving the translation-, rotation-, and reflection-symmetry of the whole system. Finally, formal expressions are obtained for the two-dimensional traveling-wave amplitude and phase patterns, generated by any given distribution of mutually-coherent excitation sources.

1 - BASIC ASSUMPTIONS.

The considered square-lattice clusters are composed of N^2 circular-cylindrical cavity resonators, that are regularly spaced (side by side and with parallel axes) along the N rows and N columns of a square lattice. The resonators are assumed to be all mutually identical, and directly coupled by way of common-wall resonant irises. Each resonator has four coupling irises, all equally oriented and symmetrically located, at the mid-point between the top and bottom shorting planes of the resonators, and spaced azimuthally (around the cylinder axis) by equal 90° angles.

The considered square-lattice clusters have, therefore, a square perimeter, with N cavity resonators along each side, with a total of $4(N-1)$ resonators along the whole perimeter.

Each of the $4(N-2)$ resonators along the sides has one 'external' coupling iris, but the four resonators on the corners have two external irises. There are therefore $4(N-2) + 8 = 4N$ 'external' coupling irises along the perimeter of the cluster, and these irises constitute the interface between the square cluster and the external loads and sources.

2 - EDGE-FEEDING OF A COUPLED-CAVITY CLUSTER.

Each of the mutually coherent amplitude-, and phase-controlled microwave signals, injected into the cluster through any or all of the 'external' irises, fills all the N^2 cavity resonator with TM_{010} resonant fields. The amplitude and phase of the TM_{010} resonant fields, generated by each of the edge-injected signals in any of the N^2 cavity resonators of the cluster, is determined by: a) the amplitude and phase of the injected signal, b) the position (along a specified cluster side) of the signal-injection point, and c) the specific (i,j) position of the considered cavity resonator, along the rows and columns of the cluster lattice.

Further, as a consequence of the linearity of the cluster, the injection of multiple edge-feeding signals, through a set of external irises, results in a vectorial linear superposition of TM_{010} resonant-field contributions within each of the N^2 cavity resonators. The resulting, two-dimensional, TM_{010} -field amplitude and phase distribution, generated by this type of 'complex wave spectrum' cluster-excitation, can be electronically controlled, by controlling the relative amplitudes and phases of the edge-injected signals.

2.1 - PROBLEM DEFINITION.

The objective of the performed analysis, is the determination of a mathematical description of the physical process of two-dimensional guided-wave propagation, from the cluster external irises to each of the N^2 cavity resonators, the process that provides the fundamental mechanism by which the amplitudes and phases of the edge-injected signals are correlated to the amplitudes and phases of the TM_{010} resonant fields within the cavity resonators of the cluster.

The obtained mathematical description is in terms of both symbolic algorithms and numerical-computation procedures.

3 - ANALYSIS STRATEGY.

3.1 - COMPLEXITY OF THE NETWORK REPRESENTATION.

The above defined two-dimensional, guided-wave-propagation problem can be solved by applying some rather advanced, unconventional and sophisticated (but nevertheless clearly understood) methods of linear network analysis.

The substantially advanced character of the required analysis is a consequence of the complexity of the linear-network representation of the cavity-resonator cluster. Indeed, this representation is in terms of an electrically-large cluster of interconnected, multi-port 'unit-cell' network-elements, physically extending tens or even hundreds of free-space wavelengths in both width and length. Further, the required analysis must be based on the availability of experimentally-determined electrical-performance parameters, obtained by performing calibrated measurements upon precision-machined physical models of the 'unit cell' cavity resonator.

3.2 - THE POWER OF SYMMETRY ANALYSIS.

Fortunately, the considered cluster of cavity resonators is known to be reciprocal, and to exhibit: a) translational symmetry in two mutually orthogonal dimensions, b) rotational symmetry around at least two mutually-orthogonal axes, and c) reflection-symmetry with respect to at least five mutually-intersecting planes. Further, the linear, and reciprocal four-port networks, that represent the unit-cell cavity resonators, also exhibit the same rotational-, and reflection-symmetries as the whole cluster. This combination of reciprocity, rotational-, and reflection-symmetry leads to a very substantial reduction of the dimensionality of the defined network-analysis problem, a reduction of such proportions as to make the solution of an almost intractable, and daunting problem feasible.

3.3 - SYMMETRIES OF THE PARAMETER MATRICES.

Indeed, the identification of the reciprocity and of the intrinsic symmetries of both the four-port unit-cell networks, and of the whole cluster immediately specifies the intrinsic symmetry-structure of the corresponding scattering (S), impedance (Z), and admittance (Y) matrices.

All these matrices are known to be both symmetric and 'circulant'^{1,2}, already for the four-port unit-cell network that represents the cavity resonators, and further to be both symmetric and 'block-circulant' for the whole cluster of N rows and N columns.

3.4 - THE SYMMETRIES OF THE UNIT-CELL NETWORK.

The symmetry-structure of the scattering matrix S_4 of the four-port unit-cell network is known to have the symmetric and circulant form:

$$S_4 = \begin{vmatrix} S_{11} & S_{12} & S_{13} & S_{12} \\ S_{12} & S_{11} & S_{12} & S_{13} \\ S_{13} & S_{12} & S_{11} & S_{12} \\ S_{12} & S_{13} & S_{12} & S_{11} \end{vmatrix} = \begin{vmatrix} a & b & c & b \\ b & a & b & c \\ c & b & a & b \\ b & c & b & a \end{vmatrix} \quad (1)$$

and to have, therefore, only three (rather than 16) different elements ($S_{11} = a$, $S_{12} = b$, and $S_{13} = c$). The same symmetry structure is shared by the corresponding impedance matrix Z_4 , that is known to have the similar symmetric and circulant form:

$$Z_4 = \begin{vmatrix} Z_{11} & Z_{12} & Z_{13} & Z_{12} \\ Z_{12} & Z_{11} & Z_{12} & Z_{13} \\ Z_{13} & Z_{12} & Z_{11} & Z_{12} \\ Z_{12} & Z_{13} & Z_{12} & Z_{11} \end{vmatrix} = \begin{vmatrix} a & b & c & b \\ b & a & b & c \\ c & b & a & b \\ b & c & b & a \end{vmatrix} \quad (2)$$

The impedance matrix Z_4 of the unit-cell network also has, therefore, only three different elements ($Z_{11} = a$, $Z_{12} = b$, and $Z_{13} = c$, with a, b, and c representing here impedance-matrix elements rather than scattering parameters).

3.5 - THE SYMMETRIES OF THE $N \times N$ CLUSTER.

Similarly, the $4N \times 4N$ scattering matrix S_{4N} of the whole array cluster of N rows and N columns is known to have the symmetric and block-circulant form:

$$S_{4N} = \begin{vmatrix} A & B & C & B^T \\ B^T & A & B & C \\ C & B^T & A & B \\ B & C & B^T & A \end{vmatrix} \quad (3)$$

and to have, therefore, essentially only three (rather than 16) different $N \times N$ matrix-blocks (identified by the symbols A , B , and C , with the fourth block B^T of the first block-row being just the transpose of the second block B , and as such not intrinsically different from block B , in the values of its elements). Further, at least the two matrix-blocks A and C are expected to be symmetric with respect to both the main diagonal and the cross-diagonal, with consequent very substantial reduction in the total number of different elements across the $4N \times 4N$ scattering matrix S_{4N} .

Finally, the symmetry-structure of the $4N \times 4N$ impedance matrix Z_{4N} of the whole cluster is known to also be symmetric and block-circulant as that of the scattering matrix S_{4N} :

$$Z_{4N} = \begin{vmatrix} A & B & C & B^T \\ B^T & A & B & C \\ C & B^T & A & B \\ B & C & B^T & A \end{vmatrix} \quad (4)$$

Again, in the expression (4) of the impedance matrix Z_{4N} of a whole $N \times N$ cluster of directly coupled cavity resonators the symbols A , B , and C stand for $N \times N$ impedance-matrix blocks, rather than $N \times N$ scattering-matrix blocks (the use of simple block-symbols is a convenient artifice to evidence the symmetry-structure of the considered matrices!).

3.6 – THE MASSIVE MUTUAL INTERDEPENDENCE OF MATRIX ELEMENTS.

Clearly, the intrinsic physical symmetries of a whole $N \times N$ cluster of directly coupled cavity resonators results in a very substantial reduction of the number of matrix elements that truly have different values. The total number of elements of the scattering (S_{4N}) and impedance (Z_{4N}) matrices is, however, $16N^2$, and the residual number of different matrix element may still be rather large. But, if the unit-cell networks are mutually identical (or even only approximately so), as assumed in Section 1, the three different unit-cell parameters a , b , and c of expression (1) or (2) will control and characterize the guided-wave propagation process, from resonator to resonator, through the whole $N \times N$ cluster. This means that, regardless of how large or small the number E_D of different elements of the S_{4N} , and Z_{4N} matrices is relative to the $16N^2$ total, only three (any three!) of these matrix elements will be truly independent, while the remaining $E_D - 3$ elements can be expressed as functions thereof.

In conclusion, the $16N^2$ elements of the S_{4N} , and Z_{4N} matrices are mutually related by $16N^2 - 3$ mutual functional relations, and this massive mutual interdependence of matrix elements surely constitutes a unique character, not just for the S_{4N} , and Z_{4N} matrices, but for all the mutually-equivalent matrix-representations of the electromagnetic-wave propagation properties of the generalized $N \times N$ cavity resonator cluster (other useful matrix representations are provided by the $4N \times 4N$ ABCD-matrix K_{4N} , and by the $2N \times 2N$ image-impedance matrix Z_I , and image-transfer-function matrix T_{IV}).

3.7 – DIAKOPTIC NETWORK ANALYSIS.

Diakoptics is a piecewise approach to the solution of large-scale interconnected systems. The diakoptic method was conceived by G. Kron in the 1950's and developed by H. H. Happ and others. The motivation came from electric power system problems.

Kron and Happ developed a theory of diakoptics for power systems represented by linear networks, for which the diakoptic approach gives exact solutions. The basic idea, introduced by Kron is to solve large-scale network problems in at least two steps: a) the subnetwork level, and b) the interconnection level. The advantage of the diakoptic approach is that the smaller subnetworks are easier to solve.

Kron's derivation is rather obscure, and based on concepts of tensor analysis. Happ has expanded the theory and the applications along the same lines.

3.8 – APPLICATION OF DIAKOPTICS TO CLUSTER ANALYSIS.

We assume here that the integer number N of rows and column of the considered $N \times N$ cluster is not prime, and can therefore be expressed as a product of many integer factors. The application of a multi-level diakoptic approach to the analysis of a cavity resonator cluster becomes then possible, with a very substantial reduction of the required mathematical effort.

The steps of the diakoptic cluster analysis are:

- a) The subdivision (or 'tearing') of the considered cluster into a hierarchical system of progressively smaller sub-divisions, with each sub-division of any given level being further subdivided into smaller subdivisions.

- b) Solving the smallest sub-division first, then use the obtained solution to solve the next-higher level sub-division by network interconnection.

This approach becomes very clear, obvious, and advantageous if the number N of rows and columns in the cluster is a power of two ($N = 2^\alpha$ with α being an integer). In this case the considered cluster can be first subdivided in four equal parts, each having $2^{(\alpha-1)}$ rows and columns. Each of the resulting four parts can be further subdivided into four sub-sub-divisions of $2^{(\alpha-2)}$ rows and columns, and the subdivision process can be continued down to the level of the single unit-cell cavity resonator, which is a known cluster-component characterized by the three different a , b , and c elements of its S_4 scattering matrix.

3.9 – THE GENERALIZED INTERCONNECTION ALGORITHM.

A generalized diakoptic interconnection matrix-algorithm has been derived, that solves the linear-network analysis problem of interconnecting four square $n \times n$ clusters, to form a single $2n \times 2n$ cluster (Figure 1). The derived matrix-algorithm, operates on the three different blocks A , B , and C of the impedance matrix Z_{4n} of each $n \times n$ cluster, by simply enforcing Kirchoff's laws along the four common interfaces between the four component clusters, and is completely general in the sense that it is valid, rigorous, and applicable to any size cluster with any arbitrary number n of rows and columns. The derived matrix-algorithm becomes simply scalar in the case $n = 1$, which represents the interconnection of four-port cavity resonators into a minimal 2×2 cluster (Figure 2). The minimal 2×2 cluster of cavity resonators is characterized by its 8×8 impedance matrix Z_8 , which has been expressed in closed form in section 3.10.

Most importantly, the derived diakoptic interconnection matrix-algorithm includes formal expressions of the complex voltages, currents, and voltage-waves at the ports of the four $n \times n$ component-clusters, that are aligned along the interconnection interfaces.

These electrical quantities are 'internal' to the $2n \times 2n$ cluster, resulting from the interconnection, and are expressed as functions of the 'external' voltages, or currents, or voltage-waves, present at the 'external' ports of the cluster. As a consequence, all the 'internal' quantities, present along any interconnection interface between component-clusters of any level of subdivision, can be determined in terms of both amplitude and phase, if the boundary conditions around the perimeter of the whole $N \times N$ cluster are known. The boundary conditions must include the electrical characterization of both the external loads and the external sources of the edge-injected signals.

3.10 – THE IMPEDANCE MATRIX OF THE 2×2 CLUSTER.

The elements of the 8×8 impedance matrix Z_8 of the basic, minimal 2×2 cluster of cavity resonators (Figure 2) have already been expressed in closed form as functions of the different element a , b , and c of the impedance matrix Z_4 of a single unit-cell resonator. The formal, analytical expressions of the elements of the 8×8 impedance matrix Z_8 have been obtained by applying the developed, generalized diakoptic matrix algorithm to the special case ' $n = 1$, $N = 2$ ', where the four component-cluster, resulting from the subdivision of the considered 2×2 cluster, simply reduce to four, four-port unit-cell resonators. In this case, The generalized, diakoptic matrix algorithm reduces to a set of simple scalar expressions.

The 8×8 impedance matrix Z_8 only has seven different elements, rather than 64, all being functions of the same three complex impedance values a , b , and c that characterize any of the unit-cell resonators. The symmetry-structure of the impedance matrix Z_8 and the formal expressions of its seven different elements are given by the following eight equations:

$$Z_8 = \begin{vmatrix} A_1 & A_2 & B_1 & B_2 & C_1 & C_2 & B_1 & B_3 \\ A_2 & A_1 & B_3 & B_1 & C_2 & C_1 & B_2 & B_1 \\ B_1 & B_3 & A_1 & A_2 & B_1 & B_2 & C_1 & C_2 \\ B_2 & B_1 & A_2 & A_1 & B_3 & B_1 & C_2 & C_1 \\ C_1 & C_2 & B_1 & B_3 & A_1 & A_2 & B_1 & B_2 \\ C_2 & C_1 & B_2 & B_1 & A_2 & A_1 & B_3 & B_1 \\ B_1 & B_2 & C_1 & C_2 & B_1 & B_3 & A_1 & A_2 \\ B_3 & B_1 & C_2 & C_1 & B_2 & B_1 & A_2 & A_1 \end{vmatrix} = \quad (5)$$

$$= \begin{vmatrix} A & B & C & B^T \\ B^T & A & B & C \\ C & B^T & A & B \\ B & C & B^T & A \end{vmatrix} = \begin{vmatrix} Z_1 & Z_2 \\ Z_2 & Z_1 \end{vmatrix}$$

$$\begin{aligned}
A_1 &= Z_{11} = Z_{22} = Z_{33} = Z_{44} = \\
&= Z_{55} = Z_{66} = Z_{77} = Z_{88} = \\
&= a + \frac{2ab^2c - (2a^2 - b^2)(b^2 + c^2)}{4a(a^2 - b^2)}
\end{aligned} \tag{6}$$

$$\begin{aligned}
A_2 &= Z_{12} = Z_{21} = Z_{34} = Z_{43} = \\
&= Z_{56} = Z_{65} = Z_{78} = Z_{87} = \\
&= b \cdot \left\{ 1 + \frac{(b^2 + c^2)a - (2a^2 - b^2)2c}{4a(a^2 - b^2)} \right\}
\end{aligned} \tag{7}$$

$$\begin{aligned}
B_1 &= Z_{13} = Z_{31} = Z_{17} = Z_{71} = \\
&= Z_{24} = Z_{42} = Z_{28} = Z_{82} = \\
&= Z_{35} = Z_{53} = Z_{46} = Z_{64} = \\
&= Z_{57} = Z_{75} = Z_{68} = Z_{86} = \\
&= b \frac{2ac - (b^2 + c^2)}{4(a^2 - b^2)}
\end{aligned} \tag{8}$$

$$\begin{aligned}
B_2 &= Z_{14} = Z_{41} = Z_{27} = Z_{72} = \\
&= Z_{36} = Z_{63} = Z_{58} = Z_{85} = \\
&= \frac{(2a^2 - b^2)c^2 - (2ac - b^2)b^2}{4a(a^2 - b^2)}
\end{aligned} \tag{9}$$

$$\begin{aligned}
B_3 &= Z_{18} = Z_{81} = Z_{23} = Z_{32} = \\
&= Z_{45} = Z_{54} = Z_{67} = Z_{76} = \\
&= b^2 \frac{(2a^2 - b^2) - (2a - c)c}{4a(a^2 - b^2)}
\end{aligned} \tag{10}$$

$$\begin{aligned}
C_1 &= Z_{15} = Z_{51} = Z_{26} = Z_{62} = \\
&= Z_{37} = Z_{73} = Z_{48} = Z_{84} = \\
&= b^2 \frac{2ac - (b^2 + c^2)}{4a(a^2 - b^2)}
\end{aligned} \tag{11}$$

$$\begin{aligned}
C_2 &= Z_{16} = Z_{61} = Z_{25} = Z_{52} = \\
&= Z_{38} = Z_{83} = Z_{47} = Z_{74} = \\
&= b \frac{(b^2 + c^2)a - 2b^2c}{4a(a^2 - b^2)}
\end{aligned} \tag{12}$$

3.11 - THE IMPEDANCE MATRIX OF THE $2n \times 2n$ CLUSTER.

3.11.1 - ANALYTICAL STRUCTURE OF THE GENERALIZED ALGORITHM.

The formal expressions (5) of the 8×8 impedance matrix Z_8 , and the expressions (6)–(12) of the seven different elements of its three different 2×2 blocks A, B, and C, given in the previous Section 3.10, completely characterize the electrical performance of the minimum 2×2 square-lattice cluster of cavity resonators (Figure 2).

Further, the given expressions also represent the first step in the already described process of multi-level diakoptic network analysis. Indeed, the already anticipated generalized sub-array interconnection matrix-algorithm expresses the $4N \times 4N$ impedance matrix Z_{4N} of a $2n \times 2n$ cluster of cavity resonators as function of the $4n \times 4n$ impedance matrix Z_{4n} of each of the four $n \times n$ component sub-arrays ($N = 2n$).

The generalized sub-array interconnection matrix-algorithm is formulated as a relatively large set of matrix-functions. The given set of matrix-functions expresses the 64 ' $n \times n$ blocks' Z_{ij} of the $8n \times 8n$ impedance matrix Z_{4n} of the $N \times N$ square-lattice cluster, as functions of the three different $n \times n$ blocks A, B, and C of the impedance matrix Z_{4n} of the four sub-arrays.

3.11.2 – PORT-NUMBERING CONVENTIONS.

Very specific and carefully selected port-numbering sequences must be established, by convention, to firmly identify the relevant sets of port-voltages and of port-currents present at the ports of each of the four $n \times n$ sub-arrays. Indeed, first the 4 n ports of each sub-array (n ports being aligned along each of four sides) must be sequentially numbered (clockwise or counter-clockwise), in a continuous full cycle through all four sides, in order to preserve the symmetric and block-circulant structure of its impedance matrix Z_{4n} .

Further, it is convenient to have matching port-numbering sequences on either side of each of the four sub-array interconnection-interfaces (Figure 1). Matching sequences can be used if the cyclic port-numbering sequences of the sub-arrays alternate from clockwise to counter-clockwise at each of the four interconnection-interfaces.

Similarly, the 4 N 'external' ports of the resulting $N \times N$ square-lattice cluster must also be sequentially numbered (clockwise or counter-clockwise), in a continuous full cycle through all four sides, in order to preserve the symmetric and block-circulant structure of its impedance matrix Z_{4n} . As a consequence, the cyclic numbering sequence of its 'external' ports can only match the cyclic numbering sense of only two of the four sub-arrays (along two 'external' sides of each), but is necessarily reversed relative to the cyclic numbering sequence of the other two sub-arrays.

Indeed, the developed generalized diakoptic sub-array interconnection matrix-algorithm uses, as a convenient convention, counter-clockwise port-numbering sequences for sub-arrays A, and C, and clockwise port-numbering sequences for sub-arrays B, and D (Figure 1). The sequential port-numbering of each sub-array starts at the external port closest to the vertical ' $\alpha - \alpha$ ' interconnection interface (Figures 1 and 5: on top for sub-arrays A and B, and at the bottom for sub-arrays C and D).

Four different port counters i, j, h , and k are used (in the appropriate cyclic sequence around each sub-array) to identify the four sets V_{Xy} of port-voltages and the four sets I_{Xy} of port currents, present at the external ports of each of the four sub-arrays (where X stands for either A, B, C, or D, and y stands for either i, j, h , or k , where $i = 1, 2, \dots, n, j = n+1, n+2, \dots, 2n, h = 2n+1, 2n+2, \dots, 3n$, and $k = 3n+1, 3n+2, \dots, 4n$). The cyclic port-numbering sequence for the whole $2n \times 2n$ cluster, resulting from the interconnection of the four sub-arrays, starts at port 1 of sub-array A and runs counter-clockwise, thus matching the cyclic port-numbering sequences of sub-arrays A, and C, while running reverse to the sequences of sub-arrays B, and D.

Two different port counters $I = 1, 2, \dots, 4n$, and $J = 4n+1, 4n+2, \dots, 8n$, are used to identify the eight sets V_{Uv} of external-port voltages, and the four sets I_{Uv} of external-port currents, present at the $8n$ external ports of the whole $N \times N$ cluster, the ports that are aligned around its four sides (where U stands for either I or J , and v stands for either a, b, c , or d).

3.11.3 – VOLTAGE AND CURRENT VECTOR RELATIONS.

As a consequence of the above established port-numbering conventions and symbolism, eight vector-matrix relations hold between four sets of external-port voltages and the corresponding four sets of external-port currents of the whole $2n \times 2n$ cluster on one hand, and corresponding sets of external-port voltages and of external-port currents of the four sub-arrays on the other.

3.11.4 – THE KIRCHHOFF'S LAW INTERFACE RELATIONS.

Eight vector identities express Kirchhoff's voltage and current laws along the two mutually-orthogonal interconnection interface planes ' $\alpha - \alpha$ ' and ' $\beta - \beta$ ' (Figure 1). These rather obvious vector identities are fundamental for the formulation of the generalized diakoptic sub-array interconnection matrix-algorithm, where the identities are used (in combination with the four voltage/current matrix equations $V(i) = Z_{4n} \cdot I(j)$ of each sub-array) to express the four unknown sets of interconnection-interface currents I_{Ak} , I_{Bh} , I_{Ck} , and I_{Dh} , as functions of eight sets of external-port currents I_{Uv} , present at the $8n$ external ports of the $2n \times 2n$ cluster. An explicit formal expression of the sets of interconnection-interface currents I_{Ak} , I_{Bh} , I_{Ck} , and I_{Dh} has been analytically obtained.

3.11.5 – EXPRESSION OF THE IMPEDANCE MATRIX Z_{4n} .

A formal expression of the $8n \times 8n$ impedance matrix Z_{4n} of the whole $2n \times 2n$ cluster is obtained by substituting the just found expressions of the interconnection-interface currents I_{Ak} , I_{Bh} , I_{Ck} , and I_{Dh} in the four $V(i) = Z_{4n} \cdot I(j)$ voltage/current matrix equations of each sub-array. A single matrix equation is obtained, that expresses the $8n$ -order vector of the V_{Uv} external-port voltages as a linear transformation of the $8n$ -order vector of the I_{Uv} external-port currents.

The expression of the impedance matrix Z_{4n} is given by the 64 matrix functions, each of which defines one of the 64 $n \times n$ blocks of the matrix Z_{4n} . The expression of the 64 blocks of the matrix Z_{4n} are selectively collected in groups of either eight or sixteen at a time, where the blocks in each group are defined by mutually-equivalent expressions, with each group corresponding to one of the seven different $n \times n$ blocks $A_1, A_2, B_1, B_2, B_3, C_1$, and C_2 of the matrix Z_{4n} .

3.11.6 - THE MULTI-LEVEL DIAKOPTIC PROCESS.

The obtained expressions define the four basic steps of the mathematical procedure that performs the diakoptic interconnection of four $n \times n$ sub-arrays into a single $2n \times 2n$ cluster:

- First the six auxiliary matrices $\alpha_1, \alpha_2, \beta, \gamma_1, \gamma_2$, and δ are expressed as functions of the blocks A, and B of the impedance matrix Z_{4n} of an $n \times n$ sub-array.
- Second, eight auxiliary matrices q_{ij} are expressed as functions of the blocks B, and C of the matrix Z_{4n} , and as functions of the α 's, β , the γ 's, and δ .
- Third, the four unknown sets of interconnection-interface currents I_{Ak}, I_{Bh}, I_{Ck} , and I_{Dh} are expressed as functions of the eight sets of external-port currents I_{Uv} , by means of a linear transformation.
- Finally, the just found expressions of the interconnection-interface currents I_{Ak}, I_{Bh}, I_{Ck} , and I_{Dh} are substituted in the linear matrix-vector expression of the external port voltages V_{Uv} .

By performing the implied matrix product and addition, the expression of the $8n \times 8n$ impedance matrix Z_{4N} is obtained, with all its $64n \times n$ matrix-blocks listed as the already mentioned above.

REFERENCES

- P. J. Davis, "Circulant Matrices," John Wiley & Sons, Inc., Pure and Applied Mathematics Series, New York, 1979.
- R. A. Speciale, "Guided Wave Propagation on Two-Dimensional Clusters of Directly Coupled Cavity Resonators," General Dynamics Engineering Research Report, 1992.

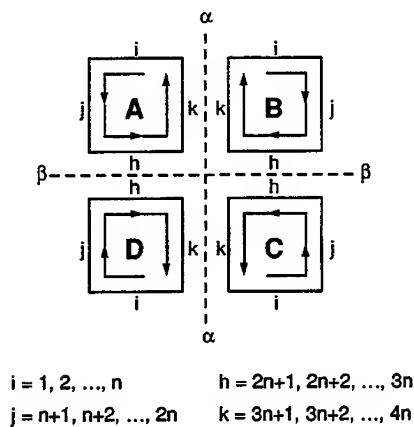


Figure 1. Port Numbering Sequence For The Four Blocks Of A $2n \times 2n$ Cluster Of Directly-Coupled Cavity Resonators.

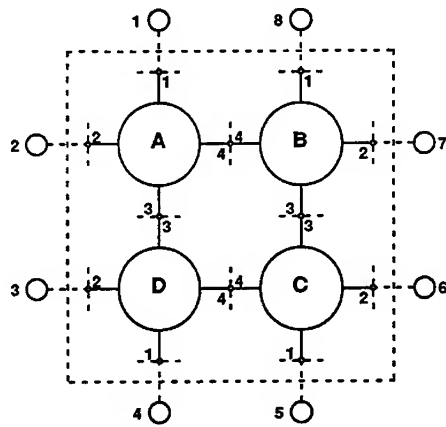


Figure 2. The Minimum 2×2 Square-Lattice Cluster.

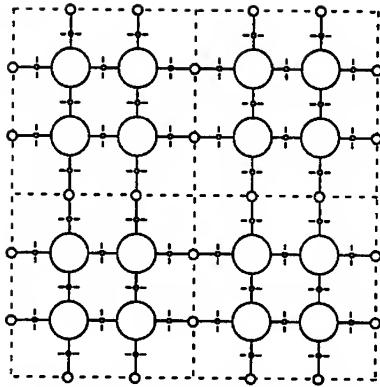


Figure 3. The 4 x 4 Square-Lattice Cluster.

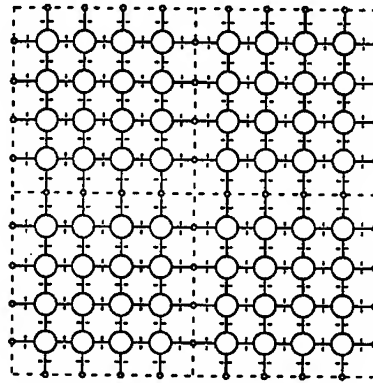


Figure 4. The 8 x 8 Square-Lattice Cluster.

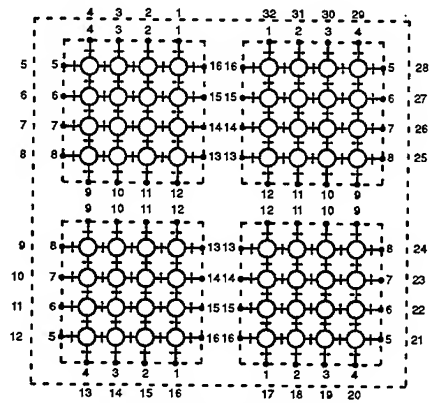


Figure 5. Port Numbering Sequence For The Four Blocks Of An 8 x 8 Cluster Of Directly-Coupled Cavity Resonators.

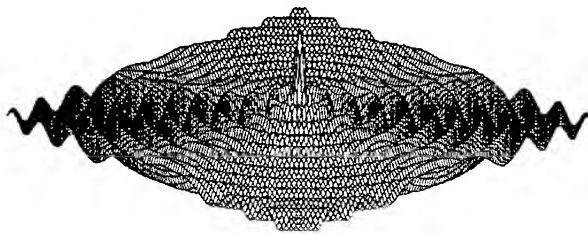


Figure 6. Two-Dimensional Wave Propagation on Isotropic Medium. Single Source Excitation.

ANALYSIS OF A MILLIMETER-WAVE FILTER USING TRANSMISSION LINE MATRIX AND MODE MATCHING METHODS AND COMPARISON WITH THE MEASUREMENTS

W. Menzel

Department of Microwaves

University of Ulm , Ulm, Germany

F. Alessandri, M. Mongiardo, R. Sorrentino

Institute of Electronics, University of Perugia

Perugia, Italy

C. Eswarappa, P. P. M. So and W. J. R. Hoefer

Department of Electrical and Computer Engineering

University of Victoria, Victoria, B.C., Canada

Abstract:

A millimeter-wave bandpass filter has been analyzed independently by frequency domain Mode Matching and time domain Transmission Line Modeling. The numerical results are compared with measurements. The features and computer expenditures associated with the different methods are presented, and error sources are discussed.

1. Introduction

The object of this study is a waveguide bandpass filter for the Ka-band at 35 GHz and a bandwidth of 1 GHz. It was designed, fabricated and measured at the University of Ulm, and subsequently analyzed independently at the Universities of Perugia and Victoria with substantially different numerical techniques, namely the mode-matching and the TLM methods. The purpose was to compare the results and computational requirements of these methods and to test them against measurements.

It appears that both numerical methods yield the Scattering Parameters of the filter within the manufacturing and measurement tolerances. In the following the techniques for the design and tuning of the filter will be described briefly, followed by a summary of the mode matching and TLM analyses of the filter. The computed and measured results will then be compared and discussed. This includes sources of error and possible corrections.

2. Design, Fabrication and Tuning of the Filter

The methods for designing, fabricating and tuning the filter have been described already in [1] and will, therefore, only be summarized here.

The design procedure was based on a mode matching formulation which involved higher order modes for the characterization of the irises separating the resonators, and the dominant mode only for the interaction between them. Irises and resonators were considered to be of perfectly rectan-

gular shape (Fig. 1a). The filter was then milled out of a brass block and covered by a 0.1 mm thick bronze sheet. Its dimensions were measured at the top side of the filter and are given in Fig. 1b. Note that all inner corners are rounded due to the finite radius (1 mm) of the milling tool, and that the measured dimensions of the filter differ from the specifications due to manufacturing tolerances. The S-parameters were subsequently optimized by tuning. To this end, steel balls were pressed against the top plate (see Fig. 2). Fig. 3 compares the measured characteristics of the filter before and after tuning.

3. Mode Matching Analysis of the Filter

The two filter geometries were analyzed using two different formulations of the mode matching (MM) technique, as briefly described below. In both cases, however, the inner corners were assumed to be rectangular, and losses were neglected.

In the conventional MM technique each discontinuity is modelled as a multiport network (usually represented by its Generalized Scattering Matrix, GSM) and then cascaded to the subsequent discontinuity through the connecting waveguide section. The algorithm is repeated till the end of the filter. For the filters of Fig. 1, eight discontinuities (when symmetry is not considered), thus 8 multiports are to be analyzed. A more efficient MM procedure was adopted here, based on the segmentation of the structure into volume cells (Cellular Segmentation, CS [2]). Each cell, occupying the volume between two irises, is modelled by a Generalized Admittance Matrix (GAM), while each iris corresponds to a waveguide section of reduced width. In this manner the analysis of the filter involves only three multiports for the cells plus two additional multiports for the remaining discontinuities located at both ends of the filter. To improve the computational efficiency of the conventional MM technique, a modified MM (MMM) technique can also be adopted [3, 4] as an alternative to CS. The field behavior at the metal edges is incorporated into the field expansions using Gegenbauer polynomials. In this manner, a very accurate representation of the field at each step is obtained with only two terms, and a substantial reduction of the number of unknowns in the final system of equations is obtained. Moreover, no relative convergence phenomenon is observed. These advantages are obtained at the price of some additional effort to evaluate series of inner products (coupling integrals) between the waveguide modes and the aperture field basis functions. In the numerical simulation, however, this is done only at the initial spot frequency, since frequency dependence extraction is adopted.

In both cases, namely with the CS and with the MMM, multimode interaction between discontinuities is fully accounted for using a maximum of 3 modes. The field representation at the discontinuities (apertures of the irises) requires 6 to 7 modes using CS and only 2 Gegenbauer polynomials using MMM. The MMM has the advantage of a better field representation at the discontinuities, but requires 8 discontinuities to be analyzed. The CS, on the contrary, involves a reduced number of multiports. As a consequence, both techniques exhibit about the same computational efficiency. To give an idea of the required computation time, the analysis of the filter on a 486 PC/33 MHz requires 87 seconds for 100 spot frequencies.

The results of the above computations are shown in Fig. 4. The difference in dimensions produces a marked difference in the return loss curve, but only a small shift of the filter characteristics. The differences between the two mode matching techniques are also very small (about 50 MHz or 0.15 percent of the mid-band frequency). Since both sets of curves have been computed with the same number of modes assumed in the various filter subsections, the potential systemati-

error is the same for all curves, and Fig. 4 can thus be regarded as representing the effect of the differences between specified and actual dimensions of the filter structure, but not including the effect of the rounding of the inner corners.

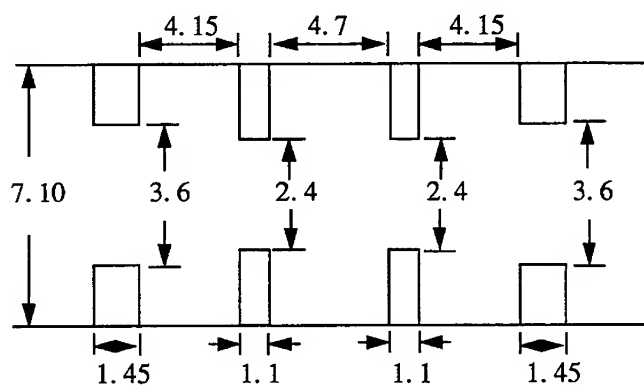


Fig. 1a : Filter Geometry with Design Dimensions (in mms)

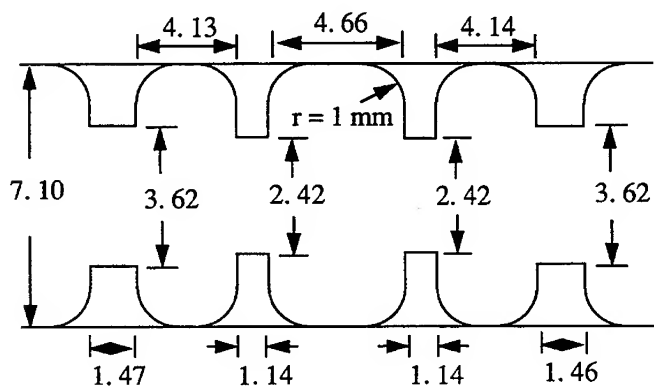


Fig. 1b : Filter Geometry with Manufactured Dimensions (in mms)

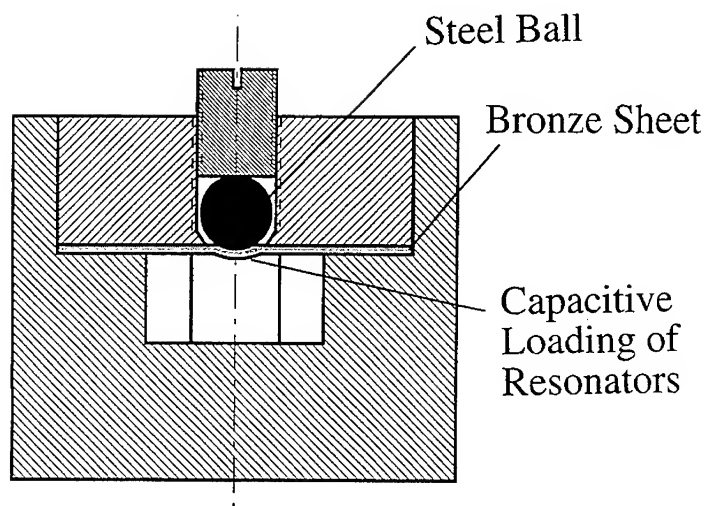


Fig. 2 : Tuning Arrangement for Bandpass Filter

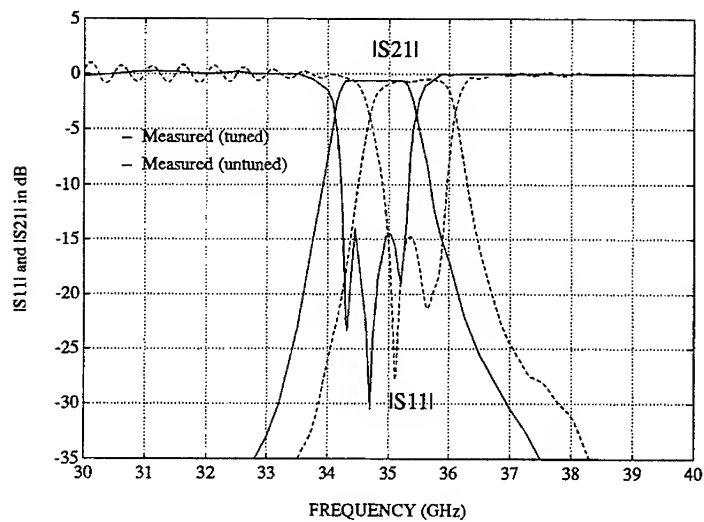


Fig. 3 : Measured Scattering Parameters of the Filters in Figs. 1 a and 1 b

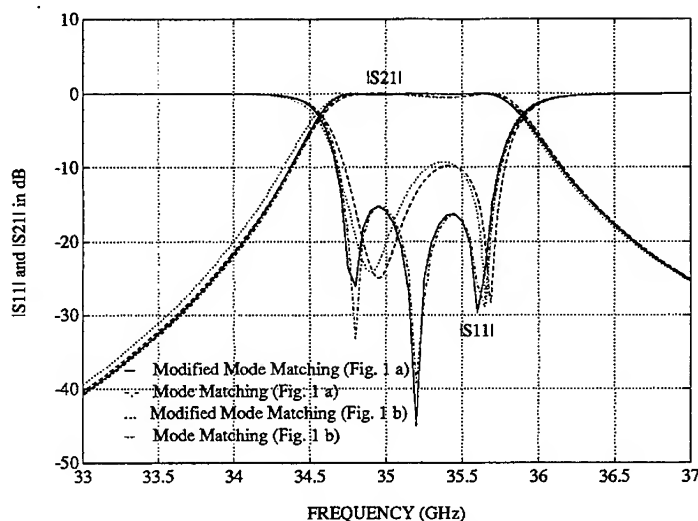


Fig. 4 : Scattering Parameters of the Filters in Figs. 1 a and 1 b Computed with Mode Matching Techniques

4. TLM Analysis of the Filter

The filter was analyzed using 2D TLM [5]. First, the structure given in Fig. 1a was modeled. Taking advantage of symmetry about the longitudinal axis, only one half of the structure was discretized using a mesh parameter $\Delta l = 0.05$ mm, resulting in a two-dimensional mesh of size 564×73 . The maximum difference between the TLM and actual filter dimensions was 0.02 mm. The input and output waveguide were terminated with wideband absorbing boundary conditions, the excitation was a Gaussian pulse with a half-sinusoidal amplitude distribution in the cross-section (TE_{10} mode). The time response in the input and output ports was Fourier transformed and processed to yield the return loss and the insertion loss characteristics.

Then the mesh parameter was reduced to 0.025 mm. For this case, the discretized mesh size was 1126×143 . With this mesh size, nominal dimensions of the filter were described with a tolerance of less than 0.01 mm, which is equal to the manufacturing tolerance. From these results, data were extrapolated linearly for $\Delta l = 0$. Fig. 5 shows the mode matching and the extrapolated TLM data for identical dimensions of the filter in Fig. 1 a. The agreement is excellent, given the fundamentally different approaches used to generate them. Fig. 6 shows the characteristics obtained with both methods for the dimensions of the actual filter (Fig. 1b), but assuming rectangular inner corners. Agreement is close. The slight difference is attributed to the deviations in TLM dimensions from those given in Fig. 1 b due to the finite resolution of the TLM mesh (± 0.01 mm). Finally, Fig. 7 shows the data measured at the University of Ulm, together with mode matching data for the dimensions in Fig. 1b (assuming rectangular inner corners) and TLM results which, this time, account for the finite radius of the inner corner by means of a stepped contour

approximation. Both the measured and TLM data are shifted upwards in frequency with respect to the mode matching results, which can partly be attributed to the effect of the rounded inner corners. The shift due to the rounding was determined by a separate TLM analysis to be 60 MHz or 0.17 percent of the midband frequency.

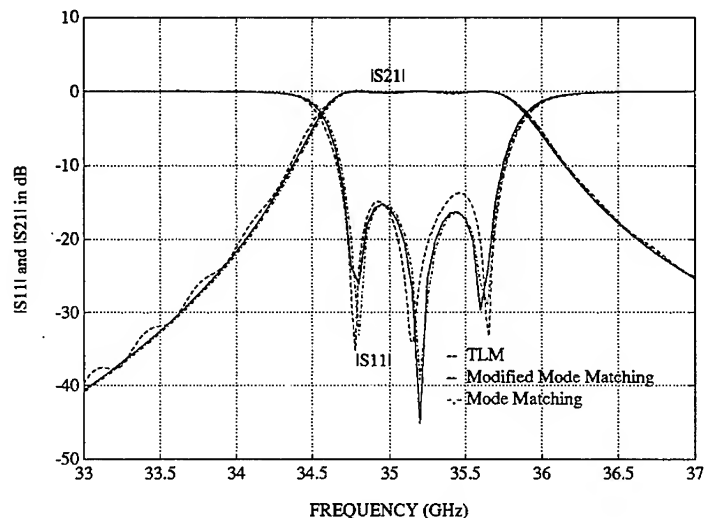


Fig. 5 : Scattering Parameters of the Filter in Fig. 1a Computed with TLM and Mode Matching Techniques.

5. Errors and their Compensation

5.1 Errors affecting the Mode Matching Analysis

Since the mode matching program allows for the entry of exact dimensions, the error estimated is of the order of the difference between regular and modified mode matching computations, i.e. ± 50 MHz.

5.2 Errors affecting the TLM Analysis

The most important error in TLM simulations is the coarseness error which is due to imperfect resolution of the fields in the vicinity of sharp edges. This error has been reduced by at least one order of magnitude by computing the structure with two different discretization steps ($\Delta l = 0.05$ and 0.025 mm) and linearly extrapolating the results for $\Delta l = 0$. The systematic error after extrapolation is estimated to be ± 10 MHz (0.03 percent of the mid-band frequency). Velocity error due to the finite discretization is negligible. 25,000 computation steps were used, yielding a negligible truncation error less than 0.00025 percent. Another error of consequence is due to the finite return loss of the absorbing boundaries used in the simulation, which is estimated to be less than 0.15 percent of the midband frequency, or ± 50 MHz.

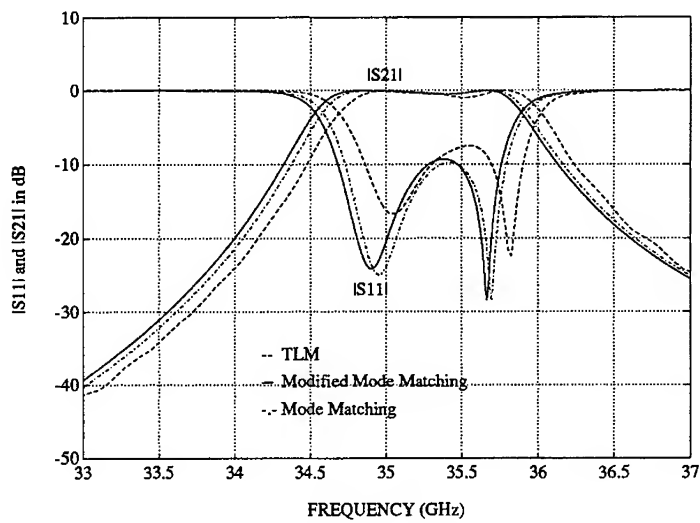


Fig. 6 : Scattering Parameters of the Filter in Fig. 1 b Computed with TLM and Mode Matching Techniques

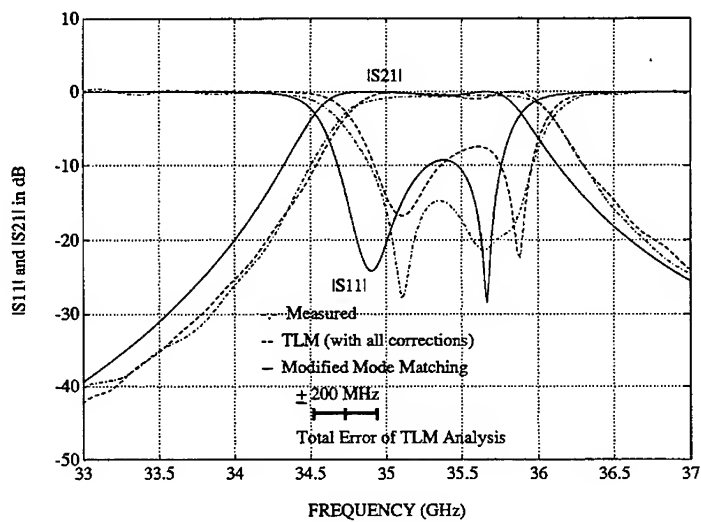


Fig. 7 : Comparison of the Computed and Measured Scattering Parameters for the Filter in Fig. 1 b

The error due to the slight differences between the actual dimensions and those of the TLM model (less than 0.01 mm for $\Delta l = 0.025$ mm) introduces an additional uncertainty in frequency of about 140 MHz. This is equivalent to the uncertainties due to the machining tolerances. In the worst case these uncertainties add together, so that the TLM computations are estimated to be accurate within ± 200 MHz or 0.6 percent of the midband frequency. Execution time on an IBM 360 RISC workstation was about 4 hours for the finest mesh, but it took only 30 minutes to enter the structure into a general-purpose TLM program, yielding a total solution time of less than 5 hours.

5.3 Errors Affecting the Measurements

There are, of course, errors in the experimental verification as well, accounting for the differences between experimental and numerical results. The measurements of the mechanical dimensions are accurate only within 0.01 mm. Additionally, these measurements were done at the surface of the filter mount, and additional variations of the dimensions occur due to the slightly trapezoidal form of the waveguide cross-section and due to imperfectly rectangular outer edges of the irises. The RF measurements are partly affected by reflections at the flanges due to improper electrical contacts to the thin cover plate; this may influence especially return loss values below -15 dB. Furthermore, conductor losses, not included in the TLM data, are responsible for slightly higher insertion loss in the measurements.

6. Conclusion

A millimeter-wave bandpass filter has been analyzed independently by frequency domain Mode Matching and time domain Transmission Line Modeling. The numerical results agree with measurements within the error bounds and manufacturing tolerances. While the computation time for the mode matching programs is shorter by several orders of magnitude, the TLM program is more general and can account for details such as rounded inner corners without additional expenditure and effort.

References :

- [1] A. Klaassen, H. Barth, W. Menzel, "Efficient Design and Realization of mm-wave Waveguide Bandpass Filters, (in German), in MIOP '90 Digest, pp. 534-537, Stuttgart, 24-26 April, 1990.
- [2] F. Alessandri, M. Mongiardo, and R. Sorrentino, "Transverse segmentation: A novel technique for the efficient CAD of 2N-port branch guide couplers", IEEE Microwave and Guided Wave Letters, Vol. 1, pp. 204-207, Aug. 1991.
- [3] R. Sorrentino, M. Mongiardo, and F. Alessandri, "Numerical analysis of printed transmission lines on semiconductor substrate", Journal of Electromagnetic Waves and Applications, Vol. 5, No. 4/5, pp. 353-370, 1991.
- [4] T. Rozzi and M. Mongiardo, "E-plane steps in rectangular waveguide", IEEE Trans. Microwave Theory Tech., Vol. MTT 39, No. 8, Aug. 1991.
- [5] W. J. R. Hofer, "The transmission line matrix (TLM) method," in Numerical Techniques for Microwave and Millimeter Wave Passive Structures, T. Itoh, Ed., New York: Wiley, 1989.

COUPLING-OF-MODES ANALYSIS OF SAW-MULTISTRIP COUPLER

R. Weigel¹, G. Scholl², P. Russer^{1,3}

¹ Technische Universität München, Lehrstuhl für Hochfrequenztechnik,
Arcisstr. 21, D-8000 München 2, Germany

² Siemens AG München, ZFE ME MS 11,
Otto-Hahn-Ring 6, D-8000 München 83, Germany

³ Ferdinand Braun Institut für Höchstfrequenztechnik,
Rudower Chaussee 5, O-1199 Berlin, Germany

Abstract — The coupling-of-modes (COM) formalism is applied to the analysis of surface-acoustic-wave (SAW) multistrip couplers (MSC's). The COM approach delivers closed-form expressions. To determine the pertinent COM-parameters, the COM-differential equations are solved and the solution is compared with analytically derived expressions from the transmission-matrix approach. By doing this, the most important physical effects such as energy storage, propagation loss and mechanical and electrical loading are fully taken into account. As an example, a 100% SAW energy transfer MSC on YZ-LiNbO₃ with 100 regular electrodes and 10 μm pitch will be discussed.

I. INTRODUCTION

A SAW multistrip coupler is a planar acoustic directional coupler with high efficiency and wide bandwidth [1,2]. It is based on the principle that a set of metal strips in the path of a SAW can be used to generate a secondary SAW, which may be displaced laterally with respect to the input wave. The MSC has a variety of forms as well as many different applications among which the improvement of the rejection and the selectivity of SAW filters are the most common ones. In practice, the MSC technique is restricted to substrates with high electromechanical coupling coefficients (high- k^2 substrates) such as lithium niobate (LiNbO₃).

The COM formalism is based on a set of differential equations relating two variables, namely forward and backward wave amplitudes. This differential coupled-mode model is phenomenological and enables the study of perturbations and excitations in a material. In 1985, a very cogent paper was written by *Chen* and *Haus*, which demonstrated the feasibility of using the COM theory for analyzing metal-strip SAW gratings [3]. The many subsequent publications on COM modeling of SAW devices confirmed the effectiveness of the COM formulation [4-6].

In the following, we will regard the SAW grating as a periodic array composed of elementary unit cells which are subdivided into concentrated electrical and mechanical reflection centers and distributed delay lines. Thus, we can take into account several physical effects including mechanical and electrical loading, energy storage, and acoustic propagation attenuation. We will relate the COM coefficients to the parameters obtained by transmission-matrix theory. Term by term comparison of the closed-form COM equations with the expressions delivered by the transmission-matrix model enables us to determine the COM parameters.

The MSC behavior will be analyzed by superimposing a symmetric and an antisymmetric mode. The MSC will be regarded as composed of two parallel tracks. In each of these tracks the wave propagation is modeled as a superposition of a forward wave and a backward wave. By doing this, we describe the MSC in terms of open-circuited and short-circuited gratings with distributed internal reflections.

II. MULTISTRIP COUPLER COM MODEL

The MSC in its simplest form is a periodic array of disconnected electrodes spanning two parallel equal aperture physical tracks 1 and 2 schematically shown in Fig. 1. We describe the behavior of the MSC from a wave amplitude point of view and in terms of a symmetric and an antisymmetric mode which are superimposed [7]. Any uniform wave incident on one track can be decomposed into these modes. From an analysis of an infinite grating it can be derived that the solutions for open-circuited and for short-circuited gratings give the symmetric and antisymmetric modes. The symmetric mode has the velocity of the wave propagating in an open-circuited grating, and the antisymmetric mode has the velocity of the wave propagating in short-circuited grating. In most practical MSC's the number of electrodes is large and so the results for a periodic structure may be applied directly to an MSC of finite length. The usefulness of COM theory for the description of codirectional coupling occurring in an MSC has already been proven [8]. In addition to conventional MSC theory, which neglects electrode reflections, we include in each of the two tracks the backward propagating waves.

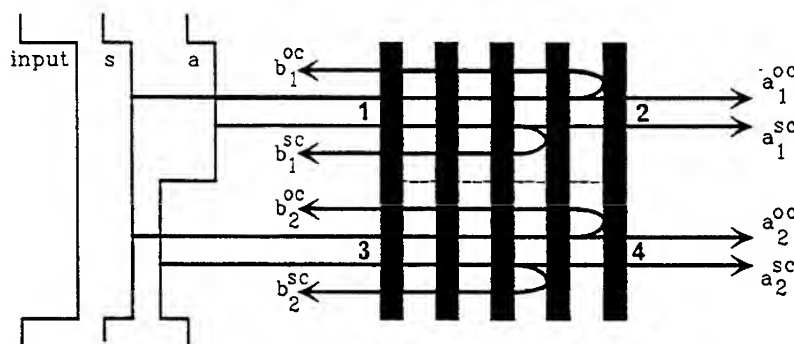


Fig. 1 Multistrip coupler with excitation resolved into symmetric mode s and anti-symmetric mode a (superscript "oc" denotes "open-circuited"; superscript "sc" denotes "short-circuited")

At first, let us suppose an array of n regular electrodes with pitch p , width a , and metalization ratio $\eta = a/p$ as shown in Fig. 2.

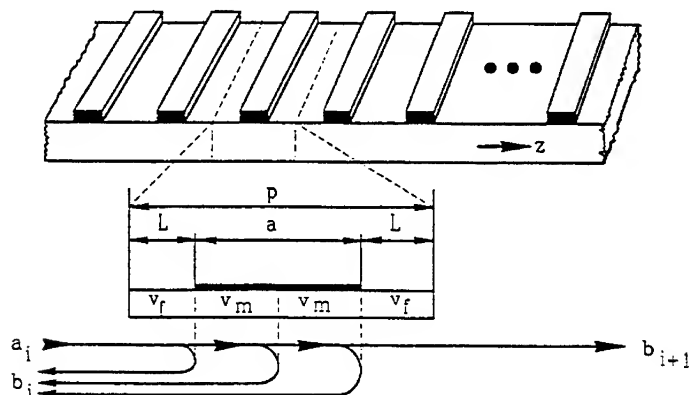


Fig. 2 SAW grating unit cell

The electrode length is assumed to be large, so that all field quantities do not depend on the length-coordinate. We assume time-harmonic forward and backward travelling surface waves $a(z)$ and $b(z)$ with slowly varying complex amplitudes $R(z)$ and $S(z)$,

$$a(z) = R(z) \exp(-jk_g z/2) \exp(j\omega t) \quad (1)$$

$$b(z) = S(z) \exp(+jk_g z/2) \exp(j\omega t) \quad (2)$$

having sufficient phase synchronism to allow significant interchange of energy. Here, $k_g = 2\pi/p$ is the wavenumber of the grating and the factor $\exp(j\omega t)$ will be dropped in the following. An accurate description of the field distributions would require an infinite number of space harmonic components, but only the two lowest order ones which are dominant were taken into account. We write the field in the form of wave amplitudes and approximate the local amplitude $u(z)$ by the superposition

$$u(z) = R(z) \exp(-jk_g z/2) + S(z) \exp(+jk_g z/2) . \quad (3)$$

The solution of the problem is well known and the reciprocal COM equations in the derivative form are written as [3]

$$\frac{dR}{dz} = (-j\delta - \alpha)R + j\kappa S \quad (4)$$

$$\frac{dS}{dz} = -j\kappa^* R + (j\delta + \alpha)S . \quad (5)$$

Here, and throughout the paper, the asterisk denotes the conjugate complex value. The parameters δ , κ , and α are the detuning parameter, the coupling coefficient, and the attenuation coefficient, respectively. The solution of the COM equations is straightforward, and after introducing

$$\gamma^2 = |\kappa^2| - (\delta - j\alpha)^2 \quad (6)$$

we have

$$R(z) = h_1 \exp(-\gamma z) + \frac{h_2 \kappa}{\delta - j(\alpha + \gamma)} \exp(+\gamma z) \quad (7)$$

$$S(z) = \frac{h_1 \kappa^*}{\delta - j(\alpha + \gamma)} \exp(-\gamma z) + h_2 \exp(+\gamma z) . \quad (8)$$

The unknown constants h_1 and h_2 can be derived from the boundary conditions that are imposed on the incident wave at the beginning of the grating and on the backward wave at the end of the grating,

$$a(0) = 1 \quad (9)$$

$$b(np) = 0 . \quad (10)$$

We get

$$h_1 = \frac{H_1 e_p}{H_1 e_p - H_2 / e_p} \quad (11)$$

$$h_2 = \frac{-H_1 \kappa^*}{(H_1 e_p - H_2 / e_p) H_1 e_p} \quad (12)$$

with

$$e_p = \exp(\gamma np) \quad (13)$$

$$H_1 = \delta - j(\alpha + \gamma) \quad (14)$$

$$H_2 = \delta - j(\alpha - \gamma) \quad (15)$$

Thus, we obtain the scattering matrix of the grating

$$S_n = \begin{bmatrix} b(0) & a(np) \\ a(np) & b(0) \end{bmatrix} \quad (16)$$

with the elements

$$b(0) = \frac{j\kappa^* \sinh(\gamma np)}{\gamma \cosh(\gamma np) + j(\delta - j\alpha) \sinh(\gamma np)} \quad (17)$$

$$a(np) = (-1)^n \frac{\gamma}{\gamma \cosh(\gamma np) + j(\delta - j\alpha) \sinh(\gamma np)} \quad (18)$$

Now, let us refer again to Fig. 1 and represent the MSC by short-circuited and open-circuited gratings as was mentioned before. In each of the tracks 1 and 2, we assume forward and backward travelling waves $a(z)$ and $b(z)$ with slowly varying amplitudes $R(z)$ and $S(z)$,

$$a_1 = [R^{oc}(z) + R^{sc}(z)] \exp(-jk_g z/2) \quad (19)$$

$$a_2 = [R^{oc}(z) - R^{sc}(z)] \exp(-jk_g z/2) \quad (20)$$

$$b_1 = [S^{oc}(z) + S^{sc}(z)] \exp(+jk_g z/2) \quad (21)$$

$$b_2 = [S^{oc}(z) - S^{sc}(z)] \exp(+jk_g z/2) \quad (22)$$

where the superscripts oc and sc denote an open-circuited and a short-circuited grating, respectively. In track 1 the symmetric and antisymmetric modes add in phase, whereas in track 2 these modes are totally out of phase. With the boundary conditions

$$a_1(0) = 1 \quad (23)$$

$$a_2(0) = b_1(np) = b_2(np) = 0 \quad (24)$$

equations (19) to (22) yield directly the following scattering parameters of the MSC:

$$2S_{c11} = S^{oc}(0) + S^{sc}(0) \quad (25)$$

$$2S_{c21} = [R^{oc}(np) + R^{sc}(np)] \exp(-jk_g np/2) \quad (26)$$

$$2S_{c31} = S^{oc}(0) - S^{sc}(0) \quad (27)$$

$$2S_{c41} = [R^{oc}(np) - R^{sc}(np)] \exp(-jk_g np/2) \quad (28)$$

Thus, due to symmetry and reciprocity of the problem the complete scattering matrix S_c of the MSC is evaluated, and we can write the scattering parameters of the MSC in terms of the scattering parameters of open-circuited and short-circuited gratings, S_n^{oc} and S_n^{sc} :

$$2S_{c11} = S_{n11}^{oc} + S_{n11}^{sc} \quad (29)$$

$$2S_{c21} = S_{n21}^{oc} + S_{n21}^{sc} \quad (30)$$

$$2S_{c31} = S_{n11}^{oc} - S_{n11}^{sc} \quad (31)$$

$$2S_{c41} = S_{n21}^{oc} - S_{n21}^{sc} \quad (32)$$

III. GRATING NETWORK MODEL

Now, let the array of electrodes which is shown in Fig. 2 be infinite, and let the unit cell consist of one metal strip and two transmission lines of length $L = (1-\eta)p/2$. The symmetry plane of the unit cell is defined to be the center of the reflector strip. The discontinuities at the two strip edges generate the mechanical reflections. The electrical reflection center is located at the strip center. We describe the mechanical reflection from the front edge of the strip by the scattering matrix

$$\mathbf{S}_m = \exp(-j\varphi_m) \begin{bmatrix} \rho_m & t_m \\ t_m & -\rho_m^* \end{bmatrix}, \quad (33)$$

and the mechanical reflection of the back edge of the strip by interchanging S_{m11} and S_{m22} in equation (33). Taking into consideration the properties of symmetry, reciprocity and non-dissipation, the scattering matrix for the electrical reflection centers can be written as

$$\mathbf{S}_{el} = \begin{bmatrix} jr_{el} & t_{el} \\ t_{el} & jr_{el} \end{bmatrix}. \quad (34)$$

Equation (34) holds for open-circuited as well as for short-circuited gratings, if r_{el} is substituted by the correct reflection coefficients r_{of} or r_{ol} . The transmission coefficients t_{of} or t_{ol} follow in both cases from power conservation: $t_{el}^2 = 1 - r_{el}^2$. The delay lines in the grating gaps are characterized by

$$\mathbf{S}_{d11} = \exp[-j(2\pi f/v_f(f) - j\alpha_f)L] \begin{bmatrix} 0 & 1 \\ 1 & 0 \end{bmatrix}, \quad (35)$$

and those for the metalized surfaces by

$$\mathbf{S}_{d12} = \exp[-j(2\pi f/v_m(f) - j\alpha_m)a] \begin{bmatrix} 0 & 1 \\ 1 & 0 \end{bmatrix}. \quad (36)$$

The coefficients occurring in equations (33) to (36) describe various physical phenomena which are taken into account. They are derived in detail in [9] and are as follows:

- (1) ρ_m , t_m , and φ_m depend on the metalization height h_m , the acoustic free-surface wavelength λ_f , and the metalization ratio η . They take into account the mechanical loading effect (mass loading and stress loading) and the energy storage effect which is due to the excitation of evanescent modes that are stored reactively near the strip edges. The mechanical transmission coefficient is a purely real value.
- (2) r_{el} and t_{el} are real quantities having differing values for open-circuited and short-circuited gratings. They depend on the electromechanical coupling coefficient k^2 , the wavenumber $k_f = 2\pi/\lambda_f$, the metalization ratio η , and pitch p .
- (3) v and α are the dispersive velocity and the attenuation coefficient due to air loading and viscosity, respectively. They depend on h_m , λ_f , k^2 , and η . The subscripts f and m denote the free-surface or the metalized-surface values.

The functional dependencies of all these coefficients are formulated using a number of material constants which were obtained by direct-field theoretical analysis and/or experimental investigations.

Neglecting multiple reflections within one metal strip, equations (33) to (36) yield the complete scattering matrix for the unit cell

$$\mathbf{S}_p = \exp[-j(\varphi_p - j\alpha_p)] \begin{bmatrix} jr_p & \sqrt{1-r_p^2} \\ \sqrt{1-r_p^2} & jr_p \end{bmatrix} \quad (37)$$

with

$$r_p = 2\operatorname{Re}\{\rho_m\}\sin(\Delta\varphi) + 2\operatorname{Im}\{\rho_m\}\cos(\Delta\varphi) + r_{e1} \quad (38)$$

$$\varphi_p = [k_f + \eta(k_m - \alpha k_f) + k_e]p \quad (39)$$

$$\alpha_p = [\alpha_f + \eta(\alpha_m - \alpha_f)]p. \quad (40)$$

In equation (38) $\Delta\varphi$ is $\Delta\varphi = \eta k_m p + \varphi_m$. The wavenumbers k_m and k_e are $k_m = 2\pi f/v_m$ and $k_e = 2\varphi_m/p$, respectively.

The scattering matrix of the unit cell, \mathbf{S}_p , is easily converted to the corresponding transmission matrix, \mathbf{T}_p ,

$$\begin{bmatrix} b_i \\ a_i \end{bmatrix} = \begin{bmatrix} T_{p11} & T_{p12} \\ T_{p21} & T_{p22} \end{bmatrix} \cdot \begin{bmatrix} a_{i+1} \\ b_{i+1} \end{bmatrix} \quad (41)$$

with a_i and b_i as the incident and reflected wave amplitudes of the i th unit cell, respectively. From basic wave analysis of periodic structures (being slow-wave structures) [10], the dispersion relation

$$2\cos(kp) = T_{p11} + T_{p22} = \operatorname{trace}(\mathbf{T}_p) \quad (42)$$

can easily be derived. For small r_p , the trace of \mathbf{T}_p can be approximated by

$$\operatorname{trace}(\mathbf{T}_p) = 2(1 + r_p^2/2)\cos(\varphi_p - j\alpha_p). \quad (43)$$

Let us define $\delta_p = \varphi_p - \pi$. Then near the first stop band, where δ_p is much less than unity, and for small r_p and α_p , we can simplify the dispersion relation to

$$kp = \pi + j\sqrt{\gamma_p^2} \quad (44)$$

with

$$\gamma_p^2 = r_p^2 - (\delta_p - j\alpha_p)^2. \quad (45)$$

The transmission matrix for n -cascaded sections, \mathbf{T}_n , is given by [11]

$$\mathbf{T}_n = P_n(y)\mathbf{T}_p - P_{n-1}(y)\mathbf{E} \quad (46)$$

where P_n , P_{n-1} are Chebychev polynomials of the second kind, \mathbf{E} is the unit matrix, and y is the trace of \mathbf{T}_p . The Chebychev polynomials may be obtained from a recurrence relation and may be written in closed form as [12]

$$P_n(y) = \frac{\sin(nkp)}{\sin(kp)}. \quad (47)$$

Then \mathbf{T}_n can be obtained by substitution of equation (44) into (47), and the scattering matrix for the complete grating, \mathbf{S}_n , can be easily derived to

$$S_n = \frac{1}{D} \begin{bmatrix} -j r_p \sinh(n \gamma_p) & (-1)^n \gamma_p \\ (-1)^n \gamma_p & -j r_p \sinh(n \gamma_p) \end{bmatrix} \quad (48)$$

where the denominator D is given by

$$D = \gamma_p \cosh(n \gamma_p) + j(\delta_p - j \alpha_p) \sinh(n \gamma_p). \quad (49)$$

Equation (48) enables us to compute the reflection and transmission behavior of both short-circuited and open-circuited gratings.

Term by term comparison of equations (17), (18), and (48) yields $\gamma_p = \gamma_p$, $\delta_p = \delta_p$, $\alpha_p = \alpha_p$, and $\kappa^* p = -r_p$. Thus, we obtain the COM parameters

$$\delta = k_f + \eta(k_m - k_f) + k_e - k_g/2 \quad (50)$$

$$\alpha = \alpha_f + \eta(\alpha_m - \alpha_f) \quad (51)$$

$$\kappa^* = |\kappa| \exp(-j\psi) = -r_p/p. \quad (52)$$

Note, that r_p may be positive or negative. The phase factor ψ depends on the location of the origin of the coordinate system relative to the location of the reflection maximum. Without loss of generality, ψ can be chosen to be 0 or π , so that κ is a real quantity.

IV. NUMERICAL EXAMPLE

The general characteristics of the scattering parameters of an MSC on YZ-LiNbO₃ with $n = 100$, $p = 10 \mu\text{m}$, $\eta = 50\%$, and $h_m = 0.1 \mu\text{m}$ are shown in Fig. 3 in a linear scale. The value $n = 100$ has been derived from the formula [13]

$$n_{\text{total}} = \frac{\pi}{p(\delta_{\text{sc}} - \delta_{\text{oc}})}. \quad (53)$$

Using this (smallest permissible) value for n_{total} one obtains full energy transfer between the two MSC tracks. The value n_{total} varies slowly with frequency, and has a minimum at $f_0 = v_f/(2p)$. However, this frequency corresponds to a stop band. To operate well away from this stop band, the separation between MSC strips typically places the operating frequency about 1.3 times above f_0 . As is seen in Fig. 3, the MSC stop band is predicted and the back scattered power is at maximum.

V. CONCLUSION

A combination of the COM formalism and the transmission matrix approach has been worked out for analysis of multistrip couplers including internal reflection effects. The analysis is based on the traditional onedimensional symmetric/antisymmetric mode description of the MSC. The corresponding computer program is incorporated into a standard microwave network analysis program thus enabling MSC optimization. This work demonstrates the usefulness of the COM model (which has originally been developed for the analysis of microwave and optical structures) for the theoretical investigation of SAW devices with small distributed reflections.

ACKNOWLEDGEMENT

The authors would like to thank A. Christ and W. Ruile of Siemens AG München, Germany, for many helpful discussions.

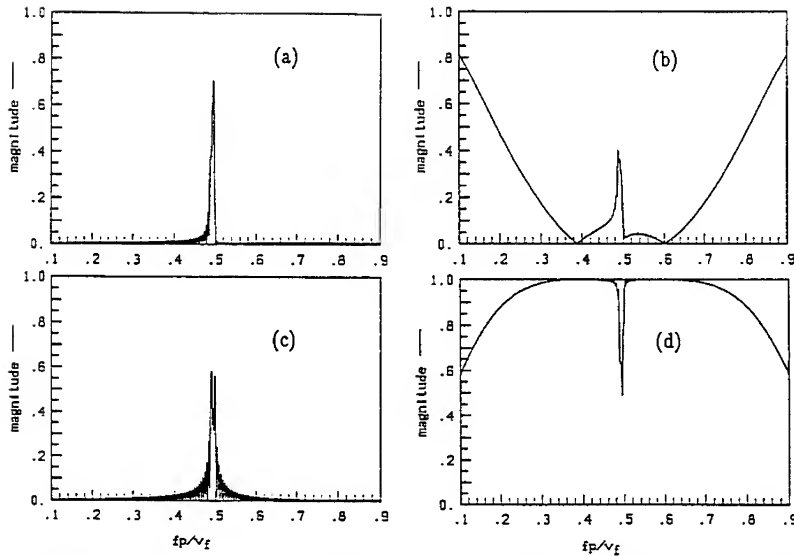


Fig. 3 MSC in-line scattering coefficients S_{c11} (a) and S_{c21} (b); MSC cross scattering coefficients S_{c31} (c) and S_{c41} (d)

REFERENCES

- [1] C. Campbell, *Surface Acoustic Wave Devices and Their Signal Processing Applications*. San Diego: Academic Press, 1989, pp. 111–118.
- [2] B.P. Abbott, D.C. Malocha, "Closed Form Solutions for Multistrip Coupler Operation Including the Effects of Electrode Resistivity," *IEEE Ultrasonics Symposium Proc.* 1990, pp. 25–30.
- [3] D.P. Chen, H.A. Haus, "Analysis of Metal-Strip SAW Gratings and Transducers," *IEEE Trans. Sonics Ultrasonics*, vol. SU-32, no. 3, pp. 395–408, 1985.
- [4] P.V. Wright, "Analysis and Design of Low-Loss SAW Devices with Internal Reflections Using Coupling-of-Modes Theory," *IEEE Ultrasonics Symposium Proc.* 1989, pp. 141–152.
- [5] E.L. Adler, M.P. da Cunha, O. Schwelb, "Arbitrarily Oriented SAW Gratings: Network Model and the Coupling-of-Modes Description," *IEEE Trans. Ultrason. Ferroelec. Freq. Contr.*, vol. UFFC-38, no. 3, pp. 220–230, 1991.
- [6] B.P. Abbott, C.S. Hartmann, D.C. Malocha, "Transduction Magnitude and Phase for COM Modeling of SAW Devices," *IEEE Trans. Ultrason. Ferroelec. Freq. Contr.*, vol. UFFC-39, no. 1, pp. 54–60, 1992.
- [7] R.L. Rosenberg, L.A. Coldren, "Fast Synthesis of Finite-Loss SAW Resonator Filters," *IEEE Ultrasonics Symposium Proc.* 1977, pp. 882–887.
- [8] A. Yariv, "Coupled-Mode Theory for Guided-Wave Optics," *IEEE J. Quantum Electron.*, vol. QE-9, no. 9, pp. 919–934, 1973.
- [9] G. Scholl, A. Christ, W. Ruile, P. Russer, R. Weigel, "Efficient Analysis Tool for Coupled-SAW-Resonator Filters," *IEEE Trans. Ultrason. Ferroelec. Freq. Contr.*, vol. UFFC-38, no. 3, pp. 243–251, 1991.
- [10] R.E. Collin, *Foundations for Microwave Engineering*. Singapore: McGraw-Hill, pp. 363–433, 1966.
- [11] P.S. Cross, "Properties of Reflective Arrays for Surface Acoustic Resonators," *IEEE Trans. Sonics Ultrason.*, vol. SU-23, no. 4, pp. 255–262, 1976.
- [12] E.K. Sittig, G.A. Coquin, "Filters and Dispersive Delay Lines Using Repetitively Mismatched Ultrasonic Transmission Lines," *IEEE Trans. Sonics Ultrason.*, vol. SU-15, no. 2, pp. 111–119, 1968.
- [13] D.P. Morgan, *Surface-Wave Devices for Signal Processing*. Amsterdam: Elsevier, 1985, pp. 113–118.

DESCRIPTION OF CONDUCTOR-LOSS EFFECTS IN PLANAR TRANSMISSION LINES

Wolfgang Heinrich

Institut für Hochfrequenztechnik, Technische Hochschule Darmstadt
Merckstr. 25, W-6100 Darmstadt / Germany

Abstract

The influence of conductor loss on the propagation characteristics of planar transmission-lines is investigated. Both a rigorous full-wave method and a simplified model are applied. The results are validated by comparison to measurements. The paper discusses the principal effects induced by conductor loss and provides data for typical coplanar waveguide and coplanar strip geometries found in mm-wave monolithic circuits. Also, the case of high- T_c superconducting materials is discussed.

1 Introduction

Today, planar transmission lines represent key elements for many high-frequency applications, especially with regard to monolithic integration of analog and digital circuits. With increasing packaging density and frequency of operation, the line geometries have become smaller and smaller. In mm-wave monolithic integrated circuits (MMIC's), for instance, metallization thicknesses t below $3\mu\text{m}$ and strip widths in the range of $10\mu\text{m}$ are in use (e.g. [1,2]).

When scaling down the cross-sectional dimensions of planar transmission lines, however, the conductor-loss phenomena gain importance and need to be included in circuit design. It is necessary, therefore, to provide computational methods that account accurately for those effects. A particular difficulty arises from the fact that most of the common approaches are based on skin-effect approximations. This requires metallization thickness t to be larger than the skin depth δ , which, however, is not fulfilled for most of the MMIC structures. A similar situation is encountered when modelling state-of-the-art high- T_c superconductive films.

Consequently, a rigorous analysis of conductor loss is required that does rely neither on skin-effect assumptions nor on perturbation techniques. Two different types of such an approach are outlined briefly in the following section.

2 Simulation Approaches

2.1 Full-Wave Mode-Matching Technique

The formulation starts from the general planar structure shown in Fig. 1. All subregions are described by their complex permittivity ϵ . Thus, conductivity κ and dielectric loss tangent can be

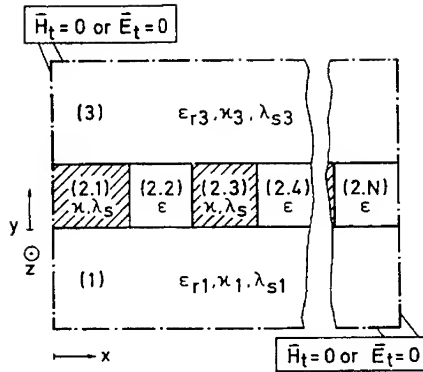


Fig. 1: The waveguide cross-section (each subregion is characterized by its complex dielectric constant $\varepsilon = \varepsilon_r \varepsilon_0 - 1/(\omega^2 \mu \lambda_s^2) - j\kappa/\omega$ including normal conductivity κ and, if applicable, superconductor penetration depth λ_s).

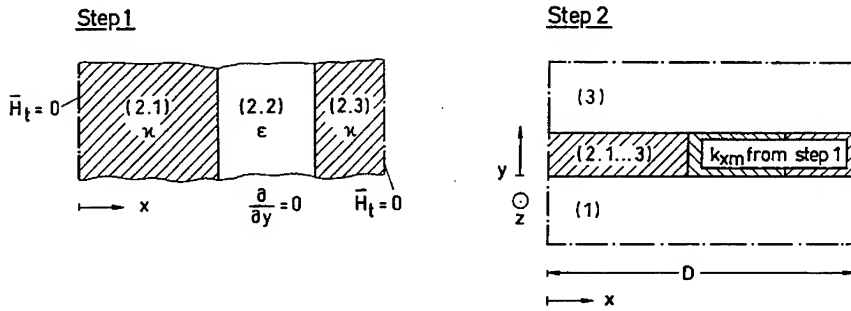


Fig. 2: The two steps of the mode-matching procedure

included in a general way and the formulation holds for arbitrary values of conductor dimensions and skin depth [3]. Superconductor penetration depth λ_s can be accounted for equally [4].

Regarding the mode-matching technique itself, two steps can be separated as illustrated by Fig. 2. First, the lateral separation constants k_{xm} are determined. In analogy to the well-known case of a layered rectangular waveguide, the k_{xm} depend only on the x -layer characteristics. This step, however, is a critical one because it involves problems due to the metallic conductivity values.

The second step corresponds to the common field-matching procedures. Using the k_{xm} values from step 1 and the y -layer data one yields the complex propagation constant $k_z = \beta - j\alpha$ and

all other field quantities.

Due to the rigorous loss description, the numerical expenses are relatively high. This type of analysis, therefore, is ideally suited for generating reference results. But the efforts involved are too high for practical MMIC circuit design. For that purpose, a simplified CPW description was developed which is presented in the following subsection.

2.2 Simplified Quasi-TEM Modelling of CPW

Because of the miniaturized transversal line dimensions, the waves are of the quasi-TEM type. Hence a distributed equivalent-circuit model as shown in Fig. 3 can be employed. Using the full-

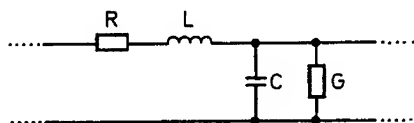


Fig. 3: The distributed equivalent-circuit model (all elements defined per unit length).

wave results as a reference and exploiting physical simplifications, closed-form approximations are derived [5]. Altogether, this leads to a very efficient formulation suitable for the practical design process.

3 Results

3.1 Principal Effects

Generally, conductor loss influences the propagation behaviour of planar quasi-TEM lines in two ways:

- (i) Naturally, finite conductivity $\kappa < \infty$ causes attenuation, i.e., a non-zero line resistance R in Fig. 3. Regarding the frequency dependence R follows a \sqrt{f} rule in the skin-effect regime and approaches a constant in the DC limit. Between these two cases an intermediate range occurs that may extend over a considerable portion of the frequency range of operation (as is the case with respect to MMIC CPW structures).
- (ii) But conductor loss also affects the phase constant β and $\epsilon_{\text{reff}} = (\beta/\beta_0)^2$. This is true particularly for line geometries that show inherently two-dimensional field characteristics (e.g. coplanar waveguide (CPW), coplanar strips (CPS), and slot line). In that case, the magnetic fields both inside and outside the conductors change when the skin depth δ falls short of $3t$ (t denotes metallization thickness). As a consequence, the line inductance L and thus ϵ_{reff} become frequency dependent to a significant amount. Fig. 4 illustrates the corresponding ϵ_{reff} curve with the characteristic negative slope. The plot also includes results obtained by the quasi-TEM model (Section 2.2) and measurement data [6,7].

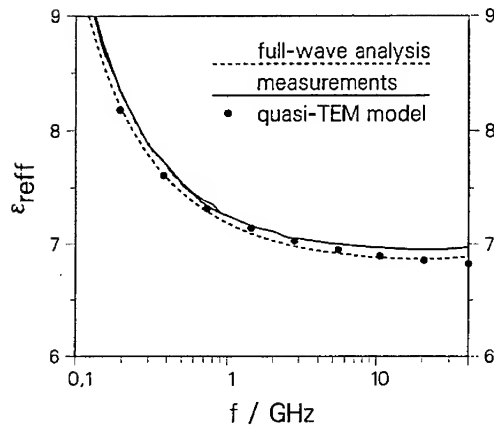


Fig. 4: CPW effective dielectric constant $\epsilon_{reff} = (\beta/\beta_0)^2$ as a function of frequency f – comparison of measurement results [6] (solid line) with full-wave analysis [3] (dashed) and quasi-TEM modelling [5] (symbols).

CPW geometry: $71\mu\text{m}$ wide center strip, slot width $s = 49\mu\text{m}$, metallization $t = 1.6\mu\text{m}$ thick with conductivity $\kappa = 3.6 \cdot 10^7 \text{ S/m}$, GaAs substrate ($\epsilon_r = 12.9$, $\tan \delta_e = 3 \cdot 10^{-4}$).

3.2 Coplanar Waveguide (CPW)

Fig. 5 presents the frequency dependence of ϵ_{reff} and α for a typical MMIC CPW geometry. Both the results of the full-wave approach (Section 2.1) and those of the quasi-TEM model (Section 2.2) are plotted.

As observed already in Fig. 4 the dispersion caused by finite metallization conductivity dominates the behaviour of ϵ_{reff} . Non-TEM effects, on the other hand, remain small and appear only around 100 GHz. Regarding the attenuation α one finds two frequency ranges that can be distinguished clearly: The skin-effect regime at high frequencies and the 'intermediate' range for lower frequencies where the α curve again follows a straight line in the log-log scale but with different slope. In general, the attenuation values reach a relatively high level because of the miniaturized line dimensions.

3.3 Coplanar Strips (CPS)

The CPS behaviour is similar to that of the CPW. Fig. 6 provides the relevant data. As in the CPW case, the negative slope of ϵ_{reff} reflects the influence of conductor loss. Also, the intermediate frequency range becomes visible in the α curve. The attenuation values are comparable to those of the CPW. Hence the CPS line represents an interesting complement to the CPW in MMIC's where anti-symmetric properties are required.

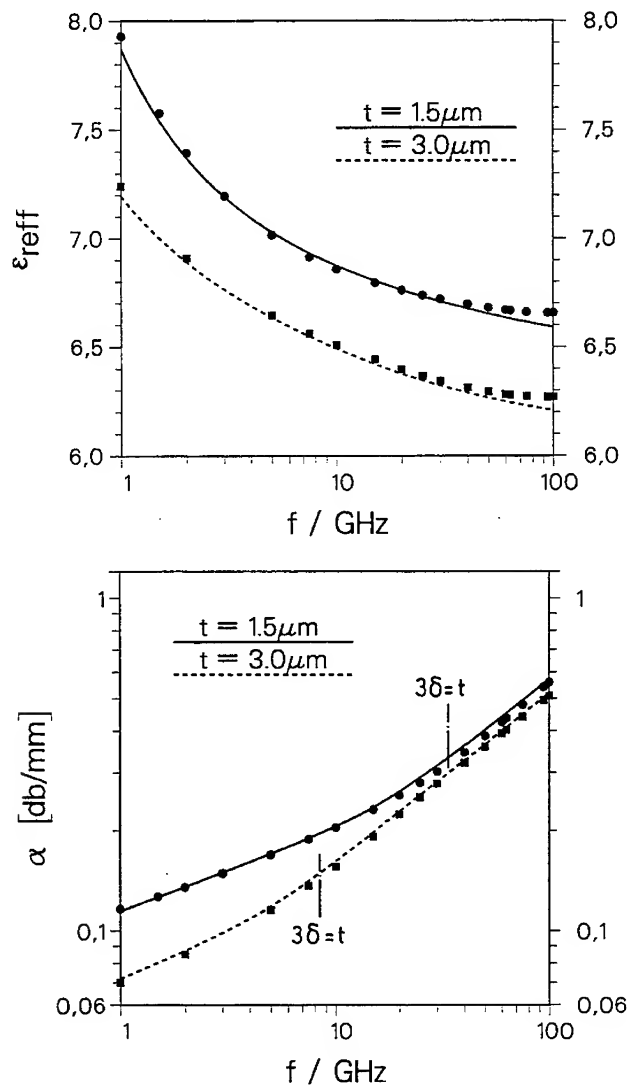


Fig. 5: CPW effective permittivity ϵ_{reff} and attenuation α against frequency f with metallization thickness t as parameter – comparison of quasi-TEM model (solid and dashed lines) with full-wave analysis [3] (symbols).
 CPW geometry: $20\mu\text{m}$ wide center strip, slot width $s = 15\mu\text{m}$, conductivity $\kappa = 3 \cdot 10^7$ S/m, $600\mu\text{m}$ thick GaAs substrate.

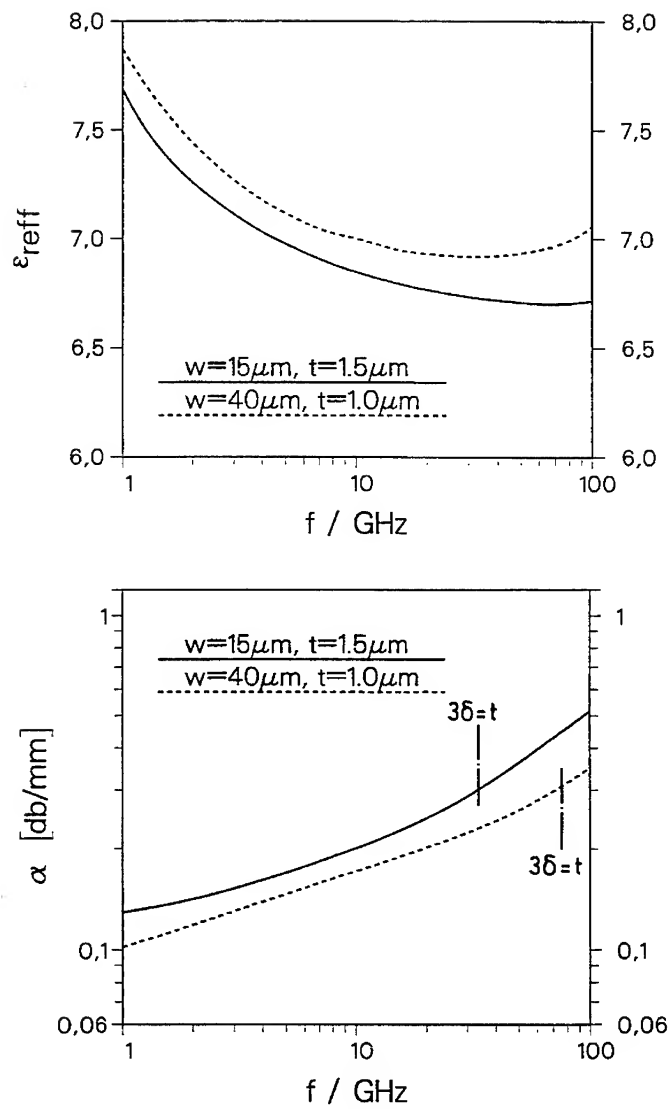


Fig. 6: CPS effective permittivity ϵ_{eff} and attenuation α against frequency f with metallization width w and thickness t as parameter;
CPS geometry: $20\mu\text{m}$ wide slot, conductivity $\kappa = 3 \cdot 10^7 \text{ S/m}$, $600\mu\text{m}$ thick GaAs substrate.

3.4 Superconducting CPW

Finally, the potential of high- T_c superconducting films with regard to MMIC CPW structures is to be highlighted. Fig. 7 compares a superconducting line with its metallic counterpart, both on LaAlO_3 substrate.

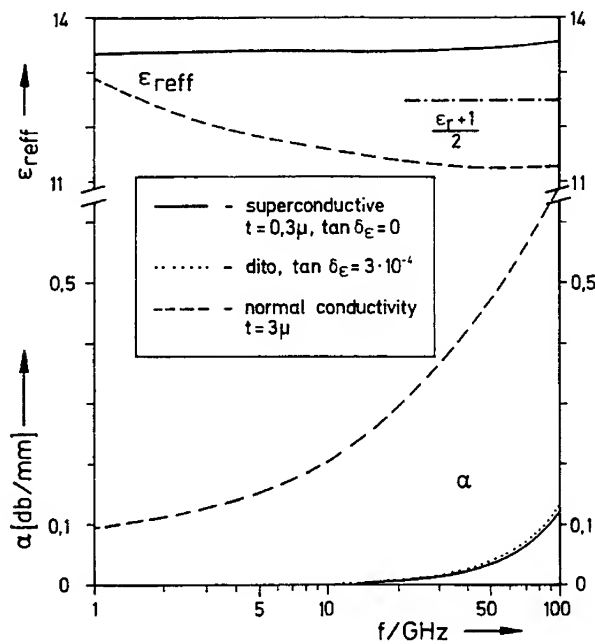


Fig. 7: Effective permittivity ϵ_{eff} and attenuation α against frequency f for superconducting CPW ($t = 0.3\mu\text{m}$) with substrate loss tangent $\tan \delta_e = 0$ (solid) and $\tan \delta_e = 3 \cdot 10^{-4}$ (dotted), respectively. The dashed curves refer to the case of metallic conductors ($t = 3\mu\text{m}$) with $\kappa = 3.0 \cdot 10^7 \text{ S/m}$. For line geometry see Fig. 5, substrate: LaAlO_3 with $\epsilon_r = 24$, superconductor [8]: $\lambda_s = 0.3\mu\text{m}$, $\kappa = 8.2 \cdot 10^5 \text{ S/m}$.

As could be expected, attenuation α decreases when introducing superconductors, although this reduction amounts only about one order of magnitude. The changes in the phase constant are significant as well. For the superconducting case, ϵ_{eff} shows excellently low dispersion. This can be attributed to the fact that the penetration depth λ_s is constant with frequency f whereas the metallic skin depth δ depends on f .

4 Conclusions

- Whenever the performance of analog and digital IC's aims at high frequencies, bit rates, or packaging densities, miniaturized structures have to be used. The transmission lines in such IC's show a distinct influence of non-ideal conductivity. Apart from the growing attenuation values, also the phase constant and thus dispersion is affected. This holds particularly for lines with inherently two-dimensional field patterns such as CPW and CPS.
- Suitable modelling tools have to be developed that describe the conductor-loss effects with sufficient accuracy. Two examples of opposite type are treated in this paper: An accurate but numerically expensive full-wave analysis and an highly efficient quasi-TEM model based on closed-form expressions for the line elements.

References

- [1] M. Aikawa, H. Ogawa und T. Sugeta, "MMIC progress in Japan," *1989 IEEE Microwave and Millimeter-Wave Monolithic Circuits Symposium, Digest* pp. 1-6.
- [2] M. Schlechtweg, W. Reinert, P.J. Tasker, R. Bosch, J. Braunstein, A. Hülsmann, and K. Köhler, "Design and characterization of high performance 60 GHz pseudomorphic MODFET LNAs in CPW-technology based on accurate s-parameter and noise models", *IEEE Trans. Microwave Theory Tech.*, vol. MTT-40, to appear in the December issue, 1992.
- [3] W. Heinrich, "Full-wave analysis of conductor losses on MMIC transmission lines," *1990 IEEE Trans. MTT*, vol. MTT-38, pp. 1468-1472, Oct. 1990.
- [4] W. Heinrich, "Full-wave analysis of superconducting coplanar waveguide with finite conductor thickness," *21st European Microwave Conference Digest*, vol. 1, pp. 667-672, 1991.
- [5] W. Heinrich, "Quasi-TEM description of MMIC coplanar lines including conductor-loss effects," *1993 IEEE Trans. MTT*, to be published in the January issue, 1993.
- [6] R.B. Marks, US National Institute of Standards and Technology, Boulder, CO, private communication.
- [7] R.B. Marks and D.F. Williams, "Characteristic impedance determination using propagation constant measurement", *IEEE Microwave and Guided Wave Letters*, vol. 1, pp. 141-143, June 1991
- [8] J. Kessler, R. Dill, P. Russer, and A.A. Valenzuela, "Property calculations of a superconducting coplanar waveguide", *1990 European Microwave Conference Digest*, pp. 798-803.

DYNAMIC ELECTRICAL MODELING OF GAP DISCONTINUITIES ON LOSSY MONOLITHIC MICROSTRIP LINE

Anne VILCOT - Smaïl TEDJINI

Laboratoire d'Electromagnétisme Microondes et Optoélectronique

ENSERG - BP 257 - 38 016 Grenoble Cédex - FRANCE

Tel : (33) 76 87 69 76 - Fax : (33) 76 46 56 36

Abstract

In this paper we consider the dynamic modeling of microwave discontinuities realised on lossy multilayer structures. We take into account the real nature of dielectrics ($\tan \delta$) and/or semiconductor (conductivity) by the use of the complex frequency concept. The classical Spectral Domain Technique in which we introduced this concept allows the calculation of complex resonant frequencies of lossy cavities. The proposed method is applied to gap discontinuities on lossy microstrip line. The physical behavior confirms well the obtained results.

Introduction

The Dynamic modeling of planar transmission lines and discontinuities is a topic of great interest, especially for monolithic microwave and millimeterwave circuits. The existing electric models for planar transmission lines include the losses phenomena due to substrate [1], ground plane[2] and strip thickness[3]. However, when considering the discontinuities on lossy substrate no equivalent models are found in the literature. The aim of this paper is a contribution to fill this gap by the development of a modeling technique which can include the real nature of dielectric or semiconductor substrates, that is to say losses. Very efficient for the analysis of uniform planar transmission lines, the well-known Spectral Domain Approach has been extended to the study of discontinuities on planar transmission lines [4] too. Up to now, the method could only treat the case of lossless lines. However, new applications appear that cannot be realistically modeled without taking losses into consideration. In this paper, we propose thus an extension of the SDA to the study of discontinuities on lossy structures. As an example of this technique, we will apply it for the modeling of a gap on a lossy microstrip structure.

General principle of the 3D SDA on lossless structures

Coupled to a type of Transverse Resonance Technique, the classical SDA may be very efficient at determining the electrical equivalent circuits of planar discontinuities [4]. We call this method the 3D Spectral Domain Approach. Consider first the case of discontinuities on lossless multilayer substrate. The 3D SDA mainly consists in putting the discontinuity in a resonant cavity with either electric or magnetic walls (Fig. 1).

Let $\begin{bmatrix} Z_{11} & Z_{12} \\ Z_{21} & Z_{22} \end{bmatrix}$ be the equivalent Z-matrix of the considered discontinuity, the resonance condition reads, when the cavity is made of electric walls :

$$[Z_{11} + j Z_{c1} \tan(\beta_1 l_1)] [Z_{22} + j Z_{c2} \tan(\beta_2 l_2)] - Z_{12} Z_{21} = 0$$

In the case of magnetic walls, it reads :

$$\left[Z_{11} - \frac{j Z_{c1}}{\tan(\beta_1 l_1)} \right] \left[Z_{22} - \frac{j Z_{c2}}{\tan(\beta_2 l_2)} \right] - Z_{12} Z_{21} = 0$$

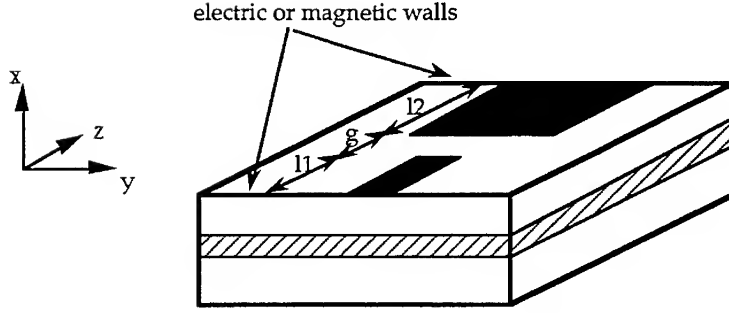


Figure 1 : Discontinuity in a resonant cavity.

The classical 2D SDA gives the values of the respective characteristic impedances of the two considered propagation lines Z_{c1} and Z_{c2} , and their respective phase constants β_1 and β_2 . The calculation of 4 couples of lengths (l_1, l_2) which make the cavity resonate, at the same frequency, allows the determination of the equivalent Z-matrix of the discontinuity.

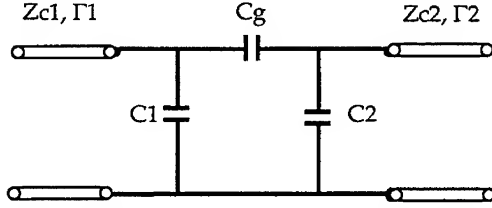


Figure 2 : Electric equivalent circuit of a gap on a lossless microstrip line.

In the case of a gap on a microstrip line, the electric equivalent circuit is given on figure 2. The resonance condition of the cavity in the presence of electric walls reads :

$$C_g^2 = \left(C_g + C_1 - \frac{1}{Z_{c1} \omega \tan(\beta_1 l_1)} \right) \left(C_g + C_2 - \frac{1}{Z_{c2} \omega \tan(\beta_2 l_2)} \right).$$

In the case of magnetic walls for the cavity, we have :

$$C_g^2 = \left(C_g + C_1 + \frac{\tan(\beta_1 l_1)}{Z_{c1} \omega} \right) \left(C_g + C_2 + \frac{\tan(\beta_2 l_2)}{Z_{c2} \omega} \right).$$

This means that, in the case of a gap on a microstrip line, only 3 couples of lengths (l_1, l_2) are required.

The 3D SDA allows the determination of the resonance lengths. The basic principle is the same as that of the classical 2D SDA. However, as metallisations are no longer uniform in the propagation direction Oz, we have a Fourier development in this direction too (added to the development in the y-direction). As in the 2D SDA, we obtain a relation between the tangential electric field and the tangential current density, in the Fourier domain :

$$\begin{pmatrix} j E_y(u,n) \\ E_z(u,n) \end{pmatrix} = \omega \epsilon_0 \begin{pmatrix} g_{11}(u,n) & g_{12}(u,n) \\ g_{21}(u,n) & g_{22}(u,n) \end{pmatrix} \begin{pmatrix} J_y(u,n) \\ j J_z(u,n) \end{pmatrix}$$

where u is the Fourier variable related to the open direction Oy and n is the Fourier variable related to the z -direction. To solve it, we use Galerkin's moment method, which consists in splitting the current density on a function basis according to the y - and the z -directions. We get then a system of linear equations which depends on one hand on the frequency and on the other hand on the lengths (l_1, l_2) . We thus solve the problem by calculating the lengths (l_1, l_2) which put the determinant of the system of linear equations to zero, at a given frequency.

Extension to lossy structures : complex frequency concept

To treat the case of discontinuities on lossy structures, we make use of the complex frequency concept. It consists in the fact that the resonance frequency of a lossy resonator is complex. Indeed, on a lossy propagation line, the fields vary as $\exp(-\Gamma z) \exp(j\omega t)$; in the case of a lossy resonator, the variation is $\exp(-j\beta z) \exp(j\omega_c t)$. Comparing the two expressions, it comes $\omega_c = \omega + j\omega'' = \omega + j\alpha \frac{d\omega}{d\beta}$. The complex frequency concept is valid

whatever the losses level is. However, in our case, we make use of it through a perturbation method added to the previous theory. The hypothesis of low losses allows to consider that, between the lossless structure and the lossy one, the equivalent circuit only changes by the addition of resistive elements as shown in Fig. 3.

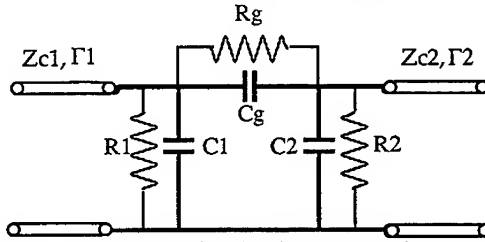


Figure 3 : Electric equivalent circuit of a gap on a lossy microstrip line.

We can show an application of this method to a symmetric gap on a microstrip line, which can be modeled through a microstrip resonator (Fig. 4). The electric equivalent circuit of that resonator is given on figure 5, in the case of a lossless structure. Adding low losses to the previous structure, we only add resistive elements to the electric equivalent circuit (Fig. 6). The calculations of the resonant complex frequencies $f_1 = f'_1 + j f''_1$ and $f_2 = f'_2 + j f''_2$, where $f'_1 = \frac{1}{\sqrt{L_1 C_1}}$ and $f'_2 = \frac{1}{\sqrt{L_1 (C_1 + 2C_2)}}$ and the quality factors :

$$Q_1 = \frac{f_1}{2 f''_1} = 2\pi R_1 C_1 f'_1 \text{ and } Q_2 = \frac{f_2}{2 f''_2} = 2\pi \frac{R_1 R_2}{2R_1 + R_2} (C_1 + 2C_2) f'_2$$

lead to :

$$C_1 = \frac{2C_2}{f_1^2 - f_2^2}; R_1 = \frac{1}{4\pi f'_1 C_1}; \frac{1}{R_2} = \frac{1}{2} \left(4\pi C_1 f'_2 \frac{f_1^2}{f_2^2} - \frac{1}{R_1} \right)$$

where C_2 has been previously determined by the 3D SDA.

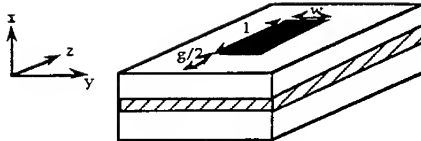


Figure 4 : Microstrip resonator.

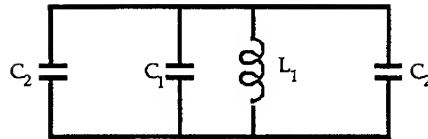


Figure 5 : Equivalent circuit of a lossless resonator.

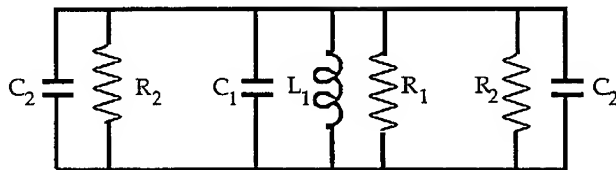


Figure 6 : Equivalent circuit of a lossy resonator.

We have applied our method to a microstrip structure previously studied by Koster and Jansen [5] (Fig. 7). At the frequency $f = 1$ GHz, we have varied the gap width g from 0 to 4 mm. The values of C and C_g obtained by the 3D SDA are presented on figure 8. The series capacitance C_g decreases as g increases, contrary to the parallel capacitance C . The limit where $g = 0$, which entails theoretically $C_g = \infty$ and $C = 0$, and the limit where $g = \infty$ which leads to $C_g = 0$, are respected, as can be seen on figure 8.

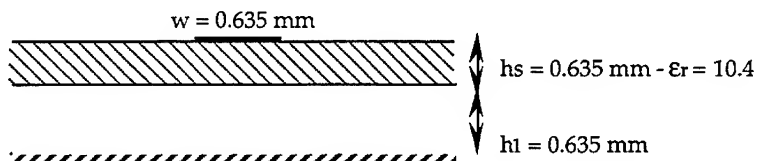


Figure 7 : Studied microstrip structure.

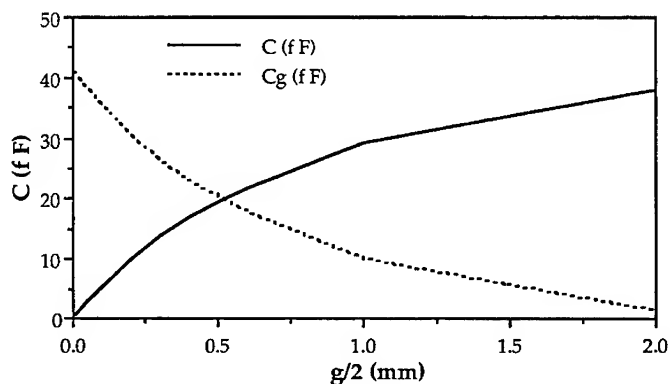


Figure 8 : Capacitances as functions of the gap width.

We added losses to the previous structure through $\tan \delta_s = 10^{-4}$. Figure 9 gives, at $f = 1$ GHz, the variation of the resistances R and R_g as functions of the gap width, obtained by means of the complex frequency concept. We can draw here the same conclusions as for the capacitances variations, as concern the limits $g = 0$ and $g = \infty$.

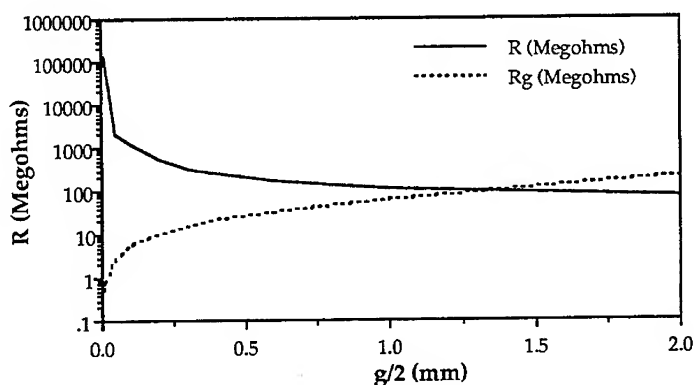


Figure 9 : Resistances as functions of the gap width - $\tan \delta_s = 10^{-4}$.

We then added losses to the same basic structure through $\sigma_s = 5 \cdot 10^{-4} \text{ S/m}$. At $f = 1$ GHz, this conductivity gives less losses than $\tan \delta_s = 10^{-4}$. As the ideal lossless case gives $R = R_g = \infty$ increasing losses must increase the values of R and R_g , which is verified on figure 10.

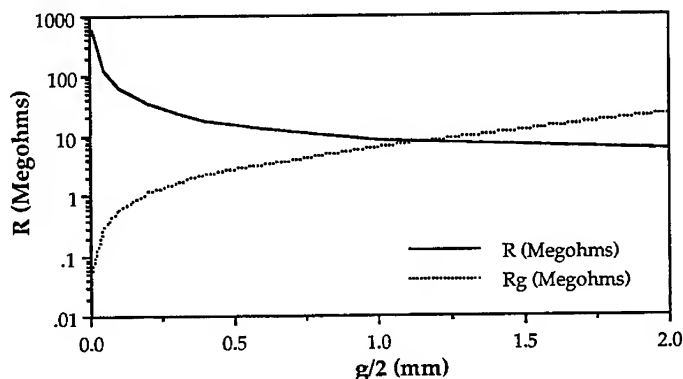


Figure 10 : Resistances as functions of the gap width - $\sigma_s = 5 \cdot 10^{-4} \text{ S/m}$.

For the same basic structure (Fig. 7), we have varied the frequency from 1 to 15 GHz, for a fixed gap width $g = 1.27 \text{ mm}$. Figure 11 shows the variations of C and C_g , which can be explained by the fact that the electric fields E_x and E_z increase with the frequency. As C is bound to E_x and C_g to E_z , the increase of the frequency leads thus to an increase of both capacitances C and C_g .

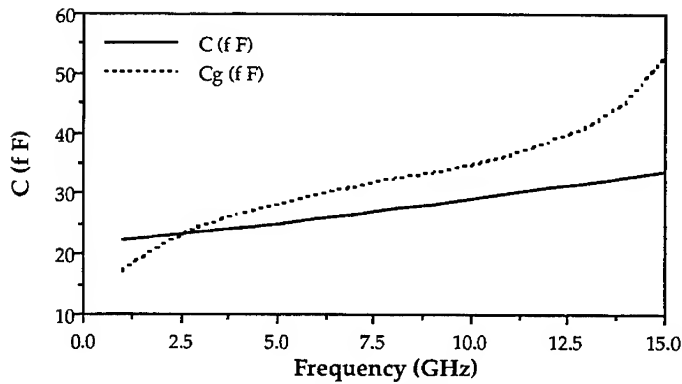


Figure 11 : Capacitances as functions of the frequency.

To this basic structure, we have added first losses through $\tan \delta_s = 10^{-4}$. Using the complex frequency concept, we have calculated the resistive elements R and R_g (Fig. 12). We can notice that R and R_g decrease as the frequency increases, indicating that losses increase with the frequency (in fact, with the electric fields E_x and E_z).

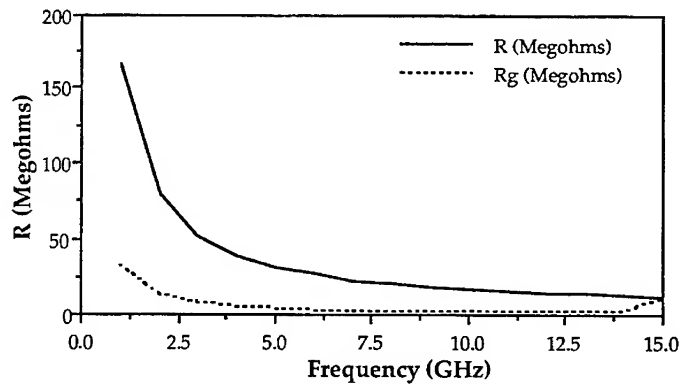


Figure 12 : Resistances as functions of the frequency - $\tan \delta_s = 10^{-4}$.

We have then added losses through $\sigma_s = 5 \cdot 10^{-4} \text{ S/m}$, which is equivalent to $\tan \delta_s = 8.65 \cdot 10^{-4}$ at $f = 1 \text{ GHz}$ and $\tan \delta_s = 5.76 \cdot 10^{-5}$ at $f = 15 \text{ GHz}$. The resistance R decreases as the frequency increases (Fig. 13). On the contrary, the resistance R_g decreases for weak frequencies and then increases. In fact, we have two opposite variations : on one hand, the equivalent $\tan \delta_s$ decreases with the increasing frequency, on the other hand and at the same time, the field increases in the dielectrical substrate, which entails increasing losses.

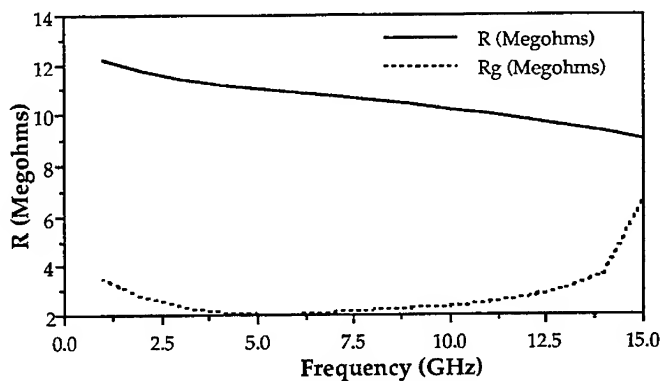


Figure 13 : Resistances as functions of the frequency - $\sigma_s = 5 \cdot 10^{-4} \text{ S/m}$.

Conclusion

The monolithic microwave and millimeterwave circuits are usually based on planar transmission lines and discontinuities. For most classical microwave applications, only the losses on transmission lines are calculated and taking losses into consideration in the modeling of discontinuities is useless. However, some particular applications, where for example the semiconductor conductivity plays an important role, require a modeling method where losses are taken into consideration. In this paper, for the first time, we study the modeling of lossy discontinuities. The developed technique is based on the well-known and very efficient Spectral Domain Approach. To introduce the substrate losses we make benefit of the complex frequency concept, which allows to get electrical equivalent circuits with resistive elements representing the losses. This technique does not depend on the losses level. However in the case of low losses it is advantageous to couple it to a perturbation method. As an example we have applied it to gaps on low lossy microstrip lines. The obtained results have been explained and agree well with the expected physical behaviour of the structure.

References

- [1] P. Kennis, L. Faucon : "Rigorous analysis of planar MIS transmission lines", Electronics Letters, vol. 17, n°13, June 1981, pp 454-456.
- [2] A. Vilcot, S. Tedjini : "Effet de masse sur les lignes intégrées monolithiques pour applications millimétriques", IEEE-MTT chapitre français, Journées d'Etudes sur les Composants Millimétriques, 21-22 novembre 1991, pp 47-50.
- [3] S. Tedjini, N. Daoud, D. Raully, E. Pic : "Analysis of MMIC's with finite strip thickness and conductivity", Electronics Letters, vol 24 n°15, July 1988, pp 965-966.
- [4] W. Wertgen, R. H. Jansen : "Efficient and iterative electrodynamic analysis of geometrically complex MIC and MMIC structures", International Journal of Numerical Modelling : electronic networks, devices and fields, vol. 2, 1989, pp 153-186.
- [5] N.H.L. Koster, R.H. Jansen : "The equivalent circuit of the asymmetrical series gap in microstrip and suspended substrate lines", IEEE Trans. Microwave Theory and Tech, vol. 30, n°8, Aug. 1982, pp 1273-1279.

SESSION 10 - "TIME-DOMAIN TECHNIQUES I

(FEATURING FDTD)"

Chair: Dr. Ray Luebbers, Co-Chair: Dr. Jiayuan Fang

Absorbing Boundary Treatments in the Simulation of Wave Propagation in Microwave Integrated-Circuits

Jiayuan Fang

Department of Electrical Engineering
State University of New York at Binghamton
Binghamton, New York 13902-6000
Tel: (607)777-4412, FAX: (607)777-4822

ABSTRACT

An absorbing boundary condition is presented in this paper for simulation of wave propagation by the finite-difference time-domain method. Unlike previously developed absorbing boundary conditions, which can only absorb outgoing propagating waves, this boundary condition can also reduce the reflection of evanescent waves significantly. The boundary condition presented in this paper is found very effective in modeling wave propagation in passive components of microwave integrated-circuits. With this boundary condition, some of the outer surfaces of computation domains can be placed much closer to modeled objects, resulting in savings in computer memory space and computation time. The application of this boundary condition is demonstrated by modeling a pulse propagation along an open microstrip line.

Introduction

In numerical modeling of wave propagation in an infinite large space by the finite-difference time-domain method, the finite-difference mesh has to be truncated at a finite distance to modeled objects due to limited computer memory space. Various absorbing boundary conditions have been developed to prevent outgoing waves being reflected back into the computation domain. These boundary conditions include the space-time extrapolation method [1-2], the impedance boundary condition [3], Engquist & Majda's [4], Liao et. al.'s [5], Higdon's [6], etc. The super-absorption technique [7-8] can be applied together with absorbing boundary conditions to improve the absorption property of boundary conditions. Although these boundary conditions have been used successfully in many applications, it has been found (see reference [2]), as will also be shown in examples presented later in this paper, that on some outer surfaces of computation domains, previously developed absorbing boundary conditions all appear to be totally ineffective.

The place where previously developed absorbing boundary conditions fail is when fields near outer boundaries are mostly evanescent waves instead of outgoing propagating waves. As a result of this fact, in numerical modeling of microwave passive components, an open microstrip line as an example, outer boundaries parallel to the microstrip line have to be placed far away from the metal strip in order to minimize the influence of reflection waves from these boundaries. It has been observed that even a modest amount of error in transient solutions, caused by the reflection from outer boundaries, can severely deteriorate the accuracy of frequency-dependent circuit parameters obtained through Fourier transform of transient solutions

[2,9]. To ensure accurate numerical results without resorting to use excessive computer resources, all the outer boundaries of computation domains need to be treated carefully. The absorbing boundary condition presented in this paper is found effective for absorbing both outgoing propagating and evanescent waves.

Proposed Absorbing Boundary Condition

Previously used absorbing boundary conditions were developed for the absorption of outgoing waves incident normally or at certain angles at outer boundaries [1-8]. Therefore, they work well only for outgoing propagating waves. The absorbing boundary condition which can be accommodated to both propagating and evanescent waves can be expressed as

$$\left[\prod_{i=1}^N \left(\frac{\partial}{\partial x} + \frac{p_i}{v} \frac{\partial}{\partial t} + \alpha_i \right) \right] E = 0, \quad (1)$$

where α_i and p_i are parameters, v is the speed of light. The outer boundary surface considered in equation (1) is at the far end in the x direction of the computation domain. The boundary condition expressed in equation (1) is an N th order boundary condition which is composed of the product of N first order boundary conditions.

Consider the boundary condition in equation (1) in its first order form, that is,

$$\left(\frac{\partial}{\partial x} + \frac{p_1}{v} \frac{\partial}{\partial t} + \alpha_1 \right) E = 0. \quad (2)$$

The reflection coefficient R_1 of this boundary condition can be found by substituting

$$E = e^{j(\omega t - k_x x - k_y y - k_z z)} + R_1 e^{j(\omega t + k_x x - k_y y - k_z z)} \quad (3)$$

into equation (2), then R_1 can be obtained as

$$R_1 = - \frac{-jk_x + jp_1 k + \alpha_1}{jk_x + jp_1 k + \alpha_1} \quad (4)$$

where $k = \omega/v$, k_x , k_y and k_z are the wavenumbers in the x , y and z directions respectively. The wavenumber k_x in general can be expressed as

$$k_x = \beta_x - j\alpha_x. \quad (5)$$

Substituting k_x expressed in equation (5) into equation (4), R_1 can be rewritten as

$$R_1 = \frac{j(\beta_x - p_1 k) + (\alpha_x - \alpha_1)}{j(\beta_x + p_1 k) + (\alpha_x + \alpha_1)}. \quad (6)$$

From equation (6), it is clear to see the general principle in selecting parameters α_1 and p_1 to minimize the reflection coefficient R_1 . For outgoing propagating waves, which correspond to $\alpha_x = 0$, α_1 can be set to zero, and p_1 is selected according to the estimated propagation speed and the incident angle of outgoing waves. For evanescent waves, which correspond to $\beta_x = 0$, p_1 can be set to zero, α_1 is chosen to be the estimated attenuation rate of fields near the outer

boundary. For attenuating-propagating waves, both α_1 and p_1 can be chosen to be some non-zero numbers.

In numerical modeling of wave propagations, exact values of the propagation constant β_x and the attenuation constant α_x of outgoing waves are usually not known. Furthermore, the propagation and the attenuation constants of outgoing waves at a boundary surface can change with position and time. Therefore, the first order boundary condition is found not good enough for many applications. The boundary condition (1) can be applied in its high order form if good absorption property of the boundary condition is required. The reflection coefficient of the N th order boundary condition can be found by substituting equation (3) into equation (1), that is,

$$R = - \prod_{i=1}^N \frac{-jk_x + jp_i k + \alpha_i}{jk_x + jp_i k + \alpha_i} . \quad (7)$$

Equation (7) shows that the reflection coefficient of an N th order boundary condition is equal to the product of the reflection coefficients of N first order boundary conditions. Since the reflection coefficients of first order boundary conditions are all less than or equal to one, their product can become a sufficiently small number. Parameters α_i 's and p_i 's in an N th order boundary condition can be selected in the way that each boundary operator is designated to absorb one particular type of outgoing wave, so the whole boundary condition can absorb outgoing waves of a wide range of propagation and attenuation constants.

Numerical Examples

Consider an open microstrip line shown in figure 1. The dielectric substrate of the microstrip line is of $\epsilon_r = 4$ and has a thickness $H = 500 \mu\text{m}$. The metal strip is of a width $W = 1000 \mu\text{m}$ and zero thickness. Let us model a Gaussian pulse propagation along this microstrip line by the finite-difference time-domain method. The pulse is excited by a current source under the metal strip. The space-step dh of the finite-difference mesh is chosen to be $125 \mu\text{m}$. The time-step $dt = 0.5 dh/v$, where v is the speed of light in air.

Fields around the near and far end surfaces in the x direction are dominantly propagating waves ($\alpha_x = 0$). All the previously developed absorbing boundary conditions can be applied at these surfaces. Liao et. al.'s and Higdon's boundary conditions are especially effective; a 2nd or 3rd order Liao et. al.'s or Higdon's boundary condition is usually good enough to obtain accurate solutions of the effective dielectric constant ϵ_{eff} and the characteristic impedance Z_0 [10]. If α_i 's in equation (1) are all set to zero, the boundary condition (1) has actually the same form as that of Higdon's boundary condition. It can be shown that, by adding some small value of α_i 's in the boundary condition, it is helpful to maintain the stability of the boundary condition [11].

Problems arise at the far end surfaces in the y and z directions, where fields are dominantly evanescent waves. Let us examine the situation at the far end surface in the y direction as an example. Suppose the far end surface in the y direction is terminated at $y = 2500 \mu\text{m}$. Let us consider the first order Engquist & Majda's boundary condition which is the same as the first order Higdon's boundary condition expressed as follows

$$\left(\frac{\partial}{\partial x} + \frac{p_1}{v} \frac{\partial}{\partial t} \right) E = 0. \quad (8)$$

The parameter p_1 is usually selected according to the estimated propagation speed of outgoing wave. Percentage errors, due to the reflection wave from the boundary, in the voltage of the microstrip line as a function of frequency for various values of p_1 are displayed in figure 2. The percentage errors in voltage displayed in figure 2 are obtained by comparing voltages with the reference solution computed with the outer surface in the y direction being placed very far away from the metal strip. Figure 2 shows that reflections from the boundary can not be substantially reduced no matter what value of p_1 is chosen. The corresponding effective dielectric constants $\epsilon_{\text{eff}}(f)$ are shown in figure 3.

Next let us consider the second order boundary condition expressed in equation (1), but keep $\alpha_1 = \alpha_2 = 0$. This boundary condition becomes the same as the second order Higdon's boundary condition, and comparable to the second order Liao et. al.'s boundary condition. Percentage errors in the voltage when $p_1 = \sqrt{4.0}$ and p_2 chosen to be different values are displayed in figure 4. It can be seen that the second order absorbing boundary conditions can not provide much improvement on the first order ones.

Consider the first order absorbing boundary condition in equation (2) again, but this time let $p_1 = 0$ and α_1 to be different values. Percentage errors in the voltage for different values of α_1 are shown in figure 5. It can be seen that reflection waves from the boundary can be substantially reduced by choosing α_1 properly. This result further confirms that the fields at this boundary can not be treated as outgoing propagating waves. The parameter α_1 can be selected according to the estimated attenuation rate of fields near the boundary; and the attenuation rate of fields can be estimated through some pre-computations to find field patterns near boundary surfaces [10].

The attenuation rate of fields near outer boundaries usually varies with position. After applying the first order absorbing boundary condition with a constant α_1 , a large portion of reflection wave can be removed, but a significant fraction of the reflection wave may still remain. Higher than the first order absorbing boundary conditions are needed to further reduce the reflection. Figure 6 shows the percentage errors in the voltage with the first to fourth order boundary conditions, and the corresponding effective dielectric constants $\epsilon_{\text{eff}}(f)$ are shown in figure 7. From figures 6 and 7, we can see that boundary operators for evanescent waves play a very important role in reducing the reflection error; and the boundary conditions of the most effectiveness are the ones with a combination of boundary operators for evanescent and propagating waves.

For the outer boundary surface in the z direction, similar results as above have been observed [10].

Conclusion

This paper presents an absorbing boundary condition which can be easily adjusted for either outgoing propagating or evanescent waves. This boundary condition has been verified to be very effective in reducing reflection errors in the modeling of wave propagation in microwave integrated-circuits. The generality of this boundary condition allows it to be applicable to other applications such as optical waveguides, interconnections in electronic packaging, etc.

Acknowledgements

This work was supported by the National Science Foundation under contract MIP-9110203 and ECD-9108850 which supports the Integrated Electronics Engineering Center (IEEC) at the State University of New York at Binghamton, and by the Cornell National Supercomputer Center.

References

- [1] A. Taflov and M. E. Brodwin, "Numerical solution of steady-state electromagnetic scattering problems using the time-dependent Maxwell's equations," *IEEE Trans. Microwave Theory Tech.*, MTT-23, pp. 623-630, Aug. 1975.
- [2] X. Zhang and K. K. Mei, "Time-domain finite-difference approach to the calculation of the frequency-dependent characteristics of microstrip discontinuities," *IEEE Trans. Microwave Theory Tech.*, MTT-36, pp. 1775-1787, Dec. 1988.
- [3] S. Yoshida and I. Fukai, "Transient analysis of a stripline having a corner in three-dimensional space," *IEEE Trans. Microwave Theory Tech.*, MTT-32, pp. 491-498, May, 1984.
- [4] B. Engquist and A. Majda, "Absorbing boundary conditions for the numerical simulation of waves," *Math. Comp.*, v. 31, pp. 629-651, 1977.
- [5] Z. Liao, H. L. Wong, B. Yang and Y. Yuan, "A transmitting boundary for transient wave analysis," *Scientia Sinica, Series A*, vol. XXVII, No. 10, pp. 1062-1076, Oct. 1984.
- [6] R. L. Higdon, "Absorbing boundary conditions for difference approximations to the multi-dimensional wave equation," *Math. Comput.*, vol. 47, No. 176, pp. 437-459, Oct. 1986.
- [7] J. Fang and K. K. Mei, "A super-absorbing boundary algorithm for solving electromagnetic problems by time-domain finite-difference method," 1988 IEEE AP-S/URSI International Symposium, pp. 472-475, Syracuse, NY, June 6-10, 1988.
- [8] K. K. Mei and J. Fang, "Superabsorption - A method to improve absorbing boundary conditions," *IEEE Trans. Antennas Propagat.*, vol. AP-40, pp. 1001-1010, Sept. 1992.
- [9] X. Zhang, J. Fang, K. K. Mei and Y. Liu, "Calculation of the dispersive characteristics of microstrips by the time-domain finite-difference method," *IEEE Trans. Microwave Theory Tech.*, MTT-36, pp. 263-267, Feb. 1988.
- [10] J. Fang, "Absorbing boundary conditions applied to model wave propagation in microwave integrated-circuits," submitted to *IEEE Trans. Microwave Theory Tech.*
- [11] J. Fang, "Investigation on the stability of absorbing boundary conditions for the time-domain finite-difference method," 1992 IEEE AP-S/URSI International Symposium, Chicago, IL, July 18-25, 1992, pp. 548-551.

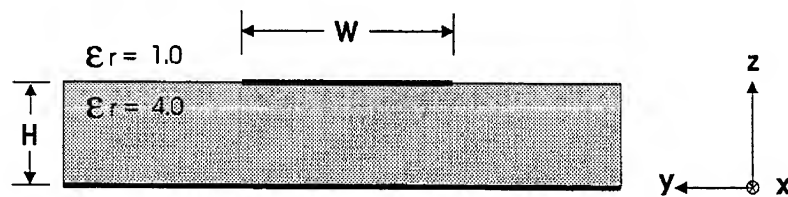


Figure 1. Structure of an open microstrip line.

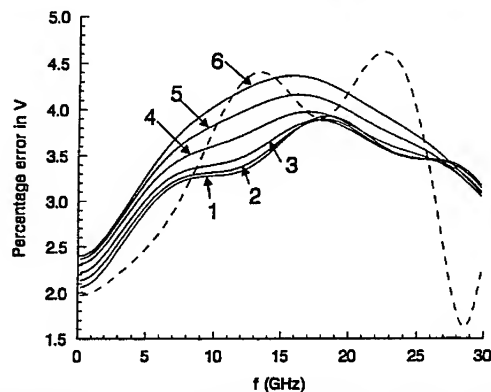


Figure 2. Percentage error in voltage when the far end boundary in the y direction is terminated by the first order boundary conditions with zero α_1 and different values of p_1 . Curves 1 to 6 correspond to $p_1 = \sqrt{4}, \sqrt{3}, \sqrt{2}, \sqrt{1}, \sqrt{0.5}$ and $\sqrt{0.25}$ respectively. The dashed curve is for the electric wall boundary.

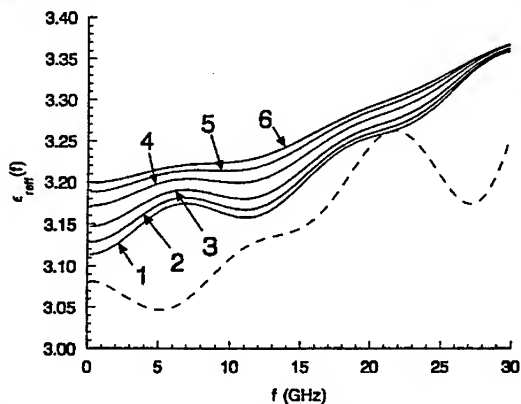


Figure 3. Effective dielectric constant of the microstrip computed with the far end boundary in the y direction being terminated by the first order boundary conditions with zero α_1 and different values of p_1 . Curves 1 to 6 correspond to $p_1 = \sqrt{4}, \sqrt{3}, \sqrt{2}, \sqrt{1}, \sqrt{0.5}$ and $\sqrt{0.25}$ respectively. The dashed curve is for the electric wall boundary.

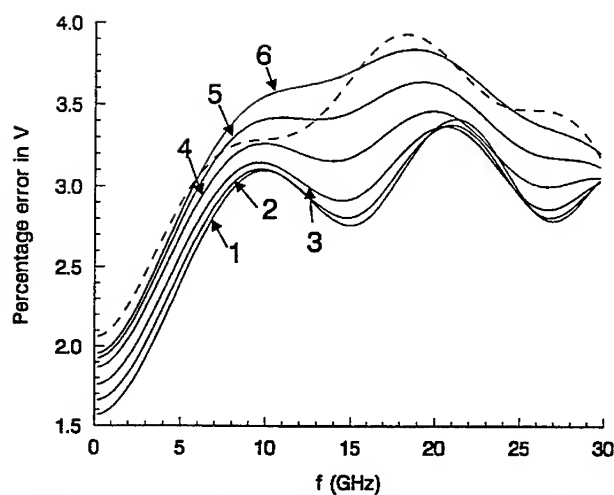


Figure 4. Percentage error in the voltage when the far end boundary in the y direction is terminated by the second order boundary conditions with $\alpha_1 = \alpha_2 = 0$, $p_1 = \sqrt{4}$ and different values of p_2 . Curves 1 to 6 correspond to $p_2 = \sqrt{4}$, $\sqrt{3}$, $\sqrt{2}$, $\sqrt{1}$, $\sqrt{0.5}$ and $\sqrt{0.25}$ respectively. The dashed curve is for the first order boundary condition with $\alpha_1 = 0$ and $p_1 = \sqrt{4}$.

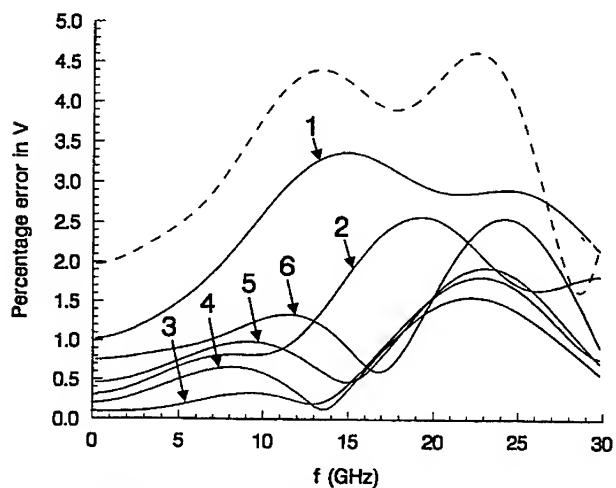


Figure 5. Percentage error in the voltage when the far end boundary in the y direction is terminated by the first order boundary conditions with zero p_1 and different values of α_1 . Curves 1 to 6 correspond to $\alpha_1 dh = 0.02$, 0.04 , 0.06 , 0.08 , 0.10 and 0.12 respectively. The dashed curve is for the electric wall boundary.

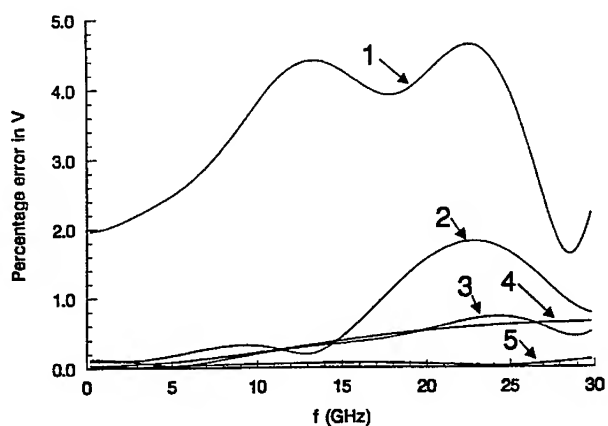


Figure 6. Percentage error in the voltage for different boundary conditions applied at the far end boundary in the y direction. Curve 1: electric wall boundary; Curve 2: 1st order ABC, $\alpha_1 dh = 0.06$; Curve 3: 2nd order ABC, $\alpha_1 dh = 0.06$, $\alpha_2 dh = 0.04$; Curve 4: 3rd order ABC, $\alpha_1 dh = 0.06$, $\alpha_2 dh = 0.04$, $p_3 = \sqrt{3}$; Curve 5: 4th order ABC, $\alpha_1 dh = 0.06$, $\alpha_2 dh = 0.04$, $p_3 = \sqrt{3}$, $\alpha_4 dh = 0.12$.

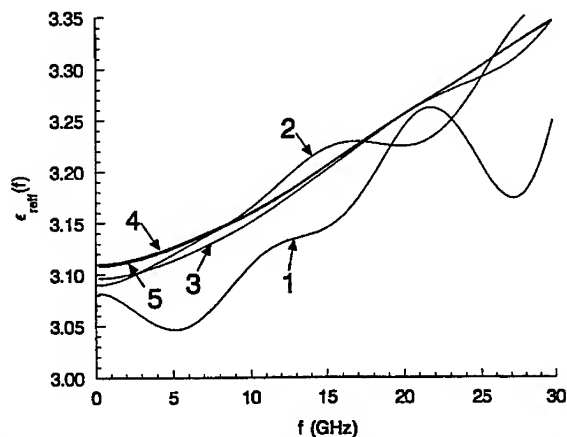


Figure 7. Effective dielectric constant $\epsilon_{eff}(f)$ computed with different boundary conditions applied at the far end boundary in the y direction. Curve 1: electric wall boundary; Curve 2: 1st order ABC, $\alpha_1 dh = 0.06$; Curve 3: 2nd order ABC, $\alpha_1 dh = 0.06$, $\alpha_2 dh = 0.04$; Curve 4: 3rd order ABC, $\alpha_1 dh = 0.06$, $\alpha_2 dh = 0.04$, $p_3 = \sqrt{3}$; Curve 5: 4th order ABC, $\alpha_1 dh = 0.06$, $\alpha_2 dh = 0.04$, $p_3 = \sqrt{3}$, $\alpha_4 dh = 0.12$.

**A HYBRID RAY/FDTD METHOD
FOR COMPUTING ELECTROMAGNETIC SCATTERING
FROM AN ENGINE CAVITY WITH A COMPLEX TERMINATION**

R. Lee and T. T. Chia
ElectroScience Laboratory
Department of Electrical Engineering
The Ohio State University
1320 Kinnear Rd.
Columbus, Ohio 43212-1191

I. Introduction

The problem of electromagnetic scattering from an open-ended cavity structure is an important problem in the area of radar scattering. Among other things, it models the radar scattering from a jet engine inlet. There has been considerable work devoted to computing the high frequency scattering from the interior of an arbitrarily shaped cavity. Two ray based techniques, the Shooting and Bouncing Rays (SBR) method [1] and the Generalized Ray Expansion Method (GRE) [2], have recently been developed to analyze cavity scattering. Both methods in principle can be used to accurately predict the scattering from the interior of practically any three-dimensional cavity within the high frequency restrictions, including the effects of material coating on the interior cavity walls. In practice, though, SBR and GRE have generally been restricted to cavities with planar or other simple terminations. The terminations of cavities of practical interest are often fairly complex. The complexities of the terminations are such that high frequency ray techniques are usually unable to provide an accurate solution. It should be possible, however, to analyze the scattering from a cavity with a complex termination using a hybrid technique. A hybrid modal-moment method has previously been implemented and proven to be successful at modeling perfectly conducting, arbitrarily-shaped terminations [3].

In this paper, we propose another hybrid method which combines GRE with the finite difference time domain (FDTD) method [4, 5]. GRE has been chosen over SBR because the former has proven to be more accurate [6]. The coupling between FDTD and GRE is first described. This is followed by a discussion on the advantages of the hybrid method. Finally, two numerical results are presented for two-dimensional cavities.

II. Coupling FDTD to GRE

The GRE method has been well described in [2] and therefore is not presented here. Similarly, the FDTD method, which has become a standard method in electromagnetics, is not derived in this paper. However, the coupling between GRE and FDTD requires some explanation. Let us consider the cavity in Figure 1. The cavity has been divided into three regions. GRE is used to compute the solutions in Region 1 and Region 3, while FDTD is applied to Region 2. In Regions 1 and 3, the cavity geometry is assumed to be simple enough for high frequency approximations to be valid, i.e., smoothly varying cavity cross-sections. In Region 1, the rays are traced from the aperture of the cavity to the surface S_{T1} . The field solution associated with all the rays are summed together to produce a high frequency solution on S_{T1} . The solution on S_{T1} can be used as the excitation for the FDTD computation in Region 2.

Since the GRE method is a frequency domain method, it is necessary to choose a suitable time variation for the excitation. One possible choice would be a sinusoidal steady-state time variation. For this case, the GRE computation is performed only at the frequency of interest. Another possible choice would be a Gaussian pulse excitation. In this instance, a GRE solution must be determined over a range of frequencies which properly accounts for the frequency content in the Gaussian pulse. Then the inverse Fourier transform of the product of the GRE solution with the Fourier transform of the Gaussian pulse can be used as the excitation for the FDTD computation. Actually, any desired time variation can be substituted in place of the Gaussian pulse in the above description.

The excitation at S_{T1} produces a wave which propagates toward the termination and eventually interacts with it. In general, part of the wave is transmitted through S_{T2} into Region 3, and the remainder is reflected back toward S_{T1} . If we assume that the waves which exit Region 2 through S_{T1} and S_{T2} do not return, then an absorbing boundary condition such as the ones introduced by Higdon [7] or Mur [8] can be applied to the FDTD calculations in Region 2. This assumption is usually valid because most jet engine inlets are shaped in such a way that there is very little energy which returns to Region 2 once it has exited it. For those engine inlets where the assumption is not true, we can convert the waves leaving Region 2 back into rays by applying the GRE method at S_{T1} and S_{T2} . The rays which return to Region 2 act as additional excitation.

To determine the radar scattering of the cavity, we must use the appropriate information from the field solution in Region 2. One way to do this is to use the FDTD solution at S_{T1} to launch rays into Region 1. These rays can then be tracked out of the cavity and used to determine the scattered field. Unfortunately, this method

requires that rays be traced both into the cavity for the initial excitation of Region 2 and out of the cavity for the scattered field calculation. To eliminate the need to trace the rays out of the cavity, we can use the reciprocity formulation developed in [9] to find the scattered electric field exterior to the cavity. In this formulation only the tangential electric and magnetic fields at S_{T1} are needed to compute the scattered field.

III. Advantages of the Hybrid Ray/FDTD Method

A hybrid method is the only feasible way that the cavity problem can be solved in the near future. High frequency techniques do not provide a solution that is accurate enough for many applications, while low frequency methods such as FDTD are incapable of modeling electrically large structures because of the tremendous computational costs. For example, a rectangular cavity of cross-section $30\lambda \times 40\lambda$ and a depth of 100λ , requires 5.76 billion unknowns for FDTD with a mesh density of 20 nodes/ λ .

The hybrid method seems to be ideal for the engine cavity. A high frequency method is applied to the region where it is best suited, and a low frequency method is used where it is needed. Currently, hybrid methods have been employed to solve the cavity problem in the frequency domain. In some cases, an integral equation technique such as the method of moments is used to handle the termination in the cavity. Because the termination can have dimensions which are many wavelengths long, the majority of the computation time is spent in the solution of the integral equation. More specifically, the computation time is spent in the solution of a large matrix equation. The number of floating point operations needed to solve a matrix equation is approximately $n^3/6$ where n is the number of unknowns in the matrix equation. In addition, the n^2 elements of the matrix must be stored. For a three dimensional penetrable termination, the number of unknowns can become so large that the solution of the matrix equation is infeasible in terms of both memory storage and computation time.

A frequency domain finite element method may be more efficient than integral equation methods because the resulting matrices are sparse. However, the computation time necessary to solve the matrix equation is still very expensive for large problems. Time domain methods such as FDTD overcomes many of the difficulties associated with a frequency domain solution. This method evaluates the solution directly in the time domain by stepping the solution in time. Although the solution must be obtained for a multiple number of time steps, it is still very efficient since it

does not require the solution of a matrix equation. Instead, the field at a given position in space is computed in terms of the field values in neighboring positions at the previous time step; therefore, the number of floating point operations is proportional to the number of unknowns n . In addition, the memory storage is proportional to n .

There are several major disadvantages with FDTD: (1) it cannot easily handle non-conforming geometries, (2) the solution must be rerun for every incident angle, and (3) for pulsed excitations, dispersive materials are difficult to model. At this time, research is continuing to improve upon this hybrid method to eliminate these disadvantages.

IV. Numerical Results

To test the validity of the hybrid GRE-FDTD method, a two-dimensional steady-state time variation code has been written for a parallel-plate waveguide cavity with a variety of terminations. We will provide numerical results here for two cavities. The first cavity has a planar termination. The second cavity has an additional wedge-shaped plug attached to its planar termination. The height of the wedge-shaped plug is 2λ and its base width is 4λ . Both cavities are 30λ long with apertures of 9.6λ . The walls of the cavity and the termination are assumed to be perfectly conducting. Region 2 is 4λ long while Region 3 is absent in our examples.

Figure 2 shows the radar cross-section (RCS) patterns of the first cavity using the modal-method of moment (Modal-MM) [3] and the hybrid GRE-FDTD method for the TE case. The pattern obtained via the former method is used as a reference solution.¹ From Figure 2, the RCS pattern obtained via the hybrid GRE-FDTD method agrees very well with the reference solution.

The RCS patterns of the second cavity is shown in Fig. 3 using the two hybrid methods for the TE case. The pattern obtained by the hybrid GRE-FDTD method is again in good agreement with the reference pattern of the modal-MM, except for θ greater than 54° . The difference between the two patterns at these large angles could be due to the higher order modes excited by the wedge-plane termination through diffraction of fields from its edges and multiple reflections of fields from its surfaces. These higher order modes have large modal angles which the second-order Mur [8] absorbing boundary condition used in our FDTD scheme does not absorb as well as it does the lower order modes with smaller modal angles. If these higher order modes are significant, then their non-physical reflections from S_{T1} back to the termination will ultimately affect the fields transmitted through S_{T1} .

¹The contribution to the scattered field from the fields diffracted from the edges of the aperture has been removed from the original modal-MM code in [3] for comparison with our results.

V. Summary

A hybrid ray/FDTD method has been introduced. This method allows for the modeling of complex terminations to the order of the FDTD cells. From the numerical results, we have shown that this method is very accurate.

VI. References

- [1] R.-C. Chou, *Reduction of the radar cross section of arbitrarily shaped cavity structures*. Ph.D. dissertation, University of Illinois, Urbana-Champaign, IL, 1987.
- [2] R. J. Burkholder, *High-Frequency asymptotic methods for analyzing the EM scattering by open-ended waveguide cavities*. Ph.D. dissertation, The Ohio State University, Columbus, OH, 1989.
- [3] C. W. Chuang, P. H. Pathak and R. J. Burkholder, *A hybrid asymptotic modal-moment method analysis of the EM scattering by 2-D open-ended linearly tapered waveguide cavities*. The Ohio State University ElectroScience Laboratory Technical Report No. 312436-1, prepared for McDonnell Douglas Corporation, St. Louis, MO, December, 1988.
- [4] K. S. Yee, "Numerical solution of initial boundary value problems involving Maxwell's equations in isotropic media," *IEEE Trans. Antennas Propagat.*, vol. AP-14, pp. 302-307, May 1966.
- [5] A. Taflov and M. E. Brodwin, "Numerical solution of steady-state electromagnetic scattering problems using the time-dependent Maxwell's equations," *IEEE Trans. Microwave Theory Tech.*, vol. MTT-23, pp. 623-630, August 1975.
- [6] R.-C. Chou, T. T. Chia and R. Lee, "The energy flow inside a waveguide cavity using the SBR and GRE methods", presented at the *IEEE AP-S International Symposium, URSI Radio Science Meeting and Nuclear EMP Meeting*, July 18-25, 1992, Chicago, IL.
- [7] R. L. Higdon, "Numerical absorbing boundary conditions for the wave equation", *Math. Comp.*, vol. 49, no. 179, pp. 65-90, July 1987.
- [8] G. Mur, "Absorbing boundary conditions for the finite-difference approximation of the time-domain electromagnetic-field equations", *IEEE Trans. Electromagn. Compat.*, vol. EMC-23, pp. 377-382, November 1981.

- [9] P. H. Pathak and R. J. Burkholder, "A reciprocity formulation for the EM scattering by an obstacle within a large open cavity," to appear in *IEEE Trans. Microwave Theory Tech.*

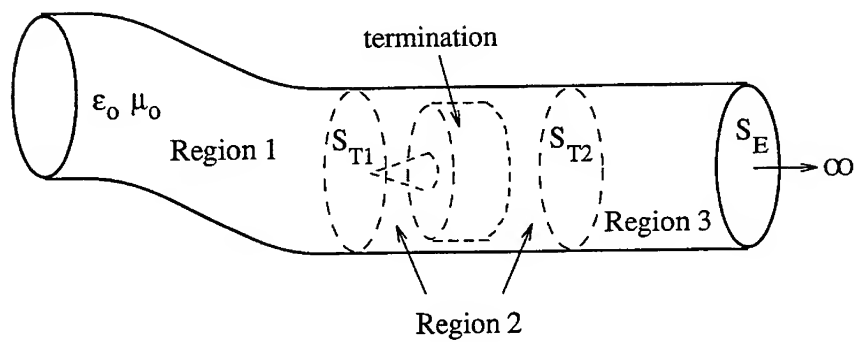


Figure 1: Geometry of cavity with termination.

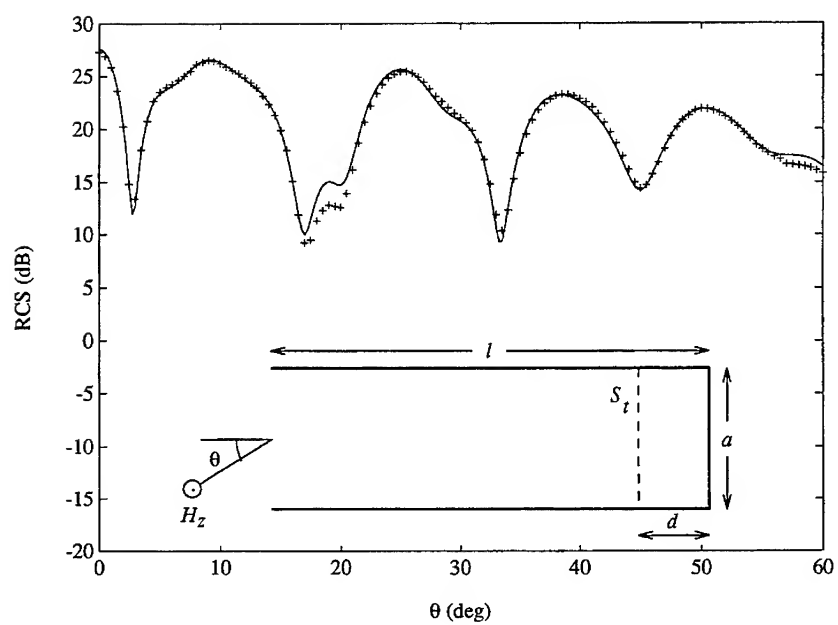


Figure 2: Radar cross-section patterns of parallel-plate cavity with planar PEC termination using the hybrid Modal-MM & the hybrid GRE-FDTD methods. $a = 9.6\lambda$, $l = 30\lambda$, $d = 4\lambda$; TE: — Modal-MM, + GRE-FDTD (3 subapertures).

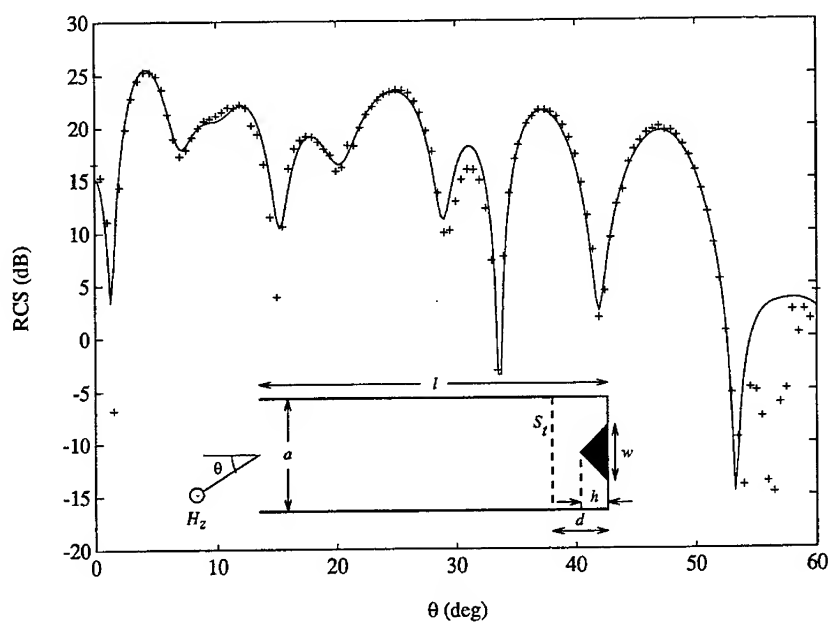


Figure 3: Radar cross-section patterns of parallel-plate cavity with a wedge-shaped PEC plug termination using the hybrid Modal-MM & the hybrid GRE-FDTD methods. $a = 9.6\lambda$, $l = 30\lambda$, $d = 4\lambda$, $h = 2\lambda$, $w = 4\lambda$; TE: — Modal-MM, +: GRE-FDTD (3 subapertures).

FDTD Modeling of the Resonance Characteristics of Realistic Enclosures

Kent Chamberlin and Lauchlan Gordon
University of New Hampshire

Bruce Archambeault
Digital Equipment Corporation

Abstract

As part of an effort to characterize radiation from computer enclosures, the resonant behavior of closed and partially closed, finitely-conducting structures has been studied using closed-form solutions, FDTD, and measurements. Finitely-conducting materials are modeled in FDTD by a perfect conductor backed by a one-cell-thick, conducting layer with very low conductivity. Lossy seams are modeled by lossy magnetic regions near the seams. This paper presents measured and modeled data comparisons as well as a discussion of practical considerations such as model parameters, geometry, computer running time and measurement techniques.

Introduction

FDTD has been used to model perfect electric conductors (PEC) and slightly lossy dielectric and magnetic materials for some time and has been shown to produce satisfactory results. In contrast, FDTD modeling of finitely-conducting metals generally estimates much lower loss than would be expected. For instance, one work[1] in which an attempt was made to include the finite conductivity of the walls of a ported cavity mentioned in passing that "the inclusion of aluminum's conductivity had only a negligible effect", and that the conductivity had to be increased 4 orders of magnitude before conductivity losses equalled the radiation losses of even a small aperture.

FDTD does not accurately model losses in realistic conductors for practical applications because the skin depth is generally much smaller than the cell size; linear interpolation is used in the algorithm, and there may be considerable truncation error, particularly when using single precision computation techniques. For example, in the work presented here, computer running time and storage constraints mandated the use of a cell size of around one-half inch. This cell dimension is considerably larger than the skin depth for aluminum, which is less than 3 micrometers at 1 GHz. The standard FDTD approach, as defined by Yee, employs an explicit central differencing scheme that retains only first-order terms[2]. A direct consequence of this simplification is that field values between grid points are determined by linear interpolation. To demonstrate how linear

interpolation affects the estimation of loss in a conductor, consider an illuminated metal plate represented by a one-cell thick region where the conductivity is equal to the conductivity of the metal. If the cell thickness is much greater than the skin depth, FDTD will correctly estimate a near-zero field on the unilluminated side of the conductor. On the illuminated side, FDTD will calculate a small, non-zero tangential E-field on the conductor surface. Intermediate values of E within the cell are interpolated linearly, rather than exponentially, which causes an unrealistic estimate of the boundary value parameters as seen at the illuminated conductor surface. The resultant error may be several orders of magnitude for good conductors. When combined with word-length truncation errors, conductivity effects may not be estimated correctly, if at all.

In an actual conductor, the current density decays exponentially and the skin depth is the point at which the current density has decayed to 36.8% of its value at the surface. If the curve of current density versus distance is integrated, and then divided by the value of the current density at the surface, the resulting value is the skin depth[3]. If the current decays linearly, as it will when linear interpolation is used, applying the former definition results in a skin depth of at least .632 cell. Applying the latter definition results in a skin depth of at least $\frac{1}{2}$ cell. Restating, linear interpolation FDTD programs cannot model an α greater than two divided by the cell size in meters, and will lose accuracy for values of α approaching that limit.

Solutions to achieving a more accurate estimate of loss in good conductors are: 1) using cell sizes much smaller than the skin depth (obviously, not a practical solution), 2) employing an exponential interpolation technique at conductor boundaries (an idea worth pursuing), 3) retaining some of the second-order, central-difference terms at the conductor-dielectric interface (also, worth pursuing) or, 4) using a heuristic approach such as the one described in this paper.

Heuristic Approach to Modeling Realistic Conductors

In the approach presented here, realistic conductors are represented by an infinitesimally-thin perfect electric conductor (PEC) backed by a very-slightly-lossy material one cell thick, with the PEC at the location of the conductor boundary. The one-cell thickness has proven convenient in this work, although the approach should work equally well for greater thicknesses. The lossy material used may be either electric or magnetic, or combinations of both.

Using the above approach, losses due to imperfect reflection at a finite-conductor boundary are approximated by dissipation in the lossy medium. For modeling good conductors, the conductivity of that lossy medium will generally be such that reflection from the surface of that medium, as well as refraction, will be negligible. An exception to this is when the angle of incidence for a wave is near to or greater than the real part of the complex critical angle, although this will not be a problem for most practical geometries. It is recognized that some of the dependencies for the lossy material will be different than the dependencies for a metal conductor (*viz*, dependency on frequency, polarization, and angle of incidence). However, as indicated by the agreement between

measured and modeled data obtained in this work, those dependencies do not prevent this approximation from providing good results over a broad range of frequencies.

To approximate the conductivity of the lossy material, consider Figure 1, which shows a fundamental mode ray trajectory inside a 2-dimensional square box. The objective in selecting the conductivity for the lossy material is to have the loss incurred by propagating through that region equal to the loss that would occur due to imperfect reflection at the real metal boundary, which is given by the reflection coefficient at the assumed angle of incidence. For the values presented here, the angle of incidence has been determined based upon the fundamental mode ray trajectory, as shown in the figure. The loss due to propagating in the lossy material is $e^{-\alpha d}$, where d is the optical path length traveled in the lossy material. An example of these types of calculations are given in [4]. Clearly, values of conductivity are dependent upon aspect ratio, the thickness of the lossy material, and frequency.

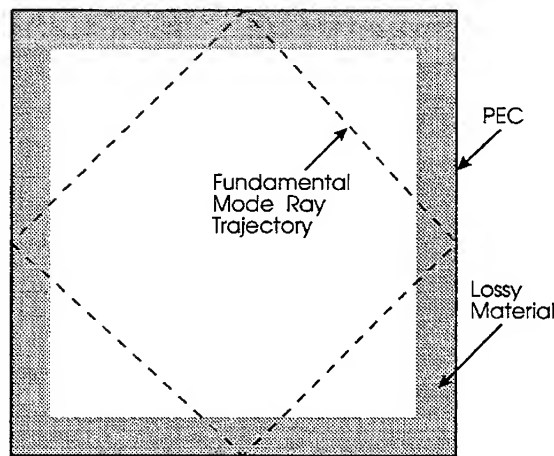


Figure 1 Geometry Used To Approximate Conductivity In Lossy Region.

There are other factors that need to be considered when using this technique relating to the way in which FDTD deals with dielectric and magnetic materials. When a dielectric material is backed by a PEC, four of the E-field elements in each cell will define the PEC, and the remaining eight may be used to define the dielectric. Because elements are shared by adjacent cells, there is an average of one E_x , E_y , and E_z field element available in each cell to describe the dielectric, except at the edges of the slab. On the PEC, the normal component of the E-field terminates and the tangential components vanish. However, total E-field values of all three components in the dielectric may be significant. It should be recognized that the parallel E-field components are required to present a true dielectric boundary at the side of the lossy dielectric layer bounded by the original dielectric material [5][6].

When using lossy magnetic materials for this approach, the lossy material region will be $\frac{1}{2}$ or more cells thick on one or both sides of a PEC, due to the spacial offset between the electric and magnetic fields. When using magnetic materials, only H-field components parallel to the PEC are used to model the lossy magnetic material, since these are sufficient to produce an acceptable magnetic surface

Validation

Comparison of FDTD with closed-form solution. A rectangular PEC cavity of 31 x 21 x 11 cm was modeled in FDTD using 1 cm³ cells, and was lined with a one-cell-thick, lossy dielectric layer. The wall material of the cavity to be modeled was selected to have a conductivity of 9×10^6 seimens/meter (lead). This very lossy conductor was selected in order to reduce the number of time steps required to accurately evaluate the cavity Q. The modeled cavity was excited with a 1 element E-field placed vertically on the 31x21 cm side, one cell away from a corner. The E-field was monitored at the opposite end of the cavity at the center of the 21x11 cm side. The theoretical TE₁₀₁ frequency of this cavity is 862.16 mHz, with a theoretical Q of 9917. It should be noted that the theoretical value of Q was derived using the assumption that the field distribution in the finitely-conducting cavity is identical to the field distribution in a lossless cavity. In the case of a lead cavity, this assumption may be only marginally true.

Using a ray path expansion of the TE₁₀₁ mode for a cavity[7], the wave reflects from the mid points of the 31 x 21 cm cavity sides, and has parallel polarization. An average angle of incidence of 45° was assumed to determine the path length in the lossy dielectric as described above. These calculations yielded a σ of 1.935×10^{-5} S/m for the lossy dielectric. The FDTD model was run on a VAXstation 3540 using 3 parallel processors and executed for 1,050,000 time steps in 61 hours of CPU time. The FFT of the time domain response revealed a TE₁₀₁ frequency of 861.7 MHz and a Q of 11020.

Thus, the FDTD estimate of the TE₁₀₁ mode resonance was in error by .46 MHz, or .053% in frequency, and 11% in the Q. Results for other modes were similar.

Comparison of FDTD with measured data. The theoretical cavity, as modeled above, has continuous conductivity through all of the seams comprising the cavity. However, practical enclosures, which are the topic of interest in this study, typically have seams that are not bonded, a factor that significantly affects Q. To determine whether the approach for modeling real conductors described here could be modified to account for lossy seams, an effort was undertaken to measure and model the resonances of a real enclosure with lossy seams.

That cavity was constructed by lining the inside of a commercially-produced box with six copper plates that were held to the inside of the box and each other with screws spaced several inches apart. A ½ inch overlap was used on eight of the edges, while the other four were butted; none of these edges were brazed. This produced a rather lossy cavity in which the losses of the seams were unknown and probably varied considerably from seam to seam, and along the length of the seams. It was intended to be typical of a practical equipment enclosure rather than a high-Q microwave cavity. The internal dimensions of this enclosure are 42.4x13x32.4 cm.

Measured resonance data were collected using a Hewlett-Packard 8753 network analyzer. The signal was radiated within the enclosure by a 1.08 mm long monopole, which was located in the center of the 42.4x13 cm side, and an identical receiving antenna was on

the facing side. The measured result was received signal strength as a function of frequency for a constant transmitted signal strength.

This cavity was modeled in FDTD by a $40 \times 30 \times 12$ cell PEC cavity with cell dimensions slightly over 1 cm. The cavity was lined with a 1 cell thick dielectric to model the conductivity loss of the copper. The loss associated with the cavity seams was modeled with a 1×1 cell block of lossy magnetic material running the length of the seams with a $\frac{1}{2}$ cell spacing from the PEC. It should be noted that the dielectric material was present in the same space where the magnetic material was used, and conductivity losses from both materials were present in these regions.

The modeled signal was injected into the cavity by a one-cell E-field at the cell location corresponding to the transmitting antenna location in the actual box. An infinitesimally-thin PEC wire was used to model the receive antenna. The modeled E field was monitored at the co-linear E-field element at the end of the receive antenna. The ray optics method was used to calculate a value of 8.68×10^{-6} for the dielectric. The value of magnetic conductivity was adjusted by trial and error to give a TE_{110} Q value close to that measured in the actual box. The FDTD data were normalized by the gaussian pulse as actually propagated by the one-element E field. A normalization for the receive antenna in the model was not included. Two FDTD model runs were made for this configuration: one using a lossy dielectric layer, and the other using a lossy magnetic layer. The results for these two cases were nearly identical.

Plots of measured and modeled data are shown in Figure 2. As can be seen from the figure, the measured and modeled TE_{110} and TE_{111} Q's are well matched. In most cases,

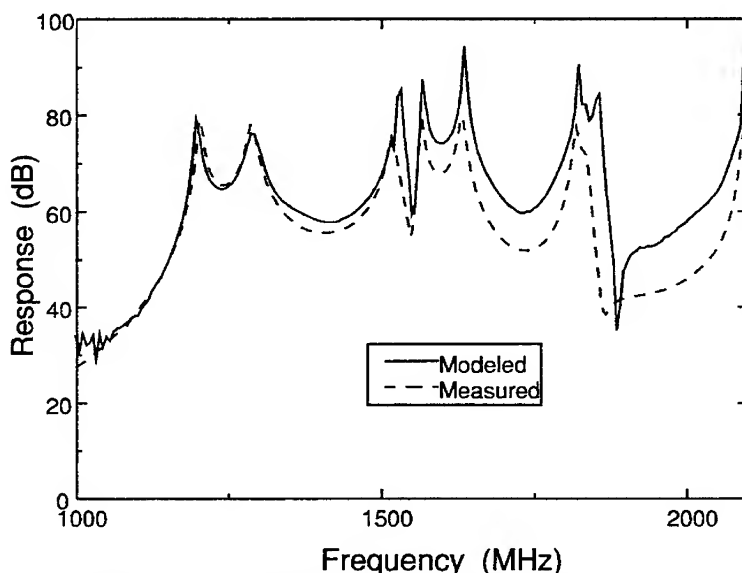


Figure 2 Plot of Measured and Modeled Data for a Realistic Enclosure.

the remaining Q's are lower in the FDTD model than in the measured box. It is possible that improved modeling of the receive antenna and its loading effects on the cavity response would improve the modeled Q's. It is probable however that much of the difference between the modeled and measured Q's is the result of the nonuniformity of the effective conductivity in the seams. Four hours of CPU time were required to generate the modeled data of Figure 2.

Acknowledgements

The authors would like to thank Dr. Raymond Luebbers of The Pennsylvania State University for providing the FDTD code used in this study, as well as for his helpful comments and suggestions. The authors would also like to thank Mr. Rich Mellitz of Digital Equipment Corporation, who collected the measured data presented in this paper.

References

- [1] K.S.Kunz, D.J. Steich and R.J. Luebbers, "Low Frequency Shielding Effectiveness of a Conducting Shell with a Varying Size Aperture on the Response off an Internal Wire.", Penn State ECE department internal document, p.12.
- [2] K.S. Kunz, and R.J.Luebbers, "*The Finite Difference Time Domain Method For Electromagnetics*," Chapter 2, CRC Press, due to be published Spring 1993.
- [3] C.A. Balanis, *Advanced Engineering Electromagnetics*, Wiley, New York, 1989, pg 209.
- [4] *Op. Cit.*, Balanis, pp. 206-214.
- [5] *Op. Cit.*, K.S.Kunz and R.J. Luebbers, Section 3.5
- [6] Beggs, *et al*, "User's Manual for Three Dimensional FDTD Version C Code for Scattering from Frequency-Independent Dielectric and Magnetic Materials", Electrical and Computer Engineering Department, The Pennsylvania State University, University Park, PA 16802, 16 June 1992, pp. 8-11.
- [7] S. Ramo and J Winnery, "Fields and Waves in Modern Radio", Wiley, New York, 1944, p 381.

A METHOD FOR REDUCING RUN-TIMES OF OUT-OF-CORE FDTD PROBLEMS

J. Raley Marek and Jeff MacGillivray
Computational Electromagnetics Group
Phillips Lab/WSR
Kirtland AFB, NM 87117-5776

ABSTRACT

This study investigates a simple method for reducing the run-times of Finite-Difference Time-Domain (FDTD) models that are larger than a computer's main memory. To operate on the entire model, portions of the problem must be swapped (paged) to and from disk. This method reduces the amount of swapping (input/output) that is required by advancing time more than just one step for certain portions of the problem in main memory. This time advance can take place in one, two, or three dimensions, with corresponding software control complexity. Actual results are obtained and compared to in-core, single step swapping, and predicted times. Whereas a standard swapping technique with single step time advance can increase run-time by a factor of ten, a one-dimensional time advance technique applied to the same problem increases run-time by a factor of less than 1.1.

I. Study Definition

The objective of this study was to speed up FDTD run-times for large problems where the problem space is larger than the core memory of the computer solving the problem. This paper presents a method for slicing up an FDTD problem and operating on these slices in such a way that time is advanced for more than just a single time step while the slices reside in memory. This method is referred to as a time advance or slicing method. Results are based on predictions and FDTD code run-time measurements. For the purposes of this study, run-time is defined as total clock time to run a FDTD problem for a specified number of time steps, Input/Output (I/O) time is the clock time spent reading and/or writing to disk for the same problem, and calculation time is that part of run-time that is not I/O time.

II. Problem Background

The memory storage required for the FDTD method scales on the order of the cube of the electrical length (in terms of the shortest wavelength present in the problem) of the object to be modeled. For electrically large problems, one cannot fit the data arrays of the entire problem in main memory and must resort to storing some portion of them on mass storage. In the FDTD method, one might typically swap into main memory a portion of the problem that is on disk, advance its fields by a time step, then swap it back out and bring in the next portion[1]. The time to move data to and from disk, however, is often much more than that required for the computations alone. A FDTD problem which must swap to disk may run from 5-10 times longer than one that does not.

The basis of the time advance algorithm is the computational concept called principle of locality[2]. The principle of locality simply states that all programs tend to use certain portions of memory more than others. Computer architects attempt to take advantage of this principle by designing computers with a hierarchy of memory. Small amounts of fast (expensive) memory are available for data the program requires the most, and large amounts of slower (cheap) memory are available for the rest. This hierarchy runs the spectrum from CPU registers and high-speed cache to hard disk and tape archive. The time advance algorithm takes advantage of the principle of locality and the hierarchy of memory by advancing FDTD several time steps while data is in main memory, before swapping it to disk.

III. The Method

As stated earlier, the time advance method iterates on cell data residing in core for more than just one time step before writing the data to disk. This method makes use of the fact that information in the FDTD method travels no faster than one cell per time step and that the speed of light is the information speed divided by root 3. Since we retreat from the boundary at the information speed, no information is lost, and causality is not violated. This comes about from the stability criterion which states (for square cells) [3]:

$$c\Delta t \leq \frac{\Delta x}{\sqrt{3}} \quad (1)$$

This equation is used to select Δt for computations. It also shows that for any time step Δt , light can, at most, travel only $1/\sqrt{3}$ of a cell. Therefore, by retreating by a cell every time step, the time boundary moves faster than the speed of light. This, however, is not enough. The coupled, explicit E and H equations show that

numerical information can travel one-half cell every one-half time step. Fortunately, by retreating one-half cell every one-half time step, the method keeps pace with this numerical speed as well.

Initially, as much of the mesh is read into core as is possible. Note that the problem extent is truncated in only one dimension, whereas the other two are preserved. That is, if one wishes to slice in z , the x and y dimensions of the problem are the same as the x and y dimensions of the data in core. Since we are starting with H at time step .5 and E at time step 0, we update all of the E values. This brings them all to time step 1. All interior H 's are updated to 1.5. Next we retreat in the z direction one cell and all E 's except the first layer on the slice boundary are updated. All H 's interior to these updated E 's are updated. We retreat again in the z direction and calculate as before. This continues until we have retreated back to the $z=0$ boundary. What is left is a staircase in time of all the slices, as shown in Figure 1. (Only E field times are shown.) If n is the number of slices, the first slice of E is at time step 1 and the last slice of E is at time step n . (In the case of a Mur radiation boundary at $z=0$, the last 2 slices are at time step $n-1$ since the boundary cannot advance ahead of the slice of cells interior to it.[4]) The $z=0$ slice is written to disk and the $z=n+1$ slice

is read from the disk (Figure 2). Even though the slice written is on the opposite side as the slice read, with some extra coding we contain and keep track of all of the slices in a single data structure that uses the entire core. The read slice is updated to time step one. The next slice (at time step one) is advanced to time step two. This continues until the last slice is advanced to time step n (Figure 3). This slice is written to disk and a new slice is read (Figure 4). The new slice is update to 1, the next to 2, the next to 3, ... and the last to n . Therefore, as the problem moves through this window of core slice by slice, it enters at time step 0

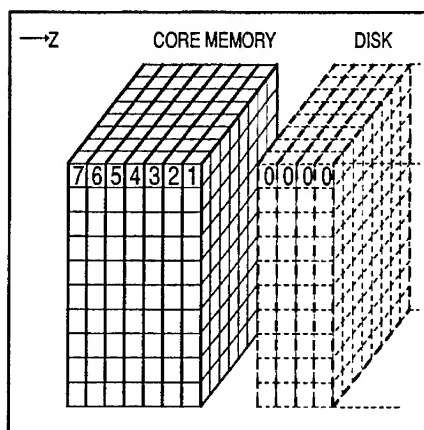


Figure 1

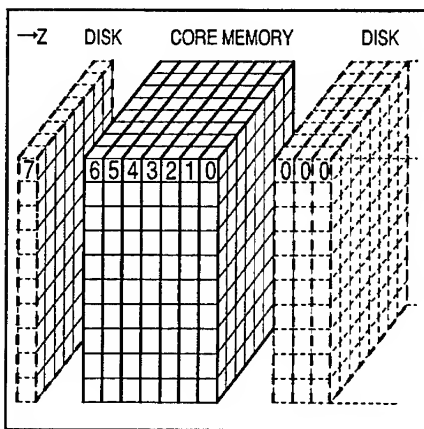


Figure 2

and exits at time step n . When the end of the problem is reached, the entire problem in core is brought to time step n . Therefore with one pass through the entire mesh, the method requires less than one full read and one full write of the mesh to bring the problem to time step n . The process is started again, this time progressing in the reverse direction (because we already have the last core-load of the problem in memory). Note that during this entire process, every slice is within one time step of its neighbors.

Contrast to this is the traditional out-of-core technique which reads in a core-load of the problem, updates the core part by one time step, writes this to disk and then reads in the next core-load. As the problem passes through this window of core, it enters at one time step and exits at the next time step [1]. This new time advance method advances time a factor of $n-1$ more than the traditional technique for each pass of the problem through core. This manifests itself as a $n-1$ factor of reduction of the amount of Input/Output (I/O) to and from disk. This method has no substantial effect on the actual computation time, but can reduce the I/O time significantly, perhaps to the point that it is cheaper to run some problems out-of-core on existing machines, rather than purchase larger computers to perform the computation.

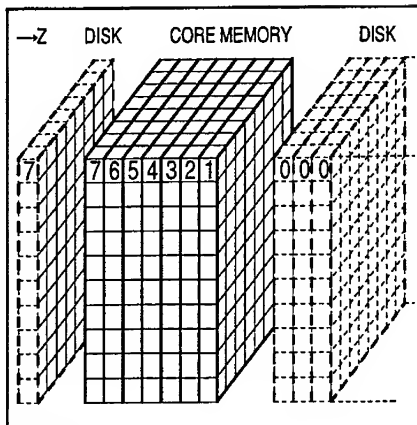


Figure 3

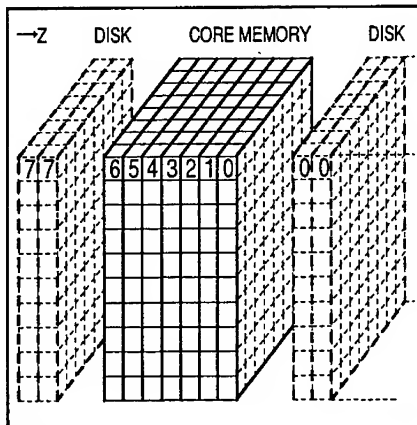


Figure 4

IV. Results

A prediction code was written to estimate the run times of very large out-of-core problems using the one-dimensional and two-dimensional time advance methods. The code was developed to predict how much time savings could be achieved by implementing the time advance methods. The code uses the computer FLOPS (Floating Point Operations per Second) rating, number of cells, number of

time steps desired, and number of operations per cell to predict the computation time. It then employs the mesh dimensions and core memory size to determine how many slices can fit into the core memory and thus how many time steps the mesh can be advanced for one mesh pass. Once the number of mesh passes for solving the problem is determined, the code calculates the I/O time by considering the computer I/O speed (obtained experimentally) and number of bytes to swap between the hard disk and core memory. The prediction time code also makes coarse run-time estimates for massively parallel computers, but the accuracy of this feature has not been verified.

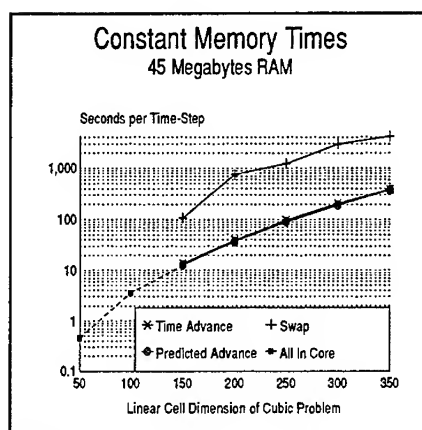


Figure 5

The results using the standard swap method, the one-dimensional time advance method, and the prediction time advance code are shown in Figure 5 and Figure 6. The problem tested was an existing Transverse Electric (TE) perfectly conducting cylinder problem (a brief note on this later). The two dimensions are the orthogonal radii of the cylinder (x and y), the third dimension being the axis (z) of the cylinder. The core memory size was simulated by controlling the number of slices in main memory. All times were obtained on Sun SPARC II and SPARC IPX workstations (each with 64-96 Mbytes of RAM) storing data on external SCSI hard drives. All cases were compiled with the "-fast" option of the Sun FORTRAN compiler and real numbers were calculated with single precision. Calculated field results for the various methods for each problem size agreed to within the limits of the accuracy of the computer. Some of the variances in the data may be attributable to times obtained on different machines.

In Figure 5, the core memory size is held constant while the mesh size is increased. The last five sets of points show predicted times, slice times and swap times. (Corresponding number of slices is 100, 56, 36, 25, 18). The swap times are consistently an order of magnitude greater than the slice times for this range of problem size. The accuracy of the predictions is revealed in this figure, as well. Surprisingly, the first slice point and the last in-core point (150 cells) nearly coincide. (The slice time is about 11% greater, showing that, for this case, the I/O time has been reduced from a dominant run-time contributor to a relatively minor one). The swap technique was not optimized, otherwise its curve would eventually join the slice/in-core curve at the lower mesh sizes. (Our results appear to show this downward trend.) Although not tested, we would expect the in-core curve to

continue on below the slice curve as the mesh size increases. We would also expect the slicing curve to eventually join to the swap curve at the large mesh slices (i.e., the number of slices in the core approaches one).

In Figure 6, the mesh size is held constant while the core memory (slices) is increased. Corresponding memory sizes are 5, 10, 20, 40, 60, and 80 Mbytes. This results in a gradual speedup since more slices can be stored in main memory. Note that, as the number of slices approaches one, the slice technique reduces to a standard swap technique.

But just sixteen slices offers a factor of ten reduction in run-time. The upward trend toward larger memory sizes was unexpected (note the predictions) and affects both cases. (We suspect that this may be due to the approaching physical main memory limit on our workstations. As the limit is approached, the operating system may start swapping out pages of memory and increasing run-times, something we were specifically trying to avoid!) The greatest speedup is sixteen times faster than the standard swapping method (the fifth point in Figure 6). In this case a user would wait roughly ten hours for a wave to travel across the length of the mesh as opposed to more than one week days using standard swapping.

The time advance method works almost as if the hard disk were merely an extension of the main memory. In many cases, the I/O time for out of core problems is much less than the computation time. (NOTE: these results underestimate the total run-time of a general problem since the problem solved a pure TE cylinder inscribed in the problem space. The interior fields are in free space, there is no axial E field component, the walls are perfectly conducting, and the fields are updated in the inside only. Therefore, calculation time is lower than in a full featured FDTD code. However, the amount of I/O time is the same. This means that the percentage increase in total time for a slice versus in-core technique will be reduced from that reported here. This is the important result.)

V. Future Work

As problems grow much larger than core memory, the one dimensional time advance technique becomes more ineffective at reducing the run-time over swapping, since fewer slices can be accommodated and I/O time savings decrease.

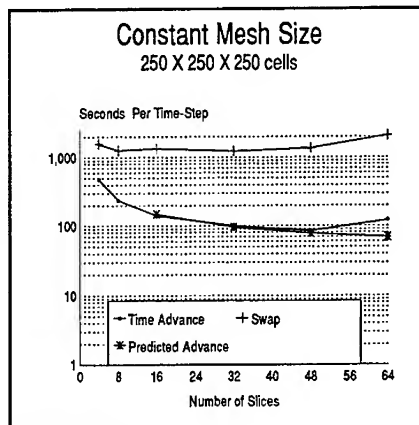


Figure 6

Current work involves two and three dimensional time advance techniques, which advance time in two and three dimensions respectively. These techniques allow for a greater number of time advances for a given amount of memory (for the three dimensional case, the number of advances increases as the cube root of memory size, i.e. it is problem size and geometry independent). Preliminary results show that although they live up to predictions, usefulness may be an issue. Computers can typically be obtained with enough RAM to keep them busy for hours on a full core FDTD problem. Just the computations alone for problems that are much greater than the core memory size tend to push run-times beyond the reasonable range. The algorithms themselves are also much more complicated. Therefore, it may be possible that a need for these higher dimension time advance algorithms (especially the 3D method) may never materialize.

Work is also progressing on implementing this method on an out-of-core large object FDTD solver for a parallel supercomputer. Given the fact that massively parallel supercomputers tend to have a higher ratio of (reported) computational power to I/O bandwidth than workstations, as well as less memory per CPU, we believe that this method will be useful for computations on these architectures. The 1-D method appears to map well to mesh connected architectures, while the 2-D method seems best suited for a linearly connected architecture. With these geometries, the nodes are uniformly load balanced.

The simplicity of this method suggests that it might be easily applied to other computational modeling problems besides FDTD, especially those which are traditional finite-difference type problems (particle-in-cell, seismic modeling, heat transfer in solids, etc).

VI. Conclusions

This paper demonstrates that a one-dimensional time advance technique for FDTD problem can reduce run-times for out-of-core problems by a factor of three (with four slices) to ten (with more than eighteen slices) depending on problem size and computer resources. Run-times for out-of-core problems increase as little as 10% over the same in core problem.

ACKNOWLEDGEMENTS

The authors wish to thank Professor Karl Kunz of The Pennsylvania State University for his expertise and guidance, as well as Dr. C. Y. Pan of The Utah State University for his enthusiasm and support.

REFERENCES

1. Holland, Richard, Larry Simpson and R.H. St. John. "Code Optimization

for Solving Large 3-D EMP Problems," *IEEE Transactions on Nuclear Science*, 26: 4964-4969 (December 1983).

2. Hennessey, John L. and David A. Patterson. *Computer Architecture -- A Quantitative Approach*. San Mateo, California: Morgan Kaufmann Publishers, Inc., 1990.
3. Taflov, Allen and Morris E. Brodwin. "Numerical Solution of Steady-State Electromagnetic Scattering Problems Using the Time-Dependent Maxwell's Equations," *IEEE Transactions on Microwave Theory and Techniques*, 23: 623-630 (August 1975).
4. Mur, Gerrit. "Absorbing Boundary Conditions for the Finite-Difference Approximation of the Time-Domain Electromagnetic-Field Equations," *IEEE Transactions on Electromagnetic Compatibility*, 33: 377-382 (November 1991).

INVESTIGATION OF THE USE OF CHIMERA FOR SOLVING MAXWELL'S EQUATIONS FOR ELECTROMAGNETIC PROPAGATION IN THE TIME DOMAIN[†]

M. D. White and J. J. Chattot
Department of Mechanical, Aeronautical, and Materials Engineering
University of California, Davis
Davis, Ca. 95616

Abstract

As simulations become more geometrically complex, defining a grid around the individual surfaces becomes a problem. Complex geometries can be gridded using either a structured or unstructured approach. While creating an unstructured grid is relatively simple, there is a large increase in both memory storage and computing efficiency compared to the structured approach. Structured grids tend to be more difficult to generate for either complex geometries or multiple bodies and can have problems with monotonicity in the grid mapping. One way to alleviate this problem is to use the Chimera approach. With Chimera, complex geometries are broken up into simpler geometries and overlapping or overset grids are generated with information being interpolated from one grid to another. Overset grids are grids which lie completely within another grid. These underlying grids must have a hole cut in the grid so that information may be interpolated from the overset grid back to the underlying grid.

The application of Chimera techniques to the problem of solving Maxwell's Equations using a finite difference-time domain method is investigated. The scheme used is the Ni scheme, first proposed by Ron Ho Ni as a finite volume scheme but which can also be viewed as a finite difference scheme à la Lax-Wendroff. Errors caused by applying Chimera to the situation of waves propagating on two rectangular meshes with the smaller of the two overset on the larger and having translational and rotational freedom are considered. The convergence of the scheme is found to be second order with grid refinement if the analytical (exact theoretical) function and its first derivative are continuous. If the first derivative of the analytical function is not continuous, it is found that second order accuracy is not insured. The next case of a scatterer is presented using Chimera and comparing to a single uniform grid. All results are for the case of 2-D transverse magnetic (TM) waves.

Introduction

Recently, CFD methods are being increasingly applied to solving Maxwell's Equations with complex geometries in which a uniform Cartesian mesh becomes undesirable [i.e. 1,2]. One often wishes to use body-fitted coordinate systems which is fine if there is a single body. For multiple bodies, the grids must either be manipulated so that the two grids match or data must be interpolated back and forth on overset grids (Chimera). The

[†] Funds for the support of this study have been allocated by the NASA-Ames Research Center, Moffett Field, California, under Interchange No. NCA2-572.

issues behind applying this method to Maxwell's Equations has recently been introduced for both the Yee scheme[3] by K. S. Yee, et. al. [4] and with a finite-volume / finite-difference scheme (the Ni Scheme [5,6]) by the present authors[7]. The effect that overset grids has on the propagation of electromagnetic waves will be discussed with a simple application.

The first problem investigated here consists of two rectangular grids, one overset on the other, and a TM wave passing through the domain. The computational plane is divided into a total field zone (TFZ) and a scattered field zone (SFZ). The TFZ formulation was chosen for the comparison of Chimera results. The second problem is a comparison of the scattering of a circular cylinder using a body fitted mesh around the cylinder and a Cartesian mesh in the far field.

Maxwell's Equations:

Maxwell's equations are given by:

$$\mathbf{E}_t = \nabla \times \mathbf{H} - \mathbf{J}, \quad \mathbf{H}_t = -\nabla \times \mathbf{E} \quad \text{and} \quad \nabla \cdot \mathbf{E} = \rho, \quad \nabla \cdot \mathbf{H} = 0$$

with the normalization of $\mu_0 = \epsilon_0 = c = 1$, and $\mathbf{B} = \mu_0 \mathbf{H}$ and $\mathbf{D} = \epsilon_0 \mathbf{E}$. For the TM case the vectors are $\mathbf{E} = (0, 0, E_z)$ and $\mathbf{H} = (H_x, H_y, 0)$ and in free space $\mathbf{J} = 0$ and $\rho = 0$. The latter situation allows the two divergence conditions to be derived from the time dependent equations.

Computational Scheme

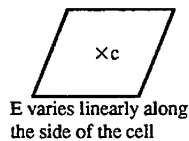
The scheme developed by Ni [5], solves the derivatives inside cells surrounded by four nodes and then distributes those values to the nodes. While Ni developed this scheme as a finite volume scheme, it is identical to solving an explicit box scheme, with higher derivatives summed up in the method of Lax-Wendroff[6].

$$E_i^{n+1} = E_i^n + \Delta t (\partial E / \partial t)_i^n + \Delta t^2 / 2 (\partial^2 E / \partial t^2)_i^n + \dots$$

The derivatives in a cell are obtained by assuming that the nodal functions vary linearly along the sides and that the derivatives are constant in the cells. Thus:

$$\iint (\partial E / \partial x) dx dy \approx (\partial E / \partial x)_c \iint dx dy$$

$$\iint (\partial E / \partial y) dx dy \approx (\partial E / \partial y)_c \iint dx dy$$



and applying the divergence theorem, one obtains:

$$\begin{aligned} \iint (\partial E / \partial x) dx dy &= \oint (E, 0) \cdot \hat{n} \, dl \Rightarrow (\partial E / \partial x)_c \approx \oint (E, 0) \cdot \hat{n} \, dl / \iint dx dy \\ \iint (\partial E / \partial y) dx dy &= \oint (0, E) \cdot \hat{n} \, dl \Rightarrow (\partial E / \partial y)_c \approx \oint (0, E) \cdot \hat{n} \, dl / \iint dx dy \end{aligned}$$

The line integrals around the perimeter of the cell are obtained by determining the outward normal of the control cell sides and using the trapezoidal rule to evaluate the line integrals. Now the first derivatives are distributed to the nodes based on the fraction of the area of the control volume intersecting the area of the control cell (see fig. 1). Thus:

$$Ex_{j,k} = \frac{1}{4} (Ex_{cell1} + Ex_{cell2} + Ex_{cell3} + Ex_{cell4}).$$

To cancel the second time derivative contribution, the first time derivatives are differenced in the same manner as before and is distributed to the node surrounded by the first time derivatives. Thus, for example for the E field:

$$\left(\frac{\partial E^z}{\partial t} \right)_c = \left(\frac{\partial H^y}{\partial x} \right)_c - \left(\frac{\partial H^x}{\partial y} \right)_c \quad \& \quad \left(\frac{\partial^2 E^z}{\partial t^2} \right)_n = \left(\frac{\partial H^y / \partial t}{\partial x} \right)_n - \left(\frac{\partial H^x / \partial t}{\partial y} \right)_n$$

where the subscript c indicates that the quantity is evaluated at the center of a cell as mentioned previously, and the subscript n indicated that the quantity is evaluated at the nodes surrounded by the four centers of the neighboring cells.

In generalized coordinates the cells are mapped onto local coordinates of the cell volume and the derivatives are determined using the chain rule;

$$\left(\partial H^y / \partial x \right)_c = \left(\frac{\partial \xi}{\partial x} \right)_c \left(\partial H^y / \partial \xi \right)_c + \left(\frac{\partial \eta}{\partial x} \right)_c \left(\partial H^y / \partial \eta \right)_c$$

and then distributed to the nodes as before. The stability of the scheme is found by Ni to have a CFL condition of $\Delta t = \min(\Delta x, \Delta y)$ [5].

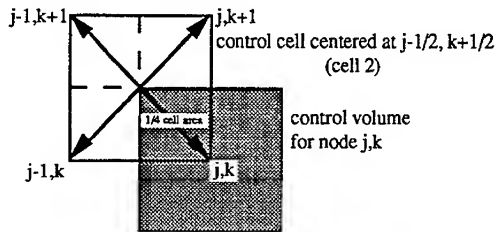


Figure 1: Distribution of derivatives from the center of the control cell to the surrounding nodes.

Chimera

Chimera typically consists of two or more grids either overlapping or one grid wholly on another[8]. In the latter case, a hole must be cut in the primary grid to allow the information to travel between both grids[8]. The interpolation used was second order and achieved by assuming a bilinear variation of the values in a given cell volume. Thus, for a given field variable, it is assumed that in the cell:

$$F_{cell} = a + b\xi + c\eta + d\xi\eta$$

with the four field values at the nodal points of the cell, $F_i(\xi, \eta)$, forming a unit square. It is sometimes necessary to determine the precise values of ξ and η . In this case ξ, η are found using Newton's method in two dimensions (with the initial guess in the middle of the cell: $\xi, \eta = 0.5, 0.5$) which becomes:

$$\begin{aligned}\xi^{n+1} &= \xi^n + (X_{target} - X(\xi^n, \eta^n)) \left(\frac{\partial \xi}{\partial x} \right)^n + (Y_{target} - Y(\xi^n, \eta^n)) \left(\frac{\partial \xi}{\partial y} \right)^n \\ \eta^{n+1} &= \eta^n + (X_{target} - X(\xi^n, \eta^n)) \left(\frac{\partial \eta}{\partial x} \right)^n + (Y_{target} - Y(\xi^n, \eta^n)) \left(\frac{\partial \eta}{\partial y} \right)^n\end{aligned}$$

where

$$\begin{pmatrix} \partial \xi / \partial x & \partial \xi / \partial y \\ \partial \eta / \partial x & \partial \eta / \partial y \end{pmatrix} = \frac{1}{Det} \begin{pmatrix} \partial y / \partial \eta & -\partial x / \partial \eta \\ -\partial y / \partial \xi & \partial x / \partial \xi \end{pmatrix}.$$

This method usually converges in one or two iterations.

The first set of test cases for applying Chimera were simple ones consisting of two grids overset on top of one another with no scatterer (figure 2a). The reason that these test cases were chosen was to provide the simplest possible case in which a wave is propagated to see what the effect of the interfaces is.

The first test case consisted of two rectangular grids with a lower (primary) grid of 31x31 points having a hole that was 9x9 points and a secondary, overset grid with 11x11 points. The errors in propagation were determined for the two grids and the norm 1 errors were recorded as both grids were refined by a factor of two. The error involved in both the discretization and the interpolation is formally second order accurate by Taylor series expansions. In verifying this, the three tests from the second test case were rerun calculating the norm 1 error each time as the grid was refined by a factor of two. The norm 1 error is defined as:

$$N1_{err} = \frac{1}{N} \sum_{ij} |u_{ij} - u_{exact}|$$

A plot of $\ln(err)$ verses $\ln(\Delta)$ where $\Delta = \Delta x_1 = \Delta y_1$ will result in a slope that is roughly equal to the order of accuracy.

At first, the wave ($\sin k(x-t)$) was propagated halfway into the domain and the slopes were determined. The results showed a wide range of slopes ranging from just over one to around two. If the wave was allowed to pass clear through the field, however, the slopes were consistently around two (with the exception of the 45° case on grid two which has a slope around 1.2 for the H^x field). These results were confusing as the Taylor series expansions showed that the convergence should be second order regardless of how far in the wave had propagated. It was believed that the culprit might be the fact that while the incoming wave was continuous everywhere, its first derivative was discontinuous at the leading edge (i.e. $E = E_0 \sin k(x-t)$ if $x \leq t$ and $E = 0$ if $x \geq t$). To check this, the incoming wave was given a bias so that both the function and the first derivative would be continuous everywhere (i.e. $E = [E_0 \cos k(x-t) - 1]$ if $x \leq t$ and $E = 0$ if $x \geq t$). This wave was then allowed to propagate halfway into the domain and indeed the slopes all showed that the solution was converging quadratically (see figure 3).

Based on these results we ran the case of the circular cylinder with a body-fitted mesh in a uniform Cartesian grid and compared the solution to the same case with a single body fitted mesh. In both cases, the cylinder had a diameter of 1. and 150 points around the body. The initial Δr was calculated from $.5 * \sin(\Delta\theta)$ (≈ 0.021) and was stretched by 2% in the radial direction. The single mesh case had 75 points in the radial direction and its outer boundary was just beyond a radius of 2 from the center of the cylinder. The total field zone (TFZ) was located seven points from the body. The Chimera test had the same parameters for the body fitted mesh but only 6 points in the radial direction (with the seventh being interpolated from the Cartesian mesh) and the TFZ was on the Cartesian mesh more than 20 points from the body. The primary grid in the Chimera run had 191×191 points in a domain of ± 2 in both X and Y. This roughly corresponds to the 75 points in the radial direction in the previous case and gives a CFL condition on the Cartesian grid of ≈ 0.995 . All points on the lower mesh with a radius less than the 4th radial point were initially blanked out but a few were added back in based on the number and position of nodes around them. The surface current and scattered field contour plots are given in figures 4 and 5 respectively. Both cases match well with the exact solution of the surface current. Looking at the contour plots it is difficult to tell where the Chimera overlap is.

Conclusions

These preliminary results show that application of Chimera to solving Maxwell's Equations is promising. A second order interpolation seems to be enough to ensure second order convergence, and even when there is excess error from a discontinuous derivative in the wave front, that error tends to propagate out of the domain. The solution of the cylindrical scatterer shows that good results can be obtained without too much effort; however,

errors involved with the interpolation coupled with small CFL conditions, grid stretching or large difference in CFL numbers between grids still need to be examined more thoroughly.

Acknowledgments: The authors would like to acknowledge the help of the late Joseph L. Steger, whose discussions and insight into the workings of Chimera and grid generation made the work so much easier.

References

- [1] Fusco, M., "FDTD Algorithm in Curvilinear Coordinates," *IEEE Trans. on Antennas and Propagat.*, 1990 Jan, V38 N1:76-89.
- [2] V. Shankar, W. F. Hall, and A. H. Mohammadian, "A Time-Domain Differential Solver for Electromagnetic Scattering Problems," W.R. Stone (Ed.), IEEE Press, 1989, pp.127-139.
- [3] K. S. Yee, "Numerical Solution of Initial Boundary Value Problems Involving Maxwell's Equations in Isotropic Media," *IEEE Trans. on Antennas and Propagat.*, 1966 May, Vol AP-14, pp.302-307.
- [5] Ni, R. H., "A Multiple-Grid Scheme for Solving the Euler Equations", AIAA Paper 81-1025 (also: *AIAA Journal*, 20 1565-1571, 1982).
- [6] Chattot, J. J., "Box Schemes for First Order Partial Differential Equations," (NASA report, unpublished), 1991.
- [7] M. D. White, JJ Chattot, "Investigation of the use of a Finite-Volume Scheme with Edge Singularities and Application of Chimera for Electromagnetic Propagation in the Time Domain," (NASA progress report, unpublished), Oct. 1992.
- [8] J. L. Steger, "Studies of the Chimera Method of Flow Simulation", unpublished.

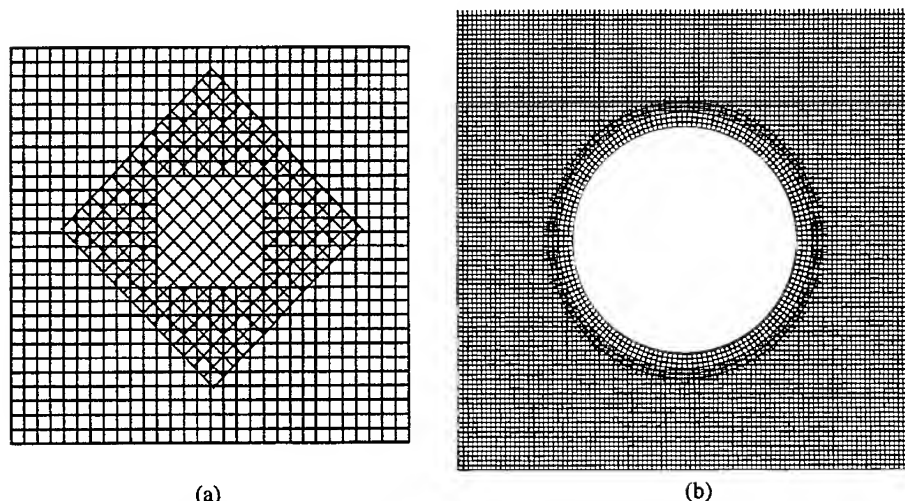


Figure 2: (a) Mesh for wave passing through two grids. (b) Cylindrical mesh overset on a Cartesian mesh for the circular scatterer.

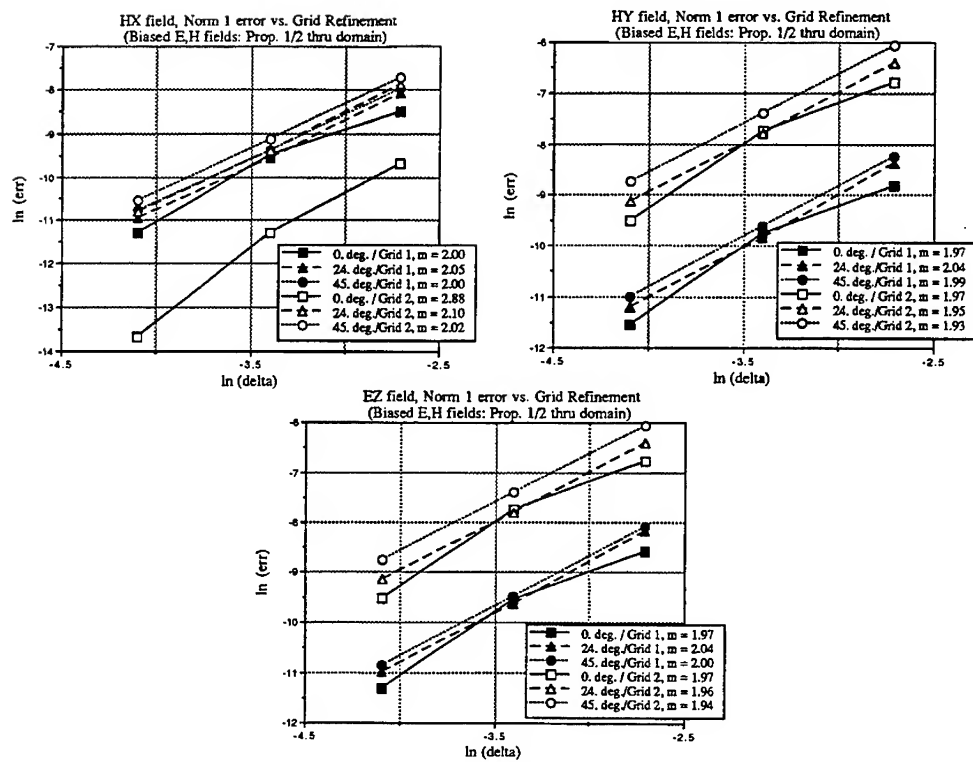


Figure 3: Convergence plots for a (cosine - 1) wave when passed half-way into the domain.

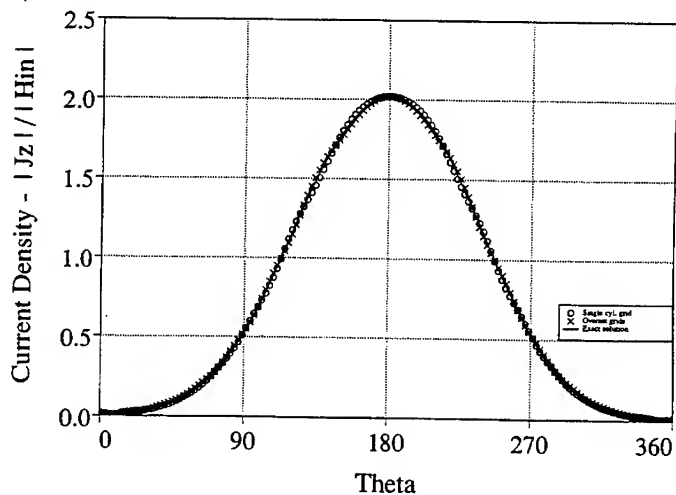


Figure 4: Surface current of a circular cylinder (diameter = 1) with a incident plane wave with wavelength $= \pi/7$.

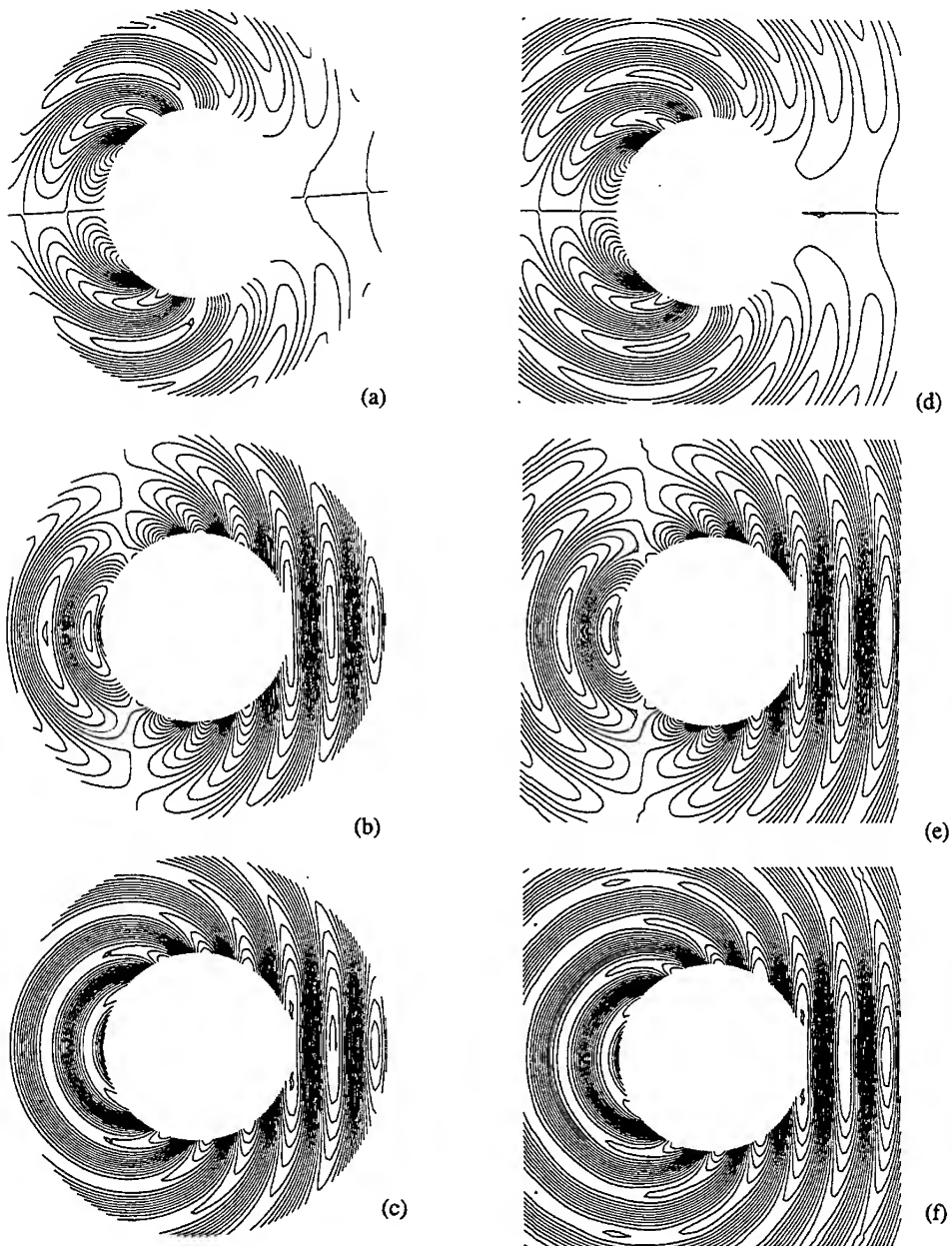


Figure 5: Scattered field contours from the cylinder: (a), (b), (c) are H_x field, H_y field, and E_z field, single grid; (d), (e), (f) are H_x field, H_y field, and E_z field, Chimera; respectively.

RADAR-CROSS-SECTION AND AERODYNAMIC-FORCE CALCULATIONS USING FINITE-DIFFERENCE METHODS

H. Vinh *, C. P. van Dam **, H. A. Dwyer ***
Department of Mechanical, Aeronautical and Materials Engineering
University of California
Davis, CA 95616

ABSTRACT

The use of finite-difference methods to analyze the aerodynamic efficiency and observability of two-dimensional configurations is described and several examples are presented to demonstrate the capability of these numerical analysis techniques.

INTRODUCTION

Since the early days of aviation, shaping for good aerodynamic characteristics has been an integral part of aircraft design. However, with the introduction of aircraft such as the F-117A and the B-2, it is clear that low observability is also rapidly becoming an important criterion in the design of new aircraft. Thus, today the designer is not only faced with shaping for maximum aerodynamic efficiency but also with shaping for low radar cross section (RCS) which is most influenced by the shape of the aircraft. This type of multidisciplinary design requires accurate analysis of the aerodynamic and RCS characteristics of the entire aircraft. In this paper, the use of finite-difference methods to analyze the aerodynamic and RCS characteristics of two-dimensional configurations is described. The RCS of a configuration is determined from the Computational Electromagnetics (CEM) solution of the time-domain Maxwell's equations while its lift and drag are found from the Computational Fluid Dynamics (CFD) solution of the full-potential equations. The two sets of governing equations are transformed to generalized curvilinear coordinates and solved on body-conforming grids using proven finite-difference methods. The resulting RCS and lift/drag characteristics determine the observability and aerodynamic efficiency of a given configuration. A selection between several different configurations can then be made or the shape of the configuration can be modified accordingly to obtain the desired aerodynamic and RCS characteristics. The aerodynamic and RCS analysis methods described in the following sections provide the basic elements of a multidisciplinary design technique for aerodynamic configurations being developed at UC Davis.

AERODYNAMIC ANALYSIS

The aerodynamic analysis is based on the finite-difference solution of the inviscid, irrotational, full-potential equations. The full-potential formulation is chosen over the more general Euler formulation because the full-potential equations give accurate prediction of wave drag at low transonic Mach number [1] and, more importantly, methods based on the full-potential equations are much faster in terms of CPU time required to obtain a fully converged solution than methods based on the Euler equations [2]. Numerous numerical methods have been developed for solving the full-potential equations. Since these methods are described extensively in the literature, only a general description of one of the methods is presented here.

In two dimensions, the full-potential equations in Cartesian coordinates can be written in conservation form:

$$(\rho\phi_x)_x + (\rho\phi_y)_y = 0 \quad (1)$$

$$\rho = \left[1 - \frac{\gamma-1}{2} M_\infty^2 (u^2 + v^2) \right]^{\frac{1}{\gamma-1}} \quad (2)$$

* Research Assistant
** Associate Professor
*** Professor

where

$$u = \phi_x \quad \text{and} \quad v = \phi_y$$

Here ϕ is the velocity potential, ρ is the fluid density, u and v are the respective x and y velocity components, and γ is the specific heat ratio. In this formulation, the density and the velocity components are nondimensionalized by the freestream values. Equations (1) and (2) are solved subject to the tangency condition $\phi_n = 0$ at the body. In the present algorithm, Eqs. (1) and (2) are transformed to the generalized curvilinear coordinate system and discretized using second-order accurate central differences. The resulting system of equations is solved iteratively using the conventional successive-line-over-relaxation (SLOR) method [3]. Artificial viscosity is added in the supersonic region by upwinding the density as suggested by Holst and Ballhaus [4]. The pressure distribution across the aerodynamic configuration is computed using the isentropic-flow equations. The lift and drag are calculated by integrating the surface pressure.

RCS ANALYSIS

The RCS analysis is based on the time-domain solution of the Maxwell's equations obtained using the Lax-Wendroff scheme which was developed for CFD and is now being applied to CEM [5, 6, 7]. The time-domain Maxwell's equations governing the propagation of electromagnetic wave in free space are:

$$\begin{aligned} 1. \text{ Gauss' electric law: } & \vec{\nabla} \cdot \vec{E} = 0 & (3) \\ 2. \text{ Gauss' magnetic law: } & \vec{\nabla} \cdot \vec{H} = 0 & (4) \\ 3. \text{ Ampere's law: } & \epsilon_0 \vec{E}_t - \vec{\nabla} \times \vec{H} = 0 & (5) \\ 4. \text{ Faraday's law: } & \mu_0 \vec{H}_t + \vec{\nabla} \times \vec{E} = 0 & (6) \end{aligned}$$

where \vec{E} and \vec{H} are the electric and magnetic field intensities, respectively, and ϵ_0 and μ_0 are the respective permittivity and permeability coefficients in free space. For the purpose of simulating electromagnetic scattering, the last two equations representing Ampere's and Faraday's laws are solved. These two equations are transformed to the generalized curvilinear coordinate system and solved on body-conforming grids.

In two dimensions, the Maxwell's equations decouple into the transverse-magnetic (TM) and transverse-electric (TE) modes. In this paper only the TM mode is considered. The corresponding Maxwell's equations in Cartesian coordinates can be written in conservation form:

$$\bar{Q}_t + \bar{F}_x + \bar{G}_y = 0 \quad (7)$$

where

$$\bar{Q} = \begin{bmatrix} \epsilon_0 E^z \\ \mu_0 H^x \\ \mu_0 H^y \end{bmatrix} \quad \bar{F} = \begin{bmatrix} -H^y \\ 0 \\ -E^z \end{bmatrix} \quad \bar{G} = \begin{bmatrix} H^x \\ E^z \\ 0 \end{bmatrix}$$

Equation (7) comprises a system of hyperbolic equations which can be marched in time. As a result of the transformation from the Cartesian coordinate system to the generalized curvilinear coordinate system where $\xi = \xi(x, y)$ and $\eta = \eta(x, y)$, Eq. (7) takes the following form:

$$Q_t + F_\xi + G_\eta = 0 \quad (8)$$

where

$$Q = \frac{1}{J} \begin{bmatrix} \epsilon_0 E^z \\ \mu_0 H^x \\ \mu_0 H^y \end{bmatrix} \quad F = \frac{1}{J} \begin{bmatrix} \xi_y H^x - \xi_x H^y \\ \xi_y E^z \\ -\xi_x E^z \end{bmatrix} \quad G = \frac{1}{J} \begin{bmatrix} \eta_y H^x - \eta_x H^y \\ \eta_y E^z \\ -\eta_x E^z \end{bmatrix}$$

Here $J = \xi_x \eta_y - \xi_y \eta_x$ is the Jacobian of the coordinate transformation. The vectors F and G in Eq. [8] can be expressed as functions of Q :

$$\begin{aligned} F &= AQ \\ G &= BQ \end{aligned} \quad \begin{aligned} (9) \\ (10) \end{aligned}$$

where

$$A = \begin{bmatrix} 0 & \frac{\xi_y}{\mu_o} & -\frac{\xi_x}{\mu_o} \\ \frac{\xi_y}{\epsilon_o} & 0 & 0 \\ -\frac{\xi_x}{\epsilon_o} & 0 & 0 \end{bmatrix} \quad \text{and} \quad B = \begin{bmatrix} 0 & \frac{\eta_y}{\mu_o} & -\frac{\eta_x}{\mu_o} \\ \frac{\eta_y}{\epsilon_o} & 0 & 0 \\ -\frac{\eta_x}{\epsilon_o} & 0 & 0 \end{bmatrix}$$

Equation (8) is solved numerically using the Lax-Wendroff scheme [8]. This explicit scheme is computationally efficient and is generally less dispersive than implicit schemes. In addition, it is easily extendible to multidimensions.

Lax-Wendroff scheme

The Lax-Wendroff scheme is an explicit scheme widely used in CFD. It is second-order accurate in both time and space. For the one-dimensional form of Eq. (7):

$$\bar{Q}_t + \bar{F}_x = 0 \quad (11)$$

where

$$\bar{Q} = \begin{bmatrix} \epsilon_o E^z \\ \mu_o H^y \end{bmatrix} \quad \bar{F} = \bar{A}\bar{Q} = \begin{bmatrix} -H^y \\ -E^z \end{bmatrix} \quad \bar{A} = \begin{bmatrix} 0 & -\frac{1}{\mu_o} \\ -\frac{1}{\epsilon_o} & 0 \end{bmatrix}$$

the Lax-Wendroff scheme is derived starting from the Taylor series expansion:

$$\bar{Q}_i^{n+1} = \bar{Q}_i^n + \Delta t \bar{Q}_t + \frac{\Delta t^2}{2} \bar{Q}_{tt} + O(\Delta t^3) \quad (12)$$

Using Eq. (11), the time derivatives in Eq. (12) are replaced with spatial derivatives:

$$\bar{Q}_t = -\bar{F}_x \quad (13)$$

$$\bar{Q}_{tt} = -\bar{F}_{tx} = -\bar{A}\bar{Q}_{tx} = \bar{A}\bar{F}_{xx} \quad (14)$$

which upon substituting into Eq. (12) give:

$$\bar{Q}_i^{n+1} = \bar{Q}_i^n - \Delta t \bar{F}_x + \frac{\Delta t^2}{2} \bar{A} \bar{F}_{xx} \quad (15)$$

Finally, the Lax-Wendroff algorithm for the one-dimensional Maxwell's equations is obtained by replacing the spatial derivatives in Eq. (15) with central differences:

$$\bar{Q}_i^{n+1} = \bar{Q}_i^n - \Delta t \frac{\bar{F}_{i+1}^n - \bar{F}_{i-1}^n}{2\Delta x} + \frac{\Delta t^2}{2} \bar{A} \frac{\bar{F}_{i+1}^n - 2\bar{F}_i^n + \bar{F}_{i-1}^n}{\Delta x^2} \quad (16)$$

In one dimension, the Lax-Wendroff scheme is numerically stable for $CFL \leq 1$ where CFL is the Courant-Friedrichs-Lewy number [8] defined as $CFL = c_o \Delta t / \Delta x$ where $c_o = 1/\sqrt{\mu_o \epsilon_o}$ is the wave velocity. In multidimensions, Δx is defined as the smallest grid spacing in the computational grid. Therefore, the maximum allowable time step for the Lax-Wendroff scheme, and all explicit schemes in general, is directly dependent on the resolution of the computational grid. In addition, the Lax-Wendroff scheme is both dissipative and dispersive but these numerical errors tend to be small near the stability limit.

In general, the derivation of the Lax-Wendroff scheme for the one-dimensional Maxwell's equations presented here can be extended directly to multidimensions.

Boundary conditions

For perfectly-conducting scatterers, the reflecting boundary condition for the electric and magnetic fields at the body are:

$$\hat{n} \times \vec{E}^t = 0 \quad (17)$$

$$\hat{n} \cdot \vec{H}^t = 0 \quad (18)$$

where \hat{n} is the unit vector normal to the body, \vec{E}^t is the total electric field, and \vec{H}^t is the total magnetic field. Here the total field represents the sum of the incident and the scattered fields. These boundary conditions are enforced using the scattered-field formulation in which the incident field is propagated analytically and only the scattered field is computed.

At the outer boundary, the approximate absorbing boundary condition derived by Mur [9] is imposed to allow the scattered wave to propagate out of the computational domain:

$$\phi_t + c_0 \phi_n = 0 \quad (19)$$

where

$$\phi = \begin{bmatrix} E^z \\ H^x \\ H^y \end{bmatrix}$$

Here η represents the coordinate normal to the outer boundary. Since this is only an approximation of a perfectly absorbing boundary, the outer boundary is placed far away from the scatterer to minimize the effects of any wave reflection.

RESULTS

Code validation

The aerodynamic and RCS analysis algorithms were validated using standard test cases. The test case for the aerodynamic analysis involves transonic flow over the NACA-0012 airfoil at $M_\infty = 0.82$ and $\alpha = 0^\circ$ where M_∞ is the freestream Mach number and α is the angle of attack. Figure 1 shows the partial grid used in the calculation. The grid is relatively coarse with 140x30 points. Figure 2 shows the computed Mach contours and Fig. 3 shows the corresponding pressure coefficient, C_P , on the airfoil surface along with the lift and drag coefficients, C_L and C_D , of the airfoil. These aerodynamic coefficients are defined as:

$$C_P = \frac{2(P - P_\infty)}{\gamma P_\infty M_\infty^2} \quad C_L = \frac{2L}{\gamma P_\infty M_\infty^2 c} \quad C_D = \frac{2D}{\gamma P_\infty M_\infty^2 c}$$

where P is the local static pressure, P_∞ is the ambient static pressure, $\gamma = 1.4$ is the specific heat ratio, c is airfoil chord length normalized to 1, L is the lift force per unit width, and D is the drag force per unit width. Both the lift and the drag coefficients are in good agreement with the Euler results presented in Ref. [3]. Note that the full-potential equations apply to inviscid flow only and, therefore, the computed drag coefficient represents only the wave drag generated by shock waves on the airfoil surface.

The test case for the RCS analysis involves a right-propagating TM plane wave striking a perfectly-conducting, infinite circular cylinder. The cylinder has an electrical size of $ka = 10$ where a is the radius of the cylinder and k is the wave number defined as $k = 2\pi/\lambda$ with λ representing the nondimensionalized wavelength of the incident wave. Figure 4 shows the partial grid used in the calculation. The grid contains 150x75 points with the

outer boundary located at 5λ from the cylinder surface. The corresponding scattered electric field contours are shown in Fig. 5. The computed bistatic RCS of the cylinder is shown in Fig. 6 along with the exact solution [10]. Overall, the numerical results are in excellent agreement with the exact solution.

Effects of airfoil thickness on the aerodynamic efficiency and observability

The first example of airfoil analysis using the CEM and CFD algorithms involves a simple study of the effects of airfoil thickness on the aerodynamic and RCS characteristics of an airfoil. The study was conducted using two NACA-00XX series airfoils where XX represents the ratio of the airfoil maximum thickness to its chord length, t/c . The two airfoils, NACA-0012 and NACA-0024 [11], are shown in Fig. 7. For simplicity, the aerodynamic analysis was done for nonlifting flow, i.e. $\alpha = 0^\circ$ since the airfoils are symmetrical. Therefore, the only variable needed to be examined when comparing the aerodynamic characteristics of the two airfoils is the wave drag. The computational grids used in this part of the analysis all contain 140×30 points. The RCS analysis was done for a right-propagating TM plane wave with a wavelength of $\lambda = 0.25c$. Both airfoils are perfect conductors. The computational grids used in this part of the analysis all contain 120×60 points with the outer boundary located at approximately 4λ from the airfoil.

The computed drag coefficients of the two airfoils are shown in Fig. 8 as a function of the freestream Mach number. The wave drag of each airfoil is zero or near zero up to the drag-divergent Mach number where it begins to increase rapidly due to shock waves forming on the airfoil surface. Figure 8 shows that the drag-divergent Mach number increases as the maximum thickness of the airfoil is decreased. Therefore, aircraft employing the thinner airfoil can cruise at a higher Mach number without having to overcome a large amount of wave drag than those employing the thicker airfoil.

The computed bistatic RCS of the two airfoils are shown in Fig. 9. As expected, the bistatic RCS in the back-scattering region near the 180° viewing angle, which is often the most important threat sector for combat aircraft, increases as the maximum thickness of the airfoil is increased. Therefore, together with the result of the aerodynamic analysis, it can be concluded that the thinner airfoil has better aerodynamic efficiency and lower observability than the thicker airfoil.

Effects of leading-edge radius on the aerodynamic efficiency and observability

The second example of airfoil analysis using the CEM and CFD algorithms involves a study of the aerodynamic efficiency and observability of the NACA-0012 and NACA-0012-34 airfoils. The two airfoils are shown in Fig. 10 [11]. Both airfoils have a maximum thickness of $0.12c$. However, the NACA-0012-34 airfoil has a leading-edge radius of $0.00391c$ compared to $0.0158c$ for the NACA-0012 airfoil and, consequently, the location of the maximum thickness of the NACA-0012-34 airfoil is at $0.4c$ as opposed to $0.3c$ for the NACA-0012 airfoil. Both the aerodynamic and RCS analysis were performed for the same conditions as those described in the previous section.

The computed drag coefficients of the two airfoils are shown in Fig. 11 as a function of the freestream Mach number. The NACA-0012-34 airfoil has a slightly higher drag-divergence Mach number than the NACA-0012 airfoil. However, the biggest difference between the two airfoils is in their bistatic RCS shown in Fig. 12. The bistatic RCS of the NACA-0012-34 airfoil is significantly lower than that of the NACA-0012 airfoil in the back-scattering region near the 180° viewing angle. This is expected since the leading edge of the NACA-0012-34 airfoil is much smaller than the leading edge of the NACA-0012 airfoil. Note that the bistatic RCS in the forward-scattering region near the $0^\circ/360^\circ$ viewing angle is the same for both airfoils since they have the same maximum thickness.

CONCLUSION

The use of finite-difference methods to analyze the aerodynamic efficiency and observability of two-dimensional configurations was described. Using these numerical methods, a configuration such as an airfoil can be designed to be both aerodynamically efficient and low observable. Example analyses showed that the aerodynamic efficiency and observability of an airfoil can be improved by simply reducing its maximum thickness and/or leading-edge radius.

Future plans include improving the computational efficiency of the CFD method by introducing a direct solution algorithm to solve the governing equations. The present iterative solution algorithm tends to be computationally inefficient at higher Mach numbers when strong shocks occur. In addition, the capabilities of the present methods will be expanded by the addition of a numerical optimizer. The optimizer will modify the design

variables (i.e. variables which describe the shape of the airfoil) to minimize the objective function (i.e. the aerodynamic drag of the airfoil) at given flow conditions while satisfying certain constraints such as $RCS \leq RCS_{max}$ and $t/c \geq t_{min}/c$. Last but not least, the CFD and CEM methods will be expanded to allow the analysis of three-dimensional configurations. These additions to the present analysis methods will significantly reduce the computational cost and/or enhance the usefulness of the CFD and CEM methods in the developmental phase of an aerodynamic configuration.

ACKNOWLEDGMENT

This research is supported by the NASA Ames Research Center under Joint Research Interchange Agreement No. NCA2-568.

REFERENCES

- [1] J. W. Slooff, "Computational Drag Analysis and Minimization; Mission Impossible?" in *Aircraft Drag Prediction and Reduction*, AGARD R-723, Addendum I, 1986.
- [2] J. Flores, J. Barton, T. Holst, and T. Pulliam, "Comparison of the Full-Potential and Euler Formulations for Computing Transonic Airfoil Flows," NASA TM 85983, June 1984.
- [3] C. Hirsch, Numerical Computation of Internal and External Flows, Vol. 2, Wiley & Sons, 1990, pp. 77-81, p. 106.
- [4] T. L. Holst and W. F. Ballhaus, "Fast Conservative Schemes for the Full Potential Equation Applied to Transonic Flows," AIAA Journal, Vol. 17, 1979, pp. 145-152.
- [5] H. Vinh, "An Investigation of the Numerical Characteristics of Finite-Difference Methods as Applied to the Time-Domain Maxwell's Equations," Master's Thesis, University of California, Davis, 1991.
- [6] H. Vinh, H. A. Dwyer, and C. P. van Dam, "Finite-Difference Methods for Computational Electromagnetics (CEM)," IEEE Antennas and Propagation Society International Symposium, July 1992, Chicago, 1992 Digest, Vol. III, pp. 1682-1685.
- [7] H. Vinh, H. A. Dwyer, and C. P. van Dam, "Finite-Difference Algorithms for the Time-Domain Maxwell's Equations - A Numerical Approach to RCS Analysis," AIAA paper 92-2989, July 1992.
- [8] D. A. Anderson, J. C. Tannehill, and R. H. Pletcher, Computational Fluid Mechanics and Heat Transfer, Hemisphere Publishing, 1984, pp. 101-102, p. 75.
- [9] G. Mur, "Absorbing Boundary Conditions for the Finite-Difference Approximation of the Time-Domain Electromagnetic-Field Equations," *IEEE Transactions on Electromagnetic Compatibility*, Vol. EMC-23, No. 4, Nov. 1981, pp. 377-382.
- [10] G. T. Ruck, D. E. Barrick, W. D. Stuart, and C. K. Krichbaum, Radar Cross Section Handbook, Vol. 1, Plenum Press, 1970, p. 212.
- [11] I. H. Abbott and A. E. van Doenhoff, Theory of Wing Sections, Dover, 1959.

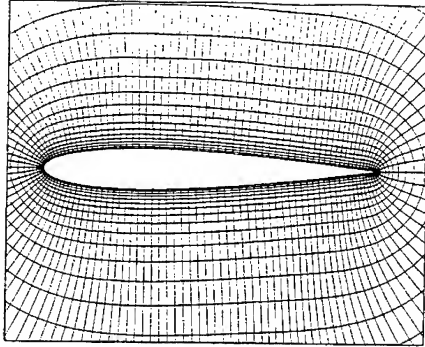


Figure 1: Computational grid for the NACA-0012 airfoil.

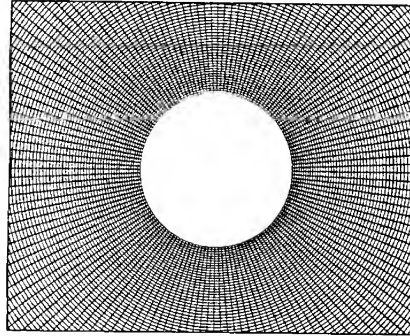


Figure 4: Computational grid for the circular cylinder ($ka = 10$).

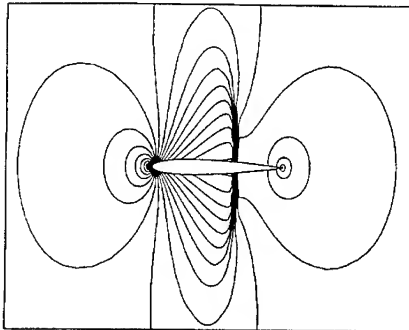


Figure 2: Mach contours of the NACA-0012 airfoil.

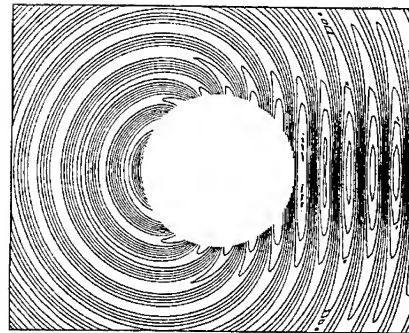


Figure 5: Scattered E^z contours of the circular cylinder ($ka = 10$).

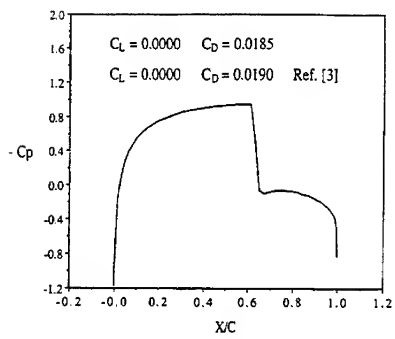


Figure 3: C_p distribution on the NACA-0012 airfoil.

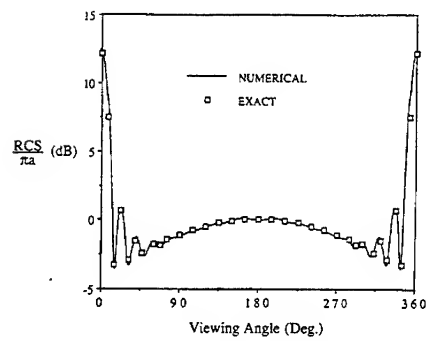


Figure 6: Bistatic RCS of the circular cylinder ($ka = 10$).

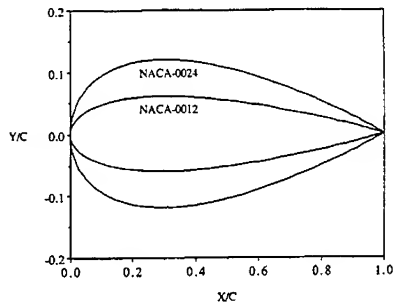


Figure 7: NACA-0012 and NACA-0024 airfoils.

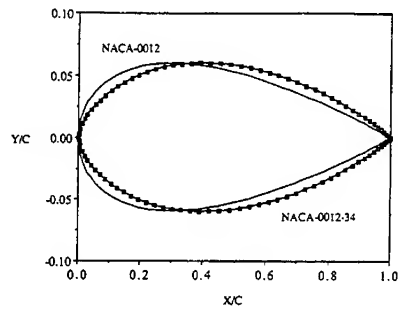


Figure 10: NACA-0012 and NACA-0012-34 airfoils.

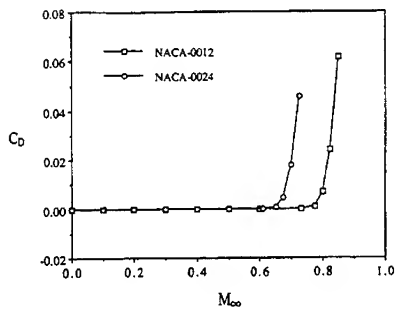


Figure 8: Variation of drag coefficient with Mach number.

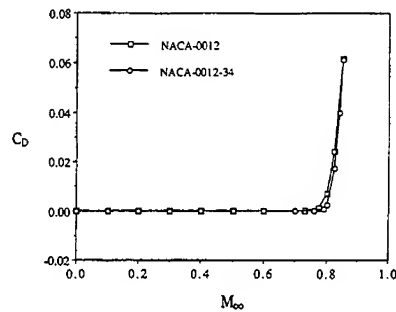


Figure 11: Variation of drag coefficient with Mach number.

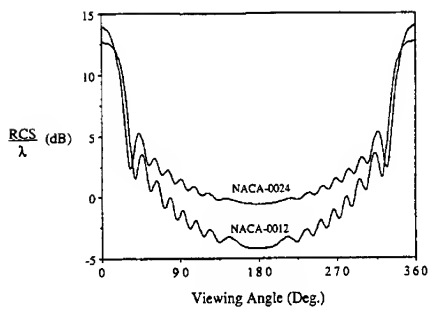


Figure 9: Bistatic RCS of the NACA-0012 and NACA-0024 airfoils.

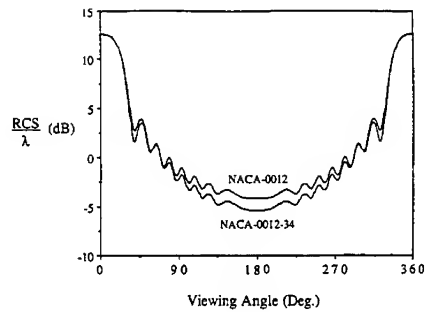


Figure 12: Bistatic RCS of the NACA-0012 and NACA-0012-34 airfoils.

SESSION 11 - "REMOTE SENSING

AND

MONTE CARLO TECHNIQUES"

Chair: Professor Leung Tsang, Co-Chair: Dr. Chi Chan

MONTE-CARLO PO SIMULATION OF SCATTERING FROM ROUGH SURFACES NEAR GRAZING INCIDENCE

H. Bender¹, R. Suchar³ and P. Russer^{1,2}

¹ Lehrstuhl für Hochfrequenztechnik, Technische Universität München,
Arcisstraße 21, D-8000 München 2, Germany
phone: +49-89-2105-3373, fax: +49-89-2105-3365

² Ferdinand Braun Institut für Höchstfrequenztechnik,
Rudower Chaussee 5, O-1199 Berlin, Germany
phone: +49-30-6704-5717, fax: +49-30-6704-4542

³ IABG, Einsteinstraße 20, D-8012 Ottobrunn, Germany
phone: +49-89-6088-2051, fax: +49-89-6088-2954

I. Introduction

In rough surface scattering numerous methods are known dealing with scattering at nearly normal incidence. If the incident or scattering angle is near grazing most of the known methods fail. The best known theory for calculating the scattered field from two-dimensional random rough surfaces with large radii of curvature compared to the wavelength is the Kirchhoff approach. This approximation method gives the statistical properties of the scattered field in dependence of the statistical properties (standard deviation σ , autocorrelation length l_c) of the considered rough surface [1]. In this approach shadowing effects, which are important near grazing incidence, were taken into account by using the well known shadowing functions of Smith [4]. Because measurements in this angle range are difficult and have not been published until now the shadow-corrected Kirchhoff approach was never validated. One possibility for verification, already investigated in the case of monostatic scattering [7], is a Monte-Carlo simulation based on the PO approach, in which shadowing effects are taken into account using an hidden surface algorithm (HSA).

II. Generation of random rough surfaces

Fung has already investigated the scattering from a one-dimensional random height distribution [2]. In this contribution we calculate the scattering from a rough surface with two-dimensional random height distribution. The height coordinates $C_{k,l}$ at the points (k, l) of the discretized random height profiles are given by

$$C_{k,l} = \sum_{i=-L}^{+L} \sum_{j=-L}^{+L} W_{i,j} U_{k+i, l+j} \quad (1)$$

where the U_i are uncorrelated random variates with Gaussian density function and $W_{i,j}$ is a two-dimensional weighting function, to take the correlation of neighbouring values in the surface profile into account. The weighting coefficients are then given by

$$W_{i,j} = \sqrt{\frac{2}{\sqrt{\pi} l_c}} \exp(-2 \frac{j^2 + i^2}{l_c^2}). \quad (2)$$

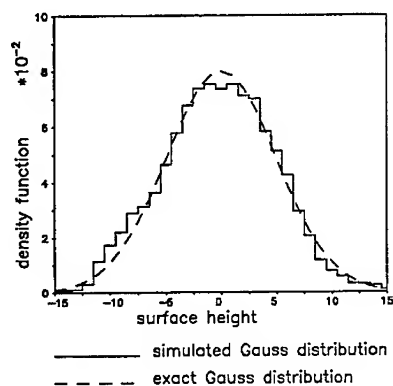


Figure 1: comparison of the density functions of surface B

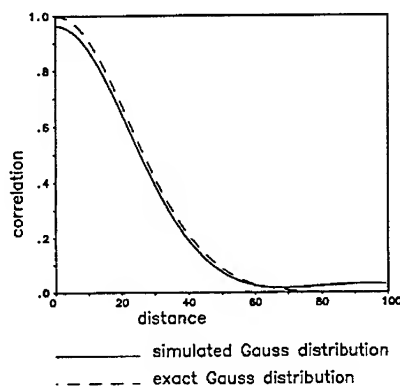


Figure 2: comparison of the correlation functions of surface B

Several two-dimensional profiles were generated using these weighting coefficients; surface A with standard deviation $\sigma = 5 \text{ mm} (= 1\lambda)$ and surface B with $\sigma = 50 \text{ mm} (= 10\lambda)$. The sum parameter L has to be chosen depending on the correlation length of the surface (here: $L = 60$). The results for the probability density function and autocorrelation function for surface B are given in figs.1-3. Figs. 1 and 2 compare the simulated probability density and correlation functions with the ideal ones. In both cases very good agreement can be seen. Fig. 3 shows a two-dimensional plot of the surface height. As expected there are no edges or discontinuities though only every 10th point was plotted.

III. Monte-Carlo Simulation of Scattering

Modelling complex scatterers by flat plates, it is a relatively simple procedure to compute the backscattered field with the physical optics (PO) method. Here we discretized the

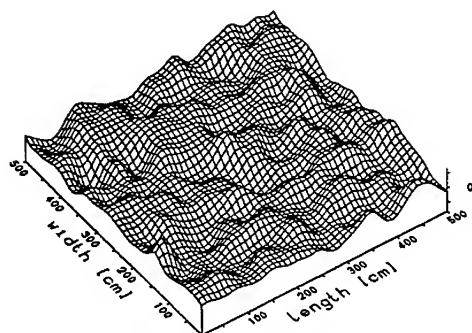


Figure 3: two-dimensional plot of the surface height

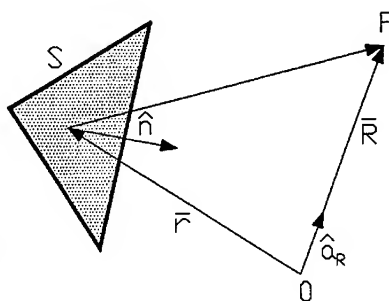


Figure 4: geometry of vectors for surface integrals

rough surface, with dimensions $500 \times 500 \text{ cm}^2$, using about 5000 triangles. The simulation frequency was 60 GHz, so that all sides of the triangles were at least 20λ long. On each triangle the surface current is given by

$$\vec{J}_s = \begin{cases} 2\hat{n} \times \vec{H}_i & \text{for illuminated parts} \\ 0 & \text{for non-illuminated parts} \end{cases} \quad (3)$$

where \hat{n} is the surface unity normal vector and \vec{H}_i the incident field vector. The scattered field far from the induced sources is given by the following integral [5] (according to fig. 4).

$$\vec{E}_s(P) = \frac{j\omega\mu_0 \exp(-jkR)}{4\pi R} \int_{S_{ill}} [\vec{J}_s - (\vec{J}_s \cdot \hat{a}_R)\hat{a}_R] \exp(jk\vec{r} \cdot \hat{a}_R) dS \quad (4)$$

Near grazing incidence shadowing plays a dominant role. Removing parts, which are not seen by the incident ray is necessary. This is done using a hidden-surface algorithm. It is now possible to calculate the scattered field realization-by-realization, to find the mean scattered intensity and its statistical properties. The mean field indicated by $\langle \dots \rangle$ is given by

$$\langle \vec{E}_s \rangle = \frac{1}{N} \sum_{i=1}^N \vec{E}_{s,i} \quad (5)$$

and the variance by

$$\text{var}(\vec{E}_s) = \langle \vec{E}_s \vec{E}_s^* \rangle - \langle \vec{E}_s \rangle \langle \vec{E}_s^* \rangle \quad (6)$$

$$= \langle I_s \rangle - \langle \vec{E}_s \rangle \langle \vec{E}_s^* \rangle \quad (7)$$

$$= \frac{1}{N} \sum_{i=1}^N I_{s,i} - \frac{1}{N^2} \sum_{i=1}^N \vec{E}_{s,i} \sum_{i=1}^N \vec{E}_{s,i}^* \quad (8)$$

It follows:

$$I_{coh} = |\langle \vec{E}_s \rangle|^2 \quad (9)$$

and

$$I_{diff} = \text{var}(\vec{E}_s) \quad (10)$$

where I_{coh} is the coherent and I_{diff} is the diffuse scattered intensity.

In the Kirchhoff approach shadowing effects which are important near grazing incidence are taken into account using shadowing functions $S(\theta)$ [4].

$$S(\theta) = \frac{[1 - \frac{1}{2}\text{erfc}(\mu/\sqrt{2}w)]}{[\Lambda(\mu) + 1]} \quad (11)$$

with

$$\Lambda(\mu) = \frac{1}{2} \left\{ \sqrt{\frac{2}{\pi}} \frac{w}{\mu} \exp(-\mu^2/2w^2) - \text{erfc}(\mu/\sqrt{2}w) \right\} \quad (12)$$

and

$$\mu = \cot \theta, \quad w = \sqrt{2} \frac{\sigma}{l_c} \quad (13)$$

Using this function we get the following expressions for the coherent scattered intensity

$$I_{coh} = S(\theta_i) \cdot S(\theta_s) \cdot \exp(-4\Sigma^2) \cdot I_{plate} \quad (14)$$

where I_{plate} is the scattered intensity of the equivalent flat plate and Σ is the well known Rayleigh roughness parameter and given by

$$\Sigma = 2\pi \frac{\sigma}{\lambda} \cos \theta \quad (15)$$

Using the same shadowing function in the case of diffuse scattering we get

$$I_{diff} = S(\theta_i) \cdot S(\theta_s) \cdot \text{var}(\bar{E}_s) \quad (16)$$

IV. Numerical Results

As seen from eq. 14 coherent scattering depends on the Rayleigh roughness parameter. This parameter given in eq. 15 can be varied by changing the roughness of the surface or by changing the angle of incidence. In fig. 5 we can see the results varying the roughness of the surface. The incident angle was constant ($\theta = \theta_i = \theta_s$) and chosen that no shadowing takes place. As you can see the agreement between the Kirchhoff approach results and the results of the Monte Carlo simulation is very close up to $\Sigma = 1.5$. For values of $\Sigma > 1.5$ there is a significant deviation which was already seen in experimental results given by Desanto and Brown in [6].

Fig. 6 shows the same ratio by varying the incident angle from 75° to 90° . The roughness of the surface was constant ($\sigma = 2\lambda$). In this case shadowing plays a dominant role and dominates the curves at $\Sigma \rightarrow 0$. But again up to $\Sigma = 1.5$ agreement between the shadow corrected Kirchhoff approach and the Monte Carlo Simulation is very close. We also made diffuse scattering simulation in the monostatic and bistatic case and found good agreement. Fig. 7 shows the diffusely scattered intensity for an angle of incidence of 30° . This means that shadowing is negligible in the given angle range. The convergence of our Monte Carlo simulation is given in fig. 8. The sums in eq. 8 can be truncated after averaging over 80 independent surface realizations. If the transmitter/receiver systems

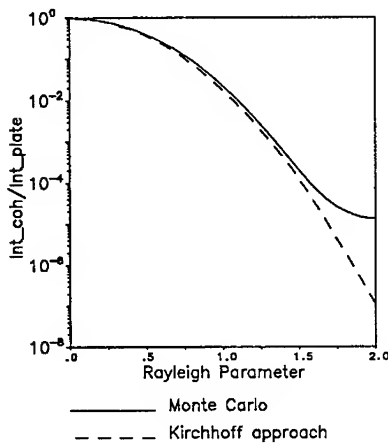


Figure 5: Ratio of I_{coh}/I_{plate} in dependence of the Rayleigh parameter, incident angle $\theta_i = \text{constant}$

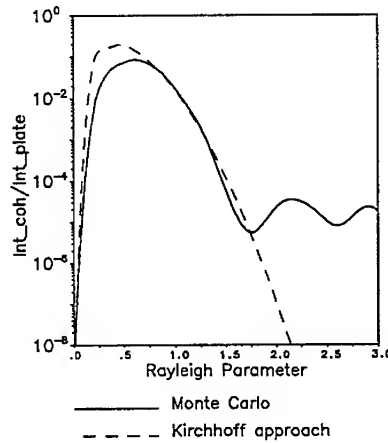


Figure 6: Ratio of I_{coh}/I_{plate} in dependence of the Rayleigh parameter, roughness $\sigma = \text{constant}$

are on the earth incident and scattering angle are near grazing. Fig. 9 compares the shadow corrected Kirchhoff results with the Monte Carlo results where the incident angle was chosen to 89° . This means that shadowing dominates the scattering process. Again the Kirchhoff approach is an acceptable approximation.

Fig. 10 shows the comparison of the monostatic RCS results calculated with the Kirchhoff approach and the numerical results of the Monte Carlo simulation with different roughness of the surface (surface A: $\sigma/\lambda = 1$, surface B: $\sigma/\lambda = 10$, both surfaces: $l_c/\lambda \gg 1$). As you can see the agreement in the main beam near normal incidence is very good.

V. Conclusion

We have shown new results in scattering of electromagnetic waves from two-dimensional random rough surfaces using a shadow including Monte Carlo technique. We've seen that the shadow corrected Kirchhoff approach gives good results in the main beam. The shadowing functions well known from the literature describe shadowing very well as it was seen in the case of diffuse and coherent scattering. Outside the main beam there is a significant deviation between our results and the results of the Kirchhoff approach, but we think that our results are much more realistic. Future work will be measurements of scattering from rough surfaces.

Acknowledgment

The authors want to thank Dr. H.-J. Geile from the IABG, Ottobrunn for helpful discussions and support.

References

- [1] L. Tsang, J.A. Kong and R.T. Shin: *Theory of Microwave Remote Sensing*, Wiley Series in Remote Sensing, 1985.
- [2] A.K. Fung and M.F. Chen: *Numerical Simulation of Scattering from Simple and Composite Random Surfaces*, J. Opt. Soc. Am. A, vol. 2, pp. 2274-2284, 1985.
- [3] R. M. Axline and A. K. Fung: *Numerical Computation of scattering from a Perfectly Conducting Random Surface*, IEEE Trans. Antennas Propagat., vol. AP-26, pp. 482-488, 1978.
- [4] B.G. Smith: *Geometrical Shadowing of a Randomly Rough Surface*, IEEE Trans. Antennas Propagat., vol. AP-15, pp. 668-671, 1967.
- [5] W. V. T. Rusch: *Reflector Antennas* in: Numerical and Asymptotic Techniques in Electromagnetics, R. Mittra Editor, Springer-Verlag Berlin, 1975.
- [6] J. A. Desanto and G. S. Brown: *Analytical Techniques for Multiple Scattering from Rough Surfaces*, Progress in Optics, vol. 23, Elsevier Science Publishers B.V., pp. 1-62, 1986.
- [7] H. Bender, R. Suchar and P. Russer: *Shadow Including PO Simulation of Backscattering from Two-Dimensional Random Rough Surfaces in a Wide Angle Range*, Proc. 1992 Int. Symp. Ant. Prop. (ISAP), Sapporo, Japan, pp. 285-288, 1992.

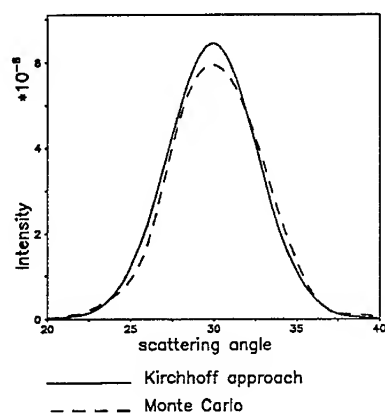


Figure 7: Comparison between Kirchhoff and Monte Carlo results ($\theta_i = 30^\circ$)

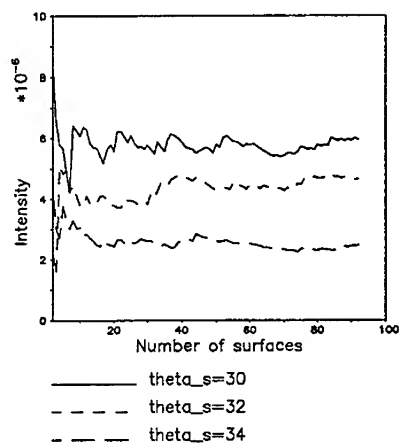


Figure 8: Convergence of the Monte Carlo Simulation according to fig. 7

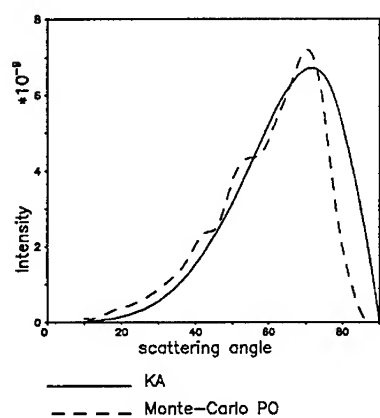


Figure 9: Comparison between Kirchhoff and Monte Carlo results near grazing incidence ($\theta_i = 89^\circ$)

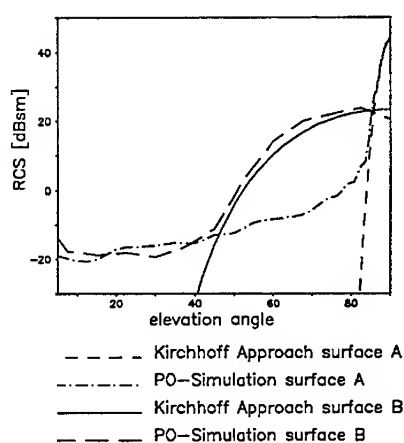


Figure 10: Monostatic results for different roughness scales

Polarimetric Thermal Emission from Rough Ocean Surfaces: A Numerical Study

J. T. Johnson, J. A. Kong, and R. T. Shin
Department of Electrical Engineering and Computer Science
and Research Laboratory of Electronics
Massachusetts Institute of Technology, Cambridge, MA

S. H. Yueh, S. V. Nghiem, and R. Kwok
Jet Propulsion Laboratory
California Institute of Technology, Pasadena, CA

Abstract A numerical study of the polarimetric thermal emission from ocean surfaces randomly rough in one dimension using a Monte Carlo technique is presented. In this study, a set of finite length surface profiles with desired statistics was generated using a spectral method. Each surface was extended periodically to create an infinite rough surface, and the thermal emission was computed using the extended boundary condition method (EBC) and the method of moments (MOM). The results from the set of surfaces were then averaged to obtain the Monte Carlo estimate of polarimetric thermal emission. The surface statistics chosen were intended to model a wind perturbed ocean surface in the X to K_u band microwave region. The results of the study show that the third Stokes parameter, U_B , is sensitive to the azimuthal angle between the surface periodicity and the looking angle, the rms height of the surface, and the surface power law spectrum slope, and that this parameter is insensitive to variations in polar angle, permittivity, and surface spectrum high frequency content as an indicator of the azimuthal asymmetry of the surface.

1 Introduction

Recent theoretical works have suggested the potential of passive polarimetry in the remote sensing of geophysical media [1–5]. It has been shown that the brightness temperature in the third Stokes parameter, U_B , may become large for azimuthally asymmetric fields of observation. In references [4] and [5], values of U_B as high as 30 K were measured from sinusoidal water surfaces at 10 and 14.6 GHz. In order to investigate the potential applicability of passive polarimetry to the remote sensing of rough ocean surfaces, a numerical study of the polarimetric thermal emission from ocean surfaces randomly rough in one dimension was performed. A Monte Carlo technique utilizing an exact integral equation method for calculating thermal emission was chosen for the study.

The next section presents a brief background on the theory of polarimetry and describes the passive polarimetric brightness vector. The method of calculation for the numerical experiment is discussed in Section 3 and the numerical results are presented in Section 4.

2 Theory of Polarimetry

In passive polarimetry, brightness temperatures corresponding to all of the four modified Stokes parameters are measured. The brightness temperature Stokes vector is defined as

$$\bar{T}_B = \frac{1}{C} \bar{I} = \frac{1}{C} \begin{bmatrix} I_h \\ I_v \\ U \\ V \end{bmatrix} = \frac{1}{\eta C} \begin{bmatrix} \langle E_h E_h^* \rangle \\ \langle E_v E_v^* \rangle \\ 2\text{Re}\langle E_v E_h^* \rangle \\ 2\text{Im}\langle E_v E_h^* \rangle \end{bmatrix} \quad (1)$$

where E_h and E_v are the emitted electric fields received from the horizontal and vertical polarization channels of the radiometer, η is the characteristic impedance, and $C = K/\lambda^2$ with K denoting Boltzmann's constant, λ the wavelength. The first two parameters of the brightness temperature Stokes vector correspond to the powers received in the horizontal and vertical polarization channels, respectively. The third and fourth parameters correspond to the complex correlation between the electric fields received by the horizontal and vertical channels. We will label the four parameters T_{Bh} , T_{Bv} , U_B , and V_B respectively in this paper. It is shown in [3] that the third and fourth Stokes parameters may be related to the brightness temperature in a 45 degree linearly polarized measurement (T_{Bl}) and a right hand circularly polarized measurement (T_{Br}) as follows:

$$U_B = 2T_{Bl} - T_{Bh} - T_{Bv} \quad (2)$$

$$V_B = 2T_{Br} - T_{Bh} - T_{Bv} \quad (3)$$

Thus, to calculate all four parameters of the brightness temperature Stokes vector, the brightness temperatures in horizontal, vertical, 45 degree linear, and right hand circular polarizations are first calculated, and the above equations are used to obtain U_B and V_B .

In the passive remote sensing of rough surfaces, the parameter that is actually of interest is the emissivity, which relates the brightness temperature emitted by an object to its actual physical temperature, under the assumption that the object is at a constant physical temperature and that the emission from the object is the only source of brightness:

$$T_{Ba} = e_a(\theta, \phi) T_{phys} \quad (4)$$

In the above equation, the subscript a refers to the polarization of the brightness temperature, θ to the polar observation angle, and ϕ to the azimuthal observation angle. Through the principles of energy conservation and reciprocity, Kirchhoff's law relates this emissivity to the reflectivity of the surface [6]:

$$e_a(\theta, \phi) = 1 - r_a(\theta, \phi) \quad (5)$$

The reflectivity $r_a(\theta, \phi)$ for the given incident polarization a is defined as the fraction of the power incident from direction (θ, ϕ) that is rescattered and can be evaluated by

integrating the bistatic scattering coefficient $\gamma_{ba}(\theta, \phi; \theta', \phi')$ over all scattering angles in the upper hemisphere and summing the results of both orthogonal scattering polarizations.

$$r_a(\theta, \phi) = \frac{1}{4\pi} \sum_b \int_0^{\pi/2} d\theta' \sin \theta' \int_0^{2\pi} d\phi' \gamma_{ba}(\theta, \phi; \theta', \phi') \quad (6)$$

In the above expression, (θ, ϕ) and (θ', ϕ') represent the incident and the scattered directions, respectively, and the subscripts a and b represent the polarizations of the incident and the scattered waves, respectively.

Thus, to calculate the fully polarimetric emission vector, the bistatic scattering coefficient for each of four polarizations is first calculated and integrated over the upper hemisphere to obtain the reflectivity for that particular polarization. Multiplication of the corresponding emissivity by the physical temperature of the object under view yields the brightness temperature for this polarization. The fully polarimetric brightness vector is then calculated as described previously. A physical temperature of 300 K was assumed for the surfaces in this experiment.

3 Method of Calculation

Scattering from randomly rough surfaces has been studied extensively by a number of researchers. Numerous approximate techniques, such as the Kirchhoff approximation and the small perturbation method, exist and work well under certain restrictions for providing the statistically expected values of scattered fields and power [6]. However, it was found in [2] that in order to measure large U_B values from a sinusoidal surface, a large height to period ratio was required. The large slopes of such a surface fall into the regions of non-applicability for the above methods, so a Monte Carlo method was chosen for the study.

In this Monte Carlo method, a set of surface profiles with given statistics was generated, and the fully polarimetric brightness vector from each surface was calculated using an exact integral equation approach. The results for the set were then averaged to obtain the final Monte Carlo estimate of the average brightness vector for those particular surface parameters. The surface generation and analysis procedure are described in more detail in the next section.

3.1 Random Surface Generation

A spectral method, described in [7-8], was used to generate a finite sample of a rough surface with desired statistics. In this method, a set of normally distributed (both real and imaginary part) Fourier coefficients is generated and then weighted by a spectral density function in the frequency domain. The resulting Fourier coefficients are then transformed back into the space domain using an inverse FFT algorithm to obtain a surface profile

sampled in space. The surface profiles were linearly interpolated between the specified points.

Since only a finite surface profile could be generated, an infinite surface was created by extending this finite surface periodically. The Floquet modes obtained from the periodic surface are thus a discrete approximation to the continuous spectrum of a truly infinite random rough surface. The effect of this periodic extension on the polarimetric brightness temperature was investigated by comparing the results from a set of surfaces with a given period with the results from a set of surfaces a longer period and the same frequency spectrum. A period of 20 wavelengths was found to be sufficient to provide convergence of the U_B results to within 0.3 K for longer period surfaces. The surfaces were continuous when made periodic due to the periodic properties of the FFT series from which they were generated.

The surface profiles generated were rough in one dimension only due to the complexity of the calculations for surfaces rough in two spatial directions. The rough profile along the x direction was extended infinitely along the y direction in the calculations (see Figure 1). Three dimensional angles of incidence were allowed, however, so that polarimetric effects could be observed from the resulting 'conical diffraction' problem. While this model is extremely simple when compared to an actual wind perturbed ocean surface, its results should give some indication as to the properties of U_B for general rough surfaces.

The surface statistics chosen for the calculations were intended to model ocean surfaces in the microwave frequency range. For this purpose, a dielectric constant of $50 + i30$ was chosen for the medium and a power-law spectral density function for the surfaces was used. This function, $\phi(k)$ is described by:

$$\phi(k) = \begin{cases} k^{-s} & \frac{2\pi}{5\lambda} \leq k \leq k_c \\ 0 & \text{otherwise} \end{cases} \quad (7)$$

where k is the spatial wavenumber of the surface in rads/m , s is the slope of the power law spectrum, and k_c is the cutoff wavenumber of the surface set. The effects of varying the slope of the spectrum and its high frequency cutoff were investigated in the experiment. The surface in Figure 1 is one of the surfaces generated with -3 slope power law spectrum and a high frequency cutoff of $k_c = 4\pi/\lambda$.

Each surface was normalized independently of the others to a specified rms surface height; rms heights of $\lambda/20$, $\lambda/25$ and $\lambda/30$ were chosen to investigate the effect of varying the surface height on the polarimetric brightness temperature. The 20λ requirement for the surface period prevents larger rms heights from being studied due to computational limitations. Each generated surface consisted of 400 points within this period, so that the surface profile was sampled every $\lambda/20$ along the \hat{x} direction. This sampling frequency is well above all of the Nyquist frequencies of the power spectral density functions used in the experiment. The surface statistics calculated from the generated surface sets were compared to their desired theoretical values and found to be in good agreement.

The results from ten surface profiles were averaged for all of the points in the exper-

iment. The convergence of the results with the number of surface profiles averaged was investigated by comparing the results from independent groups of ten surfaces. The results for U_B were found to be within 0.2 K.

3.2 Integral Equation Method

Numerous studies have been made of scattering from a periodic surface. The Extended Boundary Condition (EBC) method [9] is one of the most efficient methods, but has been found to become ill conditioned for steep surfaces. The Method of Moments (MOM) for a periodic surface, described in [2], is another solution of the problem that does not have the steep surface problems of the EBC, but is more computationally intensive. The calculations from these two methods were compared for a sample surface for each case in the experiment and found to give similar results in all of the cases. This agreement indicates that the surface slope limitations of the EBC were not exceeded, and this more efficient method of calculation was used for the larger surface sets of the experiment.

4 Results of Calculations

Figure 2 is a plot of the average U_B value for the $\lambda/20$, $\lambda/25$, and $\lambda/30$ rms height surfaces as a function of azimuthal angle for a polar angle of 20 degrees. A power law slope of -3 , cutoff wavenumber of $k_c = 4\pi/\lambda$, and dielectric constant of $50 + i30$ were used. Points were calculated every 15 deg in azimuthal angle, so that the interpolating lines shown should not be taken to be exact. It is seen that the U_B value is small for viewing angles parallel or perpendicular to the direction of periodicity of the surface, and that the highest values of U_B are obtained at azimuthal angles of approximately 45 or 135 degrees. The magnitude of U_B is determined by the rms height of the surface, with rougher surfaces giving higher values. The small values of U_B obtained in these results (2 K) are due to the convergence requirements for the Monte Carlo technique: larger U_B values could be obtained by analyzing rougher surfaces, but would require more computer time than was available for this study. Also, data collected from the SSM/I and reported by Wentz [10] indicates that the azimuthal variation in T_{Bh} and T_{Bv} for real wind perturbed ocean surfaces at both 37 and 19 GHz is typically less than 3 K, as is obtained for these rms heights. The U_B channel is seen to indicate the azimuthal direction of the surface in all cases where it is observable. Note that negative values for U_B are possible, as this parameter corresponds only to a correlation between real observables. Also, the symmetry about $\phi = 90$ deg seen in Figure 2 and the following figures is due only to the statistical symmetry of the surface set about this angle; individual surfaces are not symmetric about $\phi = 90$ deg. This gives an indication that the average of the ten surface profiles is converging to the true statistical average.

Figure 3 investigates the effects of polar angle on the U_B . Plotted are the results at polar angles of 20, 40, and 50 degrees for the $\lambda/20$ rms height, -3 slope, $k_c = 4\pi/\lambda$,

50 + i30 dielectric constant surfaces. The results are surprisingly similar, demonstrating that this parameter is relatively insensitive to polar angle as an indicator of surface azimuthal direction. These larger polar angles are important due to the need for large polar angles in satellite borne sensor applications.

Figure 4 illustrates the effect of permittivity on U_B . Results for polar angle 20 degrees, rms height $\lambda/20$, -3 slope, $k_c = 4\pi/\lambda$, and dielectric constants of 40 + i25, 50 + i30, and 60 + i35 are plotted. The results again indicate that the U_B channel is insensitive to a change in the dielectric constant around 50 + i30.

Figure 5 displays the variation in U_B with the slope of the power law spectrum, s . The results for $\lambda/20$ rms height surfaces with power law slopes of -3, -2.5, and -4.5 are compared for a polar angle of 20 degree, cutoff wavenumber $k_c = 4\pi/\lambda$, and dielectric constant of 50 + i30. The results show that the U_B parameter is larger for the -2.5 slope surface, which has more high frequency content and hence larger slopes, and that U_B is smaller for the smoother -4.5 slope surface. However, U_B exists for all three cases and indicates the direction of surface periodicity in each case.

Finally, Figure 6 investigates the effect of the high frequency cutoff wavenumber, k_c on U_B . Plotted are the results from $\lambda/20$ rms height -3 slope surfaces for a polar angle of 20 degrees and dielectric constant 50 + i30. Cutoff wavenumbers of $4\pi/\lambda$, $8\pi/\lambda$, and $16\pi/\lambda$ are shown. This change in the cutoff wavenumber is seen to have little effect on the U_B results.

5 Conclusions

A numerical study of polarimetric thermal emission from randomly rough ocean surfaces using a Monte Carlo method has been carried out. This study indicates that polarimetric information can be useful in the remote sensing of anisotropic rough ocean surfaces. One proposed application is the remote sensing of wind direction over the ocean, as the rough surface created on the ocean has an anisotropic structure. Since the U_B parameter is shown to be relatively insensitive to the polar angle, the permittivity of the medium, and the cutoff wavenumber of the surface spectral density function as an indicator of surface azimuthal direction, a wind direction sensor could feasibly operate under a wide variety of these conditions. Further research into this area and into the use of a more realistic ocean surface model will continue.

Acknowledgements This work was supported in part by ONR Grant N00014-92-J-1616, NASA grant NAGW-1617, and a National Science Foundation Graduate Research Fellowship.

6 References

- [1] Tsang, L., "Polarimetric passive microwave remote sensing of random discrete scatterers and rough surfaces," *J. Electromag. Waves Applic.*, Vol. 5, No. 1, 41-57, 1991.
- [2] Veysoglu, M. E., H. A. Yueh, R. T. Shin and J. A. Kong, "Polarimetric passive remote sensing of periodic surfaces," *J. Electromag. Waves Applic.*, Vol. 5, No. 3, 267-280, 1991.
- [3] Nghiem, S. V., M. E. Veysoglu, J. A. Kong, R. T. Shin, K. O'Neill, and A. W. Lohanick, "Polarimetric passive remote sensing of a periodic soil surface: microwave measurements and analysis," *J. Electromag. Waves Applic.*, Vol. 5, No. 9, 997-1005, 1991.
- [4] Johnson, J. T., J. A. Kong, R. T. Shin, K. O'Neill, and A. Lohanick, "Third Stokes parameter emission from a periodic water surface," submitted to *IEEE Trans. Geosci. Remote Sensing*, 1992.
- [5] Yueh, S. H. S. V. Nghiem, R. Kwok, F. K. Li, J. T. Johnson, and J. A. Kong, "Polarimetric thermal emission from periodic water surfaces," submitted to *Radio Science*, 1992.
- [6] Tsang, L., J. A. Kong, and R. T. Shin, *Theory of Microwave Remote Sensing*, John Wiley, New York, 1985.
- [7] Thorsos, E. I., "The validity of the Kirchhoff approximation for rough surface scattering using a Gaussian roughness spectrum," *J. Acoust. Soc. Am.*, Vol. 83, No. 1, 78-92, 1988.
- [8] Fung, A. K. and M. F. Chen, "Numerical simulation of scattering from simple and composite random surfaces," *J. Opt. Soc. Am. A*, Vol. 2, No. 12, 2274-2284, 1985.
- [9] Chuang, S. L. and J. A. Kong, "Wave scattering from a periodic dielectric surface for a general angle of incidence," *Radio Science*, Vol. 17, No. 3, 545-557, 1982.
- [10] Wentz, F. J. "Measurement of oceanic wind vector using satellite radiometers," *IEEE Trans. Geosci. Remote Sens.*, Sept. 1992.

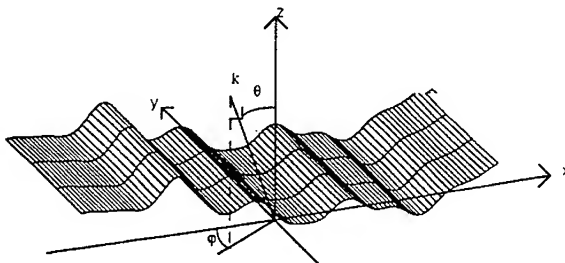


Figure 1: Geometry of the problem

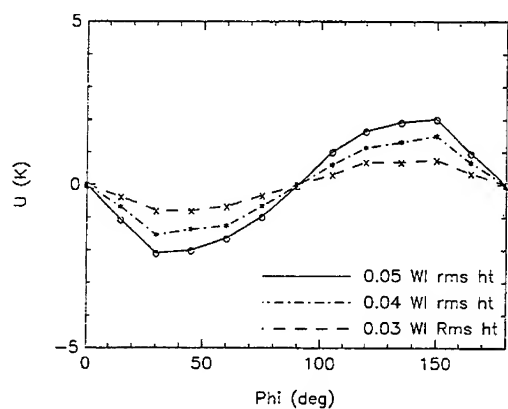


Figure 2: Variation of U_B with rms height

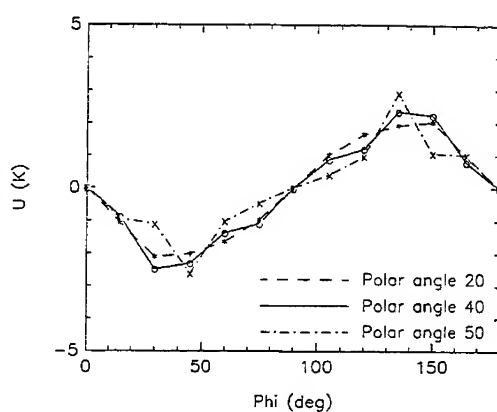


Figure 3: Variation of U_B with polar angle

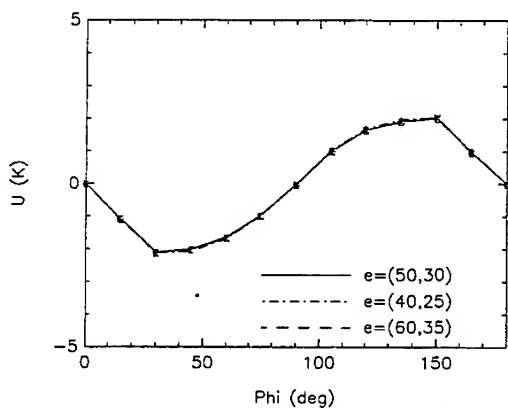


Figure 4: Variation of U_B with surface permittivity

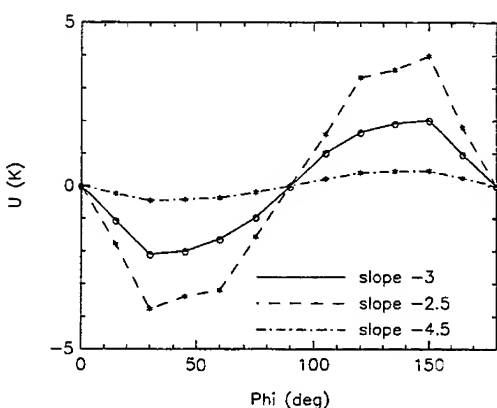


Figure 5: Variation of U_B with power law slope

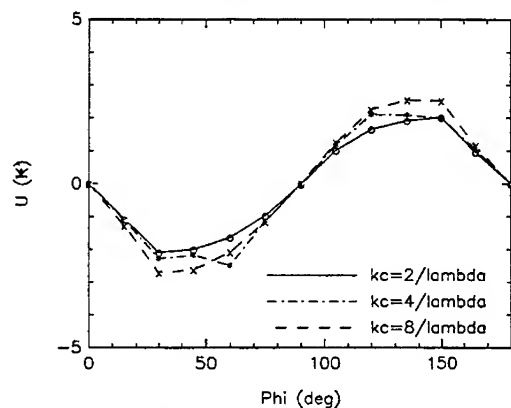


Figure 6: Variation of U_B with high frequency cutoff

A Banded Matrix Iterative Approach to Monte Carlo Simulations of Large-Scale Random Rough Surface Scattering: TE Case

by

Leung Tsang, Chi H. Chan and Haresh Sangani
Electromagnetics and Remote Sensing Laboratory
Department of Electrical Engineering, FT-10
University of Washington
Seattle, Washington 98195

Introduction

The study of wave scattering by random rough surfaces is a topic of continuing interest [1-3]. The classical analytic approaches of Kirchhoff approximation and small perturbation method [1-3] have been used to solve these problems, however, both are restricted in domain validity. With the advent of modern computers, the Monte Carlo simulations of one-dimensional rough surfaces can be calculated. The standard method is the method of moments [4]. An integral equation method in the space domain is formed and then converted to a matrix equation with a full matrix inversion [5-7]. However, the full matrix inversion requires $O(N^3)$ number of operations where N is the number of unknowns. The typical number of unknowns used is between 300-400 with 5 to 10 unknowns per wavelength. However, for large-scale rough surface problems, a much larger surface length is required. Large-scale problems include cases of large rms heights, large correlation lengths, large incidence angles, composite rough surfaces with small-scale roughness superimposed on large-scale roughness, etc. Thus recently, increasing effort has been invested in finding a more computationally efficient method than the integral equation method of full matrix inversion.

In this paper, a banded matrix iterative approach (BMIA) [8] is applied to study scattering of a TE incident wave from a perfectly conducting one-dimensional random rough surface. The original full matrix equation is decomposed into a banded matrix which represents strong interaction and the remainder of the full matrix represents the weak interaction part. This is based on the physical interpretation that in random rough surface scattering only points in the vicinity of each other will interact strongly in scattering. Points that are outside the neighborhood interact weakly due to both the decay of amplitude with distance and the random phase fluctuation which is a characteristic of random media scattering. An iterative approach is then adopted. A key feature of BMIA is that very few iteration steps (typically no more than ten) are required to give solutions of sufficient accuracy. The size of the neighborhood varies depending on the rough surface statistics and the incidence angle. However, it is always much less than the required surface length and is also much less than the tapering g parameter. Thus the method is much faster than the full matrix inversion approach (EMI) or the conjugate gradient method (CGM). Because very few iterations are required, the memory requirement can be reduced by storing only the strong interaction matrix for problems of very large surface length. BMIA includes coherent wave interactions among all parts of the rough surface within the entire surface length. Numerical results are illustrated for a variety of rough surface parameters with particular application to large-scale problems.

Formulation

Consider a tapered plane wave $\psi^{\text{inc}}(x, z)$ with time dependence $\exp(-i\omega t)$ impinging upon a 1-D rough surface with a random height profile $z=f(x)$. It is tapered [6] so that the illuminated rough surface can be confined to surface length L .

$$\psi^{\text{inc}}(\mathbf{r}) = e^{i\mathbf{k}\cdot\mathbf{r}[1+W(\mathbf{r})]} e^{-(x+z\tan\theta_{\text{inc}})^2/g^2} \quad (1)$$

where

$$W(\mathbf{r}) = [2(x+z\tan\theta_{\text{inc}})^2/g^2 - 1] / (kg \cos\theta_{\text{inc}})^2; \mathbf{k} = k(x \sin\theta_{\text{inc}} - z \cos\theta_{\text{inc}})$$

and g is the parameter that controls the tapering of the incident wave. In (1), bold face represents a vector quantity. The boundary condition is the wave function ψ equal to zero on the random surface. This is the Dirichlet problem that corresponds to a TE electromagnetic wave impinging upon a perfect electric conductor. A Fredholm integral equation of the first kind can be formed [4] for a point $\mathbf{r} = \mathbf{x} + z\mathbf{f}(x)$ on the rough surface such that

$$0 = \psi^{\text{inc}}(\mathbf{r}) - \int dx' \sqrt{1 + \left(\frac{df(x')}{dx'}\right)^2} G(\mathbf{r}, \mathbf{r}') \frac{\partial \psi(\mathbf{r}')}{\partial n'} \quad (2)$$

where $G = i H_0^{(1)}/4$ is the two-dimensional free space Green's function and $H_0^{(1)}$ is a Hankel function of the first kind. The BMIA approach can be directly applied to the Fredholm integral equation of the first kind. Equation (2) can be cast into a matrix equation by discretizing in the space domain with the points labeled consecutively in the 1-D rough surface profile

$$\bar{\bar{Z}}\bar{X} = \bar{C} \quad (3)$$

with the column vector \bar{X} of dimension N denoting the unknown values on the rough

surface and the column vector \bar{C} corresponding to the first term on the right-hand side of (2). Z_{mn} is the mn element of the $N \times N$ matrix and represents the interaction between two points on the rough surface as represented by the Kernel of Eq. (2) and is calculated by the method of moments [4]. The matrix Z_{mn} is symmetric. The number of points is N where usually $N = N_p L$ and N_p is the number of points per wavelength and L the surface length in wavelengths. To ensure numerical accuracy, we have used N_p equal to 8 or 10. When the matrix equation is solved directly, it is known as the exact matrix inversion. In the banded

matrix iterative approach, the $\bar{\bar{Z}}$ matrix is decomposed into a banded part $\bar{\bar{Z}}^{(s)}$ consisting of strong interactions and the remainder into the weak interaction part $\bar{\bar{Z}}^{(w)}$

$$\bar{\bar{Z}} = \bar{\bar{Z}}^{(s)} + \bar{\bar{Z}}^{(w)} \quad (4)$$

For the 1-D case, since the points are labeled consecutively, we have $Z_{mn}^{(s)} = Z_{mn}$ for $|m-n| < b$ and $= 0$ otherwise. Thus for the 1-D case, $\bar{Z}^{(s)}$ is banded. We have used the half bandwidth $b = N_p r_d$, where r_d is the maximum distance in wavelength of strong interaction. Then the iteration procedure is for the first-order solution,

$$\bar{Z}^{(s)} \bar{X}^{(1)} = \bar{C} \quad (5)$$

and higher order solution is

$$\bar{Z}^{(s)} \bar{X}^{(n+1)} = \bar{C} - \bar{Z}^{(w)} \bar{X}^{(n)} \quad (6)$$

The choice of r_d varies depending on the rough surface characteristics and the incidence angle. As indicated by the numerical results, it is generally much smaller than the surface length L and tapering g parameter. In order to take full advantage of the banded matrix, a direct sparse matrix solver (LU decomposition and backsubstitution) [9] is used to solve (6). The LU decomposition requires $O(b^2N/2)$ operations while the backsubstitution only requires $O(2bN)$ operations. The matrix multiplication $Z^{(w)}X^{(n)}$ requires $O(N^2)$ steps. Thus computing the solution up to the n th order requires $O(b^2N) + O(nN^2)$. One key feature of this approach is that very few orders are required (5 or 10 orders are required for all the calculations presented in this paper). The valid test of convergence of this approach is how well it agrees with the exact full matrix inversion and the conjugate gradient method. For a large-scale problem with a large N , the memory requirement can be reduced (at the expense of CPU) by storing only the banded matrix $Z^{(s)}$ and calculating the full matrix $Z^{(w)}$ each time it is needed. Note that no approximation has been made and the iterated solution represents the result for a surface length L with all coherent wave interactions over the entire surface length included. In all our calculations, the symmetric property of the matrix is exploited to reduce CPU time and memory storage. Contrary to the TE case, asymmetric banded matrix solutions are required for the TM case [8].

Results and Discussions

In the implementation of BMIA, the order of solutions is fixed at 5 to 10, and then $b = N_p r_d$ is increased until the solution converges. The result converges for r_d much less than the surface length L and the tapering parameter g . The results are illustrated for different order of solutions and different bandwidths. Comparisons are made for one realization as well as for averaged results over many realizations. All the calculations presented in this section are performed on a VAX-6000-440 computer. The tapering parameter g is set at $L/4$.

Figure 1 shows the bistatic radar cross section of a random surface with surface length $L = 100\lambda$, rms height $h = 0.575\lambda$ and correlation length $l = 1.05\lambda$ at an incident angle of 20° for one realization. With a discretization of 8 points per wavelength, the total number of unknowns is 800. Three different combinations of order of solutions (n) and half bandwidth (b) of BMIA are compared with EMI. The CPU times for the EMI, BMIA with $n = 10$ and $b = 50$, $n = 20$ and $b = 50$, and $n = 10$ and $b = 60$ are 415.41, 28.28, 51.46, and 29.75 seconds, respectively. Except for the case of $n = 10$ and $b = 50$, the results completely overlie those of EMI for all scattering angles θ_s including the backscattering direction at $\theta_s = -20^\circ$. For $n = 10$ and $b = 50$, there is a slight difference between BMIA and EMI at θ_s close to 90° . It is evident that by increasing the half

bandwidth, we can reduce the order of solutions required to achieve the same accuracy without sacrificing computational efficiency as the total CPU time is proportional to $O(b^2N) + O(nN^2)$. The choice of b , however, also depends on the angle of incidence.

Figure 2 shows the bistatic radar cross section of the same rough surface at 80° incidence for one realization. The region of focus is in the vicinity of the backscattering direction at $\theta_s = -80^\circ$ while the results overlie those of EMI for the remaining scattering angles similar to Figure 1. A larger b ($=90$) is required when the angle of incidence is close to grazing. The number of iterations is set at 10. Numerical experiments show that the larger half bandwidth required for the large incident angle does not significantly affect the computational efficiency of BMIA. A reduction in CPU time by a factor of 12 can still be achieved when compared to EMI.

After the accuracy and convergence of BMIA have been established, we apply this new method to studying large-scale rough surfaces that have not been previously attempted. Two different examples are shown here. The first example is a large-scale rough surface with $h = 3\lambda$ and $l = 10\lambda$. The second example is a composite rough surface which has a small-scale roughness superimposed on the first large-scale surface. In this composite surface case, $f(x) = f_1(x) + f_2(x)$ where $f_1(x)$ and $f_2(x)$ are independent gaussian random processes with a zero mean and the rms heights and correlation lengths are equal to $(h_1 = 3\lambda, l_1 = 10\lambda)$ and $(h_2 = 0.3\lambda, l_2 = 0.6\lambda)$ respectively. The incident angle is set at 30° . We use $L = 400\lambda$. A discretization of 8 points per wavelength is employed for both surfaces and hence, the total number of unknowns is 3200. The matrix size is prohibitively large for the exact matrix inversion to be performed on the VAX-6000-440 computer. Comparison for this case is made with the CGM method.

Monte Carlo simulations are performed for both large-scale surfaces using BMIA. The bistatic radar cross sections after 100 realizations are shown in Figure 3. For the first large-scale rough surface, the radar cross section peaks at the forward scattering direction at $\theta_s = 30^\circ$ and there is no backscattering enhancement at $\theta_s = -30^\circ$. In contrast, the bistatic radar cross section of the composite rough surface peaks at the backscattering direction. These results suggested that the small-scale roughness, because of its larger slope, contributes to and may dominate the backscattering.

To validate our calculation, we compare the bistatic radar cross section for one realization of the first large-scale surface with the conjugate gradient method. In CGM, we also compute the matrix each time it is needed in the iteration. The maximum normalized residual norm of CGM is set at 1% [10] and the number of iterations required is 47. Perfect agreement between CGM and BMIA is shown in Figure 4, however, the CPU seconds required by CGM for this 3200 unknown problem is 77500 versus 3968 seconds of BMIA. The symmetric property of the matrix is exploited in both methods. When computers with larger RAM are available to store all the matrix elements, we can avoid calculating the matrix anew for each new order of solution for BMIA and for each iteration of CGM. However, the relative speed between BMIA and CGM will remain unchanged.

Conclusions

A banded matrix iterative approach is presented for the scattering of a TE incident wave from a perfectly conducting one-dimensional random rough surface. The accuracy and convergence of the method are shown numerically for various surface statistics, surface lengths, and incident angles. This method is much faster than the exact matrix inversion or the conjugate gradient method for all surface lengths. This method is applied

to large-scale problems that have not been previously attempted with all the coherent wave interactions for the entire surface length included. It is shown that backscattering can be dominated by the small roughness that is superimposed on the large scale roughness.

Acknowledgments

This work is in part supported by the National Science Foundation (ECS-9158040).

References

- [1] P. Beckmann and A. Spizzichino, *The Scattering of Electromagnetic Waves from Rough Surfaces*, Pergamon, Oxford, 1963.
- [2] A. Ishimaru, *Wave Propagation and Scattering in Random Media*, Academic Press, New York, 1978.
- [3] L. Tsang, J. A. Kong, and R. T. Shin, *Theory of Microwave Remote Sensing*, Wiley-Interscience, 1985.
- [4] R. Harrington, *Field Computation by Moment Methods*, Macmillan, 1968.
- [5] R. M. Axline and A. K. Fung, "Numerical computation of scattering from a perfectly conducting random surface," *IEEE Trans. on Antennas and Propagat.*, AP-26, 1978, pp. 482-488.
- [6] E. I. Thorsos, "The validity of the Kirchhoff approximation for rough surface scattering using a gaussian roughness spectrum," *J. Acoust. Soc. Am.*, vol. 82, 1988, pp. 78-92.
- [7] J. S. Chen and A. Ishimaru, "Numerical simulation of the second order Kirchhoff approximation from very rough surfaces and study of backscattering enhancement," *J. of Acoustical Society of America*, vol. 88, 1990, pp. 1846-1850.
- [8] L. Tsang, C. H. Chan, and H. Sangani, "Application of a banded matrix iterative approach to Monte-Carlo simulations of scattering of waves by random rough surface: TM case," *Microwave and Optical Technology Letters*, in press, 1993.
- [9] O. C. Zienkiewicz and R. L. Taylor, *The Finite Element Method--Basic Formulation and Linear Problems*, 4th Edition, McGraw-Hill, Volume 1, 1989.
- [10] C. H. Chan and R. Mittra, "Some recent developments in iterative techniques for solving electromagnetic boundary value problems," *Radio Science*, vol. 22, no. 6, 1987, pp. 929-934.

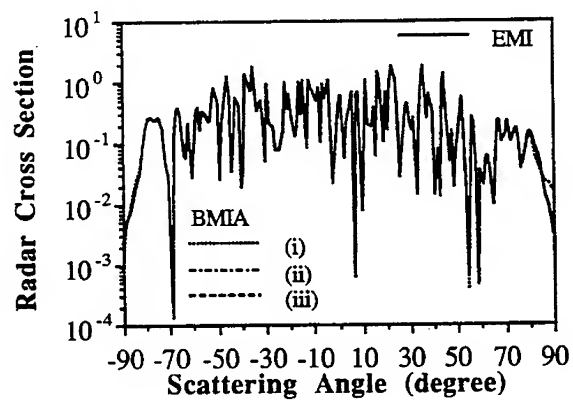


Figure 1. Convergence of BMIA with various order of solutions at 20° incidence with surface length $L = 100\lambda$, rms height $h = 0.575\lambda$, correlation length $l = 1.05\lambda$ and 800 unknowns for one realization. (i) $n = 10$, $b = 50$; (ii) $n = 20$, $b = 50$; (iii) $n = 10$, $b = 60$.

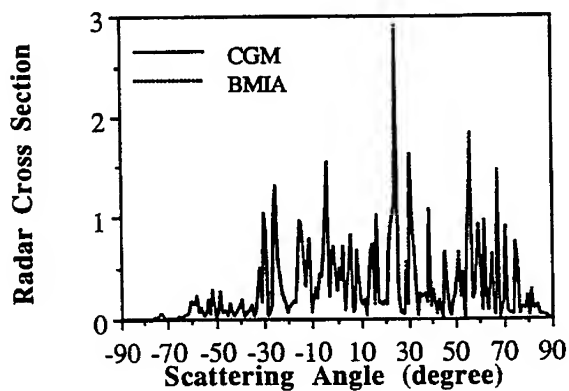


Figure 2. Comparison of bistatic radar cross sections using BMIA and EMI at 80° incidence. The surface length $L = 100\lambda$, rms height $h = 0.575\lambda$, correlation length $l = 1.05\lambda$, $b = 90$, $n = 10$ and 800 unknowns for one realization.

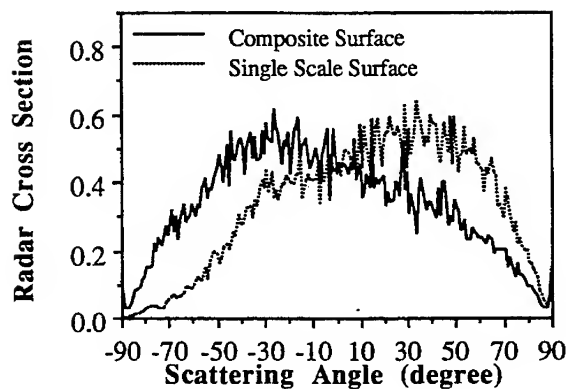


Figure 3. Comparison of bistatic radar cross sections of the assemble average of 100 realizations of two random rough surfaces. The single scale surface has ($h = 3\lambda$ and $l = 10\lambda$). The composite surface is a summation of two independent zero mean gaussian surfaces with rms heights and correlation lengths ($h_1 = 3\lambda$, $l_1 = 10\lambda$) and ($h_2 = 0.3\lambda$, $l_2 = 0.6\lambda$), respectively. BMIA is used for both cases. The surface length is 400 wavelengths with 3200 unknowns.

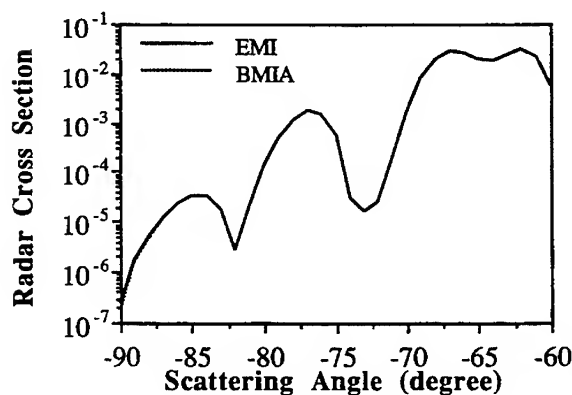


Figure 4. Comparison of bistatic radar cross sections of a surface length 400 wavelength random surfaces ($h = 3\lambda$ and $l = 10\lambda$) calculated by BMIA and CGM for a single realization. Number of unknowns is 3200.

A Banded Matrix Iterative Approach to Monte Carlo Simulations of Large-Scale Random Rough Surface Scattering: Penetrable Case

by

C. H. Chan, L. Li and L. Tsang
Electromagnetics and Remote Sensing Laboratory
Department of Electrical Engineering, FT-10
University of Washington
Seattle, Washington 98195

Introduction

Monte Carlo simulation of one-dimensional penetrable rough surfaces has been a topic of continued study for many years because of its broad applications. The most common method used in solving random rough surface scattering problems is the integral equation method [1-4] with a Gaussian tapered incident wave. A large surface is required to include many correlation lengths. Unlike the perfectly conducting random rough surface case in which the unknowns are the field values sampled on the surface, two unknowns are required for each sample point on the penetrable surface, namely, the field on the surface (Ψ) and its normal derivative ($\partial\Psi/\partial n$). In the actual implementation, the discretized $\partial\Psi/\partial n$ can be related to those of Ψ through a matrix inversion followed by two matrix multiplications. Therefore, the memory and CPU time required for the penetrable case is about twice that of the perfect conducting case for the same surface length. Consequently, the application of the integral equation method to a large scale penetrable surface is limited by the available computer memory and CPU time. Furthermore, for the Monte Carlo simulation, the scattered field intensity is averaged over many realizations and, hence, it is important to minimize the computation time for each realization.

In this paper, we discuss the implementation of a banded matrix iterative approach (BMIA) [5] which allows us to perform Monte Carlo simulations of random penetrable rough surfaces of much larger surface length than otherwise can be studied. Numerical studies show that BMIA is faster than the conventional matrix inversion method as well as other iterative schemes such as the conjugate gradient method (CGM).

Integral Equation Formulation

The scattered field from a penetrable rough surface shown in Fig. 1 can be solved using the coupled integral equation. If the fields on either side of the surface S are denoted by Ψ_1 and Ψ_2 , respectively, for medium 1 and medium 2, they satisfy the following equation [3]:

$$h_1 \Psi_1(r) = h_2 \Psi_2(r) + \int_S \left[\Psi_1(r') \frac{\partial G_i(r, r')}{\partial n'} - G_i(r, r') \frac{\partial \Psi_1(r')}{\partial n'} \right] dr' \quad (1)$$

$$h_1 = 0.5 \text{ and } h_2 = 1 \text{ when } i = 1; h_1 = -0.5 \text{ and } h_2 = 0 \text{ when } i = 2,$$

where \int_S denotes a Cauchy integral and G_i is the Green's function in medium i . Ψ_1 and Ψ_2

are related through the boundary conditions on the surface S, namely,

$$\Psi_1(r) = \Psi_2(r) \text{ and } \frac{d\Psi_1(r)}{dn} = \frac{1}{\rho} \frac{d\Psi_2(r)}{dn} \quad (2)$$

where ρ equals μ_1 / μ_2 and ϵ_1 / ϵ_2 for TE and TM polarizations, respectively. Applying the boundary conditions in conjunction with the point-matching method, we arrive at a matrix equation

$$\Psi_{in}(x_m) = \sum_{n=1}^N a_{mn} F_1(x_n) + \sum_{n=1}^N b_{mn} F_2(x_n) \quad (3)$$

$$0 = \sum_{n=1}^N c_{mn} F_1(x_n) - \sum_{n=1}^N \rho d_{mn} F_2(x_n) \quad (4)$$

where $F_1(x) = \Psi_1(x)$ and $F_2(x) = \sqrt{1 + f(x)^2} \partial \Psi_1 / \partial n$, respectively, and $x_m = (m-0.5) \Delta x - L/2$. a_{mn} and c_{mn} are functions of $f(x_n)$, $f(x_m) - f(x_n)$ and $H_1^{(1)}(k|r_m - r_n|)$. b_{mn} and d_{mn} , on the other hand, are functions of $H_0^{(1)}(k|r_m - r_n|)$. k is equal to k_1 for a_{mn} and b_{mn} and is equal to k_2 for c_{mn} and d_{mn} . Note that when the dielectric is lossy, c_{mn} and d_{mn} involve evaluations of Hankel functions with complex argument.

In the conventional matrix solution, F_2 is eliminated in Eq. (3) through the relation in Eq. (4). However, such elimination is not possible for an iterative solution.

Banded Matrix Iterative Approach for the Penetrable Case

To apply BMIA, the two sets of unknowns F_1 and F_2 are labeled alternatively along the one-dimensional surface discretized with N sample points resulting in the matrix equation as follows:

$$\begin{bmatrix} a_{11} & b_{11} & a_{12} & b_{12} & \dots & a_{1N} & b_{1N} \\ c_{11} & -\rho d_{11} & c_{12} & -\rho d_{12} & \dots & c_{1N} & -\rho d_{1N} \\ a_{21} & b_{21} & a_{22} & b_{22} & \dots & a_{2N} & b_{2N} \\ \dots & \dots & \dots & \dots & \dots & \dots & \dots \\ c_{N1} & -\rho d_{N1} & \dots & \dots & \dots & c_{NN} & -\rho d_{NN} \end{bmatrix} \begin{bmatrix} F_1(x_1) \\ F_2(x_1) \\ F_1(x_2) \\ \vdots \\ F_2(x_N) \end{bmatrix} = \begin{bmatrix} \Psi_{in}(x_1) \\ 0 \\ \Psi_{in}(x_2) \\ 0 \\ \vdots \\ \Psi_{in}(x_N) \end{bmatrix} \quad (5)$$

or

$$\bar{\bar{Z}} \bar{\bar{F}} = \bar{\bar{C}} \quad (6)$$

In BMIA, the matrix $\bar{\bar{Z}}$ is divided into a banded matrix $\bar{\bar{Z}}^{(s)}$ representing strong interactions and the remainder of the matrix $\bar{\bar{Z}}^{(w)}$ representing weak interactions

$$\bar{\bar{Z}} = \bar{\bar{Z}}^{(s)} + \bar{\bar{Z}}^{(w)} \quad (7)$$

It is evident that the matrix $\bar{\bar{Z}}$ is asymmetric. The iterative solution is given as

$$\bar{\bar{Z}}^{(s)} \bar{F}^{(1)} = \bar{C} \quad (8)$$

$$\bar{\bar{Z}}^{(s)} \bar{F}^{(n+1)} = \bar{C} - \bar{\bar{Z}}^{(w)} \bar{F}^{(n)} = \bar{C} - \bar{D}^{(n)} \quad (9)$$

To determine the convergence of the BMIA, we can define a residual as

$$\bar{R}^{(n)} = \bar{C} - \bar{\bar{Z}} \bar{F}^{(n)} \quad (10)$$

It is not difficult to see that

$$\bar{R}^{(1)} = -\bar{D}^{(1)} \quad (11)$$

and

$$\bar{R}^{(n)} = \bar{D}^{(n-1)} - \bar{D}^{(n)} \quad (12)$$

There truncation criterion of the iterative procedure is then defined as

$$\sqrt{\frac{\langle \bar{R}^{(n)}, \bar{R}^{(n)} \rangle}{\langle \bar{C}, \bar{C} \rangle}} \times 100 \% < \epsilon \quad (13)$$

For solving a large problem, only the banded matrix $\bar{\bar{Z}}^{(s)}$ is stored and the remainder of the matrix $\bar{\bar{Z}}^{(w)}$ is recomputed for every iteration. To eliminate the need of repetitive calculations of Hankel functions with complex arguments for the lossy penetrable surface, we create a look-up table which allows efficient evaluation of $\bar{\bar{Z}}^{(w)}$ through interpolations.

Numerical Results

All the numerical results shown in this section are computed on a Vax-6000-440 computer. Medium 1 in Fig. 1 is assumed to be free space and medium 2 has a dielectric constant of $(5 + i2)$. The incident angle is fixed at 10° and the tapering factor [3] of the incident field is equal to 4. Δx is set at 0.1λ where λ is the free-space wavelength.

Figure 2 shows the comparison of bistatic normalized cross sections calculated by the exact matrix inversion method (EMI) and BMIA for one realization. The incident wave is TM polarized. The surface length L is 100λ , the root-mean-square height h is 0.575λ and the correlation length l is 1.05λ . The number of unknowns in this example is 2000. While BMIA solves for a 2000×2000 matrix, EMI only inverts matrices of 1000×1000 . BMIA with 3 iterations completely overlies EMI. The half-bandwidth is 13λ . Figure 3 shows the comparisons of CPU between EMI and BMIA for various half-bandwidths. BMIA with a look-up table and interpolations is six times faster than EMI at the optimal half-bandwidth of 13λ .

Figure 4 shows the comparison of normalized scattering sections using BMIA and CGM for one realization. The incident wave is TE polarized. The surface length and statistics of the surface are: $L = 150 \lambda$, $h = 2.875 \lambda$ and $l = 5.25 \lambda$. The number of sample points on the surface is 1500 which is too big for EMI. We compare the normalized cross

sections calculated by BMIA with the half-bandwidth equal to 17λ and CGM. In the CGM, the banded portion of the matrix is stored while the remainder of the matrix elements are recomputed for each iteration. Excellent agreement between results obtained by BMIA and CGM is achieved. Figure 5 shows the convergence of BMIA and CGM. For each iteration, the CPU time for CGM is about 9.5 minutes. For BMIA, the first iteration which only involves a banded matrix (strong interaction) solution is 6.33 minutes. For the subsequent iteration which involves one banded matrix solution and a weak interaction matrix multiplication takes 8.5 and 15.5 minutes with and without look-up table interpolations, respectively. To truncate the iterative process for the same percentage error, CGM requires as many as 100 iterations while BMIA only requires 3. BMIA is definitely more efficient than CGM.

Figures 6a and 6b show the Monte Carlo simulation of 200 realizations of the surface used in Fig. 4 for $L = 150$ and 75λ , respectively. The presence of the third peak around -50° in Fig. 6b indicates that the surface length 75λ is not long enough for the large correlation length of 5.25λ .

Conclusions

In this paper, we have employed the banded matrix iterative approach to perform Monte Carlo simulations of random penetrable surfaces. BMIA is much faster than both the exact matrix inversion method and the conjugate gradient method. BMIA only stores the banded portion of the matrix and hence, it allows one to solve a larger problem than the conventional method.

Acknowledgments

This work is in part supported by the National Science Foundation (****)

References

- [1] R. M. Axline and A. K. Fung, "Numerical computation of scattering from a perfectly conducting random surface," *IEEE Trans. Antennas Propagat.*, vol. AP-26, pp. 482-488, 1978.
- [2] A. A. Maradudin, E. R. Mendez, and T. Michel, "Backscattering effects in the elastic scattering of p-polarization light from a large amplitude random grating," in *Scattering in Volumes and Surfaces*, M. Nieto-Vesperinas and J. C. Dainty eds., Elsevier Science Publishers, North-Holland, 1990.
- [3] E. I. Thorsos, "The validity of the Kirchhoff approximation for rough surface scattering using a Gaussian roughness spectrum," *J. Acoust. Soc. Am.*, vol. 83, pp. 78-92, 1988.
- [4] J. S. Chen, "Wave scattering from very rough surfaces and a study of backscattering enhancement," Ph. D. Dissertation, University of Washington, Seattle, 1990.
- [5] L. Tsang, C. H. Chan and H. Sangani, "Application of a banded matrix iterative approach to Monte-Carlo simulations of scattering of waves by random rough surface: TM case," *Microwave and Optical Technology Letters*, in press, 1993.

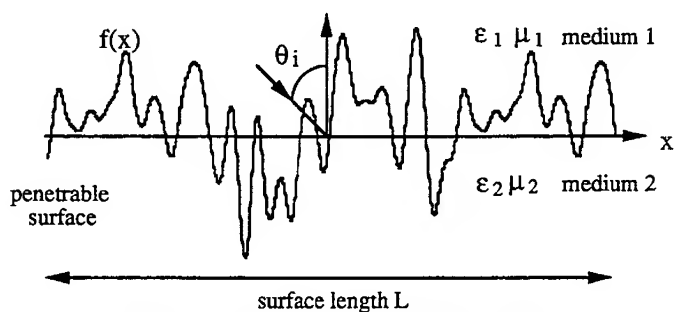


Figure 1. A random rough penetrable surface.

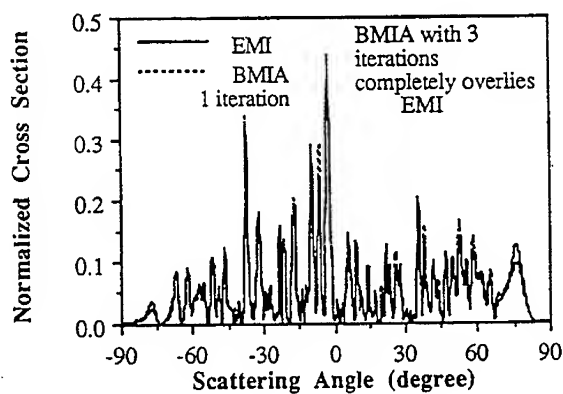


Figure 2. Comparison of bistatic normalized cross sections calculated by EMI and BMIA for one realization.

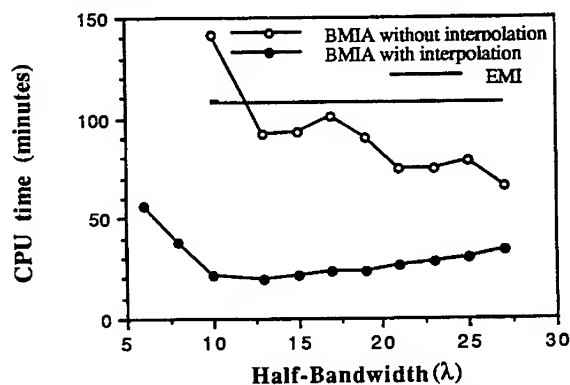


Figure 3. Comparisons of CPU between EMI and BMIA for various half-bandwidths.

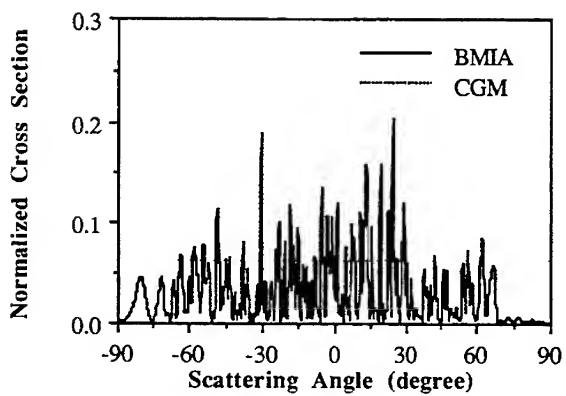


Figure 4. Comparison of normalized scattering cross sections using BMIA and CGM for one realization.

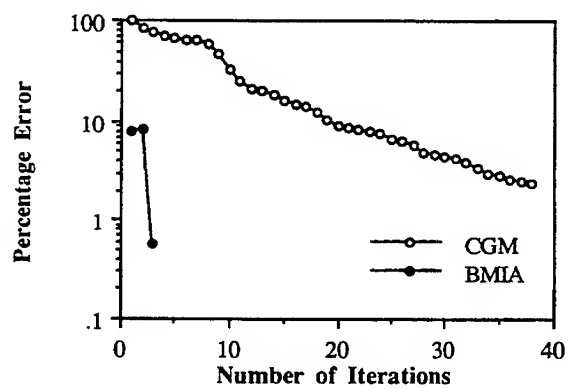
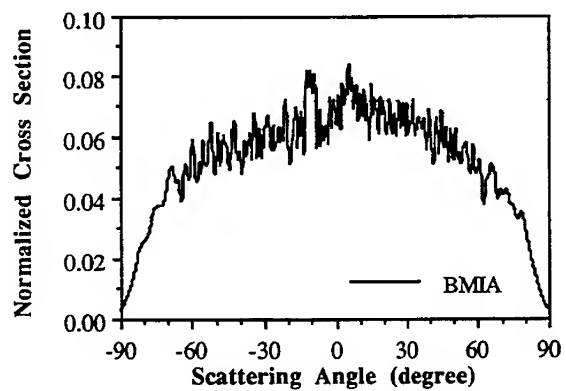
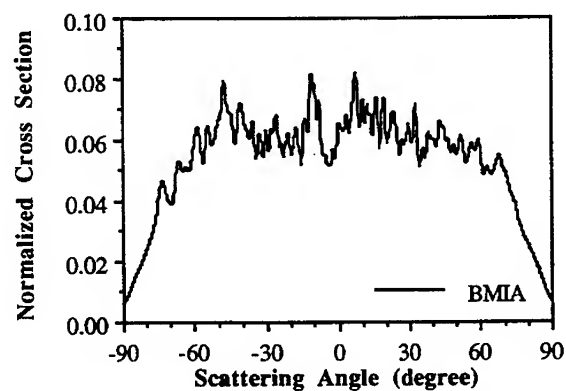


Figure 5. Convergence of BMIA and CGM.



(a)



(b)

Figure 6. Monte Carlo simulations of penetrable random rough surfaces. (a) $L = 150 \lambda$ and (b) $L = 75 \lambda$.

SESSION 12 - "BIOELECTROMAGNETIC COMPUTATIONS"

Chair: Dr. Imre Gyuk

BIO-ELECTROMAGNETIC COMPUTATION IN THE LOW FREQUENCY RANGE: AN INTRODUCTION

Imre Gyuk, EMF Program Manager, U. S. Department of Energy

Biological Effects of Electric and Magnetic Fields

In recent years it has become increasingly clear that electric and magnetic fields (EMF) of low frequency (<150 Hz) and fairly low intensity (<1 Gauss) can have biological effects - usually under carefully controlled laboratory conditions. Correspondingly, there has also been increasing concern that these biological effects might result in health effects.

Although the energy involved in electric and magnetic fields (EMF) of extremely low frequency is quite small, there is a common consensus that there are indeed biological effects due to these fields. The locus of cell-field interaction is apparently the cell membrane. In particular, it is the flux of calcium ions and other biologically important messengers which appears to be altered by the presence of EMF. Following changes at the cell surface, the subsequent cascade of intracellular processes, can be altered as well. Although there is not enough energy for direct interaction with DNA, gene expression and protein synthesis are apparently affected. Melatonin represents an important hormone linked to diurnal rhythms of the body and regulating most other hormone systems. Even short exposure of rodents to EMF may affect the nightly rise of production of this hormone. Sheep, baboons and humans may be more resistant. There is also some indication that EMF may influence the immune system. Although experimentation with humans must proceed with extreme caution, it has been shown that human heart rate is slightly lowered by mixed EMF. Human reaction time is apparently also decreased.

Unlike ionizing radiation or most other chemical factors, the effect of EMF at low frequencies appears to be highly non-linear. In fact, there seem to be 'windows' in intensity range and possibly even resonance like phenomena. Intermittency, transients, and, perhaps, the geomagnetic field may play a role. The dose effect relationship is little known thus far.

Observed effects are to be considered as biological effects only - they do not constitute actual health effects. Nonetheless, concern is focused by these studies on potential risks of abnormal cell growth, reproductive issues and neurophysiology. Epidemiological studies have not yielded conclusive evidence of health hazards. Instead, there appears to be a linkage of diseases such as childhood leukemia with exposure surrogates such as wiring codes. Risk factors appear to have a value of 2.0 approximately, barely out of the noise level.

Interest and attention of potential health effects of EMF have largely been focused on power transmission lines. However, more recently, concern has widened to distribution lines, electrical transportation modes and electrical appliances. In particular, concern over potential health effects of EMF may well result in serious impediments to the introduction of novel technologies such as magnetically levitated trains (maglev), superconducting magnetic energy storage (SMES), electric cars, robotics and a host of other applications.

Calculation of Fields from Complex Sources

Maxwell's equations, particularly in their covariant form, have an ineffably beautiful simplicity, unrivalled by any other relation in the physical universe. But unfortunately, gross reality soon disturbs this elegance and forces us into more and more elaborate schemes of calculation and evaluation. Certainly, the tangle of wires represented by a substation is a far cry from vacuum electrodynamics. Yet, with increasing public concern about possible health effects from EMF, it becomes important to calculate fields due to fairly complex geometries. Facilities impinging electrically on our daily lives from substations to the distribution network and house wiring, from the subway to office equipment, not forgetting toasters and telephones, electric shavers, blankets and hairdriers, suddenly become worthwhile objects of calculational virtuosity.

Appropriate codes must be developed to allow generic evaluation of fields due to a wide variety of facility or equipment. As field considerations become criteria of design, such codes must be made interactive, so that the engineer can develop design solutions minimizing external fields. Graphic display may give considerable help in this task.

Exposure Studies

Although accurate evaluation of fields from specific sources is important, this does not yet give us the field as experienced by a person. To determine the 'exposure', the pattern of movement among various sources or the method of utilizing an electrical appliance must be taken into account. Some measurements have been taken by attaching portable field meters to individuals. Time analysis of such measurements indicates rather spiky, almost fractal, fluctuations in value. Very little theory is yet available to connect measured or calculated field values with this empirical exposure. A statistical approach would appear to be indicated - something reminiscent of a probabilistic Greens function to relate sources to human exposure.

Epidemiology underscores both the difficulty and the importance of the exposure issue. Residential epidemiological EMF studies attempt to relate the incidence of rare diseases like childhood leukemia to residences divided into a number of exposure classes. Although statistically significant correlations have been found between disease and exposure class, no direct relation to actual measurements has been proven. Most occupational studies attempt to relate disease incidence to job classifications such as 'electrical transport worker'. Here too, some significant correlations have been found. Obviously a much better connection with source fields is essential, particularly since people, except very young children, spend about a third of their time at home and a third at school or work.

Dosimetry

Given the external fields, it yet remains to be determined what the actual dosage received by a human or animal will be. In the case of most environmental toxins one is dealing with a single parameter, such as parts per billion in the ambient air. One then has to determine what percentage will be deposited in the lungs of a person. For electric and magnetic fields this problem is much more complicated. One deals with many more parameters: field strengths for both

electric and magnetic fields, angles and phases between them, frequency distribution, intermittency and transients - even the angle with the earth magnetic field may be of importance. At this time we do not know which of the parameters are biologically relevant. It is not even clear whether cells interact with induced currents or with the fields directly.

Dosimetry, the calculation of current and field distributions inside the body of an animal or a human becomes an important, and by no means trivial task. Originally, estimates were made considering a mouse as half of a prolate spheroid. Later, the body was subdivided into biological zones with more detailed boundary conditions. Actually, matters are rather more complicated, because biological organisms are not only inhomogeneous, but they are so in a minutely organized fashion. Tissues, bones, blood vessels, and nerves, each with quite different electrical properties, do not occur at random. Instead they are organized into extensive structures.

The situation becomes even more complex, because the creatures just won't sit still ! As a human walks under a transmission line, a baboon sits down in his metal cage or rats shield each other from electric fields by huddling. Field values, let alone the induced currents vary wildly. Moreover, transients, which may be biologically very important, will be occurring throughout.

Biophysics of Interaction

Once an adequate evaluation of fields and currents inside the body has been obtained, one still has to find a mechanism of interaction with the cell surface. At 60 Hz, a wavelength stretches from Washington to Monterey. The energy available for interaction is, therefore, truly minute. Moreover the applied fields have to compete with substantial endogenous fields on the one hand and random thermal motion on the other. One can imagine that collective phenomena involving integration over time and space are at work. The structure of the cell membrane has to take relatively minute differences and compound them into qualitative, localized phenomena (the Ising model comes to mind). Alternatively, to avoid the limit of random noise, superfast non-equilibrium processes, such as free radical formation, may be occurring. In either case, the relationship between field and effect will certainly be non-linear. Numerical evaluations may well have to deal with the realm of chaotic phenomena. Indications from the biology seem to support this.

Conclusion

Obviously, the increasing concern for electric and magnetic fields in our environment and their potential health effects, presents a considerable challenge to the mathematician, engineer or physicist. Fields due to a variety of sources need to be calculated with a view to field management through design. Actual exposure must be determined to interface with epidemiology. Dosimetry must calculate the changing field and current distribution throughout the body. Finally, on a microscopic and very fundamental level, the interactions between field and cell need to be determined.

CALCULATION OF ELECTRIC AND MAGNETIC FIELDS NEAR GROUND LEVEL IN 187KV AC SUBSTATION

by

K. Isaka, N. Hayashi, and Y. Yokoi

Department of Electrical and Electronic Engineering, Faculty of
Engineering, The University of Tokushima, Tokushima, Japan 770

In order to calculate electric fields, the complex electrode systems are approximated by cylindrical conductor segments each of which has uniform charge on its outer surface. In addition, the charge simulation method is applied to predict the shielding effect by a tree. As for the magnetic fields, the current-carrying conductors are approximated by straight line segments, to each of which the Biot-Savart law is applied. The predictions are compared with the measured results.

1. INTRODUCTION

In 1970's the characterization of electric fields near ground level in electric power substations came to be needed for the evaluation of possible occupational health problems of substation workers. The analog (reduced scale) modeling was used to determine the electric field distributions in a 345 kV substation in the late 1970's (Sebo and Caldecott, 1979). Due to the increased interest in magnetic field effects since 1979, a number of studies have been made regarding the characterization of magnetic fields from power systems and at homes as well. However, only a small number of papers dealing with substation magnetic field characteristics are found in the literature. In The Ohio State University the extensive research on 345kV substation magnetic fields is being performed using both the analog and digital modeling techniques (Sebo et al., 1989 ; Kasten et al., 1989 ; Caldecott et al., 1991 ; Kasten et al., 1991 ; Sebo, 1991).

We made the studies on magnetic field distributions in a 187kV substation by using the digital modeling(Hayashi et al., 1989 and 1992). In parallel with those studies, the analysis of the electric field characteristics was made. Although the calculations of electric fields in substations cannot be easily handled because of complex physical systems of electrical wirings, the computer modeling technique was applied to make a trial calculation of electric fields. So far there is little literature on substation electric field calculations.

This paper describes the calculated results of electric and magnetic fields and their comparisons with the experimental ones. All calculations and measurements have been related to one meter height above ground level.

Figure 1 shows the layout plan of the 187 kV switchyard of a 187/66 kV substation as well as the location of calculations and measurement traverses (broken lines denoted by #1, #2, #3, and #4). The one-line diagram of the two-bus arrangement examined is shown in Figure 2. The current distribution on the bus and line conductors, as indicated in Figure 2, was numerically determined and partly estimated using the substation operation data during the experiments. It is assumed in the calculations that the current distribution is constant throughout the experiments. Actually the variations of current magnitudes were several percent for the measurement period.

The diagram shows a horizontal transmission line with five buses labeled #1, #2, #3, #4, and #5 from left to right. Below the line, there are three transformers labeled 'To TR (300MVA)', 'To TR (120MVA)', and 'To TR (200MVA)'. The line segments between buses have impedances: 152 between #1 and #2, 556 between #2 and #3, 250 between #3 and #4, and 375 between #4 and #5. There are also shunt impedances at each bus: 403 at #1, 403 at #2, 341 at #3, 16 at #4, and 15 at #5. The transformers are connected to the line at buses #2, #3, and #4 with impedances of 540, 216, and 360 respectively.

404

3. CALCULATION OF ELECTRIC FIELDS

The following assumptions are employed in the calculations: (1) Metallic structures are neglected, (2) No free charges exist in the air, (3) The earth is a perfect conductor, (4) The substation apparatuses and line conductors can be approximated by cylindrical conductor segments, (5) The effect of the bus can be ignored when calculating electric fields in the areas remote from the bus.

The elevation of the current transformer (CT), gas-insulated circuit breaker (GCB), lightning arrester (LA), and the line conductors is shown in Figure 3. As the first approximation, each apparatus is replaced by a cylindrical conductor having the uniform distribution of surface charge on its outer surface (Zahn, 1979). The calculation method employed in this study is the same as used for the analysis of transmission line electric field shielding by objects (Deno et al., 1987) except that the distribution of charge density on each segment is assumed to be constant instead of being linearly varying from one end to the other.

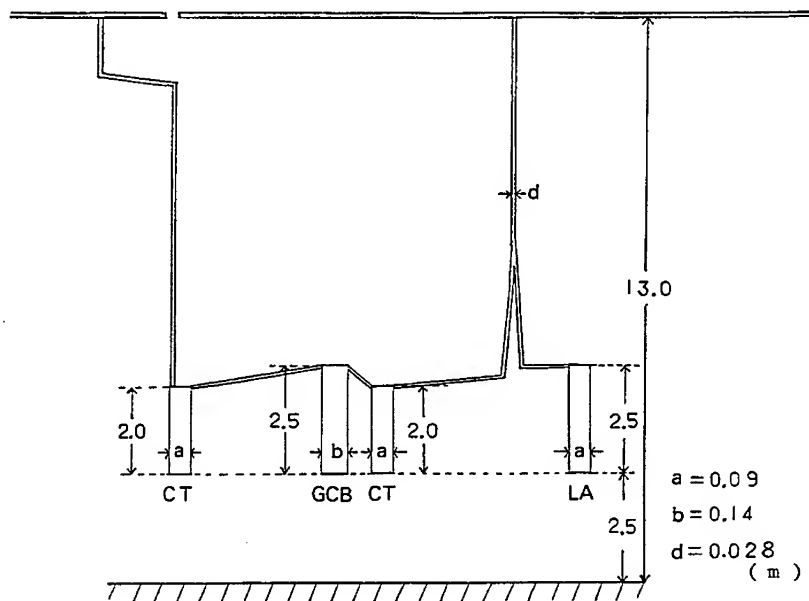


Figure 3. Elevation of apparatuses and lines approximated by cylindrical conductor segments. The apparatuses are placed at a height of 2.5 m above ground level (CT: current transformer, GCB: gas-insulated circuit breaker, LA: lightning arrester).

Figure 4 shows the electric field profile along the path #1 together with the experimental results. The disagreement between the calculated and experimental results is partly due to the electrostatic shielding effects by the trees and the metallic fence. In order to calculate the electric field profile along the path #2 having a tree at its ending position, the effect by a tree is taken into consideration. The tree examined is cone-shaped as shown in Figure 5, which is 4.0 m in height, and approximately axisymmetrical. The method presented here uses the approximation of the tree as the grounded object. The charge simulation method (Singer et al., 1974) is employed, in which the fictitious ring charges are distributed so that the potentials of the tree's surface contour points become all zero. Figure 6 shows how 8 ring charges are placed on a horizontal cross-section of the tree. It is found from Figure 7 that the calculated results agree well with the experimental ones.

Since the effects of the bus and the metallic structures supporting the apparatuses on field calculations are neglected, the field profiles along the paths #3 and #4, which are closer to the bus and apparatuses, cannot be discussed here.

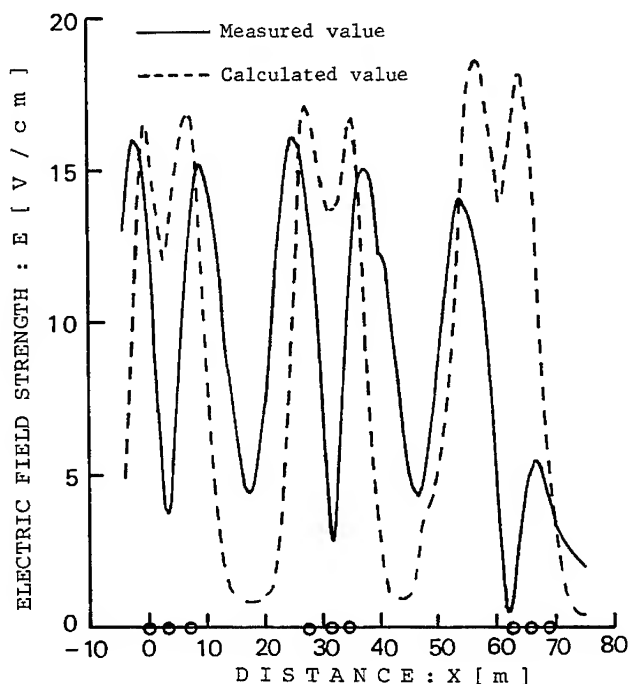


Figure 4. Profile of electric fields along the path #1.



Figure 5. Shape of tree examined.
(4 m in height and axi-
symmetrical)

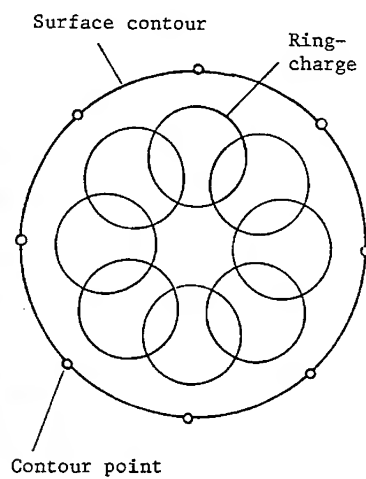


Figure 6. Ring-charges placed on
horizontal cross-section.

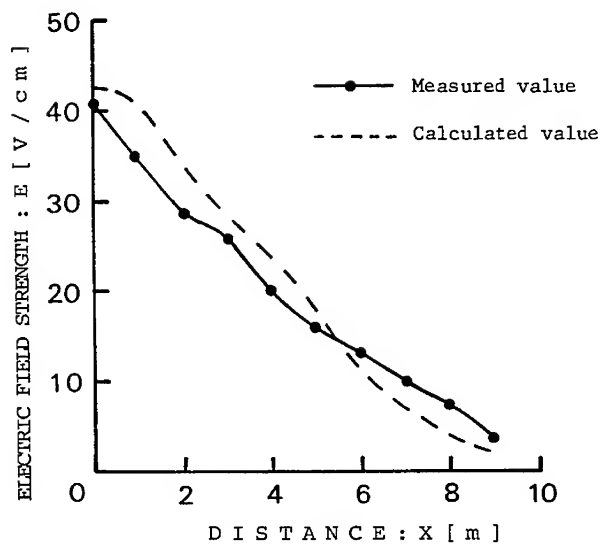


Figure 7. Profile of electric fields along the path #2
having a tree at its ending position.

4. CALCULATION OF MAGNETIC FIELDS

The following assumptions are employed in the calculations of power frequency magnetic flux density: (1) Metallic structures are neglected, (2) The three-phase currents are balanced, (3) The current path can be approximated by straight line segments, and the current on each segment is constant, (4) The earth is non-magnetic, (5) No image current is taken into account, and (6) Currents induced in counterpoise wires and ground wires are ignored.

A closed form solution of the Biot-Savart law developed for a straight line segment is used (IEEE Magnetic Fields Task Force, 1988). All current-carrying conductors are approximated by 450 straight line segments. Figures 7 and 8 show the results calculated along the paths #1 and #4, respectively, together with the experimental ones. It is found that a reasonably good agreement has been obtained between the predictions and experiments. The digital modeling technique has also been used (Sebo, 1991), and a user-friendly computer program is being developed (Pappa and Ben-Yaacov, 1992).

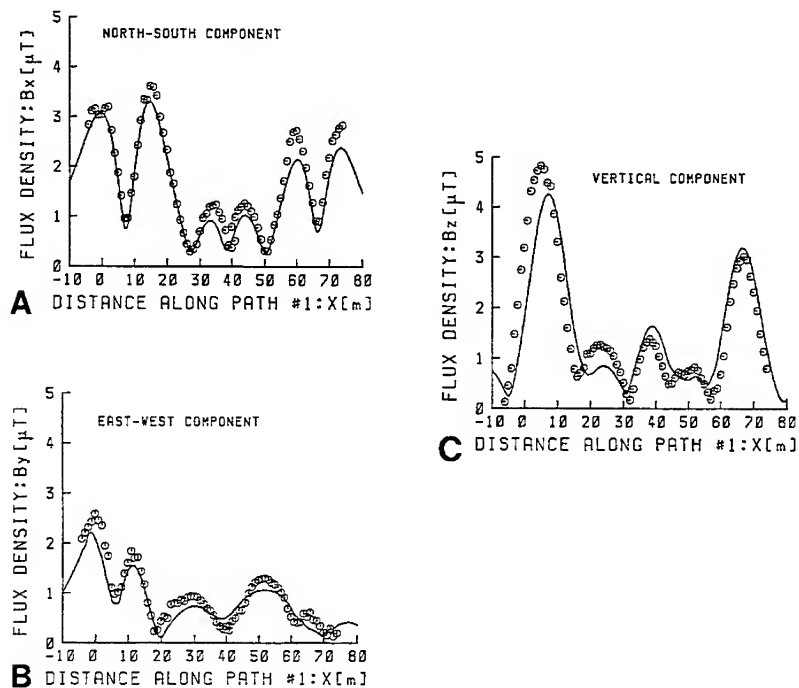


Figure 8. Profiles of magnetic fields along the path #1.
(solid line: calculated, circle: measured)

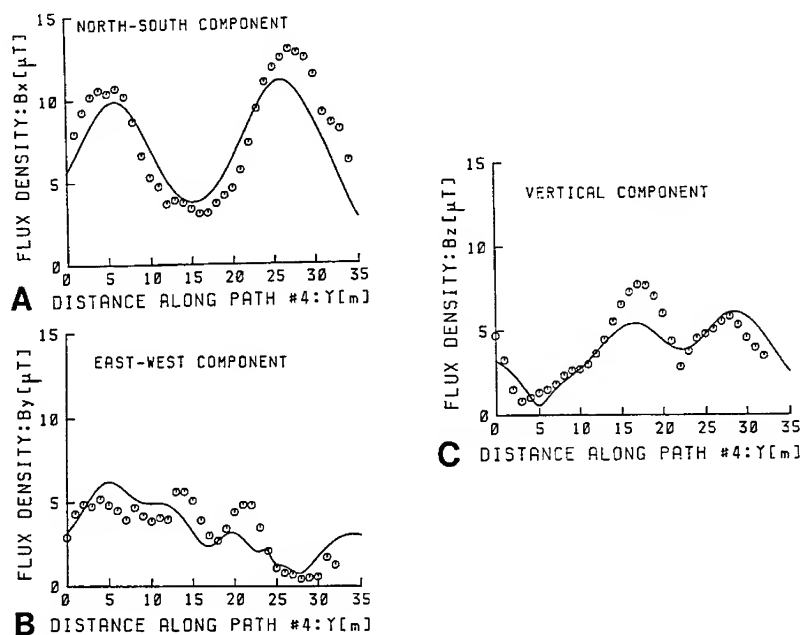


Figure 9. Profiles of magnetic fields along the path #4.
(solid line: calculated, circle: measured)

5. CONCLUSIONS

The substation electric and magnetic fields have been calculated. It is shown that the electric fields at locations remote from the bus can be predicted with roughly approximated electrode systems. It is found from this study that the Biot-Savart law is applicable to the prediction of substation magnetic fields once the current paths are exactly identified.

Generally, both the energized and grounded objects affect the characteristics of electric fields to a greater extent than those of magnetic fields. Even the trees provide a remarkable effect of electrostatic shielding. The calculated results described in this paper are very limited. More research is still needed for the precise computer modeling of substation electric fields.

ACKNOWLEDGMENTS

The authors would like to thank Messrs. M. Okamoto, S. Hase, K. Kume, T. Matsumoto, and Y. Kamiji for their technical assistance, and to express their appreciation to Shikoku Electric Power Co., Ltd., for

its support of this work. This work was funded in part by a Grant-in-Aid for Scientific Research from the Ministry of Education, Science, and Culture, Japan.

REFERENCES

- Caldecott, R., English, W. E., Sebo, S. A., and Addis, G. I. (1991): Scale modeling of the electromagnetic field in hv ac substations, Proceedings of the 7th International Symposium on High Voltage Engineering, Dresden, Germany, Paper No. 93.08.
- Deno, D. W., Zaffanella, L. E., and Silva, J. M. (1987): Transmission line electric field shielding by objects, IEEE Trans. on Power Delivery, Vol. 2, No. 1, pp. 269-279.
- Hayashi, N., Isaka, K., and Yokoi, Y. (1989) : ELF electromagnetic environment in power substation, Journal of the Bioelectromagnetic Society, Vol. 10, No. 1, pp. 51-64.
- Hayashi, N., Isaka, K., and Yokoi, Y. (1992) : Analysis of 60-Hz magnetic fields near ground level in 187-kV switchyard of a 187/66-kV ac substation, IEEE Trans. Power Delivery, Vol. 7, No. 1, pp. 237-244.
- IEEE Magnetic Fields Task Force (1988) : Magnetic fields from electric power lines -theory and comparison to measurements-, IEEE Trans. on Power Delivery, Vol. 3, No. 4, pp. 2127-2136.
- Kasten G. D., Zhang, W., and Addis, G. I. (1991) : Calculation of the magnetic flux density in high voltage ac substations, Proceedings of the 7th International Symposium on High Voltage Engineering, Dresden, Germany, Paper No. 93.02.
- Kasten, G. D., Sebo, S. A., and Caldecott, R. (1989) : Development of a computer program for modeling of magnetic fields in high voltage ac substations, Proceedings of the 6th International Symposium on High Voltage Engineering, New Orleans, USA, Paper No. 24.05.
- Pappa, J., and Ben-Yaacov, G. (1992) : Windowed access to electric and magnetic fields software, IEEE Computer Applications in Power, Vol. 5, No. 4, pp. 24-28.
- Sebo, S. A. (1991) : Magnetic fields in substations, prepared for the panel session of Effects of Transmission and Distribution Design Parameters and Constraints on Magnetic Fields at the 12th IEEE/PES T&D Conference and Exhibition, Dallas, Texas.
- Sebo, S. A., Caldecott, R., and Kasten, G. D. (1989): Analog modeling of magnetic fields in high voltage ac substation, Proceedings of the 6th International Symposium on High Voltage Engineering, New Orleans, USA, Paper No. 40.04.
- Sebo, S. A., and Caldecott, R. (1979) : Scale model studies of ac substation electric fields, IEEE Trans. on Power Apparatus and Systems, Vol. PAS-98, No. 3, pp. 926-939.
- Singer, H., Steinbigler, and Weiss, P. (1974): A charge simulation method for the calculation of high voltage fields, IEEE Trans. Power Apparatus and Systems, Vol. 93, pp. 1660-1668.
- Zahn, N. (1979) : Electromagnetic field theory, p. 71, John Wiley & Sons.

NUMERICAL METHODS FOR DOSIMETRIC CALCULATIONS: ELF TO MICROWAVE FREQUENCIES

Om P. Gandhi
Department of Electrical Engineering
University of Utah
Salt Lake City, Utah 84112

We will review some of the efficient numerical methods that have been used for calculations of internal E- and H-fields, induced currents, and specific absorption rates (SARs) in anatomically based models of the human body. The methods to be discussed are the impedance method and the finite-difference time-domain (FDTD) method. In the impedance method, usable for low-frequency exposures where quasi-static approximation may be made (≤ 30 MHz for the human body), the biological body or the exposed parts thereof may be represented by a three-dimensional network of impedances whose individual values are obtained from the complex conductivities $\sigma + j \omega \epsilon_0 \epsilon_r$ for the various locations of the body. This method is capable of allowing for anisotropic properties (σ , ϵ_r) for various tissues that are important in the ELF region. The impedance method has, in the past, been used for a number of exposure situations, such as spatially variable vector-magnetic fields of an RF induction heater (450 kHz), linearly or circularly polarized H-fields of an MRI machine, or for hyperthermia applicators such as RF needles, capacitor plates, etc. Recently, the method has been used to calculate currents induced in the human body due to power-frequency magnetic fields of overhead transmission lines, electric hand drills, hair dryers, etc., for average tissue properties specified for cubic cells of dimensions 1.31 cm for each of the sides.

Using time-dependent Maxwell's curl equations, the FDTD method is usable at any frequency where the model has been discretized into cells of dimensions less than or equal to $\lambda_e/10$ where λ_e is the wavelength within the tissues with the highest complex dielectric constant $\epsilon^* (= \epsilon_r - j \sigma/\omega \epsilon_0)$. For bioelectromagnetic problems, the FDTD method has been found to be extremely versatile and has been used for induced current and SAR calculations for whole-body or partial-body exposures due to spatially uniform or nonuniform incident fields (far-field or near-field) that may be sinusoidally varying continuous-wave (CW) or transient, such as those for an electromagnetic pulse. Recently, the FDTD method has also been adapted for exposure of biological bodies to EMFs at power frequencies that may be sinusoidally varying or transient in nature. The method has also been modified to include frequency-dependent properties of the tissues and used to calculate time-dependent induced currents for exposure to nanosecond pulses with wide bandwidths in excess of 1 GHz.

In addition to describing some of the recent applications of these numerical methods from ELF to microwave frequencies, we will also show video displays of some of the calculated results.

THIS PAGE
INTENTIONALLY BLANK

A MATRIX FORMULATION OF DIELECTRIC IMAGING, DOSIMETRY AND COMPUTATION OF VECTOR ELECTROMAGNETIC FIELDS

Wendy W. Guo and Theodore C. Guo
Potomac Research, Inc., Potomac, Maryland 20854

Abstract

A matrix technique for dosimetry, scattering, and imaging of arbitrary three-dimensional objects is presented. An integral equation for the vector electric field is first derived from Maxwell equations, then converted to a sum of integrals over small cells (voxels). The unknown quantities are separated from the integrand and the remaining integral may be integrated analytically with some approximation or integrated digitally. The final formulation involves two matrix equations, one for fields inside (dosimetry) the target and another for fields outside (scattering). The scattering matrix equation may be inverted to yield an imaging equation, which gives the target's quantitative dielectric profile, both real and imaginary parts, in terms of the measured scattering fields; the matrix inversion is performed by a singular-value decomposition technique. Both scattering and dosimetry matrices are independent of the target and may be computed off-line once and for all. In this paper, the dosimetry and scattering results for homogeneous spheres are compared to those from Mie formula and are found to be accurate to the order of 10^{-3} or better for spheres discretized to 179 cells, and for a wide range of frequencies, with wavelength ranging from order of the target's size to 10^6 times the target's size. The imaging results for various highly inhomogeneous targets are shown to have a 3-D resolution of $1/35$ of the wavelength. Indeed, resolution as high as $1/165$ of the wavelength has been obtained and is found to depend only on signal-to-noise ratio, and independent of wavelength.

1. Introduction

Due to recent renewed interests in electromagnetic field environment and its biological effects,¹ there is increasing demand for an accurate and effective method for dosimetry and scattering computation. Analytic solution of vector electromagnetic fields may be obtained only in simple cases, such as Mie scattering from a uniform dielectric sphere or concentric spheres.^{2,3} Still, as we shall show, Mie formula does not provide a good solution for long wavelengths (comparing to the sphere size) due to slow convergence of the series expansion of $\exp(ikr\cos\theta)$ in spherical Bessel functions. For arbitrary objects, there are several numerical approaches, mostly for one-dimensional or two-dimensional objects. Born approximation by iteration may be used for weak scatterers, including three-dimensional objects, if it converges.⁴ The moment method developed by Richmond applies to scalar fields, viz. TE waves or TM waves, in two-dimensional objects with cylindrical symmetry.^{5,6} The moment method has been used on three-dimensional dielectric body,^{7,8} but it was found that the numerical solutions tend to diverge with respect to degree of discretization;⁹ a testing procedure was developed to analyze the numerical stability and reduce the computation time.¹⁰ These approaches approximate the field inside the scatterer by a linear combination of some basis functions and then numerically solve the linear coefficients. The finite element (FE) method has developed for bodies of revolution and for waveguide problems.^{11,12} Recently, it has been shown that the finite-difference time-domain (FDTD) method, originated by Yee¹³ and extended by Taflov and Brodwin,¹⁴ appears to be quite promising for two-dimensional geometry and time-dependent problems;¹⁵ though it has been applied to three-dimensional problems as well,¹⁶ it is still limited to simple 3D geometries and a homogeneous dielectric medium. The shortcoming of the FDTD method is that, due to the nature of the finite-difference algorithm which essentially solves Maxwell equations and fits boundary conditions from cell to cell, a field discontinuity between neighboring cells will artificially introduce fallacious dielectric discontinuities. Furthermore, the solution is sometimes unstable with respect to the truncation function which must be introduced to terminate the computation.^{14,15}

Here we present a matrix formulation for dielectric imaging and for computation of vector electromagnetic fields inside (dosimetry) and outside (scattering) arbitrary three-dimensional dielectric objects. It is based on discretization of the integral equation for the field.^{17,18} An integral equation for the vector electric field is first derived from Maxwell equations, then converted to a sum of integrals over small cells (voxels). The unknown quantities are separated from the integrand and the remaining integral may be integrated analytically with some approximation or integrated digitally. The final formulation involves two matrix equations, one for dosimetry and another for scattering. The scattering matrix equation may be inverted to yield an imaging equation, which gives the target's quantitative dielectric profile, both real and imaginary parts, in terms of the measured scattering fields; the matrix inversion is performed by a singular-value decomposition technique.^{18,19} Both dosimetry and scattering matrices are independent of the targets and may be computed off-line once and for all.

The difference between the matrix method presented here and other discretization method, such as the FE or FDTD methods, is that the matrix method discretizes the integral equation whereas FE and FDTD discretizes the differential equation. As a discretized integral equation, the fields in all cells are essentially solved simultaneously, where all boundary conditions between neighboring cells are included in the dosimetry and scattering matrices, denoted by G_s and G_v , respectively, and in the algorithm that they operate on the fields. On the other hand, in discretized differential equations, fields are matched from cell to cell by boundary conditions, therefore field discontinuities between neighboring cells may introduce fallacious dielectric discontinuities. As to the external boundary conditions, for example, boundary conditions with respect to surrounding apparatus, they are embedded in the incident field, which is defined as the field without the scatterer. One distinctive advantage of the matrix method is that, once the dosimetry and scattering matrices and their inversions are computed, field computation and imaging become trivial and take little computation time, even if the target is changed.

The matrix formulas provide a fast and accurate method for dosimetry and near- or far-field computation anywhere inside or outside a three-dimensional object with any distribution of dielectric permittivity and electric conductivity, both of which may be complex numbers, and for any form of incident field. To demonstrate the accuracy of the matrix technique, vector fields are computed inside and outside a uniform dielectric sphere for which fields from the analytic Mie formula are used for comparison. It is found that the matrix method provides a 99.9% accuracy for all three components of the fields for a sphere discretized to 179 cells. Furthermore, it is found that the small differences are mostly due to the fact that the two methods provide fields for two different objects, viz., discretized sphere and perfect sphere.

On dielectric imaging, since the matrix method does not rely on any Fourier transform relationship, such as that used in Fraunhofer or Fresnel diffraction method of imaging, the resolution is not limited by wavelength, though it will still be subject to limitation of signal-to-noise ratio. Many highly inhomogeneous target models have also been performed, and 3-D resolution of as high as $1/165$ of the wavelength has been obtained. Some of the imaging results are presented here; input scattering fields are computed by Mie formula when possible, and by the matrix method when the target is highly inhomogeneous. The results also show that, for targets much smaller than the cell size, such as a collection of small bubbles, the reconstructed image provides an accurate description of average dielectric permittivities within the cells. Dielectric imaging by RF or microwave inverse scattering may be applied to non-destructive evaluation, remote target identification, and medical imaging.^{20,24}

2. The Integral Equation

Consider that an electromagnetic wave is incident upon a target. As we are interested in the field inside as well as outside the target, we shall denote by V_0 the region occupied by the target, and by V a region outside where fields may be of interest. Either inside or outside the target, the term "scattering field" is to be defined as the difference between the total field and the incident field. The target is assumed to be electrically linear so that its response to a pulsing field may be Fourier transformed to a superposition of frequency components. Thus, for some frequency component of the incident field ω , let ϵ_m and $\epsilon(x)$ denote, respectively, the dielectric permittivity of the background medium and that of the target; both ϵ_m and $\epsilon(x)$ may have real and imaginary parts. Thus the quantity $\epsilon(x) - \epsilon_m$ vanishes outside V_0 . We shall limit the target to non-conductive and non-magnetic objects, though the formulation may be easily extended to include conductivities σ_m and $\sigma(x)$, as well as magnetic permeability μ_m and $\mu(x)$. Using Dirac's bra-ket notation for a linear space, with the space elements denoted by kets $|... \rangle$ and their conjugate elements denoted by bras $\langle ... |$, it can be shown that Maxwell's equations of the system may be written in the form: $M|f \rangle = 0$, where M represents Maxwell's differential operators and f the field quantities. Here $|f \rangle$ can be any combination of electric and magnetic fields or any of their derivatives, such as the one-dimensional scalar potential $|\varphi \rangle$, or the four-dimensional potential $|A \rangle = |\varphi, A \rangle$, etc.^{22,23} Specific expression of M depends on the definition of $|f \rangle$. In this paper we shall define f as the three-dimensional electric field E ; the expression of M for f being the four-dimensional potential has also been derived previously.²² The total field may be expressed as the sum of the scattering field and the incident field: $f = f^{(s)} + f^{(i)}$. We also separate the operator M into two parts: $M = M_m - S$, with M_m representing Maxwell's operator in a homogeneous background and $-S$ the operator due to the excess dielectric permittivity, $\epsilon(x) - \epsilon_m$. Then Maxwell's equation may be written as $M_m|f^{(s)} \rangle + M_m|f^{(i)} \rangle = S|f \rangle$. Since $M_m|f^{(i)} \rangle = 0$, the equation becomes: $M_m|f^{(s)} \rangle = S|f \rangle$. We shall restrict our function space to scattering fields only, so that M_m has an inverse, denoted by G_m ; in the x -representation, $G_m(x, x')$ is the well known Green's function. Operating both sides by G_m , one then gets:

$$|f^{(s)} \rangle = G_m S |f \rangle. \quad (1)$$

In the x -representation, the above equation is the integral equation:

$$f^{(0)}(x) = \int dx' \int dx'' G_m(x, x') S(x', x'') f(x''). \quad (2)$$

Thus the dosimetry and scattering problem has been reduced to a source-field problem in a homogeneous medium, with the source being $S|f\rangle$. Adding $|f^{(0)}\rangle$ to both sides of (1) and rearranging terms, the equation gives $(1 - G_m S)|f\rangle = |f^{(0)}\rangle$, or,

$$|f\rangle = (1 - G_m S)^{-1} |f^{(0)}\rangle \quad (3)$$

Equation (3) gives the total field in terms of the incident field; the scattering field may be easily computed from the total field: $f^{(s)} = f - f^{(0)}$. Note that $f^{(0)}$ may be any wave such that $M_m |f^{(0)}\rangle = 0$, viz., it may be any eigenwave of the electromagnetic environment in the absence of the target.

To compute the total field from (3), one must first establish the integral operators G_m and S , which, like M , depend on the definition of $|f\rangle$ and are derivable from Maxwell's equations. Noting that (1) defines only the product $G_m S$, once (1) is obtained, the product may be re-factorized to any pair of operators, (G_m', S') , such that $G_m' S' = G_m S$. So, for the case $|f\rangle$ being the electric field $|E\rangle$, we first write Maxwell's equations in the form: $M_m' |f^{(0)}\rangle = S' |f\rangle$, where, in the Gaussian system of electromagnetic unit, the operators M_m' and S' are as follows:

$$M_m' = [\nabla^2 + k_m^2] \cdot \tilde{I} \quad (4)$$

$$S'(x, x') = - [\nabla \nabla \cdot + k_m^2 \tilde{I}] \frac{\epsilon(x) - \epsilon_m}{\epsilon_m} \cdot \delta(x - x') \quad (5)$$

where a time-dependency of $e^{i\omega t}$ has been assumed, $k_m = 2\pi/\lambda_m$ is the wave number in the background medium, and \leftrightarrow denotes a 3×3 dyadic; \tilde{I} represents the identity dyadic. From (4) one obtains the x -representation of the inverse of M_m' :

$$G_m'(x, x') = - \frac{1}{4\pi} \frac{\exp(ik_m |x - x'|)}{|x - x'|} \cdot \tilde{I} \quad (6)$$

Since $[\nabla \nabla \cdot + k_m^2 \tilde{I}]$ commutes with M_m' , it commutes with its inverse, G_m' . Therefore, from (5), $G_m' S' = [\nabla \nabla \cdot + k_m^2 \tilde{I}] G_m' [-\epsilon(x) - \epsilon_m]/\epsilon_m$. Defining G_m as $[\nabla \nabla \cdot + k_m^2 \tilde{I}] G_m'$, we may re-factorize $G_m' S'$ to the product of the following pair of (G_m, S) :

$$G_m(x, x') = - \frac{1}{4\pi} [\nabla \nabla \cdot + k_m^2 \tilde{I}] \frac{\exp(ik_m |x - x'|)}{|x - x'|} \quad (7)$$

$$S(x, x') = - \frac{1}{\epsilon_m} [\epsilon(x) - \epsilon_m] \delta(x - x') \cdot \tilde{I} \quad (8)$$

The operator S vanishes outside the target and is diagonal in the sense that $S(x, x') = S(x) \delta(x - x')$. The diagonal elements of S are exactly the negative of the fractional variations of the target's dielectric permittivity with respect to the background medium.

With the operators G_m and S derived as above, one may compute the scattering field, as well as the total field, from (3). The next task is to discretize these two operators and convert the equation into matrix form.

3. The Dosimetry and Scattering Matrix Equations

We shall now convert (3) to a matrix form by discretization. Since we are only concerned in the regions V_t (the target) and V (the scattering region), we shall project all operators and fields onto these two regions. To this end, we use x to denote a point in V , and y a point in V_t , and denote by f_v and f_t , respectively, the projection of a field onto V and V_t . Also, we denote by G_v the projection of G_m onto V on the left and onto V_t on the right, and by G_t the projection of G_m onto V_t from both sides:

$$G_v = V G_m V_t \quad (9)$$

$$G_t = V_t G_m V_t \quad (10)$$

Similarly, S_o denotes the projection of S onto V_o from both sides:

$$S_o = V_o S V_o \quad (11)$$

Note that S_o is effectively equal to S because S vanishes outside the target V_o ; so $S f > = S_o f_o >$ for any field f . Thus, in the integral form, G_v is $G(x, y')$, G_v^{-1} is $G^{-1}(y, x')$, and G_o is $G_o(y, y')$. With the above notation, (1) then decomposes into a V part and a V_o part:

$$|f_v^{(o)} > = G_v S_o |f_o > \quad (12)$$

$$|f_o^{(o)} > = G_o S_o |f_o > \quad (13)$$

Following the same procedure in deriving (3) from (1), one derives, from (13), the equivalence of (3) for f_o :

$$|f_o > = (1 - G_o S_o)^{-1} |f_o^{(o)} > \quad (14)$$

To get the scattering field both outside and inside the target, one substitutes (14) into, respectively, (12) and (13). With some simple manipulation, it gives:

$$|f_v^{(o)} > = G_v (S_o^{-1} - G_o)^{-1} |f_o^{(o)} > \quad (15)$$

$$|f_o^{(o)} > = G_o (S_o^{-1} - G_o)^{-1} |f_o^{(o)} > \quad (16)$$

Equations (15) and (16) are, respectively, the basic scattering and dosimetry equations, both given in terms of the incident field inside the target and the distribution of the target's dielectric permittivity; the total field deposition inside the target may be obtained by adding $f_o^{(o)}$ to the right hand side of (16). For a pulsing field, the field for each frequency component may be computed by replacing $f_o^{(o)}$ by the corresponding frequency component of the incident field, and replacing S_o by the dielectric permittivity profile of the target for that frequency; the matrices G_o and G_v will also be changed accordingly based on the matrix expressions to be established below (see (20)-(22)).

After having developed the dosimetry and scattering formulas, (15) and (16) respectively, the rest of the problem is to establish the two matrices, G_o and G_v , and the matrix S_o . G_o and G_v are referred to as the Green's matrices or the scattering matrices, while S_o is a diagonal matrix with its elements representing the distribution of the target's dielectric permittivity. To this end, we divide V_o into a number of small cells. Label the cells by τ_j and their centers by y_j . Each cell τ_j must be small enough that the field inside may be approximated by its value at y_j . This means that the dimension of the cells must be smaller than a fraction, say 1/4 or smaller, of the electromagnetic wavelength inside the target. Then integration over V_o may be converted into summation of integrals over cells τ_j as below:

$$\iiint_{V_o} G(x, y') f_o(y') dy' \approx \sum_j \left[\iiint_{y' \in \tau_j \subset V_o} G(x, y') dy' \right] f_o(y_j) \quad (17)$$

Let $\{x_i\}$ represent the set of points where scattering fields are to be computed, and denote by G_{ij} the integral inside the bracket for $x = x_i$:

$$G_{ij} = \iiint_{y' \in \tau_j \subset V_o} G(x_i, y') dy' \quad (18)$$

where $G(x, y')$ is given by (7). We shall refer to G_{ij} as the Green's matrix. With the above definition, (17) may be written in the matrix form:

$$\iiint_{V_o} G(x, y') f_o(y') dy' = \sum_j G_{ij} f_o(y_j) \quad (19)$$

Equation (18) defines the matrix elements of G_v if x_i is outside the target, and that of G_o if it is inside the target. By approximating the cell with a sphere of equal volume, the integral may be evaluated analytically. Denoting by a the radius of the spherical cell, the matrix elements of the Green's matrices G_o and G_v are:^{17,18}

$$(G_o)_{ii} = \tilde{Y} \left[1 + \frac{2}{3} \cdot a^2 \cdot \frac{d}{da} \left(\frac{\exp(ik_m a)}{a} \right) \right] \quad (20)$$

$$(G_o)_{ij} = a \cdot \frac{\exp(ik_m |y_i - y_j|)}{|y_i - y_j|} \cdot \left[\cos(k_m a) - \frac{1}{k_m a} \cdot \sin(k_m a) \right] \cdot \left[\tilde{Y} \left(1 - \frac{1}{ik_m |y_i - y_j|} + \frac{1}{(ik_m |y_i - y_j|)^2} \right) - \frac{y_i - y_j}{|y_i - y_j|} \frac{y_i - y_j}{|y_i - y_j|} \left(1 - \frac{3}{ik_m |y_i - y_j|} + \frac{3}{(ik_m |y_i - y_j|)^2} \right) \right] \quad (21)$$

$$(G_r)_{ij} = a \cdot \frac{\exp(ik_m |x_i - x_j|)}{|x_i - x_j|} \cdot \left[\cos(k_m a) - \frac{1}{k_m a} \cdot \sin(k_m a) \right] \cdot \left[\tilde{Y} \left(1 - \frac{1}{ik_m |x_i - x_j|} + \frac{1}{(ik_m |x_i - x_j|)^2} \right) - \frac{x_i - x_j}{|x_i - x_j|} \frac{x_i - x_j}{|x_i - x_j|} \left(1 - \frac{3}{ik_m |x_i - x_j|} + \frac{3}{(ik_m |x_i - x_j|)^2} \right) \right] \quad (22)$$

Note that the off-diagonal matrix elements of G_o and G_r are of identical form; $(G_o)_{ij}$ may be obtained by replacing x_i in $(G_r)_{ij}$ by y_i . As to the S_o operator, (8) gives:

$$(S_o)_{ij} = -\frac{1}{\epsilon_m} [\epsilon(y_i) - \epsilon_m] \delta_{ij} \cdot \tilde{Y} \quad (y_i \in \tau_j \subset V_o) \quad (23)$$

So S_o is diagonal with the diagonal element $(S_o)_{ii}$ being the negative of the fractional variation of the dielectric permittivity of the i^{th} cell in the target with respect to the background medium.

With the above analytic expressions for the matrix elements of G_o , G_r , and S_o , one may calculate both phase and amplitude of the field anywhere, using (15)-(16). It can be shown that the scattering field computed from the matrix formula converges.¹⁹ Note that, since each element of the column vectors $f_i^{(o)}$ and $f_i^{(r)}$ represents an electric field, which is a vector field, each element of the matrices, G_o , G_r , and S_o , is itself a 3x3 submatrix. Although (15)-(16) involve the inversion of the matrix $(S^{-1} - G_o)$, we have found that this matrix is very stable for inversion. The fields f_e and f_r may also be solved without matrix inversion: One first solves (13) for f_e by Gauss reduction or by iteration, then uses (12) to obtain f_r . Note also that the scattering matrices G_o and G_r depend only on the geometry of V_o and V_r and the geometrical arrangement of the cells inside them, and are independent of the target S_o . Therefore these matrices, as well as $(S_o^{-1} - G_o)^{-1}$, may be computed off-line once and for all. This increases the speed of dosimetry and scattering prediction greatly.

4. The Dielectric Imaging Equation

In our matrix formulation, the target is represented by S_o . Therefore dielectric imaging is to obtain S_o in terms of incident field and measured fields outside the target. Since S_o is a diagonal matrix, its diagonal elements are equal to the ratio of the corresponding elements of $S_o |f_o\rangle$ and $|f_o\rangle$. From (12), one gets:

$$S_o |f_o\rangle = G_o^{-1} |f_o^{(o)}\rangle. \quad (24)$$

Substituting this into the right hand side of (13) and add $f_o^{(o)}$ to both sides, (13) gives:

$$|f_o\rangle = |f_o^{(o)}\rangle + G_o G_o^{-1} |f_o^{(o)}\rangle. \quad (25)$$

Dividing the i th element $S_o |f_o\rangle$ by the corresponding element of $|f_o\rangle$, one gets, from the above two equations:

$$(S_o)_{ii} = \frac{-1}{\epsilon_m} [\epsilon(y_i) - \epsilon_m] = \frac{\sum_j (G_o^{-1})_{ij} f_j^{(o)}(x_j)}{f_i^{(o)}(y_i) + \sum_{j \neq i} (G_o)_{ij} (G_o^{-1})_{jk} f_k^{(o)}(x_k)} \quad (26)$$

Equation (26) is the dielectric imaging equation. It gives the scatterer's dielectric permittivity $(S_o)_{ii}$ in the i th cell in terms of the scattering field $f_i^{(o)}(x_i)$ outside the scatterer, and the incident field $f_i^{(o)}(y_i)$ inside the scatterer, which is a known quantity. The computation of the inverse G_o^{-1} may be very time-consuming, however, as mentioned earlier, G_o^{-1} , as well as G_o and G_r , may be computed off-line once and for all, since they are independent of the scatterer S_o . In the next two sections, we present results for dosimetry and scattering field computation and for imaging of highly inhomogeneous objects.

5. Results - Dosimetry and Scattering Computation

To analyze the accuracy of the dosimetry and scattering matrices, we perform some computation for scattering of a plane wave from a dielectric sphere in a homogeneous background, and compare the results with Mie's scattering formula.³ All quantities relating to length, such as wavelength, distance, etc., are measured with respect to the size of an arbitrary cube and thereby treated as dimensionless. So, consider a unit cube with its center located at (.5, .5, .5), and a dielectric sphere of radius .25 centered at (.501, .501, .501) and complex permittivity ϵ in a background medium of permittivity $\epsilon_m=1$; the slight displacement of the sphere from the cube's center is to avoid divergence when the coordinate origin is moved to that point for computing the Mie field. The incident wave travels in the z-direction with its electric field polarized in the x-direction with unit amplitude: $E^{(0)} = \hat{x} \exp[ik_m(z-0.5)]$, where $k_m = (\omega/c)\sqrt{\epsilon_m}$.

The unit cube is discretized with a $(N+1) \times (N+1) \times (N+1)$ mesh, yielding $(N+1)^3$ lattice points (nodes), each of which is the center of a cell; all border cells are halfway outside the target region. From (23), S_0 is diagonal and its elements take only two values, 0 or $S \equiv (\epsilon - \epsilon_m)/\epsilon_m$, depending on whether its corresponding cell is inside or outside the dielectric sphere. A cell is considered inside the dielectric sphere if the distance from its center to that of the sphere is less than the sphere's radius, otherwise it is considered to be outside the sphere. As to the matrix elements of G_0 and G_1 , they are computed from (20)-(22). To save computation time, the dimensions of S_0 and G_0 are reduced to the number of non-vanishing elements in S_0 , i.e., the target region V_0 is taken to be the space occupied by the discretized sphere. Though the number of matrix elements in the G matrices is proportional to N^6 , only $\sim N^3$ of them are independent because the value of each matrix element depends only on the relative position of the corresponding pairs of cells. In order to save memory, these independent elements are computed and stored as an array, and a mapping scheme is devised to find each matrix element from the array.

Though the fields outside and inside the target may be computed from, respectively, (15) or (16), we find that it takes less time to first solve f_0 from (13) by iteration, and then compute $f_1^{(0)}$ and $f_2^{(0)}$ from (12)-(13). Adding $f_0^{(0)}$ to both sides of (13), one gets:

$$If_0 > = f_0^{(0)} + G_0 S_0 If_0 > \quad (27)$$

Solved by iteration, the above equation provides a rapidly converging solution for f_0 ; 15 iterations suffice to converge to an error of 10^{-6} . Once f_0 is solved for, computing $f_1^{(0)}$ is trivial and takes very little computer time; computing operations needed for each field point is of the order of $4 \cdot 3 \cdot N$, where the factor of 4 is for complex number multiplication and 3 for the three components of a vector field.

The results of the matrix method are compared to the Mie formula in the contour plots of scattering field $|E^{(0)}|$ in Figure 1 - Figure 6 for three different wavelengths, dielectric contrasts, and discretizations. In each figure, fields from the matrix method are shown on the left and that from Mie formula on the right. The model parameters in these figures are: For Figure 1 and Figure 2, wavelength $\lambda_m = 5$, sphere's permittivity $\epsilon = 2+0.2i$, discretization $N = 30$; for Figure 3 and Figure 4, wavelength $\lambda_m = 10^6$, sphere's permittivity $\epsilon = 2$, discretization $N = 30$; for Figure 5 and Figure 6, wavelength $\lambda_m = 10^4$, sphere's permittivity $\epsilon = 60+60i$, discretization $N = 20$. Figure 1, Figure 3, and Figure 5 show the fields in the planes $y=.5$, $x=.4$, and $x=.5$, respectively, all of which cut through the target sphere. Figure 2, Figure 4, and Figure 6 show the fields in the planes $z=1$, $y=1$, and $z=0$, respectively, all of which are separated from the target sphere by radius distance. Figure 3 shows that the Mie fields are distorted inside the target sphere, which is due to slow convergence of the series expansion of $\exp(ikr \cos \theta)$ in spherical Bessel functions; it is found that the 14-term expansion has a 10^{-3} error for $kr = 10^6$ and only 10^{-11} error for $kr = 10^3$. Therefore, it is difficult to compare the matrix formula with the Mie formula for long wavelengths. Nevertheless, from the fact that the field pattern from the matrix formula is much more consistent with the symmetry of the target, the matrix formula possibly provides more accurate result. Other than that, the results show a near perfect fit for a wide range of wavelengths and dielectric contrasts; the slight deviations for fields on the target's surface are due to the fact that the matrix method provides fields for a discretized sphere, which has a zigzag surface.

Discrepancy of the fields between the matrix method and the Mie formula may be due to the geometric difference between the discretized target and the spherical target, as well as the approximations employed in discretizing the integral equation. With this in mind, we analyze the field discrepancies by examining their dependency on various parameters. Since the incident wave is polarized in the x-direction, we consider only discrepancies in E_x , which dominates the discrepancies in $|E|$. The discrepancy ΔE_x is defined as the maximum value of the percentage differences between E_x computed from the matrix method and E_x from the Mie formula over all six faces of the unit cube that encloses the target sphere:

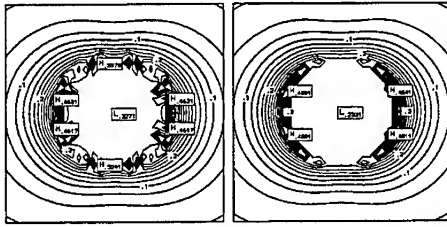


Figure 1. Field contours in $y=0.5$ plane for $\lambda_m=5$ from a $\epsilon=2+2i$ sphere computed from $N=30$ discretization (left) and Mie formula (right).

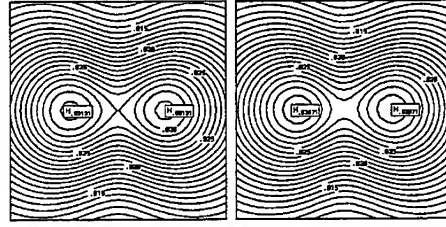


Figure 2. Field contours in $z=1.0$ plane for $\lambda_m=5$ from a $\epsilon=2+2i$ sphere computed from $N=30$ discretization (left) and Mie formula (right).

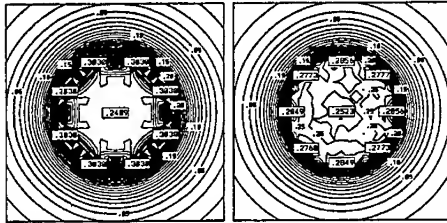


Figure 3. Field contours in $x=0.4$ plane for $\lambda_m=10^4$ from a $\epsilon=2$ sphere computed from $N=30$ discretization (left) and Mie formula (right).

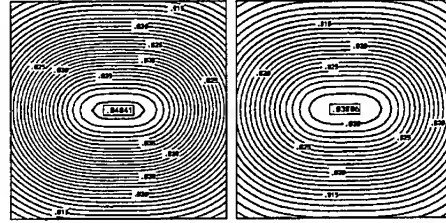


Figure 4. Field contours in $z=1.0$ plane for $\lambda_m=10^4$ from a $\epsilon=2$ sphere computed from $N=30$ discretization (left) and Mie formula (right).

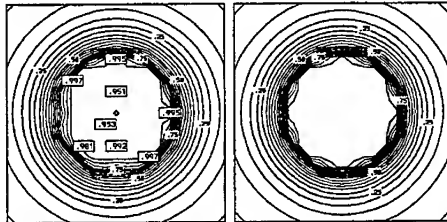


Figure 5. Field contours in $x=0.5$ plane for $\lambda_m=10^4$ from a $\epsilon=60+60i$ sphere computed from $N=20$ discretization (left) and Mie formula (right).

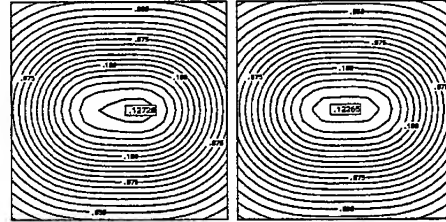


Figure 6. Field contours in $z=0$ plane for $\lambda_m=10^4$ from a $\epsilon=60+60i$ sphere computed from $N=20$ discretization (left) and Mie formula (right).

$$\Delta E_x = \text{Max} \left\{ \frac{|\mathbf{E}_x^{\text{matrix}} - \mathbf{E}_x^{\text{Mie}}|}{|\mathbf{E}_x^{(0)}|} \right\} \quad (28)$$

Figure 7 shows the dependency of ΔE_x on wavelength for $\epsilon = 2$ and discretization of $N = 14$, plotted against $\lambda_m/\Delta s$ where $\Delta s = 1/14$ is the cell size; the target sphere is represented by 179 cells. It shows that the discrepancy is less than 10% for $\lambda_m > 5\Delta s$, less than 1% for $\lambda_m > 15\Delta s$, and less than 0.1% for $\lambda_m > 42\Delta s$. It also shows that the discrepancy stays flat at slightly less than .1% even when λ_m increases to $140\Delta s$. This asymptotic discrepancy possibly is due to the finite discretization of $N = 14$; finer discretization may be needed to render a sphere with higher precision. Figure 8 shows the field discrepancy as a function of target's dielectric permittivity for $N = 16$ and $\lambda_m = 5$. One sees that the discrepancy is not very sensitive to the target's dielectric permittivity. Also it shows that the discrepancy peaks at about 0.5% for ϵ around 4 and decreases for small ϵ as well as large ϵ . This is rather unexpected since one would expect ΔE_x to increase as ϵ increases. It is possible that at about $\epsilon = 4$ there is a resonance between wavelength inside the sphere and the sphere's geometry, which produces strong scattering and thereby gives higher discrepancy. This hypothesis may be tested by plotting ΔE_x versus ϵ while keeping $(R/\lambda)^2 = (R/\lambda_m)^2 \epsilon$ constant; it shall show a flat curve if the hypothesis is valid. One may also make a similar plot for various values of N and the over-all feature of the curve shall not depend on N .

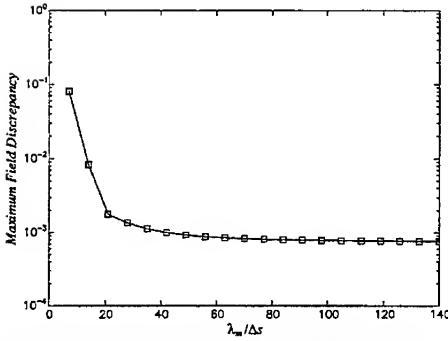


Figure 7. Dependency of field discrepancy $\Delta E_s = \text{Max}\{ |E_s^{\text{meas}} - E_s^{\text{calc}}| / |E_s^{\text{meas}}| \}$ on wavelength for $\epsilon=2$ and $N=14$ discretization ($\Delta s=1/14$).

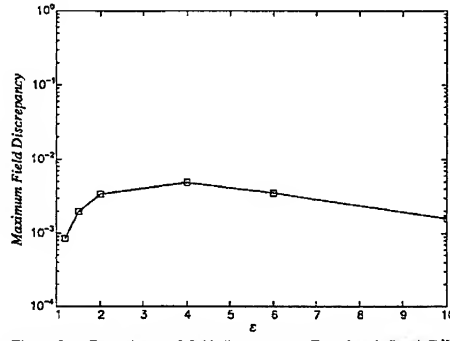


Figure 8. Dependency of field discrepancy $\Delta E_s = \text{Max}\{ |E_s^{\text{meas}} - E_s^{\text{calc}}| / |E_s^{\text{meas}}| \}$ on target's permittivity for $\lambda_0=5$ and $N=16$ discretization.

An interesting behavior of the field discrepancy against grade of discretization is shown in Figure 9 for $\lambda_0 = 5$ and $\epsilon = 2$, which shows an oscillatory behavior as N increases. Also plotted is the volume mismatch between the discretized target and the real target, which is defined as the difference between the volume of the dielectric sphere and that of the collection of all cells representing the sphere:

$$\Delta V = \left| \frac{4\pi}{3} R^3 - \frac{1}{N^3} N_{\text{sphere}} \right| \quad (29)$$

where R is the radius of the dielectric sphere and N_{sphere} is the number of cells that collectively represent the sphere; each cell is yet represented by a small sphere of volume $1/N^3$. Field discrepancy may be caused by volume mismatch as well as shape mismatch between the discretized sphere and the real target sphere. Simply a problem of geometric configuration, the degrees of these mismatches do not vary monotonously with N , as certain sizes of cells may pack more uniformly in a sphere. This leads to the oscillatory behavior of the dependency of field discrepancy ΔE_s on N .

6. Results - Inverse Scattering and Dielectric Imaging

Equation (26) provides the formula for dielectric imaging. To use this formula, the scattering matrix G_s must first be inverted. We have found that, while inversion of the dosimetry matrix G_d is easy, G_s may be unstable for inversion. If so, some stabilizing technique must be employed. To this end, we employ the singular value decomposition technique.^{25,26} To further stabilize the inversion, the number of scattering fields are almost doubled so as to make it an over-determined problem. In essence, we seek the best-fit solution (as opposed to exact solution) for almost twice as many equations as the number of unknowns.

Computer simulation of many highly inhomogeneous models have been performed, four of them are presented below. As in field computations, all quantities relating to length, such as wavelength, distance, etc., are measured with respect to the size of a cubic target region and thereby treated as dimensionless. The target region is discretized into $7 \times 7 \times 7$ cells, yielding $8 \times 8 \times 8$ lattice points (nodes), with the centers of the cells located at $x, y, z = 0, 1/7, \dots, 1$; thus there are $8 \times 8 \times 8$ cells in the target region, with border cells being halfway outside the target region. The matrices G_s , G_d , and G_s^{-1} are computed and stored, the same matrices are then used for all target models. Scattering fields on the surface of the cube or at about $1/14$ distance away from the surface are used as input fields. In all cases, the incident field propagates in z -direction and is polarized in \hat{x} : $E^{(0)} = \hat{x} \exp(ik_z z)$, and the wavelength is $\lambda_0 = 2\pi/k_0 = 5$. Input and imaged dielectric distributions are shown using

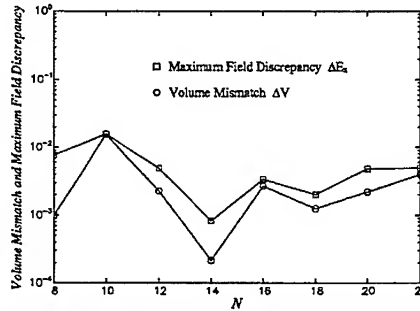


Figure 9. Dependency of field discrepancy on number of discretization and its correlation to mismatch in volume of discretized target, for $\lambda_0=5$ and $\epsilon=2$.

a gray scale for each of the slices $z = 0, 1/7, 2/7, \dots, 1$. With $\lambda_m=5$, the $7 \times 7 \times 7$ discretization yields a 3-D resolution of $\lambda_m/35$; images with resolution as high as $1/165$ have been obtained.

In the first model, three small spheres are placed in three different cells in the $z=4/7$ section. Each sphere has a permittivity of $\epsilon = 10+3i$ and radius $r=0.05$, and the background medium is $\epsilon_m = 80+3i$, giving a volume-averaged permittivity of $67+3i$. Scattering fields approximated by first order linear superposition of the Mie fields from each of the three spheres are used as "measured" fields; errors in this approximation represent possible errors when actual measurements are taken. Figure 10 shows the eight slices of reconstructed real part of the dielectric permittivity of the target region, with $z = 0, 1/7, 2/7$ and $3/7$ (left to right) in the first row of the figure and the rest in the second row. In the second model, of which similar image slices are shown in Figure 11, the same three spheres are placed in different planes. In both cases, the reconstructed image data consistently give $\epsilon = 64+3i$ in the cells that contain a sphere, which is within 4% of the average value, and $(80 \pm 1) + (3 \pm 0.3)i$ in cells that do not contain a sphere. Note that, for cells that do not contain a sphere, the gray-scale figures appear to show more contrast than the actual image data because $\epsilon=80$ is used as a dividing point of gray levels; reading from the image data, cells with lighter shade generally have permittivity in the range of $79.7-80.0$, and those with darker shade are in the range of $80.0-80.3$.

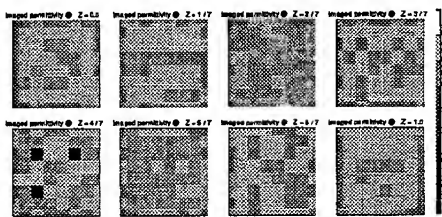


Figure 10. Image of $\text{Re}(\epsilon)$ of three spheres in $z=4/7$ plane with radius 0.05 and permittivity $\epsilon=10+3i$ in a background medium of $\epsilon_m=80+3i$.

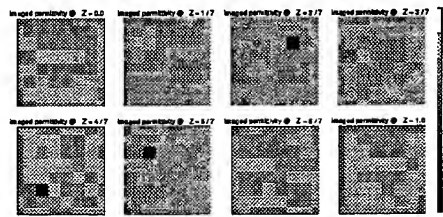


Figure 11. Image of $\text{Re}(\epsilon)$ of three spheres in three different z -slices with radius 0.05 and permittivity $\epsilon=10+3i$ in a background of $\epsilon_m=80+3i$.

In the third model, each cell in the target is given a randomly generated real value of $S \equiv (1 - \epsilon/\epsilon_m)$. The scattering fields are computed using the iteration method described in Section 5. Figure 12 shows both input and imaged S for the eight slices. The first row of the figure gives the $z = 0$ (left pair) and $1/7$ (right pair) slices, and so forth; for each pair, the input S is on the left and imaged S on the right. In the fourth model, the target region is given a discretized double Gaussian distribution for both real and imaginary parts of S , peaks at $a = (.5 \ .5)$ and $b = (.7 \ .7)$:

$$S_j = -(1+i) \cdot [\text{Exp}(-10|y_j - a|^2) + \text{Exp}(-10|y_j - b|^2)] \quad (30)$$

where y_j is the center of the j th cell. Scattering fields are computed in the same way as the third model. Figure 13 shows both input and imaged $\text{Re}(S)$ and $\text{Im}(S)$ for the eight slices, with the left half of figure giving $\text{Re}(S)$ and the right half giving $\text{Im}(S)$; the slice arrangement for each half is the same as in Figure 12 described above. Both models show exceptional image quality.

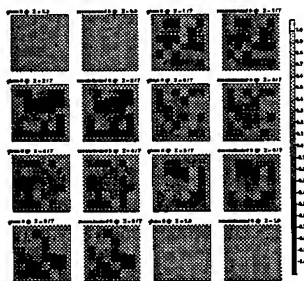


Figure 12. The z -slices of input and imaged $S \equiv (1 - \epsilon/\epsilon_m)$ of a random dielectric distribution.

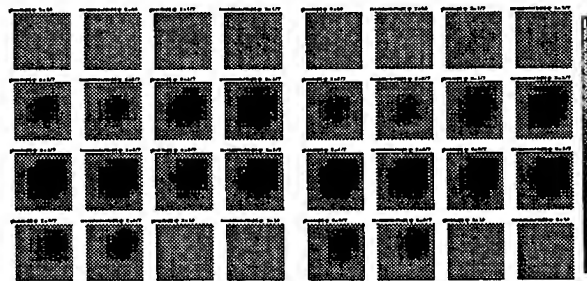


Figure 13. The z -slices of input and imaged $\text{Re}(S)$ (left half) and $\text{Im}(S)$ (right half) of a double Gaussian dielectric distribution; in each slice, input (left) and image (right) are paired side-by-side.

7. Discussion and Conclusion

In the matrix formulation, the field in each cell is a 3-D vector and S_i is a 3×3 diagonal submatrix, of which each element is the relative permittivity in the corresponding polarization. Therefore the imaging formula gives not only real and imaginary parts of dielectric permittivity, but also its anisotropic components. Owing to its quantitative nature, imaging of objects much smaller than the discretized cells is possible, as it is demonstrated in the imaging results (see discussion on Figure 10 and Figure 12 in Section 6.) Note also that the formulation is scalable with respect to ϵ/ϵ_m and λ_w/L , where L is the characteristic length of the target region. Thus, given a fixed discretization and fixed locations of measurements, the image quality is unchanged as long as ϵ/ϵ_m and λ_w/L are unchanged. As to computation time, for $8 \times 8 \times 8$ cells, it takes about 900 CPU seconds on a Cray C-90, most of which is for inverting G_+ . However, only one set of matrices is needed for all target models, and each image reconstruction time takes less than a second.

On dosimetry and scattering computation, we like to discuss further the field discrepancy between matrix method and the Mie formula, keeping in mind that most part of the discrepancy is due to different target rather than errors in the matrix formula. From the strong correlation between field discrepancy and volume mismatch as shown in Figure 9, it appears that volume mismatch may contribute substantially to field discrepancy. We have analyzed this subject by inspecting the geometry of the discretized sphere as represented by a collection of cells, for the cases of $N = 14$ (179 cells) and $N = 16$ (257 cells), as shown in Figure 14. $N = 16$ has higher volume mismatch, with $\Delta V = 0.003384$ as compared to 0.000831 for $N = 14$. It gives higher field discrepancy in spite of having finer discretization and being more spherically shaped. We thus conclude that the field discrepancies are mostly due to the geometric difference between the discretized sphere and the perfect sphere, and that volume mismatch has more effect on field accuracy than shape mismatch does, and, to some extent, also has more effect on field accuracy than the degree of discretization does.

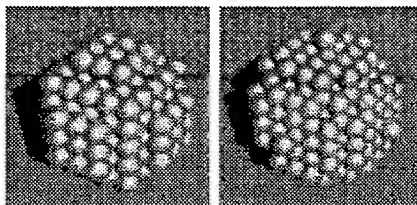


Figure 14. Collection of spherical cells that represent the discretized sphere of $R=25$ for $N=14$ (left) and $N=16$ (right). The volume mismatch ΔV is .000831 for $N=14$ and .003384 for $N=16$.

One may then expect that the field discrepancy may be reduced by renormalizing the volume of the discretized sphere. In deriving (20)-(22) for the G matrices, each cubic cell is replaced by a spherical cell of equal volume. The volume renormalization process is to readjust the volume of the spherical cells so that the collection of cells that represent the discretized sphere has the same volume as the real sphere. We have performed volume renormalization and found that it does reduce field discrepancy, but eliminates neither the discrepancy completely nor the oscillatory behavior; furthermore, the locations of maxima and minima in the ΔE_x versus N plot are changed by volume renormalization. This implies that both shape mismatching and volume mismatching contribute to the oscillatory behavior. The change in the locations of maxima and minima following volume renormalization is due to the fact that volume and shape mismatching are not synchronous in terms of N . For the cases of $N = 14$ and $N = 16$, the latter gives higher ΔE_x in spite of finer discretization and less shape mismatching, because it has higher volume mismatch. Upon volume renormalization in both cases, $N = 16$ yields lower ΔE_x owing to its better shape matching as well as finer discretization.

Another approach to reduce field discrepancy may be to smooth the border of the discretized sphere. Without a method of border smoothing, we have performed a dielectric-border smoothing by half the permittivity for border cells, but it failed to reduce the oscillatory dependency of ΔE_x on N . It appears that, to reduce shape mismatching, geometric smoothing instead of dielectric smoothing is needed.

We have developed a matrix formulation for three-dimensional quantitative dielectric imaging and for computation of vector fields inside and outside any arbitrary three-dimensional dielectric object. The formulation provides accurate fields with a viable degree of discretization and for a wide range of frequencies and dielectric contrasts. It also makes possible high resolution quantitative dielectric imaging, which will find many applications, particularly medical applications.^{20,21,24}

Acknowledgement

Computer simulations were performed by Dr. Hasan Oguz of Potomac Research, Inc. Computer time for this work has been provided by the Department of Energy Office of Energy Management through NERSC at Lawrence Livermore Laboratory, and by NASA through the Center for Computational Sciences at Goddard Space Flight Center. The authors also wish to express their appreciation to NERSC Consultant Group for their support.

References

1. C. Polk and E. Postow, eds., *CRC Handbook of Biological Effects of Electromagnetic Fields*, CRC Press, 1986.
2. M. Born and E. Wolf, *Principles of Optics*, pp. 633-656, Macmillan, 1964.
3. E. Argence and T. Kahan, *Theory of Waveguides and Cavity Resonators*, pp. 181-187, Hart Publishing, 1967.
4. J. B. Keller, "Accuracy and validity of the Born and Rytov approximations," *J. Opt. Soc. Am.* **59**, 1003-1004 (1969).
5. J. H. Richmond, "Scattering by a Dielectric Cylinder of Arbitrary Cross-Section," *IEEE Trans. Ant. Prop.* **13**, pp. 334-341 (1965).
6. J. H. Richmond, "TE-Wave Scattering by a Dielectric Cylinder of Arbitrary Cross Section Shape," *IEEE Trans. Ant. Prop.* **14**, pp. 460-464 (1966).
7. R. H. Harrington, *Field Computations by Moments Methods*, McGraw-Hill, New York, 1968.
8. D. E. Livesay and K.-M. Chen, "Electromagnetic Fields Induced Inside Arbitrarily Shaped Biological Bodies," *IEEE Trans. Micr. Th. Tech.* **22**, pp. 1273-1280 (1974).
9. H. Massoudi, C. H. Durney, and M. F. Iskander, "Limitations of the Cubical Block Model of Men in Calculating SAR Distributions," *IEEE Trans. Micr. Th. Tech.* **32**, pp. 746-752 (1984).
10. C. T. Tsai, H. Massoudi, C. H. Durney, and M. F. Iskander, "A Procedure for Calculating Fields Inside Arbitrarily Shaped, Inhomogeneous Dielectric Bodies Using Linear Basis Functions with the Moment Method," *IEEE Trans. Micr. Th. Tech.* **34**, pp. 1131-1139 (1986).
11. M. A. Morgan and K. K. Mei, "Finite-Element Computation of Scattering by Inhomogeneous Penetrable Bodies of Revolution," *IEEE Trans. Antenna and Propagation AP-27*, pp. 202-214 (1979).
12. S. Ratnajeevan H. Hoole, "An Integrated System for the Synthesis of Coated Waveguides from Specified Attenuation," *IEEE Trans. Microwave Theory Tech. MTT-40*, pp. 1564-1571 (1992).
13. K. S. Yee, "Numerical Solution of Initial Boundary Value Problems Involving Maxwell's Equations in Isotropic Media," *IEEE Trans. Ant. Prop.* **14**, pp. 302-307 (1966).
14. A. Taflovie and M. E. Brodwin, "Numerical Solution of Steady-State Electromagnetic Scattering Problems Using the Time-Dependent Maxwell's Equations," *IEEE Trans. Micr. Th. Tech.* **23**, pp. 623-630 (1975).
15. D. T. Borup, Dennis M. Sullivan, and O. P. Gandhi, "Comparison of the FFT Conjugate Gradient Method and the Finite-Difference Time-Domain Method for the 2-D Absorption Problem," *IEEE Trans. Micr. Th. Tech.* **35**, pp. 383-395 (1987).
16. P. C. Cherry and M. F. Iskander, "FDTD Analysis of Power Deposition Patterns of an Array of Interstitial Antennas for Use in Microwave Hyperthermia," *IEEE Trans. Micr. Th. Tech.* **40**, pp. 1692-1700 (1992).
17. T. C. Guo and W. W. Guo, "Scattering of Vector Waves by Arbitrary Three-Dimensional Dielectric Objects," *Proceedings of the 1987 International Microwave Symposium*, pp. 307-312, Rio de Janeiro, Brazil, July 1987, IEEE Publication 87TH0183-4, Library of Congress No. 87-80089.
18. T. C. Guo and W. W. Guo, "Computation of Electromagnetic Wave Scattering from an Arbitrary Three-Dimensional Inhomogeneous Dielectric Object," *IEEE Trans. Magn.* **25**, pp. 2872-2874 (1989), and *Proceedings of the Third Biennial IEEE Conf. Electromagnetic Field Computation*, Washington, DC, Dec. 1988.
19. T. C. Guo and W. W. Guo, "Three-Dimensional Dielectric Imaging by Inverse Scattering with Resolution Unlimited by Wavelength," *Annual Report of the Conf. on Electrical Insulation and Dielectric Phenomena*, pp. 65-74, Leesburg, Virginia, October 1989, IEEE Publication 89CH2773-0, Library of Congress No. 79-649806.
20. L. E. Larsen, J. H. Jacobi, W. W. Guo, T. C. Guo, and A. C. Kak, "Microwave Imaging Systems for Medical Diagnostic Applications," *Proc. 6th Annual Conf. IEEE Eng. in Medicine and Biology Soc. - Frontiers Eng. and Comp. in Health Care*, pp. 532-539, ed. John L. Semmlow and Walter Welkowitz, Los Angeles, September 1984, IEEE Publication 84CH2058-6, Library of Congress No. 84-81384.
21. L. E. Larsen and J. H. Jacobi, eds., *Medical Applications of Microwave Imaging*, IEEE Press, New York, 1986.
22. T. C. Guo and W. W. Guo, "Physics of Image Formation by Microwave Scattering," *SPIE Proceedings 767*, pp. 30-39, SPIE Press, Bellingham, WA, February 1987.
23. T. C. Guo, W. W. Guo, and L. E. Larsen, "Recent Development in Microwave Medical Imagery - Phase and Amplitude Conjugations and the Inverse Scattering Theorem," in *Medical Applications of Microwave Imaging*, ed. L. E. Larsen and J. H. Jacobi, pp. 167-183, IEEE Press, 1986.
24. J.-C. Bolomey, "Recent European Developments in Active Microwave Imaging for Industrial, Scientific, and Medical Applications," *IEEE Trans. Micr. Th. Tech.* **37**, pp. 2109-2117 (1989).
25. G. H. Golub and C. F. Van Loan, *Matrix Computations*, Ch. 6, The Johns Hopkins University Press, Baltimore, 1983.
26. G. E. Forsythe, M. A. Malcolm, and C. D. Moler, *Computer Methods for Mathematical Computation*, p. 41, Prentice-Hall, 1977.

Explanation of Biological Effects of Low-intensity Electric, Magnetic and Electromagnetic Fields by Nonlinear Dynamics

F. Kaiser

Institute of Applied Physics, Theory, Nonlinear Dynamics, Technical University of Darmstadt, Hochschulstr. 4A, D-6100 Darmstadt, FRG

This paper proposes concepts to explain biological effects created by interactions of low-intensity electromagnetic fields with cellular systems. Based on externally driven nonlinear oscillations, frequency and intensity dependent responses of the perturbed systems are analyzed with the methods of nonlinear dynamics. A recently developed model for cytoplasmic Ca^{2+} -oscillations is presented and results for a combined chemical and electromagnetic stimulus interacting with the signal transduction pathway are discussed.

1. Introduction

Oscillating phenomena play a dominant role in the creation, stabilization and maintenance of special biological order and function. The systems involved range from the molecular to the macroscopic level, the corresponding periods are from below the sub- μ sec level to hours, days and even years. Oscillation dynamics define biological clock functions and are of essential importance in inter- and intracellular signal transmission and in cellular differentiation. The functional complexity of biological systems and subsystems necessitates the application of macroscopic theories for their description. Under certain far from equilibrium conditions living systems can achieve multiple steady states, quasiperiodic states and irregular states, in addition to the regularly oscillating states. Nonlinearity and cooperativity are necessary prerequisites for these states to occur.

Nonlinear dynamics impose both, spatio-temporal structures and spatio-temporal constraints on the system. Nonlinear equations govern the spatio-temporal configurations. Thus the control of and the response to a certain internal or external stimulus are a manifestation of the cooperative dynamics within the system. Well-known examples are: (1) cyclic AMP and glycolytic oscillations, (2) the occurrence of cytosolic Ca^{2+} -oscillations after the onset of a certain signal transduction mechanism by a chemical and/or an electromagnetic stimulus, (3) the onset of trains of action potentials ("nerve pulses") and of oscillations of the electromagnetic potential in the brain ("brain waves", EEG).

The interaction of electric and magnetic fields (e.g. ELF) and of electromagnetic fields (e.g. microwaves) with biological systems leads to responses or effects, which are directly related to (1) absorption of field energy (thermal effects), (2) classical effects (e.g. field-induced forces) and (3) quantum effects (e.g. breaking of intermolecular bonds or intramolecular changes). In addition interaction mechanisms of fields with cooperative or coherent states (i.e. nonequilibrium states) have to be considered.

In the present contribution only those interaction mechanisms are discussed, where (1) changes of the temperature are not significant, (2) no thermal thresholds exist and (3) no direct processes determine the whole sequence of events. Only those specific processes where nonlinear dynamics dominate, are considered.

Since many years internally and externally perturbed oscillating states on a cellular and macroscopic level have been investigated. The combined interaction of both the internal frequencies and amplitudes of the active oscillators with the frequencies and amplitudes of the stimuli offers a great variability of the system's response. Frequency regulated processes and amplitude dependent processes compete and cooperate with one another. To get an insight into the fundamental differences exhibited by nonlinear systems in relation to the conventional linear ones, a series of different nonlinear oscillators is discussed. When perturbed from the outside, sub- and superharmonic resonances, complex periodic, quasiperiodic and chaotic states result. This inherent nonlinear behaviour leads to an extreme frequency and intensity sensitivity, including extreme low thresholds and windows. Frequency and amplitude modulations create additional oscillatory specificities in the nonlinear system [1,2].

Meanwhile experimental results exist which show that in certain situations nonthermal interactions of electromagnetic fields with cellular systems occur (see refs. [3,4] for a review). Important experimental examples are (1) frequency- and intensity-dependent cellular response to microwave radiation [5], (2) extremely-low-frequency magnetic field effects on Ca^{2+} -mediated signal transduction events in lymphocytes [6]. In the first part some results for externally driven nonlinear self-excited oscillators are presented. In the second part a detailed and complicated model is discussed which describes a signal pathway for a concrete biological situation: onset of cytoplasmic Ca^{2+} -oscillations. The whole pathway is discussed, i.e. from the external signal to the cellular response via transduction, amplification and expression. Special emphasis is given to those steps in the pathway, where extremely weak electric, magnetic or electromagnetic fields can interact.

2. Nonlinear Oscillations

Oscillating nonlinear systems are either of passive or active type. Whereas passive nonlinear systems are in a stable, nonoscillating steady state when no external drive is present, an active system is oscillating even without any external or internal stimulus.

This oscillation of limit cycle type results from competing internal processes of energy input and energy dissipation, where at least one of these processes has to be nonlinear. The limit cycle oscillation represents a specific state of order and function; a necessary requirement for their creation, stabilization and maintenance are nonlinear dynamic processes. If such an oscillation exists, e.g. as a certain biological oscillation or rhythmic state, no fast dissipation of energy into nonoscillating degrees of freedom occurs. Thus a specific state gets stabilized far from equilibrium, consequently no thermalization destroys this state within a relevant period of time. In addition, the structurally stable nonlinear states

are influenced by internal and external fluctuations (stochastic forces). In this contribution, main emphasis lies on the influence of external static and periodic signals (deterministic forces).

The combined interaction of stochastic and regular signals with nonlinear oscillations or rhythmic states will not be discussed. However, it is well-known that weak, noisy internal or external signals can significantly amplify very weak external periodic signals. These regular signals extract a coherent component from the noisy or fluctuating background. Such a situation is exhibited by bi- and multistable systems (lasers, nonlinear optics) for both, additive and multiplicative noise.

Periodically driven limit cycles offer a rich variety of behaviour. One has the interaction of at least two frequencies, the internal limit cycle frequency and the frequency of the external stimulus. Depending on both, the frequency and the amplitude of the external drive, complex periodic, quasiperiodic and chaotic, i.e. irregular states are exhibited. Some of these results are briefly presented. Fig. 1 shows the possible stable states (attractors) of nonlinear systems: static attractors (fixed points), periodic attractors (limit cycles), quasiperiodic attractors (motion on a torus) and strange attractors (chaotic motion).

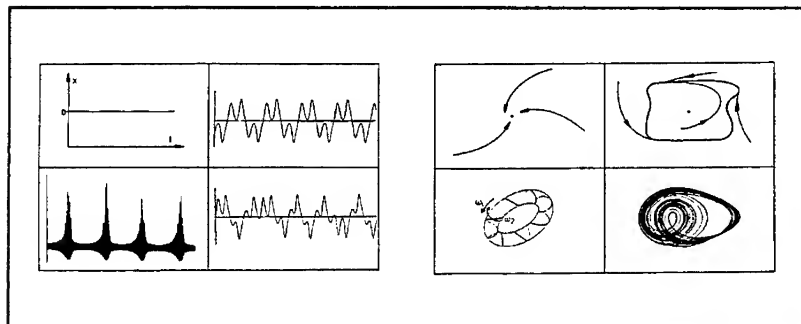


Fig. 1: *stable states (attractors). Oscillation diagrams (amplitude x versus time t) and phase plane diagrams (x versus \dot{x}) for fixed point, periodic, quasiperiodic and chaotic states.*

The stable steady state responses of limit cycles are given in Figs. 2 and 3, where the nonlinear resonances for different external field parameters are displayed. The first model is a generalized von der Pol oscillator. Its equation of motion reads:

$$\ddot{X} + \mu(-1 + \alpha X^2 - \beta X^4 + \gamma X^6)\dot{X} + X = F_1 \cos(\omega t) \quad (1)$$

In Fig. 2 the superharmonic (lhs) and the subharmonic (rhs) resonances exhibit a rich periodic behaviour. Between the resonance horns the driven oscillation

is quasiperiodic. In regions where the periodic states start to overlap, chaotic oscillations can occur.

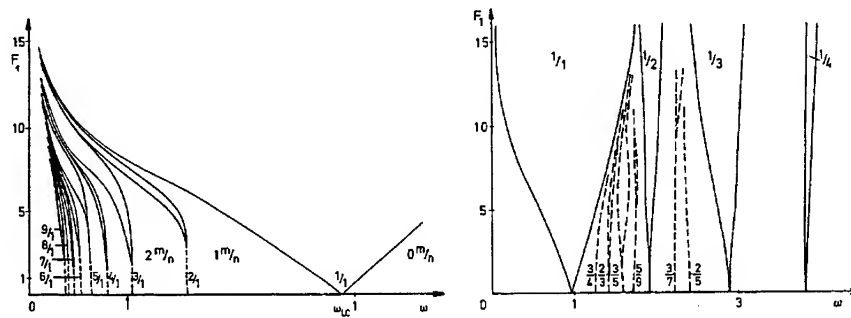


Fig. 2: resonances as a function of the external field parameters (ω : frequency, F_1 : field strength). m/n is a specific type of a winding number, it gives the ratio of internal to external oscillations per period n .

From a biological point of view the combined interaction of static and periodic fields is important. This can be demonstrated with the following nonlinear oscillator, the coherent oscillation model [1]. The equations read:

$$\dot{X} = \gamma X + \alpha XY + (c^2 e^{\Gamma^2 X^2} - d^2)X + F_0 + F_1 \cos(\omega t) \quad (2)$$

$$\dot{Y} = -\beta Y - \alpha XY \quad (3)$$

Some nonlinear resonances are shown in Fig. 3 for $F_0 = 0$.

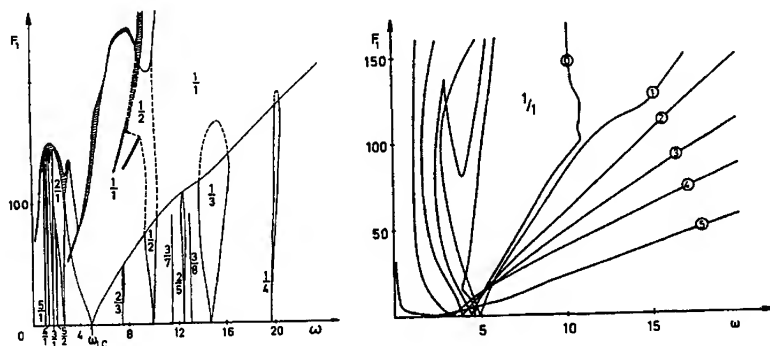


Fig. 3: resonances as a function of the external parameters ω and F_1 for model eqns. (2)-(3). On the rhs the main resonances ($1/1$) are given for different F_0 values, F_0 increases from $F_0 = 0$ to $F_0 = 200$ (circled numbers $1 \rightarrow 5$).

Some F_0 -values offer types of motion, which are completely new and unexpected [8]. Fig. 4 gives an example. For $F_0 = -40$ (depolarizing case) the 1/1, 1/2 and 1/3-resonance (vid. Fig. 3) exhibit "side resonances", which overlap and proceed like "channels" to smaller F_1 and ω values. Contrary to what one would expect, the amplitudes of the oscillations increase strongly towards the end of the "channels" i.e. for decreasing stimulus. A detailed analysis is required to understand the bifurcations related to these additional "side resonances". Fig. 4 shows the dependence of the subharmonic 1/3-resonance as a function of F_0 . With decreasing F_0 , the closed resonance horn gets bigger, the overlapping zone with the 1/1-resonance increases.

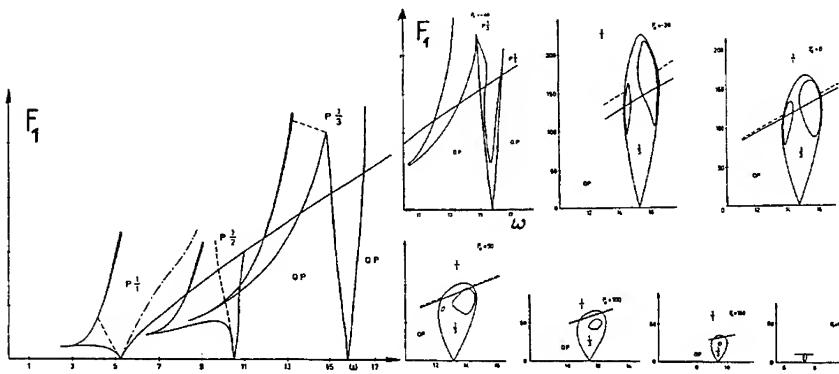


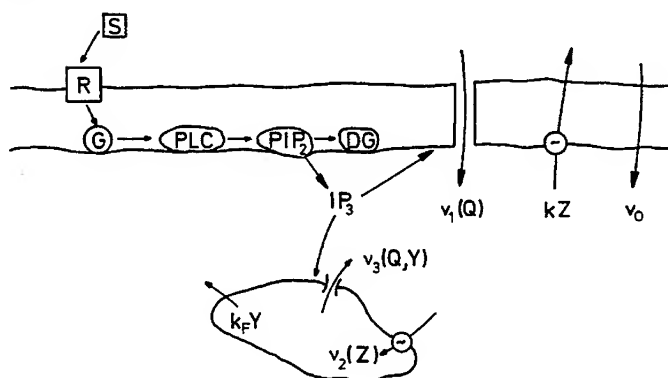
Fig. 4: resonances with "side channels" for model eqns. (2)-(3). lhs: $F_0 = -40$; rhs: 1/3-resonance for 8 different F_0 -values (straight and broken line: lower boundary of the 1/1 resonances including quasiperiodic-periodic coexisting regions).

Eqns. (1)-(3) and Fig. (2)-(4) are typical examples of externally driven limit cycle oscillators. Sharp resonances and quasiperiodic and chaotic states allow for an extreme sensitivity to external influences. The response includes frequency and intensity windows and very large transients (for details see [1,2,7]). From the point of view of nonlinear dynamics low-intensity field effects with an extreme frequency dependence are conclusive. In addition, responses with increasing or decreasing strength (positive or negative effects) can occur for nearly the same situation. This is completely impossible for linear dynamics and for thermally stimulated effects.

From the point of view of irradiated biological systems, the above results are very exciting. But important questions remain: 1. location and type of the relevant biological oscillator, 2. what are possible interaction mechanisms between oscillating states in the active biosystem and external electromagnetic fields; these problems are discussed in the next chapter, first results are given.

3. Model for Receptor-controlled Cytosolic Calcium Oscillations

The model describes the signal pathway which leads to cytosolic calcium oscillations. These oscillations are induced by a single positive feedback loop on the basis of inositol (1,4,5) triphosphate. In this contribution only the resulting set of equations is given (vid. ref. [8] for details). It should be stressed that Ca^{2+} -oscillations (intra-and intercellular) play a dominant role on the cellular level. Starting from an external signal (chemical/hormonal and/or electromagnetic) as a first messenger a whole sequence of reception, transduction and amplification processes leads to the cellular response. The following scheme displays the essential steps:



S external signal, *R* receptor, *G* G-protein, *PLC* phospholipase C, *PIP₂* and *IP₃* inositolphosphates, *DG* diacylglycerol. Intracellular concentrations for *IP₃*, Ca^{2+} and Ca^{2+} in Ca-store are *Q*, *Z*, *Y*; v_i are nonlinear fluxes.

For this conceptual model the following set of equations can be derived [8]:

$$\frac{d\Gamma}{dt} = V_T \frac{\beta^l}{K_H + \beta^l} \frac{1 - \Gamma}{K_T + 1 - \Gamma} - \kappa_T \Gamma \quad (4)$$

$$\frac{dQ}{dt} = \sigma \Phi(\Gamma, Z) - \kappa_Q Q \quad (5)$$

$$\frac{dY}{dt} = \nu_2(Z) - \nu_3(Q, Y) - k_F Y \quad (6)$$

$$\frac{dZ}{dt} = -\nu_2(Z) + \nu_3(Q, Y) + k_F Y + \nu_0 + \nu_1(Q) - k Z \quad (7)$$

$$\sigma \Phi(\Gamma, Z) = \sigma \frac{\mu_1 K_C^p + (\mu_1 + \Gamma^j) Z^p}{\mu_2 K_C^p + (\mu_2 + \Gamma^j) Z^p} \quad (8)$$

$$\nu_1(Q) = V_{M1} \frac{Q^q}{(K_M + Q)^q} \quad (9)$$

$$\nu_2(Z) = V_{M2} \frac{Z^n}{K_P + Z^n} \quad (10)$$

$$\nu_3(Q, Y) = V_{M3} \frac{Q^m}{(K_R + Q)^m} Y \quad (11)$$

When the cell is stimulated, different oscillations result, depending on the specific choice of the parameters determining the internal calcium fluxes. Fig. 5a shows four different forms, all of which have been found in experiments. If in addition to the chemical stimulus, a periodic external field is applied, a variety of responses is possible. In Fig. 5b an example is given. In this case the set of equations has been modified to allow for certain interaction processes of the external field with ion channels in the membrane. The modification is based on the additional interaction of a coherent membrane oscillator with the calcium oscillation and the stimulus.

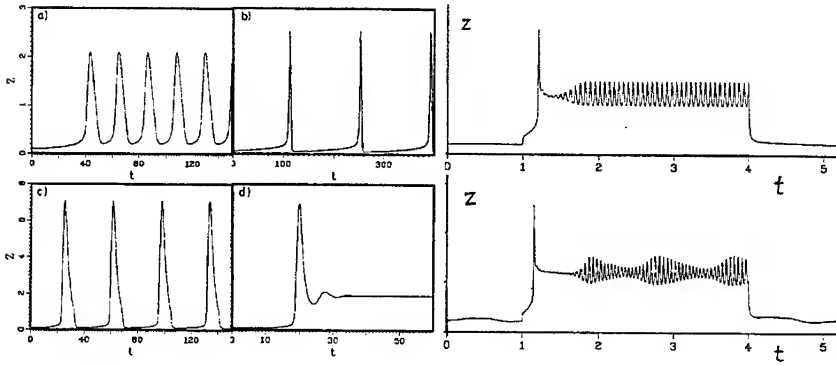


Fig. 5: oscillation diagrams. Internal Ca^{2+} -oscillation Z as a function of time, Lhs: stimulus after 10 sec., no field; rhs: modified model, no field (top), field (bottom).

For certain parameter regions, bistable situations occur, leading to switching processes between low- and high-amplitude oscillations. In the coexistence or hysteresis region the system can be influenced by small fluctuations. An investigation with multiplicative noise has shown that the oscillations are much less sensitive to noise than one would expect, only small shifts in the bifurcations are created.

The question where electric, magnetic or electromagnetic fields can interact is open. Typical examples of possible processes are [4] (1) changes in the G-protein and ion-channel conformation by the E-component of ELF-fields, (2) changes in

free radical reactions, triplet-singlet interchanges and Zeemansplitting by the ELF- and static B-field component, (3) changes in reaction rates and reaction kinetics and paramagnetic resonances in the RW- and MW region.

A detailed experimental and theoretical investigation is required to find the relevant interaction mechanisms. Besides the conformational, ion- and spin-mediated electromagnetic effects coherent macroscopic nonthermal states have to be considered. Finally, the temporal dynamics offer no complete description. The spatio-temporal behaviour and related structures, e.g. the formation of calcium waves, have to be included.

4. Conclusions

Since neither the primary nor the consequential steps are known for a specific cellular system by which low level, electric, magnetic and electromagnetic fields can interact with biological systems all possible primary interaction mechanisms have to be investigated. The models have to take into account the possibility of cellular transduction and amplification mechanisms and their alterations by external additional stimuli. Nonthermal states and nonlinear dynamics are indispensable for an understanding of the observed specific cellular effects.

The results of both the general concept and detailed model calculations and a series of highly sophisticated experiments lead to the conclusions: (1) for specific nonlinear processes in biosystems the kT -argument is meaningless, nonthermal effects can exist, (2) no contradiction to physical laws results, since nonlinear effects can – under certain conditions and restrictions – occur below the thresholds of linear theory.

Acknowledgement

The author is grateful to C. Eichwald for the development and investigation of the calcium oscillation model.

References

1. F. Kaiser, Theory of Nonlinear Excitations, in *Biological Coherence*, H. Fröhlich(ed.), 25-48, Springer Berlin (1988).
2. F. Kaiser, Biophysical Models Related to Fröhlich Excitations, *Nanobiology* 1, 149-161, 1992.
3. W. Grundler, F. Kaiser, Experimental Evidence for Coherent Excitations Correlated with Cell Growth, *Nanobiology* 1, 163-176, 1992.
4. W. Grundler, F. Kaiser, F. Keilmann, J. Walleczek, Mechanisms of Electromagnetic Interactions with Cellular Systems, *Naturwissenschaften* 79, 551-559, 1992.
5. W. Grundler, F. Keilmann, Sharp Resonances in Yeast Prove Nonthermal Sensitivity to Microwaves, *Phys. Rev. Lett.* 51, 1214-1216, 1983.
6. J. Walleczek, Electromagnetic Field Effects on Cells of the Immune System: the Role of Calcium Signalling. *FASEB J.* 6, 3177-3185, 1992.
7. F. Kaiser, C. Eichwald, Bifurcation Structure of a Driven, Multi-limit-cycle van der Pol Oscillator. *Int. J. Bif. and Chaos* 1, 485-491. 1991.
8. F. Kaiser, T. Rathert (in preparation) and T. Rathert, Diploma Thesis, Darmstadt 1992.
9. C. Eichwald, F. Kaiser, Model for Receptor-controlled Cytosolic Calcium Oscillations and for External Influences on the Signal Pathway, submitted to *Biophys. J.*

Calculation of absorbed power density in the human arm due to induced currents at 1-30 MHz

PR Wainwright, National Radiological Protection Board, Chilton, Didcot, Oxfordshire OX11 0RQ, UK.

Abstract

An anatomically realistic numerical model of the lower human arm has been constructed for the computation of current density and specific absorption rate (SAR) which result from a given current received by contact with a metal object in a radiofrequency electromagnetic field.

This study treats frequencies in the range 1-30 MHz. Current density and SAR distributions were obtained using a finite-element solution of the quasistatic field equation. The distribution of SAR is presented for each of the major tissues in the arm to illustrate the nature of the 'hot-spot' which occurs at the wrist.

I. Introduction

Previous work by several authors [1,2,3,4] has highlighted the possibility of high local current densities occurring in the ankle when the human body acts as an antenna in a vertically polarized E -field near its resonance frequency (about 40 MHz for a well-grounded person).

A similarly high absorption rate will be expected in the wrist if current is received by the hand, for example by contact with a metal object acting as an antenna in a radiofrequency electromagnetic field. In this paper an anatomically realistic mathematical model of the arm is used to calculate the distribution of current and SAR to be expected in the wrist under these conditions.

II. The Mathematical Model

In order to calculate the current density and absorbed power distributions in the lower arm the quasistatic approximation to Maxwell's equations has been used. It is known [2] that the resonant frequency for a grounded man in a

vertical E -field is about 40 MHz, at which point the vertical extent of the body contains one quarter-wavelength; even at this frequency the length of the lower arm is considerably smaller than the wavelength of the radiation, and under these circumstances the quasistatic approximation is known to be valid. This means that the electric field can be derived from an electrostatic potential ϕ satisfying the partial differential equation

$$\nabla \cdot \{(\sigma + i\omega\epsilon)\nabla\phi\} = 0 \quad (1)$$

where σ is the conductivity of the tissue, ϵ is the permittivity, and ω the circular frequency of the current. The current density J is related to the gradient of the potential by

$$J = (\sigma + i\omega\epsilon)E = -(\sigma + i\omega\epsilon)\nabla\phi \quad (2)$$

and its normal component is required to be continuous at tissue interfaces. The specific absorption rate is then given by

$$\frac{1}{\rho} \nabla\phi \cdot \sigma \nabla\phi \quad (3)$$

The area of the hand which is in contact with the metallic object will be at a uniform potential, so the homogeneous Dirichlet condition $\phi = 0$ is applied on that portion of the boundary. Near the proximal boundary of the modelled region (just below the elbow) the cross-sectional configuration of the arm changes quite slowly with height, and therefore the equipotential surfaces are approximately flat and oriented at right angles to the bones of the arm. Using this property the known current input to the model can be distributed over the proximal boundary of the model to provide a Cauchy condition on the current density J . On the remaining parts of the boundary there is no normal current flow, so the normal derivative of ϕ vanishes.

In order to solve the above equations and boundary conditions, the Galerkin finite element (FE) method has been used. By expanding the

approximate solution ϕ in terms of elementary basis functions $\alpha_i(x,y,z)$

$$\phi(x,y,z) = \sum_{i=1}^N \phi_i \alpha_i(x,y,z) \quad (4)$$

and demanding that the residual of the partial differential equation (1) be orthogonal in L^2 -norm to each of the basis functions α_i , the linear system

$$\sum_{j=1}^N A_{ij} \phi_j = b_i \quad (5)$$

is obtained, where the coefficient matrix A and the vector right hand side b are given by

$$\begin{aligned} A_{ij} &= \int \nabla \alpha_i \cdot \sigma \nabla \alpha_j dV \\ b_i &= - \int J \alpha_i dS \end{aligned} \quad (6)$$

In this project, *linear tetrahedral* elements were used. The spatial region under consideration is approximated by a mesh of tetrahedral elements (not necessarily regular in shape), whose vertices are called *nodes*. To the node numbered i there corresponds a basis function α_i with the properties:

- (1) α_i is a linear function of the coordinates on each element;
- (2) α_i is continuous at the interface of any two adjacent elements;
- (3) $\alpha_i = 1$ at the node numbered i ;
- (4) α_i vanishes at all other nodes.

Using this basis, the unknown ϕ_i is just the electrostatic potential at the node i .

The Cauchy boundary conditions are already incorporated in the right-hand side of the linear system (5). The Dirichlet condition at the earthed part of

the surface is imposed subsequently by the following device: the diagonal matrix element A_{ii} corresponding to the node i to be earthed is multiplied by a large scale factor (10^{10}) and the corresponding right-hand side element b_i is replaced by zero. When solving the linear system this will ensure that $\phi_i = 0$.

III. Construction of the Mesh

The region of interest was bounded by the surface of the arm together with cutting planes at the metacarpophalangeal joint (upper joint of the thumb), and at about one centimetre below the elbow. The remainder of the hand was not modelled, since the current distribution there depends critically on the geometry of the contact area.

The finite element mesh contains 6784 nodes and 33637 tetrahedral elements. The model contains four kinds of tissue:

- (1) a composite skin/fat outer layer
- (2) other fat and connective tissue
- (3) muscle
- (4) bone

In the region considered there is no current flow through the external surfaces of the model, and therefore the current will be very nearly parallel to the skin/fat interface. It is therefore appropriate to treat the skin and subcutaneous fat as a pair of parallel resistances, and an effective conductivity for the composite outer layer can be calculated on this basis.

IV. Results

Calculations of SAR and current density have been performed for a current of 100 mA at frequencies 1, 10, 20 and 30 MHz. Several averaging procedures have been employed to present the data. Figures 1 to 3 present the SAR for 10 MHz radiation, averaged over the elements of skin, muscle and bone in *each layer* of the model. The layer position is measured from the distal end of the model (metacarpophalangeal joint). In the neighbourhood of the wrist muscles from the hand and of the arm both terminate, and near their ends the current is therefore channelled into a narrowing region surrounded by relatively insulating connective tissue. The graphs clearly show the effects of current concentration at the wrist in all tissues, but particularly so in the muscle. In a few slices of the wrist the amount of muscle present was so low that it could not

be accurately modelled; therefore here (at about the 6.0 cm level) no results were obtained. However, the amount of tissue in the affected layers is so small (no more than a few grams) that excessive power deposited here will rapidly and efficiently be removed by thermal conduction and blood perfusion, so this omission is not significant in thermal terms. Figure 4 shows the SAR averaged over *all* tissues in each layer.

The two prominent peaks which occur in the bone SAR (Figure 3) seem to be associated with the points at which major muscles terminate, depositing their current in the bone and connective tissues. The higher peak (2.5 W/kg) occurs at the terminus of the pronator quadratus muscle; the lower peak (2 W/kg) is located at the point where in the model the bones of the hand have been fused together, terminating the first dorsal interosseous muscle.

V. Outlook

Future work is planned to integrate the electromagnetic model with a thermal model of the arm and to calculate the resultant temperature distributions.

VI. Acknowledgements

The author would like to thank Peter Dimbylow for helpful discussions.

This project was supported by the Ministry of Defence under contract NSM708A/1044.

References

1. P.J. Dimbylow. The calculation of induced currents and absorbed power in a realistic, heterogeneous model of the lower leg for applied electric fields from 60 Hz to 30 MHz, *Phys. Med. Biol.*, **33** No 12, 1453-1468 (1988).
2. P.J. Dimbylow. Finite-Difference Time-Domain Calculations of Absorbed Power in the Ankle for 10-100 MHz Plane Wave Exposure. *IEEE Trans. Biomed. Eng.*, **38** No 5, 423-428 (1991).

-
3. J-Y. Chen and O.P. Gandhi. Thermal implications of high SARs in body extremities at the ANSI-recommended MF-VHF safety limits. *IEEE Trans. Biomed. Eng.*, **35**, 435 (1988).
 4. M. Hoque and O.P. Gandhi. Temperature distributions in the human leg for ULF-VHF exposures at ANSI-recommended safety levels. *IEEE Trans. Biomed. Eng.*, **35**, 442 (1988).

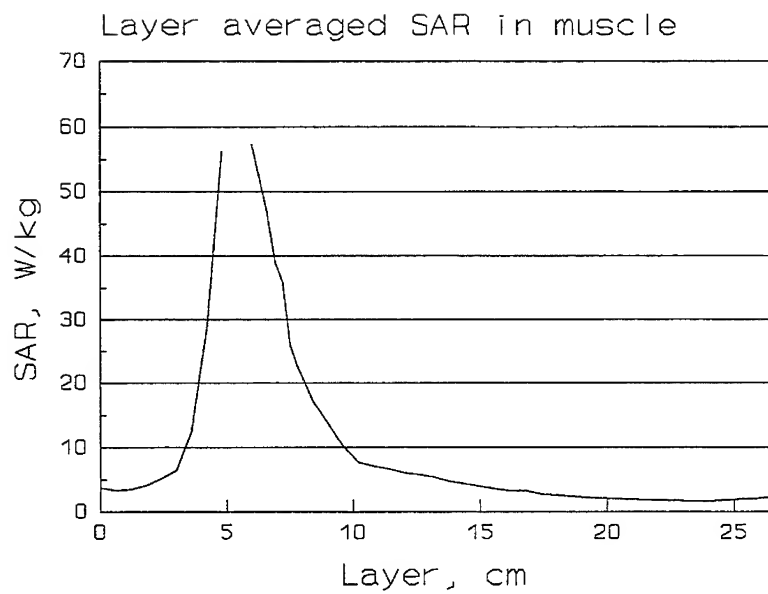


Figure 1

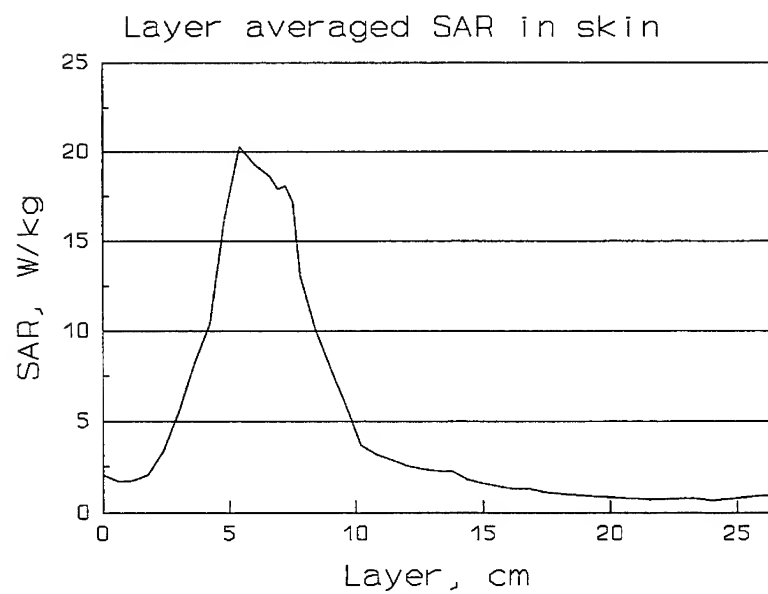


Figure 2

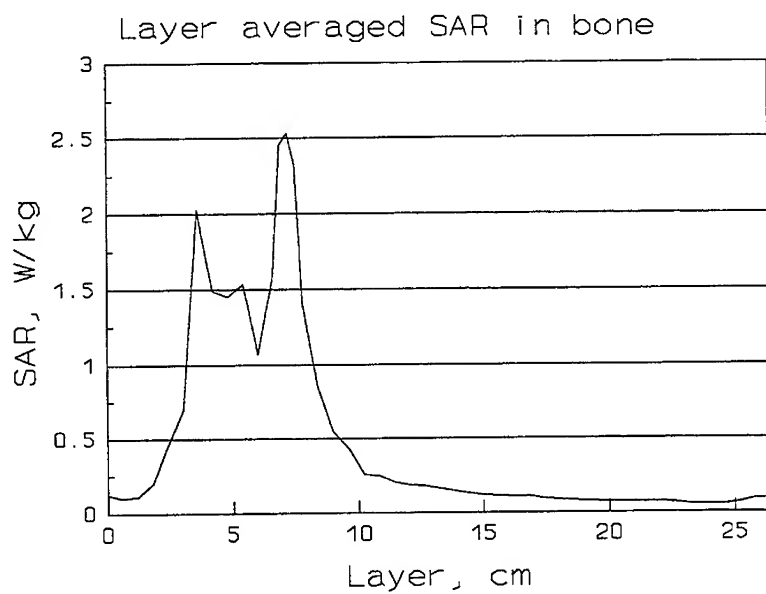


Figure 3

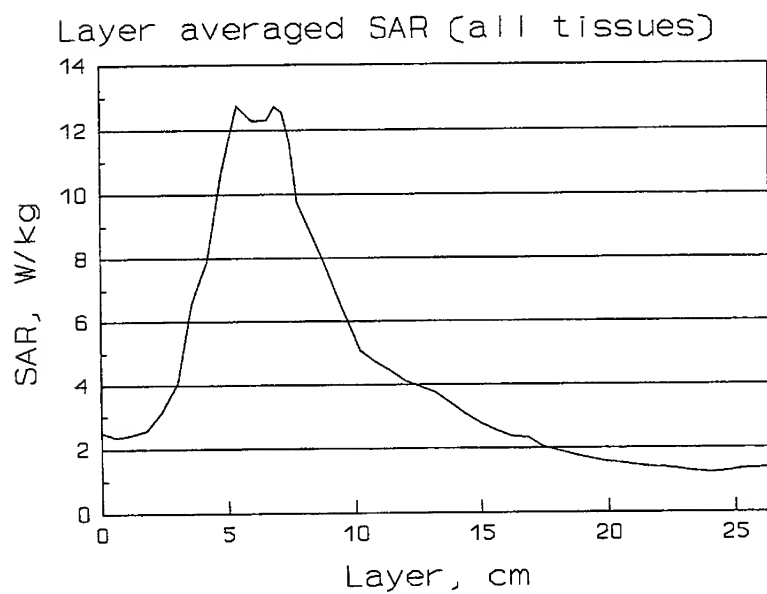


Figure 4

SESSION 13 - "TIME-DOMAIN TECHNIQUES II

(FEATURING TLM)"

Chair: Dr. Wolfgang J.R. Hoefer, Co-Chair: Dr. Fred German

A COMPARISON OF CURRENTS INDUCED ON SCATTERING BODIES
USING THE TRANSMISSION LINE MODELING (TLM) METHOD
AND THE METHOD OF MOMENTS (MOM)

Griffin K. Gothard

Sadasiva M. Rao

Department of Electrical Engineering
Auburn University, AL 36849

ABSTRACT

The transmission line modeling (TLM) method and the marching-on-in-time (MOT) technique are used to predict transient current densities on scattering bodies due to an incident Gaussian plane wave. The results from these two methods are compared and analyzed. Example calculations are presented for two-dimensional and three-dimensional geometries.

I. INTRODUCTION

Direct time-domain analysis of various scattering bodies is accomplished using the transmission line modeling (TLM) method and the marching-on-in-time (MOT) method. A simulated Gaussian plane wave is used to induce currents on the scattering bodies, and the TLM and MOM results are compared. The TLM method is an iterative numerical time-domain technique based on the differential form of Maxwell's equations, while the MOT is based on the integral equation solution and uses the well known method of moments (MOM). A comparison between these two techniques will help point out the relative strengths and weaknesses of each method.

In the next section, a brief overview of the TLM method is provided. In section III, an outline of MOT is provided. In section IV, transient current densities, as predicted by TLM and MOT, are compared and analyzed. Finally, in section V, appropriate conclusions are summarized.

II. TRANSMISSION LINE MODELING (TLM) METHOD

The TLM method, an iterative numerical time-domain technique, is based on the equivalence between voltages, currents, and lumped circuit elements, and electric fields, magnetic fields, and constitutive material parameters, respectively, in some region of space [1]. These equivalencies are obtained by relating the differential equations describing a small length of transmission line to the differential Maxwell's equations describing a block of space.

Three dimensional formulations of TLM include the expanded node [2], the condensed node [3], and the symmetrical condensed node [4]. For this work, the code GTEC (which utilizes the symmetrical condensed node) developed by German [5] is used. The theory behind the symmetrical condensed TLM method is presented in [4].

III. MARCHING-ON-IN-TIME (MOT) METHOD

The marching-on-in-time (MOT) technique is an iterative technique based on the method of moments (MOM). In this work, the MOT equation is obtained by solving the electric field integral equation (EFIE) directly in the time domain and approximating the conducting body with planar triangular patches. Crucial to the development of an accurate solution is the usage of specially developed basis functions in the MOM solution.

One disadvantage of the MOT technique is the occurrence of late-time oscillations. However, by employing specially designed averaging techniques [7,8] one can effectively eliminate this problem. For more details refer [6-8].

IV. NUMERICAL RESULTS

In this work, an incident Gaussian plane wave was used and of the form

$$E^{inc}(r,t) = E_0 e^{-\gamma^2}$$

where

$$\gamma = \frac{[t - t_0 - (r-k)/c]}{\sigma}$$

Note that E^{inc} is the incident field, E_0 is the polarization vector with unit magnitude, k is the unit vector in the direction of propagation of the incident field, σ is the standard deviation, $E_0 \cdot k = 0$, r is a position vector relative to the origin, c is the velocity of propagation in the external medium, and t_0 is a time delay which represents the time at which the pulse peaks at the origin. The scattering bodies include a two-dimensional strip and a square cylinder (infinite in the z -direction), and a three-dimensional cube, plate, and parallel plate structure. A Sparc-2 SUN Workstation was used for all numerical calculations.

Figure 1 shows the induced transient current on an infinitely long 1.0m width strip illuminated by a transverse magnetic (TM) Gaussian plane wave ($\sigma = 1.25\text{ns}$, $t_0 = 7.50\text{ns}$) as predicted by TLM and MOT. To generate the transient currents, the TLM method (with one symmetry boundary) uses a problem space of $30 \times 35 \times 1$ nodes, and implements 800 time steps (iterations). For the MOT, the strip was divided into 9 equal segments. The cpu time for both cases is similar. As is evident from the figure, we see good early time agreement, which, however, deviates in the late time. The currents predicted by the TLM method decay much faster than the MOT. Also, since the MOT has been validated using inverse discrete Fourier transform techniques, it is assumed that its solution is more accurate. Using a larger problem space, the TLM results appear to approach the MOT results but the improvements are not substantial.

Figure 2 shows the transient current on an infinite (in the z -direction) square cylinder, 1.0m to a side, illuminated by a TM Gaussian plane wave ($\sigma = 1.25 \times 10^{-9}$, $t_0 = 7.5\text{ns}$) as predicted by TLM and MOT. To generate the transient currents, the TLM method (with one symmetry boundary) uses a problem space of $60 \times 40 \times 1$ nodes, implements 1000 iterations, and requires 2min 31sec of cpu time. For the MOT solution, the cylinder was approximated by 76 linear segments, and the cpu run time was approximately 45min. Again in Figure 2, both results

exhibit good early time agreement but a faster decay in the late time by the TLM method.

Next, we consider the three-dimensional problems. For all cases, the incident wave is assumed to be x-polarized and travelling along the z-direction.

Figure 3 shows the x-directed transient current at the center of a $2.0\text{m} \times 2.0\text{m}$ plate located in the xy plane illuminated by a Gaussian plane wave ($\sigma = 2.5\text{ns}$, $t_0 = 15\text{ns}$) as predicted by TLM and MOT. The TLM method (with two symmetry boundaries) uses a problem space of $40 \times 40 \times 30$ nodes, implements 800 iterations and requires 58min 40sec of cpu time. For the MOT problem the plate is approximated by 20 triangular patches and requires a cpu time of approximately 5min. In Figure 3 we see good overall agreement between the TLM and MOT predicted transient currents, both in the early time and late time. In fact, by increasing the TLM problem space, the TLM results approach those predicted by the MOT technique.

Figure 4 shows the x-directed transient current at the center of the front face of a cube, 1.0m to a side, illuminated by a Gaussian plane wave ($\sigma = 5.0\text{ns}$, $t_0 = 30.0\text{ns}$) as predicted by TLM and MOT. The TLM method (with two symmetry boundaries) uses a problem space of $60 \times 30 \times 30$ nodes, implements 1000 iterations and requires 53min 26sec of cpu time. For the MOT problem, the cube is approximated by 136 triangular patches and requires 20min of cpu time. In Figure 4, we see good overall agreement between the TLM and MOT predicted transient currents. Again, as the TLM problem space is increased, the TLM solution approaches the MOT solution.

Figure 5a and 5b shows the x-directed transient current at the center of the top and bottom plate, respectively, of a parallel plate structure illuminated by a Gaussian plane wave ($\sigma = 5.0\text{ns}$, $t_0 = 30.0\text{ns}$) as predicted by TLM and MOT. The plates (2.0m to a side and separated by 2.333m) are each oriented parallel to the xy plane. The TLM method (with two symmetry boundaries) uses a problem space of $65 \times 35 \times 35$ nodes, implements 1000 iterations and requires 1hr 8min 20sec of cpu time. For

the MOT problem, the two plates are approximated by 40 triangular patches and requires approximately 10min cpu time. Again, as seen in Figures 3 and 4, Figure 5 shows good overall agreement.

V. CONCLUSIONS

In three dimensions, the TLM method is capable of accurately predicting the transient current densities on scattering bodies. However, the TLM method applied to two-dimensional scattering bodies exhibits accuracy problems in the late time. These inaccuracies can be improved upon, but not totally eliminated, by increasing the TLM problem space. Further investigation of this problem is underway.

REFERENCES

- [1]. G. Kron, "Equivalent circuit of the field equations of Maxwell-I," Proc. IRE, 32, 289-299 (1944).
- [2]. S. Akhtarzad and P. B. Johns, "Solution of Maxwell's equations in three space dimensions and time by the T.L.M. method of numerical analysis," Proc. IEE, 122 (12), 1344-1348 (1975).
- [3]. P. Saguet and E. Pic, "Utilisation d'un nouveau type de noeud dans la methode TLM en 3 dimensions," Electron. Lett., 18 (11), 478-479 (1982).
- [4]. P. B. Johns, "A symmetrical condensed node for the TLM method," IEEE Trans. Micro. Theory Tech., MTT-35 (4), 370-377 (1987).
- [5]. F. J. German, G. K. Gothard, L. S. Riggs and P. M. Goggans, "The calculation of radar cross-section (RCS) using the TLM method," Int. J. Numerical Modeling, 2 (4), 267-278 (1989).
- [6]. S. M. Rao and D. R. Wilton, "Transient scattering by conduction surfaces of arbitrary shape," IEEE Trans. Antennas Propagat., 39 (1), 56-61 (1991).
- [7]. B. P. Rynne, "Time domain scattering from arbitrary surfaces using the electric field integral equation," J. Electromag. Waves Appl., 5, 93-112 (1991).
- [8]. D. A. Vechinshi and S. M. Rao, "A stable procedure to calculate the transient scattering by conducting surfaces of arbitrary shape," IEEE Trans. Antennas Propagat., 40 (6), 661-665 (1992).

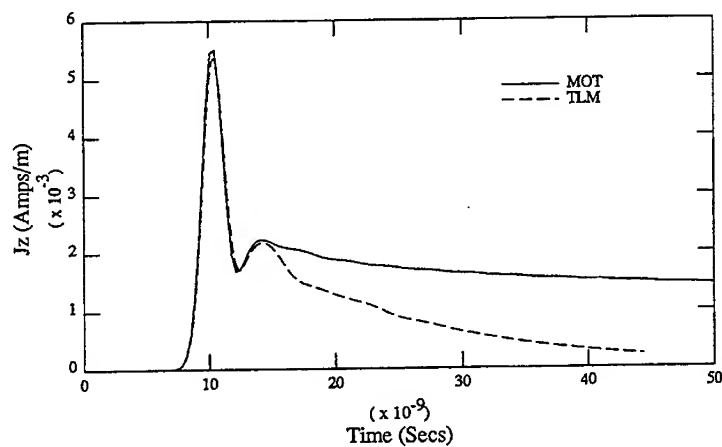


Figure 1. The induced transient current at the center of an infinite 1.0m strip illuminated by a normally incident TM Gaussian plane wave with $\sigma = 1.25\text{ns}$ and $t_0 = 7.5\text{ns}$.

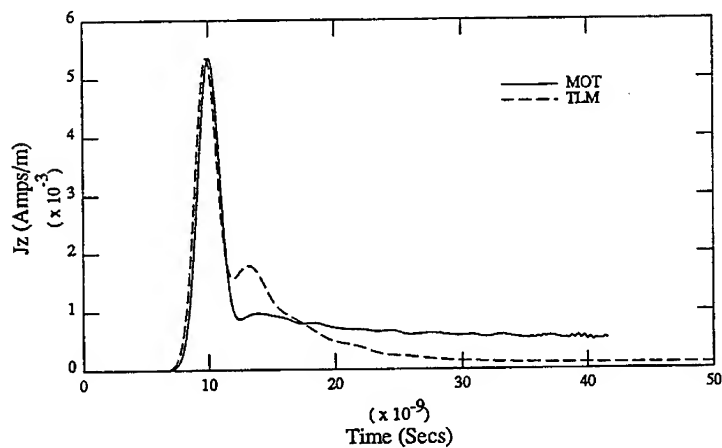


Figure 2. The induced transient current at the center of the front side of an infinite square cylinder, 1.0m to a side, illuminated by a normally incident TM Gaussian plane wave with $\sigma = 1.25\text{ns}$ and $t_0 = 7.5\text{ns}$.

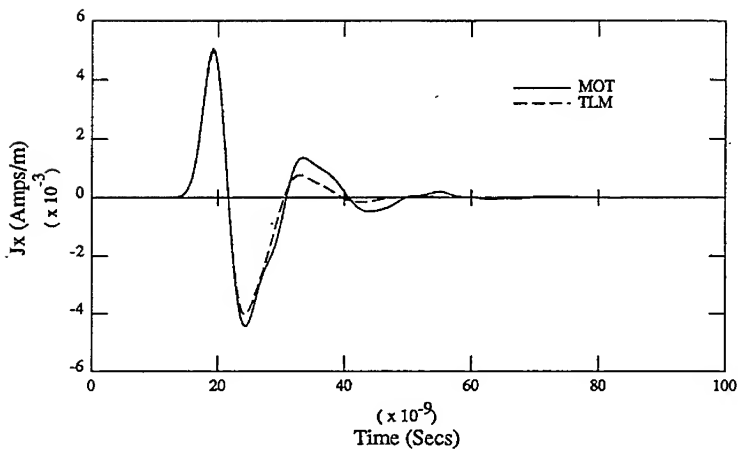


Figure 3. The x-directed transient current at the center of a $2.0\text{m} \times 2.0\text{m}$ plate, located in the xy plane, illuminated by a Gaussian plane wave with $\sigma = 2.5\text{ns}$ and $t_0 = 15.0\text{ns}$.

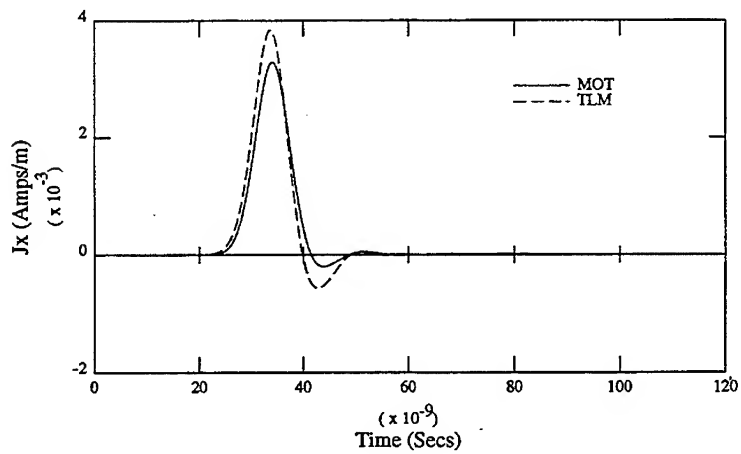
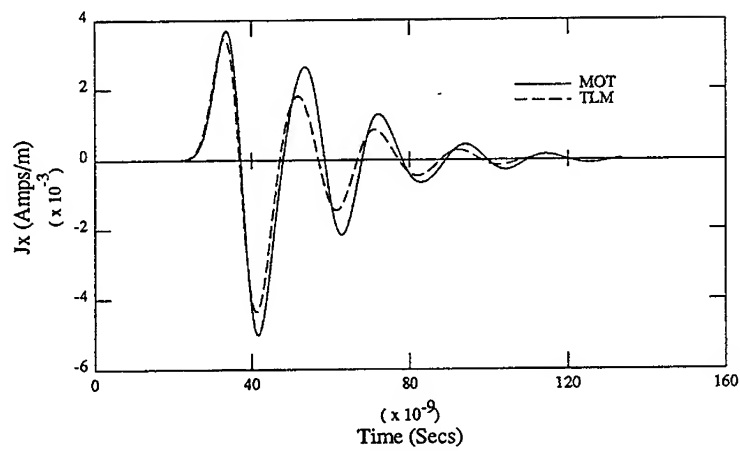
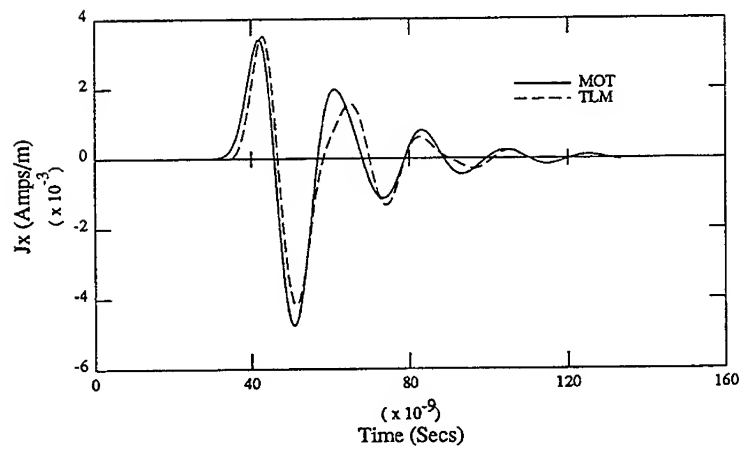


Figure 4. The x-directed transient current at the center of the front face of a cube, 1.0m to a side, illuminated by a Gaussian plane wave with $\sigma = 5.0\text{ns}$ and $t_0 = 30.0\text{ns}$.



a.)



b.)

Figure 5. The x-directed transient current at the center of a.) the top plate and b.) the bottom plate of a parallel plate structure illuminated by a Gaussian plane wave with $\sigma = 5.0\text{ns}$ and $t_0 = 30.0\text{ns}$. The plates, $2.0\text{m} \times 2.0\text{m}$, are separated by 2.333m .

Transmission Line Matrix (TLM) Modeling of a Stepped-Septum Square-Waveguide Polarizer

Lloyd S. Riggs, G. K. Gothard, and Fred J. German
Department of Electrical Engineering
Auburn University, AL 36849
(205) 844-1866

and

Chuck Chandler
Jet Propulsion Laboratory
4800 Oak Grove Drive, MS 161-213
Pasadena, CA 91109

Abstract

The TLM in conjunction with a wideband absorbing boundary method based on a time domain diakoptics (Johns Matrix) approach is used to compute the VSWR, isolation, axial ratio, and tilt angle of a stepped-septum, square-waveguide polarizer.

Introduction

This paper presents a transmission line matrix (TLM) investigation of a stepped-septum square waveguide polarizer. The design investigation is in support of the dual frequency low gain antenna for NASA's Cassini Spacecraft emergency command and low data rate link. NASA also has a general interest in creating an analytic tool capable of assessing and optimizing polarizer designs based on various mission requirements (typically 7-9 GHz).

Operation of the Polarizer

Figure 1. shows a simple schematic of a stepped-septum square-waveguide polarizer and its equivalent network. According to Chen and Tsandoulas [1], even mode excitation of the rectangular waveguide region (i.e. $a_1 = a_3 = 1$, $a_2 = a_4 = 0$) results in propagation of an even mode wave which will be unaffected by the septum and will transfer its total energy into the TE_{10} mode in the square waveguide. Furthermore, they point out that for odd mode excitation (i.e. $a_1 = 1$, $a_2 = -1$, $a_3 = a_4 = 0$) there will be no coupling to the TE_{10} mode and the odd-mode energy will be partially transferred to the TE_{01} mode in the square waveguide and partially reflected. When only port one is excited, which is equivalent to a superposition of the even and odd mode cases just described, the polarizer is in operation and some of the incident energy will be transferred to the TE_{10} mode and some to the TE_{01} mode. In Figure 1, b_1 is the power reflected back to the input port, which determines the VSWR of the device, and b_2 represents the power coupled to the nonexcited input, which determines the isolation. The relative amplitude and phase

of b_3 and b_4 determine the axial ratio and major-axis tilt angle of the elliptically-polarized wave. The design objective is to obtain perfect circular polarization and under this condition b_3 and b_4 will be equal in magnitude and 90° out of phase.

The TLM Method

The TLM method is ideally suited to the analysis of the stepped-septum polarizer first proposed in [1] for several reasons. First, the geometry of the structure can be very easily specified using only rectangular primitives, which allows the basic and efficient TLM algorithm in the cartesian coordinate system to be utilized. Since the characteristics of the device over the 7.1 to 8.5 GHz frequency band is desired, the TLM simulation can be used, in conjunction with techniques recently developed by Hoefer et. al. [2]-[5] for simulating wideband absorbing boundaries, to yield the required results at all frequencies within the desired bandwidth in a single run of the program. This gives the TLM a significant advantage over the integral equation based method of moments (MOM) which would require a large set of simultaneous equations to be resolved at each frequency of interest. Because of the ease with which the geometry is specified and the ability to obtain wide band data in a single run, the TLM method is a very attractive technique to use for optimization of the polarizer.

The Symmetrical Condensed Node

The symmetrical condensed TLM node developed by Johns [6] and shown in Figure 2 will be used to analyze the polarizer. The condensed node has six branches and each branch consist of two uncoupled two-wire transmission lines. A three-dimensional grid of these elements is used to model the polarizer as described in greater detail subsequently. Excitation of the grid (or mesh) is accomplished by forcing ideal impulses to propagate on selected transmission line branches. Impulses propagating along a transmission line encounter an impedance discontinuity upon arriving at the center of the node and consequently are scattered according to the following scattering matrix originally derived by Johns [6],

$$\begin{bmatrix} v_1 \\ v_2 \\ v_3 \\ v_4 \\ v_5 \\ v_6 \\ v_7 \\ v_8 \\ v_9 \\ v_{10} \\ v_{11} \\ v_{12} \end{bmatrix}^r = \frac{1}{2} \begin{bmatrix} 0 & 1 & 1 & 0 & 0 & 0 & 0 & 0 & 1 & 0 & -1 & 0 \\ 1 & 0 & 0 & 0 & 0 & 1 & 0 & 0 & 0 & -1 & 0 & 1 \\ 1 & 0 & 0 & 1 & 0 & 0 & 0 & 1 & 0 & 0 & 0 & -1 \\ 0 & 0 & 1 & 0 & 1 & 0 & -1 & 0 & 0 & 0 & 1 & 0 \\ 0 & 0 & 0 & 1 & 0 & 1 & 0 & -1 & 0 & 1 & 0 & 0 \\ 0 & 1 & 0 & 0 & 1 & 0 & 1 & 0 & -1 & 0 & 0 & 0 \\ 0 & 0 & 0 & -1 & 0 & 1 & 0 & 1 & 0 & 1 & 0 & 0 \\ 0 & 0 & 1 & 0 & -1 & 0 & 1 & 0 & 0 & 0 & 1 & 0 \\ 1 & 0 & 0 & 0 & 0 & -1 & 0 & 0 & 0 & 1 & 0 & 1 \\ 0 & -1 & 0 & 0 & 1 & 0 & 1 & 0 & 1 & 0 & 0 & 0 \\ -1 & 0 & 0 & 1 & 0 & 0 & 0 & 1 & 0 & 0 & 0 & 1 \\ 0 & 1 & -1 & 0 & 0 & 0 & 0 & 0 & 1 & 0 & 1 & 0 \end{bmatrix} \begin{bmatrix} v_1 \\ v_2 \\ v_3 \\ v_4 \\ v_5 \\ v_6 \\ v_7 \\ v_8 \\ v_9 \\ v_{10} \\ v_{11} \\ v_{12} \end{bmatrix}^i \quad (1)$$

where the "i" and "r" superscripts correspond to incident and reflected voltage pulses respectively and the subscript "k" identifies the iteration number (i.e. TLM is a time domain method). Pulses scattered at one node are connected to (become incident upon) adjacent nodes whereupon the process is repeated and so on until eventually pulses have propagated throughout the mesh. Repeated application of the scattering-connection process results in an output function at some chosen observation position (output node) which consist of a train of pulses in time. Typically, output in the frequency domain is desired which can be obtained by Fourier transforming the output time domain sequence.

From [6], the cartesian field components at any given node are related to the incident voltage pulses at that node by

$$E_x = 1/2 (V_1^i + V_2^i + V_9^i + V_{12}^i) \quad (2a)$$

$$E_y = 1/2 (V_3^i + V_4^i + V_8^i + V_{11}^i) \quad (2b)$$

$$E_z = 1/2 (V_5^i + V_6^i + V_7^i + V_{10}^i) \quad (2c)$$

$$H_x = 1/2Z_o (V_4^i - V_5^i + V_7^i - V_8^i) \quad (2d)$$

$$H_y = 1/2Z_o (-V_2^i + V_1^i + V_9^i - V_{10}^i) \quad (2e)$$

$$H_z = 1/2Z_o (-V_3^i + V_6^i + V_{11}^i - V_{12}^i) \quad (2f)$$

where Z_o is the characteristic impedance of the individual transmission lines.

Boundaries

Figure 2 presents the critical dimensions and the TLM discretization scheme for the polarizer of reference [1]. A symmetrical condensed node is contained within each square in Figure 2A so that a total of $24 \times 24 \times 120 = 69,120$ nodes will be used in the TLM model. The waveguide walls and septum are easily modeled by inverting and reversing the direction of propagation (multiplying by -1) all voltages pulses incident upon perfectly conducting boundaries. It is necessary to match the input and output ports of the polarizer in order to compute the desired scattering parameters. A narrow band match is easily achieved by multiplying voltages pulses incident on the input and output plane by the reflection coefficient

$$\Gamma = \frac{Z_g - Z_o}{Z_g + Z_o}$$

where $Z_g = Z_o / [1 - (f_c/f)^2]^{1/2}$ is the frequency dependant fundamental waveguide impedance (f_c is the waveguide cutoff frequency and f is the operating frequency). Since, in general, we wish to compute scattering parameters over a band of frequencies the use of (3) to match the input and output ports will require that a new time domain response be computed and Fourier transformed at each frequency of interest. Alternatively, a much more efficient means of achieving a wide band absorbing boundary has been presented by Hoefer et. al. [2]-[5]. There method represents a refinement of a time domain diakoptics approach first presented by Johns and Akhtarzad [7]. Because the input and output ports of the polarizer support

only the fundamental waveguide mode (orthogonal fundamental modes in the square waveguide section) a particularly simple method can be used to create a wide band match. First, we excite only the nodes across the front face of a long section of waveguide making sure that the amplitude of the excitation pulses follow the half sine wave distribution of the fundamental mode. This excitation will cause a stream of impulses to flow out of the nodes across the face of the waveguide and since this output stream also has a half sine distribution one need only store the impulse train associated with the condensed node at the center of the guide. (Note that the condensed nodes along the input face must be match terminated during this process.) The stored impulse train constitutes what has been termed [5] a one-dimensional Johns Matrix. The Johns Matrix will be used, as described next, to match terminate the input and output ports of the polarizer. When the input plane of the polarizer is excited in the half-sine distribution just described, voltage pulses will flow out of the nodes located at the input and output plane. According to the procedure outlined in detail in [3], pulses injected back into the input and output plane nodes are found by convolving these reflected pulses with the one-dimensional Johns Matrix. This convolution process can be written as

$$V_2^r(k) = \sum_{k'=0}^k J(k') V_2^i(k-k') \quad (4)$$

$$V_9^r(k) = \sum_{k'=0}^k J(k') V_9^i(k-k') \quad (5)$$

$$V_8^r(k) = \sum_{k'=0}^k J(k') V_8^i(k-k') \quad (6)$$

where (4) pertains to the front face where only the TE_{10} mode is excited and (5) and (6) pertain to the square waveguide section of the polarizer where both the TE_{10} and TE_{01} modes are excited. It should also be pointed out that (4) (5) and (6) explicitly apply only to the condensed node at the center of the front and back faces. Reflected pulses at the other nodes on the input and output planes are found by scaling (4), (5) and (6), whichever is appropriate, by the half-sinusoidal distribution. Other methods may be used to compute the Johns Matrix. For example, as demonstrated by Chen et al. [4], one can compute the Johns Matrix by inverse Fourier transforming (3). Eswarappa et al. [3] have also demonstrated that a better absorbing termination can be generated by exponentially tapering the Johns Matrix. A Johns Matrix computed from a long section of waveguide (no exponential taper) was used to generate the results presented here.

Results and Conclusions

In order to compute the VSWR and isolation of the polarizer we first excite E_x on port 1, or equivalently excite V_2 on all the condensed nodes at the input plane, with the half-sinusoidal distribution previously described. Next, the total x-directed field, E_x , (incident plus reflected) is computed at the center and 10 nodes within the excitation port using (4a). Subtracting the incident field, E_x^i , (which is computed using a long section of empty waveguide) from the total field yields the scattered or reflected field, E_x^r , at input port 1 ($E_{x,1}^r = E_{x,1} - E_x^i$). The reflection coefficient is found by dividing the reflected and incident fields, $\Gamma = E_{x,1}^r/E_x^i$, and the VSWR = $(1+|\Gamma|)/(1-|\Gamma|)$, " $|\Gamma|$ " indicates magnitude. Isolation is

computed by dividing the x-directed field at port 2 by the incident field or Isolation = $20 \log(E_{x,2}/E_x)$. Finally, the axial ratio is computed from the magnitude of the ratio of the \hat{x} - and \hat{y} - directed fields in the square waveguide section $AR(\text{dB}) = 20 \log(|E_x^T|/|E_y^T|)$, and E_y^T is found using (2b). The tilt angle is computed by subtracting the angle of E_y^T from E_x^T . Figure 3 shows the VSWR, isolation, axial ratio and tilt angle for the polarizer of Figure 2 computed using the method outlined above. The oscillations observed in Figure 3A and 3B might be due to imperfect absorbing boundaries used to terminate the input and output planes of the polarizer. It is probable that these oscillations could be reduced by using the exponentially tapered Johns Matrix discussed above. This issue is currently under investigation and will be reported on during the oral presentation of this work.

References

- [1] M. Chen and G. Tsandoulas, "A Wide-Band Square Waveguide Array Polarizer", IEEE Trans. on Antennas and Propagation, pp 380-393, May 1973.
- [2] Eswarappa, G. Costache, and W. Hoefer, "Transmission Line Matrix Modeling of Dispersive Wide-Band Absorbing Boundaries with Time-Domain Diakoptics for S-Parameter Extraction, IEEE Trans. on MTT, vol 38, No. 4, pp 379-386, April 1990.
- [3] Eswarappa, and W. Hoefer, "Diakoptics and Wideband Dispersive Absorbing Boundaries in the 3-D TOM Method with Symmetrical Condensed Nodes, IEICE Transactions, vol. E 74, NO. 5, May 1991, pp 1242-1250.
- [4] Z. Chen, W. J. R. Hoefer, and M. M. Ney, "A New Procedure for Interfacing the Transmission Line Matrix (TLM) Method with Frequency Domain Solutions, IEEE Trans. on MTT, vol 39, No. 10., pp 1788-1791.
- [5] W. J. R. Hoefer, "The Discrete Time Domain Green's Function or Johns Matrix - A New Powerful Concept In Transmission Line Modeling (TLM)", International Journal of Numerical Modeling: Electronic Networks, Devices and Fields, Vol. 2, 215-224, (1989).
- [6] P. B. Johns, "A Symmetrical Condensed Node for the TLM Method", IEEE Trans. MTT, vol. 35, No. 4, April 1987, pp. 370-377.
- [7] Johns P. B. and Akhtarzad K.: "The Use of Time Domain Diakoptics in Time Discrete Models of Fields", Int J. Num. Methods Eng., 17, pp. 1-14 1981).

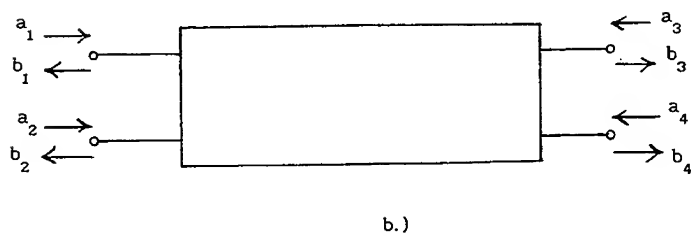
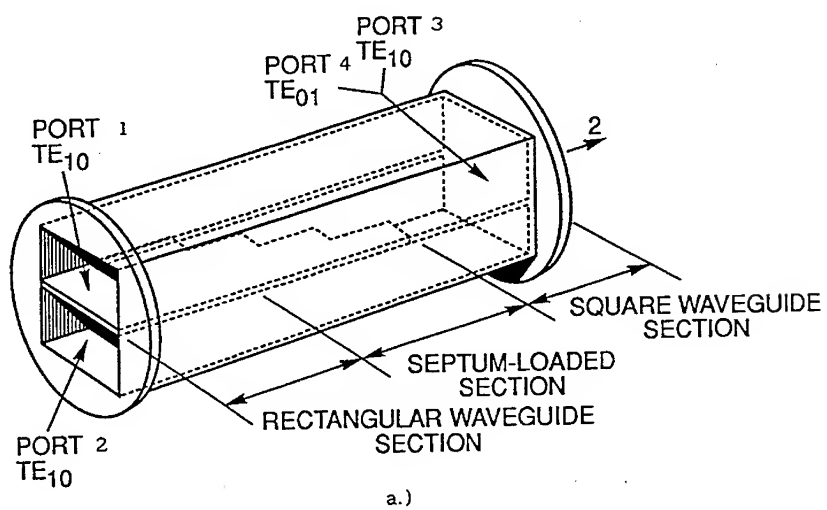


Figure 1. a.) Stepped-Septum Square-Waveguide Polarizer and b.) Equivalent Polarizer Network.

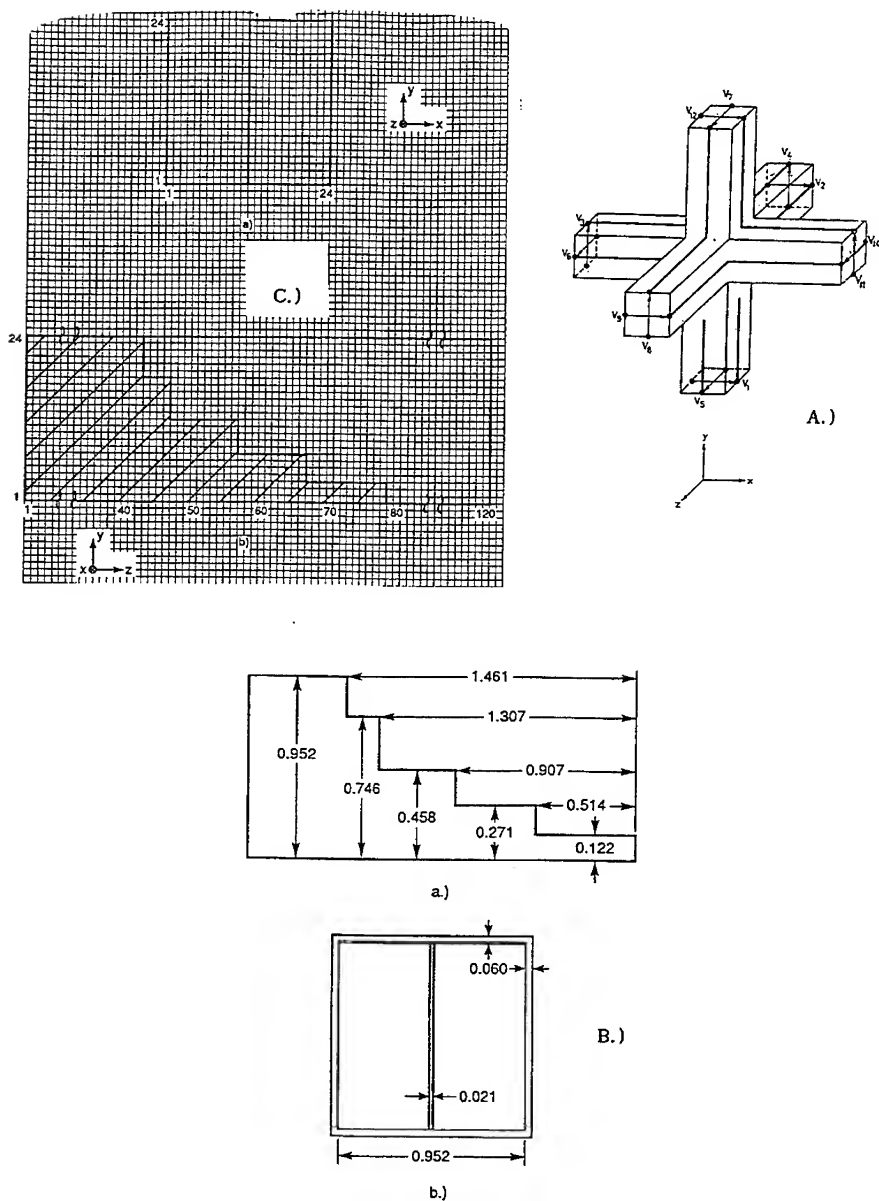
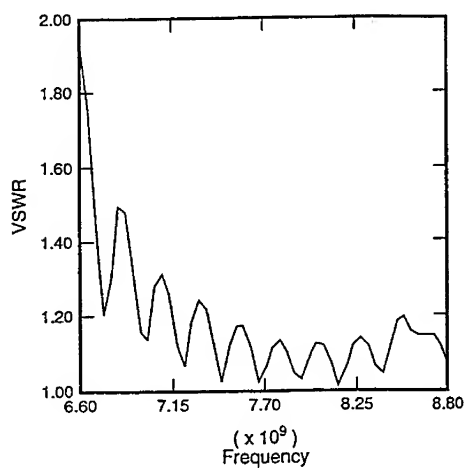
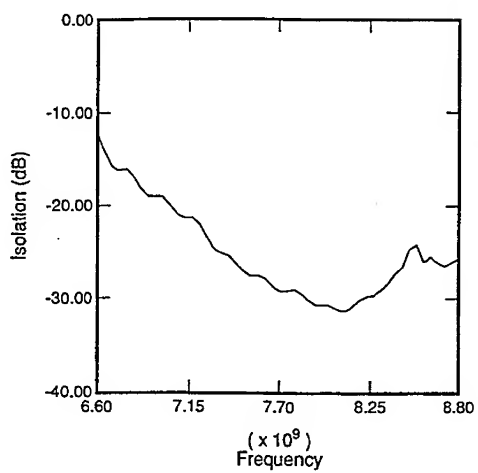


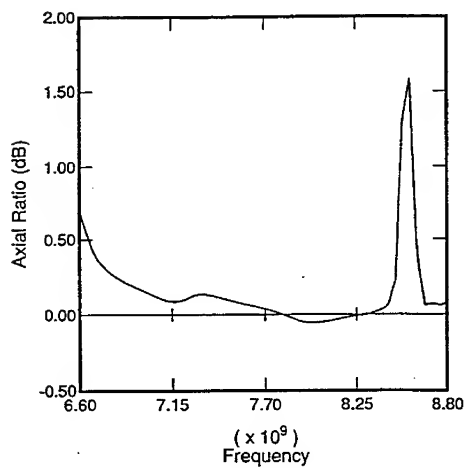
Figure 2. A.) Symmetrical Condensed Node After [6], B.) Critical Dimensions (In Wavelengths) of the Stepped-Septum Polarizer, C.) TLM Discretization Scheme for the Polarizer of Reference [1].



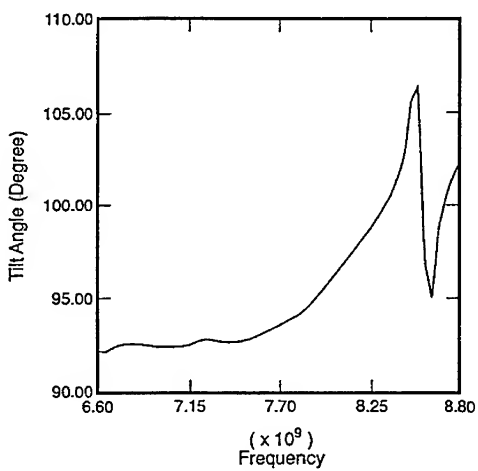
A.)



B.)



C.)



D.)

Figure 3. A.) VSWR, B.) Isolation, C.) Axial Ratio D.) and Tilt Angle for the Stepped-Septum, Square-Waveguide Polarizer of Reference [1] Computed Using TLM.

DISCRETE TIME-DOMAIN GREENS FUNCTIONS FOR THREE-DIMENSIONAL TLM MODELLING OF THE RADIATING BOUNDARY CONDITIONS

M. Krumpholz and P. Russer

Ferdinand-Braun-Institut für Höchstfrequenztechnik
Rudower Chaussee 5, O-1199 Berlin, Germany
Phone: +49 (30) 6704 2360, Fax: +49 (30) 6704 4542

Abstract

Based on the Hilbert space representation of the TLM method for time domain computation of electromagnetic fields, a method for the algebraic computation of three-dimensional discrete Green's functions describing spatial domains in TLM is presented. The Green's function is nonlocal with respect to space and time and allows an exact formulation of the absorbing boundary conditions in TLM.

I Introduction

In the TLM-method, the electromagnetic field is modelled by wave pulses propagating on a mesh of transmission lines [1,2,3]. We use the three-dimensional symmetric condensed TLM node of Johns [4]. In this case, the mesh node is modelled by a twelve port. The Hilbert space representation of the TLM method allows the algebraic description of the time evolution of the electromagnetic field [5]. In the Hilbert space representation, the complete field state is mapped into a point in Hilbert space. Spatial domains and boundary conditions may be specified by projection operators.

In the TLM-model, the field is described by wave amplitudes instead of field quantities. The reaction to a wave pulse incident on a boundary of a spacial domain is nonlocal with respect to space and time. It may be represented by discrete Green's function [6]. In this paper, the discrete Green's functions for the three-dimensional half-space are calculated algebraically. The boundary of the halfspace is intersected by two ports of the TLM condensed node twelve-ports representing horizontal and vertical polarization, respectively. Therefore, there exist four Green's functions relating the two incident wave polarizations to the two reflected wave polarizations. The consequence of the rotational invariance of the problem is that only two out of the four Green's functions have to be calculated algebraically. These two Green's

functions are calculated from a system of partial difference equations which can be solved by transforming it to frequency- and momentum-space.

II The Discrete Field State Space

In the three-dimensional TLM-method, in each of the three spatial directions, two lines represent the two possible directions of polarization. Using the three-dimensional symmetric condensed TLM node of Johns (Fig. (1)), the mesh node is modelled by a twelve port with the scattering matrix S given by

$$S = \begin{bmatrix} 0 & \mathbf{T} & \mathbf{T}^T \\ \mathbf{T}^T & 0 & \mathbf{T} \\ \mathbf{T} & \mathbf{T}^T & 0 \end{bmatrix} \quad \text{with} \quad \mathbf{T} = \begin{bmatrix} 0 & 0 & \frac{1}{2} & -\frac{1}{2} \\ 0 & 0 & -\frac{1}{2} & \frac{1}{2} \\ \frac{1}{2} & \frac{1}{2} & 0 & 0 \\ \frac{1}{2} & \frac{1}{2} & 0 & 0 \end{bmatrix} \quad (1)$$

The wave amplitude vector is given by $\mathbf{a} = [a_1, a_2, \dots, a_{11}, a_{12}]^T$ and $\mathbf{b} = [b_1, b_2, \dots, b_{11}, b_{12}]^T$. The incident wave pulses ${}_k \mathbf{a}$ at $t = k\Delta t$ and the scattered wave pulses ${}_{k+1} \mathbf{b}$ at $t = (k+1)\Delta t$ are related by

$${}_{k+1} \mathbf{b} = S {}_k \mathbf{a} \quad (2)$$

In the TLM model, the field state at a given discrete time is described completely by specifying the amplitudes of the twelve incident or reflected wave pulses per mesh node. According to [5], all incident and reflected voltage waves are represented by

$$|a\rangle = \sum_{k=-\infty}^{+\infty} \sum_{l,m,n=-\infty}^{+\infty} {}_k \mathbf{a}_{l,m,n}^T |k; l, m, n\rangle \quad \text{and} \quad |b\rangle = \sum_{k=-\infty}^{+\infty} \sum_{l,m,n=-\infty}^{+\infty} {}_k \mathbf{b}_{l,m,n}^T |k; l, m, n\rangle \quad (3)$$

in the Hilbert space \mathcal{H} . The bra-ket notation introduced by Dirac [7] is used. The basis vectors $|k; l, m, n\rangle$ fulfill the orthogonality relations

$$\langle k_1; l_1, m_1, n_1 | k_2; l_2, m_2, n_2 \rangle = \delta_{k_1, k_2} \delta_{l_1, l_2} \delta_{m_1, m_2} \delta_{n_1, n_2} \quad (4)$$

We define the shift operator X and its Hermitian conjugate X^\dagger by

$$X |k; l, m, n\rangle = |k; l+1, m, n\rangle \quad \text{and} \quad X^\dagger |k; l, m, n\rangle = |k; l-1, m, n\rangle \quad (5)$$

and in an analogous way ([5]) the shift operators Y , Y^\dagger , Z , Z^\dagger and T for the spatial coordinates m , n , and the time coordinate k respectively.

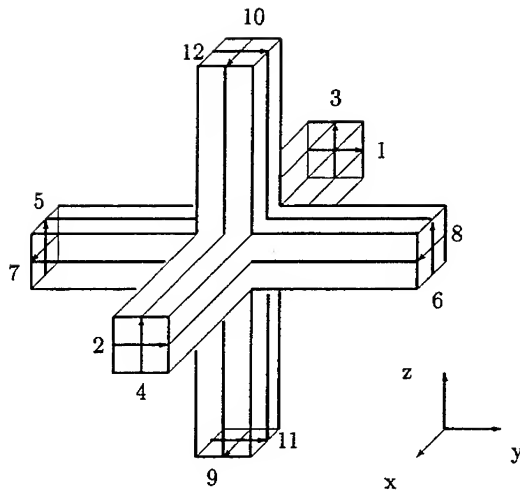


Figure 1: Three-dimensional symmetric condensed TLM node.

We introduce the connection operator Γ given by

$$\begin{aligned} \Gamma = & X(\Delta_{1,3} + \Delta_{2,4}) + X^\dagger(\Delta_{3,1} + \Delta_{4,2}) + Y(\Delta_{5,7} + \Delta_{6,8}) \\ & + Y^\dagger(\Delta_{7,5} + \Delta_{8,6}) + Z(\Delta_{9,11} + \Delta_{10,12}) + Z^\dagger(\Delta_{11,9} + \Delta_{12,10}) \end{aligned} \quad (6)$$

with the 12×12 (m,n)-matrix $(\Delta_{i,j})_{m,n} = \delta_{i,m} \delta_{j,n}$. The propagation of the wave pulses between adjacent condensed node ports is described by

$$|a\rangle = \Gamma |b\rangle \quad (7)$$

The equation

$$|b\rangle = T S |a\rangle \quad (8)$$

describes the simultaneous scattering within all the mesh node twelve-ports according to Fig. 1. The scattering by a mesh node causes the unit time delay Δt .

Using the discrete Green's function for TLM [6] and proceeding in the same way as [5] we obtain the *boundary state evolution equation*

$$|b\rangle_B = G |a\rangle_B \quad (9)$$

The subscripts I and B denote the projection of Hilbert space vectors on the boundary and the inner part of a spatial domain, respectively. Hilbert Space operators are projected from the left and from the right and therefore, they exhibit two subscripts. The discrete Green's operator G is given by

$$G = \left[TS_{BB} + S_{BI} \left(\sum_{l=0}^{\infty} T^{l+2} (\Gamma S_{II})^l \right) \Gamma S_{IB} \right] \quad (10)$$

The *boundary state evolution equation* relates the states of the wave pulses propagating into the boundary $|a\rangle_B$ to the states $|b\rangle_B$ reflected from the boundary. It is the general formulation of the boundary element problem in the Hilbert space. Since the Green's operator is represented by a Neumann series in the operators T , Γ and S_{II} , it is nonlocal with respect to space and time.

III The Discrete Three-dimensional Green's Function

As an example, we derive the discrete Green's functions for the half-space by mapping equation (9) onto configuration space for a point-like initial state $|a\rangle_B$. The solution of the resulting system of difference equations provides algebraic expressions for the Green's functions.

The half-space is defined by the domain projection operator P_D given by

$$P_D = \sum_{k,l,m} \sum_{n=0}^{\infty} |k; l, m, n\rangle \langle k; l, m, n| \quad (11)$$

The boundary of the halfspace is intersected by the ports 1 and 3 of the TLM condensed node twelve-ports in the y - z -plane at $x = 0$, representing horizontal and vertical polarization, respectively (Figure 1). Therefore, there are four Green's functions: The Green's function G^{11} describes the impulse response at port 1 to an incident unit impulse into port 1. We define the Green's function G^{13} as the impulse response in port 3 of an incident unit impulse in port 1. In the same way, we define the Green's functions G^{33} and G^{31} .

The functions G^{11} and G^{13} can be calculated algebraically. G^{33} and G^{31} are obtained by a positive 90° -rotation of G^{11} and G^{13} around the x -axis. According to Figure 1, we obtain

$${}_k G_{m,n}^{33} = {}_k G_{m,n}^{11} \Big|_{90^\circ} \quad (12)$$

since by a positive 90° -rotation around the x -axis, a_1 is transformed into a_3 , and

$${}_k G_{m,n}^{31} = - {}_k G_{m,n}^{13} \Big|_{90^\circ} \quad (13)$$

because by the same 90° -rotation, a_3 is transformed into $-a_1$.

A positive 90° -rotation of a function $f(m, n)$ around the x -axis is described by the transition $f(m, n) \rightarrow f(n, -m)$. Using the symmetries ${}_k G_{n,-m}^{11} = - {}_k G_{m,n}^{11}$ and ${}_k G_{n,-m}^{13} = - {}_k G_{m,n}^{13}$ yields

$${}_k G_{m,n}^{33} = - {}_k G_{m,n}^{11} \quad (14)$$

and

$${}_k G_{m,n}^{31} = {}_k G_{m,n}^{13} \quad (15)$$

For calculating the Green's functions G^{11} and G^{13} , we choose the incident unit impulse

$$|a\rangle_B = \begin{bmatrix} 1 \\ 0 \\ \vdots \\ 0 \end{bmatrix} |0; 0, 0, 0\rangle \quad (16)$$

in $l' = 0$, $m' = 0$ and $n' = 0$ at the time $k' = 0$.

The discrete Green's operator is given by

$$\begin{aligned} G = & \sum_{m,m'=-\infty}^{\infty} \sum_{n,n'=-\infty}^{\infty} \sum_{k,k'=-\infty}^{\infty} {}_{k-k'} G_{m-m', n-n'}^{11} \\ & |k; 0, m, n\rangle \langle k'; 0, m', n'| \begin{bmatrix} 1 & 0 & \cdots & 0 \\ 0 & 0 & \cdots & 0 \\ \vdots & \vdots & \ddots & \vdots \\ 0 & 0 & \cdots & 0 \end{bmatrix} \\ & + \sum_{m,m'=-\infty}^{\infty} \sum_{n,n'=-\infty}^{\infty} \sum_{k,k'=-\infty}^{\infty} {}_{k-k'} G_{m-m', n-n'}^{13} \\ & |k; 0, m, n\rangle \langle k'; 0, m', n'| \begin{bmatrix} 0 & 0 & \cdots & 0 \\ 0 & 0 & \cdots & 0 \\ 1 & 0 & \cdots & 0 \\ 0 & 0 & \cdots & 0 \\ \vdots & \vdots & \ddots & \vdots \\ 0 & 0 & \cdots & 0 \end{bmatrix} \end{aligned} \quad (17)$$

Then, for $|b\rangle_B$, it yields

$$|b\rangle_B = \sum_{m=-\infty}^{\infty} \sum_{n=-\infty}^{\infty} \sum_{k=-\infty}^{\infty} \begin{bmatrix} {}_k G_{m,n}^{11} \\ 0 \\ {}_k G_{m,n}^{13} \\ 0 \\ \vdots \\ 0 \end{bmatrix}_{m,n} |k; 0, m, n\rangle \quad (18)$$

Our result will be the function ${}_k G_{m,n}^{ij}$. The general Green's function is given by the transition ${}_k G_{m,n}^{ij} \rightarrow {}_{k-k'} G_{m-m', n-n'}^{ij}$.

Mapping eqs. (9) with (10) to configuration space by multiplication from the left side with $\langle k; l, m, 0|$, we obtain the following system of partial difference equations for $l = 0, 1, 2, \dots, \infty$ and $m, n = -\infty, \dots, -1, 0, 1, \dots, \infty$:

$$\begin{aligned} {}_{k+1} [b_1]_{l+1, m, n} &= \frac{1}{2} {}_k [-b_7 + b_8 + b_{11} + b_{12}]_{l, m, n} \\ {}_{k+1} [b_2]_{l, m, n} &= \frac{1}{2} {}_k [b_7 - b_8 + b_{11} + b_{12}]_{l+1, m, n} \\ {}_{k+1} [b_3]_{l+1, m, n} &= \frac{1}{2} {}_k [b_5 + b_6 - b_9 + b_{10}]_{l, m, n} \\ {}_{k+1} [b_4]_{l, m, n} &= \frac{1}{2} {}_k [b_5 + b_6 + b_9 - b_{10}]_{l+1, m, n} \\ {}_{k+1} [b_5]_{l, m+1, n} &= \frac{1}{2} {}_k [b_3 + b_4 - b_{11} + b_{12}]_{l, m, n} \\ {}_{k+1} [b_6]_{l, m-1, n} &= \frac{1}{2} {}_k [b_3 + b_4 + b_{11} - b_{12}]_{l, m, n} \\ {}_{k+1} [b_7]_{l, m+1, n} &= \frac{1}{2} {}_k [-b_1 + b_2 + b_9 + b_{10}]_{l, m, n} \\ {}_{k+1} [b_8]_{l, m-1, n} &= \frac{1}{2} {}_k [b_1 - b_2 + b_9 + b_{10}]_{l, m, n} \\ {}_{k+1} [b_9]_{l, m, n+1} &= \frac{1}{2} {}_k [-b_3 + b_4 + b_7 + b_8]_{l, m, n} \\ {}_{k+1} [b_{10}]_{l, m, n-1} &= \frac{1}{2} {}_k [b_3 - b_4 + b_7 + b_8]_{l, m, n} \\ {}_{k+1} [b_{11}]_{l, m, n+1} &= \frac{1}{2} {}_k [b_1 + b_2 - b_5 + b_6]_{l, m, n} \\ {}_{k+1} [b_{12}]_{l, m, n-1} &= \frac{1}{2} {}_k [b_1 + b_2 + b_5 - b_6]_{l, m, n} \end{aligned} \quad (19)$$

We have used the abbreviation ${}_k [b_1 + b_2 + b_3]_{l, m, n} = {}_k [b_1]_{l, m, n} + {}_k [b_2]_{l, m, n} + {}_k [b_3]_{l, m, n}$. The initial conditions are given by ${}_0 [b_7]_{0, 1, 0} = {}_0 [b_8]_{0, -1, 0} = {}_0 [b_{11}]_{0, 0, 1} = {}_0 [b_{12}]_{0, 0, -1} = \frac{1}{2}$ and ${}_0 [b_i]_{l, m, n} = 0$

for all other l, m, n . The boundary conditions are ${}_k[b_1]_{0,m,n} = {}_k[b_3]_{0,m,n} = 0$. Furthermore, we demand that in the halfspace, the amplitude of exponential increasing solutions must be zero. This is equivalent to the Sommerfeld radiation condition.

The Green's functions for $k \geq 2$ are given by

$${}_k G_{m,n}^{11} = \frac{1}{2} {}_{k-2} [b_7 - b_8 + b_{11} + b_{12}]_{0,m,n} \quad (20)$$

and

$${}_k G_{m,n}^{13} = \frac{1}{2} {}_{k-2} [b_5 + b_6 + b_9 - b_{10}]_{0,m,n} \quad (21)$$

respectively. The Green's functions are zero for $k = 0, 1$.

We solve this system of difference equations by transforming it to frequency- and momentum-space. The Green's functions are given by

$$\begin{aligned} {}_k G_{m,n}^{11} = & {}_{k+1} g_{m+1,n} + {}_{k+1} g_{m-1,n} - {}_{k+1} g_{m,n+1} - {}_{k+1} g_{m,n-1} \\ & + {}_{k-1} g_{m+1,n} + {}_{k-1} g_{m-1,n} - {}_{k-1} g_{m,n+1} - {}_{k-1} g_{m,n-1} \end{aligned} \quad (22)$$

and

$${}_k G_{m,n}^{13} = {}_k g_{m+1,n+1} + {}_k g_{m-1,n-1} - {}_k g_{m-1,n+1} - {}_k g_{m+1,n-1} \quad (23)$$

The functions ${}_k G_{m,n}^{11}$ and ${}_k G_{m,n}^{13}$ can be expressed by a superposition of one function ${}_k g_{m,n}$. The symmetries and properties

$${}_k g_{m,n} = {}_k g_{-m,n} = {}_k g_{m,-n} = {}_k g_{-m,-n} \quad (24)$$

$${}_k g_{m,n} = {}_k g_{n,m} \quad (25)$$

$${}_k g_{m,n} = 0 \quad \text{for even } k \quad (26)$$

$${}_k g_{m,n} = 0 \quad \text{for odd } m+n \quad (27)$$

save memory and computer-time when performing the convolution process to simulate the open halfspace.

For $k \geq -1$, the function ${}_k g_{m,n}$ is given by

$$\begin{aligned} {}_{k+2} g_{m,n} = & \sum_{c=0}^{\frac{k+1}{2}} \frac{(-1)^c}{8} \left(2 - \delta_{c, \frac{k+1}{2}} \right) {}_{\frac{k+1}{2}-c} I(2c+1, -1)_{m,n} \\ & + \sum_{c=0}^{\frac{k-1}{2}} \frac{(-1)^c}{8} \left({}_{\frac{k-1}{2}-c} I(2c+2, 0)_{m,n} - {}_{\frac{k+1}{2}-c} I(2c+2, -2)_{m,n} \right) \\ & - \sum_{c=0}^{\frac{k-1}{2}} \frac{(-1)^c}{8} {}_{\frac{k-1}{2}-c} I(2c, 0)_{m,n} \end{aligned}$$

$$\begin{aligned}
& + \sum_{c=0}^{\frac{k-3}{2}} \frac{(-1)^c}{8} \left(\frac{k-1}{2} - c I(2c+2, -2)_{m,n} - 2 \frac{k-3}{2} - c I(2c+1, -1)_{m,n} \right) \\
& + \sum_{c=0}^{\frac{k-3}{2}} \frac{(-1)^c}{8} \frac{k-3}{2} - c I(2c+2, -2)_{m,n} \\
& - \sum_{c=0}^{\frac{k-5}{2}} \frac{(-1)^c}{8} \frac{k-5}{2} - c I(2c+2, -2)_{m,n} \\
& + \frac{1}{16} \left(\frac{k+3}{2} I(0, -2)_{m,n} - (1 - \delta_{k,-1}) \frac{k+1}{2} I(0, -2)_{m,n} \right) \\
& + \frac{1}{16} \left(-\frac{k-1}{2} I(0, -2)_{m,n} + \frac{k-3}{2} I(0, -2)_{m,n} \right)
\end{aligned} \tag{28}$$

For the integral ${}_k I(t, s)_{m,n}$, we obtain in case of $t = s = 0$

$${}_k I(0, 0)_{m,n} = 2 \sum_{i=0}^k \sum_{j=0}^{k-i} \binom{2i}{i} \binom{2j}{j} \binom{k+i+j+1}{k-i-j} (-1)^{k+i+j} A_m^{i,j} A_n^{i,j} \tag{29}$$

with

$$A_m^{i,j} = \sum_{k=k_{min}}^j \binom{j}{k} \binom{2i+2k}{i+k-|m|} (-1)^k \left(\frac{1}{2} \right)^{2i+2k} \tag{30}$$

and $k_{min} = \max\{0, |m| - i\}$. For all other t and s , we obtain

$$\begin{aligned}
{}_k I(t, s)_{m,n} = & \sum_{i=0}^k \sum_{j=0}^{k-i} \binom{2i}{i} \binom{2j}{j} \binom{k+i+j+1}{k-i-j} (-1)^{k+i+j} \\
& \sum_{c=-i-j}^{i+j} \sum_{d=-i-j}^{i+j} A_c^{i,j} A_d^{i,j} (1/2)^{2s} \sum_{e=-t}^t \binom{2t}{t-e} (-1)^e \\
& (B(l+d+e, n+c+e) + B(l+d+e, n+c-e))
\end{aligned} \tag{31}$$

with

$$B(m, n) = \frac{1}{4} \begin{cases} \binom{\frac{|m+n|+t-s}{2}-1}{\frac{|m+n|-t+s}{2}} \binom{\frac{|m-n|+t-s}{2}-1}{\frac{|m-n|-t+s}{2}} & \text{for even } m-n \geq t-s \\ 0 & \text{for even } m-n < t-s \text{ and all odd } m+n \end{cases} \tag{32}$$

The algebraic formulae of the Green's functions provides the same numerical values as the Green's functions calculated by injecting a unit impulse into a TLM mesh representing the open halfspace.

IV Conclusion

We have presented a method for the algebraic computation of the three-dimensional discrete Green's functions. The Green's functions allow a correct formulation of the absorbing boundary conditions in TLM.

The absorbing boundary conditions for an open halfspace are described by four Green's functions. Two of them may be derived by using the rotational invariance of the halfspace. The Green's functions can be expressed by a superposition of the single function ${}_k g_{m,n}$. Due to the symmetry of this function, only a minimum of the numerical values have to be stored. The convolution process which has to be performed to simulate the absorbing boundary condition can be reduced considerably.

References

- [1] P.B. Johns, R.L. Beurle, "Numerical Solution of 2-Dimensional Scattering Problems using a Transmission-Line Matrix", Proc. IEE, vol.118, no. 9, pp 1203-1208, Sept 1971.
- [2] W.J.R. Hoefer, "The Transmission Line Matrix Method-Theory and Applications", IEEE Trans. Microwave Theory Tech., vol. MTT-33, no.10, pp.882-893, Oct 1985.
- [3] W.J.R. Hoefer, "The Transmission Line Matrix (TLM) Method", Chapter 8 in "Numerical Techniques for Microwave and Millimeter Wave Passive Structures", edited by T. Itoh, New York, 1989, J. Wiley, New York 1989, pp. 496-591.
- [4] P.B. Johns, "A Symmetrical Condensed Node for the TLM-Method", IEEE Trans. Microwave Theory Tech., Vol. MTT-35, Nr.4, S. 370-377, April 1987.
- [5] P. Russer, M. Krumpholz, "The Hilbert Space Formulation of the TLM Method", to be published in: International Journal of Numerical Modelling : Electronic Networks, Devices and Fields, 1992.
- [6] W.J.R. Hoefer, "The Discrete Time Domain Green's Function or John's Matrix - a new powerful Concept in Transmission Line Modelling", International Journal of Numerical Modelling : Electronic Networks, Devices and Fields, Vol. 2, 215-225, 1989.
- [7] P.A.M. Dirac, "Quantum Mechanics", fourth edition, Oxford University Press, Oxford

Transmission Line Matrix Method on Massively Parallel Processor Computers

Poman P.M. So, Eswarappa Channabasappa, and Wolfgang J.R. Hoefer

NSERC/MPR Teltech Research Chair in RF Engineering
Department of Electrical and Computer Engineering
University of Victoria, Victoria, B.C., Canada, V8W 3P6

Tel: (604) 721-6511
Fax: (604) 721-6230
Email: Poman.So@ECE.UVic.CA

Abstract

The Transmission Line Matrix (TLM) method is a time domain method for modeling the behaviour of electromagnetic waves. This method is based on Huygens' Principle which, in its original form, is a localized recursive definition of electromagnetic wave propagation in the time domain. A parallel algorithm for the TLM method results, which is highly suitable for implementation on computers with massively parallel processors.

Introduction

The theory of the 2D-TLM method is well described in [1], [2] and [3]. The basic building block of this method is a node which is formed by connecting four transmission lines together, Figure 1a. A 2D-TLM mesh is built by cascading a network of these nodes as shown in Figure 1b. To simulate electromagnetic wave propagation in the mesh, scattering and transfer of voltage impulses must be performed.

Scattering of impulses is local to each node. Impulses incident from a transmission line are scattered into all four transmission lines (Figure 2). Transfer of impulses requires communication among adjacent nodes (Figure 3a). This operation needs to be modified if boundaries are to be placed between nodes (Figure 3b).

Both scattering and transfer of impulses are highly localized operations. The former is totally localized within each node and the latter is localized within the immediate surrounding region of a node, namely its four adjacent nodes. Therefore, scattering of impulses can be carried out in each node simultaneously, and transfer of impulses can be carried out in each region simultaneously as long as synchronization among adjacent nodes is preserved. In other words, these two operations can be carried out in parallel at each node and in the region of each node

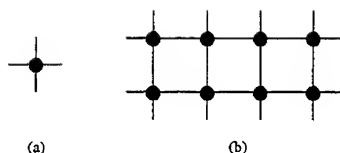


Figure 1: (a) A node, the basic building block of a 2D-TLM mesh.
(b) A 2D-TLM mesh formed by a network of nodes.

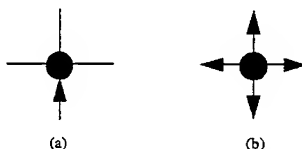


Figure 2: Scattering of an impulse at a node.
(a) An incident impulse.
(b) The scattered impulses.

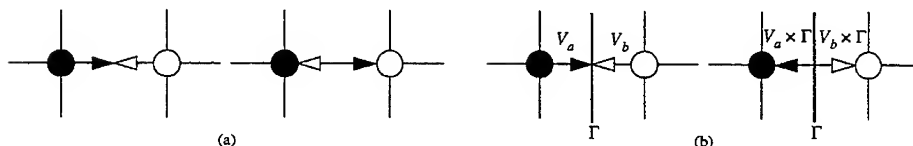


Figure 3: Transfer of impulses between two adjacent nodes.
(a) When there is no boundary between two nodes.
(b) When there is a boundary between two nodes. Γ is the impulse reflection coefficient of the boundary.

The DECmpp 12000

The DECmpp 12000 has a master processor and a large amount of parallel slave processors (the one we used has 8K). The master processor is called the Array Control Unit (ACU) and the parallel slave processors are called the Processor Elements (PE). These PEs have 16K of random access memory each and are connected with each other in a rectangular toroidal wraparound fashion [4]. MPL and MPF are the two high level languages available for programming the machine.

MPL is a C-like language. It has serial and parallel instructions which are executed on the ACU and PEs, respectively. It also has singular and plural data which are allocated on the ACU and PEs, respectively, Figure 4a. Communications among PEs are achieved via the MPL's X-net or global router instructions, [4]. Object libraries written in MPL can be called from other popular serial high level languages (C, C++ and Fortran) through the MPL callRequest function. In that case the ACU and PEs are collectively called the back-end (BE) and the work-station that executes the serial module is called the front-end (FE), Figure 4b.

MPF is a Fortran-77 like language with Fortran-90 array features. Data declared and/or used in the Fortran-90 array formats are allocated on the PEs, otherwise on the FE. Instructions written in the Fortran-90 array formats are executed on the PEs, otherwise on the FE. The ACU is not available for use to MPF programs; the PEs are also transparent to MPF programs. MPF modules cannot be called by other languages but they can call MPL modules, Figure 5.

MPL and MPF have their advantages and disadvantages that depend on the types of applications. We have implemented a 2D-TLM and a 3D-TLM simulation module in both MPL and MPF; the MPL versions run nearly twice as fast as the MPF versions.

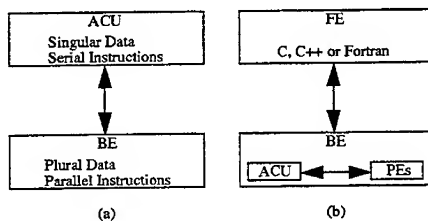


Figure 4: The DECmpp 12000 MPL programming models.
 (a) Stand-alone MPL programs.
 (b) MPL modules driven by other high level front-end languages.

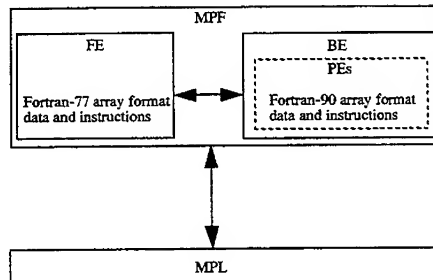


Figure 5: The DECmpp 12000 MPF programming model.

A Parallel 2D-TLM Algorithm

The plural data and parallel instruction constructs of MPL are two very important features for implementing parallel algorithms on the DECmpp 12000. Our MPL 2D-TLM module consists of a plural data structure of node to represent a mesh and a set of parallel functions (*scatter*, *transfer*, ...) to operate on the plural data structure, Listing 1. In the object oriented programming methodology, such a collection of data and functions is called an object. In other words, our MPL 2D-TLM module has a mesh object. Each node of the mesh object is physically located in a PE of the DECmpp 12000. Therefore all the nodes of the mesh can perform the 2D-TLM simulation operations in parallel.

The *scatter* function in Listing 1 shows some parallel features of MPL. The function has no *do-loop*, all the statements in it are parallel statements. An invocation of this function causes all PEs in the DECmpp 12000 to perform the same scattering operation in parallel. The *transfer* function in Listing 1 shows some features of the *parallel-if* and the *X-net* constructs of MPL. The *parallel-if* statement causes all PEs to perform the same logical operation with their local data; if the result of the operation is *TRUE* then execute the block of statements following the *if* statement else *do-nothing*. The *X-net* statements in the *transfer* function exchange impulses between adjacent nodes if there is no boundary between them.

We have implemented the above algorithm in MPF by using its Fortran-90 array features and *parallel-if* constructs. The MPL version runs nearly twice as fast as the MPF version. The main reason is that MPL programs can access the hardware more directly than MPF. But MPF has multi-dimensional array features and a higher level of abstraction which make the PEs and *X-net* communication transparent to MPF programs.

Performance of the Parallel 2D-TLM Algorithm

We have combined the above 2D-TLM parallel simulation module with the UNIX version of our 2D-TLM simulator, [3]. The FE component, Figure 4b, of the simulator, consisting of code for graphics and control of general program execution, is written in C, X Windows Xlib and Motif Xm libraries. This FE component is the master of the simulator; it receives commands from the user and directs the operations on both the FE and BE.

Table 1 summarizes the execution times of the serial and parallel version of the 2D-TLM simulator for a number of test cases. The mesh size used in the simulation is 128×64 , which is equal to the number of PE's available in the DECmpp 12000 that we used. In all the cases, only the execution time related to the 2D-TLM simulation, sampling of results and performing Fourier Transform (if applicable) is recorded, i.e. execution time related to graphical I/O operations is subtracted from the total time. The serial version is executed on the DEC5000 front-end and the parallel version is on the DECmpp 12000 with its GUI module executed on the DEC5000 front-end. The number of computation steps for all the cases is 1000 and the number of frequency points for cases 2 and 3 is 100.

The result in Table 1 shows that the parallel version of the 2D-TLM simulator performs very well for plain simulation. The performance of the parallel version starts to decrease when we try to sample data from the mesh (case 2) or inject signals into the mesh (case 3). This decrease in performance does not appear in the serial version because much of the work is done to perform the 2D-TLM simulation; the work for the injection and sampling of data is negligible. In the parallel version, the 2D-TLM simulation is performed in parallel in the DECmpp 12000 BE while the injection and sampling of signal are performed in series in the DEC 5000 FE. A major reason for such a decrease in performance when the DEC5000 FE is involved is the overhead of the `blockin`, `blockout` and `callRequest` functions for the FE-BE (front-end-back-end) communication. These functions are called before and after each computation step to inject signals into the mesh and sample signals from the mesh. Another reason is that the output point causes the FE to do some extra work, such as performing a Fourier Transform. The former problem can be solved by keeping the sampled data and the input signal in the BE and transferring the sampled data to the FE after the simulation is completed. The latter problem can be solved by implementing a parallel Fourier Transform algorithm and execute it in the BE.

Case	Simulation Feature	Serial (sec.)	Parallel (sec.)	Speeded up (times)
1	Plain Simulation	54.5	2.0	27
2	Impulse, 1 Output Point	54.5	2.3	24
3	Gaussian, 1 Output Point	54.5	3.0	18

Table 1: Performance comparison between the serial and parallel versions of the 2D-TLM Simulator. The mesh size is 128×64 , which is equal to the number of PEs available in the DECmpp 12000 that we used. The serial version is executed on the DEC5000 front-end and the parallel version is on the DECmpp 12000 with its GUI module executed on the DEC5000 front-end. The number of computation steps for all the cases is 1000 and the number of frequency points for cases 2 and 3 is 100.

A Parallel 3D-TLM Algorithm

We have also implemented the 3D-TLM condensed node algorithm, [5], [6] and [7], in MPL and C*. This section shows some important concepts and steps of converting a potentially parallel algorithm from its serial implementation to an equivalent parallel implementation.

Listing 2 shows some code fragment from the 3D-TLM Simulator, [8]. This code fragment shows a small but important part of a big program, the 3D-TLM impulse scattering operation. Listing 2a is from the serial version of the 3D-TLM Simulator. In the serial version a Mesh class is used to encapsulate the 3D-TLM operations; Mesh::Scatter is one of the member functions and it performs 3D-TLM scattering. Listing 2b shows how this function is modified to call the MPL Node_Scatter function. Listing 2c depicts in detail the actual MPL implementation.

The PEs of the DECmpp 12000 are connected with each other in a rectangular toroidal wraparound fashion, [4]. Therefore, the physical layout of the PEs can only be used to represent a plane, say xy -plane, of a volume in the 3D-TLM mesh. The remaining dimension, say z -direction, must be represented by a one-dimensional array in each PE. That is, each PE of the DECmpp 12000 is used to represent a column of nodes in the z -direction, Figure 6. This can be done easier if MPF is used to implement the algorithm because it has the multi-dimensional array feature of Fortran-90 but the drawback is that the MPF module cannot be called by other languages. Unless one is prepared to rewrite the whole application in MPF, MPL is a better language to use. C* is a very good language for applications with multi-dimensional arrays; it offers the flexibility of MPL and the multi-dimensional array feature of MPF. C* is supported by Thinking Machine Corporation on their Connection Machines. We have implemented a similar algorithm on the CM2 with 8K of processors.

We have compared the performance of the serial and parallel versions of the 3D-TLM Simulator; the result is similar to that of Table 1.

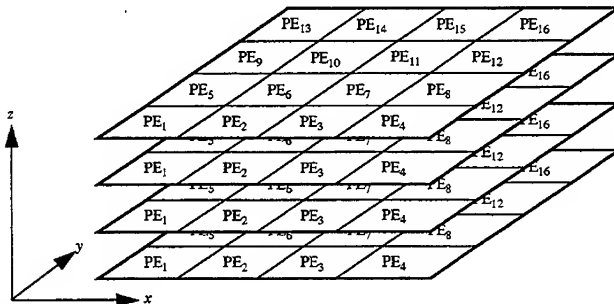


Figure 6: A hypothetical situation. A 16-PE mpp is used to represent a 64-node mesh. Each PE represents 4 nodes in the mesh: PE₁ represents nodes (1,1,1), (1,1,2), (1,1,3) and (1,1,4), PE₂ represents nodes (2,1,1), (2,1,2), (2,1,3) and (2,1,4), and so on.

Conclusion

We have implemented the two-dimensional TLM method on the DECmpp 12000 in MPF and MPL, the three-dimensional TLM method on the DECmpp 12000 in MPL and on the Connection Machine CM2 in C*. These parallel implementations give more than an order of magnitude of improvement in performance when using 8192 processors.

Since MPL object modules can be called by other popular serial high level languages, the 2D-TLM and 3D-TLM MPL modules are combined with the 2D-TLM and 3D-TLM Simulators by using mixing language programming technique. The graphical user interface (GUI) components of the Simulators are implemented by using C/C++, X Windows Xlib and Motif Xm libraries, and is executed in the DEC5000 front-end. The MPL object modules are executed in the DECmpp 12000 back-end. The GUI components are the masters of the Simulators which control the simulation components through the MPL callRequest function. The performances of these simulators are compared with their equivalent serial versions, and the result is that the parallel versions are more than an order of magnitude faster than their serial versions.

Some important concepts and steps of converting a potentially parallel algorithm from its serial implementation to an equivalent parallel implementation are also outlined in the form of an example. The advantages and disadvantages of MPL, MPF and C* are also addressed. We feel that massively parallel computation is a good way to solve complicated electromagnetic wave problems and it is important for the computing engineers to grasp the parallel computing concept.

References

- [1] W.J.R. Hoefer, *The Transmission Line Matrix Method - Theory and Application*, IEEE Trans. Microwave Theory Tech., vol. MTT-33, pp.882-893, Oct. 1985.
- [2] W.J.R. Hoefer, *The Transmission Line Matrix (TLM) Method*, Chapter 8 of *Numerical Techniques for Microwave and Millimeter-Wave Passive Structures*, edited by T. Itoh, John Wiley & Sons, New York, 1989.
- [3] W.J.R. Hoefer and P.P.M. So, *The Electromagnetic Wave Simulator - A Dynamic Visual Electromagnetics Laboratory based on the Two Dimensional TLM Method*, John Wiley & Sons Ltd., 1991.
- [4] *DECmmp Sx V1.1 Programming Language Reference Manual*, Digital Equipment Corporation, 1992.
- [5] Peter B. Johns, *A Symmetrical Condensed Node for the TLM Method*, IEEE Trans. Microwave Theory and Tech. vol.MTT-35, No.4, pp.370-377, April 1987.
- [6] D.A. Al-Mukhtar and J.E. Sitch, *Transmission-line Matrix Method with Irregularly Graded Space*, IEE PROC. vol.128, Pt.H, No.6, pp.299-305, December 1981.
- [7] C.E. Tong and Y. Fujino, *An Efficient Algorithm for Transmission Line Matrix Analysis of Electromagnetic Problems Using the Symmetrical Condensed Node*, IEEE Trans. Microwave Theory and Tech. vol.MTT-39, No.8, pp.1420-1424, August 1991.
- [8] P.P.M. So and W.J.R. Hoefer, *3D-TLM Time Domain Electromagnetic Wave Simulator for Microwave Circuit Modeling*, IEEE MTT-S vol.2, pp.631-634, June 1991.

```
typedef struct{
    float VS,VW,VN,VE; /* voltages on mesh lines; */
                        /* S: South, W: West */
                        /* N: North, E: East, */
                        /* which is the same as the */
                        /* X-net communication */
                        /* arrangement of the DECmmp */
    float VL; /* voltage on the stub */
    float yo,go; /* material constants */
    float rNS,rEW; /* reflection coefficients */
                  /* of the boundaries */
                  /* half-a-delta-1 from the */
                  /* node */
    int rNSco,rEWco; /* North-South and East-West */
                    /* reflection types */
                    /* 0: no boundary, */
                    /* 1: reflection boundary, */
                    /* 2: Johns Matrix. */
}shunt_node; /*--- shunt_node ---*/

plural static shunt_node node; /* A 2D-TLM mesh */
.
.
.
visible void scatter(){
    register plural float tf;
    register plural double td;
    td = 2.0/(4.0+node.yo+node.go);
    tf = td*(node.VS+node.VW+node.VN+node.VE+
             node.VL*node.yo);
    node.VS = tf - node.VS;
    node.VW = tf - node.VW;
    node.VN = tf - node.VN;
    node.VE = tf - node.VE;
    node.VL = tf - node.VL;
} /*--- scatter ---*/

visible void transfer(){
    if (node.rNSco==0) /* i.e. no boundary */ {
        t = xnetS[1].node.VN;
        xnetS[1].node.VN = node.VS;
        node.VS = t;
    }
    if (node.rEWco==0) /* i.e. no boundary */ {
        t = xnetE[1].node.VW;
        xnetE[1].node.VW = node.VE;
        node.VE = t;
    }
} /*--- transfer ---*/

visible void reflect(){
    .
    .
    .
    .
}
```

Listing 1: Our MPL 2D-TLM simulation module code fragment. shunt_node is the data type definition used to collect all the information that is local to a 2D-TLM shunt node. node is the actual declaration to allocate memory on each PE. Since node is a plural data type, there is a node on each PE. In other words, it represents a mesh. scatter and transfer are functions that perform parallel scattering and transfer of impulses on the mesh. Note that transfer of impulses, when there are boundaries among nodes, is handled separately by a function named reflect.

Listings


```

(a)
void Mesh::Scatter() {
  int x,y,z;
  for (z=0; z<z_dimension; z++)
    for (y=0; y<y_dimension; y++)
      for (x=0; x<x_dimension; x++)
        node(x,y,z)->Scatter();
}/*--- Mesh::Scatter ---*/

```

```

(b)
void Mesh::Scatter() {
  callRequest(Node_Scatter,0);
}/*--- Mesh::Scatter ---*/

```

```

(c)
typedef struct {
  Real u,v,w; /* unit length in the*/
              /* x,y & z-direction */
  Real ex,ur,dt; /* mat. constants */
              /* and time step */
  Real yx,yy,yz, /* normalized y, */
              /* z */
  Real gx,gy,gz; /* and g values */
  Real s1,s2,s3, /* scattering */
  s4,s5,s6, /* coefficients */
  s7,s8,s9;
  Real rx,ry,rz, /* refl. coefficient*/
  rx,ry,rz; /* at half-way between nodes */
  Real v1, v2, v3, /* incident voltages*/
  v4, v5, v6,
  v7, v8, v9,
  v10,v11,v12,
  v13,v14,v15,
  v16,v17,v18;
} Node;

.
.
.
.
plural Node *node;
.
.
.

```

```

visible void Node_Scatter() {
  plural Real a,b,c,Jx,Jy,Jz,Jxv16,Jyv17,
  Jzv18,Kx,Ky,Kz,Ux,Uy,Uz,Wx,Wy,Wz;
  int z;
  for (z=0; z<nznnode; z++) {
    a=node[z].v1+node[z].v12;
    b=node[z].v2+node[z].v9;
    Ux=a+b+node[z].v13; Wx=b-a;
    a=node[z].v3+node[z].v11;
    b=node[z].v4+node[z].v8;
    Uy=a+b+node[z].v14; Wy=b-a;
    a=node[z].v5+node[z].v7;
    b=node[z].v6+node[z].v10;
    Uz=a+b+node[z].v15; Wz=b-a;
    a=node[z].v4+node[z].v8;
    b=node[z].v5+node[z].v7;
    Jx=b-a+node[z].v16; Kx=a+b;
    a=node[z].v6+node[z].v10;
    b=node[z].v2+node[z].v9;
    Jy=b-a+node[z].v17; Ky=a+b;
    a=node[z].v1+node[z].v12;
    b=node[z].v3+node[z].v11;
    Jz=b-a+node[z].v18; Kz=a+b;
    node[z].v13 = node[z].s1*Ux+node[z].v13;
    node[z].v14 = node[z].s2*Uy+node[z].v14;
    node[z].v15 = node[z].s3*Uz+node[z].v15;
    node[z].v16 = node[z].s4*Jx;
    node[z].v17 = node[z].s5*Jy;
    node[z].v18 = node[z].s6*Jz;
    Jxv16 = Jx+node[z].v16; Jyv17 =
    Jy+node[z].v17; Jzv18 =
    Jz+node[z].v18;
    a=Ux-(node[z].v13+node[z].s7*Ux);
    b=Kz+Jzv18; c=a+Wx;
    node[z].v1=0.25*(c+b);
    node[z].v12=0.25*(c-b);
    b=Ky-Jyv17; c=a-Wy;
    node[z].v2=0.25*(c+b);
    node[z].v9 =0.25*(c-b);
    a=Uy-(node[z].v14+node[z].s8*Uy);
    b=Kz-Jzv18; c=a+Wy;
    node[z].v3=0.25*(c+b);
    node[z].v11=0.25*(c-b);
    b=Kx+Jxv16; c=a-Wy;
    node[z].v4=0.25*(c+b);
    node[z].v8 =0.25*(c-b);
    a=Uz-(node[z].v15+node[z].s9*Uz);
    b=Kx-Jxv16; c=a+Wz;
    node[z].v5=0.25*(c+b);
    node[z].v7 =0.25*(c-b);
    b=Ky+Jyv17; c=a-Wz;
    node[z].v6=0.25*(c+b);
    node[z].v10=0.25*(c-b);
  }
}/*--- Node_Scatter ---*/

```

Listing2: (a) The serial scattering function of the 3D-TLM Simulator.
 (b) The front-end function in (a) calls the MPL scattering function in (c).
 (c) The MPL implementation of the 3D-TLM scattering operation called in (b).

Fast Frequency-Domain TLM Analysis of 3D Circuit Discontinuities

Jifu Huang, Ruediger Vahldieck and Hang Jin

*Laboratory of Lightwave Electronics, Microwaves and Communications
(LLiMiC)*

*Department of Electrical and Computer Engineering
University of Victoria, PO Box 3055, Victoria, B. C. Canada V8W 3P6*

Abstract

An improved steady-state frequency-domain TLM algorithm is presented. Instead of using the symmetrically condensed 3D node with inductive and capacitive stubs to model dielectric and magnetic permeability, which led to a symbolic 15-port node scattering matrix, only a 12-port symbolic scattering matrix is used. This is possible by eliminating the stubs which are necessary in the time-domain to preserve time synchronism, but not in the frequency-domain. The efficiency of this approach will be illustrated for three typical analysis and design problems.

Introduction

The Transmission Line Matrix (TLM) method is known as a versatile and general purpose numerical simulation tool for electromagnetic field problems (i.e.[1],[2]). Although the TLM is basically a time-domain method, frequency-domain data can be obtained from a Fourier transform of the impuls response of the network. Therefore, like the FDTD technique, the TLM combines the advantages of time-domain and frequency-domain analysis in one method. Besides transient analysis and visualization of electromagnetic wave phenomena also modelling of passive and nonlinear devices can be done with the TLM.

For many applications, however, steady-state circuit analysis and design is required, and usually only a small frequency range -in time-domain terms- is of importance (i.e 100MHz to 60GHz). Then, computationally (computer memory and CPU-time) and in comparison to some methods which work entirely in the frequency-domain, time-domain methods are at a disadvantage. This is in particular the case for circuit design problems. Furthermore, while the FDTD is complemented by a frequency-domain finite difference (FD) scheme, which allows the user to stay within the framework of one method, the TLM method was lacking such a frequency-domain pendant until recently. In [3] Hang and Vahldieck have introduced a

frequency-domain TLM (FDTLM) algorithm which uses the same space discretization network as in the time-domain TLM, but due to a novel impuls excitation (impuls train of sinusoidally modulated amplitude), the use of complex quantities and network theory, the method works entirely in the frequency-domain. Therefore, the FDTLM not only retains the flexibility of the time-domain TLM (TDTLM) to analyse arbitrarily shaped circuit structures, but eliminates also a number of problems associated with the TDTLM approach. In particular frequency-domain circuit design is now possible using the same space discretization network as in the time-domain but without requiring extensive computer resources.

In this paper we present an improved FDTLM with even better computational efficiency in terms of computer memory and CPU-time than the one described in [3]. While in [3] we have still utilized a 15-port symbolic scattering matrix for each node, because we have assumed the same propagation constant in all space directions. This assumption made it necessary to include the stubs to represent the case where $\Delta x \neq \Delta y \neq \Delta z$ and $\epsilon_r \neq 1$ and $\mu_r \neq 1$. In the improved FDTLM we eliminate these stubs by introducing different propagation constants in all three space directions. The resulting 12-port node is shown in Fig.1. To illustrate the numerical efficiency and accuracy of this approach we will analyze three different types of discontinuity problems and compare the results with other techniques and measurements.

Theory

In [3] the FDTLM approach was still based on the 3D hybrid condensed node known from the time-domain TLM. This node was represented by a 15-port symbolic scattering matrix, because we have assumed equal propagation constant in each of the branches which made the stubs necessary. However, as we found out recently, these stubs can be eliminated if we assume different propagation constants in each of the branches. Then, by assuming a sinusoidally modulated impulse train excitation [3], we can connect the incident and reflected voltages between neighboring nodes in the following way:

$$V_x^i = \lambda_x C_x V_x^r \quad (1)$$

$$V_y^i = \lambda_y C_y V_y^r \quad (2)$$

C_y and C_x are the connection matrices which connect the neighboring branches and λ_x and λ_y are the propagation factors in the X and Y directions. Defining the z-axis as the propagation direction of the wave, the branches of the hybrid node are classified into two types (Fig.1):

exterior branches: $+zx, +zy, -zx, -zy.$

interior branches: $+xy, +xz, -xy, -xz;$

$+yz, +yx, -yz, -yx.$

The exterior branches point into the propagation direction of the wave, while the interior branches between neighboring nodes are connected through (1) and (2). Therefore, a so-called intrinsic scattering matrix can be defined as [3]

$$\begin{bmatrix} V_z^r \\ V_x^r \\ V_y^r \end{bmatrix} = \begin{bmatrix} S_{zz} & S_{zx} & S_{zy} \\ S_{xz} & S_{xx} & S_{xy} \\ S_{yz} & S_{yx} & S_{yy} \end{bmatrix} \begin{bmatrix} V_z^i \\ V_x^i \\ V_y^i \end{bmatrix} \quad (3)$$

which is the resulting s-matrix, combining the symbolic node matrices with which the entire cross-section is discretized. This intrinsic s-matrix can represent one or more slices of a three-dimensional mesh. From (1-3) we can now find a relationship between the incident and reflected voltages of the exterior branches, that are the branches which point in propagation direction:

$$V_z^r = [S_{zz} + \lambda_x S_{zx} C_x P (MS_{zz} + \lambda_y MS_{zy} C_y NS_{yz}) + \lambda_y S_{zy} C_y Q (NS_{yz} + \lambda_x NS_{yx} C_x MS_{xz})] V_z^i \quad (4)$$

where

$$M = (1 - \lambda_x S_{xx} C_x)^{-1}_3$$

$$N = (1 - \lambda_y S_{yy} C_y)^{-1}$$

$$P = (1 - \lambda_x \lambda_y MS_{xy} C_y NS_{yx} C_x)^{-1}$$

$$Q = (1 - \lambda_x \lambda_y NS_{yx} C_x MS_{xy} C_y)^{-1}$$

This step is necessary to connect subsequent s-matrices (from other discontinuities) together to form the overall s-matrix of the 3D structure. Once (4) is known, the eigenvalues of a guiding structure can be determined and the scattering parameters for two guiding structures connected through a discontinuity can be computed. This procedure is described in [3] and for further details the reader is referred to this paper. The difference to reference [3] and this paper is that here only a 12-port node is involved which leads to a

smaller size of matrix (3). This 12-port node is shown in Fig.1 and the corresponding symbolic scattering matrix is shown in Fig.2. The matrix coefficients are derived using the principle of power conservation which leads to the well know unitary relation:

$$S^T Y S^* = Y \quad (5)$$

Y denotes the diagonal admittance matrix normalized to the admittance of free space. Applying (5) with current and voltage conservation leads to a set of nonlinear equations. After some manipulations one finds three solutions which correspond to the shunt node, series node and hybrid node, respectively. By further assuming that the characteristic admittance of each branch is the same and equals the intrinsic admittance of the medium, the coefficients of the symbolic s-matrix are reduced to $a_n = c_n = 0$, $b_n = d_n = 1/2$, which corresponds to P.B.John's node matrix without stubs. The normalised propagation constants are also chosen to give

$$\begin{aligned} \tilde{\gamma}_x &= \frac{1}{2} \left(\frac{v+w}{vw} - \frac{vw}{u^2} \right) \\ \tilde{\gamma}_y &= \frac{1}{2} \left(\frac{u+w}{uw} - \frac{uw}{v^2} \right) \\ \tilde{\gamma}_z &= \frac{1}{2} \left(\frac{u+v}{uv} - \frac{uv}{w^2} \right) \end{aligned} \quad (6)$$

where u, v , and w are the dimensions of the node in x, y , and z directions, respectively.

Results

The following numerical results have been compared with other the mode matching method and measurements. At the time this paper was written results from a time-domain TLM analysis were not available. We have selected three sets of problems which are of practical relevance. The first structure (Fig.3) is a planar circuit with composite layers of substrates (insulating and semiconducting) and cascaded discontinuities. Such a circuit combines a very thin layer of substrate (SiO_2) with a relatively thick layer of substrate (GaAs). The ratio is 1:200. Also the ratio between center conductor ($100\mu\text{m}$) and slots ($20\mu\text{m}$) is 5:1. Furthermore, the metallization thickness is $t=5\mu\text{m}$ and the structure is enclosed by a metallic box which can support box modes. To resolve such a structure with space discretization methods generally requires significant computer resources because the discretization size is normally determined by the smallest substructure to be resolved. Furthermore, since this is a spatially three-dimensional structure, the entire

(3D) space must be discretized. Although non-equidistant discretization can be used to reduce memory space and CPU-time, this is not easily done (or virtually impossible) with time-domain methods, because of stability problems which may lead to considerable uncertainties with respect to accuracy of the results.

The new FDTLM method does not suffer from these problems because it uses diakoptics to subdivide a large structure into smaller substructures, which alleviates the large memory requirements known from other space discretization methods significantly. Furthermore, in the FDTLM the reference plane for the s-parameter computation is placed directly in the interface. No additional line length is required to ensure fundamental mode propagation left and right from a discontinuity. The s-matrix of the discontinuity contains fundamental and higher order mode interaction within the discontinuity plane. This s-matrix can be combined with s-matrices of subsequent discontinuities to form the overall s-matrix of a cascaded arrangement. Also stability problems known from the time-domain TLM in case of extreme non-equidistant discretization are non existent. Therefore, the numerical analysis of the structure in Fig.3 was done within 16 minutes CPU-time on a IBM RS6000 (530). This corresponds to approximately 1minute and 20 seconds per frequency point.

The analysis for the structures shown in Fig.4 and 5 is much faster. Fig.4 shows an E-plane filter which has been published in [4]. Not only is the agreement between the mode matching results [4] and the measurements excellent, but the CPU-time was down to 0.23 seconds per frequency point. Similar results are obtained for a ridged waveguide structure [5] given in Fig.5. Also here the agreement between the mode matching method, measurements and the FDTLM are very good. The CPU-time was 0.53 seconds per frequency point. In particular in the last case the mode matching method requires significantly more computation time. The dimensions for both structures are given in Table I.

Table I

Filter	Waveguide housing	Number of resonators	Insert thickness t (mm)	l1=l7 (mm)	l2=l6 (mm)	l3=l5 (mm)	l4 (mm)
E-plane metal insert filter	WR-28	3	0.51	1.009	4.778	3.87	4.796
E-plane ridge insert filter	WR-62	3	0.90	2.60	8.95	10.25	10.50

Conclusion

We have presented an improved version of the frequency-domain TLM method. Instead of using a 15-port symbolic scattering matrix for the 3D hybrid condensed node, only a 12-port node is utilized. This is possible by introducing three different propagation constants for each of the three space directions. The resulting algorithm is approximately 5 times faster than the original approach.

References

- [1] P.B.Johns, "Use of condensed and symmetrical TLM nodes in computer-aided electromagnetic design," *Proc. IEE Pt.H.*, vol. 133, pp.368-374, 1986.
- [2] W.J.R.Hoefer, "The transmission-line matrix method: Theory and applications," *IEEE Trans. Microwave Theory Tech.*, vol. MTT-33, pp. 882-893, Oct. 1985.
- [3] H.Jin and R. Vahldieck, "The Frequency-domain Transmission Line Matrix Method - A New Concept," appears in *IEEE Trans. Microwave Theory and Technique*, vol 40, No. 12, Dec. 1992.
- [4] J.Bornemann, R.Vahldieck, F.Arndt, and D.Grauerholz, "Optimized low-insertion-loss millimetre-wave fin line and metal insert filters", *The Radio and Electronic Engineer*, vol.52, No. 11/12, PP.513-521, 1982.
- [5] J.Bornemann and F.Arndt, "Transverse resonance, standing wave, and resonator formulations of the ridge waveguide eigenvalue problem and its application to the design of E-plane finned waveguide filters", *IEEE Trans. Microwave Theory Tech.*, vol. MTT-38, pp.1104-1113, Aug. 1990.

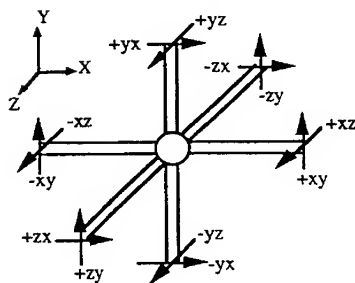


Fig. 1 The symmetrical condensed node

Row Number	Column Number											
	+xy	+xz	-xy	-xz	+yz	+yx	-yz	-yx	+zx	+zy	-zx	-zy
+xy	a_3	c_3	d_1	$-d_1$	b_4	b_4						
+xz	a_6	c_6	b_5	b_5	d_2	d_2						
-xy	c_3	a_3	d_1	$-d_1$	b_4	d_2	b_4	d_2				
-xz	c_6	a_6	b_5	b_5	d_2	d_2	b_4	d_2	d_4			
+yz	d_3	$-d_3$	a_1	c_1	b_2	$-d_4$	b_2	d_4				
+yx	d_3	$-d_3$	b_5	c_5	a_5	b_2	$-d_4$	b_2	d_4			
-yz	$-d_3$	d_3	a_1	c_1	b_2	$-d_4$	b_2	d_4				
-yx	$-d_3$	d_3	b_5	c_5	a_5	b_2	$-d_4$	b_2	d_4			
+zx	b_3	d_6	b_3	d_5	d_5	b_1	a_2	a_4	c_2	c_4		
+zy	b_3	d_6	b_3	d_5	d_5	b_1	a_2	a_4	c_2	c_4		
-zx	b_3	d_6	b_3	d_5	d_5	b_1	a_2	a_4	c_2	c_4		
-zy	b_3	d_6	b_3	d_5	d_5	b_1	a_2	a_4	c_2	c_4		

Fig. 2 New symbolic scattering matrix

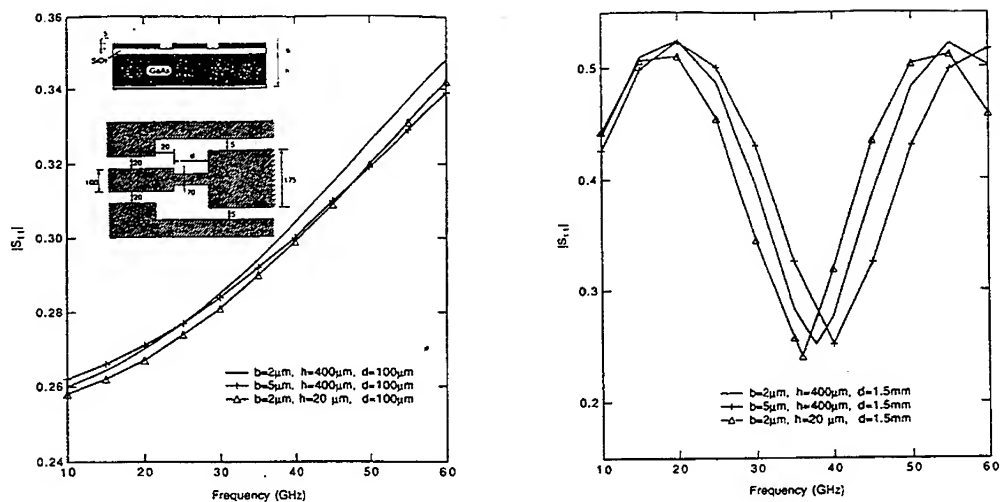


Fig. 3 Frequency-dependant s-parameters of cascaded discontinuities on MIS coplanar waveguide.

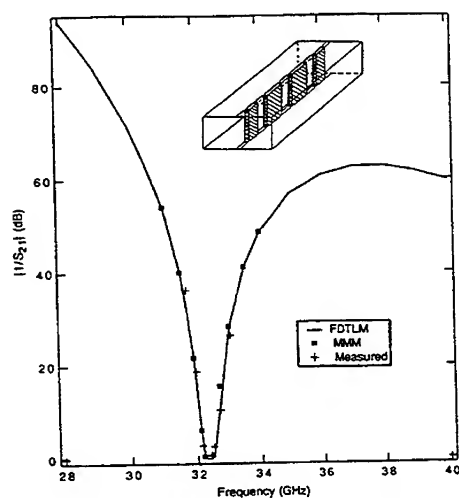


Fig. 4 Calculated and measured insertion-loss as a function of frequency of a Ka-band metal insert filter

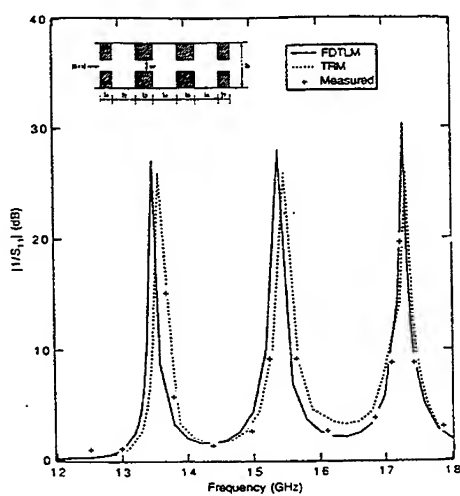


Fig. 5 Calculated and measured input reflection coefficient $|S_{11}|$ versus frequency of a simple E-plane ridge-waveguide filter

Infinitesimally Adjustable Boundaries In Symmetrical Condensed Node TLM Simulations

Fred J. German
Texas Instruments, Inc.
2501 W. University, MS 8019
McKinney, Texas 75070
Phone: (214)952-3723 FAX: (214)952-3773
email: fgerman@lobby.ti.com

INTRODUCTION

The symmetrical condensed node TLM (SCN-TLM) method is well established for the time domain solution of complex electromagnetic interaction problems in three dimensions. Recent improvements to the TLM method such as edge nodes [1], corner nodes [2] and thin wire nodes [3,4] have increased both the accuracy and applicability of the technique. Still, one of the major limitations of the TLM method is the requirement that boundary conditions be enforced either at mesh nodes or at points which lie exactly midway between them. This restriction is required in order to preserve time synchronization which insures the arrival of voltage pulses at all nodes in the TLM mesh simultaneously. As a consequence, problems must be discretized such that all boundaries are located at half-integer multiples of the mesh spacing. This requirement leads to unacceptable computational requirements for a large class of problems that require an accurate placement of boundary conditions. In addition, the standard cartesian mesh requires that curved surfaces be approximated using a stair-casing approximation. In many cases, such as the calculation of scattering from complex targets, this stair-casing approximation leads to substantial errors, and the use of increasingly finer meshes does not converge quickly to the desired result for the continuous curved boundary.

A method has been proposed by Johns and Slater [5] which allows the link-lines of a two dimensional TLM mesh to be adjusted at reflective boundaries in order to achieve boundary placement at any point lying between two adjacent nodes. This technique requires a modified scattering matrix for the TLM nodes. For the two dimensional series and shunt connected TLM nodes, the derivation of this scattering matrix is straightforward. In the case of the three dimensional SCN-TLM node, however, there is no equivalent lumped circuit model and so the derivation of the scattering matrix is not so simple.

In order to overcome this difficulty, Muller et. al. have proposed a method which retains the usual scattering matrix. In this technique, the affected link-lines are loaded with impedance elements to simulate the additional distance to the boundary. The differential equations relating the voltage and current at these elements are then replaced by difference approximations which yield recursive formulas for updating the voltage pulses reflected from the boundary. This requires knowledge of the voltage pulses at the boundary not only at the current time step but the previous one as well which must be

stored in the computer. In addition, the stability of these recursive formulas only allows for the link-lines to be lengthened, and not shortened, to accomodate boundary conditions.

In this paper, the scattering matrix for a general three dimensional SCN with differing link-line characteristic impedances is presented. This allows for the application of the Johns and Slater technique for adjusting boundaries. The development of this node allows for reflective boundaries to be placed at any point on the link-lines connecting two adjacent nodes.

THEORY

Figure 1 shows a SCN with unequal link-line lengths. By allowing the length of the link-lines to vary in this way, the point at which reflective boundary conditions are applied can be positioned at any point between adjacent nodes. An example where this capability is advantageous is demonstrated by the slanted boundary shown in Figure 2. Using the method presented here, the boundary conditions can be applied at the exact points where the boundary intersects the link-lines in the mesh. A stepped approximation to the boundary resulting from the placement of boundaries at the midpoint between nodes is also shown.

In any TLM simulation, time synchronization must be maintained. One way of preserving time synchronism while varying the link-line lengths involves changing the characteristic impedance of the lines [5]. Therefore, the scattering matrix for the SCN with variable impedance link-lines is required. Because each arm of the node contains two link-lines (corresponding to two orthogonal polarizations) there is the possibility of having, at most, six different characteristic impedances associated with a single SCN since

$$Y_1=Y_5, Y_2=Y_4, Y_3=Y_6, Y_7=Y_{12}, Y_8=Y_9, Y_{11}=Y_{10}$$

where the original port numbering used by Johns [6] has been used here.

The scattering matrix for the new node is obtained by applying Maxwell's equations along with the conservation condition that the scattering matrix be unitary. Figure 3 shows the symbolic form of the scattering matrix which is assembled based on symmetry considerations [6]. Using arguments similar to Johns' to discretize Maxwell's equations in terms of the voltage pulses on the link-lines and by requiring the unitary condition, a complicated set of equations results which can be solved, after considerable manipulation, for a,b,c,d and e. These values are given by the following:

$$a = \frac{Y_i}{Y_i + Y_j} \left(1 - \frac{2(Y_k + Y_l)}{Y_i + Y_j + Y_k + Y_l} \right) + \frac{Y_j}{Y_i + Y_j} \left(1 - \frac{2(Z_m + Z_n)}{Z_i + Z_j + Z_m + Z_n} \right)$$

$$b = \frac{2Y_k}{Y_i + Y_j + Y_k + Y_l}$$

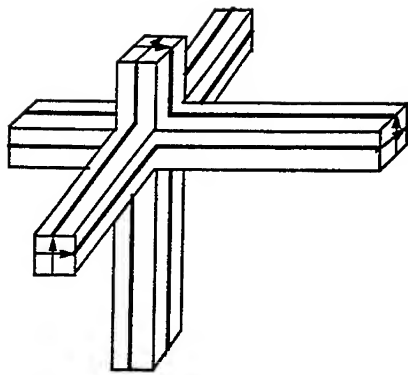


Figure 1. Symmetrical condensed TLM node with varying link line lengths for the arbitrary placement of boundaries.

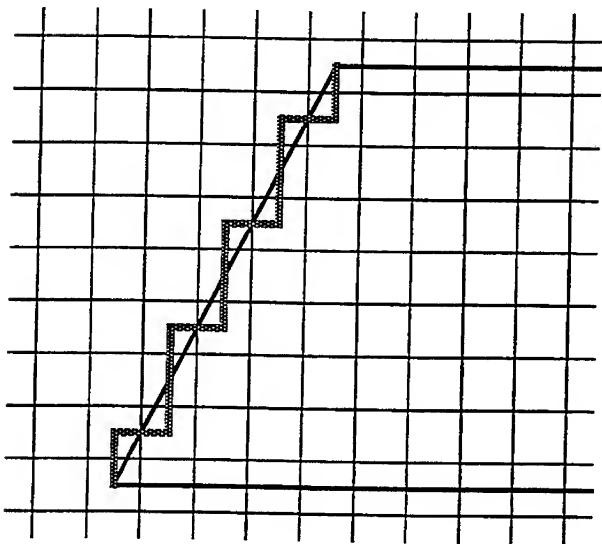


Figure 2. A TLM mesh with a slanted boundary modeled using a fitted boundary and a stepped boundary approximation.

i	j	k	l	m	n	1	2	3	4	5	6	7	8	9	10	11	12
1	1	2	9	3	1	a	b	d						c		-d	e
2	9	1	1	2	6	b	a			d				e	-d		c
3	1	1	4	8	1	d		a	b				c			e	-d
4	8	3	1	1	5			b	a	d		-d	e			c	
5	7	6	1	0	4				d	a	b	e	-d		c		
6	1	0	5	7	2		d			b	a	c		-d	e		
7	5	6	1	0	4				-d	e	b	a	d		c		
8	4	3	1	1	5			b	e	-d		d	a			c	
9	2	1	1	2	6	b	e				-d			a	d		c
10	6	5	7	2	9		-d			b	e	c		d	a		
11	3	4	8	1	1	-d		e	b				c			a	d
12	1	2	9	3	1	e	b	-d						c		d	a

Figure 3. The scattering matrix for the new TLM node.

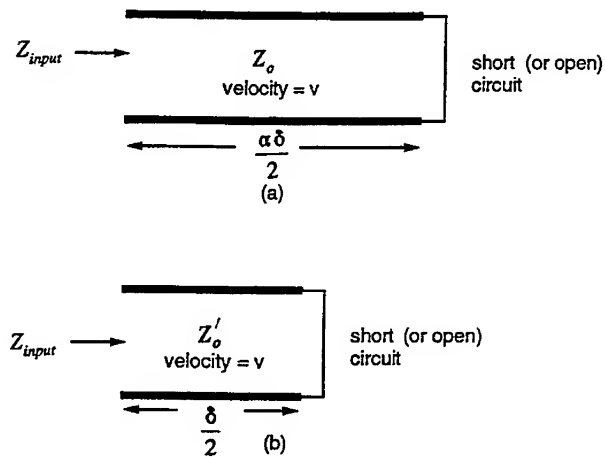


Figure 4. Transmission line equivalents for the placement of a short (or open) circuit load. (a) The physical problem, and (b) electrically equivalent problem.

$$c = \frac{2Y_l}{Y_l + Y_j + Y_k + Y_i}$$

$$d = \frac{2Z_l}{Z_l + Z_j + Z_m + Z_n}$$

$$e = \frac{2Y_l}{Y_l + Y_j} \left(1 - \frac{Y_k + Y_i}{Y_l + Y_j + Y_k + Y_i} - \frac{Z_m + Z_j}{Z_l + Z_j + Z_m + Z_n} \right)$$

where the subscripts for the admittances and impedances are obtained from Figure 3.

With the scattering matrix now available, its application to adjustable boundaries must be considered. For the standard SCN all link-lines are $\delta/2$ long where δ is the inter-nodal spacing in the coordinate directions. Suppose we wish to apply a boundary condition at a point that is $\alpha\delta/2$ from a node where $0 < \alpha < 2$. A single link-line for this situation is shown in Figure 4(a). Clearly, time synchronism is violated. However, if we replace this physical situation with the electrically equivalent one shown in Figure 4(b), time synchronism is maintained. To see how this is done, note that the input impedance for the case of Figure 4(a) is given by

$$Z_{input} = jZ_o \tan\left(\frac{\beta\alpha\delta}{2}\right)$$

which for small $\beta\delta$ is

$$Z_{input} = jZ_o \frac{\beta\alpha\delta}{2}$$

For the case in Figure 4(b).

$$Z_{input} = jZ_o' \tan\left(\frac{\beta\delta}{2}\right)$$

which reduces, for small $\beta\delta$, to

$$Z_{input} = jZ_o' \frac{\beta\delta}{2}$$

For the two situations to be electrically equivalent we equate the input impedances which gives the requirement that

$$Z_o' = \alpha Z_o$$

for a short circuit (PEC) boundary. For the case of an open circuit (PMC) boundary we

find that the required impedance is

$$Z_o' = \frac{Z_o}{\alpha}$$

Thus, by applying the above properties, it becomes evident how a reflective boundary a distance of $\alpha\delta/2$ from a node can be simulated by adjusting the characteristic impedance of the affected $\delta/2$ link-lines, thus preserving the required time synchronization.

NUMERICAL RESULTS

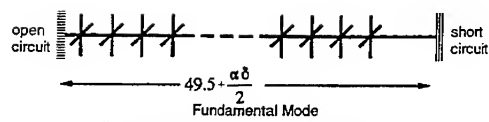
The first example is a simple one dimensional resonator built out of a string of 50 SCN's. The resonator is terminated on one end with a stationary magnetic wall (open circuit) and at the other with an adjustable electric wall (short circuit). The enclosing walls are terminated using appropriate symmetry conditions. The resonant frequencies for the first and fifth resonant modes were calculated for various values of the length parameter α and are presented in the figure where good accuracy is observed. For the same TLM mesh without adjustable boundaries only the $\alpha=1$ solution can be obtained. This example demonstrates not only the accuracy of the proposed method, but also the versatility that can be achieved with regard to the positioning of boundaries on a sub-cell size scale.

Next we examine the use of the proposed method for simulating a circular waveguide. Due to symmetry only one-fourth of the structure need be considered as shown in Figure 6. A radius of 5δ is used to calculate the cutoff frequencies for several TE modes in the guide. The results in Figure 5 are presented for a stepped approximation to the boundary and for a fitted boundary using the present method. In all cases except the TE₀₁ mode (where the stepped boundary result is very accurate) improvement in the results is observed. To investigate the convergence of the resonant frequency with increasing mesh resolution, the same waveguide was used to calculate the TE₁₁ cutoff frequency for different mesh sizes. The results are shown in Figure 7. Overall, the fitted boundary yields more accurate answers than the stepped boundary for a given mesh coarseness, and approaches the exact result faster with increasingly finer meshes.

As a final example, the problem of a rectangular waveguide with a slightly off-center fin is examined. The geometry is shown in Figure 8. If a mesh size of 1 mm is chosen, then the boundary condition for the fin cannot be placed exactly using the usual ungraded TLM mesh. The problem has been solved using a 1 mm mesh size using the fitted boundary technique and with the standard TLM algorithm by approximating the fin as being centered. As a reference solution, the problem was also solved using a fine ($\delta=0.5\text{mm}$) mesh which allows the fin to be placed exactly in a normal mesh. The results are shown in the figure for the cutoff frequencies of the first two TE modes. Clearly, an advantage is gained from the use of the adjustable boundaries described here.

CONCLUSIONS

A method for the accurate positioning of reflective boundaries in the SCN-TLM method has been presented. It is based on the earlier work of Johns and Slater, and a newly derived scattering matrix for the SCN. Some simple examples have demonstrated the advantages of the technique when the accurate placement of boundaries is called for.

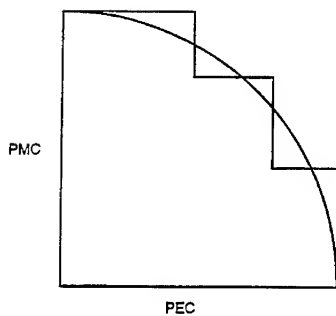


α	fr (TLM)	fr (Exact)	% Diff.
0.0	1.508	1.515	0.462
0.5	1.504	1.507	0.199
1.0	1.504	1.500	0.267
2.0	1.496	1.485	0.741

Fifth Resonant Mode

α	fr (TLM)	fr (Exact)	% Diff.
0.0	7.540	7.576	0.475
0.5	7.524	7.538	0.186
1.0	7.504	7.500	0.053
2.0	7.472	7.426	0.619

Figure 5. One dimensional resonator with the first and fifth resonant frequencies calculated using adjustable boundaries.



MODE	Exact	Stepped	Fitted
TE 01	0.6099	0.6108 (0.14)	0.6283 (3.02)
TE 11	0.2930	0.2833 (3.31)	0.2883 (1.60)
TE12	0.8485	0.8275 (2.47)	0.8392 (1.10)
TE 21	0.4861	0.4517 (7.08)	0.4558 (6.23)
TE22	1.0673	1.0283 (3.65)	1.0392 (2.63)

Figure 6. Geometry and cutoff frequencies for various TE modes in a circular waveguide using fitted boundaries and a stepped approximation. Parenthetical values are percent error.

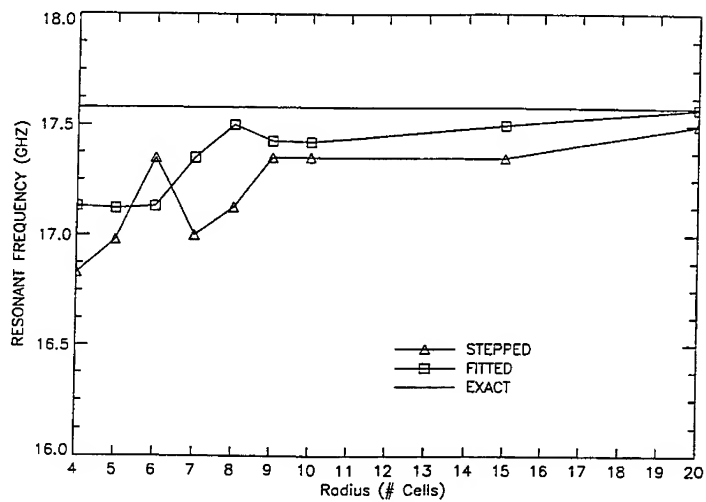
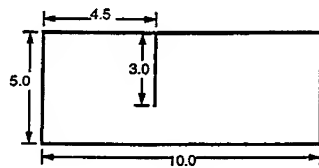


Figure 7. Convergence of the fitted and stepped boundaries for the TE₁₁ mode of a circular waveguide.



	Fine Mesh	Coarse Mesh	Coarse Mesh (Fitted)
f1	10.94 GHZ	10.66 GHZ (2.56)	10.74 GHZ (1.83)
f2	28.31 GHZ	30.02 GHZ (6.04)	27.14 GHZ (4.1)

Figure 8. Finned waveguide geometry and cutoff frequencies of the first two TE modes. (Percent difference from fine mesh is in parenthesis)

The TLM code GTEC [7] has been modified for the present work. Since GTEC implements pre-calculation of the scattering matrices in the mesh, the additional computational expenditure required by the use of adjustable boundaries is in the pre-processing stage when these are calculated and is negligible. The technique does, however require slightly more memory since more scattering matrices must be stored. The actual TLM algorithm remains unchanged. Further work is underway to more fully characterize the accuracy of the new method.

REFERENCES

- [1] J.S. Nielsen and W.J.R. Hofer, "Modification of the Condensed 3-D TLM Node to Improve Modeling of Conductor Edges," IEEE Microwave and Guided Wave Letters, vol. 2, no. 3, 1992.
- [2] U. Muller, P.P.M. So and W.J.R. Hofer, "The Compensation of Coarseness error in 2D TLM modeling of Microwave Structures," 1992 IEEE MTT-S Int. Symp. Dig., Albuquerque, NM.
- [3] P. Naylor and Christopoulos, "A New Wire Node for Modeling Thin Wires in Electromagnetic Field Problems Solved By Transmission Line Modeling," IEEE Trans., vol. MTT-38, no. 3, 1990.
- [4] J.A. Porti et. al., "Comparison of Thin-Wire Models for TLM Method," Electron. Lett., vol. 28, no. 20, 1992.
- [5] P.B. Johns and G.F. Slater, "Transient Analysis of Waveguides With Curved Boundaries," Electron. Lett., vol. 9, no. 21, 1973.
- [6] P.B. Johns, "A Symmetrical Condensed Node for the TLM Method," IEEE Trans., vol. MTT-35, no. 4, 1987.
- [7] F.J. German and L.S. Riggs, "GTEC User's Manual", Electrical Engineering Department Report, Auburn University, AL, 36849, 1986.

SESSION 14 - "GENERAL PURPOSE CODE APPLICATIONS"

Chair: Dr. Jim Breakall, Co-Chair: George Hagn

Rhombic Illuminator Performance at High Frequency

J. Patrick Donohoe and Clayborne D. Taylor

Mississippi State University
Department of Electrical and Computer Engineering
P.O. Drawer EE
Mississippi State, MS 39762

ABSTRACT

The high frequency characteristics of a rhombic illuminator under common-mode excitation are studied in this paper using the Numerical Electromagnetics Code (NEC-2). The electrical length of the overall wire structure ranges from approximately 700 wavelengths at 500MHz to approximately 1400 wavelengths at 1GHz. Efficient segmentation schemes are required to extend the analysis up to 1GHz. Based on the damping characteristic of the rhombic illuminator current at these frequencies, only a portion of the wire structure must be modelled. This technique allows one to analyze such a structure efficiently at very high frequencies.

INTRODUCTION

A rhombic illuminator (RI) is characterized by a rhombic transmission line configuration over ground with the ends of the transmission line connected to ground through a source at one end and a matched load at the opposite end as shown in Figure 1. The height of the transmission line above ground rises from the source and the load to an apex somewhere in the midsection of the transmission line. The wires on the source end of the RI are referred to as the *launch wires* (wires #1 and #3) with voltage sources V_1 and V_3 driving these wires relative to the ground plane. The wires on the load end are referred to as the *termination wires* (wires #2 and #4) with loads Z_2 and Z_4 connecting these wires to the ground plane. These terminations are chosen to be the characteristic impedance of the two-wire transmission line over ground. The dimensions of the RI considered in this paper are shown in Figure 2.

The RI is typically designed to produce near uniform fields of a given polarization within some specified volume below the conductors. This volume of interest is commonly referred to as the *working volume*. The polarity of the voltage sources relative to each other dictates the direction of field polarization within the working volume. The common-mode excitation ($V_1=V_2$) generates fields in the working volume which are predominately vertically polarized such that E_z is the principal component of the transverse electric field. The x-component of the electric field under common-mode excitation is designated as the nonprincipal component of the transverse electric field. The differential-mode excitation ($V_1=-V_2$) generates fields in the working volume which are predominately horizontally polarized such that E_x is the principal transverse component of the electric field while E_z is the nonprincipal transverse component.

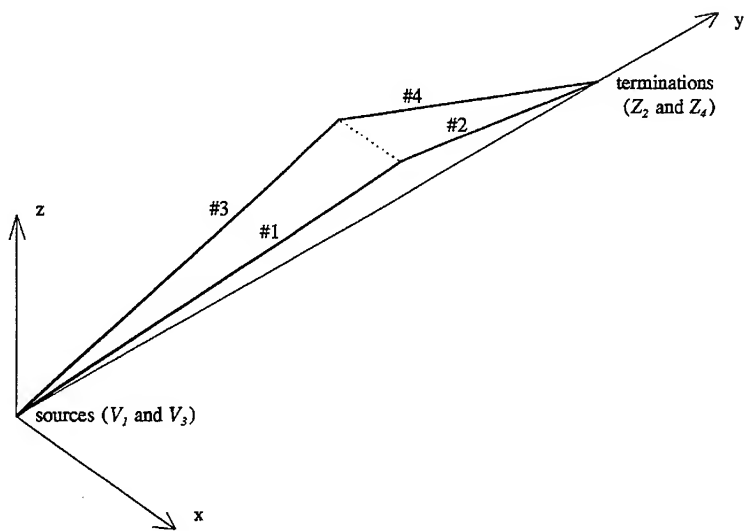


Figure 1. Rhombic Illuminator (RI) wire configuration.

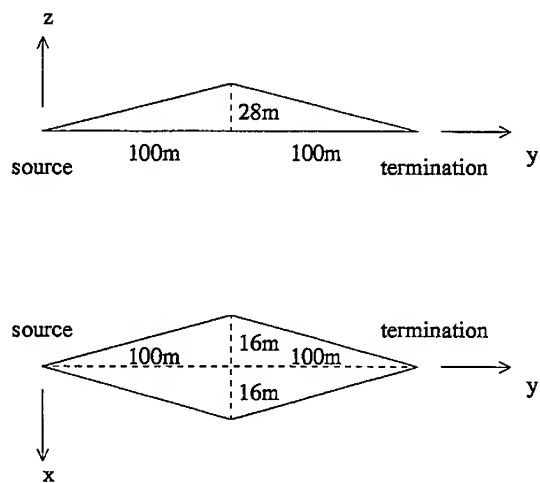


Figure 2. Dimensions of the Rhombic Illuminator.

LOW FREQUENCY PERFORMANCE OF THE RHOMBIC ILLUMINATOR

At low frequencies, the RI may be modelled as a two-wire transmission line over ground [1]. The transverse electromagnetic fields within the working volume may be approximated by the fields of the two-wire line TEM mode. The TEM electric fields of the two-wire line under common-mode or differential-mode excitation are obtained by considering the static fields of equivalent line charges over ground. The principal and nonprincipal transverse electric fields under common-mode excitation given a perfectly-conducting ground plane are

$$E_z = \frac{\eta_o V}{4\pi Z_{cm}} \left[\frac{(z-b)}{(x-a)^2 + (z-b)^2} + \frac{(z-b)}{(x+a)^2 + (z-b)^2} - \frac{(z+b)}{(x-a)^2 + (z+b)^2} - \frac{(z+b)}{(x+a)^2 + (z+b)^2} \right] \quad (1)$$

$$E_x = \frac{\eta_o V}{4\pi Z_{cm}} \left[\frac{(x+a)}{(x-a)^2 + (z-b)^2} + \frac{(x-a)}{(x-a)^2 + (z-b)^2} - \frac{(x+a)}{(x-a)^2 + (z+b)^2} - \frac{(x-a)}{(x-a)^2 + (z+b)^2} \right] \quad (2)$$

where $2a$ is the distance between the wire centers, b is the height of the wires above the ground plane, V is the wire potential, η_o is the intrinsic impedance of the surrounding medium (modelled here as free-space) and Z_{cm} is the characteristic impedance of the common-mode two-wire line given by

$$Z_{cm} = \frac{\eta_o}{4\pi} \left\{ \ln \left[\frac{1 + \sqrt{1 + (r/b)^2} - r/b}{1 - \sqrt{1 + (r/b)^2} + r/b} \right] + \frac{1}{2} \ln [1 + (b/a)^2] \right\} \quad (3)$$

where r is the radius of the wires. Below approximately 100MHz, the electric field distributions defined in Equations (1) and (2) are quite similar to the working volume fields obtained using *NEC-2*. The RI wire current magnitude at 1, 10 and 100MHz is shown in Figure 3 where the variable s defines the distance along the wires. The current distribution along the RI wires at these frequencies, while exhibiting a damped standing-wave characteristic from the source to the termination, is relatively constant. Thus, the similarity of the field distribution with that of the TEM mode is not surprising. As the frequency of operation is increased, the RI becomes a more effective radiator and the current decay along the RI wires becomes more pronounced. The standing wave behavior of the RI current is attributable to reflections from the wire bends and the terminations.

HIGH FREQUENCY PERFORMANCE OF THE RHOMBIC ILLUMINATOR

The high frequency characteristics the given RI are evaluated using *NEC-2*. The RI is excited in the common-mode configuration. The total wire length for the RI is approximately 420 meters and the frequency range of interest is 500MHz to 1GHz. Thus, the electrical length of the overall wire structure to be modelled with *NEC-2* ranges

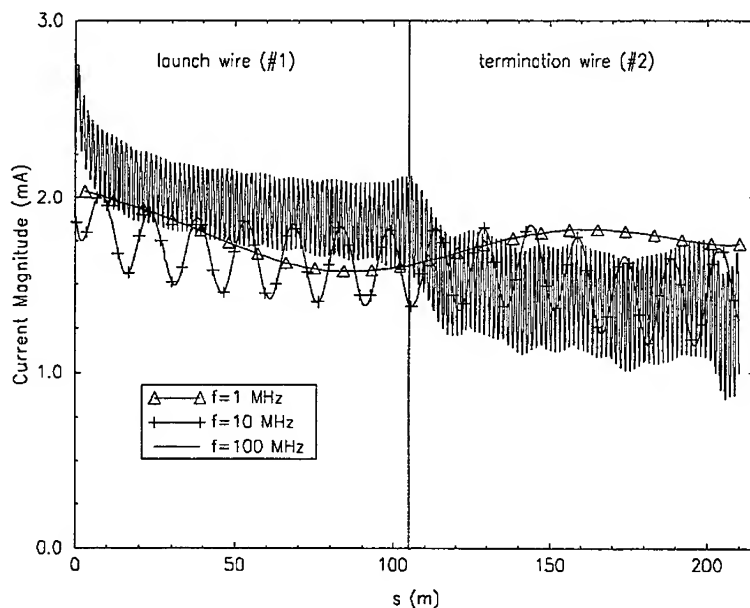


Figure 3. RI current at 1, 10 and 100MHz.

from a minimum of approximately 700 wavelengths to a maximum of approximately 1400 wavelengths. The complexity of the analysis is reduced somewhat by the fact that the RI configuration possesses one plane of symmetry. Efficient segmentation schemes [2] are required to extend the analysis of the RI up to 1GHz using a code like *NEC-2* which utilizes sub-domain basis functions. The segment lengths are increased from a minimum at the source ($\sim 0.01\lambda$) to the specified maximum length ($\sim 0.4\lambda$) using a 10% increase in length from segment to segment. The remaining portion of the launch wire and the complete termination wire are divided into uniform segments of maximum allowable length ($\sim 0.4\lambda$).

The RI current was computed at 500 and 550MHz using *NEC-2* and the segmentation technique described above and is shown in Figure 4. At 500MHz, the current magnitude is significant along the entire structure. However, at 550MHz, the current decays such that the termination wire current becomes negligible over a portion of the wire. At higher frequencies (600MHz and higher), the current decays to a negligible magnitude over a larger portion of the termination wire. This characteristic allows for analysis of the RI at higher frequencies by modeling only the portion of the antenna over which the current is significant. The antenna currents from 600MHz to 1GHz at 50MHz intervals are shown in Figures 5 through 8.

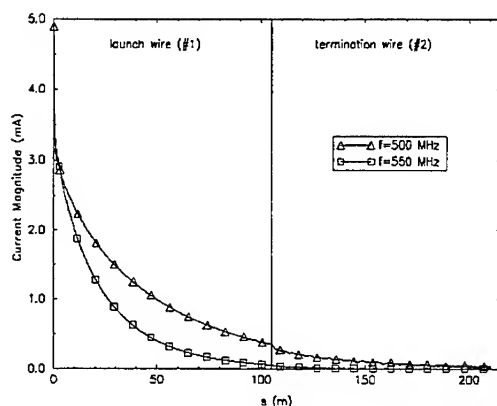


Figure 4. RI Current at 500 and 550 MHz.

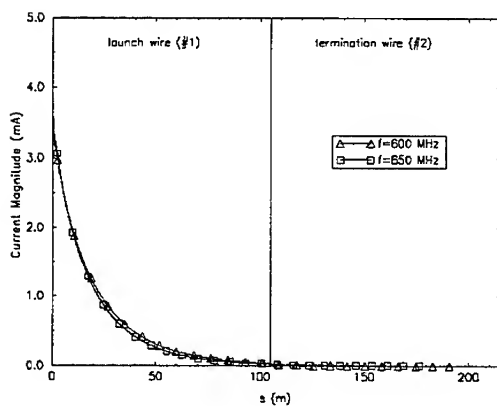


Figure 5. RI current at 600 and 650 MHz.

The principal electric field magnitude is determined along a line normal to the antenna axis at both 500 MHz and 1 GHz for a perfect ground plane and an inhomogeneous lossy ground plane consisting of wire radials over a lossy material. The ground material properties are assumed to be ($\epsilon_r=7.55$, $\sigma=0.124 \text{ U/m}$) at 500 MHz and ($\epsilon_r=6.4$, $\sigma=0.258 \text{ U/m}$) at 1 GHz. The plots of the working volume fields are given in Figures 9 and 10.

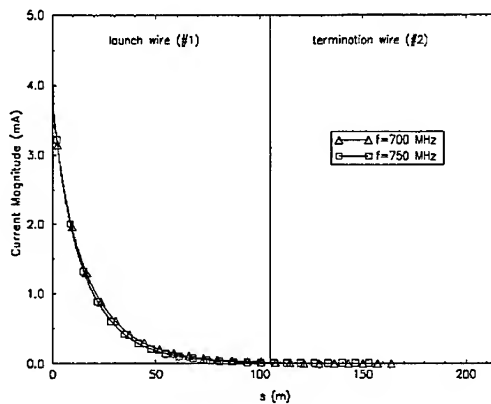


Figure 6. RI current at 700 and 750 MHz.

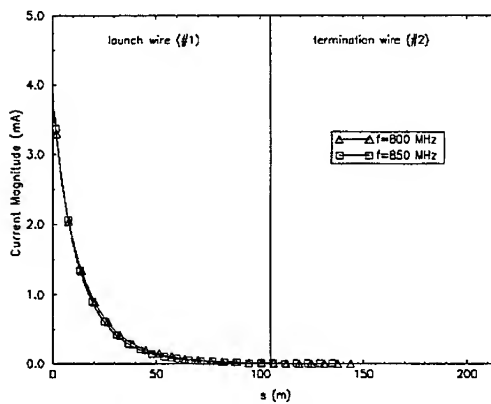


Figure 7. RI current at 800 and 850 MHz.

CONCLUSION

The damping coefficient associated with the RI currents increases as the frequency increases. A significant change in the current distribution is noted from 500 MHz to 550 MHz. Further increases in frequency produce smaller changes in the shape of the current by comparison. The peak value of the current, located at the source, shows a continual increase with frequency. From the current distribution results given here, we find that the terminations wires would have little effect on the basic operation of the RI at frequencies above 1 GHz. The technique for reducing the actual length of the antenna

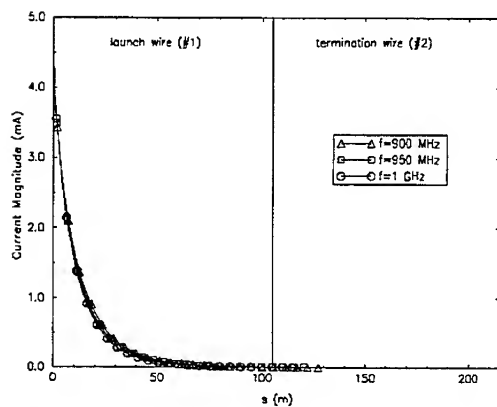


Figure 8. RI current at 900, 950 and 1000MHz.

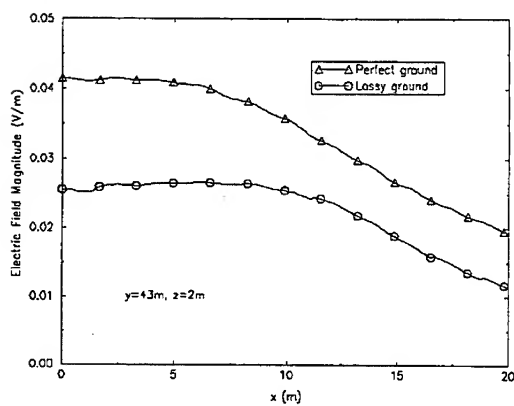


Figure 9. RI principal transverse electric field magnitude at 500MHz.

in the analysis could be applied to the HSI at frequencies above 1 GHz. Such an analysis would yield accurate results assuming the damping characteristics of the antenna follow the same trend as seen from 500MHz to 1GHz.

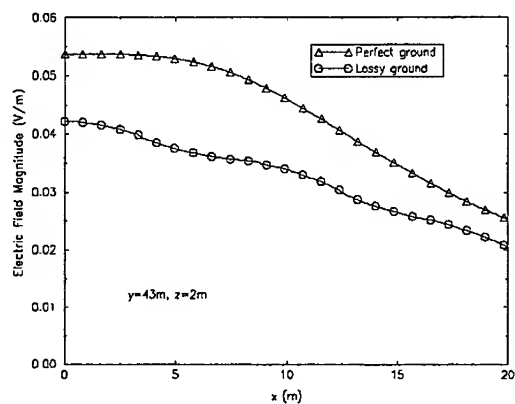


Figure 10. R1 principal transverse electric field magnitude at 1 GHz.

REFERENCES

- [1] H. M. Shen and R. W. P. King, "The Rhombic EMP Simulator," *IEEE Transactions on Electromagnetic Compatibility*, Vol. EMC-24, No. 2, pp. 255-265, May 1982.
- [2] S. N. Tabet, J. P. Donohoe, and C. D. Taylor, "Using Nonuniform Segment Lengths with NEC to Analyze Electrically Long Wire Antennas," *Applied Computational Electromagnetics Society Journal*, Vol. 5, No. 2, pp. 2-16, Winter 1990.

High Resolution Spectral Analysis of HF Coupling Modes on the EC-130 Aircraft

Q.C. Luu, S.J. Kubina, and C.W. Trueman
Concordia University
7141 Sherbrooke St. W.
Montreal, Quebec, Canada H4B 1R6

D. De Carlo
Naval Air Test Center
Patuxent River
MD 20670

Abstract

The complex HF antenna installation on the EC-130 aircraft presents an unusual opportunity for the study of inter-antenna and antenna-to-airframe coupling. A complex wire-grid model of the aircraft was developed for use with the Numerical Electromagnetic Code (NEC) to analyze the HF coupling modes on the aircraft. NEC runs were executed as frequency sweeps with very fine frequency stepping so that the detailed variations in radiation characteristics can be revealed. The numerical results provide a valuable and complete information set which is difficult to obtain by experimental measurements.

I. Introduction

The EC-130 is a U.S. Navy communication platform which is equipped with five external HF wire antennas for long range communication. They include two top mounted antennas that run from either side of the forward fuselage to the vertical stabilizer, two symmetrical "dog-leg" antennas running from mid-fuselage towards the horizontal stabilizer and then to the vertical stabilizer, and one receive antenna, centred on top of the fuselage, aft of the other two longer top mounted antennas, as shown in Fig. 1. Such a complex HF antenna installation presents an unusual opportunity for the study of inter-antenna and antenna-to-airframe coupling. The coupling between the HF antennas gives rise to two main concerns : (1) the magnitude of the induced voltage across the feed points of an antenna could be high enough to cause operational interference or even damage to the receiver connected to the passive antenna; (2) the radiation pattern of each individual antenna could be profoundly altered by the strong currents induced on other antennas and/or on the airframe due to phase additions or cancellations. The exact frequencies where these strong couplings occur are very difficult if not impossible to identify by direct measurements or simplified calculations. Therefore, numerical modelling techniques are employed to study the coupling phenomena on this complex structure. The use of numerical modelling techniques not only allows one to obtain a complete set of critical frequencies associated with strong couplings by fine frequency stepping sweeps, but also to calculate the values of the induced voltages at antenna terminals and the currents on any part of the structure, as well as the radiated field patterns of the antennas. This paper presents the results obtained from running NEC for excitations of two different antennas and three different passive antenna loading conditions. Part of the results had been published in the proceedings of ANTEM'92 [1].

II. Model Development and Validation

A complex wire-grid model of the aircraft consisting of 924 wire segments was developed for use with the numerical electromagnetic code (NEC) to analyze the radiation characteristics of the aircraft as a whole. The wire-grid model had been carefully designed to minimize the difference between the real structure and the model in terms of electromagnetic properties. As can be seen in Fig. 5, measures that were taken in the design of the model include a denser wire-grid in the antenna feed regions and smooth transition of wire density in regions such as wings and stabilizers where the width of the conducting surface is not constant. These two arrangements will ensure the continuity of current flows on the airframe. Moreover, the "same surface area" rule was applied to calculate the radius of each wire in the model. The calculation of wire radii was done systematically using computer programs called "MESHES" and "FNDRAD" [2]. The first program identifies all the meshes in the wire-grid model, and the latter one finds the radius for each wire based on the area(s) of the mesh(es) to which the wire belongs. For complicated wire-grid models such as the one used in this study, the use of a computer program for radius calculation eliminates the chance of making mistakes and speeds up the process considerably. It is of great concern that the wire-grid model complies with the known modelling guidelines of NEC [3] so that meaningful numerical results can be obtained. Thus the program "CHECK" [4] was used to detect any violation of NEC guidelines and no errors were reported. The validity of the model was further confirmed by the good agreement between the measured and computed radiation patterns at selected frequencies [5].

III. Antenna Input Impedance Values as Coupling Indicators

One of the major advantages of using numerical modelling techniques to analyze electromagnetic problems is the ease in repeating the analysis for the same problem with different parameter values. This allows one to see the detailed variation in the results with respect to a parameter such as frequency. In the study of HF coupling, it is desirable to find out the exact frequencies in the HF range where strong couplings occur. Strong couplings are revealed by abrupt changes in input impedance values of an antenna. If the input impedance curve of an antenna is compared with a reference curve which represents the coupling-free input impedance, then all the couplings can be found by examining the input impedance curve. With the increase in computing power on modern computers, it is possible to complete a frequency sweep on the model with very fine frequency stepping in a relatively short period of time. This allows one to obtain very high resolution input impedance curves and hence greatly reduces the chance of missing some strong couplings occurring over a very narrow frequency band. After obtaining the input impedance curve, one can analyze all the couplings present in the HF range. Figures 2 and 3 show the input impedances of antennas HF1 and HF4, respectively. Compared with the input impedance of a dipole antenna in free space, as shown in Fig. 4, it is seen that the input impedance curves of HF1 resemble that of the dipole except there are additional peaks and valleys at certain frequencies. Due to its special shape and orientation with respect to the airframe, the impedance curves of the "dog-leg" antenna HF4 are less similar to that of the dipole, but they still possess the typical pattern of open-circuit transmission line impedances. The most obvious inter-antenna coupling is observed as a small bump on the resistance curve between 3.0 and 4.8 MHz. Couplings to the airframe are generally less intense and occur over a wider frequency band, they do not show up as spikes or steep edges on the impedance curves as a result.

The existence of the couplings observed from the impedance curves can be verified by examinations of current distributions or the induced voltages across the feed points of the loaded passive antennas. Induced voltages are calculated by multiplying the currents at the feed elements of the passive antennas by the load impedances, and the results are plotted versus frequency. The coupling modes are then investigated by examining the current magnitude and phase on the wire antennas and on the airframe as well as the induced voltages at the passive antenna terminals. For very practical reasons, the radiation patterns at the critical frequencies will also be plotted and compared with the patterns at adjacent frequencies where no strong couplings are observed.

IV. Analysis of Coupling Modes

(a) HF1 as the active antenna.

Compared with the input impedance curve of a dipole in free space, the input impedance for the short-circuit and open-circuit conditions exhibit high degree of anomaly at certain frequencies, whereas the input impedance for the $50\ \Omega$ loading condition basically follows the pattern of a dipole antenna in free space with the exception near 4 MHz and weaker indications elsewhere.

In the short-circuit case shown in Fig. 2(a), there is an oscillation of input reactance at frequencies near 3.6 MHz. This oscillation was found to be related to the strong couplings between the two "dog-leg" antennas (HF4 and HF5) and the active antenna (HF1) by an examination of the current distribution at those frequencies. As shown in Fig. 5(c), the magnitudes of the currents induced on HF4 and HF5 are comparable to that on the active antenna at 3.65 MHz. The notch on the input resistance curve near 4.7 MHz was identified as the indication of the coupling between HF1 and HF3, which is shown in Fig. 5(b). It is also observed that there is a spike near $f = 3.15$ MHz and three other notches on the input resistance curve near $f = 10.4$, 17.65, and 24.9 MHz corresponding to couplings between HF1 and HF2. These strong couplings occur at the resonant frequencies of HF2, which incidentally are also the resonant frequencies of HF1 (HF1 and HF2 are of the same length). This is an important clue to the coupling modes between antennas. Fig. 5(a) shows the current distributions on HF1 and HF2 at 3.15 MHz, where the strongest coupling between HF1 and HF2 occurs.

In this paper, the frequencies at which the input reactance changes from negative to positive are referred to as resonant frequencies, and the frequencies where the input reactance changes from positive to negative are referred to as anti-resonant frequencies. The resonant and anti-resonant frequencies for the five antennas on the aircraft in the frequency range from 2 to 30 MHz are listed in Table 1.

For the open-circuit case shown in Fig. 2(b), it was surprising to find that the input resistance and reactance of the active antenna are quite different from those in the short-circuit case. First of all, no oscillation of input reactance is found near 3.6 MHz, instead, the oscillation occurs at frequencies near 29.2 MHz. In addition, the notches on the input impedance curve do not occur at the resonant frequency of HF2. There is a spike followed by a notch near 9 MHz, a small "bump" followed by a shallow notch near 19 MHz, and another spike at 29.2 MHz. The

anomalous points near 9 and 19 MHz are due to couplings between HF3 and HF1, which is something unexpected since these frequencies correspond to the anti-resonant frequencies of HF3 rather than its resonant frequencies. Fig. 5(d) shows the current distributions on HF1 and HF3 at 9 MHz, HF3 is seen to be at anti-resonance. The spike at 29.2 MHz, which is close to the anti-resonant frequencies of both HF2 and HF3, is the result of strong couplings to both HF2 and HF3. Besides significant induced currents, strong couplings also result in high induced voltages across the feed points of the passive antennas. The voltage values in this case were calculated by multiplying the current on the feed element of each antenna by the simulated open-circuit load of 1 M Ω . Fig. 6 (a) shows the plots of the induced voltages versus frequency. These plots give even clearer pictures regarding the bandwidth as well as the magnitude of each coupling. Obviously, HF2 and HF3 have much higher induced voltages than HF4 and HF5. This is probably due to the fact that these two antennas are farther away from HF1 than the other two passive antennas. The highest induced voltage is found at HF3 near 19.0 MHz which is 5 times the excitation voltage at HF1. The following inferences were drawn based on a careful examination of the frequencies at which voltage peaks occur :

High induced voltages appear at the terminals of the passive antennas near frequencies corresponding to : (1) the resonant frequencies of the active antenna; (2) the anti-resonant frequencies of the passive antennas.

Table 1 Resonant and Anti-Resonant Frequencies of the HF Antennas on the EC-130.

Antenna	Frequency (MHz)							
	1st order		2nd order		3rd order		4th order	
	Resonant	Anti-Res.	Resonant	Anti-Res.	Resonant	Anti-Res.	Resonant	Anti-Res.
HF1	3.2	6.4	10.4	12.8	17.6	21.0	25.0	28.8
HF2	3.2	6.4	10.4	12.8	17.6	21.0	25.0	28.8
HF3	4.7	9.0	14.1	19.0	25.0	29.2		
HF4	3.6	7.0	10.8	13.0	17.8	22.0	25.2	27.0
HF5	3.6	7.0	10.8	13.0	17.8	22.0	25.2	27.0

With the passive antennas being terminated in 50 Ω resistances, the magnitudes of couplings are reduced throughout the HF range. The only strong coupling visible on the input resistance curve is the one occurring near 3.3 MHz. The induced voltages were obtained by multiplying the currents on the feed elements of the passive antennas by 50 Ω and were plotted versus frequency as shown in Fig. 6 (b). It is noted that the highest induced voltage in this case occurs at HF2 near 3.5 MHz and is 1.1 times the excitation voltage at HF1. Voltage peaks are found at frequencies close to the resonant frequencies of the active antenna HF1. Unlike the open-circuit case, no high induced voltages are found near the anti-resonant frequencies of the passive antennas. It is also observed that the magnitude of coupling decreases as the relative distance between the active and passive antennas increases. HF2 is closest to HF1, thus it experiences strongest coupling. Being the farthest passive antenna from HF1, HF5 has lowest coupled voltages among the four.

(b) HF4 as the active antenna.

Although HF4 is a bent wire antenna, its input impedance pattern is still comparable with

that of a dipole in free space. As shown in Fig. 3, the input impedances for all three passive antenna loading conditions are very similar, except near 4.7 MHz where there is tiny notch on the resistance curve for the short-circuit case but not for the other two cases. That notch is found to be related to a coupling between HF4 and HF3 by an inspection of the current distribution shown in Fig. 5 (e). The induced voltages for open-circuit and 50 Ω loading are plotted in Figures 7 (a) and Fig. 7 (b), respectively.

For open-circuit loading, the coupling modes observed when HF1 acts as an active antenna also apply here. High induced voltages are found near resonant frequencies of the active antenna HF4 and near the anti-resonant frequencies of the passive antennas. Compared with HF1 excitation, the magnitudes of the induced voltages, however, are much lower.

Similarly, the induced voltages for the 50 Ω loading case also fit in the modes described for HF1 excitation. High coupled voltages are observed near the resonant frequencies of the active antenna HF4. Again, the magnitude of coupling is much lower compared to HF1 excitation.

Coupling to the airframe is present throughout the HF range for all three loading conditions. There are two major current paths : (1) the path along antenna HF4 and the port (left) wing of the aircraft; (2) the path along antenna HF4, port side of the fuselage, and the port horizontal stabilizer starting near the feed point of HF4. The magnitude of coupling varies with frequency. Strongest couplings to the left wing are found near 4, 12, 20, and 27 MHz. The magnitudes of the couplings to the fuselage and stabilizer are also found to be strongest near the frequencies mention above, but are less sensitive to frequency change compared to those to the wing. As an example, at 6 MHz, the coupling to the wing has diminished whereas the coupling to the fuselage and horizontal stabilizer is still strong, as shown in Fig. 5 (f).

V. Effects of Coupling on Radiation Patterns

The patterns of radiated fields depend not only on the active antenna but also on the passive antennas and the aircraft structure because currents induced on any part of the aircraft are radiation sources as well. We are particularly interested in the radiation patterns at frequencies where strong inter-antenna couplings are present. At these critical frequencies, induced currents on the passive antennas could be so strong that the radiation patterns could be entirely different from the patterns at other frequencies. Fig. 8 shows the volumetric radiation patterns for two polarizations of the E-field.

For HF1 excitation under short-circuit loading condition, the patterns at 3.15 and 3.65 MHz are very different from the patterns at 3.0 and 4.0 MHz, as shown in Figures 8 (a) through 8 (d). This indicates that the couplings between HF1 and HF2 at 3.15 MHz, and between HF1, HF4 and HF5 at 3.65 MHz alter the radiation pattern substantially. Similarly, a comparison between the radiation patterns at 4.0 and 4.7 MHz shown in Fig. 8 (d) and Fig. 8 (e) reveals that the coupling between HF1 and HF3 at 4.7 MHz also results in significant radiation pattern changes. These profound changes in radiation patterns within such a narrow frequency band are very difficult to detect by experimental measurements. Changes in radiation patterns are also

found for other couplings occurring at higher frequencies and for the couplings present in the open-circuit and 50 Ω loading cases.

VI. Conclusions

It is observed from the numerical results that the most striking couplings on the aircraft are those between the HF wire antennas mounted on the airframe, especially between the three straight antennas that extend from the top of the fuselage to the vertical stabilizer. Currents induced on passive antennas are higher or comparable to the current on the active antenna at certain frequencies. When acting as active antennas, the two "dog-leg" antennas can induce relatively high current along the wings and the sides of the fuselage due to their special locations and orientations. As far as the induced voltages are concerned, voltages as high as 5 times the source voltage of the active antenna are observed to be induced across the feed points of a passive antenna under the open-circuit condition. Under the 50 Ω loading condition, the induced voltages are lower, but still can be as high as 1.1 times the source voltage. It is noted that for short-circuit and 50 Ω termination, strong inter-antenna couplings occur near the resonant frequencies of the active and passive antennas, whereas high magnitude couplings are found near the resonant frequencies of the active antenna and the anti-resonant frequencies of the passive antennas for the open-circuit case.

Acknowledgement

This work was supported by the National Science and Engineering Research Council of Canada.

References

- [1] Q.C. Luu, S.J. Kubina, C.W. Trueman, and D. De Carlo, 'Study of HF Antenna Coupling Modes on the EC-130 Aircraft', Conference Proceedings, Symposium on Antenna Technology and Applied Electromagnetics, Winnipeg, Canada, August 1992.
- [2] C.W. Trueman, 'Automated Radius Calculation for Wire-Grid Models', 7th Annual Review of Progress in Applied Computational Electromagnetics Computational Society, Monterey, California, March 18-22, 1991.
- [3] G.J. Burke and A.J. Poggio, 'Numerical Electromagnetic Code (NEC) -- Method of Moments, Naval Ocean System Center, Technical Document 116, July 1977.
- [4] C.W. Trueman and S.J. Kubina, 'Verifying Wire-Grid Model Integrity with Program "CHECK"', Appl. Comput. Electromagnet. Soc. J., Vol. 5, No. 2, Winter 1990.
- [5] B.R. Rosenzweig, 'Numerical Modelling of EC-130 Airframe and Antenna Installation for Prediction of Radiation Characteristics over the HF Band', M. ENG. Thesis, Department of Electrical and Computer Engineering, Concordia University, Montreal, Quebec, Canada.

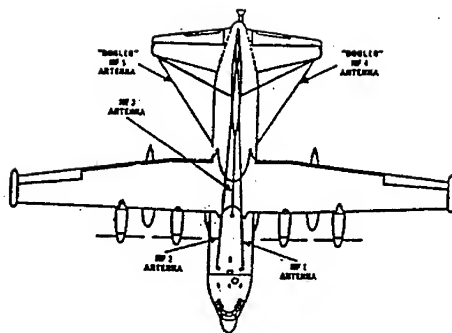
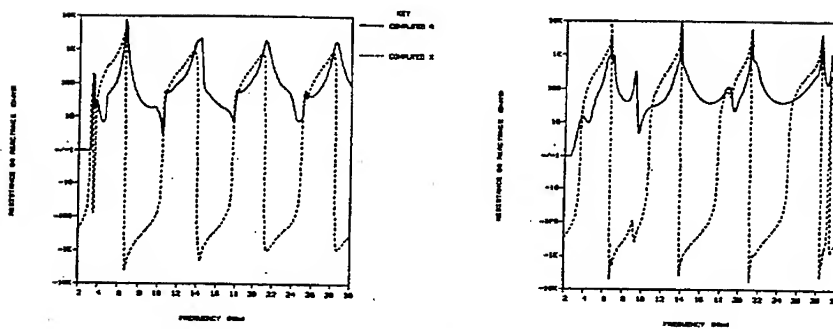
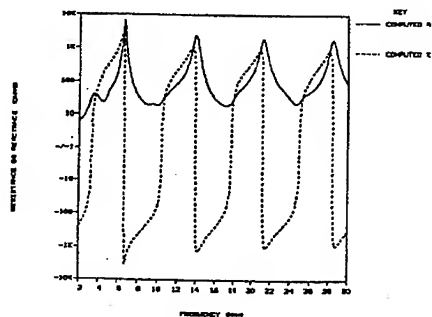


Fig. 1 EC-130 HF Antenna Installation.



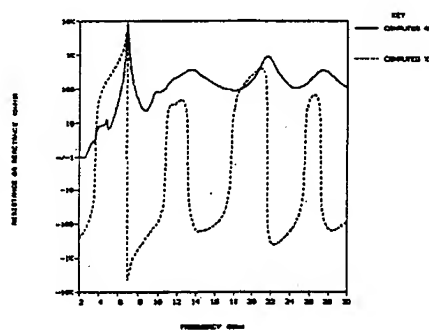
(a) Passive Antennas Short-Circuited.

(b) Passive Antennas Open-Circuited.

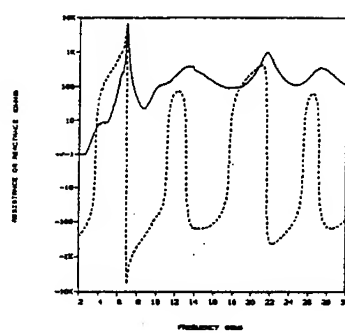


(c) Passive Antennas Loaded with 50 Ω Resistances.

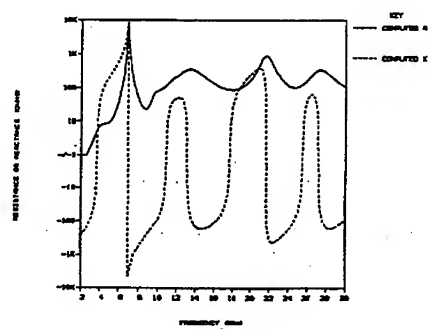
Fig. 2 HF1 Input Impedance.



(a) Passive Antennas Short-Circuited.



(b) Passive Antennas Open-Circuited.



(c) Passive Antennas Loaded with 50 Ω Resistances.

Fig. 3 HF4 Input Impedance.

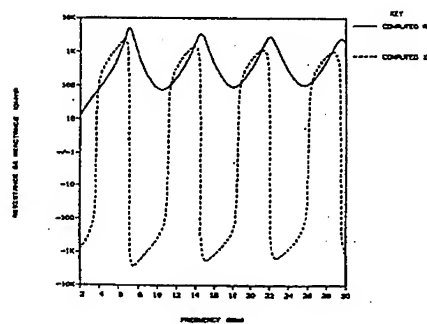
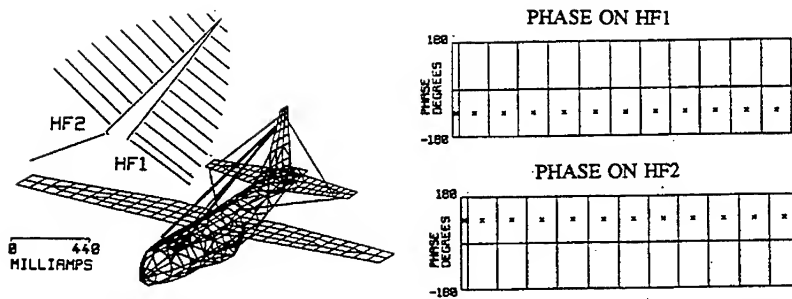
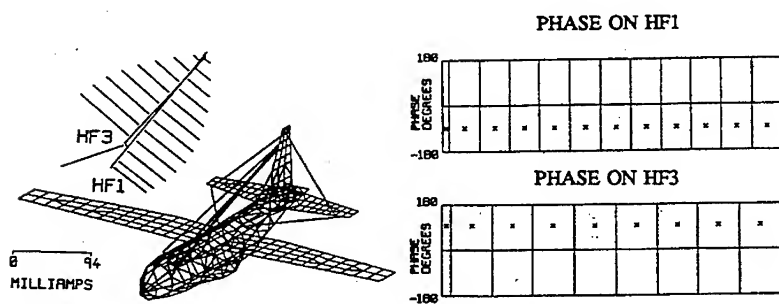


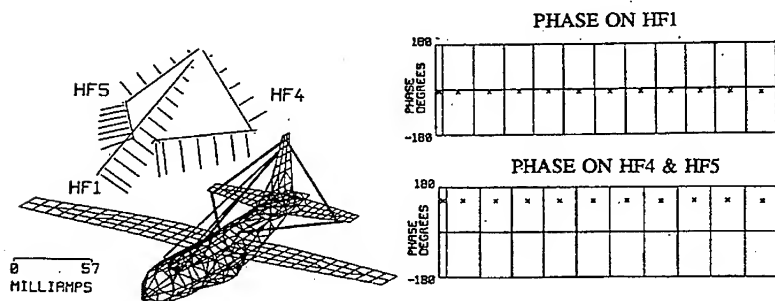
Fig. 4 Input Impedance of a 40 m Long Dipole in Free Space.



(a) $f = 3.15$ MHz. Active Antenna : HF1. Passive Antennas Short-Circuited.



(b) $f = 4.7$ MHz. Active Antenna : HF1. Passive Antennas Short-Circuited.



(c) $f = 3.65$ MHz. Active Antenna : HF1. Passive Antennas Short-Circuited.

Fig. 5 Magnitudes and Phases of the Coupled Currents.

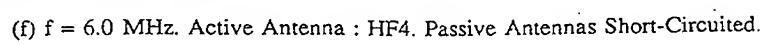
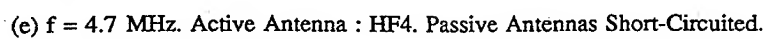
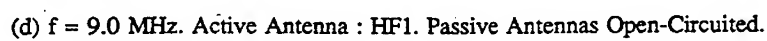
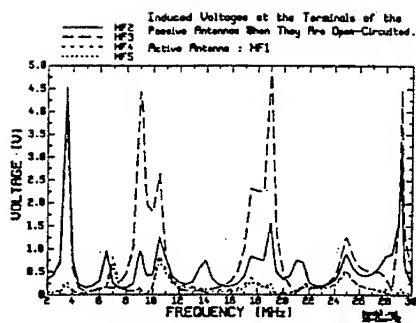
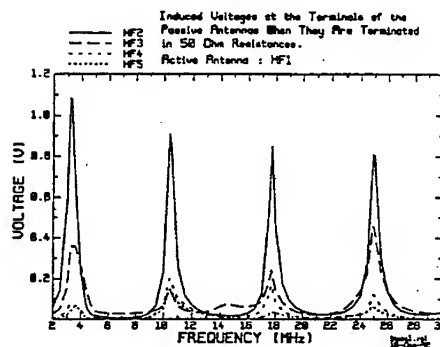


Fig. 5 (Cont'd)

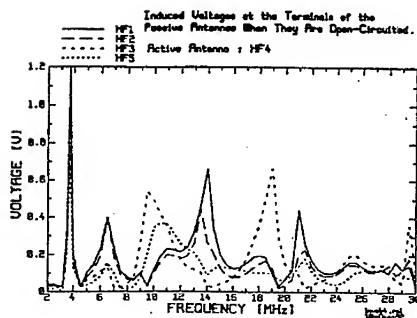


(a) Open-Circuited.

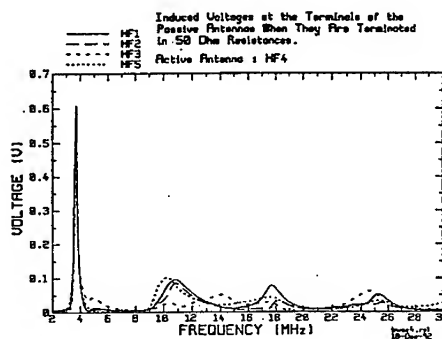


(b) Loaded by 50 Ω .

Fig. 6 Voltages Induced at the Terminals of the Passive Antennas by HF1.



(a) Open-Circuited.



(b) Loaded by 50 Ω .

Fig. 7 Voltages Induced at the Terminals of the Passive Antennas by HF4.

Helicopter Antenna Pattern Analysis Using NEC-BSC

R. M. Herkert, J. A. Woody, D. W. Acree, and D. P. Millard
Georgia Tech Research Institute
Georgia Institute of Technology
Atlanta, Georgia 30332

ABSTRACT

This paper details the evaluation of the pattern degradation due to protruding structures for several antennas mounted on a military helicopter tail boom. Models of the antennas under investigation and of the helicopter structure were created for use with the Numerical Electromagnetic Code - Basic Scattering Code (NEC-BSC) Version 3.1 [1]. To determine the effects of the main rotor compartment, the engines, and the tail section on the antennas' patterns, two separate models of the helicopter structure were required: a partial aircraft model and a full aircraft model. The partial aircraft model did not include the main rotor compartment, the engines, or the tail section, while the full aircraft model included these structures. NEC-BSC was run using these models to perform the analysis. The pattern degradation due to the protruding structures was determined by comparing the antenna patterns resulting from the two models.

INTRODUCTION

Antenna placement on a military helicopter presents many challenging problems because there are a limited number of suitable mounting surfaces and because of the large number of antennas required on such a platform. These problems include the necessity for placing antennas within close proximity of each other and the likelihood of having protruding helicopter structures affect the antennas' intended area of coverage. On a complex military helicopter, such as the one shown in Figure 1, one antenna location of choice is on the top of the tail boom. This is a good location because not only is there enough area for mounting several antennas with adequate spacing, but there is also little helicopter structure to obstruct the antennas. The main protruding structures that are likely to affect the patterns of antennas placed on the tail boom are the main rotor compartment, the engines, and the tail section.

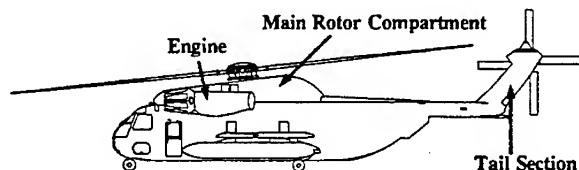


Figure 1. Complex Military Helicopter.

The antennas typically placed on the tail boom are associated with electronic systems which operate at different frequencies in the range from 100 to 1600 MHz. There is a definite need for a technique to analyze the pattern coverage of these antennas as a precursor to a measurement program. The analysis can be used to help avoid placing antennas in areas with excessive pattern blockage or to compare the placement of antennas in various locations for performance trade-offs.

NEC-BSC can be used for this type of investigation because it is based on the Uniform Geometrical Theory of Diffraction (UTD), an approach which is ideal for a high frequency study of antennas in which only the most basic structural features of an otherwise very complicated structure need to be modeled. This allows for a complex helicopter to be modeled using a small number of perfectly conducting plates and cylinders. Because the model need not be very complicated, its creation is a relatively easy task and computer run times are short enough to not become a major drain on personnel or resources.

This paper will focus on the analysis of three different antennas operating at three distinct frequencies all using the same helicopter models. The first two antennas are blades operating at 130 and 1090 MHz, respectively. The third antenna is a turnstile operating at 260 MHz.

MODEL DEVELOPMENT

Antenna Models

In this investigation, the blade antennas were modeled as vertically polarized half-wavelength dipoles. The turnstile antenna was modeled as two orthogonal, horizontally polarized, half-wavelength dipoles fed with a 90° phase differential to obtain circular polarization. Models for two different orientations of the crossed dipoles were created (rotated 45° relative to each other) because their true orientation was unknown due to the antenna casing.

Helicopter Models

The helicopter structure was modeled using perfectly conducting plates and cylinders. Use of UTD generally requires that each plate have edges at least a wavelength long and that each antenna be at least a wavelength from all plate edges. Since the lowest operating frequency of any of the antennas is 130 MHz, which corresponds to a maximum wavelength of 90.9 inches, the requirements of UTD could not be met. However, the NEC-BSC's User's Manual [1] states that in many cases the wavelength limit can be reduced to a quarter wavelength for engineering purposes. Since the helicopter model could be built to conform to the quarter wavelength limit, which required a minimum edge length of 22.7 inches, NEC-BSC was used assuming this limit was valid. It should be noted that the rotors were not included in the helicopter model. The inclusion of the spinning rotors would have a modulating affect on the patterns that were generated without them.

To determine the effects of the protruding structures on the antennas' patterns, two separate models of the helicopter structure were created: a partial aircraft model and a full aircraft model. A comparison of the antenna patterns of these two models identified the effects of the engines, the main rotor compartment, and the tail section. An isometric view of the partial aircraft model is shown in Figure 2. This model conforms to the quarter wavelength

limit and contains a total of nine plates; it does not include the engine sections, the main rotor compartment, or the tail section. An isometric view of the full aircraft model is shown in Figure 3. This model conforms to the quarter wavelength limit and contains a total of eighteen plates and two cylinders; it includes the engine sections, the main rotor compartment, and the tail section.

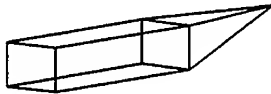


Figure 2. Partial Aircraft Model.

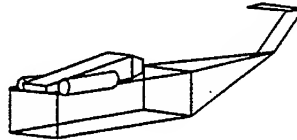


Figure 3. Full Aircraft Model.

OUTPUT VISUALIZATION

The pattern cuts that were used to display the outputs from NEC-BSC were: 1) azimuth cut (top view), 2) longitudinal elevation cut (side view), and 3) crosswise elevation cut (front view). Three cuts were necessary to examine the entire pattern for each of the antennas. Patterns were calculated with one degree increments in the appropriate pattern angle because this proved to be a good tradeoff point for pattern resolution versus NEC-BSC run time.

Four antenna patterns were calculated for each pattern cut. The patterns corresponded to the following conditions: 1) the antenna in free space with no aircraft model, 2) the antenna mounted on a perfectly conducting horizontal infinite ground plane, 3) the antenna mounted on the partial aircraft model, and 4) the antenna mounted on the full aircraft model. The first two conditions were selected because their patterns were already known and they proved to be good test cases for the antenna models. The third and fourth conditions were used to determine the degradation due to the protruding structures on the helicopter.

A computer program was written to convert the results obtained from NEC-BSC into a form that could be loaded into GRAFTOOL [2], a commercial scientific visualization package. Overlaying the plots of the differing conditions on the same graph provided an easily readable method of comparison.

SAMPLE ANTENNA PATTERNS

E-field patterns for the blade antenna at 130 MHz are shown in Figures 4 through 9 for the following conditions: 1) in free space, 2) mounted on an infinite ground plane, 3) mounted on the partial aircraft model, and 4) mounted on the full aircraft model. The blade was placed on the tail boom roughly halfway between the main rotor compartment and the tail section and slightly off center. For all of these patterns, only the theta (horizontal) component has been shown, because the theta component of the field is the dominant component.

E-field patterns for the blade antenna at 1090 MHz for conditions 3 and 4 are shown in Figures 10 through 12. The patterns for conditions 1 and 2 match those of the blade at 130 MHz and are not repeated. This blade was placed on the tail boom roughly one third of the way from the tail section to the main rotor compartment and slightly off center. Once again, only the theta (horizontal) component has been shown.

E-field patterns for the turnstile antenna at 260 MHz for all four conditions are shown in Figures 13 through 16. The turnstile was placed on the tail boom roughly one fourth of the way from the tail section to the main rotor compartment and slightly off center. Results for the two orientations of the crossed dipoles (rotated 45° relative to each other) gave results within 1 dB for all patterns, therefore, patterns for only one orientation are given. For this antenna, theta and phi components are of the same relative magnitude, so both components are shown. Due to space limitations, only patterns for the longitudinal elevation cut are presented.

CONCLUSIONS

A technique to analyze the pattern coverage of antennas placed on the tail boom of a helicopter using NEC-BSC has been presented. The analysis is centered on NEC-BSC's ability to predict far zone patterns of antennas in the presence of scattering structures. This type of analysis is helpful as a precursor to a measurement program for several reasons. By using NEC-BSC, models of the complex helicopter need only contain its most basic structural features. Once the antennas and the helicopter are modeled, trade-off analyses can be easily performed by moving the antennas to various locations on the tail boom and re-running the evaluation. Comparisons of the outputs of these runs can be used to minimize the effects of the protruding structures and maximize antenna coverage.

REFERENCES

1. R.J. Marhefka and J.W. Silvestro, "Near Zone - Basic Scattering Code User's Manual with Space Station Applications," Grant No. NSG 1498, ElectroScience Laboratory, The Ohio State University, March 1989.
2. *GRAFTOOL Graphical Analysis System, Version 3.3*, 3-D Visions Corporation, 1990.

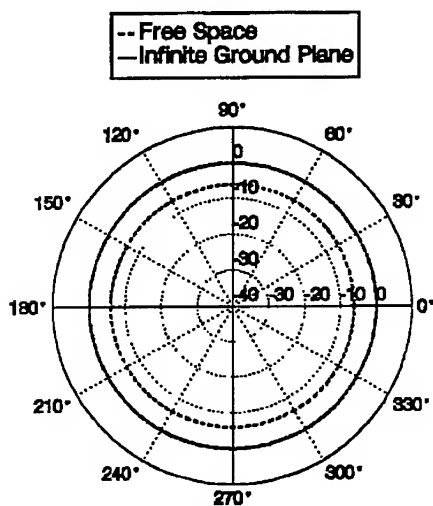


Figure 4. Blade Patterns at 130 MHz
Azimuth Cut, Theta Component.

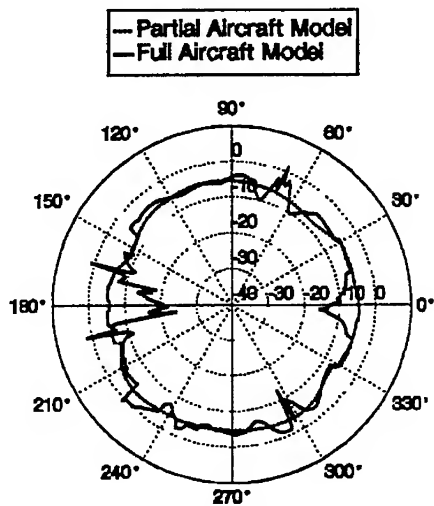


Figure 5. Blade Patterns at 130 MHz
Azimuth Cut, Theta Component.

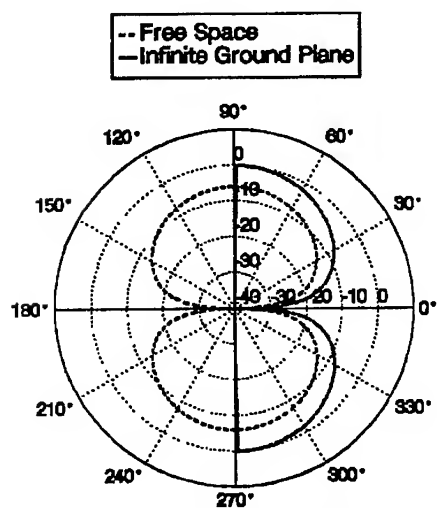


Figure 6. Blade Patterns at 130 MHz
Long. Elevation Cut, Theta Comp.

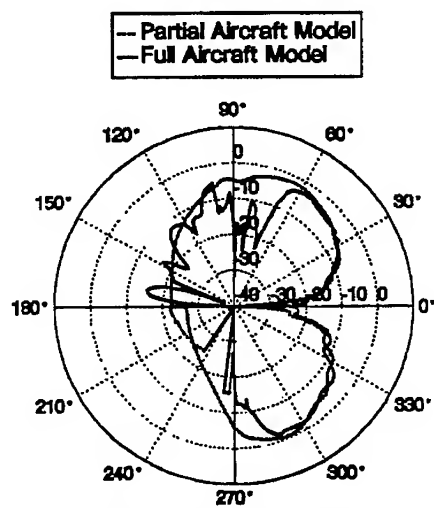


Figure 7. Blade Patterns at 130 MHz
Long. Elevation Cut, Theta Comp.

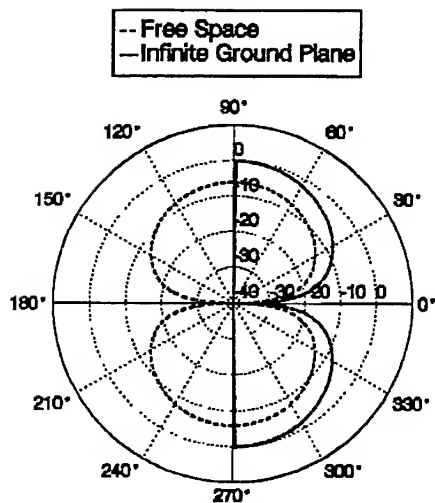


Figure 8. Blade Patterns at 130 MHz
Cross. Elevation Cut, Theta Comp.

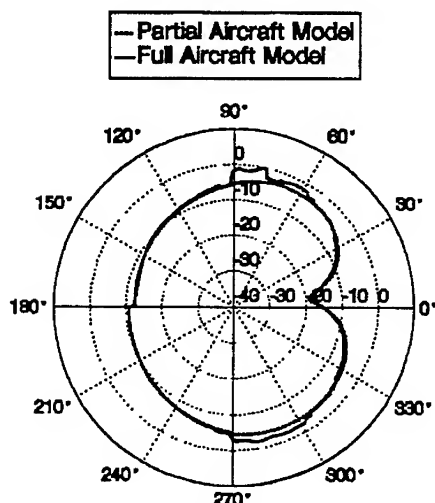


Figure 9. Blade Patterns at 130 MHz
Cross. Elevation Cut, Theta Comp.

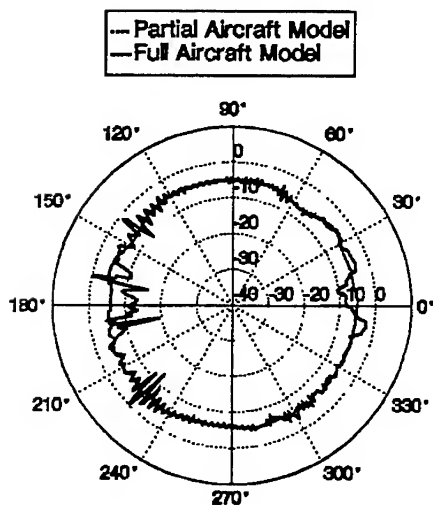


Figure 10. Blade Patterns at 1090 MHz
Azimuth Cut, Theta Component.

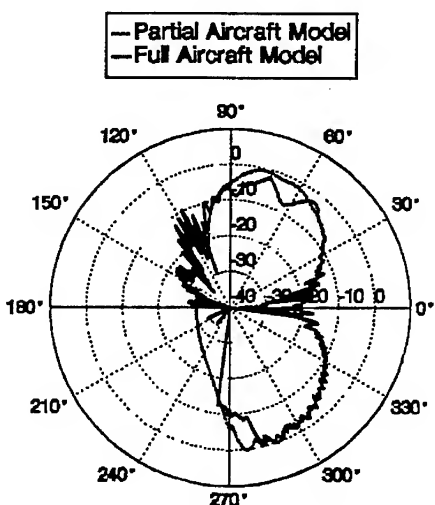


Figure 11. Blade Patterns at 1090 MHz
Long. Elevation Cut, Theta Comp.

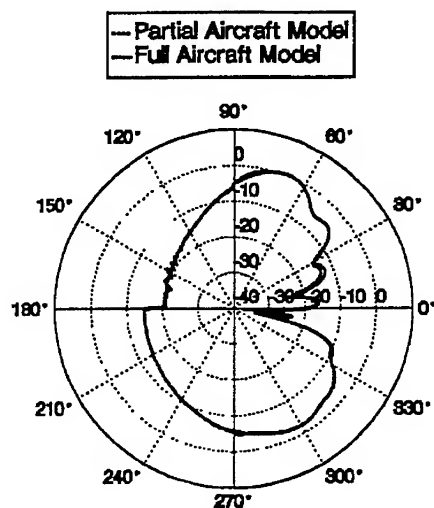


Figure 12. Blade Patterns at 1090 MHz
Cross. Elevation Cut, Theta Comp.

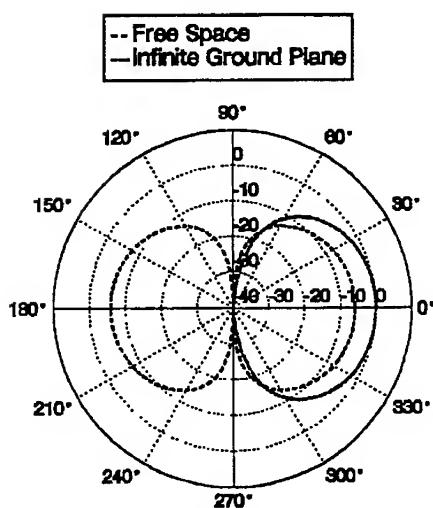


Figure 13. Turnstile Patterns at 260 MHz
Long. Elevation Cut, Theta Comp.

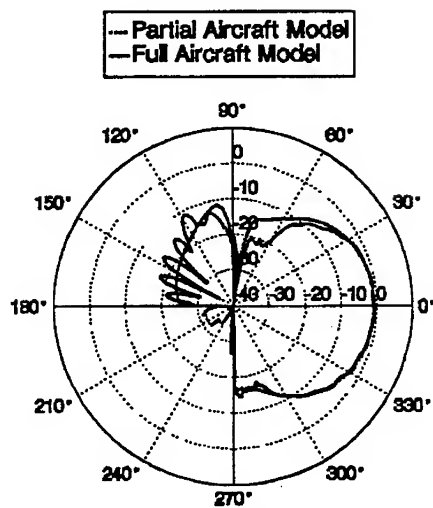


Figure 14. Turnstile Patterns at 260 MHz
Long. Elevation Cut, Theta Comp.

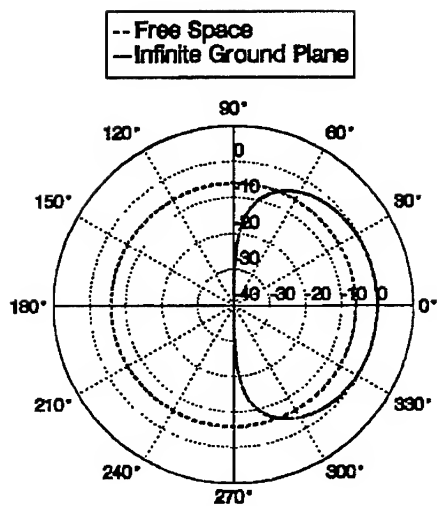


Figure 15. Turnstile Patterns at 260 MHz
Long. Elevation Cut, Phi Comp.

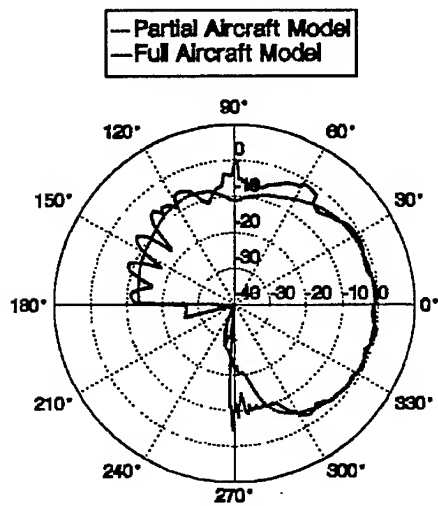


Figure 16. Turnstile Patterns at 260 MHz
Long. Elevation Cut, Phi Comp.

**AIRBORNE TX/RX ANTENNA PAIR LOCATION INVESTIGATION--
EXPERIMENTAL AND NEC-BSC RESULTS**

Scott Townley
ESL Inc. A Subsidiary of TRW
495 Java Drive
Sunnyvale, CA 94086

ABSTRACT

Aircraft are fitted with numerous blade antennas for a variety of missions. Equipment additions and system upgrades often result in conflicts in locating all the required antennas. Frequently, resolving the conflict requires moving an antenna system to another fuselage location. Naturally, the end user of the platform desires to maintain full effectiveness of all on-board systems.

This article describes an antenna relocation study where a blade dipole antenna is moved from a wingtip position to the tail. The effect of this move on the antenna radiation patterns and another nearby antenna array is determined using the Basic Scattering Code (NEC-BSC) from Ohio State, and experimentally verified using a full-scale mockup of the airframe.

INTRODUCTION

The airframe as modeled in NEC-BSC is illustrated in Figure 1 along with the relevant antennas and their positions. One system's antennas were originally located near each wingtip. Recently, a system upgrade was proposed which required antennas from another system be located within only a few inches of the first. Preliminary analysis revealed that the existing system would produce cross-modulation products in the new system, seriously degrading its performance; therefore, the wingtip antenna would have to be moved to another mounting position in order to successfully implement the system upgrade. The most obvious place was the high horizontal stabilizer of the T-tail assembly.

However, relocating the wingtip antenna was subject to several constraints. The performance of the existing system could not be degraded--in particular, it was feared that blockage due to the proximity of the vertical stabilizer would severely compromise the azimuthal coverage of a tail-mounted antenna. Of secondary concern was that the antenna pair isolation would be greatly reduced since the antennas would have less spatial separation.

Most critically, the new system location could not result in increased coupling to a second antenna array located on the bottom of the aircraft fuselage. Very expensive interference cancellers were integrated with this array, and increased

coupling from the newly tail-mounted system would require an even more expensive redesign and retrofit of the interference cancellers.

NEC-BSC [1] was used to predict the effects resulting from the relocation of the wingtip antenna system. Azimuthal radiation patterns and antenna coupling calculations were made for four different antenna positions on the horizontal stabilizer. These calculations were later verified using a full-scale wood and copper screen mockup of the airframe at ESL's outdoor testing facility in Fremont, CA.

NEC-BSC CALCULATIONS

NEC-BSC Airframe Model.

Figure 1 illustrates the NEC-BSC model and antenna positions used in the calculations. As the full-scale mockup used later has no nose radome, the NEC-BSC model did not include that feature. Antenna positions are in inches, and the origin of the coordinate system corresponds roughly to the center of rotation of the full-scale mockup.

Two additional features are incorporated in the NEC-BSC model. First, the full-scale mockup is actually mounted upside down, so the RT command was used initially to build the aircraft in that position. Additionally, the outdoor test site is not the customary anechoic chamber--ground reflections from the earth play a role in the illumination of the mockup and antennas. The GP command was used to incorporate a lossy half-space ground with parameters $\epsilon = 4$ and $\sigma = 0.005$. These ground parameters were estimated from ground probe measurements and are consistent with "poor" ground as is typically found in low coastal hills [2].

Illuminating a Plate on Both Sides.

A third feature was quickly added to the NEC-BSC model to reflect actual measurement conditions. Figure 2 illustrates the antennas used to simulate the wingtip mounted system. The antenna consists of two monopole blades located on either side of the wing (or horizontal stabilizer), fed with a wideband hybrid junction, so that the antenna (now essentially a dipole) radiates equally well on both sides of the mounting surface.

However, NEC-BSC considers plates as being illuminated from one side only. The illuminated side is defined by the ordering of the plate vertices according to the right-hand rule. This requirement presents a difficulty in that the dipole antenna illustrated in Figure 2 must necessarily illuminate both sides of the plate simultaneously.

This problem was addressed by defining a second plate immediately underneath, with its vertices ordered such that its normal pointed away from the first plate. Sample calculations with this plate geometry showed that accurate dipole patterns were obtainable in this frequency range with a spacing between plates of 0.01", and that it was not necessary to "short out" the slot between the plate edges or otherwise enclose this volume with additional plates. The wing and tail surfaces of the NEC-BSC model of Figure 1 were all treated in this fashion.

The Model Antenna Elements.

In order to properly normalize the coupling results obtained in the NEC-BSC analysis (using the PR command), specific characteristics of the experimental antennas need to be known. Since a vector network analyzer would be available for the experimental portion of this study, it was decided to calculate the complex mutual impedance Z_{12} between antenna pairs. In order to perform the calculation, the SG command is given the test antenna's postulated current distribution and physical length, and the complex current flow on the element. Additionally, the PR command is supplied with the complex terminal current for the desired antenna pair.

The non-conventional nature of the test antenna illustrated in Figure 2 required some further calculation in order to use the correct terms. For each antenna position, two elements (sources or receivers) were defined, such that the orientation of their current flow was as shown. NEC-BSC internally "integrates" these separately defined sources into a single antenna. The terminal current (used in the PR command) supplied to NEC-BSC was the input current at the hybrid junction input port. This current was calculated using the known available source power of the vector network analyzer and the measured input impedance of the hybrid with the antenna elements attached.

The determination of the individual element currents for use in the SG command was more involved. The current input to the element is 0.7071 times the (hybrid) terminal current, but the current input to the SG command is that portion of the element input current which actually flows through the radiation resistance. This is found by current division between the shunt matching resistor and the input impedance of the element measured without the matching resistor. This calculation also yields the antenna radiation efficiency (neglecting internal hybrid losses) which can be used with the PR command in radiation pattern calculations to normalize the calculated pattern to dBi.

MEASUREMENTS

Full Scale Model and Outdoor Test Range.

A full scale model was used in the experimental phase for NEC-BSC verification. The mockup is mounted atop a 30' high wooden pyramid. The skin of the mockup is copper screening, and antennas are attached to the aircraft using screws and foil shielding tape. The mockup is located on a large azimuth turntable capable of turning vehicles as heavy as a Bradley Fighting Vehicle.

An HP 8753C Vector Network Analyzer (VNA) is located inside the body of the mockup. The VNA is used as a transmit source and a tuned receiver for the generation of antenna patterns, as well as for directly measuring the complex antenna-to-antenna isolation (S21). Due to the fairly large isolation expected between antennas, the full error-correcting capabilities of the VNA must be used to guarantee accurate and noise-free data [3].

The transmit site for pattern generation is located approximately 700 feet downrange. A 25 watt instrumentation amplifier is fed by the output of the VNA, and the mockup is illuminated with a LPDA at a height of 40 feet. This test geometry yields a 3.27 degree constant elevation angle which is used in the NEC-BSC pattern calculations.

Procedure.

Antenna patterns are measured using the VNA under computer control by an HP300 computer system, using software developed at ESL for that purpose. Patterns were measured at five frequencies in all the positions shown in Figure 1a.

Antenna coupling is measured using the VNA and an HP 85047A S-Parameter Test Set, using full two-port error correction. The use of full two-port calibration compensates for the effects of the long coaxial cables used to feed the antenna pair under test. Additionally, both scalar and complex coupling data can be obtained using the VNA and S-Parameter Test Set together. Although the VNA measures scattering parameters, these can easily be converted to Z-parameters (which NEC-BSC outputs) after measurement [4].

Isolation data was taken from the wingtip transmit position to the wingtip receive position and each belly array element position; from each transmit tail position to the wingtip receive position; and from the #7 tail position to each belly array position.

RESULTS

Radiation Patterns.

A representative measured-predicted radiation pattern pair is shown in Figure 3, for the wingtip-mounted dipole position. Fairly good agreement in the pattern ripple is evident. It is particularly interesting how well the pattern ripple frequency correlates between experimental and theoretical data. Measured and calculated radiation intensity also agree fairly well. The discrepancy is largely due to the accuracy with which the lossy ground parameters can be measured. The measured radiation patterns for the tail-mounted antennas showed similar agreement to NEC-BSC predictions.

The most significant disagreement between theory and experiment was that NEC-BSC did not predict the prominent broadside null in the wingtip-position radiation pattern. This difference was attributed to a lack of modelling accuracy, in that the wings on the airframe mockup attach to the bottom of the fuselage and sweep up, whereas the NEC-BSC model has straight, center-mounted wings. Another source of model inaccuracy is in locating the exact center of rotation of the mockup. As has been pointed out numerous times by other experimenters, model accuracy and attention to details is paramount for fine scale agreement with NEC-BSC results!

Mutual Impedance.

Figure 4 shows a table of measured and predicted mutual impedances and the resultant antenna pair isolation, for the wingtip mounted case. Antenna pair isolation can be calculated using Z-parameters as $I=20*\log(z_{21}/(z_{22}+z_{load}))$ [5]. This method of calculating antenna pair isolation is to be preferred as the other coupling normalization options in NEC-BSC are valid only for idealized situations (conjugate-matched source and load, maximum available gain, or far-field conditions).

Fairly good agreement is shown except for the highest frequency. It is believed that the experimental data is in error at that point, since the coupling increases so dramatically in a small frequency interval. Agreement in coupling phase is not as accurate, due to the difficulty in precisely locating the experimental antennas on the mockup. For the range of frequencies that NEC-BSC is valid, experimental placement errors of only a few inches can greatly impact predicted coupling phases. Antenna pair isolations for the tail-mounted positions showed similar agreement to the NEC-BSC predictions.

CONCLUSIONS

NEC-BSC predictions of antenna pair mutual impedance and radiation patterns were validated by experimental measurements on a full scale airframe mockup. In spite of the fact that larger mockups are usually considered as potentially more accurate, and this mockup was about as large as they get, highly accurate dimensioning is still very much a basic requirement. Further, the use of an outdoor test range brings the constitutive parameters of the earth into play, which are difficult to accurately measure. Finally, it is critical in the prediction of antenna coupling using NEC-BSC to have fully characterized antennas, especially if experimental validation is contemplated.

REFERENCES

- [1] R. J. Marhefka, "Numerical Electromagnetic Code-Basic Scattering Code NEC-BSC (Version 2)", Ohio State University, 1982.
- [2] F. E. Terman, Radio Engineers' Handbook, McGraw-Hill, 1943, Section 10, "Propagation of Radio Waves".
- [3] Hewlett-Packard Corporation, HP 8753C Users Manual, Chapter 5, "Measurement Calibration".
- [4] G. Gonzalez, Microwave Transistor Amplifiers, Prentice-Hall, 1984, pp. 24-25.
- [5] G. Zelinger, Basic Matrix Analysis and Synthesis, Pergamon Press, 1966, p. 33.

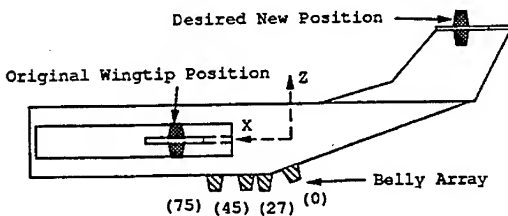


Figure 1a - NEC-BSC Model and Antenna Positions (side)

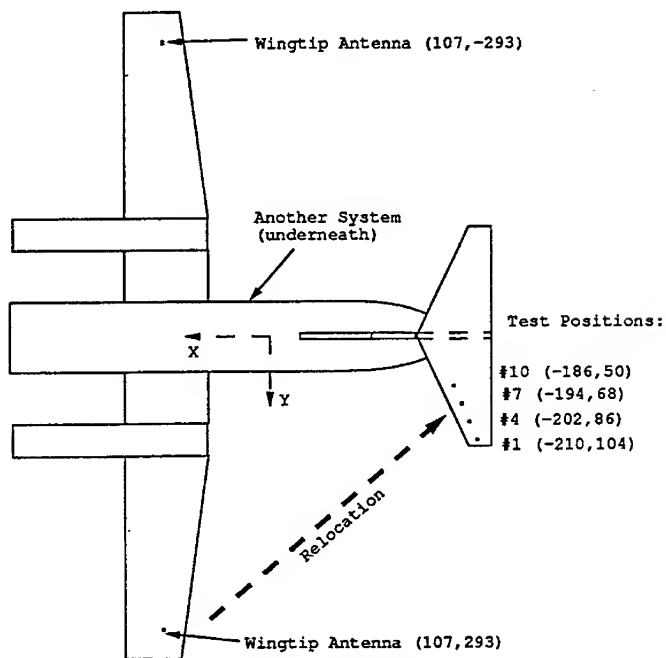


Figure 1b - NEC-BSC Model and Antenna Positions (plan)

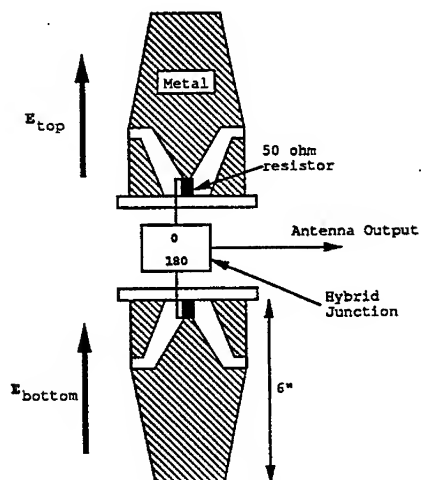
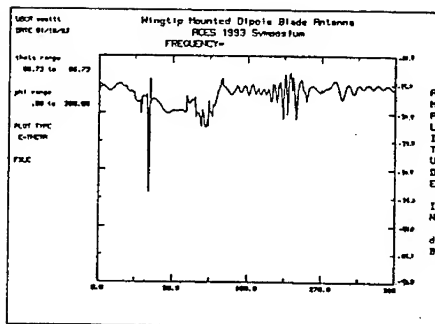
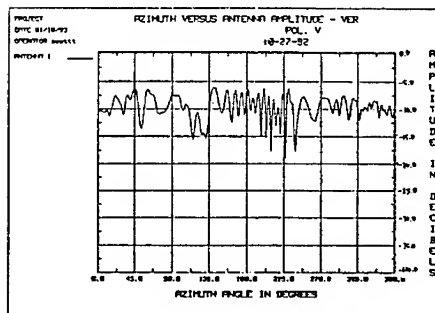


Figure 2 - Dipole Blade Antenna Configuration



NEC-BSC result



Measured Result

Figure 3 - Dipole Blade Antenna Radiation Patterns
(wingtip mounting)

Z21:						
Freq	Measured		Calculated		Δ mag, dB	Δ phase
#1	9.597e-3	@-120	11.554e-3	@-153	1.6	-33
#2	21.846e-3	@-68	27.549e-3	@-34	2.0	34
#3	34.7e-3	@-100	31.439e-3	@-135	-0.86	-35
#4	60.466e-3	@173	53.61e-3	@232	-1.04	59
#5	337.06e-3	@-162	65.378e-3	@-198	-14.25	-36

Figure 4 - Measured and Calculated Mutual Impedance
(wingtip-wingtip mounting)

THE ANALYSIS OF ASYMMETRIC LOG-PERIODIC DIPOLE ANTENNAS USING NEC

Jacqueline A. Schaefer
ARINC Research Corporation
2551 Riva Rd.
Annapolis, MD 21401

ABSTRACT: *The purpose of this paper is to present results of an investigation of the performance of asymmetric log-periodic dipole array (LPDA) antennas using the Numerical Electromagnetics Code (NEC). Asymmetric LPDAs have been shown, both theoretically and experimentally, to exhibit anomalous behavior across frequency due to unwanted radiation from the feed line of the antenna. For extreme cases of asymmetry, this behavior can lead to pattern distortions and boresite gain reductions. When using NEC to model asymmetric LPDAs, care must be taken to model the feed line of the antenna properly. This paper establishes the need to model the feed line using wire segments instead of using the transmission line option built into the NEC program to produce valid results for asymmetric LPDAs.*

INTRODUCTION

The use of log-periodic dipole arrays (LPDAs) in order to achieve high, and relatively constant gain across frequency has long been a popular practice. When using this type of antenna for lower frequencies, however, the size of the array may become a cause for concern. This is especially true when the antenna must be installed within some limited space. One solution to the installation problem of such an antenna is to bend the dipole elements of the array in such a configuration as to accommodate the space constraints. This bending however causes the LPDA to become asymmetric which may lead to significant degradations in performance of the antenna across frequency.

The existence of very narrow high-Q resonances resulting in side radiation from asymmetric log-periodic dipole antennas was described in an article by Balmain and Nkeng [1] and expanded upon in later research by Hilbert, Tilston, and Balmain [2] and Vainberg and Balmain [3]. These resonances involve a net current flowing in the transmission line which feeds the dipole elements. This phenomena would not occur in a symmetric LPDA because perfectly symmetric LPDAs being fed symmetrically would have an equal and opposite current flowing on each of the two wires of the parallel wire feed. In the asymmetric case, however, the currents on the two wires are not equal and the net feeder current gives rise to radiation to the side of the antenna. In extreme cases, this side radiation can result in the reduction in boresite gain of the antenna and some resulting distortion in the radiation pattern.

DESCRIPTION OF LPDAs MODELED

In order to demonstrate the phenomena of such gain reductions and pattern distortions arising in asymmetric LPDAs, the Numerical Electromagnetics Code (NEC) was used to model both a perfectly symmetric and an asymmetric LPDA.

The LPDA chosen to be modeled was a 14-element array covering a frequency range of 3 octaves mostly residing in the low VHF region. The scaling factor (τ) and spacing factor (σ) for this antenna are .843 and .0592 respectively. The first antenna was a perfectly symmetric version of this LPDA, as shown in Figure 1. The elements were modeled using wire segments of lengths no greater than $.1\lambda$, where λ is the wavelength of the highest frequency of operation for the LPDA, in accordance with the guidelines of wire grid modeling.[4] The second antenna was a variation of the first with the elements bent into the configuration shown in Figure 2. The asymmetry of this second antenna arises from the bending of these bottom elements. The elements for this antenna were also modeled using $.1\lambda$ wire segment lengths.

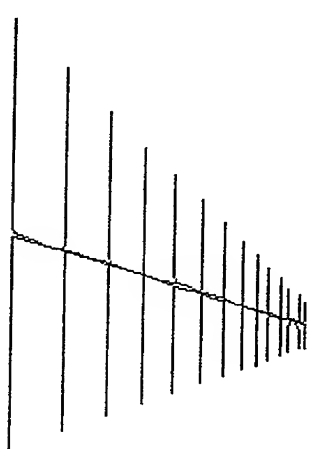


FIGURE 1
Symmetric LPDA

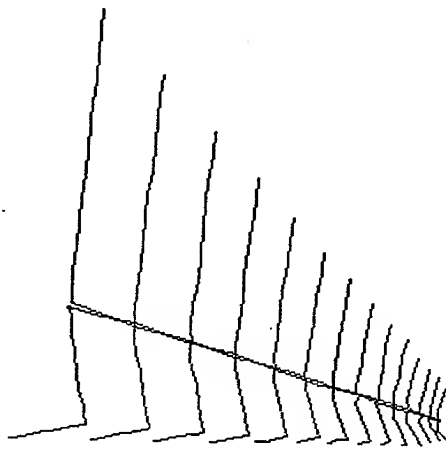


FIGURE 2
Asymmetric LPDA

Next the method for feeding the elements of the array had to be chosen. The proper way to feed an LPDA is with a crossed transmission line. This means that the top half of the first dipole element is at the same potential as the bottom half of the next adjacent dipole element. This method of feeding the array provides the necessary excitation for each consecutive dipole element in the array. To model the feed line using NEC, there are two options which can be employed. One is the transmission line option (the TL card) provided by the NEC code. This option allows the user to specify a crossed transmission line merely by choosing the correct parameters for the

TL card. The characteristic impedance of the transmission line for the LPDA was chosen to be 300 ohms. The second method for feeding the array is to use wire segments to connect the elements keeping in mind that the top half of the first dipole must be connected to the bottom half of the next consecutive dipole element. In addition the lateral spacing of the parallel wire segments used to feed the array elements must be such as to approximate the characteristic impedance of the feed line. Equation 1 describes the characteristic impedance of an air insulated parallel wire transmission line.

$$(1) Z_c = 276 \log (2S/d)$$

where:

Z_c = characteristic impedance

S = lateral spacing between the two wires

d = diameter of the wires

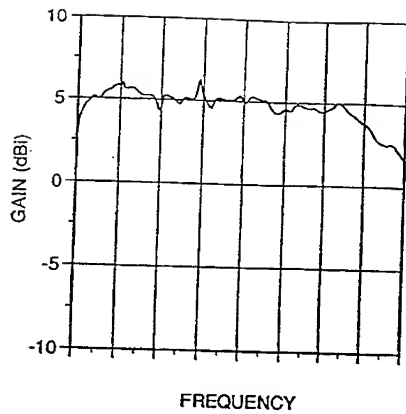
This equation was used to calculate the lateral spacing needed between the two wires of the feed line given a characteristic impedance of 300 ohms and a wire diameter of 1/8 inch.

Using the two different transmission line options with the symmetric and the asymmetric LPDA designs, four different NEC models were constructed.

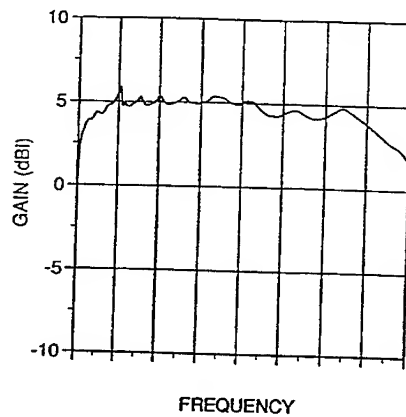
- 1) A symmetric LPDA (with straight elements) using the transmission line option to feed the dipole elements.
- 2) An asymmetric LPDA (with bent elements) using the transmission line option to feed the dipole elements.
- 3) A symmetric LPDA (with straight elements) using a wire segment transmission line to feed the dipole elements.
- 4) An asymmetric LPDA (with bent elements) using a wire segment transmission line to feed the dipole elements.

RESULTS OF THE MODELS

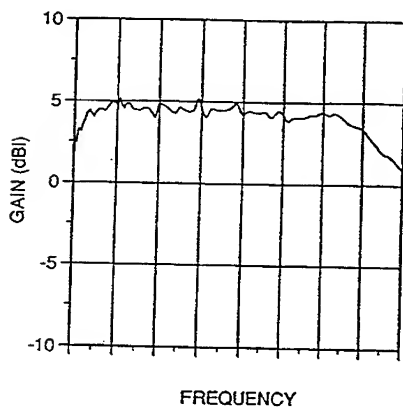
The radiation patterns resulting from the four antennas over the operating frequency range were examined. The boresite gain versus frequency results are shown in Figure 3 for each of the antenna configurations. The gains shown in these figures represent the gain adjusted to account for the impedance mismatch loss for each frequency. This was accomplished by calculating the average impedance of the antenna, seen from the feed point, across frequency and using that average as the feed point impedance in calculating mismatch loss. The mismatch loss is calculated using equation 2 and is subtracted from the gain predicted by NEC to give the adjusted gain.



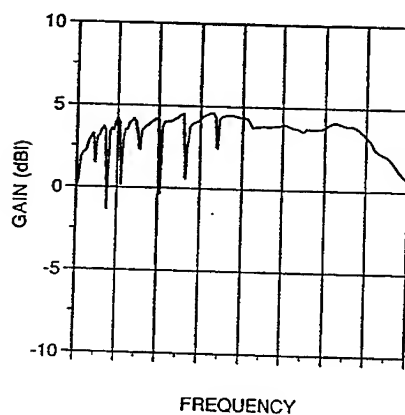
(a) Symmetric LPDA w/ transmission line option feed



(b) Asymmetric LPDA w/ transmission line option feed



(c) Symmetric LPDA with wire segment feed



(d) Asymmetric LPDA with wire segment feed

FIGURE 3: COMPARISON OF BORESITE GAIN VERSUS FREQUENCY

$$(2) \text{ Mismatch loss} = 10 \log [(S + 1)^2 / 4S]$$

$$\text{where: } S = \text{VSWR} = (1 + |\Gamma|) / (1 - |\Gamma|)$$

$$\Gamma = (Z_L - Z_0) / (Z_L + Z_0)$$

Z_0 = Feed point impedance

Z_L = Load impedance (calculated by NEC)

It is apparent from Figure 3b that the presence of the boresite gain reductions/pattern distortions predicted by the research of Balmain et. al are not present when the asymmetric LPDA is modeled using the transmission line option to feed the dipole elements. This finding is as expected given the premise of the asymmetry resonance theory which states that the resonances, which cause the reductions in boresite gain and resulting radiation pattern distortions, are a result of a net current flowing in the transmission line which feeds the dipole elements. By using the NEC transmission line option to model the transmission line, we have effectively eliminated the possibility of this net current existing because, this option "neglects interactions between the transmission line and the antenna and its environment" and its use is "justified only if the currents on the line are balanced".¹ This means that the currents on each wire of the parallel wire system are assumed to be equal and opposite when the transmission line option is used.

Another result of the models that can be examined to further provide support for the Balmain et. al research is the frequencies at which the resonance anomalies occur. The previously mentioned papers by Balmain and Nkeng [2] as well as the one by Vainberg and Balmain [3] suggest a method of calculating the frequencies at which the boresite gain reductions will occur. The papers assert that the resonant half wavelength frequency of each distorted "cell" of the asymmetric LPDA will be approximately where the anomaly will occur. A "cell" is defined as the length of the upper half of the first dipole element plus the length of the lower half of the next adjacent dipole element plus the length of the transmission line connecting the two. This would suggest that for a 14 element LPDA having 13 cells, that there would be 13 resonance anomalies (boresite gain reductions). The experimental results studied in the Balmain and Nkeng paper however, showed that for most of the antennas the number of anomalies was less than the number of cells. This suggests that in general a given resonance occupies slightly more than one cell.

In the NEC results of the 14 element asymmetric LPDA at least 8 anomalies are evident. The anomalies are represented as a drop in boresite gain of at least .5 dB in one frequency step (1 MHz). A table comparing the frequencies at which the anomalies occur using the NEC model and the ones predicted using the resonant cell postulate are presented in Table 2.

¹ Reference [4] Part I: Program Description - Theory p. 72

TABLE 2
FREQUENCIES AT WHICH BORESITING GAIN ANOMALIES OCCUR

Theoretical Frequency of Anomaly	NEC Predicted Frequency of Anomaly	Percent error
f1	0.9718 f1	2.81%
f2	NOT APPARENT	—
f3	1.0014 f3	0.14%
f4	1.0189 f4	1.89%
f5	1.0307 f5	3.07%
f6	1.0550 f6	5.50%
f7	1.0640 f7	6.40%
f8	1.0734 f8	7.34%
f9	1.0907 f9	9.07%
f10	NOT APPARENT	—
f11	NOT APPARENT	—
f12	NOT APPARENT	—
f13	NOT APPARENT	—

The resonant cell postulate, while not an exact method for predicting the frequencies at which anomalies will occur, provides a means to identify approximate frequencies at which the antenna may not perform optimally.

ANGLED ASYMMETRY

Further study was undertaken to examine different configurations of the asymmetric LPDA which would adhere to the space constraints of the installation while endeavoring to reduce or eliminate the asymmetry resonances. One such configuration consisted of angled lower elements instead of the sharply bent elements of our first asymmetric LPDA. The new angled bottom elements of the LPDA are shown in Figure 4. The boresite gain versus frequency performance of this antenna is much more consistent across frequency than the asymmetric one with the bent elements as demonstrated in Figure 5.

The angled element LPDA exhibits better performance than the bent element LPDA because the currents are coupled to the dipole elements more effectively rather than staying on the feed line. By examining the impedance of the different antenna configurations across frequency, we can gain insight into this phenomenon. A large fluctuation in the impedance indicates that the current is not being coupled to the elements at specific frequencies and tends to stay on the feed line. This is what causes the resonance anomalies. Figure 6 shows the impedance variations across frequency for the symmetric LPDA, the asymmetric LPDA with bent elements and the asymmetric LPDA with angled elements. It is clear from this figure that the impedance varies much less drastically for the symmetric and angled element LPDAs than for the

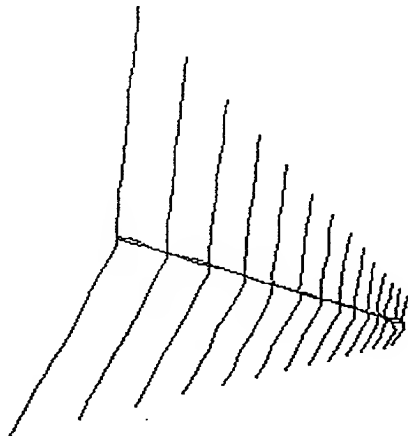


FIGURE 4
ASYMMETRIC LPDA WITH ANGLED ELEMENTS

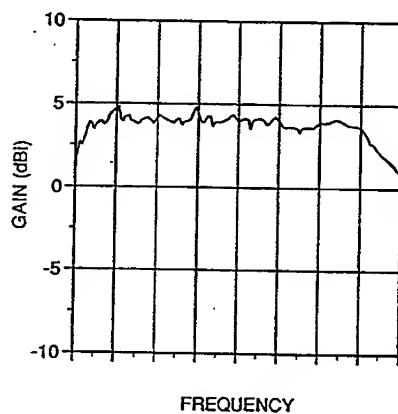


FIGURE 5
BORESITE GAIN VERSUS FREQUENCY OF ANGLED LPDA

bent element LPDA. It is also evident that the large spikes in the impedance for the bent element LPDA occur at the same frequencies as the boresite gain anomalies for this antenna.

Another way to reduce the impedance fluctuations across frequency of the antenna and thus reduce the effect of the asymmetry resonances is to tune the LPDA by either removing or adding lengths of wire to the elements which are causing problems. This method, however, is probably most effectively accomplished empirically using an impedance meter or network analyzer to optimize impedance across frequency.

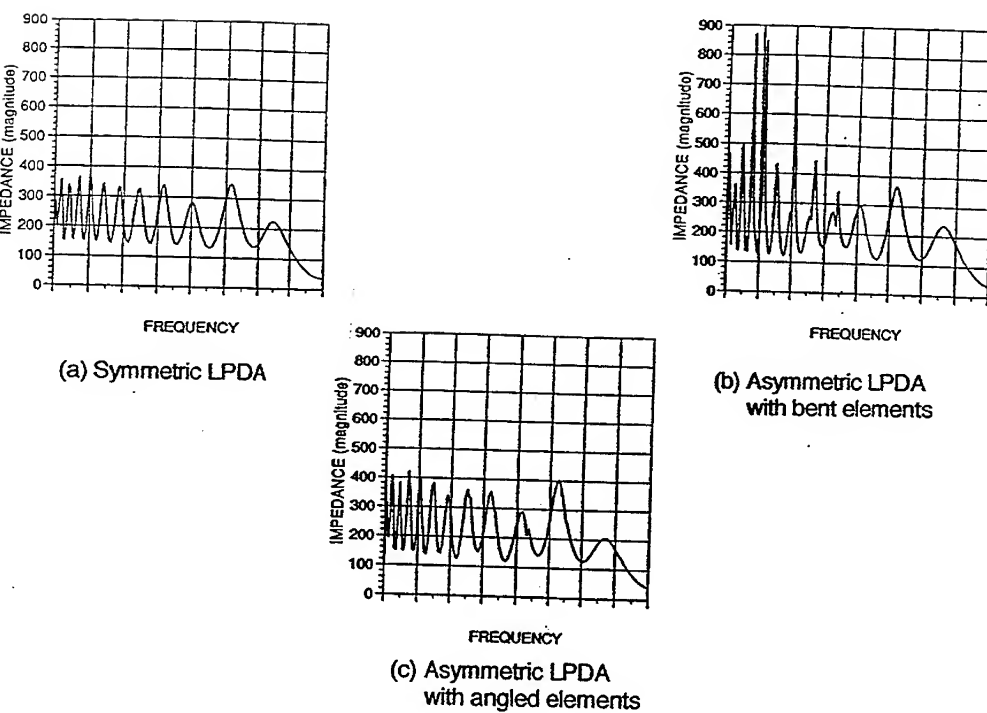


FIGURE 6: IMPEDANCE VARIATION ACROSS FREQUENCY
FOR THE DIFFERENT LPDA CONFIGURATIONS

REFERENCES

- [1] Keith G. Balmain and Joseph N. Nkeng, "Asymmetry Phenomenon of Log-Periodic Dipole Antennas" *IEEE Transactions on Antennas and Propagation*, Vol. AP-24 pp. 402-410, July 1976.
- [2] Martin Hilbert, Mark A. Tilston, and Keith G. Balmain, "Resonance Phenomena of Log-Periodic Antennas Characteristic-Mode Analysis", *IEEE Transactions on Antennas and Propagation*, Vol. 37 No. 10 pp. 1224-1233, October 1989
- [3] M. Vainberg and K. G. Balmain, "On Prediction of the Asymmetry Resonance Phenomenon of Log-Periodic Antennas", *Canadian Electrical Engineering Journal*, Volume 6 No. 3, 1981.
- [4] G. J. Burke and A. J. Poggio, "Numerical Electromagnetics Code (NEC) - Method of Moments", NOSC Technical Document 116

SESSION 15 - "CAEME"

Chair: Dr. Magdy Iskander

INTERACTIVE VIDEO LESSONS FOR ELECTROMAGNETIC EDUCATION

Magdy F. Iskander and Thomas Reed
Electrical Engineering Department
University of Utah
Salt Lake City, UT 84112

ABSTRACT

With the availability of a significant amount of software for EM education from CAEME and other commercial sources, it is important to assess the effectiveness of these new tools in classroom teaching and develop procedures that promote their effective use in education. Routine classroom teaching is significantly different from computer-based instruction, and concerted efforts must focus on developing new teaching techniques. These new procedures are intended to help students understand the physical principles underlying results from simulations and also help instructors integrate software and simulations in their teaching.

In this paper, we present the features of four interactive video lessons in EM developed by CAEME to aid in the inclusion of computer-based instruction and simulation in the student learning process. These lessons include tutorials, simulations from CAEME software and videos, and quizzes to evaluate student understanding. The lessons use animated graphics to illustrate specific dynamic phenomena and measurement procedures. They also keep a record of student quiz scores for instructor use. These, as well as other features of the three developed interactive video lessons, will be described.

INTRODUCTION

With the proliferation of computers on university campuses, and based on initial experiences of many educators, it is generally agreed that computers provide an exciting opportunity for boosting engineering education [1]. Animated graphics of dynamic phenomena, visualization of abstract and highly mathematical subjects, one-on-one and self-paced tutoring, and the ability to mimic often-unavailable and expensive laboratory experiments are among the most cited benefits of a computer-based engineering curriculum. As instructors continue to integrate computers in their classroom teaching, however, they are beginning to realize more of the limitations of using computers in engineering education. For example, it is not clear if students will effectively and independently be able to understand basic phenomena from the numerical or graphical representations of simulations. Also, avenues for the effective integration of simulation, demonstration, and computer-based homework assignments and tests in and outside of typical classroom teaching are not clearly defined. Many courses need to be restructured and even the role of the university professor needs to be redefined to fit the era of a computer-based curriculum.

Fortunately, this uncertainty in understanding the role of computers and software tools in engineering education has coincided with rapid growth in the area of multimedia presentations [2]. Interactive video applications integrate the visual power of video, interactivity of software, and an ability to structure educational lessons that include tutorials, quizzes, and maintenance of scores for the instructor's use. Furthermore, the availability of authoring software such as QUEST [3] to help develop these applications, the affordability of the required hardware, and the publication of the CAEME software book and videos made the preparation of multimedia lessons in electromagnetics is not only justifiable but also an efficient and cost-effective way for using software in education.

In response to the need to promote the effective use of software in classroom teaching, CAEME developed four interactive video lessons using the QUEST authoring software [4]. The main features of the developed lessons include

- Access to and specific assignments from software packages in the *CAEME Software Book*, Vol. I.
- Access to all or part of the experimental or computer-generated videos distributed by CAEME. Portions of these videos have been transferred to two laser discs (30 minutes each), and specific frames of the video sections are accessed by QUEST through a videodisc player (e.g., Sony LDP 1450).
- Animated graphics of various dynamic phenomena associated with the topic of the lesson. QUEST [3, 5], as well as other authoring systems, provides relatively easy-to-use capabilities for creating animated graphics so valuable to the effective explanation of dynamic electromagnetic fields. Examples of some of the developed animated graphics will be discussed in the following section.
- Quiz sessions that help evaluate the students' understanding of key topics in the lesson, guide students through correct solution procedures, and suggest specific avenues (additional reading, software simulation, or video review) to help students in their understanding. In all cases, the multimedia lessons were structured such that results from the quiz sessions are reported to the instructor.

In the following section, features of the four developed EM multimedia lessons will be described.

EXAMPLES OF MULTIMEDIA LESSONS IN ELECTROMAGNETICS

In all the four multimedia lessons developed by CAEME thus far, the animation, access to video, simulation, and quiz features described above were implemented. In each of the following examples, however, we will attempt to highlight one of these features.

Example 1: Electromagnetic Waves

The objective of this lesson is to introduce the student to basic propagation characteristics of traveling and standing waves. The main menu of the lesson is shown in Fig. 1, where it may be seen that the lesson provides access to video demonstrations on standing waves [6] and to two software packages from the CAEME book [7, 8]. It includes animated graphics and tutorials on some basic properties of traveling and standing waves and a quiz session.

We will use this example to demonstrate the animated graphics and access to video features of a multimedia lesson.

Video Frames of Traveling and Standing Waves

When this option is selected from the main menu, the screen shown in Fig. 2 is displayed. This screen gives the student the option of selecting and focusing on the topic of either traveling or standing waves. Let us briefly consider the content of each topic.

Traveling waves: In this section, the student is introduced to the basic propagation properties of a traveling wave and the relationship between the associated electric and magnetic

fields. An example screen in this option is shown in Fig. 3, where the electric and magnetic fields associated with a plane wave propagating in air are demonstrated dynamically using animated graphics. This dynamic presentation of the propagation characteristics of waves makes the use of computers far superior to routine textbook static-type teaching. At the end of the traveling wave section of the lesson, it is suggested that the student access and perform independent simulations of some specified aspects of wave propagation using the CAEME software [7, 8].

Standing waves: Selecting the standing-wave option in the menu of Fig. 2 offers another menu which allows the student to access a short section of video that experimentally demonstrates mechanical standing waves, a brief tutorial with animation of standing wave characteristics, and additional captured small sections of the video on experimental demonstrations of standing electromagnetic waves. The video sections on mechanical waves and the electromagnetic waves are included in the video available with the CAEME book [6].

The Electromagnetic Standing Waves Tutorial briefly introduces the cause and propagation properties of standing waves. An animation that demonstrates the interference between two waves of equal magnitude, of the same frequency, and propagating in opposite directions is included in this section (see Fig. 4). The basic properties of a standing wave are also summarized. Aspects such as distances between successive nulls in electric and magnetic fields and locations of nulls from short- and open-circuit terminations of TEM lines are discussed. Once again, the animated graphics illustrating the interference between two waves and the visualization of the characteristics of the resulting standing wave provide excellent demonstrations of the advantages of using computers to teach dynamic electromagnetic fields.

Example 2: Electrostatic Charges and Coulomb's Law

The purpose of this lesson is to review basic concepts concerning interactions between charged particles. To accomplish this, the student views a video presentation on the measurement of charge and an experimental verification of Coulomb's law. The main menu of the lesson that appears after the student signs his/her name is shown in Fig. 5. This lesson provides access to a section of the video on experimental demonstrations for teaching electromagnetic fields and energy [6], to CAEME simulation software relevant to the lesson's topic [8-10], and also to tutorials on electrostatic charges, their forces, and techniques for their measurement.

Besides the access to sections of the video on Coulomb's law and measurement of electrostatic charges, the lesson provides an attractive computer-based quiz session. This includes animated graphic features wherever appropriate and also interactive remediation for helping and guiding the student in solving the quiz problems. For example, in quiz problem number 3, the student is asked to determine the angle between an electrostatic charge Q and an infinitely large plane charged with a charge density ρ_s . If the student clicks on the wrong answer, the program will first advise the student that his/her answer is incorrect (see Fig. 6) and then will proceed to provide guidance through one aspect of the required analysis. For example, in this case, the student will be asked to calculate the electric field associated with the infinitely large plane charged with a charge density ρ_s . It will be pointed out that he/she needs to apply Gauss' law for the electric field, and to do this a Gaussian surface that takes advantage of the symmetry consideration and the resulting direction of the electric field needs to be established [11]. The student's selection of the direction of the electric field resulting from an infinitely large charged plane is indicated by clicking on the appropriate option as shown in Fig. 7. If a wrong selection is made, the student will be guided so as to recognize aspects of the symmetry consideration, and he/she will even be led to the selection of an appropriate Gaussian surface as shown in Fig. 8. Upon the selection of the suitable Gaussian surface and the correct calculation of the electric field from an infinitely large charged surface, the student will be asked to attempt a

second answer to the quiz. If the answer is still incorrect, the student will receive a second level of remediation with the additional analysis needed to answer this question. In particular, the analysis concerning balancing the electric and gravitational forces on the suspending string with the substitution of the correct value of the electric field, as described in the earlier portion of the analysis, should be fairly simple for the student to identify the correct answer to the quiz.

It should be emphasized that through this example, we attempted to demonstrate the integration of the visualization, animation, and interactive features of the multimedia lesson. The inclusion of sections of video help visualize experimental aspects of measuring charges, while access to CAEME software and interactive guidance of the student through the quiz session clearly distinguish multimedia lessons from classical static or textbook-type teaching.

Example 3: Dielectric and Conducting Materials

The objective of this lesson is to review the conducting and dielectric properties of materials, describe various polarization mechanisms, and quantify the conduction and polarization currents as well as the polarization charge that results from the interaction of materials with an externally applied electric field. The main menu of the developed lesson is shown in Fig. 9, where it may be seen that traditional features such as access to video segments, CAEME software, and a quiz session are included.

This lesson, however, has additional attractive features. This includes interactive animations and specific software assignments to help lead students to understand some fundamental concepts of the lesson, and also a hypertext type of tutorial whereby key words are highlighted and additional explanations are made available to students upon request.

Regarding the interactive animation feature, let us consider the explanation of the various polarization mechanisms. In the lesson, it is initially stated that there are three main polarization mechanisms in pure substances, and a menu is provided to access an explanation of each of these mechanisms. Upon access of the electronic polarization option, for example, the student is shown a classical atomic model of a positively charged nucleus surrounded by a cloud of orbiting electrons. The student is then asked to apply an external electric field by clicking the mouse and watching the shifts in the centers of the positive and negative charges in opposite directions, thus creating the electric dipole. In the orientational polarization case, a color graph of a section of material is shown and the permanent electric dipoles are displayed in random motion under the influence of their thermal energy. When the student applies an external E-field, he/she watches, in real time, the alignment of these dipoles in the direction of the E-field and, although still in motion, they maintain their alignment along the field. Figure 10 shows stills that illustrate this process.

Based on these types of animated graphics which provide an avenue for the student to interact with the process by applying the E-field or changing the type of material, concepts such as polarization and induced polarization currents and charges may conveniently be introduced. Their presence is further appreciated by students.

The other new feature of this lesson is providing students with specific assignments to use CAEME software. Figure 11a shows a simulation example that will help students understand the reduction of the electric-field strength inside a dielectric material as a result of the material's polarization. The first part of the assignment provides access to the ROSEM software [12] and shows the student the expected result from their simulation effort "screen display." Upon continuing, a second screen with the remaining part of the assignment is shown. Once again, access to the software and to a display of the expected results is provided as shown in Fig. 11b. After performing the simulation, the student is asked to explain the results in an interactive

fashion as shown in Fig. 12. Depending on the answer, the student may either be asked to carefully compare the results as shown in Fig. 13 or be guided through a detailed, often graphical explanation of the expected answer.

The above discussion provides an example of a specific software simulation assignment that may help guide students through an understanding of a physical phenomenon. Other examples are available in this as well as other multimedia lessons developed by CAEME.

Example 4: Tic-Tac-Toe Review Test in Electromagnetics

The purpose of this multimedia application is to provide a review test of basic concepts in electromagnetics. As the student accesses the application and enters his/her name, the overall Tic-Tac-Toe board shown in Fig. 14 appears on the screen. The various question categories include elements of an introductory course in electromagnetics such as vector algebra, fields, Maxwell's equations, EM waves, and dielectric polarization. It may also be noted that the question board includes a video category in which the student is shown a short section of a video and then asked to answer a question. In addition to the fun nature of this lesson, many of the questions include animation; this emphasizes an additional advantage of having this Tic-Tac-Toe game played on a computer. The arrangement of the remaining categories is randomized after each question to avoid a fixed arrangement of the topics.

In designing this review test, each question category was divided into subcategories, each of which includes several questions. For example, the category on Maxwell's equations includes subcategories on general aspects of these equations, Ampere's law, Gauss' law, and Faraday's law. Also, the category on vector operations includes subcategories on vector algebra, integral operations, and differential operations. An example of the questions in the vector differential operation subcategory is shown in Fig. 15, in which the student is asked to identify the relationship between the differential vector operations and the flux representations of some vector fields. It is difficult to demonstrate in this paper some of the dynamic, animation, and interactive aspects of these questions, but it suffices to indicate that students find this lesson fun, exciting, and most important, instructionally useful and certainly helpful in solidifying their understanding.

SUMMARY

In this paper, we presented four examples of multimedia lessons developed for electromagnetic education. These lessons provide an attractive avenue for the integration and interactive use of motion and still videos, audio, software simulations, and animated graphics in tutorials, application exercises, and assessment tools.

Specifically, each lesson includes tutorials, animations, access to specific topics of CAEME software, and access to sections of videos that demonstrate practical applications or experimental demonstrations of some aspects of the lesson. Based on instructor and student comments on these lessons, it is generally believed that multimedia applications will play a significant role in future integration of computers and software tools in classroom teaching. Future developments such as the use of CD ROM and digitized video will improve the construction, distribution, and accessibility of these new highly interactive and visual lessons.

REFERENCES

1. Z. Fazarinc, "Harnessing Computer Power for Teaching Concepts," *Symposium Digest, IEEE Antennas and Propagation Symposium*, Dallas, Texas, May 7-11, 1990, pp. 1663-1670.
2. H. J. Bailey and N. E. Thornton, "Interactive Video: IEEE (Innovative Episodes for Enhancing Education)," *Computer Applications in Engineering Education*, Vol. 1, No. 1, pp. 97-108, 1992.
3. "Comparing Authoring Systems: Where Do You Start?," *Computer Based Training (CBT) Directions*, pp. 15-29, May/June 1992. QUEST is available from Allen Communication, 140 Lakeside Plaza II, 5225 Wiley Post Way, Salt Lake City, UT 84116.
4. M. F. Iskander, T. Reed, and J. Breen III, "Interactive Video Lessons for Electromagnetic Education," *Computer Applications in Engineering Education*, Vol. 1, No. 2, 1993.
5. M. Fritz, "Authoring Systems in Action," *Computer Based Training (CBT) Directions*, pp. 11-22, September/October 1992.
6. M. Zahn, J. R. Melcher, and H. A. Haus, "Experimental Demonstrations for Teaching Electromagnetic Fields and Energy," Chapter 7, *CAEME Software Book*, Vol. I, September 1991.
7. W. L. Stutzman, A. B. Garrett, and M. Cerny, "Electromagnetic Waves -- A Video Tutor Graphics Package," Chapter 5, *CAEME Software Book*, Vol. I, September 1991.
8. N. N. Rao, "Elements of Engineering Electromagnetics," Chapter 2, *CAEME Software Book*, Vol. I, September 1991.
9. R. Cole and C. Brune, "Visualization, Simulation, and Computing: New Tools for Learning, New Paradigm for Teaching," *Computer Applications in Engineering Education*, Vol. 1, No. 1, pp. 65-72, 1992.
10. K. E. Lonngren and W. B. Lim, "MacEM," Chapter 4, *CAEME Software Book*, Vol. I, September 1991.
11. M. F. Iskander, *Electromagnetic Fields and Waves*, Prentice Hall, Englewood Cliffs, NJ, 1992.
12. M. Melton, J. Engel, and J. Lebaric, "Electromagnetic Software for Solving Static and Dynamic 2D Field Problems on a Personal Computer," Chapter 6, *CAEME Software Book*, Vol. I, September 1991.

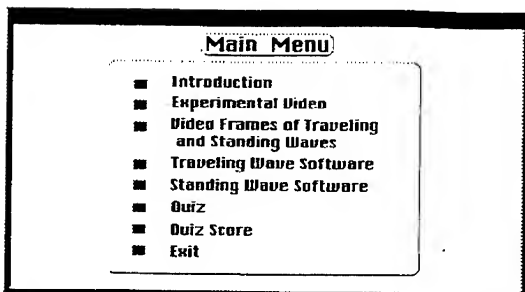


Fig. 1. Main menu of the multimedia lesson on electromagnetic waves. The lesson includes access to experimental video, two CAEME software packages [7, 8], animated graphics, and a quiz that consists of five questions.

Fig. 2. A menu that provides access to the traveling and standing waves topics.

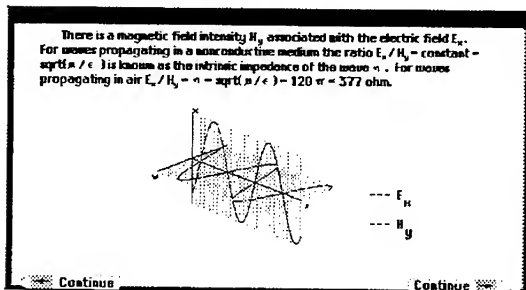
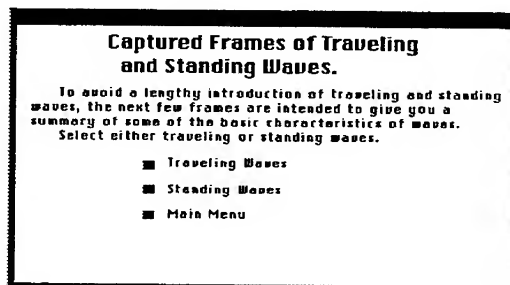
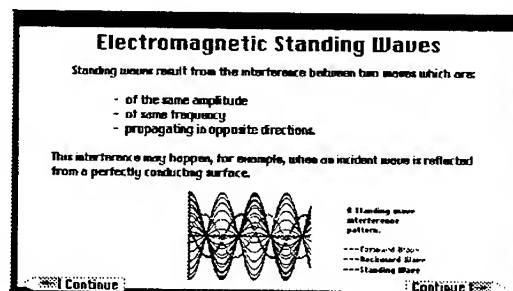


Fig. 3. An example that demonstrates the animated graphics capabilities of the "electromagnetic wave" multimedia lesson. The figure shows in phase sinusoidal electric and magnetic fields. These fields are perpendicular to each other and to the direction of propagation (z).

Fig. 4. Dynamic illustration of the concept of standing waves. Two sinusoidal plane waves of the same frequency and propagating in opposite directions (green and purple curves) interfere to produce the resulting standing wave (white curve).



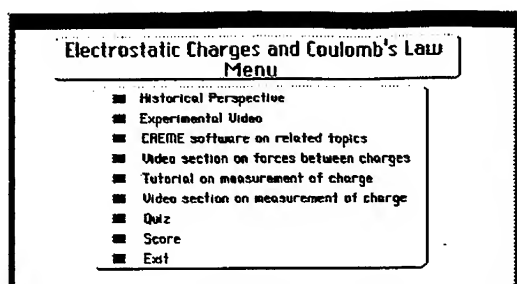


Fig. 5. Main menu of the multimedia lesson on electrostatic charges and Coulomb's law.

Fig. 6. An example of the response a student receives when a wrong answer is selected. Multimedia lessons are structured so as to provide remediation for helping and guiding the students when solving the quiz problems.

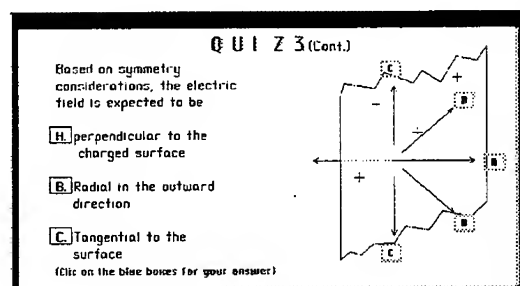
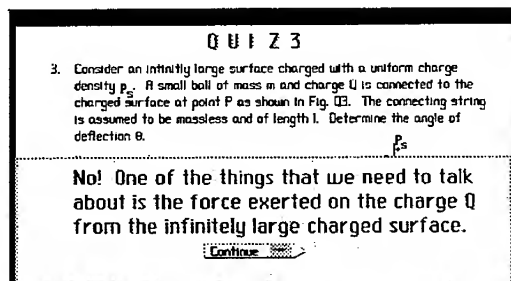
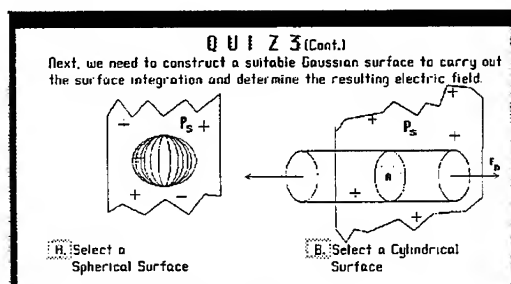


Fig. 7. A display of a multiple-choice question intended to help students identify the correct direction of the electric field associated with an infinitely large charged plane.

Fig. 8. A schematic demonstrating (a) an incorrect and (b) a correct option of selecting a Gaussian surface for evaluating the electric field associated with an infinitely large plane charged with a charge density ρ_s . If a wrong answer is selected, the student is advised to select option B to take advantage of simplifications when integrating the electric field E_n over the closed surface.



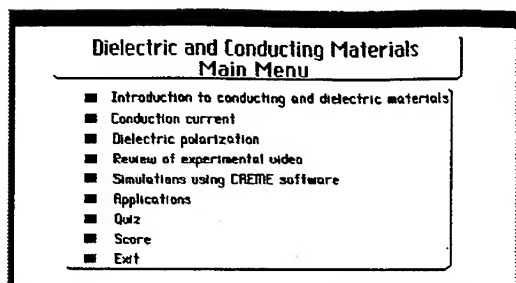
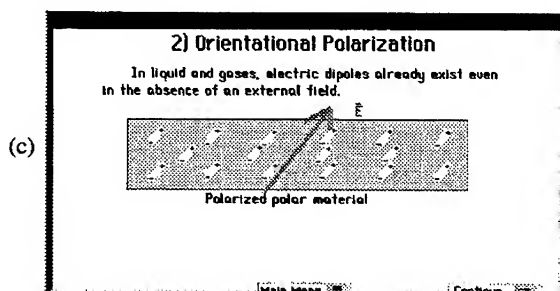
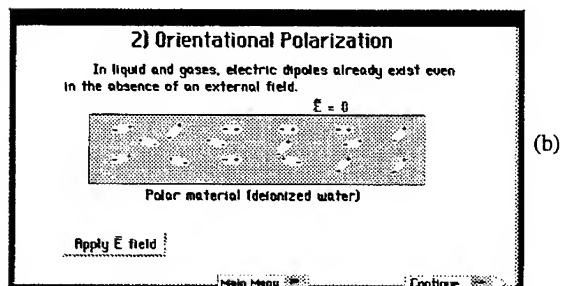
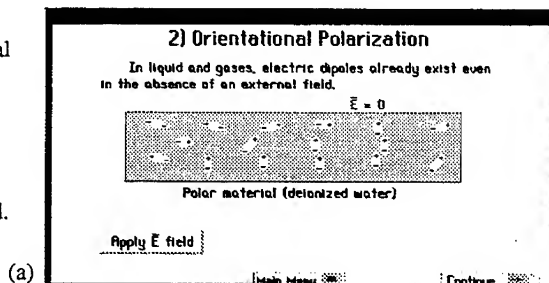


Fig. 9. Main menu of the multimedia lesson on dielectric and conducting materials.

Fig. 10. A series of stills that illustrates the concept of orientational polarization. (a) and (b) show the random orientation of permanent electric dipoles and their continuous motion in the absence of an external electric field. (c) Alignment of the permanent electric dipoles in the direction of the external electric field.



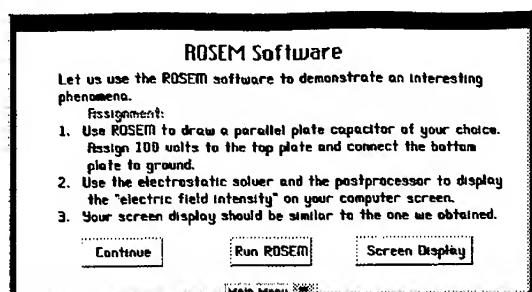


Fig. 11. An example of software assignment that helps guide students through simulation using CAEME software (e.g., ROSEM [12]). (a) Simulation example of an electric field in a parallel-plate capacitor. (b) Simulation of the electric-field intensity in part (a) when a dielectric slab is inserted between the plates.

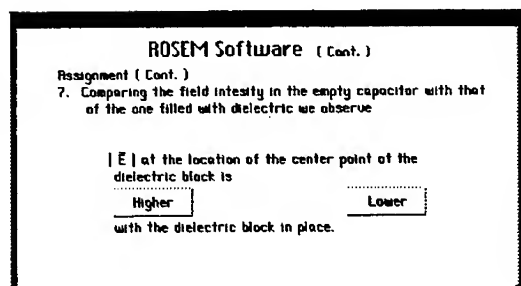
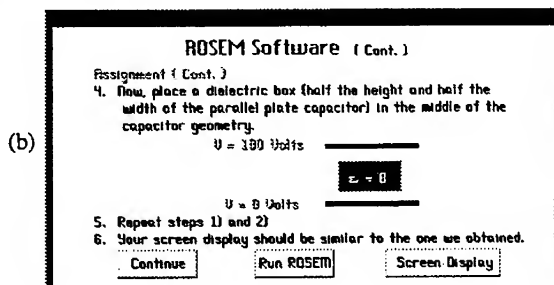
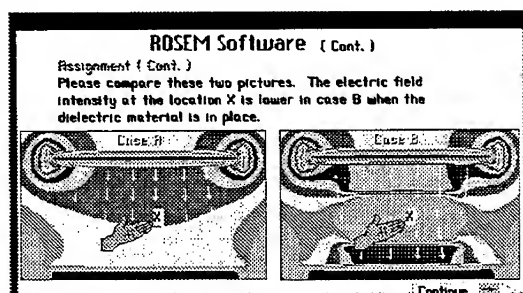


Fig. 12. A quiz prepared to evaluate students' understanding of the simulation results. The electric field inside the dielectric is expected to be lower than its value before inserting the dielectric slab. The student is asked to make a selection between the two choices.

Fig. 13. Electric-field intensity in the region between the plates of a parallel-plate capacitor. Option A is for the air-filled capacitor, while option B is for the case when the dielectric slab of $\epsilon_r = 8$ is inserted in a central subregion between the plates.



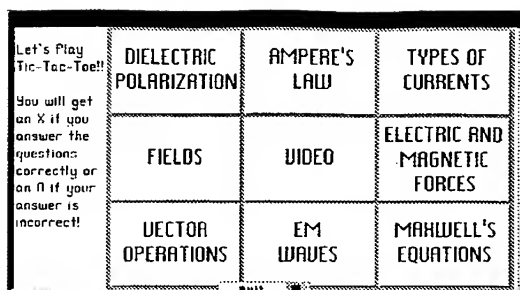


Fig. 14. Main menu of the Tic-Tac-Toe interactive video lesson. This is a review lesson on some basic concepts in introductory electromagnetics.

Fig. 15. An illustration of the type of questions included in the Tic-Tac-Toe review lesson. Flux representations of vector fields are sketched and the student is asked to match the flux representation with the appropriate expression of the vector field.

Vector Fields **Question 1**

1) A flux representation of vector fields provides a visual illustration of the spatial variation of the field quantities.

Match the flux representations given below with the corresponding vector field

$A = kx\hat{a}_x$ $B = k\hat{a}_x$ $C = kx^2\hat{a}_x$

Below each flux representation are three boxes labeled A, B, and C for matching.

A Generic Finite Element Model for Plane Problems

Kyran D. Mish
Imbsen & Associates, Incorporated
Sacramento, California

LaDawn Haws
Department of Mathematics and Statistics
California State University, Chico

Abstract

Much of the effort of developing finite element computational models is independent of the particular problem being solved. It is therefore possible to develop a generic finite element solver for large classes of problems that can be used for a wide variety of applications with only minimal modifications by the programmer/analyst. The authors have developed such an analysis package for two-dimensional problems for the Macintosh family of computers, and this generic application has been used successfully by hundreds of students. The analysis environment includes modules appropriate for static and transient analyses of heat conduction, plane elasticity, plates, flow problems, and electromagnetism. The analysis programs are tightly coupled to visualization codes that support appropriate graphical displays including color contouring, vector field plots, and animation of time-dependent analyses. The overall architecture of these codes will be presented, and various forms of output will be demonstrated.

Overview

Research and educational applications utilizing finite-element approximation are commonly performed on commercial finite-element codes. While such proprietary codes are widespread in engineering practice and are well-supported and error-free, commercial codes suffer from a few basic flaws. First, since they are generally proprietary, the source code is seldom available for study or modification. Many of the more successful codes are extensible through the device of standard interfaces for new element types, but are not otherwise modifiable by the analyst interested in a new formulation, or by the student looking for examples of finite-element coding principles. In addition, commercial codes are generally expensive, unless distributed in a low-cost form (which is generally a hamstrung version of the full-scale commercial solver).

There is a definite need for finite-element programs that are "lean and mean", in the sense of performing a *limited* range of problems without modification (which leads to a compact code), and performing analyses without all the attendant variety of model generation, analysis, and interpretation options available with commercial programs. The relatively simple family of finite-element codes described in this document is intended to

allow researchers and educators using finite-element approximation to use codes that are reasonably advanced (in terms of solution algorithms, code architecture, and solution visualization schemes), reasonably efficient, relatively straightforward to use, and very simple to modify or extend. The codes presently are optimized for use on the Apple Macintosh II and Quadra microcomputer series (since these micros provide the graphical support and memory addressing required in system software), but the library of codes is being ported by the authors to IBM's OS/2v2.0 operating system and to the range of Unix workstations supporting X/Windows. It is anticipated that the codes will ultimately be available for computers running Microsoft's Windows/NT operating system once that software platform becomes widely available.

Principles of Program Design

Most of the components of a finite-element application are completely independent of the particular problem to be solved. Commercial codes exploit this fact by collecting a wide variety of approximation types into generic element libraries, thus allowing the analyst to specify the class of solution interpolant to be used at run-time. As the variety of elements and solution schemes available in an application increases, the underlying code complexity increases accordingly. An alternative scheme is to limit the class of elements that can be used at run-time, while instead making the program source sufficiently easy to modify so that the generic element type is simple to change. In the code presented here, the basic element type is a four-node bilinear quadrilateral. This element is preferred for many problems because it is relatively simple to create arbitrary quadrilateral meshes, because this simplest two-dimensional Lagrange element is reasonably accurate for a variety of problems, and because it can be made very efficient by using appropriate reduced quadrature rules. In addition, its three-dimensional generalization (the eight-node trilinear hexahedron) is easily obtained by only minor modifications of an analogous two-dimensional analysis program.

Once a generic element type has been established, the overall code architecture can be segregated into two distinct classes of computer procedures and data structures: those that depend upon the particular problem to be solved, and those that are independent of the problem. In the setting of a static analysis, there are only four tasks that are dependent upon the particular problem:

- (1) formation of the element matrices, whose size and composition depends upon the number of unknowns defined at each interpolation node, and upon the material data of the problem to be solved
- (2) calculation of the derived (i.e., secondary) solution parameters, which are generally some form of spatial derivative of the primary unknowns (e.g., simple gradients in scalar potential problems; strains or strain rates in solid and fluid mechanics applications)

- (3) input and verification of the material data, whose form and size depends upon the problem to be solved
- (4) optionally, the preparation of formatted "verbose" output suitable for printing if a graphical solution display is not used.

All other aspects of the problem, including mesh generation, interpolation overhead, equation assembly and solution, and most of the postprocessing burden, can then be coded so that all dependence on the problem solved is through a set of fundamental constants (implemented via the PARAMETER statement of FORTRAN). These fundamental constants include the number of solution unknowns to be interpolated at each node; the number of nodes, quadrature points, and derived solution parameters per element; the maximum sizes permitted for the finite-element mesh and associated equation set, and other similar constants. Extension of a root analysis scheme (such as a static scalar potential problem) to a new class of problems consists of coding the four classes of procedures described above (for which all overhead data structures are available through appropriate data structures calculated within the generic part of the program), and then modifying all the global problem parameters using a standard "find and replace" function of a text editor. Similar modifications can be used to customize the accompanying visualization codes to optimize display of results.

Classes of Analysis Protocols

There are several standard modules presently available in this application family. At present, only linear constitutive models are used in each code, but modification of most of the individual codes to account for nonlinear material behavior is straightforward. The various classes of analysis methods available are enumerated below:

- static analyses $Kd = f$

In the linear static case, the analyst must complete procedures for evaluating the element stiffness matrices, the element load vectors, reading and verifying appropriate material data, and calculation of the secondary solution parameters (e.g., determining strains from the displacement field in a mechanics application).

- quasi-static analyses $Cv + Kd = f$

The analyst must provide all the same parameters as for the static case, but must also code a procedure to evaluate element contributions to the damping matrix C . A standard one-parameter time-stepping scheme is used to provide a robust temporal integration algorithm.

-
- dynamic analyses $Ma + Cv + Kd = f$

The analyst must provide the same parameters as for the quasi-static case, but must also code a procedure to evaluate element contributions to the system mass matrix M . A standard three-parameter time-stepping scheme is used to provide simultaneous optimal error control (i.e. a quadratic convergence rate), and user-specified damping control to attenuate high-frequency noise common to discretized dynamic problems.

- eigensolution analyses $Kd = \lambda d$

Input to this analysis scheme is the same as for the static case, except that no load vectors are required. A full eigensolver is used to determine all eigenvalues and eigenvectors (which typically takes only several minutes on a current-generation microcomputer). The authors will ultimately extend the eigensolution schemes available to include forward- and inverse- Lanczos schemes to provide only a partial construction of the full matrix spectrum.

- generalized eigensolution analyses $Kd = \lambda Md$

Input to this analysis scheme is the same as for the standard eigensolver, except that element mass routines must be provided. Either the system mass M or the system stiffness K must be positive-definite, since in the alternative case, it is not possible to guarantee construction of a real diagonal form.

In each case, representative graphical postprocessing facilities are available to produce plots of finite-element results, including mesh drawings, line, grayscale, and color contours of the primary and secondary solution parameters, and (in the case of time-dependent analyses) animation of the solution history using standard animation file formats (e.g. the PICS and QuickTime formats for the Macintosh platform).

Representative problems that are already coded include thermal analyses, plane elasticity problems, incompressible solid and fluid mechanics problems, plate bending analyses, and electromagnetic problems involving potential, magnetic, and electric fields. In many of these problems (e.g. incompressible or electromagnetic cases), a divergence-free constraint on the primary solution is required, and simple selective/reduced integration schemes are easily implemented within the existing code architecture. The analyst interested in extending the generic code to solve a new problem can generally start with a similar problem by examining the existing classes of implemented schemes available with the program distribution.

Sample Problems

Conventional publication technology precludes the inclusion of the sort of color visualization schemes that are an essential component of the generic finite-element code described above. The results below show only a black, white, and grayscale sample of solution behavior from the finite-element application family. Complete results are available in the code distribution kit that can be obtained by correspondence with the second author.

The first sample shown arises from a generalized eigensolution scheme appropriate to constructing approximate solutions for the scalar Helmholtz equation. The particular example is from the preliminary investigation of a four-vane birdcage resonator used in medical imaging applications. The eigensolution scheme was used to verify electrostatic results which are at present being verified by a full vector Helmholtz analysis of the magnetic field in three space dimensions. Figure 1 shows the finite-element mesh used to perform the analysis. Figure 2 is a grayscale contour map of the fundamental mode for the resonator.

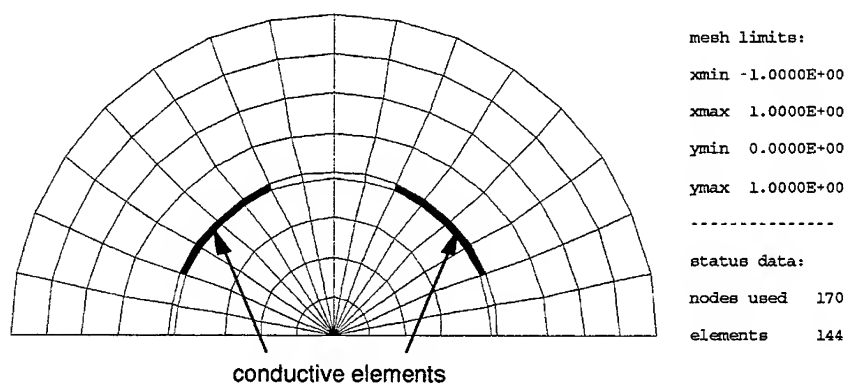


Figure 1: Mesh Used in Scalar Helmholtz Example

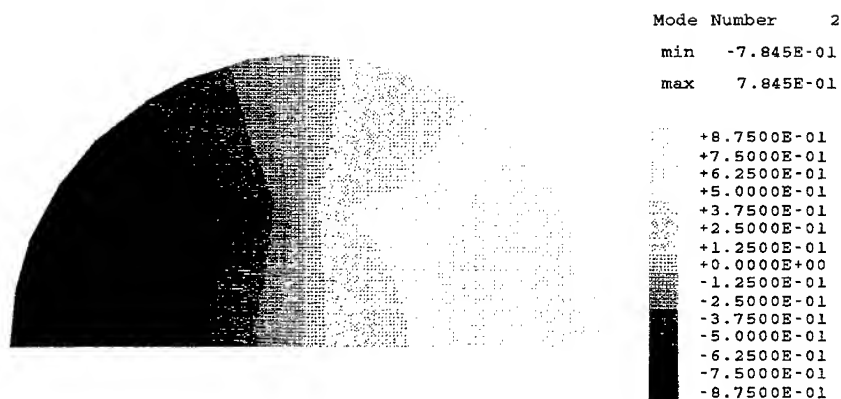


Figure 2: Grayscale Contours of Fundamental Mode

Many important physical problems must be solved in the presence of a constraint equation, such as the divergence-free condition required by Maxwell's equations on the magnetic field. One of the most important advantages of finite-element models is the relatively simple incorporation of such constraint equations into the underlying functional minimization principle that defines the finite-element approximation. The mathematical theory underlying convergence of discrete approximations for constrained problems is sufficiently difficult so as to preclude (in most cases) *a priori* examinations of whether the resulting constrained discrete model suffers from any common pathological behavior. One of the best ways to determine whether spurious solution behavior is present is to draw a visual representation of the solution, which allows the analyst to identify anomalous results. For example, in figure 3, the transverse displacement of a plate is shown. The square plate is supported only at one point at its center, and loaded out of the plane of the paper with a uniform load. The effect of the naive implementation of the appropriate mechanical constraint for this problem is the introduction of a spurious oscillatory mode that is immediately apparent from the graph shown in figure 3. A related variety of this "hourglass" oscillation is common in magnetic field problems, where the naive implementation of a divergence-free condition on the solution results in a similar erosion of solution accuracy. A close coupling between analysis code and visualization application helps to identify and rectify such potential solution errors.

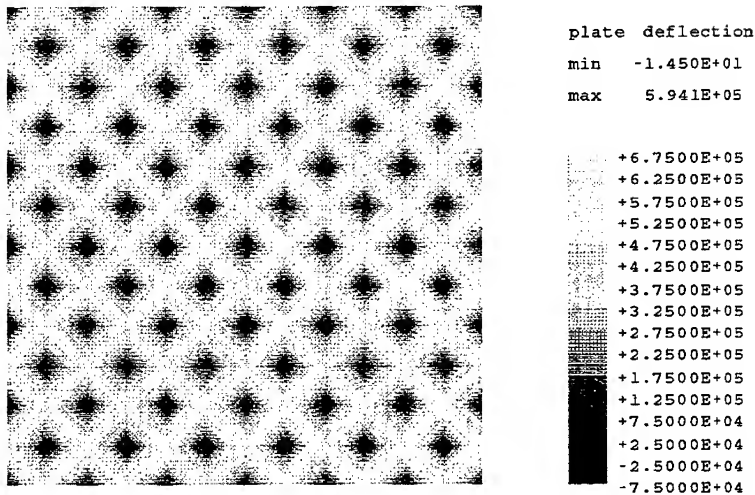


Figure 3: Contamination of Solution by Hourglass Mode

Summary

The simple generic finite-element application presented here is sufficiently concise so that it is easily understood by students of finite-element analysis, reasonably easy to modify or to generalize to accommodate new types of element approximation, and accurate enough to justify its use in research, academia, and engineering practice. The code is available for a nominal distribution fee by correspondence with:

LaDawn Haws
 Department of Mathematics and Statistics
 California State University, Chico
 Chico, California, 95926

At present, the analysis code runs on virtually any high-performance microcomputer or engineering workstation. The graphical visualization applications are presently supported only on the Apple Macintosh-II or Quadra series of computers. It is anticipated that the visualization codes will be available on most engineering workstations and under OS/2v2 for IBM and IBM-clones by the end of 1993.

ANALYSIS OF ELECTROMAGNETIC FIELDS IN ELECTRICAL MACHINES FROM EXPERIMENTAL DATA FOR EDUCATIONAL PURPOSES

Osama A. Mohammed & Howard Gordon
Dept. of Elec. & Comp. Engineering
Florida International University
Miami, Florida 33199

Abd A. Arkadan
Dept. of Elec. & Comp. Engineering
Marquette University
Milwaukee, Wisconsin

Abstract: This paper presents a system for the analysis of electromagnetic fields in electrical machines and their operational concepts from experimental data. The analysis can be performed directly while hands-on experimentation is in progress in the laboratory. The proposed system consists of three modules; data acquisition, data control and analysis modules. The analysis module contains finite element programs for the numerical analysis of electric machines at no load and at various load conditions. The system also includes a laboratory workstation which includes the rotating machines, personal computers and a data base for the geometrical, material and electrical data of the machines. Operational and control data are sent directly to the analysis programs during experimentation using the control and data acquisition modules.

The presented system is aimed at developing a tool that would help improve the student's understanding of electromagnetic field distribution and their use in calculating performance measures as well as operational concepts pertaining to the practical study of electrical machines. Furthermore, the developed system will help boost student's creativity and increase participation in understanding the concepts and theories. The presented system also provides a foundation for its implementation on a multi media environment to meet the ever changing need in educational tools and electrical engineering curricula.

INTRODUCTION

It is a common feeling in electrical engineering education that it is of extreme importance to boost creativity and student ability to analyze practical problems under various conditions. The ability to compare laboratory results with theoretical expectations concurrently is an important step to achieve this goal. Furthermore, the capability of visualizing the concept will certainly increase the student's ability to understand the theory and the topics being taught.

The utilization of computer systems in the study and analysis of electric machines has been proposed earlier by energy conversion educators. References [1] to [3] are examples of some of the efforts devoted to this area. These papers provided comprehensive analyses on the relevant subjects as well as described useful experimental treatments. The presented system adds a component providing finite element analysis of electric machines during the hands-on experimentation.

Electric machinery courses and the associated laboratories are requirements for most electrical engineering students in many universities. At Florida International University this laboratory consists of experiments on various analytical and operational characteristics of electric machines. These machines are in the form of separate components and include single- and three-phase transformers, three-phase induction machines, three-phase synchronous machines as well as single-phase multi-function and universal motors. All of the rotating machines treated here are rated at 1/3 hp. In addition to these components, an assortment of measuring instruments and other coupling and related components are housed in a mobile unit, which is referred to in this paper as the "workstation". For the development of the proposed system, each workstation has been upgraded to contain personal computers, a signal conditioner, a printer, a plotter and control circuits. The computers are equipped with A/D and D/A cards, a communication software, a data base which include magnetic circuit and other relevant manufacturer data, and an analysis module which utilize a Finite Element (FE) mesh generator and a set of finite

element analysis programs.

In addition to manually connecting the various components for a given experiment, the student is also required to make connections to the signal conditioner, control circuits as well as the computers. Once the student sets up the experiment for a given study manually, the data acquisition module is used to read and record the data. The menu-driven data acquisition software allows the sampling of the exact data points obtained from the experiment. From the computers, the student is able to control the operating parameters such as speed, voltage, current etc., as well as observe associated changes. The controlled excitation parameters are directly sent to the corresponding FE analysis program which performs a field solution for the machine under

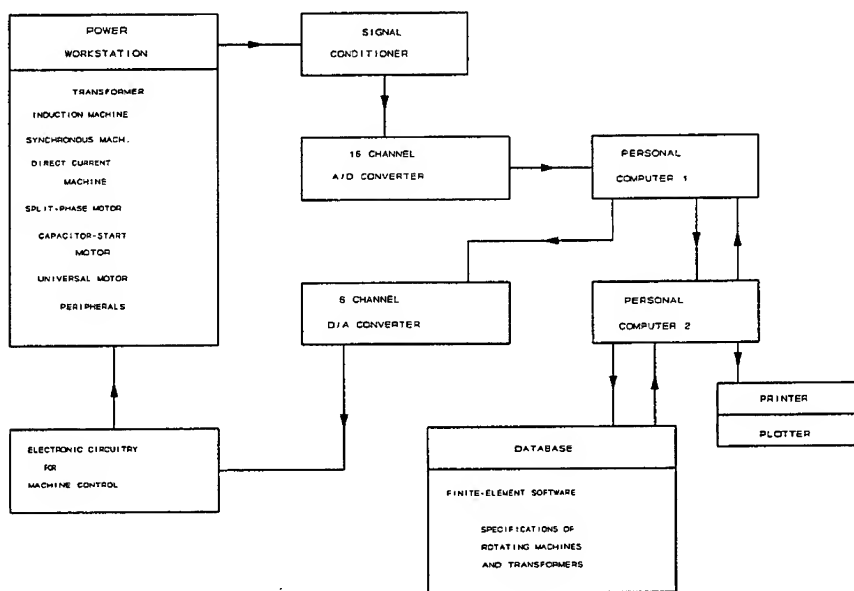


Fig. 1. Schematic block diagram of the system

test and calculate its performance measures from the machine's model stored in the data base. The comparison of experimental and analysis results takes the form of tables and/or graphs either on the computer monitors or in hard copy. The corresponding electromagnetic field pattern of the machine under study is also generated and displayed for the experimented conditions.

Examples are provided here to illustrate the use of the proposed system. The chosen examples are experiments dealing with the analysis of the no-load and load characteristics of transformers and rotating machines.

DESCRIPTION OF THE SYSTEM COMPONENTS

The main objective of the proposed system is *not* to eliminate the work involved in the laboratory but to clarify doubts or abstract ideas the students may have. It is not intended to reduce the amount of work required from students with that of a computer. The proposed system was developed in three main modules; (1) *The Data Acquisition Module*, (2) *The Analysis*

Module and, (3) *The Control Module*. An overall schematic block diagram of the system is shown in Fig. 1, giving an outline of the various components involved.

The Data Acquisition Module:

In addition to the hardware upgrades described above, this module also consists of a software that enables the user to sample data directly from a computer keyboard. In addition, this software also allows the user to link the entire system. This software is known as the Data Acquisition Program (DAP). The DAP is used in *Personal Computer 1*, and it is made up of several sub-programs. This program was written primarily to enable effective sampling and monitoring of the machine. The DAP consists of three main routines responsible for the overall data acquisition performance. The programs are; a) data acquisition, b) control, and c) data acquisition and control. Two other routines allow the user to display and graph the results obtained at any point during sampling. Once the program is loaded, a menu appears which allows the user to select the desired part of the program to be utilized. The main menu of the DAP is shown in Table I. The DAP allows the user to acquire data either through the A/D converter or to store data manually entered from the keyboard. The control program enables the user to send messages via the keyboard to the various machines for response. The data acquisition and control programs allows the user to simultaneously sample data from the machines and relay a command or message to the same machine or some other directly related machine. The data display menu allows the user to observe the acquired data in the sampling sub-routine. This sub-routine will print the data acquired and/or display it on the screen.

TABLE I. A/D AND D/A TRANSLATE MASTER MENU

1	SAMPLING MENU
2	CONTROL MENU
3	SAMPLING & CONTROL MENU
4	DISPLAY DATA
5	GRAPH DATA
6	ANALYSIS MENU
7	EXIT PROGRAM

After providing all input information, the program returns to the SAMPLE MENU program. At this point, the user may now sample the data for a given experiment or return to the main program. The next step is to enable the user initialize the channels and then commence the data acquisition procedure. Once the initialization is completed, the sampling takes place by means of an A/D converter in Personal Computer 1. By reading the appropriate ports, the sampling data is recorded and corrected. Each sample data point stored is read three times and then averaged. There are three modes of operation during data acquisition; A/D sampling, manual sampling, simultaneous A/D and manual sampling. The A/D sampling takes place when using the signal conditioner and the A/D board. The manual sampling is used when there are signals that cannot be coupled to the signal conditioner.

During control, there are two modes of operation; a) control with and 2) control without memory. In both cases, the D/A converter is used. The output of the D/A converter is set at a range of 0 - 5 volts depending on the maximum output to control. The user needs to provide the channel to be controlled and the maximum output for the system. Once the control output number is provided, the system will send the information to the D/A converter. The second mode of operation is similar to the first mode except for the creation of a file for the control outputs. The data acquisition and control system allows the user to acquire data and simultaneously control the devices and components involved in the experiments.

The Analysis Module:

This module was developed in order to provide the user with a comprehensive tool capable of analyzing the behavior of the electromagnetic fields in electric machines. All relevant data including manufacturers' specifications, physical geometries and material properties are contained within a data base. The Analysis Module Program (AMP), shown in Fig. 2, allows the user to

TABLE II. FIRST SUB-MENU OF AMP

1	TABULATION
2	GRAPH
3	FINITE ELEMENTS
4	QUIT

analyze any choice of machine(s) under study. The AMP is developed to provide an automatic interface with the data acquisition and the analysis modules. The main menu of the analysis module permits the user to select one of the following machines to analyze using the FE programs; 1) Transformer, 2) Induction Motor, 3) Induction Generator, 4) Synchronous Motor, 5) Synchronous Generator, 6) Direct Current Motor, and 7) Direct Current Generator.

Once the user selects one of the options, a sub-menu as shown in Table II. appears. If "Tabulation" is chosen, a unit is called which will retrieve all the data files created by the DAP. If the user wishes to plot any set of parameters from these data files, then option 2, Table II. is selected. The "selection file" unit presents the data files and allows the user to choose which

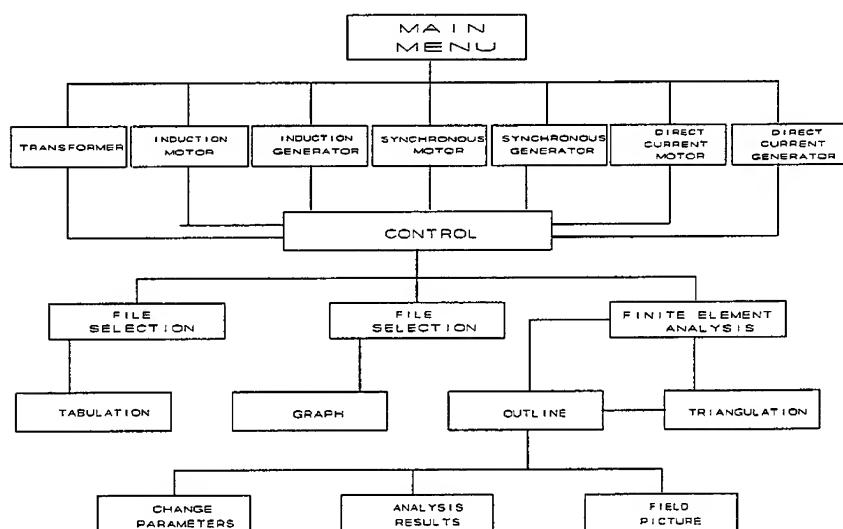


Fig. 2. The Analysis Module

variables are to be graphed. Graphs generated may combine results from experimental data, numerical analysis or utilizing information in the data base.

The third option in Table II. provides the FE analysis menu shown in Table III. Option 1, Table III., gives the outline of the machine's magnetic circuit cross-section showing the constructional features and main geometry as shown in Fig. 3. Option 2, Table III., produces the FE grid, Fig. 4, of the machine under study. The third choice, Table III., gives the results of the FE analysis and creates the magnetic field picture at a particular test instant, Fig. 5. The FE programs used here are base on work presented earlier by Mohammed et.al. [4]. The FE solution is based the magnetic vector potential (mvp) formulation [4]. The numerical solution is then used to calculate a variety of performance measures and produce the corresponding curves for comparison with experimental data.

TABLE III. SECOND SUB-MENU OF AMP

- | | |
|---|-----------------------------|
| 1 | MAGNETIC CIRCUIT OUTLINE |
| 2 | GRID GENERATION |
| 3 | FE ANALYSIS & FIELD PICTURE |
| 4 | QUIT |

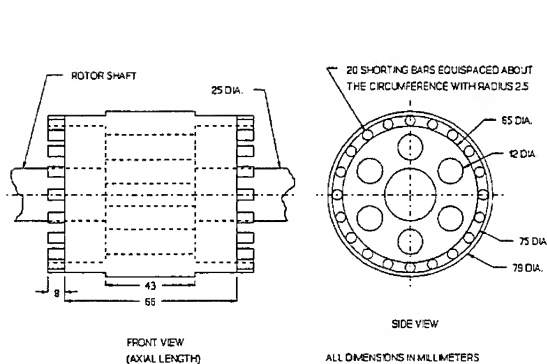


Fig. 3. Main geometry of the machine

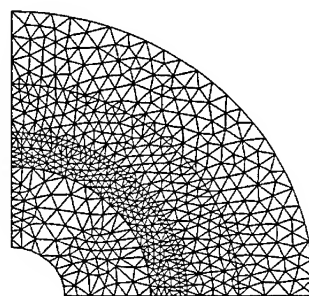


Fig. 4. Finite element grid

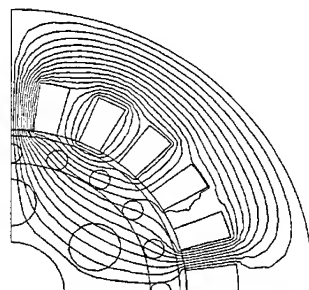


Fig. 5. Magnetic field picture

The Control Module:

The control module was developed in order to provide the user with a way of controlling the rotating machine experiments directly from the keyboard. A feedback system, which is capable of sensing the speed of rotation, adjusting the speed if necessary by making comparisons to a specified reference value, and making the results available for immediate display, was developed. This module comprises

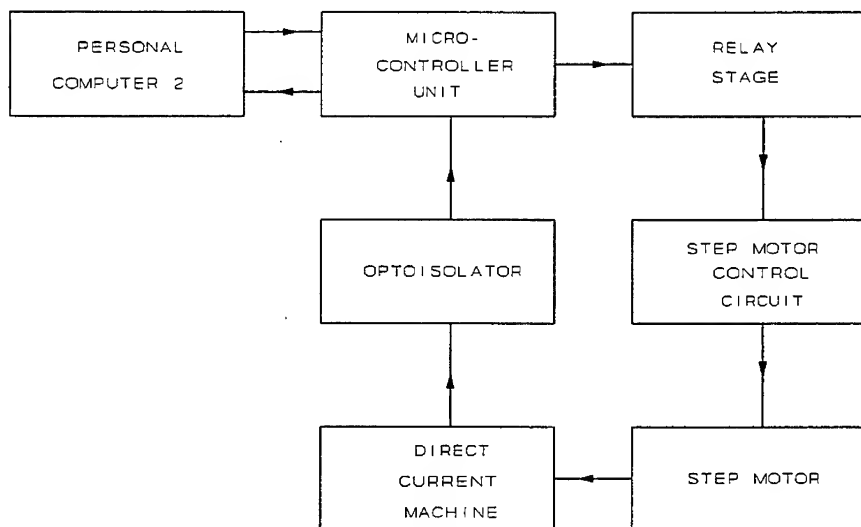


Fig. 6. Block diagram of the Control Module

of several main components such as personal computers 1 and 2, Fig. 1, a Motorola's HCMOS single-chip microcontroller, stepper motor, stepper motor controller circuit, optoisolator (Omron Photo Microsensor with built-in amplifier), and a perforated disk. A direct current motor was used to perform all prime moving tasks with respect to the rotating machine experiments. Figure 6 shows a block diagram of the control module. The Control Module is accessed from the main menu by choosing item 2 as shown in Table I.

The Control Module Program (CMP) was developed to provide speed control and speed monitoring of a DC motor. The sequence of operation begins with the perforated disk and the optoisolator. As the mounted disk rotates with the shaft of the motor, the ON/OFF signals triggered by the light sensors of the sensing section of the optoisolator, are sent to the microcontroller in the form of a square wave. The program displays the resulting speed in real-time fashion on the computer screen after detecting two consecutive rising edges generated by consecutive holes on the perforated disk. The program then finds the difference in time between the rising edges and convert it to period, frequency, and revolutions per minute. If the speed has to be changed, the desired result is entered from the keyboard, at which point the program prompts the step motor to adjust the field rheostat of the DC motor until the desired speed is obtained. This system forms a closed-loop feedback controller. The step motor control circuit, was modified to operate in both manual and automatic modes. The manual mode is directly controlled by the user with the speed control and direction control knobs.

SAMPLE APPLICATIONS

Two experiment are selected to show the effectiveness of the proposed system as an educational tool. The objectives of the first experiment is to study the electromagnetic field in a single phase transformer under no-load and load conditions as well as compare the laboratory and analysis data for its performance. The objectives of the second experiment is to study the no load and load characteristics of a synchronous alternator.

The procedures outlined above were implemented and appropriate experimental setups were made. The load on the transformer is a resistance varied in six steps from 333 to 2000 Ω . The produced field distribution is shown in Figs. 7.a-c for no-load, 333 Ω and 2000 Ω , respectively. The efficiency of the transformer under test was calculated from the experiment, and from a set of FE solutions. The two results are shown in Fig. 8.

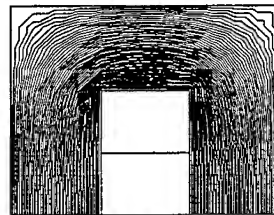
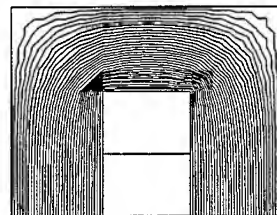
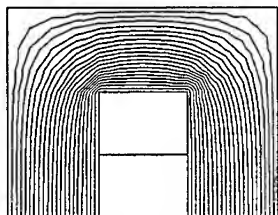


Fig. 7.a. Field dist at no load

Fig. 7.b. Field dist. at 333 Ω load

Fig. 7.c. Field dist. at 2000 Ω load

For the second experiment, the synchronous alternator is coupled to a dc motor and appropriate connections were made. The field current was varied in steps and the armature voltage was measured as well as calculated from the FE field solutions. The no-load characteristic of Fig. 9.a shows a comparison between experimental and FE results. A resistive load was connected to the synchronous alternator and the motor's field rheostat was adjusted to its minimum resistance. The motor is started and the speed is adjusted to 2000-rpm by varying the field rheostat. The excitation was controlled simultaneously to maintain the output voltage to 220-V from the alternator while the speed is maintained at 2000-rpm. A load test is carried out from no-load to approximately 0.35 Amperes. The same test was repeated at 1600-rpm. The load characteristics from both experiments and FE solutions are shown in Figs. 9.b-c. The magnetic field distribution at no-load, 1600-rpm and 2000-rpm are shown in Figs. 10.a-c.

One important aspect of the system proposed here is the FE and other analysis programs. This aspect has been reached with the currently available 386 personal computers. One of the main objectives of this system is that the user can visualize the change in the field picture inside the machine being tested and obtain analytical results during experimentation. At this time we have been able to produce the field picture and obtain analysis data from the electromagnetic field modelling for various cases within few minutes of processing due to the large number of equations being solved at each experimental instant. A faster computer will reduce the processing time significantly. We believe that the proposed additions to the conventional energy conversion workstation are feasible in terms of cost, as well as its overall educational benefits.

CONCLUSION

The comparison of laboratory results with theoretical expectations is a crucial step in providing knowledge and clarifications on the various concepts that students need for laboratory experiments and classroom instructions. The system proposed here provides a complete analytical and practical approach to the understanding of electrical machines and energy conversion concepts.

The overall system is designed to be user friendly using menu-driven setups. The system is made of three modules; Data Acquisition, Analysis, and Control Modules. A major result of the system described in this paper is that an energy conversion laboratory could become an in-depth analytical and practical experience in addition to performing the experiments and observing associated results.

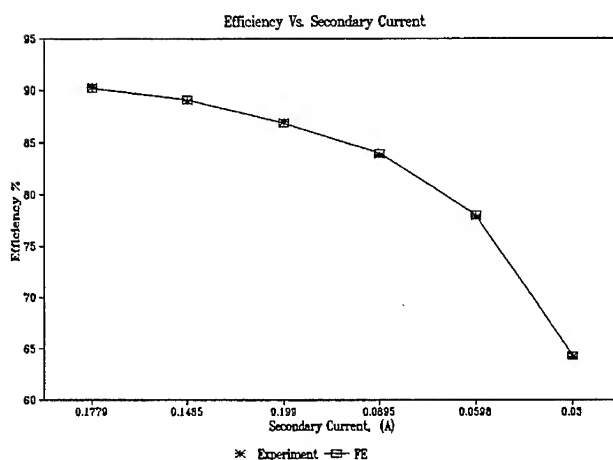


Fig. 8. Efficiencies calculated from experiment and FE solution

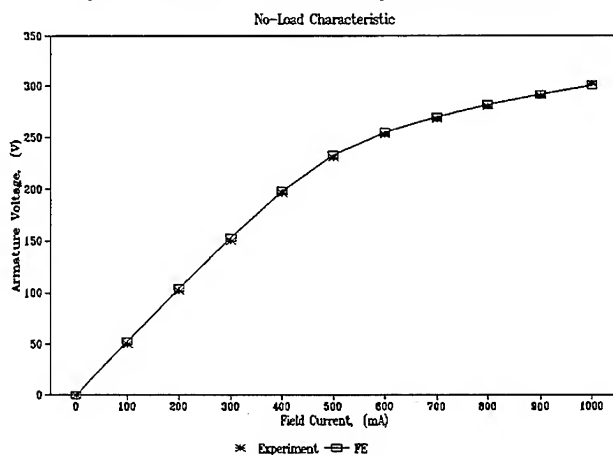


Fig. 9.a. No load characteristics for the dc motor

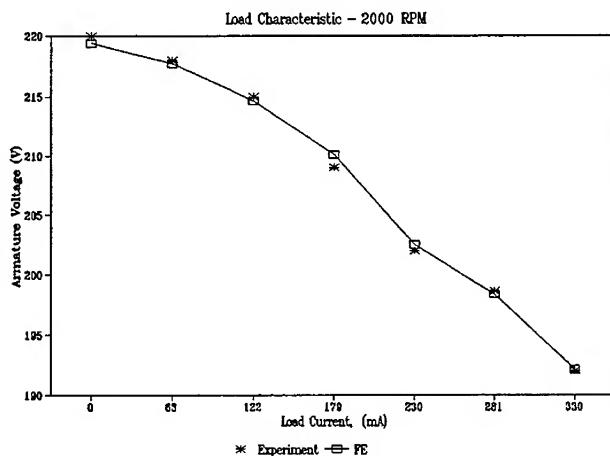


Fig. 9.b. Load characteristics at 1600 rpm

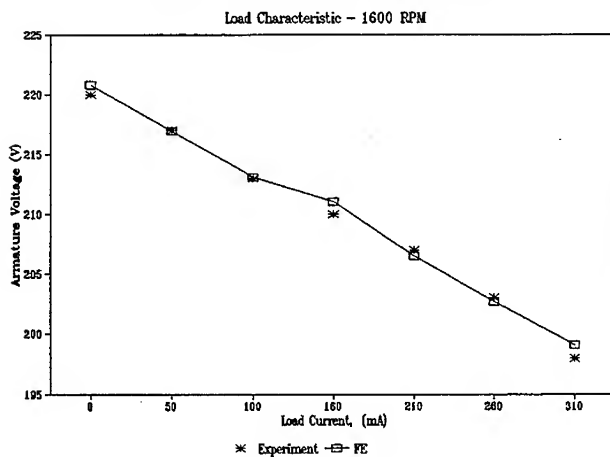


Fig. 9.c. Load characteristics at 2000 rpm

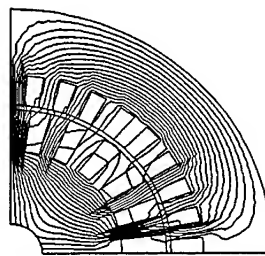


Fig. 10.a. Field dist. at no load

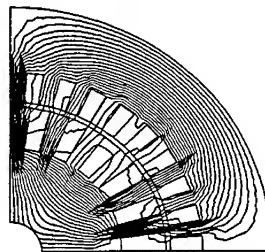


Fig. 10.b. Field dist. at 1600 rpm

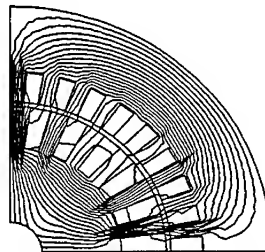


Fig. 10.c. Field dist. at 2000 rpm

REFERENCES

- [1] H.A. Smolleck, "Modeling and Analysis of the Induction Machine: A Computational/Experimental Approach;" Paper# 89 SM 650-3 PWRs, presented at the IEEE/PES 1989 Summer Meeting, Long Beach, California, July 9 - 14.
- [2] M.A. El-Sharkawi, T.C. Huang, and M. Chen, "Laboratory Setup for Instruction and Research in Electric Drive Control;" Paper# SM 652-9 PWRs, presented at the IEEE/PES 1989 Summer Meeting, Long Beach, California, July 9 - 14.
- [3] A.J. Goetze, "Introducing Computers to the Undergraduate Machinery Laboratory - Computer Control of a DC Generator and Motor;" (Paper# 84 WM 178-0), presented at the IEEE/PES 1984 Winter Meeting, Dallas, Texas, January 29 - February 3.
- [4] O.A. Mohammed and L. Garcia, "An Optimum Finite Element Automatic Grid Generator for Electromagnetic Field Computations;" *IEEE Trans. on Magnetics*, November 1988.

Learning About EM Theory and EM Modeling by Analyzing Printed Circuit Boards in an Enclosure

T. H. Hubing and M. W. Ali
University of Missouri-Rolla
Rolla, MO 65401

Abstract

Understanding electromagnetic theory requires more than an ability to apply Maxwell's equations to specific problems. Students in electromagnetics should be taught to visualize field distributions and anticipate solutions to basic problems in electromagnetics. Numerical EM modeling codes can be an excellent visualization tool. They also allow students to solve a variety of real-world problems that emphasize the relevance of the EM concepts presented in a course. This paper shows how simple printed circuit board structures can be used to illustrate basic field theory concepts. After modeling a number of these structures, students learn to visualize solutions to new structures even before they are modeled.

Introduction

Undergraduate electromagnetics classes tend to be among the most difficult courses in an electrical engineering curriculum. Students in these classes must be taught vector calculus and learn to work in different coordinate systems just to solve the most basic electromagnetic problems. The relationship between these basic problems and real-world engineering problems can be difficult for students to grasp.

Because the courses are difficult, many students convince themselves that EM theory is not relevant to the type of electrical engineering work they will eventually be doing. Many of them do not expect ever to solve another field problem once they have completed the required undergraduate EM courses. Electromagnetics instructors may even encourage this attitude among students if the classroom examples and demonstrations fail to illustrate applications of EM theory to other areas of electrical engineering. Traditional class demonstrations involving tin cans, balloons, ping-pong balls, and pendulums are both educational and entertaining, but they do not convince the students who are interested in computers or communications that EM theory is relevant to their engineering careers.

Trends in EM Education

There are two engineering trends that promise to revolutionize electromagnetics education. The first trend is the proliferation of high-speed microprocessor circuitry. Microprocessors are found in all kinds of electric and electronic appliances including televisions, audio equipment, coffee makers, pencil sharpeners, and electric shavers. A new automobile may have dozens of microprocessors and commercial jet aircraft may have hundreds. It is becoming very difficult for graduating electrical engineers to find a job that does not require designing or working with high-speed microprocessor circuits. It is also becoming much more difficult to get high-speed microprocessor systems to function properly and meet electromagnetic compatibility requirements without a basic understanding of EM theory.

The second trend that promises to have a significant impact on electromagnetics education is the increasing availability and sophistication of computer EM modeling techniques. Computer modeling enables students to solve problems that are much too complex to solve analytically. This means that EM instructors can assign problems that demonstrate applications of EM theory to real-world engineering challenges.

Computer modeling techniques also make it much easier for the student to visualize the solution by plotting the results over a region in space. Once a problem has been solved, it is relatively little extra work to make minor modifications to a structure and analyze it again. This makes it easier for the student to learn what effect various attributes of the structure have on the solution.

Teaching Electromagnetics

There are arguably three levels at which students may learn electromagnetic theory,

1. understanding the math
2. being able to work the problems
3. being able to visualize the important parameters.

For example, a student who understands the algebra and complex number theory necessary to solve a simple transmission line matching problem has a level 1 understanding of transmission line stub matching. If the student can consistently calculate the correct stub length and location, then level 2 has been achieved. The student who can visualize the standing wave pattern (perhaps with the aid of a few calculations), and then come up with a reasonable estimate for the best stub length and location has attained a level 3 understanding of transmission line stub matching. This student can probably estimate the bandwidth over which a "reasonable" match will be achieved and is generally able to determine the best stub matching solution under various conditions.

These same three levels of understanding exist for other aspects of electromagnetic theory such as field propagation in waveguides, modes in resonant cavities, current distributions on antennas, and antenna field patterns. These levels of understanding usually occur in the order presented, however it is possible for a student to achieve them in any order. For example, engineering technicians who frequently work with radio and microwave frequency hardware, often achieve a level 3 understanding of many aspects of electromagnetic theory without ever achieving level 1 or level 2. Engineers who rely on computers and numerical methods to do field calculations may not be familiar with the mathematics involved in the calculations and yet they still may have a level 2 and level 3 understanding of the topic. Undergraduate and graduate courses in electromagnetic theory must strive to instruct students at all three levels.

Students who develop just a level 1 or level 2 understanding of EM theory are not likely to apply it to real engineering problems and will soon forget most of what they learned. For example, a student who is proficient at calculating the length and position of matching stubs may be well prepared for situations involving a mismatched line that needs to be matched with a stub. However, this particular situation may never arise. The student may encounter a number of similar problems (e.g. the need for notch filter) where a stub may be the perfect solution, but the potential for applying the theory to these new problems may not be recognized.

The best way to instill a level 3 understanding in students is to encourage them to plot fields and/or currents rather than to ask for a specific numerical answer. Also, students should be asked

questions of the form "If this parameter is changed in this way, how will the result be affected?" These types of questions get the student to think about physics of the problem.

While many college instructors already use this approach to teach transmission line theory, it is not as common for 3D field theory. The primary reason for this has been that 3D field calculations are tedious and there are a limited number of problems that students can be expected to solve. However, with the help of numerical modeling codes, it is becoming easier to solve a number of interesting EM field problems with real-world applications and quickly plot the results.

PCB Structures in an Enclosure

One type of structure that is useful for demonstrating EM field theory concepts, and also has practical applications, is the printed circuit board in a metal enclosure. A simple example is illustrated in Figure 1. Normally, currents in the circuit are calculated using transmission line or circuit theory and the enclosure is ignored.

As an example of how students can use numerical modeling techniques to help develop a level 3 understanding of a basic field problem, the structure in Figure 1 was analyzed using the EMAP finite element modeling code [1]. The amplitude of the x-component of the electric field in the plane of the circuit is plotted in Figure 2 at four frequencies.

At most frequencies, the circuit behaves like a shorted transmission line and the field is primarily confined to the region between the conductors. However, at frequencies away from the circuit resonance, the field away from the circuit can be much stronger than the field within the circuit. This is especially true at frequencies that excite a resonance of the enclosure.

These results may not surprise engineers with EM modeling or measurement experience, but they make a lasting impression on students in undergraduate electromagnetics classes. Students learn to recognize that the fields within the circuit may not be the only fields of importance and that under some conditions a circuit's enclosure can have an effect on the operation of the circuit. By experimenting with various circuit sizes, positions, frequencies, and dielectric materials; students can develop a feeling for the way in which different parameters affect the results. Pretty soon, students can predict how new configurations will behave without even running the modeling code.

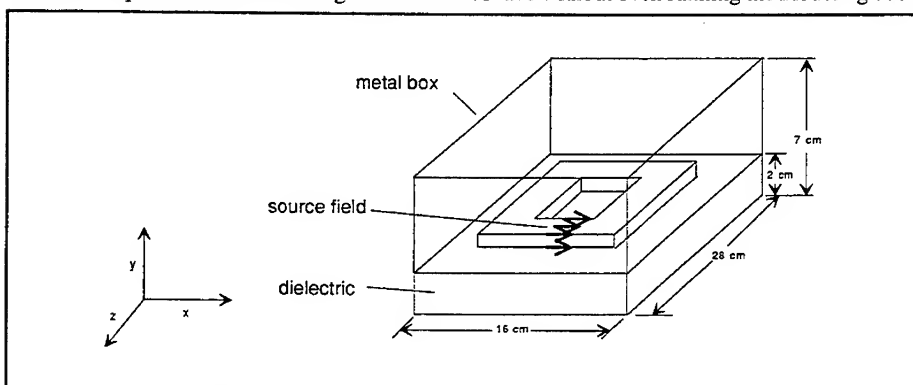


Figure 1: Printed circuit board structure in an enclosure

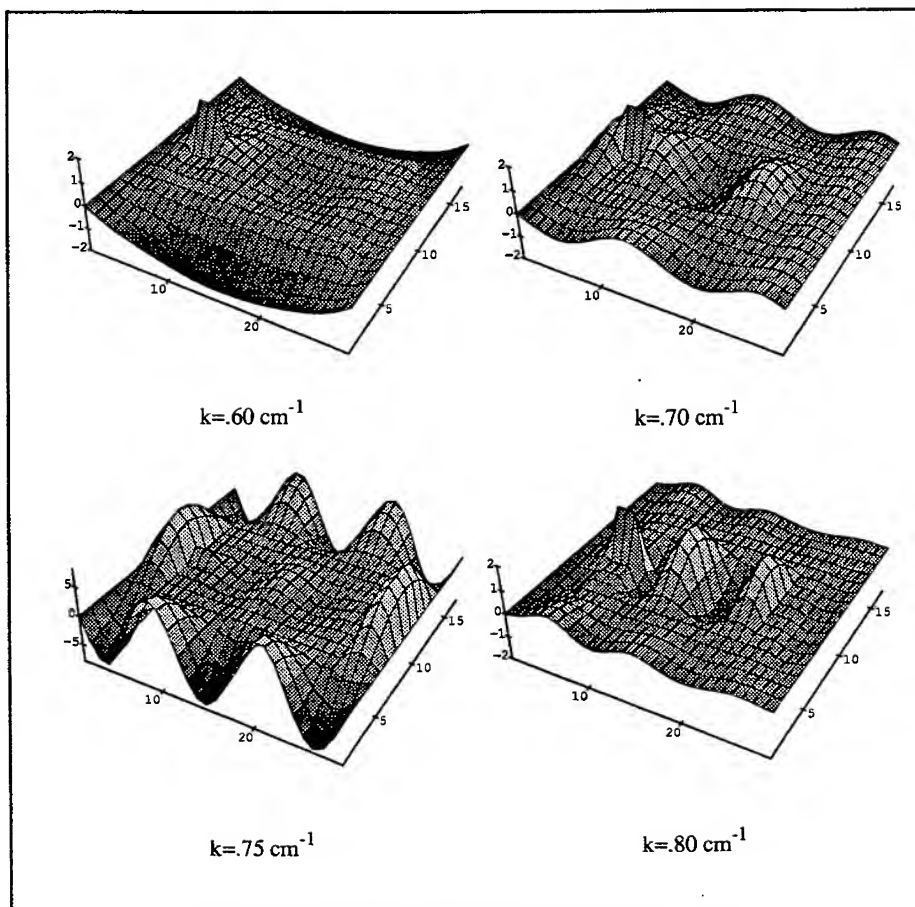


Figure 2: x-component of electric field at four frequencies

With two loop circuits placed in an enclosure as shown in Figure 3, it is relatively easy to demonstrate how fields from one circuit are coupled to another. With a little practice, students can learn to design and orient circuits to maximize or minimize the coupling between them.

Conclusions

The availability of easy to use 3D numerical modeling techniques provides instructors of undergraduate and graduate electromagnetics classes with a unique opportunity to give students hands on experience with electromagnetic field calculations. Using these techniques, students gain an awareness of the practical applications of EM theory and develop a feeling for how fields behave in different circumstances. Numerical modeling assignments can make the course more interesting

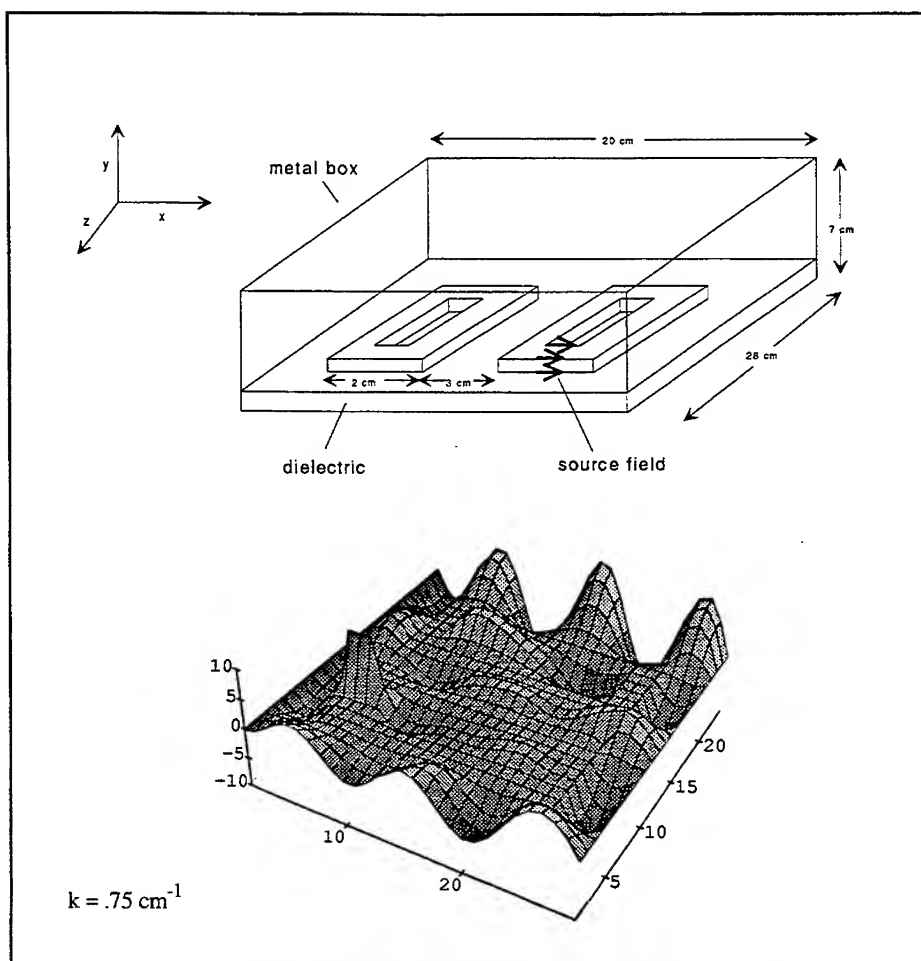


Figure 3: Two loop circuits in an enclosure

for the students and at the same time help the student to achieve a level 3 understanding of the topic. With a little practice, students can learn to design and orient circuits to maximize or minimize the coupling between them.

References

- [1] T. Hubing, M. Ali, and G. Bhat, "EMAP: A 3-D, Finite Element Modeling Code for Analyzing Time-Varying Electromagnetic Fields," to be published in the *ACES Journal: Special Issue on Computer Applications in Electromagnetics Education*

Relativistic Foundation of Electric Current - A Model for Transmission Lines

by *Zvonko Fazarinc*

Hewlett-Packard Laboratories, Palo Alto, California
Stanford University, California

Abstract

A computerizable model of electric current flow in conductors is proposed which holds the potential for a seamless curriculum of electromagnetics from the early secondary to late college instruction. The model is based on parameters like electron velocity and their relative spacing and is as such intuitively accessible to the uninitiated. At the same time it is based on relativistic principles captured in Maxwell's equations and represents as such a firm foundation for further analytical development. The paper is accompanied by live computer demonstrations.

1. Introduction

Teaching of electromagnetics continues to suffer from problems rooted in limitations imposed by chronology of mathematical tool acquisition. A case in point: It is unthinkable to teach Maxwell's equations or their derivatives like transmission lines and radiation to high school students. The obvious reason is that high school students are not expected to be proficient in partial differential calculus. Yet, the current flow in conductors which obeys those same natural laws, captured so elegantly in Maxwell's equations is being courageously taught by most science teachers in high schools. They can only rely on algebra and maybe ordinary differential equations and are therefore forced to resort to fluid flow analogies and instantaneous action across space. Delayed space-time relationships are understandably being avoided. When computer aids are available, images of current flow that show electrons moving in unison along the whole circuit are usually presented. While this is close to the truth it is not good enough to forestall many problems the students encounter later, in college. The price they must pay is disproportionately high when we consider that they have to first part with erroneous analogies before they can become receptive to the "new ways" in which the electric current behaves. With the image of electric current starting simultaneously at all points of the wire it is very difficult for the teacher to explain why one wire would be positive and the other negative. The fact that the electron velocity in the positive wire is higher than in the negative defies all reasonable expectations. The Ohm's Law, the unshakable fortress of "everything electrical" also becomes suspect. Legitimate questions which are rarely asked and even less frequently answered are keeping the student in a constant state of uncertainty. For many, the true revelation never materializes and the misconceptions imposed in secondary school often stand in the way of successful problem solving. Here is one such question that persists until the student gains full comprehension of the concept of characteristic impedance and that of the reflection, i.e. the comprehension of transmission lines. "If the current does not start simultaneously at all points of the wire how does the voltage source V know to send the current V/R into the wire even if the resistor R is far away from the source?" The second question may persist well into graduation and beyond and one may therefore be tempted to dismiss its importance. Yet, it is at the root of understanding the mechanism of electric current flow and as such legitimate to ask: "How is it possible that the electric field travels down the wire at nearly the velocity of light, and terminates on charges which typically travel ten orders of magnitude slower?"

We could make the life of students and teachers of electromagnetics much easier if we could, without the need for proficiency in partial differential calculus, present a "Maxwell-correct" concept of electric current flow to high school students. This paper attempts to do just that and shows, in association with a dynamic computer display, how a relativistic model of electric current conveys to the uninitiated

student the answers to the above two questions and to many more. The static nature of the medium in which this paper must be published makes it difficult to communicate in a convincing manner the ease with which this is accomplished. The paper shows how this same model provides a direct starting point for a later development of the transmission line theory without the need for any "midcourse corrections".

2. Relativistic Model of Current Flow.

The special relativity is based on a single observation of the most straightforward kind. The light, or in our case the electric field emanates from a source at constant speed c regardless of the velocity v of the source. In our case the source is the electron. Each electron can be viewed as having a spherically symmetrical radial field which terminates at infinity. If an electron is jerked into a new position the radial field surrounding it must be rebuilt with the new position of the center and the disturbance flows outward from the the electron to infinity at speed c . When such disturbance encounters an electron this senses it as a force field and is normally put in motion if free to move. The whole radiation and antenna theory is based on this concept. We wish to display the effect of propagating force fields on adjacent electrons within a conductor. The inability to display moving pictures makes it awkward to describe the processes which can be easily followed on a computer screen. We are faced with the task of conveying the direction of motion of electrons, the direction of propagation of the force field and of the direction of the force on electrons when encountering the field. To this end we have tagged the middle electron with the symbol e_0 and the reader must infer the direction of its motion from successive snapshots by watching its subsequent positions. All the other electrons are moving in the same direction or are standing still, as the case may be. The direction of force on a negatively charged particle is identified by the symbol "<" or ">". The propagation direction of the force field, on the other hand, is indicated with an arrow under the force symbol.

In Fig. 1. we see seven uniformly spaced small dots representing free electrons, and seven larger ones representing stationary positively charged atoms. There is no motion possibility beyond the two boundaries.

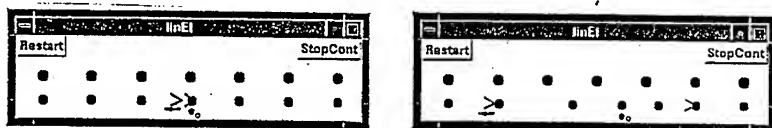


Fig. 1 Computer Demo of Interaction Between Accelerated Electrons.

The snapshot on the left shows the instant of acceleration to the right of the middle electron e_0 . The force field starts propagating away from the electron and the force exerted on an electron when encountered is always in the direction of acceleration. The orientation of the force is shown by symbol ">". The arrow indicates the direction of motion of the respective force field. The other ">" travels to the right. The speed of the force field is constant and therefore it takes the same amount of travel from the accelerated electron to the one behind it and to the one ahead of it. This is the only relativistic rule imposed on our model. The electrons travel at one third of the speed of field in our example.

The moving electron closes in on the one ahead of it which we will refer to as e_{+1} during the field travel time. It also separates from the one behind it, which we denote by e_{-1} , during the field travel time. After that the three travel in a new formation which is characterized by a compression in front and by a rarefaction behind e_0 . The acceleration of the two new travel companions sends out new disturbances, i.e. force fields which bring two more electrons into the moving formation. These we

refer to as e_{+2} and e_{-2} . The snapshot on the right of Fig.1 shows the moment when the force field reaches them and all five are in motion from then on.

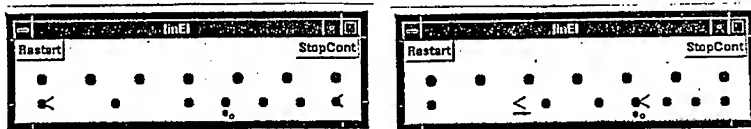


Fig. 2 Computer Demo of Interaction Between Accelerated Electrons (continued).

As the force field emitted by electron e_{+2} reaches the electron at the boundary this is accelerated forward but because it has no place to go it is immediately decelerated and sends a reverse force field toward the approaching electron e_{+2} . This exact moment is captured in the snapshot on the left in Fig. 2. During the field travel time from the boundary to e_{+2} the approach continues for a new, further reduced spacing. Then the field stops e_{+2} and its deceleration sends a new force field towards e_{+1} . Again e_{+1} has a chance to come nearer the now resting e_{+2} until it is stopped. The exact instant when the decelerating field encounters e_0 and stops it is captured in the right-hand side snapshot of Fig. 2. The decelerating force field emitted from e_0 later stops e_{-1} while the force field arriving from the left-hand side boundary catches e_{-2} at the same time the field from e_{+1} encounters it. Instead of just stopping e_{-2} this combined action accelerates e_{-2} to the left. Events similar to those described at the beginning and which can be followed very easily on a dynamic computer screen require too many words to describe how, in turn, all five electrons are set in motion, this time to the left. Reaching the boundaries, the fields reverse again and gradually stop the formation in the original, uniformly spaced state.

3. From Continuous to Relativistic Current Flow Model

In Fig. 3 we see the electron flow presented with the ratio of field speed and electron velocity of 150 at the left and three to one on the right. The positive voltage source terminal is at the bottom. The relativistic effects become visible in the second case. The current does not start instantly everywhere and results in compression in the top wire and in rarefaction in the lower.

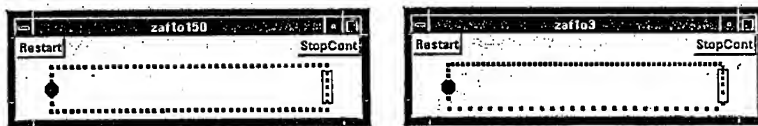


Fig. 3 Current Flow with Different Ratios of Field to Electron Velocity.

The source keeps pumping against the compressed electrons and leaves behind the rarefied formation. The termination does exactly the opposite. It allows the compressed electrons entering the resistor to spread out gradually and, with proper termination, they exit with the exact separation demanded by the source. A detailed study of collisional interaction with the lattice can explain this quite readily and answers another profound question: "What is so special about that one resistor value that produces no reflection?" This paper is restricted to ideal conductors and we defer any further discussion of resistive effects to another paper.

4. Quarter-Wave Resonance Explained With the Relativistic Model

We can now experiment with the model and choose an open transmission line driven by a pure voltage source shown in Figs. 4 and 5. To the microwave engineer this is unmistakably a resonant structure and as such subject of interest. Again the larger dots represent positive atoms and the smaller ones free electrons. The upper terminal of the voltage source is negative which means that the source tends to crowd electrons there after withdrawing them from the lower terminal. The spacing of atoms is denoted by D and that of electrons in the lower wire by S . Initially S and D are equal which assures neutrality of the conductor. As the spacing of electrons along the wires changes the net charge changes accordingly. This is directly proportional to the difference $1/D - 1/S$ which is plotted in the lower graph. For a uniform line geometry this plot represents the voltage. The electron flux is proportional to the velocity of electrons V times their density. The latter is proportional to $1/S$ so the plot of V/S below the conductors represents the flux of electrons. The quantities D, S and V are read from the simulation of electron interaction along the line as time progresses.

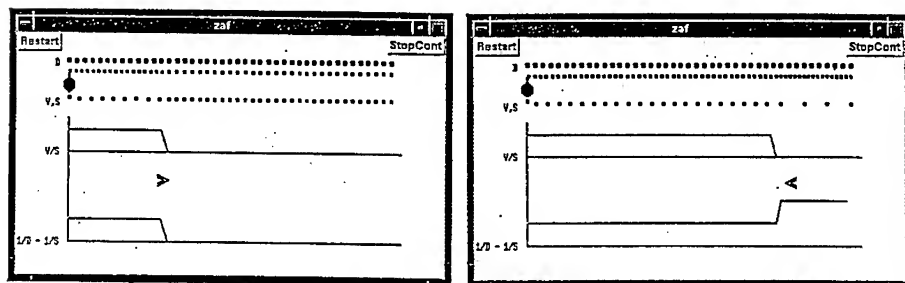


Fig. 4 Open Transmission Line Driven by a Voltage Source - First two Passes

On the left of Fig. 4 we see a snapshot of the dynamic display during the first pass after the voltage source has been turned on. The rarefaction of electrons in the lower wire gives rise to a positive net charge whose locus travels at the field speed to the right as indicated by the symbol " $>$ ". The electron flux travels also at the speed of rarefaction, i.e., at the speed of accelerating field while the electrons themselves travel much slower. The second snapshot in Fig. 4 was taken after the boundary electron has emitted a decelerating field backwards which is gradually bringing the electrons to a standstill starting at the open end. The accompanying increased rarefaction (or compression in the upper wire) gives rise to a double charge the locus of which is now traveling towards the source. The flux plot shows that the motion has been arrested.

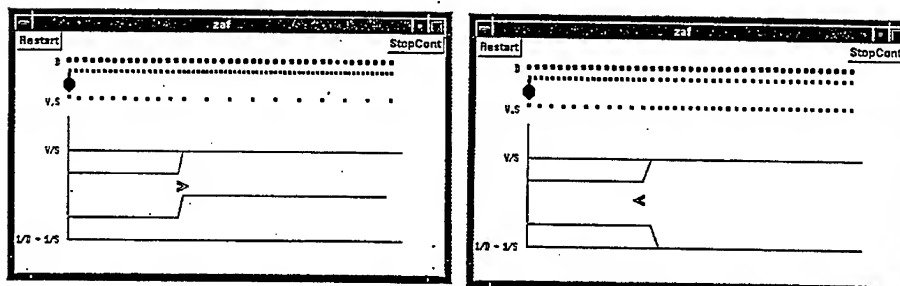


Fig. 5 Open Transmission Line Driven by a Voltage Source - Third and Fourth Pass

In Fig. 5 we see two more snapshots taken after those in Fig. 4. The one of the left shows the state after the double charge (double potential) has reached the source (single opposing potential). This forced electrons into reverse motion and we see now a tightening of the spacing in the lower wire and a relaxation in the upper. The net charge consequently drops back to a single value and the locus travels to the right, gradually setting electrons into reverse motion. Finally, when the deceleration starting at the boundary propagates towards the source we see the electrons being stopped exactly when they reach a mutual separation equal to D . This is commensurate with a neutral state and the line charge and flux go to zero. The right-hand side snapshot in Fig. 5 shows the line in the process of being cleared.

The fourth pass ends up with the initial state and if the voltage source is still present another cycle is initiated by acceleration of the source electron(s). Thus it took four passes for the pattern to repeat and the quarter wave resonance phenomenon can be intuitively understood if attention is paid to what the electrons are doing along the line. Observation of say one point in the upper wire would reveal that the electron is moving first to the right, then it stops, after which it moves to the left and finally stops again. After that the whole cycle repeats itself.

5. From Qualitative to Quantitative Analysis.

The electron flux f per unit area is defined as the number of electrons crossing a unit area in a unit of time. If we assume that the electrons are moving in only one dimension of the three-dimensional space then we can define the flux as the velocity of electrons v in that one dimension divided by their density. In a neutral, singly ionized conductor the density of electrons is equal to the density of ionized atoms. If the spacing of these atoms is d then the average spacing of electrons in the neutral conductor is also d and their respective densities are $1/d^3$. The electron flux per unit area in a neutral conductor is then simply

$$f = \frac{v}{d^3} \quad (1)$$

If the conductor is not neutral, i.e. it has an excess of positive or negative charges, the density of electrons differs from that of the ionized atoms. In our case such deviations are caused by motion of electrons in presence of delayed electric fields and consequently the spacing of electrons is affected only in the direction of electron motion. If we denote the spacing of electrons along the length of the negatively charged wire by s_n (less than d), then the electron density in that wire is $1/(d^2 s_n)$. Similarly in the positively charged wire we would expect the electron spacing s_p to be larger than d and the electron density would amount to $1/(d^2 s_p)$. For the continuity of flux f such as expressed in (1) the following relationships must be true

$$f = \frac{v}{d^3} = \frac{v_p}{d^2 s_p} = \frac{v_n}{d^2 s_n} \quad (2)$$

In (2) v_n and v_p are the respective electron velocities in the negatively and positively charged wires. The respective net charge densities in the two wires identified by subscripts n and p can be expressed in terms of defined quantities as

$$q_n = \frac{e}{d^2} \left(\frac{1}{d} - \frac{1}{s_n} \right) \quad (3)$$

and

$$q_p = \frac{e}{d^2} \left(\frac{1}{d} - \frac{1}{s_p} \right) \quad (4)$$

We take now advantage of our relativistic model to evaluate the spacings s_n and s_p . The speed of electric field propagation is denoted by c . Consequently the time for the field to traverse a distance d amounts to d/c . In the negative wire the electrons are forced against each other to a final spacing s_n . If the velocity of such an electron is v_n it traverses a distance $v_n d/c$ while the field travels from it to the neighbouring electron a distance d away. The resulting spacing at that moment is

$$s_n = d - v_n \frac{d}{c} = d \left(1 - \frac{v_n}{c}\right) \quad (5)$$

Similarly in the positive wire the electrons are forced to separate from each other. If an electron is moving at velocity v_p away from the neighbouring electron a distance d away it will travel undetected for a time d/c before the field disturbance reaches the neighbour. The spacing at that instant is

$$s_p = d + v_p \frac{d}{c} = d \left(1 + \frac{v_p}{c}\right) \quad (6)$$

During the initial transient the adjacent electrons are set in motion when the field reaches them and they continue to move at the velocity of the originators. We will prove this later on. The spacings s_n and s_p are consequently established along the whole length of the two wires unless a discontinuity is encountered.

From (2) and (3), using (5) and (6) we can write for the charge densities

$$q_n = -\frac{e}{d^2 s_n} \left(\frac{s_n}{d} - 1\right) = -\frac{e}{d^2} \frac{v_n/c}{s_n} \quad (7)$$

and

$$q_p = \frac{e}{d^2 s_p} \left(\frac{s_p}{d} - 1\right) = \frac{e}{d^2} \frac{v_p/c}{s_p} \quad (8)$$

For flux continuity (2) must hold and consequently charges q_n and q_p are recognized as being the negatives of each other. The first important result we can get out of this analysis is the relationship between the charge density q and the current density j . The latter is equal to the electron flux density f multiplied by the electron charge $-e$. So from (2) combined with (7) and (8), respectively, we find

$$q_n = -\frac{j_n}{c} \quad q_p = \frac{j_p}{c} \quad (9)$$

Relationship (9) holds for any geometry of conductors as long as it is not re-entrant. For re-entrant structures the field disturbance may reach the conductor electrons sooner through the intervening space than along the conductor in which case the model does not apply. For non-reentrant structures analyzed here the inductance and capacitance per unit length are directly related to each other by

$$LC = \frac{1}{c^2} \quad (10)$$

Expression (9) immediately yields the characteristic impedance of the structure if we can assume a uniform geometry for which the linear relationship between the potential and charge applies, such as $Q = VC$. Then (9) multiplied by the cross-sectional area of the conductor in association with (10) results in

$$VC = \frac{I}{c} \quad \text{or} \quad \frac{V}{I} = \sqrt{\frac{L}{C}}$$

Let us now take a look at the temporal/spatial relationships between the charge and the flux. To this end we expand the notation to a spatial coordinate x and a temporal t . In the sketch below we see three electrons with their spacings and velocities identified.

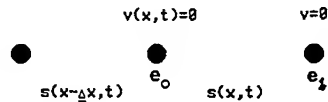


Fig. 6 Snapshot at time t when e_0 has been accelerated.

We know that in absence of discontinuities the spacing reduction and spacing enhancement travel in the respective wires at velocity c . We choose the spatial increment Δx and the temporal one Δt such that their ratio is equal to c . Then the spacing enhancement or reduction along the wire can be described by the relationship

$$s(x, t + \Delta t) = s(x - \Delta x, t) \quad (11)$$

which simply states that whatever was at $x - \Delta x$ at time t will be at x a time Δt later.

Referring to Fig. 6 we can find the value of the spacing $s(x, t + \Delta t)$ which is created from $s(x, t)$ during the field travel from e_0 to e_1 . This amounts to

$$s(x, t + \Delta t) = s(x, t) + v(x) \frac{s(x, t)}{c}$$

From the above we can find the change of velocity of e_0 between time t and $t + \Delta t$. (Recall that $v(x)$ started out as $v(x, t) = 0$ and was constant throughout the field travel time $s(x, t)/c$).

$$v(x, t + \Delta t) - v(x, t) = v(x) = \frac{s(x, t + \Delta t) - s(x, t)}{s(x, t) c}$$

Divide both sides by $s(x, t + \Delta t) c d^2$, substitute (11) for $s(x, t + \Delta t)$ and add and subtract $1/d^3$ to obtain

$$\frac{v(x, t + \Delta t)/c - v(x, t)/c}{d^2 s(x - \Delta x, t)} = \frac{1}{d^3} - \frac{1}{d^2 s(x, t)} - \left[\frac{1}{d^3} - \frac{1}{d^2 s(x - \Delta x, t)} \right] \quad (12)$$

We readily recognize the left-hand side of (12) as the temporal change of flux density and the right-hand side as the spatial difference of net charge densities at x and at $x - \Delta x$. If we multiply both sides by the electronic charge, divide them by Δt , divide and multiply the right-hand side by Δx , we obtain

$$\frac{\Delta j}{\Delta t} = -c^2 \frac{\Delta q}{\Delta x} \quad (13)$$

where we have substituted c for $\Delta x/\Delta t$. In association with (10) the above translates into one of the familiar transmission line equations. The other one can be obtained by substituting the current-charge relationship (9) into (13). This produces

$$\frac{\Delta q c}{\Delta t} = c^2 \frac{\Delta j}{\Delta x}$$

or

$$\frac{\Delta q}{\Delta t} = - \frac{\Delta j}{\Delta x} \quad (14)$$

6. Conclusions

A computerizable model of electric current flow has been proposed. With the aid of a dynamic display the concept of delayed propagation can be conveyed to the uninitiated student and phenomena like quarter-wave resonance and reflections on transmission lines can be made understandable to pre-partial differential calculus students. Not described in this paper were a number of other phenomena that the model can correctly conceptualize for the layman and the professional alike. The concepts of inductance and capacitance, the reasons for current-voltage relationships in inductors and capacitors, the nature of voltage and current sources, lossy conductors, skin effect and the reason for ejection of magnetic field when superconductivity sets in are just a few examples.

We have restricted our main example to the open line but the model can just as well handle the shorted case. As a matter of fact the relativistic nature of the current flow model really stands out when one studies the events taking place at the shorted end. There the fluxes from the two wires add up while the condensations arriving on the negative wire cancel the rarefactions in the positive wire and vice versa. A neutral state is established and the current is being carried by an electron density $1/d^3$. The question is what is the velocity v_x of electrons that carry this sum of fluxes. The following relationship applies

$$\frac{v_x}{d^3} = \frac{v_n}{d^2 s_n} + \frac{v_p}{d^2 s_p}$$

When (5) and (6) are substituted respectively for s_n and s_p we get after some simple algebraic manipulation

$$v_x = \frac{v_n + v_p}{1 + \frac{v_n v_p}{c^2}}$$

The reader will recognize the above as the famous relativistic velocity addition formula that applies always when particles which are emitting fields are interacting. It assures that no matter what the constituent velocities may be their sum can never exceed that of velocity of emitted field c .

While the model is intuitive it yields a firm analytical basis from which the mathematical theory of conduction can be developed. Examples of characteristic impedance and transmission line equations and this last example illustrate the point.

Reflector Antenna Analysis Software: An Educational Approach

B. Houshmand and Y. Rahmat-Samii
Department of Electrical Engineering
University of California, Los Angeles
Los Angeles, CA 90024-1594

ABSTRACT

Reflector antennas are one of the most frequently used antenna systems for a wide range of applications such as radar, communications, and remote sensing. In this paper a reflector antenna software package is presented which provides the electromagnetics students with an analysis tool to study the performance of realistic reflector antenna systems. The use of such software package in an antenna course enables the students to gain insights into antenna concepts such as directivity, antenna gain, side-lobe level, beamwidth, reference/cross polarization, and near-far field relationship. This software package complements the existing Computer Applications for Electromagnetics Education (CAEME) array and wire antenna software packages. This software is dedicated to single reflector geometry, and designed to be user-friendly with a reasonable turnaround time in a PC environment. It can be effectively integrated with reflector antenna chapters in one of the standard antenna textbooks. In addition to antenna concepts, this software is designed to address some basic computational aspects such as convergence, as well as some fundamental electromagnetic concepts such as the Huygens' principle. In this talk several examples are presented to highlight various features of this software package.

I. Introduction

Reflector antennas are one of the most frequently used antenna systems for a wide range of applications such as radar, communications, and remote sensing. The purpose of this project is to provide the electromagnetics students with a software tool to study the performance of realistic single reflector systems and gain insights into antenna concepts such as directivity, antenna gain, side-lobe level, beamwidth, reference/cross polarization, and near-far field relationship. This software package complements the existing Computer Applications for Electromagnetics Education (CAEME) array and wire antenna software packages.

Reflector antennas have been the subject of much attention in the past several decades. As a result, a wealth of information in the form of antenna handbooks, and more recently, software packages are available for design and analysis of complex reflector antenna systems. These materials are used primarily by antenna engineers and researchers in the field, and their use might be beyond the scope of the interest of undergraduate electromagnetics students. In addition, software packages dealing with general multiple reflector antenna systems are too large in terms of memory requirement and computational time to be useful for educational purposes. In this project, we are focusing our attention on single reflector antennas with single feed. The antenna configuration can consist of a symmetrical or offset reflecting surface and a feed with arbitrary orientation. Many properties and radiation characteristics of reflector antenna systems such as directivity, side-lobe level, beamwidth, polarization, scanning, and near-far field relationship can be addressed by studying such an antenna system. The software package is designed to be user-friendly and has a reasonable turnaround time in a PC environment. This software package can be effectively integrated with reflector antenna chapters in one of the standard antenna textbooks such as [1-3].

This paper is organized as follows. The method of procedure is described in section II. Software capabilities are described in section III, and the concluding remarks are given in section IV.

II. Explanation of Procedure

The radiation characteristics of reflector antennas are commonly computed using two methods, Equivalent current distribution method and Aperture distribution method [4-6]. Both methods produce similar far field radiation characteristics for the main beam and nearby side lobes. The far-away lobes are dominantly affected by the reflector boundary

and reflector support structure. The treatment of these effects are beyond the scope of the interest of the undergraduate electromagnetics students, and are not addressed here. The current distribution method makes use of the Physical Optics approximation of the equivalent current distribution on the main reflector. This current distribution is then integrated over the reflector surface to yield the radiated field. The aperture distribution method is based on the computation of the reflector scattered field on an equivalent aperture plane perpendicular to the reflector axis. The radiated field is then computed using an aperture technique such as the Plane Wave Spectrum (PWS) method.

In this project, we develop a software which produces the near, Fresnel, and far radiated fields. Both the equivalent distribution method and the aperture method are implemented for comparison purposes, using the following formulations.

i. Equivalent Current Distribution Method. The equivalent current distribution on the main reflector is

$$\vec{J}(\vec{r}) = 2\hat{n} \times \vec{H}^i(\vec{r}) \quad (1)$$

where \vec{H}^i is the incident field due to the feed, and \hat{n} is the unit normal vector to the reflecting surface. The feed radiation pattern is modeled by a $[\cos\theta]^q$ type feed which can control the polarization state and the radiation taper [4]. Realistic feeds such as open-ended circular and rectangular waveguides can be represented by proper adjustment of the parameters of this feed model [5].

Using the current distribution in Equation (1), the radiated field is calculated using the Physical Optics integration

$$\vec{E}(\vec{r}) = -j\omega \left(\vec{I} + \frac{\nabla\nabla}{k^2} \right) \vec{A}(\vec{r}) \quad (2a)$$

$$\vec{H}(\vec{r}) = \frac{1}{\mu} \nabla \times \vec{A}(\vec{r}) \quad (2b)$$

$$\vec{A}(\vec{r}) = \frac{\mu}{4\pi} \int_{\text{surface}} \vec{J}(\vec{r}') \frac{e^{-jkR}}{R} d\vec{r}' \quad (2c)$$

where k is the wave number, μ is the permeability, \vec{r}' is the position of the current on the reflector surface, and R is the distance from the current element to the observation point. \vec{I} is the unit dyad.

There are various techniques to evaluate this integral in the near, Fresnel, and far regions of the antenna system. It is well known that Equation (2) can be simplified in the far field region, and becomes

$$\vec{E}(\vec{r}) = -j\omega [\vec{I} - \hat{r}\hat{r}] \vec{A}(\vec{r}) \quad (3a)$$

$$\vec{H}(\vec{r}) = -j\frac{\omega}{\eta} \hat{r} \times \vec{A}(\vec{r}) \quad (3b)$$

$$\vec{A}(\vec{r}) = \frac{\mu}{4\pi r} e^{-jk r} \int_{\text{surface}} \vec{J}(\vec{r}') e^{jk \hat{r} \cdot \vec{r}'} d\vec{r}' \quad (3c)$$

where r is the distance from a reference point on the reflector antenna system (e.g., reflector apex) to the observation point, \hat{r} is the unit vector in this direction, ω is the operating radian frequency. Equation (3) is the standard equation which is normally covered in the undergraduate electromagnetics antenna courses. We use this equation as the building block to perform our computations. We compute the field quantities (E and H vector fields) by representing the current distribution by

$$\vec{J}(\vec{r}) = \sum_i \sum_j \vec{J}_{ij}(\vec{r}_{ij}) P_{ij}(\vec{r}) \quad (4)$$

where P is a mask function which takes on the value 1 when \vec{r} is within a neighborhood of a cell defined around \vec{r}_{ij} , and 0 elsewhere. Simply stated, the original current distribution is approximated by a set of current segments. The antenna radiated field is the Cartesian vector sum of the fields produced by these current segments, each computed in its local coordinate system [6]

$$\vec{E}(\vec{r}) = \sum_{ij} \Delta \vec{E}(\vec{r} - \vec{r}_{ij}) \quad (5)$$

where $\Delta \vec{E}(\vec{r} - \vec{r}_{ij})$ is due to the r_{ij} .th current segment, evaluated at the observation point \vec{r} . This particular representation of the current allows the use of Equation (3) for the near and Fresnel zones as long as the observation point is in the far field of the current segments

even if it is located in the near field of the reflector. This approach avoids some of the complicated mathematical manipulations for the computation of (2) in the near and the Fresnel zones which are typically presented in the graduate level antenna courses. This computational method can be implemented efficiently on a Personal Computer, and provides a clear picture of the computational issues in reflector antenna analysis.

ii. Aperture Integration Method. The aperture field is computed using Equations (2-4) by setting the aperture plane as the observation plane. The radiated field beyond the observation plane can be computed by the virtue of the Huygens' principle. We use the PWS method to perform this computation. The radiated field at any point beyond the aperture is

$$\vec{E}(x,y,z) = \int_{k_x} \int_{k_y} dk_x dk_y \vec{E}(k_x, k_y) e^{-j(k_x x + k_y y + k_z [z - z_{\text{aperture}}])} \quad (6)$$

where $\vec{E}(k_x, k_y)$ is the Fourier transform of the aperture field, and (k_x, k_y, k_z) satisfy the dispersion relationship, and k_z is

$$k_z = -\sqrt{k^2 - (k_x^2 + k_y^2)} \quad (7)$$

and specifies the propagating as well as the evanescent spectral components of the aperture field. Equation (6) is used to compute the radiated field parallel to the aperture plane. These two-dimensional field distributions can be used to animate the field propagation away from the radiating structures.

It will be illuminating for electromagnetics students to compare the two computational methods for field computation. In the far field region it can be shown that both methods produce the same analytical expressions, starting from an aperture distribution. We will provide all the relevant equations to demonstrate this equivalence in a chapter for the CAEME book.

III. Software Package

This software package consists of an input file, main program and an output file. The input file is self-explanatory and is divided into four segments which allow the specification of the operating frequency, reflector type, feed parameters, and observation points of interest, respectively. The main program is written in FORTRAN and

documented well for clear understanding of the program flow and the employed algorithms. The output file is formatted and the output variables are labeled clearly.

This software package can be used as a design tool for single reflector antennas. As such, this software can be used to study various properties of single reflector antenna system such as directivity, side lobe level, beamwidth, reference and cross polarization for linear, circular and elliptical polarized feeds. Specialized topics such as beam squinting and cross-pol minimization by feed rotation for offset configurations can also be addressed [7-8]. Field quantities in the near and Fresnel zones can also be computed by specifying the proper observation surfaces in the input file. These computations illustrate the transition of the collimated beam in the near field to far field radiation pattern. Near field computations are of importance in applications such as beam waveguide design, and field strength evaluations for biological studies.

Representative numerical results due to an aperture distribution are illustrated in Figures 1 and 2. Figure 1 shows the axial field computation for a uniform aperture distribution. The PWS method (Equation 6) and the P.O. integration method (Equation 5) are used for this computation. Figure 2 shows the three dimensional view of the electric field due to a uniform aperture distribution at several observation planes.

IV. Concluding Remarks

The objective of this project is to develop a user-friendly educational electromagnetics software for analysis and design of single reflector antennas. This software computes the near, Fresnel, and far radiated fields by the induced current method and the aperture integration method. Both computational methods are included to illustrate some fundamental electromagnetics concepts such as the Huygens' Principle, near to far field relationship, and the equivalence of the two methods. A flow chart of these methods is shown in Figure 3. This software can be effectively integrated in an undergraduate antenna course to study the characteristics of reflector antennas.

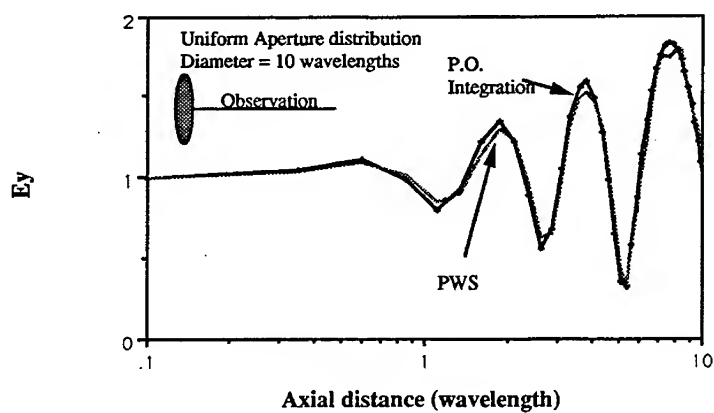


Figure 1. Axial field due to a uniform aperture distribution. The field is computed using the PWS method (Eq. 6) and the P.O. integration (Eq. 5).

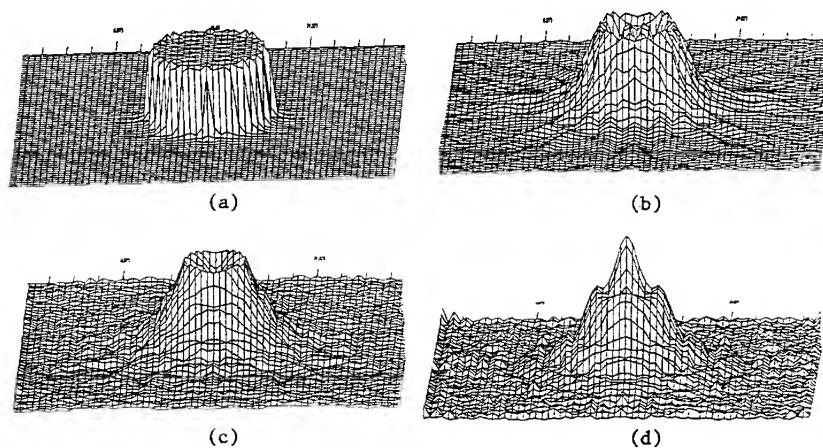


Figure 2. Field due to a uniform aperture distribution at several observation planes. (a) $Z=0.1$, (b) $Z=5.0$, (c) $Z=10.0$, (d) $Z=20.0$ wavelengths from the aperture.

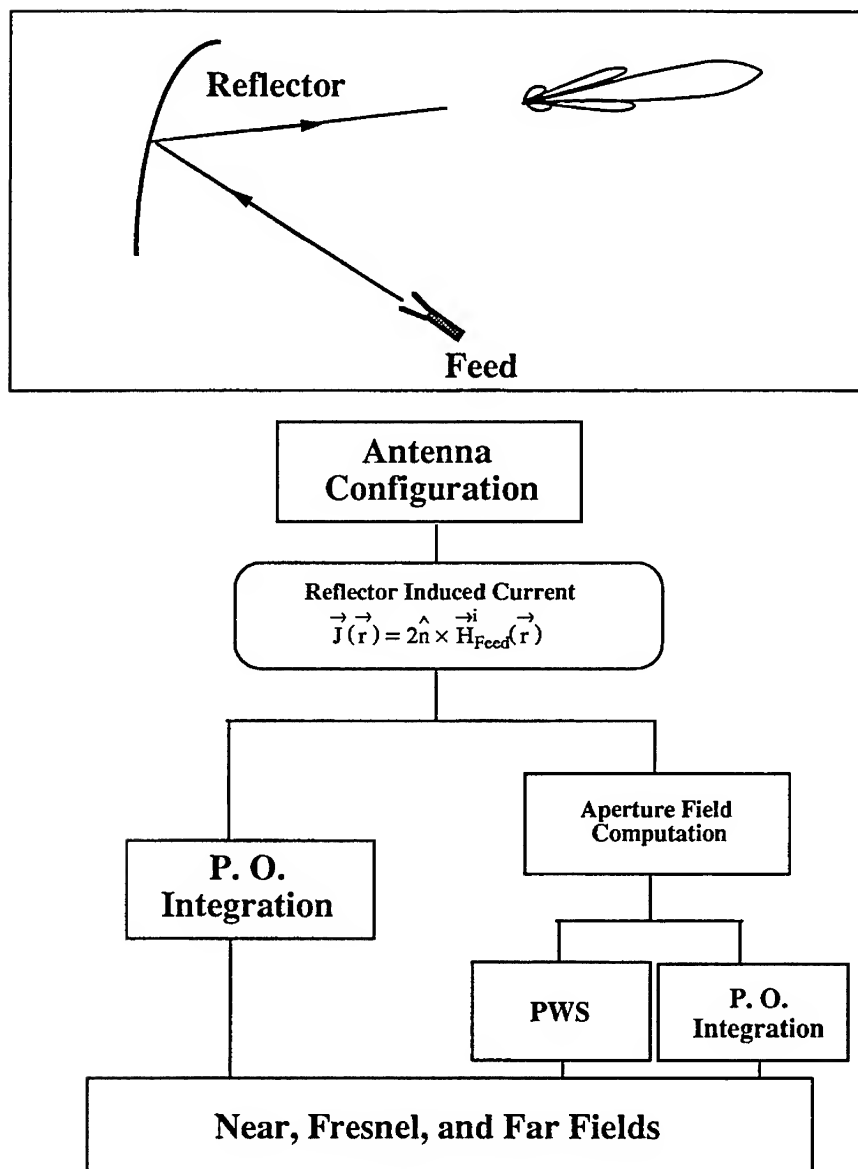


Figure 3. Block diagram of the computational methods for calculation of the near, Fresnel, and far fields of a reflector antenna.

Reference

- [1] C.A. Balanis, *Antenna Theory, Analysis and Design*, Harper & Row, Publishers, New York, 1982.
- [2] R.S. Elliot, *Antenna Theory and Design*, Prentice-Hall, Inc., New York, 1981.
- [3] W.L. Stutzman and G.A. Thiele, *Antenna Theory and Design*, John Wiley & Sons, Inc., New York, 1981.
- [4] B. Houshmand, S.W. Lee, Y. Rahmat-Samii, P.T. Lam, "Analysis of Near-Field Cassegrain Reflector: Plane Wave vs. Element by Element Approach," *IEEE Trans. Antennas Propagat.*, Vol. 38, No. 7, 683-701, 1990.
- [5] Y. Rahmat-Samii, "Reflector Antennas," Chapter 15, *Antenna Handbook Theory, Application, and Design*, eds. Y.T. Lo and S.W. Lee, New York: Van Nostrand Reinhold, 1988.
- [6] B. Houshmand, S.W. Lee, Y. Rahmat-Samii, "An Efficient Method for Analysis of Beam Waveguide Fed Cassegrain Reflector Antenna," *Journal of Electromagnetics Waves and Applications*, Vol. 4, No. 7, 683-701, 1990.
- [7] D.W. Duan and Y. Rahmat-Samii, "Beam Squint Determination in Conic-Section Reflector Antennas With Circularly Polarized Feeds," *IEEE Trans. Antennas Propagat.*, Vol. 39, No. 5, 612-619, 1991.
- [8] B. Houshmand, "Cross Polarization in Beam Waveguide Fed Cassegrain Reflector Antennas," *IEEE Trans. Antennas Propagat.*, Vol. 39, No. 2, 262-265, 1991.

Computer-Graphics-Aided Teaching and Learning Tool for Antennas

Authors:

Hamid Moradi, Swapan Chakrabarti and Prasad Gogineni
Department of Electrical and Computer Engineering
University of Kansas

Abstract

This paper presents a computer graphics aided software that is used for investigating the radiation pattern of antennas as functions of their design parameters. Electromagnetic field solutions for antenna problems consist of complex mathematical expressions, representing a three-dimensional distribution of radiated fields. Consequently, it is difficult to develop a clear understanding about how the overall shape of an antenna pattern depends on its design parameters. A visualization tool that can synthesize a radiation pattern in three dimensions will be very useful to study the behavior of the pattern as a function of its design parameters. This software will first synthesize the radiation pattern of an antenna as a 3D surface, and then it will provide numerical information about the pattern characteristics, such as the location of the principal maxima, half-power beamwidth, and the main-lobe to side-lobe power ratio. The combination of the 3D view and numerical information serves as a useful teaching and learning tool for basic antenna patterns. This software is developed using a 386-based PC that is equipped with a math coprocessor and a VGA card.

I. Introduction

For antenna problems, the electromagnetic (EM) field solutions are mathematically complex[1]. Even for simple antennas it is difficult to develop a clear understanding regarding the distributions of the radiation patterns as functions of their design parameters. Consequently, a visualization tool [2] that will provide three dimensional views of the radiation pattern of an antenna as functions of its design parameters, will be very useful for both teaching and learning. At the University of Kansas, we have developed a computer-graphics aided software to enhance student's understanding about the characteristics of the radiation pattern of antennas. This software allows students to get an interactive learning experience about the affect that each antenna design parameter has on the radiation pattern of that antenna. In order to run this software, the students should be aware of the theoretical foundations behind the design of the antenna of interest. The rest of the paper will be used to develop a thorough understanding of the effective usage of this software.

In Section II, we will present the computer-graphics techniques used to synthesize the 3D radiation pattern of antennas. In Section III, the hardware and software requirements to run the program will be introduced, and a global view of the different stages of software execution will be presented. In Section IV, we will show how this

software can be used to learn about the characteristics of the 3D radiation pattern of a planar array. In Section V, concluding remarks and future extensions of this project will be presented.

II. Synthesis of the Radiation Pattern of Antennas

Antennas are basically metallic devices, usually available in the form of wires, discs, or horns, whose primary purpose is to receive or transmit electromagnetic waves. When used as a transmitter, the antenna will be excited electrically, so it can radiate electromagnetic waves out of the antenna into the open space. Depending on the specified requirements such as directivities, half power beamwidths, and main-lobe to side-lobe power ratio [1], different types of antennas can be selected. The geometric and excitation parameters of the antennas can be varied to satisfy the design requirements with good precision. Although mathematical expressions are readily available to describe the radiation pattern of most antennas, approximate solutions are frequently used to describe antenna characteristics. Hence a visualization tool aided with numerical results will be useful not only to see the entire pattern in 3D space but also to study the affect of the design parameters on the antenna's radiation pattern.

Since the magnitude of the electric field ($|E|$) radiated from an antenna is expressed as functions of the polar (γ) and azimuthal angle (δ), our next objective will be to introduce a modified coordinate system that is widely used for representing 3D radiation pattern of antennas. Mathematically, the transformation between the conventional and modified coordinate system can be given by

$$P = \frac{(2.a)}{\pi} \gamma \cdot \cos \delta \quad (1)$$

$$Q = \frac{(2.a)}{\pi} \gamma \cdot \sin \delta \quad (2)$$

$$R = |E| \quad (3)$$

where a is the size of the semimajor axis used for accommodating maximum value of the polar angle γ . The points A,B,C,D shown in Fig. (1a) will take the positions of A' , B' , C' and D' , respectively, in the modified coordinate system shown in Fig.(1b). It is clearly evident that the points A' , B' , C' and D' constitutes a surface element in the three dimensional space whose projection on the computer screen plane (Q-R plane) will be a polygon. At this point we can treat the surface bounded by A' , B' , C' , D' as a solid surface and use a conventional shading rule to provide a realistic view of the surface element by computing the normal direction to this surface element. In this investigation we assumed a backscattering configuration and used a shading scheme derived from the full-wave solution of the scattering of the electromagnetic waves from metallic surfaces[3]. Using the above procedure, several radiation patterns are synthesized in Section-IV. In the next section we will discuss the hardware and software requirements that are necessary to synthesize the radiation pattern of antennas.

III. Hardware and Software Requirements.

(a). Hardware requirements

The hardware requirements can be outlined as follows:

1) Intel's 386 or 486 microprocessor based PC. A math coprocessor will be needed if 386 based system is used.

2) VGA Monitor.

3) Graphics board with ET4000 chip and

a) 1Meg memory for 1024x768 resolution with 256 colors

or,

b) 512K memory for 640x480 resolution with 256 colors.

Other graphics boards can also be used, but the graphics driver should be compatible with HGRAPH5 graphics library.

(b). Software requirements

The software requirements can be given as follows:

1) Executable program PATTERNS.EXE; the source code is written using Lahey FORTRAN and HGRAPH5 graphics Library.

2) Appropriate driver for the graphics board. For example, ET256.SCR for ET4000 chip.

3) A screen configuration file SCREEN.CFG, in which the driver and other graphic-board parameters are specified.

4) File BESS.OUT which provides data for the Bessel function of the first kind.

5) File FRES.COEF which tabulates the values of Fresnel Integrals for arguments over the range of 0 to 15.

(c). Different steps of software execution

This menu-driven software calculates and plots three dimensional radiation patterns of various antennas. The program proceeds as follows:

(1) First the user is prompted for the viewing parameters, such as the direction of light incidence, orientation of the pattern, etc.

(2) After the viewing parameters are entered, the main menu will pop-up. The user will then be required to select a type of antenna from the following list.

(a) Dipole Antennas, (b) Arrays, (c) Aperture Antennas, (d) Horns, (e) Loop Antennas, and (f) Reflector Antennas.

Within each type, there could be several antennas with different configurations, and the user will be required to select one for synthesizing its radiation pattern.

(3) Once the desired antenna is selected, a geometrical representation of the antenna, along with a brief description about that antenna, will pop-up on the next screen. At this time the user is prompted to type in the values of the design parameters of the antenna. These design parameters are highlighted in the geometrical description.

(4) After the user has typed in all the requested parameters, the program will calculate and plot a three-dimensional radiation pattern of that antenna. It usually takes between one to three minutes to plot a 3D radiation pattern.

(5) After a radiation pattern is synthesized, the user will be given the option to compute and print out the characteristics of the pattern, such as, location of the principal maxima, half-power beamwidth, etc. Then the software will present the following options to the user:

- a) Generate a radiation pattern for the same antenna with different design parameters, but without altering the viewing parameters. If this option is selected, the program returns to step (3).
- b) Select a new antenna without altering the viewing parameters. This option will take the program back to step (2).
- c) Select a new antenna and change the viewing parameters. This option takes the program back to step (1).
- d) Exit from this program.

This software has a modular structure. Hence a new antenna pattern can be easily added to our collection as follows:

- (i) Write a FUNCTION that calculates the distribution of the magnitude of the electric field for a new antenna.
- (ii) Add this antenna as a menu option so that it can be selected in step (2), if needed.
- (iii) A call to the FUNCTION is then included in the Case Statement of the GETLINE subroutine.

This software is developed to provide protection against system crashing due to the typing of illegal characters and out-of-bound values.

IV. Pattern Analysis for a Planar Array: An Example.

The configuration of a planar array is shown in Fig. 2. The magnitude of the far-field radiation pattern for such an antenna is given by [1]

$$|E(\gamma, \delta)| = \frac{1}{mn} \frac{\sin(\frac{m\psi_x}{2})}{\sin(\frac{\psi_x}{2})} \frac{\sin(\frac{n\psi_y}{2})}{\sin(\frac{\psi_y}{2})} \quad (4)$$

where

$$\psi_x = (k \cdot dx) \cdot \sin \gamma \cos \delta + \alpha_x \quad (5)$$

and

$$\psi_y = (k \cdot dy) \cdot \sin \gamma \sin \delta + \alpha_y \quad (6)$$

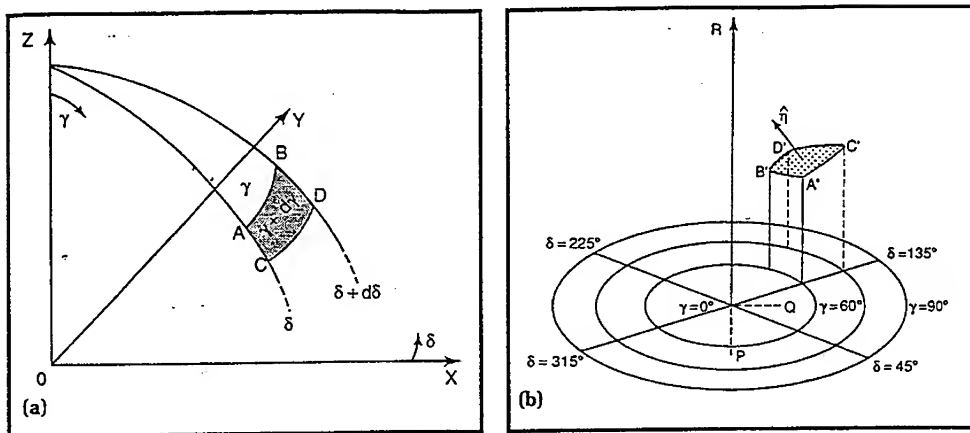
In equations (5) and (6), k represents the wavenumber of excitation, and m and n represent the number of elements used along the x and y direction. Also γ and δ define the polar and azimuthal angle of the far field observation point as shown in fig (1a). For $\alpha_x = \alpha_y = 0$; $m = n = 7$, and for $dx = dy = 0.5\lambda$, the radiation pattern for the planar array is shown in Fig.(3). In this case, the main lobe appears along $\gamma = 0$, $\delta = 0$ direction, and the half-power beamwidth is estimated by the software to be nearly equal to 0.14 radians. Next, keeping m, n, dx, dy fixed, we set $\alpha_x = -2.0$ and $\alpha_y = -1.0$, and the radiation pattern is found to have the principal maxima near $\gamma = 45$ and $\delta = 30$ degrees (see Fig.(4)). For $m = n = 11$ and $\alpha_x = \alpha_y = 0$, the radiation pattern is shown in Fig.(5). Figures(3) to (5) can be used to study the effect of the design parameters upon the radiation pattern of a planar array. It is clearly visible from Figs.(3) and (4) that the effect of changing progressive phase shifts is to change the direction of the main lobe. From Fig.(3) and Fig.(5) we can see that by increasing the number of antenna elements in both directions, the main beam can be focussed sharply, but at the same time more unwanted minor lobes appear in the pattern.

V. Concluding Remarks and Future Extensions

In this paper we have presented a computer-graphics aided software that can be used for teaching and learning about radiation pattern of antennas. This software is modular in nature, and therefore, information about any new antenna can be easily added as a new FUNCTION. One of the main drawbacks of running this software in a PC environment is that the software does not provide real-time performance. However, as a teaching or learning tool, it provides necessary information over a reasonable time interval (1 to 3 minutes). With the introduction of the next generation microprocessors, pattern generation time might be reduced significantly.

References

1. C. A. Balanis. 'Antenna Theory- Analysis and Design'. Ch: 6,11,12. Harper Row Publishers. N.Y. 1983.
2. S. Chakrabarti, J.C. Wong and P. Gogineni. 'Visualization of radiation pattern of antennas for synthesis and analysis'. IEEE Computer Graphics and Applications. vol. 10, No. 1, pp. 41-49, June 1990.
3. E.Bahar and S. Chakrabarti. 'Full-wave theory applied to computer aided graphics of 3-D objects'. IEEE Computer Graphics and Applications. vol. 7, No. 7, pp 46-60, Jan. 1987.



(a) Conventional 3D coordinate system (b) Modified 3D coordinate system

Figure 1. Surface element in two different coordinate systems.

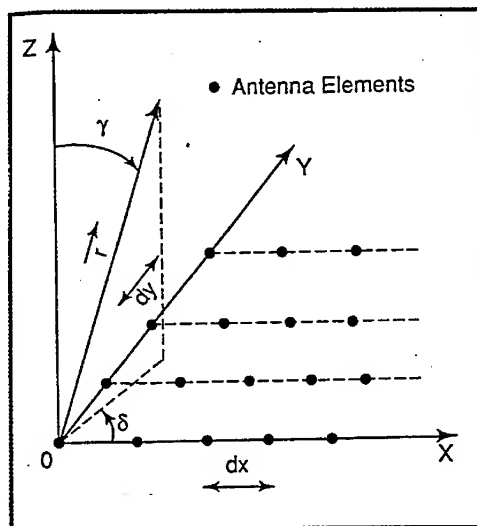


Figure 2. Configuration of a planar array.

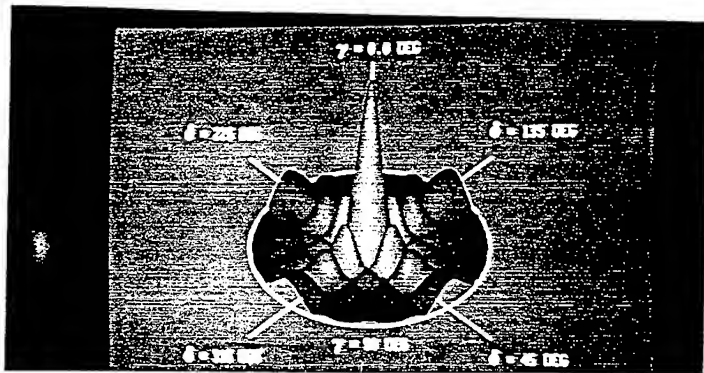


Figure 3. 3D radiation pattern for a planar array
 $m = n = 7, \alpha_x = \alpha_y = 0$

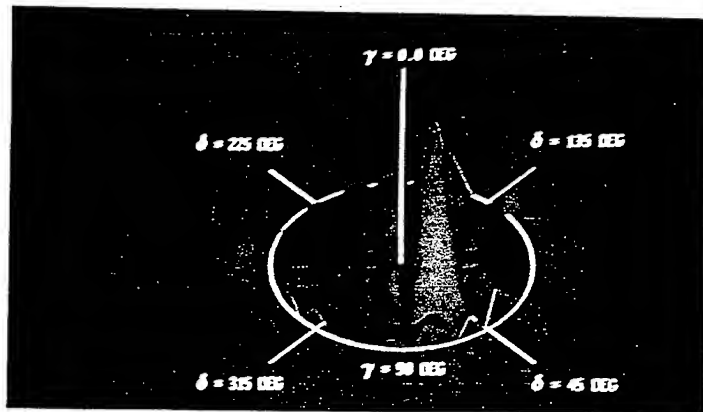


Figure 4. 3D radiation pattern for a planar array
 $m = n = 7, \alpha_x = -1.90, \alpha_y = -1.11$

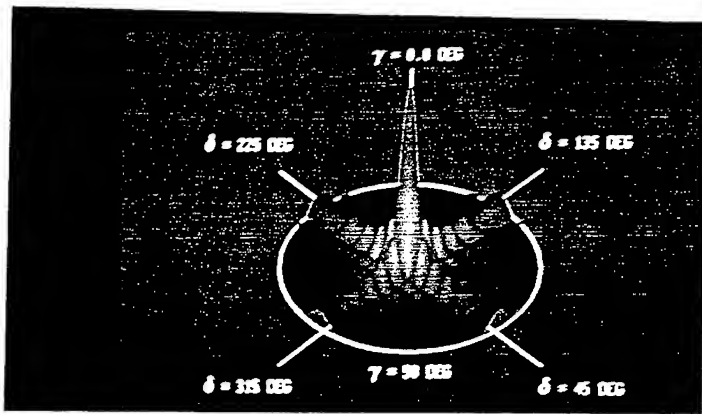


Figure 5. 3D radiation pattern for a planar array
 $m = n = 11, \alpha_x = \alpha_y = 0$

INTERACTIVE ANALYSIS OF ANTENNA ARRAYS WITH A PERSONAL COMPUTER

Atef Z. Elsherbeni and Patrick H. Ginn

Department of Electrical Engineering
University of Mississippi

INTRODUCTION

An antenna array is a group of antennas arranged in such a way to produce a radiated field with specific radiation characteristics which cannot be achieved by a single antenna. There are several different configurations used for grouping individual antennas into arrays. The most common array configurations are linear (uniform, nonuniform, binomial, etc.), two-dimensional (circular, rectangular, etc.), and three-dimensional (cubic, spherical, etc.). Different aspects of the analysis of antenna arrays have been dealt with in several text books [1-4]. Computer aided instructions are also available for selected types of arrays [5-7]. The objective of this software package is to provide a comprehensive coverage for the analysis of antenna arrays that can be used for undergraduate education. The "ARRAYS" (version 2) software package is designed to help students understand, in an interactive and visual procedure, the analysis of many types of antenna arrays using the principle of pattern multiplication. Furthermore, this software provides a visual response, almost immediately, of the effects of changing any of the antenna parameters on its radiation pattern. This feature is important in familiarizing students with the elementary patterns of different types of antennas before using them in an array.

Version 2 of "ARRAYS" is developed as an upgrade of the first version of "ARRAYS" [8]. The most important features of this upgrade are: menu windows that can be controlled with a mouse or the keyboard cursor keys; multiple planes for calculating and observing the radiation patterns (the user can now choose up to three planes of observation which can be toggled during the viewing screens); single item editing, (the user can edit a single piece of data instead of re-inputting the entire list of data); the ability to save the computed radiation patterns for future display and analysis, user-defined data for element patterns and pattern scanning for specific levels by two distinct pointers.

HARDWARE SPECIFICATIONS

The "ARRAYS" program requires, as a minimum configuration, the following: 8088 Processor, 512 kbytes of memory, DOS 3.0, EGA Color Display, and One 360k Floppy Drive. The performance of the program can be enhanced if any of the following items is available: 386 or 486 processor, Math co-processor, Microsoft Mouse or compatible, and printer. To make a hard copy of any of the screens, the user should execute the command "GRAPHICS.COM" which is a part of DOS operating system before executing the "ARRAYS" program.

This work was supported in part by a grant from CAEME center and by a grant from NASA-Mississippi Space Grant Consortium.

PROGRAM DESCRIPTION

The "ARRAYS" program was developed to be as self explanatory as possible. There is, however, a need for the user to have a fundamental knowledge of antenna theory to receive the full benefit of the program. This section is provided to explain the screens of the program and other related parameters. The user should note that all distances and lengths are entered in wavelengths, and all phases are entered in degrees. Every screen has an exit option, and the function key "F10" may be used at any time in the program to quit.

Upon starting the program, the user will first see the main menu screen as shown in Fig 1. In the center of the screen is a menu window. Menu windows are evident by the red pointer and highlighted option. This particular menu prompts the user to choose either one-, two-, or three-dimensional array, arbitrary arrays, or to retrieve data from a file on disk saved by the program in a previous run. The user can use a mouse, if available, or use the up and down arrow keys to highlight the option of his or her choice, or press the first character of one of the shown options. Once the user has chosen the basic type of the array, a menu window will prompt the user to select the specific type of the array which depends on the previous selection. For example, if the user chose the three-dimensional array, the next menu would prompt the user for either a cubic or a spherical array. The user also has the option to return to the main menu from the secondary menu.

```

      ANTENNA ARRAYS
      Version 2.0

  -> 1-dimensional array
     2-dimensional array
     3-dimensional array
     Arbitrary array
     Retrieve data
     Quit

  Authorized user: CAEME members .... December 1992

  Copyright (c) 1992 Atef Elsherbeni
  Electrical Engineering Department, University of Mississippi

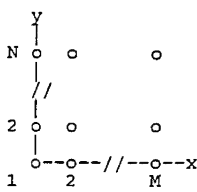
```

Fig. 1 The main menu screen of the ARRAY program.

After selecting the array type, the main menu screen will be replaced by the data input screen for whichever array was selected. As an example, Fig. 2 shows the input screen for a cubic array. A simplified array geometry is displayed on the right side of the screen. The type of array is printed at the top of the screen in the title section. On the left side of the screen, the user will be prompted to enter the array parameters. Some of the information will have to be entered from the keyboard, or the menu windows which have been included whenever possible.

FIELD PATTERNS OF A UNIFORM CUBIC ARRAY

Enter number of elements in x (1-25)



Array geometry
P levels in
z direction

Fig. 2 The input parameters screen for a cubic array.

If the user choses to continue, after entering all necessary array parameters, the input echo screen for the array will be displayed as shown in Fig. 3. The actual array geometry is shown on the right side of the screen and the parameters entered during the previous screen are listed on the left side of the screen. The options for this screen are displayed at the lower left corner of the screen. These options are to edit, continue, return to main menu, or quit.

CUBIC ARRAY

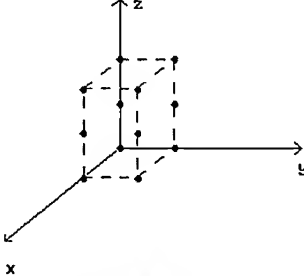
Number of elements in x direction = 2
y direction = 2
z direction = 3

Spacing in x direction = .5 lambda
y direction = .5 lambda
z direction = .5 lambda

Phase shift in x direction = 45 °
y direction = 45 °
z direction = 0 °

Observation plane: x-y
x-z
 $\phi = 90^\circ$

Press C to contiune
E to edit data
M to return to main menu
Q to quit



Array geometry

Fig. 3 The data verification screen for a cubic array.

The edit screen, if selected, will replace the echo screen as shown in Fig. 4. On the right side of the screen, the array parameters are displayed. By choosing an option, the user can change a single piece of input data and then, when all the editing is finished, can return to the echo screen by selecting the end edit option.

CUBIC ARRAY

→ Number of elements
 Spacing
 Phase shift
 End edit

Number of elements in x = 2
 y = 2
 z = 3
 Total number of elements = 12
 Spacing in x direction = .5
 y direction = .5
 z direction = .5
 Phase shift in x direction = 45 °
 y direction = 45 °
 z direction = 0 °
 Observation plane: x-y
 x-z
 φ = 90

Fig. 4 The editing screen for a cubic array.

When the user is satisfied with the input parameters, he or she can continue and proceed to the antenna element selection screen as shown in Fig. 5. This screen lists the available antenna elements in a mouseable window menu. The user should choose the element of preference followed by the desired orientation of the antenna element. The length of the antenna will be requested next if applicable. Additional parameters will be requested in accordance with the chosen antenna. As an example, if the user chooses the finite line source, he or she will have the following options for the current distribution on the element: triangular, cosine, or cosine on a pedestal. If the cosine distribution is chosen, the user will be prompted to enter n, which controls the roll-off. A value of 0 will create a uniform distribution, i.e., no roll-off.

By selecting the user defined pattern option from the element menu, the user may enter the pattern from the keyboard or load a pattern from a disk file (if a pattern was previously stored). Note that if a pattern is to be loaded from a disk file, the retrieved pattern must have the same number of observation planes as those chosen by the user when inputting the data for the array type. Otherwise, the pattern will be invalid and the program will return to the main menu. When the pattern is entered from the keyboard, the user will enter the pattern with normalized power levels. The user will have the option to save this pattern on a disk file if desired.

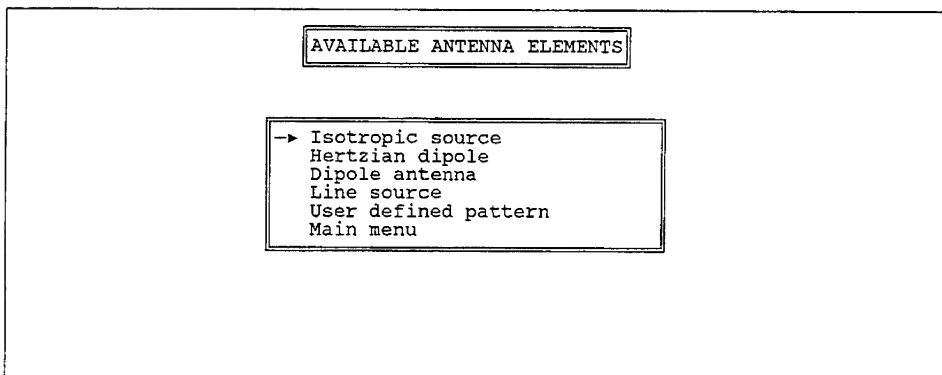
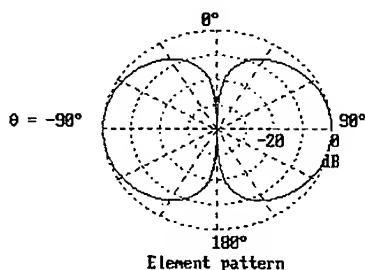


Fig. 5 The antenna element selection screen.

When the user continues, the element echo screen will appear as shown in Fig. 6. The radiation pattern for the element is displayed on the upper right corner of the screen. If the user has chosen more than one plane of observation, he or she can view the pattern in the other planes by pressing "V". On the lower right corner of the screen, the current distribution on the element will be displayed if applicable. Note that the isotropic element will not have a current distribution displayed since an isotropic source is simply a point source. On the left side of the screen the antenna element type and parameters are listed. The user can choose to try a different element by pressing "T" or to continue by pressing "C".

FIELD PATTERN OF THIN WIRE DIPOLE

Length of antenna = .45 lambda
Antenna oriented parallel to z axis
Observation plane: x-z



Press C to calculate the array pattern
I to try another element type
M to return to main menu
V to view pattern in next plane
Q to quit

Current distribution I(z)

Fig. 6 The element pattern screen for a dipole antenna.

After computing and displaying the element pattern, the program will calculate the array factor and the total pattern. The monitor will show a screen similar to the main menu screen except that the center of the screen will be flashing the statement "Calculating... please wait" and a horizontal bar graph will appear below this message. This bar graph will increase from left to right showing the user how far along the calculations are. Note that if more than one plane of observation was chosen, the bar graph will run through a complete cycle for each chosen plane.

When the calculations are finished, the final screen will appear as shown in Fig. 7. Pertinent information will be displayed at the top left corner of the screen. The element pattern will be displayed at the top center of the screen, the array factor will be displayed at the upper right corner of the screen, and the total pattern will be displayed at the lower right corner of the screen. User options will be listed at the lower left corner of the screen. One can choose to quit, return to the main menu, edit array parameters, try different elements, save the data to a disk file, or scan any of the displayed patterns.

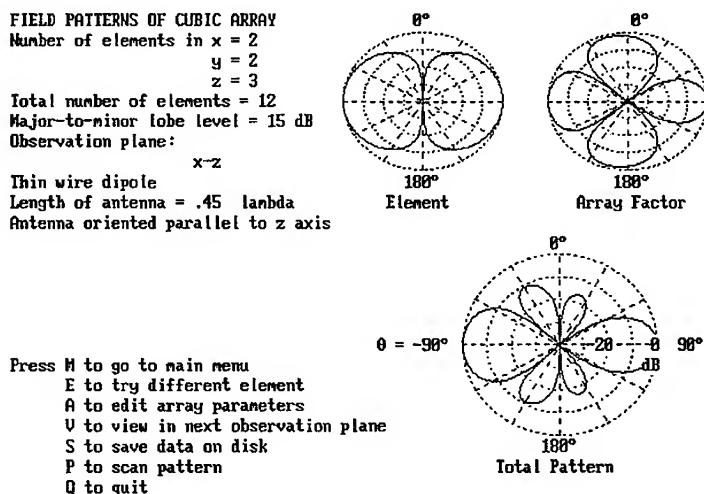


Fig. 7 The output screen for the patterns of a cubic array of dipole antennas.

The scan menu window will allow the user to choose the element, the array factor, or the total pattern to be scanned. Once the user chooses one pattern, the pattern scan screen will appear as shown in Fig. 8. The chosen pattern will be displayed at the right of the screen. On the left side, the angular positions and amplitudes of the scanning dots are displayed. The user can use the left and right arrow keys to move the dots clockwise or counterclockwise. By pressing "T" the user can change control from one scanning dot to the other one. The user can choose to scan a different pattern or return to the main menu.

CUBIC ARRAY

Scanning total pattern

Observation plane:

x-z

Active dot	Angle	Amplitude (dB)
dot 1	22	-16.697
	330	-18.798
Difference =	52	-5.899
	dot1 - dot2	

Current scanning step = 1 °

Press I to increase scanning step
 D to decrease scanning step
 T to toggle between scan dots
 S to scan a different pattern
 R to return to output screen
 M to return to main menu
 → or > to scan clockwise
 ← or < to scan counterclockwise

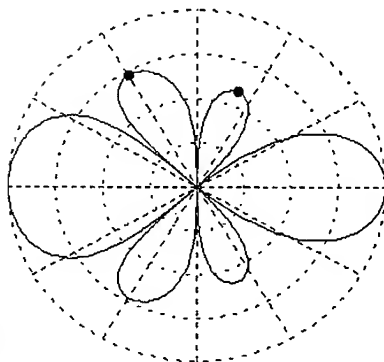


Fig. 8 The scan screen for the total pattern of a cubic array of dipole antennas.

If the user chooses to use the save pattern option in the final output screen, another screen will appear which will ask for a data drive and a name for the disk file. It is not necessary to put an extension to the file name since the program will supply "ARD" as an extension. To retrieve pattern data from the main menu, the program will ask for a data drive and will show all files on that chosen drive with the extension "ARD". The user can enter the name of the file without using any extension. Once the data is loaded, the program will proceed directly to the final screen. The user can then manage the data normally.

REFERENCE

- [1] W.L. Stutzman and G.A. Thiele, *Antenna Theory and Design*. John Wiley & Sons, New York, 1991, Ch. 3.
- [2] C. Balanis, *Antenna Theory*. Harper & Row, New York, 1982, Ch. 6.
- [3] J.D. Kraus, *Antennas*. McGraw-Hill, New York, 1988, Ch. 4.
- [4] E.A. Wolff, *Antenna Analysis*. Artech House, Inc., MA, 1988, Ch. 6.
- [5] D. Pozar, *Antenna Design Using Personal Computers*. Artech House, Inc., MA, 1985.
- [6] N.N. Rao, *Elements of Engineering Electromagnetic*. Third Edition, Prentice Hall, 1991, pp. 584-591.
- [7] S.J. Blank and S.L. Wang, "Tutorial Computer-Aided Instruction for Linear Antenna Array Theory and Design," in NSF/IEEE Center for Computer Applications in Electromagnetic Education Software Book, Vol. I, Editor: M.K. Iskander, Salt Lake City, 1991, Ch. 12.
- [8] A.Z. Elsherbeni and P.H. Ginn, "ARRAYS: A Software Package for the Analysis of Antenna Arrays," *Journal of Computer Applications in Engineering Education (CAE)*, Vol. 1, No. 1, pp. 109-117, September/October 1992.

SESSION 16 - "RCS"

Chair: Dr. Shian U. Hwu, Co-Chair: Dr. A.K. (Tony) Brown

Computing the Time Domain EM Scattering from Large Open-Ended Cavities Using the SBR and GRE Ray Shooting Methods¹

Robert J. Burkholder and Prabhakar H. Pathak
The Ohio State University ElectroScience Laboratory
1320 Kinnear Road, Columbus, Ohio 43212

1 Introduction

The electromagnetic (EM) scattering from electrically large open cavities can be a very significant contributor to the overall radar cross section (RCS) of objects containing such cavities. In particular, the EM scattering from jet engine inlets and exhausts is often the most prominent feature contributing to the RCS of modern jet aircraft. The time domain EM scattering from aircraft, i.e., the reflected radar return from a target as a function of time, may be used for radar target identification. It is therefore important to understand and accurately predict the time domain behavior of EM fields scattered by large cavities, such as jet inlets and exhausts. In particular, it is known that open cavities scatter dispersively in the time domain, i.e., the reflected radar pulse is distorted and spread out in time, depending on the depth, complexity and electrical size of the cavity. This is in contrast to a simple scattering mechanism, such as corner diffraction or specular reflection ("glint"), which would generally not change the shape of the reflected radar pulse. Therefore, it is important that the analysis method be able to predict the time dispersive behavior of cavities. Unfortunately, it is generally not possible to obtain an exact solution to this problem, either in closed form or by using a numerical technique, due to the size and complexity of these types of cavities.

Two versatile but approximate high-frequency asymptotic ray shooting methods have been developed for calculating the RCS of electrically large arbitrarily shaped cavities: the shooting and bouncing ray (SBR) method [1, 2], and the generalized ray expansion (GRE) method [2, 3]. It is of interest here to apply these two ray methods for cavity RCS prediction, and evaluate their ability to accurately and efficiently predict the time domain response. This is achieved by analyzing rectangular and circular open-ended waveguide cavity geometries for which there exists a waveguide modal reference solution [4]. The cavities are perfectly conducting and terminated by a flat plate (short circuit) at the closed end. Furthermore, the cavities are surrounded by free space and have no external supporting structure. Although these geometries have nowhere near the complexity of an actual jet engine cavity supported by an airframe, they are useful for evaluating the merits of the ray methods for modeling the coupling into and propagation of fields inside open-ended cavities.

¹Sponsored by the Air Force Wright Laboratory Target Recognition Technology Branch, Wright-Patterson AFB, Ohio, and funded by the AFOSR Summer Research Program.

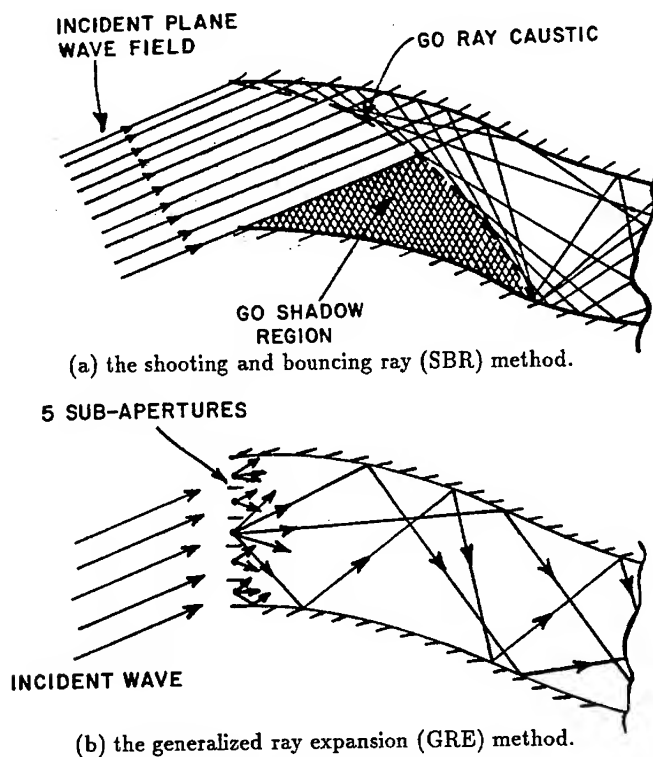


Figure 1: Ray launching methods (shown in 2-D).

2 The SBR and GRE Ray-Shooting Methods

This section presents a qualitative description of the SBR and GRE ray-shooting methods. Details concerning their implementation may be found [1-3], and a description of the waveguide modal reference solution may be found in [4].

In the SBR method, a dense grid of parallel ray-tubes is launched into the cavity, representing the geometrical optics (GO) portion of the incident (illuminating) plane wave which is intercepted by the open end, as shown in Figure 1(a). The individual ray-tubes are tracked inside the cavity via multiple reflections (or bounces) from the inner cavity walls using the laws of GO, until they exit again through the open end (Figure 2). The scattered field is obtained by performing an aperture integration over the equivalent Huygen's sources defined by the projections (or footprints) of the ray-tubes in the open end as they exit the cavity.

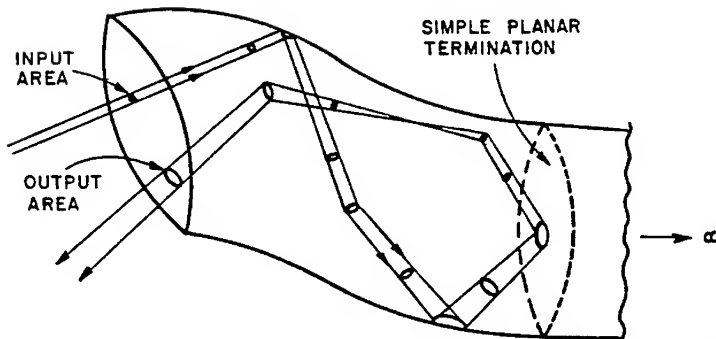


Figure 2: GO ray-tube tracked inside a waveguide cavity until it exits through the open end.

The SBR method is very versatile and easy to apply, but it tracks only the GO field inside the cavity, ignoring the fields diffracted into the cavity by the rim at the open end. As Figure 1(a) shows, this leaves GO shadow regions which in reality contain the diffracted field. The GRE method intrinsically includes these diffracted fields by launching rays in all directions into the cavity. Specifically, the aperture at the open end is broken up into a small number of subapertures, and ray-tubes are launched radially into the cavity from the phase centers of the subapertures, as shown in Figure 1(b). Each ray-tube is weighted by the far-field radiation pattern of its subaperture when the subaperture is excited by an external field incident on the open end of the cavity. The subaperture far-field radiation pattern is obtained by integrating equivalent currents over the subaperture, which are defined by the incident field. Once launched in this manner, the ray-tubes are treated in exactly the same manner as the SBR ray-tubes, i.e., they are tracked inside the cavity via multiple GO bounces and aperture integration is used to obtain the scattered field.

In the SBR method, a new grid of ray-tubes must be tracked for each plane wave incidence angle. An advantage of the GRE method is that only the amplitude weighting of the ray-tubes is dependent on the incident field, and not the initial launch directions. Therefore, a sufficiently large number of ray-tubes can be launched, tracked inside the cavity, and stored; later the rays can be weighted and summed to give the cavity scattered field for any number of incidence angles. However, a much larger number of GRE ray-tubes is required compared with the number of ray-tubes used in SBR for a single incidence angle. Therefore, SBR is generally more efficient than GRE unless a sufficiently large number of incidence angles is required (typically, on the order of 100 or more). On the other hand, GRE is expected to be more accurate because it includes diffraction effects.

3 Numerical Results

The open-ended waveguide cavities analyzed here are axially straight with square, rectangular or circular cross-sections and have a flat plate termination normal to the waveguide axis. They are perfectly conducting and only the scattering from the cavity interior is included. All external scattering effects are ignored, such as the direct scattering from the rim at the open end. The cavities are illuminated by a vertically polarized EM plane wave incident in the horizontal plane. The time domain scattering is obtained by inverse Fourier transforming the frequency domain RCS in the band from 8 to 12 GHz at 128 equally spaced steps. The frequency domain data is weighted with a Kaiser-Bessel windowing function ($\alpha = 2$) before transforming to minimize unwanted sidelobe contamination of the time domain response. The result is a "band-limited" time domain impulse response.

Figure 3 shows the time domain impulse response of an open-ended waveguide cavity with a square cross-section. At midband this cavity is 6.67 wavelengths across and 26.67 wavelengths long. The SBR method predicts well the main impulse, corresponding to the GO field return, but misses the side impulses which are dispersed in time. The dispersion is due to the fields diffracted into the cavity by the edges at the open end which propagate inside the cavity along different paths than the GO field. These paths are shorter or longer than the GO paths, and so the diffracted fields may arrive back at the observer advanced or delayed in time with respect to the GO field. Notice that the GRE solution predicts both the main impulse and the most significant time dispersive effects because both the GO and diffracted fields are intrinsically included in the method. However, the amplitudes of the peaks are not in perfect agreement because of the approximations associated with the GRE ray launching scheme and ray shooting methods in general.

Figure 4 shows the impulse response for a much larger rectangular cavity². The dimensions of this cavity are comparable to an F-15 engine inlet duct. At midband the cavity is 30.48 wavelengths high, 20.32 wavelengths wide, and 152.40 wavelengths long. For this case the dispersion effect is still noticeable in the modal and GRE results, but is much less significant than in the smaller cavity of Figure 3. As before, the SBR method predicts the main impulse well, but not the time dispersed impulses.

Figure 5 shows the impulse response of a very large open-ended circular waveguide cavity. Again, the dimensions of this cavity are comparable to an F-15 engine inlet duct. At midband the cavity is 27.09 wavelengths in diameter and 152.40 wavelengths long. The curved walls of this cavity cause the GO fields to diverge as they bounce around inside, giving rise to dispersion-like effects in the time domain. So in this case, the SBR method gives a more spread out time domain impulse response compared with a rectangular waveguide cavity which has planar walls, and agrees very well with the modal reference solution. The dispersion caused by diffraction effects is still present in the modal and GRE solutions, but these effects are not noticeable on the scale of the plots used in Figure 5. The GRE result

²In Figures 4 and 5, the time scale is shifted by 30 nanoseconds (ns) due to the particular inverse Fourier transform routine used to obtain the time domain response from the frequency domain data. The actual times for the impulse responses of Figures 4 and 5 are exactly 30 ns greater than those shown.

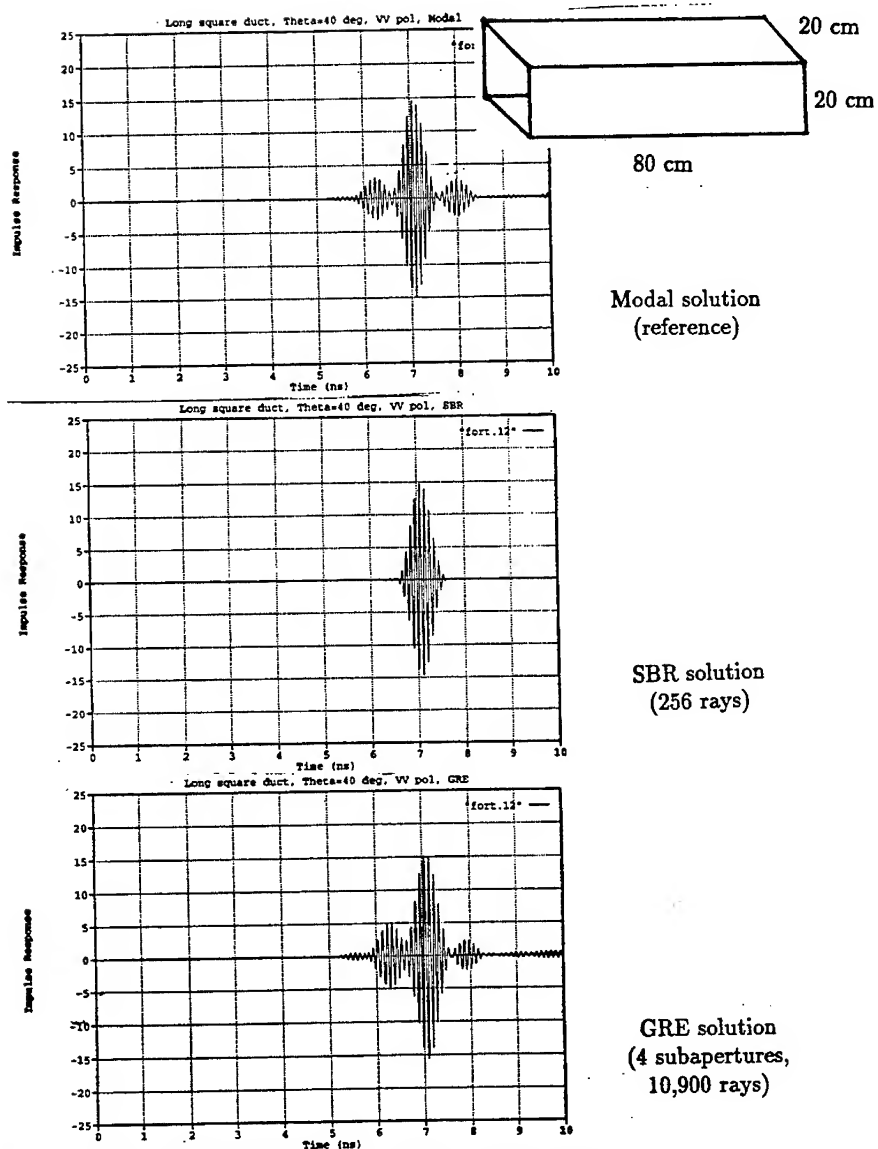


Figure 3: Cavity impulse response of an open-ended square waveguide cavity, illuminated 40° off-axis.

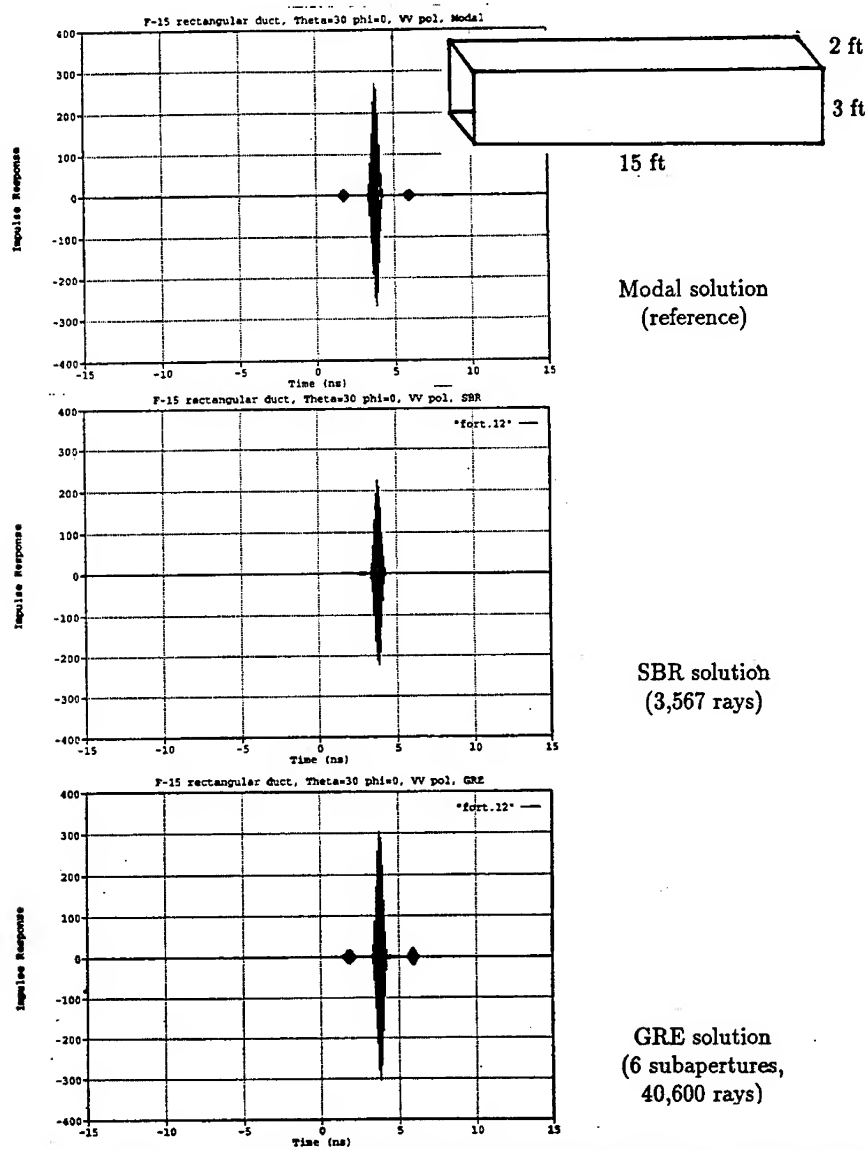


Figure 4: Cavity impulse response of an F-15 sized open-ended rectangular waveguide cavity, illuminated 30° off-axis.

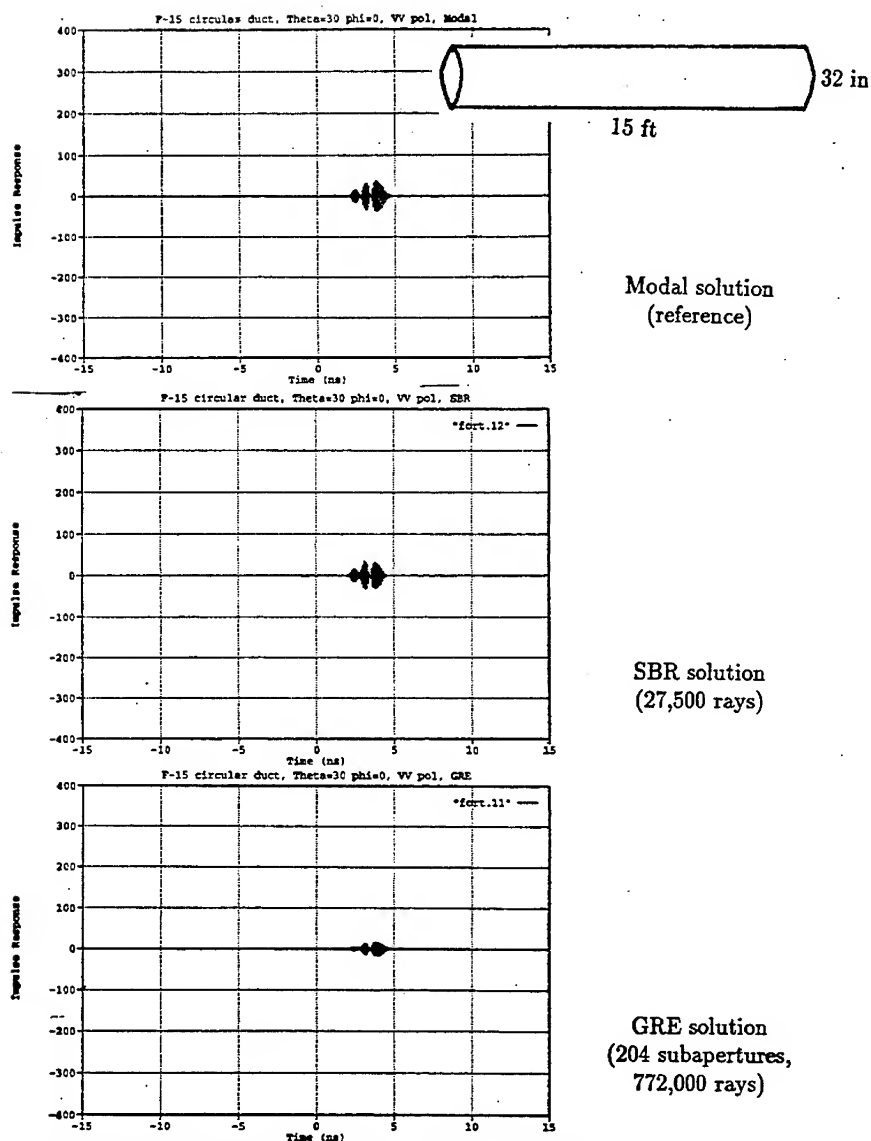


Figure 5: Cavity impulse response of an F-15 sized open-ended circular waveguide cavity, illuminated 30° off-axis.

predicts the peaks in the right location, but the amplitudes of the peaks are in somewhat worse agreement.

4 Conclusions

It has been shown that open cavities exhibit a dispersive effect on the EM scattering of a plane wave in the time domain. This is due to the fields diffracted into the cavity by the rim at the open end, which undergo multiple bounces inside the cavity before re-radiating out through the open end. This time dispersive effect differentiates open cavities from simple scatterers which would exhibit a more localized return in the time domain.

The SBR method is very versatile and easy to implement, but it does not predict cavity time dispersion effects caused by diffraction because the fields diffracted into the cavity by the open end are not included. However, it has been shown that for very large cavities the diffracted field is much weaker than the GO field, and the SBR method predicts very well the dominant time domain return associated with GO.

The GRE method is versatile and predicts cavity time dispersion effects because the fields diffracted into the cavity by the open end are intrinsically included. However, this method is not as straightforward to implement as the SBR method because the aperture at the open end of the cavity must be gridded up into subapertures. The GRE method is sometimes not as accurate as the SBR method for very large cavities because additional approximations are introduced by the subaperture gridding. Nevertheless, dispersive effects are expected to be very significant for realistically complex jet engine cavities because the engine face will diffract strongly, unlike the flat "short circuit" terminations used here; therefore, a method such as the GRE which includes dispersion will be required.

References

- [1] H. Ling, R. Chou, and S.W. Lee, "Shooting and Bouncing Rays: Calculating RCS of an Arbitrary Cavity," *IEEE Trans. on Antennas and Propagation*, Vol. AP-37, No. 2, pp. 194-205, February 1989.
- [2] R.J. Burkholder, R. Chou and P.H. Pathak, "Two Ray Shooting Methods for Computing the EM Scattering by Large Open-Ended Cavities," *Computer Physics Communications*, Vol. 68, pp. 353-365, 1991, North-Holland Science Publishers.
- [3] R.J. Burkholder and P.H. Pathak, "High-Frequency Electromagnetic Scattering by Open-Ended Waveguide Cavities," *Radio Science*, Vol. 26, pp. 211-218, January-February 1991.
- [4] P.H. Pathak and R.J. Burkholder, "Modal, Ray and Beam Techniques for Analyzing the EM Scattering by Open-Ended Waveguide Cavities," *IEEE Trans. on Antennas and Propagation*, Vol. AP-37, pp. 635-647, May 1989.

Target Facetization Level and the Effect on Xpatch Predictions

E. M. Miller, D. J. Andersh, A. J. Terzuoli Jr.
Air Force Institute of Technology
Wright-Patterson AFB Ohio

1 Abstract

Xpatch V4.0¹ [1] is a Radar Signature prediction code that provides both frequency domain radar cross section predictions and time domain results for a flat faceted triangular geometry file. It is a fully polarimetric code that performs mono-static and bi-static predictions and provides the capability to rotate facets, calculate shadowing and blockage, perform multi-bounce calculations, and calculate scattering from radar absorbing materials (RAM). The prediction method is based on the Shooting Bouncing Ray method, Physical Optics and the Incremental Length Diffraction Coefficient Formulation (ILDC) [2] to obtain the target scattered field.

This paper² analyzes the limitations of 3-D model facetization on the radar signature predicted by Xpatch. Predictions are compared against exact solutions and different facetizations for two primitives and one complex target. A more detailed analysis is available in the thesis, "Validation of Xpatch Radar Signature Predictions Using Flat Facet Geometries" [3].

2 Introduction

Before Xpatch is used to predict the radar signature of facetized models, the limitations of the flat facet approach must be understood because measurements we use as reference are not always exact. There is an uncertainty associated with the target's position when it is put on the rotator in the measurement chamber. Depending on the care taken, and measurement equipment used, the target's position could easily be off by 1° or more in both azimuth and elevation. These small changes in position will effect the measured azimuth scans and range profiles. In addition, changing the level of flat facetization on the associated geometry file will have an effect on the signature prediction. Therefore, predictions cannot be judged blindly against the measured data. To minimize the uncertainty, a target with an exact solution, such as a sphere, is an excellent choice for comparison against Xpatch predictions. A test was conducted to evaluate Xpatch's frequency response predictions on a set of 6" spheres, each with four different facetization levels. In addition, the effect on the azimuth scan of an almond and the range profile of a complex missile are evaluated. This paper presents the results of a facetization study performed on these three models. Comparisons are not made against measured data, only between predictions.

2.1 Sphere

A 6" sphere was chosen to test the frequency response prediction with respect to facetization level. The exact Mie series was used for comparison and is shown in Figure 1 along with a curved facet prediction made

¹A High Frequency RCS Computation Code for Flat Patches with Interactions, written by S. W. Lee of the University of Illinois

²This research was sponsored by the US Air Force Wright Laboratory, Avionics Directorate, Target Recognition Branch, WL/AARA, ASC WPAFB OH

by CADDSCAT [4], on the sphere. Notice the curved surface model only needed 112 facets to show good agreement with the Mie series.

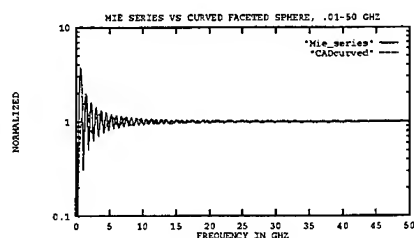


Figure 1: 6 inch Sphere, 112 Curved Facets at 0AZ, 0EL

Four, Advanced Computer Aided Design (ACAD) [5], models were built for the 6 inch sphere by progressively increasing the number of flat facets in each. The number of facets ranged from 360 to 9,800 as noted under the plots.

Figures 2(a) through 3(d) give a visual representation of the the four facetization levels and their associated test plots. Each sphere is "shown" at the aspect angle of 45° azimuth and 45° elevation. Xpatch frequency predictions on each sphere, however, were made, at four different aspect angles. Only one quadrant was included since the facetization is symmetric.

The chosen aspect angles were:

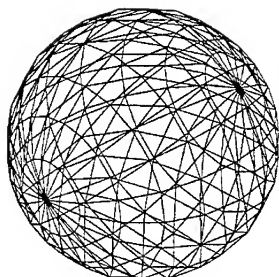
- "0" = 0° AZ and 0° EL
- "90" = 90° AZ and 0° EL
- "9090" = 90° AZ and 90° EL
- "45" = 45° AZ and 45° EL

Combining two pieces of information, you obtain the legend for the test plots. For example: sph290 is sphere #2 at aspect angle 90.

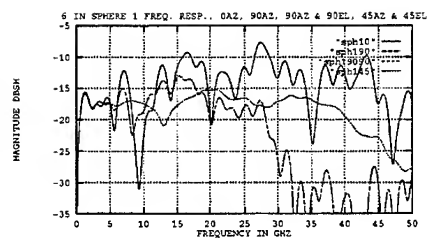
The fluctuations of the frequency response are a direct result of the number of facets. Sphere #1 has the smallest number and the prediction fluctuates wildly over nearly the whole range. The best prediction, compared to the Mie series, is the expected sphere #4 since it has the highest number, or smallest facets.

Figure 4(a) is a plot of the most forgiving aspect angle (45° azimuth and 45° elevation) for each facetization level. All predictions were compared against the exact Mie series for the sphere, with the 9,800 facet model deviating very little. The error associated with flat facet geometries is most easily seen by comparison with the curved model. This is shown in Figure 4(b). While the 45° AZ, 45° EL aspect agrees with the curved model and hence the Mie series, the 0° AZ and 0° EL deviates considerably as the frequency increases beyond 30 GHz.

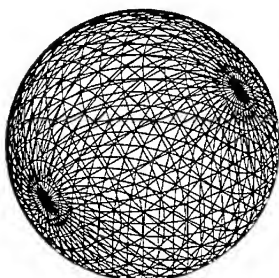
Clearly, the flat faceted model has problems associated with it. The curved faceted model prediction was closest to the exact solution and was aspect angle invariant, while, the flat faceted model can fluctuate badly with an aspect change. In addition, the curved model uses two orders of magnitude fewer facets than its flat counterpart to obtain equal results. If a flat faceted model is to be used in the prediction of a target, care must be taken to understand how the facets are laid out. If not, the results could have a larger error associated with them than anticipated.



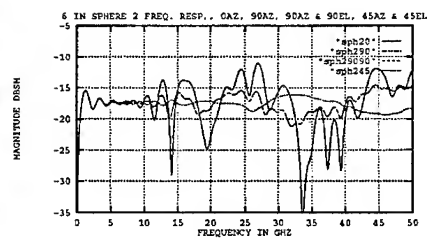
(a) Sphere 1



(b) 360 Facets, 4 Aspect Angles

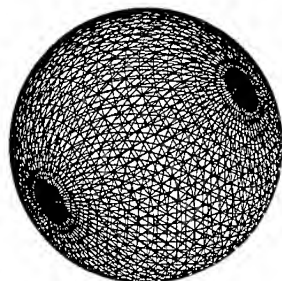


(c) Sphere 2

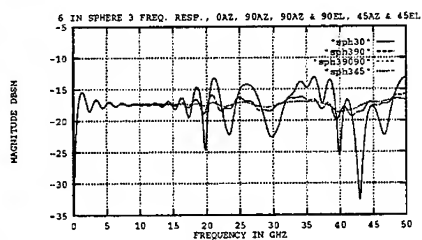


(d) 1520 Facets, 4 Aspect Angles

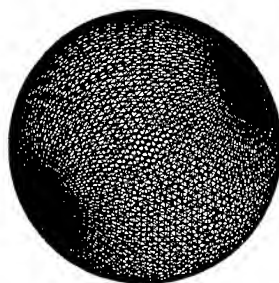
Figure 2: Sphere Facetization Effects With Changing Aspect



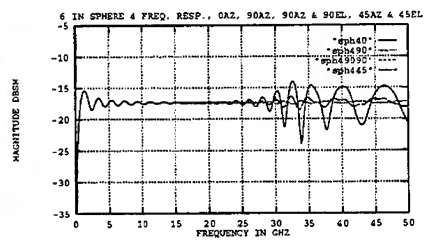
(a) Sphere 3



(b) 3480 Facets, 4 Aspect Angles



(c) Sphere 4



(d) 9800 Facets, 4 Aspect Angles

Figure 3: Sphere Facetization Effects With Changing Aspect

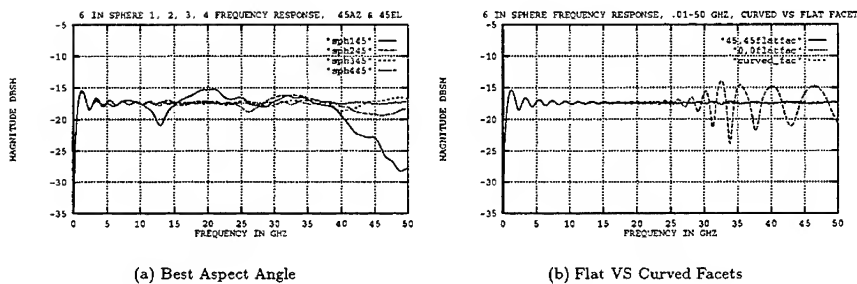


Figure 4: Frequency Response VS Facetization

2.2 Almond

One of the stealthiest of the primitive targets is the almond. The shape and triangular flat facet layout can be seen in Figure 5(a). The almond was sized to match the bench marked primitive measurements made by China Lake [6]. Therefore the dimensions were: $l = 9.936''$, $h = 1.28''$, $w = 3.842''$. In order to ensure at least five wavelengths over the target as recommended by Knott[7], the prediction was made at 18 GHz. In order to have a reasonable facet distribution, the following three levels were used:

coarse 454 facets
 medium 8,032 facets
 fine 29,394 facets

Figure 5(b) shows the variations in the Xpatch prediction for each facet level. A good agreement is obtained between all three models over the majority of the azimuth range. The tip of the almond is located at the 180° point and it is there that the models differ the most. The prediction in the region of the tip can't be seriously considered for two reasons. First, the tip itself is not predicted by any code, and secondly the RCS value of -60 dBSM is extremely low and could be in the measurement noise floor depending on the RCS chamber used. The only other deviation is noted at near broadside where the coarse geometry deviates. This model had so few facets, that there were noticeable grooves on both sides of the ACAD model including the tip. This segmentation would be expected to give erroneous results.

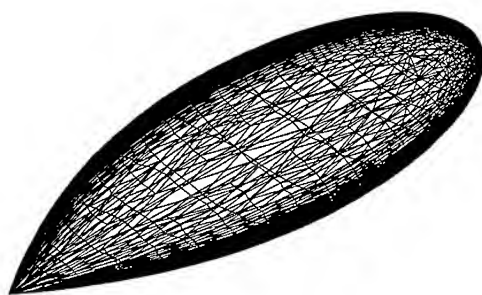
The final analysis indicated that 10,000 facets were adequate for predictions made by Xpatch. Any increase in the number of facets, increased the run time and did not add to the accuracy.

2.3 Complex Missile

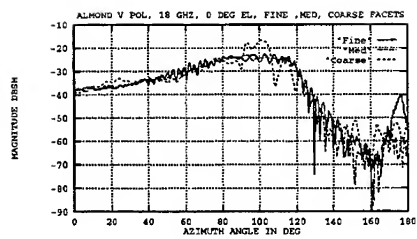
To test the effect on time domain range profile predictions, three models were built for the complex missile shown in Figure 6. The following facetizations were used:

coarse 2,758 facets with 294 edges
 medium 4,246 facets with 326 edges
 fine 9,706 facets with 458 edges

The variations in the predicted range profiles, for each facetization, are shown in Figure 7(a). The interesting result is that the amplitudes are not all the same at each scattering center. Starting from the



(a) Triangular Faceted Almond



(b) Three Facetization Levels

Figure 5: Almond Effect Of Facetization Level

left, the first scatterer is off the nose. Notice that the more coarse nose gives the highest return, but, the oddity is that the medium faceted nose gave the lowest value. This would be attributed to the layout of the facets on the nose. In this case, it was simply coincidence that the facets were facing in a direction which yielded a slightly lower return. The reason the hanger and pad at the 19 and 26 inch points did not show up is because they are shadowed by the the front hanger when looking directly nose on, as in this case. This was also expected and supports Xpatch's ability to account for shadowing.

Figure 7(b) shows the effect of a change in facetization on the frequency response of the missile. With a few exceptions, all three models track very well across the 27-36 GHz band. This is encouraging but shows there is a difference in the prediction depending on the facet fidelity of the ACAD model. When comparing these predictions against measured data, both these effects must be kept in mind.

3 Conclusions

Xpatch V4.0 uses flat faceted geometry files to predict the radar signature. Clearly, the flat faceted model has problems associated with it. If this type of geometry is to be used in the prediction of a doubly curved target, care must be taken to understand how the facets are laid out on the ACAD model. If not, the results could have a larger error associated with them than anticipated. The test results show that a higher number of facets gives a better prediction, but, it comes at the expense of CPU time. Since faster run times are desired, care must be taken in building the geometry files to strike a balance between speed and accuracy.

References

- [1] S. Lee, "Xpatch-4.0 a high frequency rcs computational code for flat patches and interactions," tech. rep., Defense Electromagnetic Analysis Company, Dec. 1991.
- [2] K. M. Mitzner, "Incremental length diffraction coefficients," technical report afal-tr-73-296, Northrup Corp., Aircraft Division, AF Avionics Laboratory Wright-Patterson AFB OH 45433, April 1974. DTIC AD918861.
- [3] E. M. Miller, "Validation of xpatch radar signature predictions using flat facet geometries," aflt/ge/eng/92d-27, Air Force Institute of Technology, AFIT, Wright-Patterson AFB OH 45433-6583, Dec. 1992.
- [4] J. Roedder, *CADDSCAT User's Manual for CADDSCAT version 3 Jan 1992*. McDonnell Douglas, McDonnell Douglas, Saint Louis, MO 63166-0516, Jan. 1992.
- [5] P. D. M. Group, *Advanced Computer Aided Design (ACAD) Version 7.2 User's Manual*. MZ 2635, General Dynamics, Fort Worth Division, General Dynamics Boulevard, Fort Worth, TX 76108.
- [6] H. T. Wang, L. Sanders, and A. Woo, "Radar cross section measurements data on low cross-section targets part 1 and part 2," Tech. Rep. TM-7002, Radio Frequency Guidance Division Intercept Weapons Department, Naval Weapons Center, China Lake, CA 93555-6001, Oct. 1991.
- [7] E. F. Knott, J. F. Shaeffer, and M. T. Tuley, *Radar Cross Section*. Artech House, 1985.

SESSION 17 - "MULTIPOLE TECHNIQUES"

Chair: Dr. Richard K. Gordon

COMPARISON OF MULTIPOLE AND MULTIFILAMENT TECHNIQUES

D. REUSTER and M. KAYE

Department of Electrical Engineering
University of Dayton
Dayton, OH 45469

ABSTRACT

This paper presents a comparison of the multipole and multifilament techniques as applied to the problem of scattering by periodically deformed dielectric cylinders. Comparisons are made on the performances of the two techniques with respect to variations of the cylinder's cross section. Theoretical development is given for both techniques, along with comments regarding the uniqueness of each technique. Comparisons are made with respect to run time, number of special function calls, matrix sizes required for convergence, and numerical stability. RCS results are presented for dielectric cylinders of various cross sections. Conclusions and general rules of thumb are given for the use of each technique.

I. INTRODUCTION

Multipole and multifilament techniques have been used in recent years to solve two dimensional electromagnetic propagation and scattering problems for dielectric and metallic structures [1]-[4]. In the multipole technique (MPT) the unknown fields are expressed in terms of a finite number of multipoles (classical series solutions to Maxwell's equations in cylindrical coordinates) situated at one location. In the multifilament technique (MFT) the unknown fields are expressed in terms of a finite number of monopoles (first order solutions to Maxwell's equations in cylindrical coordinates) distributed around the boundary of the structure. In both cases, the unknown expansion coefficients and propagation constants are found by imposing the boundary conditions at selected matching points along the boundary, thus forming a linear system of equations in terms of the unknown coefficients. Solving the system of equations then provides the coefficients for the approximate series solutions.

II. MATHEMATICAL DEVELOPMENT

Fig.1 shows the cross section of an infinitely long homogeneous dielectric cylinder, of permeability μ_0 and permittivity ϵ_d , with its axis along the \hat{z} direction. The region surrounding the cylinder is free space with permeability μ_0 and permittivity ϵ_0 . In this paper we shall consider cylinders with contours described by the following parametric equation :

$$R(\phi) = a(1 + \delta \cos(3\phi)) \quad (1)$$

It will be assumed that the cylinder is illuminated by a transverse magnetic (TM) plane wave, of unit amplitude, propagating in the x-y plane.

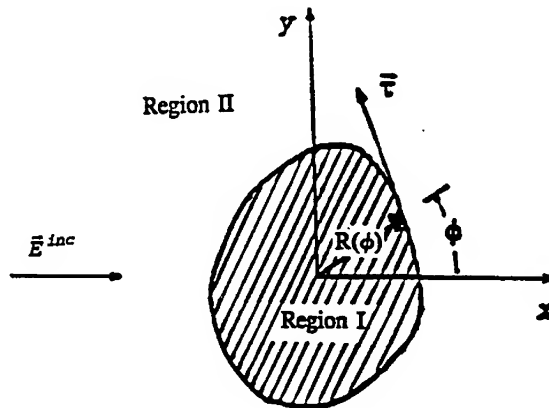


Figure 1 Dielectric cylinder and related coordinate system.

A) MULTIPOLE TECHNIQUE

Let the electric field inside the dielectric cylinder be expressed by the following series expansion:

$$\vec{E}_{die1} = \sum_{n=-\infty}^{\infty} a_n J_n(k_d \rho) e^{jn\phi} \hat{z} \quad (2)$$

From Maxwell's equations, the corresponding magnetic field may be expressed as follows :

$$\vec{H}_{die1} = \frac{-j}{\eta_d} \sum_{n=-\infty}^{\infty} a_n J'_n(k_d \rho) e^{jn\phi} \hat{\phi} - \frac{1}{\eta_d k_d \rho} \sum_{n=-\infty}^{\infty} n a_n J_n(k_d \rho) e^{jn\phi} \hat{\rho} \quad (3)$$

where η_d and k_d are, respectively, the intrinsic impedance and wavenumber of the medium. Similarly, the scattered electric and magnetic fields at an observation point external to the dielectric cylinder are given by :

$$\vec{E}_{scat} = \sum_{n=-\infty}^{\infty} b_n H_n^{(2)}(k_0 \rho) e^{jn\phi} \hat{z} \quad (4)$$

$$\vec{H}_{scat} = \frac{-j}{\eta_0} \sum_{n=-\infty}^{\infty} b_n H_n^{(2)'}(k_0 \rho) e^{jn\phi} \hat{\phi} - \frac{1}{\eta_0 k_0 \rho} \sum_{n=-\infty}^{\infty} n b_n H_n^{(2)}(k_0 \rho) e^{jn\phi} \hat{\rho} \quad (5)$$

where, η_0 and k_0 are, respectively, the intrinsic impedance and wavenumber of free space.

From the boundary conditions, the tangential components of the electric and magnetic fields must be continuous across the contour of the cylinder. This leads to the following two equations :

$$\sum_{n=-\infty}^{\infty} a_n J_n(k_d R(\phi)) e^{jn\phi} = \sum_{n=-\infty}^{\infty} b_n H_n^{(2)}(k_0 R(\phi)) e^{jn\phi} + E_{inc} \quad (6)$$

and

$$\begin{aligned} & \frac{-j}{\eta_d} \sum_{n=-\infty}^{\infty} a_n J_n'(k_d R(\phi)) e^{jn\phi} \tau_\phi - \frac{1}{\eta_d k_d \rho} \sum_{n=-\infty}^{\infty} n a_n J_n(k_d R(\phi)) e^{jn\phi} \tau_\rho \\ &= \frac{-j}{\eta_0} \sum_{n=-\infty}^{\infty} b_n H_n^{(2)'}(k_0 R(\phi)) e^{jn\phi} \tau_\phi - \frac{1}{\eta_0 k_0 \rho} \sum_{n=-\infty}^{\infty} n b_n H_n^{(2)}(k_0 R(\phi)) e^{jn\phi} \tau_\rho + \vec{H}_{inc} \cdot \vec{\tau} \end{aligned} \quad (7)$$

where $\vec{\tau} = \tau_\phi \hat{\phi} + \tau_\rho \hat{\rho}$ is the unit tangent vector at any point on the contour $\rho = R(\phi)$. Approximating the above series by the first $2N+1$ terms and enforcing the resulting equations at $2N+1$ matching points on the contour results in the following matrix equation :

$$\begin{bmatrix} [E_{die}] & [-E_{scat}] \\ [H_{die}] & [-H_{scat}] \end{bmatrix} \begin{bmatrix} a_n \\ b_n \end{bmatrix} = \begin{bmatrix} E_{inc} \\ \vec{H}_{inc} \cdot \vec{\tau} \end{bmatrix} \quad (8)$$

Solving Eq. (8) provides the series expansion coefficients for both the fields inside the dielectric cylinder and the scattered fields outside the cylinder.

B) MULTIFILAMENT TECHNIQUE

Let the electric field inside the dielectric cylinder be expressed as the superposition of the electric fields radiated by N electric line sources located outside the dielectric cylinder and radiating in a medium equivalent to that of the dielectric body as shown in Fig. 2. The electric field in region I is, therefore, given by :

$$\vec{E}_{die1} = -\frac{k_d \eta_d}{4} \sum_{n=1}^N a_n H_0^{(2)}(k_d \rho_n) \hat{z} \quad (9)$$

where $\rho_n = \sqrt{(x-x_n)^2 + (y-y_n)^2}$ and (x_n, y_n) is the location of the n^{th} line source.

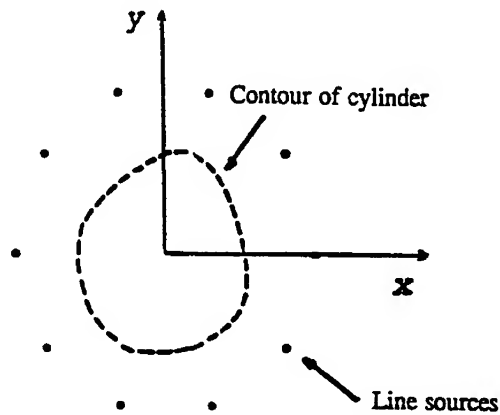


Figure 2 Geometry for computing fields in region I

From Maxwell's equations, the corresponding magnetic field in region I is given by:

$$\vec{H}_{die1} = \frac{k_d}{4j} \sum_{n=1}^N \frac{a_n (y_n - y)}{\rho_n} H_1^{(2)}(k_d \rho_n) \hat{x} + \frac{k_d}{4j} \sum_{n=1}^N \frac{a_n (x - x_n)}{\rho_n} H_1^{(2)}(k_d \rho_n) \hat{y} \quad (10)$$

Likewise, the scattered electric field outside the dielectric cylinder may be expressed as the superposition of the electric fields radiated by N electric line sources located inside the dielectric cylinder and radiating in free space, as shown in Fig. 3.

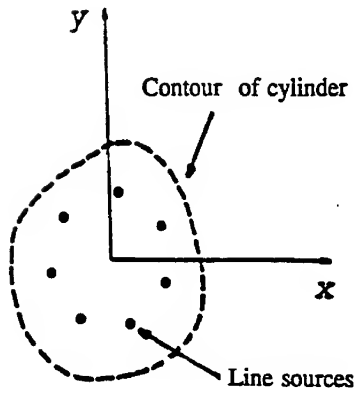


Figure 3 Geometry for computing fields in region II

The scattered electric field in region II is, therefore, given by :

$$\vec{E}_{scat} = -\frac{k_0 \eta_0}{4} \sum_{n=1}^N b_n H_0^{(2)}(k_0 \rho_n) \hat{z} \quad (11)$$

From Maxwell's equations the corresponding scattered magnetic field in region II is given by :

$$\vec{H}_{scat} = \frac{k_0}{4j} \sum_{n=1}^N \frac{b_n (y_n - y)}{\rho_n} H_1^{(2)}(k_0 \rho_n) \hat{x} + \frac{k_0}{4j} \sum_{n=1}^N \frac{b_n (x - x_n)}{\rho_n} H_1^{(2)}(k_0 \rho_n) \hat{y} \quad (12)$$

Continuity of the tangential field components across the contour of the cylinder leads to the following relationships :

$$-\frac{k_d \eta_d}{4} \sum_{n=1}^N a_n H_0^{(2)}(k_d \rho_n) = -\frac{k_0 \eta_0}{4} \sum_{n=1}^N b_n H_0^{(2)}(k_0 \rho_n) + E_{inc} \quad (13)$$

and

$$\begin{aligned} & \frac{k_d}{4j} \sum_{n=1}^N \frac{a_n (y_n - y)}{\rho_n} H_1^{(2)}(k_d \rho_n) \tau_x + \frac{k_d}{4j} \sum_{n=1}^N \frac{a_n (x - x_n)}{\rho_n} H_1^{(2)}(k_d \rho_n) \tau_y \\ &= \frac{k_0}{4j} \sum_{n=1}^N \frac{b_n (y_n - y)}{\rho_n} H_1^{(2)}(k_0 \rho_n) \tau_x + \frac{k_0}{4j} \sum_{n=1}^N \frac{b_n (x - x_n)}{\rho_n} H_1^{(2)}(k_0 \rho_n) \tau_y \end{aligned} \quad (14)$$

Enforcing Eqs.(13) and (14) at N matching points on the contour results in a matrix equation for the unknown expansion coefficients a_n and b_n .

III. COMPARISONS

Three periodically deformed dielectric cylinders of radii 0.3λ , 1.0λ , and 3.0λ were chosen as test targets for the comparison of the two methods. Each method was applied to the three cylinders for deformation constants of 0.0, 0.2, and 0.4 (see Fig. 4).

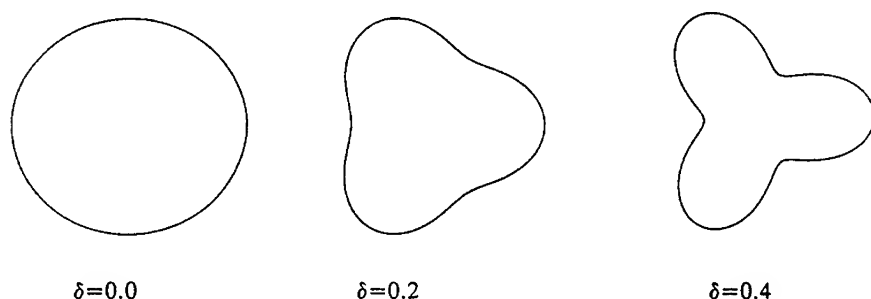


Figure 4 - Periodically deformed test targets.

Table I presents the run time and matrix sizes required to produce a converged bistatic radar cross section plot for each of the scatterers for an incident TM plane wave. All test cases were run on an HP 9000 model 730 using double precision and IMSL libraries. It should be noted that for some test targets no convergence (NC) was obtained. Figs. 5 and 6 show the convergence patterns for each of the methods.

For targets near circular, the MPT requires smaller matrix sizes than the MFT; however, as the target's cross section becomes less circular, the matrix size quickly increases. Limits on the maximum allowable matrix size for the MPT are directly related to the minimum electrical dimension of the body. If the number of matching points greatly exceeds the minimum electrical dimension of the body, numerical problems associated with the behavior of the Bessel functions used in the series expansion causes the matrix to become ill-conditioned (see Table II).

While the MFT does not suffer from an upper bound on the number of matching points allowed, it is, in general, slower than the MPT. This is, in part, due to the need for more matching points and a greater number of special function calls. For the MFT $2N^2$ special function calls are required, whereas for the MPT only $2N$ are required. The rate of convergence for the MFT is also dependent on the location of the fictitious line sources about the contour of

the target. Leviatan [3] suggests that the line sources be placed within 20% of the radius of the body. This was found to be generally true; however, as the number of matching points became large, it was found that the location of the line sources needed to be moved closer to the body in order to keep the matrix from becoming ill-conditioned. This phenomenon again places an upper limit on the number of matching points allowed. This limit is much larger than the limit on the MPT; hence, making the MFT more versatile than the MPT. As a benchmark, both methods were compared to the classical Method of Moments solution [5] for the 0.3λ dielectric cylinder. Both the MPT and the MFT require a system matrix that is at least five times smaller than the Method of Moments matrix with run times correspondingly smaller.

IV. CONCLUSIONS

Comparison of the MPT and the MFT shows a trade off between speed and versatility. For bodies suitable for MP analysis, the MPT shows a substantial run time improvement. However, the MPT is limited to the class of near circular problems whereas the MFT is capable of handling more irregular bodies. Thus, the principle factor when choosing between the two techniques is the general shape of the body under analysis.

REFERENCES

- [1] J. E. Goell, "A circular-harmonic computer analysis of rectangular dielectric waveguides," *Bell Syst. Tech. J.*, vol.48, pp. 2133-2160, Sept. 1969.
- [2] E. Yamashita and K. Atsuki, "The point matching method," in *Analysis Methods for Electromagnetic Wave Problems*, E. Yamashita, Ed. Norwood, MA: Artech House, 1990, ch.3.
- [3] Y. Leviatan and A. Boag, "Analysis of electromagnetic scattering from dielectric cylinders using a multifilament current model," *IEEE Trans. Antennas Propagat.*, vol. AP-35, pp. 1119-1127, Oct. 1987.
- [4] C. Hafner, *The Generalized Multipole Technique for Computational Electromagnetics*, Norwood, MA: Artech House, 1990.
- [5] J. H. Richmond, "Scattering by a dielectric cylinder of arbitrary cross section shape," *IEEE Trans. Antennas Propagat.*, vol. AP-13, pp.334-341, May 1965.

Table I

Dielectric Cylinder	Approximate matrix size for convergence		Run time in seconds	
	Multipole	Multifilament	Multipole	Multifilament
$r=0.3, \delta=0.0$	30	60	0.2	1.3
$r=0.3, \delta=0.2$	40	60	0.6	1.3
$r=0.3, \delta=0.4$	NC	80	NC	2.2
$r=1.0, \delta=0.0$	70	90	0.4	3.0
$r=1.0, \delta=0.2$	110	100	1.2	3.4
$r=1.0, \delta=0.4$	NC	NC	NC	NC
$r=3.0, \delta=0.0$	120	150	1.5	8.0
$r=3.0, \delta=0.2$	NC	NC	NC	NC
$r=3.0, \delta=0.4$	NC	NC	NC	NC

Table II

n	$J_n(2.0)$
0	0.223 E 00
10	2.515 E-07
20	3.918 E-19
30	3.650 E-33
40	1.196 E-48

MULTIPOLE TECHNIQUE

MULTIFILAMENT TECHNIQUE

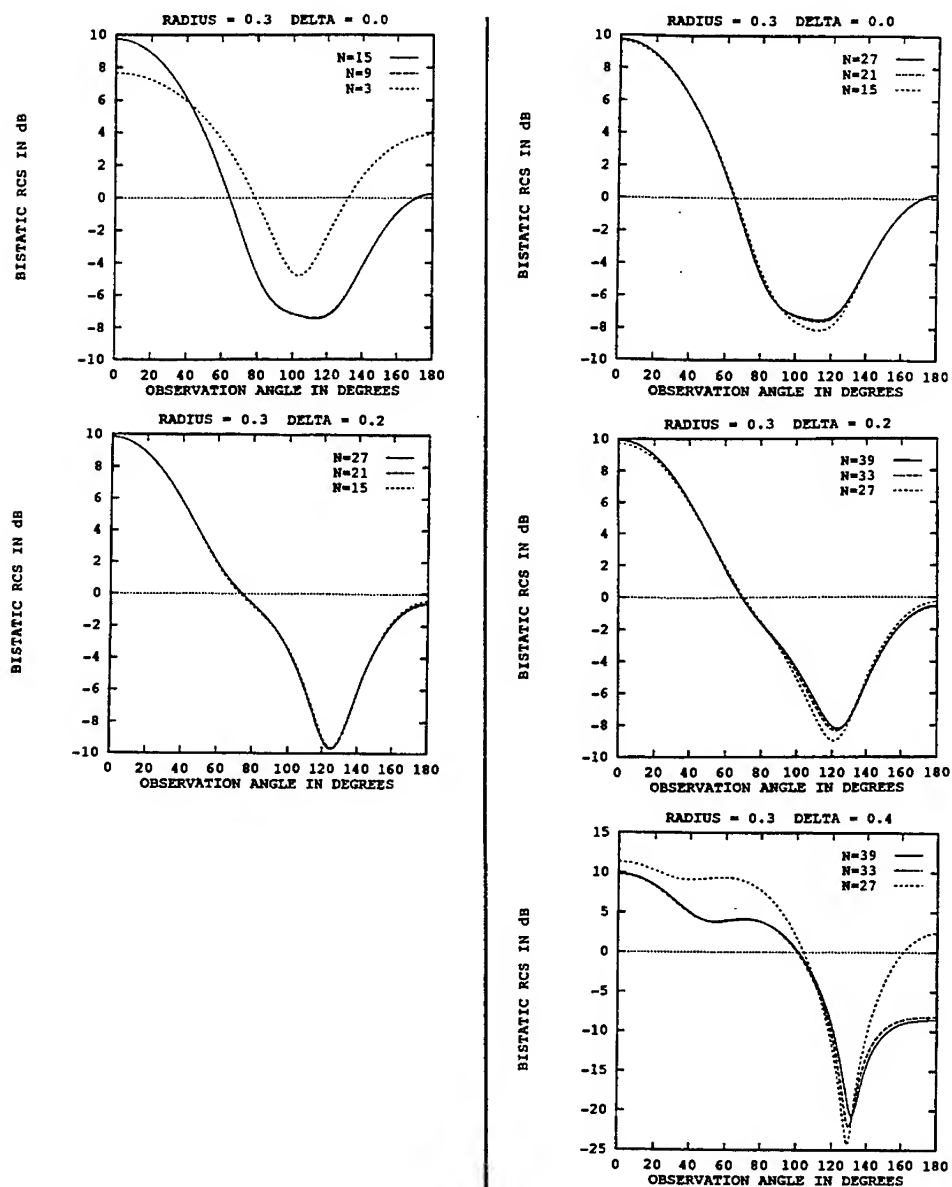


Figure 5 Bistatic RCS for periodic deformed dielectric cylinders with $r = 0.3$, $\epsilon_d = 3.0\epsilon_0$, and $\delta = 0.0, 0.2, \text{ and } 0.4$.

MULTIPOLE TECHNIQUE

MULTIFILAMENT TECHNIQUE

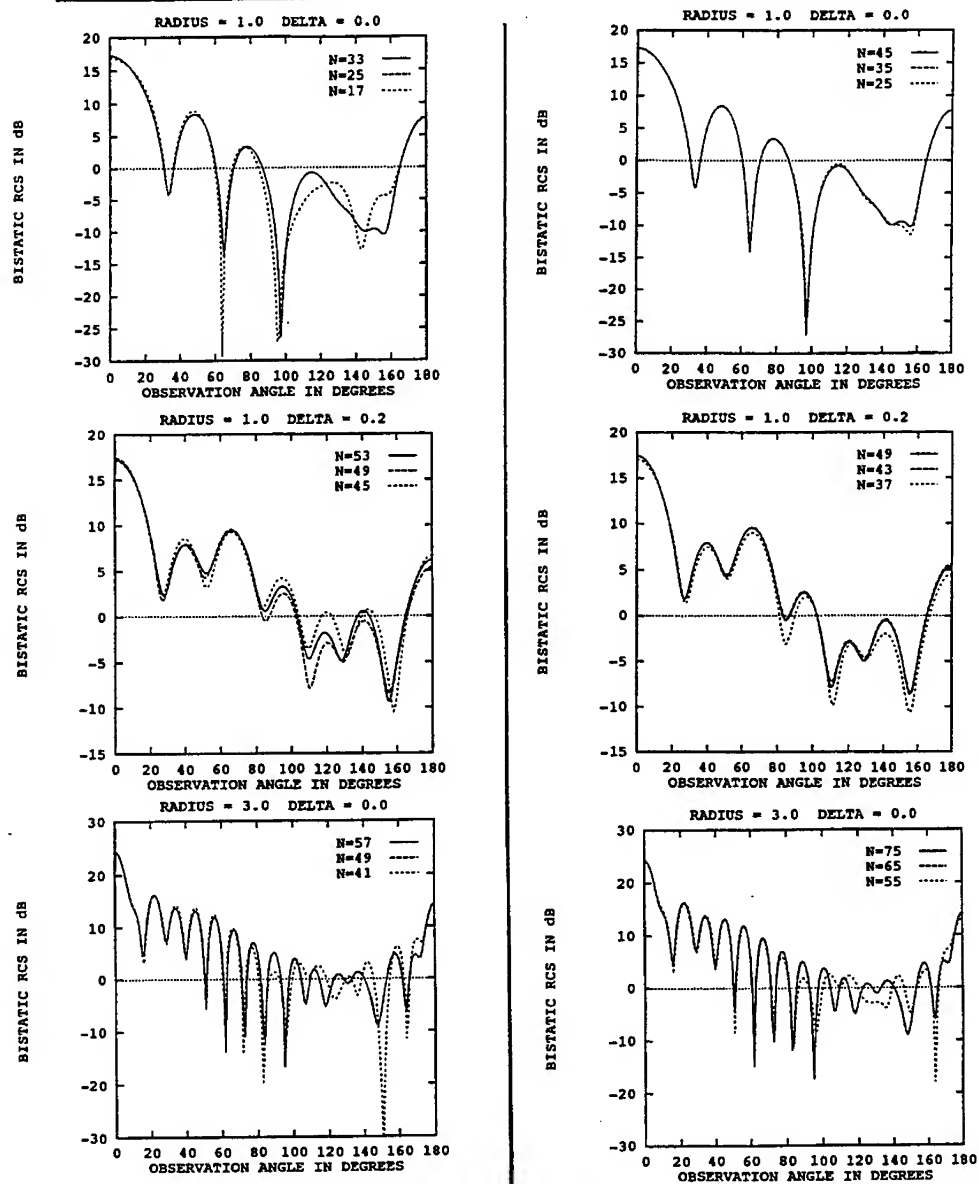


Figure 6 Bistatic RCS for periodic deformed dielectric cylinders with $r = 1.0, 3.0$, $\epsilon_d = 3.0\epsilon_0$, and $\delta = 0.0, 0.2$.

New Thin Wire Expansions for Long Wires in the MMP-Code

Pascal Leuchtman and Marcel Gnos

Laboratory of El.-mag. Fields and Microwave Electronics, ETH Zurich
CH-8092 Zürich, Switzerland

Abstract: A class of special thin wire expansion functions have been added to the MMP-program package. The new functions may be used if thin wires are involved in situations to be analysed. The basic concept of the new functions is described and some general remarks to the choice of basis functions are given. In the part on the numerical examples, an appropriate definition of the percentage error is defined and first experiences with the use of the new functions are described. Some suggestions are given how to overcome existing problems.

1. Introduction

The MMP-program package [1,2,7] is a top level tool for computational electromagnetics in frequency domain. It is possible to perform rigorous far- and near-field calculations in scattering problems, as long as the scatterer(s) is (are) smaller than some wavelengths and the materials involved are piecewise homogeneous, linear and isotropic.

The present version of MMP offers a number of different types of expansion functions. (Remember: An MMP-expansion function is a complete solution of Maxwell's homogeneous equations. It consists of six complex space functions, the components of the electric field \vec{E} and of the magnetic field \vec{H} .) Some of them are specially adapted to certain geometrical shapes of the boundaries. In particular, the ordinary multipoles are useful for spherelike parts of the boundaries, the thin wire expansions [3] are adapted to long circular and relatively thin wires and the line multipoles [4] do the same job for long thick wires as well as for edges.

2. The basic idea of the new expansion type

This paper deals with a new type of thin wire expansions which have been implemented in the MMP-code. The most important difference to the 'old' thin wire expansion [3] is the fact that the number of unknowns is significantly reduced. Using the old thin wire expansion, an arbitrary current distribution along a long wire is modelled using a segmentation of the wire, where each segment is (a) short compared to the wavelength λ (typically shorter than $\lambda/20$) and (b) short compared to strong current variations (the unknown current distribution is actually represented by a (approximately) linear distribution on each segment). This second request is necessary due to the matching concept used in the MMP-code [5]. The actual unknowns are the currents at the boundaries of the segments. In the case of a fine segmentation, this leads to a large number of unknowns.

The new expansion functions are essentially thin wire expansions with a fine segmentation (to avoid matching problems [5]) but have a total number of unknowns, which

is significantly smaller than the number of segments. The reduction of the number of unknowns is obtained as follows.

Let z be the coordinate along a particular long wire and $I(z)$ the current distribution on this wire. Then

$$I(z) = \sum_{n=1}^N a_n f_n(z) + \eta(z) \quad (1)$$

where $f_n(z)$ are suitable functions discussed below, a_n are unknown parameters and $\eta(z)$ is a (hopefully!) small error. Obviously, the total number of unknowns to represent the current distribution $I(z)$ is N . This general concept includes the old thin wire expansion, which uses essentially¹ triangular functions $f_n^T(z)$, defined as follows: Given a certain segmentation with S segments and cuts at positions $z_0, z_1, z_2, \dots, z_S$ on the wire, it is

$$f_n^T(z) := \begin{cases} \frac{z - z_{n-1}}{z_n - z_{n-1}} & \text{if } z_{n-1} < z < z_n \\ -\frac{z - z_{n+1}}{z_{n+1} - z_n} & \text{if } z_n < z < z_{n+1} \\ 0 & \text{elsewhere on the wire} \end{cases} \quad (2)$$

Using functions $f_n(z)$ being nonzero all along the wire, the segmentation is no longer needed. However, the evaluation of the electromagnetic field due to the current $f_n(z)$ requires an integration along the whole wire. It is this integration which makes it necessary to introduce again a segmentation. Since the functions in the 'old' thin wire expansion are based on current distributions whose electromagnetic field may be evaluated analytically [3], it is convenient to use the same current distributions here. Following this idea the wire is segmented and all the f_n are actually polygon approximated. Note, that the evaluation of the electromagnetic field of the constant and of the linear current distribution has to be performed only once for each segment. Hence, the number of segments S becomes independent from the number of functions N . It is always $N \leq S$. The segmentation is adapted to the variation of the f_n 's in such a way, that the polygon approximation of each f_n looks smooth.

3. The choice of the basic current distributions

From a general point of view the functions $f_n(z)$ in eq. (1) must be chosen in such a way, that 'any' current distribution $I(z)$ may be approximated with a small error $\eta(z)$. In practice, the requirements are less restrictive: Only a class of rather smooth current distributions $I(z)$ should be representable. Since in any practical case, the solution of a given problem is unique and does exist — this is known from physics — one could even ask only for the ability to expand the solution itself (and nothing else!) by the set of the f_n 's. Since the solution is not known a priori, this gives no practical hints for the choice of the functions f_n . But we can keep in mind, that this is the point where we could introduce a priori knowledge on the solution.

¹ This is only part of the truth: The constants c and s in the 'linear' current distribution $I_l(z) = c + sz$ on each segment are actually weak functions of z ($c = \cos kz$, $s = (\sin kz)/z$ where $kz \ll 1$ on the whole segment).

From a mathematical point of view the problem is reduced to the following: Give a complete set of functions $f_n(z)$, which are defined on the finite interval of length L (the length of the wire). Among others, there are powers ($f_n^p(z) := z^n$) and trigonometric functions ($f_n^c(z) := \cos n \frac{2\pi z}{L}$ or $f_n^s(z) := \sin n \frac{2\pi z}{L}$). The criteria to find a suitable and practically useful set of functions are:

- All the f_n must be linearly independent. This is a strict requirement. Otherwise, the degree of freedom is actually less than N , and the MMP-solver results in a singular matrix.
- On the other hand, orthogonality of the f_n is not required, even if it is the optimum form of independence. Due to the fact that not the current distribution itself but its electromagnetic field is used to find the unknowns, it would be more efficient to have orthogonal *fields* rather than orthogonal *currents*. Unfortunately, this does not fit into our general concept of given basis *currents*.
- The importance of the terms within the series in (1) should decrease with increasing n . This is not strict, but highly recommended. A small increase of the number N should not drastically change the solution but just perform some 'fine tuning'.
- The meaning of the first terms should be physical. This is helpful in the first view interpretation of the results.
- The error should have a similar magnitude along the whole wire. This makes the trigonometric functions less useful for all those cases where the currents at the beginning of the wire is not equal to the current at the end, since a Fourier series has very bad convergence at all those places where the function to be expanded is not continuous. This effect is known as Gibbs' phenomenon.

The last criterion eliminates the trigonometric functions $f_n^c(z)$ and $f_n^s(z)$ and favours the simple powers z^n . Obviously, they are independent, but they turn out to be somewhat dependent from each other. This dependency is a purely numerical dependency and can be observed in the fact, that the plots of say z^6 and z^7 look very similar, if only the finite interval $0 \leq z \leq L$ is considered.

A suitable combination of the powers to polynomials of n -th degree make the functions more independent from each other. One can find several families of orthogonal² polynomials [6]. In the interval $-1 \leq z \leq 1$, the Jacobi Polynomials $P_n^{(\alpha, \beta)}$ are orthogonal with respect to the weight function $w(z) = (1-z)^\alpha(1+z)^\beta$, the Gegenbauer Polynomials $C_n^{(\alpha)}$ with $w(z) = (1-z^2)^{\alpha-\frac{1}{2}}$, the Chebyshev Polynomials of the first kind, T_n with $w(z) = (1-z^2)^{-\frac{1}{2}}$, the Chebyshev Polynomials of the second kind, U_n with $w(z) = (1-z^2)^{\frac{1}{2}}$ and the Legendre Polynomials P_n with $w(z) = 1$. For sake of simplicity we do not consider the polynomials $P_n^{(\alpha, \beta)}$ and $C_n^{(\alpha)}$, because this would require a decision for the parameters α and β . All the remaining Chebyshev and Legendre Polynomials seem to be useful for our task. One just has to map the interval $-1 \leq z \leq 1$ onto the wire with length L .

The most simple among the mentioned functions are the Legendre Polynomials. Hence, the investigation has been done with this class of functions, the more as a simple recursion for them being already implemented in the MMP-code. Beside the Legendre Polynomials,

² Orthogonality depends on a weight function $w(z)$ and an interval $a \leq z \leq b$. Two functions $f_1(z)$ and $f_2(z)$ are called orthogonal on the interval $a \leq z \leq b$, with respect to $w(z)$, if $\int_a^b w(z) f_1(z) f_2(z) dz = 0$.

a second class of weighted Legendre Polynomials has been considered as well. Figure 1 shows plots of the first orders of all the investigated polynomials. In addition to these, a sinusoidal half wave has been implemented, in order to study the interaction between functions of different classes.

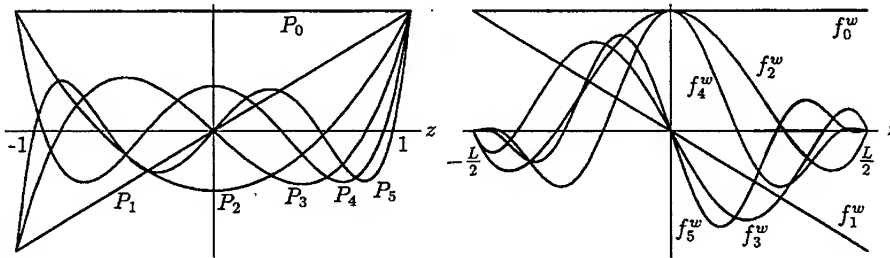


Figure 1 The Legendre Polynomials $P_n(z)$ (left) oscillate in the interval $-1 \leq z \leq 1$. In order to obtain more oscillation in the center of the interval and less oscillation at its ends, the Legendre Polynomials $P_n(z)$ have been weighted by Associated Legendre Functions of the first kind (right, see also eq. (3) for an exact definition of $f_n^w(z)$).

4. Numerical Examples

Two basic types of examples have been studied, (1) a straight wire in free air, illuminated by a plane wave and (2) a rectangular loop connected to an infinite ground plane, illuminated again by a plane wave.

All the examples have been calculated both as electrically small objects (overall dimension $\approx \lambda/10$) and as electrically large objects (overall dimension $\approx 2\lambda$).

Comparisons have been made between a current expansion using the conventional basic current distribution $f_n^T(z)$, which are defined in eq. (2), the Legendre Polynomials $f_n^L(z) := P_n(2z/L)^3$ (see fig. 1, left hand side) and the weighted Legendre polynomials

$$f_n^w(z) := \begin{cases} \frac{P_n(2z/L)P_n^n(2z/L)}{P_n(0)P_n^n(0)} & \text{if } n \text{ even} \\ \frac{P_n(2z/L)P_{n-1}^{n-1}(2z/L)}{P_{n-1}(0)P_{n-1}^{n-1}(0)} & \text{if } n \text{ odd} \end{cases} \quad (3)$$

(see fig. 1, right hand side). Both Legendre type current expansions were also examined under the addition of the function

$$f^C(z) := \cos(\pi z/L). \quad (4)$$

³ The coordinate $z = 0$ on the wire is in the center of the wire, i.e., z varies on the wire from $-L/2$ to $L/2$.

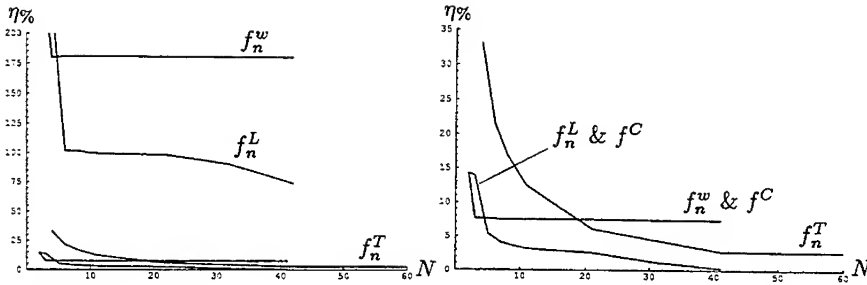


Figure 2 The overall percentage error $\eta\%$ as a function of the total number of unknowns N for a short wire ($L = \lambda/10$). Different sets of basic current functions f_n show different convergence properties.

The quality of the solution is measured by the following error definition [7]. Suppose M is the total number of matching points, \vec{r}_i is the position vector of the i -th matching-point,

$$F_i := \sqrt{\frac{1}{6}|\vec{E}(\vec{r}_i)|^2 + |Z^2| \cdot |\vec{H}(\vec{r}_i)|^2} \quad (5)$$

is a positive scalar value for the electromagnetic field amplitude ($Z = \sqrt{\frac{\mu}{\epsilon}}$ is the impedance of the medium (air) and \vec{H} is the magnetic field amplitude) and $\eta_i := |\vec{E}(\vec{r}_i) \cdot \vec{u}_i|$ is the component of the total electric field along the wire (the error on the i -th matching-point). The unit vector \vec{u}_i points parallel to the wire in this point. Then $F := \frac{1}{M} \sum_{i=1}^M F_i$ is the mean value of the field on the wire and $\eta := \frac{1}{M} \sum_{i=1}^M \eta_i$ is the mean value of the absolute errors. With these definitions, we define the percentage error as

$$\eta\% = \frac{\eta}{F} 100\%. \quad (6)$$

Note, that $\eta\%$ may be more than 100%. This is due to the factor 6 in (5) — the electromagnetic field has 6 components, but in our particular case the error is composed of only one component.

4.1 The straight wire in the air

A straight wire with circular cross-section (diameter = 2 mm) of length $L = 10$ cm and pointing into direction \vec{u} is illuminated by a plane wave which is linearly polarized parallel to the wire ($\vec{E}_{inc} = E_0 \vec{u}$). The situation has been calculated both at a frequency of 300 MHz ($\rightarrow L = \lambda/10$) and at a frequency of 6 GHz ($\rightarrow L = 2\lambda$). The two cases are referenced to as the short wire (300 MHz) and the long wire (6 GHz) respectively, even when the physical dimensions are the same.

For all the calculations using Legendre Functions the same segmentation of 98 segments of equal length has been used and on $M = 198$ matching-points, the longitudinal component of the total electric field is set to zero (in a least squares sense, as usual in MMP). For the calculations with the triangular functions f_n^T , the matching points are set following the suggestions in [5].

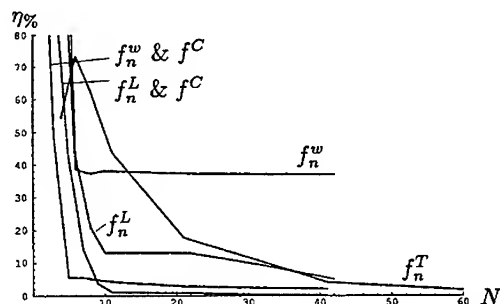


Figure 3 The overall percentage error $\eta\%$ as a function of the total number of unknowns N for a long wire ($L = 2\lambda$). Different sets of basic current functions f_n show different convergence properties.

In fig. 2 and 3, the error $\eta\%$ is shown as a function of the total number of parameters. For both the short wire and the long wire, the results from the weighted functions f_n^w are always worse than those from the ordinary Legendre Polynomials f_n^L , and the addition of the function f^C improves the results significantly. In fact, it is rather hard to model the short wire (fig. 2) without f^C , whereas the convergence is better at the long wire, even without f^C . In general, the convergence with the weighted functions f_n^w is bad, even not monotonous. Hence, for this particular problem, the use of the f_n^w is not recommended.

The comparison with the conventional thin wire expansion using the triangular functions f_n^T shows, that the Legendre Polynomials f_n^L do have significant advantages compared to the f_n^T , in particular for a low number of unknowns.

Figure 4 shows the current distributions for approximately 20 unknowns, which look very similar as soon as the error $\eta\%$ is below 10%. (See also fig. 2 and 3.) Higher error values lead to bad results.

4.2 The rectangular loop over a ground plane

The second example is a rectangular loop connected to an infinitely well conducting ground plane, the x - y -plane (see fig. 5). The excitation consists of a plane wave which is linearly polarized in y -direction. The loop is $L = 5$ m wide and 1 m high and the diameter of the wire is 8 mm. The situation has been calculated both at a frequency of 100 MHz ($\rightarrow L \approx 1.7\lambda$) and at a frequency of 10 MHz ($\rightarrow L \approx .17\lambda$).

Due to symmetry, only one half ($y \geq 0$) of the loop has to be modelled, and the ground plane is taken into account using the image principle.

For the horizontal 2.5 m-wire, 164 segments and 328 matching points and for the vertical 1 m-wire, 84 segments and 168 matching points have been used. The longitudinal component of the total electric field on the surface of the wires is set to zero. For the calculations with the triangular functions f_n^T , the matching points are set following the suggestions in [5].

The investigations have shown that in general, the Legendre Polynomials f_n^L are more suitable than the weighted functions f_n^w . The same fact has been observed already in the previous example. But other than there, the convergence is worse in comparison to the

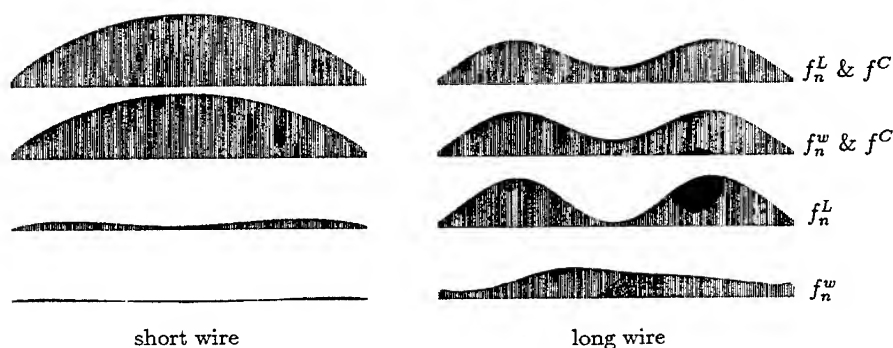


Figure 4 The current distributions $I(z)$ (instantaneous value) on the short (left) and the long wire (right) look rather different, if different basic current distributions f_n are used. At the very right, the basis functions are indicated. In all cases, 21 functions of Legendre type — and in the first two lines additionally the function f^C — have been used. A comparison with fig. 2 and 3 shows that the accuracy decreases from top to down.

conventional thin wire expansions with f_n^T . In this example, the use of the new thin wire expansion functions give only small advantage compared to the conventional thin wire expansions.

5. Conclusions and future work

It has been shown that the new thin wire expansion functions may have significant advantages compared to the conventional thin wire expansions (reduction of the number of unknowns up to a factor of 10 at the same accuracy). In more complicated situations, the advantages are less clear and may even disappear.

Future work using other basic current distributions such as Chebyshev's Polynomials and others, as well as an adaptive segmentation and curved wires will show whether the concept will really beat the conventional thin wire expansions.

References

- [1] Ch. Hafner, *The generalized multipole technique for computational electromagnetics*, Artech House Books, 1990.
- [2] L. Bomholt, P. Regli, Ch. Hafner, and P. Leuchtman, "MMP-3D: A package for computation of 3D electromagnetic fields on PC's and workstations," in *6th Annual Review of Progress in Applied Computational Electromagnetics (ACES), Conference Proceedings*, (Monterey), Mar. 1990.
- [3] P. Leuchtman and L. Bomholt, "Thin wire feature for the MMP-code," in *6th Annual Review of Progress in Applied Computational Electromagnetics (ACES), Conference Proceedings*, (Monterey), Mar. 1990.

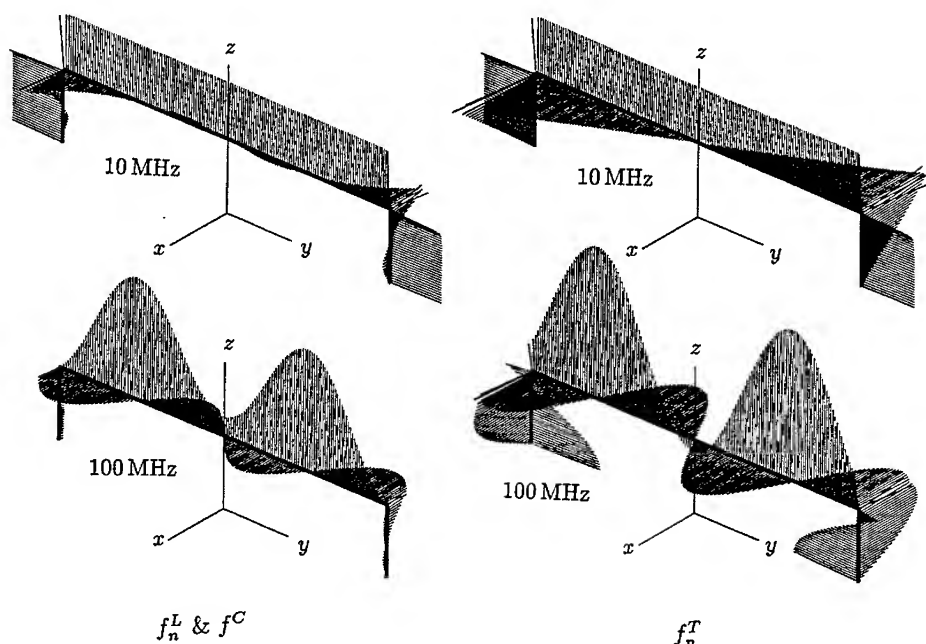


Figure 5 The picture shows the instantaneous values of both the magnetic field (field arrows mainly in the loop plane) and of the electric field (mainly perpendicular to loop plane) on the surface of the wire at $x = 4$ mm. In the left column, the functions f_n^L have been used (41 plus f^C for the horizontal (2.5 m-)part and 21 plus f^C for the vertical (1 m-)part). The right column shows the results from the conventional functions f_n^T (164 horizontal segments and 84 vertical segments). At the top the frequency is 10 MHz and at the bottom it is 100 MHz. Note that the magnetic fields (=current) are much more equal at left and right than the electric fields, in particular for the lower frequency. At the loop corners, the oblique electric arrows indicate some errors in the calculation.

- [4] P. Leuchtman, "New expansion functions for long structures in the MMP-code," in *7th Annual Review of Progress in Applied Computational Electromagnetics (ACES), Conference Proceedings*, (Monterey), Mar. 1991.
- [5] P. Leuchtman, "Optimal locations for matching points for wire modelling with MMP," *Applied Computational Electromagnetics Society (ACES) Journal*, vol. 6, pp. 21-37, Dec. 1991.
- [6] M. Abramowitz and I. A. Stegun, *Handbook of Mathematical Functions*. Dover Publications, 1972.
- [7] L. Bomholt, *MMP-3D — A Computer Code for Electromagnetic Scattering Based on GMT*. PhD thesis, Diss. ETH Nr. 9225, 1990.

SESSION 18 - "NUMERICAL MODELLING IN COMPLEX MEDIA"

Chair: Dr. Weng Chew

**Toward an FDTD Analysis of the Standard Approximations
for Propagation in Randomly Structured Ionization**

L. J. Nickisch
Mission Research Corporation
2300 Garden Road, Suite 2
Monterey, California 93940-5326

and

P. M. Franke
University of Illinois at Urbana-Champaign
Department of Electrical and Computer Engineering
323 CSRL MC-229
1308 W. Main Street
Urbana, IL 61801

Abstract

Much progress has been made in our understanding of the scattering of electromagnetic waves from small scale ionization structure. This progress has been made by taking advantage of a sequence of approximations which render the random media propagation calculations tractable, at least numerically. However, regimes of interest exist for which the limits of validity of these approximations are exceeded and suitable extensions cannot be found. Thus, for lack of an alternative, the results of computations performed under these approximations are being applied in the invalid regime with the hope that the breakdown of the approximations is more or less graceful. A tool now exists which can allow the limits of validity of the standard random media propagation theory approximations to be explored. We have recently shown that the Finite Difference - Time Domain (FDTD) method can be extended to account for the effects of temporal dispersion in frequency dependent media, and can therefore be applied to ionospheric propagation. The FDTD method solves the Maxwell equations directly in the time domain by temporal integration. No approximations beyond that of finite differencing are necessary, although the direct enforcement of certain approximations is possible. By doing so the method can be used to explore the breakdown of the standard random media propagation approximations. We present the results of an initial effort toward such an analysis.

Introduction

During propagation through ionization, RF signals are subject to dispersion (due to the frequency dependent ionospheric index of refraction), absorption, refraction and associated focusing/defocusing. Random structure in the ionization can further cause angular signal scatter (spreading the signal in delay and reducing its frequency coherence), pulse arrival time wander, and Doppler spreading (or loss of temporal signal coherence). All of

these effects have been studied utilizing various approximation methods. However, regimes of interest exist for which the standard approximation methods fail and suitable extensions have not been found. Thus results obtained under the standard approximations are speculatively pushed into the invalid regime with the hope that the approximations, when violated, do not break down catastrophically but rather degrade gracefully. For example, parabolic equation results which are valid at SATCOM frequencies are regularly applied to HF propagation with results which are in direct contradiction of assumptions used in the calculations themselves (the computed signal correlation lengths are often smaller than the field wavelength, while the assumption that $\ell_c \gg \lambda$ is specifically made in the theoretical development). In this case we have some indication (via analysis of HF channel probe data from the disturbed polar ionosphere [Nickisch, 1992]) that this misapplication of the standard approximations seems to work fairly well for oblique propagation; yet there is no firm proof. Even at UHF and higher frequencies, certain of the standard approximations can be violated when propagation along the geomagnetic field is considered (the assumption that many correlation scales of the propagation medium are traversed by the signal is violated, and the Markov assumption is suspect).

We have recently developed an efficient method for incorporating the dispersive, absorptive, anisotropic nature of the ionospheric channel into the Finite Difference - Time Domain (FDTD) method [Nickisch and Franke, 1992], and have shown that the method is capable of extreme accuracy. Since the FDTD method requires no approximations other than that implicit in the finite differencing, it is ideal for the application which we report on here, that of examining the way in which the standard random media approximations degrade when applied outside their regime of validity.

FDTD in Ionization

The basic FDTD methodology introduced by Yee [1966] is now well established. However, the treatment of temporally dispersive media within the FDTD formulation has only recently received attention. Yet, when considering ionospheric propagation, the dispersive nature of the medium is of paramount importance.

The difficulty in treating dispersive media in the time domain stems from the relation of the electric displacement \vec{D} to the electric field \vec{E} . It is in the frequency domain that the relation $\vec{D}(\omega) = \vec{\epsilon}(\omega) \cdot \vec{E}(\omega)$ holds. The corresponding expression in the time domain involves a convolution of the dielectric tensor with the field. Two difficulties arise when one attempts to apply this convolution in the FDTD methodology. First the time domain dielectric constant must be obtained as the Fourier transform of the frequency domain expression. Then the convolution itself must be evaluated at each mesh point for each time step, and this convolution requires knowledge of the entire signal history. These problems have been dealt with by at least two independent groups for specific dielectrics. Bui, et al. [1991] considered a linear, isotropic, homogeneous Debye dielectric for which the time domain expression is easily obtained. They were able to obtain a recursive expression for the convolution of this Debye dielectric which circumvented the need to store the

signal's entire history. Luebbers, et al. [1990,1991] (whose work precedes that of Bui, et al.) in addition to Debye dielectrics, considered the dispersive plasma of interest in this article. They also showed that for the particular functional form of their temporal dielectric, a recursion relation can be obtained which necessitates only the updating of certain quantities at each time step to accomplish the convolution. The functional form of which they made use, however, diverges as the electron collision frequency goes to zero, and hence is restricted to plasmas exhibiting significant absorption.

Our method [Nickisch and Franke, 1992] avoids the convolution altogether by solving the plasma equation of motion for the electric polarization. It applies to collisionless as well as absorptive plasmas, as easily incorporates anisotropy, and applies not only to plasmas, but to general media by simply altering the medium equation of motion. Joseph, et al. [1991] have explored a related technique which supplants the convolution approach with the solving of a differential equation relating \vec{D} to \vec{E} . Although we developed our method independently, we have learned that Kashiwa, et al. [1988] have developed an equivalent scheme, but have cast it in the language of the Transmission Line Matrix (TLM) method.

Rather than dealing with the dielectric tensor, in our approach the equation of motion for the ionospheric electrons (from which the dielectric tensor is derived) is solved simultaneously with the FDTD field equations. This dynamical equation, for a charged cold plasma, is [Budden, 1985],

$$-e\vec{E} + \frac{1}{N_e} \frac{\partial \vec{P}}{\partial t} \times \vec{B}_E = \frac{m_e}{N_e e} \left(\frac{\partial^2 \vec{P}}{\partial t^2} + \nu_e \frac{\partial \vec{P}}{\partial t} \right) \quad (1)$$

which relates the forces on the charged plasma to the plasma acceleration. We have included in (1) the forces on a charge due to the applied field of our wave of interest and the external geomagnetic field \vec{B}_E responsible for magneto-ionic splitting. The collisional forces responsible for signal absorption are incorporated through the electron collision frequency ν_e in the last term. Equation (1) has been written in terms of the electric polarization \vec{P} . Our approach is to discretize (1) on the FDTD grid and solve for the polarization P at the current time step in terms of the polarization and field at previous time steps. We then use the relation $\vec{D} = \epsilon_0 \vec{E} + \vec{P}$ in the FDTD versions of the Maxwell curl equations (with $\vec{B} = \mu_0 \vec{H}$), or, as we tend to prefer, in an FDTD version of the vector wave equation,

$$\frac{1}{c^2} \frac{\partial^2 \vec{E}}{\partial t^2} = \nabla^2 \vec{E} - \vec{\nabla}(\vec{\nabla} \cdot \vec{E}) - \mu_0 \frac{\partial^2 \vec{P}}{\partial t^2} . \quad (2)$$

The Standard Approximations

The standard approximations used in the current theory for propagation in randomly structured ionization generally follow this progression: First the true vector wave equation is reduced to the scalar Helmholtz wave equation by neglecting the polarization coupling

contribution (generally valid when the field wavelength is small relative to the ionospheric structure scale size). Then it is assumed that the field is dominantly forward scattering; all backscattered contributions are ignored. It is further assumed that this forward scattered field is scattered through only small angles, resulting in the so-called parabolic approximation in which a second derivative contribution in the propagation direction is neglected relative to other terms (generally valid when the field correlation length is large relative to the field wavelength). From the parabolic wave equation, stochastic equations are formed for higher field moments, usually under the assumption the fluctuations in the refractive index are small relative to the mean, and the Markov assumption is used (the propagation medium is assumed to be delta correlated in the propagation direction). From this point further analytical progress is made by assuming that many correlation distances of the medium are traversed by the signal. Finally, it is often assumed that the medium can be collapsed to one or more thin screens with intervening free space. All of the above approximations can be explored using the FDTD technique.

Preliminary Results

We have performed some initial random media propagation calculations with our FDTD code. Figure 1 displays the time history at a receiver plane of an incident Gaussian pulse plane wave after propagation through a slab of ionization irregularities described by Gaussian statistics. The slab parameters were chosen to provide strong scatter within the computational grid ($L_o = 32 \text{ m}$, $\xi = \Delta N_e / \langle N_e \rangle = 0.8$, $\langle f_p \rangle = 4 \text{ MHz}$, slab thickness = 320 m). The incident pulse width was $0.0267 \text{ } \mu\text{sec}$ at the $1/e$ point. Extreme dispersion of the pulse is evident in the received waveform as the pulse is spread over several microseconds. Angular scatter is evident in the contorted wavefronts. In Figure 2 the corresponding frequency domain signal is displayed (magnitude only), and illustrates one of the greatest advantages of the time domain approach over spectral approaches: In a single calculation we have computed the response a very large portion of the HF band. Frequency domain approaches would have required numerous calculations to obtain such coverage. We note that signal absorption due to electron collisions was accounted for in this calculation, and thus much of the lower frequency component of the incident signal has been removed by the medium.

The reader familiar with RF signal propagation in randomly structured ionization will note that the calculation parameters associated with Figure 2 (quoted parenthetically above) put this calculation way outside the regime of validity of the standard random media propagation approximations. It is of interest, then, to see what the theory which makes use of all the approximations predicts in this case. To perform such a comparison, we computed the two position mutual coherence function (MCF) of the received field across the frequency band for several realizations similar to Figure 2, but for varying fractional electron variances ($\xi = 0.2, 0.4, 0.6, 0.8$). We then computed the correlation lengths of these MCFs and compared them to the results of an analytical calculation which made full use of all the standard approximations [Knepp, 1985]. The results are shown in Figure 3, where the FDTD results are shown as crosses and the standard approximate results

appear as solid curves (denoted *thin screen PE*). We point out that these computations were performed with minimal FDTD grid resolution due to the capacity of our current computer and are definitely preliminary (the 4 meter grid spacing employed corresponds to an adequate 8 points per wavelength near 10 MHz, but corresponds to only 4 grid points per wavelength at 20 MHz, which likely accounts for the oscillations and apparent plateau evident at the higher frequencies; results at the lower frequencies should be quite good). The first thing to note about Figure 3 is the remarkable agreement of the two methods considering how far away from the regime of validity the approximate theory was applied. The numerical values are at least of the same order of magnitude, and such accuracy is often all that is required when considering system performance issues in severely structured environments.

This apparent agreement is deceptive, however. Figure 4 displays a subset of the mutual coherence functions computed from the FDTD realizations and illustrates the manner in which the FDTD coherence lengths were computed to produce Figure 3. The standard definition of the coherence length is the $1/e$ point of the mutual coherence function. The weaker scatter cases, however, did not actually decorrelate to the $1/e$ point, so we instead chose to compute the correlation length as the $1/e$ point of the best fit Gaussian to the central peak of the mutual coherence function, as illustrated by the dotted curves of Figure 4. For the stronger scatter cases this definition proves to be substantially the same as the standard definition. For the weaker scattering cases the definitions are markedly different. In fact, Figure 4 shows that the field actually does not substantially decorrelate for the weakest case, although blind application of the standard theory predicts quite small correlation lengths. The apparent agreement shown in Figure 3 is actually a true agreement for only the strongest scattering cases. The prediction of the approximate theory for the weaker cases really only applies to the "initial" decorrelation represented by the central MCF peak. The difference could be very important to coherently processing systems such as OTH radar whose performance, by the misapplication of the standard theory, would be predicted to be severely degraded when, in fact, it could operate in the presence of substantially stronger ionospheric structure.

The above results are very preliminary and certainly do not constitute an analysis, but they provide some indication of the potential afforded by FDTD analysis of frequency dependent media. We hope in the near future to begin a careful analysis of each of the standard approximations described above. An approach for exploring the breakdown of the standard approximations is to create a data base of FDTD calculated fields for propagation through random media with specified statistical characteristics. The data base must be created under circumstances appropriate for each test. For example, comparisons between FDTD runs including and excluding the polarization coupling terms of the vector wave equation can elucidate the relative importance of those contributions to mutual coherence functions formed from the data base (we have performed a preliminary test of the neglect of polarization coupling and find definite differences in the coherence structure of the fields). The limits of viability of the other random media propagation theory

approximations can be explored similarly by creating data bases for propagation through irregular slabs of varying thickness (or strength, etc.) and comparing the resulting mutual coherence functions and stochastic signal structure parameters to those obtained directly from propagation theory or by comparison to the results of numerical multiple phase screen propagation.

References

- Budden, K. G., The Propagation of Radio Waves, Cambridge University Press, 1985.
- Bui, M. D., S. S. Stuchly, and G. I. Costache, "Propagation of Transients in Dispersive Dielectric Media," *IEEE Trans. Microwave Theory Tech.*, **39**, no. 7, pp.1165-1171, July 1991.
- Luebbers, R., F. Hunsberger, K. Kunz, R. Standler, and M. Schneider, "A Frequency-Dependent Finite-Difference Time-Domain Formulation for Dispersive Materials," *IEEE Trans. Electromagn. Compat.*, **EMC-32**, pp. 222-227, Aug. 1990.
- Luebbers, R., F. Hunsberger, and K. Kunz, "A Frequency-Dependent Finite-Difference Time-Domain Formulation for Transient Propagation in Plasma," *IEEE Trans. Ant. Propag.*, **AP-39**, no. 1, pp. 29-34, 1991.
- Joseph, R. M., S. C. Hagness, and A. Taflov, "Direct time integration of Maxwell's equations in linear dispersive media with absorption for scattering and propagation of femtosecond electromagnetic pulses," *Optics Letters*, **16**, no.18, pp. 1412-1414, Sept 15, 1991.
- Kashiwa, T., N. Yoshida, and I. Fukai, "Transient Analysis of a Magnetized Plasma in Three-Dimensional Space," *IEEE Trans. Ant. Propag.*, **AP-36**, no. 8., pp. 1096-1105, 1988.
- Knepp, D. L., "Aperture Antenna Effects After Propagation Through Strongly Disturbed Random Media," *IEEE Ant. Propag.*, **AP-33**, no. 10., pp. 1074-1084, 1985.
- Nickisch, L. J. and P. M. Franke, "Finite Difference - Time Domain Solution of Maxwell's Equations for the Dispersive Ionosphere," *IEEE Antennas and Propagation Magazine*, Vol. 34, No. 5, October 1992.
- Nickisch, L. J., "Non-uniform motion and extended media effects on the mutual coherence function: An analytic solution for spaced frequency, position, and time," *Radio Sci.*, **27**, no. 1, pp. 9-22, 1992.
- Yee, K. S., "Numerical Solution of Initial Boundary Value Problems Involving Maxwell's Equations in Isotropic Media," *IEEE Trans. Ant. Propag.*, **AP-14**, no. 3, pp. 302-307, 1966.

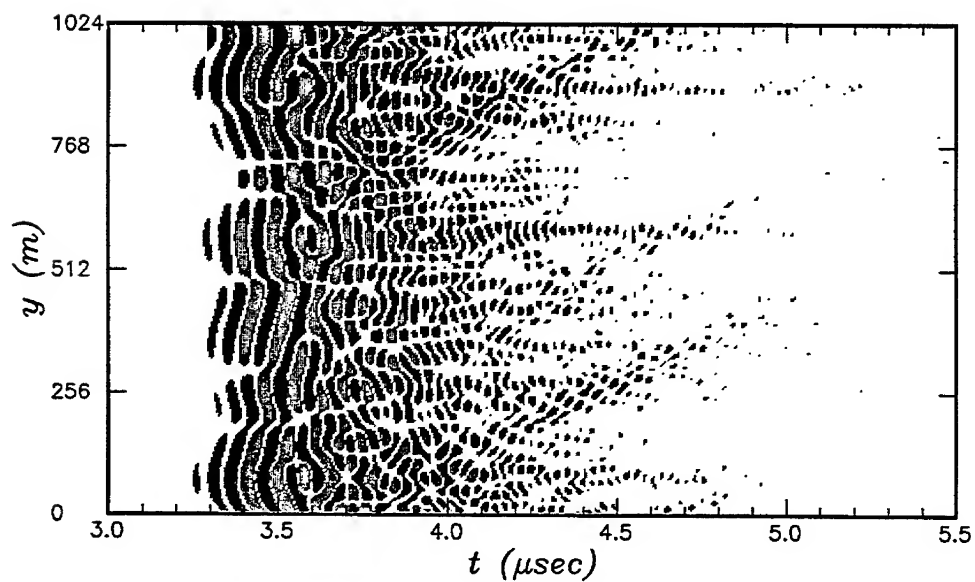


Figure 1. Time history of an initially gaussian plane wave pulse after propagation through a slab of gaussian distributed electron density.

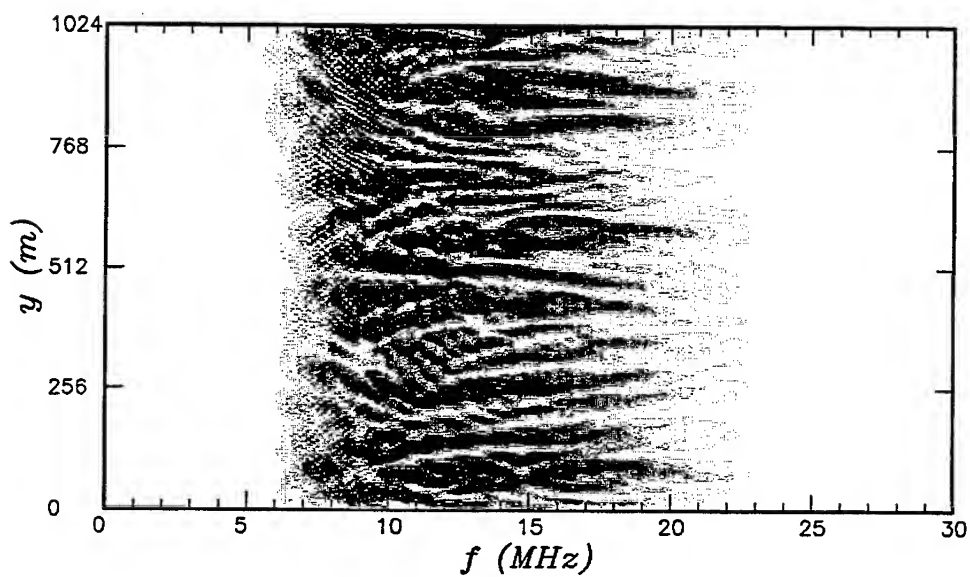


Figure 2. Frequency domain field magnitude corresponding to Figure 1.

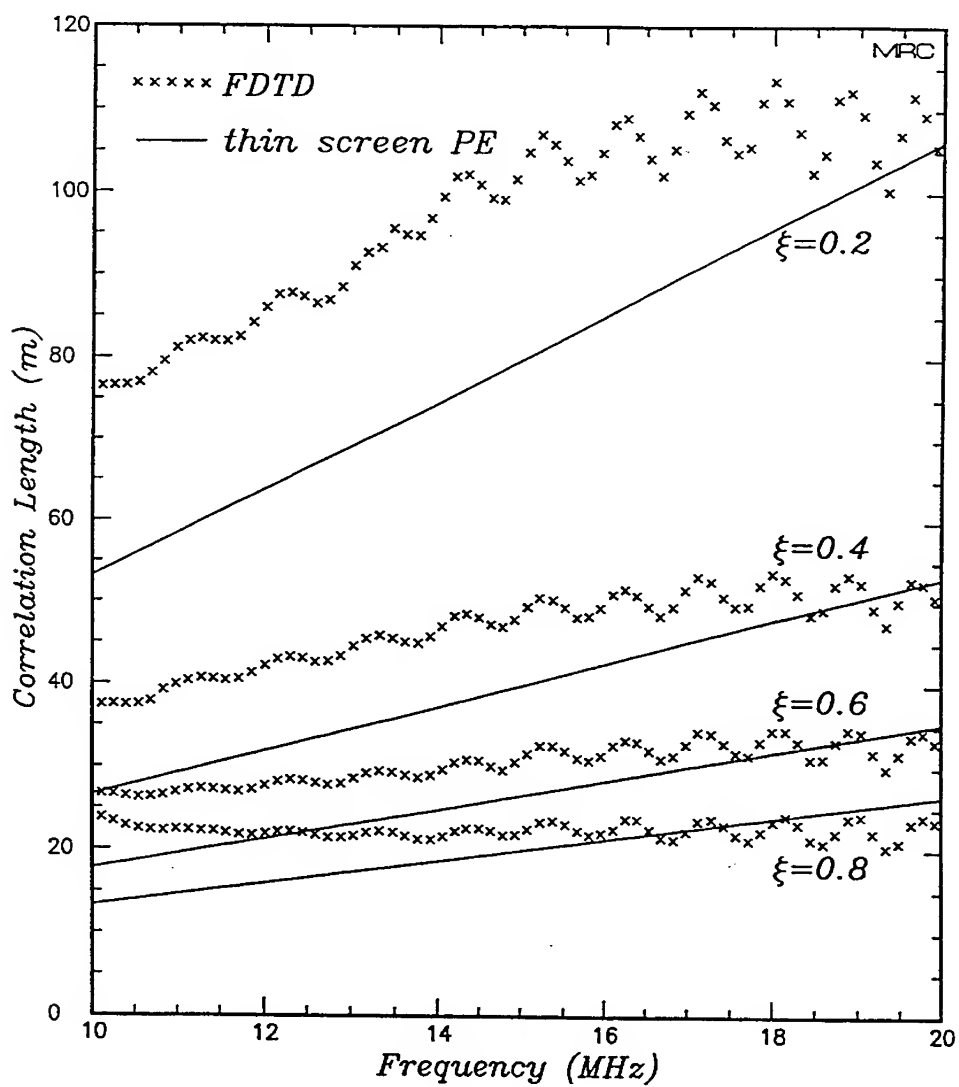


Figure 3. Comparison of FDTD computed correlation lengths (crosses) with the theoretical thin screen parabolic equation result (solid curves).

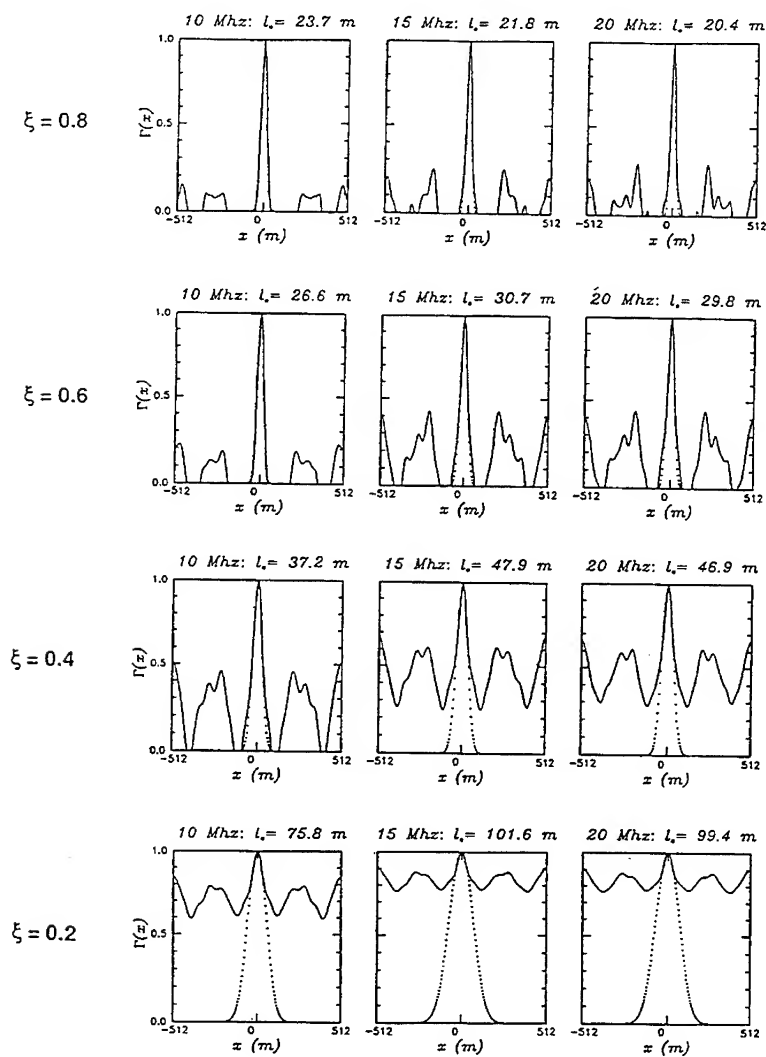


Figure 4. FDTD computed two position mutual coherence functions and best fit gaussians.

A RAY-BASED APPROACH TO SCATTERING FROM INHOMOGENEOUS DIELECTRIC OBJECTS

Hao Ling and Hyeongdong Kim

Department of Electrical and Computer Engineering
The University of Texas at Austin
Austin, TX 78712-1084

1. Introduction

A ray-based approach is developed to calculate the scattering from inhomogeneous dielectric objects. This approach is a natural extension of the "shooting and bouncing ray" (SBR) technique developed earlier for calculating the radar cross section of cavity structures and complex targets [1],[2]. In this formulation, a dense grid of rays representing the incident field is shot toward the scatterer (Fig. 1). The curved trajectory, amplitude, phase and polarization of the ray fields inside the inhomogeneous object are computed numerically based on the laws of geometrical optics. The contributions of the exiting rays to the exterior scattered field are then calculated by using the equivalence principle in conjunction with a ray-tube integration scheme.

This work is initially motivated by our effort to characterize the effect of space plasma from an arcjet thruster plume on the performance of microwave reflector antennas on-board communication satellites. The ray method is used to compute the ray optics field transmitted through the plume. The far field patterns of the reflector in the presence of the plume are computed for several plume-to-reflector configurations. For arcjet prototypes in the 1-kW class, the plume effect on the antenna performance is small. As the electron density increases (corresponding to higher arcjet power), a gradual degradation of the main beam and sidelobe level is observed. In addition, the main beam tends to squint away from the plume region. The resulting quantitative data are crucial in determining realistic constraints on the location and maximum power output of the arcjet for spacecraft integration.

We also generalize the ray approach to characterize the backscattering from inhomogeneous objects with well-defined boundaries. At the scatterer boundary, reflected and refracted rays are generated due to discontinuity of the medium parameters. Whenever the rays cross the scatterer surface, additional reflected/refracted rays are generated and are tracked. This process is repeated until the intensities of the refracted/reflected rays become negligible and the ray tracing algorithm can be terminated. The extended formulation is used to calculate the backscattering from inhomogeneous targets. For circular cylinders with simple permittivity profiles, good agreement with the exact series solutions is observed in the high frequency range. The ray approach not only complements other low-frequency numerical techniques, but also provides a simple physical picture of the backscattering mechanisms in penetrable objects.

2. Arcjet Plasma Study

An arcjet thruster is an electrothermal propulsion device being developed by NASA and the aerospace industry for stationkeeping and attitude control on future generation satellites. Because of its high efficiency, this device could significantly extend the lifetime of modern communication satellites. The operating principle of the arcjet consists of

heating a gas mixture (e.g., nitrogen-hydrogen) by means of a high temperature arc discharge. The heated propellant is then ejected through a nozzle to produce thrust. One important issue which arises in the actual spacecraft integration of arcjet technology is the environmental impact of the arcjet plume, especially on microwave communication systems. The arcjet produces a weakly ionized plasma, which modifies the free space normally surrounding the satellite and causes refraction and attenuation of the microwave signals to and from the spacecraft (Fig. 2). This is a primary user concern that must be addressed quantitatively before the arcjet technology can be fully accepted by the communication satellite industry. In this work, the effect of an arcjet plume on the performance of on-board reflector antennas is studied [3]. The arcjet plume is modeled as an inhomogeneous scatterer with a smoothly varying index of refraction. The spatial distribution of the refractive index is related to the measured electron density data based on the cold plasma model. To study the propagation of the microwave signal through the inhomogeneous plasma plume, geometrical optics is used. Choosing geometrical optics to attack this problem is motivated by several considerations: (a) the plume size of interest is more than several wavelengths in extent, (b) the permittivity distribution of the plume is smoothly varying, and (c) a ray approach is compatible with existing reflector analysis codes. Once the ray optics field transmitted through the plume is found on a near-field aperture, the far field performance degradation of the reflector in the presence of the plume can be fully characterized.

Shown in Fig. 3(a) is the geometry of the case under study. The reflector is assumed to have a diameter of 60 cm (20λ at 10 GHz) and a 10-dB aperture edge taper. The initial ray bundle after reflection from the reflector surface is assumed to be perfectly collimated and has perfect linear polarization in the y-direction. Also shown in the figure are ray trajectories through a plume with parameter $a_1 = 1 \times 10^{14} \text{ cm}^{-1}$ which corresponds to approximately 3 kW of arcjet power. It is observed that the rays tend to bend away from the high electron density region near the nozzle. The direction, phase, amplitude and polarization of the ray field transmitted through the plume are computed on an exit aperture plane. The far field of the reflector in the presence of the plume can be related to the transmitted field on the aperture plane through the standard radiation integral. The reflector patterns along the two principal planes for the geometry in Fig. 3(a) are computed and plotted in Figs. 3(b) and (c). Small but noticeable degradations in the main beam and the sidelobe regions are observed. In particular, the main beam is found to squint away from boresight in the H-plane. This effect can be interpreted physically if we ignore, to the first order, the refraction of the rays through the plume. We can then argue that the rays traveling closer to the nozzle must experience a smaller total phase shift than those farther away from the nozzle due to the lower permittivity of the inner plume region. Consequently, the transmitted field on the exit aperture $z=z_a$ has a tilted phase distribution which leads to the main beam squinting away from the plume region. In this example, the beam (beamwidth= 3.0°) experiences a 0.75° (0.25 BW) beam squint away from the boresight. This translates into a 0.94 dB gain loss. For very narrow beam antennas, this effect could become more serious. The E-plane pattern in Fig. 3(c) shows a higher sidelobe level than the H-plane pattern, and a noticeable cross polarization level due to the plume. The plume effect on reflector performance is strongly dependent on the actual plume-to-reflector configuration. An actual case study of the arcjet-reflector configuration has been carried out for the General Electric Series-7000 satellite and reported in detail in [4].

3. Backscattering from Arbitrary Inhomogeneous Objects

We next generalize the ray approach to characterize the backscattering from inhomogeneous objects with well-defined boundaries. The refractive index of the scatterer

is assumed to be smoothly varying, except at the scatterer boundary. To represent the incident plane wave, a large number of rays are shot toward the inhomogeneous object. The incident rays encounter the scatterer boundary and reflected rays and refracted rays are generated, e.g., at point 1 in Fig. 4. The refracted rays propagate inside the object and eventually encounter the scatterer boundary (point 2 in Fig. 4). Again reflected rays and refracted rays are generated, except this time the refracted rays exit the scatterer while the reflected rays bounce off the boundary and remain inside the inhomogeneous object. The intensities of the reflected rays should become weaker after every bounce against the boundary and this process can be terminated after several bounces. To account for the ray reflection and refraction at the curved scatterer boundary, the geometrical optics solution is implemented. Whenever a ray exits the scatterer boundary, the contribution of the ray to the total scattered field is calculated by a ray-tube integration scheme. The integration is taken over the projection of the ray tube on an arbitrary Huygens' surface and the fields on the surface are approximated by the ray fields (Fig. 5). The detail formulation can be found in [5].

Scattering results for a radially inhomogeneous circular cylinder are shown in Fig. 6. To establish a reference solution, the radially inhomogeneous cylinder can be modeled as a cylinder of many layers with different refractive indices. The series expansion solution to scattering from a radially multilayered cylinder is implemented and more than 10 layers per wavelength are used to approximate the exact solution for the inhomogeneous cylinder. This reference solution will be considered numerically exact. Cylinders with the following smooth permittivity profile are studied:

$$\epsilon_r(\rho) = n^2(\rho) = d + b(1 - c \cos \frac{\pi \rho}{a}) \quad (1)$$

where

$$d = \epsilon_r(a) - 1, \quad b = \frac{1 + [\epsilon_r(0) - d]}{2}, \quad c = \frac{1 - [\epsilon_r(0) - d]}{1 + [\epsilon_r(0) - d]}$$

This profile is an arbitrarily chosen function which varies smoothly between $\epsilon_r(0)$ at the cylinder center and $\epsilon_r(a)$ at the outer boundary. Fig. 6 depicts the results for $\epsilon_r(0)=2.1$ and $\epsilon_r(a)=2.5$. Plots of the echo width (normalized with respect to the free space wavelength) versus frequency are shown on the left column for the TE polarization. Good agreement between the exact series solution and the ray results is observed for $k_0 a > 10$ (cylinder diameter $> 3 \lambda_0$). In the low frequency range, the ray results deviate from the exact solution as expected. It is also observed from the results that there are two types of oscillations in the echo width versus frequency plots. These features correspond to different scattering mechanisms in the dielectric object and can be easily interpreted in terms of the ray picture. The small-scale local oscillations are due to the interference between the direct reflected ray and the once internally reflected ray. The large-scale global oscillations (with nulls occurring at $k_0 a=21$ and 39) are due to the interference between the reflected rays and the so-called "glory ray." Both types of oscillations as well as the overall echo width levels are accurately predicted by the ray formulation. The TM results are shown on the right column of Fig. 6. Again, good agreement between the ray results and the exact solution is observed. For the case of the TM incidence, the ray tracing data are identical to the TE case except for the reflection/transmission coefficients at the scatterer boundary. Since the on-axis rays have the same reflection/transmission coefficients for both polarizations, the local oscillation which are due to the interference between the on-axis rays should be the same for both polarizations. This is indeed the case by a detail comparison of the results for the two polarizations. The global oscillations, on the other hand, are very different for the TM and TE cases.

4. Discussions

A numerical ray tracing approach has been presented to calculate the scattering from electrically large, inhomogeneous objects. We conclude with several remarks concerning the numerical aspect of the ray approach. First, it is found from numerical experimentation that launching incident rays from a nonuniform grid is more efficient computationally than using uniform ray density. A higher ray density should be used on the outer region of the scatterer so that the number of rays per unit perimeter (or in the three-dimensional case, per unit surface area) launched toward the scatterer boundary is fixed. Convergence test is performed and it is found that more than four rays per wavelength along the scatterer boundary are necessary for convergent results. Second, the total scattered field should theoretically be independent of the choice of the Huygens' surface where the ray-tube integration is carried out. The most natural choice for the Huygens' surface is the scatterer boundary. However, when caustic points are located close to the scatterer boundary, the geometrical optics fields on the boundary are not accurate and the scattered field calculated based on the surface GO fields will not be accurate. This problem can be overcome by choosing a Huygens' surface larger than the scatterer boundary so that the caustic points are far away from the Huygens' surface where the geometrical optics fields are needed. In our calculations, the Huygens' surface is usually chosen to be about $8-10 \lambda_0$ away from the scatterer boundary. Finally, due to the large number of rays which need to be traced in the object, the scattering calculation using ray tracing is computationally intensive, especially for three-dimensional scatterers. However, since ray tracing is independent of frequency, once ray tracing is done for one frequency, the ray data for other frequencies can be trivially calculated by proper scaling. In conclusion, it has been shown that the ray approach is an effective method for characterizing the electromagnetic scattering from large inhomogeneous objects. For objects with smoothly varying medium parameters, the ray results agree well with the available exact solutions in the high frequency range. In addition, the ray approach provides a simple physical picture of the scattering mechanisms in penetrable objects. It serves as a good complement to other low-frequency techniques.

Acknowledgement

This work was supported by National Science Foundation grant ECS-8657524, NASA Lewis Research Center Cooperative Agreement NCC3-127 and General Electric Aerospace contract P.O. 55618080-F66.

References

- [1] H. Ling, R. Chou and S. W. Lee, "Shooting and bouncing rays: calculating the RCS of an arbitrary shaped cavity," *IEEE Trans. Antennas Propagat.*, vol. AP-37, pp. 194-205, Feb. 1989.
- [2] J. Baldauf, S. W. Lee, L. Lin, S. K. Jeng, S. M. Scarborough and C. L. Yu, "High frequency scattering from trihedral corner reflectors and other benchmark targets: SBR versus Experiment," *IEEE Trans. Antennas Propagat.*, vol. AP-39, pp. 1345-1351, Sept. 1991.
- [3] H. Ling, H. Kim, G. A. Hallock, B. W. Birkner and A. J. M. Zaman, "Effect of an arcjet plume on satellite reflector performance," *IEEE Trans. Antennas Propagat.*, vol. AP-39, pp. 1412-1420, Sept. 1991.
- [4] G. A. Hallock, H. Ling, D. Hastings, H. Kim and R. Chatterjee, "Arcjet plume plasma analysis," Final Report to GE-Aerospace Contract P.O. 55618080-F66, May 1991.
- [5] H. Kim and H. Ling, "Electromagnetic scattering from an inhomogeneous object by ray tracing," *IEEE Trans. Antennas Propagat.*, vol. AP-40, pp. 517-525, May 1992.

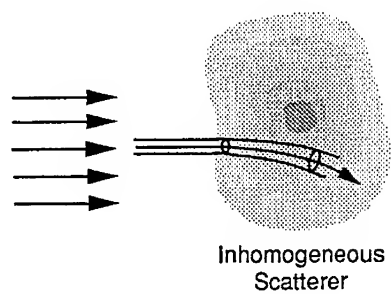


Fig. 1. Scattering from an inhomogeneous object by a ray shooting approach.

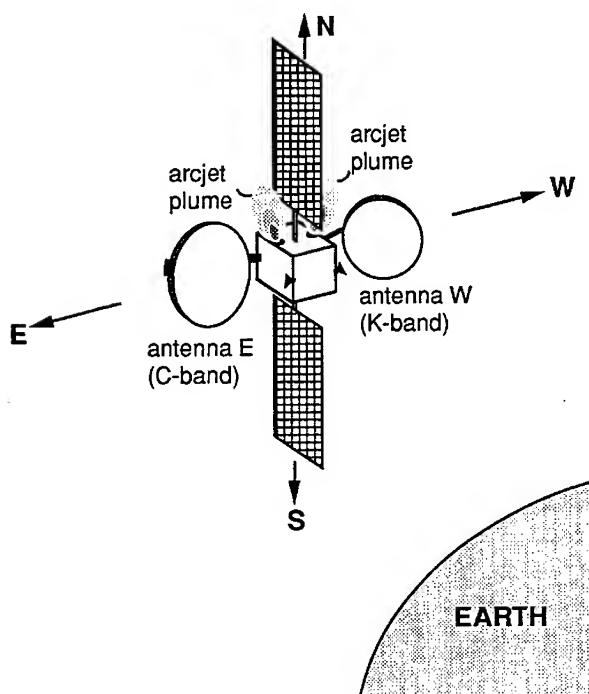


Fig. 2. Arcjet plume plasma effect on satellite reflector performance.

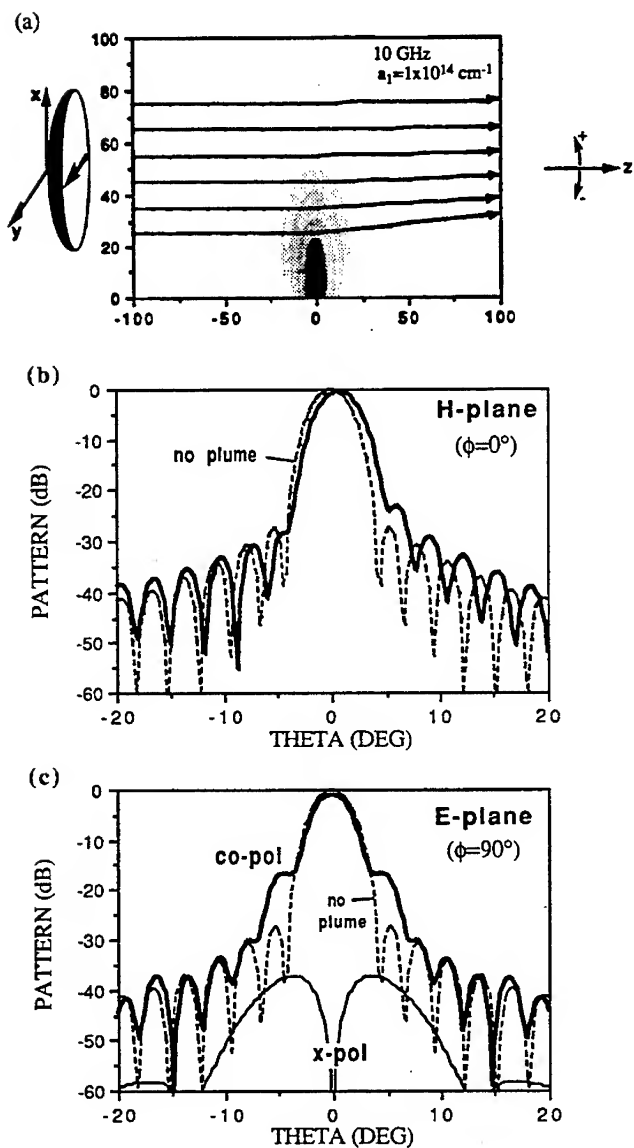


Fig. 3. Reflector pattern degradation due to a plasma plume. (a) Reflector and plume configuration. The reflector has a diameter of 60 cm (20λ at 10 GHz) and an assumed aperture taper of 10 dB. The polarization is linear in y. (b) H-plane pattern. (c) E-plane pattern.

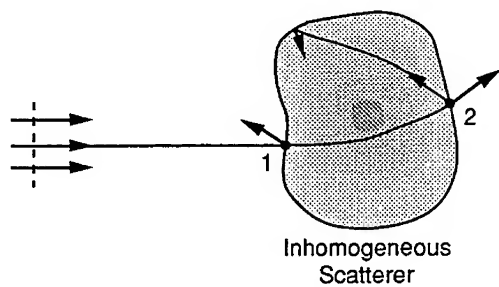


Fig. 4. Reflected and refracted rays are generated due to the medium discontinuity at the scatterer boundary.

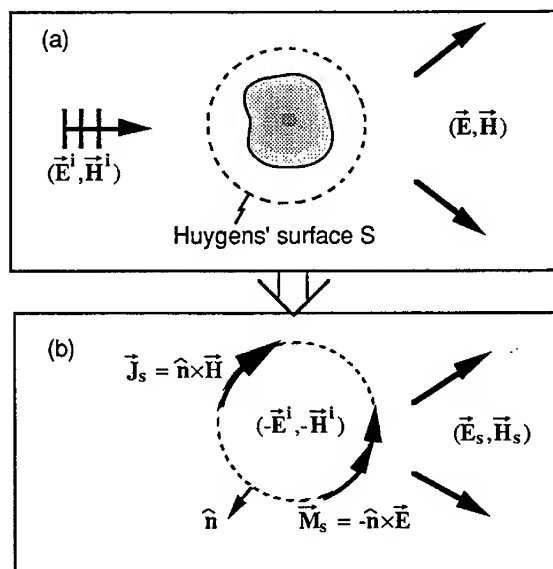


Fig. 5. Scattering formulation for inhomogeneous objects.
(a) Original problem. (b) Equivalent problem.

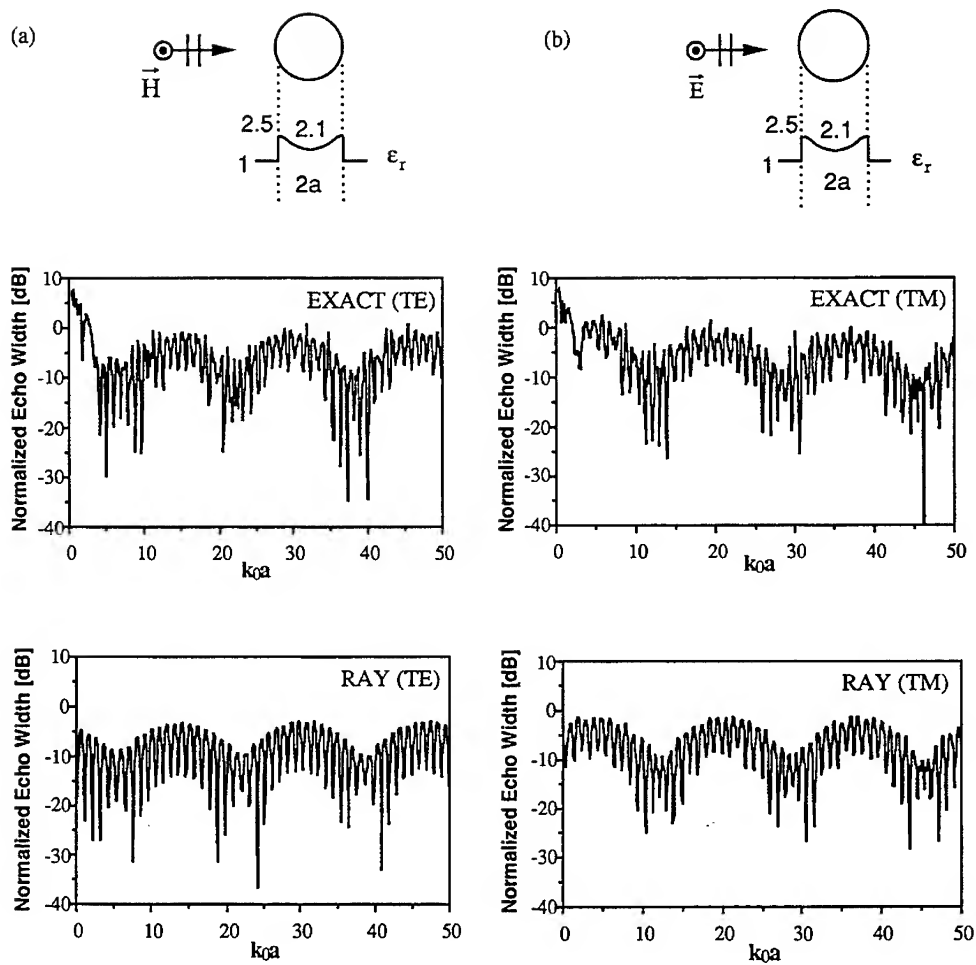


Fig. 6. Backscattering from an inhomogeneous cylinder computed from the exact multilayered solution and the ray solution for (a) TE incidence and (b) TM incidence.

Hierarchical Basis Functions for 3D Finite Element Methods¹

John R. Lovell
Schlumberger-Doll Research
Old Quarry Rd
Ridgefield, CT 06877

Introduction

In this paper, we consider FEM methods applied to complicated 3D structures that arise in borehole geophysics. The methodology we present applies to general solutions of Maxwell's equations but for notational simplicity we shall restrict ourselves to a scalar fields subject to Helmholtz's equation (or Laplace's equation if the problem is DC). We shall suppose that we do not want to use a general purpose 3D mesh generator in order that we can retain control over the properties of the resulting stiffness matrix. In particular, we would like to choose basis functions for the finite element solution that will provide enhanced structure to the matrix thereby allowing faster solution techniques. A typical example of a structured matrix is that stiffness matrix arising from a 3D mesh generated by rotating a 2D triangular mesh in ρ, z mesh about the z -axis. The triangles in the 2D mesh become pentahedra in the 3D domain Ω . The mesh topology within each azimuthal plane does not change with ϕ and so the matrix is block tridiagonal. Fast methods have been developed for such matrices, most recently on parallel machines (e.g., [7]).

The choice of mesh is intimately related to the choice of basis function. For example, with piecewise linear elements on a triangular mesh in ρ, z then within a triangle with nodes $(\rho_1, z_1), (\rho_2, z_2), (\rho_3, z_3)$ a scalar field is given as

$$(1) \quad u(\rho, z) = u_1 B_1^{\rho z}(\rho, z) + u_2 B_2^{\rho z}(\rho, z) + u_3 B_3^{\rho z}(\rho, z),$$

where

$$(2) \quad B_1^{\rho z}(\rho, z) = \frac{(\rho - \rho_3)(z_2 - z_3) - (\rho_2 - \rho_3)(z - z_3)}{(\rho_1 - \rho_3)(z_2 - z_3) - (\rho_2 - \rho_3)(z_1 - z_3)}$$

and similarly for $B_2^{\rho z}$ and $B_3^{\rho z}$. $B_i^{\rho z}$ can also be defined as that unique piecewise linear function on the domain which is 1 on the i th node and 0 on all of the other nodes and we see that u_i is the value of u at the i th node. If the mesh is rotated in ϕ then the triangle becomes a prism in cylindrical coordinates with triangular faces $(\rho_1, z_1, \phi_j), (\rho_2, z_2, \phi_j), (\rho_3, z_3, \phi_j)$ for $j = 1, 2$. With respect to this mesh, a scalar field u is given as

$$(3) \quad u = \sum_{i=1}^3 \sum_{j=1}^2 u_{ij} B_i^{\rho z}(\rho, z) B_j^{\phi}(\phi)$$

¹To be presented at Ninth Annual Review of Progress in Applied Computational Electromagnetics, Monterey, March 22nd - 26th, 1993.

where the $B^{\rho z}$ are the basis functions above and

$$(4) \quad B_1^\phi(\phi) = \frac{\phi_2 - \phi}{\phi_2 - \phi_1}, \quad B_2^\phi(\phi) = \frac{\phi - \phi_1}{\phi_2 - \phi_1}.$$

This type of 3D basis is traditionally also called a tensor product and written $B^{\rho z} \otimes B^\phi$. The corresponding approximation space is then written as $V_h^{\rho z} \otimes V_h^\phi$ where $V_h^{\rho z}$ is the space of piecewise linear functions over the mesh in ρ, z and V_h^ϕ is the space of piecewise linear functions in ϕ . If the material properties are separable then stiffness matrix will also take on a tensor product structure. For example, if we want to solve the differential equation

$$(5) \quad -\nabla \cdot \frac{1}{\sigma_1(\rho, z)\sigma_2(\phi)} \nabla u + i\omega\mu_1(\rho, z)\mu_2(\phi)u = f,$$

we can cast this as a Galerkin problem and look for $u \in V_h^{\rho z} \otimes V_h^\phi$ such that

$$(6) \quad -\int_{\Omega} v \nabla \cdot \frac{1}{\sigma_1 \sigma_2} \nabla u + \int_{\Omega} i\omega\mu_1\mu_2 v u = \int_{\Omega} v f$$

for all $v \in V_h^{\rho z} \otimes V_h^\phi$. Applying integration by parts (and assuming appropriate boundary conditions on $\partial\Omega$) gives

$$(7) \quad \int_{\Omega} \frac{1}{\sigma_1 \sigma_2} \nabla v \cdot \nabla u + i\omega \int_{\Omega} \mu_1 \mu_2 u = \int_{\Omega} v f.$$

In terms of the tensor product basis vectors this reduces to solving for u_{pq} such that

$$(8) \quad \sum_{pq} A_{ijpq}^{\rho z \phi} u_{pq} = f_{ij} \quad \text{for all } ij$$

where $A^{\rho z \phi} = A^{\rho z} \otimes M^\phi + M^{\rho z} \otimes A^\phi + i\omega M^{\rho z} \otimes M^\phi$. Here

$$(9) \quad A_{ip}^{\rho z} = \int d\rho dz \frac{1}{\sigma_1} \nabla B_i^{\rho z} \cdot \nabla B_p^{\rho z}, \quad M_{ip}^{\rho z} = \int d\rho dz \mu_1 B_i^{\rho z} \cdot B_p^{\rho z},$$

$$(10) \quad A_{jq}^\phi = \int d\phi \frac{1}{\sigma_2} \nabla B_j^\phi \cdot \nabla B_q^\phi, \quad M_{jq}^\phi = \int d\phi \mu_2 B_j^\phi \cdot B_q^\phi,$$

and

$$(11) \quad f_{ij} = \int d\rho dz d\phi B_i^{\rho z} B_j^\phi f.$$

Many techniques exist to solve this, so called, 2 1/2 D problem, typically involving some kind of Fourier decomposition in ϕ and direct or iterative matrix inversions in ρz (e.g., [3],[6]).

More generally, σ and μ will not separate along coordinate directions but may be constant within each pentahedral element. In this case, the matrix A still has a block structure but the tensor products must be weighted to account for the varying material properties. For such problems, Fourier transforms are

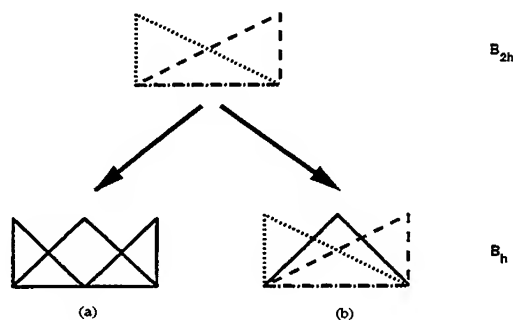


Figure 1: 2-level hierarchical bases on $[0, 1]$

inapplicable but good solution techniques are still available such as alternating direction implicit (ADI) with appropriately chosen Chebyshev acceleration parameters ([9],[12]).

For some remaining problems, however, it is not appropriate to suppose the material properties to be piecewise constant. For example, the cylindrical mesh will not be aligned with structures which are deviated with respect to the cylindrical axis. Such configurations arise in borehole geophysics when the borehole has not been drilled perpendicular to bedding planes – an increasingly common exploration procedure. There can be sharp variations in conductivity across these dipping beds, or else high conductivity deviated fractures can intersect the borehole. Such anomalies will significantly affect the response of borehole logging tools. For good accuracy, with as few node points as possible, it has generally been accepted that the mesh should be conformal with the bed boundaries and fractures.

An obvious solution is to use a general purpose mesh generator. Unfortunately, the resulting stiffness matrices will be completely unstructured. One node may have few neighbours, another very many. Moreover, horribly skewed tetrahedra can result far from the bed boundaries thereby severely degrading the accuracy (to the point where one would probably have been better off approximating the bed profiles as piecewise constant within a *non-conformal* mesh).

Another approach is to include the bed boundary into an existing structured mesh by subdividing appropriate pentahedra or hexahedra into tetrahedra aligned with the discontinuity. This can be performed in a straightforward manner but subdividing one face typically implies that the neighbouring element must also be subdivided, and so the next, and so on, until one arrives at the mesh of tetrahedra we had tried to avoid.

In the next section we show how to use embedded or hierarchical systems of basis functions to add nodes along interfaces without having to subdivide pentahedra far from bed boundaries. Moreover, we shall show how the resulting stiffness matrix is well structured allowing the use of advanced inversion techniques.

Hierarchical Bases

A sequence of basis vectors is called hierarchical if each basis is a subset of the next. For a simple example consider a basis consisting of the two functions defined on $[0, 1]$ shown in the top of Figure 1. The lower figures show two choices of basis for a vector space defined on a mesh V_h which is half the diameter of the original mesh. The upper set of basis functions is denoted B_{2h} . Figure 1a shows a non-hierarchical basis, whereas Figure 1b shows a hierarchical scheme. In the latter case, the basis vectors of B_{2h} are also basis vectors of B_h . Hierarchical bases in FEM offer many of the advantages found in nested dissection or substructuring and their use also drastically improves the stiffness matrix condition number ([11]). Such bases also offer intriguing connections with multigrid, ([10]), and with the (different) aggregation methods of Chatelin & Miranker ([2]), Chew ([4]), and Douglas ([5]). There is also currently interest in the hierarchical properties of wavelet bases (e.g., [8]).

For a more complicated example of nested basis, consider Laplace's equation with Dirichlet boundary conditions

$$(12) \quad \nabla \cdot \sigma \nabla u = 0, \quad u = f \text{ on } \partial\Omega$$

discretized using the two meshes shown in Figure 2. We suppose that σ is constant above and below the diagonal interface, Γ , shown in Figure 2b. The set of piecewise bilinear basis functions used in Figure 2a will be denoted B_1 . The basis functions used in Figure 2b will be the linear elements on triangles given in equation (2) and denoted B_2 . We suppose that we do not want to use the triangular basis functions over the whole domain, but instead choose $B_1 \cup \tilde{B}_2$ where \tilde{B}_2 denotes those triangular basis functions which are zero at any node of B_1 . In this way, we gain the ability to model sharp changes in the field across the interface without changing the basis functions away from the interface. Suppose that V_i is the space of functions generated by B_i , then we want to write the scalar field u as $u_1 + u_2$ with $u_i \in V_i$. This decomposition would not normally be unique. We enforce uniqueness by insisting that $u_2 = 0$ on all of the nodes of B_1 . u_2 is thus only non-zero on the area shown shaded in Figures 2a and 2b, which we denote Ω_2 . The non-zero nodes of u_2 lie only along the 1D interface, Γ .²

At the boundaries of the domain, we suppose that $f \in V_1$ so that we can set $u_2 = 0$ everywhere on the boundary $\partial\Omega_2$. We write V_1^0 for the space of piecewise bilinear functions in V_1 which are zero on the boundary $\partial\Omega$. We thus obtain a well-defined Galerkin scheme by choosing test functions $v_1 \in V_1^0$ and $v_2 \in V_2$ such that

$$(13) \quad \int_{\Omega} \sigma \nabla v_1 \cdot \nabla (u_1 + u_2) = 0 \quad \text{and} \quad \int_{\Omega} \sigma \nabla v_2 \cdot \nabla (u_1 + u_2) = 0$$

for all v_1 and v_2 , with $u_1 = f$ on $\partial\Omega$ and $u_2 = 0$ on $\partial\Omega_2$. This obviously corresponds to a stiffness matrix with block structure

$$(14) \quad \begin{pmatrix} A_{11} & A_{12} \\ A_{12}^T & A_{22} \end{pmatrix}.$$

²In purely formal terms, we can think of u_2 being the restriction to Γ of a function in $H^1(\Omega)$ with $u_2|_{\partial\Omega} = 0$, so that $u_2 \in H_0^{1/2}(\Gamma)$. We have chosen a decomposition $H^1(\Omega) = \bar{H}^1(\Omega) \oplus H_0^{1/2}(\Gamma)$ where $\bar{H}^1(\Omega)$ is that space of functions u with $\langle u, v \rangle_{\Gamma} = 0$ for all $v \in H_0^{1/2}(\Gamma)$. I.e., we have specifically removed from $H^1(\Omega)$ those functions which have discontinuous normal derivative across Γ and put those functions into $H_0^{1/2}(\Gamma)$ instead. The FEM discretization inherits the decomposition of these function spaces.

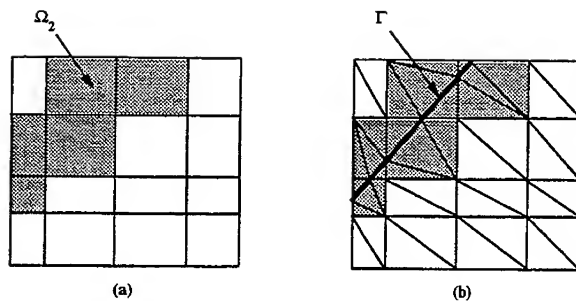


Figure 2: Meshes on $[0, 1]^2$

A_{11} denotes the discretized Laplace equation using piecewise bilinear functions over Ω and A_{22} represents the discretized Laplace equation using piecewise linear functions over Ω_2 . A_{11}^{-1} produces a function whose normal derivative is continuous across Γ , so that the normal current is discontinuous and leads to a charge build up. u_2 is the extra contribution needed to make the normal current continuous again. The coupling matrix A_{12} will take on a similar form to that from Figure 1b. One can think of the solid triangle being a basis function in \tilde{B}_2 and the basis functions $B_{2h} \subset B_h$ are the B_1 .

This example was a little contrived because on $\partial\Omega_2$, u_2 is linear and so could match perfectly against a bilinear function defined on the rectangles. A simple strategy would have been to remove the bilinear basis functions from Ω_2 and have a well-defined finite element scheme with triangles inside Ω_2 and rectangles outside.

This strategy is *not* possible in 3D. An intersecting plane will result in a mesh of tetrahedra on Ω_2 and give rise to piecewise linear functions defined on the triangles of the boundary $\partial\Omega_2$. These would *not* match up against the bilinear elements on the square faces of $\partial(\Omega - \Omega_2)$. In effect, $u_1 + u_2$ would not be continuous. The only ways to enforce continuity are either (i) extend Ω_2 to encompass the whole domain or (ii) set $u_2 = 0$ on $\partial\Omega_2$. The first case, that of extending Ω_2 to the entire domain requires a tetrahedral mesh everywhere, which was what we had tried to avoid. In the second case, we see that $u_1 + u_2$ is continuous precisely because the zero function is equally well defined as bilinear on a square mesh or linear on a triangular mesh.

Our strategy for 3D meshing is thus to rotate a 2D mesh of triangles to form a mesh of pentahedra. The stiffness matrix A_{11} will be block tridiagonal. Each bed boundary defines an intersecting plane which cuts through the domain. We convert each intersected pentahedra into a sum of tetrahedra, but we *only* subdivide those pentahedra which are actually intersected. We write Ω_2 for the sum of tetrahedra. We solve for $u_1 + u_2$ where u_2 is defined on the mesh of tetrahedra and, for continuity, u_2 is zero on $\partial\Omega_2$. A_{22} represents Laplace's equation on the tetrahedra. A_{11} represents the differential equation relative to the original discretization scheme.³

³ A_{11} could also correspond to a finite difference discretization.

Because the stiffness matrix has retained a rich structure, many iterative and direct inverse methods suggest themselves. We shall give examples based on conjugate gradient with suitable preconditioners. The preconditioned conjugate gradient algorithm is well known, e.g., see [1], and will not be repeated here.

We shall consider preconditioners based upon ILU factorization which requires that we decompose the stiffness matrix A as $LU + C$ where L is lower triangular with unit diagonals, U is upper triangular. C is chosen so that $L_{ij} = U_{ij} = 0$ if $A_{ij} = 0$.⁴ An advantage of this decomposition is that L and U can be stored with the same sparse matrix structure as A . The standard (unmodified) ILU algorithm given in [1] is

```

do r = 1 to N - 1
  do r = 1 to N - 1
    d = A(r, r)
    do i = r + 1 to N
      if A(i, r) ≠ 0 then
        e = A(i, r)/d
        A(i, r) = e
        do j = r + 1 to N
          if A(r, j) ≠ 0 then
            if A(i, j) ≠ 0 then
              A(i, j) = A(i, j) - e × A(r, j)
            end if
          end if
        end do
      end if
    end do
  end do
end do

```

At the end of the algorithm, A has been overwritten by L and U with L having unit diagonals which are not stored (i.e., the diagonal elements that are stored in A after the ILU algorithm are the diagonal elements of U). If A is complex symmetric, C will be also and $U = DL^*$ for some diagonal matrix D . (Clearly, $D_{ii} = U_{ii}$ because $L_{ii} = 1$.)

A disadvantage of the ILU algorithm above is that even if A is positive definite then LU need not be. Only in some restricted cases (see [1] for references) can the matrix LU be shown to be positive definite. Recall that the preconditioned conjugate gradient algorithm generally converges faster if the preconditioner is positive definite, although this is by no means a necessary condition.

We have found that the positivity of LU depends strongly on the node numbering chosen. In particular, if we choose a 'natural' ordering, with the overlay nodes listed after the pentahedral nodes then the convergence was almost invariably poor. Nor did choosing a profile minimizing scheme such as reverse

⁴We are ignoring the block structure so here $i, j = 1, \dots, n$ where n is the total number of nodes.

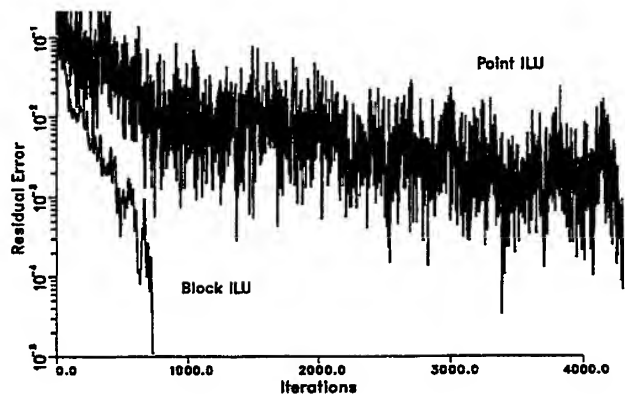


Figure 3: Point versus Block ILU Preconditioning

Cuthill – Mckee help.⁵ The problem is that we are trying ‘point-oriented’ preconditioners. We are ignoring the block structure of A and that is a mistake.

A better preconditioner is to write $A_{11} = L_{11}U_{11} + C_{11}$ and $A_{22} = L_{22}U_{22} + C_{22}$ so that

$$(15) \quad \begin{pmatrix} A_{11} & A_{12} \\ A_{12}^t & A_{22} \end{pmatrix} = \begin{pmatrix} L_{11} & 0 \\ 0 & L_{22} \end{pmatrix} \begin{pmatrix} U_{11} & 0 \\ 0 & U_{22} \end{pmatrix} + \begin{pmatrix} C_{11} & A_{12} \\ A_{12}^t & C_{22} \end{pmatrix}$$

Although the defect matrix, C , is now bigger than it was for point-ILU, the number of iterations will be greatly decreased, even if $L_{11}U_{11}$ or $L_{22}U_{22}$ are not positive definite. A comparison of the two preconditioners is shown in Figure 3. This example involved a Dual Laterolog[†] in a $0.01\Omega m$ borehole with one semi-infinite bed of resistivity $1\Omega m$ beneath another of resistivity $100\Omega m$. The interface was inclined by 80 degrees. We compare point-ILU preconditioning with block ILU preconditioning. The former required 4300 iterations and the latter only 740. For this problem, there were 3329 nodes in each of 32 ρz planes and an additional 7629 tetrahedral nodes, making a total of 114157 unknowns. For this example, if we chose to *not* add the additional basis functions on the tetrahedra, the number of iterations fell to 720 and the accuracy degraded by 8%.

In conclusion, we have developed a robust method of adding basis functions which are conformal with sharp changes in material properties. If appropriate block preconditioners are chosen then these additional functions do not cause any significant increase in the number of iterations required for convergence.

⁵Moreover, an RCM numbering will destroy the structure of A that we have been trying to maintain!

[†]Trademark of Schlumberger

NEPAL—The Use of Huygens' Equivalence Principle for Solving the Volume Integral Equation of Scattering *

WENG CHO CHEW AND CAI-CHENG LU
DEPARTMENT OF ELECTRICAL AND COMPUTER ENGINEERING
UNIVERSITY OF ILLINOIS
URBANA, IL 61801

Abstract

A new algorithm is proposed to solve the volume integral equation whereby the scatterer is first divided into N subscatterers. Smaller problems are nested within larger problems so that the problem can be solved in $\log N$ steps. The use of Huygens' equivalence principle reduces the number of unknowns at each stage. The resultant algorithm has reduced computational complexity whose CPU time is proportional to $N^{1.5}$ in two dimensions, and N^2 in three dimensions. Unlike the conjugate gradient method, the solution is valid for all incident waves. Hence, effectively, the matrix equation that is related to the volume integral equation is inverted with reduced computational complexity.

1. Introduction

Recently, we have developed a recursive aggregate T-matrix algorithm (RATMA) to solve volume integral equation valid for all incident waves with reduced computational complexity compared to a direct solution via a matrix equation with Gaussian elimination [1-4]. The method has a computational complexity of N^2 for two dimensional scattering problems ($N^{7/3}$ for three dimensions) where N is the total number of unknowns needed to characterize the volume of the scatterer.

In this paper, we present an algorithm [5] to solve volume integral equations valid for all incident waves with computational complexity of $N^{1.5}$ in two dimensions and N^2 in three dimensions. This is of reduced computational complexity compared to RATMA. We shall call this the nested equivalence principle algorithm (NEPAL).

The nested equivalence principle algorithm (NEPAL) is similar to many fast algorithms like FFT [6] and the nested dissection ordering approach in finite element method [7,8]. The principal idea of this approach is to nest one

* This work was supported by the Army Research Office under contract DAAL03-91-G-0339, and the Office of Naval Research under grant N00014-89-J-1286. The computer time was provided by the National Center for Supercomputer Applications at the University of Illinois.

algorithm within another so that a smaller problem is solved before a larger one. The size of the problem increases by a factor of 2^n at each stage where n is the dimension of the problem. In this manner, an N unknown problem is solved in $\log_2 N$ steps. Moreover, the use of Huygens' principle reduces the number of unknowns at each stage so that the computational labor is being reduced. The resultant complexity is $N^{1.5}$ in two dimensions and N^2 in three dimensions.

2. The Volume Integral Equation

A volume integral equation has the form [4]

$$\phi(\mathbf{r}) = \phi_{inc}(\mathbf{r}) + \overbrace{\int_V d\mathbf{r}' g_0(\mathbf{r} - \mathbf{r}') k_0^2 [\epsilon_r(\mathbf{r}') - 1] \phi(\mathbf{r}')}^{\phi_{sca}(\mathbf{r})} \quad (1)$$

or

$$\phi(\mathbf{r}) = \phi_{inc}(\mathbf{r}) + \underbrace{\int_V d\mathbf{r}' \nabla g_0(\mathbf{r} - \mathbf{r}') [\epsilon_r^{-1}(\mathbf{r}') - 1] \cdot \nabla' \phi(\mathbf{r}')}_{\phi_{sca}(\mathbf{r})} \quad (2)$$

where $g_0(\mathbf{r} - \mathbf{r}')$ is the Green's function. In electromagnetics, the first form is for the scattering of E_z polarized waves while the second form is for the scattering of H_z polarized waves.

A usual practice in solving (1) and (2) is to discretize the scatterer into N discrete pieces and approximate the integrals in (1) with summations. Hence,

$$\phi_{sca}(\mathbf{r}) = \sum_{i=1}^N \psi^i(k_0, \mathbf{r}_i) \cdot \mathbf{b}_i, \quad (3)$$

where $\mathbf{r}_i = \mathbf{r} - \mathbf{r}'_i$, and $\psi^i(k_0, \mathbf{r}_i)$ is a row vector containing outgoing-wave cylindrical harmonics in two dimensions and spherical harmonics in three dimensions [4, p. 460]. The column vector \mathbf{b}_i contains the magnitudes of the harmonic expansions. For monopole subscatterers, \mathbf{b}_i is a one-component vector corresponding to the monopole harmonics, while for dipole subscatterers, \mathbf{b}_i is a three-component vector corresponding to three harmonics. For instance, Equation (1) will yield principally monopole subscatterers while Equation (2) will yield principally dipole subscatterers. The unknown \mathbf{b}_i can be found by imposing a boundary condition on all the N subscatterers.

3. The Huygens' Equivalence Principle

The Huygens' equivalence principle stated mathematically is

$$\phi_{sca}(\mathbf{r}) = \oint_S dS' \hat{n} \cdot [\phi_{sca}(\mathbf{r}') \nabla' g_0(\mathbf{r} - \mathbf{r}') - g_0(\mathbf{r} - \mathbf{r}') \nabla' \phi_{sca}(\mathbf{r}')] \quad (4)$$

It can be used to shift the scattering centers of the subscatterers to the surface as shown in Figure 1. In this manner, the number of scattering centers can be reduced. If the number of volume subscatterers is $O(n)$, the number of surface subscatterers is then $O(n^{0.5})$ in two dimensions, and $O(n^{0.66})$ in three dimensions. This reduction in the number of scattering centers can be used to reduce the computational labor of solving for the scattering solution of a volume scatterer as illustrated by NEPAL.

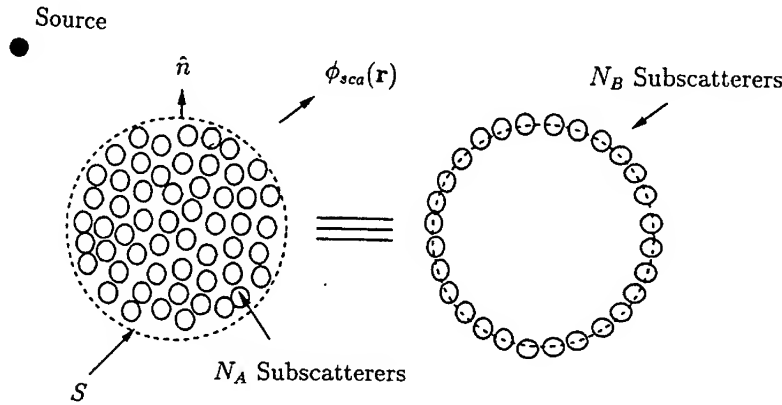


Figure 1. Huygens' equivalence principle helps to reduce the number of scattering centers.

Mathematically, the reduction in the number of scattering centers can be expressed as follows. Initially, we have N_A volumetric subscatterers as illustrated in Figure 1. The scattered field from these N_A scattering centers, in the manner of Equation (3), can be expressed as

$$\phi_{sca}(\mathbf{r}) = \sum_{i=1}^{N_A} \psi^i(k_0, \mathbf{r}_i) \cdot \mathbf{b}_i \quad (5)$$

where $\psi^i(k_0, \mathbf{r}_i)$ represents a column vector of spherical harmonics emanating from the center \mathbf{r}_i . Huygens' principle states that this scattered wave can be replaced by wave radiating from equivalence surface sources on a surface enclosing the N_A subscatterers (see Figure 1). In other words, the N_A volumetric scattering centers can be replaced by N_B scattering centers residing on the surface. Mathematically, we now have

$$\phi_{sca}(\mathbf{r}) = \sum_{m=1}^{N_B} \psi^i(k_0, \mathbf{r}_m) \cdot \mathbf{c}_m \quad (6)$$

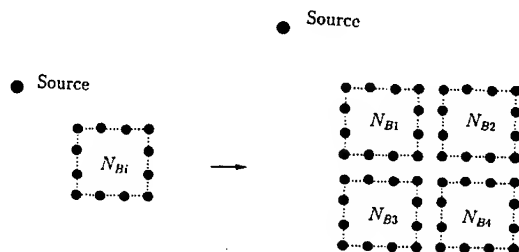


Figure 2. NEPAL—Nested equivalence principle algorithm.

where now, the wave emanates from \mathbf{r}'_m residing on the surface S . Since the wave equation is linear, a linear relationship exists between \mathbf{c}_m and \mathbf{b}_i . This relationship can be found via the use of Huygens' principle. Consequently, we have

$$\mathbf{c}_m = \sum_{i=1}^{N_A} \mathbf{h}_{mi}^{(0)} \cdot \mathbf{b}_i, \quad m = 1, \dots, N_B \quad (7)$$

Note that $N_B \approx \sqrt{N_A}$, so a large reduction in the number of scattering centers ensues when N_A is large.

4. Nested Equivalence Principle Algorithm (NEPAL)

The nested equivalence principle algorithm (NEPAL) is similar in spirit to fast Fourier transform [6] and nested dissection ordering in finite element method [7,8]. The idea is to divide the original problem into subgroups. The subgroups are then further divided into sub-subgroups until the lowest level of subgroups is reached. In two dimensions, the lowest level is in groups of four (see Figure 2) while in three dimensions, it is in groups of eight. (For 1D FFT, it is in groups of two.)

For instance, in two-dimensions, first, at the lowest level, the scattering solutions for groups of four subscatterers are solved. Then, at the next higher level, the scattering solution from four groups each consisting of four subscatterers are solved. Hence, the scattering solution from a group of 16 subscatterers are known. Then, the Huygens' equivalence principle is used to replace 16 scattering centers with 12 scattering centers. Then at the next higher level, the scattering solutions for four groups of scatterers each consisting of 12 subscatterers (i.e. 48 subscatterers) are solved. The process is repeated until the scattering solution for the entire scatterer is obtained.

Because of the use of Huygens' equivalence principle at each stage, the number of subscatterers involved or the number of unknowns is reduced by

roughly a factor of two at stage i when i is large. Hence, even if Gaussian elimination is used at each stage to solve for the scattering solution, reduction in computational labor ensues. It shall be shown in the next section that when N gets sufficiently large, this is asymptotically an $O(N^{1.5})$ algorithm in two dimensions.

5. Computational Complexity

The most important aspect of this algorithm is its reduced computational complexity of $O(N^{1.5})$. This fact can be appreciated even without understanding the details of the algorithm. It is the consequence of nesting a smaller problem within a larger one and the use of Huygens' equivalence principle.

If a scatterer can be modeled by N scattering centers, a straightforward approach to solve this problem valid for all incident waves is to convert the problem into an N unknown problem with an $N \times N$ matrix. The matrix equation can be solved for all possible right-hand side (equivalent to all possible incident waves) by Gaussian elimination, for instance, and this results in an $O(N^3)$ solution technique.

On the other hand, if we use a divide-and-conquer strategy, a more efficient algorithm can be developed. Assume that $N = 4^L$, where $L > 2$. Then, we can first divide the N subscatterers into groups each containing 16 subscatterers, resulting in $N/16$ groups.* We first solve the 16 subscatterer problem using the $O(n^3)$ algorithm mentioned in the previous paragraph, making the 16-subscatterer solution valid for all incident waves. This is repeated $N/16$ times, which is the number of groups present. Hence, in the first stage, the operation count is proportional to

$$(16)^3 \times \frac{N}{16} = 16^2 N \quad (8)$$

The next step is to replace the interior scattering centers of each group by surface scattering centers, which is the execution of Equation (7). This is a procedure with subdominant operation count compared to (8). With the interior scatterers of each group removed now, then we regroup four previous groups into one larger group, and solve a new scattering problem involving the larger group. Because of the removal of the interior scattering centers, the number of unknowns of the new larger group is not 4×16 , but a number

* We start with groups of 16 subscatterers at the lowest level because Huygens' principle cannot be used to reduce the number of scattering centers for groups of 4 subscatterers at the lowest level.

less than that. (In this case, it is 4×12 .) Approximately, the use of Huygens' principle halves the number of unknowns. Hence, asymptotically, the number of unknowns per group doubles when one goes from stage i to stage $i+1$. (This is an approximation at the early stage, but becomes increasingly accurate when i becomes large.) However, the number of the larger groups now to be solved separately is $N/(16 \times 4)$. Hence, the CPU time in the second stage is approximately

$$(16 \times 2)^3 \frac{N}{16 \times 4} = 16^2 2^2 N. \quad (9)$$

Hence, repeating the same argument, and assuming that the number of unknowns only doubles at each stage, in the i -th stage, the CPU time is proportional to

$$T_i = 16^2 2^i N \quad (10)$$

and the problem is solved in $P = \log_4 N - 1$ steps. The total CPU time is then

$$\begin{aligned} T &= 16^2 N + 16^2 2^2 N + \dots + 16^2 2^P N \\ &= 16^2 N \sum_{i=0}^P 2^i = 16^2 N (2^{P+1} - 1) \end{aligned} \quad (11)$$

Since $2^{P+1} = 2^{\log_4 N} = \sqrt{N}$, when $N \rightarrow \infty$, the above becomes

$$T \approx 16^2 N^{1.5} \quad (12)$$

Hence, it is an $O(N^{1.5})$ algorithm. The reduction in computational complexity is the result of nesting a smaller problem within a larger one, and reducing the number of unknowns by Huygens' equivalence principle at each stage. The solution is valid for all incident waves.

6. Numerical Results and Conclusions

We have implemented NEPAL to solve volume integral equations (1) and (2) and compared the results with directly solving the volume integral equations by the method of moments (MOM) [9]. The results are in good agreement for both E_z and H_z -polarized waves. We illustrate the comparison for the E_z and H_z polarized waves in Figure 3.

We have also studied the growth of computer time with the number of unknowns in the problem and found that NEPAL is very competitive with RATMA in this preliminary investigation as shown in Figure 4. It is certainly more efficient than MOM using Gaussian elimination. Moreover, the solution

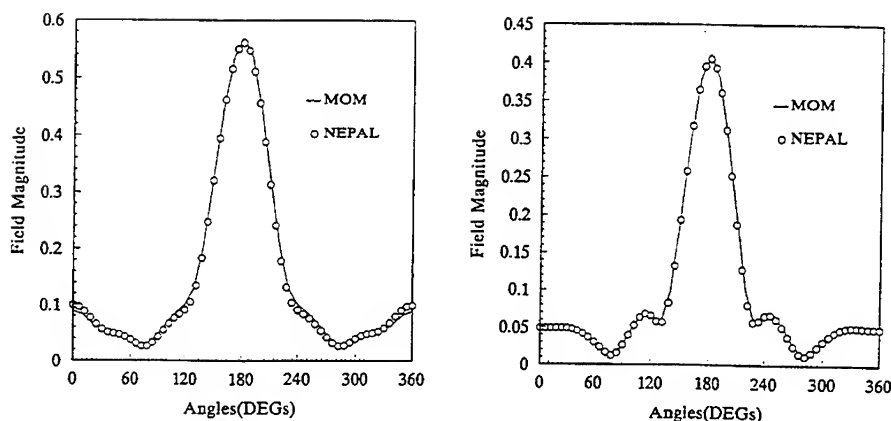


Figure 3. Comparison of NEPAL with method of moments for (a) E_z , and (b) H_z wave scattering.

it provides is valid for all angles of incident unlike conjugate-gradient-type methods [10].

The idea of NEPAL can also be used to expedite the calculation of a matrix-vector multiplication in the conjugate-gradient algorithm. It can be shown that in such a case, the computational complexity of the matrix-vector multiplication can be reduced to $O(N)$ from $O(N^2)$.

REFERENCES

- [1] W. C. Chew, "An N^2 algorithm for the multiple scattering solution of N scatterers," *Microwave Optical Tech. Lett.*, vol. 2, no. 11, pp. 380-383, 1989.
- [2] Y. M. Wang and W. C. Chew, "An efficient algorithm for solution of a scattering problem," *Microwave Optical Tech. Lett.*, vol. 3, no. 3, pp. 102-106, 1990.
- [3] W. C. Chew and Y. M. Wang, "A fast algorithm for solutions of a scattering problem using a recursive aggregate τ matrix method," *Microwave Optical Tech. Lett.*, vol. 3, no. 5, pp. 164-169, 1990.
- [4] W. C. Chew, *Waves and Field in Inhomogeneous Media*, Van Nostrand

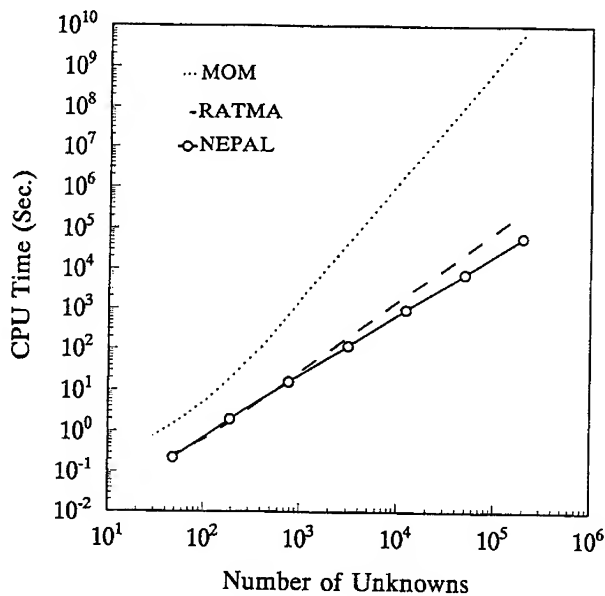


Figure 4. Comparison of CPU time of NEPAL with RATMA and MOM.

Reinhold, New York, 1990.

- [5] W. C. Chew and C. C. Lu, "NEPAL—An N^{1.5} algorithm for solving the volume integral equation," *IEEE Antennas and Propagation Society International Symposium Digest*, pp. 184-187, July 18-25, Chicago, 1992.
- [6] J. W. Cooley and J. W. Tukey, "An algorithm for the machine computation of complex Fourier series," *Math. Comp.*, vol. 19, pp. 297-301, 1965.
- [7] A. George, "Numerical experiments using dissection methods to solve $n \times n$ grid problems," *SIAM J. Numer. Anal.*, 14, pp. 161-179, 1977.
- [8] A. George and J. W. Liu, *Computer Solution of Large Sparse Positive Definite Systems*, Prentice-Hall, Englewood Cliffs, New Jersey, 1981.
- [9] R. F. Harrington, *Field Computation by Moment Methods*, Krieger Publishing Co., Malabar, Florida, 1983.
- [10] D. T. Borup and O. P. Gandhi, "Fast-Fourier-Transform method for calculation of SAR distributions in finely discretized inhomogeneous models of biological bodies," *IEEE Trans. Micro. Theory Tech.*, vol. 32, no. 4, pp. 355-360, 1984.

A CG-FFHT Method for the Solution of EM Field in Axisymmetric Inhomogeneous Media

QING-HUO LIU
SCHLUMBERGER-DOLL RESEARCH
OLD QUARRY ROAD
RIDGEFIELD, CT 06877

AND

WENG CHO CHEW
DEPARTMENT OF ELECTRICAL AND COMPUTER ENGINEERING
UNIVERSITY OF ILLINOIS
URBANA, IL 61801

In this paper, we propose a CG-FFHT method for the solution of electromagnetic field in an axisymmetric inhomogeneous medium. This method combines the conjugate gradient (CG) method with the fast Fourier transform (FFT) and the fast Hankel transform (FHT). It is similar in spirit to the CG-FFT method in Cartesian coordinate system [1, 2].

In an axisymmetric inhomogeneous medium with dielectric constant $\epsilon_r(\rho, z)$ and conductivity $\sigma(\rho, z)$, a coaxial loop antenna with current I will generate a nonzero electric field component E_ϕ governed by

$$\left(\frac{\partial}{\partial \rho} \frac{1}{\rho} \frac{\partial}{\partial \rho} \rho + \frac{\partial^2}{\partial z^2} + k^2\right) E_\phi = -i\omega I \mu_0 \delta(\rho - \rho_0) \delta(z - z_0), \quad (1)$$

where ρ_0 is the radius, and $z = z_0$ is location of the antenna; the magnetic permeability is assumed to be a constant μ_0 . The wavenumber k is related to the complex permittivity $\epsilon = \epsilon_0(\epsilon_r + \frac{i\sigma}{\omega\epsilon_0})$ by $k^2 = \omega^2 \mu_0 \epsilon(\rho, z)$.

The Green's function for a homogeneous background medium with constant complex permittivity ϵ_b (wavenumber k_b) can be shown as

$$g(\rho, \rho', z, z') = -\frac{1}{2\pi} \int_{-\infty}^{\infty} dk_z \int_0^{\infty} dk_\rho \frac{\rho' J_1(k_\rho \rho') e^{-ik_z z'}}{(k_b^2 - k_\rho^2 - k_z^2)} k_\rho J_1(k_\rho \rho) e^{ik_z z}. \quad (2)$$

Note that the Green's function is expressed in terms of an inverse Hankel transform in ρ direction and an inverse Fourier transform in z direction.

Using the definition of the Green's function and the principle of linear superposition, one derives the integral equation for the electric current density as

$$\frac{J(\rho, z)}{(k^2 - k_b^2)} - \int_{-\infty}^{\infty} dz' \int_0^{\infty} d\rho' g(\rho, \rho', z, z') J(\rho', z') = E_\phi^{\text{inc}}(\rho, z), \quad (\rho, z) \in R, \quad (3)$$

where the induced current density is defined as $J(\rho, z) = (k^2 - k_b^2)E_\phi(\rho, z)$, R stands for the inhomogeneous region, and $E_\phi^{\text{inc}}(\rho, z)$ is the incident electric field. By substituting Equation (2) into (3), and using the definitions for the Hankel transform and Fourier transform, we arrive at

$$S(\rho, z)J(\rho, z) - \mathcal{FH}^{-1} \left\{ \hat{L} \mathcal{FH}[J(\rho, z)] \right\} = E_\phi^{\text{inc}}(\rho, z), \quad (4)$$

where \mathcal{FH} and \mathcal{FH}^{-1} stand for the forward and inverse Fourier-Hankel transforms in z and ρ respectively. In Equation (4), the operator \hat{L} and function S are

$$\hat{L}(k_\rho, k_z) = \frac{1}{(k_\rho^2 + k_z^2 - k_b^2)}, \quad S(\rho, z) = \frac{1}{k^2(\rho, z) - k_b^2}. \quad (5)$$

Therefore, the integral equation in (4) can be rewritten as

$$\mathcal{L}J(\rho, z) = E_\phi^{\text{inc}}(\rho, z). \quad (6)$$

This integral equation can be solved by using the conjugate-gradient method. In each iteration of a conjugate-gradient method, the most expensive operation is a matrix-vector multiplication, or equivalently, operator-vector action illustrated by the left-hand side of (6). If $J(\rho, z)$ is discretized into N unknowns, the cost of a simple matrix-vector multiplication is $O(N^2)$. However, with the use of fast Fourier-Hankel transform (FFHT) [3], the cost of this matrix-vector multiplication can be reduced to $O(N \log_2 N)$, greatly reducing the computation time. Moreover, the memory requirement in a CG method is $O(N)$, much less than the direct solution of the matrix equation via Gaussian elimination.

In order to demonstrate the use of the CG-FFHT method, we show a numerical example for the application in the electromagnetic subsurface sensing. The sensor consists of one loop antenna transmitter and one receiver in the measurement along the z axis. The receiver-transmitter spacing is 1.016 m; so if the midpoint of the receiver and transmitter is at z , the locations of the transmitter and receiver are at $z - 0.508$ and $z + 0.508$ respectively. The transmitter is operating at an induction frequency 20 kHz. At this frequency, the small-loop antennas can be regarded as dipole antennas. The receiving antenna measures the electric field, which is then converted into an apparent conductivity. In the inhomogeneous medium considered here, we assume $\epsilon_r = 1$, and the conductivity σ is a function of space since only the conduction current dominates at this frequency.

The example shown in Figure 1 is a two-body inhomogeneous medium in a background of conductivity 1.0 S/m. The conductivities of the two bodies are $\sigma = 0.01$ S/m and $\sigma = 2.0$ S/m respectively. The calculated real and imaginary parts of the current density is shown in Figures 2a and 2b; and the apparent conductivity obtained by the CG-FFHT method is shown in Figures 3a and 3b. The number of iterations in the CG procedure is less than eight for all points. Excellent agreement has been found between our result and that obtained by the numerical mode-matching (NMM) method [4].

In summary, it is shown in this paper that the two-dimensional integral equation for the induced current density in an axisymmetric inhomogeneous medium can be formulated using the Hankel transform in ρ and Fourier transform in z . The CG-FFHT method is developed to solve the integral equation for the unknown current density using the combination of the CG method and the FHT and FFT algorithms. In each iteration of this method, the number of complex multiplications is $O(N \log_2 N)$, which is much faster than a straightforward MOM solution with Gaussian elimination or the CG method with a simple matrix-vector multiplication.

References

- [1] D. T. Borup and O. P. Gandhi, "Calculation of high-resolution SAR distribution in biological bodies using the FFT algorithm and the conjugate gradient method," *IEEE Trans. Microwave Theory Tech.*, vol. MTT-33, pp. 417-419, 1985.
- [2] T. K. Sarkar, E. Arvas, and S. M. Rao, "Application of FFT and the conjugate gradient method for the solution of electromagnetic radiation from electrically large and small conducting bodies," *IEEE Trans. Antennas Propagat.*, vol. AP-34, pp. 635-639, 1986.
- [3] H. K. Johansen, and K. Sorensen, "Fast Hankel transform," *Geophy. Prospect.*, vol. 27, pp. 876-901, 1979.
- [4] W. C. Chew, Z. Nie, Q.-H. Liu, and B. Anderson, "An efficient solution for the response of electrical well logging tools in a complex environment," *IEEE Trans. Geosci. Remote Sensing*, vol. GE-29, pp. 308-313, 1991.

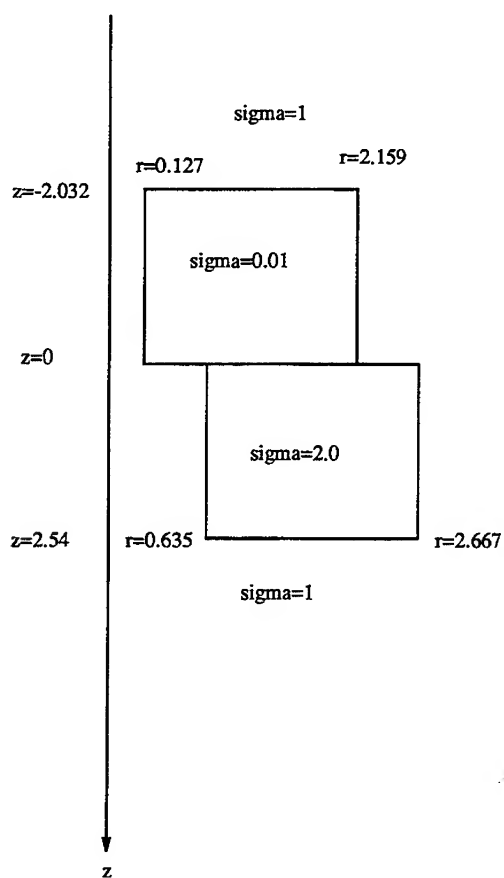


Figure 1. Geometry of the example showing the dimension of the inhomogeneous region in meters. The conductivity is in S/m.

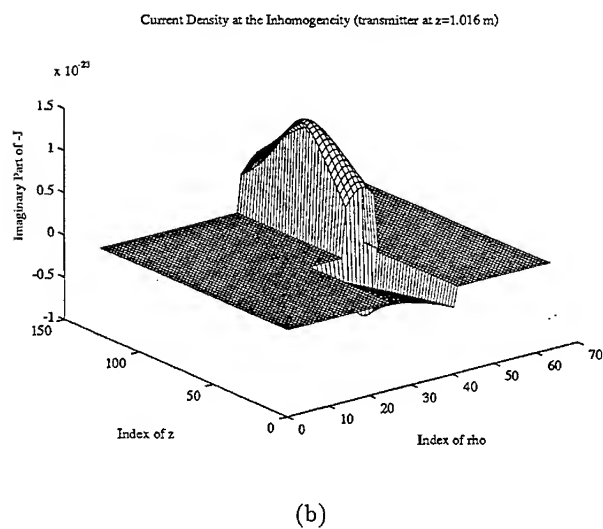
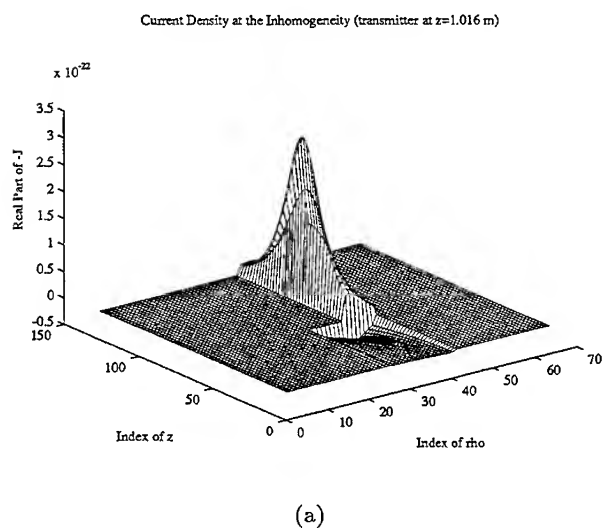
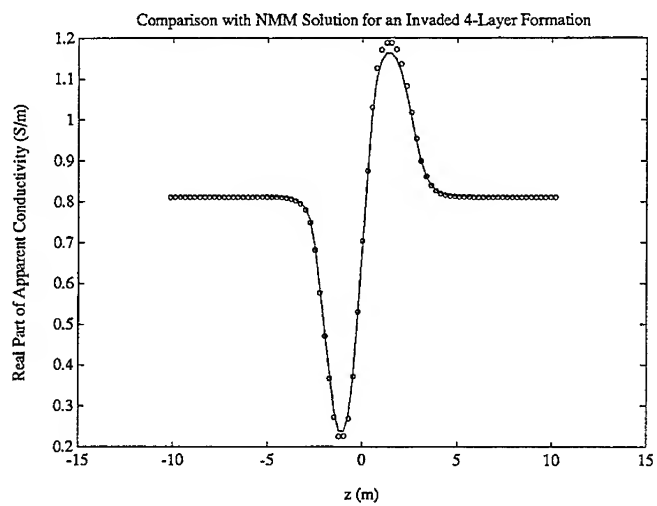
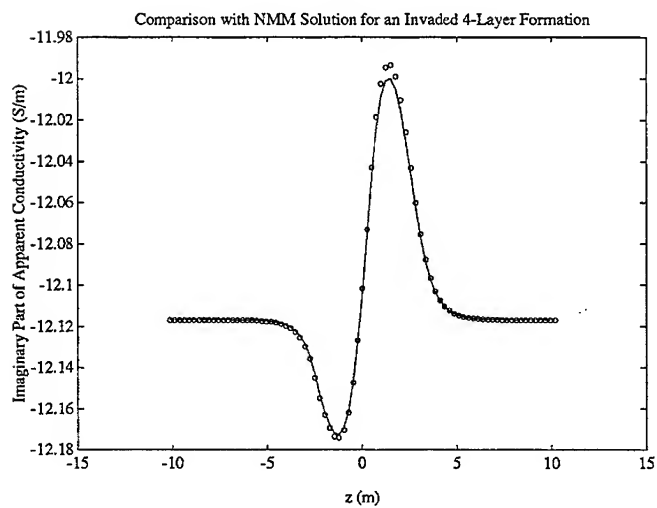


Figure 2. The real and imaginary parts of the current density distribution obtained from the CG-FFHT method for transmitter at $z = 1.016$ m.



(a)



(b)

Figure 3. Comparison of apparent conductivity obtained using CG-FFHT method and the numerical mode-matching (NMM) method. Solid line: NMM result; circles: CG-FFHT result.

SCATTERING COMPUTATIONS FOR MULTI-REGION CYLINDRICAL OBJECTS

Michael A. Morgan

Electrical and Computer Engineering Department
Naval Postgraduate School, Monterey, CA 93943

Abstract

A class of 2-D scattering problems involving sectorized and layered regions containing penetrable materials, with optional conducting surfaces, is solved using multi-region cylindrical harmonic expansions. The numerical approach is easy to implement and provides accurate frequency-domain solutions of a wide range of geometrical configurations. Solutions programmed using MATLAB are shown for bistatic scattering from: (1) a split region circular cylinder; (2) a half circular cylinder, and; (3) a penetrable half-shell.

Introduction

Scattering by an infinite length dielectric circular cylinder was first solved using cylindrical harmonics for the electromagnetic case by Lord Rayleigh early in this century [1]. Since that time, numerous others have extended the use of cylindrical harmonics to solutions for scattering by metallic cylinders coated with dielectrics, plasmas and magnetic materials, as well as multi-layered dielectric cylinders, as exemplified in references [2-5]. Cylindrical harmonics in multiple regions have recently been used to solve for scattering by a conducting wedge [6] and for radiation from finite length monopole antennas having a top-hats and dielectric loadings [7-8]. Cylindrical harmonics used in local regions, but with variable multipole points, are also employed with the 2-D generalized multipole technique (GMT) [9]. The approach here could be considered as a special case of the GMT where all multipole expansions are centered at the origin and material boundaries are restricted to separable contours, thus providing an exact analytical formulation as a starting point for the numerical solution.

The objective of this paper is to propose and then demonstrate a simple technique for extending the use of cylindrical harmonics to scattering problems involving both layered and sectorized regions of penetrable or conducting material. This formulation is theoretically exact, although numerically approximated. It provides a powerful tool for simple and accurate analysis of a wide range of configurations which can be modeled under the restriction to radial and circumferential material boundaries. An important practical application of this method is providing benchmark solutions of multi-region scattering

problems for use in the validation of more general 2-D scattering codes which may employ finite elements or integral equations to handle arbitrary material configurations.

Formulation

Time-harmonic ($e^{j\omega t}$ suppressed) plane wave scattering will be considered for 2-D circular objects having layered and sectorized regions, as illustrated in Fig. 1. These regions are each filled with specified homogeneous material or free space. Note that each region is labeled with a double index, (l, s) , where $l = 1, 2, \dots, L$ defines the layers and $s = 1, 2, \dots, S(l)$ corresponds to sectors within the l -th layer. The unbounded outer "layer" (outer boundary at $r \rightarrow \infty$) has $l = 1$, with $S(1) = 1$, while the inner core layer has $l = L$.

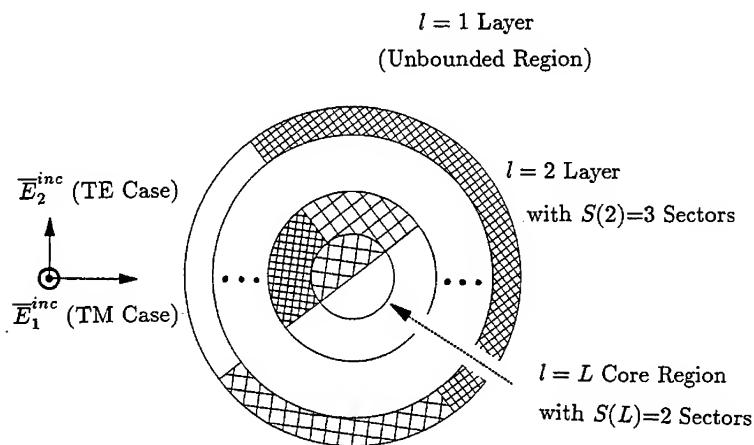


Figure 1 Scattering by a Multi-Region Cylindrical Object

Both the structure and the fields are invariant to translations in z . Two orthogonal, linearly polarized incident plane waves, \vec{E}_i^{inc} are considered, corresponding to transverse magnetic (TM) and transverse electric (TE), to \hat{z} , with respective subscripts $i=1$ and 2.

All field components can be generated through a knowledge of the z -components of \vec{E}_1 and $\eta_0 \vec{H}_2$. These field components will be respectively denoted as $\psi_1(\rho, \phi)$ and $\psi_2(\rho, \phi)$ in an effort to consolidate common equations for the TM and TE cases. Applying Maxwell's equations in cylindrical coordinates (with z invariance), shows that each $\psi_i(\rho, \phi)$ solves the Helmholtz equation while the transverse (to z) field components are given by [10]

$$\eta_0 H_\rho(\rho, \phi) = \frac{j}{\mu_r k_0 r} \frac{\partial \psi_1}{\partial \phi} \quad (1a)$$

$$\eta_0 H_\phi(\rho, \phi) = \frac{-j}{\mu_r k_0} \frac{\partial \psi_1}{\partial \rho} \quad (1b)$$

$$E_\rho(\rho, \phi) = \frac{-j}{\epsilon_r k_0 r} \frac{\partial \psi_2}{\partial \phi} \quad (1c)$$

$$E_\phi(\rho, \phi) = \frac{j}{\epsilon_r k_0} \frac{\partial \psi_2}{\partial \rho} \quad (1d)$$

The general solution for ψ_i in each of the (l, s) regions which is penetrable can be approximated by the truncated cylindrical harmonic expansion

$$\psi_i(\rho, \phi) \doteq \sum_{n=-N}^N [a_n J_{\nu(n)}(k\rho) + b_n H_{\nu(n)}^{(2)}(k\rho)] e^{j\nu(n)\phi} \quad (2)$$

where N and $\nu(n)$, as well as $k = \sqrt{\mu_r \epsilon_r} k_0$, are specified in each penetrable region and are thus each implicit functions of (l, s) . It should be noted that all $b_n = 0$ in the core layer L while the a_n 's in the exterior $l = 1$ layer are known through specification of the incident field. For example, a plane wave incident at an angle ϕ_0 , with form $\psi_i = \psi_0 e^{-jk_0 \rho \cos(\phi - \phi_0)}$, has $a_0 = 0.5\psi_0$ and $a_n = j^{-n} e^{-jn\phi_0} \psi_0$ for $n \neq 0$.

Note that $\nu(n) = n$ in the case of the $l=1$ exterior layer, or in any other layer having only one segment. Periodicity of 2π in such cases is required so the solution can be single-valued. Another special case is with fixed pec or pmc radial boundaries to a given sector, say at angles ϕ_1 and $\phi_2 = \phi_1 + \Delta\phi$. Resultant null conditions on either ψ_1 or ψ_2 at both ϕ_1 and ϕ_2 quantizes the angular frequencies to $\nu(n) = n\pi/\Delta\phi$, with eigenmodes of the form $\sin[\nu(n)(\phi - \phi_1)]$. The summation index in (2) is then forced to run from 1 to N .

Aside from these special cases, $\nu(n)$ will be of the form $n\alpha$ with selection governed by the usual rules of Fourier series expansion of an arbitrary function over a domain of length $\Delta\phi$. Such an expansion will be periodic in $2\pi/\alpha$ and this interval must exceed $\Delta\phi$. The usual selection is $\alpha = \pi/\Delta\phi$, which makes the expansion periodic in $2\Delta\phi$. To simplify the programming in MatLab, which only has intrinsic Hankel functions of integer order, we will use $\nu = n$ in all regions. Since the periodicity of this selection is 2π the expansion of an arbitrary function over a narrow interval $\Delta\phi$ could require many more terms relative to an expansion using, say $\nu = n\pi/\Delta\phi$. Optimization of numerical efficiency by using noninteger ν 's is postponed for later efforts.

Referring to Figure 1, moment equations based on continuity of tangential fields around the perimeter of each region are used to define the linear system for the solution of

the unknown expansion coefficients. For example, the following integral form is evaluated over a perimeter contour of the (l, s) region

$$\oint_{C_{l,s}} E_{tan}^{(l,s)}(c) w_m^{(l,s)}(c) dc = \sum_{(l',s')} \int_{C_{l,s} \cup C_{l',s'}} E_{tan}^{(l',s')}(c') w_m^{(l',s')}(c') dc' \quad (3a)$$

$$\oint_{C_{l,s}} H_{tan}^{(l,s)}(c) w_m^{(l,s)}(c) dc = \sum_{(l',s')} \int_{C_{l,s} \cup C_{l',s'}} H_{tan}^{(l',s')}(c') w_m^{(l',s')}(c') dc' \quad (3b)$$

where the RHS includes contributions from all regions (l', s') which are adjacent to (l, s) . The weighting functions, $\{w_m^{(l,s)}(c)\}$ are selected to be asymptotically complete over the integration contour. A good choice is the Fourier set over the perimeter path length $\Delta C_{l,s}$ of the form

$$w_m^{(l,s)}(c) = e^{j2m\pi c/\Delta C_{l,s}} \quad (4)$$

The linear equations in (3) relate the cylindrical harmonic coefficients between adjacent regions and have the form

$$\begin{aligned} & \sum_{n=-N_{l,s}}^{N_{l,s}} A_{m,n}^{(l,s)} a_n^{(l,s)} + B_{m,n}^{(l,s)} b_n^{(l,s)} \\ & + \sum_{(l',s')} \left\{ \sum_{n'=-N_{l',s'}}^{N_{l',s'}} A_{m',n'}^{(l',s',l,s)} a_{n'}^{(l',s')} + B_{m',n'}^{(l',s',l,s)} b_{n'}^{(l',s')} \right\} = 0 \end{aligned} \quad (5)$$

where the system coefficients $A_{m,n}$ and $B_{m,n}$ are evaluated as moment integrations, weighted by $w_m(c)$, of cylindrical harmonic terms involving regional values of either $J_{\nu(n)}(k\rho)e^{j\nu(n)\phi}$ or $H_{\nu(n)}^{(2)}(k\rho)e^{j\nu(n)\phi}$, as well as radial or azimuthal derivatives of these terms depending upon the tangential field values being considered. Specifics can be easily derived by substituting the appropriate tangential fields into (3) as either found from (2), or via operations on (2) as given in (1). In forming the linear system from the moment equations in (5), the terms for $l=1$ involving known a_n 's which expand the incident field are transferred to the RHS and used as the driving array for the system.

Truncation estimates for $N_{l,s}$ in each region depend upon the Fourier indices $\nu_{l,s}$ selected within the region. Using the expedient form $\nu = n$ employed here, very good convergence is obtained using $N_{l,s} = 2|k|\rho_l$, where $k = k_0\sqrt{\epsilon_r\mu_r}$ within the region and ρ_l is the outer radius of the l -th layer. This applies except for the $l=1$ exterior region, where $N_1=2k_0\rho_2$ is used. Good convergence is usually reached when using these truncations because the angular frequency (radians per radian in the ϕ coordinate) of traveling waves within the region is bounded by half this value, $|k|\rho_l$. For $n > |k|\rho_l$ Bessel and Hankel functions within the region will behave as their "small argument" forms indicate, with

the series terms dominated by the Neumann functions within the $H_n^{(2)}$ portion. Thus, the series terms much beyond $|k|\rho_l$ can be identified as evanescent fields which contribute to the reactive storage of energy. With the exception of hi-Q enclosed cavities (with null-field boundaries) the contributions of the evanescent field terms diminish rapidly with increasing n . Our truncation estimate, which is twice the transition bound $|k|\rho_l$, thus allows a generous surplus of modes in all but hi-Q cavity region cases.

Once the linear system in (5) is solved, the scattered field is found through use of the b_n 's for $l = 1$. In the far-zone of the scatterer, defined by the three conditions $\rho \gg \lambda_0$, $\rho \gg D$ and $\rho > 2D^2/\lambda_0$, where D is the outside diameter of the scattering object, the scattered field may be simplified through use of the large argument approximation to the Hankel functions,

$$H_n^{(2)}(k_0\rho) \rightarrow \sqrt{\frac{2j}{\pi k_0\rho}} j^n e^{-jk_0\rho} \quad (6)$$

The resultant far-zone scattered field becomes

$$\psi_i^s(\rho, \phi) \doteq \sqrt{\frac{j}{2\pi k_0\rho}} e^{-jk_0\rho} \sum_{n=-N_1}^{N_1} b_n e^{jn(\phi+\pi/2)} \quad (7)$$

The 2-D bistatic radar cross section per unit length, also known as the "scattering width", is given by

$$\sigma_i(\phi) = \lim_{\rho \rightarrow \infty} 2\pi\rho \frac{|\psi_i^s(\rho, \phi)|^2}{|\psi_i^{inc}|^2} = \frac{4}{k_0} \left| \sum_{n=-N_1}^{N_1} b_n e^{jn(\phi+\pi/2)} \right|^2 \quad (8)$$

where the incident field magnitudes of either E_z (TM case) or $\eta_0 H_z$ (TE case) are assumed to be unity: $|\psi_i^{inc}| = 1$.

Computations

Simple examples of the multi-region cylindrical harmonic technique will now be shown. These were originally used for validation of a powerful and quite general finite element based 2-D code which allowed conformal (to the object's surface) mesh termination using the Field Feedback Formulation (F^3), [11]. In fact, the approach described in this paper was developed by the author to provide simple but highly accurate computational benchmarks incorporating piecewise inhomogeneous scatterers for verification of the F^3 algorithm or other codes.

The first comparison is shown in Figure 2 for the case of a split-region circular cylinder of diameter $2\lambda_0$ where $\epsilon_r=2$ in the left half and $\epsilon_r=4$ in the right half. The bistatic scattering width computed using the multi-region cylindrical harmonic (MRC) approach agrees very well with the finite element method (FEM) even at angles having low scattering.

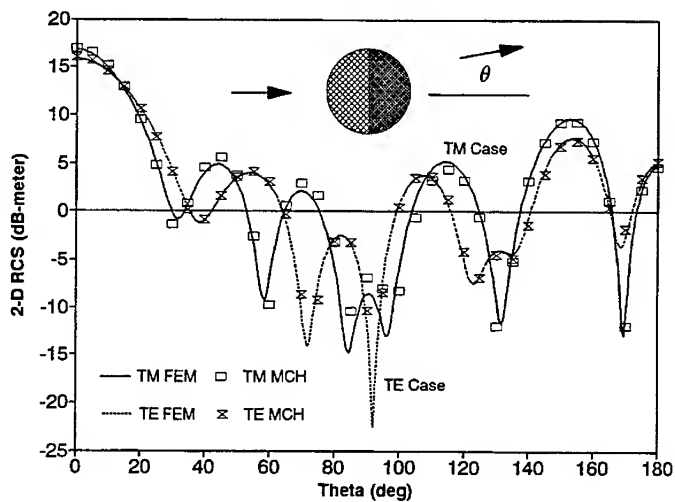


Figure 2 Comparison of Bistatic RCS for a Split-Region Dielectric Cylinder having $2\lambda_0$ Diameter, Left-Half $\epsilon_r = 2$, and Right-Half $\epsilon_r = 4$

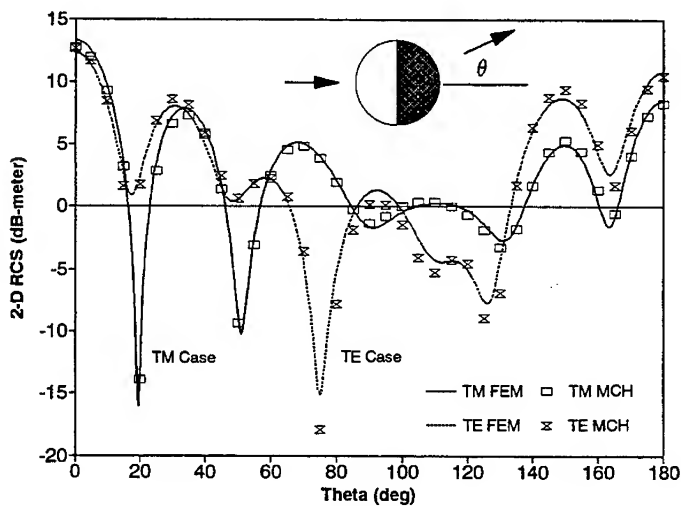


Figure 3 Comparison of Bistatic RCS for a Half-Circular Dielectric Cylinder having $2\lambda_0$ Diameter and $\epsilon_r = 4$

By setting ϵ_r to unity in the left-half region, the split-region cylinder is converted into a half-circular cylinder. Comparison with the finite element method solution is shown

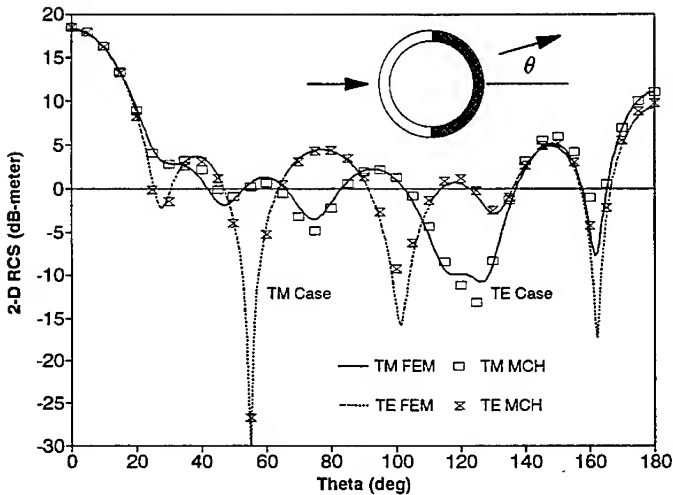


Figure 4 Comparison of Bistatic RCS for a Semi-Circular Dielectric Shell with $0.25\lambda_0$ Thickness, Outer Diameter = $2\lambda_0$ and $\epsilon_r = 4$

in Figure 3, with excellent agreement again observed. The conversion of the split-region cylinder to the half cylinder illustrates the effective removal of regions from the scatterer by setting $\epsilon_r=1$ in those regions. It is still necessary to represent the fields within these free space regions using the appropriate cylindrical harmonic expansions.

A final example is shown in Figure 4, where an $\epsilon_r=4$ dielectric half-shell is constructed using a two-sector $l=2$ layer (with left half $\epsilon_r=1$) and a single sector free space $L=3$ core. Quite good agreement is once again demonstrated in comparing to the bistatic patterns computed using the finite element method with F^3 mesh termination.

Conclusions

This paper has introduced the general formulation and demonstrated the utility of employing cylindrical harmonic expansions in multiple regions to solve for scattering by a special class of inhomogeneous scatterers. The approach is simple to program and has been highly accurate for the cases considered. Further, the method is very efficient since the basis functions are exact solutions to the field equations in each region and quickly converge. Computation times using this technique, when optimized for array processing under MatLab 386, averaged over 50 times faster than a highly optimized F^3 based finite element code compiled under NDP386.

As mentioned, the multi-region cylindrical harmonic method was developed to pro-

vide a suite of benchmark 2-D scattering problems with reliable solution accuracy. The approach appears to be highly robust and further validations are planned for additional objects which include pec surfaces and lossy material. Comparisons will be made using both the F^3 code and the generalized multipole technique.

References

- [1] Lord Rayleigh, "The dispersal of light by a dielectric cylinder," *Phil. Mag.*, vol. 36, p. 365, 1918.
- [2] C. C. H. Tang, "Backscattering from dielectric-coated infinite cylindrical obstacles," *J. Appl. Phys.*, vol. 28, pp. 628-633, May 1957.
- [3] W. V. T. Tusch and C. Yeh, "Scattering by an infinite cylinder coated with an inhomogeneous and isotropic plasma sheath," *IEEE Trans. Antennas Propagat.* vol. AP-15, pp. 452-457, May 1967.
- [4] R. E. Evans, "Electromagnetic scattering from a conducting circular cylinder with a circumferentially magnetized ferrite," *IEEE Trans. Antennas Propagat.*, vol. AP-24, pp 190-197, March 1976.
- [5] H. E. Bussey and J. H. Richmond, "Scattering by a lossy dielectric circular cylindrical multilayer, numerical values," *IEEE Trans. Antennas Propagat.*, vol. AP-23, pp 723-725, Sept. 1975.
- [6] C. A. Balanis, *Advanced Engineering Electromagnetics*, Section 11.6 "Scattering by a Conducting Wedge", New York: Wiley, 1989.
- [7] M. A. Morgan, R. C. Hurley and F. K. Schwing, "Computation of monopole antenna currents using cylindrical harmonics," *IEEE Trans. Antennas Propagat.* vol. AP-38, pp. 1130-1133, July 1990.
- [8] M. A. Morgan and F. K. Schwing, "Eigenmode analysis of dielectric top-hat monopole antennas," in review by *IEEE Trans. Antennas Propagat.*
- [9] C. Hafner, *The Generalized Multipole Technique for Computational Electromagnetics*, Boston: Artech House, 1990.
- [10] R. F. Harrington, *Time-Harmonic Electromagnetic Fields*, Chapter 5, New York: McGraw-Hill, 1961.
- [11] M. A. Morgan and T. B. Welch, "Field Feedback Computation of Scattering by 2-D Penetrable Objects," *IEEE Trans. Antennas Propagat.* vol. AP-40, pp. 445-450, April 1992.

SESSION 19 - "LOW-FREQUENCY TECHNIQUES
AND APPLICATIONS"

Chair: Dr. Osama Mohammed, Co-Chair: Dr. Abd A. Arkadan

COMPUTATION OF ELECTRIC MACHINES PARAMETERS IN THE ABC FRAME OF REFERENCE USING FINITE ELEMENT ANALYSIS

A.A. Arkadan R.H. VanderHeiden
Electrical and Computer Engineering Department
Marquette University
Milwaukee, WI 53233, USA

Abstract: A computer-aided method which is based on the use of state space models in the abc frame of reference and finite element models for the analysis of magnetic fields in electric machines is presented. The resulting finite element models are suited for the analysis of such machines under any load condition, and account for saturation and space harmonics effects due to material nonlinearities and machine geometry. The method is implemented to determine the parameters of a synchronous generator. The parameters include the self and mutual inductances as well as the armature induced back emfs. A description of the modeling approach used as applied to an example synchronous generator is presented. In addition, a verification of this modeling approach is presented by comparing simulation results to experimental data.

Introduction

Before the advent of applying computer-aided methods to the analysis of electric machinery, saturation and parameters nonlinearity were accounted for by empirical or semi-empirical methods. Also, the state space models describing electrical machines in the abc frame of reference were simplified by proper substitution (transformation) of variables and using transforms such as the Park's transformation and the resulting dq0 frame parameters and associated models [1-3]. However, with advances in numerical techniques one can solve directly the state space models resulting from modeling electrical machines in the natural abc frame of reference [4-6].

In this paper, some advantages of using the natural abc frame modeling approach are discussed, and the state space model in this frame of reference for a synchronous generator is presented. In addition, the machine winding inductances and armature induced emfs are determined from series of nonlinear finite element (FE) magnetic field solutions which are obtained throughout the machine cross-section for different load conditions. Moreover, these computed parameters are compared to measured data for verification.

Machine State Space Model Description

A lumped parameter state space model in the natural abc frame of reference for the dynamic performance prediction of synchronous generators is presented. An advantage of using the natural abc frame modeling approach is that one can easily account for inherent harmonics in flux linkages and inductances. Another advantage is that the abc frame approach can be used easily to study internal or terminal faults resulting from abnormal winding connections as was demonstrated in earlier works [4-7]. Furthermore, the method enables one to directly use readily available FE based methods to determine the emfs and the nonlinear self and mutual inductances of various machine windings from field solutions. These are the key parameters of the state models in the abc frame of reference. Also, the method makes it easier to compare simulated results with corresponding test data since most of the testing processes on electrical machines lead to measurements of (a), (b), and (c) phase and line currents and voltages. Another important advantage of this approach, is that it makes it easier to incorporate such abc machine models into an overall modeling effort of the machine-load system network including inverter drives or rectifier loads [6,7].

The differential equations used to model the dynamic performance of electrical machines in general, and 3-phase ac machines in particular, are derived from the interaction between

the armature windings, field, and damping circuits. For the synchronous generator under consideration, the machine is represented by six windings as shown in Figure (1). The windings (a), (b), and (c) represent the armature three phases. The winding (f) represents the rotor field winding. In addition, the shorted windings (kd) and (kq) represent the damper bars which are embedded in the pole faces of the rotor structure. Accordingly, the lumped parameter state space model in the abc frame of reference which is based upon a six winding representation is given as follows:

$$\underline{V} = \underline{R}\underline{I} + \omega \frac{\partial}{\partial \theta} \{ \underline{L} \} \underline{I} + \underline{L} \frac{d\underline{I}}{dt} \quad (1)$$

where θ is the electrical rotor position angle, measured from a fixed reference, and ω is the angular speed in electrical rad/s. The array, \underline{I} represents the currents of the six windings. That is the armature phase currents i_a , i_b , and i_c , the field current i_f , and the damper bars equivalent currents i_{kd} and i_{kq} . Meanwhile, the array \underline{V} represents the voltages of the six windings. The diagonal matrix \underline{R} represents the resistances of the machine equivalent windings, and the matrix \underline{L} represents the machine self and mutual inductance terms. In expanded matrix form, this inductance matrix can be written as follows:

$$\begin{bmatrix} L_{aa} & L_{ab} & L_{ac} & L_{af} & L_{akd} & L_{akq} \\ L_{ba} & L_{bb} & L_{bc} & L_{bf} & L_{bkd} & L_{bkq} \\ L_{ca} & L_{cb} & L_{cc} & L_{cf} & L_{ckd} & L_{ckq} \\ L_{fa} & L_{fb} & L_{fc} & L_{ff} & L_{fkd} & L_{fkq} \\ L_{kda} & L_{kdb} & L_{kdc} & L_{kdf} & L_{kdkd} & L_{kdkq} \\ L_{kqa} & L_{kqb} & L_{kqc} & L_{kqf} & L_{kqkd} & L_{kqkq} \end{bmatrix}$$

It should be noted that the values of the currents, i_a through i_{kq} , in equation (1), can be determined numerically for any set of initial conditions and terminal voltages, v_a , v_b , and v_c . As can be appreciated from equation (1), the main parameters of the state model are the inductances. Methods for determining the inductances and the armature induced back emfs are discussed next.

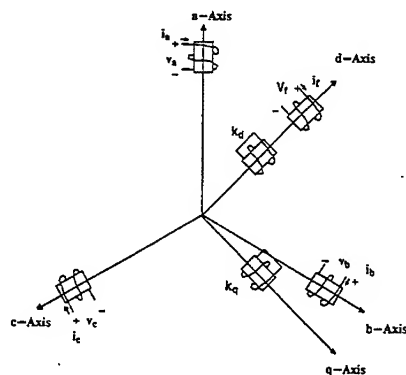


Figure (1) Machine Windings Schematic

Determination of Machine Inductance Profiles

The self and mutual inductances given in equation (1) are complicated functions of the machine winding currents, the nonlinear magnetic characteristics of the material used in the

machine construction, and the relative position of its stationary and moving parts. Accordingly, the profiles of the machine windings self and mutual inductances must be calculated at different rotor positions which cover a complete ac cycle for a given load condition. In this paper, the values of the inductances for an example synchronous generator are calculated from nonlinear finite element magnetic field solutions using an energy perturbation technique. A crucial advantage of the energy perturbation method is that it results in all winding self and mutual inductances at any given load condition. Thus for a machine with (n) windings the method can be used to determine the (nxn) inductance matrix for each set of specified winding currents and corresponding rotor positions.

Based on the energy perturbation method [8-10], the self inductance L_{jj} and the mutual inductance L_{jk} can be determined from the following energy expressions:

$$L_{jj} = [W(i_j - \Delta i_j) - 2W + W(i_j + \Delta i_j)]/(\Delta i_j)^2 \quad (2)$$

$$\begin{aligned} L_{jk} = & [W(i_j + \Delta i_j, i_k + \Delta i_k) \\ & - W(i_j - \Delta i_j, i_k + \Delta i_k) - W(i_j + \Delta i_j, i_k - \Delta i_k) \\ & + W(i_j - \Delta i_j, i_k - \Delta i_k)]/(4 \cdot \Delta i_j \cdot \Delta i_k) \end{aligned} \quad (3)$$

where i_j is the current in winding j , Δi_j is the perturbation of current i_j , and $W(i_j, i_k)$ is the global energy of the machine. It should be noted that the remainder of the machine winding currents, i_{k+1} through i_n , are not shown in the equations since those are not perturbed when calculating L_{jj} or L_{jk} . Moreover, it should be mentioned that equations (2) and (3) can be used to calculate both apparent and incremental inductances. However, for nonlinear problems, depending on the choice of inductances, one must be careful to use the proper permeabilities for the energy perturbation [8-10]. In this paper, the apparent inductances are calculated. Accordingly, the apparent permeabilities are used.

In order to numerically compute the self inductance given in equation (2), using the results of the finite element field solutions, one calculates the global energy, W , at the quiescent (operating) point for a given load condition. In doing so, one needs a field solution requiring a complete Newton-Raphson set of iterations. In addition, one needs two more perturbed field solutions which are obtained in one iteration for the positive perturbation ($i + \Delta i$) and another for the negative perturbation ($i - \Delta i$), using the apparent reluctivities for all the nonlinear elements in the FE grid. That is, no iterative process is required for these perturbed solutions. Meanwhile, to calculate the mutual inductance given by equation (3), one needs four perturbed field solutions in addition to the complete solution obtained at the quiescent point. Again, the four perturbed solutions do not require any iterations. For example, in order to determine the mutual inductance, $L_{ab}(\theta_i)$, for a given load condition and rotor position, θ_i , one has to calculate the energy at the operating point, $W(i_a, i_b)$. In addition, one needs to obtain the energies for four perturbed field solutions corresponding to four sets of current perturbations which are $W(i_a + \Delta i_a, i_b + \Delta i_b)$, $W(i_a + \Delta i_a, i_b - \Delta i_b)$, $W(i_a - \Delta i_a, i_b + \Delta i_b)$, and $W(i_a - \Delta i_a, i_b - \Delta i_b)$.

As can be seen from the expressions in equations (2) and (3), one needs to calculate the energy throughout the machine corresponding to a given current and/or its perturbation. Accordingly, these currents should be properly injected in the regions of the FE grid corresponding to the armature winding, field, and damper bars. The details of determining the excitation currents are given below.

Determination of Excitation Currents for a Load Condition

The governing equation for magnetostatic field solutions in two dimensions is given as follows:

$$\frac{\partial}{\partial x}(\nu \frac{\partial A}{\partial x}) + \frac{\partial}{\partial y}(\nu \frac{\partial A}{\partial y}) = -J \quad (4)$$

where A is the z-component of the magnetic vector potential (mvp), ν is the magnetic reluctivity, and J is the z-component of the excitation current density vector. The excitation current density vector values are determined as follows:

Field Winding: Using closed form expressions and the associated phasor diagram, Figure (2), the dc value of the field current is estimated for a given load condition. Given the value for the excitation field current and the number of field turns, the field current density used in equation (4) is determined by dividing the ampere-turns product by the area of the field winding region in a finite element model.

Armature Winding: To determine the instantaneous values of the armature winding currents, one needs to determine the value of the rotor position angle σ_0 for a given load condition. This angle is defined as the angle at time $t=0$ between the rotor's direct axis, and the axis of phase (a). This angle is estimated using the phasor diagram shown in Figure (2). Next, the current density in each armature slot in the FE grid is determined as was described in reference [11].

Rotor Damping Circuits: As shown by Figure (1), the rotor damper bars are represented by two equivalent windings (kd) and (kq). In order to compute the self and mutual inductances associated with these rotor damping circuits using the expressions of equations (2) and (3), one needs to inject currents and/or their perturbations in the rotor damping circuits to determine the energy. For instance, the calculation of the inductance L_{akq} which is the mutual inductance between the armature phase (a) and the damping bars q-axis equivalent winding, (kq), requires the distribution of the induced damper bars currents in a manner that produces a predominant component of damper winding mmf, $F_{kq}(\theta)$ along the quadrature-axis. This was done by distributing the current in the damper bars from a sinusoidally distributed current sheet, $C_{kq}(\theta)$, such as shown in Figure (3). For full details, reference [10] should be consulted.

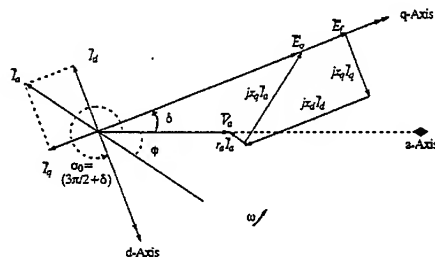


Figure (2) Developed Phasor Diagram

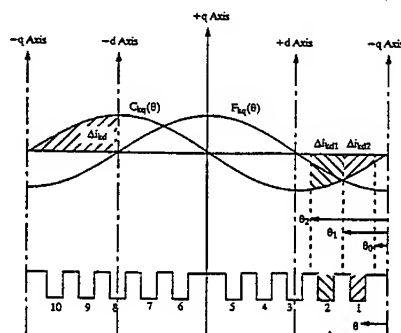


Figure (3) Damper Bars Current Perturbation Distribution

Synchronous Generator Inductance Calculations

The results of implementing the approach outlined above to compute the values of the self and mutual inductances of a synchronous generator at no-load and 1.0 per unit (p.u.) load conditions are given in this section. Using the FE model for the generator, a series of nonlinear magnetic field solutions were obtained over a set of rotor positions. This required automatic mesh generation with the capability of moving the rotor with respect to the stator. In the case of the generator under consideration, the rotor was stepped forward at increments of quarter stator slot pitch to account for ripple effects due to slotting in the calculated inductance data. Thus profiles of the variations of the various self and mutual inductances with respect to the rotor position, were obtained. Sample plots for the armature self inductance L_{aa} and the mutual inductance L_{ab} versus the rotor position are given here in Figures (4) and (5) respectively, for no-load and 1.0 p.u. load conditions. Furthermore, the profile for mutual inductance between the armature phase (a) winding and the field winding, L_{af} , is given in Figure (6). Moreover, the resulting inductance profile of L_{akq} , the mutual inductance between phase (a) and the quadrature axis equivalent damping circuit, (kq), versus rotor position is given here in Figure (7). As can be appreciated from these waveforms, the effects of loading (saturation) and rotor angle are clearly visible.

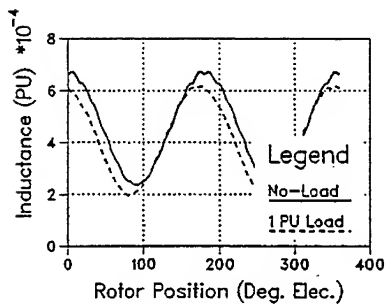


Figure (4) Self Inductance L_{aa}

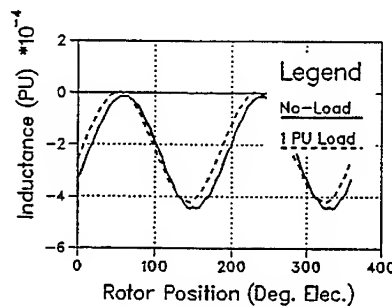


Figure (5) Mutual Inductance L_{ab}

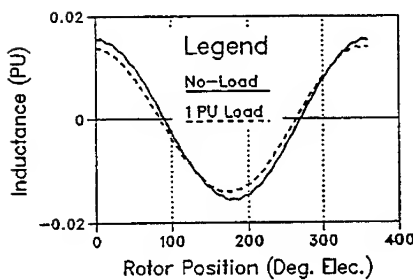


Figure (6) Mutual Inductance L_{af}

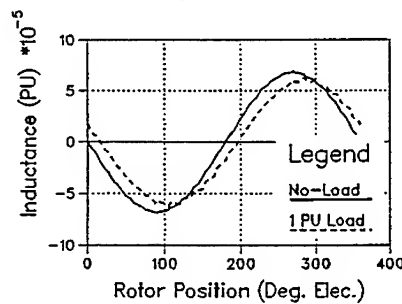


Figure (7) Mutual Inductance L_{akq}

Once the inductance values are calculated, a Fourier analysis of the complete profile of these inductances can be obtained. This results in Fourier Series type expressions of the form:

$$L_{jk} = a_0 + \sum_{n=1}^{\infty} [a_n \cos(n\theta) + b_n \sin(n\theta)] \quad (5)$$

where a_0 is the dc value of the inductance, and a_n and b_n are the coefficients for the cosine and sine terms of the n^{th} harmonic. Doing so will allow one to use the calculated inductances in the state model of equation (1) to predict the performance characteristics of the machine under different operating conditions [4,5].

Determination of Armature EMF Values

Two approaches for the calculation of the emf waveforms in rotating electrical machines using finite element field solutions are presented. The first approach is based on the use of the speed voltage concept. The second approach uses the mutual inductance concept. Both approaches are applied to predict the emf values for the example synchronous generator. Moreover, the computed values are verified by comparison to test results.

Method #1: Speed Voltage Approach

The speed voltage approach can be implemented for the calculation of the induced emf per phase in the armature winding of a rotating machine. In this method, one utilizes the values of the magnetic vector potential (mvp) in the airgap to determine the midgap radial flux density waveform. Since two dimensional (2D) finite element analysis is used in this work, only the z component of the mvp, A_z , exists.

The radial flux density can be calculated from A_z as follows:

$$B_r(\zeta) = \sum_{M=1}^{NH} \frac{(2M-1)A_{2M-1}}{\rho_{mean}} \sin((2M-1)\zeta + \gamma_{2M-1}) \quad (6)$$

where M is the harmonic counter, ζ is the angle measured in a counter clockwise (ccw) direction from the machine grid reference which is the (lagging) quadrature axis in our case, γ_{2M-1} is the phase shift, NH is the highest harmonic order used, and ρ_{mean} is the radial distance from the axis of the machine to the middle of the armature slot as shown by Figure (8).

Consider a conductor (j) which is located at an angle θ from the machine stationary A-axis reference, Figure (8). The induced emf in a conductor (j) at any θ location, can be written as follows:

$$e_{cj}(\theta) = l_c v_{cj} B_r(\zeta_{cj} - \theta) \quad (7)$$

where l_c is the effective embedded length of a stator conductor, ζ_{cj} is the angle between conductor (j) and the lagging q-axis of the machine grid in-ccw-direction, and v_{cj} is the linear relative speed between conductor (j) and the magnetic field. By calculating the emf in a conductor, and knowing the sequence these conductors are connected and their locations in the stator slots, one can find an expression of any phase induced emf.

The mvp waveform along the airgap was determined for the synchronous generator from FE nonlinear magnetic field solutions. Using the approach outlined above, the armature induced back emf was determined for different field excitations (ampere turns) at no-load condition. The resulting voltage values are given in Figure (9) together with test data for comparison. As can be seen from this figure, good agreement exists between the calculated and measured values. Moreover, effects of saturation are evident in both curves, as one expects.

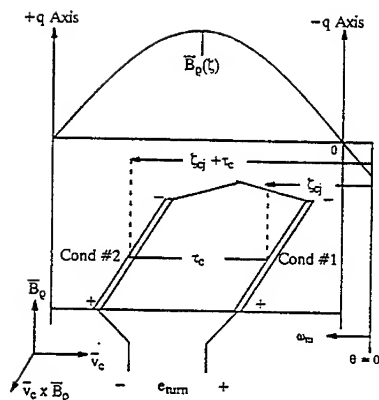


Figure (8) EMF Calculation in a Conductor

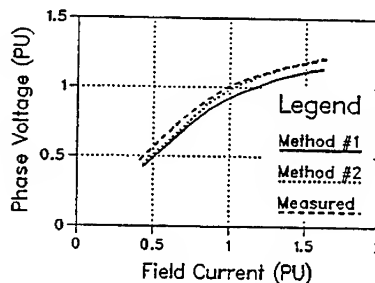


Figure (9) EMF Values

Method #2: Mutual Inductance Approach

In this second approach the waveform of the machines emf is calculated in terms of the mutual inductance between the armature phase winding and the field winding, L_{af} . The mutual inductance L_{af} can be expressed as follows:

$$L_{af}(\theta) = \sum_{n=1,3}^n A_n \cos(n\theta - \psi_n) \quad (8)$$

where A_n and ψ_n are the amplitude and the phase angle of the n^{th} harmonic, respectively, and θ is the rotor angle as defined earlier. Accordingly, the instantaneous value of the machine emf can be expressed as follows [12]:

$$e_a = \omega i_f \frac{dL_{af}(\theta)}{d\theta} \quad (9)$$

where, ω is the angular frequency in rad/s, and i_f is the field current. Using values of $L_{af}(\theta)$ which were calculated from field solutions using the energy perturbation approach, for different field excitations, resulted in the curve shown in Figure (9). As can be seen from this curve, the computed values of the emf agree with the test values, and saturation effects are clearly evident in both the measured and calculated data. This further demonstrates the validity of the computed emf and inductance values and verifies the validity of the modeling approach.

Conclusion

A computer-aided method for the analysis of magnetic fields in electric machines was presented. The method was implemented to determine the machine parameters of a synchronous generator. The method is based on the use of state space models in the natural abc

frame of reference and a series of nonlinear finite element magnetic field solutions throughout the machine cross-section. Accordingly, the effects of saturation and space harmonics due to material nonlinearities and machine geometry were accounted for in the analysis. In addition, a verification of this modeling approach was presented by comparing simulation results to experimental data.

References

- [1] Fuchs, E.F. and Erdelyi, E.A., "Nonlinear Theory of Turboalternators Part II: Load Dependent Synchronous Reactances", *IEEE Trans. on Power Apparatus and Systems*, vol. 92, pp. 592-599, 1973.
- [2] Chari, M.V.K., Cendes, Z.J., Minnich, S. H., Tandon, S. C. and Berkery, J., "Load Characteristics of Synchronous Generators by the Finite Element Method", *IEEE Trans. on Power Apparatus and Systems*, vol. PAS-100, pp. 1-13, 1981.
- [3] Hannalla, A.Y., "Analysis of Transient Field Problems in Electrical Machines Allowing for End Leakage and External Reactances", *IEEE Transaction on Magnetics*, vol. MAG-17, pp. 1240-1243, 1981.
- [4] Kulig, T.S., Buckley, G.W., Lambrecht, D., and Liese, M., "A New Approach To Determine Generator Winding and Damper Currents In Case of Internal and External Faults and Abnormal Operation. Part I: Fundamentals, Paper No. 87 WM 203-3, *IEEE-PES Winter Meeting*, New Orleans, Feb. 1-6, 1987.
- [5] Arkadan, A.A., and Demerdash, N.A., "Modeling of Transients in Permanent Magnet Generators with Multiple Damping Circuits Using the Natural abc Frame of Reference," *IEEE Transactions on Energy Conversion*, vol. EC-3, No.3, pp. 722-731, 1988.
- [6] Arkadan, A.A., Hijazi, T.M., and Demerdash, N.A., "Computer-Aided Modeling of a Rectified DC Load Permanent Magnet Generator System with Multiple Damper Windings in the Natural abc Frame of Reference," *IEEE Transactions on Energy Conversion*, vol. EC-4, No. 3, pp. 518-525, 1989.
- [7] Arkadan, A.A., and Kielgas, B.W., "Switched Reluctance Motor Drive Systems Dynamic Performance Prediction Under Internal and External Fault Conditions," A Paper Accepted for Publication and Presentation at the 1993 IEEE-PES, Winter Meeting, Columbus, Ohio.
- [8] Nehl, T.W., Fouad, F.A., and Demerdash, N.A., "Determination of Saturated Values of Rotating Machinery Incremental and Apparent Inductances by an Energy Perturbation Method", *IEEE Transactions on Power Apparatus and Systems*, vol. 101, pp. 4441-4451, 1982.
- [9] Demerdash, N.A., and Nehl, T.W., "Determination of Winding Inductances in Ferrite Type Permanent Magnet Electric Machinery by Finite Elements", *IEEE Transactions on Magnetics*, vol. MAG-18, pp. 1052-1054, 1982 .
- [10] Arkadan, A.A., Demerdash, N.A., Vaidya, J.G., and Shah, M.J., "Impact of Load on Winding Inductances of Permanent Magnet Generators with Multiple Damping Circuits Using Energy Perturbation," *IEEE Transactions on Energy Conversion*, vol. EC-3, No. 4, pp. 880-889, 1988.
- [11] Demerdash, N.A., and Hamilton, H.B., "A Simplified Approach to Determination of Saturated Synchronous Reactances of Large Turbogenerators Under Load," *IEEE Transactions on Power Apparatus and Systems*, vol. 95, pp. 560-569, 1976.
- [12] Fitzgerald, A.E., Kingsley, C., and Kusko, A., *Electric Machinery*, McGraw-Hill Publishing Company, Inc., 1971, New York, NY.

An Efficient 3-D Finite Element Mesh Generator for Electromagnetic Analysis in Complex Volumes

Fuat G. Üler and Osama A. Mohammed
Department of Electrical and Computer Engineering
Florida International University
Miami, Florida, 33199

Abstract – A 3-D mesh generator for finite element analysis of electromagnetic field problems has been developed. The software is capable of handling a wide variety of geometries. In addition to ease of use, the mesh generator provides the user with good control over many significant characteristics of a finite element grid. These include the number of elements and their size in different regions, the orientation of these elements, as well as the material type associated with every region. The algorithm is capable of modeling complex topologies such as the organs of the human body. Also the grid is optimized by performing Delaunay correction to the elements after each node insertion. The efficiency of the algorithm is enhanced by the use of digital image processing techniques to extract topological information from digital images.

An application example shows simplified model of the human thorax created using the grid generator. It should be noticed that this problem includes most of the difficulties encountered in 3-D mesh generation for the finite element method. The 3-D mesh grid generator is easy to use because the work to be performed prior to running the program is kept at a minimum level.

I. INTRODUCTION

As far as today's grid generation techniques are concerned, complicated regions such as those found in modeling the human body present an exceedingly difficult task. The application efficiency of the grid generator algorithms vary with the problem. A method that is useful for one type of problem may not be applicable to another type. A prototype grid generator, developed by the authors, is quite competent for applications which present rather regular geometries which can be represented by simple algebraic equations [1]. Many practical cases, however, comprise regions that show no topological regularity. Any object, like the human body, that is created naturally possesses this trait. An algorithm that seeks standard shapes for modeling becomes futile when used for modeling an irregular geometry. Thus a new algorithm that can handle irregularities in complex topologies is necessary.

For an irregular mesh, the need for the optimization of elements is inevitable. An irregular grid, created by *node insertion* has ill-conditioned elements that result in vital numerical errors. However, no ill-shaped elements can be allowed in the final model. In the case of the presented algorithm, which follows the node insertion method, the final grid must be optimized.

II. THE 3-D GRID GENERATION

A. Data Preparation

The first task in modeling the problem is to represent all of its significant features in a format compatible with the grid generator. In this section a simple example, shown in Fig. 1, is

provided as various phases of data preparation are described. Determining the various regions based on the material types and the desired element size is the first step of the modeling process. All parameters that define the topology of the regions, their connectivity, and their material and element characteristics are compiled into a data base.

1) *Identification of the regions:* The regions in the model can be of any arbitrary shape. A boundary can be shared by a number of regions. Its outline can contain convex or concave surfaces, however, it can not touch itself. This restriction implies that if the boundary of a region touches itself, that region has to be represented by at least two regions. It also denotes that a region cannot be located inside the closed boundary of another region. If a region is to be defined inside another, the latter needs to be divided into two regions, leaving an empty space in between for the former.

Region 1 is of major importance. It is usually a hexahedral box that is large enough to contain the whole geometry of the actual problem. This region defines the initial grid that serves as the womb to the actual model.

Numbering the regions does not follow a predefined pattern. If N is the number of regions identified in the problem, then any number from 2 to $N + 1$ can be assigned to a region, as long as it is not used repeatedly.

The regions of the sample problem are indicated in Fig. 1. With the outer box, the hypothetical Region 1, there are three regions in the model.

2) *Identification of the initial nodes:* All region boundaries are defined by initial nodes placed on the surfaces of the regions. There are no restrictions for placing the nodes on the boundary surfaces. Any location that serves in defining the region is acceptable. The number of nodes placed on a boundary surface determines how finely that surface is modeled.

The numbering of the initial nodes is also done arbitrarily. As long as no duplicates are used, any number can be assigned to the nodes. Skipping a number does not constitute a problem in this case, however it is not recommended because it sometimes causes confusion. Even though the initial nodes are placed without following any predefined convention, slicing the object proves to be an efficient method of determining the initial nodes. The initial nodes are placed along the outlines of these two dimensional projections.

For modeling the sample problem, the object is cut by six planes parallel to the x-y plane. Fig. 2 shows the outlines of the regional projections on one of these planes. This particular plane has cross sections from all three regions.

3) *Coordinates of the initial nodes:* Based on the coordinate system the object is placed in, the x-, y-, and z-coordinates of all initial nodes are determined and listed in the data base in ascending order of the node numbers.

4) *Regional material identifications:* For each region specified in the model, a parameter is assigned for identifying the material it is made of. There are as many different values for this parameter as the number of materials in the actual problem.

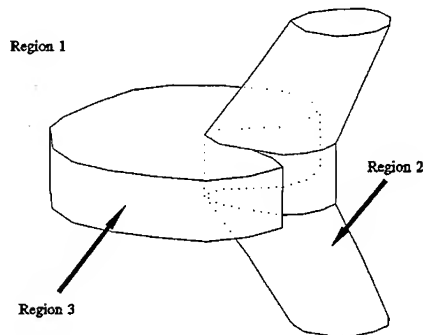


Fig. 1. The outlines of the three dimensional regions of the sample problem

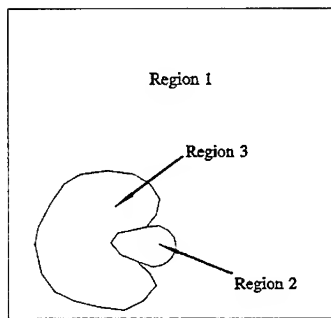


Fig. 2. One of the cross sections used for defining the problem: It reveals all three regions.

5) *Regional element size*: The size of a tetrahedral finite element is measured by its volume. The maximum element size a region can have is identified in the input data. During grid generation, the algorithm divides the elements that are larger than the specified maximum size into smaller ones until all elements in a region comply with the size requirements.

6) *Definition of the regions using the initial nodes*: The regions in the model have been identified by their region numbers, material types, element sizes, and boundary node numbers. The definition of the region by the initial nodes is done by listing all nodes that

are placed on the boundary surface of a region. For the layering method the two dimensional outlines of the region maps are traced by the initial nodes, counterclockwise.

B. The initial grid

The first phase of the automatic 3-D grid generation is to create a grid using all initial nodes. To achieve this, each node is inserted into the mesh one by one and after each insertion the grid is optimized. The result is an initial grid that is to be used for the refinement process to obtain the final model.

1) *Delaunay optimization in three dimensions*: Its efficiency and simplicity in 2-D makes the Delaunay method a desirable tool to be used in three dimensional applications. In 3-D, the dual concepts for a triangle and its circumcircle are the tetrahedron and its circumsphere, respectively. Hence, the optimality check for two neighboring tetrahedra is performed by determining if the fourth vertex of the second element is located inside the circumsphere of the first. Up to this point, the analogy between the 2-D method and the 3-D method works well. When it comes to the correction of the elements, however, a major problem is encountered. The swapping method for 2-D dictates that the common connection of the two triangles is replaced by the other diagonal and two new triangles are created. Following the analogy, it is expected that the common connection of the two tetrahedra, their shared face, will be replaced and two new elements will be created by the five vertices. For triangles, the replacement is confined to the quadrilateral formed by the four vertices and does not place any effect on the sides. Hence, the elements surrounding the pair do not get affected. In the tetrahedral application of the same idea, however, the replacement is not confined into the polyhedra formed by the faces of the original tetrahedron pair. It modifies the outer connections of the polyhedra altering the overall geometry. The polyhedra, created by the new tetrahedra, does not occupy the same volume anymore. Thus, if the surrounding elements are not corrected accordingly, overlaps or empty spaces between the finite elements result. This affect is demonstrated in Fig. 3.

To avoid the problem described above, a surrogate method is employed for optimizing the tetrahedral grid. This method is merely based on the algorithm suggested by Watson and also utilized by Cavendish [2, 3]. It forms a polyhedron around a newly inserted node by deleting all tetrahedra that are not optimal relative to the new node. Then, connecting the faces of the polyhedron to the kernel node, it creates new tetrahedra, which now satisfy the Delaunay criterion.

Optimization is performed every time a new node from the initial nodes list is inserted or a node is created for refinement. In the original algorithm it is stated that the entire process starts with a large enough tetrahedron to contain all the nodes to be inserted. For the method developed for this study, the six tetrahedra of Region 1 do this job. With the insertion of the new nodes these tetrahedra are divided into smaller elements to form the mesh.

2) *Insertion of the initial nodes:* When a new node is inserted, the algorithm locates the tetrahedron that contains it. Then, the optimization procedure takes over and creates the new tetrahedra, satisfying the optimality criterion. It is not always the case that a new node is inserted into a tetrahedral element. Three different types of *degeneracies* may occur during the node insertion process. These are encountered when a new node is located 1) on a face of a tetrahedron, 2) on an edge of a tetrahedron, and 3) on a vertex of a tetrahedron. The first degeneracy is resolved by starting the optimization process from a polyhedra that is formed by the two tetrahedra sharing the face on which the new node is located. The third form of degeneracy is trivial and should not occur if no more than one node is defined at a certain point in space. Only the second degeneracy requires special care. When it is encountered, the algorithm slightly perturbs the location of that node until it is not located on an edge anymore. After the elements are successfully created, that node is shifted to its original location in the mesh.

Currently, the model is in its initial grid state. All regions, including Region 1, are discretized. The mesh is optimized in the Delaunay sense. The initial grid is an intact model of the problem. There are, nevertheless, no internal nodes inside the regions. The entire grid is made of the initial nodes that define the boundaries. Thus, every element of the mesh stretches between the boundary surfaces. It is a correct model, however, for computational purposes, refinement of the mesh is required. This process will introduce additional nodes inside the closed boundaries of the regions and create new elements.

The sample problem's initial grid is exhibited in Figs. 4.a and 4.b, each separately.

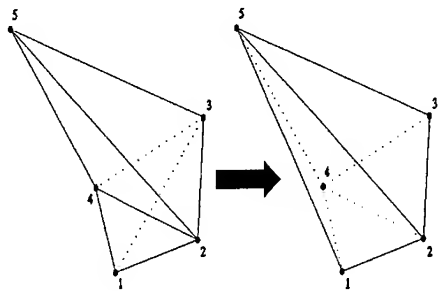


Fig. 3. Expansion of the swapping rule to three dimensions: The geometry around the element pair is altered.

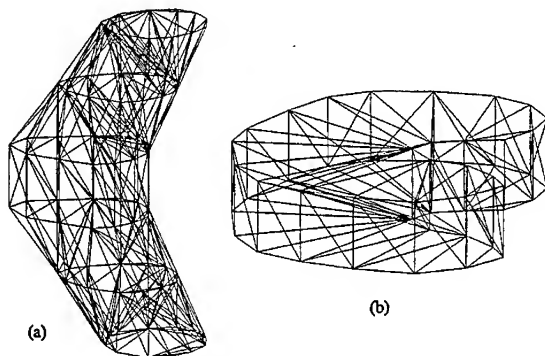


Fig. 4. Sample problem's initial grid: (a) Region 2, (b) Region 3.

C. Mesh refinement

For every element in the mesh, the refinement procedure first calculates its volume. By comparing this value with the specified parameter of the regional element size, it determines whether the element complies with the requirement. If the volume of the element is larger than the preset maximum element size of that region, a node creation process is initiated. The new node is placed at the center of mass of the tetrahedral element. Introducing a new node into the mesh results in the creation of new elements. All elements are processed until all tetrahedra comply with the size requirements of their regions. In Figs. 5.a and 5.b the model of the problem is shown from two different view angles with individual regions' hidden lines removed.

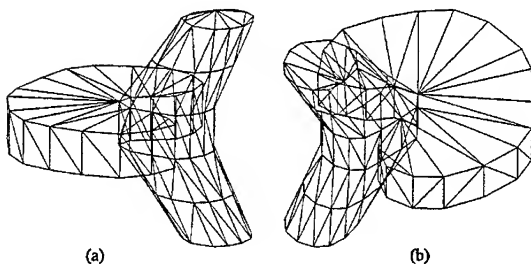


Fig. 5.(a), (b). The model for the sample problem viewed from two different angles; hidden lines of the individual regions are removed.

D. Use of Digital Image Processing

Grid generation is a completely geometrical process. First, the topology of the problem needs to be introduced to the grid generator. This is done by defining the contours of various regions in the problem by assigning nodes along them. The coordinates of these nodes and the node sequences that define the regions of the problem have to be identified. If the contours of the problem's regions cannot be represented by standard shapes, an automated process which will place nodes along the boundaries becomes a challenging task. Digital image processing is a powerful tool used at this stage of the modeling.



Fig. 6. Original image obtained from CT scan

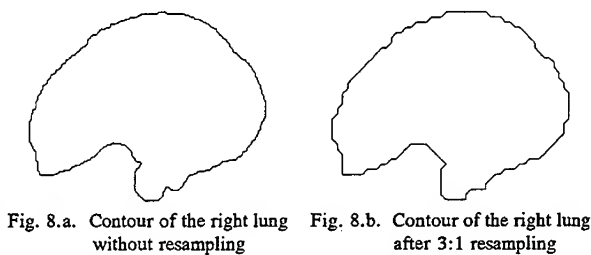


Fig. 7. Boundary of the lungs after edge detection

With the image for the problem given, image processing can extract the boundaries of the regions and because the problem is already represented by pixels, node placing can

be done quite easily following contour extraction [4, 5].

This method is applied to extract the contour of the right lung in an actual CT scan image. The image is scanned from film provided by the clinic into a 179x249 image to include only the region that contains the lungs. Figure 6 exhibits the original image. Gradient of the image is computed to detect the boundaries. Figure 7 reveals the boundary of the regions after edge detection is performed. In Fig. 8.a, the contour extracted from the boundary of the right lung is shown. Figure 8.b shows the contour after 3:1 resampling. For the 3-D applications, each layer of the CT describing the CT image is processed and the information extracted is combined by the grid generator.



III. MODEL OF THE HUMAN THORAX

The developed grid generator is used to model a portion of the human thorax. This problem presents highly complicated topologies as the grid generator must closely follow the outlines of the organs.

A. Anatomical Data and Simplifications

A cross sectional study of the human anatomy is used based on slices 1 or 2 cm thick [6].

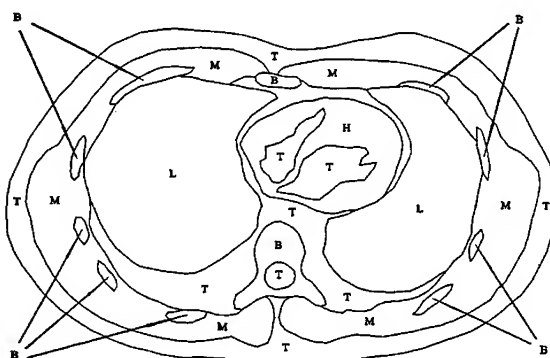


Fig. 9. Outlines of the modeled regions on a complete cross section of the thorax; M: skeletal muscle, H: cardiac muscle, B: bone, T: inner tissue, L: lungs

Images of the sections are taken from below so that the right side of the body is on the reader's left. All of the ten sections forming the thorax are used. Instead of the entire thorax, however, a portion that surrounds the heart and its close proximity is defined as the domain of the model. Data is extracted for those regions confined to this rectangular prism shaped volume. On every cut plane, a rectangle, representing the cross section of the modeling area, is placed. As there is no reference point provided for aligning these sections, after the nodal coordinates are

determined, two dimensional corrections are carried out to straighten the model.

Further simplifications are performed on every cross section. Many superfluous details are eliminated from the modeling area. The outline of the regions are smoothed, the thoracic aorta and the esophagus are removed, and the heart is reduced to a homogeneous body. From the grid generation point of view, the reason for simplifying the problem is to reduce the number of nodes in the mesh. For a highly detailed model, more nodes are required in the grid to accurately follow the outlines of the various regions of the problem. Figure 9 shows the outline of the modeled regions on a complete cross section of the thorax.

B. Identification of the regions

For identifying the regions of the problem, the layering approach is employed. As stated in the previous chapter, this method of region and node identification seems to be most efficient.

Advantageously, the anatomical data is also provided in a layered format.

Based on the procedure discussed in the section of data preparation, each organ or tissue is identified as various three dimensional regions throughout the layers. The location of different regions vary in the volume to be modeled. For example, the region that is identified as the heart starts at Layer 5 and stretches up to the tenth layer. Both lungs appear on each of the layers. The spine also goes down through the entire model.

Outside the modeling area, another rectangular prism is defined as Region 1, which holds the auxiliary elements. The heart,

the right lung, the sternum, and the spine, are modeled as a preliminary test of the application of the 3-D grid generator to this particular problem. Several views of this simplified model from different angles are shown in Figs. 10 and 11.

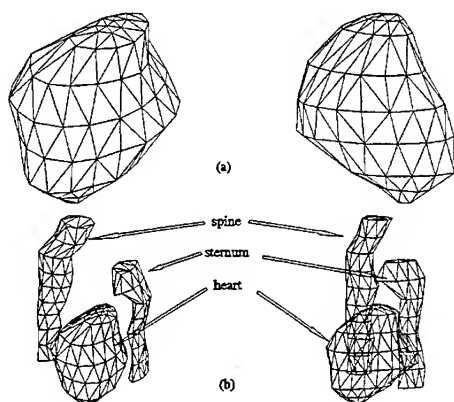


Fig. 10. Views of the 3-D model showing (a) the heart, (b) the sternum, the spine, and the heart.

IV. DISCUSSION AND CONCLUSION

For many reasons, the developed algorithm proves to be a powerful tool in three dimensional finite element grid generation. First, it is capable of modeling extremely complex geometries with great simplicity. The concept of arbitrariness combined with the process of identifying the mesh parameters, as the regions, the initial nodes, the element sizes, and the material types, provides remarkable flexibility in defining the topology of the model. This flexibility also minimizes the effort made for any alterations to the model. Some of the changes that can be performed quite easily are redefining the regions, modifying the material types, or changing the element size.

Although a layered type is used for the examples given in this paper, this mode is only an

option for data preparation. As opposed to many commercial 3-D grid generators' data entry schemes, a layering of the object is not required. The outlines of the boundaries can be specified by nodes placed anywhere on the boundary surface. This feature furnishes the algorithm with the immense capability of fitting the virtual geometry of the problem attacked.

In order to avoid ill-shaped elements, the algorithm performs optimization on the grid. This is an excessively significant characteristic of the grid generator presented here. Another feature of this 3-D grid generator is the error-based refinement mechanism. The separated refinement process of this algorithm sustains a potential for an implementation as a corrector step after the solution program.

An implementation of the proposed 3-D grid generator is presented utilizing the human thorax with a demonstrated success.

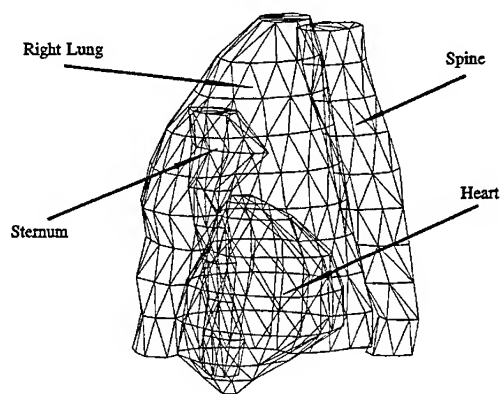


Fig. 11. 3-D finite element model of the thorax including the right lung

REFERENCES

- [1] F. G. Üler and O. A. Mohammed, "A new 3-D Finite Element Grid Generator for Electromagnetic Analysis," *SOUTHCON'92 Conference Record*, pp. 84-87, 1992.
- [2] D. F. Watson, "Computing the n -dimensional Delaunay tessellation with application to Voronoi polytopes," *The Computer Journal*, vol. 24, no. 2, pp. 167-172, 1982.
- [3] J. C. Cavendish, D. A. Field, and W. H. Frey, "An approach to automatic three-dimensional finite element mesh generation," *IJNME*, vol. 21, pp. 329-347, 1985.
- [4] R. C. Gonzalez and R. E. Woods, *Digital Image Processing*, Addison-Wesley, Reading, MA, 1992.
- [5] E. L. Hall, *Computer Image Processing and Recognition*, Academic Press, New York, NY, 1979.
- [6] R. R. Peterson, *A cross-sectional Approach to Anatomy*, Year Book Medical Publishers, Inc., Chicago, 1980.

Modern numerical techniques for high precision MRI magnet design

Sergio Pissanetzky. Texas Accelerator Center. 4802 Research Forest Drive. The Woodlands, TX 77381. USA

Abstract. Superconducting magnets for whole body magnetic resonance imaging (MRI) of humans are the single largest commercial application of superconductivity. Numerical techniques based on an expansion of the magnetic scalar potential or field in spherical zonal harmonics, which originated a century ago, are still in use for the design of MRI magnets. In the last decade, as the world market became more competitive, active and iron shields were introduced, and new, elaborate methods were developed to deal with cost minimization and nonlinearity. We review some of these techniques, with particular emphasis on the recently introduced structured coil methodology, and their impact on the MRI industry.

1. Introduction

A typical whole body superconducting MRI magnet has a bore diameter of 90 to 100 cm, and delivers a field of 0.5 to 4 T, uniform within 10 part per million (ppm), in a spherical volume of interest (VOI) of 40 to 50 cm diameter centered in the bore. The bore contains a set of pulsed gradient coils, several shim coils which improve the homogeneity to better than 1 ppm, and a set of RF coils. The final clear opening left for the patient is 60 to 70 cm in diameter. Magnets with fields stronger than 2 T are used only for research since current FDA regulations prohibit the use of such fields for clinical applications.

Normal conducting magnets are also used for MRI and are similar, except that the field range is from very low to about 0.3 T. Magnets used for nuclear magnetic resonance spectroscopy (MRS) are also similar, with fields up to 18.8 T for a proton resonance frequency of 800 MHz, and clear bores from 5.4 to 30 cm diameter. In-vivo whole body spectroscopy at fields of 2 to 4 T is currently in an experimental stage, and will soon become a clinical practice.

Issues involved in the design of MRI and MRS magnets are cost, field homogeneity, stability, shielding, shimming, patient access, patient encapsulation, maintenance, weight, power, footprint, and a few others. In the case of superconducting magnets, quench protection and cryogenic boil-off rate are also important considerations.

2. Review of traditional design methods

An infinitely long solenoid produces a perfectly uniform field. So also does a spherical winding with current density proportional to $\cos \theta$ (Everett and Osemeikhian, 1966). Neither one is practical, however. The design problem is to create a set of coaxial coils of reasonable dimensions, such that the required field strength and uniformity in the VOI are realized. If z is the axis, then $\nabla^2 B_z = 0$, and B_z can be expanded in a series of spherical zonal harmonics with reference to a system of spherical coordinates r, θ, ϕ :

$$B_z = \sum_{n=0}^{\infty} C_n r^n P_n(\cos \theta) \quad (1)$$

The expansion is valid in the largest sphere centered at the origin which does not contain electric current. A uniform field is obtained when C_0 is the dominant coefficient, and the remaining coefficients are small and can be considered as field errors. The C_n 's depend only on the distribution of current, and the question of how to calculate them for a given coil geometry is therefore of central importance. A. Gray (1892) addressed this question a century ago. Garrett (1951) presented a more complete account, giving analytical expressions for the C_n 's due to infinitely thin loops of current, solenoids of finite axial length but infinitely small radial thickness, and solid solenoids with finite dimensions both axially and radially. In 1967, Garrett presented a fundamental piece of work, listing hundreds of solenoid systems with homogeneities of the 6th to the 20th order (n -th order means that the first nonzero coefficient is C_n), including solenoids with inside and outside notches. The question of coaxial polygonal coil systems, where tesseral harmonic coefficients are also present, has been discussed by Garrett and Pissanetzky (1971), with extensive listings of square, hexagonal and octagonal systems with homogeneity of the 4th to the 8th order, and comparison with their cylindrical counterparts. These ideas are still in use, and some commercial MRI magnets available today are based to some extent on Garrett's designs. Iron shields were not considered by Garrett, but since magnetization is equivalent to current, the same analytical methods can be used once the magnetization is known.

3. Modern methods

More recently, as the world market became more competitive, active and iron shields were introduced, and new, elaborate methods were developed to deal with cost optimization and nonlinearity. Many of these methods assume a prescribed set of cylindrical coils with rectangular cross section in the ρ, z plane and a uniform current density. The only degrees of freedom are the radial and axial positions of the boundaries of the coil cross sections, and the value of the current density. The effect of a change in each one of these parameters on the C_n 's is numerically determined, and the parameters are systematically readjusted until the undesirable coefficients become small.

Siebold (1988) proposed a method where the coils and iron are discretized into solid rings, the magnetization in the iron is calculated by an integral method, and the zonal harmonics are obtained by numerical quadrature over a set of field sampling points. The coils are then reshaped until the desired spectrum is obtained. The field at the sampling points is calculated by Urankar's (1982) elaborate method, which could have been avoided if Garrett's simple analytical expressions had been used.

Ogle and D'Angelo (1991) used the finite element (FE) method to obtain the mag-

netization in the iron. A set of target points, equal in number to the number of degrees of freedom of the system, is chosen in the VOI. The contribution from the iron is described in terms of a spherical harmonic expansion, with coefficients calculated by weighting the magnetization with suitable expansion functions. The spherical harmonic expansion is used to calculate the fields at the target points due to the iron alone. The contribution from the coils is obtained by subdividing each coil into a grid of circular wire loops, and using an elliptic integral to calculate the field of each loop. The locations of the coils are then adjusted until the target field values are met. The magnetization in the iron is recalculated, and iterations continue until convergence is achieved. The elaborate procedure involving the spherical harmonics could have been avoided if a grid of circular wire loops had been used to represent the magnetization in the iron.

Thompson (1992) used a combination of numerical techniques and variational approach with constraints introduced via Lagrange multipliers to determine optimal currents and coil locations. Ishiyama (1987 and 1991) also used the FE method for the iron and the boundary element method for field calculations in the volume of interest. The FE method is not considered accurate enough for the high precision field calculations required in the VOI.

All these methods share three common assumptions: (1) the number of coils is prescribed, (2) the cross section of each coil by a ρ, z plane is a rectangle, and (3) the current density is uniform in the cross section. These assumptions appear quite reasonable, since a coil is always wound layer after layer into a bobbin, resulting in a rectangular cross section and a uniform current density. The assumptions, however, are extremely rigid and leave very few degrees of freedom for the optimization to take advantage of. In the next Section we examine a new methodology where all three assumptions have been removed. The methodology provides practical coil systems that can be wound in the traditional way and exhibit a superior performance.

4. The structured coil methodology

Coil structure was introduced as a design parameter for the first time by Pissanetzky (1992) for coil systems, and by Pissanetzky (1993) for magnets comprising coils and ferromagnetic components, with either planar or cylindrical symmetry. In the case of a cylindrical MRI magnet, a system of cylindrical coordinates ρ, z, φ is attached to the magnet, and a cross section defined by a $\rho, z, \rho \geq 0$ half-plane is considered. The current density $j(\rho, z)$ defined in the plane is used to describe the coil system, since all electric currents cross the plane normally. In a traditional optimization method, the coils are described by a set of rectangles in the plane, and the assumption is made that $j(\rho, z) = j_i$ inside rectangle i , and $j(\rho, z) = 0$ outside the rectangles. The j_i 's and the dimensions of the rectangles are, then, readjusted for better field quality.

In the structured coil methodology, a **tiling** is defined in the ρ, z half-plane, covering a region where $j(\rho, z)$ is allowed to be nonzero, while $j(\rho, z) = 0$ is assumed outside

the tiling. The tiling has a large number T of tiles, typically several hundred to several thousand tiles. No other assumptions are made as to the number of coils, or the positions or shapes of their cross sections inside the tiling, and no requirement is enforced on $j(\rho, z)$ to be uniform in any particular region. Instead, $j(\rho, z)$ is described by a set of T independent currents i_t , $t = 1, \dots, T$, one in each tile, thus providing T independent degrees of freedom. Constraints are enforced on the currents i_t not to exceed a certain range, usually dictated by critical current considerations in a superconducting magnet, or by heat generation considerations in a normal conducting magnet. A typical set of constraints is:

$$0 \leq i_t \leq I, \quad t = 1, \dots, T \quad (2)$$

if negative currents are not allowed, or

$$-I \leq i_t \leq I, \quad t = 1, \dots, T \quad (3)$$

when negative currents are allowed, where I must be specified by the magnet designer. Next, treating each tile as a solid solenoid, Garret's (1967) analytical expressions are used to find the zonal harmonic coefficients of the z component of the field contributed by the *unit* current in that tile. If C_{nt} is the n -th zonal harmonic coefficient for tile t , then C_{nt} depends only on the geometry of the tile. The coefficients C_n for the expansion of the *total* field are given by:

$$C_n = \sum_{t=1}^T C_{nt} i_t, \quad n = 1, \dots, N \quad (4)$$

where N is the largest order desired by the magnet designer. An objective function is now defined as the sum of the squares of the errors expressed in terms of the coefficients C_n . For example, if we would like $C_0 = C$ and $C_n = 0$ for $n > 0$ for a uniform field, we would define the following objective function:

$$F = (C_0 - C)^2 + \sum_{n=1}^N C_n^2 \quad (5)$$

Function F is quadratic in the tile currents i_t , since matrix C_{nt} is given. To obtain the optimum values for the currents i_t , F is minimized by Simplex constrained quadratic optimization. The properties of the Simplex algorithm with linear constraints play a fundamental role in creating a practical coil. The linear constraints define a hyper-polyhedron in the T -dimensional space of the currents i_t . All feasible solutions are inside the polyhedron, but the *optimum* solutions are on the boundary

of the polyhedron, usually at vertices. But the polyhedron is rectangular, and a vertex is a point where all i_t 's acquire the value of either the upper or the lower constraint, 0 and I if negative currents are not allowed, or $-I$ and I if negative currents are allowed (actually, since this is a quadratic problem, one or two of the i_t 's may end up having values other than the extremes). Furthermore, tiles with like currents coalesce into clusters, resulting in a subdivision of the initial region into areas of either one of two types: (1) areas where all tiles have the same current I , and (2) areas where all tiles have the same current 0 (or $-I$ if negative currents are allowed). Typically, there are two or three areas of each type, and the shape of the areas is irregular. Each area with current represents a coil that can be built by the traditional procedure of winding wire into a bobbin. Each area without current represents space where no winding is necessary. The optimization process determines, in one shot, all important parameters: the number of coils and the shapes and positions of their cross sections.

When iron is present, iterations are necessary. An initial guess is made for the tile currents i_t , and a finite element method is used to obtain the magnetization $M(\rho, z)$ in the iron. With M known, Garret's methods are used to obtain the zonal harmonic coefficients contributed by the iron alone. These are included in F , and a new iteration is performed. For an MRI magnet with a close fit external iron yoke, convergence is typically achieved in 7 to 8 iterations.

The objective function F can be defined in many different ways. In previous publications (Pissanetzky, 1992, 1993) F was defined in terms of field errors at a set of target points defined on the boundary of the VOI, which is also a quadratic function of the i_t 's. Fringe fields evaluated at target points outside the magnet can also be included in F , with appropriate weights, when an actively shielded magnet is being designed. Several tilings can be used if there is a need to confine the coils to specific regions. The important feature of the structured coil methodology is the very large number of degrees of freedom, which results in a better optimization for the objective function. Traditional trade-offs such as size, shielding, field quality and cost improve significantly, and better designs are obtained, some never tried before.

5. An example

We present a design example for a 2 T, 1 m bore actively shielded MRI magnet for whole body imaging, with a 50 cm diameter VOI centered in the bore of the magnet, our internal code *ey*. Commercial magnets with these characteristics are about 2.5 to 2.8 m long. A patient introduced into such a long magnet feels encapsulated. Besides, access to the patient by medical personnel is severely restricted, and life support equipment attached to the patient has to be removed. Therefore, the purpose of the optimization is to design a 2 T magnet not much longer than a person, say 1.8 m long. To realize how ambitious is this goal, compare with currently available actively shielded commercial magnets which provide one-fourth of the field, 0.5 T, and are 1.6 m long (Hawksworth, 1991).

Figure 1 shows a cross section of one quadrant of the ρ, z plane, where 3 tilings have been defined, T_1 , T_2 and T_3 . Tiling T_1 is the region allocated for the main coils. It is divided into 7 divisions horizontally and 20 divisions vertically, for a total of 140 tiles, with a current density constrained to be between 0 and 30 KA/cm². Tiling T_2 has 10 horizontal divisions by 7 vertical divisions, for a total of 70 tiles, and a current density in the range -30 KA/cm². Tiling T_3 is divided 7 x 12, and its current density is restricted between -30 KA/cm² and 0. Tilings T_2 and T_3 contain negative coils for flux confinement and active shielding. The current densities are compatible with the expected peak fields at the coils for NbTi superconducting wire.

The commercial program Opus is used for all calculations and plots. The objective function F was expressed in terms of target fields, with 21 target points selected on the quarter circle at radius 50 cm for field quality, and 11 targets on a quarter ellipse of semiaxes 180 and 280 cm for shielding. Since no iron is present, the optimization converges in just one iteration. The resulting field lines are shown in figure 1. The active shield is very effective, with the 5 G line at 1.5 m from the side of the magnet, and 4.7 m from the front, and the field quality in the 50 cm diameter VOI is 12 ppm. The total magnetic energy is 12.2 MJoule. Figure 2 shows the current map for the three tilings, with currents given in KA per tile. Tiling T_1 contains 3 structured coils in the region $z \geq 0$, which can all be wound on a single bobbin of 58 cm radius. This radius has been chosen large enough to accommodate to thickness of the bobbin and the cryostat, and still leave a clear bore of 1 m diameter. If the bobbin and cryostat could be made thinner, the magnet would be proportionally shorter. Tiling T_2 has one structured coil with negative current on each side of the midplane, and tiling T_3 has only one negative coil of rectangular cross section centered on the midplane. Peak fields, zonal harmonic coefficients and forces on the windings have all been calculated by Opus, and found to be acceptable.

6. References

- J. E. Everett and J. E. Osemeikhian (1966). J. Sci. Instr., Vol. 43, pp. 470-474.
- M. W. Garrett (1951). J. Appl. Phys., Vol. 22, pp. 1091-1107.
- M. W. Garrett (1967). J. Appl. Phys., Vol. 38, pp. 2563-2586.
- M. W. Garrett and S. Pissanetzky (1971). Rev. Sci. Instr., Vol. 42, pp. 840-857.
- A. Gray (1892). Phil. Mag. (V), Vol 33, p. 62.
- D. Hawksworth (1991). Magn. Res. in Medicine, Vol. 17, pp. 27-32.
- A. Ishiyama et al. (1987). IEEE Trans. Magn. Vol. MAG-23, pp. 603-606.
- A. Ishiyama et al. (1991). IEEE Trans. Magn. Vol. 27, pp. 1692-95.
- M. D. Ogle and J. D'Angelo (1991). IEEE Trans. Magn., Vol. 27, pp. 1689-1691.
- S. Pissanetzky (1992). IEEE Trans. Magn., Vol. 28, pp. 1961-68.
- S. Pissanetzky (1993). IEEE Trans. Magn., to appear.
- H. Siebold (1988). IEEE Trans. Magn., Vol. 24, pp. 408-410, and pp. 419-422.
- M. R. Thompson, R. W. Brown and V. Srivastava (1992). MRI in the Applied Sciences Symposium, Durham, North Carolina, October 26-28.
- L. K. Urankar (1982). IEEE Trans. Magn., Vol. MAG-18, pp. 1860-67.

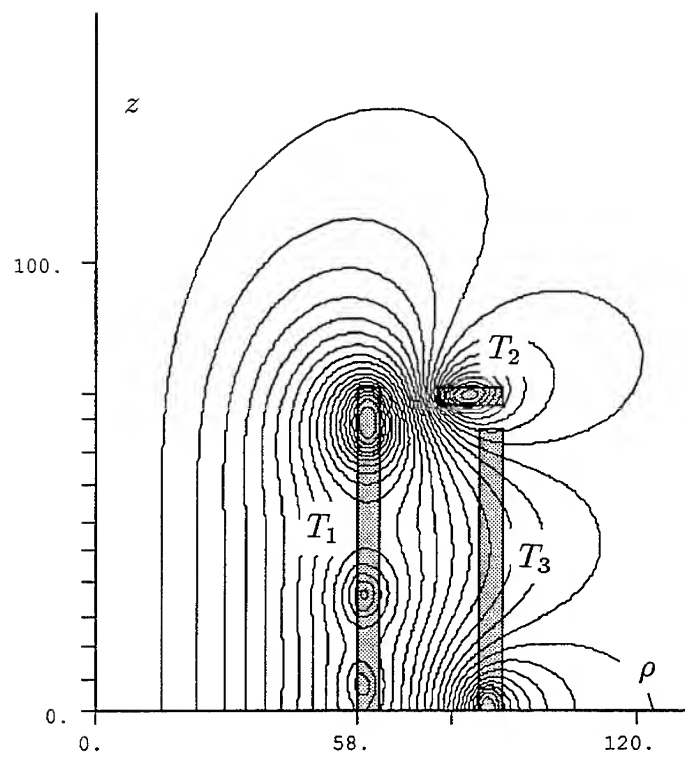


Figure 1. Tilings and field lines for the example discussed in Section 5 of the text.

77.14	77.14	77.14	77.14	77.14	77.14	77.14
77.14	77.14	77.14	77.14	77.14	77.14	77.14
77.14	77.14	77.14	77.14	77.14	77.14	77.14
77.14	77.14	77.14	77.14	77.14	77.14	20.94
0.00	0.00	0.00	0.00	0.00	0.00	0.00
0.00	0.00	0.00	0.00	0.00	0.00	0.00
0.00	0.00	0.00	0.00	0.00	0.00	0.00
0.00	0.00	0.00	0.00	0.00	0.00	0.00
0.00	0.00	0.00	0.00	0.00	0.00	0.00
0.00	0.00	0.00	0.00	0.00	0.00	0.00
0.00	0.00	0.00	0.00	0.00	0.00	0.00
75.83	0.00	0.00	0.00	0.00	0.00	0.00
77.14	77.14	77.14	77.14	77.14	0.00	0.00
77.14	77.14	77.14	39.78	0.00	0.00	0.00
0.00	0.00	0.00	0.00	0.00	0.00	0.00
0.00	0.00	0.00	0.00	0.00	0.00	0.00
0.00	0.00	0.00	0.00	0.00	0.00	0.00
77.14	64.33	0.00	0.00	0.00	0.00	0.00
77.14	77.14	77.14	77.14	0.00	0.00	0.00
14.67	0.00	0.00	0.00	0.00	0.00	0.00

-24.00	-24.00	-24.00	-24.00	-24.00	-24.00	-24.00	-24.00	-24.00	0.00
-24.00	-24.00	-24.00	-24.00	-24.00	-24.00	-24.00	-24.00	0.00	0.00
-24.00	-24.00	-24.00	-24.00	-24.00	-24.00	-24.00	-24.00	0.00	0.00
-24.00	-24.00	-24.00	-24.00	-24.00	-24.00	-24.00	-24.00	0.00	0.00
-24.00	-24.00	-24.00	-24.00	-24.00	-24.00	-20.51	0.00	0.00	0.00
-24.00	-24.00	-24.00	-24.00	-24.00	-24.00	0.00	0.00	0.00	0.00
-24.00	-24.00	-24.00	-24.00	-24.00	0.00	0.00	0.00	0.00	0.00

0.00	0.00	0.00	0.00	0.00	0.00	0.00
0.00	0.00	0.00	0.00	0.00	0.00	0.00
0.00	0.00	0.00	0.00	0.00	0.00	0.00
0.00	0.00	0.00	0.00	0.00	0.00	0.00
0.00	0.00	0.00	0.00	0.00	0.00	0.00
0.00	0.00	0.00	0.00	0.00	0.00	0.00
0.00	0.00	0.00	0.00	0.00	0.00	0.00
0.00	0.00	0.00	0.00	0.00	0.00	0.00
0.00	0.00	0.00	0.00	0.00	0.00	0.00
0.00	0.00	0.00	0.00	0.00	0.00	0.00
-112.50	-112.50	-112.50	-112.50	-66.13	0.00	0.00

Figure 2. Current maps for tilings T_1 , T_2 and T_3 of figure 1. The currents are given in KA per tile. The structured coils have been outlined.

An Artificial Neural Network Environment for the Optimal Design of Geometric Boundaries in Electromagnetic Devices

Osama A. Mohammed, Dong C. Park, Riaz Merchant and Fuat G. Üler
Department of Electrical and Computer Engineering
Florida International University, Miami, Florida 33199, U. S. A.

Abstract - A neural network based environment for optimization of geometric boundaries of electromagnetic devices is presented. The method utilizes Artificial Neural Networks (ANNs) in a system which encompasses numerical computations and expert's input for generating a variety of ANN training data for different topologies. The environment is aimed at producing the smallest possible size of the electromagnetic devices for a specific performance measure.

The proposed ANN environment is composed of four modules. The input module prepares the data based on practical examples for different topologies. The ANN module utilizes a layered type perceptron which is trained using the error back propagation algorithm. The optimization module utilizes finite element solutions combined with a Hopfield Network and Simulated Annealing. A conventional search technique may also be used in the optimization module. The produced optimal solution is then adapted by an adaptive ANN module.

Optimal designs are obtained quickly once the ANN is trained with a variety of topologies. Results of implemented examples are provided to show the validity of the proposed mechanism.

I. INTRODUCTION

Optimization of geometric boundaries in electromagnetic devices is receiving widespread attention and interest by many researchers. Recently, several design optimization techniques have appeared in the literature ranging from evolution strategies to simulated annealing, and search techniques for global minima [1-4].

During the past few years, ANNs have been successfully applied to many engineering problems involving associative operations, search operations, classification and regression, as well as pre-processing [5-6]. ANNs can be utilized to provide a parallel computation alternative and high speed for a variety of problems in electromagnetics [7-8].

The optimal design problem seeks an optimal output (minimum size, best performance, etc.) for a given set of constraints (inputs). In order to apply the ANNs to the design optimization of electromagnetic devices, consider the optimal design problem as an inverse problem: given an output specification (O), find the input geometries (I) which satisfy given specification in an optimal fashion. Assume that there exists a set of equations, F (such as the finite element equations or the expert's rule), which govern the relationship between I and O such that $O = F(I)$. That is, a set of geometries which produces an output specification by the existing set of equations, F . It should be noticed that I is the set of geometries which gives the specified output, either linear or nonlinear. The steps involved can be described as follows:

1. Create N data sets by applying sets of inputs to the set of governing equations F ; (I_i, O_i), $i=1, \dots, N$.
2. Train the ANN with O_i as input and I_i as desired output of the ANN.
3. Give the desired performance for which optimal geometry is sought to the ANN. The ANN responds with a practical solution which may or may not be the optimal one.

4. The ANN output is passed on to the optimization module. This step involves optimization and testing till the optimal geometry is found.
5. The optimal geometry is adapted into the training set of step 2 and the ANN adapted with this new data.

Although the first two steps are computationally extensive, these are done off line. However, once trained, the ANN provides a response within a few milliseconds.

This paper explores the suitability of applying ANNs to the optimal design problem in electromagnetic devices. Results obtained from the implemented examples show that using ANN is a viable approach with accurate results and quick response time.

II. DESCRIPTION OF FUNCTIONAL MODULES

The proposed design environment consists of four modules as shown in Figure 1. The first module deals with the preparation of the ANN training data based on a particular topology. This procedure is done only at the beginning of the training procedure and could be deemed as a system initialization. The second module is the trained ANN. Test examples are given to the ANN and the response is fed into the third module which is the optimization module. The optimization module responds with an optimal solution. This optimal geometry is later incorporated into the ANN training set by an adaptation algorithm.

A. Input Module

The input module consists of an example generator and off-line training of the ANN. The examples are generated by using equations governing the geometry of the devices and inputs from experts. Sufficient examples are generated to adequately train the network for a good response.

An ANN can be defined as a network that resembles the functional architecture of the brain. It consists of a highly connected array of elementary processors called neurons. In this paper, the multilayer perceptron (MLP) type ANN with back-propagation is considered [6].

The MLP type ANN consists of several layers; one input layer, one or more hidden layers, and one output layer. Neurons in a layer are generally interconnected to all the neurons in the adjacent layer with different weights. Each neuron receives its inputs from the neurons in the higher layer through interconnections and propagates its activation to the neurons in the next lower layer. Except for the input layer, each neuron receives a signal which is a linearly weighted sum of all the outputs from the neurons of the former layer.

When h hidden layers exist, the layer 0 and layer $(h+1)$ denote the input and output layers, respectively. Then, the activation of a neuron j in the layer k , is defined as:

$$u_k^{(k)} = f_j \left(\sum_i w_{ji} u_i^{(k-1)} \right) \quad (1)$$

where

$$f_j(x) = \begin{cases} \frac{1}{1 + \exp^{-x}} & \text{if neuron } j \text{ is a hidden neuron} \\ x & \text{otherwise} \end{cases}$$

and i covers all the neurons in the layer $(k-1)$. Note that the activation of the j^{th} neuron in k^{th} layer, $u_j^{(k)}$ in (1), is only a function of the activations of the neurons in the $(k-1)^{\text{th}}$ layer and weights which connect the j^{th} neuron in k^{th} layer and the neurons in the $(k-1)^{\text{th}}$ layer. The nonlinearity $f_j(x)$ does not necessarily have to be the sigmoid function $(1/(1+\exp^x))$. Other monotonic functions which are differentiable in the domain of x can also be used for $f_j(x)$.

The ANN is trained off-line with the geometry of the device as the input and the performance as the output. The training is stopped once the ANN gives adequate response to the test data. When on-line, the user specifies the desired performance measures as his requirement and the output from the network is the geometry for that performance criteria. This is called inverse solution.

B. ANN Module

The trained ANN is put on-line after the training is complete. The output from the ANN is a practical one. This is a safe assumption because the training set consisted of practical examples. The ANN serves to reduce the search time encountered in other methods [1-4]. The optimization procedure can now be applied on the output from the ANN.

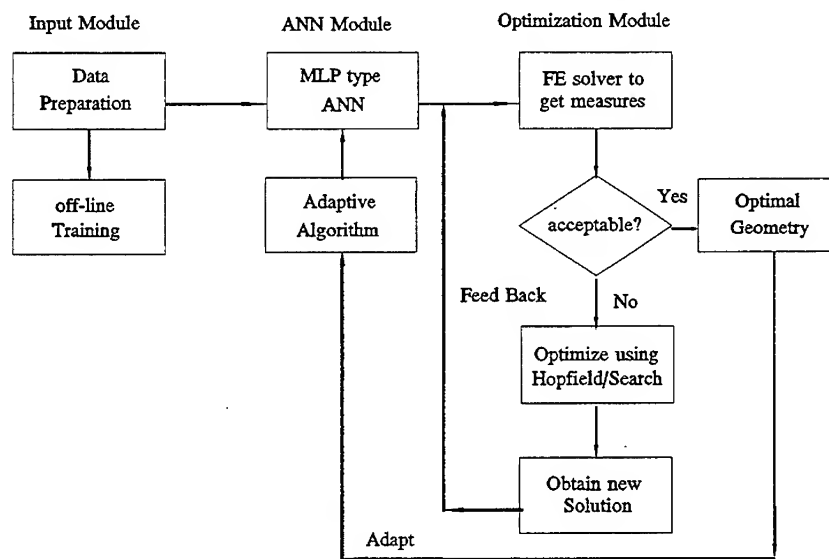


Fig. 1. System flow diagram of the design environment

C. Optimization Module

The next step is to optimize the results obtained from the ANN. The ANN solution is passed on to the finite element solver to obtain the field solutions for the geometry obtained from the ANN. This solution will give an indication about the optimality of the geometry after

comparison with the specified performance criteria based on an energy function. If the solution has been found to be acceptable, then we say that it is the optimal solution. If not, then the geometry obtained from the ANN is passed on to the optimization routine. The optimization routine can either be a combined Hopfield network/simulated annealing method or a conventional search technique [9]. The optimization routine tries to reduce the objective function related to the topology of the device under consideration. The objective function could be based on specified parameter that is required, core loss value, energy or the mmf values. Other measures may also be used.

In the case of electromagnetic devices implemented here, the main aim is to minimize the size for a specified value of flux density. First, the flux density of the geometry obtained from the ANN is calculated using the finite element solution. Then, the difference of the calculated flux density value and the specified value is minimized in the least square sense to achieve optimization. If the value is found to be acceptable, then the geometry is said to be an optimal one and is adapted. If not, then the output from this routine is fed back into the finite element solver to obtain another geometry (smaller or larger). This loop continues until an optimal solution is obtained. Since the ANN solution is a practical one which is near optimal, the optimization loop can be completed quickly provided that the ANN is trained with sufficient example. The main objective of the optimization loop is to find a smaller size than the one obtained by the ANN module. It essentially represents a design perturbation mechanism to check if smaller design can be achieved while still satisfying the objective function. More details on this module can be found in [9].

D. Adaptive Module

The final stage is the adaptation of the optimal geometry. This is done by appending the optimal geometry obtained earlier into the training set of the ANN. The ANN is then trained for a few more iterations, and the weights allowed to change, to learn the new data. The adaptation is important for obtaining a quicker response from the system whenever a similar performance measure or optimal design is required.

IV. RESULTS AND DISCUSSION

The above procedure is put into application for the optimal design of two examples. The initial geometries and the geometrical variables for a C-core magnetic circuit and a dc motor are shown in Figs. 2 and 3.

For the C-core example, the training set for the ANN module has 140 examples derived from the original geometry. The geometrical position of the 10 variables, determining the shape of the magnetic circuit, Figure 2, are changed by $\pm 5\%$ until a $\pm 30\%$ offset from the original is reached. Thus different positions for each of the variables are defined and, including the original, a total of 145 different geometries are created. After normalization of the training set, 5 of these examples are picked up as test set and are not used in the training set. This is done to check the response of the trained ANN. The remaining 140 examples are used for training the ANN. For the optimization module, the objective function is based on a specified value of flux density in the gap while reducing the size.

For the 2-pole dc motor example of Fig. 3, the objective is to obtain the size that would minimize the mmf per pole while maintaining uniform flux density. The dc motor magnetic circuit is separated into several parts; pole, air gap, rotor, yoke and pole face. The cross sectional area, flux density, field intensity, mean length and mmf for each part are calculated.

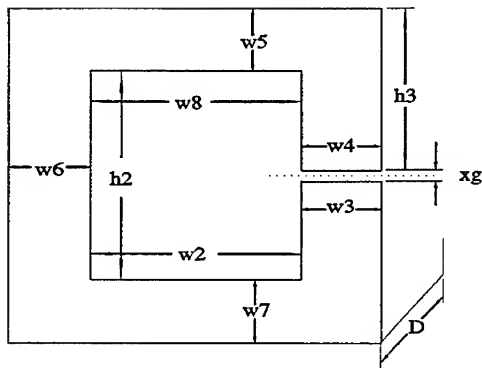


Fig. 2. C-core magnetic circuit example.

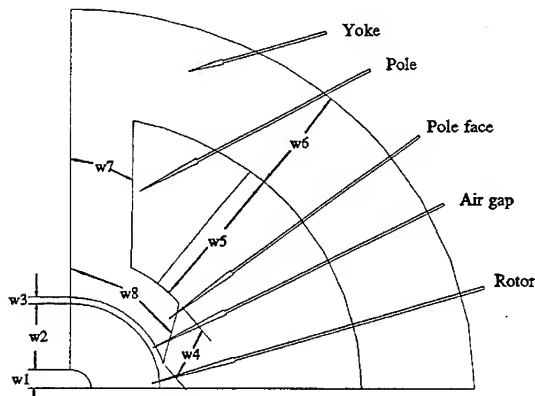


Fig. 3. 2-pole dc motor example.

For this example, the training set is composed of 145 examples derived from the initial geometry. The geometrical position of the 9 variables determining the shape of the dc motor magnetic circuit are changed by $\pm 5\%$ until a $\pm 30\%$ offset from the initial geometry is reached.

The input variables of the ANN are derived from finite element solutions for both examples representing the performance of the magnetic circuit for the various shapes included in the training set. The output variables of the ANN represent coordinate points defining the geometries. The input-output pairs are presented to the ANN as examples not including the test set which is used to check the performance of the trained ANN.

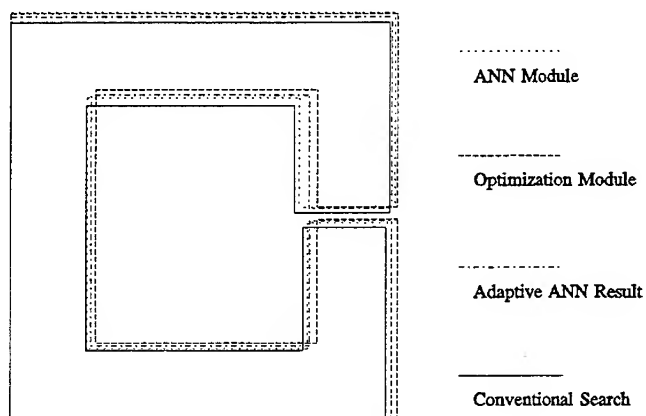


Fig. 4. C-core magnetic circuit

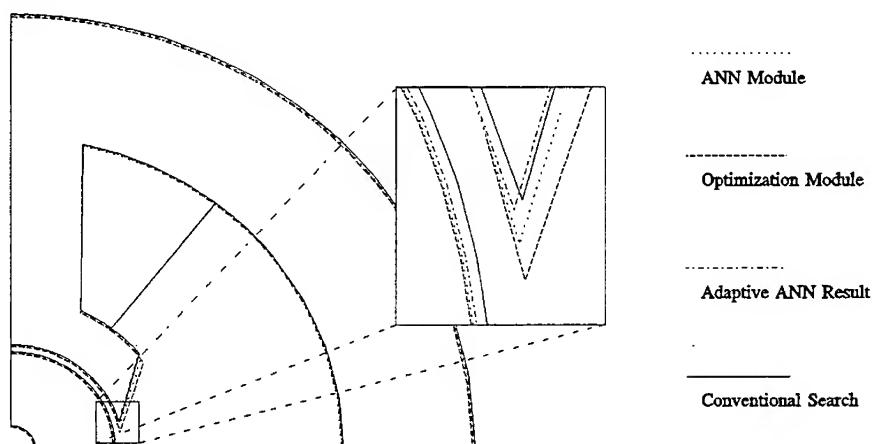


Fig. 5. Results for the 2-pole dc motor example.

For the two examples, the results of the ANN module, optimization module and the adaptation module are given in Tables I, II and III and are illustrated in Figures 4 and 5. These results are shown in comparison with the results obtained from using a conventional search technique [4]. The core size of the magnetic circuit (iron only) was determined by adding the triangular finite element areas using the FE grids from various solutions. As can be seen from these results, the various modules contribute to the improvement of the design and overall shape of the device being optimized. The results of the adaptive ANN module show that the ANN has

learned new geometry close to the optimal design. More examples appended to the training set and used in retraining has contributed to such an improvement. It should be emphasized here that continual adaptation will always produce better results than previous adaptation. The response time of the proposed ANN environment is much quicker than in conventional training.

TABLE I. COMPARISON OF OPTIMAL DESIGN RESULTS FOR THE C-CORE EXAMPLE

Optimization Method	Design Parameters (Constant Depth) in cm									
	W2	W3	W4	W5	W6	W7	W8	h2	h3	xg
ANN Module	4.182	1.589	1.826	1.725	1.441	1.441	4.013	5.061	3.922	0.305
Optimization Module	4.203	1.515	1.515	1.531	1.601	1.552	4.202	5.113	3.875	0.257
Adaptive ANN Module	4.155	1.546	1.553	1.572	1.504	1.501	4.147	5.062	3.841	0.261
Conventional Search Method	4.120	1.565	1.798	1.681	1.420	1.405	3.953	4.935	3.824	0.297

TABLE II. COMPARISON OF OPTIMAL DESIGN RESULTS FOR THE 2-POLE DC MOTOR EXAMPLE

Optimization Method	Design Parameters in cm								
	W1	W2	W3	W4	W5	W6	W7	W8	sl
ANN Module	0.4623	1.5433	0.1498	1.0074	3.3337	2.5884	1.4293	2.9512	15.0
Optimization Module	0.4503	1.5510	0.1501	1.0091	3.3499	2.5625	1.423	3.0471	15.0
Adaptive ANN Module	0.4623	1.5526	0.1473	1.0169	3.3344	2.5931	1.4311	2.8714	15.0
Conventional Search Method	0.4781	1.5633	0.1461	1.0172	3.3278	2.6021	1.4312	2.8842	15.0

TABLE III. COMPARISON OF CORE SIZES (IRON CROSS-SECTIONAL AREA* IN cm²) OBTAINED WITH DIFFERENT METHODS

	Proposed ANN Optimization Mechanism			Search Method
	ANN Module	Optimization Module	Adaptive Module	
C-Core	37.624	37.414	37.152	36.933
dc Motor	136.361	135.621	135.033	134.792

* Iron area is calculated by adding element areas of associated FE grid.

In Tables I and II, values for the geometry variables, defining the shape, obtained by the proposed method for the two examples are shown in comparison with the dynamic search procedure, presented earlier [4]. Table III shows a comparison of the different core sizes obtained by the ANN method and the conventional dynamic search method.

V. CONCLUSION

The new method which utilizes ANNs for the optimal design of electromagnetic devices is presented. A major advantage of the method is its quite short response time in obtaining the optimal geometry. The results of examples implemented in this paper show the excellent potential of ANNs in design optimization. The accuracy of the end result depends on the size and content of the training data which encompasses the designer's input. The adaptation makes it possible to respond even more quickly to new data not present in the training set.

The solution obtained from the ANN serves as an initial state of a design optimization procedure. This significantly reduces the search time required compared with other search based methods since the solution from the ANN is already a practical one.

A combined Hopfield network and simulated annealing procedure is used in the optimization module. The suitability of an optimization method depends on the problem under consideration. The optimization procedure thus may vary from problem to problem and should not be confined to Hopfield networks and simulated annealing.

REFERENCES

- [1] K. Preis and A. Ziegler, "Optimal design of electromagnetic devices with evolution strategies," *Proc. of International Symposium on 3-D Electromagnetic Fields*, Okayama, Japan, pp. 119-122, 1990.
- [2] J. Simkin and C. W. Trowbridge, "Optimization problems in electromagnetics," *Digests of Computational Electromagnetic Fields Conference*, Toronto, Canada, 1990.
- [3] A. Gottwald, "Comparative analysis of optimization methods for magnetic," *IEEE Trans. Mag.*, vol. 24, no. 1, pp. 411-414, 1988.
- [4] O. A. Mohammed and W. K. Jones, "A dynamic programming -finite element procedure for the design of nonlinear magnetic devices," *IEEE Trans. Mag.*, vol. 26, no. 2, pp. 666-669, March 1990.
- [5] L. Atlas, J. Connor, D. C. Park, et al., "A performance comparison of trained multi-layer perceptrons and trained classification trees," *Proc. of IEEE: Special Issue on Neural Networks*, vol. 78, no. 10, pp. 1614-1619, Oct. 1990.
- [6] D. E. Rummelhart, G. E. Hinton, and R. J. Williams, "Learning internal representations by error propagation," *Parallel Distributed Processing*, vol. 2, pp. 318-362, MIT Press, Cambridge, 1987.
- [7] O. A. Mohammed, et. al. "Design Optimization of Electromagnetic Devices using Artificial Neural Networks", *IEEE Transactions on Magnetics*, vol. 28, No. 5, pp 2805 - 2807, September 1992.
- [8] D. N. Dyck and D. A. Lowther "Determining an approximate Finite Element Mesh Density using Neural Network Technique", *IEEE Transactions on Magnetics*, Vol. 28, No.2, pp 1767-1770, March 1992.
- [9] O. A. Mohammed, et. al., "A New Method for the Optimal Design of Electromagnetic Devices using Artificial Neural Networks and Improved Simulated Annealing", *INTERMAG*, Stockholm, Sweden, April 1993.

SENSITIVITY ANALYSIS OF THE INTEGRODIFFERENTIAL FINITE ELEMENT - GREEN'S FUNCTION METHOD

Qiushi Chen, A. Konrad and P.P. Biringer

Department of Electrical and Computer Engineering, University of Toronto
Toronto, Ontario, CANADA M5S 1A4

Abstract — This paper presents a sensitivity analysis of the modified hybrid integrodifferential finite element - Green's function method. This hybrid formulation is developed for the solution of open eddy current problems with exterior sources. It is an efficient alternative to existing unbounded eddy current approaches. The Green's function method in this formulation is based on the concept of fictitious magnetic charges. In this study, the effects of the locations of the fictitious charges and the interface upon the accuracy of the computation results are examined. The problem solved in this paper is an infinitely long circular cylindrical conductor under uniform transverse magnetic field. Power losses are obtained and compared with analytic results. Guidelines are established for locating the fictitious magnetic charges.

Introduction

The use of the finite element method for the solution of unbounded problems requires the employment of special techniques to account for the exterior region. The spectrum of these techniques is evident in the literature [1]-[10]. While these techniques make it possible for the finite element method to solve unbounded problems, they are limited by various shortcomings. The integrodifferential finite element - Green's function method introduced in [11] is an efficient method for unbounded eddy current problems. In this formulation, the integrodifferential finite element method is used in the interior region and the Green's function method is employed in the exterior region. It has been used for the calculation of eddy currents due to exterior current sources and uniform transverse magnetic fields [12],[13].

Because the Green's function method is based on the concept of fictitious magnetic charges, it is desirable to have a clear idea of the effects of the locations of the fictitious sources on calculated results. To this end, this paper presents a sensitivity analysis of the modified integrodifferential finite element - Green's function method. The sensitivity analysis determines how the positioning of the fictitious charges and the interface with the exterior region affects the accuracy of the computation results. The study also seeks to clarify the effects of conductor skin depths.

For two-dimensional eddy current problems formulated in terms of the magnetic vector potential A , a constraint equation should be added to ensure that the total current in the conductor cross-section equals the value dictated by the circuit connection. This can be achieved through the integrodifferential finite element method [14].

Formulation

In this section, the modified hybrid integrodifferential finite element - Green's function method is formulated for the solution of 2D unbounded eddy current problems. The unbounded eddy current problem is represented by interior and exterior regions as shown in Fig. 1. The modified integrodifferential finite element method is introduced to account for the

possible inhomogeneity of conductivity. The source field is produced in the exterior region.

The *essential features* of the modified integrodifferential finite element - Green's function method are as follows:

- (1) The use of the modified integrodifferential finite element method in the interior region consisting of conductors and air;
- (2) The use of the Green's function method in the exterior region consisting of air and current sources or an impressed transverse magnetic field.

The following *assumptions* are made in the formulation that follows:

- (1) The magnetic field is quasistatic and time-harmonic with an angular frequency ω ;
- (2) All currents are in the z direction and the field is two-dimensional;
- (3) The conductivity of the conductor and the magnetic permeability are piecewise constant.

The diffusion equation governing eddy currents is expressed as

$$\frac{1}{\mu} \nabla^2 A_t - j\omega\sigma A_t = 0 \quad (1)$$

where A_t is the z -component of the total magnetic vector potential given by

$$A_t = A + A_0 \quad (\text{interior region}) \quad (2)$$

Here A is the reduced magnetic vector potential and A_0 is a constant defined in (5) below. In the conductor, the total current density J_t corresponding to A_t is given by

$$J_t = -j\omega\sigma A_t = -j\omega\sigma A - j\omega\sigma A_0 \quad (3)$$

The introduction of the constant A_0 ensures the correct circuit connection for the conductor. When the conductor carries no net current, (3) can be rewritten as

$$I_t = -j\omega \int \sigma A \, dS - j\omega \int \sigma A_0 \, dS = 0 \quad (4)$$

where the integrations are over the conductor cross-section. From (4), we obtain

$$A_0 = - \frac{\int \sigma A \, dS}{\int \sigma \, dS} \quad (5)$$

The substitution of (2) and (5) into (1) leads to

$$\frac{1}{\mu} \nabla^2 A - j\omega\sigma A + j\omega\sigma \frac{\int \sigma A \, dS}{\int \sigma \, dS} = 0 \quad (6)$$

Equation (6) is the modified integrodifferential equation with the condition (4) built in.

In the exterior region, the field is decomposed into the source field and the reaction field which is *Laplacian*. For the exterior *Laplacian* field, the magnetic vector potential is represented as follows:

$$A_e = \sum_{i=1}^M C_i G(\mathbf{r}, \mathbf{r}_i) - \frac{\mu_0}{2\pi} C_0 \quad (7)$$

where M is the number of fictitious magnetic charges, G is the appropriate 2D Green's function, C_i and \mathbf{r}_i are the strength and location of the i th fictitious magnetic charge, respectively. The fictitious magnetic charges are located inside the interior region. C_0 is a constant and C_i satisfies the following condition

$$\sum_{i=1}^M C_i = 0 \quad (8)$$

G is expressed as

$$G(\mathbf{r}, \mathbf{r}_i) = -\frac{\mu_0}{2\pi} \ln |\mathbf{r} - \mathbf{r}_i| \quad (9)$$

The source field is represented by the magnetic vector potential A_s which is derived analytically. The total magnetic vector potential in the exterior region is therefore given by

$$A_t = A_e + A_s \quad (\text{exterior region}) \quad (10)$$

Equation (6) is transformed into the finite element matrix equation using the Galerkin criterion. The coupling of the interior and exterior regions is accomplished through the interface conditions given by the following constraint equations:

$$A + A_0 = A_e + A_s \quad (11)$$

$$-\frac{\partial(A + A_0)}{\partial r} = -\frac{\partial(A_e + A_s)}{\partial r} \quad (12)$$

The resultant system of equations is written in matrix form:

$$\begin{bmatrix} S & V \\ Q & G \end{bmatrix} \begin{Bmatrix} A \\ C \end{Bmatrix} = \begin{Bmatrix} F \\ 0 \end{Bmatrix} \quad (13)$$

The matrices in (13) are defined in [11]. The inversion of the matrices yields the solution to the problem.

For transverse magnetic field, the magnetic vector potential A_s representing the source field can be obtained as

$$A_s = -B_0 R \cos\theta \quad (14)$$

where B_0 , R and θ are shown in Fig. 2.

Sensitivity Analysis

The sensitivity analysis of the integrodifferential finite element - Green's function method is based on the calculation of eddy current losses in an infinitely long circular cylindrical conductor under uniform transverse magnetic field excitation as shown in Fig. 2.

In this section, the effects of the location of the fictitious magnetic charges and the location of the interface of the two regions are examined. Power loss errors with respect to analytic losses [15] are obtained.

Results of the study are depicted in Figures 3 through 6. Power loss errors are plotted against the relative distance K_r between the fictitious charges and the interface. K_r is expressed as

$$K_r = (R - r_0)/R \quad (15)$$

where r_0 is the radius of the fictitious charge circle and R is the radius of the interface circle. The relationship between loss errors and relative distances is plotted for three different skin depths (frequencies). The variation of the skin depth is expressed by the ratio τ of the interface radius R to conductor skin depth δ :

$$\tau = \frac{R}{\delta} \quad (16)$$

The power loss errors shown in Figures 3 through 6 correspond to four different materials under three different frequency excitations (ratio τ). It is observed that for all three frequencies, the errors are very small and almost constant when K_r is between 0.07 and 0.5. The errors increase significantly when K_r is very small. For all the cases, the threshold is around 0.05. It should be kept in mind that the plots in Figures 3 and 4 have the same corresponding skin depths even though they have different material constants.

It can be concluded that the relative distance K_r , in a certain range, may have little effect on the solution accuracy. This range is generally between 0.07 and 0.5. Within this range, the accuracy for all the different conductors with different skin depths is stabilized. The range is larger for problems with smaller ratios τ of interface radius to conductor skin depth. When K_r is greater than 0.5, the errors may increase or decrease depending on the ratio τ . When the ratio is large, the error may go up while for small ratios the error may go down or stay at the same level. The larger errors in the plots for smaller skin depths are due to the discretization. In this study, the discretization is the same for all three frequencies.

Note that the interface circle need not be placed far from the conductor surface. Generally, it is sufficient to keep the distance between the interface and the conductor surface equal to the discretization size or twice the size. It is suggested that the fictitious charges should be located such that K_r is 0.1 for most problems. This is a conservative guideline. The interface circle can be placed away from the conductor surface at the discretization size or twice the size. The discretization size should be at least a third of the skin depth.

Conclusions

This paper presents a sensitivity analysis of the modified integrodifferential finite element - Green's function method. Guidelines for locating the fictitious magnetic charges and the interface circle are provided. The study reveals that as long as the relative distance K_r lies at a certain range from 0.07 to 0.5, the accuracy of the solution does not depend on the locations of the fictitious magnetic charges. The interface circle need not be placed far away from the conductor. It is sufficient to keep the interface away from the conductor surface at a distance equal to or twice the mesh size. This study also shows that the integrodifferential finite element - Green's function method is a robust method since the accuracy is not strongly dependent on the locations of the fictitious charges for all the different skin depths.

References

- [1] P. Bettess, "Finite element modelling of exterior electromagnetic problems," *IEEE Trans. Magn.*, Vol.24, No. 1, Jan. 1988, pp. 238-243.
- [2] P. Silvester, D.A. Lowther, C.J. Carpenter and E.A. Wyatt, "Exterior finite elements for two-dimensional field problems with open boundaries," *Proc. IEE*, Vol. 124, Dec. 1977, pp. 1267-1270.
- [3] H. Hurwitz, Jr., "Infinitesimal scaling - a new procedure for modeling exterior field problems," *IEEE Trans. Magn.*, Vol. 20, No.5, Sep. 1984, pp. 1918-1923.
- [4] R.L. Ungless, *An Infinite Finite Element*, MSc Thesis, Univ. of British Columbia, 1973.
- [5] I.R. Ciric and S.H. Wong, "Inversion transformation for the finite-element solution of three-dimensional exterior-field problems," *COMPEL*, Vol. 5, No. 2, 1986, pp. 53-64.
- [6] D.A. Lowther and E.M. Freeman, "Further aspects of the Kelvin transformation method for dealing with open boundaries," *IEEE Trans. Magn.*, Vol. 28, No. 2, Mar. 1992, pp. 1667-1670.
- [7] B.H. McDonald and A. Wexler, "Finite element solution of unbounded field problems," *IEEE Trans. Microwave Theory Tech.*, Vol. 20, No. 12, Dec. 1972, pp. 841-847.
- [8] S. R. H. Hoole, *Computer-aided Analysis and Design of Electromagnetic Devices*, New York: Elsevier, 1989, pp. 384-391.
- [9] T.G. Moore, J.G. Blaschak, A. Taflove and G.A. Kriegsmann, "Theory and application of radiation boundary operators," *IEEE Trans. Antennas Propagat.*, Vol. 36, No. 12, Dec. 1988, pp. 1797-1812.
- [10] M. Feliziani, "Numerical solutions of low-frequency scattering problems," *IEEE Trans. Magn.*, Vol. 28, No. 2, Mar. 1992, pp. 1224-1227.
- [11] Qiushi Chen, A. Konrad and P.P. Biringer, "An integrodifferential finite element - Green's function method for the solution of unbounded eddy current problems," to appear in *IEEE Trans. Magn.*, Vol.29, No. 2, Mar. 1993.
- [12] Qiushi Chen, A. Konrad and P.P. Biringer, "Eddy current shielding for the reduction of induced stray power losses in structural steel," in *Proc. Canadian Conf. on Electrical and Computer Engineering*, Toronto, Canada, Sep. 1992, pp. TM10.11.1-TM10.11.4.
- [13] Qiushi Chen, A. Konrad and P.P. Biringer, "A hybrid approach to the solution of open boundary eddy current problems under TM field," accepted for presentation at the *INTERMAG Conference*, Stockholm, Sweden, April 13-16, 1993.
- [14] A. Konrad, "The numerical solution of steady-state skin effect problems - an integrodifferential approach," *IEEE Trans. Magn.*, Vol. 17, No. 1, Jan. 1981, pp. 1148-1152.
- [15] M.P. Perry, *Low Frequency Electromagnetic Design*, New York: Marcel Dekker, Inc., 1985, pp. 135-144.

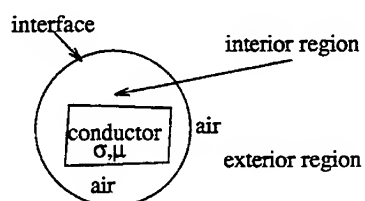


Fig. 1 A general eddy current model in 2D.

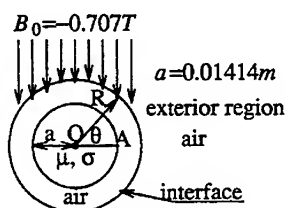


Fig. 2 A circular cylindrical conductor excited by a TM field.

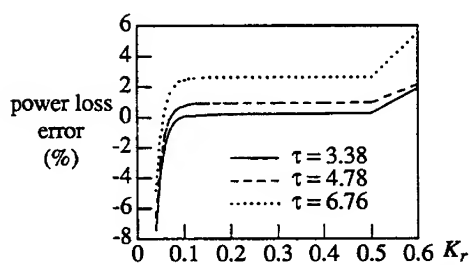


Fig. 3 Loss errors as a function of the relative distance K_r .
 $\sigma = 0.1 \times 10^7 \text{ Sm}^{-1}$; $\mu_r = 100$.

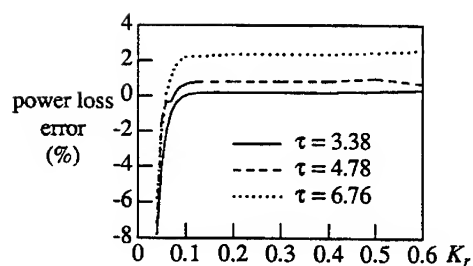


Fig. 4 Loss errors as a function of the relative distance K_r .
 $\sigma=0.01 \times 10^7 \text{ Sm}^{-1}$; $\mu_r=1000$.

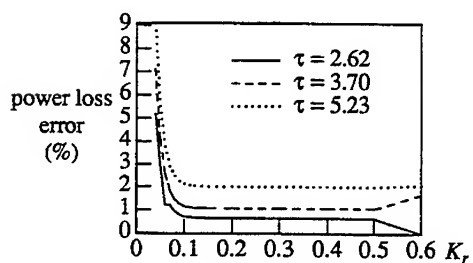


Fig. 5 Loss errors as a function of the relative distance K_r .
 $\sigma=6 \times 10^7 \text{ Sm}^{-1}$; $\mu_r=1$.

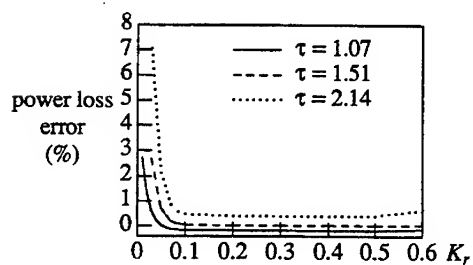


Fig. 6 Loss errors as a function of the relative distance K_r .
 $\sigma=1 \times 10^7 \text{ Sm}^{-1}$; $\mu_r=1$.

SESSION 20 - "EMC/EMI"

Chair: Dr. Todd Hubing, Co-Chair: Dr. Reinaldo Perez

EMI ANALYSIS OF TRANSIENT EVENTS VIA METHOD OF MOMENTS
ON THE TITAN IV/CENTAUR ROCKET MAIN BATTERIES

Reinaldo Perez
Jet Propulsion Laboratory
California Institute of Technology

Abstract

Expendable rockets, like the Titan IV/Centaur, constitute one of the main delivery systems used for satellites and other space instruments. For the Centaur, the electric power consumption during separation (from Titan IV) and ascent is supplied by several batteries located within this upper stage. Thermostats within the Centaur stage help to keep a constant temperature range within the battery during ascent to geosynchronous orbit. The Lithium Chloride Active Battery is a new and upgraded battery design for the Titan IV/Centaur. Large transient current in the batteries ON/OFF switching events can produce significant amounts of conducted and radiated Electromagnetic Interference (EMI) which can adversely affect the normal operating environment of nearby electronics. This paper first conducts a brief review of the physics involved in the arcing process. The major portion of the paper will then be devoted to modeling the radiated EMI caused by thermostats' transients using the Method of Moments (MoM). This paper will also address in details the validation of MoM data with obtained measurements.

1.0 INTRODUCTION

In the middle 1980's a new and upgraded launch vehicle was acquired by the Air Force to deliver larger and heavier payloads to geosynchronous orbit (22,000 miles). The 3-stage Titan IV launch vehicle contains, as part of its third stage, a Centaur Inertia Upper Stage (IUS) responsible for carrying the intended cargo (e.g satellite) into the required orbit. As part of a new design for the IUS new batteries were developed for supplying the needed electric power. The Lithium Chloride Active Battery is a new battery design capable of supplying 60 amps of uninterrupted current for up to 5 hours. The IUS carry four of these batteries and the current demand during the first few minutes of IUS ascent can reach up to 75 amps. Each battery is made up of nine cells in series, each located within its individual cavity in the battery housing. The total supply voltage for the battery is 29 volts.

In order to meet the functional requirements of the Lithium Chloride Active Battery four thermostats are installed within the

battery housing. Thermostats are needed to keep a constant operating temperature during large variations of ambient temperature experienced by the battery during ascend of the Titan IV/Centaur IUS. The four thermostats are synchronized to operate at different temperature ranges as needed. Each thermostat is individually connected to a thermally radiating heating element. The heating elements are distributed on the walls of eight of the nine cavities where the battery cells are installed as shown in Figure 1. The heating elements consist of teflon coated ($\epsilon_r=2.1$), gauge 12 copper wiring which are laid out on the interior surface of the battery walls. Each thermostat connects to an RC network which serve as "arrestor" circuit for suppressing the arcing phenomena which occurs during thermostats ON/OFF switching operations. The figure also shows the schematic of the thermostats and arrestor circuits.

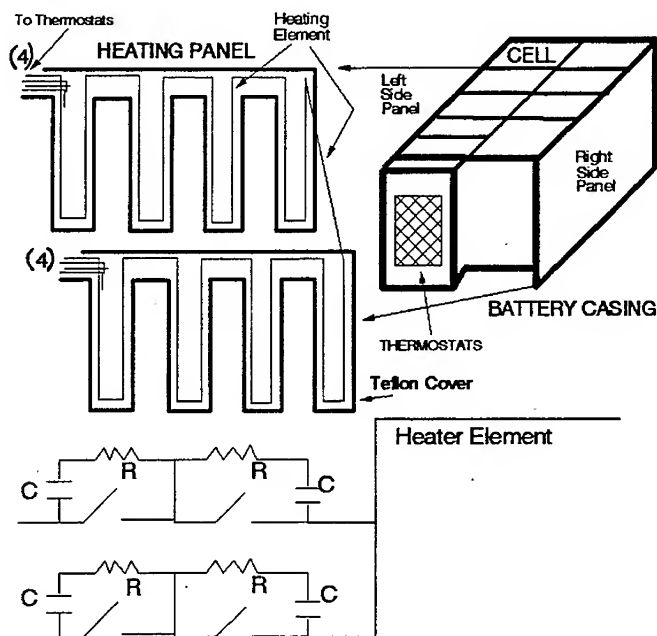


FIGURE 1. THERMOSTATS & HEATING ELEMENTS OF BATTERY

Each of the four thermostats draws about 1.6 amps of nominal current. However, transient currents of up to 4.7 amps can be measured across the thermostats during the ON/OFF switching cycles. Transient currents constitute one the major sources of conducted and radiated Electromagnetic Interference (EMI) [1] which can adversely affect the behavior of nearby electronics. Conducted EMI is of importance to eliminate because such conducted noise can be propagated to other electronic devices which are connected to the same battery. Radiated EMI is of importance to eliminate because the propagated noise can be pick up by sensitive receiver circuits through antennas and other electromagnetic field sensors commonly used in spacecraft. While considerable effort has been done in the past in analyzing conducted emissions through network representation of transient phenomena and associated circuits [2-4], less effort has been invested in analyzing the radiated EMI due to transients because of the complex nature of the transient-caused radiate emissions phenomena. There is a need to understand better and predict the amount of radiated EMI from transient circuits such that the proper electronics can be develop to avoid interferences among sensitive spacecraft instruments.

2.0 RADIATED EMI FROM TRANSIENT EFFECTS.

Radiated noise from transient current events, such as those found in thermostats ON/OFF switching, are the results of two different types of events: a) arcing processes (e.g across thermostats contacts), and b) "temporal" behavior of transient circuit elements as an antenna.

Arcing occurs is the result of mechanical switches ON/OFF operations. When the voltage across the contacts of mechanical switches is large enough it can cause the breakdown of the intervening gas. This is known as the "long arc". For smaller contact spacings, in a vacuum, the arc can be initiated by a "field-induced" emissions wherein the electric fields at the highest and sharpest points on the cathode liberate electrons. The voltage across the contacts divided by the contact spacing exceeds the breakdown field strength of the gas.

In a transient event the resulting transient current is responsible for the temporary antenna behavior of the heating elements. Though small in duration (only a few microseconds), such transients can be large enough to cause significant fields to be radiated as the wiring of the heating elements behave as a radiating antenna. In this paper we will first discuss briefly the physics of arcing phenomena. The major portion of this paper will then be devoted to modeling the antenna behavior of the thermostats/heating element, during ON/OFF switching operations using the method of moments.

2.1 RADIATED EMISSIONS DUE TO ARCING

In the arcing process the external circuit has a pronounced effect on the type of discharge or even whether a discharge occurs. Switches are frequently used to interrupt loads that are resistive and inductive (e.g. heater elements in a thermostat circuit) in nature as shown in Figure 2.

Interruption of these types of circuits leads to an interesting phenomena called "showering arc." An inevitable parasitic capacitance is in parallel with the inductive load. When the switch is closed, a steady-state current $I = V_{dc}/R$ is established in the inductor. When the switch opens, the inductor attempts to maintain this current. It is therefore diverted through the capacitance, charging the latter. The switch voltage $V(t) = V_c + V_{dc}$, therefore increases. As this switch voltage increases, it may exceed the switch breakdown voltage, whereby a short arc forms and the switch voltage drops. The capacitor discharges through the switch, with the current being primarily limited by the local resistance and inductance of the wiring diagram. If the switch current exceeds the minimum arc-sustaining current, the arc is sustained. If not, the arc is extinguished and the capacitor begins to recharge. The switch voltage once again exceeds the switch breakdown voltage, and the switch voltage drops again. If the arc is not sustainable, the capacitor begins to recharge once again. Eventually the energy stored initially is dissipated, and the capacitor voltage decays to zero, leaving $V = V_{dc}$. This leads to a sequence of rising (as the capacitor charges) and rapidly falling (as the switch breaks down) voltages across the contact separation, which has been referred to as the showering arc.

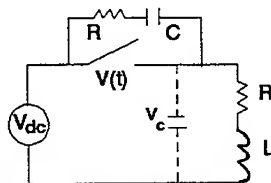


FIGURE 2. THERMOSTAT SWITCH AND ARRESTOR CIRCUIT

Showering arcs clearly have significant spectral content, and may therefore create EMI problems [6-8]. The wiring carrying these currents may cause significant radiated emissions, thereby creating interference problems. These signals may also be directly conducted along interconnected wiring paths, creating a potentially more troublesome effect, since the signal levels that are directly conducted to other points will be of the order of the switch voltages. Since these potential effects are recognized, various suppression measures are usually employed in conjunction with a mechanical switch.

A suppression technique for the arcing process is to prevent the

switch voltage from exceeding the breakdown voltage of the switch. This can be implemented by placing a sufficiently large capacitor in parallel with the inductor, thereby reducing the peak available circuit voltage and also reducing the initial rise of the available circuit voltage. This scheme has the drawback in that contact damage can occur during switch closure because of large capacitor charging currents. A solution is to limit the discharge current that occur on contact closure by adding a resistor in series with the capacitor as shown in Figure 2. The minimum value of R is chosen to limit the discharge current during switch closure to below the minimum arcing current: $V_{dc}/R < I_{min}$.

To obtain an estimate of the amount of radiated EMI from arcing a thermostat was removed from the battery and place on a wooden platform inside a semianechoic room in order to measure the radiated emissions for several samples of ON/OFF switching. The thermostat was fed from a DC battery and a broadband antenna was used for the measurements. A resistive load to simulate the heater was used while keeping wiring to a minimum. The small load was selected to draw 1.6 amps of continuous current from the thermostats. Figure 3 shows the results of arcing-induced broadband emissions as compared to MIL-STD-461 EMI broadband (BB) emissions limits.

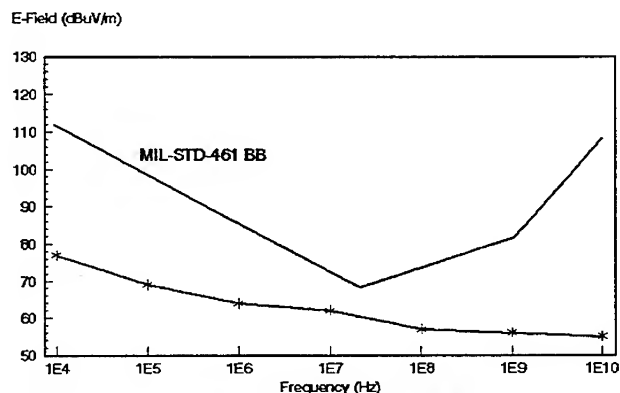


FIGURE 3. E-FIELD EMISSIONS DUE TO ARCING

2.2 RADIATED EMISSIONS FROM ANTENNA BEHAVIOR

One of the major objectives in this work is to simulate the amount of radiated electric field emissions from the heater element as it behaves temporarily as an antenna from thermostats' ON/OFF switching transients. This task will be accomplished by using the method of moments for modeling the thermostat switch/heater element as a radiating structure.

The first step in the analysis of this type of EMI emissions problem is to calculate the transient currents and voltages across the thermostats switch, hence, across the heater load, using the pSPICE network analysis program [5]. Figure 4 shows the pSPICE model for two thermostats (S7, S8 in the figure) and the heater load (87 ohms). The figure also shows the RC arrestor circuit for each thermostat and system's switch. In the calculations it is assumed that the system switch in conjunction with one of the thermostats are already close at $t=0^+$ before the other thermostat switch closes. This is consistent with the fact that during most ON/OFF switching cycles at least two thermostats will be conducting at a time. In the simulation the first thermostat (S7) closes at $t=0$ with a rise time $t_r=1.0\mu\text{S}$. The other thermostat switch closes at $t=40\mu\text{S}$ ($t_r=1.0\mu\text{S}$ also) and stays closed for $30\mu\text{S}$ before it opens. The parasitic inductances for each of the switches are also shown in the figure (L_2 & L_3 of $1\mu\text{H}$) likewise the parasitic inductance of the connector between the system switch and the thermostat is shown ($L_1=4\mu\text{H}$). The terms V_3 - V_4 in the figure are used by pSPICE as voltage controllers to simulate the times ON/OFF in the thermostats. For the pSPICE run we assume $R_{\text{ON}}=0.1$ ohms and $R_{\text{OFF}}=1000$ Mega-ohms. "Dummy" voltages V_5 - V_6 are used to monitor the thermostats' currents when the switch closes (V_6 - V_5) and the current toward the heater load. The transient currents can be calculated at any point in the circuit. Figure 5 shows the results of simulating the transient current and voltages at several locations in the circuit. Of special interest is the transient current across the thermostat switch, which from the figure can be observed to be of magnitude 4.7 amps with a rise time $t_r=0.2\mu\text{S}$. This transient current is responsible for the antenna behavior of the heating element. By multiplying the magnitude of the transient current by the impedance of the heater element we can obtain the equivalent transient voltage across the thermostat as a function of time.

To establish a benchmark for method of moment modeling, a series of electric field measurements were made to determine the spectrum profile of the radiating structure during ON/OFF switching. Two thermostats and a heating element were removed from the battery casing for these measurements. The shape of the heater element was preserved to be that it had when installed in the battery. The thermostats were encased using a shield cover, the shield was grounded so that the effects of possible arcing will not become part of the recorded spectrum. The two thermostat and heater assembly was then positioned on a wooden platform inside an semianechoic chamber. Ambient temperature was changed to simulate the needed switching cycles. During the ON/OFF switching operations a broadband antenna was used for recording the emissions of the heater element as it temporarily behaves as an antenna for a period of about $1.5\mu\text{S}$ for each ON/OFF switching operation. Measurements were made in the 100KHz-50MHz frequency range using a spectrum analyzer. A series of six (6) highest peaks (i.e frequency .vs. largest magnitude in dB $\mu\text{V/m}$) for the measured electric field were recorded. Figure 6 shows the set up obtaining the measurements together with the six peaks identified for those measurements.

Modeling the radiating structure was accomplished using the method of moments. Figure 7 shows a thin-wire representation of the heater element. The thermostat switch is represented as a transient voltage source. Important information concerning the modeling can be described: total length of heater element is 4.52m, number of segments used for the radiating structure is 10, length of segments (minimum of $\lambda/10$ criteria was used) is 45 cm, radius of wire segments (same as radius of heater element) is 2.03 mm, and conductivity is 5.8×10^7 S/m. Furthermore, since the heater elements were wrapped with teflon the modeling included an insulating dielectric ($\epsilon_r=2.1$) sleeve around the wire conductor of 2.0 mm in thickness. Since the measurements were made over a wooden platform (1.5m x 1.5m) with a metal ground plane on top, the modeling in the Figure 7 also shows a thin-wire representation of the ground plane (40 segments) and the image of the radiating structure. The transient voltage sources (i.e transient voltage magnitude .vs. frequency) shown in Figure 7 were obtained by calculating the FFT of the transient current across the thermostat in Figure 5 multiplied by the heater elements's impedance. In order to calculate the radiated electric field emissions at a particular frequency, the corresponding transient voltage at that frequency is used as the source input in Figure 7.

In order to compare the accuracy of the method of moments modeling, the six previously identified measured peaks were used as the measured values. The transient voltage sources whose frequencies match those corresponding to the measured ones were used as the driving inputs for the radiating structure of Figure 7 and they are given in Table 1. Table 2 shows the calculated values of the emitted electric fields at the six frequencies of interest using the driving inputs in Table 1. The table shows a comparison between the calculated and measured values for the frequencies of interest. Comparison of the results show good agreement between the measured and calculated data above 24 MHz with about 6 dB difference. For frequencies below 24 MHz the difference goes up to 10-12 dB.

3.0 CONCLUSION

Radiated EMI in the form of arcing and antenna radiation, due to transient events, can contribute significantly to the noise which can threatens sensitive receivers in a spacecraft. The method of moments can be used for estimating the amount of radiated EMI as a result of transient currents produced by circuit elements. Though the example described in this paper is for a thermostat circuit and its associated heater elements, the modeling principles herein discussed are applicable to other types of circuits where transients are observable and measurable. Two important principles to follow in transient modeling are: a) understand the physics of the transient phenomena taking effect for that particular circuit, and b) exercise care in the method of moments modeling.

REFERENCES

- [1] Paul, Clayton, Introduction to electromagnetic Compatibility, Chapter 12, Wiley InterScience, 1992.
- [2] Paul, Clayton, et al. "Prediction of crosstalk due to showering arcs at switch contacts," IEEE Int. Electromagnetic Compatibility Symposium, Cherry Hill, NJ, August 12-16, 1991.
- [3] Howell, E.K., "How switches produce electrical noise," IEEE Trans. Electromagnetic Compatibility, Vol 21, 1969.
- [4] Curtis, A.M., "Contact phenomena in telephone switching circuits," Bell Systems Technical Journal 19, 1940.
- [5] pSPICE, "personal-Simulation Program with Integrated Circuit Emphasis," MicroSim Corp., 20 Fairbanks, Irvine, CA, 1990.
- [6] P. Wilson, M. Ma, and A. Ondrejka, "Fields radiated by electrostatic discharges--Theory and experiment," NBS Tech. Note 1314, NIST, Boulder, Colorado, Feb. 1988.
- [7] P. Wilson, M. Ma, "Fields radiated by electrostatic discharges," IEEE Trans. Electromagnetic Compatibility, Vol 33, No 1., February 1991.
- [8] Uchimura Keiichi, "Electromagnetic Interference from discharge phenomena of electric contacts," IEEE Trans. Electromagnetic Compatibility, Vol 32, No. 2, May 1990.

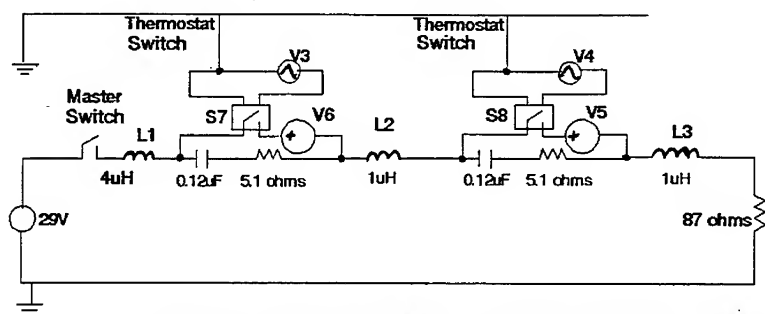


FIGURE 4. pSPICE THERMOSTATS SWITCHING MODELING

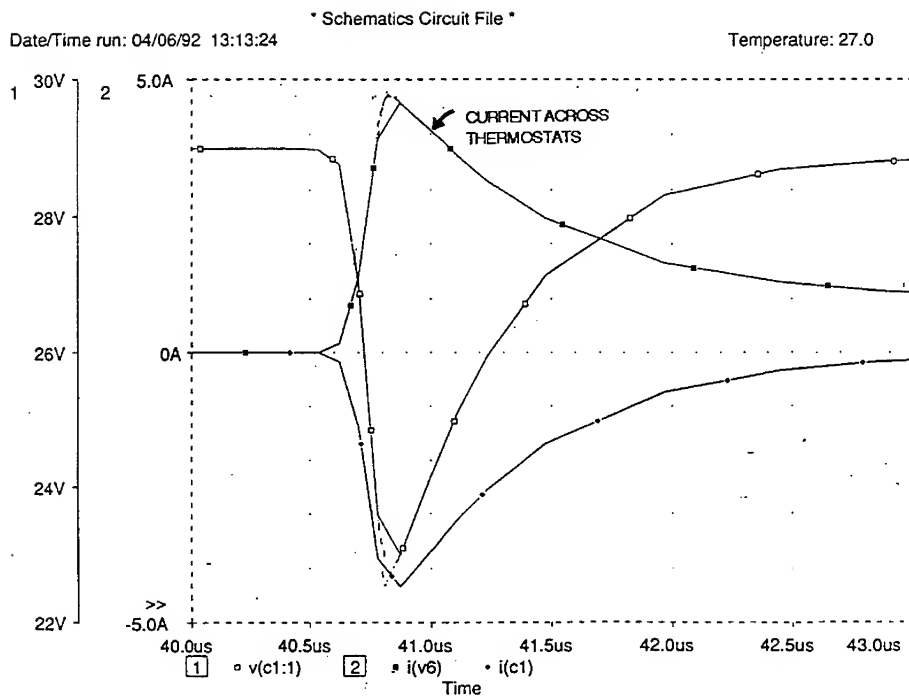


FIGURE 5. TRANSIENT RESPONSE OF THERMOSTATS DURING SWITCHING

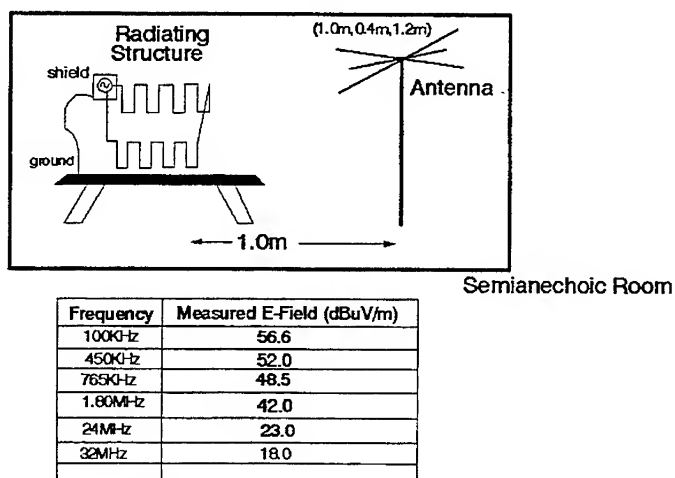


FIGURE 6. MEASUREMENT OF E-FIELD FROM TRANSIENTS

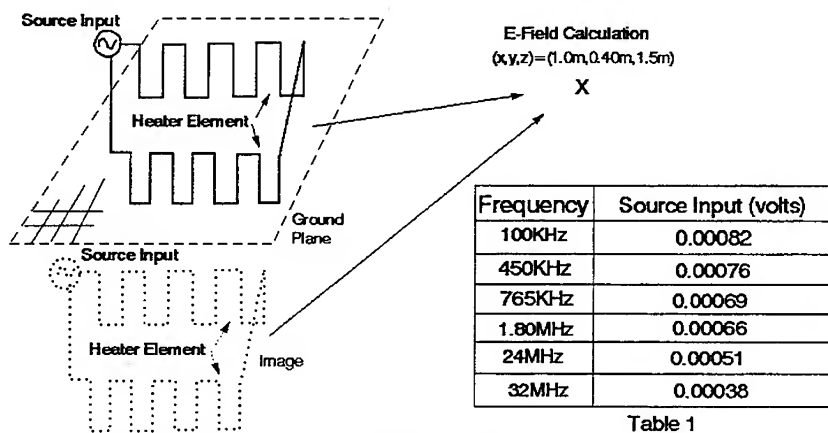


Table 1

FIGURE 7. METHOD OF MOMENTS MODELING

Frequency	Measure E-field (dBuV/m)	Calculated E-field (dBuV/m)
100KHz	56.6	45
450KHz	52.0	41
765KHz	48.5	36
1.80MHz	42.0	31
24MHz	23.0	15
32MHz	18.0	12

Table 2.

Detailed Analysis of a Realistic Canonical Structure in Electromagnetic Radiation Problems

Shahrokh Daijavad and Barry J. Rubin
IBM T.J. Watson Research Center
Yorktown Heights, NY 10598

Abstract

A canonical structure, devised by an earlier investigator to simplify the computation of radiation from small table-top products and their peripherals, was recently analyzed and the results were published. The structure involves a 1 meter cable feeding a signal line situated above a large rectangular plate. In our earlier effort, the structure was modeled, without simplifications, using a powerful moment-method code. A more complicated structure that also included a finite-size microstrip transmission line was studied as well. In this paper, we briefly describe improvements to the analysis code that allow the analysis of larger, more complex problems. We then present results obtained on a more realistic version of the earlier structure. A relationship is established between common-mode current and the radiated field, in agreement with the contentions of other EMI investigators.

1 Introduction

In [1], a "challenge" was issued to model the second canonical problem in [2]. The problem involves thin metal surfaces and a thin electrically long wire in an unbounded geometry as shown in Fig. 1. Inclusion of dielectrics yields a structure that represents a simple, yet realistic EMI source; it includes a printed circuit board, a partial metal enclosure, and an attached cable.

In the last few months, we have analyzed this structure and extensions to it using our electromagnetic analysis code. Early results have been described [3] and a brief summary of the results follows. The entire canonical structure was analyzed, and very good agreement with measurements was shown. Numerical convergence studies indicated that the numerical results were accurate and suggested that the differences between measured and calculated results were due to features of the measurement set-up that were omitted in the analysis. Though a simplified version of the structure (making the cable solid

and placing the source above the plate) was also analyzed, as first done by Hubing [2], results were not as good as those obtained by modeling the entire structure; this shows that the value of a powerful analysis code lies in its ability to handle structures without having to resort to questionable simplifications.

The code used to analyze the above structures was a prototype code capable of handling structures defined on a non-uniform grid. It was generated by making rather crude modifications to a uniform-grid version that was used to generate the results in some of our earlier papers [4]. This prototype code did not have a table lookup facility and required inordinately long times to generate the matrix elements. Further, the original code was found to be overconservative with regard to the accuracy it employed in calculating each matrix element. As described in [4], a matrix element may be calculated using point approximations or through the use of Taylor expansions. For matrix elements where source and test points are relatively far apart, the faster point calculation may be used. By including a table look-up facility, making more extensive use of the point calculations, and optimizing numerical integration routines, a dramatic speed-up in the matrix generation was achieved. To further increase the speed, a preconditioned conjugate-gradient routine developed by researchers at IBM Haifa Research Center is used in place of the standard LU decomposition routine—and this has led to a large increase in speed when many frequencies are analyzed. The new code allows us to run more complicated structures, as described below. A typical run-time for the original Hubing structure involving 985 current elements (matrix size) for analysis of 37 frequency points is 3580 seconds on an RS/6000 model 530 workstation.

The original structure is made more realistic by the following changes. A cover box is included above the plate in order to better represent the actual enclosure in a personal system product. Further, apertures are placed in the cover to represent openings such as those required for air flow or for the attachment of peripheral devices. We then reanalyze the structure and look for features of the common mode current and radiation that may have been missed in the original analysis. We search for, and find, a strong correlation between common-mode current and radiated field, one that has been suggested by Paul [5]. Paul contends that common-mode current on cables is usually the main culprit for excessive far-field radiation from computing devices. Paul's observation is based on measuring the common-mode current for a simple device and then showing excellent correlation between the far-field computed using this current and the measured field. We support Paul's contention through results based entirely on computer simulation.

2 Analysis

The original structure in [2, 3] is shown in Fig. 1. Fig. 2 shows the modified structure. The cable and source are exactly the same as in the original structure, but a perfectly conducting cover is placed over the plate region. To reduce the number of current elements required to model the structure, the original plate is reduced to zero thickness. The height of the cover is 10.7cm. We also investigated the effect of apertures of two different configurations. A single aperture having dimensions 2.3x9.0 cm is located on one side of the cover transverse to the signal line, or two identical apertures having dimensions 2.3x7.9 cm are placed on the walls that run parallel to the signal line. The shapes and locations of the apertures do not reflect those of any particular personal system, but rather serve as first-pass attempts to ascertain the effect of apertures in general. The structures with apertures will also be referred to as partially shielded structures.

The common mode current in the cable of Figs. 1 and 2 is plotted against frequency in Fig. 3 for the original, the fully shielded, and the aperture structures. Corresponding curves of the maximum electric field (maximum among 13 selected points at a distance of 300m) are shown in Fig. 4. One would expect the fields to be much smaller for the shielded structures, and, if common-mode currents and electric fields are related, that the currents display the same behavior. Perfectly shielded structures, in fact, should display absolutely no radiated fields and exactly zero common-mode current. We observe the following. The currents for the shielded and partially-shielded structures are very similar across the entire frequency range. The current for the original structure is significantly higher than the others at frequencies below about 400 MHz, but comparable above 400 MHz. The maximum field, however, is far greater across the entire frequency spectrum for the original structure, with greater variation existing between the fully and partially shielded cases. The current and field for the fully shielded structure are not zero, and in fact are at times comparable to the unshielded structure. These results can be explained as follows.

The field and currents from the fully shielded structure are nonzero because of inherent errors associated with the computer simulations. For an enclosure to perfectly shield a source, the field must be exactly zero over each point on the shield; since the matrix solution technique can only enforce constraints over a finite number of points, perhaps several thousands, our "numerically generated" shield is imperfect and cannot completely shield the source. However, as the numerical grid becomes finer, one would expect the numerical shield to be more perfect, and the field to decrease. The structure of Fig. 2, in fact, is extremely sensitive to any mathematical leakage of the field because of the long cable attached. If even a few microamps of current are induced on the cable, which behaves as a long

and thus efficient dipole antenna, significant radiation occurs.

The radiated field and common-mode current are related, but this correlation is obscured by the field radiated directly from the horizontal strip segment. We will refer to the radiation from the strip, which is not caused by the common mode current on the cable, as differential radiation. Fig. 5 shows the computed radiated field from the enclosure when no cable is present; the source is moved from the cable near the ground plane to within the enclosure. We observe about a 40 dB reduction in field associated with the full shield, with more modest reductions associated with the partially shielded structures. (And this indicates that, for the analysis of partially shielded structures with shielding effectiveness that is about 40 dB or more, it is necessary to model the structure with a finer grid.)

The peaks associated with the shielded structures are due to an internal resonance of the rectangular box forming the shield. Upon closer inspection, we observe that the differential radiation from the original structure accounts for nearly all the field in Fig. 4, except at the resonance located near 34 MHz. Since the shielded structures do a much better job of containing the radiation, we do see that for these structures the resonant peaks in the current (Fig. 3) are well correlated with those in the field (Fig. 4). Thus, the common-mode currents and radiated fields show similar behaviors, provided the differential fields are sufficiently small. Though the field (Fig. 5) at about 600 MHz for shielded structures exceeds that of the original structure, this is not cause for concern and can be explained as follows. First, larger currents are drawn at resonance, resulting in larger fields. Second, the current flow on the shield must be such that it reduces the far-field produced by the source. However, at resonance, there is also a current component on the shield corresponding to the resonant mode of the box or cavity. This last current distribution, which physically produces a field only within the cavity, also contributes to the external far-field because of the finite grid-size limitations of the code described earlier.

The correlation between the common-mode current and field can be shown more clearly by modeling a structure that does not have differential radiation. If we consider the original structure of Fig. 1, remove the cable's inner shield and the horizontal strip, and place the source between the outer shield of the cable and the ground plane, we have a pure common-mode structure that consists of a 1 meter dipole with a plate at one end. The current and field for this structure are plotted in Fig. 6. The peaks in the current are the resonances of the structure, and each is associated with a corresponding peak in the field. The plots are smoother than in the previous figures because many more frequency points were considered here. For the field curves, since only 13 points were considered, the true maximum may have been missed.

To further investigate the relationship between common-mode current and field, we again consider

the original structure, except that the source impedance is set to zero. This introduces a whole series of resonances associated with the differential current in the cable (Fig. 7). Looking from the horizontal strip toward the source, instead of a perfectly terminated cable (which looks like a resistance), a 1 meter stub (the relative dielectric constant is one for the cable in this simulation) with all its resonances is seen. The first such resonance is at 72 MHz and corresponds to the quarter wavelength resonance in the cable (the horizontal strip represents a loading capacitance that reduces the resonant frequency below the expected 75 MHz value). As in circuit analysis, where the poles of a circuit are generally observable from any point in the circuit, the resonances introduced above are seen on the cable as peaks in the common mode current. Numerous peaks in the field are also observed. Interestingly, for each peak in the field, there is a corresponding peak in the common-mode current, but not vice versa. This suggests, at least for this structure, that if there is a resonant peak in the field, it is associated (or caused) by a peak in the common-mode current. However, by observing the field, some of the peaks in the common-mode current may be missed, perhaps because of differential radiation as seen in Fig. 4. Further investigations are warranted.

3 Conclusions

We have found for the Hubing structure [2] that there is a strong correlation between common-mode current and radiated field. Such correlation was observed after properly accounting for differentially-generated radiation that obscures the relationship. In the case of practical structures, this means that common-mode current cannot always be counted upon to provide EMI decisions. Only when the radiation from the signal lines and other differential sources is significantly shielded, so as not to dominate the field, does the common-mode current behavior follow that of the field.

Further, the fundamental constraints in modeling such systems must also be considered; specifically, it is not possible to exactly model the shielding efficiency of a perfect shield, and care must be taken to extract correct results for partially shielded structures.

We have observed that resonances within a structure will appear on the "outside" of the structure as peaks in the common-mode current. Thus, there exists a coupling between the excited modes within an enclosure and those modes associated with the external regions of the enclosure such as the cable. Apertures and other imperfections in the shield, physically, must allow such coupling to take place; but it also can occur in a computer simulation because of mathematically induced imperfections in the shield.

References

- [1] T.H. Hubing, "Numerical techniques for EMI source modeling: a review of progress," *Proceedings of the 8th Annual Review of Progress in Applied Computational Electromagnetics*, (Monterey, CA), pp. 413-417, Mar. 1992.
- [2] T.H. Hubing, "Calculating the currents induced on wires attached to opposite sides of a thin plate," *The ACES Collection of Canonical Problems, Set 1*, published by the Applied Computational Electromagnetics Society, pp. 9-13, Spring 1990.
- [3] S. Daijavad and B. Rubin, "Detailed analysis of a canonical structure in electromagnetic radiation problems", *accepted for publication in IEEE Trans. Electromagn. Compat.*
- [4] B. J. Rubin and S. Daijavad, "Radiation and scattering from structures involving finite-size dielectric regions," *IEEE Trans. Antennas Propagat.*, vol. AP-38, pp. 1863-1873, Nov. 1990.
- [5] C.R. Paul, "A comparison of the contributions of common-mode and differential-mode currents in radiated emissions", *IEEE Trans. Electromagn. Compat.*, vol. EMC-31, pp. 189-193, May 1989.

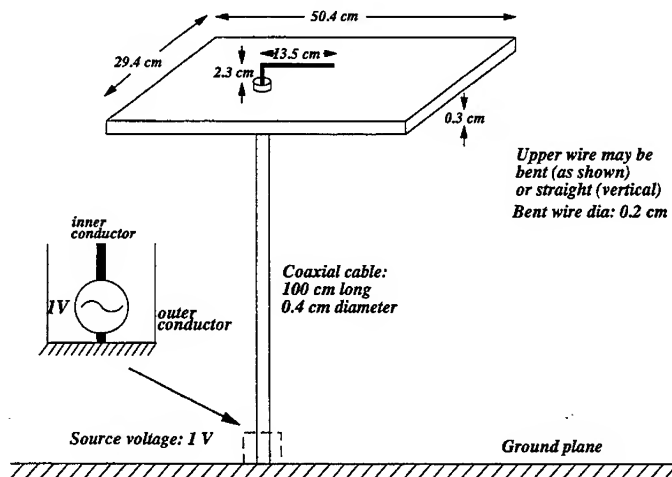


Figure 1: Original Hubing structure.

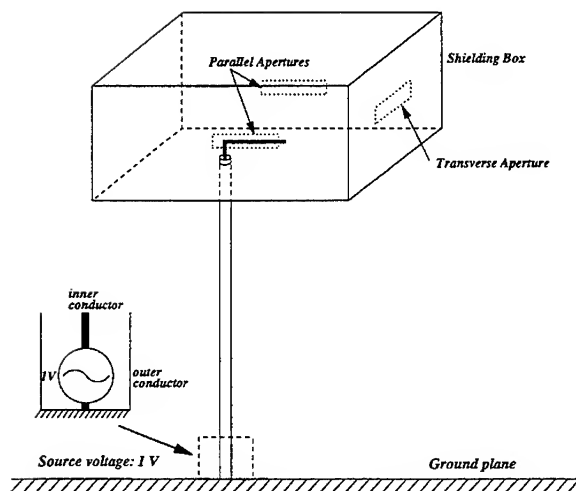


Figure 2: Modified structure featuring the shield and apertures.

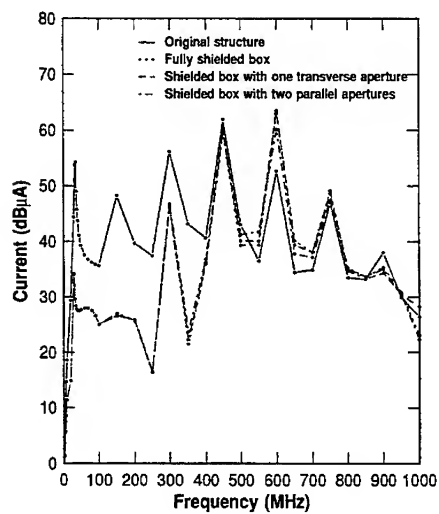


Figure 3: The common-mode current in the cable for unshielded, fully or partially shielded structure.

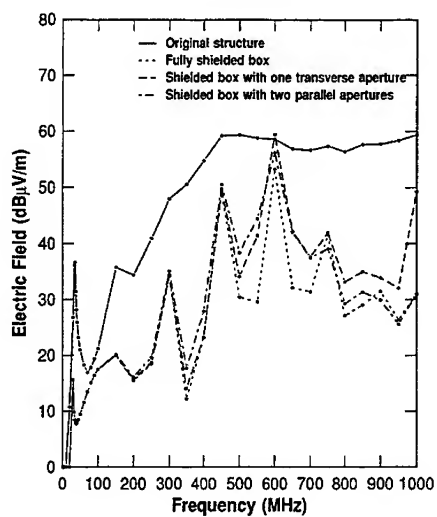


Figure 4: *Maximum electric field at 300m for unshielded, fully or partially shielded structure.*

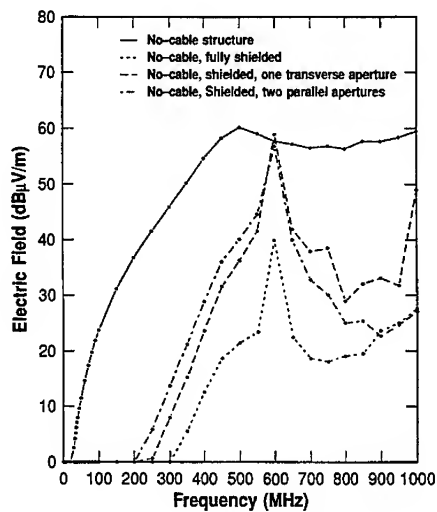


Figure 5: *Maximum electric field at 300m for unshielded, fully or partially shielded "no-cable" structure.*

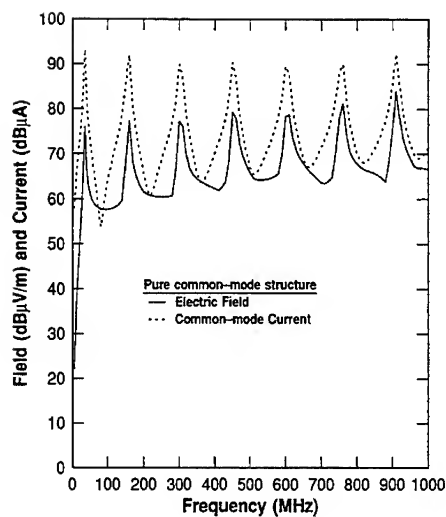


Figure 6: Correlation between electric field and common-mode current in a pure common-mode structure.

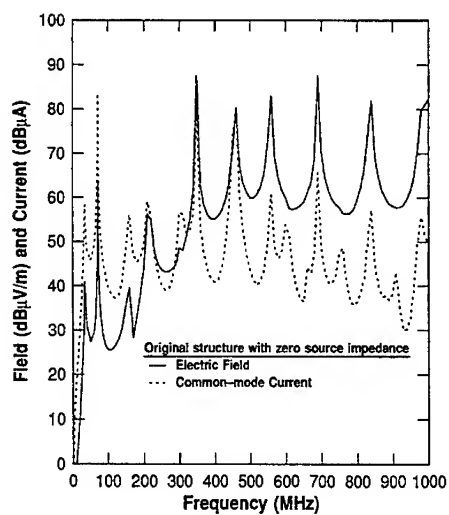


Figure 7: Relationship between electric field and common-mode current in the original structure with zero source impedance.

EMI Prediction using Wire Mesh Boxes in NEC

**Bruce Archambeault
Rich Mellitz**

Digital Equipment Corporation
TDA/EPT/STT
December 1992

Introduction

The need to accurately predict the electromagnetic emissions from computer equipment is more important than ever. Goals to reduce time-to-market and lower product development cost have resulted in an increased emphasis in numerical modeling tools to reduce the number of design iterations necessary before achieving EMI regulatory compliance. Typically, 3-5 iterations may be necessary for some products with a serious first customer shipment delays and significant extra development costs. Modeling can reduce the delays and cost by providing design engineers with a tool to predict the effect of design changes without the need to try-it-and-see, or use out-of-context equations.

The Numerical Electromagnetics Code (NEC) has been widely used for many different applications. The use of NEC has been extended to prediction of EMI emissions from computer devices towards meeting the EMI regulations of the FCC/VDE/CISPR, etc. Such modeling requires the accurate representation of the device's expected test configuration (e.g. attached wires, height above a refer-

ence plane, etc.). Therefore, the model must include the attached data and power cables. If the computer device is electrically small, then a simple wire can replace the actual device. However, any device with an appreciable size must be modeled as a box with attached wires, and with a source at the point where one of the wires is attached to the box. EMI emissions are predicted by merging voltages, either measured or derived, at the wire/enclosure junctions into the NEC simulations.

Solid Plane Inaccuracies

It has been documented that NEC can not accurately handle the case of a solid conductor plane with a source at the point a wire connects to the plane. This causes difficulty for this modeling approach since the computer device is replaced with a metal box with attached wires and a source at the point where a wire attaches to the box.

This problem was overcome by replacing the solid conductor box with a wire frame box. Wire frame models have been used extensively in other applications, and were expected to provide better accuracy

in this application. However, the wire frame box model introduces a number of variables that can affect the model accuracy. This paper describes the effect of these variables and compares predicted and measured results to validate the selected model configuration.

Approach

There are many, many different wire configurations possible. Naturally, as the wire frame box configuration becomes more complex, more wire segments are required, resulting in very large computation times. Therefore the goal of this effort was to evaluate the errors associated with wire frame boxes (in this application) by comparing the "best" configuration with a set of measured data, and then compare the various wire frame configurations against this benchmark configuration. Although some errors are inevitable, it was found that many configuration options did not provide significant errors (for this application), allowing the model to be reduced to a lower time/complexity configuration without significant loss of accuracy.

A number of wire frame box configurations were examined. A general configuration is shown in Figure 1 and a listing of the various configurations considered is given in Table 1. The wire patterns were varied independently for the source side, adjacent side, and inactive side as shown in Figure 1 and Table 1.

In addition to the wire pattern variations described above, other important parameters were varied to allow their effect to be examined. These parameters included the number of wire segments required (within the box wire patterns), the box wire diameter, and the source seg-

ment size.

Variations in the results are analyzed to determine the minimum configuration useful over various frequency ranges, allowing the minimum solution computation time.

Naturally, some determination of overall accuracy was needed to insure that the errors in the above analysis were meaningful. The configuration in Figure 1 is difficult to measure without affecting the parameter we wished to measure. Therefore, the full box measurement was replaced with a half-box and a single wire over a reference plane and rotated 90 degrees (as shown in Figure 2). These measurements were then compared to various NEC modeled configurations. The source impedance was measured using a network analyzer and compared to the source impedance from the NEC models. The 'benchmark' configuration was selected from these results.

A number of different physical configurations of the wire half-box were modeled, and the results compared to the measured case. Once the benchmark configuration was selected, all evaluations of the full box configuration (Figure 1) were compared to the benchmark configuration of the full wire box.

Relative Error

At the beginning of this effort, it was decided to find a model that provided errors that are low *relative to the errors typically expected during open field site testing* (e.g. FCC testing). This meant that errors less than 6 dB (using 20 log Magnitude) would be considered acceptable. It was recognized that many disciplines would consider a 6 dB error (50% error) to be unacceptable. However,

within the commercial EMI discipline, errors greater than 6 dB are routine and a model with less than 6 dB error would be useful.

Model Verification

It was considered important to verify that the model correctly predicted the effect of the RF voltage at the point of the cable or wire point of contact to the metal enclosure. Unfortunately, it is physically very difficult to measure the radiated field strength over the entire range of receive antenna locations, while maintaining the proper RF voltage on the cable. Source impedance is relative to the total radiated field strength therefore it was decided to use the source impedance as the unit of measure to show the relative goodness of the wire frame box models.

Although the true Open Area Field Site (OAFS) measurement typically contains the device under test (DUT) with the attached cables (similar to a box with a cable on opposite sides), this configuration was difficult to measure the source impedance without corrupting the measurement with cables leading to the network analyzer, etc. Therefore, it was decided to measure the source impedance of a half box with a single wire above a reference plane. (See Figure 2.) The effect of the measurement cable was minimized by placing the cable under the box. Although this changed the DUT configuration (because of the image, there would be two sources), this allowed accurate measurements to be made and allowed modeling using NEC. A number of configurations of wire frame half-boxes were modeled and compared to the measured data to determine the best configuration, or benchmark configuration.

The half-box model and test system were frequency scaled by a factor of three to make the physical size of the measured test set more manageable.

[Note: Due to space limitations in this document, complete details of the measured data, and the half-box models are not included here. Please contact the authors for a report containing all data.]

The segment size of the wires within the box, wire configuration, wire diameter, and source segment length were all examined individually. The configuration with the least error from the measured results were used in the full box configurations.

Full Box Optimization

As mentioned earlier, the primary interest was in determining the necessary wire frame configuration for the full box DUT while maintaining the deviation at an acceptable level and minimizing computational time. Since the full box performance could not be conveniently measured, the half box was used to find a benchmark configuration and then the various full-box wire frame configurations were compared against the same benchmark configuration. No frequency scaling was used during the modeling of the full wire frame box configurations. The frequency range of 30 - 1000 MHz was modeled.

Table 1 summarizes the results of the various full box wire frame configurations. [Note: specific plots of the data comparisons are omitted due to space limitations in this document. Please contact authors for complete copy of the report.] There are three types of box sides;

source side, lateral side, and inactive side as shown in Figure 1. Each type of side was varied and the deviation listed. Note that although both the maximum antenna impedance deviation and the maximum horizontal and vertical polarization spectral deviations are listed, the vertical/horizontal received signal strength deviation is of greater interest.

The received signal strength is the maximum signal for antenna heights of 1 to 4 meters, at a distance of 10 meters, with the DUT rotated throughout 360 degrees (as required for typical FCC tests). The deviation listed in Table 1 compares this maximum signal strength for the benchmark case against the maximum signal strength for the case under consideration.

As can be seen from Table 1, the source side of the box should remain with the full radial (spoke) configuration shown.

The inactive side (opposite the source side) has much less effect on the accuracy of the received signal strength. Only 2-4 dB of additional deviation is added under these configurations.

The lateral side variation has a significant effect if the primary current direction (source to inactive sides) is interrupted. The case of 'box 10' has the least additional deviation since it maintains this primary current flow.

The best overall case is shown in Table 1 as 'box 5-10'. This configuration was selected as the best configuration since it provided the best compromise between accuracy and computation time. The deviation (when compared to the benchmark configuration) for this case are shown in Figure 4. Note that the deviation is less than 1 dB over most of the

frequency range except in the 400-700 MHz frequency range.

Run Time

The time to run these models is of great concern. It is common knowledge that Method of Moment (MoM) programs (such as NEC) can take very long times to run when the problem includes many segments. For these modeling cases, the number of segments is listed in Table 1. The CPU run time is listed per frequency since the number of frequencies will vary depending upon the application. For all the cases in this effort, frequencies of 30 MHz to 1 GHz were used (using 5 MHz steps), so that no resonance effect would be missed. All modeling was performed on a VAX8800 cpu. Therefore cpu run times will have to be adjusted accordingly for the actual cpu in use. However, the percent time savings by optimizing the wire frame box configuration will remain constant.

Users are encouraged to determine the maximum amount of error that is acceptable, and then determine the minimum configuration that provides that total error.

Notice that the errors/deviation are not constant across the frequency range. Although the maximum error is displayed in the various tables (for clarity), over most of the frequency range the error/deviation is less than listed in the tables. It should also be noted that the deviation is at a minimum at resonant frequencies (where radiation would be greatest).

General NEC Guidelines

The general NEC guidelines were used to create the initial half-box benchmark configuration. Care was taken to not violate any important standard guideline. Wire segments were maintained between .001 and .1 times the wavelength. All wires must connect/cross only at wire segment ends.

The full box configuration use many more wire segments than the half box configuration. It was decided to limit the total number of segments to 300 to avoid excessive computation times so the guideline for segment length (relative to the wavelength) had to be violated. In this case, the segments along the axial spokes were 118 mm long (about $1/2.5$ lambda at 1 GHz) and non-spoke wires were 125 mm long (about $1/2.4$ lambda at 1 GHz). The test results indicate good accuracy (for this application) even with the long segments. The final recommended configuration is shown in Figure 3.

Summary

A number of different wire frame box configurations were considered for use in EMI modeling. The errors/deviation between the various configurations and measured data were shown. The configuration that minimized the errors (to an acceptable level for this application) and that minimized the computation time was selected as the best overall wire frame box configuration.

Figure 1 General Configuration (Full Box)

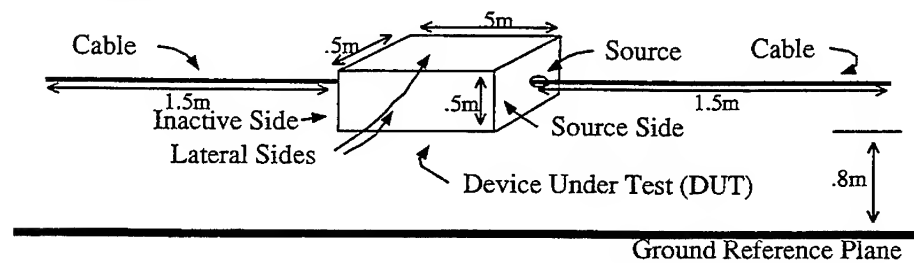


Figure 2 Measurement Configuration (Half Box)

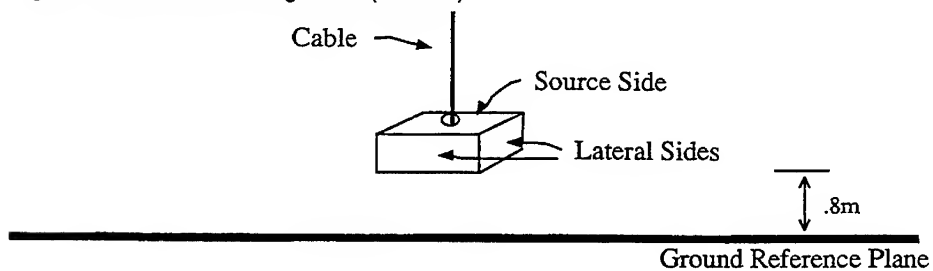


Figure 3 Recommended Full Box Configuration

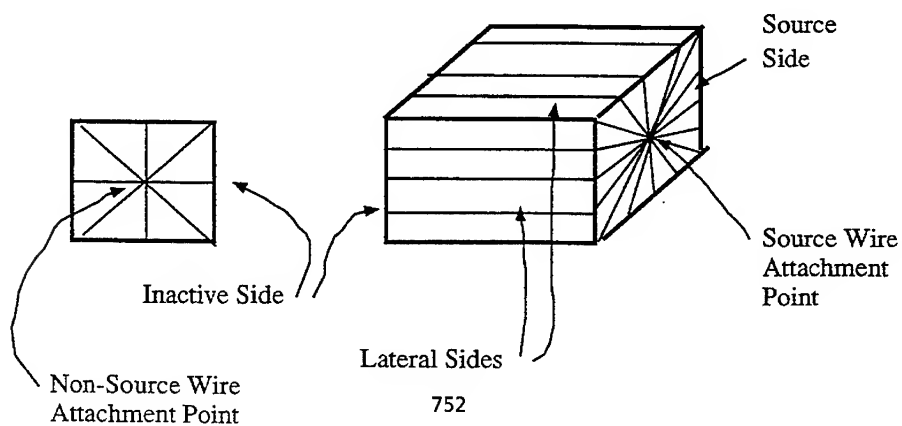


Table 1 Full Box Comparisons

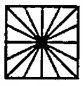
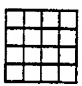
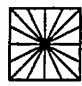
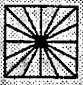
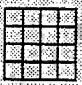
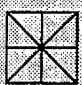
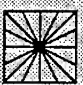
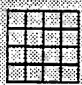

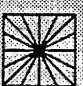
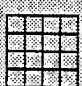
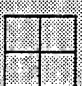
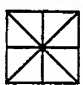
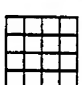
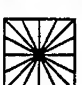

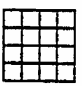
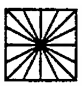
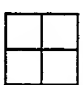
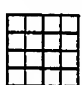
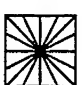
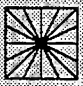
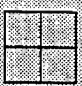
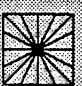
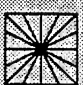
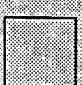
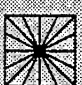
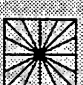

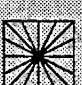
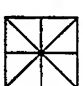

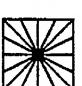
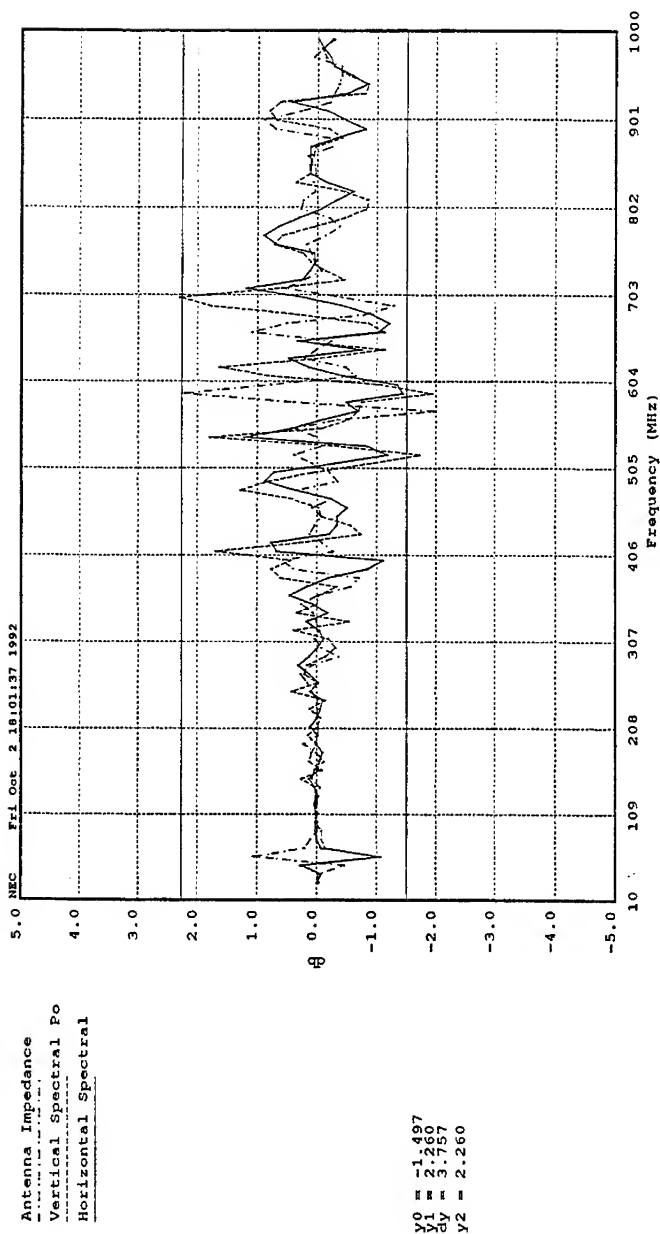
Inactive Side	Lateral Side	Source Side	id	Antenna Z Deviation (dB)	Horiz. Spectrum Deviation (dB)	Vert. Spectrum Deviation (dB)	CPU Time / Freq.	Number of Segs.
			16 box	-	-	-	188 sec.	279
			box 2	5.3	5.0	6.5	146 sec.	255
			box 3	22.0	12.9	13.0	130 sec.	243
			box 4	13.8	10.0	13.2	130 sec.	243
			box 5	0.8	2.0	3.2	144 sec.	255
			box 6	1.5	3.4	4.0	133 sec.	243
			box 7	1.0	2.6	4.4	135 sec.	243
			box 8	1.0	2.4	7.6	99 sec.	215
			box 9	2.5	5.0	7.7	60 sec.	183
			box 10	5.2	1.7	1.9	121 sec.	231
			box 5-10	2.3	1.5	2.3	87 sec.	207

Figure 4 Composite Full Box Case 5-10



Full Box Comparison - Composite Case
 Impedance and Spectral Power dB from Base Line

THE APPLICATION OF DIFFERENT MESHING TECHNIQUES TO EMC PROBLEMS

J L Herring and C Christopoulos
University of Nottingham, UK

Abstract

The transmission-line modelling (TLM) method and its application to EMC type problems are described with particular reference to issues regarding its efficient implementation and different meshing techniques. Results are presented for improving the description of open boundaries and calculating the current induced on a wire attached to a thin plate.

Introduction

A particular aspect of the numerical modelling of electromagnetic compatibility problems is the requirement to simultaneously represent both fine features and large volumes which sometimes extend to infinity. A regular uniform mesh can be used for this purpose, with the advantages of simplicity and low dispersion, but with the serious disadvantage that storage and run-time requirements are excessive since they are determined by the finest feature of interest. A practical alternative is to use a fine mesh only where it is required and a coarse mesh elsewhere. These so-called variable mesh schemes suffer from the disadvantages of more complicated problem definition and data input and also introduce additional dispersion. In the area of transmission-line modelling, schemes have been developed for a single graded mesh using both the symmetrical condensed node with stubs (stub-loaded node) and the hybrid node, as well as a multigrid technique. Before describing these methods, implementation issues common to all methods will be discussed. Finally, some examples will be presented.

Run-time efficiency

In a TLM calculation most of the run-time is taken up in the scattering procedure. The procedures for connect, boundaries and outputs are much less computationally intensive. It is therefore advantageous to optimise the scattering algorithm as far as possible. Further gains can be made, particularly when there are large regions of empty space, by implementing several procedures of increasing generality since, for example, the scattered pulses for a standard 12-port node can be computed much more quickly than those for a node with stubs. The decision on which procedure to use can be made on a per node basis as the calculation proceeds.

The scattering procedure for the hybrid node will now be derived from first principles so that an efficient algorithm can be directly obtained. A similar method may be used for the stub-loaded node. Although based on knowledge of the scattering matrix originally obtained by *Johns 1987*, the conditions imposed are reasonable and give insight into the physical characteristics of the node.

In the hybrid node, as described by *Scaramuzza and Lowery 1990*, the link-lines are allowed to take different impedances such that they incorporate all of the required inductance. Three distinct impedances are used (at each node) and these are assigned to the three sets of link-lines contributing to the magnetic field in each of the coordinate directions. The capacitance associated with the link-lines is chosen to maintain synchronism and open-circuit stubs are added at the node to make good any deficit. The connect procedure is modified to take into account any difference in impedance of link-lines from adjacent nodes.

In the following derivation, the numbering scheme originally used by *Johns* is abandoned in favour of more meaningful port names. For the link-lines, a three character suffix is used: the first

character gives the direction parallel to the link-line, the second is 'n' or 'p' for the port on the negative or positive side of the node and the third gives the polarisation. For the stubs, a two character suffix is used: the first character is 'o', 'e' or 'h' for open-circuit, electric loss or magnetic loss stubs and the second gives the polarisation. Superscript 'i' or 'r' is used to denote voltage pulses incident upon or scattered from the node and, if omitted, the total voltage is assumed. \hat{Y} and \hat{Z} are used to denote link-line admittance and impedance with \hat{Y}' and \hat{Z}' used for normalized quantities. Superscript 's' is used for stub admittance.

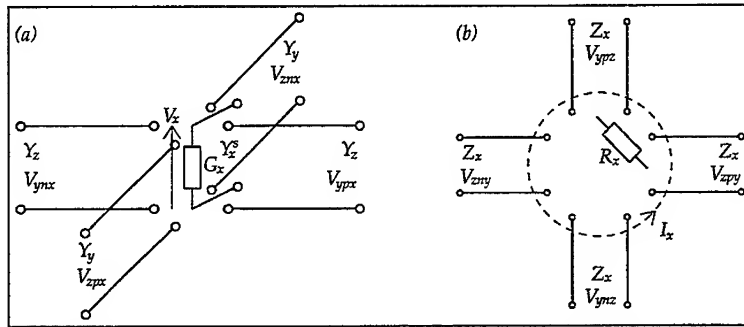


Fig. 1 - Transmission-lines contributing to the x-components of (a) electric field and (b) magnetic field

i) Conservation of charge

Consider the ports contributing to the x-component of the electric field, as shown in fig. 1a.

Voltages V_{ynx} and V_{ypx} on link-lines each of capacitance $\frac{1}{2}\hat{Y}_x Y_0 \Delta t$.

Voltages V_{ynz} and V_{ypz} on link-lines each of capacitance $\frac{1}{2}\hat{Y}_y Y_0 \Delta t$.

Voltage V_{ox} on open-circuit stub of capacitance $\frac{1}{2}\hat{Y}_z Y_0 \Delta t$.

Let V_x be the voltage across the total capacitance ($V_x \sum C_i = \sum V_i C_i$).

$$V_x = \frac{\hat{Y}_y(V_{ynx}^i + V_{ynx}^r + V_{ypx}^i + V_{ypx}^r) + \hat{Y}_z(V_{ynz}^i + V_{ynz}^r + V_{ypz}^i + V_{ypz}^r) + \hat{Y}_x(V_{ox}^i + V_{ox}^r)}{2\hat{Y}_y + 2\hat{Y}_z + \hat{Y}_x} \quad (1)$$

Let the total incident charge be equal to the total scattered charge

$$\begin{aligned} \hat{Y}_y(V_{ynx}^i + V_{ypx}^i) + \hat{Y}_z(V_{ynz}^i + V_{ypz}^i) + \hat{Y}_x V_{ox}^i &= \\ \hat{Y}_y(V_{ynx}^r + V_{ypx}^r) + \hat{Y}_z(V_{ynz}^r + V_{ypz}^r) + \hat{Y}_x V_{ox}^r & \end{aligned} \quad (2)$$

V_x may be expressed solely in terms of incident pulses (which are known) by substituting the scattered pulses from (2) into (1) and writing $V_{ox}^r = V_x$ (no incident pulse from loss stub). The pulse scattered into the open-circuit stub may be obtained directly from $V_{ox}^r = V_x - V_{ox}^i$.

ii) Conservation of magnetic flux

Consider the ports contributing to the x-component of the magnetic field, as shown in fig. 1b.

Currents I_{ynx} , I_{ypx} , I_{ynz} and I_{ypz} on link-lines each of inductance $\frac{1}{2}\hat{Z}_x Z_0 \Delta t$.

Let I_x be the current through the total inductance ($I_x \sum L_i = \sum I_i L_i$).

$$I_x = \frac{1}{4\hat{Z}_x Z_0} [(V_{ynx}^i - V_{ynx}^r) + (V_{ypx}^i - V_{ypx}^r) - (V_{ynz}^i - V_{ynz}^r) - (V_{ypz}^i - V_{ypz}^r)] \quad (3)$$

Let the total flux linked with the incident pulses equal the total flux linked with the scattered pulses.

$$V_{yz}^r + V_{zy}^r - V_{yz}^r - V_{zy}^r + V_{xz}^r = -(V_{yz}^i + V_{zy}^i - V_{yz}^i - V_{zy}^i) \quad (4)$$

I_x may be expressed in terms of incident pulses by substituting the scattered pulses from (4) into (3) and writing $V_{xz}^r = \hat{R}_x Z_0 I_x$.

iii) Continuity of electric field

Consider the x-component of the electric field. Make the electric field due to pulses on link-lines parallel to the y-axis equal that due to pulses on link-lines parallel to the z-axis.

$$V_{yz}^i + V_{zy}^r + V_{yz}^i + V_{zy}^r = V_{xz}^i + V_{zx}^r + V_{xz}^i + V_{zx}^r \quad (5)$$

iv) Continuity of magnetic field

Consider the x-component of the magnetic field. Make the magnetic field due to pulses on link-lines parallel to the y-axis equal that due to pulses on link-lines parallel to the z-axis.

$$(V_{zy}^i - V_{zy}^r) - (V_{zy}^i - V_{zy}^r) = (V_{yz}^i - V_{yz}^r) - (V_{yz}^i - V_{yz}^r) \quad (6)$$

Solving equations (2), (4), (5) and (6) and the corresponding equations for the other directions yields the required scattering matrix. *Naylor and Ait-Sadi 1992* have found that the scattering procedure is most efficiently implemented by first calculating the total voltages (V_x , V_y , V_z) and the total currents (I_x , I_y , I_z) from the incident pulses. The voltage pulses scattered into stubs can then be directly obtained and voltage pulses scattered into the link-lines can be found from expressions of the form $V_{yz}^r = V_x - Z_0 I_z - V_{yz}^i$.

The scattering procedure for the standard 12-port node requires 36 additions/subtractions and 12 multiplications by a constant. The new algorithm would require 42 additions/subtractions and 6 multiplications by a constant. The most efficient algorithm will depend on machine architecture and on whether floating-point or fixed-point arithmetic is used. For a fully featured stub-loaded node, with both electric and magnetic losses, the new requirement is for 54 additions/subtractions and 12 multiplications, provided that two scattering coefficients are stored for each node type. The new algorithm is therefore more efficient than that proposed by *Tong and Fujino 1991* in which 6 multiplications, 66 additions/subtractions and 12 divisions by 4 are required. When implementing the hybrid node, which is generally used for graded meshes, the storage required to store scattering coefficients at every node is excessive and it may be necessary to recalculate the coefficients at each iteration. A choice also has to be made as to whether the link-line and stub admittances are stored or recalculated. As a rough guide, the total run-time for the authors' code, written in C (single-precision) and running on a Hewlett-Packard 710 workstation, is 63 μ s/node/iteration for the 12-port node and 13 μ s/node/iteration for the hybrid node with no losses (in which only link-line and stub admittances have been stored).

Storage Efficiency

In the implementation of the TLM method, particularly with graded meshes, there is an obvious tradeoff between space and speed efficiency as regards the scattering coefficients. For the hybrid node, if storage is required for both the link-line and stub admittances, this leads to a total of 21 quantities per node. The situation is less severe for a uniform mesh in which there are only a small number of different material properties to be considered since the scattering coefficients need only be stored for each material type rather than for each node. This method can also be used with the graded mesh provided that the total number of distinct node sizes is small.

Space savings may be made by only allocating storage for stubs on nodes which actually require them. These savings will be significant for systems in which a large part of the volume is free-space. The disadvantage is that it becomes necessary to keep track of stub storage for each node. A compromise solution is to divide the problem space into a number of cuboid meshes in which stub storage is allocated on a per mesh basis.

In principle, virtual memory systems can be used to run problems where the storage requirement exceeds the available physical memory. If the code is written in a straightforward manner (e.g. scatter for all nodes then connect for all nodes) then the entire mesh must be brought into memory several times during each iteration. A more efficient approach is to divide the mesh into a number of overlapping regions each of which will fit into physical memory. A number of iterations are then performed in each region before the next region is processed. The interface between any two regions is moved within the overlap to take account of the temporary loss of connectivity. There is very little overhead involved in using this method although the code does become more complicated. Particular care must be taken when dealing with features which intersect the overlap. A significant reduction in page faults and hence in elapsed time can be made even when relying on the default paging mechanism built into the operating system. For example, by introducing two regions with an overlap of 10 nodes into a problem requiring 19 Mbyte of storage, the CPU time was reduced from 87 to 62 minutes and the elapsed time was reduced from 308 to 79 minutes on a VAXstation 3100 (VMS 5.4) with a working set limit of 18 Mbyte. Greater savings would be expected if custom paging routines were used.

Graded mesh

In the graded mesh technique, the node size is varied so that high resolution is applied only in areas where it is needed. The grading is uniquely defined by the node dimensions along each of the coordinate axes. The time taken for a voltage pulse to travel between any two nodes is kept constant and so the bulk wave must be slowed down with stubs. To ensure that all stub impedances are positive there is an upper limit on the timestep. Originally, the stub-loaded node, as described by *Johns 1987* was used. The maximum timestep is determined by satisfying inequalities of the form

$$\Delta t \leq \frac{\mu_r \Delta y \Delta z}{2c \Delta x} \text{ and } \Delta t \leq \frac{\epsilon_r \Delta y \Delta z}{2c \Delta x}$$

for all three directions and for all nodes. The required open-circuit stub admittances and short-circuit stub impedances are then given by expressions of the form

$$\hat{Y}_x^s = \frac{2\epsilon_r \Delta y \Delta z}{c \Delta t \Delta x} - 4 \text{ and } \hat{Z}_x^s = \frac{2\mu_r \Delta y \Delta z}{c \Delta t \Delta x} - 4$$

The stub-loaded node has now been largely superseded by the hybrid node which has the advantage of fewer stubs and can sometimes be operated with a larger timestep. It also appears to have better dispersive properties. Further details can be found in papers by *Scaramuzza and Christopoulos 1991* and *Scaramuzza et al 1991*. The maximum timestep is determined from inequalities of the form

$$\Delta t \leq \frac{\Delta y \Delta z}{c} \sqrt{\frac{\mu_r \epsilon_r}{2\Delta y^2 + 2\Delta z^2}}$$

The link-line and stub admittances are then obtained from equations of the form

$$\hat{Y}_x = \frac{2c \Delta t \Delta x}{\mu_r \Delta y \Delta z} \text{ and } \hat{Y}_x^s = \frac{2\epsilon_r \Delta y \Delta z}{c \Delta t \Delta x} - \frac{4c \Delta t}{\mu_r \Delta x \Delta y \Delta z} (\Delta y^2 + \Delta z^2)$$

The main disadvantages of the graded mesh technique are that the fine mesh often extends into regions where it is not required, the same small timestep must be used for all nodes and increased dispersion due to the presence of stubs.

Multigrid technique

In the multigrid technique, the principles of synchronism and connectivity are violated so that separate meshes of different spatial resolution can be connected together to form a complete system. The restrictions are imposed that the meshes are ungraded and are defined in the same coordinate system. At the interface between these meshes there is an abrupt change in both mesh size and timestep. The transfer of pulses across the interface must ensure continuity of fields as well as minimizing any delay. Further details about the conversion process may be found in papers by *Herring and Christopoulos 1991* and *Christopoulos and Herring 1992*. A general formula for the conversion of pulses from mesh 2 to mesh 1 is given by

$$V_{1i} = \frac{l_2}{n_2 l_1} \sum_{j=1}^{n_2} V_{2j}$$

where l_1 link-lines from mesh 1, in each direction, are to be connected to l_2 link-lines in mesh 2 and n_2 is the total number of pulses to be taken from mesh 2.

The advantages of the multigrid technique over the graded mesh are that fine mesh regions can be completely localised, larger timesteps can be used in coarse mesh regions and there is no need for stubs unless they are required for material properties. A standard 12-port node can therefore be used with savings in run-time and storage as well as a reduction in dispersion. The disadvantages are that there are problems with applying large reduction ratios and there is an inevitable loss of energy when converting pulses from the fine mesh to the coarse mesh (although this is only at high frequencies). Conversion schemes can be devised in which there is no loss of energy but the storage requirement is increased and there is no significant improvement in results.

Open boundaries

Open boundaries may be approximated by terminating the link-lines adjacent to the boundary with a matched load. This method works perfectly when a plane wave is normally incident upon the boundary but works less well for waves incident at an angle. In this section the graded mesh and multigrid techniques will be used to increase the modelled volume so that the boundaries are distant from the region of interest. This method may also be applicable when improved open boundary descriptions are used and high accuracy is required.

Fig. 2a shows a quarter section of the field profile around a point source (in the bottom left corner) at frequencies of 100MHz and 200MHz for a 40° uniform mesh with a node spacing of 10cm. The lines, which are contours of constant electric field magnitude, should be a set of concentric circles but distortion is apparent in the top right corner. This distortion is worse at the higher frequency. Fig. 2b shows the same area but with the multigrid technique used to embed the 10cm mesh inside a 40° mesh of 40cm node spacing. The boundary was therefore moved away by 12m. The distortion has effectively been removed at 100MHz although some distortion is still apparent at 200MHz. In fig. 2c, a graded mesh, utilizing the hybrid node, has been used to increase the node dimensions by 2cm for each successive node beyond the 40° uniform region. A mesh of 50° nodes was used so that the total number of nodes was the same as for the multigrid case. The results are slightly worse. Extremely bad results were obtained when the node spacing was increased to 40cm. A comparison of the computer requirements is shown below.

Mesh	Relative storage	Relative run-time
$40^3 \Delta l=10\text{cm}$	1.00	1.00
$40^3 \Delta l=10\text{cm}, 40^3 \Delta l=40\text{cm}$	1.95	1.28
$50^3 \Delta l=10, \dots, 10, 12, 14, 16, 18, 20, 22, 24, 26, 28, 30\text{cm}$	3.15	3.78

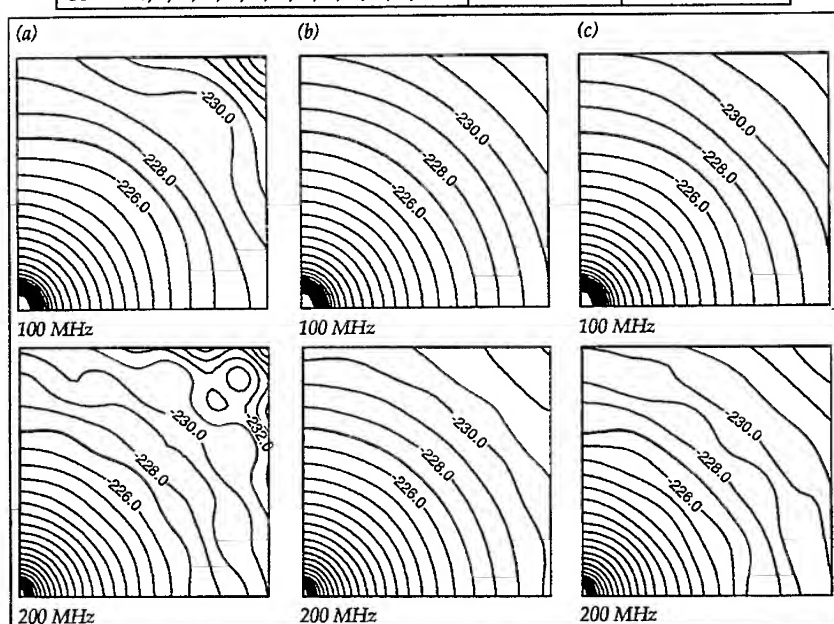


Fig. 2 - Field profile around a point source (a) uniform mesh (b) multigrid (c) graded mesh

Currents induced on wires attached to opposite sides of a thin plate

In this section, different meshing techniques will be applied to the problem of determining the currents induced on wires attached to opposite sides of a thin plate, as described by Hubing 1990, in the ACES book of canonical problems. The system consists of a 1m vertical wire attached to a thin plate measuring $50.4 \times 29.4\text{cm}^2$ above a ground plane. Above the plate, a wire either extends vertically by 15.8cm or is bent so that it measures 23cm vertically and 13.5cm horizontally. The metal of the structure was modelled with short-circuits at the mid-point of link-lines and the wires were modelled with a single node cross-section. Symmetry was not exploited and the open boundary conditions were approximated by matched boundaries. The source, which was used to connect the plate to the top wire, was modelled by four impulse voltage sources, each with 200Ω series resistance, arranged around the centre node. The output was taken as the current at the base of the long wire, normalized to 1 volt source potential. 2000 iterations were performed (with respect to the coarse node spacing) to allow the signal at the output to reach a steady state.

The multigrid models were based on a $90 \times 90 \times 45$ node coarse mesh, with a node spacing of 10cm. The boundaries were therefore 33m away from the nearest part of the structure. Two fine mesh regions, measuring $0.4 \times 0.4 \times 0.9\text{m}^3$ and $1.0 \times 1.0 \times 0.4\text{m}^3$ were used. Fig. 3a shows typical results for current (measured in dB above $1\mu\text{A}$) against frequency for the straight wire. Comparisons with experiment are shown in fig. 4, for both the the straight and bent wires, when an additional very

fine mesh region was placed around the top wire. There is reasonable agreement, at higher frequencies, considering the fact that the wire diameters and plate thickness were not modelled accurately.

The graded mesh models were based on a mesh of $81 \times 81 \times 57$ nodes with 10cm as the largest node dimension. The size of the nodes was reduced, gradually, near to the plate and the wires to provide a better description. Typical results are shown in fig. 3b for minimum node dimensions around the wire of 2cm and 1cm. These results are similar to those obtained with the multigrid method. A comparison of the computer resources required (on a Hewlett-Packard 710 workstation), for all of the examples, is given below.

Mesh	Storage (Mbyte)	Run-time (min.)
$90 \times 90 \times 45(10\text{cm})$	16.8	77
$90 \times 90 \times 45(10\text{cm}), 8 \times 8 \times 18 + 20 \times 20 \times 8(5\text{cm})$	18.4	93
$90 \times 90 \times 45(10\text{cm}), 16 \times 16 \times 36 + 40 \times 40 \times 16(2.5\text{cm})$	19.9	119
$90 \times 90 \times 45(10\text{cm}), 16 \times 16 \times 36 + 40 \times 40 \times 16(2.5\text{cm}), 32 \times 8 \times 16(1.25\text{cm})$	20.2	123
$81 \times 81 \times 57$ hybrid node, graded $\Delta l_{\min} = 2\text{cm}$	30.2	806
$81 \times 81 \times 57$ hybrid node, graded $\Delta l_{\min} = 1\text{cm}$	30.2	1612

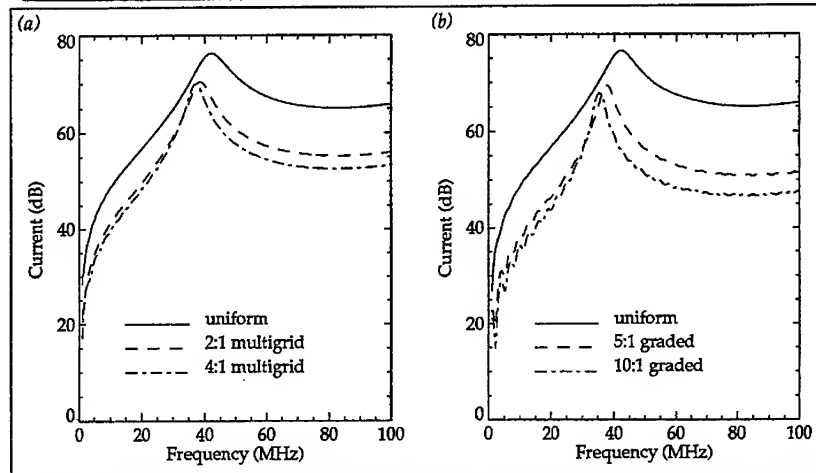


Fig. 3 - Current induced on wire modelled at different resolutions (a) multigrid (b) graded mesh

Conclusions

In the examples shown, the multigrid technique has been found to be the most efficient method. The graded mesh technique should not, however, be immediately discounted. There are many ways in which to mesh a given system and issues such as the maximum frequency of interest and proximity of matched boundaries will have differing importance in different situations. A graded mesh may well become more efficient when large reduction ratios or non-cubic nodes are used. In addition, the graded mesh can just as easily be defined in cylindrical or spherical coordinates, as in Cartesian coordinates. Ultimately, a combined graded and multigrid technique may provide the best solution.

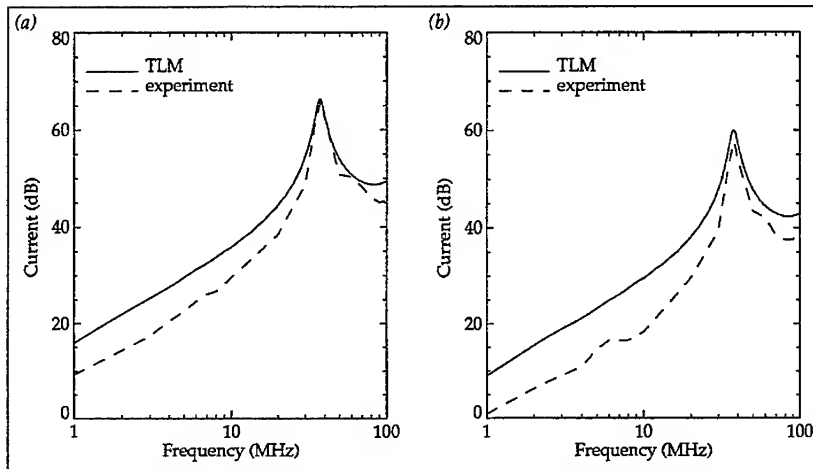


Fig. 4 - Current induced on wire: comparison with experiment (a) straight wire (b) bent wire

Acknowledgements

The authors acknowledge financial support from DRA, UK.

References

- Christopoulos C and Herring J L (1991) : "Developments in the transmission line modelling (TLM) method", Proc 8th Annual Review of Progress in Applied Computational Electromagnetics (ACES), March 16-20 1992, Monterey, pp 523-30
- Johns P B (1987) : "A symmetrical condensed node for the TLM method", IEEE Trans, MTT-35, pp 370-377
- Herring J L and Christopoulos C (1991) : "Multigrid transmission-line modelling method for solving electromagnetic field problems", Electr Letts, 27, pp 1794-1795
- Hubing T H (1990) : "Calculating the currents induced on wires attached to opposite sides of a thin plate", in Special Publ of the Applied Electromagnetics Society, The ACES Collection of Canonical Problems, Set 1, ed H A Sabbagh, pp 9-13
- Naylor P and Ait-Sadi R (1992) : "Simple method for determining 3-D TLM nodal scattering in nonscalar problems", Electr Letts, 28, pp 2353-2354
- Scaramuzza R A and Christopoulos C (1991) : "Developments in transmission-line modelling and its applications in electromagnetic field simulation", Proc Int Symp on EM Fields in Electrical Eng, Sept 18-20 1991, Southampton (UK), pp 65-68
- Scaramuzza R A and Lowery A J (1990) : "Hybrid symmetrical condensed node for the TLM method", Electr Letts, 26, pp 1947-1949
- Scaramuzza R A, Naylor P and Christopoulos C (1991) : "Numerical simulation of field-to-wire coupling problems using transmission-line modelling", Proc Int Conf on Computation in Electromagnetics, Nov 25-27 1991, London, IEE Conf Publ 350, pp 63-66
- Tong C E and Fujino Y (1991) : "An efficient algorithm for transmission line matrix analysis of electromagnetic problems using the symmetrical condensed node", IEEE Trans, MTT-39, pp 1420-1424

Optimization of FDTD for EMI Modeling Applications

Bruce Archambeault
EMI Consultant Engineer
Digital Equipment Corporation

Louise Lemaire
Principal Software Engineer
Digital Equipment Corporation

1 Introduction

The use of the Finite-Difference Time-Domain (FDTD) numerical modeling technique has become widespread among a large number of disciplines requiring the solution of Maxwell's equations. The FDTD technique offers wide flexibility for applications and provides a solution in the time domain, allowing wideband frequency response with a single model execution. The FDTD technique often requires simulation of a large number of time steps, so the total model run time can be significant. This paper describes two opportunities to save run time and maintain model accuracy by adapting the boundaries of the computational space during run time.

2 Background

When using the FDTD technique, the computational domain is divided into a grid. FDTD solves Maxwell's equations directly by converting the differential equations into difference equations and then solving the Electric (E) and Magnetic (H) fields at all grid locations within the computational domain for a single time step. The time is then incremented, and the E and H field values recomputed. This time stepping and E and H field solution continues until the simulation has completed a sufficient number of time steps for the application. A more complete description of the FDTD numerical modeling technique can be found in a number of excellent papers. [1][2][3]

The size of each cell in the grid must be kept small relative to the smallest wavelength being considered. It is common, therefore, to have computational domains with hundreds of grid segments on each side. The time domain pulse must be given sufficient time to propagate throughout the computational domain and include all reflections from conducting surfaces. It is common to run a FDTD model for many thousands (or even millions) of time steps. Depending on the application and the speed of the computer, a model simulation may run for many hours or even days.

3 EMI Modeling Using FDTD

The use of the FDTD technique for modeling Electromagnetic Interference (EMI) applications is gaining popularity. Shielding performance of apertures in a conducting wall [4], coupling between conductors within a partially or fully shielded enclosure, and radiation from a metallic structure are among the applications for FDTD which can utilize the flexibility of the technique. The time domain solution allows a wideband frequency response to be obtained by using a Fast Fourier Transform (FFT).

FDTD can be used to perform EMI modeling in either two or three dimensions. One example of a two-dimensional model would be to analyze the shielding performance of an air vent panel in a shielded enclosure [4]. The largest dimension of the vent openings will be the greatest contributor to the shielding performance so the vent panel can be reduced to a two-dimensional cut-away view of the vent panel as shown in Figure 1. With this model, the effect of varying the vent hole size, hole spacing, vent hole thickness, and source wire location can be determined simply without the added complexity of the third dimension of an enclosed shielded box. In this example, the computational boundaries are absorbing boundaries so no reflections from the computational boundary occur. The remainder of this paper will deal with an optimization of 2-dimensional EMI modeling.

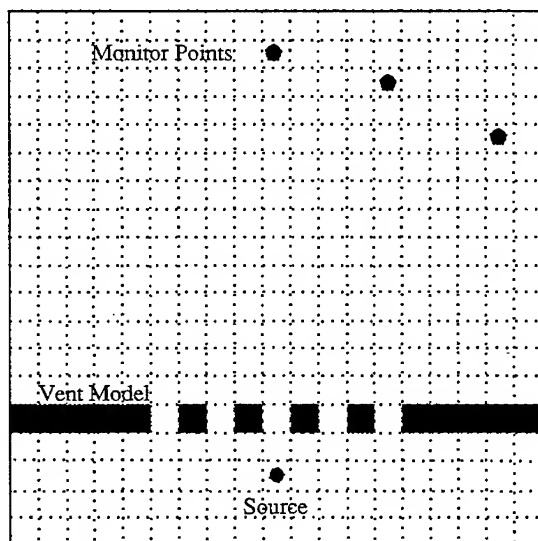


Figure 1 - Air Vent Model Example

4 Computational Domain Optimization

There are two opportunities to save computation time. Either or both techniques can be used depending on the structure and content of the model. Both techniques take advantage of the fact that many of the FDTD grid locations have zero (or near-zero) field values during much of the computational time. There is no need to waste CPU time recomputing a zero electric and magnetic field during those times when nothing computationally interesting is occurring at those cell locations.

One optimization technique is to expand the computational domain in front of the advancing time domain pulse. Figure 2 shows an example of the computational domain expanding in steps during the computational time. Although there is a slight added overhead to the program to determine when the computational domain must expand to the next size, the CPU time saved due to the smaller computational domain far exceeds the extra overhead.

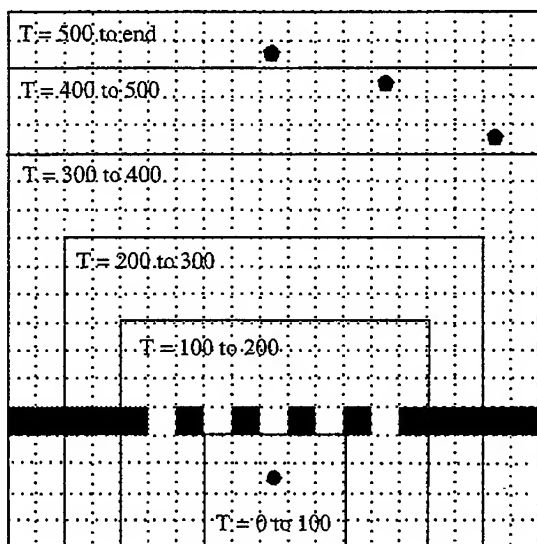


Figure 2 - Expanding Computational Domain Boundaries

The second optimization technique is to retract the computational domain behind the decaying time domain pulse. Figure 3 shows an example of the computational domain retracting. Note that care must be taken to insure the computational domain is not made smaller before the time domain pulse has completely passed through an area. In the example of Figure 1, once the pulse has completely passed through the air vent area, the bottom of the computational domain can be moved up past the air vent, since there are no more conductors to reflect the pulse. If additional reflections are expected, however, then the computational domain can not be made

smaller. The amount of shrinkage allowable at any time step is determined by the error tolerance required by the application.

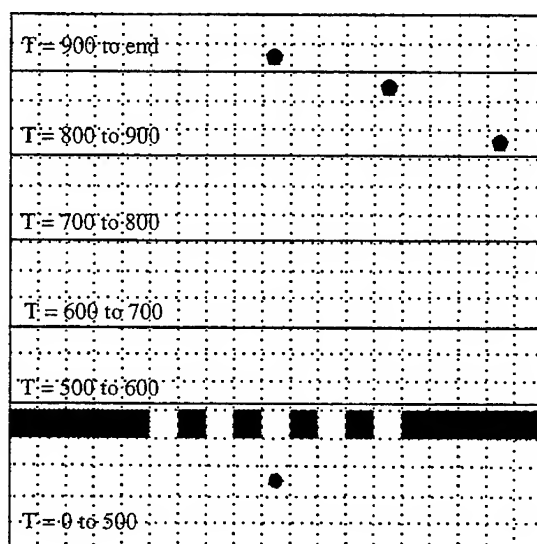


Figure 3 - Retracting Computational Domain Boundaries

5 Examples of Computational Domain Optimization

An example of both an expanding computational domain and a retracting computational domain FDTD model will be presented. Although the techniques are applied to a two dimensional model, the techniques apply to three dimensional problems as well. The two dimensional shielded air vent model described earlier will be used to illustrate this example. Figure 1 shows the general model.

5.1 Allowable Error

Different applications have different accuracy requirements. In many electromagnetic modeling applications tenths of a dB are important. However, in the field of EMI, typical measurement uncertainty is 6-10 dB. If an EMI modeling tool is able to predict the performance of a product to within 6 dB, the tool is considered very accurate for this application. The examples shown base their allowable error on the EMI application.

For the examples used in this paper, the error is calculated for frequencies in the range from 1.0E+08 Hz to 3.0E+10 Hz. There is not enough energy in the source pulse for frequencies

greater than 30 MHz to produce reliable simulation results. The frequency domain for the source pulse is shown in Figure 4.

5.2 Expanding Computational Domain

Figure 2 shows the expansion of the computational domain at specific time steps. The number of time steps before the advancing time domain pulse reaches a given point is computed so that the computational domain is always large enough to contain all active grid locations.

Figure 4 shows the frequency domain results for the base case. For each frequency, it shows the maximum amplitude over all monitor points, and the source amplitude..

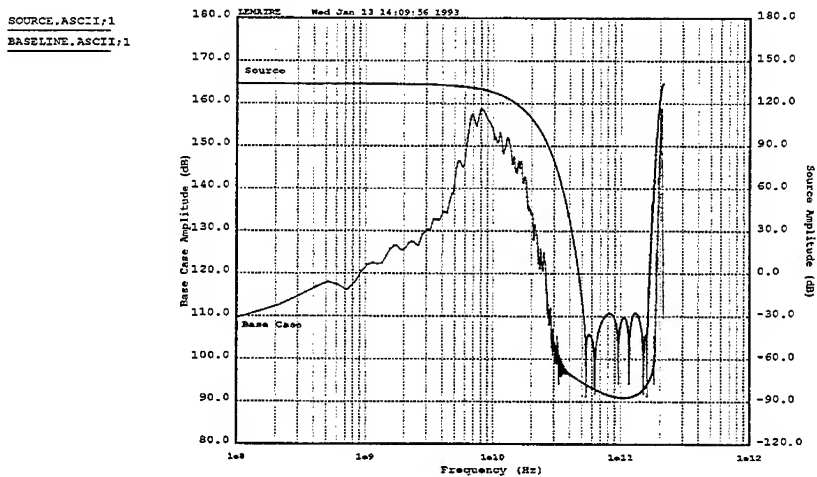


Figure 4 - Frequency Response for Base Case and Source Pulse

The frequency response curves for the expansion examples are virtually indistinguishable from the base case curve, because of the extremely small difference between them. Table 1 shows the comparative run times for different examples. In all cases, the expanding edge of the computational domain was kept out ahead of the advancing time domain pulse. The variable in the examples was the number of time steps in between recalculation of the boundaries of the active

computation space. The table data supports the selection of 25 time steps as a recalculation interval that yields good performance without adding undue recalculation overhead.

Recalculation Interval	Run Time	Percentage Savings	Maximum Error
N/A (Base case)	1 h. 24 m. 8.4 s.	N/A	N/A
10	57 m. 30.93 s.	31.64 %	0.001 dB
25	56 m. 42.43 s.	32.6 %	0.002 dB
50	57 m. 38.74 s.	31.49 %	0.002 dB
75	58 m. 27.46 s.	30.52 %	0.003 dB
100	1 h. 13.28 s.	28.43 %	0.003 dB

Table 1 - Expansion Optimization Results

The typical time savings for these examples was approximately 30% over the base case run with no optimization. These models were run on a VAX6000-440 system. Although the time savings will vary from computer to computer, the percentage time savings will remain constant.

5.3 Retracting Computational Domain

Figure 3 shows the retraction of the computational domain at specific time steps. The number of time steps lapsed before the computational domain is retracted is calculated based upon the amount of allowable error for the particular EMI application.

When the E field values were observed in space by taking a cut-away view through the center of the computational domain, the trailing edge of the pulse did not resemble the Gaussian shape of the source pulse. Where the source pulse is a symmetric curve with relatively steep rise and fall slopes, the E field value curve does not rapidly converge to zero. As the computational domain is retracted, a portion of the trailing edge of the E field value curve will be truncated, causing a modeling error especially at lower frequencies. The accuracy requirements of a particular model will control the amount of truncation allowed and the speed at which the computational domain can be retracted.

Table 2 shows the comparative run times for different retraction examples. In all examples, a recalculation interval of 25 time steps was used. The variable in the examples is the number of time steps used as a delay before retracting the computation space. A delay of 100 time steps means that the computation space was not retracted to a cell location until 100 time steps after the trailing edge of the pulse had passed through the cell location. Thus the time delay directly translates to the amount of time that the E and H field values in the cell are given to decay after the pulse energy has passed by. This relates directly to how much of the tail of the pulse energy

is truncated. The typical time savings for these examples was approximately 20% over the base case run with no optimization. These models were run on a VAX6000-440 system.

Retraction Delay	Run Time	Percentage Savings	Maximum Error
N/a (base case)	1 h. 24 m. 8.4 s.	N/A	N/A
100	1 h. 2 m. 32.87 s.	25.66 %	4.250 dB
125	1 h. 5 m. 30.82 s.	22.14 %	2.692 dB
150	1 h. 9 m. 40.32 s.	17.20 %	0 dB
175	1 h. 9 m. 34.94 s.	17.30 %	0 dB

Table 2 - Retraction Optimization Results

5.4 Combining Expanding and Retracting Computational Domains

The two optimization techniques are independent, and can be used separately or together for greater time savings. Table 3 shows the time savings possible with a combination of the two optimization methods.

Retraction Delay	Run Time	Percentage Savings	Maximum Error
N/A (base case)	1 h. 24 m. 8.4 s.	N/A	N/A
125	37 m. 27.48 s.	55.48 %	2.692 dB
135	38 m. 14.39 s.	54.55 %	0.194 dB
145	38 m. 16.66 s.	54.51 %	0.002 dB
155	39 m. 42.87 s.	52.80 %	0.050 dB

Table 3 - Combined Expansion and Retraction Optimization Results

6 Summary

This paper has presented two techniques to optimize EMI models using the FDTD numerical technique. The computational space can be expanded in front of an advancing time domain pulse, and the computational space can be retracted behind the decaying time domain pulse. An example is given with the errors introduced due to the expansion and retraction of the computational domain.

When the basic model allows the use of these techniques, significant run time reductions of the order of 50% are possible.

References

- [1] K. S. Yee, "Numerical solution of initial boundary value problems involving Maxwell's equations in isotropic media," *IEEE Trans. Antennas Propagat.*, vol. AP-14, pp. 302-307, May 1966.
- [2] A. Taflov and M. E. Brodwin, "Numerical solution of steady-state electromagnetic scattering problems using the time-dependent Maxwell's equations," *IEEE Trans. Microwave Theory Tech.*, vol MTT-23, pp. 634-630, Aug 1975.
- [3] G. Mur, "Absorbing boundary conditions for the finite difference approximation of the time-domain electromagnetic field equations," *IEEE Trans. Electromagn. Compat.*, vol EMC-23, pp. 377-382, Nov 1981.
- [4] B. Archambeault, "EMI modeling of air vents and slots in shielded cabinets," *Proceedings 1992 IEEE International Symposium on Electromagnetic Compatibility*, pp. 44-52, Aug 1992

Applications of MiniNEC to EMI Modeling

Colin E. Brench
Digital Equipment Corporation
146 Main Street, Maynard MA 01754

Abstract

MiniNEC is a code specifically designed for modeling wire antennas and so may be directly applied to the analysis of EMI problems involving cable radiation. In addition, MiniNEC can be used for much broader analysis from enclosures down to the component level. This paper explores some of these applications of MiniNEC for EMC system design and analysis.

Introduction

The main reasons for using MiniNEC [1] are availability and ease of use. Many EMI engineering tasks do not require a highly accurate initial model (within 6 dB is often adequate) but rather an understanding of the sensitivity of the system to different factors. MiniNEC models can be quickly and easily modified to provide radiation characteristics and similar information to the EMC engineers designing new computer systems [2].

It is important to consider the starting point and time frame for many commercial EMC designs. Commonly, during the concept phase of product development, EMC issues will arise that need to be resolved, often within a week. In most cases these issues are addressed based entirely upon the experience of the responsible EMC engineer. Since this is generally relative information, anything that can help quantify the situation is helpful. It is often known that "A is better than B" but usually it is not known by how much. To use MiniNEC in these applications it is necessary to produce a geometry that models the portion of the system being considered, making certain it is as simple as possible, focusing on a single element of concern. The data resulting from the MiniNEC analysis also has to be evaluated in light of the operating environment. Extra geometry variations may be needed to account for such effects.

Five cases involving EMI related problems were examined using MiniNEC. They are listed below.

- prediction of radiated emissions for a simple system
- I/O cable position effects on radiation
- heatsink influence on radiated emissions
- effects of the test unit on the measurement antenna
- design of a reference antenna

The use of MiniNEC was similar in many of the cases. Initially, the problem geometry was defined and the terminal impedance was calculated. Then, changes were made to the geometry to simulate variations that could be expected in the real application. Whenever significant changes were found, further study was required: first to ensure that the initial models were adequate, and second to determine which geometry changes were most important to the system behavior. Once the reason for the sensitivity was determined, it could be controlled in the final application.

The input impedance was chosen as the working data set rather than the radiated field distribution, in most cases. This is because the terminal impedance of an antenna can be used in conjunction with circuit analysis to determine the total energy that is radiated. For most EMC applications, the radiation pattern is unimportant since it is influenced by the presence of other conductors attached to the equipment under test (EUT). In cases where the pattern is of interest, it can be estimated from a knowledge of the system geometry.

Prediction of System Level Radiated Emissions

To aid in product design, an experiment was planned to measure the radiated emissions coupled from a source inside an enclosure to an I/O cable. MiniNEC was used to identify and separate the resonances observed in the measured data, into those due to the antenna and those due to the source and/or coupling mechanism.

The enclosure was selected to be relatively thin, so a two dimensional model could be used to represent the enclosure and I/O cable. The geometry of the test was simplified to facilitate both modeling and measurement accuracy. The enclosure was bonded to the test site groundplane and the I/O cable positioned vertically. Measurements were made from 200 MHz to 1 GHz. It is important to note that only the frequencies of maximum radiation were calculated, not the amplitudes.

Good correlation was obtained to about 600 MHz as shown in Figure 1. At this time, no work was done to improve the MiniNEC model; however, the confidence gained in obtaining these results led to its use for more complex EMI problems such as those covered in this paper.

Interface Cable Position Effects On Radiated Emissions

When making EMI measurements, some agencies require that cable and/or peripheral placement is varied to ensure that the maximum emission level is achieved, while others require that a given fixed position is used. There is much in favor of a fixed geometry. It simplifies testing greatly, aids repeatability and ensures consistency between different test houses. In consequence, there was much interest in determining just how closely the fixed position method matched with the maximum emission method [2, 3].

To model this, the problem was eventually simplified to a single cable above a ground plane. It took a number of steps to show that this was a sufficient representation to show how the radiation varied with cable position. Using MiniNEC, the orientation and shape of the radiating cable was varied and its terminal impedance was tabulated against the geometry.

The results obtained from MiniNEC indicated that the specified fixed position would provide the highest levels of emissions in many cases. However, as expected, repositioning the cable was effective in maximizing levels in other cases, particularly if there was a peripheral attached. This information has brought a better understanding of the differences in the EMI test methods.

Heatsink Influence on Radiated Emissions

With computer speeds increasing to greater than 200 MHz, there comes a point when the heatsink becomes significantly large relative to low harmonic frequencies of the clock. Two questions were raised. What is the influence of the heatsink on radiated emissions, and could the heatsink be made large enough to cool a number of devices? Due to product constraints, the time available to resolve these questions was limited to only three weeks, so it was not possible to look to more complex analysis tools.

From the modeling standpoint, there is only one model needed as the effects of larger vs. smaller heatsinks can be considered as a shift in the frequency response. There were, however, a number of other factors that needed to be evaluated. These included adjacent PC boards with groundplanes and the proximity of an enclosure side wall.

The heat sink was initially modeled as a 3D wire frame above a smaller wire frame representing the module groundplane. This was simplified, step by step, to a single monopole the height of the heatsink with four long horizontal elements, modeling the length and width, over a small radial groundplane. To account for the proximity of adjacent planar conductors, the model was evaluated both with and without an infinite groundplane, and at various heights. These models are shown in Figure 2.

The results of this work enabled the selection of the various heatsinks to be made in a way that would not cause EMI problems on the current design and was compatible with future upgrade plans. At a later stage this approach was compared to a FDTD code [4]. Consistent differences of about 6 dB in total radiated power were found but, for the application, this was quite acceptable.

Influence of the Test Unit on the Measurement Antenna

It has become apparent to the EMC community that during site attenuation measurements the direct coupling between transmit and receive antennas has to be taken into account. This is reflected in the ANSI procedures [5]. However, for real emission measurements, the transmit antenna is effectively replaced by the EUT which can range from very small to being spread across a 1.5 m x 1 m table and extend from the groundplane to 1.5 m or more in height.

To analyze these situations, a series of models were developed [6, 7]. These models included looking at the antennas alone at various heights above a groundplane for both vertical and horizontal polarizations. A further set of models were used that put various arrays of conductors at the location of the EUT. These cases included both horizontal and vertical conductors, with both grounded and ungrounded cases being examined, and simulated the interconnect and power cables as well as the EUT system components.

It was clear from the results obtained that different antennas, or similar antennas with different baluns, responded differently and so produced diverse results. Further, the results obtained from MiniNEC made it possible to estimate the magnitude of these effects and the frequency range and test distances at which they were most important.

Reference Antenna Design

The design of a simple, well characterized, electrically short dipole was needed for use as a reference antenna. A number of designs were quickly compared using MiniNEC for the influence of element length and diameter. After initial measurements of the antenna factors, the design was fine tuned to the best practical dimensions and the final antenna analyzed.

MiniNEC was used to calculate not only the terminal impedance and current distribution but also to determine the effect that nearby objects would have on the antenna factor. The effects of concern included the test site ground plane and the presence of a source antenna or, in the case of emissions measurements, the equipment under test. This enabled an estimate of the calibration uncertainty to be obtained.

This work is not complete; however, the results obtained so far are well within experimental error. As part of this project a series of different segment selections will be compared to help determine exactly what part of the design uncertainty can be attributed to MiniNEC.

Conclusions

MiniNEC has been used for a wide variety of EMI modeling tasks. Some were accurate while others were just approximations, but in all cases the information derived provided valuable design inputs and permitted a faster time to market with lower design risk.

For greater in-depth analysis, NEC or FDTD codes would be more appropriate; however, these require far greater computer resources than a basic PC, as needed for MiniNEC.

While MiniNEC may not be custom built for this type of work it can be used to provide a surprising range of design information. It is most important to realize that MiniNEC has to be used carefully; an experienced engineer is needed to ensure that the results obtained are not erroneous. However, its speed and simplicity make MiniNEC a valuable EMI design tool.

References

- [1] J. C. Logan and M. J. Rockway, "The new MININEC (Version 3): A Mini Numerical Electromagnetics code"; NOSC TD 938, Sept. 1986.
- [2] Colin E. Brench and Bronwyn L. Brench, "Effect of Cable and Peripheral Placement on Radiated Emissions", 1989 IEEE National Symposium on Electromagnetic Compatibility, pp 351 - 356.

- [3] T. H. Hubing, "The Effect of Cable Terminations on EMI Measurements", 1989 IEEE National Symposium on Electromagnetic Compatibility, pp 357 - 359.
- [4] C. F. Lee, K. Li, S. Y. Poh, R. T. Shin, and J. A. Kong, "Electromagnetic Radiation From a VLSI Package and Heatsink Configuration", 1991 IEEE International Symposium on Electromagnetic Compatibility, pp. 393 - 398.
- [5] ANSI C63.4
- [6] Colin E. Brench, "Antenna Differences and Their Influence on Radiated Emission Measurements", 1990 IEEE International Symposium on Electromagnetic Compatibility, pp. 440 - 443.
- [7] Colin E. Brench and Bronwyn L. Brench, "Reference Antenna Options for 30 MHz to 80 MHz", 1991 International Symposium on Electromagnetic Compatibility, pp. 273 - 276.

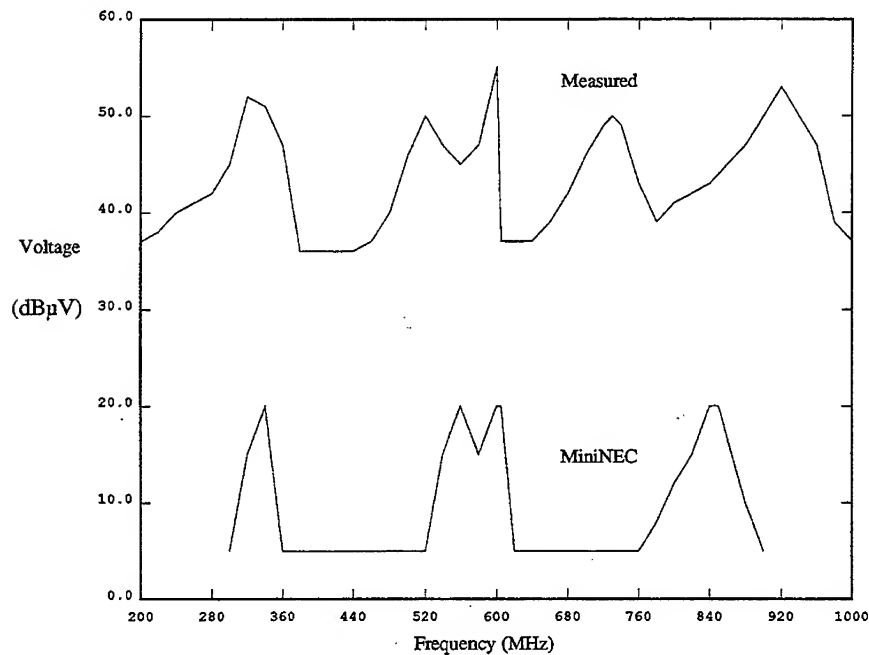


Figure 1. Measured and MiniNEC Data

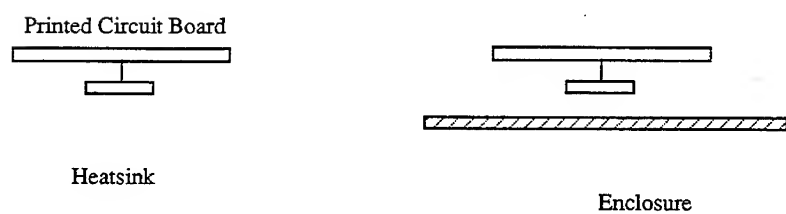


Figure 2. Models of Heatsink With and Without the Enclosure (Infinite Groundplane)

Nonlinear Effects Errors Encountered In Performing Interference Analysis Using An RF Circuit Analysis Code.

Frank E. Walker and Sperry H. Goodman
Boeing Defense and Space Group; Seattle, WA

Abstract

This effort was to analyze the effects of electromagnetic (EM) environments upon Monolithic Microwave Integrated Circuits (MMIC). This paper will discuss the results of analyzing an S-band MMIC RF receiver amplifier circuit operating in the 2 to 4 GHz range. Intermodulation and 1 dB compression effects of in-band and out-of-band CW interference are modeled. The analysis attempts to predict circuit susceptibility to EM environments by calculating nonlinear effects for a two-stage RF receiver circuit model. Modeled data were compared with measured data to determine the accuracy of the computed results.

Introduction

As high-frequency amplifiers that employ MMIC designs are developed, there is a need to evaluate electromagnetic effects on these designs. Traditional techniques of EM environmental testing at the end of development prohibit effective incorporation of EM effects mitigation into the design phase.

Prior work to investigate EM effects on MMIC devices is based on the results of laboratory testing. In these efforts, references 1 and 2, testing methodology is recommended to identify EM effects, and interference measurements are conducted to determine EM susceptibility. The investigation reported in this paper is directed, in part, to develop an analytical approach to EM susceptibility prediction for RF devices. This effort is sponsored by Rome Laboratory, under contract F30602-89-C-0004, entitled, "Electromagnetic Effects Mitigation Techniques for Advanced Arrays".

As computational radio frequency (RF) circuit analysis software development progresses, we are tempted to use these codes to investigate EM susceptibility effects while designing the circuit. In this effort the EEsof software system Academy and the nonlinear RF circuit analysis code Libra were used to model and analyze the circuit model response to interference level signals. Without knowledge of circuit detail, the RF port circuitry was modeled in Touchstone from measured S parameters. Libra was then used to model circuit performance with various combinations of normal and interference signal power levels and frequencies. Although the development of reliable EM effects analysis software seems imminent, the high-frequency analysis codes currently available are hard pressed to analyze circuits accurately when they are driven into saturation with high power levels characteristic of EM susceptibility.

The modeling results were reasonably accurate for functional performance but did not agree well with test results for intermodulation distortion. The modeling performed with the use of commercial RF circuit analysis software did not account for small signal

suppression associated with amplifier desensitization for two or more input signals. The modeling did not accurately predict power limitations in the amplifier that should result in suppression of the primary signal with the introduction of a second, high-power, in-band signal. The nonlinear distortion error in the modeling analysis is most probably the result of incomplete circuit modeling.

Linear Analysis of RF Amplifier Equivalent Circuit Model

In our effort to model the RF receiver we were unable to obtain detailed circuit design parameters from the module developer, Raytheon. This was due to the proprietary nature of the design. In order to approximate the design we matched measured device S-parameters to model circuit S-parameters and iterated the model design until the model S-parameters closely matched those of the original design. This is a practical approach because actual design data is often unavailable, and rapid modeling is needed.

In this modeling effort we employed a simple, two-stage RF amplifier model. The circuit of figure 1 is a two-stage FET amplifier with a bandpass from 2 to 4 GHz. This model was created with the EEsof Touchstone software. The linear S-parameter plots of input impedance, (S11), shown in figure 2 and gain, (S21), shown in figure 3 are compared with measured data for the RF receiver amplifier. This first model confirmed that a two-stage model was adequate to model the amplifier, but improvement in S-parameter match between measured and modeled performance was necessary.

The simple model of figure 1 was improved with the use of a parameter matching routine in Touchstone. This optimizing routine produced the more detailed two-stage amplifier model of figure 4. Modeled S11 and S21 data from the improved RF amplifier circuit model are compared to measured data in figures 5 and 6, respectively. In these comparisons there is good agreement between the modeled and measured data.

Nonlinear Modeling of Receiver Amplifier Susceptibility

With this improved, two-stage RF circuit model we were able to perform EM susceptibility modeling. In order to do this we modeled the 1 dB compression point of the circuit at various frequencies. We then evaluated the effect on the 1 dB compression point of introducing a second signal. This interfering signal could be either in- or out-of-band. The nonlinear RF circuit analysis was performed with the use of the EEsof software Libra.

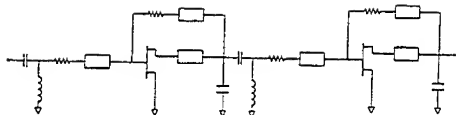


Figure 1: Simple Two-Stage Model of RF Receiver Amplifier.

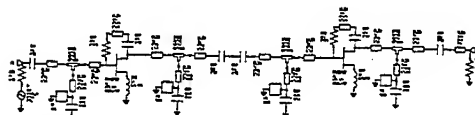


Figure 4: Improved Model of RF Receiver Amplifier.

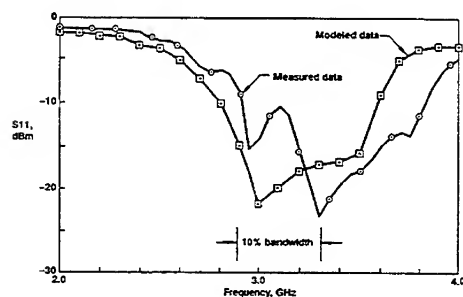


Figure 2: Input Reflection Coefficient (S11) of Simple RF Amplifier Model Versus Measured Data.

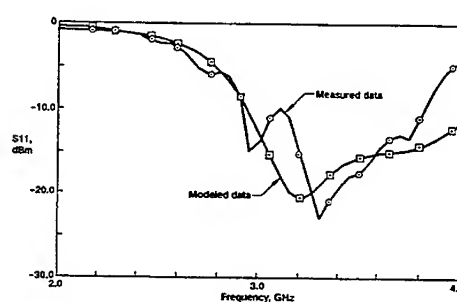


Figure 5: Input Reflection Coefficient (S11) of Improved RF Amplifier Model Versus Measured Data.

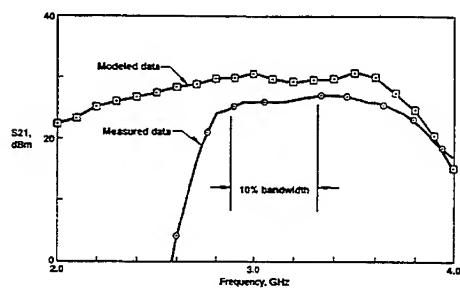


Figure 3: Gain (S21) of Simple RF Amplifier Model Versus Measured Data.

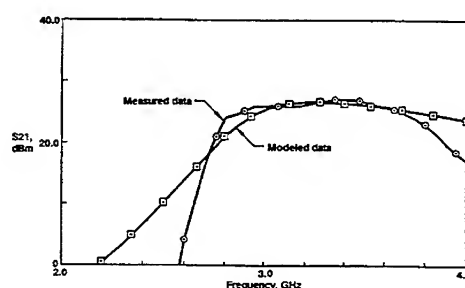


Figure 6: Gain (S21) of Improved RF Amplifier Model Versus Measured Data.

The 1 dB compression testing of the receiver port was intended to identify the threshold at which the receiver goes into nonlinear operation. Test measurements were made to allow comparison with modeled data for single-frequency and two-frequency, 1 dB compression modeling. 1 dB compression curves were measured at both out-of-band and in-band frequencies.

Single Frequency 1 dB Compression Modeling

Comparisons of modeled versus measured single-input gain are plotted in figures 7, 8, 9, and 10 for 0.3, 2, 3, and 4 GHz respectively. For the model data at low levels, the curve of the output power (P_{out}) to the input power (P_{in}) is linear. As higher input power levels are applied, the modeled output curve begins to depress (1 dB compression). As the input

level is increased further, the modeled curve plateaus. This seems to indicate simulation of FET saturation. The results are similar for the measured data. The model data exhibits greater gain above approximately 0.5 GHz (figures 7 and 8) while measured data goes into saturation earlier (figures 9 and 10).

For single-frequency operation, test and modeled results are in reasonable agreement. Modeled in-band gain is greater in magnitude and linearity than measured data. Gain is linear at low output levels up to the vicinity of compression, as expected. For in-band signals, 1 dB compression is measured to be approximately -21 dBm at the input.

Negligible gain is measured below 2.5 GHz, -67 dB at 300 MHz (figure 7), and -40 dB at 2 GHz (figure 8). Measured gain at 3 and 4 GHz (figures 9 and 10) indicates amplifier bandwidth is greater than the design specification of 3.3 GHz \pm 5%, or 3.135 to 3.465 GHz.

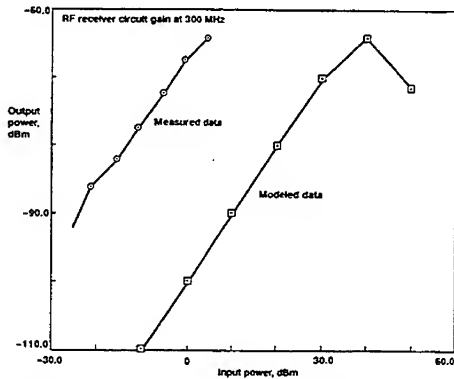


Figure 7: Comparison of Modeled Versus Measured RF Receiver Circuit Gain at 0.3 GHz.

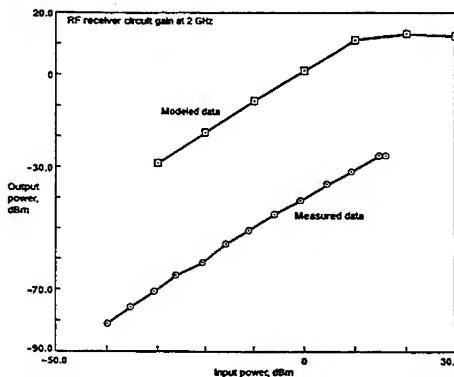


Figure 8: Comparison of Modeled Versus Measured RF Receiver Circuit Gain at 2 GHz.

At 300 MHz (figure 7), out-of-band gain is much greater for measured data than for the model.

At or above 1 GHz (figures 8, 9, and 10), out-of-band gain is greater for the model. This result primarily reflects inaccuracies in the staged amplifier model. Modeling predicts saturation for out-of-band gain whereas measured data indicates negligible out-of-band gain and therefore no associated gain suppression.

Measured compression is not observed for below-band inputs (figures 7 and 8) while compression does occur at 4 GHz (figure 10). This duplicates the high pass characteristics observed in the modeled data at these frequencies.

Two-Frequency, 1 dB Compression Modeling

More interesting results are found in our comparison of modeled and measured two-frequency, 1 dB compression data. In our two-frequency modeling, the primary signal is held at constant frequency and amplitude, (typically -30 dBm), while the fixed-frequency interfering signal amplitude is swept from a low input amplitude to beyond the 1 dB

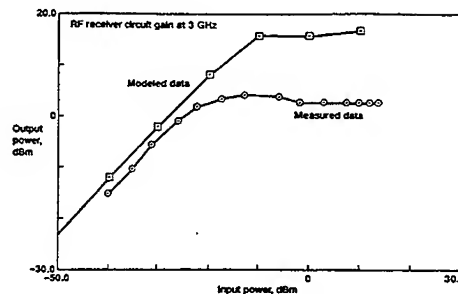


Figure 9: Comparison of Modeled Versus Measured RF Receiver Circuit Gain at 3 GHz.

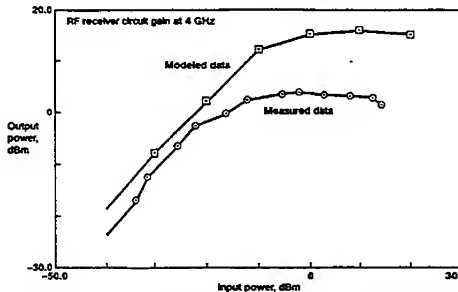


Figure 10: Comparison of Modeled Versus Measured RF Receiver Circuit Gain at 4 GHz.

compression point, (typically -50 to +10 dBm). In the data presented in figures 11 through 17, various combinations of primary and secondary frequencies are used to investigate the effects of both in-band and out-of-band EM susceptibility. In each case the primary or intended frequency is designated F2, following the convention established with the use of the EEsof analysis software, while the interfering input is designated F1. In each plot the output power of F2 is compared with the input power of F1. As the interfering input power (abscissa) is increased, the RF receiver amplifier output (ordinate) is monitored at the primary frequency with a spectrum analyzer.

Figure 11 shows both modeled and measured

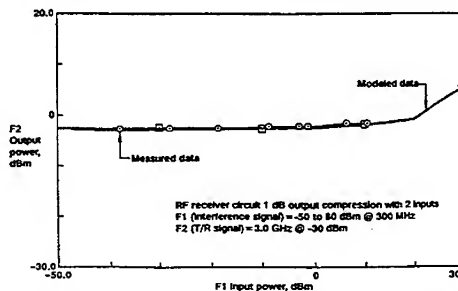


Figure 11: Comparison of Modeled Versus Measured Receiver 1 dB Compression With Inputs at F2 = 3.0 GHz and F1 = 0.3 GHz.

data for a primary signal (F2) of 3 GHz and an interfering signal (F1) at 300 MHz. In this case the interfering signal is out-of-band and has negligible effect upon the amplifier performance from -50 to +10 dBm. The measured and modeled data match well in the linear region. Note the modeled increase in primary signal gain (F1) with increasing interfering signal input (F2) above 20 dBm. This is a nonlinear error in modeling amplifier saturation.

In figure 12 the 2.0 GHz interfering signal does not appear to have a substantial effect upon the measured primary signal (F2) gain up to 0 dBm input (F1). This is in contrast to the increase in output signal gain predicted by the modeling. In figure 12 we observed an attenuation of the measured output for an interfering signal input greater than 0 dBm. This phenomenon was observed in testing whenever the interfering signal strength exceeded the primary signal, as shown in figures 13 and 14. In the case of figure 12, the effect is delayed because the interfering signal (F1) is out-of-band.

In figure 13 the test primary signal, F2, was applied at a higher level (-20 dBm instead of -30 dBm) in order to determine if an increase in primary signal strength would delay the attenuation effect. A comparison of figure 13 with figures 14 and 15 seems to indicate that the onset of primary signal reduction is delayed with an increase in primary signal strength. In addition, a comparison of figures 14 and 15 seems to indicate that the effect is delayed by input signal attenuation as the interfering signal moves out-of-band. In contrast, the modeled response for each case predicts positive gain with the application of the interfering signal.

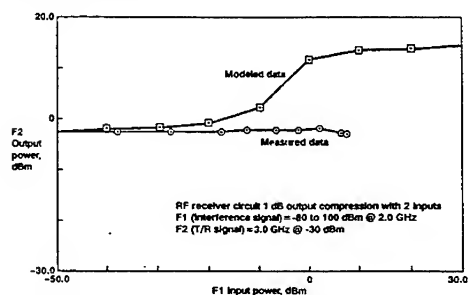


Figure 12: Comparison of Modeled Versus Measured Receiver 1 dB Compression With Inputs at F2 = 3.0 GHz and F1 = 2.0 GHz.

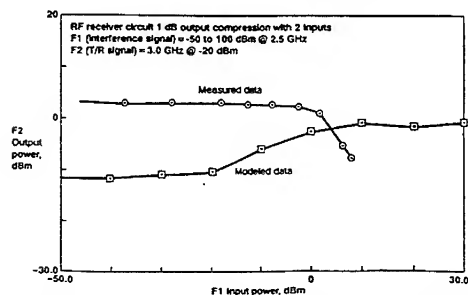


Figure 13: Comparison of Modeled Versus Measured Receiver 1 dB Compression With Inputs at F2 = 3.0 GHz and F1 = 2.5 GHz.

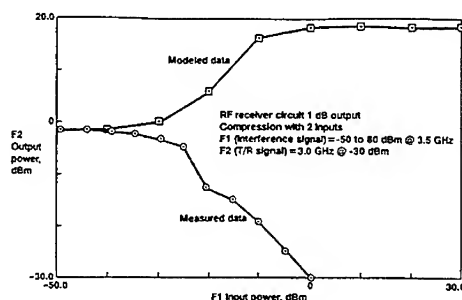


Figure 14: Comparison of Modeled Versus Measured Receiver 1 dB Compression With Inputs at F2 = 3.0 GHz and F1 = 3.5 GHz.

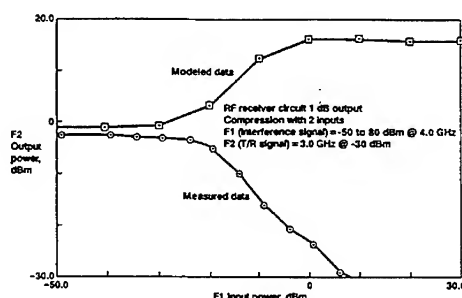


Figure 15: Comparison of Modeled Versus Measured Receiver 1 dB Compression With Inputs at F2 = 3.0 GHz and F1 = 4.0 GHz.

In figure 16, as the interfering signal is out-of-band and substantially attenuated through the amplifier, the attenuating effects of the interfering signal are not observed. The primary signal is observed to increase slightly in gain with increasing interference signal strength, as predicted by the modeling. The error in model predicted primary signal gain and measured gain with increasing interfering signal power (figure 16) is about 20 dBm.

In a comparison of the modeled and measured data the results are notably different. Out-of-band gain, for two frequencies, is greater for modeled data.

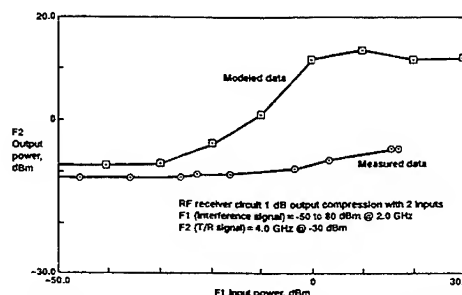


Figure 16: Comparison of Modeled Versus Measured Receiver 1 dB Compression With Inputs at F2 = 4.0 GHz and F1 = 2.0 GHz.

In the modeled data the primary signal rolls off into compression but does not decrease as in the measured data. The measured data indicates a reduction in primary signal gain as the interfering signal input power approximates or exceeds the primary signal input power (figures 13, 14, and 15). The modeled data underestimates the effects of the interfering signal when the interference signal power is greater than the primary signal. This is most likely due to small signal suppression and gain compression in the amplifier that is the nonlinear result of the high-power interference signal.

In an effort to investigate further this apparent conflict between measured and modeled response we repeated the measured response of figure 14, reducing both signals by 20 dBm. In this manner we hoped to determine if amplifier saturation was contributing to the lack of positive gain response to the interfering signal. The results of these measurements are shown in figure 17. Note in figure 17 that the output power of the primary signal (F2) of the first test is scaled on the left vertical scale, whereas the -20 dBm response of the second test is scaled on the vertical scale on the right of the plot.

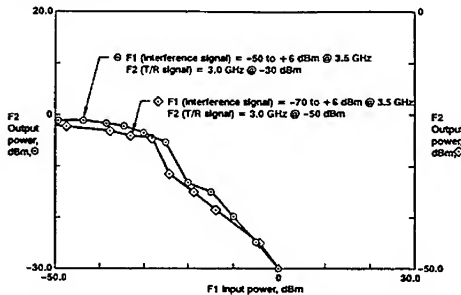


Figure 17: Comparison of Measured RF Receiver Response (with inputs at F2 = 3.0 GHz and F1 = 3.5 GHz) for -20 dBm Variation in Input Power.

Attenuation of the output at the primary frequency was identical at the reduced power levels. The results lead us to believe that amplifier saturation is not the cause of the observed gain reduction. This observation tends to support the small signal suppression theory as an explanation for the observed gain loss.

Intermodulation Effects

The observed nonlinear effects of EME susceptibility are more complex than straightforward saturation or intermodulation. The effects observed in test measurements include amplifier desensitization and small signal suppression. These effects appear to be related to power limiting in the amplifier stages but have been observed to occur at power levels below compression.

In order to better understand these effects it is useful to investigate the distortion products of two-frequency intermodulation. If we treat the amplifier output, O , in terms of the input, I , we can begin with the following simple assumption about the nonlinear performance of the amplifier:

$$O = G(I) \times I \quad \text{where} \quad G(I) = K_1 - K_2 I^2$$

Now if we look at the two-signal case:

$$\text{If } I = A_1 + A_2 \quad \text{for } A_2 \gg A_1$$

$$\text{where } A_1 = |A_1| \cos w_1 t$$

$$A_2 = |A_2| \cos w_2 t$$

then

$$O = [K_1 - K_2(A_1 + A_2)^2] (A_1 + A_2) \quad (\text{eqn. 1})$$

$$O = K_1 A_1 - K_2 A_1(A_1^2 + 2A_1 A_2 + A_2^2) + K_1 A_2 - K_2 A_2(A_1^2 + 2A_1 A_2 + A_2^2)$$

$$O = K_1 A_1 - K_2 A_1^3 - 2K_2 A_1^2 A_2 - K_2 A_1 A_2^2 + K_1 A_2 - K_2 A_1^2 A_2 - 2K_2 A_1 A_2^2 - K_2 A_2^3$$

$$O = K_1 A_1 - 3K_2 A_2^2 A_1 - K_2 A_1^3 + K_1 A_2 - 3K_2 A_1^2 A_2 - K_2 A_2^3$$

The terms in this expression may be examined to determine the distortion products. In this examination, it will be useful to note that:

$$A_1^2 = 1/2 + 1/2(\cos 2w_1 t)$$

and

$$A_2^2 = 1/2 + 1/2(\cos 2w_2 t)$$

In equation 1 the terms $K_1 A_1$ and $K_1 A_2$ are the linear output terms. The terms $-K_2 A_1^3$ and $-K_2 A_2^3$ give rise to both third-order harmonic distortion and self-compression at the fundamental frequencies. The terms $-3K_2 A_2^2 A_1$ and $-3K_2 A_1^2 A_2$ are the normal third-order intermodulation products. In addition these terms give rise to a compression at frequency w_1 due to the strength of the signal at w_2 and a compression at frequency w_2 due to the strength of the signal at w_1 . It is these cross-compression terms which can be identified with the phenomenon called "desensitization".

Small-signal suppression is related to power limiting in which multiple signals being amplified by the amplifier stages are subject to gain suppression while none of the input signals by themselves would cause the amplifier to go into compression. Small-signal suppression may be the phenomenon observed in the experiment in figure 17 in which a 20 dBm reduction of the input signals did not alter the gain loss of the primary signal, F2, as the interfering signal power, F1, was increased.

Nonlinear Modeling Errors

In our investigations, we have noted that as the input power to the model amplifier continues beyond the point of 1 dB compression, the curve begins to climb again in a linear fashion. This second linear increase, illustrated in figure 18 for a single 4 GHz input and figure 19 for two inputs at F1 = 2 GHz and F2 = 4 GHz, does not appear to be a realistic FET saturation effect.

It should be noted that the input levels for this analysis are absurdly high. This modeling does not represent real world conditions. This analysis is useful to investigate the model response to abnormally high input levels that are characteristic of some EM

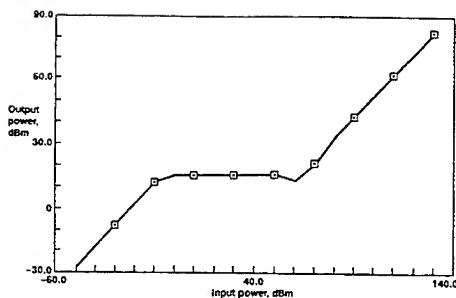


Figure 18: Modeled RF Receiver Amplifier Circuit Gain at 4.0 GHz.

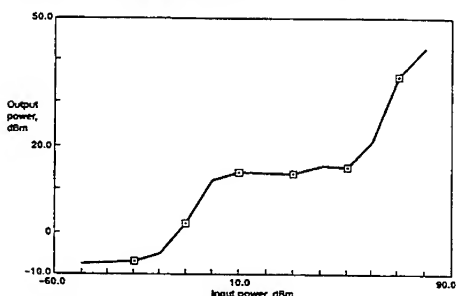


Figure 19: Modeled RF Receiver Amplifier Circuit Gain with Inputs at 4.0 GHz and 2.0 GHz.

environments. Real world exposure to these levels would result in circuit damage. We did not test real devices to abnormally high input power levels because we did not want to risk damage to our developmental test samples.

This secondary gain behavior of the model was reviewed with the developers of the analysis software (EEsof Inc). One potential explanation for the observed linear increase beyond the nonlinear gain compression plateau is a phenomenon known as "gain expansion" in the FETs. Gain expansion, or resurgence of gain in the nonlinear operating region of the amplifier, has been observed in real-world FET circuits. Another possible explanation is that nonlinear gain can have a multiple-stage effect in which the second stage of the model is providing gain after the first stage has saturated. This would require that the input signal bypass the saturated stage. A bypass mechanism has not been identified. The EEsof analysts believe that the observed gain expansion effect is due mainly to "re-biasing" of the transistors in the model. As the large signal swing is input to the device, the gate is biased positively with respect of the source, causing the gain expansion effect. In short, the software should correctly model the actual response of the circuit if breakdown effects are included in the device model. This limitation in the device modeling accuracy at interference signal levels is problematic in the evaluation of real-world EM environments effects.

Findings and Recommendations

Modeled predictions for functional performance and single-frequency operation were

reasonably accurate for the models used. Modeled predictions for intermodulation distortion did not agree with test results. Receiver two-frequency, 1 dB compression and receiver intermodulation test results indicate that there are discrepancies in modeled responses to in-band interference. Measured intermodulation effects indicate primary signal attenuation whereas the modeling predicted only gain compression. Evaluation of the measured primary signal attenuation leads us to conclude that as the interfering signal becomes greater than the primary signal, the amplifier exhibits a signal discrimination characteristic. This observed small-signal suppression is believed to be associated with amplifier desensitization for two or more input signals.

The modeling performed with the use of commercial RF circuit analysis software did not account for power limitations in the amplifier which should result in a suppression of the primary signal output with the introduction of a second, high-power, in-band signal. The nonlinear distortion error in the modeling analysis could be the result of incomplete circuit modeling or of limited device model accuracy for nonlinear gain computation.

Improved modeling of the RF amplifier is necessary in order to accurately predict out-of-band gain, in-band signal discrimination, and nonlinear distortion effects. The modeling can be improved with more precise circuit design detail. The high-input-power, nonlinear effects may require modifications to the analysis software as well as improvements to the circuit model. The typical RF circuit analysis software is not designed to accurately predict circuit behavior in response to high-energy input signals. As a result, excursions far into the nonlinear region or into saturation are not always accurate. Reliable prediction of operation in this region is necessary in order to represent coupled, high-level EM interference. Improved susceptibility prediction to EM environments can be achieved with more accurate circuit modeling and with more accurate computation of device nonlinear behavior.

Acknowledgments

The authors would like to express their gratitude to Dr. Tom Reder, Vice President of Marketing, and to Dr. Gary Otonari, Applications Engineer, with EEsof Inc. of Westlake Village, CA. Dr. Reder contributed the use of the EEsof software licenses employed in this study and Dr. Otonari provided much needed technical support in the interpretation of modeled nonlinear results.

The authors are also grateful to Mr. Michael Seifert, technical monitor for contract F30602-89-C-0004, Electromagnetic Effects Mitigation Techniques for Advanced Arrays. The results reported in this paper were performed for the U.S. Air Force at Rome Laboratory for this contract. Mr. Seifert provided valuable support and assistance in the preparation of this paper.

References

1. A. Wolski and W. Conway, EMI/EMC Assessment of MMIC Technology, RADC-TR-86-27, April 1986.
2. J. Rohrbaugh and Brian Farris, MMIC Conducted Interference Test Methodology, RADC-TR-90-312, December 1990.

SESSION 21 - "ANTENNAS"

Chair: Dr. Roger Radcliff, Co-Chair: Dr. Al Christman

COMPUTER MODEL FOR AXIALLY SYMMETRIC DIELECTRIC RADOMES IN THE NEAR FIELD OF A CIRCULAR APERTURE

D. C. Jenn
Naval Postgraduate School
Monterey, CA 93943

R. M. Francis and K. A. Klopp
U. S. Navy

I. INTRODUCTION

Rotationally symmetric radomes are frequently used in missile and aircraft applications for aero-mechanical reasons. They often shield flat-plate arrays (slotted waveguides) or paraboloids. Because of severe design requirements imposed by the operating environment, the electrical performance of the radome may be of secondary importance to the mechanical performance. The effects of the radome on the antenna radiation pattern include loss in gain, defocusing of the beam, increase in sidelobe levels, and beam pointing errors.

Ray tracing is the most common method of analyzing radomes of arbitrary shape. Typically the incident wave is assumed to be locally planar so that Fresnel reflection coefficients can be used. This requires the radome to be in the far field of the antenna. Furthermore, when the antenna scans off of the axis of symmetry of a curved radome many multiple reflections occur that make a significant contribution to the total field. Consequently many rays must be summed and the bookkeeping becomes overwhelming. Finally, if an aperture is reconstructed from the transmitted rays, the resulting aperture distribution (and therefore radome scattered field) varies with the location of reconstruction.

In this paper a method of moments (MM) solution for rotationally symmetric radomes is described. It is an extension of the Mautz and Harrington body of revolution code that has been modified to handle thin-shell dielectric radomes. The antenna is modeled as a planar circular aperture that is centered on the axis of symmetry, but can be phase-scanned. All three spherical electric field components (E_r , E_θ , E_ϕ) are considered in calculating the MM excitation vector. Thus the radome can be located in the near field of the antenna.

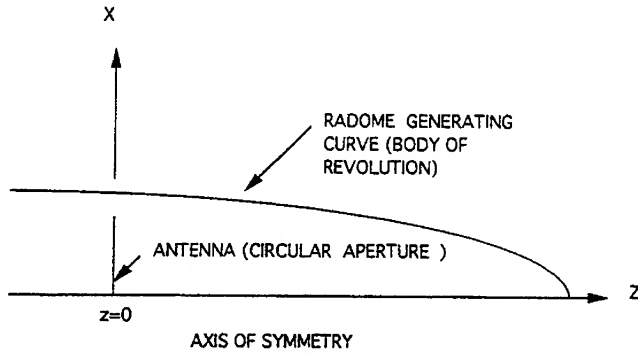


Figure 1: Antenna and radome geometry.

II. THE METHOD OF MOMENTS SOLUTION

The radome and antenna geometry of interest is shown in Figure 1. The feed is a circular aperture with a specified amplitude and phase distribution. The radome surface is a rotationally symmetric body with respect to the z axis. Thus the radome is a body of revolution (BOR) and the MM formulation developed by Mautz and Harrington [1] can be applied. The solution proceeds as if the radome were a perfect conductor, and then a correction term is added latter to account for the dielectric material properties [2]. The basis functions for the surface are:

$$\bar{J}_{ni}^t = \hat{t} \frac{T_i(t)}{\rho} e^{-jn\phi} \quad n = 0, \pm 1, \dots, \pm \infty \quad i = 1, 2, \dots, N_s - 2 \quad (1)$$

$$\bar{J}_{ni}^\phi = \hat{\phi} \frac{P_i(t)}{\rho} e^{-jn\phi} \quad n = 0, \pm 1, \dots, \pm \infty \quad i = 1, 2, \dots, N_s - 1 \quad (2)$$

$T_i(t)$ is the triangle function (which extends over two segments, i and $i + 1$) and $P_i(t)$ is the pulse function. A point on the surface of the radome is specified by the coordinates (t, ϕ) , where t is an arclength variable along the BOR generating curve. The distance of a point from the z axis is given by the cylindrical variable ρ . N_s is the number of surface generating points. A discussion leading to the choice of these basis functions is given in [1]. Finally, the surface current is expressed as a weighted sum of all the basis functions

$$\bar{J}_s = \sum_{n=-\infty}^{\infty} \left[\sum_{p=1}^{N_s-2} I_{pn}^t \bar{J}_{pn}^t + \sum_{q=1}^{N_s-1} I_{qn}^\phi \bar{J}_{qn}^\phi \right]. \quad (3)$$

Equation (3) is used in the E-field integral equation and the MM testing procedure applied using Galerkin's method (testing functions, $\bar{W}_{ni}^p = (\bar{J}_{ni}^p)^*$ where $p = t$ or ϕ).

The result is a matrix equation for the unknown current coefficients for each azimuthal mode, \mathbf{I}_n . The current coefficients for each mode can be solved for independently

$$\mathbf{I}_n = \mathbf{Z}_n^{-1} \mathbf{V}_n. \quad (4)$$

\mathbf{Z}_n is the impedance matrix for mode n , which can be partitioned into blocks associated with the vector directions \hat{t} and $\hat{\phi}$

$$\mathbf{Z}_n = \begin{bmatrix} Z_n^{tt} & Z_n^{t\phi} \\ Z_n^{\phi t} & Z_n^{\phi\phi} \end{bmatrix}. \quad (5)$$

The first superscript corresponds to the test function direction and the second to the expansion function direction. \mathbf{V}_n is the excitation vector and is defined in the next section. The detailed equations and the steps involved in obtaining equation (4) are described in [3].

The azimuthal index n runs from $-\infty$ to ∞ , but must be truncated at some finite value, say N . The value of N for a converged solution depends on the maximum radii of the antenna and radome as well as their spacing. Since the radome may be in the near field of the antenna, the current can vary rapidly and therefore more modes must be included than for a radome in the far field.

III. THIN-SHELL APPROXIMATION

The thin-shell approximation for dielectric bodies yields a correction term for the MM impedance matrix of a perfect electric conductor of the same shape [2]. Thus the impedance matrix in equation (4) becomes

$$\mathbf{Z}_n = \mathbf{Z}_{\text{MM}n} + \mathbf{Z}_{\text{L}n} \quad (6)$$

where \mathbf{Z}_{MM} is the MM impedance matrix for the perfectly conducting surface and the elements of $\mathbf{Z}_{\text{L}n}$ are given by

$$[Z_L]_{in}^{pq} = \iint_S \bar{W}_{in}^p \cdot \bar{J}_{in}^q Z_s ds \quad (p, q = t, \phi). \quad (7)$$

Orthogonality of the vectors \hat{t} and $\hat{\phi}$, requires that $p = q$

$$[Z_L]_{in}^{pp} = \iint_S \bar{W}_{in}^p \cdot \bar{J}_{in}^p Z_s ds. \quad (8)$$

The correction matrix will be tridiagonal for the Z^{tt} block in equation (5) and diagonal for the $Z^{\phi\phi}$ block.

The radome impedance

$$Z_s = \frac{1}{j\omega(\epsilon - \epsilon_o)t} \quad (9)$$

depends on the thickness of the shell t , the dielectric constant ϵ (which may be complex) and the frequency $\omega = 2\pi f$. A more convenient form of (9) is

$$Z_s = \frac{60}{n_\lambda[j(\epsilon_r - 1) + \epsilon_r \tan \delta]} \quad (10)$$

where $n_\lambda = t/\lambda$, ϵ_r is the relative dielectric constant of the radome and $\tan \delta$ is its loss tangent. If the radome material is an imperfectly conducting sheet then Z_s is purely real (surface resistivity); if the radome is lossless then Z_s is purely imaginary.

IV. CALCULATION OF THE EXCITATION VECTOR

The excitation vector is determined from the antenna radiation field

$$V_{in}^p = \iint_S \vec{W}_{in}^p \cdot \vec{E}^a ds \quad (p = t, \phi). \quad (11)$$

The electric field \vec{E}^a can be found by integrating the known current \vec{J}_i on the antenna. For a x polarized, uniformly excited aperture lying in the xy plane, with a linear phase applied to scan the beam in the direction θ_s ($\phi_s = 0$)

$$\vec{J}_i = \hat{x} J_o e^{-jkx' \sin \theta_s}. \quad (12)$$

Thus the Cartesian components of the electric field are [4]

$$E_x = \frac{-j\eta_o J_o}{4\pi k} \iint_{S_a} [G_1 + (\rho \cos \phi - \rho' \cos \phi')^2 G_2] e^{jk(\rho' \cos \phi' \sin \theta_s - R)} \rho' d\rho' d\phi' \quad (13)$$

$$E_y = \frac{-j\eta_o J_o}{4\pi k} \iint_{S_a} (\rho \cos \phi - \rho' \cos \phi')(\rho \sin \phi - \rho' \sin \phi') G_2 e^{jk(\rho' \cos \phi' \sin \theta_s - R)} \rho' d\rho' d\phi' \quad (14)$$

and

$$E_z = \frac{-j\eta_o J_o}{4\pi k} \iint_{S_a} (\rho \cos \phi - \rho' \cos \phi')^2 z G_2 e^{jk(\rho' \cos \phi' \sin \theta_s - R)} \rho' d\rho' d\phi'. \quad (15)$$

In the above, the primed coordinates refer to source (antenna) quantities and the unprimed to the observation (radome) quantities. The distance between the two points is

$$R = \sqrt{(\rho - \rho')^2 + z^2 + 4\rho\rho' \sin^2 \left(\frac{\phi - \phi'}{2} \right)} \quad (16)$$

and

$$G_1 = \frac{k^2 R^2 - 1 - jkR}{R^3} \quad (17)$$

$$G_2 = \frac{3 + 3jkR - k^2 R^2}{R^5} \quad (18)$$

where $k = 2\pi/\lambda$. The spherical components (E_r, E_θ, E_ϕ) of the antenna are obtained from the transformation

$$\begin{aligned} E_r &= E_x \sin \theta \cos \phi + E_y \sin \theta \sin \phi - E_z \cos \theta \\ E_\theta &= E_x \cos \theta \cos \phi + E_y \cos \theta \sin \phi - E_z \sin \theta \\ E_\phi &= -E_x \sin \phi + E_y \cos \phi. \end{aligned} \quad (19)$$

Using the spherical components in equation (11) yields expressions for the excitation elements that can be integrated numerically

$$V_{ni}^t = \int_0^{2\pi} \int_{t_i}^{t_{i+2}} T_i(t) e^{-jn\phi} [\sin(v_i - \theta) E_\theta + \cos(v_i - \theta) E_r] dt d\phi, \quad (20)$$

$$V_{ni}^\phi = \int_0^{2\pi} \int_{t_i}^{t_{i+1}} P_i(t) e^{-jn\phi} E_\phi \frac{\rho}{\rho_i} dt d\phi. \quad (21)$$

The quantities v_i and t_i are defined in Figure 2. Note that at every integration point in equations (20) and (21), equations (13) through (15) must be evaluated.

V. CALCULATED RESULTS AND DISCUSSION

The radiation patterns of antennas looking through various radome shapes and impedances were examined and compared to the antenna free space radiation patterns. A comparison gives the degradation in sidelobe level, increase in beam pointing error, and loss in gain. Figure 3 shows a typical result for a uniformly illuminated antenna radiating through an ogive-shaped radome. The specific values of the parameters are:

- Surface impedance, $Z_s = 0 + j1700\Omega$
- Number of azimuthal modes, $N = 20$
- Antenna radius, $a = 2\lambda$
- Radome base radius, $b = 3\lambda$
- Ogive parent circle radius, $r_o = 7.5\lambda$

The results for other shapes are given in references [3] and [5]. Figure 4 compares the patterns obtained using the complete antenna field expressions to the far-field approximation.

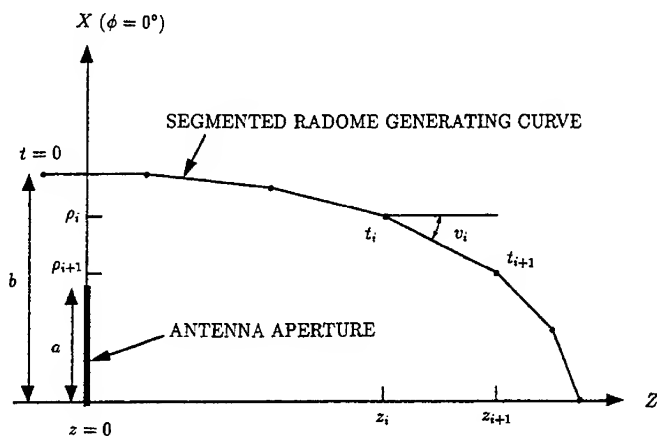


Figure 2: Geometry definition and notation.

The antenna radiation pattern is assumed to be zero in the rear hemisphere, and the radome base is open. A closed-back radome can be modeled by simply adding more segments behind the antenna that extend from the axis of symmetry to the radome edge. Note that any interaction between the antenna and radome is ignored. This should be small for a well designed radome, and primarily affect the VSWR looking into the antenna terminals.

Equation (10) was derived based on a solid homogeneous radome material of constant thickness. Radome materials that consist of multi-layers can be represented by a solid material with an equivalent dielectric constant. Radomes whose dielectric constant and thickness vary along the surface can be analyzed by a stepped index and thickness; ϵ_r , $\tan \delta$ and t can be specified independently on each segment of the generating curve.

VI. REFERENCES

- [1] J. R. Mautz and R. F. Harrington, "An Improved E-field Solution for a Conducting Body of Revolution," Syracuse University Technical Report TR-80-1, 1980.
- [2] J. R. Mautz and R. F. Harrington, "Radiation and Scattering from Loaded Bodies of Revolution," Appl. Phys. Res., vol. 26, June 1971, p.209.

[3] R. M. Francis, "A Computer Model for the Transmission Characteristics of Dielectric Radomes," Master's Thesis, Naval Postgraduate School, March, 1992.

[4] C. A. Balanis, Advanced Engineering Electromagnetics, Wiley & Sons, 1989.

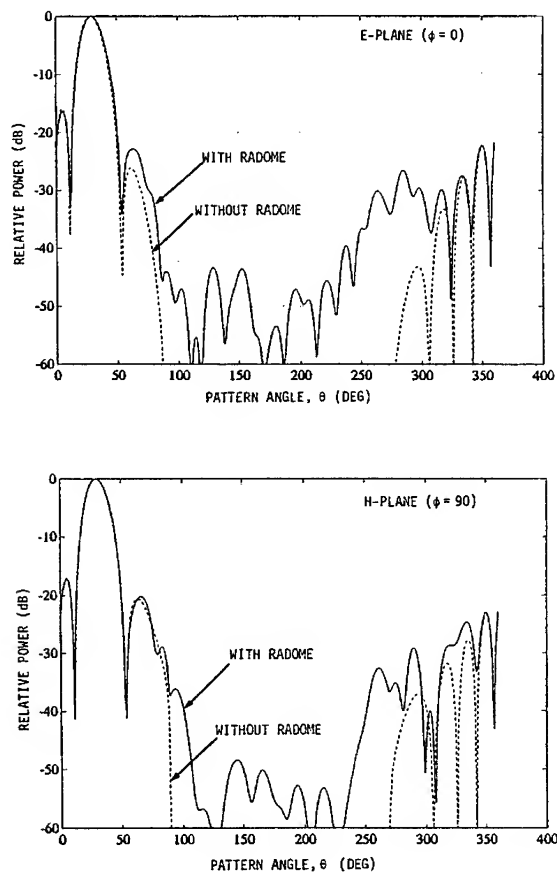


Figure 3: Radiation patterns of a 4λ antenna with and without radome.

[5] K. A. Klopp, "Antenna Gain Loss and Pattern Degradation Due to Transmission Through Dielectric Radomes," Master's Thesis, Naval Postgraduate School, March, 1993.

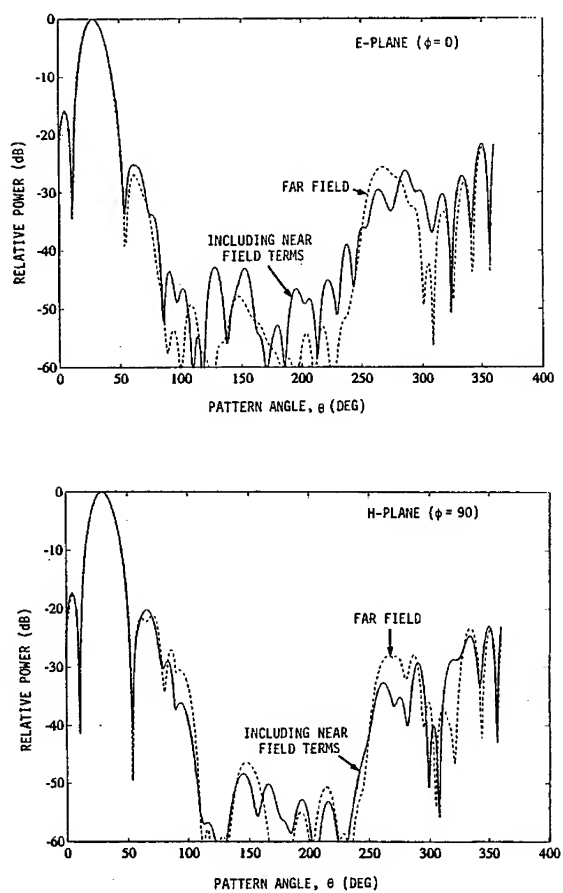


Figure 4: Radiation patterns with and without near-field terms.

AN EXACT EXPRESSION FOR THE VECTOR POTENTIAL OF A UNIFORM CURRENT CYLINDRICAL ANTENNA

D. H. Werner*

The Pennsylvania State University
The Applied Research Laboratory
P.O. Box 30
State College, PA 16804

P. L. Werner

The Pennsylvania State University
College of Engineering
DuBois, PA 15801

Abstract

This paper presents an exact formulation for the vector potential and corresponding electric fields associated with a uniform current cylindrical dipole. A mathematically exact representation of the vector potential has not previously been available for cylindrical antennas with arbitrary radius and uniformly distributed current. The exact formulation given in this paper is completely general and independent of the usual restrictions involving the wavelength, field point distance, dipole radius and length. The derivation of an exact expression for the uniform current vector potential depends upon finding an exact representation for the kernel as well as an integral of the kernel. A new expression for the exact kernel along with an exact representation for the integral of this kernel will be presented in this paper. It will be demonstrated that the integral of the kernel may be expressed in terms of a series which involves a generalized exponential integral and higher-order associated integrals. A numerically stable forward recurrence relation for the higher-order associated integrals will be presented. Various techniques will be discussed for the evaluation of the initial three terms (integrals) required by the recurrence relation.

I. The Cylindrical Wire Vector Potential

The derivation of an exact expression for the uniform current arbitrary radius cylindrical wire vector potential will be outlined in this section. The geometry for the cylindrical antenna under consideration is illustrated in Fig. 1. The length of this antenna is $2h$ and its diameter is $2a$. The cylindrical coordinates of the source point and field point are (a, ϕ', z') and (ρ, ϕ, z) , respectively. If the current is assumed to be uniformly distributed over the surface of the antenna, then the vector potential may be expressed in the form [1]

$$A_z(\rho, z) = \frac{\mu I_0}{4\pi} \int_{-h}^h K(z-z') dz' \quad (1)$$

where

$$K(z-z') = \frac{1}{2\pi} \int_0^{2\pi} \frac{e^{-i\beta R'}}{R'} d(\phi-\phi') \quad (2)$$

represents the cylindrical wire kernel, and

$$R' = \sqrt{(z-z')^2 + \rho^2 + a^2 - 2\rho a \cos(\phi-\phi')} \quad (3)$$

An exact expression for the cylindrical wire kernel was recently found by Wang [2] and later modified by Werner [3]. The exact form of the kernel obtained in [3] is given by

$$K(z-z') = -\frac{e^{-i\beta R}}{R} \sum_{n=0}^{\infty} \sum_{k=0}^{2n} A_{nk} \frac{(\beta^2 \rho a)^{2n}}{(\beta R)^{2n+k}} \quad (4)$$

where

$$A_{nk} = \binom{1/2}{n} \frac{(2n-1)}{(2i)^k} D(n,k) \quad (5)$$

$$\binom{x}{m} = \begin{cases} \frac{x(x-1)(x-2)\cdots(x-m+1)}{m!}, & m > 0 \\ 1, & m = 0 \end{cases} \quad (6)$$

$$D(n,k) = \frac{(2n+k)!}{k! 2n! (2n-k)!} = \begin{cases} \frac{1}{(2n)!}, & k = 0 \\ \frac{1}{(2n-k)!} \prod_{j=1}^k \left(\frac{2n}{j} + 1 \right), & k \neq 0 \end{cases} \quad (7)$$

$$R = \sqrt{(z - z')^2 + d^2} \quad (8)$$

$$d = \sqrt{\rho^2 + a^2} \quad (9)$$

This representation of the exact kernel has the advantages that it is easier to work with from the analytical point of view and more amenable to numerical evaluation.

Substituting the exact kernel (4) into the expression for the vector potential (1) yields

$$A_z(\rho, z) = -\frac{\mu I_0}{4\pi} \sum_{n=0}^{\infty} \sum_{k=0}^{2n} A_{nk} (\beta^2 \rho a)^{2n} E_n^k(\rho, z) \quad (10)$$

where

$$E_n^k(\rho, z) = \int_{-h}^h \frac{e^{-i\beta R}}{R} \frac{1}{(\beta R)^{2n+k}} dz' \quad (11)$$

constitute the well-known generalized exponential integral $E_0^0(\rho, z)$ and higher-order associated integrals. A numerically stable three-term forward recurrence relation may be derived which provides a computationally efficient method for evaluating the integrals in (11). The recurrence relation is given by

$$I_m = \frac{1}{(m-1)(\beta d)^2} \left[\frac{\beta \zeta_2 e^{-i\beta R_2}}{(\beta R_2)^{m-1}} - \frac{\beta \zeta_1 e^{-i\beta R_1}}{(\beta R_1)^{m-1}} \right. \\ \left. + i I_{m-3} + (m-2) I_{m-2} - i (\beta d)^2 I_{m-1} \right], \quad m \geq 3 \quad (12)$$

where

$$I_m = \int_{-h}^h \frac{e^{-i\beta R}}{R} \frac{1}{(\beta R)^m} dz' \quad \text{for } m = 0, 1, 2, \dots \quad (13)$$

$$\zeta_1 = -h - z \quad (14)$$

$$\zeta_2 = h - z \quad (15)$$

$$R_1 = \sqrt{\zeta_1^2 + d^2} \quad (16)$$

$$R_2 = \sqrt{\zeta_2^2 + d^2} \quad (17)$$

Exact solutions to the initial three integrals (I_0 , I_1 and I_2) required by the recurrence relation (12) may be derived by using a Maclaurin series expansion of the complex exponential function. Before expanding the integrands it is advantageous to express I_0 , I_1 and I_2 in the form

$$I_0 = e^{-i\beta R_0} \int_{\zeta_1}^{\zeta_2} \frac{e^{-i\beta(R-R_0)}}{R} d\zeta \quad (18)$$

$$I_1 = e^{-i\beta R_0} \frac{1}{\beta} \int_{\zeta_1}^{\zeta_2} \frac{e^{-i\beta(R-R_0)}}{R^2} d\zeta \quad (19)$$

$$I_2 = e^{-i\beta R_0} \frac{1}{\beta^2} \int_{\zeta_1}^{\zeta_2} \frac{e^{-i\beta(R-R_0)}}{R^3} d\zeta \quad (20)$$

where

$$R_0 = \sqrt{z^2 + d^2} \quad (21)$$

A term by term integration of the series expansion for the exponential function contained in these integrals yields

$$I_0 = e^{-i\beta R_0} \sum_{n=0}^{\infty} \sum_{k=0}^n \frac{(-i\beta)^k (i\beta R_0)^{n-k}}{k! (n-k)!} F_{k-1} \quad (22)$$

$$I_1 = e^{-i\beta R_0} \frac{1}{\beta} \sum_{n=0}^{\infty} \sum_{k=0}^n \frac{(-i\beta)^k (i\beta R_0)^{n-k}}{k! (n-k)!} F_{k-2} \quad (23)$$

$$I_2 = e^{-i\beta R_0} \frac{1}{\beta^2} \sum_{n=0}^{\infty} \sum_{k=0}^n \frac{(-i\beta)^k (i\beta R_0)^{n-k}}{k! (n-k)!} F_{k-3} \quad (24)$$

where

$$F_m = \int_{\zeta_1}^{\zeta_2} R^m d\zeta \quad (25)$$

Closed form solutions can be obtained for the integrals F_3 , F_2 , F_1 and F_0 while a recurrence relation can be used to determine the higher order integrals F_m for $m \geq 1$. That is,

$$F_{-3} = \frac{1}{d^2} \left[\frac{\zeta_2}{R_2} - \frac{\zeta_1}{R_1} \right] \quad (26)$$

$$F_{-2} = \frac{1}{d} \left[\tan^{-1} \left(\frac{\zeta_2}{d} \right) - \tan^{-1} \left(\frac{\zeta_1}{d} \right) \right] \quad (27)$$

$$F_{-1} = \ln \left[\frac{\zeta_2 + R_2}{\zeta_1 + R_1} \right] \quad (28)$$

$$F_0 = 2h \quad (29)$$

$$F_m = \frac{1}{(m+1)} \left[\zeta_2 R_2^m - \zeta_1 R_1^m + m d^2 F_{m-2} \right], \quad m \geq 1 \quad (30)$$

Numerical integration schemes may also be employed to evaluate I_0 , I_1 and I_2 . However, these integrals are difficult to evaluate directly using numerical techniques because their integrands are sharply peaked. This problem can be avoided by extracting the "singularity" from these integrals. Following this procedure results in

$$I_0 = F_{-1} + \int_{-h}^h \frac{e^{-i\beta R} - 1}{R} dz' \quad (31)$$

$$I_1 = \frac{1}{\beta} F_{-2} - i F_{-1} + \frac{1}{\beta} \int_{-h}^h \frac{e^{-i\beta R} + i\beta R - 1}{R^2} dz' \quad (32)$$

$$I_2 = \frac{1}{\beta^2} F_{-3} - \frac{i}{\beta} F_{-2} - \frac{1}{2} F_{-1} + \frac{1}{\beta^2} \int_{-h}^h \frac{e^{-i\beta R} + (\beta R)^2/2 + i\beta R - 1}{R^3} dz' \quad (33)$$

The integrals contained in (31), (32) and (33) may be more efficiently and accurately evaluated numerically since their integrands are much smoother. The remaining terms appearing in (31)-(33) correspond to integrals which have sharply peaked integrands but may be evaluated in closed form. Exact Bessel series expansions of I_0 , I_1 and I_2 have also been obtained in [3].

II. The Cylindrical Wire Electric Fields

The exact expression for the kernel (4) and vector potential (10) may be used to find corresponding exact expressions for the electric fields produced by a uniform current cylindrical wire antenna of arbitrary radius. The electric field components associated with the cylindrical antenna depicted in Fig. 1 may be expressed as

$$E_\rho(\rho, z) = \frac{I_0}{i4\pi\omega\epsilon} \left[\frac{\partial}{\partial \rho} K(z+h) - \frac{\partial}{\partial \rho} K(z-h) \right] \quad (34)$$

$$E_z(\rho, z) = \frac{I_0}{i4\pi\omega\epsilon} \left[\frac{\partial}{\partial z} K(z+h) - \frac{\partial}{\partial z} K(z-h) \right] - i\omega A_z(\rho, z) \quad (35)$$

For the uniform current cylindrical wire antenna of arbitrary radius, it can be shown that [3]

$$\frac{\partial}{\partial \rho} K(z \pm h) = \frac{1}{\beta^2 \rho} \frac{e^{-i\beta R_\pm}}{R_\pm^3} \sum_{n=0}^{\infty} \sum_{k=0}^{2n} A_{nk}(\beta^2 \rho a)^{2n} \left\{ \frac{(\beta \rho)^2 [(2n+k+1) + i\beta R_\pm] - 2n(\beta R_\pm)^2}{(\beta R_\pm)^{2n+k}} \right\} \quad (36)$$

$$\frac{\partial}{\partial z} K(z \pm h) = (z \pm h) \frac{e^{-i\beta R_\pm}}{R_\pm^3} \sum_{n=0}^{\infty} \sum_{k=0}^{2n} A_{nk}(\beta^2 \rho a)^{2n} \left\{ \frac{(2n+k+1) + i\beta R_\pm}{(\beta R_\pm)^{2n+k}} \right\} \quad (37)$$

where

$$R_{\pm} = \sqrt{(z \pm h)^2 + d^2} \quad (38)$$

and the exact expression for $A_z(\rho, z)$ is given in (10). These expressions for the electric field components are mathematically exact in the sense that no assumptions or approximations have been made in their derivation.

Acknowledgement

This research was sponsored by:

CDR Gus K. Lott
Chief Engineer, Code GX
Naval Security Group Command
3801 Nebraska Ave. NW
Washington, DC 20393-5452

References

- [1] R. W. P. King, "The linear antenna - Eighty years of progress," *Proc. IEEE*, Vol. 55, pp. 2-26, Jan. 1967.
- [2] W. Wang, "The exact kernel for cylindrical antenna," *IEEE Trans. Antennas Propagat.*, Vol. AP-39, pp. 434-435, April 1991.
- [3] D. H. Werner, "An exact formulation for the vector potential of a cylindrical antenna with uniformly distributed current and arbitrary radius," Submitted for publication in *IEEE Trans. Antennas Propagat.*, 1992.

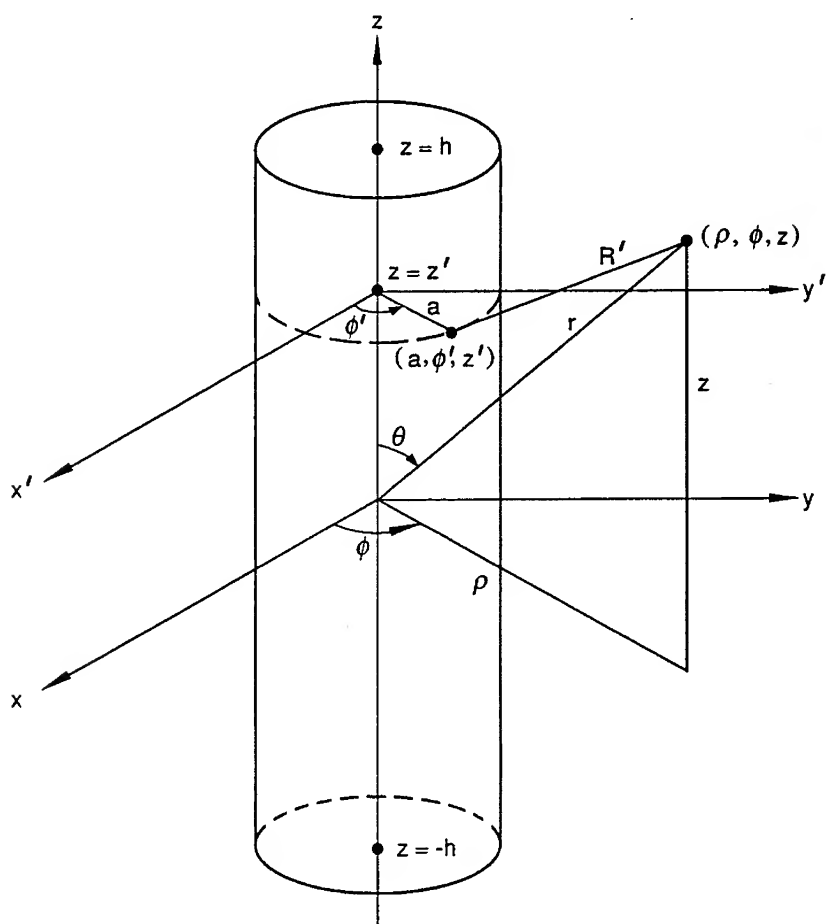


Figure 1. Cylindrical Antenna Geometry

A Simplified Approach for Modeling a Log-Periodic Dipole Antenna

Steven C. Merrill and Malcolm J. Packer
Science Applications International Corporation
300 Nickerson Road
Marlborough, MA 01752
(508)460-9500

Abstract

Numerical techniques have been developed to analyze the performance of log-periodic dipole antennas (LPDAs), which are complicated structures for which no closed form solution exists. Ma [1] and others [2] have approximated the current distribution on a wire to determine the performance of an LPDA. This paper describes a more straightforward and equally accurate approach which uses a single term (sine wave) approximation to the current distribution. Self- and mutual impedances are computed for each element and are combined with transmission line admittances to form a matrix equation. The solution to this equation gives the relative current and phase at the feed point of each LPDA element. These values are used to determine the driving-point impedance and the electric field pattern generated by each element in the array. The total radiated field is then computed as the superposition of the electric field vectors from these elements. This approach significantly decreases the computation time over other methods of moment techniques and greatly reduces the need for complicated numerical modeling. Execution times on a PC (486/33) for a 12-element LPDA are on the order of 7 seconds. This paper describes a simplified LPDA modeling approach and presents comparisons of model results with corresponding results from the Numerical Electromagnetics Code (NEC) [3]. Power gain patterns are within 1.5 dB and the radiation resistance is within 17% of NEC-generated results.

Introduction

Many applications require the use of broadband, directional antennas. Unfortunately, these requirements conflict and thus force the designer to trade-off gain and directivity for bandwidth. It is easy to design and manufacture omni-directional, broadband antennas or high-gain, narrowband antennas. It is, however, very difficult to satisfy the broadband and directional requirements simultaneously. The LPDA provides a good compromise, with reasonable gain over a wide frequency band.

One example of an application which requires broadband, directional antennas is HF automatic link establishment (ALE) radio. These radio systems are growing in popularity due to their robust adaptation to the HF skywave channel. In ALE systems, the radio automatically adjusts the radio frequency to optimize HF link performance for the existing

propagation conditions. Because the operating frequency must be varied over a wide range, nominally 1 to 30 MHz, a broadband antenna is required. Other applications which require broadband antennas include spread spectrum radio for personal communications and multi-media communications employing a single antenna system.

It is well known that antenna designs which specify the geometry of the structure entirely in terms of angles will exhibit frequency-independent characteristics [2, 4, 5, 6]. Rumsey was the first to postulate this theory which is based upon the principle of similitude [7]; the underlying concept that supports scale model design of antenna systems. If the dimensions of a given antenna are increased by a constant factor and the operating frequency is decreased by the same factor, then the performance of the antenna will remain unchanged. Of course, the permittivity, conductivity, and permeability of any media that affects the performance of the original antenna system must also be scaled. Consider a structure composed of an infinite number of adjacent cells, each of which is a scaled version of its neighbor. The structure extends to infinitely at the low frequency end and forms a vertex at the high frequency end. Because of its infinite extent and the relationship between adjacent cells, the antenna will be frequency independent with its geometry specified by a single angle.

DuHamel and Isbell [8, 9] used the single-angle principle to develop the LPDA in common use today. DuHamel began by considering a planar structure consisting of slots and teeth cut into a bi-fin. The width of adjacent slots and teeth were related by a constant scale factor and the geometry of the structure was repeated with the logarithm of the distance from the apex. This antenna produced a horizontally polarized, bi-directional radiation pattern. Isbell modified DuHamel's design to produce a uni-directional pattern by folding the structure at its apex. He then replaced the teeth of the structure with thin wire elements to produce the modern LPDA.

The LPDA is treated principally from a design perspective in the majority of the existing antenna handbooks [5, 10, 11]. Curves of directivity vs. σ and τ are typically provided to assist the engineer in selecting optimum LPDA design parameters. This data is sufficient to design an LPDA, but it is not sufficient to analyze its performance. Since no closed-form solution exists, numerical techniques must be used to obtain the key design parameters, that is, the driving-point impedance and the directivity. Although several authors have solved the resulting numerical problem, their work has received relatively little attention.

Carrel's [2] approach employed the parallel connection of two N-terminal circuits; the feed system and the dipole elements. This approach led to a matrix equation involving the impedance matrix of the dipole elements and the admittance matrix of the feeder system. Solving the matrix equation yielded the relative base currents of the dipole elements which was then used to obtain the driving-point impedance and the radiation pattern for the LPDA. Carrel assumed a sinusoidal current distribution on each of the dipole elements and created the impedance matrix using the induced-EMF method. This assumption leads to a tractable solution. With the limited computing capacity available in 1960, however,

execution times were excessive. As a result, the model could not be used to perform extensive LPDA analysis.

In a more recent work, Ma [1] expanded upon Carrel's approach by assuming a three-term approximation of the current distribution. Although this approach improved the accuracy of the solution, it also greatly increased both the complexity of the implementation and the execution time of the model. The many complex integrals, with their convergence and singularity problems, make Ma's approach difficult to implement even with modern computer systems. Ma's approach provides a relatively small increase in accuracy over the single-term approximation with a significant increase in numerical complexity.

The approach presented in this paper is similar to the approach used by Carrel in his doctoral thesis in 1961. The primary difference between the two approaches is in the determination of the mutual impedance between dipole elements. Other differences include the numerical techniques used to handle convergence and singularity problems. Since Carrel's LPDA analysis technique has received little attention in modern antenna handbooks, this paper presents a practical implementation of his approach for modeling and analysis of the LPDA.

The remainder of this paper is divided into two sections. The first section describes the approach used to model the LPDA, while the second presents results of a comparison between predictions produced by this approach and those produced by NEC.

Modeling Approach

The LPDA model described in this paper is one component of a comprehensive Electromagnetic Antenna Modeling (EAM) and analysis tool developed by Science Applications International Corporation (SAIC). EAM is a Windows-based program which includes pre- and post-processors for NEC and NEC-BSC [12] as well as a Quick-Look antenna analysis package which uses closed form solutions to compute the performance of many simple antennas. The LPDA model is one of 20 antenna models which are included in the Quick-Look software package. Among the outputs provided by the Quick-Look program are: azimuth and elevation patterns, peak gain, 3-dB beamwidth, and driving-point impedance.

The LPDA shown in Fig. 1 consists of a geometric progression of linear elements. The ratio of the length (l_i) of adjacent elements is defined as the inverse of the geometric ratio τ . This ratio also defines a similar relationship between the radius (a_i) and distance (d_i) between each element and a fixed reference point. Symbolically, this is represented as:

$$\frac{l}{\tau} = \frac{l_i}{l_{i-1}} = \frac{a_i}{a_{i-1}} = \frac{d_i}{d_{i-1}}$$

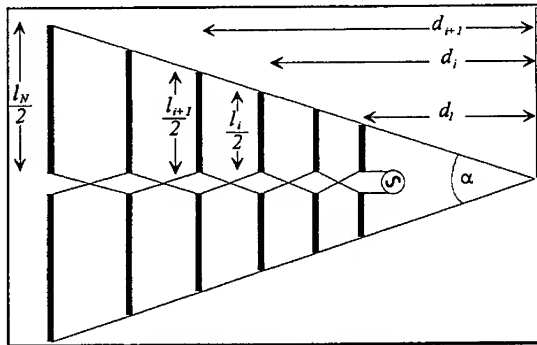


Figure 1 LPDA Geometry

The antenna elements are fed by a transmission line located in the center of the structure that connects each element with a 180-degree phase shift relative to its neighboring elements.

To analyze the performance of the LPDA, the antenna system is broken down into two N-terminal circuits; the feeder system and the dipole elements. If \mathbf{Y}_f is the

admittance matrix of the feeder system and \mathbf{V}_f and \mathbf{I}_f are vectors representing the corresponding voltage and current on the feeder system, then:

$$\mathbf{I}_f = \mathbf{Y}_f \mathbf{V}_f$$

Similarly for the dipole elements:

$$\mathbf{I}_d = \mathbf{Y}_d \mathbf{V}_d$$

Adding these equations while noting that the voltages (\mathbf{V}_f and \mathbf{V}_d) are equal yields the total input current:

$$\mathbf{I} = \mathbf{I}_f + \mathbf{I}_d = (\mathbf{U} + \mathbf{Y}_f \mathbf{Z}_d) \mathbf{I}_d \quad (1)$$

where \mathbf{U} is the identity matrix and \mathbf{I}_d is a vector representing the dipole base currents to be determined. The antenna is driven at one end and only the relative current on each dipole element need be determined. Thus define:

$$\mathbf{I} = \begin{bmatrix} 1 \\ 0 \\ \vdots \\ 0 \end{bmatrix}$$

and use matrix techniques to solve for \mathbf{I}_d .

The classical formulation of the two-port network is used to obtain values for the admittance matrix elements. These expressions can be found in Ma [1]. To compute the impedance matrix, the induced-EMF method is applied with two key assumptions. First, a sinusoidal current distribution is assumed to exist on the dipole elements. Second, the mutual impedance is computed as if the two elements were the same length. Clearly, this second assumption will produce the greatest error when used to compute the mutual impedance between elements with vastly different lengths. In the LPDA, large differences in element length are accompanied by large separation distances. This convention combined with the fact that the mutual impedance decreases with increasing element separation offsets inaccuracies caused by the assumption of equal element lengths. The

self-impedance referred to the current maximum is computed using a sinusoidal current distribution and is given in Balanis [5] as:

$$R_{ii} = \frac{\eta}{2\pi} \left\{ \begin{aligned} & C + \ln(kl) - C_i(kl) + \frac{l}{2} \sin(kl) [S_i(2kl) - 2S_i(kl)] \\ & \frac{l}{2} \cos(kl) \left[C + \ln\left(\frac{kl}{2}\right) + C_i(2kl) - 2C_i(kl) \right] \end{aligned} \right\} \quad (2a)$$

$$X_{ii} = \frac{\eta}{4\pi} \left\{ \begin{aligned} & 2S_i(kl) + \cos(kl) [2S_i(kl) - S_i(2kl)] \\ & -\sin(kl) \left[2C_i(kl) - C_i(2kl) - C_i\left(\frac{2ka^2}{l}\right) \right] \end{aligned} \right\} \quad (2b)$$

where $C = 0.5772$ is Euler's constant, a is the element radius, l is the element's length, and C_i and S_i are the familiar sine and cosine integrals [7]. Solving Eq. 2 and referring these values to the feed point yields the main diagonal elements of the impedance matrix (\mathbf{Z}_a). The off-diagonal elements are mutual impedance values which are computed using [7]:

$$R_{ij} = \frac{30}{\sin^2\left(\frac{kl}{2}\right)} \left\{ \begin{aligned} & 2(2 + \cos(kl)) C_i(kl) \\ & -4\cos^2\left(\frac{kl}{2}\right) \left[C_i\left(\frac{k}{2}(\sqrt{4d^2 + l^2} - l)\right) + C_i\left(\frac{k}{2}(\sqrt{4d^2 + l^2} + l)\right) \right] \\ & + \cos(kl) \left[C_i\left(k(\sqrt{d^2 + l^2} - l)\right) + C_i\left(k(\sqrt{d^2 + l^2} + l)\right) \right] \\ & + \sin(kl) \left[S_i\left(k(\sqrt{d^2 + l^2} + l)\right) - S_i\left(k(\sqrt{d^2 + l^2} - l)\right) \right. \\ & \left. -2S_i\left(\frac{k}{2}(\sqrt{4d^2 + l^2} + l)\right) + 2S_i\left(\frac{k}{2}(\sqrt{4d^2 + l^2} - l)\right) \right] \end{aligned} \right\}$$

$$X_{ij} = \frac{30}{\sin^2\left(\frac{kl}{2}\right)} \left\{ \begin{aligned} & -2(2 + \cos(kl)) S_i(kl) \\ & +4\cos^2\left(\frac{kl}{2}\right) \left[S_i\left(\frac{k}{2}(\sqrt{4d^2 + l^2} - l)\right) + S_i\left(\frac{k}{2}(\sqrt{4d^2 + l^2} + l)\right) \right] \\ & -\cos(kl) \left[S_i\left(k(\sqrt{d^2 + l^2} - l)\right) + S_i\left(k(\sqrt{d^2 + l^2} + l)\right) \right] \\ & + \sin(kl) \left[C_i\left(k(\sqrt{d^2 + l^2} + l)\right) - C_i\left(k(\sqrt{d^2 + l^2} - l)\right) \right. \\ & \left. -2C_i\left(\frac{k}{2}(\sqrt{4d^2 + l^2} + l)\right) + 2C_i\left(\frac{k}{2}(\sqrt{4d^2 + l^2} - l)\right) \right] \end{aligned} \right\}$$

where d is the distance between the elements in question and l is their length.

After computing the Z_d and Y_f matrices, Eq. 1 can be solved to obtain the base currents of the dipole elements. These values are used to calculate the driving-point impedance and the electric fields radiated by the structure. The driving-point impedance is computed using [1]:

$$Z_{driving} = \frac{V_1}{I_1} = V_1 = Z_{11} I_{1d} + Z_{12} I_{2d} + \dots + Z_{1N} I_{Nd} \quad (3)$$

Where the driving current, I_1 , was set to 1 A and I_{id} are the dipole base currents.

The electric field radiated by the entire structure is the sum of the fields radiated by the individual dipole elements. Individual dipole fields are computed by assuming a sinusoidal current distribution and integrating the fields produced by a hertzian dipole over the length of the dipole. For a vertically oriented dipole, this integration yields:

$$E_{\theta i}(\theta) = j\eta \frac{I_{id} e^{-jk r}}{2\pi r} \left[\frac{\cos\left(\frac{kl}{2} \cos(\theta)\right) - \cos\left(\frac{kl}{2}\right)}{\sin(\theta)} \right] \quad (4)$$

where $E_{\theta i}$ is the θ component of the electric field generated by the i^{th} element and I_{id} is the base current of the dipole under consideration (i.e., one element of the I_d vector which was computed above). Of course, the phase difference between elements must be considered when the fields are added. The base currents are complex values which reflect the amplitude and phase relationship between elements and directly determine the total electric field at a distant point. The path length differences between rays arriving from different elements results in phase differences which must also be included. The total field radiated by the LPDA is then given by:

$$E_{\theta}(\theta, \phi) = \sum_{i=1}^N E_{\theta i}(\theta) e^{jk d \sin(\theta) \cos(\phi)} \quad (5)$$

Once the electric field radiated by the LPDA has been obtained, the time averaged Poynting vector and the power gain pattern may be computed.

This approach includes two approximations which may significantly affect the performance of the model: the use of a sinusoidal current distribution applied to each element and the assumption of equal-length elements in the calculation of the mutual impedance. A comparison with NEC-generated results was performed to investigate the impact of the sinusoidal current approximation on the performance of the model. Figures 2a and 2b illustrate the current distribution predicted by the NEC model for element lengths of 0.2, 0.5, 1.0, 1.5, and 2.0 wavelengths. Superimposed on these plots are the corresponding sinusoidal distributions assumed by the LPDA model. The similarity between these curves suggests that the assumption of a sine-wave current distribution may

be adequate for many antenna modeling applications. The primary difference between the curves occurs when the length of the element is a multiple of one wavelength. For these cases, there is a dramatic difference in the feed-point current. In an LPDA, however, elements longer than about one-half wavelength will be in the unexcited region. These elements have negligible base currents and therefore do not contribute significantly to the radiated fields.

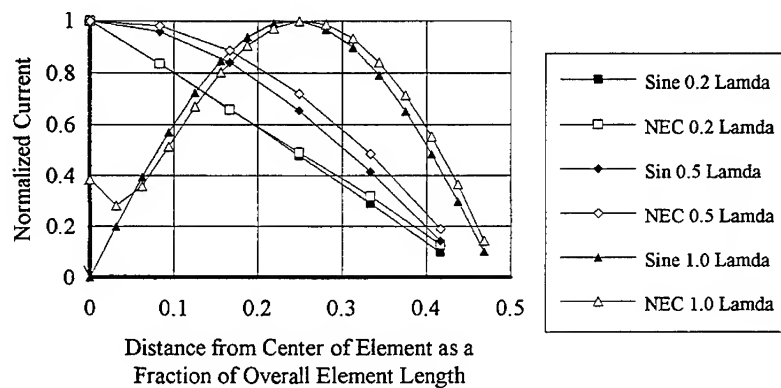


Figure 2a Current Distribution on a Thin Wire Dipole Antenna

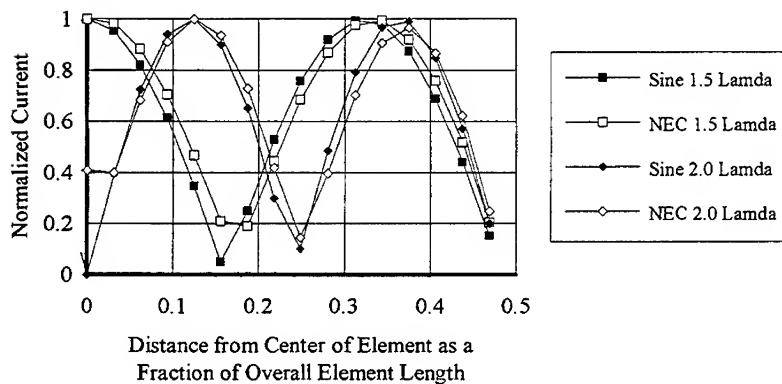


Figure 2b Current Distribution on a Thin Wire Dipole Antenna

Model results

A detailed set of comparisons between NEC model results and the Quick-Look approach has been performed to analyze the performance of the Quick-Look LPDA model. Quick-Look predictions of impedance and peak gain are compared with corresponding NEC [3] predictions as a function of frequency for a 12-element LPDA. Quick-Look and NEC predictions of radiation patterns and dipole base currents are also provided for comparative purposes.

Figures 3a and 3b are plots of the driving-point impedance (radiation resistance and reactance, respectively) as predicted by NEC and the Quick-Look LPDA modeling approach. The plots show agreement between the two models, with an rms deviation of 21Ω for the radiation resistance and 19Ω for the reactance. The maximum difference in the radiation resistance over all frequencies is less than 62Ω (17 %).

Figure 4 plots the peak gain as a function of the excitation frequency for the same 12 element LPDA. The plot illustrates that although there is a nearly constant difference of 1 to 1.5 dB between the NEC and Quick-Look predictions, they both exhibit the same behavior. Both curves are relatively flat across the frequency band with a slight decrease at the band edges. These flat curves are characteristic of frequency-independent antennas.

Figure 5 illustrates the radiation patterns produced by NEC and the Quick-Look LPDA approach. Note the good agreement in the three dB beamwidth (azimuth and elevation) and in the front to back ratio.

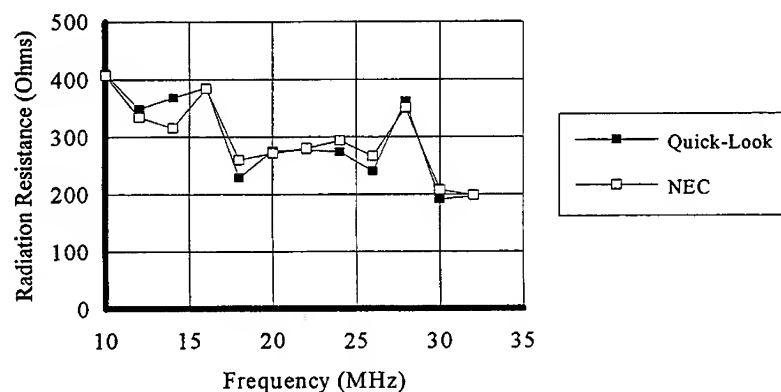


Figure 3a 12-Element LPDA Radiation Resistance vs. Frequency for Quick-Look and NEC

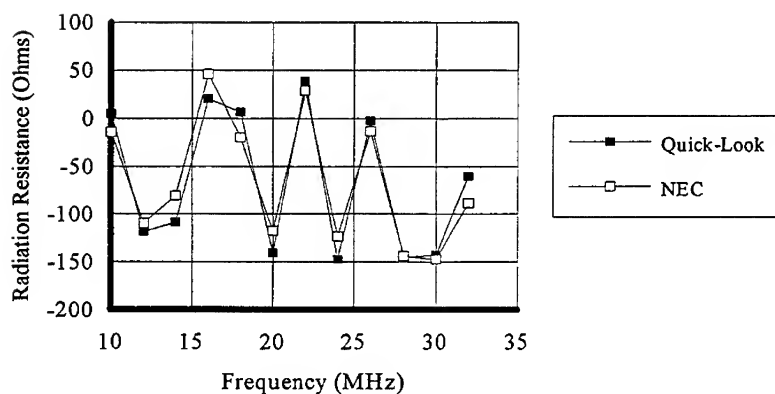


Figure 3b 12-Element LPDA Reactance vs. Frequency for Quick-Look and NEC

Figures 6a, 6b, and 6c are plots of the normalized dipole base currents generated by NEC and the Quick-Look model. The curves are parametric in frequency to best exhibit the behavior of the LPDA. Note the three distinct regions in these plots known classically as the transmission region, the active region, and the unexcited region. In the transmission region, the dipole elements are very short at the excitation frequency and therefore the base currents are small. In the active region, the dipoles are very nearly one-half wavelength long and are therefore excited by the driving signal. Because this region has

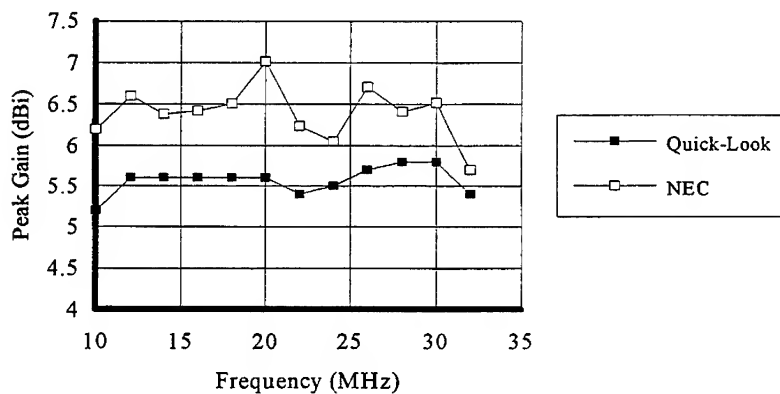


Figure 4 12-Element LPDA Peak Gain vs. Frequency for Quick-Look and NEC

the largest base currents, it is the primary contributor to the LPDA radiation pattern. In the unexcited region, the currents are almost non-existent because most of the energy in the input signal has been dissipated by elements in the excited region. Again, note the agreement between the NEC and Quick-Look predictions.

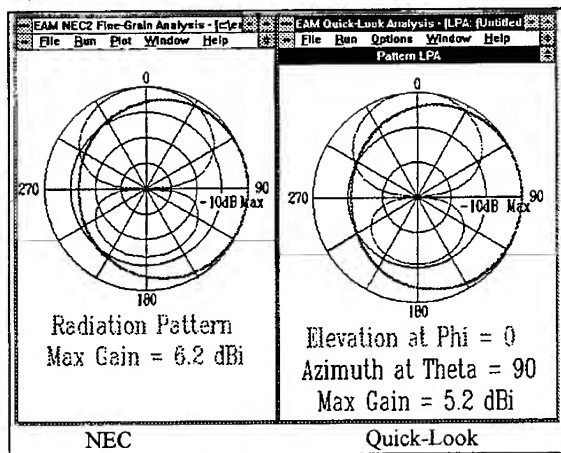


Figure 5 Comparison of NEC and Quick-Look LPDA Radiation Pattern

equation relates the dipole base currents, and the mutual impedance between element 1 (i.e., the shortest element) and every other element. Figures 6a through 6c demonstrated that most of these currents are negligible with only a few of the dipoles contributing to the input impedance. Recall that equal-length elements were assumed in the calculation of the

As an example of Quick-Look LPDA model accuracy, the radiation resistance (computed using Eq. 3 above) was compared with the corresponding value predicted by integrating the radiation pattern over a closed sphere. The two values differed by less than 0.25 dB over the entire frequency band and were nearly equal at the high-frequency end. The greatest discrepancy was observed at low frequencies, which is readily explained through an analysis of Eq. 3. This

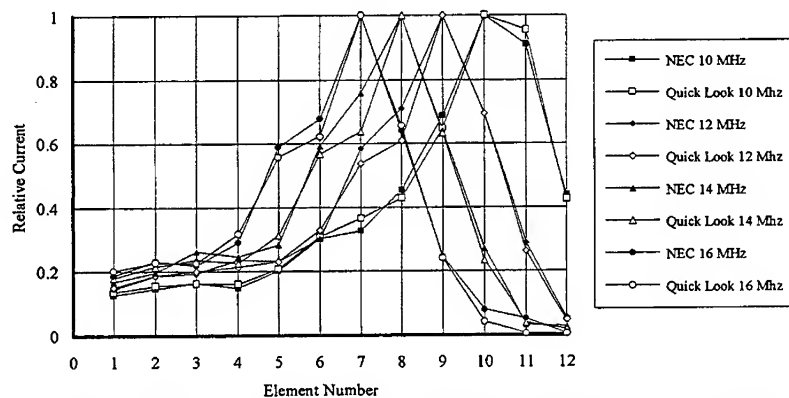


Figure 6a Base Current vs. Element # for NEC and Quick-Look, 10-16 MHz

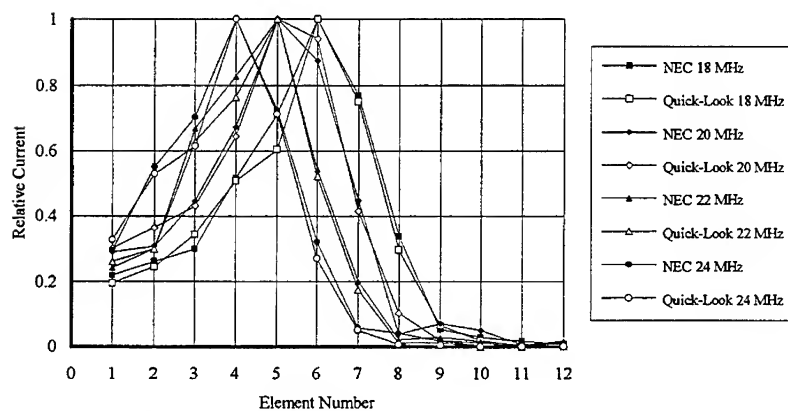


Figure 6b Base Current vs. Element # for NEC and Quick-Look, 18-24 MHz

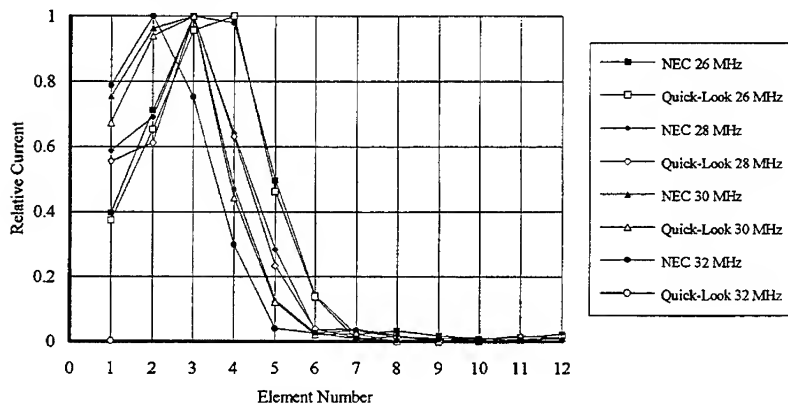


Figure 6c Base Current vs. Element # for NEC and Quick-Look, 26-32 MHz

mutual impedance between elements. This assumption may produce inaccurate results when used to compute the mutual impedance between the first (shortest) and the last (longest) elements. It is the long elements that contribute most at low frequencies, where the discrepancy in radiation resistance is greatest and the assumption becomes invalid. At higher frequencies, on the other hand, the assumption is valid and there is a much smaller discrepancy.

Figure 7 is a plot of the Quick-Look model execution time as a function of the number of elements. The run times were measured on a 486-33 PC with 8 Mbyte of memory and a 128 kbyte cache. The Quick-Look LPDA algorithm is a Turbo Pascal program written under Microsoft Windows version 3.1.

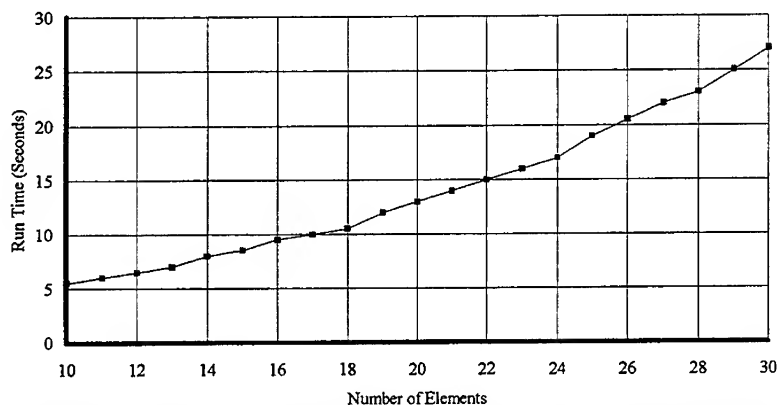


Figure 7 12-Element Quick-Look LPDA Run Time vs. Number of Elements

Summary and Conclusions

The majority of antenna handbooks treat the LPDA from a design perspective and ignore the formidable task of analyzing its performance. The engineer who needs more insight into LPDA performance is forced to rely on rigorous and time-intensive analysis tools like NEC. Although NEC is a very useful analysis tool, it is somewhat cumbersome and often difficult to use. For applications such as a log-periodic antenna, an approach similar to the one described in this paper may provide a useful alternative. With execution times on the order of 10s, numerous LPDA cases could be examined in the time required to generate and execute a single NEC LPDA model.

A numerical approach to analyzing the performance of the LPDA was presented as an alternative to NEC and other commonly used techniques. The simplified approach was implemented on a 486 PC and several comparisons with NEC were provided. In general, the Quick-Look predictions showed fairly good agreement with the corresponding NEC model, with peak gain values differing by less than 1.5 dB and radiation resistance values differing by less than 17%. This degree of accuracy is sufficient for link power budget analysis where uncertainties in other system parameters will dominate the errors induced by the Quick-Look model. Uncertainties in the background noise level, for example, almost always exceed 1.5 dB. In meteor burst communication systems [13], the statistical nature of meteor arrivals will dominate prediction accuracy. In HF performance predictions, the constantly changing ionosphere introduces prediction uncertainties that will again dominate prediction accuracy. Although the Quick-Look LPDA model is not sufficiently accurate for careful antenna analysis, it is generally effective for radio link performance predictions.

-
- 1 MA, T. M., Theory and Application of Antenna Arrays, John Wiley, New York, NY, 1974.
 - 2 Carrel, R. L., "Analysis and Design of the Log-Periodic Dipole Antenna," Phd. Thesis, University of Illinois, Urbana, IL, 1961.
 - 3 Burke, G. J., and Poggio, A. J., "Numerical Electromagnetics Code (NEC) - Method of Moments, User's Guide," Lawrence Livermore Laboratory, CA, 1981.
 - 4 Stutzman, W. L. and Theile, G. A., Antenna Theory and Design, John Wiley and Sons, New York, NY, 1981.
 - 5 Balanis, C. A., Antenna Theory and Design, Harper and Row, New York, NY, 1982.
 - 6 Mayes, P. E., "Frequency Independent Antennas and Broad-Band Derivatives Thereof," Proceedings of the IEEE, Jan, 1992.
 - 7 King, R. W. P. and Prasad, S., Fundamental Electromagnetic Theory and Applications, Prentice Hall, Englewood Cliffs, NJ, 1986.
 - 8 Duhamel, R. H. and Isbell, D. E., "Broadband Logarithmically Periodic Antenna Structures," IRE Nat. Conv. Record, 1957.
 - 9 Duhamel, R. H. and Ore, F. R., "Logarithmically Periodic Antenna Design," Collins Radio Co., Cedar Rapids, IA, 1958.
 - 10 Kraus, J. D., Antennas Second, Edition, McGraw Hill, New York, NY, 1988
 - 11 The ARRL Antenna Book, 16th Edition, The American Radio Relay League, Newington, CT, 1991.
 - 12 Marhefka, R. J. and Silvestro, J. W., "Numerical Electromagnetics Code - Basic Scattering Code - version 3 (NEC-BSC)," Electrosiences Laboratory, March, 1989.
 - 13 Desourdis, R. I., Merrill, S. C., Wojtaszek, J., and Hernandez, K., "Meteor Burst Link Performance Sensitivity to Antenna Pattern, Power Margin and Range, " MILCOM '88, San Diego, CA, October 1988 and the International Journal on Satellite Communications, vol. 8, no. 4, Wiley, July-August 1990.

PHASED ARRAY RADIATING ELEMENT DESIGN SOFTWARE*

H.K. Schuman
ARC Professional Services Group
1721 Black River Boulevard
Rome, New York 13440

1. Introduction

Several of the computer programs developed under the USAF's Rome Laboratory direction have proven useful as tools in radar systems analysis and design. One such program is the Parametric Antenna Analysis Subsystem (PAAS). PAAS contains detailed phased array antenna models and radar clutter mapping models. Detailed radiating element design is a particularly powerful function of PAAS; the Mutual Coupling Antenna Analysis Subsystem (MCAAS) encompasses the software for this function.

A new version of PAAS (Version 1.16) [1] was recently created. For this version, MCAAS was substantially revised to permit greater modeling accuracy and efficiency, to accommodate an extended set of radiator and array types that can be accurately analyzed, to facilitate the means of defining element geometry, to provide geometry verification graphics, and to provide output data graphics.

2. Overview of MCAAS

The mutual coupling analysis software in PAAS forms the basis of a powerful radiating element design and analysis tool. It enables detailed evaluation of radiating element performance in several environments: isolated element, infinite planar array or array lens, and finite array or array lens. The radiators can be of the thin conductor type (i.e., dipoles) or microstrip patch type. The environments and types are listed in Table 1. The arrays can be either of the constrained feed type or space feed (array lens) type. The constrained feed array excitations are assumed to be uniform amplitude and progressively phased Thevenin equivalent sources connected to the radiating elements via amplitude and phase adjust modules imbedded in an optional perfectly conducting, infinite ground plane. The array lens is assumed to be excited via a plane wave arbitrarily incident on the "feed side." The feed side (illuminated side) array is connected to the target side (shadow side) array via modules imbedded in a perfectly conducting, infinite ground plane. Microstrip

* This work was supported by the USAF Rome Laboratory.

TABLE 1
PAAS/MCAAS RADIATOR MODEL OPTIONS

● **ENVIRONMENT**

- **ISOLATED**
- **ARRAY (INFINITE PLANAR OR FINITE PLANAR)**
 - **GENERAL RECTILINEAR LATTICES (RECTANGULAR OR "TRIANGULAR")**
 - **INTERARRAY MUTUAL COUPLING**
- **PHASED ARRAY LENS (INFINITE PLANAR OR FINITE PLANAR)**
 - **INTERCONNECTING AMPLITUDE/PHASE ADJUST MODULES**
 - **INTERARRAY AND INTRAARRAY MUTUAL COUPLING**

● **TYPE**

- **THIN CONDUCTOR**
 - **SIMPLE DIPOLE VARIANTS (BENT OR CURVED ARMS, ETC.)**
 - **FOLDED DIPOLE VARIANTS**
 - **FEEDLINE BALUN**
 - **FEEDLINE SCATTERING**
 - **PARASITIC SCATTERERS**
 - **CURVED FEEDLINES**
 - **MULTIPLE LOAD PORTS**
- **MICROSTRIP PATCH**
 - **RECTANGULAR, CIRCULAR, ELLIPTICAL**
 - **PIN FEED (ARBITRARILY LOCATED)**
 - **EDGE FEED (ARBITRARILY LOCATED)**
 - **DUAL FEED WITH "T" COMBINER**
 - **SHORTING PINS (ARBITRARILY LOCATED)**

patch radiators always are associated with perfectly conducting, infinite ground planes in the MCAAS modeling.

Thin wire finite antenna and infinite array (plane wave expansion) moment methods underlie the radiating mode and mutual coupling mode modeling; the moment method permits a great deal of flexibility in radiator geometry. Efficient methods of combining transmission line mode and other nonradiating mode effects, such as occur with folded dipoles and with balun feed dipoles, also underlie the modeling. An efficient iterative procedure for accurately analyzing finite arrays is included in the modeling as well. Microstrip patch elements are modeled as appropriate cavities coupled to edge slots. The slots are modeled, via duality, as equivalent magnetic currents radiating in free space. The basic references for modeling details of MCAAS are [1], [2].

The recent enhancements to MCAAS (for PAAS Version 1.16) were made in the following areas [1]:

1. Accurate and flexible treatment of moment method wire junctions for analysis of thin conductor type radiating elements;
2. Automated generation of radiating mode (moment method) geometry and automated decomposition into radiating mode and transmission line mode parts;
3. Efficient, accurate iterative analysis of finite arrays and array lenses; and
4. Graphics.

The graphics enhancement provides for graphical display of principal data. Radiating mode geometry, feed port parameters (impedance, SWR, etc.), radiating mode current distribution, and gain patterns are automatically stored in files that are compatible for display via standard PAAS graphics routines.

It is noted, in particular, that the MCAAS "combined mode" modeling options for facilitating the analysis of complex radiators such as folded dipoles with integrated balun feeds have been redesigned at the user specification level. A new set of parameters has been defined that greatly facilitates the specification of a radiator of interest. The user, in fact, upon invoking these options will not need knowledge of the peculiarities related either to model decomposition into radiating mode and transmission line mode parts or to moment method segmentation. The decomposition and segmentation will be automatically performed in the software. The user need only specify the physical sizes and properties of the radiator. The dipole arms can be simple or folded; they can be inclined with respect to the array plane; and they can be composed of

circular cross section conductor or thin strip conductor. The feedlines can be balanced or, if unbalanced, contain integrated baluns; they can be bent in a general shape; and they can be composed of circular cross section conductors or thin strip conductors.

The enhanced MCAAS is accessible to the PAAS user through six PAAS procedures: WIRE, MICRO, ISOLATED, CONSTAN, LENSFED, and FINITE.

WIRE and MICRO are invoked for defining thin conductor or microstrip patch radiating elements, respectively. A graphical display of the segmentation for moment method computation of radiating mode performance is provided as part of the output. A radiator definition file is created within which all pertinent data for subsequent analysis is stored. The remaining MCAAS commands invoke routines which draw upon data within these files. Thus, the same radiator definition is used for analysis of a radiator in isolated, infinite constrained feed array, infinite array lens, or finite array (constrained feed or lens type) environments. The user need not redefine the radiator for redoing an analysis in a different environment.

ISOLATED is invoked for analysis of an isolated radiator. Port parameters, such as impedance, and pattern data, such as gain, are available for plotting over a range of frequencies. The radiating mode current distributions also are available for plotting. In addition, pertinent data is stored for later use as a potential first approximation in the efficient iterative procedure underlying the procedure FINITE for detailed analysis of large but finite arrays.

CONSTAN is invoked for analysis of an infinite planar array of identical radiators in a regular lattice. The lattice may be rectangular or triangular. The radiating elements are excited in uniform amplitude and progressive phase commensurate with a beam steering angle. Output data is similar to that of ISOLATED except that "active" impedance, etc., replace the corresponding port data, and "element" gain, etc., replace the corresponding pattern data. Pertinent data also is stored for later use as an alternative first approximation within FINITE. In addition, the nominal current distribution is available also for computation of element patterns in WELEMPAT or MELEMPAT wherein array factors are combined with element patterns to yield approximations to finite array directive gain patterns.

LENSFED is invoked for analysis of an array lens. Two infinite planar arrays sandwiching an infinite ground plane within which are imbedded amplitude and phase adjust modules comprise the lens. The illumination is a plane wave from a user specified direction. Two radiator definition files are required,

one pertaining to the illuminated side array and the other to the shadow side array. (Both files must be created by the same command, either WIRE for conducting radiator lenses or MICRO for microstrip patch lenses, but otherwise can pertain to quite different radiators.) The illuminated side array (array a) and shadow side array (array b) port voltages, currents, and impedances, etc., and radiating mode current distributions are provided on output. Port parameters also are available for each transit mode of energy, i.e., energy rereflected through the modules and back as a consequence of impedance mismatch. All transit mode port and radiating element data is available for later use in FINITE. The "single transit" mode data is available also for use in WELEMPAT or MELEMPAT.

FINITE is invoked for detailed analysis of a finite array, either constrained feed type or lens type. The effects of the array boundary, subarrays, and rings of terminated elements on mutual coupling dependent parameters can be assessed. Port parameters, such as active impedance, at each element is made available. FINITE requires data resulting from ISOLATED, CONSTAN, or LENSFED in order to initiate an iterative procedure. The array boundary selection includes circular, elliptic, or polygonal. The only limitation to polygonal is that the interior angles at vertices be less than 180° .

Realized element gain is computed in CONSTAN and LENSFED. This quantity is a particularly appropriate performance measure for large, near uniformly spaced arrays. In particular, "vector" realized element gain accounts for polarization mismatch, mutual coupling (resulting in impedance mismatch), surface waves, grating lobe loss, projected aperture loss, and any other incidental scattering loss. By comparing the principal polarization (vector) element gain with the ideal element gain, the performance of the radiating element is determined because the ideal element gain is the best conceivable element gain commensurate with the lattice. A third form of element gain, the scalar realized element gain, is an approximation to the total (polarization matched) realized element gain within the scan range for which no grating lobes enter visible space. The three forms of element gain are standard output with MCAAS.

3. Example

The enhanced software was applied to analyzing large field of view lattice phased arrays of circular cross section conductor dipoles with integrated balun

feedlines. Figure 1 shows the radiating element and lattice. Figure 2 shows the match efficiency (negative of mismatch loss) attained by scanning the array in the E-plane. Each curve corresponds to a different feedline/balun separation. A severe mismatch, thought to be a consequence of feedline scattering, is evident in each case. The mismatch moves closer towards broadside scan with increasing separation. Figure 3 shows the E-plane scan match efficiency corresponding to a 30° inclination angle. Evidently, the impedance match is substantially improved by inclining the dipole arms. Similar behavior had been observed experimentally in the development of the PAVE PAWS radar phased array antenna radiating element. (The element was designed by General Electric and the radar was built by Raytheon.)

4. References

1. H.K. Schuman, et. al., "Upgrading of the VAX Based Rome Laboratory Phased Array and Reflector Antenna Modeling Codes PAAS and ARCREP, 1990-1992," ARC Professional Services Group Final Report, Contract F30602-89-D-0028 with USAF Rome Laboratory, @ 1993.
2. H.K. Schuman, T.A. Lyon, and G.A. Bright, "SBR RF ANALYSIS/VALIDATION SBR Phased Array Radiating Element and Modeling Evaluation," RADC-TR-86-198, Vol. III, Final Technical Report, December 1986.

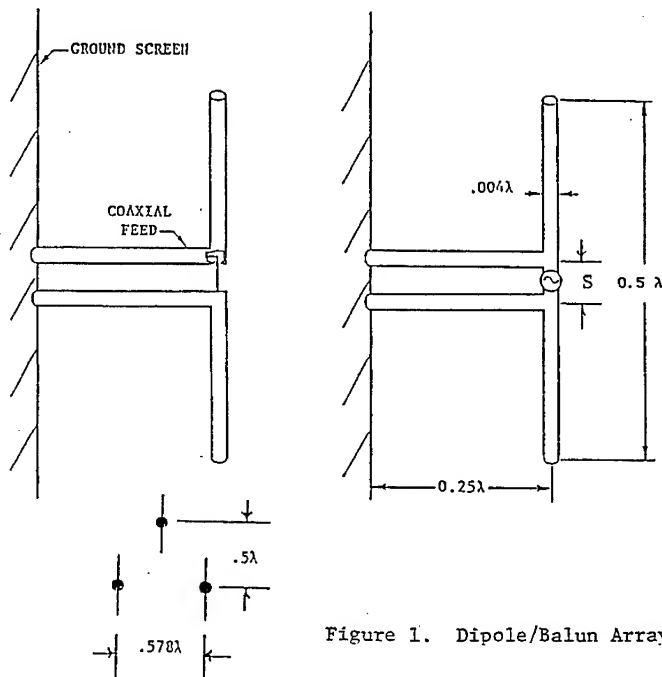


Figure 1. Dipole/Balun Array

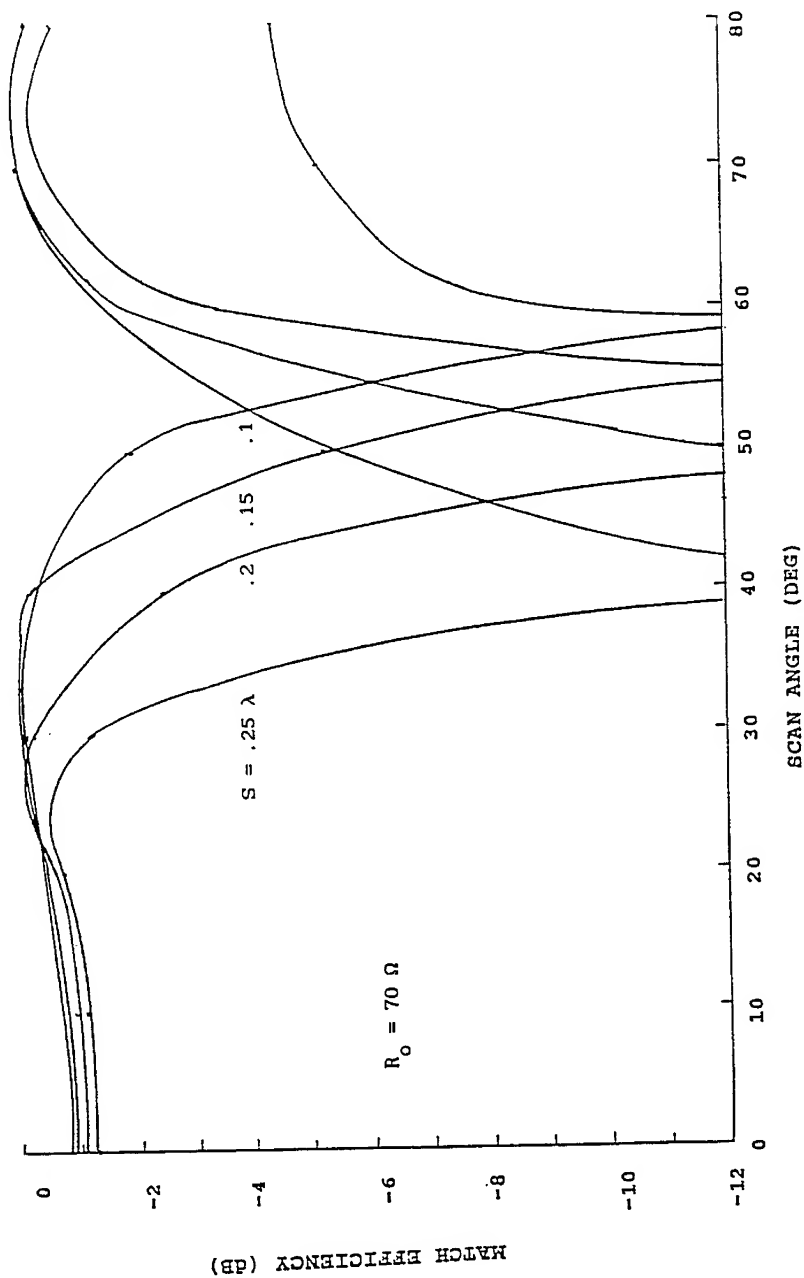


Figure 2. Straight Armed Dipole Balun Array Active Match Efficiency

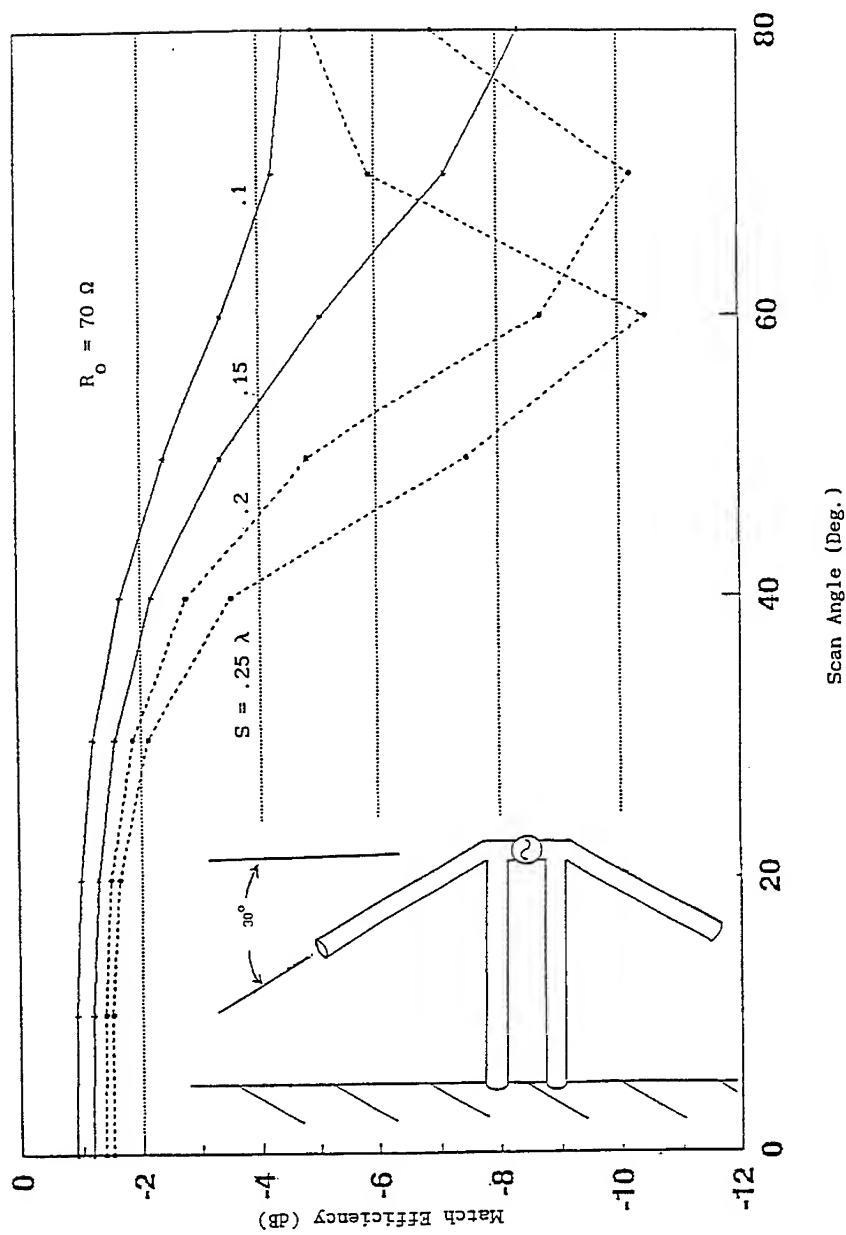


Figure 3. Inclined Arm (30°) Dipole/Balun Array Active Match Efficiency

SPECTRAL-DOMAIN ANALYSIS OF PATCH RADIATORS ON LOSSY FERRITE SUBSTRATES

Zhenglian Cai and Jens Bornemann

Laboratory for Lightwave Electronics, Microwaves and Communications
(LLiMic)

Department of Electrical and Computer Engineering
University of Victoria, Victoria, B.C. Canada V8W 3P6

Abstract A spectral-domain analysis for patch radiators on lossy ferrite substrates is presented. The theoretical model includes the losses of the substrate as well as different directions of applied d.c. magnetic bias. Moreover, the conductivity of the patch and its finite thickness is taken into account by incorporating a complex resistive boundary condition. The influence of direction and magnitude of the magnetic bias on resonance frequency and Q factor is investigated. It is demonstrated that comparable dependencies are obtained for square patches while, in the rectangular case, a bias in the narrower direction of the patch yields slightly less tunability. In applications on relatively thin ferrite substrates, the Q factor can be increased by one order of magnitude - without significantly affecting the resonance frequency - if the conventional conductor is replaced by superconducting material.

I. INTRODUCTION

Patch radiators are well known for their excellent performance in light-weight and low-cost array architectures. Many dielectric substrates commonly used to support patch radiators exhibit a significant amount of anisotropy that can either degrade the performance of printed circuits and antennas or, alternatively, have a beneficial effect once it is fully included in the design procedure [1]. Consequently, a substrate, whose material parameters can be influenced by outside parameters, offers - to a certain degree - the potential for tuning capabilities. Patch antennas on anisotropic media have been studied before, e.g. [2]-[3]. More recently, microstrip antennas on biased ferrite substrates with emphasis on linearly and circularly polarized radiation have been investigated [4], [5]. However, the field theoretical models presented neglect effects due to the finite thickness and the finite conductivity of the radiating patch and the losses of the ferrite substrate, which play an increasingly important part in the design of microstrip-integrated antenna systems.

Therefore, this paper focuses on a technique to analyze finite-thickness as well as finite-conductivity patch radiators on lossy ferrite substrate material. The theoretical model allows the d.c. magnetic bias to be applied in any direction of the cartesian coordinate system. The influence of magnitude and direction of the magnetic bias on resonance frequencies and Q values is investigated. A modified spectral-domain immittance approach is used to formulate the three-dimensional characteristic equation system. A decoupling procedure

for the electric and magnetic field leads to closed form impedance dyadic Greens functions in the spectral domain. As required and as is necessary and essential for reliable modern integrated circuit design, the theoretical model includes the loss properties of the ferrite tensor elements, the finite metallization thickness of the patch as well as its finite conductivity. The flexibility of the approach allows the patch to be realized as conventional, e.g., copper conductors or as superconductors in order to improve the radiation efficiency [6].

II. THEORY

The geometry of a patch radiator with an imperfect conductor on lossy ferrite substrate is shown in Fig. 1. The general form of the ferrite tensor in the case of magnetization in y, z and x direction can be expressed as

$$\langle \vec{\mu} \rangle = \mu_o \begin{bmatrix} \mu & 0 & j\kappa \\ 0 & \mu_y & 0 \\ -j\kappa & 0 & \mu \end{bmatrix} \quad \langle \vec{\mu} \rangle = \mu_o \begin{bmatrix} \mu & j\kappa & 0 \\ -j\kappa & \mu & 0 \\ 0 & 0 & \mu_z \end{bmatrix} \quad \langle \vec{\mu} \rangle = \mu_o \begin{bmatrix} \mu_x & 0 & 0 \\ 0 & \mu & j\kappa \\ 0 & -j\kappa & \mu \end{bmatrix} \quad (1)$$

respectively, where μ , $\mu_{x,y,z}$, and κ may be complex quantities to account for the losses in the material [7], [8].

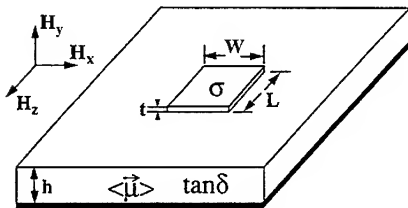


Fig. 1 Geometry of patch radiator.

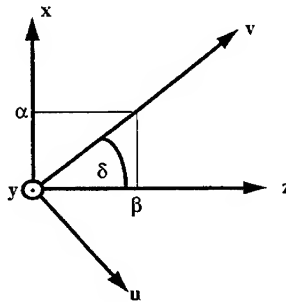


Fig. 2 Transform of coordinate systems.

By using the concept of the spectral-domain immittance approach [9], the six-component electromagnetic field considered in a coordinate system (x,y,z) can be decomposed into TM-to-y and TE-to-y waves in a (u,v,y)-system (Fig. 2).

$$u = z \sin \delta - x \cos \delta \quad (2)$$

$$v = z \cos \delta + x \sin \delta \quad (3)$$

$$\delta = \arccos \left(\frac{\beta}{\sqrt{\alpha^2 + \beta^2}} \right) \quad (4)$$

The complex elements of the permeability tensor are incorporated into Maxwell's equations which are readily applied in the transformed domain. This leads to decoupled TE and TM waves and directly yields the wave immittances of TE and TM waves with

their associated propagation constants $\gamma_{m,e}$. For magnetic bias in y direction, we obtain

$$\gamma_m^2 = -k_o^2 \epsilon_r \mu_{\perp} + \alpha^2 + \beta^2 \quad (5)$$

$$\gamma_e^2 = \frac{\mu}{\mu_y} (-k_o^2 \epsilon_r \mu_{\perp} + \alpha^2 + \beta^2) \quad (6)$$

where k_o is the free-space wave number, α, β are the propagation constants in x, z directions, respectively, and

$$\mu_{\perp} = (\mu^2 - \kappa^2) / \mu \quad (7)$$

Consequently, the the related admittances are given by

$$Y_{TM} = \frac{j\omega\epsilon}{\gamma_m} \quad Y_{TE} = \frac{\gamma_e}{j\omega\mu_o\mu_{\perp}} \quad (8)$$

Following the same steps for a magnetic bias in z direction, we find

$$Y_{TE} = \frac{(\beta^2 \mu_{\perp} + \alpha^2 \mu_z) \gamma_e + \alpha \mu_z \kappa (\alpha^2 + \beta^2) / \mu}{j\omega\mu_o\mu_z\mu_{\perp} (\beta^2 + \alpha^2)} \quad (9)$$

$$Y_{TM} = j\omega\epsilon_o\epsilon_r/\gamma_m \quad (10)$$

$$\gamma_{m,e} = \left(-\frac{q_{m,e}}{2} + \frac{1}{3} \sqrt{\left(\frac{q_{m,e}}{2}\right)^2 + \left(\frac{p_{m,e}}{3}\right)^2} \right) + \left(-\frac{q_{m,e}}{2} - \frac{1}{3} \sqrt{\left(\frac{q_{m,e}}{2}\right)^2 + \left(\frac{p_{m,e}}{3}\right)^2} \right) \quad (11)$$

with

$$q_m = 2a^3/27 - ab/3 + c \quad p_m = b - a^2/3 \quad (12)$$

$$q_e = -k_o^2 \mu_z \epsilon_r \kappa a / \mu \quad p_e = (k_o^2 \mu_z \epsilon_r - \alpha^2 - \beta^2 \mu_z / \mu) \quad (13)$$

$$a = -k_o^2 \epsilon_r \kappa / 2 \quad b = k_o^2 \mu_z \epsilon_r - \alpha^2 - \beta^2 \quad c = k_o^2 \kappa \epsilon_r (\alpha^2 - \mu_z \epsilon_r) / \alpha \quad (14)$$

For a biasing field in the x direction, the positions of α, β are exchanged in (9), (10), μ_z is replaced by μ_x , and

$$q_m = k_o^2 \kappa \epsilon_r \beta / 2 \quad p_m = k_o^2 \mu_x \epsilon_r - \alpha^2 - \beta^2 \quad (15)$$

$$q_e = k_o^2 \kappa \epsilon_r \beta / \mu \quad p_e = k_o^2 \epsilon_r - \alpha^2 / \mu - \beta^2 \quad (16)$$

in (11).

The finite thickness and conductivity of the conducting patch is taken into account

by utilizing the complex resistive boundary condition [10] which is capable of modelling conventional metal as well as superconductors. After applying Galerkins procedure and expanding the tangential current densities in sets of Bessel functions, the complex resonance frequencies $\omega_c = \omega_r + j\omega_i$ are given by the roots of the characteristic equation which is evaluated using numerical integration techniques [2]. Once ω_c is determined, the Q factor of the patch antenna is calculated as the ratio ω_r/ω_i .

III. RESULTS

The influence of a change in magnitude and direction of the d.c. magnetic bias on the resonance frequency and the Q factor of a rectangular patch radiator on ferrite substrate is shown in Figs. 3. As expected, the resonance frequency increases with the external field (Fig. 3a). The tuning range for z-direction bias is almost identical to that in y direction while the x-direction bias offers a lightly lower tuning range. A similar behavior is observed for the Q factor (Fig. 3b) which also increases with magnetic bias. This effect considerably changes the bandwidth of the patch while being tuned and needs to be considered by design engineers.

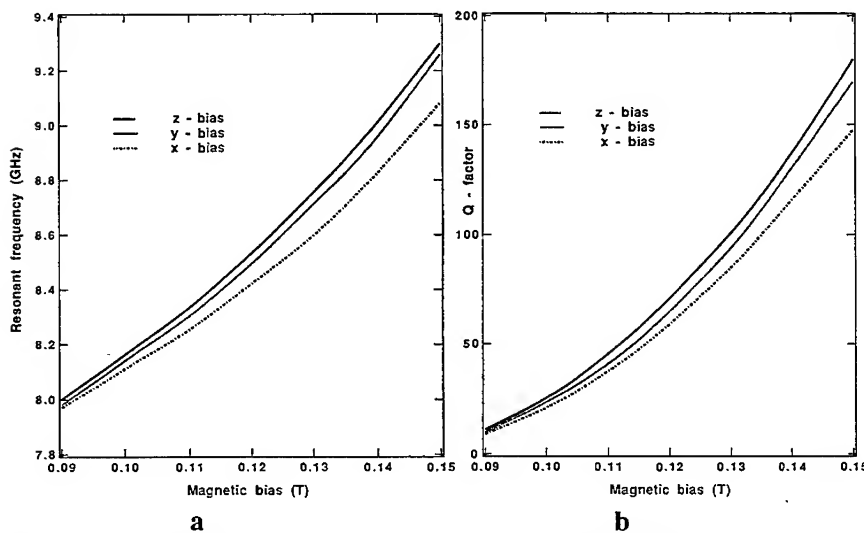


Fig. 3 Influence of direction and amplitude of magnetic bias on (a) resonant frequency and (b) Q-factor of a rectangular patch. Parameters: $\epsilon_r=16.6$, $\tan\delta=10^{-3}$, $W=2.5\text{mm}$, $L=8.0\text{mm}$, $h=1.0\text{mm}$, $t=0.2\text{mm}$, $\sigma=40\text{S}/\mu\text{m}$, $H_s=0.16\text{T}$.

For comparison with Figs. 3, Figs. 4 show the same parameters for a square patch. The resonance frequencies are slightly lower due to the enlarged patch area. The main dif-

ference, however, is that identical tuning ranges are obtained for the three investigated directions of magnetic bias (Fig. 4a). Consequently, the Q factor does not significantly depend on the direction of bias either (Fig. 4b).

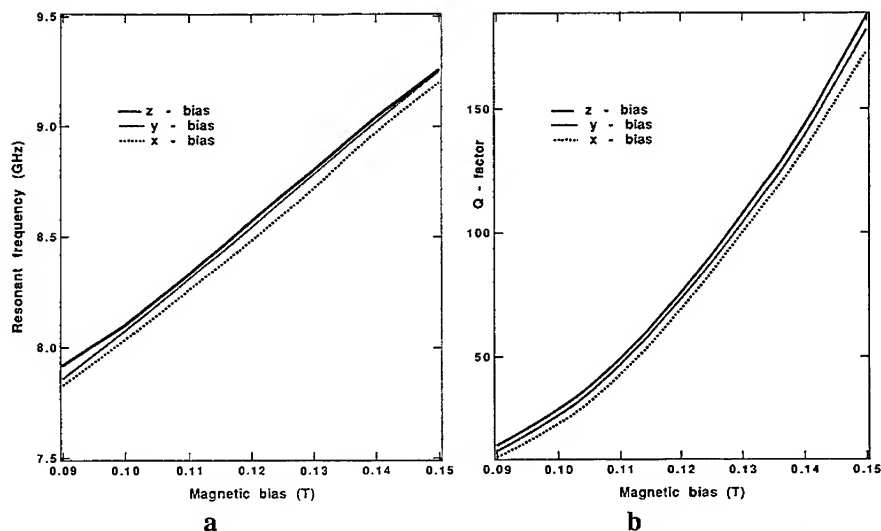


Fig. 4 Influence of direction and amplitude of magnetic bias on (a) resonant frequency and (b) Q-factor of a square patch ($W=L=8.0\text{mm}$, other parameters as in Fig. 3).

The effect of the substrate thickness on the resonance frequency and Q factor are shown in Figs. 5 with different conductors as parameter. The resonance frequencies decrease with increasing substrate height, as expected, and are relatively insensitive to the different conductor materials considered (Fig. 5a). The differences with respect to the Q factor are obvious (Fig. 5b). The superconducting patch comes close to the ideal case, and the Q factor decreases as the amount of losses contributed by the ferrite increases. The Q factor behavior of the copper patch, however, seems to be reversed. This is due to the fact that the conductor thickness is of the same order of magnitude as the substrate. Consequently, the conductor losses contribute overproportionally to the low Q factor. With further increasing substrate height, the solid curve in Fig. 5b shows a behavior similar to those of the ideal and superconductor since the substrate material then carries the majority of losses. For the relatively small substrate thicknesses displayed, however, the difference between a copper and a superconducting patch is one order of magnitude in Q-factor.

IV. CONCLUSIONS

An analysis technique for patch radiators on lossy ferrite substrates is presented. The method is based on a modified spectral-domain approach which allows the finite patch thickness as well as its finite conductivity to be taken into account. The tuning

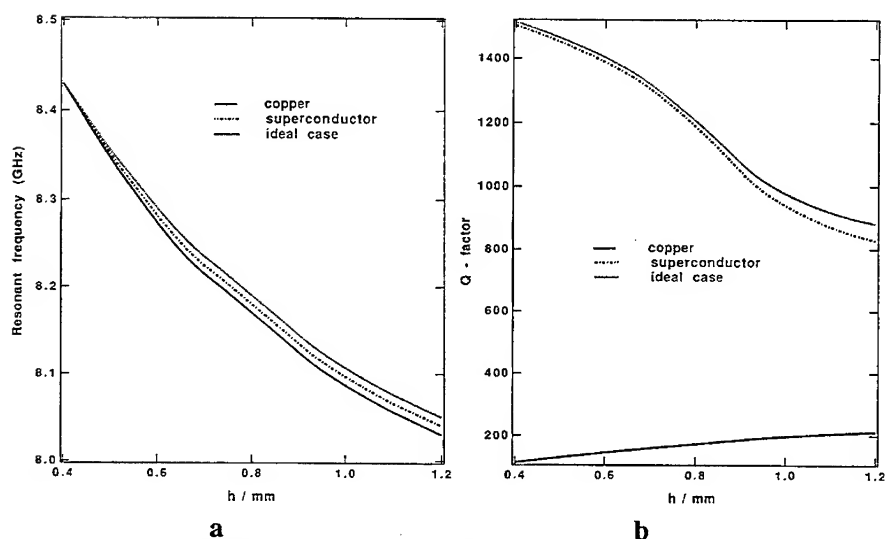


Fig.5 Effect of patch material and substrate thickness on (a) resonant frequency and (b) Q-factor. Copper: $t=0.2\text{mm}$, $\sigma=40\text{S}/\mu\text{m}$; superconductor: $t=0.4\mu\text{m}$, $\sigma_n=200\text{S}/\text{mm}$, $T/T_c=0.5$, $\lambda_{\text{eff}}=1500\text{\AA}$; ideal case: $t=0$, $\sigma \rightarrow \infty$; other parameters as in Fig. 3.

ranges and Q factors of square patches are found to be comparable for different directions of applied d.c. magnetic bias. A comparison between conventional and superconducting patches shows that the Q factor in the latter case can be improved by one order of magnitude. The influence of the conducting material on the resonance frequency is found to be extremely low.

REFERENCES

- [1] N.G. Alexopoulos, "Integrated-circuit structures on anisotropic substrate", *IEEE Trans. Microwave Theory Tech.*, vol. MTT-33, pp. 847-881, Oct. 1985.
- [2] D.M. Pozar, "Radiation and scattering from a microstrip patch on a uniaxial substrate", *IEEE Trans. Antennas Propagat.*, vol. AP-35, pp. 613-621, June 1987.
- [3] Z. Cai and J. Bornemann, "Full-wave analysis of high- T_c superconductor patch antenna on lossy bi-anisotropic substrates", in *1992 IEEE APS Intl. Symp. Dig.*, pp. 983-986.
- [4] P.J. Rainville and F.J. Harackiewicz, "Magnetic tuning of a microstrip patch antenna fabricated on a ferrite film", *IEEE Microwave Guided Wave Lett.*, vol. 2, pp. 483-485, Dec. 1992.
- [5] D.M. Pozar, "Radiation and scattering characteristics of microstrip antennas on normally biased ferrite substrates", *IEEE Trans. Antennas Propagat.*, vol. AP-40, pp. 1084-1092, Sep. 1992.

-
- [6] H. Chaloupka, N. Klein, M. Peiniger, H. Piel, A. Pischke and G. Splitt, "Miniaturized high-Temperature superconductor microstrip patch antenna", *IEEE Trans. Microwave Theory Tech.*, vol. MTT-39, pp. 1513-1521, Sep. 1991.
- [7] D. Polder, "On the theory of ferromagnetic resonance", *Phil. Mag.*, vol. 40, pp. 99-115, 1949.
- [8] J.J. Green and F. Sandy, "Microwave characterization of partially magnetized ferrites", *IEEE Trans. Microwave Theory Tech.*, vol. MTT-22, pp. 642-645, June 1974.
- [9] T. Itoh, "Spectral domain immittance approach for dispersion characteristics of generalized printed transmission lines", *IEEE Trans. Microwave Theory Tech.*, vol. MTT-28, pp 733-736, July 1980.
- [10] C. M. Krowne, "Relationships for Greens' function spectral dyadics involving anisotropic imperfect conductors imbedded in layered anisotropic media", *IEEE Trans. Antennas Propagat.*, vol. AP-37, pp. 1207-1211, Sep. 1989.

SESSION 22 - "FINITE ELEMENT METHOD

AND

APPLICATIONS AT HIGH FREQUENCIES"

Chair: Dr.Richard K. Gordon, Co-Chair: Dr.Jin-Fa Lee

ABC FINITE ELEMENTS FOR OPEN BOUNDARY ELECTROMAGNETIC PROBLEMS OF FREQUENCIES FROM DC TO GHZ

John R. Brauer, Brian S. Brown, and Mark M. Jenich

The MacNeal-Schwendler Corporation

4300 W. Brown Deer Road

Milwaukee, WI 53223 USA

414/357-0333(phone), -0347(fax). Email: j_brauer@macsch.com

ABSTRACT

This paper describes ABC finite elements used to simulate infinite space on 3D and 2D finite element models for frequencies ranging from DC to the GHz range and beyond. ABC stands for asymptotic and/or absorbing boundary condition. The ABC finite elements fill no new non-zero terms in the finite element matrices, and hence retain matrix sparsity and attendant fast CPU times. Examples of ABCs are presented for electrostatics, steady current flow, magnetostatics, and microwave antennas; in all categories the results are shown to be accurate.

INTRODUCTION

The finite element method has the capability of analyzing low frequency and high frequency electromagnetic devices of a wide range of geometries and materials, but special techniques are required to model open boundaries extending to infinity. Techniques such as hybrid boundary elements [1] and ballooning [2] all fill in many new nonzero matrix terms and hence destroy the advantageous sparsity of finite element matrix equations.

A fairly recent technique for simulating open boundaries on finite element models is called ABCs. The method was first applied to high frequencies, where the letters stand for Absorbing Boundary Condition [3]. More recently similar techniques have been applied to magnetostatic problems, where the letters stand for Asymptotic Boundary Condition [4],[5]. ABC finite elements fill no new non-zero terms in the finite element matrices, and hence retain matrix sparsity and attendant fast CPU times.

This paper describes ABC finite elements used to simulate infinite space on 3D and 2D finite element models for frequencies ranging from DC to the GHz range and beyond. First presented will be static ABCs, which will be demonstrated on electrostatic, current flow, and magnetostatic examples. None of these examples has been published before, and electrostatic and current flow ABCs have not been discussed before. Then dynamic ABCs will be discussed in the frequency and time domain, and new examples of ABCs on finite element antenna models will be presented.

THEORY

The finite element analysis software used here, MSC/EMASTM[4], based upon the potential vector $\{u\}$ made up of magnetic vector potential \vec{A} and time-integrated electric scalar potential ψ , has three matrices making up its equation [6]:

$$[M]\{\ddot{u}\} + [B]\{\dot{u}\} + [K]\{u\} = \{J\} \quad (1)$$

which can be solved for static, time domain, and frequency domain excitation vectors $\{J\}$. The derivation of (1) is based upon the energy variational equation [6]:

$$\delta W = \int_{vol} dv \{ \delta W_{el} + \delta W_{mag} + \delta W_{loss} - \delta W_{in} \} + \int_{surf} ds \int_{t_0} dt \{ \delta \vec{A} \cdot (\vec{H} \times \hat{n}) - \delta \psi [(\hat{n} \cdot \vec{J}) + \dot{\vec{D}}] \} + \left[\int_{surf} ds \delta \psi (\hat{n} \cdot \vec{D}) \right]_{t=t_0} = 0 \quad (2)$$

where the *volume* integral accounts for electric, magnetic, loss, and input energies respectively. The electric energy is proportional to permittivity and contributes to [M] of (1), the loss is proportional to conductivity and contributes to [B] of (1), and the magnetic energy is proportional to reluctivity and contributes to [K] of (1). The input energy contributes to {J} of (1).

The three *surface* integrals in (2) account for magnetic energy, power, and electric energy respectively flowing through the boundaries of the finite element model. To implement ABCs for static problems, surface integral terms are added to the three matrices depending on the type of static problem. ABC terms are added to the [M] matrix for electrostatic problems, to the [B] matrix for current flow problems, and to the [K] matrix for magnetostatic problems. The [K] matrix contributions have been derived recently for three dimensional problems [4] and for two dimensional planar problems [5]. In the two dimensional planar case, Poisson's equation is obeyed for all three types of static problems, so that the [B] and [M] matrix contributions are similar to those for [K]. However, in three dimensional and axisymmetric cases, the static ABCs for [B] and [M] differ from those for [K].

In dynamic (frequency domain or time domain) problems with high frequency content, the preceding [M], [B], and [K] matrix ABC contributions are supplemented by an additional [B] matrix contribution [7,8] that accounts for radiated power. Assuming that the ABC surface for 3D models is that of a sphere of radius r , then this additional radiation contribution can be derived from (2) to be [8]:

$$\int_{\text{surf}} ds \left\{ \delta \vec{A} \cdot (\vec{H} \times \hat{n}) \right\} = \int_{\text{surf}} ds \left\{ \frac{1}{\mu} \delta \vec{A} \cdot (\nabla \times \vec{A}) \times \hat{r} \right\} \quad (3)$$

ELECTROSTATIC EXAMPLE

To demonstrate three-dimensional electrostatics with open boundaries, we choose a problem given in a textbook by Jackson [9]. A sphere of radius $a=0.5$ meter is divided into two conducting hemispheres. The hemispheres are separated by an infinitesimally thin air gap and are surrounded by air extending to infinity. The northern hemisphere is at +1 volt and the southern hemisphere is at -1 volt.

Figure 1 shows the finite element model of a 10 degree sector of one hemisphere. The model is made up of 47 three-dimensional isoparametric finite elements, including both hexahedrons and pentahe-drons. Nine open boundary finite elements are placed at a radius of 1 meter.

Figure 1 also displays the voltage contours computed by MSC/EMAS. Note that they intersect the outer model surface at arbitrary angles, which agrees with expectations. The computed voltages can be checked by comparing them with those of the classical formula along the z axis [9]:

$$\phi = V \left[1 - \frac{(z^2 - a^2)}{z\sqrt{(z^2 + a^2)}} \right] \quad (4)$$

where the applied voltage V is here 1 volt. Figure 2 is a graph of the classical voltage $\phi(z)$ of (2) versus the MSC/EMAS voltage $\phi(z)$. The agreement is between 0.18% and 3.77%. The finite element results are somewhat in error due to the use of only 47 finite elements and due to the necessity of modeling a finite gap between the hemispheres.

STEADY CURRENT FLOW EXAMPLE

As an example of a steady current flow problem with open boundaries, consider two perfectly conducting cylinders buried in earth that extends to infinity. The conductivity σ of the earth is assumed to be 1 S/m. Figure 3 shows the cylinders, which are of radius $a=1$ meter and which are separated by $d=4$ m center-to-center. The cylinders have voltages of +1 and -1 volt, respectively.

The finite element model of Fig. 3 consists of 300 two-dimensional isoparametric finite elements, including both quadrilaterals and triangles. 24 ABC open boundary finite elements are placed at a radius of 6 m.

Figure 3 also displays the voltage contours computed by MSC/EMAS. The resistance between the cylinders is given by the classical formula [10]:

Fig. 1. Finite element model of a 10 degree sector of one hemisphere at 1 volt, with ABC boundaries at twice the hemisphere radius of 0.5 m. The computed electrostatic voltage contours are also shown.

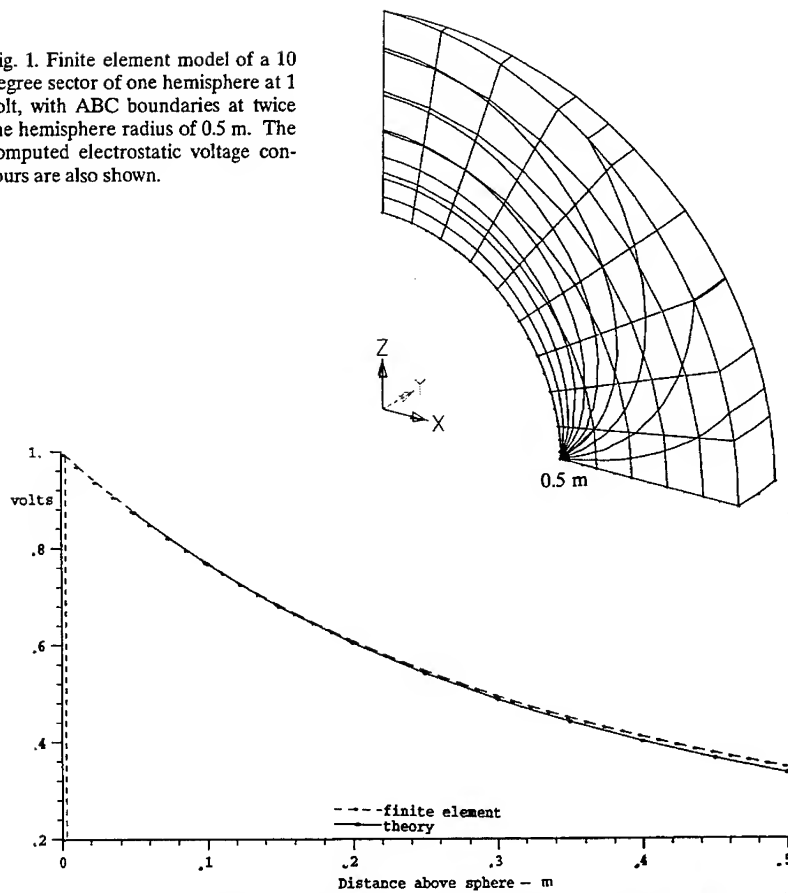
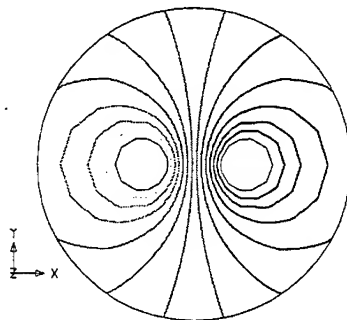


Fig. 2. Voltage versus distance along z axis of Fig. 1. Finite element and theoretical results are shown.

Fig. 3. Two buried cylinders and the computed voltage contours for the current flow between them.



$$R = \frac{\ln \left[\frac{d + \sqrt{d^2 - 4a^2}}{d - \sqrt{d^2 - 4a^2}} \right]}{2\pi\sigma} \quad (5)$$

which obtains $R = 104.80$ milliohms. MSC/EMAS obtains $R = 105.11$ milliohms, which agrees within 0.296%.

NONLINEAR MAGNETOSTATIC EXAMPLE

To demonstrate ABCs in three dimensional magnetostatic problems, we analyze a permanent magnet surrounded by air. The permanent magnet material is Alnico 8 with a nonlinear magnetization curve. This nonlinear behavior can be calculated by inputting its nonlinear $B-H$ relationship as a $B-H$ table, and by inputting its coercive force H_c of 115,387.3 A/m as a permanent magnetization excitation. The magnetic flux densities computed near the magnet will be compared with experimental results.

Only one eighth of the magnet is modeled because of its symmetry, as illustrated in Figure 4. Air is modeled around the outer edges of the magnet to a radius of 25 mm, where ABC open boundary elements are placed to simulate free space extending to infinity.

This 1/8 model is built with 2,192 first-order 3D hexahedron elements, 228 first-order ABC open boundary elements and 2,640 grid points. The magnet is built with 144 hexahedrons. The air surrounding the magnet is modelled out to a radius of 25 mm, accounting for the other 2,048 hexahedrons. Figure 4 illustrates the finite element mesh and boundary conditions.

Figure 5 shows the magnetic flux density values calculated with MSC/EMAS as a function of distance from the magnet, directly above the center of the north pole of the magnet. Experimental results, with an error of $\pm 5\%$, are shown for comparison. There are small discrepancies between MSC/EMAS results and experimental values, ranging from 2.1% to 9.7%. These could be attributed to both the measurement error and variations in the $B-H$ curve for the permanent magnet material. This finite element model converted to second order isoparametric elements obtains similar values, so the mesh density for this model is adequate.

ANTENNA EXAMPLE

A simulation of a waveguide-fed slot antenna is presented here which demonstrates the use of ABCs in the frequency domain. In this example, two and three-dimensional finite elements of first and second order are intermixed to obtain the radiation patterns and the input impedance of the simulated antenna. The radiation patterns obtained from the simulation are validated against theoretical data [11].

The slot antenna, shown in Figure 6, contains one narrow slot oriented along the broad side of the top waveguide wall and resides on an infinite groundplane. Effects of the 0.068λ waveguide wall thickness are also considered in the the simulation. The waveguide is excited with a TE_{10} mode at $f/f_c = 1.083$ where f_c is the waveguide cutoff frequency. The waveguide is terminated in a matched impedance.

Due to the geometrical symmetry of the antenna and the field symmetry of the modal excitation, only one half of the device is simulated using approximately 7900 3D and 550 2D finite elements. A hidden-line view of the finite element mesh is shown in Figure 7. All three-dimensional elements represent air; the air in the waveguide, through the finite thickness slot aperture, and above the groundplane out to a radius of 2.2λ from the center of the slot. ABC open boundary elements coat the outer surface of the air above the groundplane to simulate the air extending to infinity. Two-dimensional elements with the conductivity of copper coat the shell of the upper waveguide wall and the shell of the finite thickness slot aperture. The high conductivity of the copper elements simulates near perfect electric conductors without the use of Dirichlet boundary conditions. Two-dimensional elements are also used to terminate the waveguide in a matched impedance. Second order elements are used through the slot aperture and out to a radius of $3\lambda/8$ from the slot to capture the high field gradients throughout this region. Figure 8 illustrates the mesh detail at the slot. Four second order hexahedral finite elements

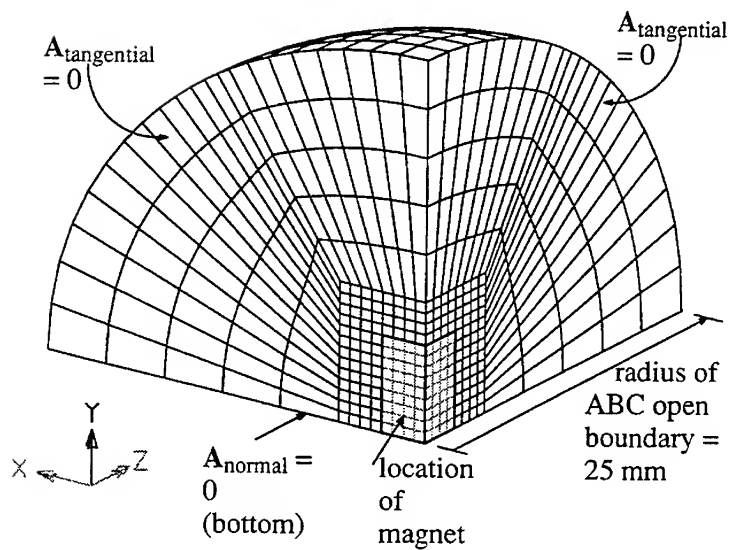


Fig. 4. Finite element mesh of one octant (2.92x2.92x6.48mm) of the magnet and air out to a radius of 25 mm. The boundary conditions properly model the symmetric flux pattern of this device.

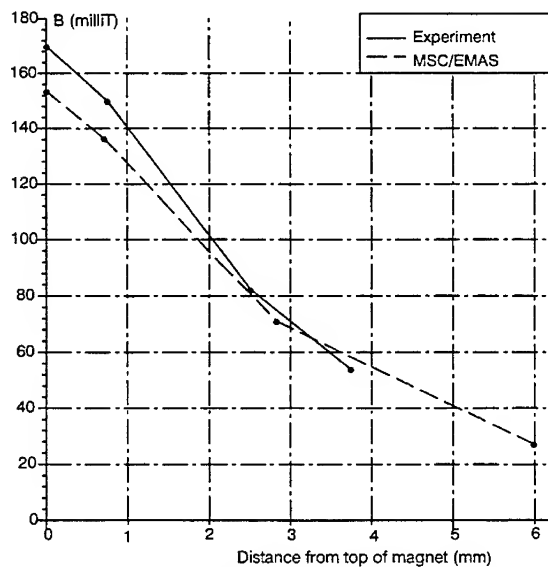


Fig. 5. Magnetic Flux Density values above the center of the north pole of the magnet, from MSC/EMAS and experimental results.

are used along the 0.068λ dimension of the slot to obtain a finite element solution free of distortion in this region. The mesh then transitions out to approximately 10 first order elements per λ out to the open boundaries.

The radiation pattern for an infinitely thin slot antenna is well-known and has an easily defined classical solution. The electric field in the E-plane is uniform at a constant radius. The electric field at a given radius in the H-plane is given as:

$$E(\theta)_{H\text{-plane}} = 20 \log E_{\max} \left[\frac{\cos\left(\left(\frac{\pi l}{\lambda}\right) \cos(\theta + 90^\circ)\right) - \cos\left(\frac{\pi l}{\lambda}\right)}{\cos(\theta)} \right] \quad (6)$$

where l is the slot length and λ is the free space wavelength.

Figure 9 depicts a graph of the electric field magnitude vs. the angle θ in the E and H planes at a radius of 1.95λ from the slot. The field strength in the E-plane is indeed close to uniform. The computed field strength in the H-plane is in excellent agreement with Equation 6. The characteristic impedance at the input port measures 1003Ω , 2% higher than theory. The magnitude of S_{11} measures -12.16 dB .

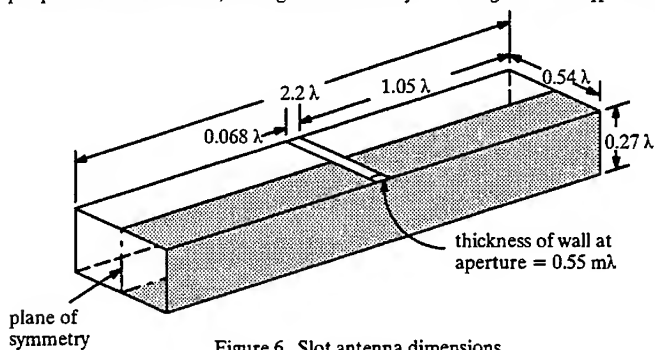


Figure 6. Slot antenna dimensions.

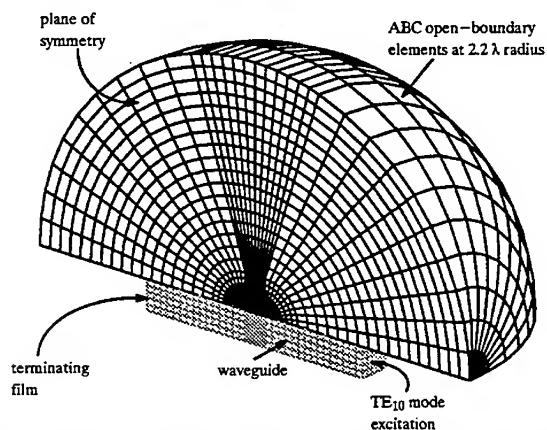


Figure 7. Finite element mesh of the air inside the waveguide and above the groundplane.

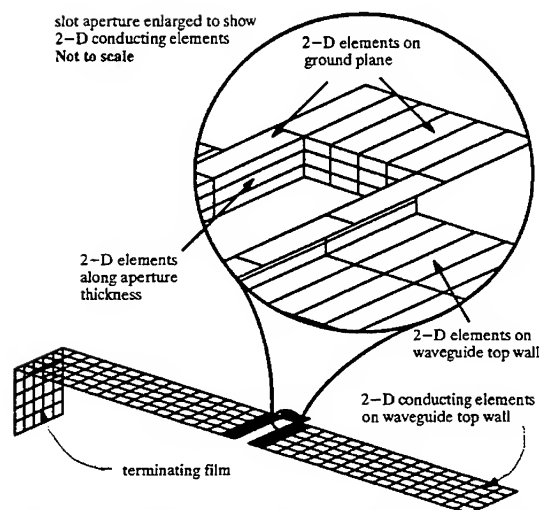


Figure 8. The finite thickness of the waveguide wall at the aperture is modeled as a shell of 2-D highly conductive elements. The 3-D elements are removed for clarity.

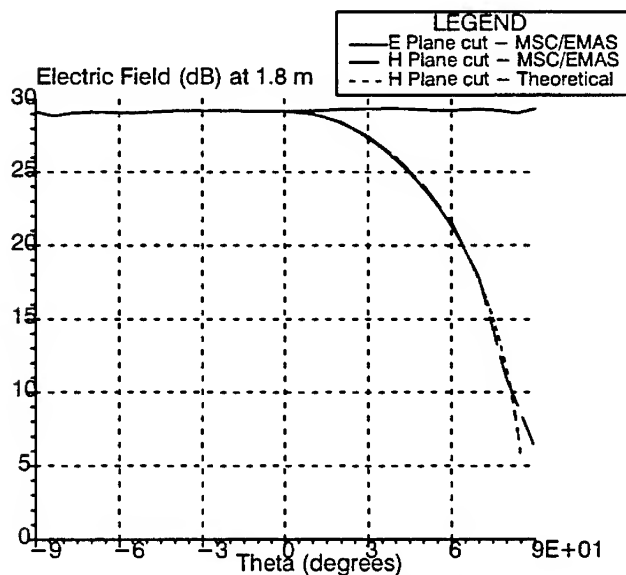


Figure 9. Computed electric field patterns in the E and H planes. The H-plane pattern is compared to Equation 5.

CONCLUSIONS

ABC finite elements have been shown able to accurately model infinite space in a wide variety of static and dynamic electromagnetic problems. An electrostatic example has obtained a voltage distribution that agrees closely with classical theory. A steady current flow example has obtained a resistance that agrees closely with a classical equation. A nonlinear magnetostatic example has obtained a magnetic field that agrees closely with measurements. Finally, a microwave antenna model has been discussed in detail, and it obtains radiation patterns that agree closely with classical theory.

REFERENCES

- [1] Jian-Ming Jin and John L. Volakis, "A Finite Element-Boundary Integral Formulation for Scattering by Three-dimensional Cavity-Backed Apertures," *IEEE Trans. on Antennas & Propagation*, January 1991, pp. 97-104.
- [2] John R. Brauer, "Open Boundary Finite Elements for Axisymmetric Magnetic and Skin Effect Problems," *Journal of Applied Physics*, November 1982, pp. 8366-8368.
- [3] R. Mittra, O. Ramahi, A. Khebir, R. Gordon, and A. Kouki, "A Review of Absorbing Boundary Condition for Two- and Three-Dimensional Electromagnetic Scattering Problems," *IEEE Trans. on Magnetics*, July 1989, pp. 3034-3042.
- [4] J. R. Brauer, S. M. Schaefer, Jin-Fa Lee and R. Mittra, "Asymptotic Boundary Condition for Three Dimensional Magnetostatic Finite Elements," *IEEE Trans. on Magnetics*, November 1991, pp. 5013-5015.
- [5] John R. Brauer and Franz Hirtenfelder, "Surface Integrals on 3D and 2D Finite Element Models for Skin Effect Excitations and Open Boundaries," *IEEE Trans. on Magnetics*, March 1992, pp. 1659-1662.
- [6] B. E. MacNeal, J. R. Brauer and R. N. Coppolino, "A General Finite Element Vector Potential Formulation of Electromagnetics Using a Time-Integrated Scalar Potential," *IEEE Trans. on Magnetics*, Sep. 1990, pp. 1768-1770.
- [7] John R. Brauer, R. Mittra, and J.-F. Lee, "Absorbing Boundary Condition for Vector and Scalar Potentials Arising in Electromagnetic Finite Element Analysis in Frequency and Time Domains," *Digest of IEEE Antennas & Propagation Society Symposium*, London, Ontario, June 1991.
- [8] John R. Brauer, J.-F. Lee and R. Mittra, "Absorbing Boundary Condition for Three Dimensional Finite Element Models with Magnetic Vector and Time-Integrated Scalar Potentials," *Digest of IEEE Antennas & Propagation Society Symposium*, Chicago, July 1992.
- [9] J. D. Jackson, *Classical Electrodynamics*, John Wiley & Sons, New York, 1962, pp. 42-44.
- [10] Robert Plonsey and Robert E. Collin, *Principles and Applications of Electromagnetic Fields*, McGraw-Hill, New York, 1961, pp. 72 and 186.
- [11] Constantine A. Balanis, *Antenna Theory Analysis and Design*, Harper & Row, New York, 1982, p. 120.

APPLICATION OF EXPLICIT FINITE ELEMENTS TO MAXWELL'S EQUATIONS

M. Hafez and P. English

Department of Mechanical, Aeronautical and Materials Engineering
University of California, Davis
Davis, CA 95616

ABSTRACT

A finite element method for the solution of Maxwell's equations is presented. The coupling problem is addressed by solving augmented equations with consistent second order space and time derivatives. A special corner treatment is introduced and the results are generated for cylinder and NACA 0012 airfoil.

1. INTRODUCTION

Lately, there is a trend to transfer existing technology from computational fluid dynamics to computational electromagnetic (CEM). Most of the technology shift entails finite difference schemes. While differencing schemes may be adequate for problems involving simple geometry on Cartesian grids, finite elements treat easily problems with complex configuration. Although methods such as the Chimera overset gridding scheme (see Benek, Buning and Steger [1]) can be applied, presently they are not widely used for CEM. The difficulties arise from the interpolation errors and the implementation of the method. The interpolation between grids with different speeds of wave propagation on different grid sizes contaminates the CEM calculations. Differencing schemes also suffer from the handicap of having material boundaries not always located on grid points. On the other hand, in the finite element method grid points can be placed at material boundaries. Many CEM finite element methods have been developed for the frequency domain. For the time domain, Lee and Madsen [2] use separate shape functions for the electric and magnetic fields to create the effect of a staggered grid. Also, a method based on the second order wave equation has been developed by Lynch and Paulsen [3].

2. METHOD

Maxwell's equations will be solved as a system of first order hyperbolic partial differential equations on unstaggered grid. The governing equations are:

$$\begin{aligned}\nabla \times \vec{E} &= -\frac{\partial \vec{B}}{\partial t} & \nabla \cdot \vec{D} &= \rho & \vec{D} &= \epsilon \vec{E} \\ \nabla \times \vec{H} &= \frac{\partial \vec{D}}{\partial t} + \vec{J} & \nabla \cdot \vec{B} &= 0 & \vec{B} &= \mu \vec{H}\end{aligned}\quad (1)$$

where \vec{E} is the electric field, \vec{H} is the magnetic field, \vec{D} is the electric displacement, \vec{B} is the magnetic induction, \vec{J} is the current density, ρ is the charge density, ϵ is the material dielectric constant, and μ is the material permeability.

For propagation in lossless and source free media, $\bar{J} = 0$, $\rho = 0$, and $\nabla \cdot \bar{B} = 0$ are automatically satisfied on the differential level.

In two dimensions, the equations decouple into the transverse electric (TE) and transverse magnetic mode (TM). In the present method, the TM mode is solved.

$$\frac{\partial(\epsilon E^z)}{\partial t} = \frac{\partial H^y}{\partial x} - \frac{\partial H^x}{\partial y} \quad \frac{\partial(\mu H^x)}{\partial t} = -\frac{\partial E^z}{\partial y} \quad \frac{\partial(\mu H^y)}{\partial t} = \frac{\partial E^z}{\partial x} \quad (2)$$

Application of standard Galerkin fine element will lead to grid decoupling (see S. Ray [4]). In the present method, weighted time balanced coupling terms are introduced in the same manner discussed in previous work by the authors [5].

$$\begin{aligned} \frac{\partial(\epsilon E^z)}{\partial t} &= \frac{\partial H^y}{\partial x} - \frac{\partial H^x}{\partial y} + \delta(\mu\epsilon \frac{\partial^2 E^z}{\partial t^2} - \frac{\partial^2 E^x}{\partial x^2} - \frac{\partial^2 E^y}{\partial y^2}) \\ \frac{\partial(\mu H^x)}{\partial t} &= -\frac{\partial E^z}{\partial y} + \delta(\mu\epsilon \frac{\partial^2 H^x}{\partial t^2} - \frac{\partial^2 H^x}{\partial x^2} - \frac{\partial^2 H^y}{\partial y^2}) \\ \frac{\partial(\mu H^y)}{\partial t} &= \frac{\partial E^z}{\partial x} + \delta(\mu\epsilon \frac{\partial^2 H^y}{\partial t^2} - \frac{\partial^2 H^y}{\partial x^2} - \frac{\partial^2 H^x}{\partial y^2}) \end{aligned} \quad (3)$$

Where δ is a small parameter of order of the element area. The coupling terms do not vanish on the discrete level thus joining adjacent nodes without the drawback of contaminating the solution with high artificial viscosity dissipation and without the complexity of having to manage two sets of shape functions. At solid walls and far field boundaries, the extra terms are dropped.

On the boundary of a perfect electric conductor (PEC), the electric field tangential to the surface is zero, and the component of the magnetic field normal to the surface vanishes.

$$E^z = 0 \quad \bar{B} \cdot \hat{n} = 0 \quad (4)$$

In the far field an absorbing boundary condition is imposed to allow the wave to travel out of the solution domain without significant reflection.

$$\frac{\partial \bar{Q}}{\partial t} = -\nabla \bar{Q} \cdot \hat{n} \quad \bar{Q} = \begin{bmatrix} E^z \\ H^x \\ H^y \end{bmatrix} \quad (5)$$

\bar{Q} is approximated with piece wise continuous elemental functions

$$\bar{Q}(x, y) = \sum_{i=1}^N \bar{Q}_i \phi_i(x, y) \quad (6)$$

where $\phi(x,y)$ are bilinear quadrilateral shape functions. With the second order terms integrated by parts, equations (3) are spatially integrated over the solution domain using the Galerkin finite element method.

The field components can be separated into scattered, \vec{Q}^S , and incident, \vec{Q}^I , fields. Regions in the solution domain where the incident field (forcing function) is subtracted out are referred to as the scattered field zones. Regions where both the incident and scattered field exist are known as total field, \vec{Q}^T , zones. Integration across different zones requires addition or subtraction of the incident component for consistency.

$$\vec{Q}^T = \vec{Q}^S + \vec{Q}^I \quad (7)$$

The elemental contributions are:

$$M_{\text{elemental}} = \begin{bmatrix} \iint_{\Omega} \epsilon \phi \phi^T dA & 0 & 0 \\ 0 & \iint_{\Omega} \mu \phi \phi^T dA & 0 \\ 0 & 0 & \iint_{\Omega} \mu \phi \phi^T dA \end{bmatrix} \quad K_{\text{elemental}} = \begin{bmatrix} 0 & -\iint_{\Omega} \phi \frac{\partial \phi^T}{\partial y} dA & \iint_{\Omega} \phi \frac{\partial \phi^T}{\partial x} dA \\ -\iint_{\Omega} \phi \frac{\partial \phi^T}{\partial y} dA & 0 & 0 \\ \iint_{\Omega} \phi \frac{\partial \phi^T}{\partial x} dA & 0 & 0 \end{bmatrix}$$

$$k_2 = \iint_{\Omega} \frac{1}{\mu \epsilon} \left(\frac{\partial \phi}{\partial x} \frac{\partial \phi^T}{\partial x} + \frac{\partial \phi}{\partial y} \frac{\partial \phi^T}{\partial y} \right) dA \quad K_{2\text{elemental}} = - \begin{bmatrix} k_2 & 0 & 0 \\ 0 & k_2 & 0 \\ 0 & 0 & k_2 \end{bmatrix} \quad (8)$$

Assembling the elemental contributions results in the following system of equations:

$$M \frac{\partial \vec{Q}}{\partial t} = K_1 \vec{Q} + \delta \left(M \frac{\partial^2 \vec{Q}}{\partial t^2} - K_2 \vec{Q} \right) \quad (9)$$

where M is the mass matrix and K_1 and K_2 are stiffness matrices. A lumped mass matrix is then formed by adding the off diagonal terms into the diagonal and then zeroing the off diagonal terms. Mass lumping results in a scheme which allows efficient solution of the equations via explicit time marching.

At the boundary of the PEC, the normal component of the magnetic field vanishes. This boundary condition was implemented by rotating the two magnetic equations based on Cartesian coordinates (2) to normal and tangential coordinates local to the boundary element.

$$\int_{\partial\Omega} \frac{\partial \mu \vec{H}_{\text{tangential}}}{\partial \theta} \psi(x,y) d\Gamma = \int_{\partial\Omega} \frac{\partial \vec{E}_n}{\partial \theta} \psi(x,y) d\Gamma \quad \int_{\partial\Omega} \frac{\partial \mu \vec{H}_{\text{normal}}}{\partial \theta} \psi(x,y) d\Gamma = - \int_{\partial\Omega} \frac{\partial \vec{E}_t}{\partial \theta} \psi(x,y) d\Gamma \quad (10)$$

where $\psi(x,y)$ is the shape function of the linear one dimensional boundary element, and the partial derivative with respect to θ is the partial derivative in the tangential direction. Since the normal component of the magnetic field is 0, only the equation for the tangential magnetic field needs to be solved.

$$\int_{\partial\Omega} \frac{\partial \mu_1^{\text{tangential}}}{\partial x} \psi(x,y) dl = \int_{\partial\Omega} \frac{\partial \bar{\psi}}{\partial x} \psi(x,y) \cdot n_x(x,y) dl + \int_{\partial\Omega} \frac{\partial \bar{\psi}}{\partial y} \psi(x,y) \cdot n_y(x,y) dl \quad (11)$$

where n_x and n_y respectively are the x and y components of the normal vector evaluated from the surface normal vectors specified at the boundary nodes. The solution for the tangential magnetic field is then rotated back to Cartesian coordinates so the values would be available for integration over Ω . The tangential electric field boundary condition is imposed by setting E^z on the boundary to zero.

The far field boundary condition (5) is imposed with:

$$\int_{\partial\Omega} \frac{\partial \sqrt{\mu \epsilon} \bar{Q}}{\partial t} \phi(x,y) dl = - \int_{\partial\Omega} \frac{\partial \bar{Q}}{\partial x} \phi(x,y) \cdot n_x(x,y) dl - \int_{\partial\Omega} \frac{\partial \bar{Q}}{\partial y} \phi(x,y) \cdot n_y(x,y) dl \quad (12)$$

3. CORNER SINGULARITY

While the scatterer boundary condition described in the above section is adequate for smooth surfaces, special treatment must be applied to corners to account for discontinuity and singularity in the magnetic field. Improper treatment of corners will result in unacceptable contamination and instability. In the present method corners are modeled as a segment of an infinitesimal cylinder. In the limit as the radius goes to zero, the cylinder segment shrinks to a single point.

Using figure 2 as a reference, the corner point is modeled as two linear elements, B1-B2 and B2-B3. The locations of B1 and B3 were chosen such that elements A-B and B-C are tangent to the infinitesimal cylinder. Since edge B-E is a common edge between two elements the location of the point, B2, on the cylinder for the edge must be the same point for the two common elements to maintain continuity between edges. The location of B2 is chosen such that in the limit as the radius of the cylinder shrinks to zero, the infinitesimal elements B1-B2, and B2-B3 approach the corner location at the same rate. The location of B2 is therefore the bisector of the circumference between B1 and B3. Accompanying the location of each point B1, B2, B3, is a normal and tangential vector to the surface of the cylinder which is used to compute the Cartesian components of the tangential magnetic field.

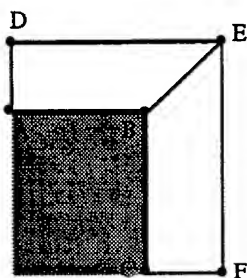


Figure 1 Physical corner.

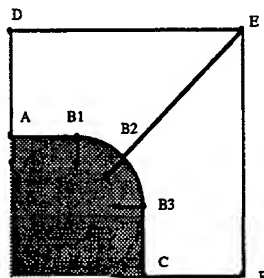


Figure 2 Corresponding model of the corner as an infinitesimal cylinder segment.

The tangential magnetic field at the corner (B) is calculated as stated in section 2 according to the model of figure 1. The result for node B is then rotated to Cartesian components for nodes B1, B2, B3 using the tangential vectors at the locations on the cylinder. Note that the nodes B1, B2, B3 which represent the corner has the same tangential magnetic field, but differ in Cartesian components.

The actual calculations for the element A-B-E-D shown in figure 1 are done using the values of the Cartesian components at B as the average of the corresponding quantities B1 and B2. Similarly for the element B-C-F-E, the average of the Cartesian components of the tangential H at B2 and B3 is used.

4. TIME INTEGRATION

The equations are advanced in time by a centered difference scheme. On non-orthogonal grids, the solution may be distorted due to the mass lumping. To correct for the distortion, the implicit equation (9) could be solved using Jacobi iteration or by the method developed by Donea [6] and used by Lee and Madsen [2]. Only three or four iterations may be needed.

$$\begin{aligned} M_L \bar{Q}_{(0)}^{n+1} &= f^n && \text{for the initial prediction.} \\ M_L \bar{Q}_{(iter+1)}^{n+1} &= f^n - (M - M_L) \bar{Q}_{iter}^{n+1} && \text{for subsequent iterations.} \end{aligned} \quad (13)$$

5. RESULTS

Scattering from a circular cylinder was used as a test case. For a practical test of the method, scattering was also computed for a NACA 0012 airfoil. For all cases unless stated otherwise, a plane wave coming from the left side of the mesh is incident on the scatterer.

5.1 Circular Cylinder Results

For the circular cylinder, a grid of 126 points circumferentially and 75 points radially was used. The incident wave was of electrical size $ka=5$. The far field was 3.18 wavelengths away from the body. Contours of the fields, surface current density, and bistatic radar cross section (RCS) were generated after 5.97 wavelengths had elapsed (see fig. 3).

The contours of the circular cylinder were very smooth. The current density and the RCS are in good agreement with series approximation results.

5.2 NACA 0012 Airfoil Results

For the airfoil, a grid of 100 points circumferentially and 100 points radially was used. The wavelength was 0.2π of the chord length. Contours of the fields, surface current density, and bistatic radar cross section (RCS) were generated after 7.16 wavelengths had elapsed (see fig. 4).

5.3 NACA 0012 Airfoil with Wave incident from Bottom

In order to compare with published results, a computation of a NACA 0012 airfoil with a wave incident from the bottom. The incident wavelength was 10 percent of the chord length. Bistatic RCS was generated after 15 wavelengths had elapsed. The grid had 100 nodal point on the body and 100 points radially.

The bistatic RCS (fig. 4) was compared with the results of Vinh [7]. The results matched well except at 0 and 180 theta. This deviation could be due to the RCS being calculated from the surface current density with a singular point represented by a finite value or due to grid density. The singularity will affect the RCS. The forward and backward scattering are practically in good agreement.

6. CONCLUSION

The results show that the present finite elements scheme can be used for CEM problems. The method is simple since only one mesh is needed for the \vec{E} and \vec{H} fields. Applications to more complex geometry using unstructured grids are under progress.

REFERENCES

- [1] Benek, J.A., Buning, P.G. and Steger, J.L., "A 3-D Chimera Grid Embedding Technique," AIAA 85-1523, July 1985.
- [2] Lee, R.L., Madsen, N.K., "A Mixed Finite Element Formulation for Maxwell's Equations in the Time Domain," *J. Comput. Phys.*, vol. 88, 1990, pp. 284-304.
- [3] Paulsen, K.D., Lynch, D.R., "Finite Element Maxwell Equations Solution in the Time Domain Using a Second Order Equation," *Proceedings of the 1989 IEEE AP-S International Symposium*, pp. 1100-1103, San Jose, CA June, 1989.
- [4] Ray, S.L., "Grid Decoupling in Finite Element Solutions of Maxwell's Equations," *IEEE Trans. Antennas Propagat.*, vol. 40, April, 1992, pp. 443-445.
- [5] English, P. and Hafez, M., "A Time Domain Method for Electromagnetic Wave Propagation and Scattering," *Proceedings of the 1992 IEEE AP-S International Symposium*, Chicago, IL, July 1992.
- [6] Donea, J., and Guiliani, S., *Int. J. Num. Methods Fluids* vol. 1, 1981, pp. 63.
- [7] Vinh, H., Dwyer, H.A., van Dam, C.P., "Finite-Difference Algorithms for the Time-Domain Maxwell's Equations - A Numerical Approach to RCS Analysis," AIAA 92-2989, July 1992.

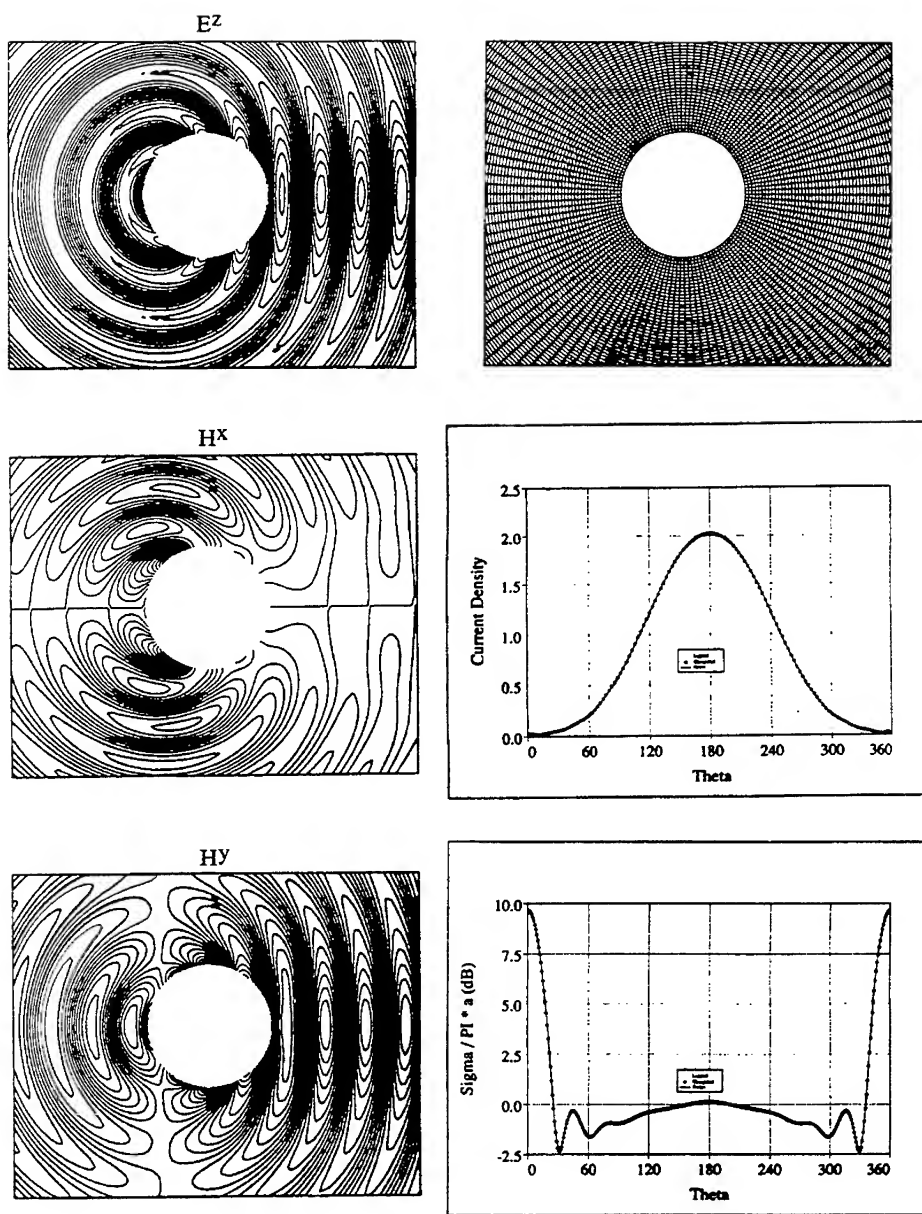


Figure 3. Results for scattering from circular cylinder.

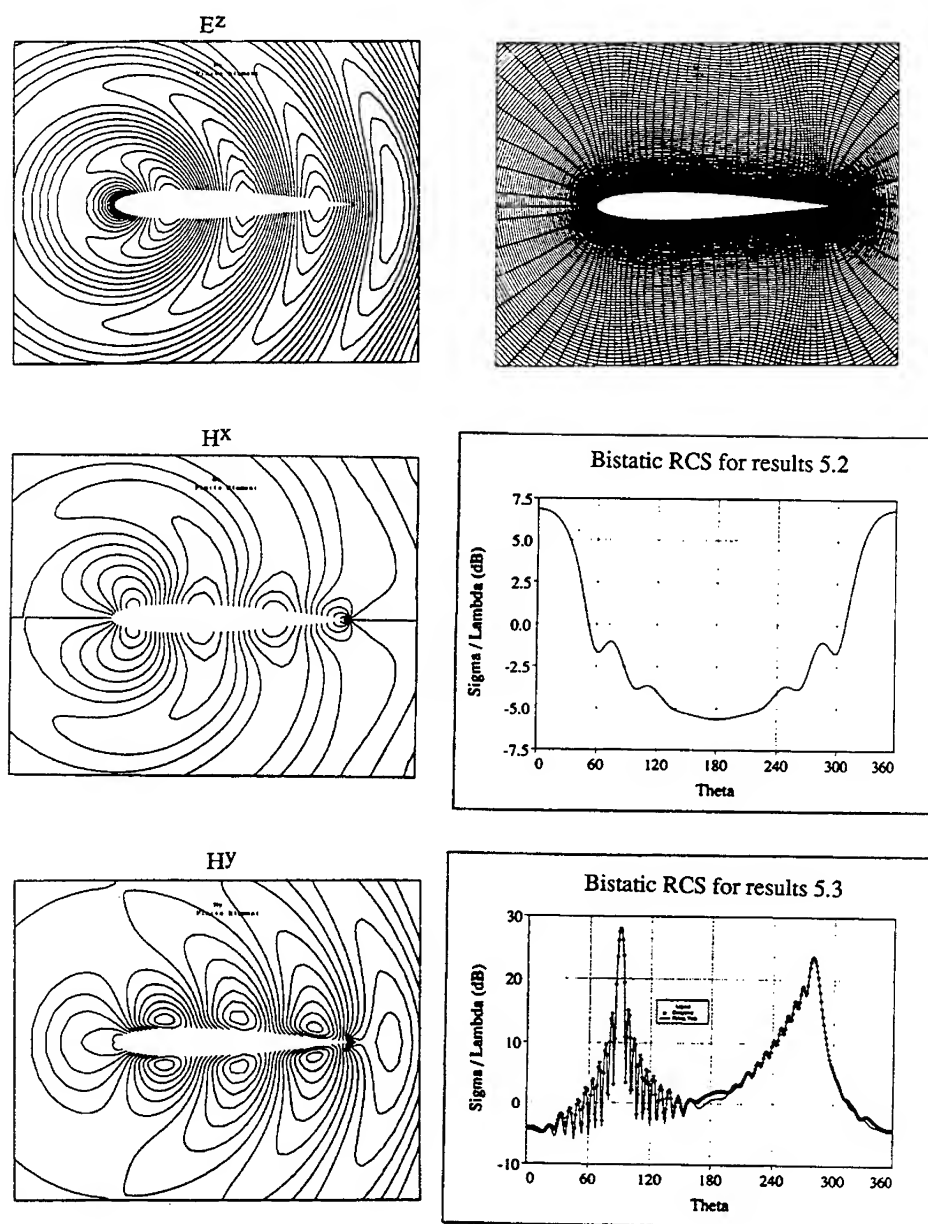


Figure 4. Results for scattering from NACA 0012 airfoil.

MICROSTRIP DISCONTINUITY ANALYSIS BY TIME DOMAIN FINITE ELEMENTS

J.O.Y. Lo*, A. Konrad*, J.L. Coulomb*, and J.C. Sabonnadiere*

*University of Toronto
Toronto, Canada, M5S 1A4

*L.E.G., E.N.S.I.E.G., BP 46,
38402 St Martin d'Heres, France

Abstract - A time domain finite element method is employed in conjunction with the planar circuit model to analyze microstrip discontinuities. By simulating the wave propagation in the circuit using the leap-frog scheme with appropriate boundary conditions enforced along the circuit periphery, the method is able to efficiently calculate the fields and scattering parameters for a variety of microstrip circuits.

Introduction

In microstrip circuits, a discontinuity arises whenever there is an abrupt variation from a straight and homogeneous line structure. This can be in the form of a bend, a step in width, a T junction, or even a change in the dielectric constant [2-4]. Though structurally simple, these discontinuities are the basic building blocks of many microstrip integrated circuits such as the microstrip filters, branch line couplers, and even patch antennas. Hence, the accurate analysis and characterization of microstrip discontinuities remains as an important and ongoing issue in microwave integrated circuit design [1,2].

Conventional analyses use one-dimensional transmission line models and lumped elements [2-4]. These approaches, however, are based on quasistatic approximations, and therefore their results are accurate for relatively low frequencies only. A better approach would be to simulate the wave propagation and scattering phenomena so that the results are also valid at higher frequencies. This idea is reflected in the recent development of the time domain finite difference methods [5,6]. The advantage of these methods over frequency domain methods such as the spectral-domain approach [7] and the moment method [8,9] is that both the time domain and the frequency domain data is readily available. However, due to the nature of finite differences, the implementation of these methods to discontinuities of arbitrary shape is difficult.

This paper describes a point-matched time domain finite element method [10] to solve microstrip discontinuities using the planar circuit concept [11,12]. This method has the advantage of the time domain analysis and yet it is more versatile than the finite difference method. To illustrate its validity and flexibility, the method is implemented on several examples of microstrip discontinuities.

Planar Circuit Model

The general concept of a planar circuit was introduced by Okoshi and Miyoshi [11] as an electrical component that has two dimensions comparable to the wavelength and a third dimension that is much smaller than the wavelength. A microstrip circuit is an example of a planar circuit because when the substrate thickness is small compared to the wavelength, the field variation in the vertical direction can be neglected. As a result, the fields can be assumed to vary only in the horizontal conductor plane (xy plane). This idea has been proved to be effective and practical because it allows the analysis of microstrip circuits of arbitrary

shape within a relatively short computation time [4,6,13-16].

In the planar circuit model, the fields inside the circuit are characterized by the following pair of two-dimensional time-dependent partial differential equations [6,16]

$$\nabla V(x, y, t) = -\mu d \frac{\partial \mathbf{J}(x, y, t)}{\partial t} \quad (1)$$

$$\nabla \mathbf{J}(x, y, t) = -\frac{\epsilon}{d} \frac{\partial V(x, y, t)}{\partial t} \quad (2)$$

with proper boundary conditions along the circuit periphery. In the above equations, V is the voltage wave function, \mathbf{J} is the surface current density vector in the plane conductor, d is the substrate thickness, and ϵ and μ are the permittivity and permeability of the substrate material, respectively.

Time Domain Finite Element Method

The time domain point-matched finite element method [10,19] is chosen to solve the above pair of equations. Because it is well suited to model the irregular boundaries of microstrip circuits. Unlike the time domain finite difference method [5,6], where stepped approximations are used to model the curved boundaries, the time domain finite element method allows a smoother approximation.

In the finite element method, the region of interest (xy plane) is discretized into a finite number of regions called elements. Each element has several points called interpolation nodes. As a result, the continuous functions V and \mathbf{J} can be approximated by

$$V(x, y, t) = \sum_{i=1}^M \phi_i(x, y) V_i(t) \quad (3)$$

$$\mathbf{J}(x, y, t) = \sum_{j=1}^N \Psi_j(x, y) \mathbf{J}_j(t) \quad (4)$$

where M and N are the number of nodes of the V and \mathbf{J} finite element grids, respectively, and $\phi_i(x, y)$ and $\Psi_j(x, y)$ are the basis functions which interpolate the field within each element using the values at the interpolation nodes. In this paper, the linear isoparametric quadrilateral element will be used [17,18].

To further simplify the computation, a pair of complementary grids as shown in Fig. 1 are used. Note that the voltage grid is slightly larger than the current density grid. This means that the microstrip circuit will be modeled with some errors. However, the advantage of doing so is that each voltage element contains an interpolation node for the current density and each current density element also contains an interpolation node for the voltage. As a result, (1) and (2) can be approximated by

$$\frac{dJ_j(t)}{dt} = -\frac{1}{\mu d} \sum_{i=1}^K \nabla \phi_i(x_j, y_j) V_i(t) \quad (5)$$

$$\frac{dV_i(t)}{dt} = -\frac{d}{e} \sum_{j=1}^K \nabla \Psi_i(x_i, y_i) J_j(t) \quad (6)$$

where $j=1,2,\dots,N$, $i=1,2,\dots,M$, and $K=4$ in this case.

The time derivatives are approximated by finite differences in the leap-frog scheme with V and J discretized in time as follows:

$$V^n = V(t = n\Delta t) \quad (7)$$

$$J^{n+1/2} = J(t = (n+1/2)\Delta t) \quad (8)$$

where $n=0,1,2,\dots$. Hence, the time derivatives in (7) and (8) can be expressed as:

$$\left. \frac{dJ_j}{dt} \right|_{n\Delta t} = \frac{J_j^{n+1/2} - J_j^{n-1/2}}{\Delta t} \quad (9)$$

$$\left. \frac{dV_i}{dt} \right|_{(n+1/2)\Delta t} = \frac{V_i^{n+1} - V_i^n}{\Delta t} \quad (10)$$

As a result, (5) and (6) can be written as follows:

$$J_j^{n+1/2} = J_j^{n-1/2} - \frac{\Delta t}{\mu d} \sum_{i=1}^K \nabla \phi_i(x_j, y_j) V_i^n \quad (11)$$

$$V^{n+1} = V^n - \frac{d\Delta t}{e} \sum_{j=1}^K \nabla \Psi_i(x_i, y_i) J_j^{n+1/2} \quad (12)$$

for $n=0,1,2,\dots$. Once the initial conditions for V at $t=0$ are known, (11) and (12) can be used alternately to simulate the wave propagation in the microstrip circuit.

Boundary Conditions

The boundary conditions along the circuit periphery where there are no external connections are the homogenous Neumann type since current flow must be tangential. In the finite element method, the elements are distorted to model the circuit boundaries and the homogeneous *Neumann* boundary condition can be satisfied by interpolating the voltage fields along the inward normal directions within the boundary elements. This is illustrated in Fig. 2. At each time step, instead of using (11) and (12), the interior voltage values are used to update the open boundary nodes of the microstrip circuits.

At the coupling ports of the microstrip circuit, absorbing boundary conditions are used because the open circuit relation is no longer valid. At these boundaries, the waves must be allowed to propagate out of the ports and at the same time the incident source voltage waves must also be allowed to propagate into the ports. To achieve these conditions, Taflové's first order absorbing boundary conditions are used [20].

Fringing Fields of Microstrip Circuits

To account for the complicated nature of the fringing fields of microstrip circuits, the permittivities and widths of the microstrip lines are adjusted according to the Wheeler, Schneider and Hammerstad formulae [21]. The authors find that this model is adequate for most applications. However, a more accurate representation based on the planar waveguide model of the microstrip lines [22] can be used in the case where the frequency dependence of the effective widths and effective permittivities must be accounted for.

Stability Considerations

The two partial differential equations in (1) and (2) constitute a hyperbolic system. For a uniform square grid with an element size of h , it has been proven [23] that the solution to the leap-frog scheme is stable if the relationship given by $u\Delta t \leq h$ is satisfied everywhere inside the grid (u denotes the velocity of propagation). For the case of a grid with distorted elements, Cangellaris *et al.* have pointed out that this stability criterion can still be used provided that "each of its irregular elements is large enough to contain a regular element of the grid" [10].

Excitations

The frequency response of the microstrip circuit can be obtained by applying a sine wave at the excitation port until steady-state is observed at the output port. Another approach would be to use a Gaussian pulse to excite the microstrip circuit, and from the transient response at the output port to extract the frequency response using the Fourier transform. This approach has the advantage that the results for a wide range of frequencies can be obtained using one computation as demonstrated in [5,24]. However, for simplicity, the sine wave approach is used in this paper.

Results

The method described above was implemented as a user-friendly package which includes: (1) a pre-processor which allows the user to specify the grid points as well as the boundary conditions, (2) a solver that simulates the wave propagation using the leap-frog scheme and enforces the assigned boundary conditions, and (3) a post-processor which displays the spatial waveforms at various time steps.

Figures 3(a) and (b) show the dimensions of a single and double open stub discontinuity, respectively. Both circuits have a dielectric constant of 9.9 with a substrate thickness of 0.254 mm. In the finite element models, the single stub was modelled with square elements of size $h = 0.046$ mm, and the double stub structure was modelled with $h = 0.02875$ mm. Figures 4(a) and (b) show the transmission magnitude as a function of frequency in the range from 6 to 26 GHz in comparison with the calculated and measured

results from Giannini *et. al.* [25]. As can be seen in the figures, the finite element method is able to predict the field behaviour within a reasonable accuracy at lower frequencies. The large discrepancies at high frequencies seem to suggest the need for a grid with finer spatial subdivisions.

One of the disadvantages of the finite difference method is that a stair-stepped approximation must be used to model a curved boundary. It has been shown that the errors due to this approximation may contaminate the field calculations significantly if the grid is not fine enough [26]. The finite element method, however, overcomes this limitation by allowing the elements to be distorted to model the boundary. Fig. 5(a) shows the dimensions of a microstrip annular ring which had been analyzed and measured by D'Inzeo *et. al.* using a modal expansion technique [27]. For finite element calculations, the widths have been adjusted according to the Wheeler, Schneider and Hammerstad formulae [21]. Note that by taking advantage of the symmetry, only half of the problem needs to be solved. Fig. 5(b) shows the grid that was used for the finite element calculations.

Figures 6(a) and (b) show calculated frequency responses along with the results from [27]. By comparing the results, one finds that there is a slight shift in dip frequencies of about 6% in the return loss of the finite element calculation. This is probably due to the fact that in the modal expansion analysis of D'Inzeo, effective parameters based on the planar waveguide model [22] were employed at each frequency, whereas in our analysis, the effective parameters were computed using the Wheeler, Schneider and Hammerstad formulae only at one frequency.

Conclusions

The paper has presented a time domain finite element method for calculating the frequency dependent scattering parameters of microstrip discontinuities. In this method, the elements are allowed to be distorted to model the circuit boundary, thus avoiding the stair-stepped approximation. In addition, this formulation does not require the evaluation and storage of a matrix of unknowns. Hence, the method is feasible for solving a large number of unknowns. However, the stability of the algorithm for the case of non-uniform grid must be further defined. Experimentation with the method reveals that the method seems to work well when the finite element grids are distorted in a conformal way. However, when this is not the case, the results will be unstable even though it appears to satisfy the criterion $\mu\Delta t \leq h$. Hence, more work has to be done in investigating the stability of the method in relation to the necessary grid generation for the case of non-uniform grid.

REFERENCES

- [1] W.K. Gwarek and C. Mroczkowski, "An inhomogeneous two-dimensional model for the analysis of microstrip discontinuities," *IEEE Trans. Microwave Theory Tech.*, vol. MTT-39, no. 9, pp.1655-1658, Sept. 1991.
- [2] B.C. Wadell, *Transmission Line Design Handbook*, Norwood, MA:Artech House, 1991.

- [3] R.K. Hoffmann, Handbook of Microwave Integrated Circuits, Norwood, MA:Artech House, 1987.
- [4] K.C. Gupta, R. Garg, and R. Chadha, Computer-Aided Design of Microwave Circuit, Dedham, MA:Artech House, 1981.
- [5] X. Zhang and K.K. Mei, "Time domain finite difference approach to the calculation of the frequency-dependent characteristics of the microstrip discontinuities," IEEE Trans. Microwave Theory Tech., vol. MTT-36, no. 12, pp.1775-1787, Dec. 1988.
- [6] W.K. Gwarek, "Analysis of arbitrarily shaped two-dimensional microwave circuits by finite-difference time-domain method," IEEE Trans. Microwave Theory Tech., vol. MTT-36, no. 4, Apr. 1988.
- [7] R.H. Jansen, "The spectral-domain approach for microwave integrated circuits," IEEE Trans. Microwave Theory Tech., vol. MTT-33, pp.1043-1056, Oct. 1985.
- [8] P.B. Katehi and N.G. Alexopoulos, "Frequency-dependent characteristics of microstrip discontinuities in millimeter-wave integrated circuit," IEEE Trans. Microwave Theory Tech., vol. MTT-33, pp.1029-1035, Oct. 1985.
- [9] S.-C. Wu, H.-Y. Yang, N.G. Alexopoulos, and I. Wolff, "A rigorous dispersive characterization of microstrip cross and T junctions," IEEE Trans. Microwave Theory Tech., vol. MTT-38, pp.1837-1844, Dec. 1990.
- [10] A.C. Cangellaris, C.-C. Lin, and K.K. Mei, "Point-matched time domain finite element methods for electromagnetic radiation and scattering," IEEE Trans. Antennas and Propagation, vol. AP-35, no. 10, pp.1160-1173, Oct. 1987.
- [11] T. Okoshi and T. Miyoshi, "The planar circuit - An approach to microwave integrated circuitry," IEEE Trans. Microwave Theory Tech., vol. MTT-20, no. 4, pp.245-252, Apr. 1972.
- [12] T. Okoshi, Planar Circuits for Microwaves and Lightwaves, Berlin:Springer-Verlag, 1985.
- [13] P. Silvester, "Finite element analysis of planar microwave networks," IEEE Trans. Microwave Theory Tech., vol. MTT-21, no.2, pp.104-108, Feb. 1973.
- [14] A. Konrad, T.J. Sober, C.T.M. Choi, L.S. Rider, and J.J. Komiak, "Planar Multipoint microwave network analysis by the finite element method" IEEE Trans. Magn., vol. 25, no.4, pp.2941-2943, July 1989.
- [15] P. Arcioni, M. Bressan, and G. Conciauro, "A new algorithm for the wide-band analysis of arbitrarily shaped planar circuits," IEEE Trans. Microwave Theory Tech., vol. MTT-36, no.10, pp.1426-1437, Oct. 1988.
- [16] A. Konrad and J.O.Y. Lo, "Time domain solutions of planar circuits", to appear in Journal of Electromagnetic Waves and Applications (JEWAW) 1992.

- [17] I. Ergatoudis, B.M. Irons, and O.C. Zienkiewicz, "Curved isoparametric quadrilateral elements for finite element analysis," Int. J. Solids Structures, vol. 4, pp.31-42, 1968.
- [18] L. Segerlind, Applied Finite Element Analysis. New York: John Wiley, 1976.
- [19] J. Joseph, T.J. Sober, K.J. Gohn, and A. Konrad, "Time domain analysis by the point-match finite element method", IEEE Trans. Magn., vol. 27, no.5, pp.3852-3855, Sept. 1991.
- [20] A. Taflove and M.E. Brodwin, "Numerical solution of steady-state electromagnetic scattering problems using the time-dependent Maxwell's equations," IEEE Trans. Microwave Theory Tech., vol. MTT-23, no.8, pp.623-630, Aug. 1975.
- [21] K.C. Gupta, R. Garg, and I.J. Bahl, Microstrip Lines and Slotlines. Dedham, MA: Artech House, 1979.
- [22] G. Kompa and R. Mehran, "Planar waveguide model for calculating microstrip components," Electron. Lett., vol.11, pp.459-460, 1975.
- [23] S. Abarbanel and D. Gottlieb, "A note on the leap-frog scheme in two and three dimensions," J. Comp. Phys., vol.21, pp.351-355, 1976.
- [24] D.M. Sheen, S.M. Ali, M.D. Abouzahra, and J.A. Kong, "Application of the three-dimensional finite difference time-domain method to the analysis of planar microstrip circuits," IEEE Trans. Microwave Theory Tech., vol. MTT-38, no.7, pp.849-857, July 1990.
- [25] F. Giannini, G. Bartolucci, and M. Ruggieri, "Equivalent circuit models for computer aided design of microstrip rectangular structures," IEEE Trans. Microwave Theory Tech., vol. MTT-40, no.2, pp.378-368, Feb. 1992.
- [26] A.C. Cangellaris and D.B. Wright, "Analysis of the numerical error caused by the stair-stepped approximation of a conducting boundary in FDTD simulations of electromagnetic phenomena," IEEE Trans. Antennas Propagat., vol. AP-39, no.10, pp.1518-1525, Oct. 1991.
- [27] G. D'Inzeo, F. Giannini, and R. Sorrentino, "Microwave planar networks: The annular structure," Electron. Lett., vol.14, pp.526-528, Aug. 1978.

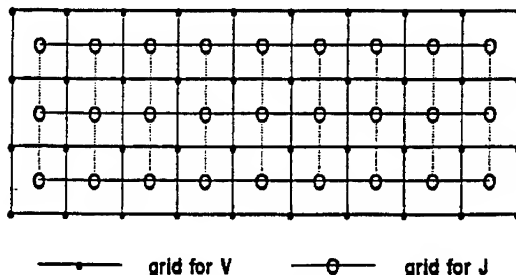


Fig. 1 A pair of complementary grids for V and J.

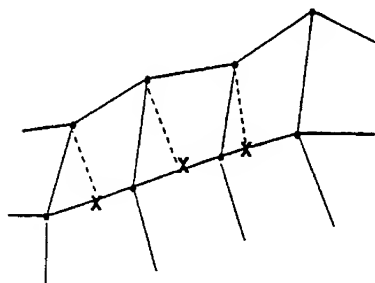


Fig. 2 Example of a Neumann boundary approximation.

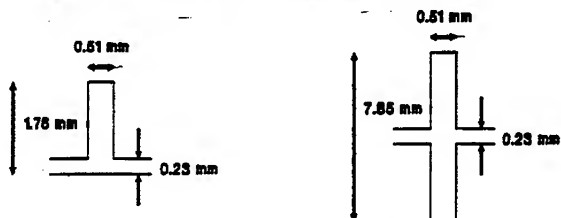


Fig. 3(a) A Single Stub discontinuity.

Fig. 3(b) A Double Stub discontinuity.

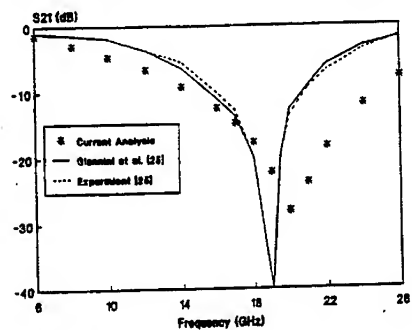


Fig. 4(a) Insertion Loss $|S_{21}|$ of the single stub discontinuity.

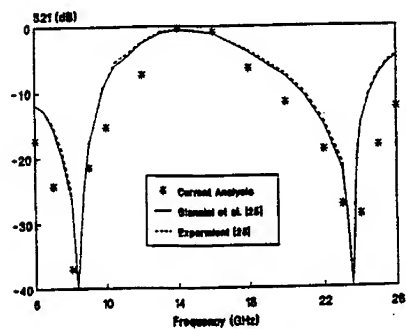


Fig. 4(b) Insertion Loss $|S_{21}|$ of the double stub discontinuity.

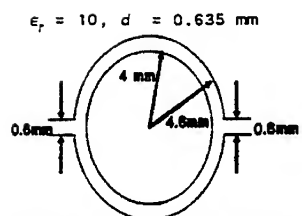


Fig. 5(a) A microstrip annular ring.

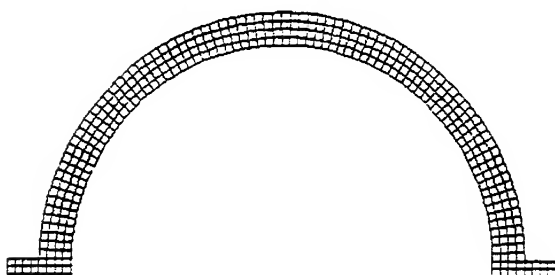


Fig. 5(b) Finite element grid for the problem shown in Fig. 5(a).

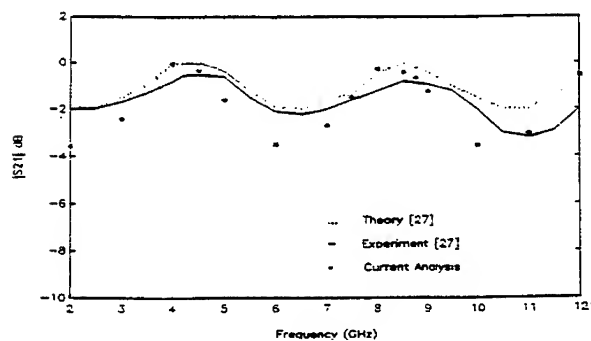


Fig. 6(a) Insertion Loss of the annular ring problem.

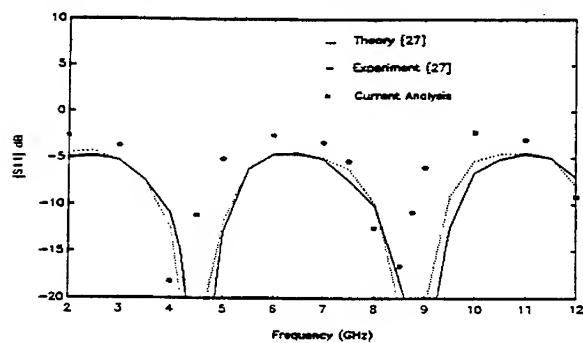


Fig. 6(b) Return Loss of the annular ring problem.

On the optimization of a finite element code for 3D scattering computation

A. Chatterjee^{*1}, J. L. Volakis¹ and D. Windheiser²
Radiation Laboratory¹; Advanced Computer Architecture Laboratory²
Department of Electrical Engineering
and Computer Science
University of Michigan
Ann Arbor MI 48109-2122

January 12, 1993

1 Introduction

Differential equation techniques are rapidly becoming the preferred solution methods for the computation of electromagnetic scattering and radiation from inhomogeneous, three-dimensional geometries [1-2]. In the finite element method, the computational domain is at first discretized using node-based or edge-based finite elements. Edge-based elements are more desirable for representing electromagnetic fields since they exhibit tangential continuity and normal discontinuity across inter-element boundaries and material discontinuities. Moreover, they can treat geometries with sharp edges and are divergenceless. The outer boundary of the finite element mesh is now artificially truncated at some distance from the target using an absorbing boundary condition (ABC). ABCs are essentially differential equations chosen to suppress non-physical reflections from the boundary, thus ensuring the outgoing nature of the waves. They are approximate boundary conditions but have the important advantage of retaining the sparsity of the matrix system.

In our implementation, we use an edge-based finite element formulation coupled with vector ABCs on conformal boundaries to compute scattering from three dimensional structures having boundaries satisfying impedance and/or transition conditions. The limiting factor in dealing with three-dimensional geometries is usually the number of unknowns and the corresponding demands on storage and solution time. Solution techniques which have $O(N)$ storage and feasible solution times are, therefore, the only way that three-dimensional problems can be solved with the available computer resources. This is one of the principal reasons for the popularity of partial differential equation techniques over integral equation (IE) approaches

which lead to dense matrices or hybrid methods which lead to full submatrices. As the body becomes large, the IE and hybrid methods (both need $O(N^l)$, $1 < l \leq 2$ storage) quickly become unmanageable in terms of storage and solution time. Another concern while solving problems having more than 100,000 unknowns - a scenario that can be envisioned for most practical problems - is to avoid software bottlenecks. The algorithmic complexity of any part of the program should increase at most linearly with the number of unknowns.

Owing to the local nature of the ABCs, the finite element matrix is very sparse resulting in $O(N)$ storage requirement. The number of unknowns is further reduced since the artificial boundary needs to be truncated only a fraction of a wavelength from the target. The sparse, symmetric matrix is initially stored in a modified ITPACK format [3] and then stored as a long vector in the main routine for reasons to be outlined later. The linear equation solver employs a preconditioned biconjugate gradient (BCG) algorithm. The preconditioners used here are a simple diagonal preconditioner and a modified version of the incomplete LU (ILU) preconditioner with zero fill-in. The trade-offs between the two types of preconditioners will be shown later. The preconditioned BCG solver was also parallelized on the KSR1 (Kendall Square Research) shared-address space distributed-cache architecture with substantial speedup.

2 Finite element discretization

The scattered electric field functional $-F(\mathbf{E}^s)$ to be discretized for the FE-ABC scheme is given in [1]. The computational volume V is subdivided into a number of small tetrahedra, each occupying the volume V^e ($e = 1, 2, \dots, M$), where M denotes the total number of tetrahedral elements. Within each element, the scattered electric field is expressed as

$$\mathbf{E}^e = \sum_{j=1}^m E_j^e \mathbf{W}_j^e = \{\mathbf{W}^e\}^T \{E^e\} = \{E^e\}^T \{\mathbf{W}^e\} \quad (1)$$

where \mathbf{W}_j^e are the edge-based vector basis functions [4], E_j^e denote the expansion coefficients of the basis and represent the field components tangential to the j th edge of the e th element, m is the number of edges making up the element and the superscript stands for the element number. The basis functions used in our implementation have zero divergence and constant curl.

The system of equations to be solved for E_j^e is obtained by a Rayleigh-Ritz procedure which amounts to differentiating $F(\mathbf{E}^s)$ with respect to each edge field and then setting it to zero. On substituting the basis expansion into the expression for the functional, taking the first variation in $F(\mathbf{E}^s)$ and assembling all M elements, we obtain the following augmented system of equations

$$\left\{ \frac{\partial F}{\partial E^e} \right\} = \sum_{e=1}^M [A^e] \{E^e\} + \sum_{s=1}^{M_s} [B^s] \{E^s\} + \sum_{p=1}^{M_p} \{C^p\} = 0 \quad (2)$$

In this, M_s denotes the number of triangular surface elements on S_k and S_o whereas M_p is equal to the sum of the surface elements on S_k , S_d and the volume elements in V_d . The elements of the matrices $[A^e]$, $[B^e]$ and $\{C^e\}$ are given in [1]. The final system can be expressed as

$$[A]\{x\} = \{b\} \quad (3)$$

where $\{x\}$ is the unknown vector representing the weighting coefficients of the basis functions.

The imposition of boundary conditions on the finite element mesh is usually quite simple. No special treatment is required at material discontinuities; the mere identification of surface elements lying on material discontinuities or inhomogeneities kicks in the contribution from the surface integrals in $F(\mathbf{E}^s)$. For perfectly conducting scatterers, the interior region is not meshed since the electromagnetic wave does not penetrate inside the scatterer. If the surface element lies on the pec boundary, a simple modification is carried out on the element matrix to preserve the symmetry of the matrix system.

2.1 Numerical considerations

The finite element code (to be referred as FEM-ATS from now on) can be classified into four main categories:

- Input/output
- Right-hand side vector (b) generation
- Finite element matrix (A) generation
- Linear equation solver

A look at Table 1 reveals that the most time-consuming portion of the code is the linear equation solver taking up approximately 90% of the CPU time. On a vector computer like the Cray YMP, it is possible to vectorize only the equation solver. The finite element matrix generation consists of too many subroutine calls and highly complex loops to permit any significant speedup through vectorization. Generating the right-hand side vector (b) as well as input/output take up a negligible portion of CPU time.

2.2 Matrix generation

The finite element mesh was usually generated using a commercial package, SDRC I-DEAS. The matrix systems arising from I-DEAS were very sparse: on the average, the minimum number of non-zero elements per row was 9 and the maximum number of non-zeros per row was 30. As stated earlier, the matrix generation was carried out using a modified ITPACK storage scheme and then stored in a long vector. The storage requirement for the entire matrix was approximately $15N$ to $16N$, where N is the number of unknowns.

The ITPACK storage scheme is attractive for generating finite element matrices since the number of comparisons required while augmenting the matrix depends only on the locality of the corresponding edge and not on the number of unknowns. However, on using the ITPACK storage scheme for our application, almost half the space is lost in storing zeros. The modified ITPACK scheme does alleviate this problem to a certain degree; however, 30% of the space is still lost in zero padding. The best trade-off between storage and speed for our application is obtained by storing the non-zero matrix elements in a long complex vector, the column indices in a long integer vector and the number of non-zeros per row in another integer vector. This data structure is referred to as the Compressed Sparse Row (CSR) format. In our implementation, a map of the number of non-zeros for each row is obtained through the modified ITPACK algorithm. The main program stores the matrix in CSR format, thus minimizing storage and sacrificing a bit of speed. The required storage is $15N$ complex words plus integers for X and PC , respectively, and N integers for the array containing the pointers to the rows' data.

2.3 Linear equation solver

For three dimensional applications, it is essential to have solvers whose memory requirements are a small fraction of the storage demand of the coefficient matrix. This necessitates the use of iterative algorithms instead of direct solvers in order to preserve the sparsity pattern of the finite element matrix. Especially attractive are iterative methods that involve the coefficient matrices only in terms of matrix-vector products with A or A^T . The most powerful iterative algorithm of this type is the conjugate gradient algorithm for solving positive definite linear systems[5]. In our implementation, the system of linear equations is solved by a variation of the CG algorithm, the biconjugate gradient (BCG) method. This scheme is usually used for solving unsymmetric systems; however, it performs equally well when applied to symmetric systems of linear equations. The conjugate gradient squared (CGS) algorithm [6] is usually faster than BCG but is more unstable since the residual polynomials are merely the squared BCG polynomials and hence exhibit even more erratic behaviour than the BCG residuals. The CGS algorithm also fails to exploit the symmetry of the matrix system. Moreover, there are cases where CGS diverges, while BCG still converges.

In our implementation, the biconjugate gradient algorithm requires 1 matrix-vector multiplication, 3 vector updates and 3 dot products per iteration. The solution scheme requires only three additional vectors of length N . The vector updates and the dot products can be carried out extremely fast on a vector Cray machine like the Cray YMP, reaching speeds of about 190 MFLOPS. However, the matrix-vector product, which involves indirect addressing and short vector lengths, runs at about 45.5 MFLOPS on 1 processor of the 8-processor Cray YMP. As a rule of thumb, the biconjugate gradient algorithm with no preconditioning consumes 4.06 microsec-

onds/iteration/unknown on the Cray YMP.

2.3.1 Diagonal preconditioner

The simplest preconditioner that was used in our implementation was the diagonal preconditioner. It consists of a vector containing the reciprocal of the diagonal element for each row. The algorithm with the diagonal preconditioner converged in about 35% of the number of iterations required for the unpreconditioned case. This suggested that the finite element matrix in our implementation was diagonally dominant since the reduction in the number of iterations was so spectacular. The diagonal preconditioner is also easily vectorizable and consumes 4.1 microseconds/iteration/unknown, a marginal slowdown over the unpreconditioned system.

2.3.2 Modified ILU preconditioner

The next step was to use a better preconditioner to improve the condition number of the system resulting in faster convergence. The traditional ILU preconditioner [7] was employed with zero fill-in; however, the algorithm took a greater number of iterations than the diagonal preconditioner to converge to a specified tolerance. Higher values of fill-in were not attempted since the preconditioner already occupied space equal to that of the coefficient matrix.

A modified version of the ILU preconditioner was then tried by eliminating the inner loop of the traditional version. The algorithm is outlined in the Appendix and basically scales the off-diagonal elements in the lower triangular portion of the matrix by the column diagonal. Since the matrix is symmetric, it retains the LDL^T form. This preconditioner is less expensive to generate and converges in about 1/3 the number of iterations taken by the diagonal preconditioner. It has been tested with reliable results for $N \leq 50000$. However, the time taken by the two preconditioning strategies is approximately the same since each iteration of the ILU preconditioned system is about three times more expensive. The forward and backward substitutions carried out at each iteration runs at 26.5 MFLOPS on the Cray YMP and proves to be the bottleneck since they are inherently sequential processes. It is, however, expected that as matrix systems grow larger, the improvement in the condition number would reduce the iteration count by a factor greater than 3 and lend viability to this type of preconditioner.

2.4 Parallelization

The parallelization of the code was carried out almost entirely on the KSR1 parallel machine. The programming model of the machine is thread-based, but it is possible to bind a thread to a processor. Parallel constructs are expressed as compiler directives that are processed by the KSR Fortran compiler but ignored by other Fortran compilers. Low-level parallelism is expressed through threads while high-level parallelism is implemented through parallel regions, parallel sections and tile families.

The solver was the first in line to be parallelized since it consumed about 90% of the CPU time. Since each vector operation is implemented as a loop, the program is parallelized by tiling these loops. In order to parallelize the application using P processors, the vectors are divided into P sections of N/P elements. Each processor is assigned a section of the vector based on the processor ID. Such partitioning of the data attempts to reduce communication while balancing the load on each processor. Significant inter-processor communication was required for the matrix-vector multiplication and the search vector update. Other vector operations needed little or no interprocessor communication since each processor used only those vector elements that they already owned.

Figure 1 shows the speedup for three versions of the sparse solver with diagonal preconditioning as the number of processors is increased from 1 to 28. The benefits of prefetching and poststoring are offset by the overhead of processing the prefetch and poststore instructions. The maximum speedup for 28 processors is about 19. The solver, therefore, runs about 3.25 times faster on the 28-processor KSR1 than on the single processor Cray YMP.

3 Results

The parallelized code was run for a $1.5\lambda \times 1\lambda \times 1\lambda$ pec inlet and the backscatter echo-area for the VV-polarization compared with measured data. For the results shown in Figure 2, the outer boundary was enclosed in a sphere of radius 1.35λ . The discretized geometry had 224476 unknowns and converged in an average of 5000 iterations on the KSR1. The agreement is quite good for most of the incident angles.

4 Appendix

In this appendix, we present the algorithm for modified ILU preconditioning. It is assumed that the data is stored in CSR format and that the column numbers for each row are sorted in increasing order. The sparse matrix is stored in the vector X and the column numbers in PC . $SIG(i)$ contains the total number of non-zeros till the i th row. The locations of the diagonal entries for each row are stored in the vector $DIAG$. The preconditioner is stored in another complex vector, LU .

```
for i=1 step 1 until n-1 do
begin
  lbeg=diag(i)
  lend=sig(i)
  for j=lbeg+1 step 1 until lend do
  begin
    jj=pc(j)
    ij=srch(jj,i)
```

```

    if (ij.ne.0) then
    begin
        lu(ij)=lu(ij)/lu(lbeg)
    end
end
end
end

```

5 References

1. A. Chatterjee, J.M. Jin and J.L. Volakis, "Application of edge-based finite elements and ABCs to 3-D scattering", *IEEE Trans. Antennas Propagat.*, February 1993.
2. D.S. Katz, M.J. Picket-May, A. Taflové and K.R. Umashankar, "FDTD analysis of electromagnetic wave radiation from systems containing horn antennas", *IEEE Trans. Antennas Propagat.*, vol. 39, no. 8, pp. 1203-12. August 1991.
3. D.R. Kincaid and T.C. Oppé, "ITPACK on supercomputers", *Numerical Methods, Lecture Notes in Mathematics*, vol. 1005, pp. 151-61, Springer, Berlin, 1982.
4. M.L. Barton and Z.J. Cendes, "New vector finite elements for three-dimensional magnetic field computation", *J. Appl. Phys.*, vol. 61, no. 8, pp. 3919-21, April 1987.
5. M.R. Hestenes and E. Stiefel, "Methods of conjugate gradients for solving linear systems", *J. Res. Natl. Bur. Stand.*, vol. 49, pp. 409-36, 1952.
6. P. Sonneveld, "CGS, a fast solver for nonsymmetric linear systems", *SIAM J. Sci. Stat. Comput.*, vol. 10, pp. 35-52, 1989.
7. H.P. Langtangen, "Conjugate gradient methods and ILU preconditioning of nonsymmetric matrix systems with arbitrary sparsity patterns", *Int. J. Numer. Meth. Fluids*, vol. 9, pp. 213-33, 1989.

TABLE I
TIMING INFORMATION ON CRAY YMP TABULATED AGAINST THE
NUMBER OF UNKNOWNNS

Type	Number of unknowns	Time (sec)			Iteration count
		I/O	Matrix gen.	Solver	
C	31563	3.992	7.255	46.571	359
C-R-D	50488	6.267	11.8	123.015	595
C	48123	6.135	11.265	80.697	408
C	40483	4.911	9.555	74.360	448
C	33239	4.138	7.571	51.587	379
C	20033	2.515	4.673	34.211	414
C	32767	4.087	8.307	60.679	452
D	18319	2.29	4.24	89.976	1200
D	11705	1.424	2.702	57.631	1200

C \equiv conductor; R \equiv resistive sheet; D \equiv dielectric

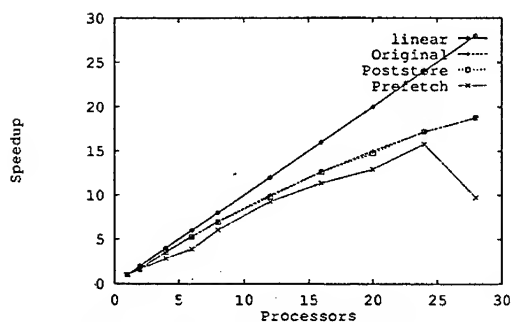


Figure 1: Speedup curves for the linear equation solver on the KSR1

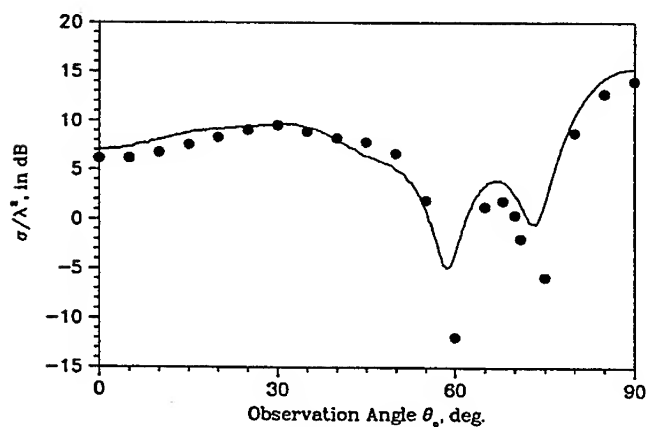


Figure 2: Backscatter pattern of pec rectangular inlet ($1\lambda \times 1\lambda \times 1.5\lambda$) for VV polarization. The black dots indicate data obtained from the KSR1 for the FE-ABC code and the solid line represents measured data.

Performance Evaluation of MEI-Based Mesh Truncation Conditions for Finite Element Modeling of Electromagnetic Scattering by Penetrable Bodies

Diana B. Wright and Andreas C. Cangellaris
Department of Electrical and Computer Engineering
University of Arizona, Tucson, AZ 85721

Abstract - The *Measured Equation of Invariance* (MEI) concept, proposed recently by K.K. Mei, for the numerical solution of time-harmonic electromagnetic wave scattering by perfectly conducting bodies in unbounded regions, is extended to handle two-dimensional penetrable scatterers. Two different approaches for developing the MEI-based truncation conditions are compared. The first approach is based on Huygen's principle while the second relies on equivalence principle arguments. Several representative numerical examples of scattering by two-dimensional penetrable targets are presented.

I. Introduction

The *Measured Equation of Invariance* (MEI) is a new concept proposed by Mei *et al* [1] to develop accurate local boundary conditions for the truncation of the numerical grid used for finite element/finite difference (FE/FD) modeling of time-harmonic electromagnetic scattering by perfectly conducting targets. An MEI is a numerically derived discrete, linear equation which relates the field at a given boundary node to the field values at neighboring nodes. Given such a condition for each boundary node, a computationally efficient and accurate FE/FD grid truncation can be achieved. Since the derivation of the MEI is not based on any assumptions about the far-field behavior of the scattered field, the truncation boundary may be placed very close to the target surface. This results in superior computational efficiency compared to finite element methods that utilize radiation-type boundary conditions for grid truncation.

Initial applications of the MEI concentrated on the finite-difference solution of electromagnetic scattering by two- and three-dimensional conducting targets in free space, as well as to scattering by perfectly conducting discontinuities in waveguides [1]. More recently, the MEI concept was also used to develop local mesh truncation conditions for the finite element modeling of electromagnetic scattering by penetrable scatterers [2].

In this paper, we compare two possible approaches for developing MEI-based truncation conditions for use in FE/FD modeling of electromagnetic scattering by penetrable targets. The first approach, which is based on Huygen's principle, was introduced in [2]. The second approach is based on equivalence principle arguments, traditionally used for the development of integral

equation formulations for electromagnetic scattering by penetrable bodies. This second approach is computationally less demanding than the Huygen's principle approach. Several representative numerical examples of scattering by two-dimensional penetrable targets are provided to facilitate the comparison between the accuracy of the two approaches.

II. The Measured Equation of Invariance

The problem of time-harmonic electromagnetic wave scattering from a two-dimensional target is used to illustrate the MEI concept and its application. Let us define a coordinate system in which the axis of the scatterer lies along the z -axis. If we assume an excitation which is invariant in z , Maxwell's equations decouple into two sets: transverse magnetic (TM_z), with an axially-directed electric field and a magnetic field which is transverse to z ; and transverse electric (TE_z), with an axially-directed magnetic field and an electric field which is transverse to z . In either case, the scattered field $\phi(\vec{r})$ must satisfy the scalar Helmholtz equation

$$(\nabla_t^2 + k^2)\phi(\vec{r}) = 0 \quad (1)$$

where $\phi = E_z$ in the TM_z case, $\phi = H_z$ in the TE_z case, and $\nabla_t^2 = \partial^2/\partial x^2 + \partial^2/\partial y^2$. The wavenumber k is related to the angular frequency ω and the velocity v of light in the surrounding medium as $k = \omega/v$. The solution to (1) may be found using either the finite difference or the finite element method. In both cases, the numerical approximation of (1) takes the form

$$\sum_{i=1}^N a_i \phi_i = 0 \quad (2)$$

where the number of nodes, N , and the values of the coefficients, a_i 's, are functions of the order of the discretization and the grid. Let us define \hat{D} to be the finite difference or finite element approximation to the operator $\nabla_t^2 + k^2$. Then any two-dimensional wave of angular frequency ω belongs to the nullspace N_D of \hat{D} (within the accuracy of the discretization scheme).

Mei [1] considered the possibility of constructing a different operator \hat{D}_s with a nullspace N_{D_s} , a subspace of N_D , consisting of all two-dimensional waves which are obtained as scattered waves from a specific target under arbitrary excitation conditions. The operator \hat{D}_s would be defined through the expression

$$\sum_{i=1}^{n+1} \hat{a}_i \phi_i = 0 \quad (3)$$

which describes a linear relationship between the field value at the node identified as $i = 1$ and the field values of its n nearby node neighbors. For each node, a separate equation would exist. These equations would be different than the FD/FE equations, but would *ideally* give the same solutions to the problem of scattering by the specific target under arbitrary excitation conditions. Each discrete equation in (3) is referred to as an MEI and can be used to relate the field at a given boundary node to the field values at neighboring nodes to produce a grid truncation condition. Of course, these conditions are not truly excitation invariant, but rather are limited by the finite accuracy of the approximation in (3) which is dependent on the number n of nodes clustered together and the proximity of these nodes to one another.

Our general problem consists of a penetrable scatterer in free space with its axis parallel to the z -axis and its boundary in the xy -plane described by the contour C_S . We denote the unbounded region exterior to the scatterer as Ω_o and the interior region as Ω_i . The interior region is characterized by a magnetic permeability $\mu(x, y)$ and a dielectric permittivity $\epsilon(x, y)$, which may be complex if losses are present. For the TM_z case, we have $\vec{E} = \hat{z}E_z(x, y)$ and $\vec{H} = \hat{x}H_x(x, y) + \hat{y}H_y(x, y)$. Assuming time-harmonic fields with $e^{j\omega t}$ dependence, we can evaluate the scattered electric field at a point $\vec{r} = \hat{x}x + \hat{y}y$ in Ω_o by applying Huygen's principle. We have

$$E^{sc}(\vec{r}) = \oint_{C_S} \left(G(\vec{r}, \vec{r}') \frac{\partial E_z(\vec{r}')}{\partial n'} - E_z(\vec{r}') \frac{\partial G(\vec{r}, \vec{r}')}{\partial n'} \right) dl' \quad (4)$$

where $k_o = \omega\sqrt{\mu_o\epsilon_o}$, $G(\vec{r}, \vec{r}') = (-j/4)H_0^{(2)}(k_o|\vec{r} - \vec{r}'|)$ is the free space Green's function, and the normal derivative is taken in the direction pointing out of Ω_o . For the TE_z case, a similar expression can be written for $H_z^{sc}(\vec{r})$ in Ω_o . We see that independent pairs of E_z and $\partial E_z/\partial n$ on C_S are required. As discussed in [2], from the uniqueness theorem we know that the values of E_z and $\partial E_z/\partial n$ for a particular pair cannot be chosen independently of one another.

To obtain the MEI for a local grid truncation condition involving a cluster of $n+1$ nodes, we require n independent functions, $f_i, i = 1, \dots, n$. We let $\partial E_z/\partial n = f_i$ on C_S and solve the i th interior boundary value problem from which we obtain E_z on C_S . By solving n such boundary value problems, we get the n pairs of E_z and $\partial E_z/\partial n$ on C_S which may be used in (4) to evaluate the scattered field at the $n+1$ nodes. By forcing these field values to satisfy (3), we produce a linear system of n equations which we solve for the unknown coefficients $\hat{\alpha}_i, i = 1, 2, \dots, n$. Repeated application of the above procedure to clusters of nodes along the outer boundary of the grid results in a set of discrete equations which are satisfied by fields scattered by the specific target and thus can be used as localized grid truncation conditions.

In the second approach for developing the MEIs, instead of evaluating the scattered field of our two-dimensional problem using Huygen's principle, we use an equivalent source integral statement

$$E^{sc}(\vec{r}) = \oint_{C_S} J_e(\vec{r}') G(\vec{r}, \vec{r}') dl' \quad (5)$$

where $G(\vec{r}, \vec{r}')$ is again the free space Green's function and J_e represents an equivalent electric current. We recall that in the equivalent source integral formulation of scattering problems J_e is postulated to be an electric current distribution on C_S , which when radiating in a homogeneous medium having constitutive parameters identical to those of the unbounded exterior region (μ_o, ϵ_o), produces the correct scattered field in the exterior region. This is the approach presented by Harrington in the *electric current formulation* used for the development of boundary integral equations [3]. In our development, we are not interested in actually formulating an integral equation and solving for the values of the equivalent currents. We simply employ this form in order to generate the scattered fields to be used in (3). Once again, we require n independent functions, $f_i, i = 1, \dots, n$. We let $J_e = f_i$ and solve for $E_i^{sc}, i = 1, \dots, n$. These field values are forced to satisfy (3) in order to develop the linear system of n equations from which we can determine the coefficients of the MEI. For the TE_z case, an expression similar to (5) can be written for $H_z^{sc}(\vec{r})$ in terms of an equivalent magnetic current M_e . In terms of computational savings, the equivalent source formulation is obviously preferable because we do not have to solve the interior problem repeatedly for the independent pairs of $(E_z, \frac{\partial E_z}{\partial n})$ as in the Huygen's

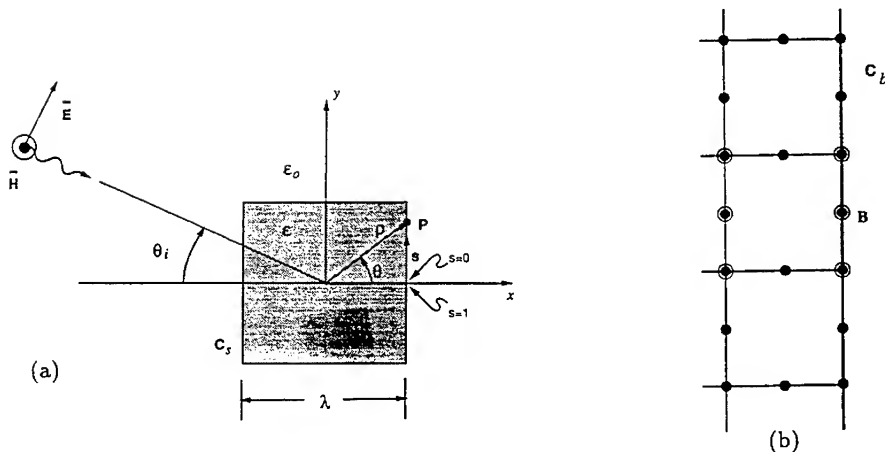


Figure 1: (a) Plane wave incident on square dielectric cylinder; (b) Boundary node and five of its nearby node neighbors.

formulation. On the other hand, it is clear that, except for the shape, the particular material composition of the scatterer is not taken into account in the generation of the scattered fields via (5).

III. Numerical Examples

The first example to be considered is that of a square dielectric cylinder (Fig. 1) having characteristic dimension $a = 1\lambda$ where λ is the wavelength in the dielectric. The plane wave is incident on the cylinder at an angle of θ_i . The TE_z polarization case is shown in Fig. 1a. For our finite element problem we employ a uniform cartesian grid with cell size $\Delta h = 0.1\lambda$ and eight-node quadratic quadrilateral elements, a situation which translates to a density of 20 nodes per wavelength. We examine the field on the boundary of the cylinder C_s . The field is plotted as a function of s , defined to be the distance along the perimeter of the cylinder normalized such that the total perimeter corresponds to a distance of $s = 1$.

Since an analytic solution to this problem is unavailable, we compare our results to those obtained using the bymoment method [4]. The bymoment method results presented herein are unpublished and were obtained by personal communication [5]. We consider a dielectric cylinder with a relative permittivity of $\epsilon_r = 4$ excited by a TE_z polarized plane wave incident at $\theta_i = 0^\circ$. Each mesh truncation condition employed is based on an MEI relating a specific boundary node B to five of its nearby node neighbors as shown in Fig. 1b. Therefore, at least five independent functions $f_i, i = 1, \dots, 5$, are required. The mesh is truncated four cells from the cylinder surface, which translates to a distance of $0.2\lambda_0$.

In Fig. 2, the magnitude and phase of the total field on the surface of the cylinder are plotted from the forward-scattered direction ($\theta = 0^\circ$, or $s = 0$) to the back-scattered direction ($\theta = 180^\circ$, or $s = 0.5$). Excellent agreement is observed. As a measure of this agreement, we consider the

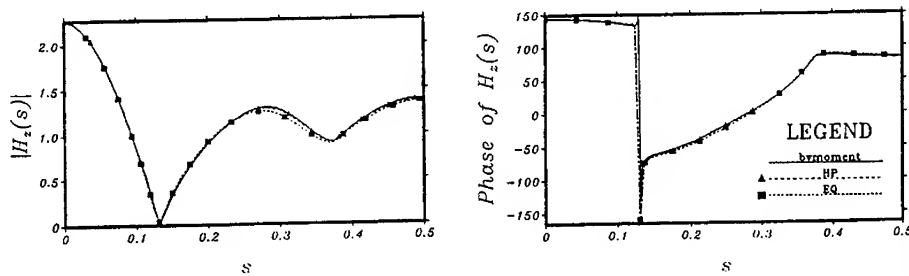


Figure 2: Total field along perimeter of square dielectric cylinder ($\epsilon_r = 4$) excited by TE polarized plane wave incident at $\theta_i = 0^\circ$.

relative RMS error defined as

$$E_{rms} = \left\{ \frac{\int_{C_s} |F_R - F|^2 ds}{\int_{C_s} |F_R|^2 ds} \right\}^{1/2} \quad (6)$$

where F_R is the *reference* field value and F is the calculated field value. Because of the previous success of the bymoment method, we consider it to be the established method. We use the results obtained with the bymoment method as our *reference* with which to compare the field values calculated using the MEI-based truncation scheme. Comparing the results from the Huygen's principle (HP) approach to the results using the bymoment method, we find that $E_{rms}^{HP} = 1.4\%$. For the equivalent source (EQ) formulation, the agreement is also extremely good with $E_{rms}^{EQ} = 4.4\%$.

Next we consider a cylinder of the same electrical size $1\lambda \times 1\lambda$, but with a relative permittivity of $\epsilon_r = 9$. In this case, the wavelength in the dielectric becomes $\lambda = \lambda_0/3$, where λ_0 is the free-space wavelength. The cell size is again chosen as $\Delta h = 0.1\lambda$ to ensure 20 nodes per wavelength. For the HP approach we truncate the mesh four cells beyond the scatterer's boundary as before. However, for the EQ approach we find that truncating four cells away does not produce acceptable results. This seems to indicate that the MEI method as originally proposed using Huygen's principle permits mesh truncation very close to the scatterer, a few elements from the surface, because the composition of the scatterer is taken into account. In contrast, the material properties of the scattering object do not enter into the EQ formulation. In order to improve the accuracy of the EQ formulation the distance between the scatterer and the mesh boundary was adjusted to be $0.2\lambda_0$, the same with the one used for the $\epsilon_r = 4$ cylinder. In this example the wavelength λ , and thus the cell size, have decreased by a factor of $2/3$ as the permittivity increased to $\epsilon_r = 9$. Therefore, in order to maintain the same distance to the mesh boundary, we increase the number of cells in this direction as the inverse of this factor ($4 \text{ cells} \times \frac{3}{2} = 6 \text{ cells}$). Obviously, it is assumed here that it is desirable to maintain the uniformity of the finite element grid. Thus, the choice of 0.1λ for the cell size in accordance with the smallest wavelength in the computational domain is maintained over the entire grid. Results for a TE_z incident plane

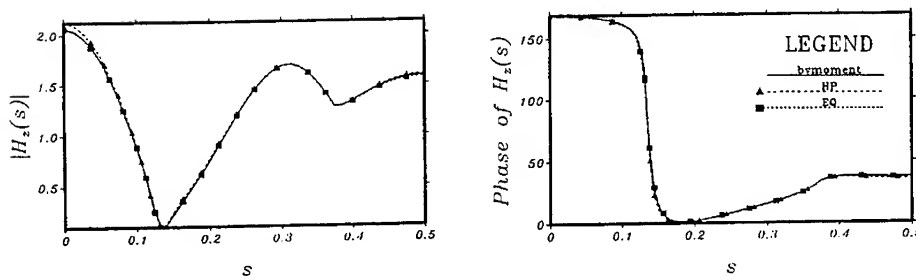


Figure 3: Total field along perimeter of square dielectric cylinder ($\epsilon_r = 9$) excited by TE polarized plane wave incident at $\theta_i = 0^\circ$.

wave scattered by the square dielectric cylinder of permittivity $\epsilon_r = 9$ are shown in Fig. 3. The agreement is extremely good with $E_{rms}^{HP} = 2.7\%$ and $E_{rms}^{EQ} = 2.0\%$.

As a second test problem geometry, we consider a substantially larger scattering object, a $5\lambda \times 1\lambda$ rectangular dielectric cylinder having a perimeter of 12λ . The problem is identical to that shown in Fig. 1a except that the cross section of the cylinder is increased in the y-dimension to 5λ . For the case of $\epsilon_r = 9$, the cylinder has a perimeter of $4\lambda_0$. A cartesian FE mesh with uniform cell size Δh is utilized. As before, the mesh is truncated four cells away from the scatterer for the HP approach and six cells away for the EQ approach. Results are shown in Fig. 4. In the TE_z case, we find $E_{rms}^{HP} = 29.1\%$ and $E_{rms}^{EQ} = 9.7\%$. If we increase the distance between the mesh boundary and the scatterer to six cells for the HP approach, we observe a marked improvement with $E_{rms}^{HP} = 11.2\%$ (labeled "HP 6h" in Fig. 4). We recall that for the $1\lambda \times 1\lambda$ case with $\epsilon_r = 9$ a four cell separation used with the HP approach provided comparable results to the EQ approach with a six cell separation. The fact that this is not true for the $5\lambda \times 1\lambda$ body would suggest that the minimum separation distance depends to some extent on the size of the scattering object. Even for the relatively large $5\lambda \times 1\lambda$ cylinder though, the distance to the mesh boundary is only one fifth of the free space wavelength.

In order to further test the observation that the minimum separation distance between the scattering object and the grid truncation boundary may depend on the size of the object, we consider the problem of plane wave scattering by a perfectly conducting circular cylinder. The plane wave is normally incident on the cylinder at an angle of 180° . Let us assume that the MEI truncation conditions, each of which clusters together six nodes ($n = 5$) near the boundary (Fig. 1b), will be used with a uniform polar grid in which 20 nodes per wavelength has been ensured and the aspect ratio of the outer elements of the mesh is approximately one. We examine the residual of the MEI (the left side of (3)), which ideally should be zero, using the known series solution for the scattered fields ϕ_i at the six nodes. Then we normalize by the scattered field at the center boundary node (node B in Fig. 1b). We fix the separation distance at four elements and let the radius of the cylinder increase. Along the boundary at an observation angle of 85° in the TM_z case, we find that this normalized residual increases from 0.016 at a radius of 5λ to 0.027 at 20λ . Thus, as the scattering object size increases, we observe that the error introduced

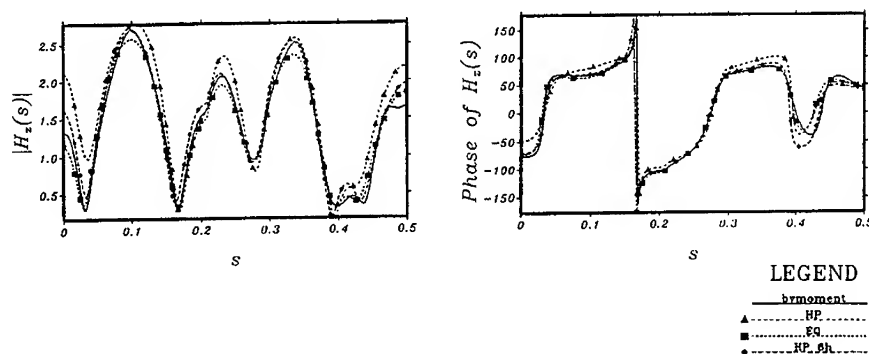


Figure 4: Total field along perimeter of rectangular dielectric cylinder ($\epsilon_r = 9$) excited by TE polarized plane wave incident at $\theta_i = 0^\circ$.

by the MEI-based grid truncation increases if the distance to the truncation boundary remains constant. Acknowledging the fact that this study is favorably biased, since the exact solution is used, we conclude that, as observed in the previous example, it is necessary to increase the separation distance for a larger scatterer.

As a final example we consider a concave scatterer, namely, the problem investigated by Richmond [6] of a circular dielectric half shell with a dielectric constant of $\epsilon_r = 4$, an inner radius $a = 0.25\lambda_0$, and an outer radius $b = 0.3\lambda_0$. Eight-node elements are used and the cell size is chosen to ensure approximately 20 nodes per wavelength. A conforming mesh which is truncated four cells from the cylinder surface is used. As before, each mesh truncation condition is based on an MEI involving a cluster of six nodes (Fig. 1b).

As shown in Fig. 5, results for the TE_z case obtained using MEI-based grid truncation (with the HP approach) compare favorably with those obtained by Lee using the bymoment method [7]. However, the MEI-based and bymoment results do not agree well with Richmond's results in the back-scattered direction ($\phi = 180^\circ$). This same disagreement in the back-scattered direction for the TE_z case was also reported by Yuan *et al.* [8].

IV. Summary

We have demonstrated that the development of the MEI for penetrable scatterers is as straightforward as for the case of perfectly conducting ones, and can be used as an accurate localized truncation condition in conjunction with finite-element/finite-difference grids that extend only a few cells away from the surface of the scatterer. An alternate approach for constructing the MEI based on equivalence principle concepts, which is computationally less demanding than the direct application of Huygen's principle, was introduced. Results from several numerical examples showed very favorable agreement between MEI-based grid truncation using both approaches and the use of other hybrid finite element and/or integral equation techniques. Preliminary results also suggest that the minimum separation distance between the grid boundary and the surface of the scattering object depends on the size of the scatterer.

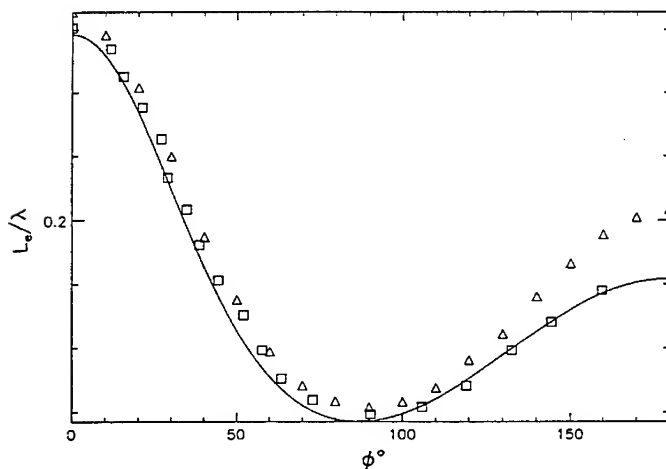


Figure 5: Echo width for dielectric circular half shell obtained with HP approach, TE case (solid line = MEI, triangles = Richmond, squares = bymoment).

References

- [1] K. K. Mei, R. Pous, Z. C. Chen, and Y. W. Liu, "Measured Equation of Invariance - Breaking through the Barrier of Radiation Condition," *Proceedings of the First European Conference on Numerical Methods in Engineering*, Sept. 1992. to appear.
- [2] A. C. Cangellaris and D. B. Wright, "Application of the Measured Equation of Invariance to Electromagnetic Scattering by Penetrable Bodies," *IEEE Transactions on Magnetics*, Mar. 1993. accepted for publication.
- [3] R. F. Harrington, "Boundary Integral Formulations for Homogeneous Material Bodies," *Journal of Electromagnetic Waves and Applications*, vol. 3, no. 1, pp. 1-15, 1989.
- [4] A. C. Cangellaris and R. Lee, "The Bymoment Method for Two-Dimensional Electromagnetic Scattering," *IEEE Transactions on Antennas and Propagation*, vol. 38, pp. 1429-1437, Sept. 1990.
- [5] R. Lee, July 1992. Personal Communication.
- [6] J. H. Richmond, "TE-Wave Scattering by a Dielectric Cylinder of Arbitrary Cross-Section Shape," *IEEE Transactions on Antennas and Propagation*, vol. 14, pp. 460-464, July 1966.
- [7] R. Lee, "Rigorous grid truncation for the finite element solution of electromagnetic scattering problems," Ph.D. dissertation, University of Arizona, Tucson, Arizona, 1990.
- [8] X. Yuan, D. Lynch, and J. Strohbehn, "Coupling of Finite Element and Moment Methods for Electromagnetic Scattering from Inhomogeneous Objects," *IEEE Transactions on Antennas and Propagation*, vol. 38, pp. 386-393, Mar. 1990.

A FINITE ELEMENT METHOD FOR DETERMINING THE SCATTERING FROM LOSSY CYLINDERS ILLUMINATED BY OBLIQUELY INCIDENT PLANE WAVES

Richard K. Gordon and Ahmed A. Kishk
Department of Electrical Engineering
University of Mississippi
University, MS 38677

I. INTRODUCTION

Although a number of papers on the scattering by cylindrical structures of normally incident plane waves have appeared in the literature, relatively few have been published on the scattering by such structures of obliquely incident fields. Rojas [1] presented a coupled integral equation formulation in which the unknowns are all six field components. Michielssen, Peterson, and Mittra [2] presented a coupled integral equation formulation in which the axial components of the electric and magnetic fields are used as unknowns. Cangellaris and Lee [3] also presented a formulation based on the use of the axial components of the electric and magnetic fields as unknowns, but used a finite element technique along with the bymoment method to solve the resulting equations.

Like [3], this paper presents a finite element solution based on an E_z - H_z formulation; but in the technique presented here we employ an impedance boundary condition (IBC) to truncate the mesh at the surface of the lossy scatterer and an absorbing boundary condition (ABC) to model the fields at the outer boundary of the mesh. The concept of the impedance boundary condition has been used extensively in numerical techniques based on integral equation formulations. In those cases where the IBC closely approximates the exact boundary condition, its use can result in a dramatic reduction in the number of unknowns needed in the numerical solution procedure. In this paper we discuss the use of the IBC concept in a partial differential equation formulation. At the outer boundary of the mesh, rather than using the bymoment method or some hybrid boundary condition, we employ an absorbing boundary condition based on an asymptotic expansion for the scattered fields [4].

This technique is particularly attractive for problems in which both inhomogeneous and large, lossy objects are in the problem domain; the presence of the inhomogeneous objects makes the use of the finite element method advantageous; the use of the IBC at the surface of the large lossy objects obviates the extension of the finite element mesh into the interior of these objects and thus dramatically reduces the number of unknowns; and the use of the ABC allows mesh truncation without an increase in the bandwidth of the finite element matrix.

II. FORMULATION

We assume that all field quantities vary in time as $\exp(j\omega t)$. The incident field is a plane wave; the wave vector of this plane wave makes an angle θ_{inc} with the positive z -axis and ϕ_{inc} with the positive x -axis. Thus, the incident field, and likewise the scattered field, vary in the z -direction as $\exp(-j\beta z)$ where $\beta = k_0 \cos(\theta_{inc})$. In order to derive the equations that will be solved using the finite element method, we first consider the behavior of E_z and H_z inside a single element, Δ . Since the material properties, ϵ and μ , are assumed to be constant within each individual element, the equations governing E_z and H_z inside Δ can be written as

$$\nabla_t \left(\frac{\epsilon}{k_s^2} \nabla_t E_z \right) + \epsilon E_z = 0 \quad (1)$$

and

$$\nabla_t \left(\frac{\mu}{k_s^2} \nabla_t H_z \right) + \mu H_z = 0 \quad (2)$$

where

$$\nabla_t = \hat{x} \frac{\partial}{\partial x} + \hat{y} \frac{\partial}{\partial y} \quad \text{and} \quad k_s^2 = \omega^2 \mu \epsilon - \beta^2.$$

If we multiply (1) and (2) by a testing function T and use the fact that $\nabla_t \cdot \nabla_t g = \nabla_t \cdot (f \nabla_t g) - \nabla_t f \cdot \nabla_t g$, we obtain the weak forms of the equations governing E_z and H_z inside Δ ,

$$\nabla_t \left(\frac{\epsilon}{k_s^2} T \nabla_t E_z \right) - \frac{\epsilon}{k_s^2} \nabla_t T \cdot \nabla_t E_z + \epsilon T E_z = 0 \quad (3)$$

and

$$\nabla_t \left(\frac{\mu}{k_s^2} T \nabla_t H_z \right) - \frac{\mu}{k_s^2} \nabla_t T \cdot \nabla_t H_z + \mu T H_z = 0. \quad (4)$$

If these equations are integrated over Δ and the divergence theorem is used, we obtain

$$\int_{\Delta} \frac{\epsilon}{k_s^2} \nabla_t T \cdot \nabla_t E_z \, dA - \int_{\Delta} \epsilon T E_z \, dA = \frac{1}{j\omega} \int_{\partial\Delta} \frac{j\omega \epsilon}{k_s^2} T \frac{\partial E_z}{\partial n} \, dl \quad (5)$$

and

$$\int_{\Delta} \frac{\mu}{k_s^2} \nabla_t T \cdot \nabla_t H_z \, dA - \int_{\Delta} \mu T H_z \, dA = \frac{1}{j\omega} \int_{\partial\Delta} \frac{j\omega \mu}{k_s^2} T \frac{\partial H_z}{\partial n} \, dl \quad (6)$$

where dA is the area element on Δ , $\partial\Delta$ is the boundary of Δ , and the partial derivative with respect to n denotes the outward normal derivative along $\partial\Delta$. If we let τ denote the tangential direction around $\partial\Delta$ defined by

$$\hat{\tau} = \hat{z} \times \hat{n}$$

and use Maxwell's equations to express the transverse components of \mathbf{E} and \mathbf{H} in terms of E_z and H_z , we find that

$$\hat{\tau} \cdot \mathbf{E} = \frac{j\omega \mu}{k_s^2} \frac{\partial H_z}{\partial n} - \frac{j\beta}{k_s^2} \nabla_t E_z \cdot \hat{\tau} \quad (7)$$

and

$$\hat{\tau} \cdot \mathbf{H} = -\frac{j\omega\epsilon}{k_s^2} \frac{\partial E_z}{\partial n} - \frac{j\beta}{k_s^2} \nabla_t H_z \cdot \hat{\tau}. \quad (8)$$

When (7) and (8) are substituted into (5) and (6) the resulting equations are

$$\iint_{\Delta} \frac{\epsilon}{k_s^2} \nabla_t T \cdot \nabla_t E_z dA - \iint_{\Delta} \epsilon T E_z dA + \frac{1}{j\omega} \int_{\partial\Delta} \frac{j\beta}{k_s^2} T \nabla_t H_z \cdot \hat{\tau} dl = -\frac{1}{j\omega} \int_{\partial\Delta} T \hat{\tau} \cdot \mathbf{H} dl \quad (9)$$

and

$$\iint_{\Delta} \frac{\mu}{k_s^2} \nabla_t T \cdot \nabla_t H_z dA - \iint_{\Delta} \mu T H_z dA - \frac{1}{j\omega} \int_{\partial\Delta} \frac{j\beta}{k_s^2} T \nabla_t E_z \cdot \hat{\tau} dl = \frac{1}{j\omega} \int_{\partial\Delta} T \hat{\tau} \cdot \mathbf{E} dl. \quad (10)$$

If we use Stokes's theorem to replace the boundary integrals on the left hand side of each equation with area integrals, we obtain

$$\iint_{\Delta} \frac{\epsilon}{k_s^2} \nabla_t T \cdot \nabla_t E_z dA - \iint_{\Delta} \epsilon T E_z dA + \iint_{\Delta} \frac{\beta}{\omega k_s^2} \nabla_t T \times \nabla_t H_z \cdot \hat{z} dA = -\frac{1}{j\omega} \int_{\partial\Delta} T \hat{\tau} \cdot \mathbf{H} dl \quad (11)$$

and

$$\iint_{\Delta} \frac{\mu}{k_s^2} \nabla_t T \cdot \nabla_t H_z dA - \iint_{\Delta} \mu T H_z dA - \iint_{\Delta} \frac{\beta}{\omega k_s^2} \nabla_t T \times \nabla_t E_z \cdot \hat{z} dA = \frac{1}{j\omega} \int_{\partial\Delta} T \hat{\tau} \cdot \mathbf{E} dl. \quad (12)$$

These equations describe the behavior of E_z and H_z inside a single element. When we put together all the elements to form the entire meshed region, Γ , we note that the area integrals on the left hand sides of these equations simply add together to form the corresponding area integrals over Γ . Because the tangential components of \mathbf{E} and \mathbf{H} are continuous across any source-free interface, the boundary integrals on the right hand sides of these equations will cancel along any interior edges; all that will remain are integrals along the inner boundary, $\partial\Gamma_{in}$, and the outer boundary, $\partial\Gamma_{out}$. Thus, the equations governing E_z and H_z inside Γ are identical to (11) and (12) except that Δ is replaced by Γ . If we make this replacement, substitute (7) and (8) into the boundary integrals on the right hand side of each equation, and multiply through by ω , we obtain

$$\begin{aligned} & \iint_{\Gamma} \frac{\epsilon_r}{\eta_o k_s^2} \nabla_t T \cdot \nabla_t E_z dA - \iint_{\Gamma} \frac{\epsilon_r}{\eta_o} T E_z dA + \iint_{\Gamma} \frac{\cos(\theta_{inc})}{k_s^2} \nabla_t T \times \nabla_t H_z \cdot \hat{z} dA - \int_{\partial\Gamma_{in}} \frac{\cos(\theta_{inc})}{k_s^2} T \nabla_t H_z \cdot \hat{\tau} dl \\ & - \int_{\partial\Gamma_{out}} \frac{\cos(\theta_{inc})}{k_s^2} T \nabla_t H_z \cdot \hat{\tau} dl = \int_{\partial\Gamma_{in}} \frac{\epsilon_r}{\eta_o k_s^2} T \frac{\partial E_z}{\partial n} dl + \int_{\partial\Gamma_{out}} \frac{\epsilon_r}{\eta_o k_s^2} T \frac{\partial E_z}{\partial n} dl \end{aligned} \quad (13)$$

and

$$\begin{aligned}
& \int_{\Gamma} \frac{\eta_o \mu_r}{k_s^2} \nabla_t T \cdot \nabla_t H_z dA - \int_{\Gamma} \eta_o \mu_r T H_z dA - \iint_{\Gamma} \frac{\cos(\theta_{inc})}{k_s^2} \nabla_t T \times \nabla_t E_z \cdot \hat{z} dA + \int_{\partial\Gamma_{in}} \frac{\cos(\theta_{inc})}{k_s^2} T \nabla_t E_z \cdot \hat{\tau} dl \\
& + \int_{\partial\Gamma_{out}} \frac{\cos(\theta_{inc})}{k_s^2} T \nabla_t E_z \cdot \hat{\tau} dl = \int_{\partial\Gamma_{in}} \frac{\eta_o \mu_r}{k_s^2} T \frac{\partial H_z}{\partial n} dl + \int_{\partial\Gamma_{out}} \frac{\eta_o \mu_r}{k_s^2} T \frac{\partial H_z}{\partial n} dl.
\end{aligned} \tag{14}$$

Note that Stokes's theorem cannot be used to rewrite the boundary integrals on the left hand side of each of these equations. The reason for this is that the integrands are not continuous over all of Γ . But this is no cause for concern; since these boundary integrals involve only the tangential derivatives of E_z and H_z along the boundaries of the mesh, they pose no difficulty in the finite element solution procedure. However, the boundary integrals on the right hand side of each equation are a different matter; their evaluation requires knowledge of the normal derivatives of the unknowns along the boundaries. Along the inner boundary, we solve this difficulty by turning to the impedance boundary conditions,

$$E_z = -\eta_{TM} H_\tau \tag{15}$$

and

$$H_z = \frac{1}{\eta_{TE}} E_\tau. \tag{16}$$

Algebraic manipulation of the equations that are obtained through substitution of (15) and (16) into (7) and (8) yields

$$\frac{\partial E_z}{\partial n} = \frac{1}{\omega \epsilon_o \epsilon_r} \left(-k_o \cos(\theta_{inc}) \frac{\partial H_z}{\partial \tau} - \frac{j k_s^2}{\eta_{TM}} E_z \right) \tag{17}$$

and

$$\frac{\partial H_z}{\partial n} = \frac{1}{\omega \mu_o \mu_r} \left(k_o \cos(\theta_{inc}) \frac{\partial E_z}{\partial \tau} - j k_s^2 \eta_{TE} H_z \right). \tag{18}$$

Thus, through use of the impedance boundary conditions (15) and (16) we are able to rewrite the normal derivative terms that appear in the inner boundary integrals in (13) and (14) in terms of the unknowns and their tangential derivatives. Substitution of (17) and (18) into (13) and (14) yields

$$\begin{aligned}
& \iint_{\Gamma} \frac{\epsilon_r}{\eta_o k_s^2} \nabla_t T \cdot \nabla_t E_z dA - \iint_{\Gamma} \frac{\epsilon_r}{\eta_o} T E_z dA + \iint_{\Gamma} \frac{\cos(\theta_{inc})}{k_s^2} \nabla_t T \times \nabla_t H_z \cdot \hat{z} dA - \int_{\partial\Gamma_{out}} \frac{\cos(\theta_{inc})}{k_s^2} T \nabla_t H_z \cdot \hat{\tau} dl \\
& + \int_{\partial\Gamma_{in}} \frac{j}{k_o \eta_{TM}} T E_z dl = \int_{\partial\Gamma_{out}} \frac{\epsilon_r}{\eta_o k_s^2} T \frac{\partial E_z}{\partial n} dl
\end{aligned} \tag{19}$$

and

$$\begin{aligned}
& \iint_{\Gamma} \frac{\eta_o \mu_r}{k_s^2} \nabla_t T \cdot \nabla_t H_z dA - \iint_{\Gamma} \eta_o \mu_r T H_z dA - \iint_{\Gamma} \frac{\cos(\theta_{inc})}{k_s^2} \nabla_t T \times \nabla_t E_z \cdot \hat{z} dA + \int_{\partial\Gamma_{out}} \frac{\cos(\theta_{inc})}{k_s^2} T \nabla_t E_z \cdot \hat{\tau} dl \\
& + \int_{\partial\Gamma_{in}} \frac{j\eta_{IE}}{k_o} T H_z dl = \int_{\partial\Gamma_{out}} \frac{\eta_o \mu_r}{k_s^2} T \frac{\partial H_z}{\partial n} dl.
\end{aligned} \quad (20)$$

The only remaining difficulty is the presence of the normal derivative terms in the outer boundary integrals. If we let k_{so} be the value of k_s at $\partial\Gamma_{out}$, which lies in the free space region outside the scatterer, and if $\partial\Gamma_{out}$ is circular and sufficiently far from the scatterer, then, along this boundary the normal derivative of u , where u represents the scattered part of either E_z or H_z , is, to a good approximation:

$$\frac{\partial u}{\partial n} = \alpha(\rho)u + \beta(\rho)\frac{\partial^2 u}{\partial \tau^2}. \quad (21)$$

where

$$\alpha(\rho) = -jk_{so} - \frac{1}{2\rho} - \frac{j}{8k_{so}\rho^2} + \frac{1}{8k_{so}^2\rho^3}$$

and

$$\beta(\rho) = -\frac{j}{2k_{so}\rho^2} + \frac{1}{2k_{so}^2\rho^3}.$$

This is the mathematical expression of the absorbing boundary condition. The derivation is explained in detail in [5]. Note that the normal derivative of u has been written solely in terms of u itself and a tangential derivative of u . Thus, the use of this boundary condition does not increase the bandwidth of the finite element matrix. As was stated above, u represents the axial component of the scattered electric or magnetic field. Thus, the absorbing boundary condition expressed by (21) can be used in (19) and (20) to obtain the final equations that are solved using the finite element method,

$$\begin{aligned}
& \iint_{\Gamma} \frac{\epsilon_r}{\eta_o k_s^2} \nabla_t T \cdot \nabla_t E_z dA - \iint_{\Gamma} \frac{\epsilon_r}{\eta_o} T E_z dA + \iint_{\Gamma} \frac{\cos(\theta_{inc})}{k_s^2} \nabla_t T \times \nabla_t H_z \cdot \hat{z} dA - \int_{\partial\Gamma_{out}} \frac{\cos(\theta_{inc})}{k_s^2} T \nabla_t H_z \cdot \hat{\tau} dl \\
& + \int_{\partial\Gamma_{in}} \frac{j}{k_o \eta_{IM}} T E_z dl - \int_{\partial\Gamma_{out}} \frac{\epsilon_r}{\eta_o k_s^2} T \left(\alpha(\rho)E_z + \beta(\rho)\frac{\partial^2 E_z}{\partial \tau^2} \right) dl = \int_{\partial\Gamma_{out}} \frac{\epsilon_r}{\eta_o k_s^2} T \left[\frac{\partial E_z^{inc}}{\partial n} - \left(\alpha(\rho)E_z^{inc} + \beta(\rho)\frac{\partial^2 E_z^{inc}}{\partial \tau^2} \right) \right] dl
\end{aligned} \quad (22)$$

and

$$\begin{aligned}
& \int_{\Gamma} \frac{\eta_0 \mu_r}{k_s^2} \nabla_t T \cdot \nabla_t H_z dA - \int_{\Gamma} \eta_0 \mu_r T H_z dA - \int_{\Gamma} \frac{\cos(\theta_{inc})}{k_s^2} \nabla_t T \times \nabla_t E_z \cdot \hat{z} dA + \int_{\partial\Gamma_{out}} \frac{\cos(\theta_{inc})}{k_s^2} T \nabla_t E_z \cdot \hat{\tau} dl \\
& + \int_{\partial\Gamma_{in}} \frac{j\eta_{TE}}{k_0} T H_z dl - \int_{\partial\Gamma_{out}} \frac{\eta_0 \mu_r}{k_s^2} T \left(\alpha(\rho) H_z + \beta(\rho) \frac{\partial^2 H_z}{\partial \tau^2} \right) dl = \int_{\partial\Gamma_{out}} \frac{\eta_0 \mu_r}{k_s^2} T \left[\frac{\partial H_z^{inc}}{\partial n} - \left(\alpha(\rho) H_z^{inc} + \beta(\rho) \frac{\partial^2 H_z^{inc}}{\partial \tau^2} \right) \right] dl. \quad (23)
\end{aligned}$$

In these equations, those field components having no superscript refer to the total field while those with the superscript "inc" refer to the incident field.

III. NUMERICAL RESULTS

As an example of the application of this technique, we consider the problem shown in Fig. 1. Along the surface of the circular cylinder of radius $a=0.32\lambda_0$ we enforce the impedance boundary conditions (15) and (16) where $\eta_{TM}=180-j40\Omega$ and $\eta_{TE}=200-j20\Omega$. The finite element mesh is truncated at a radius of $0.5\lambda_0$, i.e., $0.18\lambda_0$ from the surface of the scatterer. The obliquely incident field is TM to z . The z component of the incident electric field is:

$$E_z^{inc}(x,y,z) = \sin(\theta_{inc}) e^{-jk_0(\sin(\theta_{inc})\cos(\phi_{inc})x + \sin(\theta_{inc})\sin(\phi_{inc})y + \cos(\theta_{inc})z}$$

where $\theta_{inc}=135.0^\circ$ and $\phi_{inc}=180.0^\circ$. Figure 2 presents a comparison of the numerically determined values of the magnitudes of E_z and $\eta_0 H_z$ with the analytical values for these quantities; fig. 3 shows the comparison of the phases. In both figures, the circles and rectangles represent the numerically determined values of E_z and $\eta_0 H_z$, respectively, while the diamonds and cross marks show the analytical values of E_z and $\eta_0 H_z$, respectively. Clearly, there is excellent agreement between the numerically determined and analytical values.

IV. CONCLUSIONS

In this paper, we have presented a finite element method that employs impedance boundary conditions and an absorbing boundary condition to determine the electromagnetic scattering by lossy cylindrical structures that are illuminated by an obliquely incident plane wave. These structures may be located in the presence of materials that are inhomogeneous in both ϵ and μ . We have presented the E_z - H_z formulation that has been used in this procedure and have shown how the impedance boundary conditions and absorbing boundary condition are incorporated into the analysis. The method has been used to solve the problem of a circular impedance cylinder illuminated by an obliquely incident plane wave. The numerical results have been shown to be quite accurate.

REFERENCES

- [1] R. G. Rojas, "Scattering by an inhomogeneous dielectric/ferrite cylinder of arbitrary cross-section shape-Oblique incidence case," *IEEE Trans. Antennas Propagat.*, vol. 36, pp. 238-246, Feb. 1988.
- [2] E. Michielssen, A. F. Peterson and R. Mittra, "Oblique scattering from inhomogeneous cylinders using a coupled integral equation formulation with triangular cells," *IEEE Trans. Antennas Propagat.*, vol. 39, pp. 485-490, April 1991.
- [3] A. C. Cangellaris and R. Lee, "Finite element analysis of electromagnetic scattering from inhomogeneous cylinders at oblique incidence," *IEEE Trans. Antennas Propagat.*, vol. 39, pp. 645-650, May 1991.
- [4] J. J. Bowman, T. B. A. Senior and L. E. Uslenghi, ed., *Electromagnetic and Acoustic Scattering by Simple Shapes*, North-Holland, Amsterdam, 1969.

- [5] R. K. Gordon and J.-F. Lee, "A finite element method that employs an absorbing boundary condition for determining the electromagnetic scattering by inhomogeneous cylindrical structures that are illuminated by an obliquely incident field," to appear in *IEEE Trans. Magnetics*.

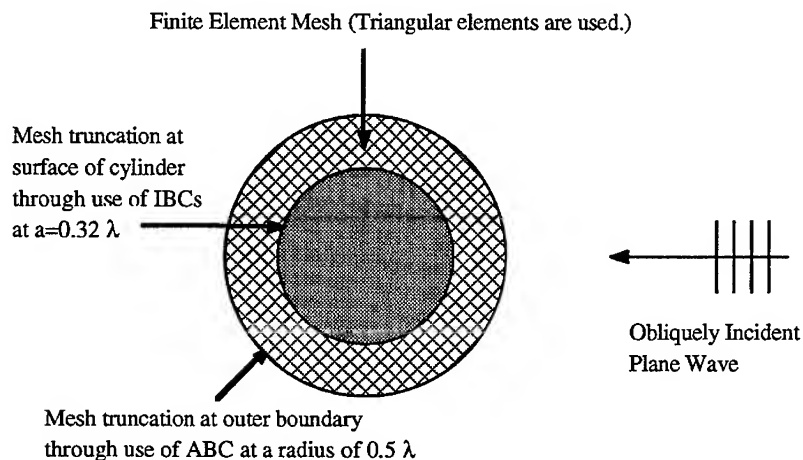


Fig. 1. Diagram of problem

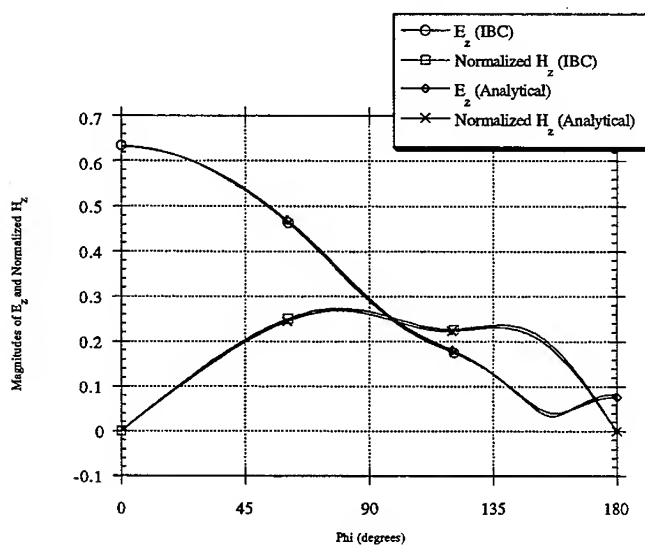


Fig. 2. Comparison of numerically determined values of magnitudes with analytical values

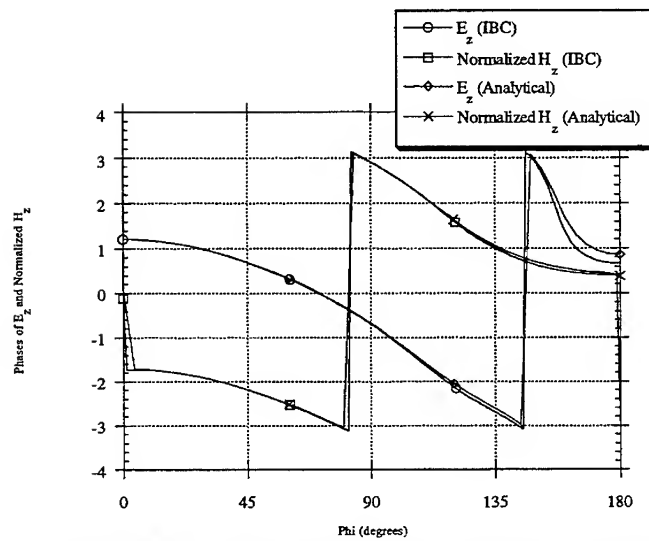


Fig. 3. Comparison of numerically determined values of phases with analytical values

NUMERICAL ANALYSIS OF MICROWAVE CAVITIES WITH ANISOTROPIC MATERIALS

Shirley Min	Jin-Fa Lee	Richard Gordon
Medtronic	Worcester Poly. Inst.	U. of Mississippi
Minneapolis, MN55432	Worcester, MA01609	University, MS38677

Abstract

The application of edge-elements for modeling three-dimensional cavities with anisotropic materials is presented in this paper. To make the computation efficient, various numerical techniques have been employed in the formulation. For example, analytical expressions for the element matrices to assemble the final finite element matrices, the minimum degree of reordering scheme to result in best unknown numbering scheme, the quasi-minimal residual (QMR) method for solving matrix equations, and the Lanczos algorithm for the solution of large-sparse generalized eigenmatrix equation.

1 INTRODUCTION

The analysis of three-dimensional inhomogeneously-filled cavities using edge-elements has been presented by Lee and Mittra [1]. The current contribution is the extension of reference [1] to include the anisotropic effects of the material properties which are often presented in real-life cavity structures.

The paper is organized as follows: Section 2 describes the variational formulation of three-dimensional cavities with anisotropic materials. The solution procedure of the variational formulation in a finite-dimensional space, or the finite element implementation, is presented in Sec. 3. Finally, numerical results of a finline cavity, and a microstrip cavity with anisotropic substrate are shown in Sec. 4.

2 VARIATIONAL FORMULATION

The basic equations that govern EM fields in source-free, time-harmonic regions are the Maxwell equations

$$\nabla \times \vec{E} = -j\omega\mu\vec{H} \quad (1)$$

$$\nabla \times \vec{H} = j\omega[\epsilon]\vec{E} \quad (2)$$

where $[\epsilon]$ and μ are the permittivity and permeability, respectively. In this paper, the permeability μ is assumed to a scalar, and the permittivity $[\epsilon]$ a diagonal tensor. The extension to most general case is straightforward and is currently under development. We note that, with $\omega \neq 0$, Eqs. (1) and (2) imply that

$$\nabla \cdot \mu\vec{H} = 0 \quad (3)$$

$$\nabla \cdot [\epsilon]\vec{E} = 0 \quad (4)$$

The substitution of \vec{E} from Eq. (2) into (1) and of \vec{H} from (1) into (2) yields the vector wave equations

$$\nabla \times \frac{1}{\mu_r} \nabla \times \vec{E} = k^2 [\epsilon_r] \vec{E} \quad (5)$$

$$\nabla \times [\epsilon_r]^{-1} \nabla \times \vec{H} = k^2 \mu_r \vec{H} \quad (6)$$

where $k^2 = \omega^2 \mu_0 \epsilon_0$, ϵ_0, μ_0 are the permittivity and permeability of air, respectively. In view of the similarity between Eqs. (5) and (6), the analysis in this paper will be presented in terms of the electric field \vec{E} .

It is well known that the field solution in a three-dimensional cavity can be formulated in a variational form [2]. If the cavity contains only lossless materials, the variational functional in terms of \vec{E} can be written as

$$F(\vec{E}) = \int_{\Omega} \frac{1}{\mu_r} \|\nabla \times \vec{E}\|^2 - k^2 \vec{E} \bullet [\epsilon_r] \vec{E} d\Omega \quad (7)$$

From the functional (7), we note that both $\nabla \times \vec{E}$ and \vec{E} need to be square integrable. Consequently, the solution is sought from the function space $L^2_{curl}(\Omega)$, which is defined by

$$L^2_{curl}(\Omega) = \{\vec{E} \in L^2(\Omega) : \nabla \times \vec{E} \in L^2(\Omega)\} \quad (8)$$

where $L^2(\Omega)$ is the linear space of square-integrable vector fields defined on the problem domain Ω .

3 FINITE-DIMENSIONAL DISCRETIZATION

The variational formulation in the previous section seeks the solution in the function space $L^2_{curl}(\Omega)$ which is infinite-dimensional. In order to solve a three-dimensional cavity problem on a digital computer, we need to convert the original continuum problem into a discretized version. This can be accomplished by using the finite element method. The basic idea of FEM can be described as follows [3]. First, we formulate the corresponding variational functional and the admissible function space, for example, $L^2_{curl}(\Omega)$ as in previous section. Then restrict the class to a smaller, finite dimensional function space $W(\Omega)$, which can be described by a finite number of parameters (the degrees of freedom). If this constraint is imposed properly, stationarity will occur at a point which is in the neighborhood of the true solution. Finally, imposition of the stationarity condition leads to a finite number of equations with respect to the degrees of freedom.

The approximate solution \vec{E}_{app} of (7) in the function space $W(\Omega)$, where $W(\Omega) \subset L^2_{curl}(\Omega)$, is the stationary point of the functional (7) in $W(\Omega)$ with respect to the variations of \vec{E} . Whatever the choice of the function space $W(\Omega)$, the functional $F(\vec{E})$ in $W(\Omega)$ may be expressed in a matrix form as

$$F(\vec{E}) = \frac{1}{2} e^t [S] e - \frac{k^2}{2} e^t [T] e \quad (9)$$

Here, e is the coefficient vector and the square matrices $[S]$ and $[T]$ are given by

$$[S]_{mn} = \int_{\Omega} \frac{1}{\mu_r} (\nabla \times \vec{\alpha}_m) \bullet (\nabla \times \vec{\alpha}_n) d\Omega \quad (10)$$

$$[T]_{mn} = \int_{\Omega} \vec{\alpha}_m \bullet [\epsilon_r] \vec{\alpha}_n d\Omega \quad (11)$$

where $\vec{\alpha}_i$ s are the vector functions that are used to span the vector function space $W(\Omega)$.

In the present approach, the problem domain Ω is broken into tetrahedra within which the material properties $[\epsilon_r]$ and μ_r are constant, although they may be discontinuous across the element boundaries. In each tetrahedron, the electric field is expressed as a linear combination of edge-elements, i.e., we write

$$\vec{E} = \sum_{i < j} e_{ij} \vec{w}_{ij} \quad (12)$$

where $\vec{w}_{ij} = \lambda_i \nabla \lambda_j - \lambda_j \nabla \lambda_i$, λ_i is the barycentric function of node i , is the Whitney 1-form associated with edge $\{i, j\}$ [7].

3.1 Element Matrices

In the finite element method, the global matrices $[S]$ and $[T]$ of Eq. (9) are the assembly of the element matrices, $[S]_e$ and $[T]_e$, i.e.

$$[S] = \sum_e [S]_e \quad (13)$$

$$[T] = \sum_e [T]_e \quad (14)$$

The constructions of the element matrices, $[S]_e$ and $[T]_e$, depend on the choice of the finite dimensional function space $W(\Omega)$. In the present approach, $W(\Omega)$ is spanned by edge-elements on a tetrahedral mesh. The analytic expression of the element $[S]_e$ using edge-elements has been shown in reference [1] and, therefore, we will not repeat the derivation here. However, since the relative permittivity $[\epsilon_r]$ is now a tensor, the element matrix $[T]_e$ has to be modified.

The geometrical identities that are useful in the derivation, given below are:

$$\nabla \lambda_i = \frac{\vec{A}_i}{3V} \quad (15)$$

$$\begin{aligned} \vec{A}_i \times \vec{A}_j &= \frac{3V}{2} s (-1)^{j-i} \vec{t}_{k,l} \\ s &= \text{sgn}(\vec{t}_{1,2} \times \vec{t}_{1,3} \bullet \vec{t}_{1,0}) \end{aligned} \quad (16)$$

for $i < j$. Here, \vec{A}_i is the area normal of the triangular face $\{j, k, l\}$ pointing into the tetrahedron, V is the volume of the tetrahedron, $\vec{t}_{k,l}$ is a vector from node k to node l ,

and $\{k, l\} = \{0, 1, 2, 3\} - \{i, j\}$, with $k < l$. With these identities, the $[T]_e$ matrix is then modified as

$$[T]_e = \int_{\Omega_e} \begin{bmatrix} \vec{w}_{0,1} \\ \vec{w}_{0,2} \\ \vec{w}_{0,3} \\ \vec{w}_{1,2} \\ \vec{w}_{1,3} \\ \vec{w}_{2,3} \end{bmatrix} \bullet [\epsilon_r] \begin{bmatrix} \vec{w}_{0,1} & \vec{w}_{0,2} & \vec{w}_{0,3} & \vec{w}_{1,2} & \vec{w}_{1,3} & \vec{w}_{2,3} \end{bmatrix} d\Omega$$

$$= \frac{1}{180V} \begin{bmatrix} 2(I_{00} - I_{01} + I_{11}) & & & & & \\ I_{00} - I_{01} & 2(I_{00} - I_{02} + I_{22}) & & & & \\ -I_{02} + 2I_{12} & I_{00} - I_{01} & I_{00} - I_{02} & 2(I_{00} - I_{03} + I_{33}) & & \\ I_{00} - I_{01} & I_{00} - I_{02} & I_{00} - I_{03} & 2(I_{00} - I_{01} + I_{11}) & & \\ -I_{03} + 2I_{13} & -I_{03} + 2I_{23} & I_{01} - I_{11} & 2(I_{01} - I_{12} + I_{22}) & & \\ I_{01} - I_{11} & 2(I_{01} - I_{12} + I_{22}) & I_{01} - I_{13} & 2(I_{11} - I_{12} + I_{22}) & & \\ -2I_{02} + I_{12} & -I_{02} + I_{22} & -I_{02} + I_{23} & I_{12} + I_{22} & & \\ I_{01} - I_{11} & I_{01} - I_{12} & 2(I_{01} - I_{13} + I_{33}) & I_{11} - I_{12} & 2(I_{11} - I_{13} + I_{33}) & \\ -2I_{03} + I_{13} & -I_{03} + I_{23} & -I_{03} + I_{33} & -I_{13} + 2I_{23} & I_{13} + I_{33} & \\ I_{02} - I_{12} & I_{02} - I_{22} & 2(I_{02} - I_{23} + I_{33}) & I_{12} - I_{22} & 2(I_{12} - I_{23} + I_{33}) & \\ -I_{03} + I_{13} & -2I_{03} + I_{23} & -I_{03} + I_{33} & -2I_{13} + I_{23} & -I_{13} + I_{33} & 2(I_{22} - I_{23} + I_{33}) \end{bmatrix} \quad (17)$$

where $I_{ij} = \vec{A}_i \bullet \vec{A}'_j$, and $\vec{A}'_i = [\epsilon_r] \vec{A}_i$.

3.2 Transformed Generalized Eigenmatrix Equation

The stationary points of the functional $F(\vec{E})$ in (9) correspond to the solutions of the following generalized eigenmatrix equation

$$[S]e = k^2[T]e \quad (18)$$

Note that the global matrices $[S]$ and $[T]$ are semi-definite and positive-definite real-symmetric matrices, respectively. Despite their sparse nature, the dimension of the generalized eigenmatrix equation is large and, hence, only iterative methods can be used to solve (20). The Lanczos algorithm [4] has been used, with much success, to solve symmetric generalized eigenmatrix equations. However, since in Eq. (20) the more dominant mode corresponds to smaller eigenvalue k^2 , the direct application of the Lanczos algorithm may converge rather

slowly. This problem can be circumvented, however, and a computationally efficient algorithm can be derived by rewriting (20). To this end, we first find an estimate k_g^2 , the lower bound of the physical modes, which can be approximated from the largest dimension and the material properties inside the cavity. We then rewrite (20) as

$$[A]x = \lambda[B]x \quad (19)$$

where $[A] = [T]$, $\lambda = \frac{1}{k^2 + k_g^2}$ and $[B] = [S] + k_g^2[T]$. The advantage of using (21) is that, except for the null vectors of the curl operator, the more dominant modes correspond to the larger eigenvalues of this equation. Due to the nature of the Krylov subspace iteration, the larger eigenpairs almost always converge faster. Therefore, by rearranging the generalized eigenmatrix equation into Eq. (21), the resonant modes of the cavity can be computed more or less in the order of dominance.

The convergence of the Lanczos algorithm for the dominant mode, with $k^2 \neq 0$, can be improved drastically by selecting an initial vector which is orthogonal to the null ($k^2 = 0$) eigenpairs [5]. To result in a practical computer simulation tool for modeling three-dimensional cavities with anisotropic materials, various numerical techniques have been incorporated in the computer codes thus developed. The flowchart of the current implementation is shown in Fig. 1. In the application of the Lanczos algorithm for the solution

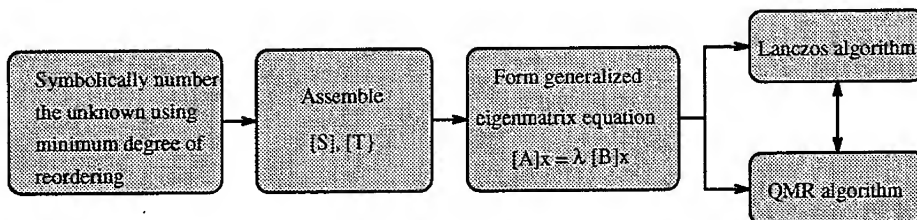


Figure 1: Computer implementation of the proposed method.

of a generalized eigenmatrix equation 19, each iteration step involves the matrix equation of the form

$$v = [B]^{-1}y \quad (20)$$

where v is the updated Krylov vector generated through iteration upon y . This matrix equation can be efficiently solved by using the quasi-minimal residual algorithm [6].

4 NUMERICAL RESULTS

4.1 Finline Cavity

Shown in Fig. 2 is a finline cavity whose dimensions are: $a = 20$ mm; $b = 15$ mm; $c = 10$ mm; $s = 1$ mm; and $d = 4$ mm. The relative permittivity of the dielectric material is

$\epsilon_r = 2.22$ Figure 3(a) summarizes a few descriptions of the finite element mesh that is used

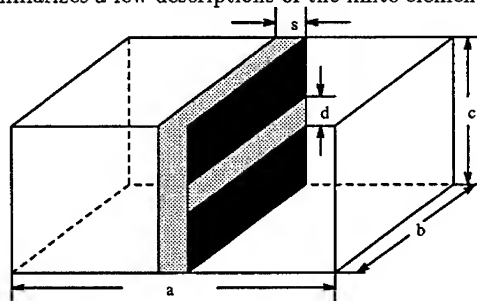


Figure 2: A finline cavity.

for the simulation. The computed resonance frequency of the dominant mode is compared with spectral-domain analysis (S.D.A) [7], variable mesh TLM [7], transmission-line method (TLM) [8], and time-domain finite-difference method (TDFD) [8] in Fig. 3(b).

element size	2 mm
# of edges	7661
# of tetrahedra	5889
# of nodes	1273
# of unknowns	6053

(a)

	Saguet		Choi etc.		
Dominant Frequency (GHz)	S.D.A.	V. M. TLM	TDFD	TLM	FEM
	10.77	10.14	10.74	10.74	10.37

(b)

Figure 3: (a) Finite element mesh information; and, (b) Numerical result compares to various methods.

4.2 Microstrip Cavity with Anisotropic Substrate

Figure 4 shows a microstrip cavity with anisotropic substrate. The dimensions and the permittivity of the substrate are: $a = 6.5$ mm; $b = 3.5$ mm; $h = 1.5$ mm; $w = 1.5$ mm; $\epsilon_{xx} = 9.4$; $\epsilon_{yy} = 11.6$; and $\epsilon_{zz} = 9.4$. The numerical results for different values of c are compared to the TDFD and TLM methods. As evidenced from Fig. 5, the FEM results are closer to the TLM results than the TDFD ones.

ACKNOWLEDGES

The authors would like to express their thanks to Mr. Eric Lucas and Prof. Stephen Gedney for providing the information on QMR algorithm and the minimum degree of reordering codes, respectively.

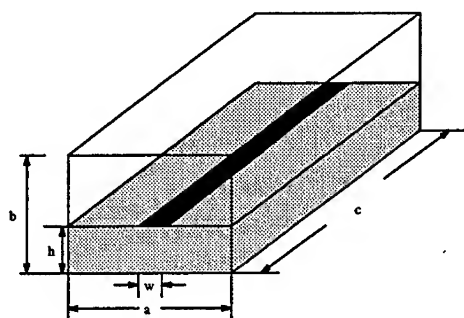


Figure 4: A microstrip cavity with anisotropic substrate.

c (mm)	3	4	5	7.5	10
TLM (GHz)	15.72	12.24	10.14	7.14	5.46
TDFD (GHz)	14.64	11.52	9.54	6.78	5.28
FEM (GHz)	15.23	12.04	10.02	7.16	5.63

Figure 5: Numerical results for different c values.

References

- [1] J. F. Lee and R. Mittra, "A note on the application of edge-elements for modeling three-dimensional inhomogeneously-filled cavities," *IEEE Transactions on Microwave Theory and Techniques*, pp. 1767-1773, Sep. 1992.
- [2] R. F. Harrington, *Time Harmonic Electromagnetic Fields*, New York: McGraw-Hill, 1961.
- [3] A. Bossavit, "Simplicial finite elements for scattering problems in electromagnetism," *Computer Methods in Applied Mechanics and Engineering*, 76, pp. 299-316, 1989.
- [4] B. N. Parlett, *The Symmetric Eigenvalue Problem*, Englewood Cliffs, NJ: Prentice-Hall, 1980.
- [5] J. F. Lee, D. K. Sun, and Z. J. Cendes, "Full-wave analysis of dielectric waveguides using tangential vector finite elements," *IEEE Trans. Microwave Theory and Tech.*, MTT-39, pp. 1262-1271, August, 1991.
- [6] R. Freund, "Conjugate gradient type methods for linear systems with complex symmetric coefficient matrices," RIACS technical report 89.54, Dec. 1989.

-
- [7] P. Saguet, "Le maillage parallelepipedique et le changement de maille dans la methode TLM en trois dimensions," *Electron. Lett.*, vol. 20, pp. 222-224, Mar. 1984.
- [8] D. H. Choi and W. J. R. Hoefer, "The finite-difference-time-domain method and its application to eigenvalue problems," *IEEE Trans. Microwave Theory and Tech.*, MTT-34, pp. 1464-1469, Dec. 1986.

LATE PAPERS

THE FOLLOWING PAPERS WERE RECEIVED

TOO LATE FOR INCLUSION

IN THEIR PROPER SESSIONS.

The Electromagnetic Modeler's Workbench for GEMACS

by

Edgar L. Coffey
Advanced Electromagnetics
Albuquerque, New Mexico

Robert Fisher
Science & Engineering Associates, Inc.
Albuquerque, New Mexico

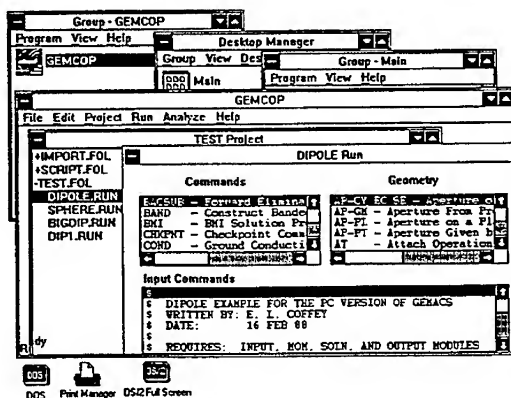
The Electromagnetic Modeler's Workbench lets GEMACS [1] users manage data, create command and geometry inputs, and extract data for analysis using a user-friendly graphical interface. Developed for the IBM OS/2 Presentation Manager, the Modeler's Workbench is a seamless application that greatly leverages the ability of the GEMACS user to create complex simulations, store all observables in a common database, and retrieve data for printing and plotting from any combination of GEMACS runs, parameters, or excitations.

The purpose of this paper is to describe the important features of the Modeler's Workbench and to illustrate how it is used in day-to-day GEMACS operations.

Overview of the Workbench

The Electromagnetic Modeler's Workbench (EMW) is the ultimate electromagnetic analyst's tool. It has been specifically designed to operate with GEMACS but is general enough to be applied to other analysis programs such as NEC or BSC with simple additions and modifications. Its operation and use are made straightforward through the graphics-based implementation in OS/2's Presentation Manager.

The EMW provides support for all your GEMACS analytic needs. You can create new run files easily from commands and geometry lists which provide full syntax reference for each statement. Check your old and new run files with a built-in syntax and statement sequence checker. Manage your projects easily with the structured subdirectory format for file handling.



This work was sponsored in part by the U.S. Air Force Phillips Laboratory under contract F29601-89-C-0074.

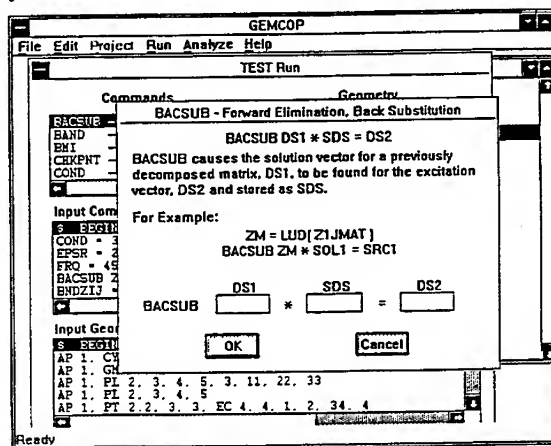
You can create and manage large numbers of projects, folders, and runs with EMW. As you build up a database of files, keyword and class-word entries associated with each run will allow you to automatically sort through the large amount of data quickly and efficiently to extract information from a single file or group of related files for analysis.

Project Management

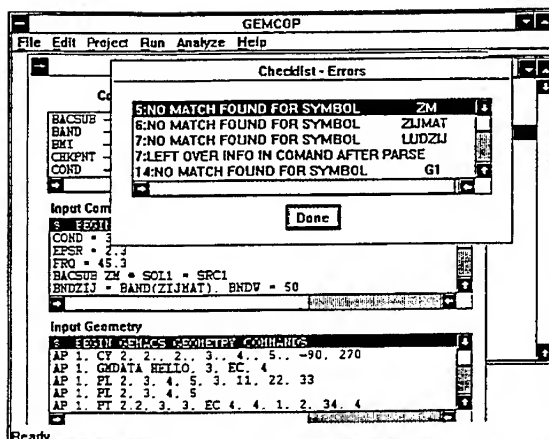
The massive amount of data accumulated in any numerical analysis can be both cumbersome to store and difficult to sift through for relevant information. The Modeler's Workbench lets you create Projects and Folders to contain the GEMACS files that will be run for that Project. Once you have begun your database, the Workbench helps you organize and select the files with which you want to work. You can even import GEMACS files which were not created with the Workbench. As you import a file, it is automatically checked for proper syntax and then written to the Workbench database in standard format. If errors are encountered, the imported file can still be used with the Workbench by editing it in the Run window (see below).

GEMACS Input Creation

Imagine creating a complex GEMACS input stream without having to refer to your old manuals! The EMW provides you a run window with all available commands and geometry statements listed for selection. You don't remember the correct syntax? The EMW does the work. Every time you make a selection from the Commands or Geometry lists, an information dialog box pops up with the description of the command and its proper syntax.



When you have completed your run file entry, or imported a GEMACS file, you can run the EMW file integrity and syntax checking software (CHEKLIST) from the Run menu. CHEKLIST provides you not only information on the errors in syntax that may be in your file; it also checks for completeness. Any errors that are found are flagged so that you can then make the corrections in the Run file list window.



Execution Management

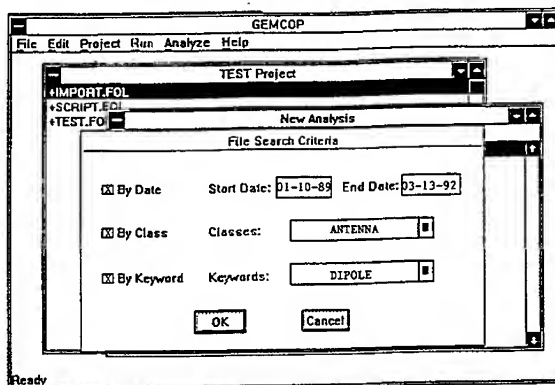
You can also run GEMACS directly from the EMW. Simply select the modules that you want to execute and click on the OK button. Your GEMACS run is on its way to execution, but you can continue to work, either within EMW or by using OS/2's multi-tasking features with another program, while GEMACS runs in background.

After the run is complete, the GEMACS symbols can be annotated with text so that you'll remember just what it was that "IX2FCT" stood for. You can also annotate the entire run file set with comments, keywords, and classifications so that they can be accessed by the ANALYZE option.

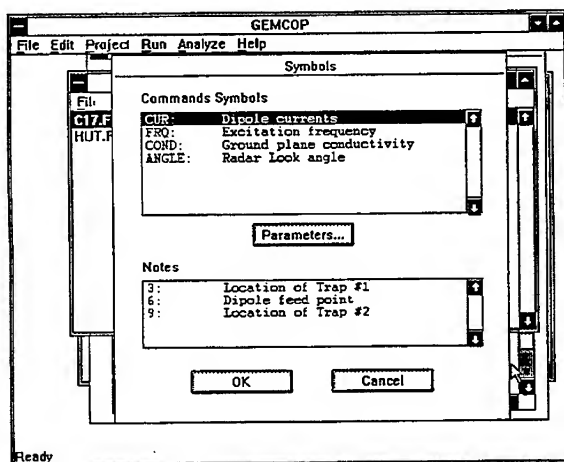
Results Analysis and Hard Copy

Ever wish you could view your GEMACS currents and fields immediately? The EMW ANALYZE feature provides immediate feedback by displaying the results of any solution or field plotted against any GEMACS parameter. Multiple GEMACS runs? No problem. ANALYZE searches your entire Project database for all runs that meet your search criteria: date, run class, and keyword list. You the user then get to selectively pick which data are to be plotted from lists automatically displayed by ANALYZE.

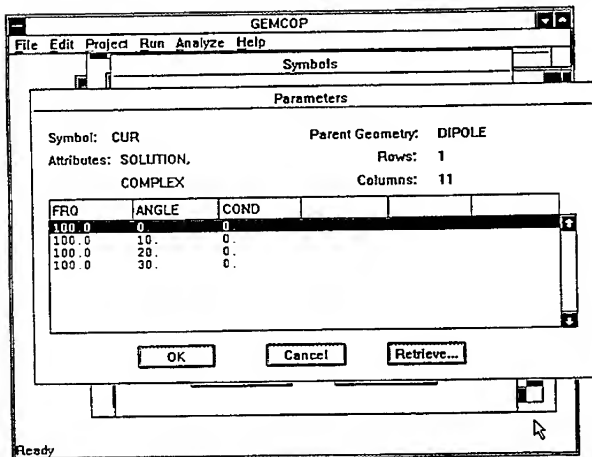
As an EMW user you have much more control over GEMACS than you would otherwise. The EMW can add lists of keywords and classes to each run, annotate GEMACS symbols with your definitions and memory joggers, and parameterize the output data before running GEMACS. These features are used by ANALYZE to search and correlate output data and to plot it however you the user desire.



Extracting data is always much harder than generating it, but ANALYZE makes this process virtually painless. First, the EMW displays a list of runs that meet your search criteria. You select a run from the list, and ANALYZE displays a list of all your GEMACS symbols associated with the run.

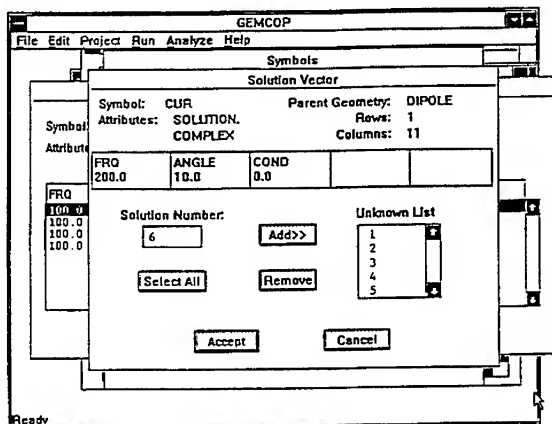


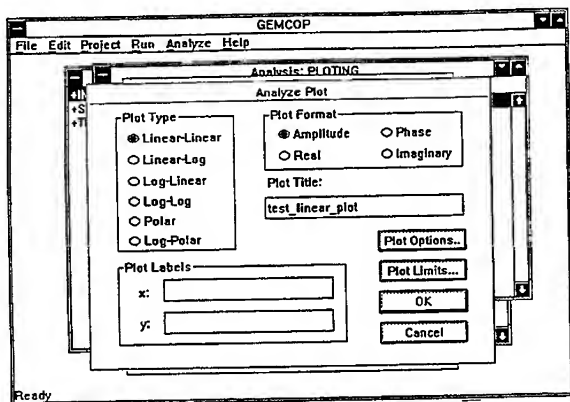
You select the symbol whose data you're interested in, and ANALYZE lists all combinations of parameters (e.g., frequency, conductivity, look angle, or any other symbol you've defined) for which data has been generated. After selecting a parameter combination, you are asked which data points you want to select for plotting, or by default you can select all the data.



The process can be repeated as many times as needed to generate many different displays from the same data. One plot might be current vs. frequency with conductivity as a parameter. Using the same data (without re-running GEMACS), a second plot might be current vs. conductivity with frequency as a parameter. Or perhaps you have a great circle pattern cut you want transformed into conical cuts.

The EMW give the user lots of control over the appearance of the plot. Multiple data files can be overlaid for comparison purposes. Data can be plotted with linear, logarithmic, or polar scales. Either linear or dB data can be entered. Axes can be labeled and a plot title generated.





Summary

This paper has described just a few of the features incorporated into the Electromagnetic Modeler's Workbench. The EMW is a commercial product of Advanced Electrodynamics and Science & Engineering Associates. It is available from the authors at nominal charge.

References

1. E. L. Coffey and D. L. Kadlec, *General Electromagnetic Model for the Analysis of Complex Systems (GEMACS)*, Volumes I-III (Version 5), Rome Air Development Center Technical Report RADC-TR-90-360, December 1990.

Recent Enhancements to GEMACS 5.2

by

Edgar L. Coffey
Advanced Electromagnetics
5617 Palomino Dr. NW
Albuquerque, New Mexico 87120

A number of new features has been added to the GEMACS (General Electromagnetic Model for the Analysis of Complex Systems) computer program since the release of version 5.0 in late 1990 [1,2]. In addition Advanced Electromagnetics has developed a much more efficient version of GEMACS as a commercial product [3]. The purpose of this paper is to describe the modifications made to the program and how these changes benefit the GEMACS user.

Array Sources

GEMACS could always model an array as a series of ESRC commands or by modeling the individual array elements and exciting them with VSRC commands. Beginning with version 5.1, GEMACS lets the user define an array as a database which can be referred to by a single ESRC command. This greatly speeds up code execution at the price of lumping all the array elements into a single "stiff" source. (More on this later.)

The GEMACS 5.1 array antennas are described by a number of elemental radiators located and oriented arbitrarily in a local coordinate system (x, y, z). This allows the user to model any antenna, including arrays with unequally spaced elements, nonplanar arrays, and arrays of mixed element types, as well as standard, planar, equally-spaced arrays.

The array description is placed in an ASCII text file. More than one array description may reside on the same file as each description is named uniquely. The general format of the file is:

```
No. of databases on file (integer)
Name of database #1 (GEMACS 6-character symbol name)
No. of elements in database #1 (integer)
Element #1 for database #1 (see below)
Element #2 for database #1 (see below)
.
.
Element #N for database #1 (see below)
Name of database #2 (GEMACS 6-character symbol name)
No. of elements in database #2 (integer)
Element #1 for database #2 (see below)
Element #2 for database #2 (see below)
.
.
Element #N for database #2 (see below)
(etc.)
```

This work was sponsored in part by the U.S. Air Force, Rome Laboratory, RL/ERPT, Griffiss Air Force Base, NY under contracts F30602-92-C-0060 and F30602-92-C-0072.

The description for each element contains the following data:

```

Element type (integer)
Element excitation (real and imaginary)
Element position (x,y,z) (meters)
Element's x-axis direction cosines (tx,ty,tz)
Element's y-axis direction cosines (tx,ty,tz)
Element length (meters)
Spare (set to 0.)

```

Below is a portion of a database that describes a 30λ array with a Taylor line source distribution (SLL = -60 dB, nbar = 16).

```

1
TAYLOR
60
1 .0006701 .00 .00 -14.75 .00 .0 .0 1.0 1.0 .0 .0 .5000 .0
1 .0008163 .00 .00 -14.25 .00 .0 .0 1.0 1.0 .0 .0 .5000 .0
1 .0011102 .00 .00 -13.75 .00 .0 .0 1.0 1.0 .0 .0 .5000 .0
1 .0015436 .00 .00 -13.25 .00 .0 .0 1.0 1.0 .0 .0 .5000 .0
1 .0020978 .00 .00 -12.75 .00 .0 .0 1.0 1.0 .0 .0 .5000 .0
1 .0027615 .00 .00 -12.25 .00 .0 .0 1.0 1.0 .0 .0 .5000 .0
...
1 .0304516 .00 .00 -3.25 .00 .0 .0 1.0 1.0 .0 .0 .5000 .0
1 .0318015 .00 .00 -2.75 .00 .0 .0 1.0 1.0 .0 .0 .5000 .0
1 .0329657 .00 .00 -2.25 .00 .0 .0 1.0 1.0 .0 .0 .5000 .0
1 .0339238 .00 .00 -1.75 .00 .0 .0 1.0 1.0 .0 .0 .5000 .0
1 .0346585 .00 .00 -1.25 .00 .0 .0 1.0 1.0 .0 .0 .5000 .0
1 .0351559 .00 .00 -.75 .00 .0 .0 1.0 1.0 .0 .0 .5000 .0
1 .0354067 .00 .00 -.25 .00 .0 .0 1.0 1.0 .0 .0 .5000 .0
1 .0354067 .00 .00 .25 .00 .0 .0 1.0 1.0 .0 .0 .5000 .0
1 .0351559 .00 .00 .75 .00 .0 .0 1.0 1.0 .0 .0 .5000 .0
(etc)

```

The array consists of 60 elements each of type 1 (electric dipole). The excitation is expressed as a complex number. For example, the first element's excitation is seen to be $0.0006701 + j0$. Next comes the element's location within the array; element #1 is at $(0, -14.75, 0)$. The element's tangents and lengths follow.

The database is accessed by the GEMACS ESRC command with the new AS ("Array Source") excitation field. To retrieve the database above we would use

```

SRC=ESRC("geometry") AS = 1.0,0.0 R = 0. THETA = 0. PHI = 0.
* LU = 55, FILEID = TAYLOR
* TANG1 = 90.,0. TANG2 = 90.,90.

```

The overall array excitation is $1 + j0$ (AS field). It is located at $(r, \theta, \phi) = (0, 0, 0)$. The data are read from the file on FORTRAN unit #55, and that file is to be searched for the database named TAYLOR. The antenna is oriented according to the TANG1 and TANG2 fields. TANG1 rotates the array's x-axis to the direction defined by $\theta = 90^\circ$ and $\phi = 0^\circ$. Likewise, TANG2 rotates the array's y-axis according to its entries.

The GEMACS symbol SRC now refers to the entire collection of elements in the database as a single source. This source may be used just like any other GEMACS ESRC source. For example, we may find the far-field pattern of the array in free space by using the inputs listed below. The results are plotted in Figure 1.

```

DISPLA ON LU=0
NUMFIL=17
FRQ = 300.0
SETINT EI
[Listing Continues on Next Page]

```

```

GMDATA = FSPACE
SRC=ESRC(FSPACE) AS = 1.0,0.0 R = 0. THETA = 0. PHI = 0.
*
* LU = 55, FILEID = TAYLOR
* TANG1 = 90.,0. TANG2 = 90.,90.
FFLD = EFIELD(FSPACE) P1=0. P2=180. T1=0. DT=0.25 T2=90.
END OF COMMANDS
$ FREE SPACE HAS NO GEOMETRY ELEMENTS
END OF GEOMETRY

```

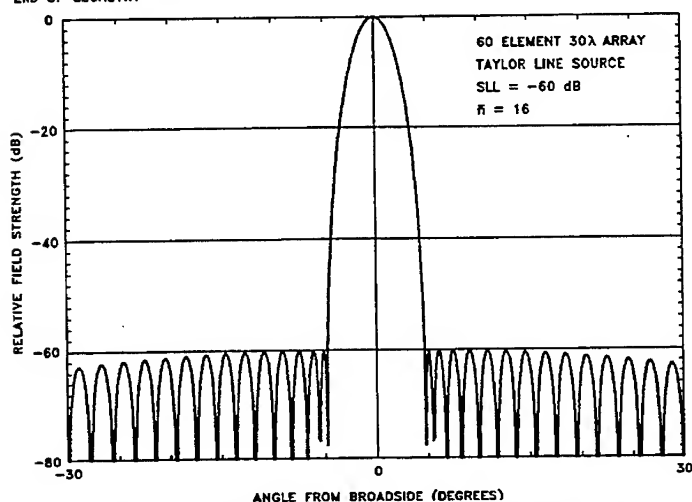


Figure 1. Far-Field Pattern from Taylor Line Source Array

The primary limitation of the array source excitation is that all array elements are lumped together as one source. When this source is used for GTD/UTD calculations, there is only one ray per path, regardless of how many elements are in the array. Hence, blockage and path length effects (e.g., phase) will cause pattern distortion if scattering centers are not in the far field of the entire array. This limitation can be overcome by creating several "subarrays" from a single large array so that potential scattering centers are in the far field of each subarray even though they may be in the near field of the entire array. Each subarray would then be associated with its own ESRC command. All subarray data could reside on the same peripheral file, however.

Pattern Sources

A second new source type for GTD and MOM/GTD hybrid problems is the pattern source command (PSRC). Pattern sources like array sources create an antenna pattern at a point in space. However, pattern sources work with patterns not array elements. There are four common antennas in the present implementation of PSRC: dipole, slot, horn, and parabolic dish with dipole feed. Others may be added at will. Each antenna has parameters which the user controls via the GEMACS command stream. For example, a slot with length of 6 cm and width of 3 cm would be entered as

```

SRC=PSRC("geometry")  SLOT = 1.0,0.0  X=0.50 Y=0.333 Z=-0.2
*                      TANG1 = 90.,0.  TANG2 = 90.,90.
*                      LENGTH=0.006  WIDTH=0.003

```

The second type of pattern data that PSRC can handle are actual pattern data stored on a peripheral file. These data can be measured data, analytic data, or data generated by a previous GEMACS simulation. For instance, say that GEMACS produced far-field patterns for an antenna that is to be placed on a large structure. The pattern data were stored on peripheral file #60 with the GEMACS symbol name ANTENA. PSRC retrieves these field data to be used as a source for the large structure with the following command sequence.

```

DISPLA ON LU=0
NUMFIL=10
FRQ = 8000.0
SETINT GTD ES EI ORDER=0-2
GMDATA = LARGE
SRC=PSRC(LARGE) V = 1.0,0.0  X=0.50 Y=0.333 Z=-0.2
*                      TANG1 = 90.,0.  TANG2 = 90.,90.
*                      LU=60  FILEID=ANTENA
FFLD = EFIELD(LARGE) P1=0. P2=180. T1=0. DT=0.25 T2=90.
END OF COMMANDS
$ LARGE STRUCTURE GEOMETRY ELEMENTS GO HERE
END OF GEOMETRY

```

The limitations described for the array source also apply to PSRC. The most important one is to realize that the pattern, perhaps created by a moderate to large antenna, is being placed at a single point. Thus ray blockage and ray path length effects may invalidate the simulation under some circumstances unless care is taken to minimize these effects.

GTD Scatterer Selection

The third enhancement made to GEMACS adds no new physics to the code. Rather, it allows the user more control over the GTD/UTD rays that will be traced. Consider the structure in Figure 2 which shows a portion of a GEMACS ship model for GTD/UTD computations. There are a number of edges that are present in the model but do not diffract, e.g., those that touch the deck from the superstructure. Though GEMACS will discard rays traced to these elements, it is more efficient for the user to *a priori* "hide" these scatterers from GEMACS.

To implement the screening process we have added a HIDE command to the GEMACS geometry processor, as well as an UNHIDE command. The HIDE command removes scattering elements (surfaces, edges, corners, and creeping waves) from the GTD calculations, though not from the ray blockage (shadowing) processor. For example the command

```
HIDE PL 3 ED 4 ED 6 CN 3 SF
```

hides edges 4 and 6, corner 3, and the entire reflective surface of plate #3. If a particular scatterer is to be singled out, the user may enter, for example,

```

HIDE ALL
UNHIDE PL 3 ED 4

```

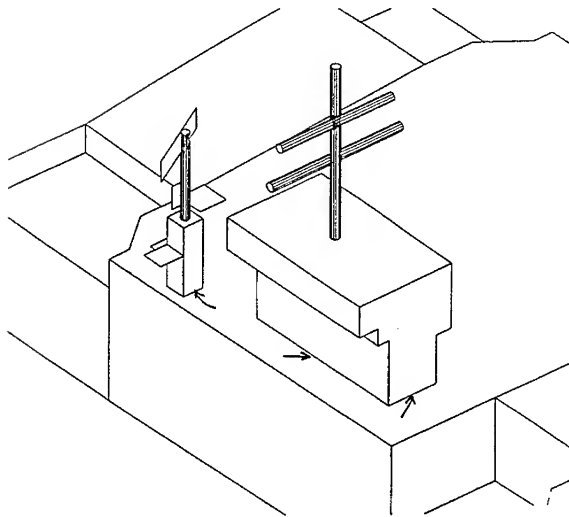



Figure 2. Illustrating Non-Scattering Elements in a GTD Problem

which will hide the entire geometry, except for edge #4 of plate 3. Hidden elements may be duplicated via the GEMACS macro geometry operations (e.g., RX, XL, RF) thus creating a powerful tool to give the GEMACS user control over selecting specific interactions to model.

MOM-MOM Multi-Region Hybrids

The development of a MOM-MOM multiple region hybrid was motivated by necessity. In a typical GEMACS hybrid, the exterior is modeled with GTD elements while the interior is modeled with finite difference (FD) elements. Difficulties arise when the object to be modeled is too small for GTD (exterior) yet too large for FD (interior). Frequently there is only a small frequency range over which the MOM-FD hybrid can work reliably.

With the development of a MOM aperture element it is possible to link MOM geometries with GTD and/or FD geometries. It is even permissible to link on MOM geometry with another.

The MOM aperture element is quite simple: it turns a MOM patch (PA) into an aperture basis function (AP). This allows boundary conditions to be enforced from one region to the next. Figure 3 shows the transformation process.

To illustrate the process, a MOM-only grid of surface patch elements was created to model a large ground plane like the one in Figure 3. An aperture was placed in the otherwise solid plane by transforming some of the patches into apertures. The object was excited with a plane wave incident from the left. Figure 4 shows the field strength on the right side of the patch grid. The MOM aperture predictions agree well with MOM-GTD predictions and even time-domain methods.

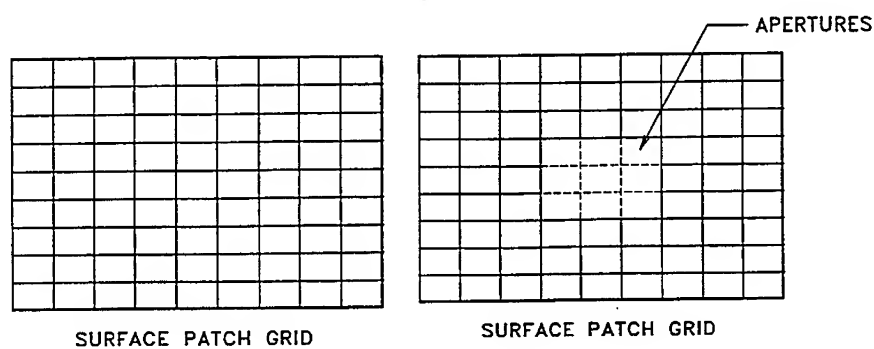


Figure 3. Change MOM Patches into Aperture Basis Functions

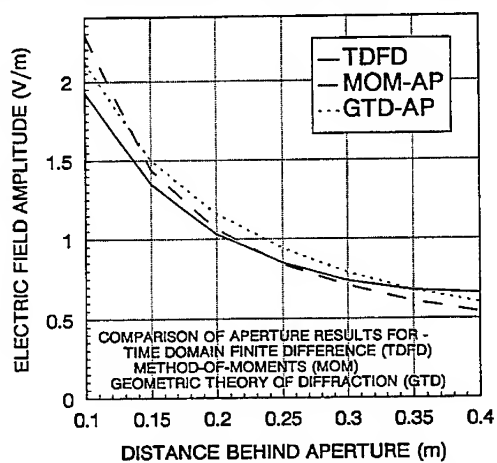


Figure 4. Results of the MOM Aperture Simulation

GEMACS-plus

Finally, it is now possible to run GEMACS as a single module on larger computers. GEMACS-plus is a product developed internally by Advanced Electromagnetics for Microsoft Windows, IBM OS/2, various UNIX work stations (Sun, Motorola, Silicon Graphics), VAX/VMS, and DEC Alpha. It contains all the features of GEMACS 5.2 as well as a rewritten file and data manager. This as well as the single module restructur-

ing of GEMACS gives tremendous execution time speed-ups, as much as 30:1 for parametric problems (e.g., sweeping frequency). More typical are factors of about 2:1.

Looking at the Future

The future of GEMACS has always been driven by user requirements. We are now looking at true 64-bit versions, rewriting the input processor to accommodate more general commands and inputs, rewriting the data manager to avoid much of the file I/O, parallel and distributed processing versions, and various physics upgrades.

Your comments are always welcome and much appreciated. It is from your input that decisions will be made concerning AE's work with GEMACS.

References

1. E. L. Coffey and D. L. Kadlec, *General Electromagnetic Model for the Analysis of Complex Systems (GEMACS)*, Volumes I-III (Version 5), Rome Air Development Center Technical Report RADC-TR-90-360, December 1990.
2. E. L. Coffey, *Installation Instructions for PC GEMACS 5.2*, Advanced Electromagnetics Report AE92R005, July 6, 1992.
3. E. L. Coffey, *GEMACS for OS/2*, Advanced Electromagnetics, June 25, 1992.

An "Object-Oriented" Approach to GTD/UTD Modeling

by

Edgar L. Coffey
Advanced Electromagnetics
5617 Palomino Dr. NW
Albuquerque, New Mexico 87120

When the GTD/UTD capabilities of GEMACS 5.0 were redesigned in 1986-89 [1], Advanced Electromagnetics took the opportunity to restructure the computational approach to one that resembles what today is called "object-oriented programming" or OOP [2]. While not a formal OOP implementation with encapsulation, inheritance, etc., GEMACS does treat each potential GTD/UTD scatterer, ray bounce, and ray path as "objects" and manipulates those objects to obtain fields for multiple bounce interactions.

This paper describes the implementation of GTD/UTD in GEMACS using the OOP paradigm. It discusses the advantages and disadvantages of the OOP approach for GTD/UTD in the hope that others may find fresh ideas in structuring their own computer codes.

What is an "Object"?

Tradition computational electromagnetic (CEM) programming, especially FORTRAN program has been task oriented. That is, the software sequences through a well-defined set of tasks in order to produce a desired results. For example, GEMACS 3.0 and 4.0 defined its GTD/UTD tasks as: (1) compute all single plate reflections, (2) compute all plate-plate reflections, (3) compute all plate edge diffractions, etc. In GEMACS 5.0, the structure was changed to emphasize collections of data, not enumeration of tasks. Hence, in GEMACS 5.0, the approach is to (1) select a source point and observation point from a collection of sources and field points, (2) select combinations of potential scatterers from a "bag" of geometry elements, compute ray paths between each pair of scattering centers, and manipulate the scatterer-to-scatterer bounces into a path that obeys the laws of GTD physics (Fermat's principle, Snell's law, etc.).

Each of the data-related entities described is a potential GTD/UTD "object":

1. Each source point (field source, MOM basis function, aperture, etc.)
2. Each observation point (field point, MOM basis function, aperture, etc.)
3. Each potential geometry scatterer (surface, edge, corner, etc.)

This work was sponsored in part by the U.S. Air Force, Rome Laboratory, RL/ERPT, Griffiss Air Force Base, NY under contracts F30602-86-C-0183 and F30602-92-C-0060.

4. Each ray path between collections of scatterers
5. Each complete ray path from source to field, including intermediate bounces.

This seemingly cumbersome division of the problem into somewhat artificial categories is what gives the OOP approach its advantages. It also lets the software designer extend the original GTD/UTD capability to hybrids with other methods such as MOM and aperture coupling. Finally, this approach lets several aspects of a complex GTD/UTD problem be formulated so that the same software can be used for each problem.

Source Point Objects

A source point object is any entity that can be the beginning of a GTD ray path. Naturally, field sources are source point objects, but MOM basis functions and apertures can also be thought of as source points in a MOM/GTD or aperture coupling hybrid.

The characteristics of a source point object are its source type, excitation, position, orientation, and perhaps a few source-specific parameters (dipole length, slot width, etc.). A source point object must also be able to generate near and far fields at any observation point.

With a data structure that can be used for every source (no matter the type), all sources can be manipulated identically by the software, and the source code for all sources can be localized to one routine. In addition, source derivatives (for slope diffraction) can all be computed in the same fashion.

In GEMACS, all sources, including MOM basis functions, etc. may be found in a single subroutine NEWSRC. To modify a source or to add a new source (as was done for GEMACS 5.1 and 5.2) it is only necessary to modify or add code to NEWSRC, ignoring user input command processing for the moment.

Observation Point Objects

An observation point object is any entity that can be the terminus of a GTD ray path. Far-field and near-field observation points are natural choices, but MOM weighting functions and aperture points can also be observation point objects for MOM/GTD.

The characteristics of an observation point are its position (or far-field direction) its field type (electric or magnetic), and its field components. For instance, a far-field object would have $\hat{\theta}$ and $\hat{\phi}$ electric field components while a surface patch weighting function might have \hat{r}_1 and \hat{r}_2 magnetic field components.

In GEMACS, all observation points, including MOM weighting functions, etc. are accessed by the single subroutine GETFLD. Thus, the GTD/UTD physics code does not have to know about a field point's orientation, tangent vectors, etc. That information is obtained from GETFLD.

Geometry Element Objects

Though it may at first seem unnatural, the basic GTD/UTD geometry element object is not a GTD/UTD modeling element (plate, cylinder, etc.). Instead, the total GTD structure is decomposed into a collection of potential scattering centers such as plate surfaces, plate edges, corners, end cap rims, etc. The GEMACS user still enters his geometry with the modeling elements, and GEMACS performs the decomposition into the basic scatterers. The scatterers are also linked together at this time (e.g., every edge bounds two surfaces, every edge is terminated by two corners, etc.) so that the GTD physics code does not have to repeatedly search for this information.

There are six basic scatterer types in GEMACS 5:

1. Flat surface reflection (plates, end caps)
2. Straight edge diffraction (plates, conductivity areas)
3. Corner diffraction (plate, conductivity corners)
4. Curved surface reflection (cylinders)
5. Creeping wave diffraction (cylinders)
6. Curved edge diffraction (end cap rim, curved conductivity edges)

The decomposition of geometry elements into combinations of these is for the most part straightforward. A single four-sided plate is decomposed into one flat surface, four straight edges, and four corners. A end cap rim, on the other hand, cannot be decomposed into a single curved edge because of the possibility of multiple scattering centers. Thus, GEMACS divides the rim into six curved segments. The corners connecting the segments are hidden from GEMACS since they are artificial entities.

The quantities associated with each geometry object are the most numerous for it is the geometry objects that the GEMACS GTD drivers manipulate the most. Obviously, each geometry object must specify position, orientation, and size data. Objects also point to their host elements (e.g., a plate edge object is hosted by a plate geometry element). There may also be auxiliary data associated with an object, such as conductivity or reflection coefficient.

In addition to the simple geometry quantities there are several functions associated with each object. An object must be able to compute a valid path for its interaction (reflection, diffraction, etc.) given a source point object, observation point object, and object parameters. That path must obey the physics laws of the object (e.g., Snell's law for reflection). Each geometry object must also supply a ray blockage routine that will detect if a ray will be shadowed by it. Some objects (edge, corner) do not shadow rays and hence have a null routine for blockage. Finally, each geometry object must have a physics routine that computes scattered field for given source and observation point objects.

There is really nothing new in the list of functions enumerated above. Any GTD code must perform the same functions. What is different is that the functions are associated with the geometry objects instead of being separate tasks for the program to perform.

Ray Path Objects

A ray path object is a collection geometry objects, a source object, an observation object, and the single interaction ray bounces among the geometry objects along a path. For example, Figure 1 shows a third order interaction with four path segments. Thus, this ray path object is composed of the source object, the field point object, the three geometry objects, and the four ray paths.

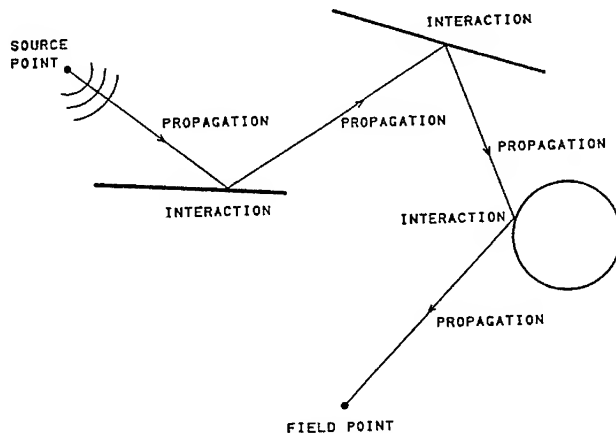


Figure 1. Third Order Interaction Example

Each path segment is computable by the geometry objects, but the ray path object provides the mechanism for connecting the paths together (Fermat's principle). It also determines ray blockage (if any) and the fields produced at the observation point (if the ray is not blocked).

Computation of Fields

With the objects defined as described above it is straightforward to compute the fields for any collection of sources and any collection of geometry elements. The geometry elements are decomposed into basic scatterers and placed into a table. For given source and observation points, all possible combinations of scatterers are formed by pulling the scatterer objects out of the table. (In a practical problem, "all" is limited to some number of bounces, say 2 or 3). One particular combination forms a ray path object. The ray path object is used to find the path, check the path validity, and compute the requested fields.

The path is computed by an iterative method that minimizes path length (Fermat's principle). The iterative technique changes the interaction points on each scatterer (e.g., specular reflection point) as it minimizes the path length. It then calls each geometry object to recompute its single-bounce path with this new source and observation point data. Iterations continue until the path length stops changing.

The path thus computed becomes a "candidate" path. Shadowing is performed by calling all geometry objects to see if any portion of the path is blocked. If so, the candidate path is discarded and zero fields returned.

If the path is valid, then the geometry objects are called to step-by-step computed the field at the observation point.

Computation of Interactions

The above procedure described a typical GTD-only scattering problem. Much of the power of GEMACS lies in its ability to hybridize dissimilar physics methods to obtain self-consistent solutions. One such hybrid is combining method of moments (MOM) with GTD. The MOM formalism requires computing an interaction matrix $[Z]$ and an excitation vector $[V]$ from which currents $[I]$ may be found by solving

$$[Z][I] = [V]$$

After currents are known, the fields can be found by

$$[F] = [GF][I] + [E^{inc}]$$

where $[F]$ are the total fields, $[GF]$ is a "Green's function matrix" generated for unit currents, and $[E^{inc}]$ is the directly incident field due to the source(s). For the MOM/GTD hybrid, these quantities include not only the direct line-of-sight paths associated with MOM but also the indirect reflections, diffraction, etc. associated with GTD, as shown in Figure 2.

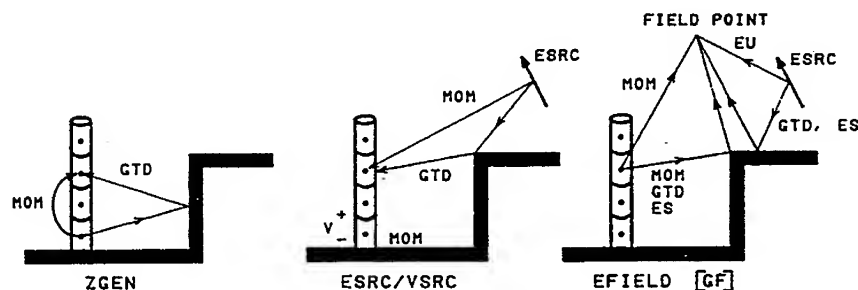


Figure 2. MOM/GTD Ray Direct and Indirect Ray Paths

There are four matrices to compute: $[Z]$, $[V]$, $[GF]$, and $[E^{inc}]$. By defining source points and observation points appropriately, the same GTD routines used for a GTD-only problem can be re-used for MOM/GTD.

For [Z], the source objects are the MOM basis functions, and the observation objects are the MOM weighting functions. The geometry objects are the GTD scatterers, as is true for the other three cases.

For [V], the source objects are the field sources (e.g., GEMACS ESRC or PSRC commands), and the observation objects are the MOM weighting functions.

For [GF], the source objects are the MOM basis functions, while the observation objects are the near-zone and far-zone field points.

For [E_{inc}], the source objects are the field sources, and the observation points are the near-zone and far-zone field points.

Software Maintenance and Expansion

Why go to the trouble to restructure an existing software program into object-oriented style? It became necessary to do so when GEMACS 5.0 was required to compute higher order interactions among any possible combination of GTD elements. The old style used in GEMACS 3.0 and GEMACS 4.0 would have required us to write a separate driver routine (task paradigm) for each combination of elements. For example, the second order interaction of double plate reflection would have required one driver, while the second order interaction of double plate edge diffraction would have required a separate driver. This is a manageable approach for a few geometry types and one or two bounces, but it quickly became unrealizable for more geometry types and higher order interactions.

In GEMACS 5.0 (OOP paradigm), there are only object drivers, not task drivers. For example, for plates only three drivers are required: reflection, edge diffraction, and corner diffraction no matter how many bounces are to be implemented. A fourth order interaction for plate reflection, then corner diffraction, next plate edge diffraction, and finally plate reflection calls the three basic drivers as needed. This concept can be extended to any number of interactions. (A tenth order plate reflection problem was run with GEMACS 5.0 for a parallel plate waveguide with very good results.)

Maintenance and troubleshooting are greatly simplified with this approach. Since all the activity associated with a function is to be found at just one location in the software, that function can be easily and quickly debugged, or even replaced if needed, without modifying the rest of the code.

Expansion of the code becomes straightforward though not trivial. To add, for example, a cone frustum to GEMACS 5.0, one would merely have to define the cone frustum geometry object and its associated functions. Once implemented for the single bounce case, the cone frustum physics becomes available to all higher order interaction cases as well.

Summary

The greatest disadvantage to using object-oriented thinking with computational electromagnetics is the amount of effort to re-orient our minds towards working with data (objects) instead of tasks (functions). However, for software maintenance efficiency,

porting to other systems, parallel and distributive processing, such a way of thinking is mandantory.

The greatest benefit to the OOP approach is not in the physics. The physics are the same. It is in the re-use of software and the isolation of physics and ray path functions to specific routines. This aids in debugging and validation of the final product as well as provides a relatively painless expansion path for the future.

References

1. E. L. Coffey and D. L. Kadlec, *General Electromagnetic Model for the Analysis of Complex Systems (GEMACS)*, Volumes I-III (Version 5), Rome Air Development Center Technical Report RADC-TR-90-360, December 1990.
2. There are many excellent books and articles on object-oriented programming theory and techniques.

Making Computer Tutorials In Electrodynamics With The CAEME Software.

Rodney Cole, Curtis Brune, and Scott Tooker
Physics Department
Learning Skills Center
University of California, Davis, 95616
(916) 752-6234, cole@ucdphy.ucdavis.edu

Abstract

Previously, making computer tutorials for electrodynamics has been a highly specialized task requiring advanced programming skills that have severely limited the number and range of computer-based tutorials developed to date. However, there have been several developments that have drastically changed this state. First, the Center for Computer Applications in Electromagnetics Education (CAEME) has sponsored the development of many programs that produce simulations of electromagnetic phenomena and the mathematics of vector fields. These programs while having tutorial value in themselves, can function as a set of tools that allow one to easily generate various simulations or problems. A suitable authoring package can import these simulations or problems allowing a complete exercise to be assembled in a short amount of time. Thus, the second major development is the existence of powerful inexpensive authoring packages on the IBM and Macintosh platforms. The exercises constructed using an authoring system can consist of simulations, compressed computer animated movies, video from laser disks, or even posing a question and launching the appropriate program to allow the student to configure a solution that satisfies the conditions of the posed question. In short, the CAEME software when coupled with authoring software allows instructors to construct computer tutorials without using advanced programming skills. We will demonstrate how an interactive computer-based tutorial can be constructed on the Macintosh.

Introduction

In the 1960's video was the technology that was going to revolutionize teaching, and in the 1980's the personal computer played a similar role. Both have not yet reached the heights envisioned by proponents perhaps for opposite reasons. Video is easy to operate and works well at depicting temporal phenomena; however, it is a linear mode of learning, sequencing events in a chain. Most importantly, straight video is not interactive. A student

cannot pose a question and receive an answer. Computer simulations on the other hand are extremely interactive, but have not played a major role in education because they tend to be difficult to use. Students can become easily lost, and often they lack the skills to adequately interpret the output which causes them to become frustrated. The challenge put forward by CAEME has been to find new and successful ways to use the computer in electromagnetics education. The first round of programs is available in Volume 1 of the CAEME software book. The software runs the gamut from full-blown computer simulations to menu-driven tutorials. However, much of the CAEME software and video tapes, are not just end products. These programs are also tools and resource material for producing new computer-based instructional software. In this presentation we will demonstrate how the CAEME software, when combined with an authoring software package and tools such as video capture hardware and software, can be used to make interesting interactive classroom exercises.

A Model For Instructional Computer Use

To make successful computer based exercises, like any mode of teaching, takes time to plan and implement. A successful development program should also make long-range plans to improve the lessons as the technology improves, and should address the needs of the student. This will include initial tutorials on how to use the computer, followed by tutorials that address the physics, i.e., those that help the student to interpret the output from the computer simulations. These tutorials should develop simple models that help the student to interpret more complicated phenomena that the student will generate in a simulation. The tutorials might consist of discussions of the graphs that might be encountered in a simulation program, including computer animations or digitized video in the form of Apple's QuickTime movies or Microsoft's Video for Windows. An example of a tutorial on superposition and the electrostatic potential is shown in Figure 1. A laser disk might also be accessed by the authoring software. The graphs can be dynamically linked to the mathematics as is done in the Electrocard software from CAEME.

The classroom or computer laboratory exercises should allow the student to pose "what if" questions perhaps with an initial exercise asking a question the student will need to run on the simulation program. These simulations can be launched directly from the tutorial program providing a very neat package that will help prevent students from breaking their concentration on the physics to deal with the host computer's operating system to navigate between simulations. In Figure 2, the "Exercise" buttons take the student to questions that require the student to run a simulation. In the exercise shown, the program SilverHammer

which is field modeling program for point charges is used. The students runs the program by clicking the mouse when the cursor is over the "SilverHammer" button. The simulation in SilverHammer is shown in Figure 3. The "what if" component is very important because it allows students to work problems that are bothering them and it can play an important role in their education. The less inventive students can get started by simulating homework problems, often sparking questions they can explore further.

We have found that there also needs to be a human component that can be in the form of a Teaching Assistant available during the lab to answer questions and help with simulations. It also helps to have students turn work into the TA or have the TA check the students' work at various milestones. Some students find that working alone at a computer terminal or PC is advantageous because they can proceed at their own pace. However, others need the human interaction that a traditional discussion section or lab provides. Both of these points can be addressed by having the students run the tutorials by themselves and then pair up for the simulations.

Another advantage is that students can take the programs with them on floppy disks when they leave the lab and run them on their own computer at home. We have had students come in during the summer, after they have completed the course, with questions from simulations they have run, showing that the learning does not end when the course ends. The result is that if the course is designed to effectively integrate computers, they can be a highly successful educational tool.

Using CAEME Software

With the development of emulation programs, many of the CAEME programs can be run on a Macintosh microcomputer. Simulations can be used to show time-domain electromagnetic processes. The individual frames can be copied to the Macintosh Scrapbook, and using a program called "Movie Converter" that is part of the "QuickTime Starter Kit", they can be compiled into an animated QuickTime movie. This allows you to quickly put together a movie using the output of any graphics program. The resulting movie can be transferred to an authoring system or word processor. The movie can also be played without change under the Windows operating system on a PC by using the QuickTime extension for Windows. We will demonstrate how to make QuickTime movies and how to incorporate them into HyperCard based tutorials. The process is so simple that we have students compiling their own QuickTime movies in the classroom exercises.

Conclusion

The ability to run applications across computer platforms and compile animated sequences that may then be used in multimedia tutorials could well make the educational use of video and computers equal the claims of their proponents. It will, however, rely on experienced educators to accomplish this feat. The computers and the tools are important, but it is the vision and creativity of the educators that will ultimately decide their role. The computer based multimedia tools are becoming easy to use, powerful, and flexible. To be effective in education, though, these tools need to be applied by imaginative teachers to develop creative exercises. They are not ends in themselves.

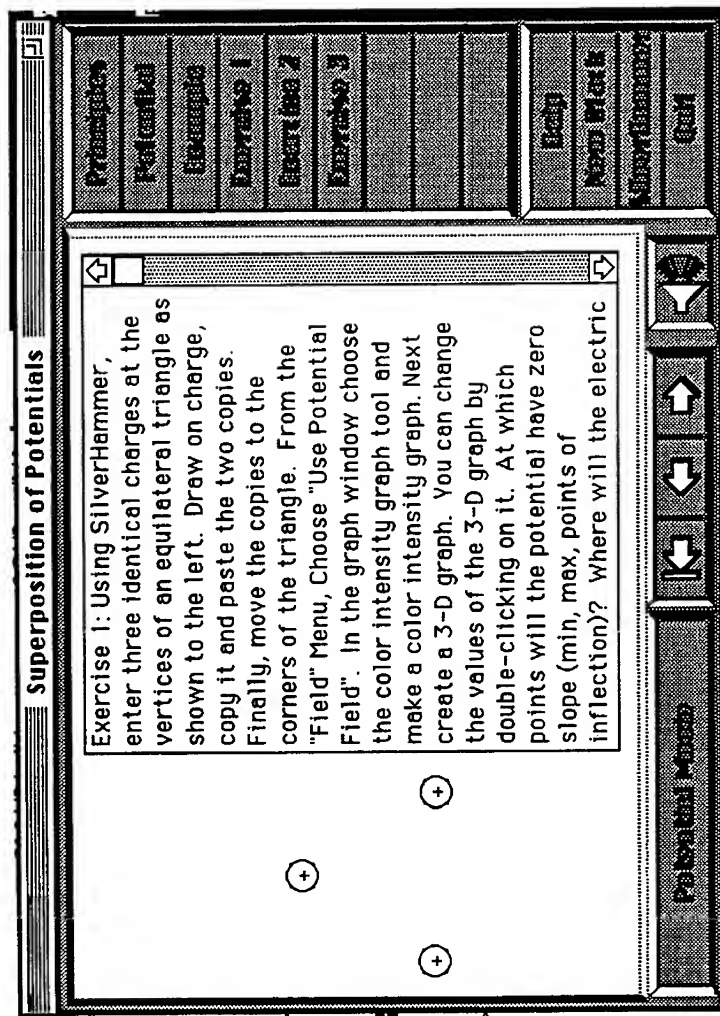


Figure 2

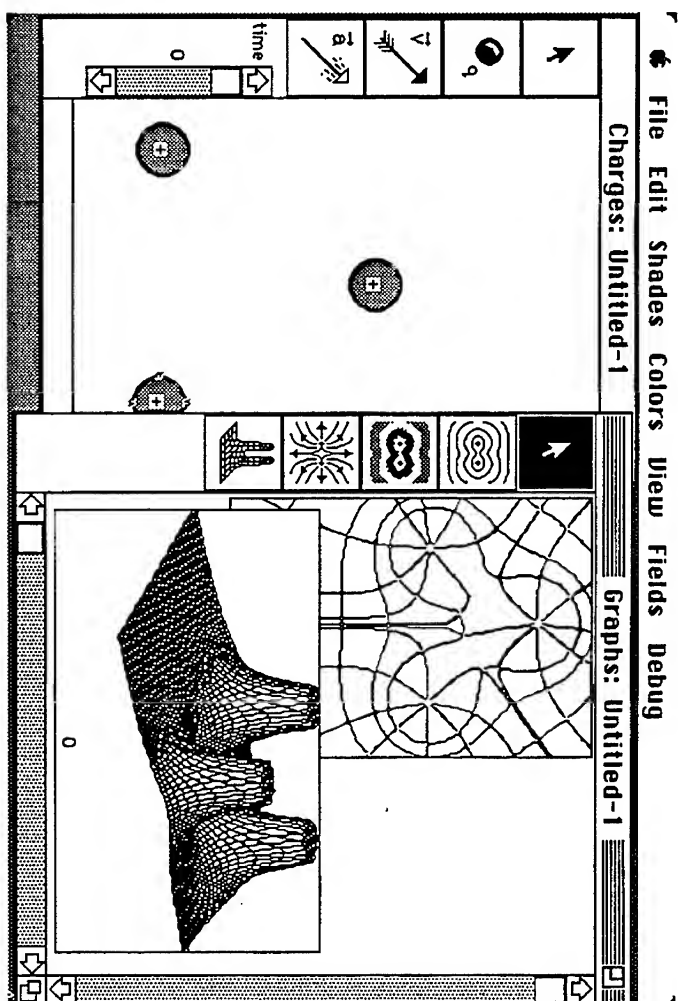


Figure 3

EMAG: Electromagnetic Software Development at Rose-Hulman Institute of Technology

Jovan E. Lebaric and Roger P. Manke, Jr.

Rose-Hulman Institute of Technology, 5500 Wabash Avenue, Terre Haute, IN 47803

Introduction

EMAG is a new electromagnetic software package developed at Rose-Hulman Institute of Technology that allows students to solve electrostatic and magnetostatic field problems. EMAG has been developed with the intention to assist in teaching electromagnetics at undergraduate level and also to offer to students and other users opportunities to modify the software, customize it to their needs, or simply be creative and add new features. EMAG, unlike most EM software packages, can be easily modified and further developed by users familiar with MATLAB since EMAG has been written in MATLAB programming language and all of EMAG source code is available to all users. Important features of EMAG are a graphical user interface and visual display of potentials and field solutions that help students in developing an intuitive feel for electrostatic and magnetostatic fields while learning the field theory concepts and its mathematics. EMAG can solve electrostatic and magnetostatic 2-D problems:

• *Electrostatic*

Media: Linear, Inhomogeneous, Isotropic, PEC (Perfect Electric Conductor)

Sources: Voltage Sources, Charges

Boundary Conditions: Open, Dirichlet;

• *Magnetostatic*

Media: Linear, Inhomogeneous, Isotropic, PMR (Perfect Magnetic Reluctor)

Sources: Magnetic Potential, Currents

Boundary Conditions: Open, Dirichlet.

EMAG solves Poisson's equation for either electric or magnetic potentials, using both direct and iterative techniques. The solution domain can be inhomogeneous (different permittivities and permeabilities), and can have Perfect Electric Conductors (PEC's) and Perfect Magnetic Reluctors (PMR's). The PMR material is defined as an ideal "anti-magnetic" material with infinite reluctivity (zero permeability). Sources in EMAG include: PEC's raised to fixed electric potentials and line charges for electrostatic problems; and PMR's raised to fixed magnetic potentials and line currents for magnetostatic problems. An open boundary condition is simulated by the Transparent Grid Termination (TGT) technique.

Brief Review of Theory

EMAG solves electrostatic and magnetostatic Poisson equation, subject to Dirichlet boundary conditions, on a uniform square grid. Starting equations are the equations of Maxwell (because of duality only one is given below):

$$\oint_S \vec{D} \cdot d\vec{S} = \int_V \rho_v dv. \quad (1)$$

When applied to the geometry in Figure 1, equation (1) can be discretized as

$$\mathbf{D}_T \Delta^2 + \mathbf{D}_B \Delta^2 + \mathbf{D}_L \Delta^2 + \mathbf{D}_R \Delta^2 = Q_{enclosed} = \rho_{l,C}(\Delta) \quad (2)$$

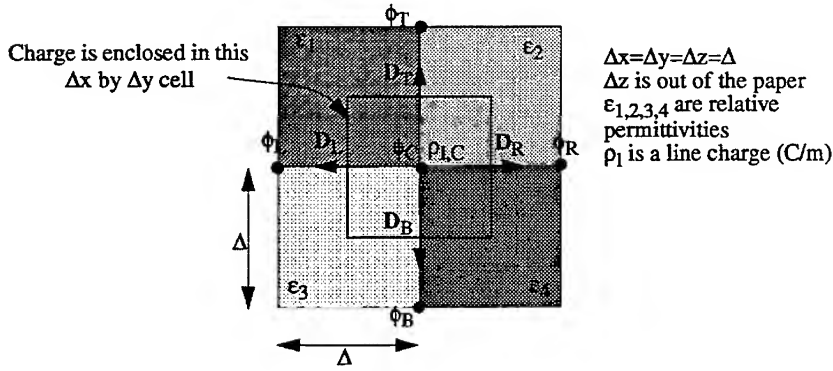


Figure 1: Geometry for interface of four arbitrary dielectrics

$$\mathbf{D}_T = \mathbf{D}_T^{\epsilon_1} + \mathbf{D}_T^{\epsilon_2} = \epsilon_o \left(\frac{\epsilon_1 + \epsilon_2}{2} \right) \left(\frac{\phi_C - \phi_T}{\Delta} \right), \quad (3)$$

$$\mathbf{D}_B = \mathbf{D}_B^{\epsilon_3} + \mathbf{D}_B^{\epsilon_4} = \epsilon_o \left(\frac{\epsilon_3 + \epsilon_4}{2} \right) \left(\frac{\phi_C - \phi_B}{\Delta} \right), \quad (4)$$

$$\mathbf{D}_L = \mathbf{D}_L^{\epsilon_1} + \mathbf{D}_L^{\epsilon_3} = \epsilon_o \left(\frac{\epsilon_1 + \epsilon_3}{2} \right) \left(\frac{\phi_C - \phi_L}{\Delta} \right), \quad (5)$$

$$\mathbf{D}_R = \mathbf{D}_R^{\epsilon_2} + \mathbf{D}_R^{\epsilon_4} = \epsilon_o \left(\frac{\epsilon_2 + \epsilon_4}{2} \right) \left(\frac{\phi_C - \phi_R}{\Delta} \right). \quad (6)$$

Equations (3) through (6) express the flux density in terms of potentials. The “averaging” of the permittivity results from variations of $\bar{\mathbf{D}}$ from one dielectric material to another for the same potential difference, or E-field in the region. When equations (3) through (6) are substituted into equation (2) and solved for ϕ_C , the resulting equation is

$$\phi_C = \frac{\frac{\rho_{l,C}}{\epsilon_o} + \phi_T \left(\frac{\epsilon_1 + \epsilon_2}{2} \right) + \phi_B \left(\frac{\epsilon_3 + \epsilon_4}{2} \right) + \phi_L \left(\frac{\epsilon_1 + \epsilon_3}{2} \right) + \phi_R \left(\frac{\epsilon_2 + \epsilon_4}{2} \right)}{\epsilon_1 + \epsilon_2 + \epsilon_3 + \epsilon_4} \quad (7)$$

Equation (7) is a discretized version of the Poisson's equation for electrostatics

$$\nabla^2 \phi = -\frac{\rho_l}{\epsilon}. \quad (8)$$

The magnetostatic duals to equations (7) and (8) are

$$A_C = \frac{\frac{I_C}{v_o} + A_T(\frac{v_1 + v_2}{2}) + A_B(\frac{v_3 + v_4}{2}) + A_L(\frac{v_1 + v_3}{2}) + A_R(\frac{v_2 + v_4}{2})}{v_1 + v_2 + v_3 + v_4} \quad (9)$$

and

$$\nabla^2 A_z = -\mu J_z \quad (10)$$

respectively, with magnetic reluctivity defined as $v = 1/\mu$. The duality between electrostatics and magnetostatics is summarized in Table 1.

Table 1: Dual Quantities

	Electric	Magnetic
Potential	ϕ	A_z
Media	ϵ	$1/\mu$
Source	ρ_l	J_z
Ideal Media	Perfect Electric Conductor (PEC)	Perfect Magnetic Reluctor (PMR)

Transparent Grid Termination

The boundary condition implemented in EMAG is a homogenous Dirichlet boundary with zero potential on the boundary. However, the solution domain does not extend all the way to the Dirichlet boundary, but rather occupies a very small portion of the grid inside the Dirichlet boundary, within another boundary we refer to as the TGT boundary. The relative sizes of the EMAG's Dirichlet and the TGT boundaries are shown in Figure 2. The Dirichlet boundary, with potential set to zero on this boundary, has been placed sufficiently far away so that the solution within the TGT boundary is not strongly affected by the Dirichlet boundary. The solution for the nodes within the TGT boundary has exactly the same accuracy as the solution for the much larger number of nodes within the Dirichlet boundary, although the number of calculations for the nodes within the TGT boundary is much smaller. This means that one can move the Dirichlet boundary as far as desired away from the TGT boundary and increase the accuracy of the solution without increasing the size of the solution domain, required memory, and the computational time. In order to accomplish that special equations have been developed for the nodes on the TGT boundary. These equations link each node on the TGT boundary to the nodes just outside the TGT boundary and to the nodes on the Dirichlet boundary. The coefficients of

these special TGT equations are only calculated once for a selected pair of Dirichlet and TGT sizes and results of these calculations are saved as a matrix of coefficients. The same set of coefficients can be used to solve any problem defined within the TGT boundary. Since the Dirichlet boundary can be moved as far away as desired (at the expense of a massive one-time calculation), the error incurred by setting the potentials to zero at the Dirichlet boundary can be made negligible. The TGT makes accurate solutions of electrostatic and magnetostatic problems feasible on a PC within reasonable time and without extensive memory requirements.

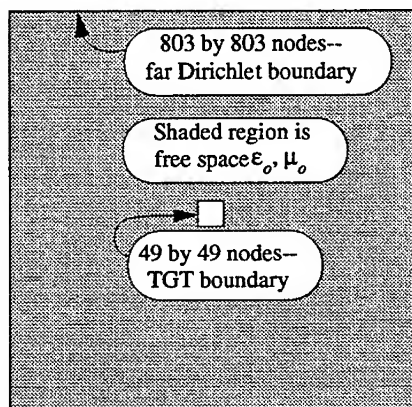


Figure 2: Relative size of the Dirichlet boundary and the TGT boundary

Listed below are the steps that can be used to generate the TGT coefficients for an N by N Dirichlet boundary and an M by M TGT boundary:

1. Define a rectangular grid (see Figure 3) of N by N nodes (N=803 for EMAG);
2. Number the grid nodes using the spiraling scheme (Figure 3), from 1 to N^2 ;
3. Write the homogeneous, source-free, discretized equations for nodes 4N-3 through node N^2-M^2 (M=49 for EMAG).

A matrix equation describing the steps 1 through 3 above looks like,

$$\begin{bmatrix} A_o & A_e & A_m & A_i \end{bmatrix} \begin{bmatrix} o \\ e \\ m \\ i \end{bmatrix} = [0], \quad (11)$$

where the subscripts of the A's indicate the nodes each submatrix A is associated with and the o, e, m, and i indicate the nodes shown in Figure 3.

4. Use forward substitution to form the upper triangular matrix for the sub-matrix $[A_e \ A_m]$ updating all rows of the system matrix when forming the upper triangular matrix,

5. Finally, use back substitution to make the last $4(M+1)$ rows of A_m into the unity matrix I . These entries are associated with the $4(M+1)$ nodes on the "m" layer. The results of steps 4-5 should appear as a matrix equation (12)

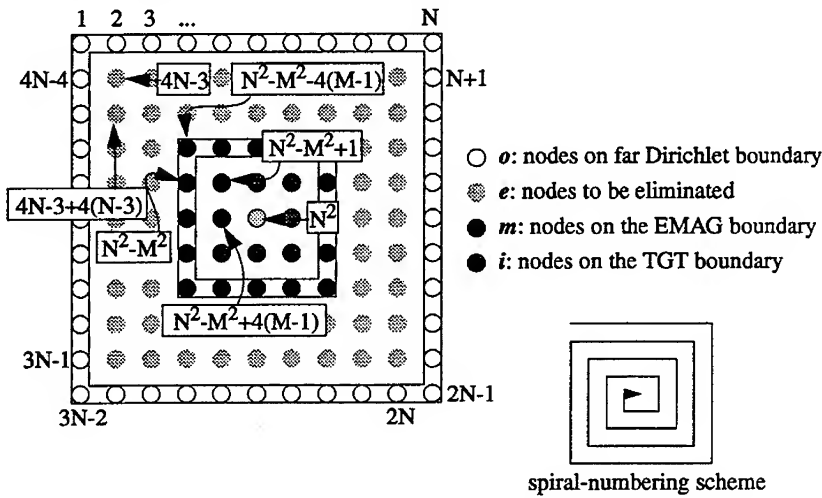


Figure 3: Spiral number scheme and terminology for nodes

$$\begin{bmatrix} C_1 & C_2 & C_3 & C_4 \\ -OUT & 0 & I & -IN \end{bmatrix} \begin{bmatrix} \phi_o \\ \phi_e \\ \phi_m \\ \phi_i \end{bmatrix} = [0], \quad (12)$$

where the C_i 's are leftovers from the forward substitution but of no interest. The last $4(M+1)$ rows of matrix equation (17) which contain OUT , I , and IN can be re-written as

$$|\phi_m\rangle = IN |\phi_o\rangle + OUT |\phi_i\rangle, \quad (13)$$

where $|\rangle$ indicate that ϕ_m , ϕ_o , and ϕ_i are column vectors. Equation (13) expresses the EMAG boundary nodes (ϕ_m) as a function of the Dirichlet boundary nodes (ϕ_o) and the TGT boundary nodes (ϕ_i).

The steps 1 through 5 can also be represented in matrix form as follows. Rewrite equation (11) as

$$(1) \Rightarrow [A_e A_m] \begin{bmatrix} \phi_e \\ \phi_m \end{bmatrix} + [A_o A_i] \begin{bmatrix} \phi_o \\ \phi_i \end{bmatrix} = [0]. \quad (14)$$

Now one can write,

$$(2) \Rightarrow \begin{bmatrix} \phi_e \\ \phi_m \end{bmatrix} = -[A_e A_m]^{-1} [A_o A_i] \begin{bmatrix} \phi_o \\ \phi_i \end{bmatrix} = \begin{bmatrix} ? & ? \\ OUT & IN \end{bmatrix} \begin{bmatrix} \phi_o \\ \phi_i \end{bmatrix}. \quad (15)$$

Note that the matrix formulation involves an inverse, while the method described on the previous page does not require the formulation of the entire inverse matrix. The “?” denote that these parts of the matrix are not needed to implement the TGT boundary condition. The TGT coefficients are used (see Figure 3) to calculate the potentials ϕ_m (nodes just outside the TGT boundary) in terms of potentials ϕ_i at the TGT boundary and the potentials on the Dirichlet boundary ϕ_o , using equation (13). If the potentials on the far boundary are set to zero ($\phi_o = 0$), then equations (13) or (15) simplify to

$$\phi_m = [IN] \phi_i. \quad (16)$$

Equation (16) expresses the potentials of the nodes just outside the TGT boundary as a function of the TGT boundary nodes! Matrix equation (16) is combined with equations for the nodes within the TGT boundary (equation (7)) to yield a set of equations which can be solved directly or iteratively. The advantage of the TGT over a Dirichlet boundary of the same size is illustrated in Figures 4 and 5 which show equal-potential lines for a point charge placed in a corner of the computational grid with Dirichlet and TGT boundary conditions imposed at the edges of the grid, respectively. The equal potential lines are circles, as they should be, for the TGT boundary while the proximity of a Dirichlet boundary at zero potential greatly distorts the solution.

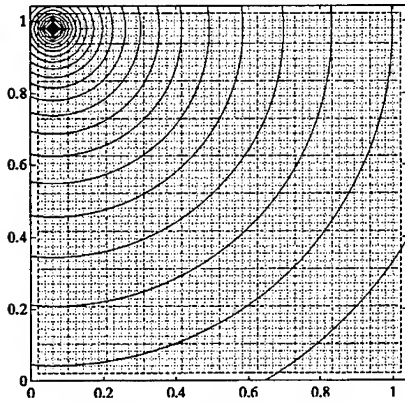


Figure 4: Line charge in corner with TGT Boundary Condition

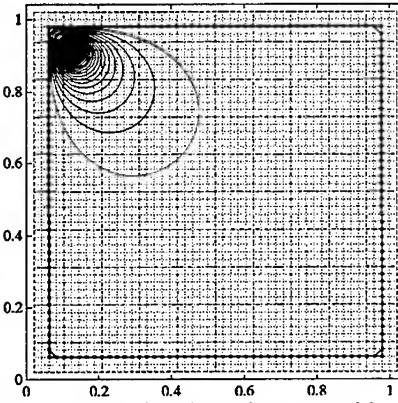


Figure 5: Line charge in corner with Dirichlet Boundary Condition

Brief Description of EMAG Program

2-D electrostatic and magnetostatic problems are formulated in EMAG in terms of discretized Poisson's equations for electrostatic and magnetostatic potentials. EMAG uses two different grids: a coarse grid and a fine grid. Two TGT matrices were thus generated, one for the coarse grid and one for the fine grid. The Dirichlet boundary for the coarse grid has 267 nodes on each side and the TGT boundary has 15 nodes on each side. Fine grid has the Dirichlet boundary with 803 nodes on each side and the TGT boundary with 49 nodes on each side. The generation of the TGT matrices for EMAG's coarse and fine grids was done "externally" (on an HP 700 series computer) and EMAG only reads them from a file each time a problem is solved. Two geometry solution "modes" are available (coarse and fine) for the problem geometry is drawn using a mouse. The "drawing pad" that is employed to define the problem geometry is a square of 51 by 51 square cells, with a cell being the smallest geometric unit. The system of equations corresponding to the "coarse" problem geometry (a program-generated 17 by 17 cell approximation of the actual geometry drawn by the user) is solved directly by Gaussian elimination. The system of equations for the 51 by 51 cell "fine" geometry is solved iteratively using a modified Jacobi method, since a direct solution (not exploiting sparsity) would require too much memory. The coarse grid solution can serve, if so selected, as the initial guess for the fine grid solution. Once the desired solution has been obtained, the results can be displayed as mesh plots of potentials, equal-potential plots, or field plots indicating field magnitudes and directions. (Electrostatic and magnetostatic fields in EMAG are obtained from their corresponding potential solutions.) Users may also calculate such quantities as the enclosed charge per unit length or the enclosed current, for a user-specified region. EMAG calculates flux integrals of electric flux density and closed line integrals of magnetic field to obtain the enclosed charge per unit length and the enclosed current, respectively. The program can also generate printouts of problem geometries and their various solutions mentioned above. Although EMAG is menu-driven and highly intuitive, a 60-page User's Guide has a number of examples to assist in using EMAG. The validity of EMAG solutions has been verified by comparing EMAG numerical solutions of electrostatic and magnetostatic problems with solutions available in the literature. EMAG has been used in a junior level electromagnetics class for electrical engineers.

Sample Results

Several examples are presented here to illustrate EMAG capabilities. Figure 6 shows the geometry of a single microstrip line and the corresponding equal-potential lines. The charge distributions for the strip and the ground plane are shown in Figure 7, with the characteristic charge peaks at the edges of the strip. Figure 8 shows the field lines of a bar-shaped permanent magnet, modelled using two sheets of current. Finally, Figure 9 shows magnetic field lines for a coil-driven, highly permeable core with an air gap (a "magnetic circuit").

NOTE: A new version of MATLAB called MATLAB 4.0 has sparse matrix algebra capabilities and significantly improved graphics capabilities (including animation). It is our intention to "port" EMAG to run under MATLAB 4.0, using its new features to further improve EMAG.

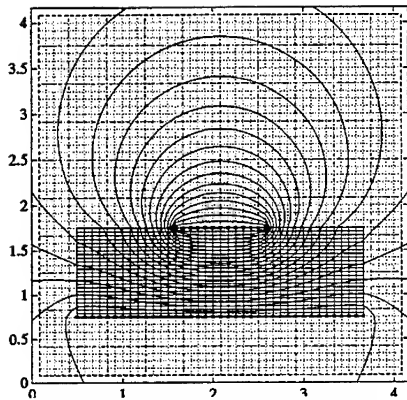


Figure 6: Equipotential Lines for a Microstrip

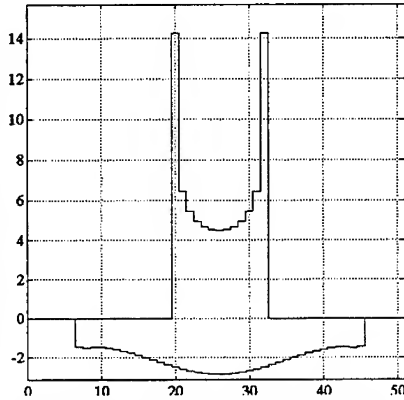


Figure 7: Charge Distributions for the Source Strip and Ground

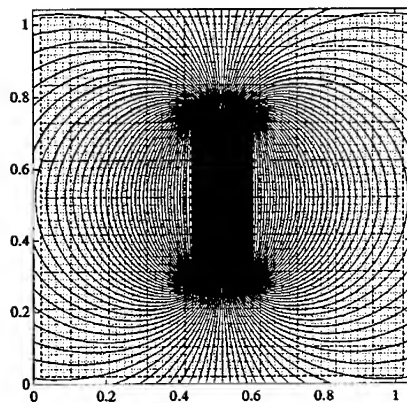


Figure 8: Magnetic Field Lines for a Permanent Magnet

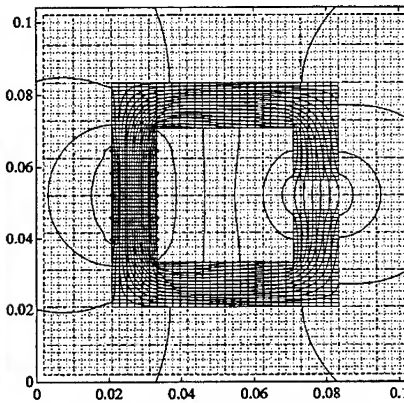


Figure 9: Magnetic Field Lines for a Core with an Air Gap

CURRENT DISTRIBUTION TOMOGRAPHY FOR DETERMINATION OF INTERNAL CURRENT DENSITY DISTRIBUTIONS

Paul C. Gailey
Oak Ridge National Laboratory

Abstract

A method is presented for determination of current densities inside a cylindrical object using measurements of the magnetic fields outside the object. The cross section of the object is discretized with the current assumed constant over each defined region. Magnetic fields outside the object are related to the internal current densities through a geometry matrix which can be inverted to yield a solution for the current densities in terms of the measured fields. The primary limitation of this technique results from singularities in the geometry matrix that arise due to cylindrical symmetry of the problem. Methods for circumventing the singularities to obtain information about the distribution of current densities are discussed.

Introduction

Public concern about the possibility of health effects resulting from exposure to power frequency electric and magnetic fields has grown rapidly during the past decade, and biological research to study this question is underway. An issue that has been largely overlooked in this research is dosimetry. Laboratory researchers typically specify the exposure fields used in a study with little further indication of dose. Unfortunately, there is no simple relationship between the external exposure fields and the internal fields experienced by various cells or tissue types. Internal fields vary with body or sample size, shape, and grounding, as well as the complex variations in electrical properties throughout the organism or sample under study. If effects are detected in these studies, a lack of accurate dosimetric information makes it difficult to develop mechanistic theories explaining the effects or to generalize the findings to other exposure situations.

Methods for predicting internal currents and fields have been developed and used extensively for dosimetry of radiofrequency fields, and are now being applied at power frequencies (Gandhi, 1993). This modeling provides valuable information about internal fields, but is necessarily limited by knowledge of tissue electrical properties. Data currently available about such properties is derived from measurements performed on excised tissues which may differ from the *in situ* properties. Discretization requirements of the model also result in averaging of the electrical properties over regions, which, although small, may contain materials with widely different properties such as bone and muscle. There has been no way to validate the modeling results for other than analytic shapes such as spheres or cylinders with known electrical properties.

The availability of a measurement method as an adjunct to these modeling techniques is clearly desirable. Invasive techniques for internal field and current measurements can be imagined, but have the disadvantage of perturbing the system, and are not acceptable for human subjects. The technique described here, current distribution tomography (CDT), is designed for determination of internal current densities using measurements of the external magnetic field distribution. It is non-invasive, and relatively simple to implement. Although related to a more general study of magnetic imaging which has been used to investigate endogenous currents in the brain and other parts of the body (Sato, 1990), CDT is restricted to currents either applied directly or induced by exposure to an external field. The formulation described in this paper is further restricted to roughly cylindrical objects such as an arm, leg, or human torso. Generalization to other shapes is possible.

Measurement of total (time-varying) current passing through a conductor is easily accomplished using a current probe. These probes surround the conductor with either a toroidal coil or a magnetic core with windings. In either case, the windings respond to the time rate of change of magnetic flux passing through them according to Faraday's law. The response of the probe to the magnetic field of the conductor is easy to visualize in the case of a single, long, homogeneous current for which the magnetic field strength is given by

$$H = \frac{I}{2\pi r} \quad (1)$$

where I is the current, and r is the perpendicular distance from the conductor to the measurement point. The field is a vector quantity and is directed along the tangent of a circle centered around the conductor. The magnitude of the field will be constant at all points along the circle. If more than one conductor carrying current is present, such as in a cable, the magnetic field at any point will be the vector sum of the fields from each conductor. The magnetic field will now vary at different points along a circle around the cable, in contrast to the single-conductor case. This variation in magnetic field magnitude and direction contains information about the current density distribution inside the cable. When current probe measurements are made, this information is lost by the summing properties of the probe. To visualize this effect, note that each turn of the toroid responds to the magnetic field at a specific location around the cable. Because the turns are connected in series, the probe as a whole responds to the additive sum of the currents in the cable. CDT preserves the information available in the field variations around the cable and uses it to compute the current density distribution inside the cable.

Multiple Line Source Approximation

The field distribution described by equation 1 is generally used for long conductors, but is reasonably accurate for measurements taken very close to short conductors. In the present analysis, it is assumed to be adequate, and the problem is reduced to two dimensions. A cross-sectional view of the cable would show the conductors as point sources with the field from each source obeying equation 1. Calculation of the total fields around the cable can be

accomplished by establishing an origin at some point inside the cable (typically at the center) and adding the vector field from each source. At a single point the equation for the magnetic field is

$$H_p = I_1 * G_{p1} + I_2 * G_{p2} + I_3 * G_{p3} + I_4 * G_{p4} + \dots$$

where H_p is the magnetic field at point p,
 G_{pm} is the geometrical factor relating wire m to point p, and
 I_m is the current flowing in wire m.

Choosing the number of field measurement points equal to the number of conductors in the cable results in a solvable set of linear equations.

$$\overline{G} \overline{I} = \overline{H} \quad (2)$$

$$G_{pm} = \frac{\sin(\frac{\pi}{2} - \alpha)}{2\pi \cdot R_{pm}} \quad (3)$$

$$\alpha = \sin^{-1} \left[\sqrt{x_m^2 + y_m^2} \cdot \frac{\sin(\theta_m - \theta_p)}{R_{pm}} \right] \quad (4)$$

$$R_{pm} = \sqrt{(x_m - x_p)^2 + (y_m - y_p)^2} \quad (5)$$

$$\theta_p = \tan^{-1} \left[\frac{y_p}{x_p} \right] \quad \theta_m = \tan^{-1} \left[\frac{y_m}{x_m} \right] \quad (6)$$

where x_p, y_p = x and y coordinates of measurement point p
 and x_m, y_m = x and y coordinates of wire m.

Once the measurement data is obtained, the system can be solved for the unknown currents.

$$\overline{G^{-1}} \overline{H} = \overline{I} \quad (7)$$

This matrix solution appears at first glance to be solvable for any distribution of currents because the number of measurements equals the number of unknowns. However, it is in general a poorly-conditioned matrix, and for systems of only 50 conductors may have a condition number of 100,000 or more. With such high condition numbers, the system is extremely sensitive to measurement errors. Random magnetic field measurement errors of 0.1%, for example, may result in completely useless current predictions with errors of 1000%. It is possible to improve the accuracy of the predictions by taking more measurements (overdetermination), and performing a least squares fit of the data.

A more fundamental issue is whether or not this point source approximation is useful for estimating currents in biological tissues. In reality, biological tissues will have a more or less continuous distribution of current rather than a set of point sources as in the case of a cable. Approximating this current distribution as a set of point sources can lead to completely erroneous results even though an apparent solution to the matrix equation may be found. The reason for this result is an inherent singularity in the problem which will be discussed later. Evidence for this problem can be found by performing a mathematical experiment. First, assume that a cylinder is divided into eight sectors as shown in Figure 1, and that the current density is constant within each sector. For a point source approximation, the current in each sector can all be assumed to be concentrated at a point at the centroid of the sector. Using this approximation, the magnetic field at any point outside the cylinder can be calculated with equation 2. Assume that this approach is used to calculate the fields at four points around the cylinder. Next, combine each pair of sectors to form four large sectors. The current must now be approximated as point sources located at the centroids of the new large sectors. If equation 7 is now used to calculate the current densities in the four large sectors, the expected result is the weighted average of the current densities in the two original sectors (to conserve total current). However, a completely erroneous result is obtained indicating that point sources are not a good approximation for continuous distributions in this formulation.

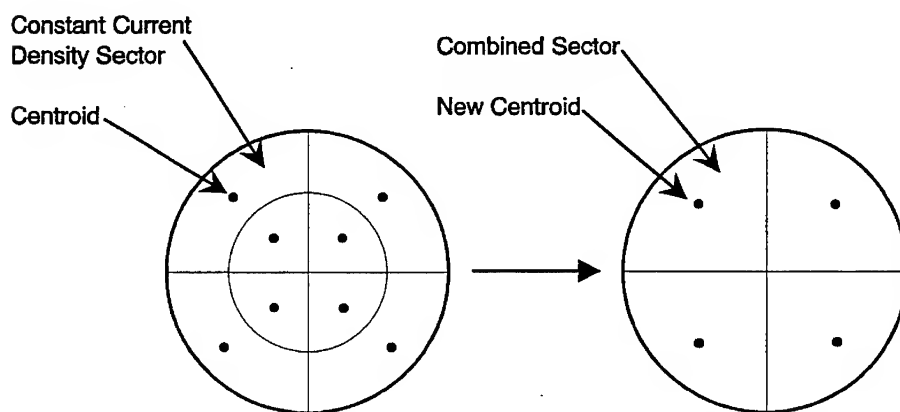


Figure 1. Point source approximation of regions with constant current density.

Constant Current Density Region Approximation

A refinement of CDT can be obtained by assuming that the current density is constant within specified regions and integrating across these regions to calculate the field values at the measurement points.

$$H = \frac{1}{2\pi} \iint \frac{J(r)}{r} dA \quad (8)$$

where $J(r)$ is the current density and r is the distance from the integration point to the measurement point. Because the magnetic field from each point is a vector quantity, the form of the integral will depend on the component of the field measured. Good results are often obtained by placing the origin near the center of the current distribution and measuring the component of the magnetic field in the theta direction (cylindrical coordinates). Then,

$$G_{ij} = \frac{1}{2\pi} \iint \frac{rp_i - r \cdot \cos(\theta p_i - \theta)}{r^2 + rp_i^2 - 2 \cdot r \cdot rp_i \cdot \cos(\theta p_i - \theta)} r dr d\theta \quad (9)$$

where rp and θp are the coordinates of the measurement points, and the integration limits are determined by the boundaries of the constant current regions. In this form, the matrix equation relates the measured field values to the current density in each region.

$$\overline{G} \overline{J} = \overline{H} \quad (10)$$

Singularities in the Matrix Solution

The G matrix formed using equation 8 produces an exact relationship between the current densities and fields if the current densities are assumed constant within the specified regions. This result contrasts with the point source approximation of equations 2 - 7 which was shown to be a poor representation of the same constant current density regions. The reason for the errors and ill-conditioning of the point source formulation now becomes clear--the G matrix formed using equation 8 is singular. It does not contain enough information to solve for the current density distribution inside the cylinder.

It is important to distinguish clearly between the two cases. When localized currents (such as in a multi-conductor cable) are considered, the point source formulation is accurate and is generally not singular. Although it typically produces an ill-conditioned matrix, least-squares fitting can usually be applied to obtain a solution. Using point sources as an approximation of constant current regions, however, introduces an intrinsic error because the exact formulation is singular. It is possible to find a solution to the point-source approximation problem that is completely erroneous.

The singularity occurring in the exact formulation represents a fundamental property of equation 1 rather than simply a numerical challenge. Consider a coaxial cable with current flowing in the same direction through both the inner conductor and outer shield. The magnetic field distribution around the cable will be constant just as in the case of a single conductor. It is impossible to determine, using magnetic field measurements outside the cable, how much current is flowing on the inner conductor and how much is flowing on the outer conductor. For example, 3 amps on the inner conductor and 2 amps on the outer conductor will produce exactly the same magnetic field distribution outside the cable as 1 amp on the inner conductor and 4 amps on the outer conductor. Any cylindrical symmetry in current distribution or conducting medium represents a singularity in the matrix equation. A point-source approximation for the coaxial example could be developed, but would only be solvable because it fails to represent the complete symmetry of the problem.

Solution Methods

Solution of equation 10 in the above form was shown above to be impossible. More information is required before the system can be solved for the unknown current densities. Shown below is the matrix equation for a cylinder split into four pie-shaped regions with four measurement points outside the cylinder.

$$\begin{bmatrix} g_{11} & g_{12} & g_{13} & g_{14} \\ g_{21} & g_{22} & g_{23} & g_{24} \\ g_{31} & g_{32} & g_{33} & g_{34} \\ g_{41} & g_{42} & g_{43} & g_{44} \end{bmatrix} \begin{bmatrix} J_1 \\ J_2 \\ J_3 \\ J_4 \end{bmatrix} = \begin{bmatrix} H_1 \\ H_2 \\ H_3 \\ H_4 \end{bmatrix} \quad (11)$$

Current densities are constant within each pie-shaped region, but may differ from one region to the next

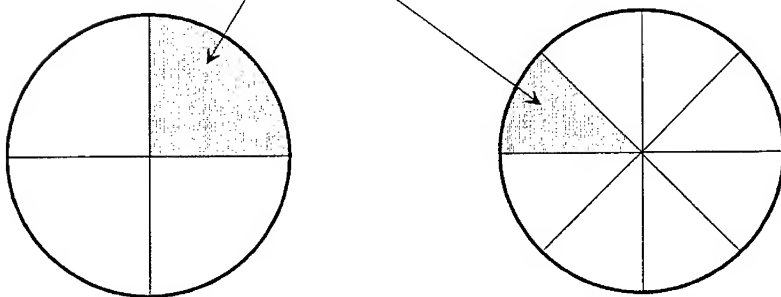


Figure 2. Cylinder divided into four or eight pie-shaped regions of constant current density

The singularity in the G matrix can be circumvented in this case if the total current flowing through the conductor is known. This information can be obtained using a current probe or a field measurement at a large distance. Substituting an equation for the total current in place of one row of the matrix equation removes the singularity. For this example, assume that the total current is I_{TOT} , and that the areas of the pie-shaped regions are A_1, A_2, A_3 , and A_4 .

$$\begin{bmatrix} g_{11} & g_{12} & g_{13} & g_{14} \\ g_{21} & g_{22} & g_{23} & g_{24} \\ g_{31} & g_{32} & g_{33} & g_{34} \\ A_1 & A_2 & A_3 & A_4 \end{bmatrix} \begin{bmatrix} J_1 \\ J_2 \\ J_3 \\ J_4 \end{bmatrix} = \begin{bmatrix} H_1 \\ H_2 \\ H_3 \\ I_{TOT} \end{bmatrix} \quad (12)$$

The method shown here can be used for any number of pie-shaped regions such as those shown in Figure 2 . Varying the location of the measurement points will vary the condition number of the matrix in equation 12 which will be called G'. In general, the condition number of G' increases as the number of regions increases, but overdetermination and least-squares fitting can be used to obtain accurate results.

An obvious limitation of the above technique is that pie-shaped regions may not offer a reasonable discretization of a particular problem. Smaller regions in more compact shapes are generally desired. The best method for defining better regions while maintaining awareness of the singularity problem is to use concentric rings to subdivide the pie-shaped regions (Figure 3). It is important to note that the number of singularities in the G matrix is equal to the number of groups of concentric regions. The case shown in Figure 3 has two sets of concentric regions resulting in two singularities. Equation 12 illustrates a technique for eliminating one of the singularities, but not both. As described earlier, any singularities resulting from concentricity or cylindrical symmetry are fundamental to the field equation, and cannot be circumvented numerically.

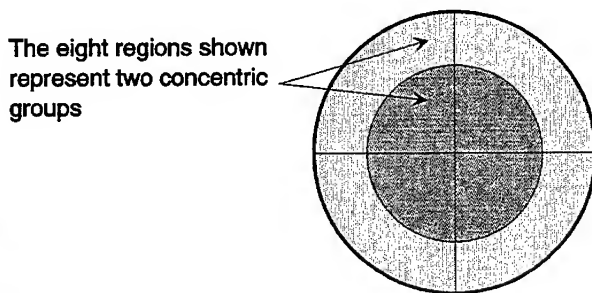


Figure 3. Eight regions of constant current density comprising two concentric groups

Before discussing a technique for examining the range of possible solutions, it is worthwhile to revisit the meaning of the singularity. Each group of concentric regions may carry some amount of concentric current or current that occurs equally in all regions of the group. This concentric current is equal to the minimum current that occurs in any region of the group. The sum of concentric currents from all groups is exactly the amount of indeterminacy of the problem. For example, if the region with minimum current in the inner group carries 2 amps while the region with minimum current in the outer group carries 3 amps, the problem will have a total concentric current of 5 amps. Using only field measurements outside the cylinder, it is impossible to tell what fraction of this concentric current occurs in the inner and outer groups of regions. CDT as a technique is only capable of determining the amount of concentric current and the distribution of non-concentric current.

Important information about the distribution of non-concentric current can be obtained by further modifying the G matrix. For the case of two concentric groups of regions, the matrix will still be singular after modification to the G' form of equation 12. If an assumption is made about the total amount of current flowing in the outer group of regions, a new equation can be included in the G' matrix equation to remove the remaining singularity. This current, IO_{TOT} , can only assume values between zero and I_{TOT} . IO_{TOT} can be varied in the G'' matrix equation below to examine the range of possible solutions.

$$\begin{bmatrix} g_{11} & g_{12} & g_{13} & g_{14} & g_{15} & g_{16} & g_{17} & g_{18} \\ g_{21} & g_{22} & g_{23} & g_{24} & g_{25} & g_{26} & g_{27} & g_{28} \\ g_{31} & g_{32} & g_{33} & g_{34} & g_{35} & g_{36} & g_{37} & g_{38} \\ g_{41} & g_{42} & g_{43} & g_{44} & g_{45} & g_{46} & g_{47} & g_{48} \\ g_{51} & g_{52} & g_{53} & g_{54} & g_{55} & g_{56} & g_{57} & g_{58} \\ g_{61} & g_{62} & g_{63} & g_{64} & g_{65} & g_{66} & g_{67} & g_{68} \\ 0 & 0 & 0 & 0 & A_5 & A_6 & A_7 & A_8 \\ A_1 & A_2 & A_3 & A_4 & A_5 & A_6 & A_7 & A_8 \end{bmatrix} \begin{bmatrix} J_1 \\ J_2 \\ J_3 \\ J_4 \\ J_5 \\ J_6 \\ J_7 \\ J_8 \end{bmatrix} = \begin{bmatrix} H_1 \\ H_2 \\ H_3 \\ H_4 \\ H_5 \\ H_6 \\ IO_{TOT} \\ I_{TOT} \end{bmatrix} \quad (14)$$

Equation 14 yields a wide range of possible solutions for J. The range can be narrowed by making the assumption that current in all regions is positive. This assumption is valid in many cases including current injection or currents induced by unidirectional electric fields. For currents induced by magnetic fields, a different approach must be taken which is not discussed here. The positive current assumption is used by eliminating all solutions which produce any negative current density values. This approach reduces the indeterminacy to exactly the total amount of concentric current flowing in the cylinder (see Figure 4). If at least one region in each group of concentric regions has zero current density (no concentric current), then there will be only one non-negative solution and it will represent the actual current distribution in the cylinder. This technique can be generalized for any number of groups of concentric regions, but preserving the symmetry of the problem is important so that the singularities can be systematically removed.

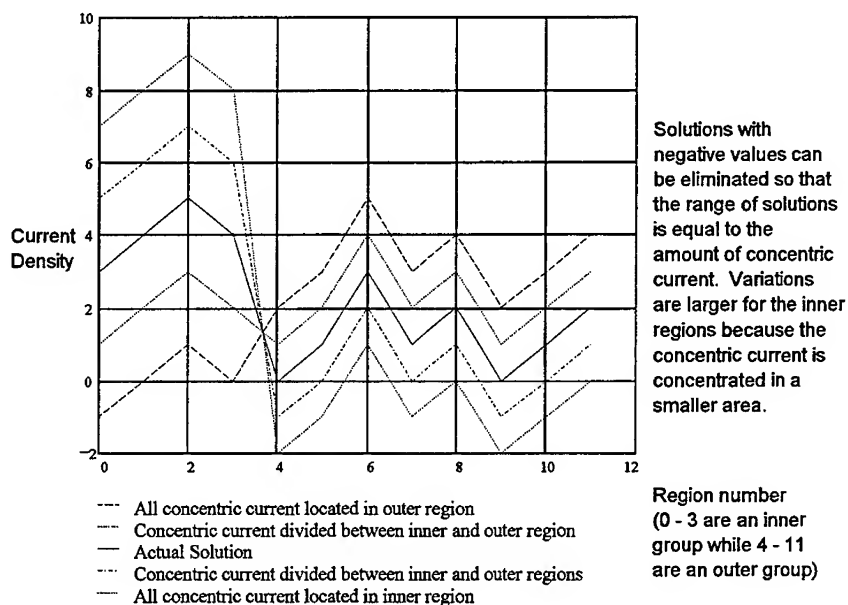


Figure 4. Range of possible solutions for a twelve region case with 2 A of concentric current

Discussion

The CDT technique described here can be used to obtain information about inhomogeneities in the current distributions in various objects, and may serve as a valuable adjunct to computational techniques. Although the absolute magnitude of the current densities cannot be determined in most cases, information about the relative magnitudes can be found. In some instances, case-specific assumptions about the distribution of concentric current can be used to further narrow the range of possible solutions. Current Distribution Tomography offers the distinct advantage of being non-invasive and relatively easy to implement.

References

- Gandhi, O.P. and Chen, J.Y. (1993). Numerical Dosimetry at Power Line Frequencies Using Anatomically-based Models, to appear in a special issue of Bioelectromagnetics based on the EPRI dosimetry workshop held in Carmel, CA, March 19-22, 1991.
- Sato, S. (1990). Magnetoencephalography. Advances in Neurology, Vol. 54, Raven Press, New York.

AUTHOR INDEX

Acree, D.W.	513	Donohoe, J.P.	492	Isaka, K.	403
Alessandri, F.	289	Dwyer, H.A.	360	Iskander, M.F.	538
Ali, M.W.	564				
Andersh, D.J.	11,610	Elsherbeni, A.Z.	594	Jenich, M.M.	830
Archambeault, B.	338,747,763	English, P.	838	Jenn, D.C.	784
Arkadan, A.A.	556,688	Eswarappa, C.	289,467	Jin, H.	266,475
Arndt, G.D.	97	Evans, J.A.	228	Johnson, J.T.	376
				Just, R.	235
Barber, P. W.	140	Fang, J.	322		
Bardarson, R.	235	Fazarinc, Z.	569	Kaiser, F.	424
Baucke, R.C.	182	Fisher, R.	888	Kashyap, S.	81
Beggs, J.H.	189	Fournet, J.S.	97	Katehi, P.B.	273
Bender, H.	370	Francis, R.M.	784	Kaye, M.	27,620
Bhalla, R.	150	Franke, P.M.	640	Khaled, E.E.M.	140
Biringer, P.P.	720			Kim, H.	649
Blocher, S.A.	158	Gailey, P.C.	923	Kishk, A.A.	871
Bomemann, J.	821	Gandhi, O.P.	411	Klopp, K.A.	784
Brauer, J.R.	830	Gaudine, D.	195	Kong, J.A.	376
Brench, C.E.	771	German, F.J.	450,482	Konrad, A.	720,846
Brown, B.S.	830	Ginn, P.H.	594	Koyama, L.	45
Brune, C.	908	Gnos, M.	630	Kruger, R.P.	122
Burkholder, R.J.	602	Goggans, P.M.	72	Krumpholz, M.	458
		Gogineni, P.	586	Kubina, S.J.	2,195,500
		Goodman, S.H.	777	Kunz, K.S.	158
Cai, Z.	821	Gordon, H.	556	Kwok, R.	376
Cangelaris, A.C.	863	Gordon, L.	338		
Cha, C.C.	56	Gordon, R.	871,879	Larose, C.	2,81
Chakrabarti, S.	586	Gordon, W.B.	173	Lebaric, J.E.	915
Chamberlin, K.	338	Gothard, G.K.	442,450	Lee, J.	879
Chan, C.H.	384,391	Guo, T.C.	413	Lee, R.	330
Chandler, C.	450	Guo, W.W.	413	Lee, T.	90,105
Chang, Y.	105	Gyuk, I.	400	Lemaire, L.	763
Chatterjee, A.	855			Leuchtmann, P.	630
Chattot, J.J.	352	Hafez, M.	838	Li, L.	391
Chen, Q.	720	Halama, B.B.	11	Ling, H.	150,649
Chew, W.C.	664,672	Haws, L.	549	Liu, Q.	672
Chia, T.T.	330	Hayashi, N.	403	Lo, J.O.Y.	846
Chowdhury, D.Q.	140	Heinrich, W.	305	Logan, J.C.	37
Christopoulos, C.	755	Herkert, R.M.	513	Louie, A.	81
Coffey, E.L.	888,894,901	Herring, J.L.	755	Lovell, J.R.	657
Cole, R.	908	Hill, S.C.	140	Lu, C.	664
Coulomb, J.L.	846	Hoefer, W.J.R.	19,289,467	Luebbers, R. J.	2,189
		Houshmand, B.	577	Luu, Q.C.	500
D'Angelo, J.	182	Huang, J.	475		
Daijavad, S.	738	Hubing, T.H.	564	MacGillivray, J.	344
Davidson, D.B.	64	Hwu, S.U.	97	Manke Jr., R.P.	915
De Carlo, D.	500	Ingham, D.	166	Marek, J.R.	344
Deneris, C.A.	37			Mellitz, R.	747

AUTHOR INDEX (continued)

Menzel, W.	289	Steyn, P.	64
Merchant, R.	712	Stytz, M.R.	213
Merrill, S.C.	800	Suchar, R.	370
Millard, D.P.	513		
Miller, E.K.	122	Taylor, C.D.	492
Miller, E.M.	610	Tedjini S.	313
Min, S.	879	Terzouli Jr., A.J.	11,213,610
Mish, K.D.	549	Tooker, S.	908
Mishra, S.	2,81	Townley, S.	521
Mohammed, O.	556,696,712	Trueman, C.W.	2,195,500
Mongiardo, M.	289	Tsang, L.	384,391
Moradi, H.	586	Tsitsopoulos, A.P.	243
Moraites, S.	122		
Morgan, M.A.	678	Uler, F.G.	696,712
Mortensen, G.E.	56		
		Vahldieck, R.	266,475
Nghiem, S.V.	376	van Dam, C.P.	360
Nickisch, L.J.	640	VanderHeiden, R.H.	688
		Vilcot, A.	313
Okoniewski, M.	252	Vinh, H.	360
		Volakis, J.L.	855
Packer, M.J.	243,800		
Panneton, R.J.	97	Wainwright, P.R.	432
Park, D.C.	712	Walker, F.	777
Pathak, P.H.	602	Weigel, R.	297
Perez, R.	728	Weller, T.M.	273
Pissanetzky, S.	704	Werner, D.H.	792
Powers, R.A.	243	Werner, P.L.	792
		White, M.D.	352
Rahmat-Samij, Y.	577	Windheiser, D.	855
Ramos, A.	195	Wojszynski, T.G.	213
Rao, S.M.	442	Woody, J.A.	513
Reed, T.	538	Wright, D.B.	863
Reuster, D.	27,620		
Riggs, L.S.	450	Yokoi, Y.	403
Rockway, J.W.	37,221	Yueh, S.H.	376
Rubin, B.J.	738		
Rudduck, R.C.	90,105	Zhang, Q.	19
Russell, L.C.	221		
Russer, P.	260,266,297, 370,458		
Ryan, D.A.	189		
Sabonnadiere, J.C.	846		
Sangani, H.	384		
Sattler, S.	260		
Schaefer, J.A.	529		
Scholl, G.	297		
Schuman, H.K.	813		
Shin, R.T.	376		
Siarkiewicz, K.R.	114		
So, P.P.M.	289,467		
Sorrentino, R.	289		
Speciale, R.A.	281		

Notes

Notes

Notes

Notes

Notes